NASA-CR-193149

Lunar and Planetary Science XXIV

(NASA-CR-193149) TWENTY-FOURTH LUNAR AND PLANETARY SCIENCE CONFERENCE. PART 3: N-Z Abstracts Only (Lunar and Planetary Inst.) 631 p

N94-20636 --THRU-- N94-20911 Unclas

G3/91 0167960

Abstracts of papers submitted to the Twenty-fourth Lunar and Planetary Science Conference

PART 3 N - Z

National Aeronautics and Space Administration

Lyndon B. Johnson Space Center
Houston, Texas

LPI / USRA

LUNAR AND PLANETARY INSTITUTE
UNIVERSITIES SPACE RESEARCH ASSOCIATION

LUNAR AND PLANETARY SCIENCE XXIV

Abstracts of Papers Submitted to the

TWENTY-FOURTH LUNAR AND PLANETARY SCIENCE CONFERENCE

Sponsored by

National Aeronautics and Space Administration
Lunar and Planetary Institute
NASA Johnson Space Center

March 15–19, 1993

Part 3

Compiled by
Lunar and Planetary Institute
3600 Bay Area Boulevard
Houston TX 77058-1113

The Lunar and Planetary Institute is operated by the Universities Space Research Association under Contract No. NASW-4574 with the National Aeronautics and Space Administration.

Preface

This volume contains abstracts accepted by the Program Committee of the Twenty-Fourth Lunar and Planetary Science Conference.

The Program Committee was co-chaired by Douglas Blanchard *(NASA Johnson Space Center)* and David Black *(Lunar and Planetary Institute)*; other members were Bruce Bohor *(U.S. Geological Survey, Denver)*, Roger G. Burns *(Massachusetts Institute of Technology)*, Bruce Campbell *(Smithsonian Institution)*, Deborah Domingue *(Lunar and Planetary Institute)*, Charles Hohenberg *(Washington University)*, Lindsay P. Keller *(NASA Johnson Space Center)*, Marilyn M. Lindstrom *(NASA Johnson Space Center)*, Glenn MacPherson *(Smithsonian Institution)*, Renu Malhotra *(Lunar and Planetary Institute)*, Kurt Marti *(University of California, San Diego)*, Gordon McKay *(NASA Johnson Space Center)*, David Mittlefehldt *(Lockheed EMSCO)*, Scott Murchie *(Lunar and Planetary Institute)*, Larry Nyquist *(NASA Johnson Space Center)*, William Phinney *(NASA Johnson Space Center)*, Jeff Plescia *(Jet Propulsion Laboratory)*, Frank A. Podosek *(Washington University)*, Ben Schuraytz *(Lunar and Planetary Institute)*, Virgil L. Sharpton *(Lunar and Planetary Institute)*, Tomasz Stepinski *(Lunar and Planetary Institute)*, Ellen R. Stofan *(Jet Propulsion Laboratory)*, Paul Warren *(University of California, Los Angeles)*, and Michael Zolensky *(NASA Johnson Space Center)*.

Papers are arranged alphabetically by the last name of the first author. There are four indexes: authors, lunar sample numbers, meteorites, and keywords.

This abstract volume was compiled through the efforts of the Publications Services Department of the Lunar and Planetary Institute. Eleta Malewitz and Jackie Lyon provided computer service support to the preparation efforts.

Logistics and administrative support for the conference were provided by the staff of the Program Services Department, Lunar and Planetary Institute.

CONTENTS

51-91
ABS ONLY

N94-20637

SO_2 ON VENUS: IUE, HST AND GROUND-BASED MEASUREMENTS, AND THE ACTIVE VOLCANISM CONNECTION: C. Y. Na, Southwest Research Institute, E. S. Barker, McDonald Obs. UT Austin, S. A. Stern, Southwest Research Institute, L. W. Esposito, LASP, U. of Colorado, Boulder.

I. SO_2 and volcanism on Venus

UV observations by Pioneer Venus from 1978 to 1986 detected a large decline of SO_2 above the clouds of Venus [1]. The decline of SO_2 has been confirmed by the International Ultraviolet Explorer (IUE) observations made in 1979 and 1987 [2]. Pioneer Venus also observed a decline in sulfuric acid aerosols from the polar regions of Venus [3]. Further still, both Pioneer Venus and Galileo have detected radio signals that have been attributed to lightning activities in the atmosphere of Venus [4,5]. Based on these observations, Esposito [6] proposed that the Venus may be volcanically active, and the large decline of SO_2 above the clouds can be interpreted as the recovery of the atmosphere following the injection of SO_2 from a volcanic eruption. If this hypothesis is correct then remote sensing of the Venus atmosphere may provide important clues to the current state of Venus geology.

In early November 1991, we obtained IUE spectra of Venus with the Long Wavelength Prime (LWP) spectrograph. On the same days, we obtained spatially resolved spectra and images of Venus using the 2.7m telescope at McDonald observatory [7]. As shown in the accompanying figure, these two observations seem to indicate that the mixing ratio of SO_2 above the cloud increased by about a factor of 2 since 1990.

More coordinated IUE and ground-based observations are planned for 1993 to determine whether the increase of SO_2 has continued. The first of the planned observation is to take place using IUE and the 2.7m telescope at McDonald observatory from 8 January to 12 January. The results from these new observations will be presented. At the time of Venus' western elongation in early June 1993, we hope to obtain (i) IUE spectra, (ii) ground-based spectra, and (iii) the first-ever Hubble Space Telescope (HST) spectra of Venus. If SO_2 is indeed increasing above the clouds, then these measurements may help us to determine the rate of increase in SO_2 above the clouds.

II. SO, S_2O and dark markings

IUE observations of Venus were used to identify SO (sulfur monoxide) in the atmosphere Venus for the first time [2]. According to photochemical models [8], SO plays an important role in the chemical processes in the upper clouds. The mixing ratio of SO was determined from IUE and rocket observations to be about 10% of SO_2 [9]. The disulfur monoxide, S_2O, which is produced from photochemical reactions involving SO may be responsible for the dark markings in the clouds [10]. Thus the IUE observations of Venus are not only important in documenting the long-term change in SO_2 and SO, but are also important in understanding the chemistry and dynamics of the Venus atmosphere.

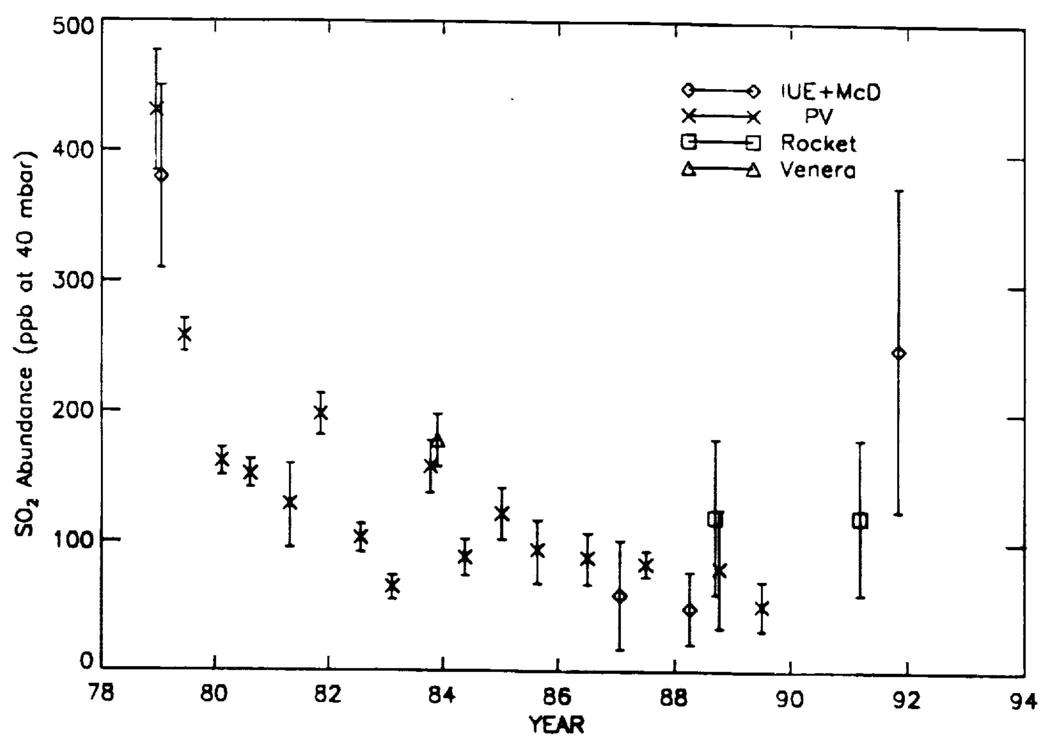
HST observations of Venus are critical because, with the end of the Pioneer Venus mission, HST will be only instrument capable of making regular observations beyond IUE which is starting its 16th year in orbit. HST can both make images and take spectral observations. The imaging capability of HST will make a valuable contribution to understanding the connection between the atmospheric dynamics and the distribution of photochemically active species.

III. Conclusion

Magellan images have shown that the volcanic features are widespread over the surface of Venus. The question of whether there is active volcanism is important for understanding both the atmospheric and the geological processes on Venus. The thick cloud cover of Venus precludes any direct observation of active volcanoes even if they exist. The only means of monitoring the active volcanism on Venus at present seems to be remote sensing from Earth. Continuous of monitoring of SO_2 is important to establish the long term trend of SO_2 abundance and to understand the physical mechanism responsible for the change.

References

[1] Esposito L. W. et al. (1988), *JGR*, **93**, 5267
[2] Na C. Y. et al. (1990), *JGR*, **95**, 7465
[3] Esposito L. W. and Travis L. D. (1982), *Icarus*, **51**, 374
[4] Kansformality, L. (1980), *Nature*, **284**, 244
[5] Gurnett, D. A. et al. (1991), *Science*, **253**, 1522
[6] Esposito L. W. (1984), *Science*, **223**, 1072
[7] Barker E. S. et al. (1992), *BAAS*, **24**, 996
[8] Yung Y. L. and DeMore W. (1982) *Icarus*, **51**, 199
[9] Na C. Y. et al. (1991) *BAAS*, **23**, 1196
[10] Hapke B. and Graham F. (1989), *Icarus*, **79**, 47



Mixing ratio of SO_2 at the cloud top level in the Venus atmosphere derived from the IUE, rocket, Pioneer Venus, Venera-15, and ground-based observations.

-10-25 ABS. ONLY N94-20633 p. 2

EVAPORATION IN EQUILIBRIUM, IN VACUUM, AND IN HYDROGEN GAS :

Hiroko NAGAHARA, Geol. Inst., Univ. Tokyo, Hongo, Tokyo 113, Japan.

Evaporation experiments were conducted for SiO_2 in three different conditions; in equilibrium, in vacuum, and in hydrogen gas. Evaporation rate in vacuum is about two orders of magnitude smaller than that in equilibrium, which is consistent with previous works. The rate in hydrogen gas changes depending on hydrogen pressure. The rate at 10^{-7} bar of hydrogen pressure is as small as that of free evaporation, but at 10^{-5} bar of hydrogen pressure it is larger than that in equilibrium. In equilibrium and in vacuum, the evaporation rate is limited by decomposition of SiO_2 on the crystal surface, but it is limited by a diffusion process for evaporation in hydrogen gas. Therefore, evaporation rate of minerals in the solar nebula can be shown neither by that in equilibrium nor by that in vacuum.

The maximum temperature of the solar nebula at the midplane at 2-3 AU where chondrites are believed to have originated is calculated to be as low as 150K [1], 1500K [2], or in between them [3]. The temperature is, in any case, not high enough for total evaporation of the interstellar materials. Therefore, evaporation of interstellar materials is one of the most important processes for the origin and fractionation of solid materials. Fundamental process of evaporation of minerals has been intensively studied for these several years [4-8]. Those experiments were carried out either in equilibrium or in vacuum; however, evaporation in the solar nebula is in hydrogen (and much smaller amount of helium) gas. In order to investigate evaporation rate and compositional (including isotopic) fractionation during evaporation, vaporization experiments for various minerals in various conditions are conducted. At first, SiO_2 was adopted for a starting material, because thermochemical data and its nature of congruent vaporization are well known.

Experiments were carried out in a vacuum furnace system descried by [4]. Capsule is either of Mo or of graphite with 1.5 or 3 mm inner diameter and 4 mm length. A capsule has two small orifices on sides and it is a Knudsen cell. Equilibrium vaporization experiments were carried out by using a capsule with a tight cap. Gas and solid are in equilibrium in the capsule, and equilibrium vapor pressure (Knudsen vapor pressure) was calculated from weight loss per time. The inside of the Knudsen cell is filled with intrinsic vapor from SiO_2 when a Mo-capsule is used, because Mo is not reactive with a silicate system. It is, however, not the case when a C-capsule is used: gas composition is affected by carbon vapor and fO_2 shifted to a lower value. Disequilibrium vaporization experiments were done by using a capsule without a cap, where generated gas is evacuated and does not condense again ("free evaporation"). Weight loss of the sample is converted to "Langmuir vapor pressure". Hydrogen gas was introduced to the chamber to investigate vaporization in a gas flow. The starting material is a single crystal of natural quartz. About 10mg of powdered sample was used for each experiment. Sample weight before and after experiment was precisely measured. Experimental temperature was 1600°C and 1700°C, the base pressure of the vacuum chamber was 10^{-11}-10^{-9} bar, and experimental duration ranged from 10 min to 1440 min. Hydrogen pressure was controlled by bleeding hydrogen gas through a micro-valve; high pressure above 10^{-5} bar was not finely controlled because an ionic gauge does not work at high pressures.

After partial evaporation, residue remains to be SiO_2 in every experiment, suggesting that SiO_2 evaporates congruently which is consistent with previous works [6,9,10]. The results are summarized in Fig. 1. Weight loss is a linear function of time regardless of temperature and fO_2 (both in a Mo or C capsule) when evaporation is in equilibrium and in vacuum. Evaporation rate in a more reducing condition (in a C-capsule) is about 3.5 times more rapid than that in equilibrium (in Mo-capsule), which is always the case for evaporation of oxides and silicates which contain oxygen. In vacuum, evaporation rate is smaller than that in equilibrium by a factor of about 0.02, which coincides with literature data (0.011-0.015 at 1560-1685°C) [6]. This lowering of evaporation rate in vacuum compared to that in equilibrium may be due to formation of metastable gas species [6] or surface kinetics in solid such as crystallographic plane, purity, surface roughness, and porosity.

EVAPORATION OF SiO_2: Nagahara, H.

In hydrogen gas, the evaporated fraction is not a linear function of time. In hydrogen gas, evaporated fraction becomes smaller than that in equilibrium, and the difference from equilibrium value becomes larger with time. At hydrogen pressure of 10^{-7} bar, evaporation rate is nearly the same as that in vacuum, but is about 3-4 times larger at 10^{-5} bar of hydrogen pressure. Contrary to higher total pressure, vaporization is more effective in hydrogen gas. This is because hydrogen is reactive with SiO_2, and the possible reaction is $SiO_2(s)+H_2(g) \rightarrow SiO(g)+H_2O(g)$.

In order to investigate vaporization rate and fundamental process controlling evaporation, the relationships are shown in logarithmic scale in Fig. 2. Equilibrium evaporation rate and free evaporation rate have slope of 1 in the figure, showing that evaporation rate is limited by decomposition of SiO_2 at the surface of the crystal. The reaction is, thus, $SiO_2(s) \rightarrow SiO(g)+1/2O_2(g)$. On the contrary, evaporation rates in hydrogen gas have slope of 1/2. Slope of 1/2 represents that the process is controlled by diffusion. Possible diffusion processes are (1) formation of $SiO+H_2O$ layer on the surface of the solid, (2) diffusion of hydrogen in solid SiO_2, and (3) formation of amorphous SiO2 layer on the solid surface. The possibility (1) is implausible, because the mean free paths in the experimental conditions is about 3m at 10^{-5} bar and 300m at 10^{-7} bar, which are far beyond the size of the experimental chamber. The generated $SiO+H_2O$ layer should be evacuated away in a second and it can not be a rate limiting factor. The possibility (2) may be implausible, because hydrogen diffusion in SiO_2 is more rapid than oxygen by 3 to 8 orders of magnitude [11]. If the data of [11] is extended to the present experimental temperatures, hydrogen diffusion distance is in the order of grain size of the present work, and it can not be a rate limiting factor. Thus the possibility (3) is the only possible explanation, although the presence of amorphous material on the surface has not been probed with the X-ray technique.

The present study suggests that evaporation rate of minerals in hydrogen gas is neither of that in equilibrium, that in vacuum, nor that in between them. The evaporation rate depends on hydrogen gas pressure. Further experimental determination for meteoritic minerals will be necessary for the discussion of evaporation of minerals in the solar nebula.

REFERENCES: [1] Wood,J.A. and Morfill,G.E. in Meteorites and the Early Solar System (eds., Kerridge, J.F. and Matthews, M.S.) pp.329-347, [2] Boss,A.P. (1992) *LPS* **XXII** 141-142, [3] Cameron,A.G.W. (1985) in Protostar and Planets II (eds., Black,D.C. and Matthews,M.S.) pp.1073-1099, [4] Nagahara, H. *et al.*(1992) *LPS* **XXII** 959-960, [5] *ibid.* 961-962, [6] Hashimoto, A. (1990) *Nature* **347** 53-55, [7] Davis, A. *et al.* (1990) *Nature* **347** 655-657, [8] Uyeda, C. *et al.* (1991) *EPSL* **107** 138-147, [9] Sata, T. *et al.* (1978) *Rep. Res. Lab. Eng. Mate. Tokyo Inst. Tech.* 3, 666-764, [10] Mysen, B.O. and Kushiro, I. (1988) *Amer. Mineral.* **73** 1-19, [11] Dennis, P.F. (1984) *J. Geophys. Res.* **89** 4047-4058; Kronenberg, A. K. *et al.* (1986) *J. Geophys. Res.* **91** 12723-12744.

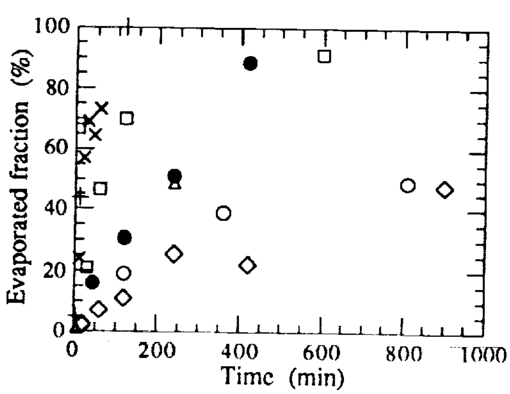


Fig. 1 Evaporated fraction of SiO2 as a function of time. Solid circle: 1600°C equilibrium, cross: 1600°C equilibrium in C-capsule, diamond: 1600°C free evaporation, circle: 1600°C in 10^{-7} bar hydrogen gas, square: 1600°C in 10^{-5}bar hydrogen gas, plus: 1700°C equilibrium in C-capsule,triangle: 1700°C free evaporation.

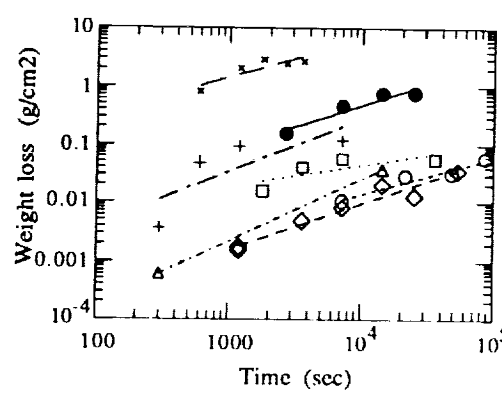


Fig. 2 Log-log relationship of weight loss and time. Symbols are the same as those in Fig. 1. Equilibrium and free evaporation rates have slope of 1, and the rates in hydrogen gas have slope of 1/2.

S3-91 ABS. ONLY

N94-20639

REE AND OTHER TRACE LITHOPHILES IN MAC88177, LEW88280 AND LEW 88763: N. Nakamura and N. Morikawa , Dept. Earth Sci., Faculty of Science, Kobe Univ., Nada, Kobe 657, Japan P-2

In order to investigate the petrogenesis of primitive achondrites, we have carried out precise isotope dilution analyses of REE, Sr, Ba, Rb, K, Li, Ca, Mg and Fe for three new meteorites; (Lodranites) MAC88177, LEW88280, (Brachinite) LEW88763, together with analyses for Acapulco. Present results are compared with those of other primitive achondrites previously reported by us [1, 2] and others.

MAC88177 was first classified as a ureilite but detailed chemical, petrographical and oxygen isotopic studies suggest that the meteorite is a new type [3-6]. As noted in [3] and/or [4], the chemical, modal mineral and oxygen isotopic compositions of the meteorite is so close to those of Yamato-74357 Lodranite. Although the meteorite specimens are generally very heterogenous, the estimated norm compositions of the Yamato-74357 specimen analyzed by us [2] is very close to those of MAC88177 reported by [3]. We studied ~100mg chip of MAC88177. The results of isotope dilution analysis (Fig. 1) indicates that MAC88177 has a light-REE depleted (La=0.17xCI, Lu=0.95xCI), highly fractionated REE pattern with a large negative Eu anomaly; CI-normalized $(Eu/Eu^*)_n = 0.34$ (Eu* is interpolated value between Sm and Gd). The Lu value obtained here is similar to that reported in [6], however, our light REE abundances are much more depleted compared to the previous results [6]. The general fractionation feature is quite similar to that of Yamato-74357 (see Fig. 1).

LEW88280 is tentatively classified as a Lordranite [7]. Although the meteorite analyzed in this work (~100mg chip) have much higher metal content (35wt%) compared to that of MAC88177 [4] (metal + sulfide = 5%), the compositions of lithophiles for both meteorites are quite similar to each other (see Fig.1a). Particularly, it is worth noting that the absolute and relative REE abundances in non-metallic fraction for both meteorites are substantially identical.

LEW88763 is classified as a Brachinite [7]. The abundances of major elements (Fe, Mg and Ca) and REE in the meteorite obtained in this work (~20mg chip) are mostly consistent with those of Brachina [8]; the relative abundances in both meteorites agree within ± 0.1xCI. The CI-normalized REE pattern for LEW88763 is almost flat but slightly light-REE enhanced relative to heavy REE of 1.5xCI (see Fig. 1b).

Among many new type of meteorites discovered recently, **Acapulco** has exceptionally a light-REE enriched pattern [9]. In order to confirm earlier INAA results [9], we have carried out ID analysis. Our results are mostly in agreement with the previous one within the analytical errors, though Rb abundance in our sample is even more depleted (see Fig. 1b).

Discussion: Previously we have reported results of REE analyses and model calculation for Antarctic primitive achondrites including Yamato-74357 [2]. Applying solid/liquid partition coefficients to modal mineral compositions at 1100°C, we suggest that the light-REE depleted pattern with negative Eu anomaly for Yamato -74357 is interpreted by the degree of ~12% melting of chondritic

REE IN MAC88177, LEW88280 and LEW88763: Nakamura N. & Morikawa N.

source material with 2xCI REE. Minor addition (<1%) of trapped melt to residual solid can meet with somewhat higher alkalis in the meteorite. Since MAC88177 (and LEW88280) have quite similar trace element and petrological features to those of Yamato-74357, they are also interpreted in terms of the similar degree of partial melting to that for Yamato-74357. The lack of plagioclase in these meteorites are considered to be consistent with the degree of ~12% melting of and almost complete removal of the felsic melt from chondritic source which might had 10-15% plagioclase. As discussed here, abundances of trace lithophiles in primitive achondrites are, in general, understandable in terms of relatively simple equilibrium melting or extensive metamorphism as envisioned previously [2]. It should be, however, clarified if the physical process of the degree of melting can also meet with the presence of sulfide in these meteorites or not.

We thank Meteorite Working Group for the meteorite samples.

References: [1] Torigoye N, Yamamoto K, Misawa K. and Nakamura N. (1992) Meteoritics 27, 297-298. [2] Torigoye, N. et al. (1992) Proc. NIPR Symp. Antarct. Meteorites No.6 (submitted) [3] Prinz M. et al. (1992) LPSC XXII 1099-1100 [4] Takeda et al. (1992) LPSC XXII 1375-1376. [5] Clayton R.N. et al. (1992) LPSC XXIII 231-232. [6] Warren P.H. and Kallemeyn G.W. (1991) LPSC XXII 1467-1468. [7] Antarctic Meteorite NEWSLETTER (ed. by Lindstrom M.) Vol. 14, No.2 (1991). [8] Nehru C.E. et al. (1983) LPSC XIV 552-553. [9] Palme H. et al. (1981) GCA 45, 727-752.

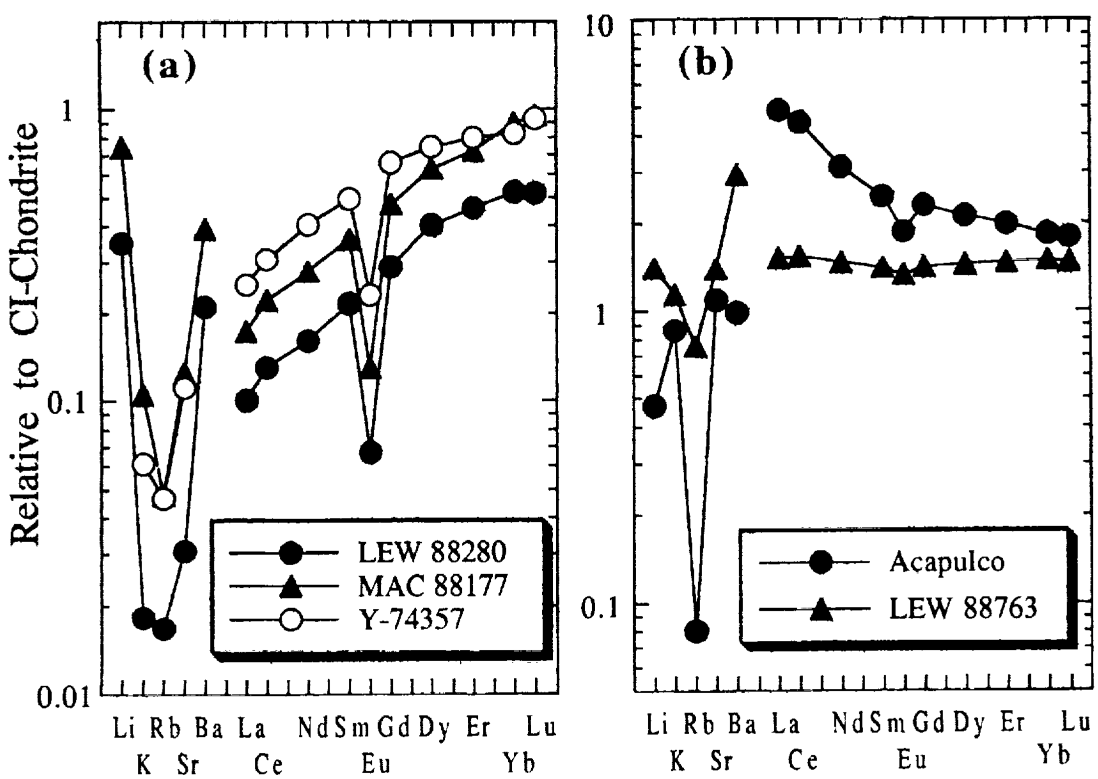


Fig. 1. CI-normalized trace element abundance patterns for bulk primitive achondrites. Data for Yamato-74357 are from [2].

54-25
ABS. ONLY

-167964
N94-20540

THE EREVAN HOWARDITE: PETROLOGY OF GLASSY CLASTS AND MINERAL CHEMISTRY. M.A.Nazarov and A.A.Ariskin. Vernadsky Institute of Geochemistry and Analytical Chemistry, Moscow 117975, Russia.

The Erevan howardite is a polymict regolith breccia [1] containing xenoliths of carbonaceous chondrites [2]. In this work we studied glassy clasts, which could be considered as primary quenched melts, and mineral chemistry of the breccia. The study reveals that the Erevan howardite consists of common rocks of the HED suite. However, unique glassy clasts, which are present some eucritic melts, were identified. The mineral chemistry and the simulation of crystallization of the melts suggest that the

compositions of the melts reflect those of some primary lithologies of EPB.

Glassy clasts. At present 3 glassy clasts have been analyzed by the broad-beam technique using the correction procedure [3]. The computer simulation of the crystallization of the melts was carried out by the method [4].

Clast ER-110 (0.3 mm) consists of a glassy material. It has a howardite composition (Table) which is close to the Erevan bulk composition. It suggests that the melt could be of impact origin. The calculated crystallization sequence of the melt is: OL (Fo 84-73); OL (Fo 72-67) + PIG (En 69-65, Wo 2); OL (Fo 66) + PIG (En 65, Wo 2.3) + PL (An 92).

Clast ER-300 (0.2*0.4 mm) is an extremly fine-grained (1-2 um) rock containing feldspar, pyroxene, ilmenite, Fe-sulphide and silica. No clasts are present in the melt. Its composition is completely different from HED compositions (Table, Fig.1). Compared to HEDs this melt is highest in Ti and Fe/Mg. The simulation [4] shows that the melt is co-saturated with feldspar (An 88) and pigeonite (En 52, Wo 11) followed by augite (En 41, Wo 33). These features suggest igneous origin of the melt as a result of a lava eruption.

Clast ER-400 (0.8 cm) contains big (1 mm) pyroxene crystals (En 48, Wo 2.5) enveloped by a basalt melt which consists of low-Ca pyroxene (En 42-46, Wo 5-8), high-Ca pyroxene (En 40, Wo 38) and feldspar (An 88-95) with minor ilmenite, Fe-sulphide and silica in a cotectic fine-grained (2-3 mm) texture. This melt has also a unique composition (Table). It is higher in Mg/(Mg+Fe) relative to noncumulate eucrites and it is higher in Ti as compared to cumulate eucrites (Fig.1). This is only the Pomozdino eucrite [5] which is close to the melt ER-400 in the composition (Table, Fig.1). According to the simulation [4] the ER-400 melt is co-saturated with olivine (Fo 71), plagioclase (An 91.5) and pigeonite (En 68, Wo 6), i.e. the composition is near to a peritectic involving these phases. The big pyroxene crystals are not equilibrated with the melt and, hence, they cannot be considered as phenocrysts. The unusual and peritectic composition of ER-400 suggests the melt to be a primary quenched liquid. If it is so then the pyroxene crystals are present a trapped material. However if the melt is of impact origin, these crystals should be considered to be a relic component of a source rock.

Mineral chemistry. Primary pyroxenes in Erevan are represented by both pigeonite and orthopyroxene. Pigeonite grains exhibit often microscopic exsolution but there are also grains without exsolution lamellae. It means that Erevan contains components of diogenites, unequilibrated (noncumulate) and equilibrated (cumulate) eucrites. Compositions of pyroxenes show some clustering (Fig.2). The Fe-rich pyroxenes (FM=Fe/(Fe+Mg)=60-62%) are typical for equilibrated eucrites. The pyroxenes with FM 44-46% could be related to the ER-300 melt. Diogenites could be a source for the pyroxenes with FM 26-28% but the same FM is a characteristic of pyroxenes which could be crystallized from the ER-110, ER-400 and Pomozdino melts. The Mg-rich pyroxenes (FM=14-16%) described also in Kapoeta and some diogenites [6,7] cannot be formed from common eucritic melts. Their source rocks are unknown.

Feldspar compositions are very variable. They range from An 72 to An 98 with the majority of analyses at An 96-97 and An 88-89 (Fig.3). However one feldspar grain showed a Na-rich composition of An 44, Or3 which has never been reported in HEDs. On the other hand, Erevan contains more calcic lagioclase (up to An 98) than other HEDs. The plagioclases of An 88 could be derived from the melt ER-300. The compositions of An 91-92 may be related to ER-110, ER-400 or other eucrites whereas source rocks of more calcic feldspars are unknown.

Olivine is a minor component of the Erevan matrix. Three groups of olivine compositions were identified (Fig.4). The olivines of Fa 30-36 could be derived from common eucritic melts which have a liquidus olivine of the same composition [6]. The Er-400 and Pomozdino melts could produce the olivines with Fa 24-28. The Mg-rich olivines (Fa 12-16) match to a liquidus olivine of the ER-110 melt.

There are Ni-poor and Ni-rich metal grains in the breccia. The Ni-poor grains are most abundant. Some of them are enriched in Co (up to 2%). The Ni-rich grains are rare and contain 6-7% of Ni and .4-.5% of Co. These grains can present a foreign material but it is also possible that they are from EPB rocks [6].

Discussion. The Erevan breccia is composed mainly of common rocks of the HED suite and contains unique glassy clasts which are present some eucritic melts. From the textural and compositional characteristics the ER-300 melt only can be considered to be of igneous origin. However mineral compositions observed in the breccia can be related to all of the melts. Thus if even all of the melts are of impact origin, the compositions of the melts reflect those of some primary lithologies of EPB. Constraints on relations between the lithologies can be obtained from the simulation of the crystallization of the melts. Some results of the simulation of equilibrium crystallization of the ER-110, ER-300, ER-400 and Pomozdino melts are shown on Fig.1. The simulation shows that the ER-300 and ER-400 melts cannot be formed by fractional or equilibrium crystallization of the ER-110 melt. However the main group of eucrites could be derived by partial melting from a source of

THE EREVAN HOWARDITE

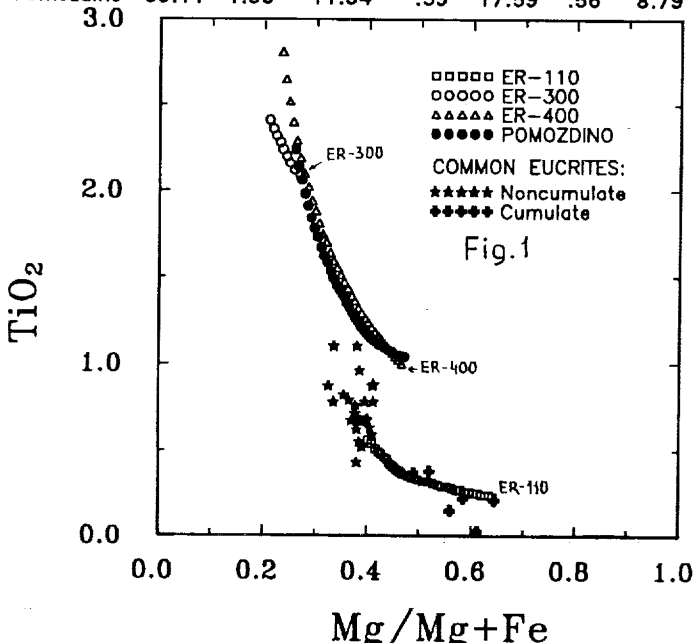
Nazarov, M.A. and Ariskin, A.A.

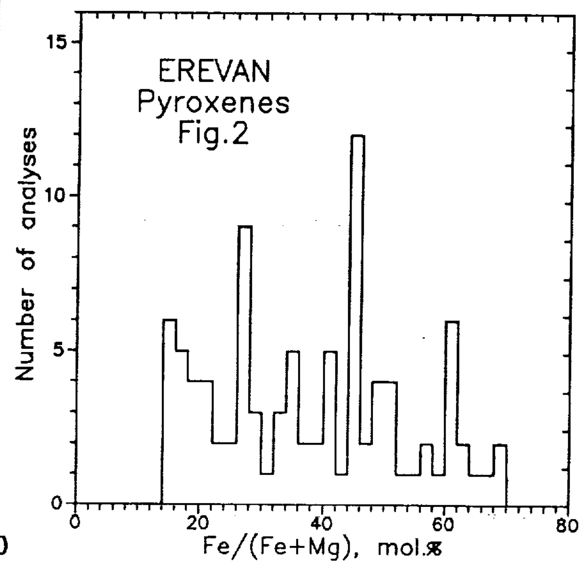
the ER-110 composition. The source could be resulted from partial melting of a silicate part of H chondrites. Therefore, at least two-stage melting should be suggested to produce the main group of eucrites from the H chondritic material. Pomozdino and the ER-400 rock can be cumulates from the ER-300 melt or melts of the Stannern group. Alternatively, Pomozdino and ER-400 could be due to a partial melting of a source enriched in Ti and Mg/Fe as compared to a source of eucrites. The ER-300 melt cannot be related to the main group of eucrites. It should be formed by a partial melting of Pomozdino or the ER-400 rock (Fig.1) or another source which must be higher in Ti and Fe/Mg than a source of eucrites. These relations suggest great heterogeneity in the mantle of EPB.

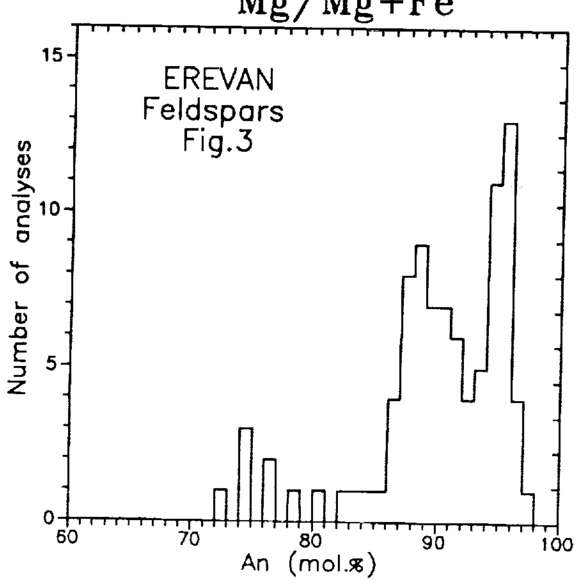
References: [1] L.Kvasha et al. (1978) Meteoritika, 37, p.80 (in Russian); [2] M.A.Nazarov et al. (1993) This volume; [3] M.A.Nazarov et al. (1982) LPSC XIII, p.582; [4] M.Frenkel and A.Ariskin (1984) Geochimiya, 10, p.1419 (in Russian); [5] P.H.Warren et al. (1990) PLSC XX, p.281; [6] E.Stolper (1977) GCA, 41, p.582; [7] R.O.Sack et al. (1991) GCA, 55, p.1111.

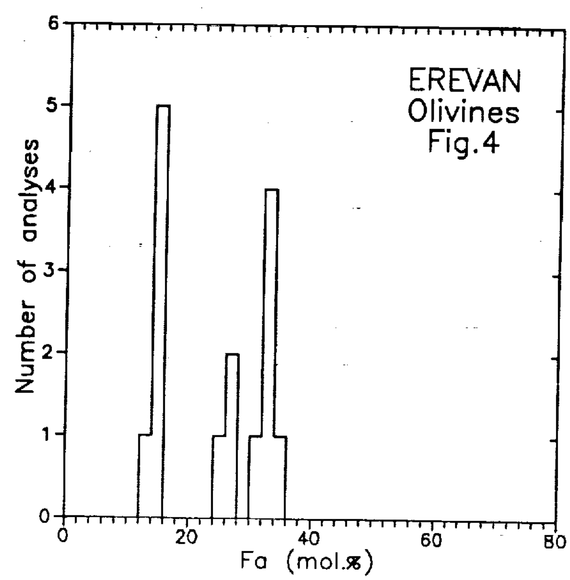
Table. Bulk Composition of Erevan glassy clasts

Sample	SiO2	TiO2	Al2O3	Cr2O3	FeO	MnO	MgO	CaO	Na2O	K2O	P2O5	FeS
ER-110	51.57	.23	5.52	.69	18.19	.56	18.26	4.75	.22	-	.02	-
ER-300	48.44	2.07	9.95	.26	21.78	.67	4.50	10.96	.41	.04	.17	.75
ER-400	49.25	.99	13.55	.16	15.73	.45	7.66	10.79	.34	.01	.17	.89
Erevan	49.81	.28	8.55	.45	15.76	.33	17.25	6.97	.27	.02	.14	-
Pomozdino	50.11	1.03	11.34	.59	17.59	.56	8.79	9.32	.59	.07	-	-









35 - 46
ABS. ONLY

N94-20641 P- 2

THE KOSHAK SECTION: EVIDENCE FOR ELEMENT FRACTIONATION AND AN OXIDATION EVENT AT THE K/T BOUNDARY. - M.A.Nazarov (1), D.D.Badjukov (1), L.D.Barsukova (1), G.M.Kolesov (1), and D.P.Naidin (2). (1) Vernadsky Institute of Geochemistry and Analytical Chemistry, Moscow 117975; (2) Moscow State University, Geological Faculty, Moscow 119899, Russia.

The Koshak site (44 47'N; 51 40'E) is a new K/T section located about 125 km EEN of the Fort Shevchenko city, Mangyshlak, Kazakhstan. In this paper we report results of geochemical and mineralogical studies of this section which indicate a deep element fractionation and an oxidation event at the K/T boundary.

Stratigraphy. The Koshak K/T boundary is marked with a 1-1.5 cm thick marl (14-16% SiO_2) layer occurring within a pelagic chalk sequence. The top and the bottom of the marl layer are not flat. The marl material penetrates into the chalk above and below it and forms veins and thin (mm in thick) sublayers. The chalk of about 1 cm thick, which covers directly the K/T layer, appears to be more cemented than the chalk above it. There is another marl layer at 1 m above the K/T boundary, which is very similar to the K/T marl in lithological characteristics.

Methods. Samples collected at the boundary were analyzed for Ir by RNAA and for major and trace elements by XRF and INAA. Concentrations of shocked quartz (SQ) grains relative to the total amount of quartz grains (SQ/Q) were measured in thin sections prepeared from HCl-insoluble fractions of the 40-120 um grain size under an optical microscope. The obtained data are shown on Fig.

Results. The K/T marl and the above-lying marl are practically the same in their major element contents. Therefore, the trace element concentrations of the above-lying marl were used as background concentrations to recognize element anomalies at the K/T boundary. No Ir was detected in the above-lying marl. In contrast, the K/T layer is characterized by a prominent Ir anomaly with the maximum content of 2 ppb at the base of this layer (Fig). The Ir enhancement is accompanied by a Ni anomaly but the Ni peak (33 ppm) is located at the top of the boundary marl. It is also interesting that there is a negative Ce anomaly at the base of the K/T marl. Other elements do not show distinct anomaleous concentrations at the K/T boundary. However Ti, Fe, Al, K, Hf, and Th appear to be higher in the K/T layer than those in the above-lying marl. The unusual characteristic of the Koshak section is an extremly high Co content (63 ppm) in the chalk which covers directly the K/T marl. This Co peak is correlated with a Mn anomaly (Fig). Similar to other K/T sections the Koshak K/T marl contains SQ which shows a highest content at the top of the marl. It suggests an additional contribution of normal quartz grains to the basal material of the marl. SQ was also detected in the chalk immediately above and below this marl. However no SQ grains were identified in the above-lying marl and the 1-2 cm sample below the boundary. The surface densities of Ir, Ni, Co, Mn and SQ were computed to be 5.4 ng/cm2, 75 ug/cm2, 170 ug/cm2, 510 ug/cm2, and 3 ug/cm2, respectively.

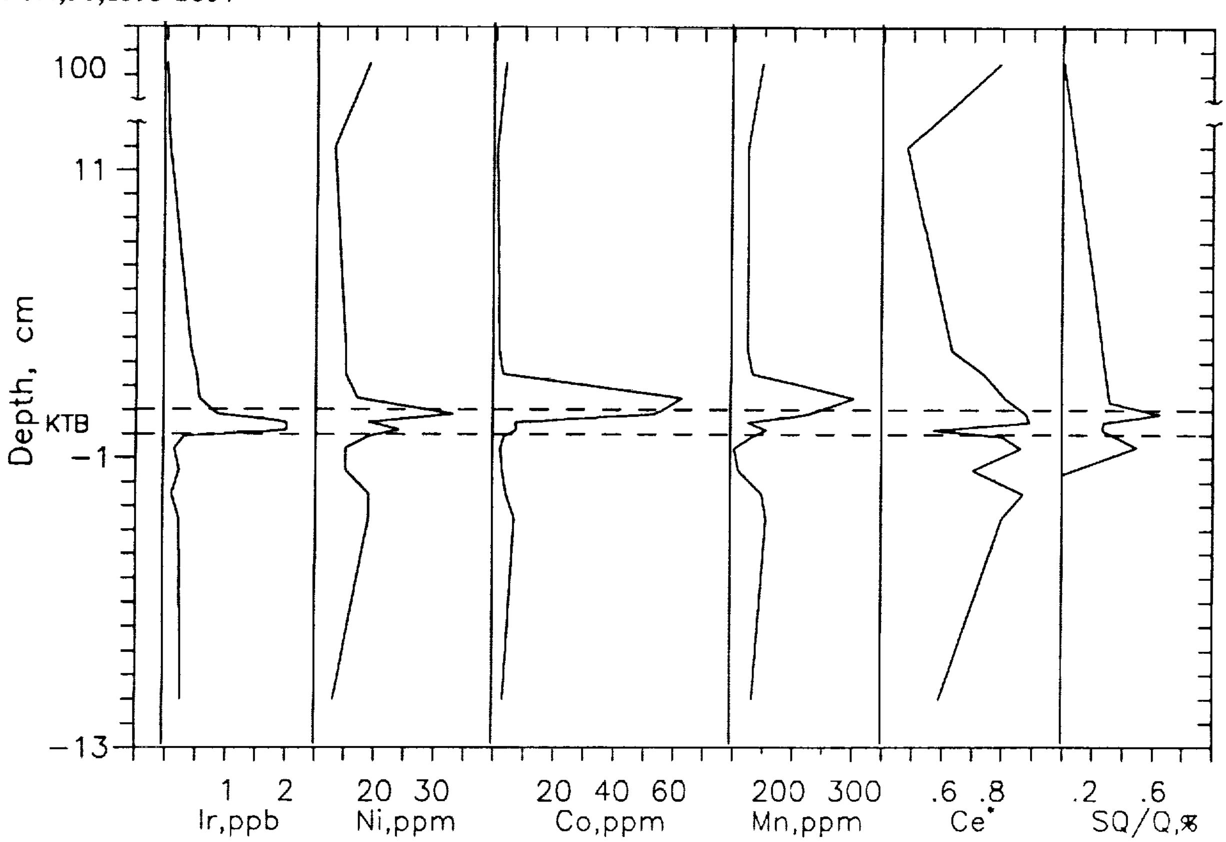
Discuission. The Koshak site is very similar in lithology and the low Ir contents to the K/T sections in Yutland [1] which are also of a pelagic type. However, the distinct separations of Ir, Ni and Co, which are believed to be of cosmic origin, has never been reported in K/T sections. In spite of the separation the Koshak Ni/Ir ratio (14 E3) in the terms of integrated amounts of Ni and Ir is close to the average Ni/Ir ratio (9.7+/-1.1 E3) at the K/T boundary which is lower than the cosmic Ni/Ir ratio (20 E3) [2]. However, the Co/Ir ratio of integrated amounts of the elements at Koshak (31.5 E3) is much higher than the Co/Ir ratio in the K/T boundary sediments (1.0+/-0.2 E3) [2] and in chondrites (1.1 E3). The same is for Co/Ni ratios. The correlation between Co and Mn suggest the Co enrichment to be of terrestrial origin. However the Mn/Co ratio at Koshak (3.0) is much lower than that in terrestrial sediments (20-100) and the present-day ocean water (150). Assuming that there was no any Mn-Co fractionation and Mn is related only to terrestrial sources, a maximum surface density of Co in the Koshak section can be estimated to be about 25 ug/cm2 that is significantly lower than the measured

value. Therefore, a most part of the Koshak Co amount should be related to the K/T extraterrestrial material. Because a low limit of siderophile contents at the K/T boundary is resulted from the atmospheric precipitation of K/T fallout, the Co enrichment relative to Ir and Ni at Koshak should be caused by a contribution of the cosmic Co deposited on a land and then transported to the basin of the sedimentation.

Thus the separation of the element peaks and the element relationship point to a significant fractionation of cosmic elements during the K/T sedimentation. The element fractionation should be due to a change of redox conditions because Co and Mn do not precipitate in a reduced environment, and, therefore, their enrichment just above the boundary clay indicates an oxidation event which followed reducing conditions during the K/T marl formation. Hence, being a mobile element under reducing conditions, the cosmic Co, deposited with K/T fallout on a land, was removed to the area of the pelagic sedimentation, and then, was fixed in the sediments under oxidizing conditions. In contrast, Ir and Ni, transported from the land, were fixed in reduced sediments near a sea shore, and, therefore, their contents at the Koshak site reflect mostly those in the atmospheric precipitation of K/T fallout.

The reduced environment after the K/T impact has been documented in many K/T sections [e.g.3] and could be due to the K/T mass mortality. The oxidation conditions are recorded clearly only in the Koshak section. However we have indicated a high Co/Ir ratio in the Tetrichkaro section (Georgia, Caucasus) and some evidence for the oxidation in Turkmenian K/T sections [4]. Therefore, it can be suggested that the oxidation environment are at least of a regional significance. In principle, the oxidation could be due to photochemical reactions [e.g.5] caused by destruction of the ozone screen after the K/T impact.

References: [1] M.A.Nazarov et al. (1983) Geochem.Int. 20, 142-159; [2] M.A.Nazarov et al. (1988) Intl.Geol.Rev. 30(7), 709-726; [3] G.-J.Jin and R.A.Schmitt (1989) LPSC XX, 464-465; [4] A.S. Alekseev et al. (1988) Intl.Geol.Rev. 30(2), 121-135; [5] A.D.Anbar and H.D.Holland (1992) GCA,56,2595-2604



CARBONACEOUS XENOLITHS FROM THE EREVAN HOWARDITE.

M. A. Nazarov, Vernadsky Institute of Geochemistry and Analytical Chemistry, Moscow 117975, Russia, F. Brandstätter and G. Kurat, Naturhistorisches Museum, Postfach 417, A-1014, Vienna, Austria.

Preliminary studies of the Erevan howardite [1] showed that the meteorite is a polymict breccia. Here we report on our study of CM-type carbonaceous xenoliths. All of these clasts are enriched in tochilinite and carbonate inclusions as compared to CM chondrites. They also contain a new, P-rich sulphide beside pentlandite. The P-rich sulphide represents a new type of P-bearing phases. It indicates a chalcophile behaviour of P under certain nebular conditions.

RESULTS Carbonaceous clasts in the Erevan howardite are usually less than 1 mm in size .Large clasts contain several textural components enclosed by a fine-grained matrix, whereas small clasts consist of matrix only. The following components were identified: **(i) Isolated olivine and pyroxene grains**. These grains are up to 0.1 mm (usually 20-40 μm) long and have compositions of Fo97-98 and En94-96 which are typical for CM chondrites. However, one olivine grain with as much as 40% Fa was found. Some olivine grains exhibit zoning with enrichment in Cr, Al and Ca towards the surface. **(ii) Carbonate inclusions**. These objects (up to 0.1 mm in size) are rounded aggregates of exceedingly fine-grained crystals. Sometimes thin veins of matrix material cut through the inclusions. In their morphology and texture they are similar to CAIs but they do not contain any relics of CAI phases and consist only of pure Ca-carbonate. In contrast, carbonate veins present in the matrix contain a relatively coarse-grained (20 μm) Ca-carbonate associated with Fe-sulphide. Thus, the observations suggest that the carbonate inclusions are of nebular origin. Similar carbonate objects were described from the CM1 chondrite Y82042 [2] but these objects contain also dolomite beside calcite. **(iii) Tochilinite inclusions** (up to 80 μm) have an irregular shape and consist mainly of tochilinite of the composition 2Fe 0.9S * 1.69(Fe 0.55,Mg 0.23,Ni 0.15,Al 0.07) (OH)2 (Table 1, No 1). Common are veins and inclusions of a S-bearing serpentine phase (Table 1, No 2) in the tochilinite aggregates. Tochilinite (or PCP) is considered to be a characteristic phase of CM chondrites [e.g.,3]. **(iv) Black clasts** (up to 0.1 mm in length) exibit a botryoidal-like texture and consist of a serpentine-tochilinite mixed phyllosilicate (Table 1, No 3) and a black fine-grained matrix. These clasts contain also isolated forsterite grains. Compared to matrices of the Erevan carbonaceous clasts the one dark clast analyzed is richer in S and poorer in Ni (Table 2, No ER-200). **(v) P-rich sulphide**. A unique fragment (40*100 μm) of P-rich sulphide was found in one carbonaceous clast. The sulphide fragment is cut by thin veins of tochilinite and serpentine. In reflected light the sulphide resembles troilite but it is slightly darker and isotropic. The composition of the sulphide (Table 1, No 4) is close to that of pentlandite (Table 1, No 5) found in the matrix of the same carbonaceous clast, but in contrast to the pentlandite, the sulphide contains P,Na,K, and Ca. Its formula: (Fe 4.59, Ni 3.71, Co 0.18, Na 0.24, K 0.08) 8.80 (S 6.90, P 1.40) 8.30, is of a pentlandite-type with a S/P ratio of 5. However, totals are between 95-97 wt.-%, and hence it is possible that the sulphide contains some oxygen. Two small grains (< 5 μm) of the same sulphide were found in the matrix of another carbonaceous clast. **(vi) Matrices**. The matrix material was analyzed in 6 carbonaceous clasts (Table 2). The matrices show some compositional variations but all of them have the chemistry of CM matrices [4] and can be well modelled by a mixing of tochilinite and serpentine. When normalized to CI composition the matrices are significantly depleted in Na, S, and Ca. Similar depletions have been found in other carbonaceous matrices and have been related to aqueous alteration in a carbonaceous parent body [5]. The presence of Ca-carbonate veins in the carbonaceous clasts supports this suggestion.

DISCUSSION The matrix composition and the presence of tochilinite are compatible with the Erevan carbonaceous clasts being a CM-type chondrite. This rock type is the only xenolith present in Erewan. This is in line with observations on other howardites which also contain mainly CM-type chondrite xenoliths [6]. This close association between howardites and CM-type chondrites either suggests a close genetic link between these meteorite classes or a dominantly CM-type chondrite flux around the EPB. CM-type chondrites are rare among terrestrial meteorite falls (e.g., [7]) but a related material apparently dominates the micrometeorite (and probably also the fine-grained dust) flux on Earth [e.g., [8]; [9]). Similar matter should also accrete on the moon but is usually destroyed by the impact. Such impact effects are not apparent in the howardite xenoliths. We have to conclude that the incorporation of CM-type rock fragments into the howardite breccia must have taken place in a very gentle way.

CARBONACEOUS XENOLITHS IN EREVAN: M. A. Nazarov et al.

Impact must be excluded leaving the alternative of co-accretion of all components - including the CM-type chondrite - into the Erevan parent body.

In comparison with other CM chondrites, the Erevan carbonaceous clasts appear to be richer in tochilinite and carbonate. Another unusual component of the clasts is the P-rich sulphide which obviously represents a new type of P-bearing compounds. Phosphorus is known to be a siderophile or lithophile element and has never been reported from sulphides associated with metal and silicate. In contrast to pentlandite , the P-rich sulphide appears not to be equilibrated with the matrix. Therefore, this sulphide must have been formed before incorporation into the carbonaceous matrix and must be considered to be of primary origin. The enrichment in Na and K demand the sulphide to be formed under reducing conditions similar to that of the enstatite chondrites where phospate phases are not stable. On the other hand this source region of the sulfide must have been characterized by a high S fugacity in order to prevent precipitation of P-rich metal and phosphide. Thus, the Erevan carbonaceous clasts seem to have sampled a highly reduced region of the solar nebular.

REFERENCES [1] L. Kvasha et al. (1978) Meteoritika, 37, 80 (in Russian). [2] F. Brandstätter et al. (1987) Meteoritics, 22, 336-337. [3] K. Tomeoka and P. Busek (1988) Geochim. Cosmochim Acta, 52, 1627-1640. [4] H. Y. McSween and S. M. Richardson (1977) Geochim. Cosmochim. Acta, 41, 1145-1161. [5] A. J. Brearley (1992) LPSC XXIII, 153-154. [6] T. E. Bunch and R. S. Rajan (1988) In "Meteorites and the Early Solar System", J. F. Kerridge and M. S. Matthews (eds), Univ.Arizona Press, Tuscon, 144-164. [7] R. T. Dodd (1981) Meteorites: A Petrological Chemical Synthesis. Cambridge Univ.Press, London, 366pp. [8] M. Maurette et al. (1991) Nature, 351, 44-47. [9] G. Kurat et al. (1992) Meteoritics 27, 246.

Table 1. Selected EMP analyses (n.d.=not detected)

	Tochil.	Serp.	Phyllo.	P.-Sulph.	Pentl.
Na	.04	.03	.10	.70	n.d.
Mg	3.3	15.1	7.0	.14	n.d.
Al	1.46	1.10	3.0	n.d.	n.d.
Si	.63	16.3	10.9	.04	.12
P	n.d.	.03	.02	5.6	n.d.
S	20.0	2.14	8.7	28.7	32.8
K	.01	.03	.06	.42	n.d.
Ca	.04	.08	.05	.10	n.d.
Ti	.04	-	-	n.d.	n.d.
Cr	.08	.13	.12	.08	.24
Mn	.10	.18	.20	.06	.08
Fe	47.1	28.9	29.1	32.6	32.5
Co	.02	.02	n.d.	1.35	1.27
Ni	4.4	.63	1.34	28.2	32.1

Table 2. Broad-beam analyses of the matrices

	ER-95	ER-100	ER-200	ER-500	ER-600	ER-700	ER-800
Na	.08	.17	.12	.11	.17	.11	.12
Mg	11.0	10.4	11.3	12.1	11.1	11.4	11.0
Al	1.27	1.25	1.52	1.03	3.6	1.21	.95
Si	15.6	14.0	13.3	13.8	12.8	12.6	13.8
P	.03	.07	.04	.03	.06	n.d.	.17
S	1.88	3.1	4.7	2.16	1.55	2.49	2.07
K	.08	.07	.05	.03	.05	.05	.03
Ca	.19	.14	.14	.20	.53	.05	.48
Ti	.10	.09	.10	.04	.19	.05	.02
Cr	.38	.36	.26	.59	.57	.41	.58
Mn	.24	.21	.20	.20	.20	.20	.20
Fe	24.4	23.5	23.2	20.0	23.3	25.2	25.5
Co	.10	.07	.02	.01	.02	.01	.02
Ni	1.15	1.14	.73	1.40	.80	.90	1.21

S7-90
ABS. ONLY

N94-20643

IGNEOUS ROCK FROM SEVERNYI KOLCHIM (H3) CHONDRITE: NEBULAR ORIGIN.

M. A. Nazarov, Vernadsky Institute of Geochemistry and Analytical Chemistry, Moscow 117975, Russia, F. Brandstätter and G. Kurat, Naturhistorisches Museum, Postfach 417, A-1014, Vienna, Austria.

The discovery of lithic fragments with compositions and textures similar to igneous differentiates in unequilibrated ordinary chondrites (UOCs) and carbonaceous chondrites (CCs) has been interpreted as to suggest that planetary bodies existed before chondrites were formed [1-3]. As a consequence, chondrites (except, perhaps CI chondrites) cannot be considered primitive assemblages of unprocessed nebular matter. Here we report about our study of an igneous clast from the Severnyi Kolchim (H3) chondrite [4]. The results of the study are incompatible with an igneous origin of the clast but are in favor of a nebular origin - similar to that of chondrules [5].

Texture and mineralogy. The Severnyi Kolchim igneous rock has an elongated rounded shape and a size of 0.8*0.5 mm. It consists of olivine (12%), orthopyroxene (46.1%), Ca-rich pyroxene (19.5%), Ca-rich feldspar (21.8%), chromite (0.2%), and mesostasis (0.3 vol.%). The rock is relatively coarse-grained (0.1 mm) and demonstrates a distinct textural zoning (Fig.1). Rounded olivine grains (light) are concentrated in the central part of the rock and group along its elongation. These grains are surrounded by Ca-rich pyroxene (dark grey) and Ca-rich feldspar (black) which form a typical ophitic texture. The outer zone of the object is composed mainly of orthopyroxene (light grey) with rare olivine inclusions. Rare chromite grains are located at olivine/feldspar contacts. The mesostasis between feldspar laths consists of fine-grained intergrowths of Na-rich feldspar, Ca-rich pyroxene, ilmenite, and silica. On the basis of the textural and compositional characteristics this rock can be classified as olivine gabbro-norite.

Mineral chemistry. Representative analyses of the phases are given in the Table. Olivine has a limited compositional range (Fig.2) of Fo80-84, and low contents of CaO (0.05%) and NiO (<.01%), typical for olivines of H chondrites. However, three minute grains of Mg-rich olivine (Fo90-92) were found enclosed in orthopyroxene of the outer zone. These relic grains resemble those in chondrules. Orthopyroxene exibits large compositional variations (Fig.2) from En80.5 to En87.7, Wo2.4-5, Al2O3 0.5-2.66%, TiO2 0.07-0.55%, Cr2O3 0.4-0.9%. It has a compositional zoning with the Fe/Mg ratio increasing towards the surface of the object. However, as compared to olivine orthopyroxene has an appreciable higher Mg/Fe ratio (Fig.2). The Ca-rich pyroxene shows the highest Mg/Fe ratio of all phases (Fig.2). Its composition is close to diopside (Table) but commonly depleted in Wo (31-44) with Al2O3 1.1-3.3%, TiO2 0.2-1.4%, Cr2O3 0.4-1.0%. Similar pyroxenes (endiopsides) were described from garnet lherzolites [6] and some chondrules [7]. The Ca-rich feldspar has a composition similar to that of eucritic feldspars, i.e. An78 - An91. It, however, is unusually rich in Cr (0.3-0.8% Cr2O3). In contrast, the feldspars in the mesostases are Na-rich (Ab84-85, Or1-3) and comparable to those in the chondrules. The chromites (Table) have typical compositions of chromites in H chondrites.

The bulk composition of the rock (Table) was calculated on the basis of the modal data and the mineral compositions. It is compatible with compositions of cumulate rocks of the gabbro-norite suite. On the other hand this composition is indistinguishable from that of the type III ferromagnesian chondrules of carbonaceous chondrites [8].

Discussion. The ophitic coarse-grained texture, the roughly cotectic proportions of feldspar and high-Ca pyroxene, the presence of orthopyroxene, instead of low-Ca clinopyroxene, and the Ca-rich feldspar composition, as well as the absence of any metal grains distinct the object from chondrule clasts and suggest it to be formed on a differentiated parent body by igneous processes. However, the mineral chemistry data conflict with this suggestion. In fact, the olivine which should be the first liquidus phase in the melt, cannot have a Fe/Mg ratio higher than the total melt, the orthopyroxene, and the cotectic feldspar-clinopyroxene liquid. The mineral compositions rather favor a mixing of different components. In addition, the textural zoning of the object and the compositional zoning of the orthopyroxene, which is similar to the zoning of olivine chondrules [9], are not compatible with an igneous origin. The textural zoning is suggestive of an accretionary process similar to that proposed for chondrules [5]. The non-equilibrated Mg/Fe distribution between and within the phases corresponds to diffusion-controlled exchange reactions with a nebular gas [5,12]. Therefore, we have to conclude, that this igneous rock has a nebular origin. It can be suggested from the chemical

IGNEOUS ROCK FROM SEVERNYI KOLCHIM: M. A. Nazarov et al.

similarity between the object and the type III chondrules that the latter could be produced by complete melting of a precursor material similar to the Severnyi Kolchim "igneous" object.

Summary. This study shows: (1) the chondrule precursor material should have a complicate nebular history including mixing of different nebular components and gas-solid reactions following the general model of chondrule formation proposed by [5,9,10]; (2) nebular processes can produce a material which is close in chemistry and texture to some types of igneous rocks and, therefore, the igneous origin of some lithic clasts in UOCs and CCs is doubtful; (3) our findings even support the suggesstion [5,13] that the basaltic achondrites might be of nebular rather than igneous origin.

References. [1] G.Kurat and A. Kracher (1980) Z. Naturforsch. 85a, 180-190. [2] I. Hutcheon and R. Hutchison (1989) Nature, 337, 238-241. [3] A. K. Kennedy et al. (1992) Earth Planet. Sci. Lett., 113, 191-205. [4] M. A. Nazarov et al. (1983) Meteoritika, 42, 40-47 (in Russian). [5] G. Kurat (1988) Phil. Trans. R. Soc. Lond. A325, 459-482. [6] F. R. Boyd (1973) Geochim. Cosmochim. Acta, 37, 2533-2546. [7] E. J. Olsen (1983) In "Chondrules and their Origins", E. A. King (ed), Lunar Planet. Inst.,Houston, 223-234. [8] H. Y. McSween (1983) ibid, 195-210. [9] J. A. Peck (1986) LPSC XVII, 654-655. [10] G. Kurat et al. (1985) LPSC XVI, 471-472. [11] G. Kurat et al. (1992) LPSC XXIII, 745-746. [12] M. Blander and J. C. Katz (1967) Geochim. Cosmochim. Acta, 31, 1015-1034. [13] G. Kurat (1990) Meteoritics, 25, 377-378.

Table: Representative EMP analyses.

	Ol	Opx	Cpx	Pl	Ch	Bulk
SiO2	38.5	53.8	52.9	45.6	0.72	51.4
TiO2	0.04	0.50	0.32	0.01	1.19	0.26
Al2O3	0.08	2.66	1.49	35.3	7.0	7.4
Cr2O3	0.15	0.89	0.67	0.85	56.0	0.71
FeO	16.9	6.00	1.67	0.82	30.3	6.4
MnO	0.43	0.15	0.07	0.04	1.16	0.21
MgO	44.3	31.5	22.2	0.09	3.1	25.2
CaO	0.07	2.58	17.9	16.6	0.37	8.1
Na2O	0.00	0.05	0.11	1.51	0.00	0.29
K2O	0.00	0.01	0.03	0.04	0.00	0.05
MG'	82.4	90.3	96.0		15.2	87.5

MG'= Mg/(Mg+Fe), at.%.



Fig.1 Distribution of Mg in igneous object from from Severnyi Kolchim.

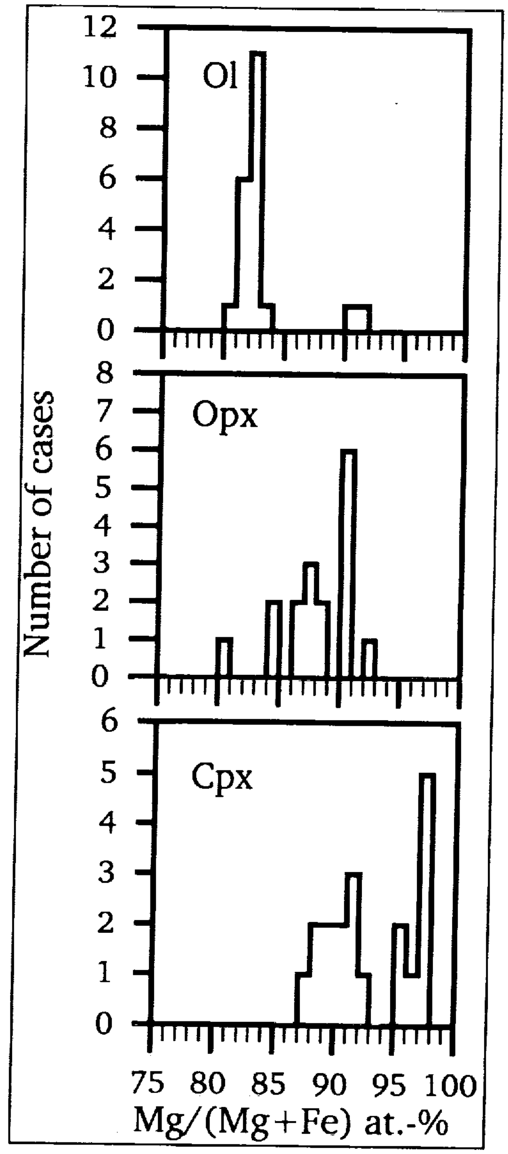
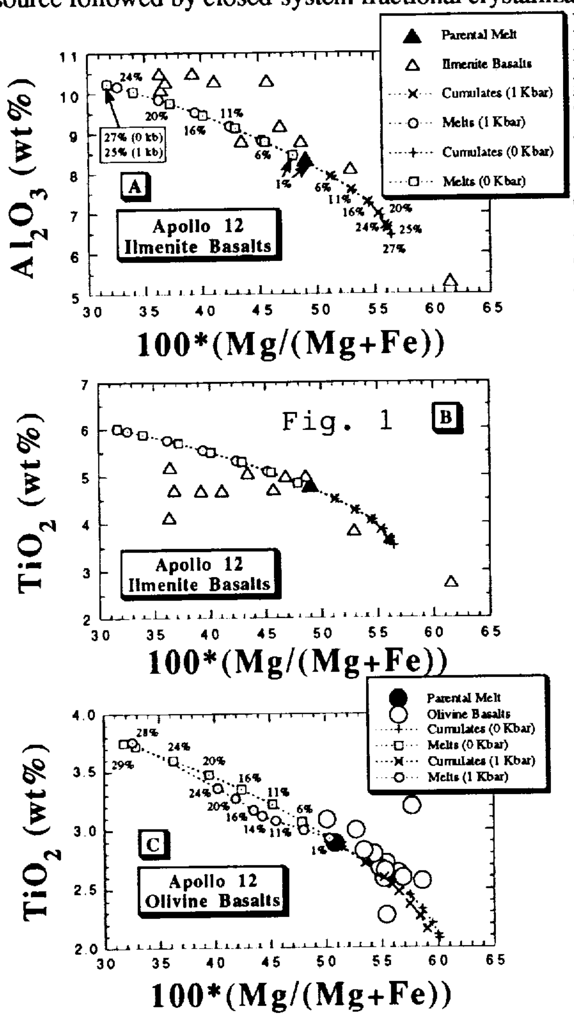


Fig.2 Mg/(Mg+Fe) ratios of olivines and pyroxenes from igneous object in Severnyi Kolchim.

PETROGENESIS OF APOLLO 12 MARE BASALTS, PART 1: MULTIPLE MELTS AND FRACTIONAL CRYSTALLIZATION TO EXPLAIN OLIVINE AND ILMENITE BASALT COMPOSITIONS.

Clive R. Neal, Dept. of Civil Engineering & Geological Sciences, University of Notre Dame, Notre Dame, IN 46556; Lawrence A. Taylor, Dept. of Geological Sciences, University of Tennessee, Knoxville, TN 37996.

Mare basalts returned by the Apollo 12 mission have been divided into 4 groups on the basis of mineralogy [1] & whole-rock chemistry (e.g., [2]): 1) Olivine Basalts; 2) Pigeonite basalts; 3) Ilmenite Basalts; & 4) Feldspathic Basalts. James & Wright [1] & Rhodes et al. [2] concluded that the olivine & pigeonite groups were co-magmatic & that the within group variations are due to fractional crystallization of olivine & minor Cr-spinel, with pigeonite replacing olivine in the pigeonite basalts. Rhodes et al. [2] concluded that the parental compositions for these suites were probably represented by the vitrophyres, & the olivine basalts are comprised essentially of cumulates & the pigeonites of evolved end-members. However, Neal et al. [3-5] have demonstrated, using trace-element considerations, that the *Apollo 12 olivine & pigeonite suites are not related*. The ilmenite basalts were studied extensively by Dungan & Brown [6] who noted that both cumulates & evolved fractionates were present within this group. In their modelling, Dungan & Brown [6] used the vitrophyre compositions as parents. Neal et al. [3-5] demonstrated that *the feldspathic suite was probably is comprised of only one member - 12038*. Herein, the ilmenite & olivine basalts are demonstrated to be the products of several non-modal partial melting events of a single source followed by closed-system fractional crystallization.



MAJOR ELEMENTS: The modelling of the olivine & ilmenite basalts was undertaken utilizing the MAGMAFOX program [7] to generate a fractional crystallization sequence for the olivine & ilmenite suites from a parental composition taken as the average of all vitrophyres in each suite, as individual vitrophyre compositions are similar. All the olivine basalts (cumulates) & those ilmenite basalts designated as cumulates [6] fall along the cumulate path (Fig. 1). In order to limit sampling errors, each composition was calculated as an average of a number of analyses conducted upon the same specimen. The single-stage model does not explain the correlations between Mg# vs. Al_2O_3 for the ilmenite basalts & Mg# vs. TiO_2 for the ilmenite & olivine basalts (Fig. 1).

TRACE ELEMENTS: The single-stage fractional crystallization model cannot generate the observed ranges in Sm/Eu & Rb/Sr ratios (Rb & Sr determined by ID) for either the ilmenite or olivine suites (Fig. 2 a,b). This is because the calculated fractionating sequence cannot radically alter the Rb/Sr or Sm/Eu ratios. Averages of several analyses were taken in order to minimize the effect of sampling errors. The modelling of ilmenite & olivine basalt petrogenesis uses the parental melt composition to calculate a source composition, similar to the method of [8], but using a non-modal batch melting approach:

$$Cs = Co/(1/(D + F(1-P)))$$

Cs = Elemental concentration in source; Co = Elemental concentration in the parent; D = Bulk Kd calculated from source mineralogy; F = Amount of partial melt; P = Bulk Kd calculated from mode going into the melt.

For the ilmenite basalts, we assumed the parent was a 6% partial melt of a source comprised of 31% olivine, 31% opx, & 38% clinopyroxene, as calculated by Nyquist et al. [8,9]. Partition coefficients used in this study have generally been determined for lunar applications [10]. However, the range in Sm/Eu & Rb/Sr ratios cannot be generated by a single parental melt generated by the parameters delineated above (Fig. 2a). Therefore, after calculating the source composition, we calculated partial melt compositions between 2-8%, but the path generated did not conform to the data. The "best fit" requires that our parental composition be a 5% partial melt of a source composed of 31% opx, 31% pigeonite, 33% augite, & 5% ilmenite melting in the proportions of 1:2:6:1. In order to generate variable Rb/Sr ratios at relatively constant Sm/Eu, modelling of 2-8% partial melts of this source appears to generate all basalt compositions (Fig. 2a). Fractional

NEAL & TAYLOR: APOLLO 12 ILMENITE & OLIVINE BASALT PETROGENESIS

crystallization will not alter the Sm/Eu & Rb/Sr ratios until plagioclase becomes a liquidus phase (> 27% FC). In this modelling, we assumed perfect adcumulates & did not incorporate a mythical "trapped liquid", & also that the crystal fractionation sequence defined for the vitrophyric samples applied to each of our model partial melts. What this model does require is some *limited* mixing/overturn) of late-stage LMO cumulates.

This approach was also used for the Apollo 12 olivine suite. Neither plagioclase nor Ca-rich cpx is a liquidus phase, so crystal fractionation cannot produce the observed ranges in Sm/Eu & Rb/Sr (Fig. 2b). The parental composition was assumed to have been derived by a 3% partial melt of a source composed of 93% olivine & 7% cpx (after [9]). However, this source, even with variable degrees of partial melting, will not generate the observed trace-element compositions. Our model requires that the olivine vitrophyres be produced by 7% non-modal equilibrium partial melting of a source of 48% olivine, 49% opx, & 3% plagioclase, melting in the proportions 3:4.5:2.5. Plagioclase in the source, more than one parent, & variable degrees of partial melting are required to generate the variation in Sm/Eu (4.0-5.5) & Rb/Sr (0.008-0.012).

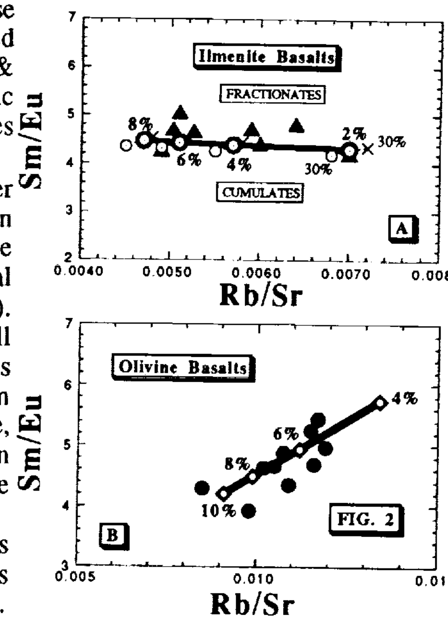


FIG. 2

ISOTOPES: The Sr isotope ratios of the ilmenite & olivine basalts [8,9,11-15] allows an evaluation of open system behavior. Initial ratios were calculated using both isochron & ^{40}Ar-^{39}Ar ages (e.g., [16-17]).

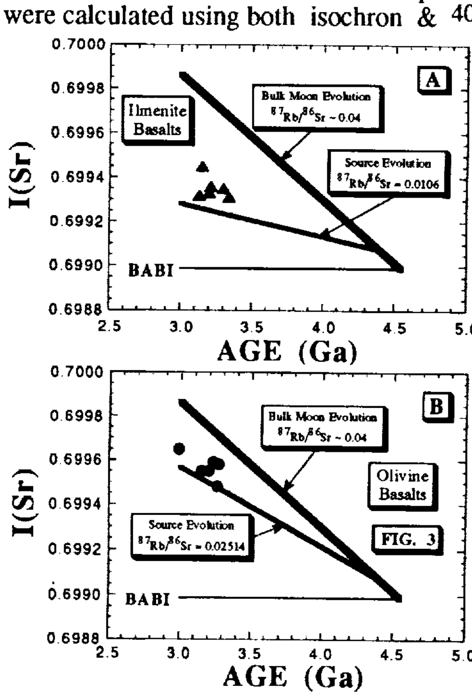


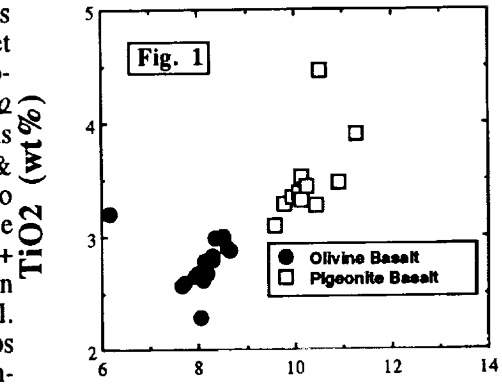
FIG. 3

The bulk moon evolution path was calculated from BABI using an $^{87}Rb/^{86}Sr$ ratio of 0.04 [18], & the ilmenite & olivine source evolution paths were generated from the Rb/Sr ratio calculated during trace-element source modelling & the present day $^{87}Sr/^{86}Sr$ ratio of vitrophyre 12008 [9] for the ilmenites & 12015 [9] (Fig. 3 a,b). Generally, the ilmenite basalts plot within error of each other, slightly above the calculated evolution path, but again are generally within error of it (Fig. 3a). The olivine basalts also plot within error of the calculated evolution path (Fig. 3b), again plotting slightly above it. Two assumptions which may account for the source evolution paths in both cases being lower than the basalts are: 1) the source departs from the bulk moon evolution path at 4.4 Ga; 2) the partition coefficients for Sr & especially Rb are not well constrained. However, initial Sr isotopic ratios of ilmenite & olivine basalts do not indicate open system behavior, supporting our multiple melt model.

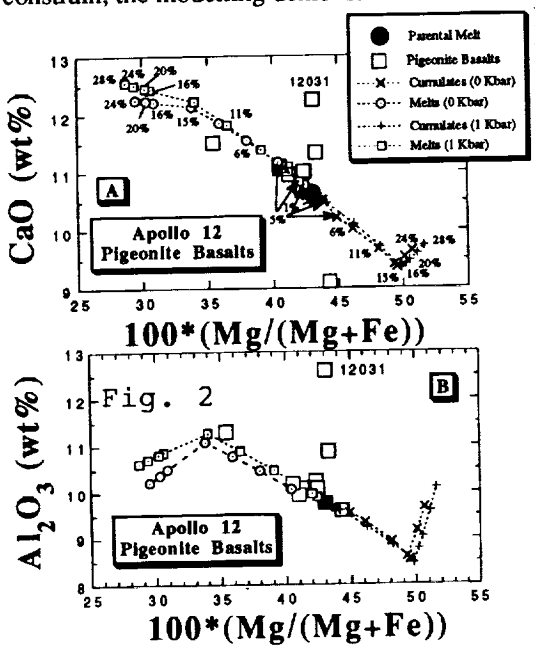
SUMMARY: The Apollo 12 ilmenite & olivine basalts cannot be explained by a petrogenesis involving a single-stage partial melting event followed by closed-system fractional crystallization. Trace-element ratios require that at least three individual partial melting events for the ilmenite & olivine basalts are required. Using the parental composition derived from the vitrophyres within each suite, a source forthe ilmenite has been calculated as 31% opx, 31% pigeonite, 33% augite, & 5% ilmenite, with the vitrophyres being a 5% partial melt of this source. Varying the degree of partial melting between 2% & 8% of this source can explain the observed range of trace-element ratios. Likewise, the olivine basalts are derived by 5-10% partial melting of a source comprised of 48% olivine, 49% opx, & 3% plagioclase. After the melts have been produced, each evolves by closed-system fractional crystallization & as the major-element compositions of each melt is similar, the trends in Fig. 1 are produced.

REFERENCES: [1] James O.B. & Wright T.L. (1972) Bull. Geol. Soc. Am., 83, 2357-2382; [2] Rhodes J.M. et al. (1977) PLSC 8th, 1305-1338; [3] Neal C.R. et al. (1992a) LPS XXIII, 975-976; [4] Neal C.R. et al. (1992b) LPS XXIII, 977-978; [5] Neal C.R. et al. (1993) Geochim. Cosmochim. Acta (submitted); [6] Dungan M.A. & Brown R.W. (1977) PLSC 8th, 1339-1381; [7] Longhi J. (1991) Amer. Mineral. 76, 785-800; [8] Nyquist L.E. et al. (1977) PLSC 8th, 1383-1415; [9] Nyquist L.E. et al. (1979) PLPSC 10th, 77-114; [10] Snyder G.A. (1992) Geochim. Cosmochim. Acta 56, 3809-3824; [11] Bottino M.L. et al. (1971) PLSC 2nd, 1487-1491; [12] Compston W. et al. (1971) PLSC 2nd, 1471-1485; [13] Murthy V.R. (1971) Geochim. Cosmochim. Acta 35, 1139-1153; [14] Papanastassiou D.A. & Wasserburg G.J. (1970) EPSL 8, 269-278; [15] Papanastassiou D.A. & Wasserburg G.J. (1971) EPSL 11, 37-62; [16] Alexander E.C. et al. (1972) PLSC 3rd, 1787-1795; [17] Stettler A. (1973) PLSC 4th 1865-1888; [18] Nyquist L.E. (1977) Phys. Chem. Earth. 10, 103-142.

PETROGENESIS OF APOLLO 12 MARE BASALTS, PART 2: AN OPEN SYSTEM MODEL TO EXPLAIN THE PIGEONITE BASALT COMPOSITIONS. Clive R. Neal, Dept. of Civil Engineering & Geological Sciences, University of Notre Dame, Notre Dame, IN 46556; Lawrence A. Taylor, Dept. of Geological Sciences, University of Tennessee, Knoxville, TN 37996.



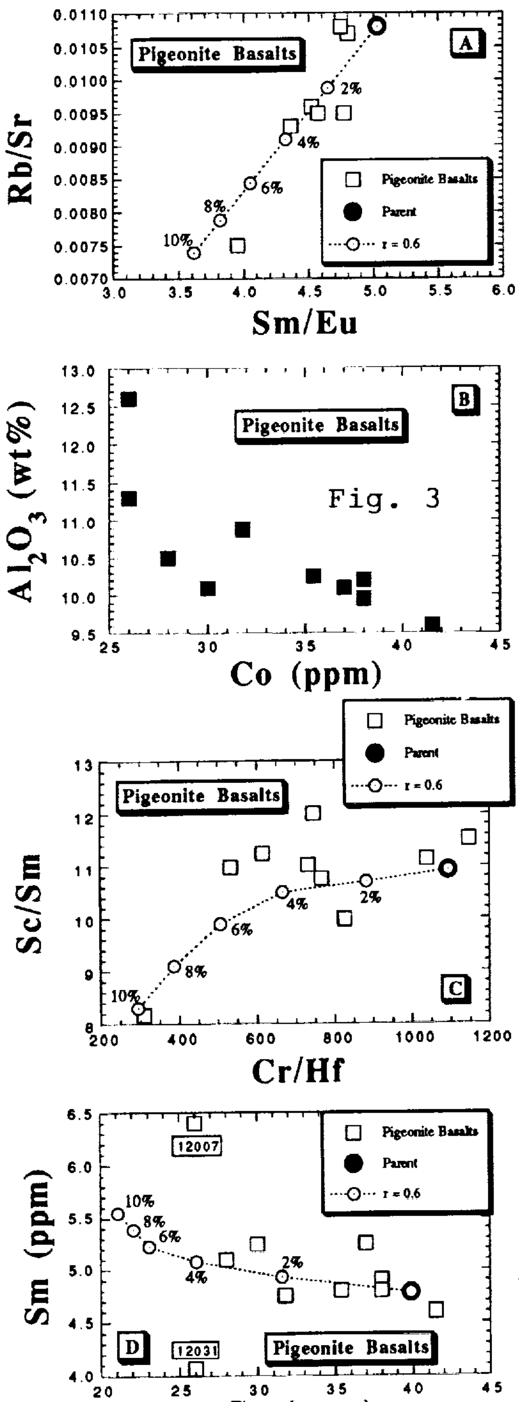
Original petrogenetic models suggested that the pigeonite basalts were the evolved equivalents of the olivine basalts (i.e., [1]). Rhodes et al. [2] concluded that the ***olivine & pigeonite*** basalts were co-magmatic, but Neal et al. [3-5] have demonstrated that these two basaltic groups are distinct & unrelated. The pigeonite suite is comprised of porphyritic basalts with a fine-grained groundmass & range continuously to coarse-grained microgabbros with ophitic to graphic textures [6]. Although it was generally recognized that the pigeonite basalts were derived from the olivine basalts by olivine + minor Cr-spinel fractionation [1,2,6], the compositional gap between these groups (Fig. 1) is difficult to reconcile with such a model. Indeed, Baldridge et al. [6] concluded that these two basaltic groups could not have been co-magmatic. In this paper, we suggest an open-system AFC model for pigeonite basalt petrogenesis. The assimilant is lunar anorthositic crust & the r value used is 0.6. While the choice of assimilant composition is difficult to constrain, the modelling demonstrates the feasibility of this model.



MAJOR-ELEMENTS: Correlations indicate that, in general, all pigeonite basalts are evolved melts from a parent represented by vitrophyre 12011 (Fig. 2 a,b). Using the MAGMAFOX program of Longhi ([7] & pers. comm.). The closed-system crystal fractionation models (at both 0 & 1 kbar) indicate the presence of plagioclase in the crystallizing sequence after 15% fractionation (Fig. 2 a-c), with the fractionating sequences being similar at each pressure. Using 12011 as a potential parent, the following fractionating sequence was determined using the MAGMAFOX program: 0-1% = olivine (100); 1-5% = olivine (80) + chromite-ulvöspinel (20); 5-15% = pigeonite (98) + chromite-ulvöspinel (2); 15-30% = pigeonite (33) + plagioclase (67). Major-element modelling suggests crystal fractionation is involved in the petrogenesis of these basalts. However, although plagioclase is a liquidus phase, crystal fractionation/cumulation of a single parent (12011) or several parents (produced by variable degrees of partial melting) can account for the trace-element data.

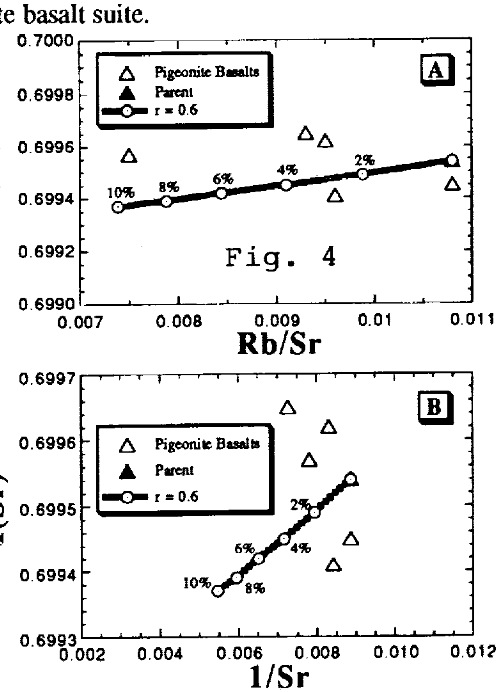
MODELLING: Modelling of pigeonite basalt petrogenesis must account for the scatter in the trace-element data (Fig. 3 a-d), decrease in Sm/Eu & Rb/Sr ratio from the parent 12011 (Fig. 3a - Rb & Sr data by ID), & the negative correlation between Al_2O_3 & Co (Fig. 3b). Our calculations indicate that these data cannot be accounted for through variable degrees of partial melting of a source containing plagioclase, as for the olivine basalts [8]. The approach used was to account for the Co vs Al_2O_3 data (Fig. 3b) by crustal assimilation, which could produce the observed trend. In elucidating a likely crustal composition, highland materials from both Apollo 14 & Apollo 12 were considered (e.g., [9-11]). On the basis of returned samples, the lunar highlands at these sites is composed predominantly of Mg-Suite & Alkali Suite compositions. For modelling purposes, we took a composition which has low-compatible elements (i.e., mafic-mineral poor), is LREE-enriched, & has a positive Eu anomaly. This composition was derived from the Apollo 12 pristine anorthosite compositions reported by Warren et al. [11] & assumes a low Rb composition because the assimilant is rich in plagioclase. The trace elements were modelled using 12011 as the parent & the method of Depaolo [12].

Results demonstrate that the Sm/Eu & Rb/Sr ratios of the majority of pigeonite basalts can be generated by 4% AFC of anorthosite by the parent, with an "r" value of 0.6 (Fig. 3a). The original feldspathic basaltic 12031 is generated after 9-10% AFC, but we consider this analysis to be unrepresentative [3-5]. When the Sc/Sm & Cr/Hf ratios are considered (Fig. 3c), the pigeonite basalts have a more scattered distribution. The parent has an elevated Cr/Hf ratio & the AFC path generated by our model is shown, & 12031 is again generated by 10% AFC. This scatter is also seen when element abundances are plotted (Fig. 3d) & illustrates the limitations of our model. While



it cannot be totally discounted, this scatter may be due to source heterogeneity coupled with multiple parents formed by variable degrees of partial melting. Equally, the scatter could be generated by an assimilant which has a heterogeneous pyroxene distribution. The Sr isotope results should be able to distinguish between these two models. Pigeonite Nd isotope data are few (e.g., [13]) & suggest closed-system processes. However, when initial Sr isotope ratios are plotted against Rb/Sr & 1/Sr (Fig. 4 a,b), it is evident that there is variation in I(Sr), but the parental composition plots in the middle of the array. Furthermore, if crustal assimilation generated the array of pigeonite basalt compositions, then the assimilant must have a Sr composition of 110-140, as 1/Sr is approximately constant (Fig. 4b). Clearly, more isotopic data are required before definitive conclusions can be made.

SUMMARY: A single-stage fractional crystallization petrogenesis is inappropriate for the Apollo 12 pigeonite basalt suite. Furthermore, trace-element ratios of the Apollo 12 pigeonite basalt suite cannot be modelled by variable degrees of partial melting followed by closed-system fractional crystallization, as in the ilmenite & olivine basalts [5,8]. Based upon major- & trace-element compositions, we have proposed a petrogenesis involving AFC with lunar crust, with an "r" value of 0.6 & using the vitrophyre composition as parental. This model can be rigorously tested by undertaking more detailed isotopic analyses of the pigeonite basalt suite.



REFERENCES: [1] James O.B. & Wright T.L. (1972) Bull. Geol. Soc. Am., 83, 2357-2382; [2] Rhodes J.M. et al. (1977) PLSC 8th, 1305-1338; [3] Neal C.R. et al. (1992a) LPS XXIII, 975-976; [4] Neal C.R. et al. (1992b) LPS XXIII, 977-978; [5] Neal C.R. et al. (1993a) Geochim. Cosmochim. Acta (submitted); [6] Baldridge W.S. et al. (1979) PLPSC 10th, 141-179; [7] Longhi J. (1991) Amer. Mineral. 76, 785-800; [8] Neal C.R. & Taylor L.A. (1993) LPS XXIV; [9] Shervais J.W. et al. (1984) PLPSC 15th in JGR 89, C25-C40; [10] Lindstrom M.M. et al. (1984) PLPSC 15th in JGR 90, C41-C49; [11] Warren P.H. et al. (1990) PLPSC 20th, 31-59; [12] Depaolo D.J. (1981) EPSL 53, 189-202; [13] Nyquist L.E. et al. (1979) PLPSC 10th, 77-114.

310-71
ABS. ONLY
N94-20346
P-2

THE COHERENT BACKSCATTERING OPPOSITION EFFECT

R. M. Nelson (1), B. W. Hapke (2), W. D. Smythe(1), V. Gharakanian(1), and P. Herrera(1), (1) Jet Propulsion Laboratory (2) University of Pittsburgh

We have measured the opposition effect, the non-linear surge in reflectance seen in particulate materials as phase angle approaches zero degrees, in a suite of materials of varying particle size and reflectance. These samples were illuminated by linearly and circularly polarized monochromatic radiation at two wavelengths, 0.442 μm and 0.633 μm. By measuring the linear and circular polarization ratios for each sample we have found that in highly reflective materials the behavior of the reflected radiation is consistent with the coherent backscattering process which has recently been proposed to explain the opposition surge that is seen in such media (1). The size and width of the coherent backscattering opposition peak vary as a function of reflectance of the sample.

The opposition effect has been observed in particulate materials studied in the laboratory and it is also observed in the radiation reflected from solar system bodies which present a regolith to the earth based observer. The traditional explanation of the opposition effect, the shadow hiding hypothesis, is that it was caused by the elimination of mutual shadows cast between the regolith grains as the phase angle of the observation became smaller (2, 3). This shadow hiding hypothesis, however, is unable to explain the opposition effect seen in highly reflective materials such as magnesium oxide and barium sulfate powders (4,5.) This is because highly reflective media will multiply scatter the incident radiation between the regolith grains. This causes the shadows to be eliminated.

It has recently been suggested that the opposition surge seen in highly reflective particulates is caused by the process of coherent backscattering (1), also known as weak photon localization (6) or time reversal asymmetry (7). The coherent backscattering hypothesis suggests that in highly reflective materials two light rays which undergo multiple scattering while traveling along identical but opposite paths in a medium will constructively interfere as the phase angle becomes small and enhance the size of the backscatter peak.

The light reflected from absorbing particulates surfaces in which shadow hiding is believed contribute to an effect opposition effect is primarily singly scattered. Therefore, as the phase angle approaches zero degrees, the linear and circular polarization ratios are expected to decrease. The radiation scattered from a very reflective surface in which coherent backscattering is expected to contribute to the opposition effect is principally multiply scattered. In this case the linear polarization ratio is expected to decrease as the phase angle approaches zero degrees. However, the circular polarization ratio is expected to increase as the phase angle of the observation decreases. Thus, the relative contribution of the shadow hiding process compared to the contribution from the coherent backscattering process may be quantified by understanding the linear and circular polarization ratios in the reflected radiation.

We have measured the angular scattering properties of a suite of materials of different reflectivity. We have observed polarization ratios in reflective particulates that are consistent with coherent backscattering as the principal process which causes the opposition surge. In

the absorbing materials, both shadow hiding and coherent backscattering contribute to the opposition surge. Figure 1 shows the phase curves of a suite of materials of varying albedo. Figure 2 shows the change in the circular polarization ratio of the same materials.

We have begun a study of the angular scattering properties of a suite of powders of varying particle size from the same material, aluminum oxide. The highly reflective materials were of five separate particle sizes. These were 0.05 µm, 0.1 µm, 0.3 µm, 0.7 µm, and 1.0 µm. All the samples were prepared with about 90% void space. We are attempting to develop an empirical relationship between the character of phase curve and the physical state of the materials. Ultimately it is our goal use these results to constrain the theoretical models that have been developed to explain both the coherent backscattering opposition effect and possibly the coherent backscattering interpretation of the negative branch of the polarization curve (8,9,10,11).

This work was performed at JPL under contract with NASA.

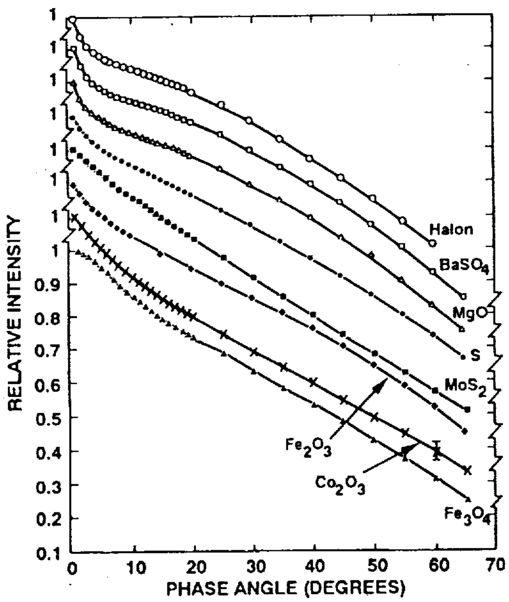


Fig 1

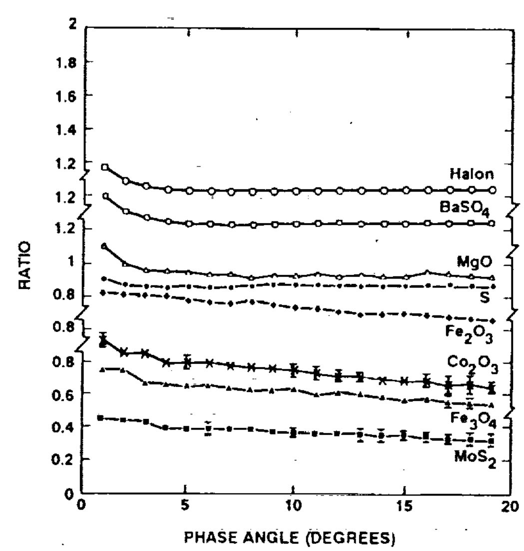


Fig 2

References

1. Hapke, B. W. Icarus, **88,** 407-417,1990. 2. Hapke, B. W. Astron J., **71,** 333-339,1966 3. Irvine, W. M. J. Geophys. Res., **71,** 2931-2937. 4. Oetking, P. J. Geophys. Res., **71,** 2505,1966 5. Pleskott, L. PhD. Thesis UCLA, 1981. 6. Etemad *et al,* 1986, Phys. Rev. Lett., **57,** 575-578. 7. MacKintosh, F. and S. John, Phys. Rev B, **37,** 1884,1897 8. Peters, K., The coherent backscatter effect. accepted in Phys. Rev. B 9. Mischenko, M. I., One the nature of the polarization Opposition effect exhibited by Saturn's Rings. Submitted to Astrophys. J. 10. Shkuratov, Astron Vestnik, **25,** 152-161, 1991 11. Muinonian, K., and K. Lumme, B.A.A.S., **22,** 1033,1990.

ON MAGNETODYNAMIC EFFECTS INITIATED BY A HIGH-SPEED IMPACT OF A LARGE COSMIC BODY UPON THE EARTH'S SURFACE

I. V. Nemchinov, P. E. Alexandrov, V. I. Artemiev, V. I. Bergelson, and V. A. Rybakov

Institute for Dynamics of Geospheres, Russian Academy of Sciences, Moscow, Leninsky prospect, 38, build. 6

The impact of a large cosmic body with typical size R ~ 1 km (mass M ~ 4-10 Gt for a stony or icy body) moving with velocity V ~ 50-70 km/s (kinetic energy of the order of 10^{21} J or 10^6 Mt of TMT) on the Earths surface leads to a full vaporization of a body and of a significant part of substance of the upper layers of the Earth and even to the ionization of this vapour cloud. As a result a hypersonic jet of air and erosion plasma is formed. The kinetic energy E_J of the jet can reach 10-20% of the kinetic energy of a cosmic body or even more. The magnitude of E_J is far above the total energy of the geomagnetic field of the Earth (approximately equivalent to the energy of 100 Mt) and the total mass of a fast-moving part of the jet $M_J \sim 10^{12}$ kg is far above the mass of atmosphere in the jet expansion cone. Thus the jet will propagate practically inertially with the constant mean velocity U ~ 10-20 km/s and even higher. The interaction of this plasma jet with the Earth's magnetic field causes magnetodynamic effects similar to those which are produced by cosmic nuclear explosions but of a larger scale.

The electric field of polarization and electric current through the ionosphere form a giant MHD-generator transforming the kinetic energy of the jet E_J into the thermal energy of ionosphere Q. A coefficient of conversion $\zeta = Q/E_J$ is approximately equal to $U^2B^2t^3/(V_AM_J)$, where B is the inductivity of the geomagnetic field near the Earth's surface and V_A is the effective Alfven velocity in the ionosphere connected with the charecteristic integral surface Pedersen conductivity of

ionosphere $\Sigma_P = c^2/(4\pi V_A) \sim 1\text{-}10\ Ohm^{-1}$, c is light velocity. Let us take for the characteristic time of interaction of the plasma jet with the magnetosphere $t = R_E/U \sim 600$ s, where R_E is the Earth's radius (for this time the interaction is already global and the reduction of the geomagnetic field at the shock wave front takes place). Hence $\zeta \sim 10^{-3}$- 10^{-2} and the total thermal energy release in ionosphere $Q \sim 10^{17}$- 10^{-18}J or 10^2- 10^3 Mt of TNT. This energy release is tens times greater then the thermal energy of the undisturbed ionosphere and energy of the geomagnetic field at the heights more than 100 km.

The substantial ionospheres heating and the deformation of the magnetosphere can lead to different immediate consequences (the destruction of the ozone layer, disruption of the radiation belts, and precipitation of the trapped energetic particles from them, to the large amplitude oscillations of the ionospheric and magnetospheric plasma, to the interruption in the transmission of the electromagnetic signals of different wavelengths which is an important factor in our information age especially in the case of the catastrophic impact etc) and to long term consequences which should be evaluated.

The preliminary results of experimental and numerical modelling of the plasma jet - magnetosphere interaction are presented.

512-90
ABS ONLY

N94-20648

DETERMINATION OF COSMIC BODIES SIZE-VELOCITY DISTRIBUTION BY OBSERVATION OF CURRENT IMPACTS ON MARS.

I.V.Nemchinov, A.A.Perelomova, V.V.Shuvalov

Institute for Dynamics of Geospheres, Russian academy of Sciences, Moscow, Leninsky prospect, 38, build 6

Collisions of cosmic bodies with terrestrial planets involve many physical processes such as deceleration and ablation during their flight through an atmosphere, the impact at a surface accompanied by cratering, melting and evaporation of surface material, generation of shock waves etc [1,2]. If body velocity is high enough then a thermal radiation is very important. All these processes on Mars proceed differently than on the other planets because of the low density of its atmosphere. In particular, this leads to the fact that smaller bodies of sizes of the order of 0.1-10 m strike the planet surface without being decelerated and perform some effects which may be detected by equipment placed on a board of artificial satellites, by a network of stations at the surface of Mars and even from the Earth. These observations can be used to determine size-velocity distribution of such bodies in the Solar System.

Numerical simulation of the impacts at the surface of Mars have been carried out using two-dimensional gasdynamic code with detailed consideration of the thermal radiative transfer. This work is an extension of our previous paper [3]. We have expanded a range of projectile sizes up to r_0=100 m. For such large-scale body the initial stage of the impact, involving cratering and ejection of surface material, is very important. Thus these effects have been taken into account.

At the beginning of the explosion a vapor plume is optically thick and radiation flux is determined by the shock velocity only. The results of numerical simulation of such intensely radiating waves in the atmosphere of Mars obtained using the code [4] have been used to calculate an energy emitted at this stage. As the plume temperature and density decrease it becomes transparent. It is this long-run stage, when the most part of the energy is emitted.

It has been shown that the wake formed during the body flight through the atmosphere [2] and thermal layer near the surface due to radiative heating [3] strongly change a form of the main shock wave. The existence of thermal layer causes a generation of vortex flow which may lead to an ejection of large quantities of sand from the surface. The sand and major portion of projectile and surface material can escape through the wake having lower density than that of an ambient gas. An evolution of impact explosion depends on a radius r_0 of an impactor. Fig.1 shows pressure distributions for the impact of bodies with r_0=10, 30 and 100 m (instances of time are chosen to have the same ratio r_0/t). The form and size of radiating region and its brightness temperature give information on the size and velocity of the

projectile. The whole radiation energy emitted achieves 60-70 percents from the explosion energy.

One else effect not being under consideration yet is generation of acoustic-gravity waves in the atmosphere of Mars. Their propagation is determined by action of two forces: the gravitational and compression ones [4]. As on the Earth such waves may turn round the planet even two or more times and may cause large-scale disturbances of an ionospheric layer. This leads to low-frequency oscillations of electron concentration which may be detected by equipment placed on a board of artificial satellites or on surface stations. Our numerical simulations of this effect show that the ionospheric disturbances achieve some percents at distances 1000-3000 km.

So the results of our investigation of the impacts on Mars show that there are some effects the observation of which may be used to determine the size-velocity distribution of small bodies in the Solar System. The following research would give particular recommendations for organization of such observations.

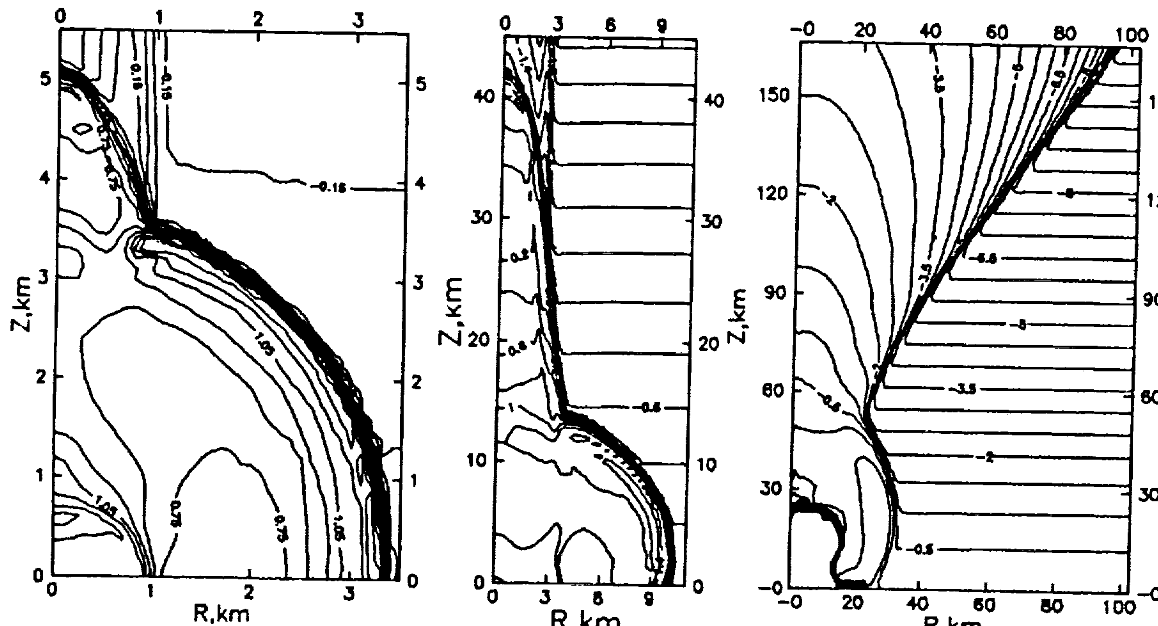


Figure 1. Pressure distributions (lines of constant ratio p/p_0) for r_0=10,30 and 100 m and t=1,3 and 10 s consequently.

References: 1. Melosh H.J. (1981) Atmospheric breakup of the terrestrial impactors, In *Multi-ring basins*, eds. P.H.Shultz and R.B.Merril, Pergamon, p.29. 2. Ahrens T.J., O'Keefe J.D. (1987), *Int. J. Impact engn.*, v.5, p.13-32. 3. Nemchinov I.V., Shuvalov V.V. (1992), *LPSC XXIII*, p.981-982. 4. Kiselev Yu.N., Nemchinov I.V., Shuvalov V.V. (1991), *Comput. Maths. Math. Phys.*, v.31, №1, p.901-921. 5. Ivanov B.A., Bazilevsky A.T., Kryuchkov K.P., Chernayya I.M. (1987), *J. Geophys. Res.*, v.12, B2, p.12,869-12,901. 6. Bergelson V.I., Nemchinov I.V., Orlova T.I., Khazins V.M. (1989), *Sov. phys. Dokl.*, v.34, №4, p.350-352. 7. Richmond A.D. (1978), *J. Geophys. Res.*, v.83, A9, p.4131-4145.

-13-110
ABS. ONLY
-167973
N94-20649

EFFECTS OF HYDRODYNAMICS AND THERMAL RADIATION IN THE ATMOSPHERE AFTER COMET IMPACTS

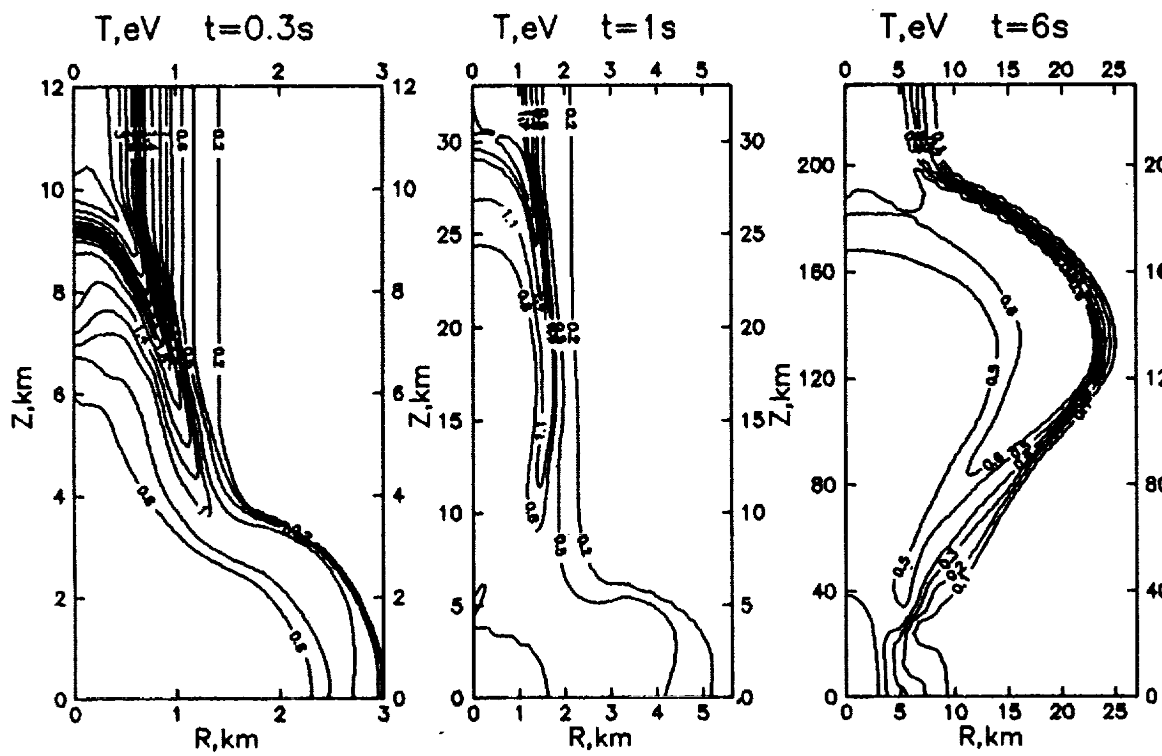
I. V. Nemchinov, M. P. Popova, L. P. Shubadeeva, V. V. Shuvalov, and V. V. Svetsov (Institute for Dynamics of Geospheres, Moscow, Russia)

Radiation phenomena in the atmosphere after impacts of cosmic bodies have special features in comparison with the surface nuclear explosions. First, initial concentration of energy after the impact is lower, and, second, a wake after the passage of the meteoroid through the atmosphere has a dramatic effect on the atmospheric flow and radiation transfer. Consequently, scaling laws [1] can not be employed for prediction of the flow in the atmosphere and the light flux on the Earth's surface.

If a density of a high-velocity impactor is low relative to the ground, as in a case of a comet impact on rocks, a major part of kinetic energy is converted to internal energy of dense and hot vapors [2]. But radiation effects can be essential even for fairly low velocities of the impactor. To clarify this issue we have undertaken calculations of 100-Mt explosions at the Earth's surface caused by small comets with velocities from 10 to 70 km/sec. That is, the initial concentration of energy has been varied. The calculations have shown that for velocities of the comet greater or about 20 km/sec a portion of energy emitted from the fireball exceeds 20% of the total energy of the explosion and this quantity does not change very much with the velocity. For an absolutely transparent atmosphere the energy of thermal radiation per unit area on the ground would be about 100 J/cm^2 at a distance of 100 km from the point of the impact. This radiation exposure is sufficient to ignite outdoor tinder materials. But atmospheric visibility reduces the radius of ignition to about 10 km for normal atmospheric conditions [3].

It had been shown in [4] that after the impact of a medium-sized comet (with radii from 200 m to 1 km) the light pulse on the Earth's surface is sufficient to ignite mass fires on continent-sized areas. The influence of the wake had not been taken into account. But the radiation flux on the ground in this case by far exceeds the magnitude necessary for ignition, and, hence, even rough estimates could give trustworthy results. In the case of the impact of a small comet (with a radius of about 100 m and smaller) it is a wake that crucially changes the atmospheric flow and enhances efficiency of radiation. We have carried out 2D radiation hydrodynamic calculations of a vertical impact of the comet. The wake was approximated by release of energy and momentum in a cylindrical layer with a radius equal to the radius of the meteoroid. It was assumed that the major part of kinetic energy of the comet was converted to heat.

Figure shows temperature contours in the atmosphere after the impact of a 100-m radius icy body at a velocity of 50



km/sec. The wake expands hydrodynamically (in 1 sec to 2 km in radius) and a great amount of mass and energy is injected into the wake. A velocity of a shock wave travelling upwards along the wake grows with the altitude and is above 40 km/sec in 1 sec after the impact. The temperatures are higher in the wake than near the ground. The plasma at the high altitudes becomes semitransparent and the radiation transfer becomes more effective than in the lower atmosphere. On the other hand, the light source, located very high, is less attenuated by atmospheric absorption. The energy per unit area is greater than 100 J/cm^2 at a distance of 300 km from the point of the impact for a perfect atmospheric visibility. The altitude of the source which emits a major portion of the light pulse is greater than 60 km. This effect severely enhances a hazard of wildfires after the impact of a small comet.

When a shock wave moves along the heated layer on the surface of the Earth, dust will be involved into the whirl inside the plume [5]. Due to the wake more dust is lofted into the upper atmosphere than in the case of the explosion of the equivalent energy.

REFERENCES: 1. Zel'dovich,Ya.B., and Raizer,Yu.P., Physics of shock waves and high temperature hydrodynamic phenomena, Acad. press, N.Y., 1967. 2. O'Keefe,J.D., and Ahrens,T.J., J. Geophys. Res., 87, 6668, 1982. 3. The effect on the atmosphere of a major nuclear exchange, Nat. Acad. press, Washington, D.C., 1985. 4. Nemtchinov,I.V.,and Svetsov,V.V., Adv. Space Res.,11, 6(65), 1991. 5. Artem'ev,V.I., Bergel'son et al., Izv. Akad. Nauk SSSR, Mekh. Zhidk. Gaza, No.2, 158, 1988.

514-35
ABS ONLY

N94-20650

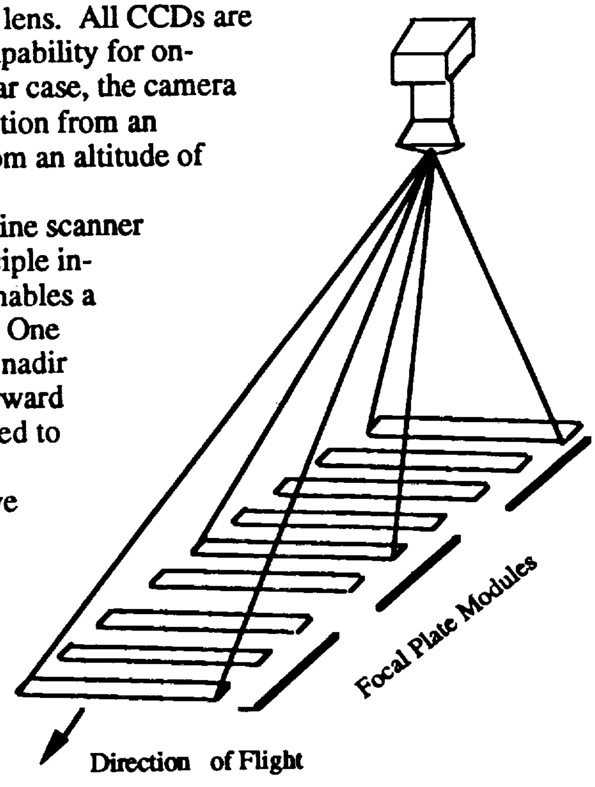
P-1

THE HIGH RESOLUTION STEREO CAMERA (HRSC) FOR THE LUNAR SCOUT I MISSION; G. Neukum, DLR, Institute for Planetary Exploration, Berlin-Adlershof/ Oberpfaffenhofen.

The High Resolution Stereo Camera (HRSC) is a planetary imaging system developed by the German Aerospace Research Establishment (DLR) with the involvement of the German Space Industry under the leadership of the German Space Agency (DARA) for the Russian Mars 94 and Mars 96 missions. The same instrument, virtually unmodified, is ideal for imaging the Moon. If flown on a Lunar Scout spacecraft, The HRSC will be operated so that it will produce data suitable for generation of a global lunar geodetic net, a global stereo image data set (both data sets produced at an orbit altitude of 200 kms approximately) and high resolution stereo imagery of areas of interest to the scientific community from an orbit altitude of 100 kms (resolution is a function of orbit altitude). All data will be digital.

The HRSC consists of a camera system and a mass memory system. The camera has one objective lens (focal length = 175 mm, f-number = 5.6 as configured for Mars) nine spectral filters and three focal plate modules. The focal plate modules have three line CCDs each for a total of nine. Each CCD (Thomson THX 7808) has 5272 7x7 micron pixels, of which 5184 are active. Each focal plate module is separately adjustable with respect to the objective lens. All CCDs are active simultaneously. There is significant capability for on-board camera parameter selection. In the lunar case, the camera system is capable of 8 meters per pixel resolution from an altitude of 200 kms and 4 meters per pixel from an altitude of 100 kms.

The HRSC operates in the "push broom" line scanner mode as shown in the figure. The basic principle involves a triple stereo image generation that enables a geometric reconstruction of the orientation. One focal plate module is forward looking, one is nadir pointing, and the third is aft looking. The forward looking focal plate module CCDs are dedicated to stereo, infrared (970nm) and photometry (675nm), the nadir module CCDs are sensitive in the blue (440nm), green (530nm) and the nadir stereo CCD in the visible (675nm), and the aft looking module has stereo, purple (750nm) and photometry (675nm). Stereo capability is provided by a viewing angle separation of 18.9 degrees between the fore and aft focal plate modules with respect to nadir.



The mass memory unit has a maximum capability of 2 Gbits and a net of 1 Gbit storage. A high degree of on-board data manipulation is possible, e.g., compression of 10:1, pixel summing and parameter selection. Capacity is sufficient for the lunar mapping modes that are planned. Software is being developed for data reduction and photogrammetric data processing for the Mars 94 / 96 missions and can be applied to the lunar case.

C-2

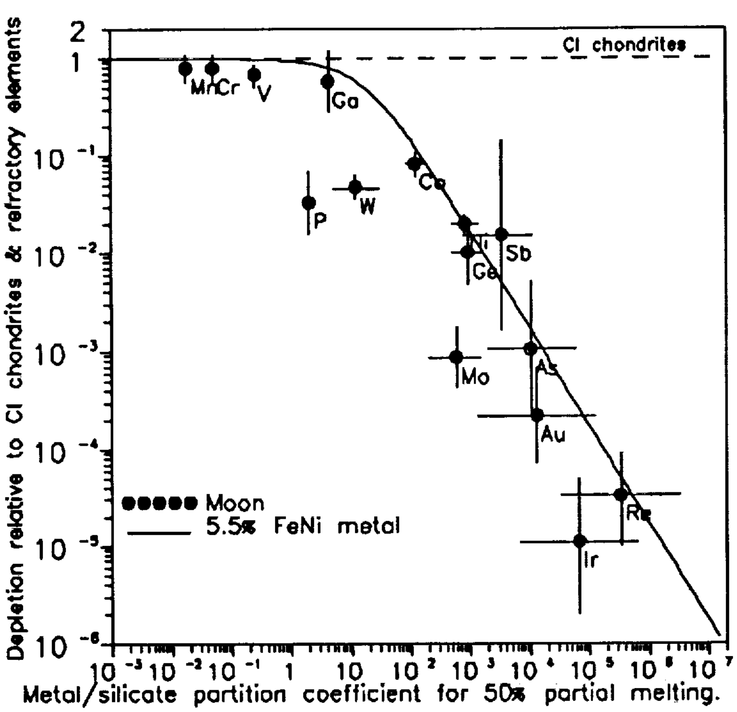
CORE FORMATION IN THE MOON: THE MYSTERY OF THE EXCESS DEPLETION OF Mo, W AND P;

H.E. Newsom and S.A. Maehr, Institute of Meteoritics and Department of Earth and Planetary Sciences, University of New Mexico, Albuquerque NM 87131

We have evaluated siderophile element depletion models for the Moon in light of our improved statistical treatment of siderophile element abundance data and new information on the physics of core formation. If core formation occurred in the Moon at the large degrees of partial melting necessary for metal segregation, according to recent estimates [1], then a significant inconsistency (not seen in the eucrite parent body) exists in the depletion of the incompatible siderophile elements Mo, W and P, compared to other siderophile elements in the Moon. The siderophile data, with the exception of Mo, are most consistent with terrestrial initial siderophile abundances and segregation of a very small core (<1 wt%) in the Moon. Our improved abundance estimates and possible explanations for these discrepancies are discussed below.

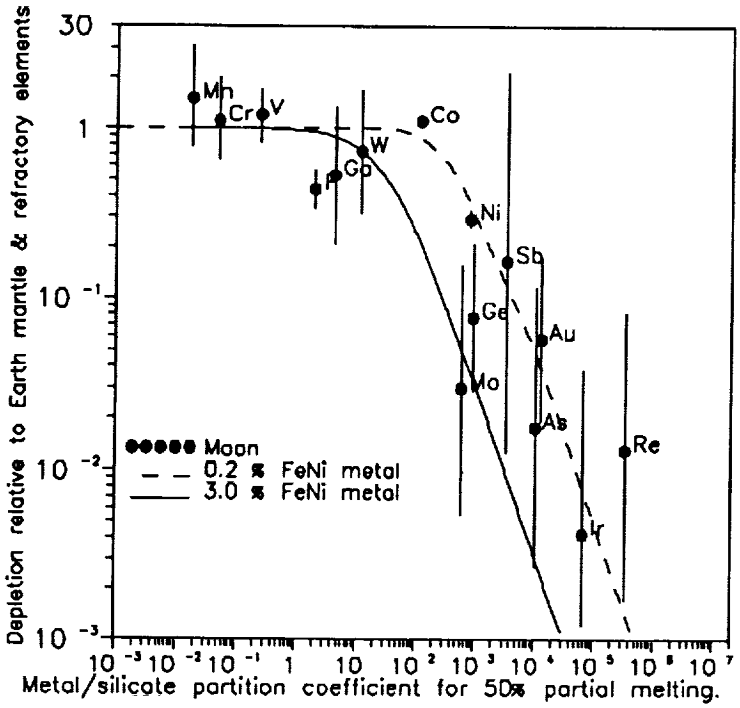
We have begun a recalculating the depletions of siderophile elements in the Earth and Moon using an improved statistical approach that takes into account the log normal behavior of siderophile element to lithophile element ratios. Preliminary results for depletions relative to CI and refractory elements are: for W in the Moon, mean 0.047, high 0.064, low 0.035, for Mo in the Moon, mean 0.00087, high 0.0018, low 0.00043, for W in the Earth, mean 0.0026, high 0.0057, low 0.0012, for Mo in the Earth, mean 0.029, high 0.045, low 0.019.

During core formation siderophile elements are depleted in the residual silicates of a parent body. Important factors controlling the pattern of siderophile element depletion include the amount of metal and the metal to silicate-melt partition coefficients. Another important factor [2] is the degree of partial melting during metal segregation, which is quantitatively controlled by the silicate-mineral to silicate-melt partition coefficients. The mineral/melt partitioning behavior for the siderophile elements varies drastically, from Ni and Co, which are strongly compatible, to elements, such as Ge, which are not strongly fractionated by mineral/melt partitioning, to W and Mo which are very incompatible. Because the behavior of these elements have an opposite dependence on the degree of partial melting, during a core formation event there will be a unique degree of partial melting for which the observed depletions of the different siderophile elements will be consistent with the same metal content.



In the case of the Moon, Newsom [3,4] showed that a smooth dependence of depletion versus metal to bulk-silicate partition coefficient only occurs for very low degrees of partial melting (5% to 10%). Recent results on the physics of metal segregation [1], however, strongly indicate that a much higher degree of partial melting, 50% or greater is needed to allow small amounts of metal to segregate from solid silicates. The problem is that metal does not wet silicates, at least at the low pressures in the Moon, and there is a finite yield strength that must be overcome for the metal to separate. Metal segregation at high degrees of partial melting is supported by the siderophile element modeling for the Eucrite Parent Body [5], which is consistent with metal segregation between 20% and 70% partial melting. If core formation in the Moon is assumed to have occurred at 50% partial melting (Fig. 1), than the observed depletions for W, Mo and P are too large, by a factor of 10 for a chondritic initial Moon. If terrestrial mantle initial abundances are assumed (Fig. 2), then the depletions of W and P may be compatible with the other siderophile elements within a factor of two, but Mo is still too depleted, by a factor of almost ten. Several possibilities can be discussed.

CORE FORMATION IN THE MOON: Newsom, H.E. and Maehr S.A.



1. W and Mo are volatile under oxidizing conditions, as seen in large depletions of several orders of magnitude in some CAI's from carbonaceous chondrites [6]. In general, however, cosmochemical fractionations of W and Mo relative to refractory siderophile and lithophile elements are surprisingly small compared to the siderophile element depletions in samples from differentiated bodies. For example, the Mo/Ce ratio in carbonaceous chondrites only ranges up to 25% greater than the CI ratio (which is the wrong direction). The LL ordinary chondrites do have a lower Mo/Ce ratio than CI's, but only by less than a factor of 2. An additional problem with this explanation is that there is no evidence of a significant oxidized component on the Moon.

2. Uncertainties in partition coefficients can probably be ruled out because a factor of ten difference for Mo would be needed. The metal/silicate partition coefficients for W, Mo, Co and Ni have been checked by several groups. Although some problems have arisen regarding the results for Co and Ni, all of the investigations are in agreement for the conditions used in the modeling (1300 °C, log fO_2=-12.6). The metal/silicate partition coefficients for some of the other elements, such as As, Sb, and the highly siderophile elements, cannot be trusted. The mineral/melt behavior of these elements is reasonably well established through experimental work and element correlations, except possibly for the behavior of Mo in the Moon.

3. Siderophile element abundances in the Moon and the Earth (a possible initial component) are well known for Ni, Co, W and Mo in the Earth, and for W in the Moon. The lunar depletion for Mo is based on less than a dozen analyses for only a few sites and could be incorrect. Additional data is also needed to check the variability of siderophile elements in different lunar reservoirs and sample sites, Ge for example is enriched in Apollo 14 samples compared to other Apollo sites [7], and variability in the abundances of P have been observed. The estimated Ni and Co abundances could be too low, if significant olivine fractionation has occurred, but this would make the discrepancy even worse. Supporting the data for Co and Ni are the depletion data for other siderophile elements, especially Ga, Ge, As, Sb and Au.

Conclusions- The currently available data and siderophile element depletion modelling suggest that for 50% partial melting during metal segregation, a better fit, with the exception of Mo, is seen for terrestrial initial abundances than for chondritic. A metal content for the Moon as large as 2-5 wt% is highly unlikely for terrestrial initial abundances. These results continue to emphasize the critical need to determine the size of the lunar core by geophysical methods. There is no obvious answer to the excess depletion problem for W, Mo and P in the Moon. However, significant progress can be made in better determination of the abundances of many siderophile elements in the Moon and their metal/silicate partition coefficients. If improved data for the other siderophile elements, such as Ga, Ge, As, Sb, and Au continue to be consistent with Co and Ni, in contrast to the data for Mo and W, a much stronger case could be made for a connection with Earth mantle initial abundances in the Moon, and for a very small lunar metal core (< 1 wt%).

References: [1] Taylor (1992) JGR Planets 97, 14,717. [2] Newsom and Drake (1982) Nature 287, 210. [3] Newsom (1984) EOS 65, 396. [4] Newsom (1986) Origin of Moon p. 203. [5] Hewins and Newsom (1988) In Meteorites and the Early Solar System 73. [6] Fegley and Palme (1985) Earth and Planet. Sci. Lett. 72 311. [7] Dickinson et al. LPSC 19th 189. *Acknowledgement*: Supported by the National Science Foundation and the Institute of Meteoritics.

DATING NATIVE GOLD BY NOBLE GAS ANALYSES; S. Niedermann[1], O. Eugster[1], B. Hofmann[2], Ch. Thalmann[1], and W.U. Reimold[3], [1] Physikalisches Institut, University of Bern, Sidlerstrasse 5, CH-3012 Bern, Switzerland; [2] Naturhistorisches Museum, Bernastrasse 15, CH-3005 Bern, Switzerland; [3] Econ. Geol. Res. Unit, Department of Geology, University of the Witwatersrand, P.O. Wits 2050, Johannesburg, RSA

Our recent work on He, Ne, and Ar in Alpine gold samples [1,2] has demonstrated that gold is extremely retentive for He and could thus, in principle, be used for U/Th-^{4}He dating. For vein-type gold from Brusson, Northern Italy, we derived a U/Th-^{4}He age of 36 Ma, in agreement with the K-Ar formation age of associated muscovites and biotites [1,3]. However, in placer gold from the Napf area, Central Switzerland, we observed large excesses of both ^{4}He and radiogenic ^{40}Ar ($^{40}Ar_{rad}$, defined as ^{40}Ar - 295.5·^{36}Ar). The gas release systematics [2] indicate two distinct noble gas components, one of which is released below about 800°C and the other one at the melting point of gold (1064°C). We now present results of He and Xe measurements in a 1 g placer gold sample from the river Krümpelgraben, as well as He and Ar data for Brusson vein-type gold and for gold from the Lily Gold Mine, South Africa [4]. We calculate reasonable U/Th-^{4}He as well as U-Xe ages based on those gases which are released at ≤800°C. Probably the low-temperature components represent in-situ-produced radiogenic He and fission Xe, whereas the gases evolving when gold melts have been trapped during gold formation. Therefore only the low-temperature components are relevant for dating purposes.

Table 1 gives the concentrations of ^{4}He, $^{40}Ar_{rad}$, and fission-type Xe (Xe_f) for the low-temperature (L) and the high-temperature (H) components separately. For Krümpelgraben and Lily gold, 80-90% of ^{4}He is released only when gold melts. In contrast, most ^{4}He and $^{40}Ar_{rad}$ in Brusson gold is outgassed below 800°C. $^{40}Ar_{rad}$ in Lily gold appears to be more abundant in the H than in the L component; however, since 40% of total $^{40}Ar_{rad}$ were released even above 1200°C, we suspect a major fraction of $^{40}Ar_{rad}$ to originate from silicate inclusions. In quartz associated with Lily gold we found huge amounts of $^{40}Ar_{rad}$: (6090 ± 110)·10^{-8} cm^3 STP/g. Therefore all $^{40}Ar_{rad}$ (H) may be from silicates. Fission-type Xe was observed in both the L and the H components for Krümpelgraben gold despite large uncertainties.

In order to find out which of the components, if any, represents in-situ-produced ^{4}He, $^{40}Ar_{rad}$, and Xe_f, we have calculated model gas retention ages based on the data from Table 1; they are presented in Table 2. For Krümpelgraben and Brusson gold, these ages can be compared with the estimated age of Alpine gold of ~32 Ma [3]. Since the H component of ^{4}He is almost completely missing for Brusson, we may assume that in-situ-produced ^{4}He is released below 800°C. As a matter of fact, the U/Th-^{4}He ages calculated from the L components are consistent with 32 Ma except for Brusson sample 1. This small (9.66 mg) sample may have contained more U than the other ones. The ^{238}U-^{134}Xe and ^{238}U-^{136}Xe ages for the L component agree also within the (very large) error limits with 32 Ma. On the other hand, the ages calculated from the H components of Krümpelgraben He and Xe are much too high, implying that ^{4}He (H) and Xe_f (H) were trapped by the forming gold from hydrothermal fluids which were already enriched in radiogenic and fissiogenic gases.

The low-temperature release of in-situ-produced gases indicates that U and Th are not homogeneously distributed in the gold, but may be concentrated in small inclusions around which radiogenic ^{4}He and Xe_f are found (α particles from U and Th decays have a range of ~10-40μm [5]). The low release temperatures might be a consequence of abundant radiation damages in these regions. In this way we can also explain variations of the U concentration between gold samples from the same location. U is actually incompatible with Au, i.e. it does not fit into the crystal lattice. On the other hand, trapped He may be sited within the crystal lattice of Au.

An interpretation of $^{40}Ar_{rad}$ (L) as being produced in situ is not valid, as demonstrated by the unreasonably high K-^{40}Ar model ages obtained for the Brusson samples (Table 2). Obviously most $^{40}Ar_{rad}$ was not produced in situ. A trapped $^{40}Ar_{rad}$ component released at low temperatures is expected to be accompanied by trapped ^{4}He and Xe_f components and, therefore, not all ^{4}He and Xe_f in the L component can be of in situ origin. However, we do not know the ratio ^{4}He/$^{40}Ar_{rad}$ in the trapped component. On the other hand, for the placer gold samples studied in [2] we obtain U/Th-^{4}He ages which are considerably lower than 32 Ma based on the L components of ^{4}He, probably due to lower U and Th concentrations than assumed.

We conclude that the ^{4}He and Xe_f components released from gold at ≤800°C may represent in-situ-produced gases, whereas essentially all $^{40}Ar_{rad}$ and the He and Xe released at the melting point of gold were trapped during formation. Currently, the ^{238}U-^{136}Xe method seems to be most promising, if the large uncertainties can be reduced. From the isochron in a ^{136}Xe/^{130}Xe versus U/^{130}Xe plot for several gold samples of the same age and the same trapped Xe composition, but with different concentrations of U or trapped Xe, we should be able to

correct for the trapped Xe_f component and derive the formation age. For this method it is, however, essential to analyze the noble gases and U in the same sample.

Acknowledgements: We thank Prof. C.R. Anhaeusser for the Lily Gold Mine samples. This work was supported by the Swiss National Science Foundation.

References: [1] Eugster O., Hofmann B., Krähenbühl U. and Neuenschwander J. (1992) *Meteoritics* **27**, 219-220. [2] Eugster O., Hofmann B., Niedermann S. and Thalmann Ch. (1993) *LPS* XXIV (this issue). [3] Diamond L.W. (1990) *Am. J. Sci.* **290**, 912-958. [4] Anhaeusser C.R. (1986) *Min. Dep. of Southern Africa*, 187-196. [5] Friedlander G., Kennedy J.W., Macias E.S. and Miller J.M. (1981) Nuclear and Radiochemistry, John Wiley & Sons.

Table 1 Radiogenic and fissiogenic noble gases in Alpine and South African gold samples (He and Ar: 10^{-8} cm^3 STP/g; Xe: 10^{-12} cm^3 STP/g).

		Low-temperature component (≤800°C)				High-temperature component (>800°C)			
Sample	Weight[g]	^{4}He	^{40}Ar	^{134}Xe	^{136}Xe	^{4}He	^{40}Ar	^{134}Xe	^{136}Xe
Krümpelgraben	1.02	540 ±30	-	0.034 +0.024 -0.019	0.017 +0.031 -0.017	2740 ±200	-	0.064 ±0.028	0.031 ±0.012
Brusson 1	0.00966	458 ±40	116 ±11	-	-	-	-	-	-
Brusson 2	0.0205	179 ±18	54 +35 -17	-	-	-	-	-	-
Brusson 3	0.0509	201 ±11	46.0 ±2.7	-	-	7.5 ±0.4	8.7 ±0.9	-	-
Lily GM2	0.00549	97.4 ±4.5	20.8 ±2.8	-	-	905 ±48	140 ±16	-	-

Table 2 Model formation ages (Ma) of Alpine gold calculated from the low- and high-temperature components of ^{4}He, $^{134}Xe_f$, $^{136}Xe_f$, and $^{40}Ar_{rad}$, respectively. The following concentrations of K, Th, and U were assumed [1]: Krümpelgraben 25 ppm K, 0.1 ppm Th, 1.3 ppm U; Brusson 40 ppm K, 0.9 ppm Th, 0.4 ppm U.

	Low-temperature component (≤800°C)				High-temperature component (>800°C)			
Sample	U/Th-^{4}He	U-^{134}Xe	U-^{136}Xe	K-^{40}Ar	U/Th-^{4}He	U-^{134}Xe	U-^{136}Xe	K-^{40}Ar
Krümpelgraben	34 +15 -8	67 +51 -43	28 +52 -28	-	169 +72 -41	126 ±65	51 ±25	-
Brusson 1	62 +30 -17	-	-	2990 +560 -400	-	-	-	-
Brusson 2	24 +12 -6	-	-	1970 +780 -520	-	-	-	-
Brusson 3	27 +14 -7	-	-	1780 +440 -290	1.0 +0.5 -0.3	-	-	500 +180 -110

5/7-90 ABS ONLY

N94-20653

HELIUM IN INTERPLANETARY DUST PARTICLES. A. O. Nier and D. J. Schlutter, School of Physics and Astronomy, University of Minnesota, Minneapolis, MN 55455, USA.

Helium and neon were extracted from fragments of individual stratosphere-collected interplanetary dust particles (IDPs) by subjecting them to increasing temperature by applying short-duration pulses of power in increasing amounts to the ovens containing the fragments. The experiment was designed to see whether differences in release temperatures could be observed which might provide clues as to the asteroidal or cometary origin of the particles. Variations were observed which show promise for elucidating the problem.

In an experiment several years ago, we determined the amounts and isotopic composition of the total He and Ne extracted from individual IDPs by heating (1). In a later experiment, particles were step-heated and the release pattern observed (2). Flynn (3), building on the work of earlier investigators, constructed a model which predicted that most cometary particles in the 20 μm diameter range may be heated to 700 to 800°C during their deceleration to the stratosphere, where they are collected; asteroidal particles of a similar size may be heated to only 600°C. The difference is attributed to the fact that, in contrast to dust particles originating in asteroids, most cometary particles enter the atmosphere with appreciable initial kinetic energy, and hence more energy must be dissipated during their fall and deceleration in the atmosphere.

Whereas in our recent step-heating experiments, oven powers were typically held constant for 5 minutes before advancing to the next step, in the present work a succession of increasing power pulses of 5 seconds duration were employed. Tests showed that due to the extremely low mass of the ovens employed, power pulses of this duration led to oven temperature variation with time approximating the heat pulse experienced by IDPs in their rapid deceleration in the earth's atmosphere (4). In the results reported in the present abstract, fragments of 24 particles were investigated. As in the earlier step-heating experiments, the particles had "diameters" of roughly 20 μm and were fragments of somewhat larger particles, other fragments of which are undergoing mineralogical and morphological investigation.

In our present experiments the amount of accumulated helium released from a particle was plotted against the peak temperatures reached during the successive pulses. For example, Figure 1 for particle No. 45 shows that as the pulse power is progressively increased, half of the helium has been extracted when the power level reaches 2.2 watts, corresponding to a peak oven temperature of 750°C. The peak temperature corresponding to the pulse where half of the total helium had been extracted was considered to be a measure of the previous thermal history of the particle. For example, if this temperature was low, it probably means that the particle had experienced little heating, and hence outgassing, in its deceleration in the earth's atmosphere, and vice versa. Moreover, there should be a correlation between this temperature and the total amount of gas extracted. Figure 2 shows the relationship

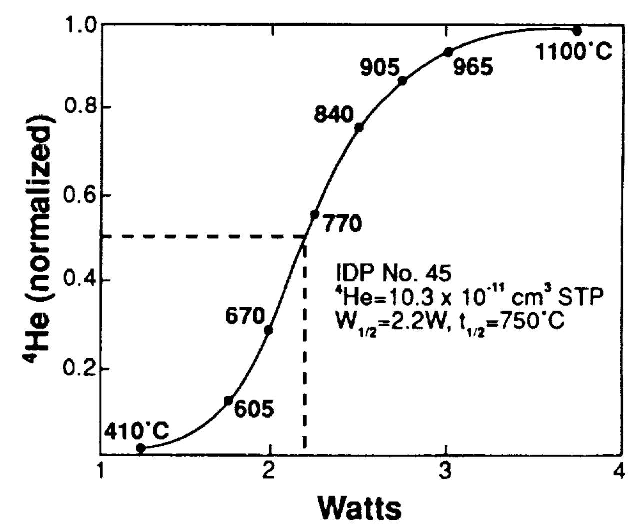


Fig. 1. Fraction of total helium released versus power applied to oven in 5 sec. pulse sequence. The power is converted to temperatures which are indicated on the curve.

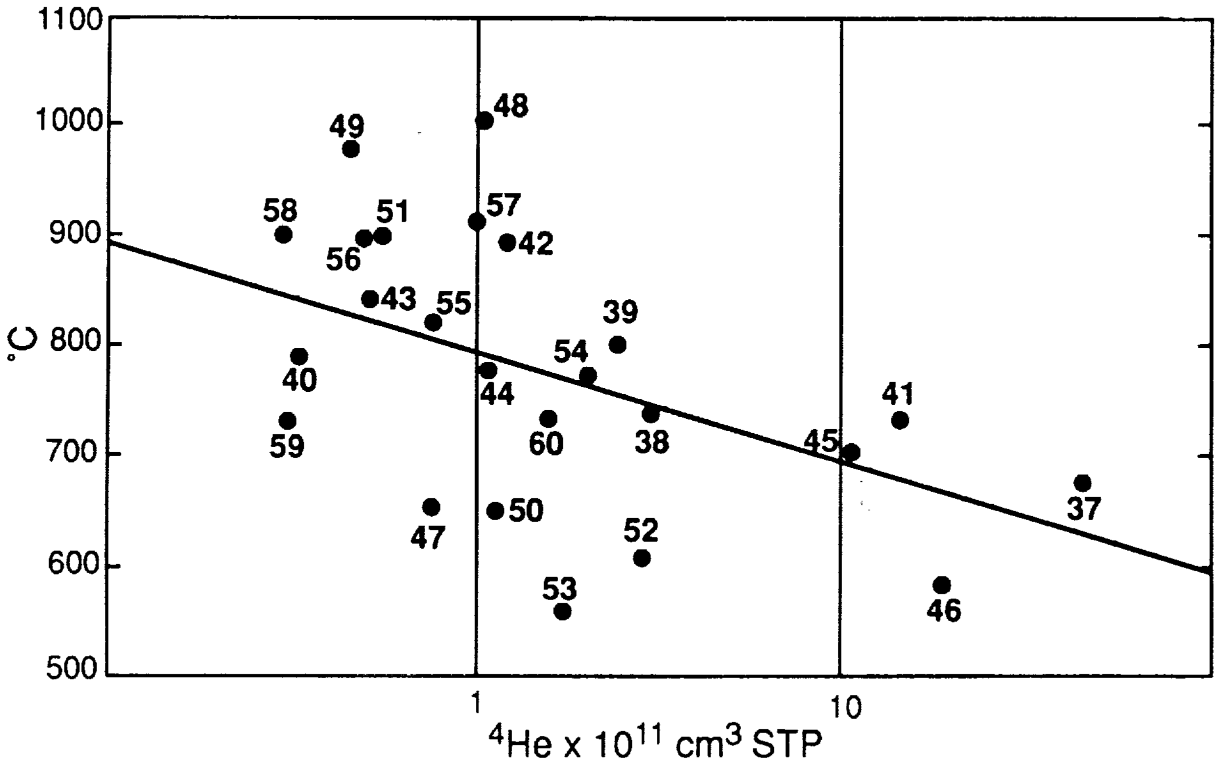


Fig. 2. Peak Temperature (°C) for removal of 50% of helium by 5 second heat pulses versus helium content of IDPs. Sloping line is least squares fit to points.

observed for the 24 particles (numbered 27 to 60, in our terminology), reported elsewhere (5, 6). The results suggest that the particles with the largest amounts of helium (and lowest extraction temperature required) are probably of asteroidal origin. Since composition and morphology also can affect the extraction temperature, final conclusion should await the results of the ancillary experiments being performed.

Since we do not know how much heating the particles experienced in their deceleration in the atmosphere, the question arises whether or not the employment of a succession of heat pulses, such as used here, does provide clues about previous heating. In several cases the progression of increasing power pulses was interrupted and a second heating progression started. It was found that essentially no additional helium was released until the power level was reached where the first sequence was interrupted. As expected, the curve for helium release for the second sequence was shifted to higher temperature. Because of the shortage of IDPs only a few such tests could be made on IDPs. On the other hand, numerous tests were made with lunar particles of comparable size, clearly illustrating the temperature shift.

REFERENCES: (1) Nier, A. O. and D. J. Schlutter, 1990, *Meteoritics* **25**, 263 - 267. (2) Nier, A. O. and D. J. Schlutter, 1992, *Meteoritics* **27**, 166 - 173. (3) Flynn, G. J., 1989, *Icarus* **77**, 287 - 310. (4) Love, S. G. and D. E. Brownlee, 1991, *Icarus* **89**, 26 - 43. (5) Nier, A. O. and D. J. Schlutter, 1992, *LPSC XXIII*, 991 - 992. (6) Nier, A. O. and D. J. Schlutter, 1992, *Meteoritics* **27**, 268 - 269.

GEOLOGIC MAPPING OF NORTHERN ATLA REGIO ON VENUS: PRELIMINARY DATA

A.M.Nikishin *, G.A.Burba **
* - Dept. of Geology, Moscow University, Moscow, 119899, Russia
** - Vernadsky Institute, Moscow, 117975, Russia

The Northern part of Atla Regio within the frame of C1-formate Magellan photomap 15N197 was mapped geologicaly at scale 1:8,000,000.

This is a part of Russia's contribution into C1 geologic mapping efforts (1). The map is reproduced here being reduced about twice (fig. 1). The map shows Northen Atla area is predominantly a volcanic plain with numerous volcanic features: shield volcanoes, domes and hills with various morphology, corona-like constructions, radar bright and dark spots often with flow-like outlines.

Relatively small areas of tessera occured in the area are mainly semiflooded with the plain material. Tesserae are considered to be the oldest terrains within the map sheet.

There are many lineated terrains in the region. They are interpreted as the old, almost-buried tesserae (those with crossed lineaments) or partly buried ridge belts (those with parallel lineaments). This lineated terains have an intermediate age between the young volcanic plains and the old tessera areas.

Two prominent high volcanic shields are located within the region - Ozza Mons and Sapas Mons.

The most prominent structure in Northern Atla is Ganis Chasma rift. The rift cuts volcanic plain and is considered to be under formation during approximately the same time with Ozza Mons shield. Ganis Chasma rift valley is highly fractured and bounded with fault scarps. Rift shoulder uplifts are typical for Ganis Chasma. There are few relatevily young volcanic features inside the rift valley. The analysis of fracturing and rift valley geometry shows the rift originated due to 5-10% crustal extention followed by the crustal subsidence.

The age sequence summary for the main terrain types in the region is (from older to younger ones):

1 - tesserae;
2 - lineated terrains with crossed lineaments (intermediate type between 1 and 3);
3 - lineated terrains with parallel lineaments;
4 - volcanic plains;
5 - prominent volcanic shields and Ganis Chasma rift valley.

The geologic structure of Atla Regio as it appeared now with the Magellan high resolution images is very close to that of Beta Regio. Such conclusion coincide with the earlier ones based on the coarser data (2,3).

References: 1. G.A.Burba, N.N.Bobina, V.P.Shashkina (1993). Russia's contibution ... (This volume). 2. D.A.Senske and J.W.Head. LPS XX (abstr.), 1989, p.986-987. 3. A.M.Nikishin. Earth,Moon,and Planets,1990, vol.50/51,p.101-125.

NORTHERN ATLA REGIO, VENUS. Nikishin, A.M. et al.

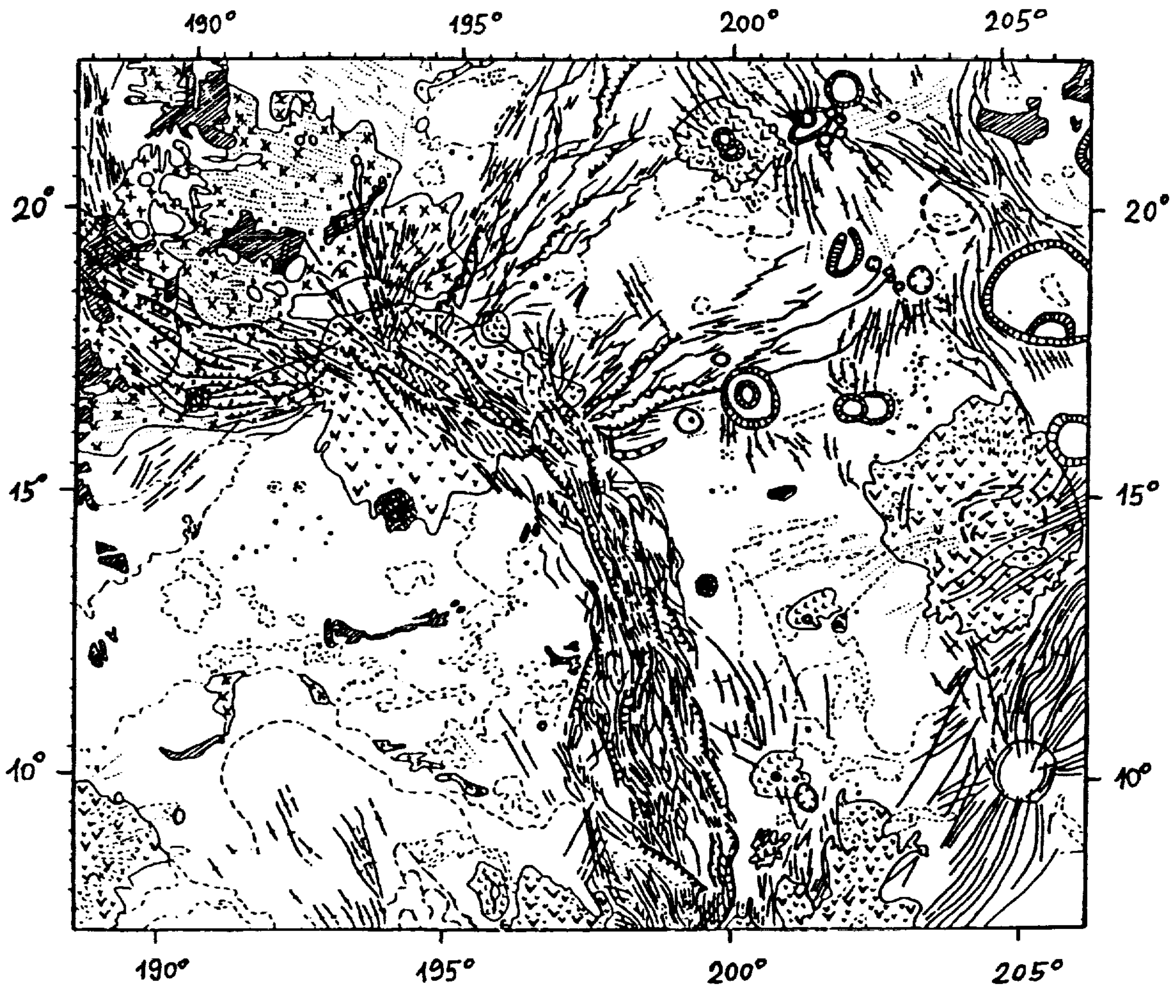


Fig.1. Geologic map of Northern Atla Regio (sheet C1-15N197)

volcanic plain, undivided
tessera
lineated terrain with parallel lineaments (ridge belt ?)
lineated terrain with crossed lineaments (intermediate type between 2 and 3)
prominent high volcanic shield
low volcanic shield
volcanic domes and hills
corona or arachnoid (ringed ridge system)
impact crater
caldera-like depression
prominent fault scarp (normal fault)
narrow grabens or normal faults
ridges
narrow radar-bright lineaments with unrevealed relief
boundaries of areas with different radar brightness (boundaries of lava flows ?)

S9-91
ABS. ONLY

N94-20655

p. 2

BETA REGIO RIFT SYSTEM ON VENUS: GEOLOGIC INTERPRETATION OF MAGELLAN IMAGES

A.M.Nikishin *, N.N.Bobina **, V.K.Borozdin **, G.A.Burba **
* - Dept. of Geology, Moscow University, Moscow, 119899, Russia
** - Vernadsky Institute, Moscow, 117975, Russia

Magellan SAR images and altimetric data were used to produce a new geologic map of the Northern part of Beta Regio within the frames of C1-30N279 map sheet. It was part of our contributions into C1-formate geologic mapping efforts. The original map is at 1:8,000,000 scale.

The rift structures are typical for Beta Regio on Venus (1-3). There are many large uplifted tessera areas on Beta upland. They occupy areas of higher topography. These tessera are partly buried by younger volcanic cover of plain material (fig. 1). These observations shows Beta upland was formed mainly due to lithospheric tectonical uplifting, and only partly was constructed by volcanic activity.

A number of rift valleis traverse Beta upland and spread to the surrounding lowlands. The largest rift crosses Beta N to S. Typical width of rifts is 40 to 160 km. Rift valleis in this region are structuraly represented by crustal grabens and half-grabens. There are symmetrical and asymmetrical rifts. A lot of them have shoulder uplifts with the relative high up to 0.5-1 km and width 40 to 60 km. Preliminary analysis of the largest rift valley structural cross-sections leads to conclusion it have originated due to 5-10% crustal extension.

The prominent shield volcano - Theia Mons - is located at the centre of Beta rift system (fig.2). It could be considered as the surface manifistation of the upper manthle hot spot. Most of the rift belts are located radially to Theia Mons.

The set of these data leads to conclusion that Beta rift system has an "active-passive" origin. It was formed due to the regional tectonic lithospheric extension. Rifting was accelerated by the upper mantle hot spot located under the centre of passive extension (under Beta Regio).

References: 1. Campbell D.B. et al., 1984, Science, vol.226, p.167-170. 2. Senske D.A. and Head J.W., 1989, LPS XX, p.986-987. 3. Stofan E.R. et al., 1989, Geol.Soc.Amer.Bull., v.101, p.143-156.

Legend for the geologic map (fig.1 - next page):

- volcanic plain, undivided
- tessera
- hilly plain (semiflooded tessera ?)
- lineated terrain with parallel lineaments (ridge belt ?)
- RP ridged plain (plain with a system of sparse ridges)
- prominent high volcanic shield
- volcanic domes or hills
- corona or arachnoid (ringed ridge system)
- impact crater
- caldera-like depression
- prominent fault scarp (normal fault)
- narrow grabens or normal faults
- ridge (compressional structure)
- structural lineaments within tessera
- boundaries of the areas with different radar brightness

BETA REGIO RIFT SYSTEM ON VENUS. Nikishin,A.M. et al.

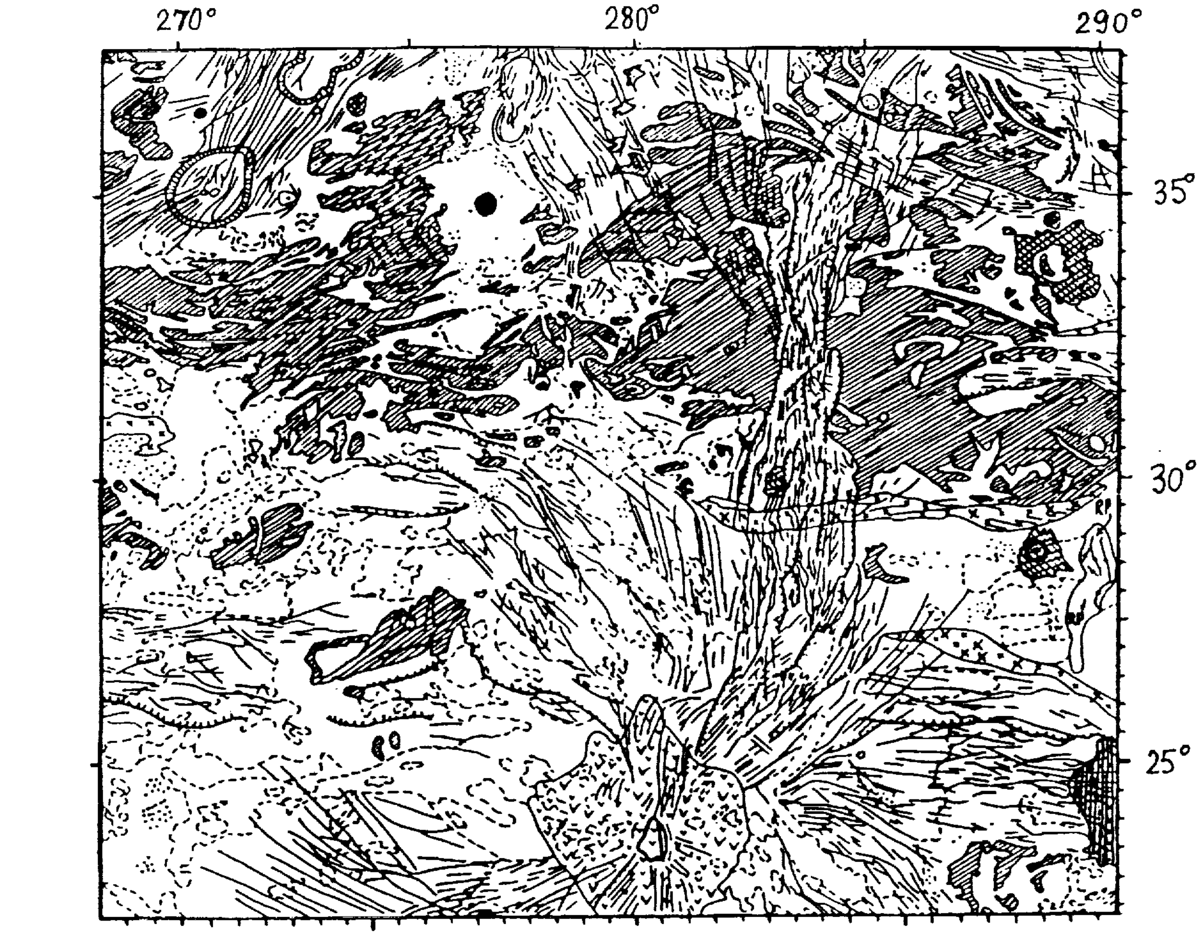


Fig.1. Geologic map of Northern Beta Regio, sheet C1-30N279
(The map's legend explanation is given at the preceding page)

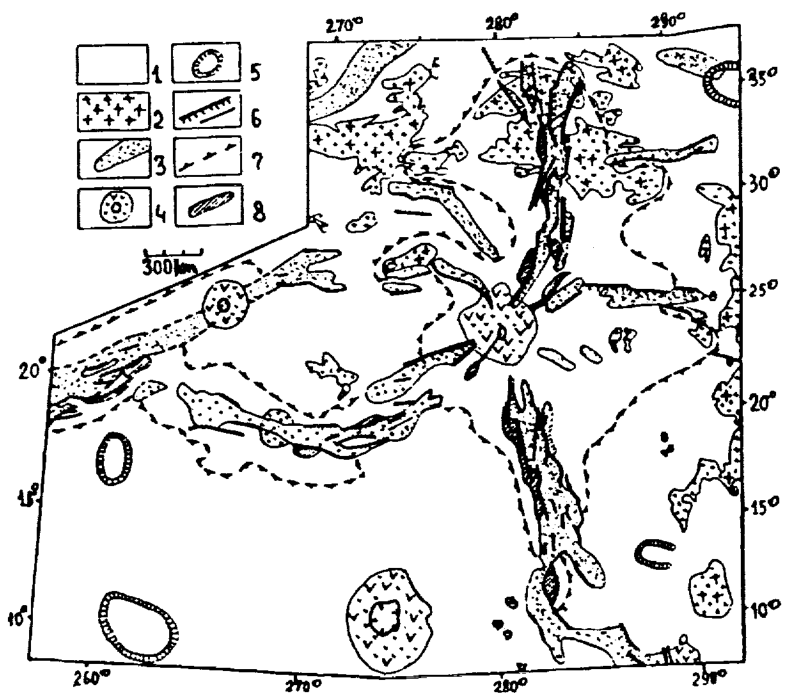


Fig.2. Tectonics sketch map of Beta Regio
Legend: 1 - mainly plain, undivided; 2 - tessera; 3 - rift valley with fractured bottom; 4 - volcanic shield; 5 - corona; 6 - normal fault; 7 - boundary of tectonic uplift; 8 - rift's uplifted shoulder

S20-91
ABS. ONLY
167980
N94-20656

BETA REGIO - PHOEBE REGIO ON VENUS: GEOLOGIC MAPPING WITH THE MAGELLAN DATA;

A.M.Nikishin *, V.K.Borozdin **, N.N.Bobina **, G.A.Burba **
* - Dept. of Geology, Moscow University, Moscow, 119899, Russia
** - Vernadsky Institute, Moscow, 117975, Russia

The geologic maps of C1-15N283 and C1-00N283 sheets were produced (preliminary versions) with Magellan SAR images. This work was undertook as a part of Russia's contribution into C1 geologic mapping efforts (1). The scale of the original maps is ~1:8,000,000 and the maps are reproduced here at a reduced size.

The oldest terrains within the sheets are tesserae. The areas of tessera have here fragment-like shapes. Tessera's margins are partly buried by younger plain materials. This is material of volcanic plains - the predominant terrain type of the area. The plains possess diverse and numerous volcanic features: shield volcanoes, domes and hills of various morphology, corona-like constructions, radar bright and dark spots and areas which often have flow-like shapes.

Devana Chasma rift crosses the surface N to S between Beta Regio in the North part of the area and Phoebe Regio in the South. Rift's normal faults dissect volcanic plains and shield volcanoes. There are shoulder uplifts along the Devana Chasma rift. Rift valleys are the youngest structures in the area. The age of volcanic shields is between that of plains and Devana Chasma rift.

The structural analysis of rift shows the rift origin was due to 5-10% crustal extension followed by the subsidence of the crust.

Reference: 1. G.A.Burba, N.N.Bobina, V.P.Shashkina(1993). Russia's contribution ... (This volume)

Legend for the geologic map (fig.1 - next page):

volcanic plain, undivided
tessera
hilly plain (semiflooded tessera ?)
lineated terrain with parallel lineaments (ridge belt ?)
RP ridged plain (plain with a system of sparse ridges)
prominent high volcanic shield
low volcanic shield
volcanic domes or hills
corona or arachnoid (ringed ridge system)
impact crater
caldera-like depression
prominent fault scarp (normal fault)
narrow grabens or normal faults
ridge (compressional structure)
structural lineaments within tessera
narrow radar-bright lineaments with unrevealed relief
boundaries of the areas with different radar brightness

BETA REGIO - PHOEBE REGIO ON VENUS. Nikishin, A.M. et al.

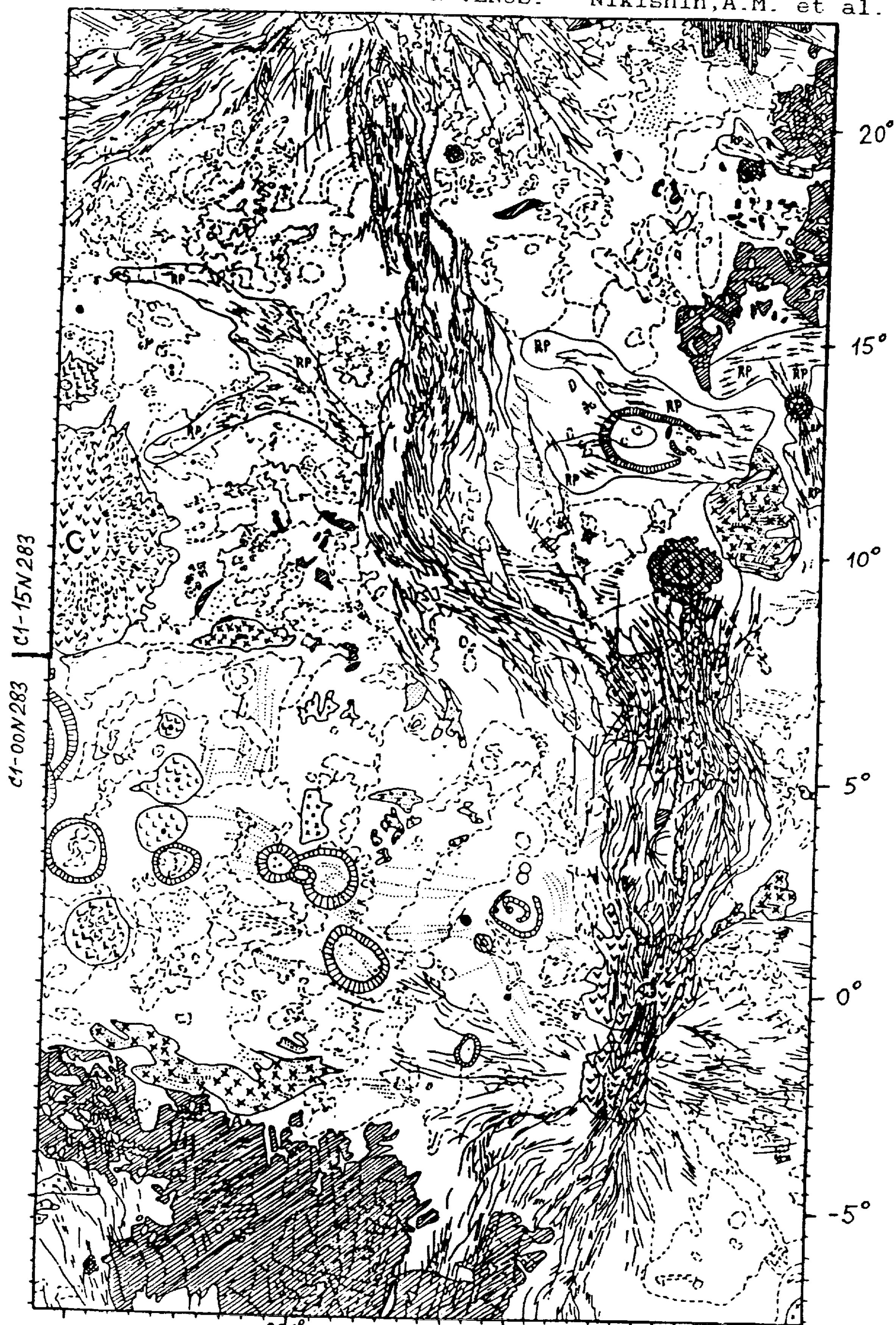


Fig.1. Geologic map of S.Beta - N.Phoebe region on Venus

52/-91 ABS. ONLY

N94-20657

LARGEST IMPACT FEATURES ON VENUS: NON-PRESERVED OR NON-RECOGNIZABLE ?

Olga V.Nikolaeva (Vernadsky Institute, 19 Kosygin str. 117975 Moscow Russia)

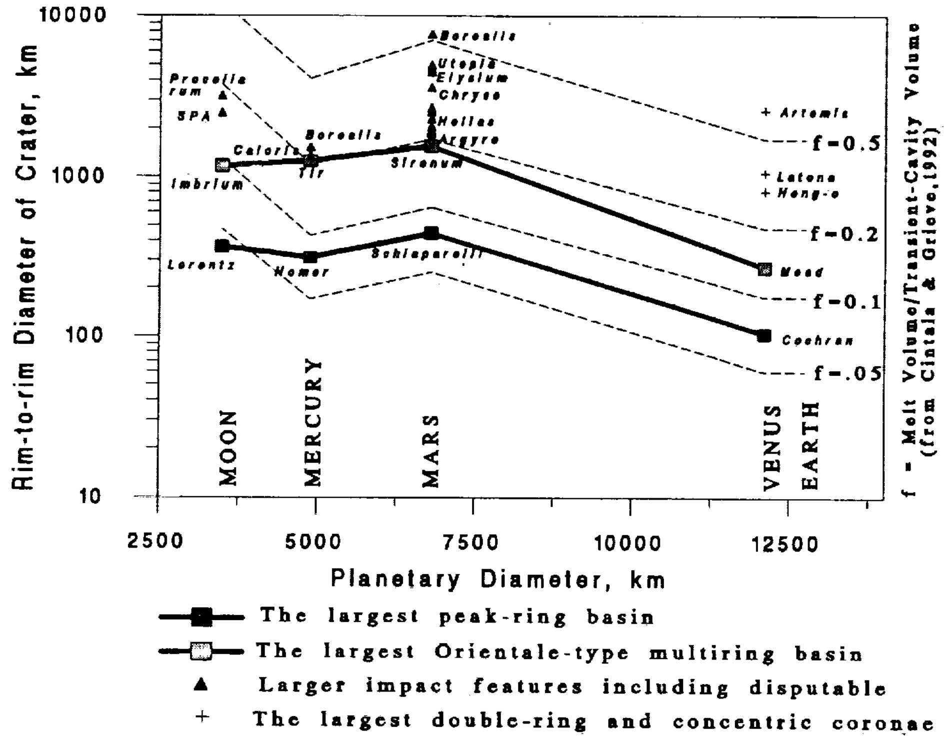
Conventional explanation of a lack of impact craters with diameters >300 km on Venus [1] is that they formed during the intense bombardment era and had lunar-like morphology, but they are not preserved now because of rapid viscous relaxation of their topograpy or/and high endogenous reworking of surface. Other explanation invokes failure to recognize these larger craters because of their non-lunar-like morphology from the moment of formation [2, 3], since larger gravity of Venus relatively to the Moon results in that largest craters on Venus may form within the mass of shock melted material while comparably sized lunar craters would be still almost "dry" [4-7]. To test this hypothesis, morphologies and rim-crest diameters of the largest peak-ring and Orientale-type basins and all larger impact features on Moon, Mercury, Mars, and Venus were compiled and compared to rim-crest diameters of model craters with different melt volume/transient-cavity volume ratios from [6]. Results show that the final diameters of model craters formed at depth of melting about twice of transient cavity depth correspond to changeover from a planet-similar morphology of all the smaller basins on any terrestrial planet to a planet-specific morphology of all the larger basins on Moon(?), Mercury, and Mars. On Venus, these largest impact features are not found and instead, a Venus-specific morphology of the largest concentric coronae appears in this size range. The coronae were suggested to form over sites of mantle upwelling and modified by subsequent volcanism and gravitational relaxation [e.g., 8-10]. The results here suggest that mantle upwelling - the first and necessary step of the corona formation models - may be induced by impact event (as a result of transient cavity collapse) and operated under cover of hot, slowly cooled impact melt in the areas of thinned crust and/or thermally active regions.

DATA ON THE LARGEST OBSERVED IMPACT FEATURES. Largest impact features on Moon, Mercury, Mars, and Venus can be groupped into three morphological types: peak-ring basins, Orientale-type multiring basins, and all the larger features whose morphology has not a lunar analogue. The morphology of a peak-ring basin (inner ring expressed as a ring of central peaks and the outer ring, as the crater rim crest.) were recognized to be similar on Moon, Mercury, Mars, and Venus [11-14]. Diameter of the largest peak-ring basin is 365km (Lorentz) on Moon [11], 310 km (Homer) on Mercury [11,12], 442 km (Schiaparelli) on Mars [11], and 104 km (Cochran) on Venus [14]. Basins of Orientale-type (at least three rings expressed as rim crests) were recognized to be similar too on all these planets [11-14]. Diameter of the largest Orientale-type basin is 1160 km (Imbrium) on Moon [11], 1250 km (Tir) on Mercury [11], 1548 km (Sirenum) on Mars [13], and 270 km (Mead) on Venus [14]. On each of the planets, except with Venus, there are still more larger impact features. Examples of these are: lunar Procellarum (D 3200 km) and South Pole-Aitken (D 2500 km) circular features with unclear morphology [15]; mercurian Caloris basin (D 1340 km) measured by fitting circles to the fragments of mapped rim crest [12]; martian Argyre-type structures (1850<D>2700 km) with an annulus and concentric graben, Chryse-type structures (3600<D>4970 km) with numerous concentric rings expressed as scarps, massifs, and channels [13], and Borealis (D 7700 km) which is a global circular depression interpreted as either impact basin [16], or mantle-plume structure [17]. So the morphology of the impact features larger than the largest Orientale-type basin is specific for a given planet.. On Venus, no impact features larger than the largest Orientale-type basin were recognized. Although a specifically venusian large circular features (coronae) have been suspected to be impact-induced by size distribution [2] and morphology [3]. The largest concentric-double ring corona (Latona) is 870x750 km in size, the largest concentric corona (Heng-o) has diameter of 1060 km, and unique corona (Artemis) is 2600 km in diameter [8]. Diameter values of all the largest features mentioned above are shown in Figure as a function of planet size.

THEORY ON IMPACT MELT PRODUCTION IN DIFFERENTLY SIZED CRATERS. Based on scaling relations, Cintala and Grieve [6] calculated and showed graphically impact melt volume/transient-cavity volume ratios as a function of rim-crest crater diameter for each of terrestrial planets. I transformed their graph into set of curves which demonstrate theoretical dependence between the diameter of craters with different values of melt volume/transient-cavity volume ratio on each of the planets and the planet size (dotted lines in Figure). Under calculations [6], all targets were assumed to be anorthosite and have a temperature of 273K except for Venus, for which diabase target and 700K was used. Typical impact velocities (from[18]), 23.6 for Mercury, 19.3 for Venus, 17.8 for Earth, 4.1 for Moon, and 12.4 km/s for Mars were employed [6].

RESULTS OF THE OBSERVED/MODEL DATA COMPARISON. Diameters of the largest observed impact features and model craters produced different volumes of impact melts are compared in the Figure. The Figure demonstrates two items. FIRST. Interplanetary trends of the largest both peak-ring and Orientale-type

LARGEST IMPACT FEATURES ON VENUS: Nikolaeva O.V.



basin diameters (solid lines) are seen to be in parallel with those of model crater diameters (dotted lines) for all the planets except for Moon. The lunar discrepancy might be due to underestimation of the Moon's impact velocity value used [6] because of much closer lunar orbit in past. At least, according to [11] the best fit of the highland crater curves of Moon and Mercury gives a Mercury/Moon impact velocity ratio of 2.18 rather than 1.67 used in [6]. (Though other causes are possible too). With this correction in mind, the model diameter trends are in surprisingly good agreement with observationaldata for the largest both peak-ring and Orientale-type basins. **SECOND**. Diameters of the largest Orientale-type basins observed on the planets are seen to correspond to those of model craters with the melt volume/transient-cavity volume ratio less than about 0.2. Diameters of the larger impact features whose morphology is a planet-specific (see above) fall in the range of the ratios of about 0.2 to 0.5 for Moon (with taking the correction above into account), Mercury, and Mars. For Venus, the diameter values of the largest concentric coronae - a specifically venusian circular structures, fall in this range. Models of the corona formation require mantle upwelling as the first and necessary step followed by volcanism and gravitational relaxation [9,10]. The result of interplanetary comparison shown in the Figure opens a possibility that the mantle upwelling could be induced by impact event of such a scale that volume of impact melt was of some 0.2 from transient-cavity volume, or depth of melting about twice of transient cavity depth (from fig.2 in [6]). The mantle upwelling as a respond on transient cavity collapse could operate under cover of hot, slowly cooling impact melt. The impact-induced corona formation is favoured, perhaps, by thinned crust (plains) and thermally active areas (linear zones).

REF: [1]Schaber G.G.et al.(1992)*JGR*,97,13257. [2]Nikolaeva O.V. et al.(1986)*Geokhimia*,5,79.[3]Hamilton .B. 1992)*LPI Contr* No 790,33. [4]Melosh H.J (1989)*Impact cratering*,Oxford,245pp. [5]O'Keefe J.D.and Ahrens T.J.(1992)*LPI Contr*.No790,25.[6]Cintala M.J.and Grieve R.A.F.(1991)*LPSC XXII*,215. [7]Grieve R.A.F.and Cintala M.J.(1992)*LPSC XXIII*, 451. [8]Stofan E.R.et al.(1992)*JGR* 97,13347.[9]Squyres S.W.et al.(1992)*JGR*,97,13611. [10]Janes D.M.et al.(1992)*JGR* 97, 16055. [11]Pike R.J.and Spudis P.D.(1987)*Earth, Moon,and Planets* 39,129. [12]Pike R.J.(1988)In: *Mercury* (F.Vilas et al.,eds.)336,Univ.Arizona,Tucson. [13]Schulz R.A.and Frey H.V.(1990)*JGR* 95,14175. [14]Alexopoulus J.S.and McKinnon W.Q.B.(1992)*JGR*(in press). [15]Wilhelms D.E.(1978)In:*The Geologic History of the Moon*,US Gov.Print. Office,Washington, 302 pp. [16]Wilhelms D.E.and Squyres S.W.(1984)*Nature* 309,139.[17]McGill G.E.and Dimitrou A.M.(1990)*JGR*,95, 12595. [18]Strom R.G.and Neukum G.(1988)In:*Mercury* (F.Vilas et. al.,eds.)336,Univ.Arizona,Tucson.

522-90
ABS. ONLY

N94-20658

EXPOSURE AGES OF CARBONACEOUS CHONDRITES - I ; K. Nishiizumi*, J. R. Arnold, Dept. of Chemistry, Univ. of Calif., San Diego, La Jolla, CA 92093-0317, M. W. Caffee, R. C. Finkel, J. R. Southon, CAMS, Lawrence Livermore National Lab, Livermore, CA 94551, H. Nagai, M. Honda, Dept. of Chemistry, Nihon Univ., Tokyo, M. Imamura, INS, Univ. of Tokyo, Tokyo, K. Kobayashi, RCNST, Univ. of Tokyo, Tokyo, P. Sharma, NSRL, Univ. of Rochester, Rochester, NY 14627

The recent exposure histories of carbonaceous chondrites have been investigated using cosmogenic radionuclides. Our results may indicate a clustering of exposure ages of C1 and C2 chondrites into two peaks, 0.2 My and 0.6 My, perhaps implying two collisional events of Earth-crossing parent bodies.

Among carbonaceous chondrites are some having short exposure ages [1, 2] which Mazor et al. hypothesized cluster into a small number of families. This hypothesis is based on spallogenic ^{21}Ne exposure ages, which in some instances are difficult to determine owing to the large amounts of trapped noble gases in carbonaceous chondrites. Also, since ^{21}Ne is stable it integrates a sample's entire exposure history, so meteorites with complex exposure histories are difficult to understand using exclusively ^{21}Ne. Cosmogenic radionuclides provide an alternative means of determining the recent cosmic ray exposure duration. To test the hypothesis of Mazor et al. [2] we have begun a systematic investigation of exposure histories of Antarctic and non-Antarctic carbonaceous chondrites, especially C2s.

Measurements of ^{10}Be ($t_{1/2}$=1.5 My), ^{26}Al (0.71 My), and ^{36}Cl (0.30 My) were obtained by AMS at Lawrence Livermore National Lab, the University of Tokyo, and the University of Rochester. ^{53}Mn (3.7 My) was measured by NAA. Only new results are shown in Table 1. ^{10}Be and ^{26}Al in some of these meteorites have been reported previously [1, 3-6]. Our ^{10}Be results are in good agreement with those of Moniot et al. [5]. The experimental errors have been significantly improved by this work.

The exposure ages of 70 carbonaceous chondrites were calculated using both cosmogenic radionuclides and noble gases [7]. With the exception of Ivuna (0.18 My by radionuclides vs. 2.3 My by ^{21}Ne), Mighei (2.0 vs. 2.7 My), ALH 77307 (0.7 vs. 16 My), and Orgueil (>10 vs. 4 My), there is reasonable general agreement. For the four noteworthy differences all but one, Orgueil, have ^{21}Ne ages older than radionuclide ages and can be plausibly explained by complex or early irradiation [3]. The situation with Orgueil is more complicated. The ^{53}Mn exposure age, which is based on bulk material, is >10 My, which is considerably longer than the ^{21}Ne exposure age from bulk material (4 My). However, Nichols et al. obtained an exposure age of 16 My, which agrees with our ^{53}Mn result, based on ^{21}Ne from olivine separates [8]. We cannot explain the apparent deficit of ^{21}Ne in bulk material at this time. Several paired falls are suggested among Antarctic carbonaceous chondrites. The concentrations of cosmogenic nuclides support the proposed pairing of ALH 83100, 83102, 84029, 84042, and 84044, although ^{26}Al in ALH 84029 [6] is somewhat lower than in the others. On the other hand, ALH 81002 and 82100 are not paired based on cosmogenic radionuclide concentrations. ALH 82100 has only a 40,000 year exposure age which is one of the shortest known meteorite ages.

The histogram of exposure ages of C1 and C2 chondrites is shown in Fig. 1. The possible paired Antarctic meteorites are plotted as an average of the ages. Exposure ages are plotted at an interval of 0.1 My to better reveal exposure age peaks which may be sharper than 0.5 My. The actual uncertainties of the ages for over a few My exposure ages are much wider than the histogram interval. Only two meteorites, Al Rais (14 My, CR2) and Orgueil (16 My, CI1) lie outside the figure. It is known that the majority of C1 and C2 chondrites have shorter exposure ages than type 3-6 carbonaceous chondrites or ordinary chondrites. About 50% of C2 chondrites have exposure ages less than 0.8 My. The ^{36}Cl concentrations indicate that Antarctic C2 chondrites reported here have terrestrial ages shorter than 0.07 My. For terrestrial ages this short no corrections are required before comparison to non-Antarctic meteorites. The distribution of exposure ages indicates that there is no significant difference between Antarctic and non-Antarctic C2s. Both Antarctic and non-Antarctic C2s have distinct groups of exposure ages at 0.2 My and around 0.6 My. The most likely explanation for this distribution is that a single breakup event of an Earth-crossing parent body is responsible for each of the two clusters. While such events undoubtedly could also occur in the asteroid belt it seems unlikely that two events occurring there would produce peaks with such short exposure ages since it is difficult to reach the earth in < 1 My [9]. The range of exposure ages observed in C1 chondrites overlaps with that of C2s, indicating no significant difference in exposure ages between C1 and C2 chondrites. The common breakup of Ivuna (CI1) and Cold Bokkeveld (CM2) was previously suggested [1].

The saturation activity of ^{36}Cl in C-chondrites (bulk) is 7.5 to 10 dpm/kg. ^{36}Cl in some C2s is higher than saturation, especially in ALH 85007 and LEW 88001. The excess ^{36}Cl in ALH 85007 and LEW 88001 was presumably produced by thermal neutron capture on ^{35}Cl. The contribution was calculated to be 50 dpm ^{36}Cl/g Cl and 165 dpm ^{36}Cl/g Cl respectively assuming 300 ppm Cl in the meteorites. The high neutron fluence in LEW

* Present address: Space Sciences Laboratory, University of California, Berkeley, CA 94720

88001 is similar to that found in Allende whose preatmospheric radius was 55-65 cm, although the recovered mass of LEW 88001 was only 45 g. Many meteorites paired with LEW 88001 would therefore be expected.

Table 1. Concentrations of cosmogenic radionuclides in carbonaceous chondrites

Name	Class	^{53}Mn dpm/kg Fe	^{10}Be dpm/kg	^{26}Al dpm/kg	^{36}Cl dpm/kg	Source
Ivuna	CI1	17.3 ± 2.5	1.76 ± 0.08*			USNM 2478
Orgueil	CI1	419 ± 20	20.48 ± 0.89*			Paris 221
Banten	CM2	237 ± 10	16.84 ± 0.59*			MTF 816
Cold Bokkeveld	CM2	25.8 ± 2.3	2.95 ± 0.14*			Me 1736,7,8
Mighei	CM2	144 ± 6	13.70 ± 0.38*			Me 1456
Murchison	CM2	131 ± 7	11.07 ± 0.31*			Me 2644
Murray	CM2	271 ± 13	17.10 ± 0.49*			ASU 635.2
Nogoya	CM2	16.4 ± 2.7	2.22 ± 0.10*			Me 1680
ALH 81002	C2		19.93 ± 0.21	31.76 ± 0.69	7.84 ± 0.17	,26
ALH 82100	C2		0.43 ± 0.02	1.79 ± 0.05	0.98 ± 0.03	,19
ALH 83102	C2		3.05 ± 0.05			,30
ALH 84033	C2		24.13 ± 0.21	40.9 ± 1.1	11.65 ± 0.19	,19
ALH 85007	C2		2.23 ± 0.04	7.25 ± 0.23	8.34 ± 0.17	,14
Belgica 7904	CM2		13.74 ± 0.17	51.0 ± 1.5	14.04 ± 0.46#	,76
EET 90021	C2		11.31 ± 0.21	24.24 ± 0.86	8.82 ± 0.32	,6
EET 90043	C2		17.35 ± 0.18	32.43 ± 0.87	5.96 ± 0.14	,5
GRO 85202	C2		2.14 ± 0.04	7.76 ± 0.18	2.92 ± 0.05	,12
LEW 88001	C2		18.82 ± 0.21	45.2 ± 1.2	57.2 ± 1.2#	,8
LEW 90500	CM2		5.24 ± 0.13	15.05 ± 0.57	5.28 ± 0.12	,16
MAC 88100	C2		20.94 ± 0.18	40.79 ± 0.76		,23
MAC 88107	C2		2.12 ± 0.03	7.63 ± 0.19		,27
MAC 88176	C2		5.67 ± 0.07	16.16 ± 0.50		,13
Y-74662	CM2	265 ± 11				
Y-86720	C2		4.47 ± 0.05	22.57 ± 0.67	6.03 ± 0.15#	,93
EET 87770	CR2		18.95 ± 0.18	51.2 ± 1.4	8.69 ± 0.21#	,8
MAC 87320	CR2		18.35 ± 0.35%	43.8 ± 1.3%		,15
Grosnaja	CV3	183 ± 10				Me 1732
EET 90007	C4		21.33 ± 0.27	47.82 ± 0.91	10.82 ± 0.25	,7
Karoonda	CK4		21.16 ± 0.34	40.01 ± 0.69	10.29 ± 0.10	offG5997
Maralinga	C5		20.31 ± 0.64	46.03 ± 0.85	8.87 ± 0.19	
Mulga (West)	C5/6		18.60 ± 0.48	31.09 ± 0.86	6.07 ± 0.07	
LEW 87009	C6		20.12 ± 0.19%	46.66 ± 0.90%		,21

* University of Tokyo, # University of Rochester; others by LLNL; % Non-magnetic phase

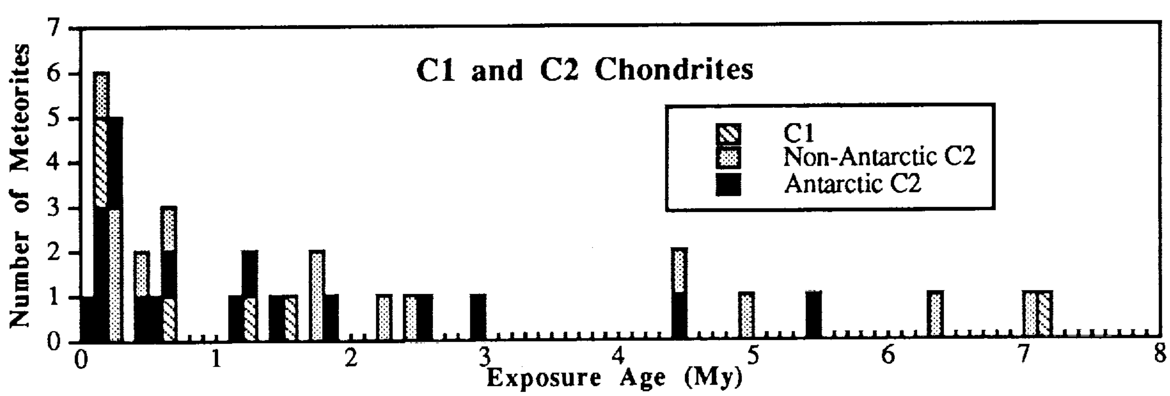


Fig. 1. Exposure ages of C1 and C2 chondrites

Ref. [1] Heymann D. and Anders E. (1967) *GCA 31*, 1793-1809; [2] Mazor E. *et al.* (1970) *GCA 34*, 781-824; [3] Fuse K. and Anders E. (1969) *GCA 33*, 653-670; [4] Rowe M.W. and Clark R.S. (1971) *GCA 35*, 727-730; [5] Moniot R.K. *et al.* (1988) *GCA 52*, 499-504; [6] Herpers U. *et al.* (1990) *LPI Tech. Rep. 90-01*, 46-48; [7] Schultz L. and Kruse H. (1989) *Meteoritics 24*, 155-172; [8] Nichols R.H. *et al.* (1992) *LPSC XXIII*, 987-988; [9] Arnold J.R. (1965) *Astrophys. J. 141*, 1536-1547.

S23-90
ABS. ONLY
167983 p. N94-20359

IDENTIFICATION OF AN INTERSTELLAR OXIDE GRAIN FROM THE MURCHISON METEORITE BY ION IMAGING; L. R. Nittler, R. M. Walker, and E. Zinner, McDonnell Center for the Space Sciences and Physics Department, Washington University, St. Louis, MO 63130-4899; P. Hoppe, Physikalisches Institut der Universität Bern, Sidlerstrasse 5, CH-3012 Bern, Switzerland; R. S. Lewis, Enrico Fermi Institute, University of Chicago, 5630 Ellis Avenue, Chicago, IL 60637-1433.

We report here the first use of a new ion-imaging system to locate a rare interstellar aluminum oxide grain in a Murchison acid residue. While several types of carbon-rich interstellar grains, including graphite, diamond, SiC and TiC, have previously been found, isotopically anomalous interstellar oxide grains have proven more elusive. For example, Virag *et al* . [1] found no evidence of an interstellar component in a study of 26 corundum grains from Murchison. Measurements by Amari *et al.* [2] on an additional 92 hibonites and 41 corundum grains in a smaller grain size fraction of Murchison gave similar negative results. A positive result was however reported by Huss *et al.* [3] who found one corundum grain, out of 23 studied from Orgueil, that had a large ^{26}Mg excess corresponding to an $(^{26}Al/^{27}Al)_0$ value of 9×10^{-4} and was thus of possible interstellar origin. A total of 550 Orgueil oxide grains and some 760 Murchison oxide grains were studied here. One corundum grain from Murchison, 83-5, showed an ^{18}O depletion ($\delta^{18}O = -244 \pm 24‰$) and an ^{17}O enrichment ($\delta^{17}O = 1072 \pm 59‰$) indicative of an interstellar origin. Grain 83-5 is also enriched in ^{26}Mg leading to an inferred $(^{26}Al/^{27}Al)_0$ of 8.7×10^{-4}, similar to that measured by Huss *et al.* [3] in their Orgueil sample. Additional data on many more oxide grains are needed to determine whether this agreement indicates a single population of presolar corundum grains or is purely coincidental.

We have developed an ion imaging system which allows us to map the isotopic composition of large numbers of grains relatively quickly and is thus ideally suited to search for isotopically exotic subsets of grains. The system consists of a PHOTOMETRICS CCD camera coupled to the microchannel plate/fluorescent screen of the WU modified CAMECA IMS-3F ion microprobe. Isotopic images of the sample surface are focused on the CCD and digitized. Subsequent image processing identifies individual grains in the images and determines isotopic ratios for each. For the present work, we have imaged in ^{16}O and ^{18}O; negligible contributions of $^{17}OH^-$ and $^{16}OH_2^-$ signals to the $^{18}O^-$ signal allow the use of low mass resolution, simplifying the measurements. Repeated imaging runs on terrestrial corundum particles showed that the system measures isotopic ratios reproducibly to about $\pm$ 40‰ (1σ). Each imaging run took about six minutes to complete, and for this study there were on average 5-15 grains in each image.

We have conducted imaging searches in 2-4 μm size separates of both Orgueil and Murchison. SEM-EDX analysis of a mount of Orgueil residue CC (ORCC) showed that it contains about 86% "chromites" (Cr-rich oxide grains with varying amounts of Mg, Al, Fe and Ti), 8% spinel, 4% TiO_2, and about 1% each of SiC and corundum-hibonite. The positions of seven corundum grains were noted and these were included in the ion mapping. The Murchison mount (KJG) contains 73% SiC, with the remainder of the grains being either corundum or hibonite. A total of 550 Orgueil oxide grains were imaged, of which we estimate 10-15 to be corundum. All but one grain appeared to be isotopically normal within analytical uncertainty. One grain showed a depletion in ^{18}O ($\delta^{18}O = -250‰$), but it unfortunately was sputtered away before it could be remeasured. Some 760 Murchison grains, all corundum or hibonite, were analyzed by imaging. All but one showed δ^{18}O values that fall within the range previously observed in Murchison oxides, from -100‰ to +80‰ with an average offset of ~ -40‰ [1,2], and are thought to have formed in the solar system. The distribution of measured δ^{18}O values (see Fig. 1) agrees well with the previous individual grain measurements although some of the higher δ^{18}O measurements in smaller grains may be artifacts of the image processing.

One Murchison corundum grain, 83-5, showed $\delta^{18}O = -210‰$ and $\delta^{18}O = -220‰$ on two consecutive imaging runs. We measured the oxygen isotopes in this grain, which is 1×3 μm in size, at high mass resolution and found an extreme enrichment in ^{17}O ($\delta^{17}O = 1072 \pm 59‰$) and confirmed the depletion in ^{18}O indicated by the imaging system ($\delta^{18}O = -244 \pm 24‰$). The actual isotopic composition of the grain may be even more extreme, since we were not able to completely eliminate secondary ions from a neighboring corundum grain for which the imaging showed δ^{18}O in the solar system range. Subsequent measurements of the Mg isotopes found a large excess of ^{26}Mg, corresponding to an initial $^{26}Al/^{27}Al$ ratio of 8.7×10^{-4}.

The unusual oxygen isotopic composition of 83-5 strongly suggests a circumstellar origin for this grain. Spectroscopic observations of red giant stars show similar isotopic signatures of enriched ^{17}O and depleted ^{18}O, presumably due to the dredging-up of CNO cycled material into the convective envelope [4-6]. The initial $^{26}Al/^{27}Al$ ratio (8.7×10^{-4}) inferred from the Mg isotopes is 17 times as high as the "canonical" solar system

value of 5×10^{-5}. The agreement with the result obtained by Huss *et al.* [3] for Orgueil Grain B (9×10^{-4}) strongly supports their interpretation of that grain as circumstellar.

The $^{17}O/^{16}O$ anomaly for Grain 83-5 is much larger than the effect in $^{18}O/^{16}O$, leading to the question whether some grains on the low edge of the $^{18}O/^{16}O$ distribution might also possess large enrichments in ^{17}O indicative of an interstellar origin. We cannot be sure on this point without further measurements but we consider it unlikely; in every previous case where ^{17}O has been measured in a single oxide grain with a ^{18}O depletion in this range, the ^{17}O was also found to be depleted [1,2]. The limited statistics available also make it impossible to decide whether the proportion of interstellar corundum is higher in Orgueil than in Murchison as suggested by Huss *et al.* [3]. We intend to use further chemical treatments to concentrate the corundum in our Orgueil separates to help answer this question.

The Murchison separates we have studied contain roughly a third as much corundum-hibonite as SiC, yet essentiallly all of the SiC grains are anomalous while only one rare oxide grain shows substantial isotopic differences from average solar system material. This result seems somewhat surprising since corundum is expected to form in stellar atmospheres [7] and the contribution of interstellar dust from oxygen stars is estimated to be similar to that from carbon stars [8]. Moreover, oxide grains should survive nebular processes that would destroy reduced phases such as graphite and SiC. Perhaps the apparent relative paucity of interstellar oxide grains is related to grain size; for example, we have previously noted that bulk measurements of a fine-grained spinel fraction from Murray showed enrichments in ^{17}O [9], and it is possible that the fraction of interstellar grains is higher for smaller grains.

The ion imaging system described here should make it possible to amass much better statistics on interstellar oxides in future work. The system should also prove useful in locating rare types of reduced interstellar grains, such as the X class of SiC grains previously identified by Amari *et al.* [10] so that these rare grains can be studied separately by complementary experimental techniques.

References: [1] Virag *et al.* (1991) *GCA* **55**, 2045. [2] Amari *et al.* (1992) *Meteroritics* **27**, 198. [3] Huss *et al.* (1992) *LPS* **XXIII**, 563. [4] Harris *et al.* (1985) *Ap. J.* **299**, 375. [5] Harris *et al.* (1987) *Ap. J.* **316**, 294. [6] Harris *et al.* (1985) *Ap. J.* **325**, 768. [7] Lattimer *et al.* (1978) *Ap. J.* **219**, 230. [8] Gehrz (1989) in *Interstellar Dust, IAU Symp. No. 135*, p. 445, Kluwer. [9] Zinner and Tang (1988) *LPS* **XIX**, 1323. [10] Amari *et al.* (1992) *Ap. J.* **394**, L43.

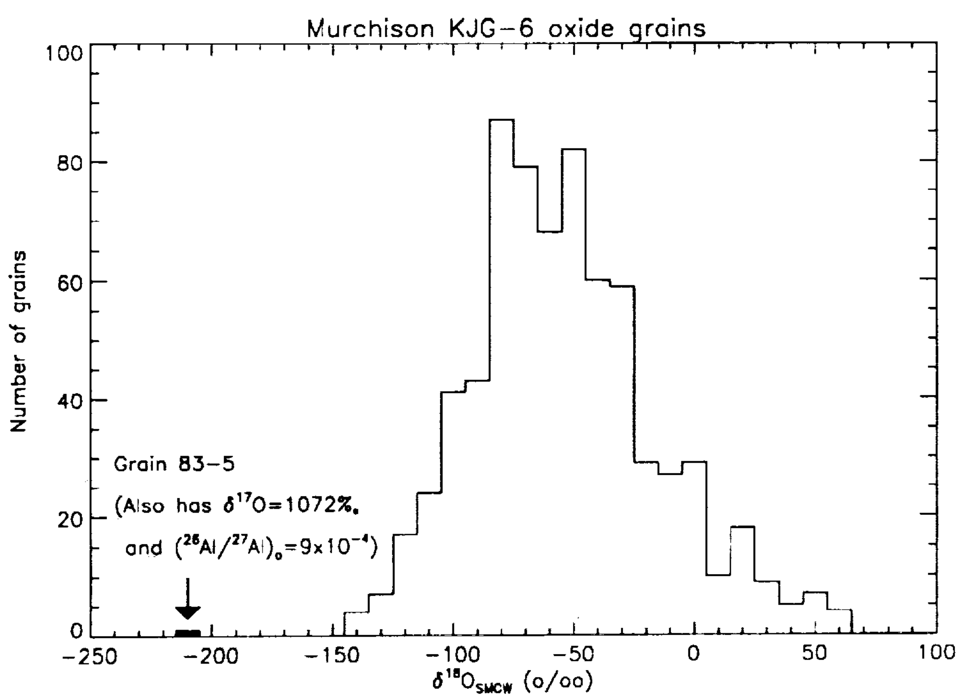


FIG. 1

S24-91 ABS. ONLY 167984

N94-20660

FRAGMENTS OF ANCIENT LUNAR CRUST: FERROAN NORITIC ANORTHOSITES FROM THE DESCARTES REGION OF THE MOON M. D. Norman (Planetary Geosciences, Dept. of Geology and Geophysics, University of Hawaii, Honolulu, HI 96822 U.S.A.) C. Alibert and M. T. McCulloch (Research School of Earth Sciences, The Australian National University, Canberra, A.C.T. 2601 Australia)

Noritic anorthosite clasts from breccia 67016 have bulk compositions similar to that of the upper crust of the Moon and petrogenetic affinities with pristine ferroan anorthosites. Rb-Sr and Sm-Nd isotopic compositions of mineral separates from one of these clasts suggest very old (≥ 4.4 Ga) ages, but interpretation of these data is complicated by the multi-stage history of the clasts which involved magmatic crystallization, brecciation, subsolidus recrystallization, and sulfide metasomatism. These clasts record some of the earliest events on the Moon, including early crust formation, accretionary bombardment, and degassing of the lunar interior.

Modal analyses of these clasts show they are now composed of about 70% plagioclase, 28% pyroxene, 2% troilite, and minor amounts of ilmenite and chromite. No metallic iron, phosphates or other trace phases were observed. Olivine is very rare, occurring only as relicts within secondary troilite+pyroxene intergrowths which may reflect reaction of olivine with sulfurous vapors [1,2]. PIXE proton microprobe analyses of the sulfides show that the metasomatism was accompanied by enrichments of Cu, Zn, Ni, Se, and Sb [3]. The clasts have been only mildly shocked since the observed texture was established. Major and minor element mineral compositions are very homogeneous and strikingly similar to those of pristine ferroan anorthosites [1]. Pyroxene compositions indicate equilibration temperatures of 850-900°C [1]. Except for the sulfide and chalcophile element metasomatism, these clasts appear to be essentially monomict and probably represent a noritic member of the ferroan anorthosite suite. Their low Ni contents and Ni/Co ratios are consistent with the interpretation of these clasts as igneous rocks which have escaped mixing with meteoritic material [4].

Whole rock powders and mineral separates from one of the noritic anorthosite clasts, and samples of the Murchison carbonaceous chondrite and the Angra dos Reis (ADOR) angrite were analyzed for Sm-Nd and Rb-Sr isotopic compositions (Tables 1,2). Two fragments of a single clast were processed separately as 67016,326 and ,328. The isotopic data show that the whole rock has a nearly chondritic $^{147}Sm/^{144}Nd$ ratio, and a $^{87}Rb/^{86}Sr$ ratio which is very low but somewhat higher than those of pristine ferroan anorthosites (0.0003-0.004; [5]). The Sm-Nd isotopic compositions of mineral separates and whole rock powders from this clast lie along a linear array suggesting either an isochron or a mixing relationship (Fig. 1). Considering all of the data together would indicate an age of 4.66 ± 0.15 Ga (MSWD = 6.26) with an I_{Nd} of 0.506568 ($\varepsilon_{Murchison}$ = -0.6) but the scatter is outside analytical uncertainty and the array cannot be considered an isochron. A 2-point minimum age would be 4.50 ± 0.07 Ga (I_{Nd} = 0.506788, $\varepsilon_{Murchison}$ = -0.4) using the ,326 pyroxene and ,328 plagioclase separates.

These data suggest the presence of ancient components in this clast. However, unless the Moon is the most ancient of objects in the Solar System, most of the Nd model ages of the mineral separates are unrealistically old (4.57-4.83 Ga) when calculated relative to our sample of Murchison. This requires the Sm-Nd system to have been open at some time subsequent to the original crystallization of this rock and dictates a cautious interpretation of the age of this clast. The Sm-Nd compositions of the pyroxenes in this clast seem to have been less affected by the disturbance than the plagioclase and may provide the best indication of the igneous crystallization age of this rock. Notable is the similarity between the 4.41 Ga Nd model age for the ,326 pyroxene split and the Sm-Nd isochron age of 4.44 ± 0.02 Ga for ferroan anorthosite 60025 (Carlson and Lugmair 1988). Young model ages of the whole rock powders (1.11 and 1.48 Ga) and the ,328 composite sample (4.31 Ga) are not meaningful due to the nearly chondritic Sm/Nd ratios of these splits.

Rb-Sr isotopic characteristics of the clast also demonstrate its primitive characteristics. Measured $^{87}Sr/^{86}Sr$ for all samples range from 0.69918-0.69950 which correct to values somewhat higher than that of ADOR at 4.55 Ga (Table 2). There is insufficient spread in the Rb-Sr data to determine an isochron age but Sr model ages can set upper limits to the crystallization age of a rock if the effect of later open system behavior is to increase Rb/Sr. However, the Rb/Sr of the Moon and its precursor materials are poorly defined so Sr model ages are not unique constraints. Relative to chondrites, Sr model ages of the noritic anorthosite clast are 4.52-4.55 Ga (Fig. 2). Relative to estimates for the bulk Earth and Moon, Sr model ages for the clast are 4.42-4.48 Ga and 4.32-4.43 Ga, respectively (Fig. 2).

Interpretation of these complex clasts requires an integrated petrologic and geochemical approach. Unrealistically old Nd model ages for both LREE-enriched plagioclase and LREE-depleted pyroxene preclude simply partially resetting the Sm-Nd isotopic system by a later thermal event, or contamination of the clast by a single component. Rather the minerals must have been open to both isotopic exchange and chemical re-equilibration with a less fractionated component, and yet retain their strong mineralogical and geochemical coherence with the ferroan

anorthosite suite. There is no petrologic evidence in these clasts for mixing of unrelated rock types such as ferroan anorthosite with Mg-suite norites or troctolites, KREEP, or evolved lithologies such as sodic ferrogabbro.

One explanation of the observed Nd isotopic compositions of the 67016 noritic anorthosite clast is that small scale redistribution of ^{147}Sm or ^{143}Nd occurred during brecciation and metamorphism. However it is difficult to see why this would affect both plagioclase and pyroxene in such an apparently regular manner, producing Nd model ages that are too old in both phases. An alternative model might involve internal redistribution of a small amount of melt created by an early impact event. This melt could change the Sm/Nd of the minerals if the melt was not a whole rock composition, e.g., if pyroxene contributed preferentially to the melt. Upon cooling or during later annealing this melt would crystallize to minerals with major element compositions identical to those of the starting material. The metamorphism which recrystallized the rock after its brecciation may have played only a minor role in establishing the isotopic compositions of this clast because it was subsolidus based on the pyroxene temperatures. This should be below the Sm-Nd closure temperature for plagioclase and pyroxene, allowing us to see through the metamorphism and dimly perceive the original partitioning of these elements during magmatic crystallization. Brecciation and recrystallization events would have hardly affected the Rb-Sr system due to the low Rb/Sr of all phases. However, later metasomatism by volatile components such as those associated with the sulfides may have increased the Rb/Sr slightly. This may be reflected in the slightly higher Rb/Sr of the bulk rock compared to all of the mineral separates.

References [1] Norman MD, Taylor GJ, Keil K (1991) GRL 18, 2081 [2] Colson RO (1992) PLPSC 22, 427 [3] Norman MD, Griffin WL, Ryan CG (1993) This volume [4] Norman MD and Taylor SR (1992) GCA 56 1013 [5] Nyquist LE (1977) Phys. Chem. Earth 10, 103

Table 1. Sm-Nd isotopic data

Sample	$^{147}Sm/^{144}Nd$	$^{143}Nd/^{144}Nd$	T(Murchison)*
,328 wr	0.1949	0.512654 (13)	1.11
,328 px+op	0.2480	0.514239 (8)	4.57
,328 pl+op	0.1694	0.511849 (10)	4.61
,328 comp	0.2061	0.512951 (13)	4.31
,326 wr	0.1995	0.512696 (6)	1.48
,326 px	0.2268	0.513564 (10)	4.41
,326 pl	0.1442	0.510999 (8)	4.83
ADOR pwd	0.1982	0.512735 (8)	
ADOR chip	0.1924	0.512546 (7)	
Murchison	0.1960	0.512662 (10)	
La Jolla (n=31)		0.511878 (13)	
BCR-1 (n=1)	0.1384	0.512661 (6)	
BCR-1 (n=1)	0.1381	0.512660 (6)	

wr = whole rock, px = pyroxene, op = opaques
pl = plag, comp = composite grain, pwd = powder
*Model age calculated relative to our sample of Murchison.

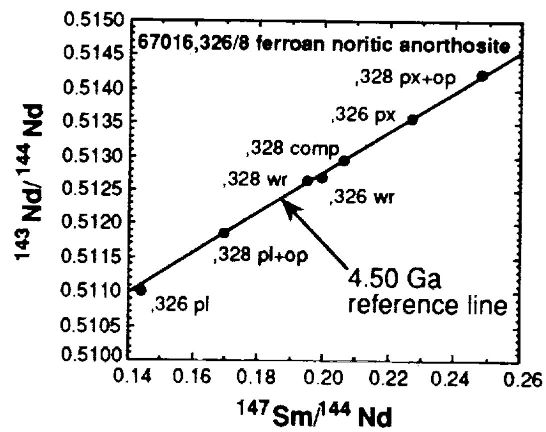


Fig. 1 Sm-Nd isotopic compositions of whole rock splits and mineral separates from the 67016 ferroan noritic anorthosite clast.

Table 2. Rb-Sr isotopic data

Sample	$^{87}Rb/^{86}Sr$	$^{87}Sr/^{86}Sr$	I_{Sr} (4.55 Ga)
,328 pl		0.699397 (10)	
,328 pl	0.004420	0.699375 (9)	0.69908
,328 pl res	0.002459	0.699175 (13)	0.69901
,326 wr	0.007274	0.699499 (18)	0.69901
,326 pl	0.003853	0.699308 (8)	0.69905
,326 px	0.004043	0.699330 (8)	0.69906
ADOR (n=8)	0.000813	0.698972 (17)	0.69892
E&A (n=10)		0.707982 (13)	
NBS987 (n=42)		0.710215 (10)	

res = residue after leaching in 1N HCL and 1N HNO_3

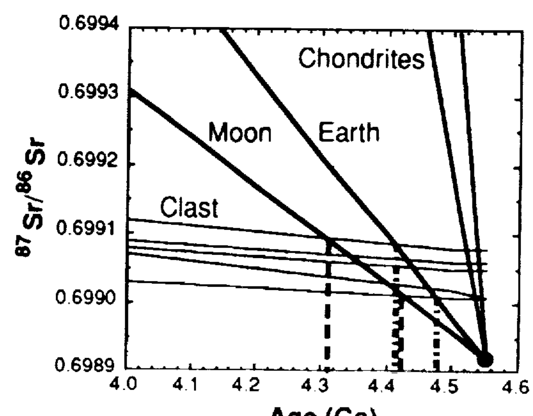


Fig. 2 Sr model ages of splits from the 67016 clast relative to chondrites and estimates of the bulk Earth and Moon. The black dot is ADOR

S25-91 ABS. ONLY 167985 N94-20661

VOLATILITY IN THE LUNAR CRUST: TRACE ELEMENT ANALYSES OF LUNAR MINERALS BY PIXE PROTON MICROPROBE M. D. Norman (Planetary Geosciences, Dept. of Geology and Geophysics, University of Hawaii, Honolulu HI 96822 U.S.A.), W. L. Griffin, and C. G. Ryan (Division of Exploration Geoscience, CSIRO, North Ryde NSW 2113 Australia)

In situ determination of mineral compositions using microbeam techniques can characterize magma compositions through mineral-melt partitioning, and investigate fine-grained or rare phases which cannot be extracted for analysis. Abundances of Fe, Mn, Sr, Ga, Zr, Y, Nb, Zn, Cu, Ni, Se, and Sb were determined for various mineral phases in a small number of lunar highlands rocks using the PIXE proton microprobe. Sr/Ga ratios of plagioclase and Mn/Zn ratios of mafic silicates show that the ferroan anorthosites and Mg-suite cumulates are depleted in volatile lithophile elements to about the same degree compared with chondrites and the Earth. This links the entire lunar crust to common processes or source compositions. In contrast, secondary sulfides in Descartes breccia clasts are enriched in chalcophile elements such as Cu, Zn, Ni, Se, and Sb, and represent a potential resource in the lunar highlands.

PIXE is a non-destructive method utilizing a beam of high energy protons to generate x-rays which can be used for trace element analysis (Fig. 1; Tables 1, 2). Methods are described by [1]. Plagioclase, pyroxene, olivine, ilmenite, and sulfide were analyzed in 5 lunar thin sections: 67016,294: A noritic anorthosite clast with ancient components, affinities with ferroan anorthosites, and abundant sulfides [2,3]. 67016,333: A poikiloblastic granulite [4]. Blocky plagioclase and euhedral olivines provide unequivocal evidence for crystallization from a melt, probably a pre-Nectarian impact melt. Fe-Ni metal compositions indicate a meteoritic component. 67016,360: A sodic anorthosite clast with mineral compositions unlike those of recognized pristine highlands rocks (An_{91-94}, opx En_{49-66}; [2]). Pyroxenes with coarse exsolution lamellae suggest this rock is igneous. 76535,52: A classic Mg-suite troctolite. 62237,8: A pristine ferroan anorthosite. Fused glass beads of USGS rock standards and one sample of natural rhyolite glass were also analyzed. Standard glasses were prepared by fusing 30 mg of rock powder on strips of either Mo (BCR) or Ir (AGV) under Ar or N_2. The rhyolite glass (Tsr-1) is a melt inclusion from a Snake River Plain tuff. Comparison of the standard data with consensus values demonstrates the utility of the method (Table 2). Potential problems with the fusion method include the loss of volatile elements and contamination of the glasses by Mo or Ir.

Sr and Ga are plagiophile elements with similar mineral-melt distribution coefficients. Sr/Ga ratios of plagioclase in the lunar samples are 40-60, reflecting the volatile-depleted nature of the lunar crust relative to chondrites and the Earth (Fig. 2). Plagioclase from ferroan anorthosites and Mg-suite cumulates have similar Sr/Ga ratios, consistent with the whole rock data [5]. Zn contents of pyroxene and olivine are remarkably low compared to their terrestrial counterparts, providing another measure of the depletion of volatile and chalcophile elements in the lunar crust. Enrichments in volatile chalcophile elements such as Cu, Zn, Ni, Sb, and Se in the 67016,294 sulfides contrast markedly with the bulk lunar crust (Table 1).

Both of the major crust-forming suites of lunar highlands rocks, the ferroan anorthosites and Mg-suite, are depleted in volatile lithophile elements to about the same degree. This links virtually the entire volume of the crust to a common set of processes or source compositions. If the Mg-suite parent magmas came from a primitive reservoir deep within the Moon, this region must have shared the depletion of volatile elements with the magma ocean, the presumed parent of the ferroan anorthosite suite. The volatile-depleted sources of Mg-suite magmas appear distinct from those of pyroclastic mare glasses with surface-correlated volatile enrichments. Alternatively, Mg-suite magmas may have been generated from refractory magma ocean cumulates [6], or by late accretion of residual planetesimals following the initial differentiation of the Moon [7]. Sulfides enriched in chalcophile elements represent a potential resource in the lunar highlands. These vapor-phase or late magmatic sulfides may be another manifestation of the fumarolic component found in certain Apollo 16 breccias [8].

References [1] O'Reilly SY, Griffin WL, and Ryan CG (1991) CMP 109, 98 [2] Norman MD, Taylor GJ and Keil K (1991) GRL 18, 2081 [3] Norman MD, Alibert C and McCulloch MT (1993) This volume [4] Cushing JA, Taylor GJ, Norman MD, and Keil K (1992) Apollo 17 Workshop LPI Tech Rept. 92-09, 4 [5] Warren PH and Kallemeyn GW (1984) PLPSC 15, 16 [6] Ryder G (1991) GRL 18, 2065 [7] Taylor SR, Norman MD, and Esat TM (1993) This volume [8] Krahenbuhl U, Ganapathy R, Morgan JW, and Anders E (1973) PLSC 4, 1325

Table 1. PIXE analyses of lunar minerals.
Data in ppm (1 sigma uncertainty, 99% minimum detection limit).

Plagioclase	Fe	Sr	Ga	Sr/Ga
67016,294 (n=3)	447 (32,10)	197 (4,1)	4.7 (0.7,1.9)	42
67016,333 (n=2)	3290 (254,13)	208 (6,2)	5.2 (0.6,2)	40
67016,360 (n=3)	2240 (178,11)	259 (7,1)	4.5 (0.6,1.8)	58
76535 (n=5)	319 (30,7)	144 (3,1)	3 (0.3,1.4)	48
62237 (n=4)	346 (66,7)	76 (2,1)	1.5 (0.3,1.4)	51

Olivine	Mn	Zn	Ni	Mn/Zn
67016,333 (n=2)	1590 (892,101)	10 (1,3)	25 (3,9)	159
76535 (n=3)	780 (55,64)	4 (1,2)	17 (2,6)	195
62237 (n=4)	1860 (126,74)	14 (1,2)	13 (3,6)	133

Ilmenite	Mn	Zn	Ni	Zr	Cu	Nb	Mn/Zn
67016,294 IL1	3870 (emp)	33.1 (3,9)	<22	326 (12,5)	<13	278 (10,5)	117

Sulfide	Mn	Zn	Ni	Zr	Cu	Se	Sb	Mn/Zn
67016,294 SU1	1935 (439,211)	<12	492 (54,36)	12 (1,4)	459 (41,19)	13 (1,5)	17 (6,13)	>161
67016,294 SU2	671 (284,200)	155 (14,12)	869 (91,37)	18 (3,4)	160 (18,19)	13 (2,5)	<14	4

Pyroxene	Mn	Zn	Ni	Zr	Cu	Y	Sr	Mn/Zn
67016,294 PX1	3615 (725,168)	8 (2,5)	<12	5 (1,4)	<7	15 (1,3)	4 (1,3)	452
67016,294 PX3	3257 (655,181)	9 (2,6)	<14	12 (2,5)	<8	16 (2,4)	64 (4,4)	362
67016,294 PX2	1711 (353,148)	<7	<17	21 (2,4)	<10	24 (4,3)	129 (4,4)	>244
67016,333 PX1	1547 (316,131)	9 (1,4)	11 (3,10)	32 (2,3)	<6	14 (1,2)	28 (2,3)	172
67016,333 PX2	1325 (272,101)	5 (1,4)	<9	26 (2,3)	<5	13 (1,2)	47 (2,3)	265
67016,360 PX1	2432 (515,174)	<6	<17	91 (3,4)	<9	61 (2,3)	23 (2,3)	>405
67016,360 PX2	2781 (591,179)	8 (2,6)	<17	70 (4,4)	<9	46 (2,4)	20 (2,3)	348
62237 PX1	3892 (796,241)	11	<21	10 (2,5)	<11	7 (2,5)	<5	354

Table 2. Standard analyses. PV = concensus values

	Mn	Ni	Cu	Zn	Ga	Rb	Sr	Y	Zr	Nb
BCR (n=2)	1203 (250,94)	<9	13 (2,5)	129 (9,4)	20 (2,3)	45 (2,2)	347 (7,3)	37 (2,3)	197 (4,4)	14 (2,5)
PV	1372	13	19	130	22	47	330	38	190	14
AGV (n=2)	784 (159,54)	17 (3,6)	45 (4,4)	69 (5,3)	17 (2,2)	71 (2,2)	708 (13,2)	16 (1,2)	249 (5,3)	12 (1,3)
PV	713	16	60	88	20	67	662	20	227	15
TSC-1 (n=2)	101 (35,65)	<8	<5	36 (3,4)	18 (2,3)	254 (4,2)	31 (2,3)	30 (3,3)	128 (4,4)	9 (2,4)
PV	101	6	2		20	250	29	30	125	12

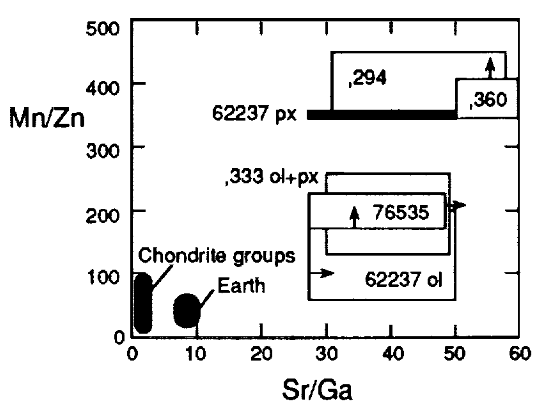


Fig. 2 An illustration of the ranges of Sr/Ga and Mn/Zn compositions of lunar plagioclase and mafic silicates, respectively, compared to chondritic and bulk Earth compositions. Samples given by split number only are from 67016. Mn/Zn values from 62237 should be interpreted cautiously because of high Zn contents found in the thin section epoxy.

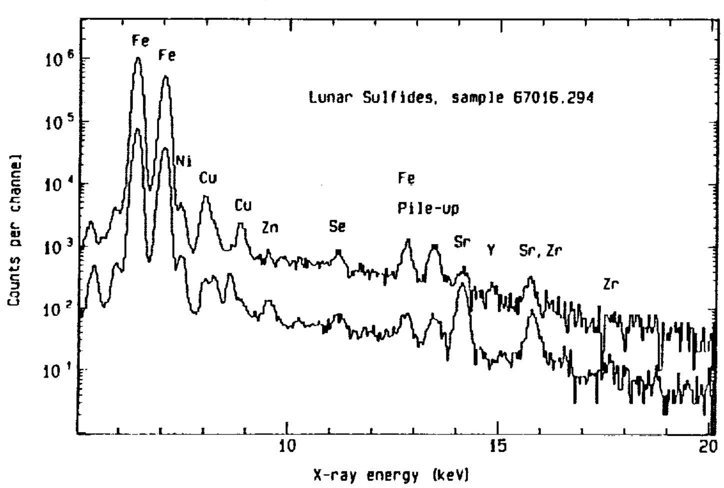


Fig. 1 PIXE spectra from 67016,294 sulfides

IMPACT GLASSES FROM THE ULTRAFINE FRACTION OF LUNAR SOILS.

J. A. Norris[1], L. P. Keller[2], and D. S. McKay[2], [1]Dept. of Geol., U. Georgia, Athens, GA 30602 and [2]Code SN, NASA Johnson Space Center, Houston, TX 77058.

Introduction. The chemical compositions of microscopic glasses produced during meteoroid impacts on the lunar surface provide information regarding the various fractionation processes which accompany these events. To learn more about these fractionation processes, we studied the compositions of submicrometer glass spheres from two Apollo 17 sampling sites using electron microscopy. The majority of the analyzed glasses show evidence for varying degrees of impact-induced chemical fractionation. Among these are HASP glasses (High-Al, Si-Poor) which are believed to represent the refractory residuum left after the loss of volatile elements (e.g. Si, Fe, Na) from the precursor material [1, 2, 3]. In addition to HASP-type glasses, we also observed a group VRAP glasses (volatile-rich, Al-poor) that represent condensates of vaporized volatile constituents and are complementary to the HASP compositions [3]. High-Ti glasses were also found during the course of this study, and are documented here for the first time.

Experimental. Samples from the <20 µm size fractions of two Apollo 17 soil samples (72501 from Station 2 at the base of the South Massif, and 78221 from Station 8 at the base of the Sculptured Hills) were embedded in low viscosity epoxy and cut into thin sections (~80-to 100-nm thick) using diamond-knife ultramicrotomy. The thin sections were analyzed using a PGT energy-dispersive X-ray (EDX) spectrometer with a JEOL 100CX TEM. EDX analyses were obtained for 107 spheres from 72501 and 115 from 78221. The apparent diameters of these spheres in thin section were typically between 100- and 400-nm, although the true diameter of any actual sphere may have been slightly larger. The relative errors associated with the EDX analyses were estimated by analyzing a grossular standard. The relative errors for Al, Si, Ca, and Fe are ~5%. These relative errors increase significantly for concentrations <5 wt.%.

The glass compositions were initially divided into a "high-Si" group (SiO_2 > 60wt.%) or a "low-Si" group (SiO_2 < 60wt.%). For the "low-Si" compositions a standard CIPW norm was calculated. However, many of these glasses (e.g. HASP) contain insufficient Si to be used with this method. For these Si-poor compositions, a new normalization scheme was developed using 3 groups of progressively Si-deficient normative minerals. Group 1 HASP compositions contain insufficient Si to calculate any normative anorthite (AN). Instead, the Group 1 normative mineralogy includes gehlenite (GH) + spinel (SP) + Ca-aluminates. Group 2 HASP compositions consist of normative GH + AN ± SP ± olivine ± Ca-aluminates. The Group 3 HASP compositions are cordierite- or mullite-normative, and contain excess Al_2O_3 and SiO_2 after using all of the Ca, Na, and K to make normative feldspar.

Results and Discussion. The compositions of the 107 glasses analyzed from sample 72501 and the 115 from 78221 are plotted in Figs. 1 and 2. The compositions range from nearly 95% refractory components to others composed entirely of more volatile components. HASP compositions comprise ~75% of the total glasses analyzed in each sample. The Group 1 HASP glasses comprise ~6% of the total analyses from both 72501 and 78221. The Group 1 HASP compositions are the most refractory and the most volatile-depleted of all the analyzed glasses. A cluster of high-Ti glasses were included within Group 1 and plot about the origin in Fig.1. The Group 1 high-Ti glasses contain little Ca or Al, but nonetheless have undergone extreme volatile loss in the form of nearly complete removal of Fe from what was once ilmenite (Tab. 1). The other Group 1 members are probably derived from mostly anorthositic material which has lost most of its original SiO_2 content. All but one of the 72501 Group 1 HASPs are high-Ti glasses, whereas 78221 contains a larger proportion of the Ca- and Al-rich members of this group (Tab. 1).

The Group 2 HASP glasses span a much wider compositional range in both samples, and comprise 29% of the analyses from 72501 and 27% of those from 78221. These have undergone a lesser degree of volatile loss than those of Group 1, and generally retain significant amounts of SiO_2 and FeO, even though considerable amounts of these components have been lost. The average composition of Group 2 glasses (in wt.%) from both samples is given in Table 1. The similarity in both the relative proportions and in the average compositions of the Group 2 HASP

glasses in these two samples reflects the similarities in bulk soil composition and soil maturity at these two sites. We note that glasses fractionated to the extent of the Group 1 & 2 HASP compositions seem to occur only among the finest size fractions.

The Group 3 glasses have the least fractionated compositions. The glasses of this compositional type in both samples comprise a larger proportion of the analyzed population than does any other single group (44% of 72501 and nearly 42% of 78221), and the average composition of this group is very similar in both samples (Tab. 1).

The high-Si glasses are comprised of the relatively volatile elements and are compositionally complementary to the HASP glasses. These compositions make up 13% of the 72501 analyses and 11% of the 78221 population. The compositions of these glasses in both samples span the range from nearly pure SiO_2, sometimes with other associated volatiles such as Na, K, P, and S, to other Si-rich compositions with high Fe concentrations (Tab. 1). It is believed that the compositions of this group represent the recondensation of impact-generated vapors [3]. As with most of the HASP glasses, these Si-rich compositions are only found among the finest size fractions of lunar soils. This suggests that such extreme fractionations only occur at sizes where the surface-area to volume ratio is high enough to allow the degree of melting and vaporization required to produce these unusual compositions.

In both samples, the glasses of basaltic composition constitute a relatively small group, being just over 8% of the analyses from 72501 and nearly 14% of those from 78221. These compositions display little or no observable volatile loss. The average composition of this group (in wt.%) from both samples is given in Table 1.

Conclusions. We found that the majority of the analyzed glasses in both soils have either refractory compositions resulting from volatile loss, or are volatile-rich condensates of impact-generated vapors. In both samples, the three HASP groups comprise ~75% or more of the total number of analyzed glasses. The HASP glasses are derived from the bulk soil and from the feldspathic component of the soils through the loss of major amounts of Si and lesser quantities of Fe and alkalis. The Si-rich glasses rival the number of the unfractionated basaltic glasses. The pronounced fractionations (volatilization and condensation) that occur in the submicrometer size range result from the large surface area to volume ratio of the glasses.

This is the first report of high-Ti glasses from lunar soils. Considering all high-Ti glasses from both samples together, a trend is observed which begins with Fe-Ti-rich compositions and extends to glasses that consist of nearly pure TiO_2. We conclude that these compositions originate by the loss of Fe from ilmenite, which is the dominant Ti-rich oxide at the Apollo 17 site. These high-Ti glasses are one of the few types of impact glasses derived from a specific mineral constituent of lunar soils.

References. [1] Naney, M. *et al.*, (1976) *Proc. 7th LPSC*, 155. [2] Vaniman, D. (1990) *Proc. 20th LPSC*, 209. [3] Keller, L. and McKay, D. (1992) *Proc. Lunar Planet. Sci.* 22, 137.

TABLE 1. Average EDX analyses for subgroups of impact glasses in soils 72501 and 78221 (1a=Group 1 HASP, 1b=Group 1, high-Ti HASP, 2=Group 2 HASP, 3=Group 3 HASP, 4=basaltic glasses, and 5=high-Si glasses).

	1a	1b	2	3	4	5*
MgO	7.0	4.0	9.0	6.0	14.0	3.1
Al_2O_3	53.0	4.0	34.0	27.0	14.0	5.2
SiO_2	10.0	7.5	30.0	49.0	46.0	65.0
CaO	23.0	1.5	18.0	11.0	9.0	2.1
TiO_2	3.3	64.0	3.0	1.0	3.0	0.6
FeO	3.7	19.0	6.0	6.0	14.0	20.0

* high-Si glasses contain <2 wt.% each of Na_2O, K_2O, SO_3, P_2O_5, MnO, Cr_2O_3.

^{146,147}Sm-^{142,143}Nd FORMATION INTERVAL FOR THE LUNAR MANTLE AND IMPLICATIONS FOR LUNAR EVOLUTION.

L.E. Nyquist, NASA Johnson Space Center, Houston, TX 77058; C.-Y. Shih, H. Wiesmann, and B.M. Bansal, Lockheed Engineering and Science Co., 2400 NASA Road 1, Houston, TX 77258.

Abstract: Small anomalies in the isotopic abundance of ^{142}Nd have been measured for two A17 high-Ti basalts, ilmenite basalt 12056, olivine-pigeonite basalt 12039, feldspathic basalt 12038, and two KREEP basalts. These anomalies correlate with ^{147}Sm/^{144}Nd for the basalt source regions as calculated from initial ^{143}Nd/^{144}Nd ratios in the basalts, and are interpreted to be from decay of ^{146}Sm ($t_{1/2}$ = 103 Ma) in distinct lunar mantle reservoirs. A three-stage model for evolution of ^{143}Nd/^{144}Nd and ^{142}Nd/^{144}Nd yields reservoir ^{147}Sm/^{144}Nd ratios which, with the ^{142}Nd/^{144}Nd ratios in the basalts, form a "mantle isochron" giving a lunar mantle formation interval of 94^{+23}_{-20} Ma (2σ). Calculated reservoir Sm/Nd ratios are in the range expected from some earlier models of basalt petrogenesis. The isochron value of ^{142}Nd/^{144}Nd at ^{147}Sm/^{144}Nd$_{CHUR}$ = 0.1967 is within error limits of the average ^{142}Nd/^{144}Nd measured for an L6 chondrite, an H5 chondrite, and the Orgueil carbonaceous chondrite. Evolution of ^{143}Nd and ^{142}Nd for high-Ti basalt 70135 was modelled precisely, starting from chondritic relative REE and Nd-isotopic abundances and using the initial $(^{146}Sm/^{144}Sm)_0$ ratio inferred from a previous study of angrite LEW86010 as the initial solar system value of this parameter. We infer that the initial Sm/Nd ratio in precursor lunar materials was very nearly chondritic (within ~8%) prior to lunar differentiation.

Reservoir ^{147}Sm/^{144}Nd and the Mantle Formation Interval: Table 1 gives Nd-isotopic data for seven lunar basalts and the average ϵ_{Nd}^{142} for three chondrites. For the lunar basalts, values of ϵ_{Nd}^{142} roughly correlate with values of ϵ_{Nd}^{143}, in spite of differences in crystallization ages (T_c). Reservoir values of ^{147}Sm/^{144}Nd were calculated from a three stage model

$$I_p^{143} = I_1^{143} + \mu_{1,2}^{147}(e^{\lambda_{147}t_1} - e^{\lambda_{147}t_2}) + \mu_{2,3}^{147}(e^{\lambda_{147}t_2} - e^{\lambda_{147}t_3}) + \mu_{3,p}^{147}(e^{\lambda_{147}t_3} - 1) \qquad \text{Eq. (1)}$$

where I_p^{143} = present-day ^{143}Nd/^{144}Nd, t_1 = lunar formation age, t_2 = lunar differentiation age, and t_3 = basalt age. Also, $\mu_{1,2}^{147}$ = present-day value of ^{147}Sm/^{144}Nd in the magma ocean at t_2, $\mu_{2,3}^{147}$ = present-day value of ^{147}Sm/^{144}Nd in the basalt source region at t_3, $\mu_{3,p}^{147}$ = present-day ^{147}Sm/^{144}Nd, and λ_{147} is the ^{147}Sm decay constant. Eq. (1) was solved for $\mu_{2,3}^{147}$ to get

$$\mu_{2,3}^{147} = \frac{I_p^{143} - I_1^{143} - \mu_{3,p}^{147}(e^{\lambda_{147}t_3} - 1)}{(e^{\lambda_{147}t_2} - e^{\lambda_{147}t_3})} - \frac{\mu_{1,2}^{147}(e^{\lambda_{147}t_1} - e^{\lambda_{147}t_2})}{(e^{\lambda_{147}t_2} - e^{\lambda_{147}t_3})} \qquad \text{Eq. (2)}$$

To a good approximation, evolution of ^{142}Nd/^{144}Nd can be expressed by

$$\epsilon_p^{142} = \epsilon_2^{142} + 1801\,(^{146}Sm/^{144}Sm)_0\,\mu_{2,2}^{147}\,e^{-\lambda_{146}(t_1-t_2)} \qquad \text{Eq. (3)}$$

in ϵ-notation, where $(^{146}Sm/^{144}Sm)_0$ is the solar system initial value. Systems having the same formation interval (t_1-t_2) and second stage ϵ_2^{142} will determine an isochron whose slope, m, gives the formation interval

$$t_1 - t_2 = -\lambda_{146}^{-1}\ln[((5.55)10^{-4}m)/(^{146}Sm/^{144}Sm)_0] \qquad \text{Eq. (4)}$$

The values of $\mu_{2,2}^{147}$ and $\mu_{2,3}^{147}$ differ only slightly due to radioactive decay of ^{147}Sm between t_2 and t_3. Thus, $\mu_{2,2}^{147}$ in Eq. (3) can be approximated by $\mu_{2,3}^{147}$ from Eq. (2), coupling the two Sm-Nd chronometers. Assuming $\mu_{1,2}^{147}$ = 0.2027, the CHUR [1] value at t_1 = 4.56 Ga ago, substituting the basalt age for t_3, and setting $t_1 = t_2$ in Eq. (2) yields a two-stage approximation to $\mu_{2,3}^{147}$. ϵ_p^{142} for the basalts can be plotted versus $\mu_{2,3}^{147}$ as in Fig. 1, to obtain an approximation to the source region

$^{146,147}Sm-^{142,143}Nd$ FORMATION INTERVAL FOR THE LUNAR MANTLE: Nyquist L.E. et al.

Table 1. Nd isotopic anomalies and source region $^{147}Sm/^{144}Nd$ for lunar basalts.

Basalt	ϵ^{142}_{Nd}	ϵ^{143}_{Nd}	T_c(Ga)	$\mu^{147}_{2,3}$†
70135	0.25±0.17	7.69±0.33	3.77	0.280
75075	0.33±0.15	7.56±0.52	3.70	0.271
12056	0.21±0.20	12.36±0.7	3.20	0.271
12038	−0.26±0.12	1.73±0.38	3.35	0.208
12039	−0.15±0.12	4.80±0.36	3.20	0.225
14078	−0.39±0.13	–	3.89	0.181
15386	−0.39±0.20	−1.30±0.3	3.85	0.181
CHUR	−0.35±0.08	0	4.558	0.1967
Mantle Formation Interval (Ma)				94±23

†$\mu^{147}_{2,3}$: $^{147}Sm/^{144}Nd$ in source if established at 4466 Ma ago.

formation interval from Eq. (4). The resulting t_2 can be used to refine the estimate of $\mu^{147}_{2,3}$ and obtain an iterated value of t_2. Values of $\mu^{147}_{2,3}$ and the formation interval (t_1-t_2) after three iterations are given in Table 1 and shown in Fig. 1.

The Fig. 1 isochron gives the formation interval of the lunar mantle as 94^{+23}_{-20} Ma (2σ) after crystallization of the angrite LEW86010 with $(^{146}Sm/^{144}Sm)_0$ = 0.0076±9 [2]. Increasing ϵ^{143}_{Moon} to ~+1 [3] lowers $\mu^{147}_{2,3}$ by ~0.005–0.01 and increases the formation interval by ~6 Ma. Average $\mu^{147}_{2,3}$ = 0.276 for the source of Apollo 17 basalts is in the range ~0.24–0.29 for model values [4,5,6,7]. Similarly, $\mu^{147}_{2,3}$ ~0.27 and ~0.21 for the sources of ilmenite basalt 12056 and feldspathic basalt 12038 are in satisfactory agreement with model values of ~0.26 and ~0.215, resp. [4,5,8], and $\mu^{147}_{2,3}$ ~0.22 for ol-pig basalt 12039 is in the model range ~0.21–0.23 [4,5,9].

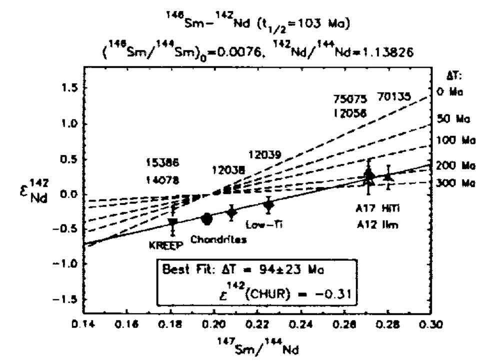


Figure 1. $^{146}Sm-^{142}Nd$ isochron for a lunar mantle formation interval of 94±23 Ma.

Comparison of ϵ^{142}_{Moon} and ϵ^{142}_{CHUR}: The weighted average ϵ^{142}_{Nd} for the three chondrites gives ϵ^{142}_{CHUR} = −0.35±0.08, nearly identical with the lunar isochron value of ϵ^{142}_{Moon} = −0.31±0.06 (2σ) at $^{147}Sm/^{144}Nd_{CHUR}$ = 0.1967. Thus, evolution of ^{142}Nd in the bulk moon appears to have been the same as in a chondritic reservoir. Fig. 2 shows the evolution of ^{143}Nd and ^{142}Nd for high-Ti basalt 70135 as modelled from CHUR parameters starting at $\epsilon^{142}_{Nd} = \epsilon^{143}_{Nd}$ = 0 at 4.558 Ga ago [10]. The model includes Nd evolution in a chondritic reservoir for 94 Ma, after which ϵ^{143}_{Nd} = +2.46 and ϵ^{142}_{Nd} = +1.26, followed by evolution in the high-Ti source of Apollo 17 basalts with $\mu^{147}_{2,2}$ = 0.2883 (present-day $^{147}Sm/^{144}Nd$ = 0.280, Table 1), and in which $\mu^{146}_{2,2}$ was increased proportionally to $\mu^{147}_{2,2}$ from 1.63×10^{-4} to 2.32×10^{-4}. ϵ^{142}_{Nd} grows about 62% in this stage, reaching a near-final value of +3.26. Growth in a chondritic reservoir would have led to ϵ^{142}_{Nd} = +2.67, explaining the ~0.6ϵ difference between present-day ϵ^{142}_{Nd} for 70135 and chondrites (Table 1).

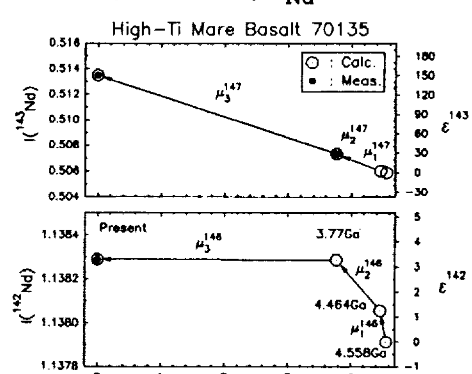


Figure 2. Modelled evolution of $^{143}Nd/^{144}Nd$ (top) and $^{142}Nd/^{144}Nd$ (bottom) in 70135.

The modelled values of $^{142}Nd/^{144}Nd$ and $^{143}Nd/^{144}Nd$ agree exactly with measured values (Fig. 2). Significant departures from chondritic evolution within the time interval (t_1-t_2), during which 38% of the total growth in $^{142}Nd/^{144}Nd$ occurred, should be detectable as a difference between calculated and measured $^{142}Nd/^{144}Nd$ ratios. Calculated growth in $^{142}Nd/^{144}Nd$ from t_1 to t_2 is ~126 ppm, and $(\epsilon^{142}_{Moon}-\epsilon^{142}_{CHUR})$ = 4±10 ppm. Thus, the $^{147}Sm/^{144}Nd$ ratio is suggested to be within ~8% of the CHUR value between lunar formation and differentiation.

REFERENCES: [1] Jacobsen S.B. and Wasserburg G.J. (1984) EPSL **67**, 137–150. [2] Nyquist L.E. et al. (1991) LPSC XXII, 989–990 and unpublished data. [3] Shih C.-Y. et al. (1993) GCA **57**, in press. [4] Nyquist L.E. et al. (1977) PLSC8, 1383–1415. [5] Nyquist L.E. et al. (1979) PLPSC10, 77–114. [6] Hughes S.S. et al. (1989) PLPSC19, 175–188. [7] Snyder G.A. et al (1992) GCA **56**, 3809–3823. [8] Nyquist L.E. et al. (1981) EPSL **55**, 335–355. [9] Hughes S.S. et al. (1988) GCA **52**, 2379–2391. [10] Lugmair G.W. and Galer S.J.G. (1992) GCA **56**, 1673–1694.

GONIOSPECTROMETRIC PROPERTIES OF A WHITE STANDARD.

A. Oehler and A. Dummel, DLR, Planetary Remote Sensing Section, 8031 Oberpfaffenhofen, F.R. Germany.

Introduction. Reflection spectroscopy is one of the fundamental tools in planetary remote sensing. Most of the laboratory work is done in terms of bidirectional reflectance R in the wavelength range of reflected sunlight (250 nm - 2500 nm). Bidirectional reflectance R is defined as the radiance of a surface relative to the radiance of an ideal Lambertian reflector, identically illuminated (radiance coefficient in [1]). For quantitative laboratory work the absolute scale of R has to be known. In addition, for many purposes it is necessary to know the dependence of R from phase angle for a large range of geometries. In many cases this can only be achieved if the goniospectrometric properties of the white standard that is used are known with high precision. For a long time Halon [3],[4] has been used as a white standard by most laboratories. Because Halon is no more available we have now analysed the goniospectrometric properties of Spectralon™ SRS-99 with the DLR-goniospectrometer [5]. Spectralon is manufactured by Labsphere Inc, North Sutton, NH 03260, USA.

Spectral, bidirectional reflectance of Spectralon at i = 8°, e = 0° (i: incidence angle, e: exit angle). Spectralon is delivered with a calibration table for the spectral, directional-hemispherical reflectance $R^{dh}(i = 8°)$, covering the wavelength range from 250 nm - 2500 nm in steps of 50 nm. To our knowledge, no data are available of the spectral, bidirectional reflectance. In order to get R of Spectralon we have calculated a scaling factor K, that can be used for the conversion of $R^{dh}(i = 8°)$ to $R(i = 8°, e = 0°)$ We found that: $K = 1.070 \pm 0.032$. K was calculated using the following formalism:

$$R^{dh}(i = 8°) = R(i = 8°, e = 0°)\ \frac{1}{\pi} \int_0^{2\pi} \int_0^{\frac{\pi}{2}} Q(i = 8°, e, \varphi)\ \cos e\ de\ d\varphi = R(i = 8°, e = 0°)\ \frac{1}{K}$$

where φ is the azimuth and Q denotes the indicatrix (the relative distribution of the reflected radiance as a function of geometry) of the material, normalized to 1 at the geometry: $(i = 8°, e = 0°)$. We have calculated K by measuring Q in the plane of incidence for exit angles from -65° to 65° in steps of 5° to 2° over the wavelength range from 300 nm to 1100 nm in steps of 25 nm. The smallest phase angle was 3°. For the numerical calculation of the integral K, Q has to be extrapolated over the whole hemisphere. This was done by fitting the photometric model of Hapke [1],[2] to the data. The following form of the Hapke-model was used: equation 37 in [1], using the definition for $B(g)$ in [2] (equation 52 and 53 in [2]) and a Legendre-polynomial of second order for the single particle phase function (equation 20 in [1]). The spectral dependence of K in the wavelength range studied was found to be not significant (relative change less than 0.3%). The error of K specified above was estimated from the statistical error of the fit and from a comparison with data at the Helium-Neon Laser wavelength (633 nm), that have been provided by Labsphere. Inc..

Bidirectional reflectance at 633 nm± 5 nm as a function of geometry. We have measured the dependence of R from geometry for $i = 0°$ and $i = 45°$ at a wavelength of 633 nm ± 5 nm for a large range of exit angles in the plane of incidence. To these data again we have fitted the photometric model of Hapke (we used the same form of the function as we used for the calculation of K). The data are shown in figure 1 and are listed in table 1. The Hapke parameters from the fit are listed in table 2 and can be used for an analytical description of the data that is correct within ±0.3% for exit angles from -60° to 60°. The modeled data also are shown in fig. 1 and are listed in table 1. Because we found that the spectral variation of the scattering properties of Spectralon is not significant, the data presented here can be used to setup the scale for any bidirectional reflectance spectrometer for a large range of phase angles within a relative uncertainty of approximately ± 3% for the absolute scale.

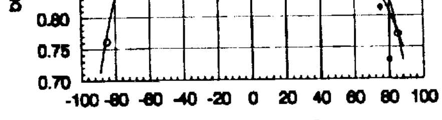


Fig. 1
R for Spectralon at 633 nm. Solid lines: fitted data. Circles: $i = 0°$, diamonds: $i = 45°$.

Conclusions. The data of the bidirectional reflectance of Spectralon presented here can be used to setup the scale for any kind of bidirectional reflectance spectrometer for a large range of phase angles over the wavelength range from 250 nm to 2500 nm. As an additional information the table of R^{dh} delivered for each standard by Labsphere Inc., is needed.

Goniospectrometric properties of a white standard. A. Oehler and A. Dummel.

Tab. 1

e [deg]	R(i=0°,e)	R fitted	e [deg]	R(i=45°,e)	R fitted
-8.50E+01	7.615E-01	7.731E-01	-8.50E+01	1.029	1.207
-8.00E+01	8.400E-01	8.328E-01	-8.00E+01	1.117	1.184
-7.50E+01	8.892E-01	8.791E-01	-7.50E+01	1.134	1.164
-7.00E+01	9.151E-01	9.149E-01	-7.00E+01	1.132	1.145
-6.50E+01	9.387E-01	9.425E-01	-6.50E+01	1.123	1.128
-6.00E+01	9.584E-01	9.638E-01	-6.00E+01	1.112	1.113
-5.50E+01	9.753E-01	9.803E-01	-5.50E+01	1.100	1.098
-5.00E+01	9.894E-01	9.931E-01	-5.00E+01	1.089	1.085
-4.50E+01	1.001	1.003	-4.50E+01	1.078	1.073
-4.00E+01	1.012	1.011	-4.00E+01	1.066	1.062
-3.50E+01	1.021	1.019	-3.50E+01	1.055	1.052
-3.00E+01	1.028	1.025	-3.00E+01	1.045	1.043
-2.50E+01	1.035	1.032	-2.50E+01	1.037	1.035
-2.00E+01	1.041	1.039	-2.00E+01	1.027	1.027
-1.50E+01	1.048	1.047	-1.50E+01	1.020	1.019
-1.00E+01	1.055	1.057	-1.00E+01	1.011	1.013
-7.50	1.059	1.062	-5.00	1.007	1.006
-5.00	1.065	1.067	0.00	1.001	1.001
-3.00	1.073	1.072	5.00	9.959E-01	9.957E-01
3.00	1.074	1.072	1.00E+01	9.925E-01	9.907E-01
5.00	1.065	1.067	1.50E+01	9.883E-01	9.861E-01
7.50	1.059	1.062	2.00E+01	9.86501	9.822E-01
1.00E+01	1.055	1.057	2.50E+01	9.846E-01	9.792E-01
1.50E+01	1.048	1.047	3.00E+01	9.824E-01	9.776E-01
2.00E+01	1.042	1.039	3.50E+01	9.835E-01	9.784E-01
2.50E+01	1.035	1.032	3.75E+01	9.851E-01	9.803E-01
3.00E+01	1.029	1.025	4.00E+01	9.895E-01	9.838E-01
3.50E+01	1.021	1.019	4.20E+01	9.859E-01	9.881E-01
4.00E+01	1.012	1.011	4.80E+01	9.761E-01	9.774E-01
4.50E+01	1.002	1.003	5.00E+01	9.627E-01	9.652E-01
5.00E+01	9.902E-01	9.931E-01	5.25E+01	9.509E-01	9.513E-01
5.50E+01	9.754E-01	9.803E-01	5.50E+01	9.344E-01	9.383E-01
6.00E+01	9.594E-01	9.638E-01	6.00E+01	9.138E-01	9.139E-01
6.50E+01	9.393E-01	9.425E-01	6.50E+01	8.885E-01	8.898E-01
7.00E+01	9.153E-01	9.149E-01	7.00E+01	8.651E-01	8.648E-01
7.50E+01	8.895E-01	8.791E-01	7.50E+01	8.138E-01	8.379E-01
8.00E+01	8.401E-01	8.328E-01	8.00E+01	7.304E-01	8.079E-01
8.50E+01	7.709E-01	7.731E-01			

	ω	*h*	*s*	*b*	*c*
R(i=0°,e)	9.4182E-01	1.2348	2.9275	2.4144	-4.4818E-01
R(i=45°,e)	9.9999E-01	1.6830E-01	6.5451E-01	-9.7603E-01	1.9216E-01

Tab. 3

Hapke-parameters for modeling the data presented in table 1 . ω: single scattering albedo; *h* : width of opposition surge; *s* : opposition surge amplitude; *b* and *c* : first and second coefficient of 2. order Legendre polynomial.

References. [1] Hapke, B.(1981),J.G.R.,86,3039. [2] Hapke, B.(1986), Icarus, 67, 264. [3] Weidner, V.R., Hsia J.J., (1981), Appl. Opt., 19,1268.[4] Weidner V.R., Hsia J.J., Adams B. (1985), Appl. Opt., 24, 2225. [5] Oehler A., Neukum G. (1992), In Lunar and Planetary Science XXIII, 1015.

529-54 ABS. ONLY

167989 N94-20365 P-1

CHARACTERIZATION OF MINNESOTA LUNAR SIMULANT FOR PLANT GROWTH

James P. Oglesby[1], Willard L. Lindsay[2] and Willy Z. Sadeh[3]
Center for Engineering Infrastructure and Sciences in Space (CEISS)
Colorado State University
Fort Collins, Colorado

Processing of lunar regolith into a plant growth medium is crucial in the development of a regenerative life support system for a lunar base. Plants, which are the core of such a system, produce food and oxygen for humans and, at the same time, consume carbon dioxide. Because of the scarcity of lunar regolith, simulants must be used to infer its properties and to develop procedures for weathering and chemical analyses. The Minnesota Lunar Simulant (MLS) has been identified to date as the best available simulant for lunar regolith. Results of the dissolution studies reveal that appropriately fertilized MLS can be a suitable medium for plant growth. The techniques used in conducting these studies can be extended to investigate the suitability of actual lunar regolith as a plant growth medium.

Dissolution experiments were conducted using the MLS to determine its nutritional and toxicity characteristics for plant growth and to develop weathering and chemical analysis techniques. Two weathering regimes, one with water and one with dilute organic acids simulating the root rhizosphere microenvironment, were investigated. Elemental concentrations were measured using inductively-coupled-plasma (ICP) emission spectrometry and ion chromatography (IC). The geochemical speciation model, MINTEQA2, was used to determine the major solution species and the minerals controlling them. Acidification was found to be a useful method for increasing cation concentrations to meaningful levels.

Initial results indicate that MLS weathers to give neutral to slightly basic solutions which contain acceptable amounts of the essential elements required for plant nutrition (i.e., potassium, calcium, magnesium, sulfur, zinc, sodium, silicon, manganese, copper, chlorine, boron, molybdenum, and cobalt). Elements that need to be supplemented include carbon, nitrogen, and perhaps phosphorus and iron. Trace metals in solution were present at nontoxic levels.

---

[1]NASA Graduate Student Fellow, CEISS, Department of Agronomy
[2]University Distinguished Professor of Soil Science, CEISS, Department of Agronomy
[3]Professor of Space Engineering and Director, CEISS, Department of Civil Engineering

S30-91 ABS. ONLY.

N94-20866

DYNAMICS OF LARGE SCALE IMPACTS ON VENUS AND EARTH; John D. O'Keefe and Thomas J. Ahrens, Lindhurst Laboratory of Experimental Geophysics, Seismological Laboratory 252-21, California Institute of Technology, Pasadena, CA 91125.

Large scale impacts are a key aspect of the accretion and growth of the planets, the evolution of their atmospheres, and the viability of their life forms [1-4]. We have performed an extensive series of numerical calculations that examined the mechanics of impacts over a broad range of conditions [5] and are now extending these to account for the effects of the planetary atmosphere. We have examined the effects of large scale impacts in which the trapping and compression of an atmosphere during impact is a significant factor in the transfer of energy to the atmosphere. Shown in Figure 1 are the various energy transfer regimes and where conventional drag and trapping and subsequent compression of atmosphere between the bolide and planetary surface are significant.

Numerical simulation of the impacts on planets with substantial atmospheres is difficult because of the large differences in the densities of the impactor, planet, and the atmosphere. Since our primary purpose was to examine the interaction of the shocked atmosphere and the cratering dynamics, we analytically calculated the flow field due to the passage of the impactor through the atmosphere and the initial interaction with the planetary surface and used these results as initial conditions in the impact calculations [6]. We calculated the state conditions behind the shock wave in front of the impactor. Given these conditions, we calculated the conditions after reflection from the surface and the subsequent adiabatic compression of the entrapped atmosphere to impactor-planet Hugoniot pressure and particle velocity. These conditions represent the work done by the impactor on the encompassed atmosphere. The relative amount of energy associated with this work is shown in Figure 1 for various regimes. We placed the encompassed atmosphere and energy associated with the work done by the impactor into a ring cell just outside the impactor and used an Eulerian numerical algorithm to calculate the resulting flow fields [7]. Specifically, we calculated the impact of a 5 km radius projectile traveling at 20 km/s on models of the Earth and Venus. Since the gravitational accelerations are similar (980 vs. 887 cm/s^2), the primary differences in the initial conditions are due to the atmospheric conditions (see Figure 2).

Samples of the calculations are shown in Figure 2. The resulting flow fields are very complex and differ for the two planets. In both cases, the entrapped atmosphere drives a strong shock wave away from the impact site. In the case of Venus, the shock wave remains lower in the atmosphere as opposed to the Earth, where the larger atmospheric density gradient refracts and accelerates the shock as it propagates to higher altitudes [8]. The refraction of the shock wave upward results in the acceleration of material upward and the blowing off of the atmosphere in the case of the Earth. The atmospheric shock pressure drives a ground shock wave. This ground shock wave initially follows the atmospheric shock wave at the surface and then at later times when the atmospheric shock decays, the ground shock wave outruns it. In addition, the projectile driven shock wave also initially lags the atmospheric shock wave and finally it also outruns the atmospheric shock wave (see Figure 2). The downward propagating wake also produces a complex series of interactions. The wake impacts the surface and stagnates, and drives a shock up and around the penetrating projectile. This shock refracts around the back of the incoming projectile and intersects other downward propagating wake gases. This produces a high pressure and temperature region behind the projectile which is seen in laboratory scale experiments [9]. The crater ejecta is propelled out of the crater after the atmospheric shock has propagated away from the crater and interacts with a low density, high temperature environment. In the case of the Earth, the atmospheric flow is in the same general direction as the ejecta. On Venus where, because of the confinement of the shock wave, the ejecta plume runs into the atmosphere and produces vortices in front of the ejecta, as seen in initial laboratory experiments of Shultz et al. [9]. The angle that the ejecta is launched changes with atmospheric pressure. In the case of Earth, the ejection angle is ~60° from the horizontal and varies little with and without an atmosphere; in the case of Venus, the angle increases to ~75°. The extent of the ejecta blanket in the case of Venus, is both restricted by the increased angle of ejection, but also by the lower atmospheric scale height.

REFERENCES: 1Wetherill G. W. (1985) *Science*, 228, 877-879. 2Ahrens T. J., *et al.* (1989) in *Origin and Evolution of Planetary and Satellite Atmospheres* (Atreya S. K., *et al.*, eds.), pp. 328-385. University of Arizona Press, Tucson, AZ. 3Ahrens T. J. (1993) *Ann. Rev. Earth Planet. Sci.*, in press. 4Sharpton V. L. and Ward P. D. (1990), Global Catastrophes in Earth History; An Interdisciplinary Conference on Impacts, Volcanism, and Mass Mortality. The Geological Society of America, Inc., Special Paper 247, Boulder, Colorado, 631 pp. 5O'Keefe J. D. and Ahrens T. J. (1992) *J. Geophys. Res.*, submitted. 6O'Keefe J. D. and Ahrens T. J. (1988) *Abstract, Lunar and Planetary Science*, XIX, 887-888. 7Thompson S. L. (1979), Sandia National Labs, Albuquerque, N.M., SAND 77-1339. 8Zel'dovich Y. B. and Raizer Y. P. (1966) *Physics of Shock Waves and High-Temperature Hydrodynamic Phenomena* Academic Press, New York, 916 pp.. 9Schultz P. H. and Gault D. E. (1981) *Geol. Soc. Am. Spec. Paper*, 190, 152-174.

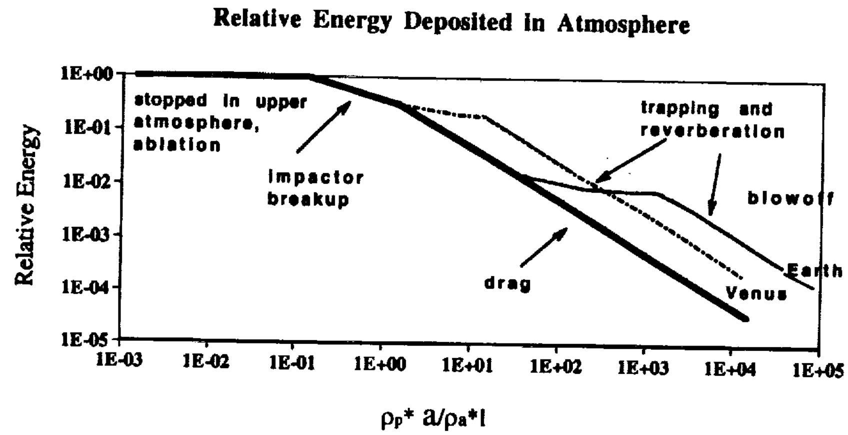


Figure 1. Regimes of relative energy deposited in atmosphere. Relative energy is given as a function of density of impactor (ρ_p) times the radius of impactor (a) divided by the product of density of atmosphere at surface (ρ_a) times scale height (ℓ). Energy is normalized to impactor kinetic energy.

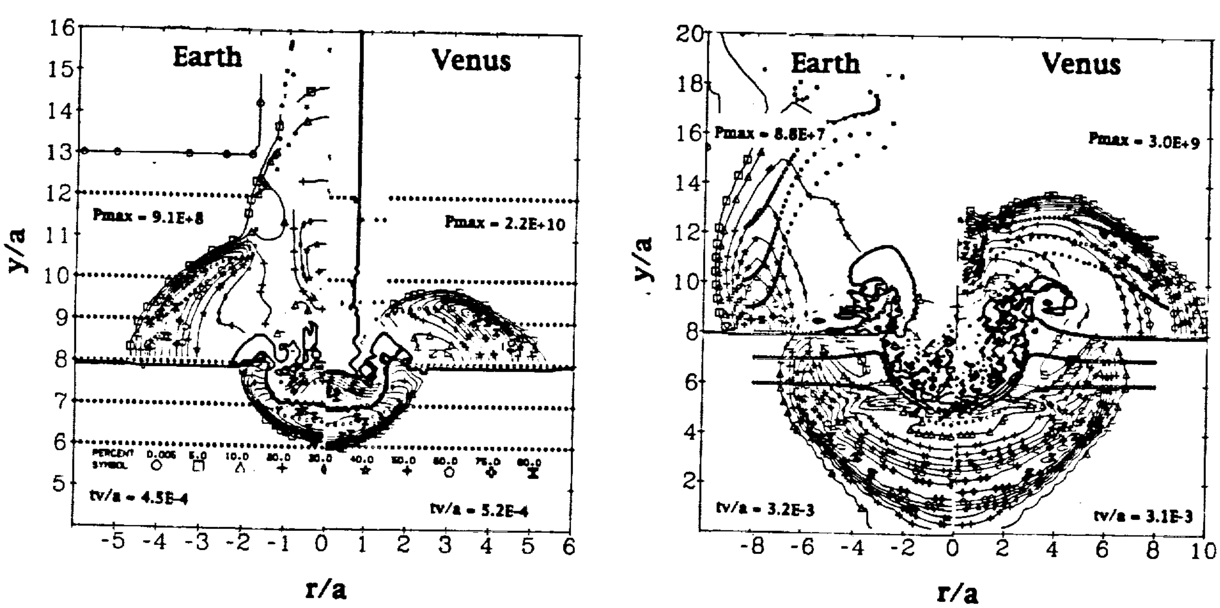


Figure 2. Impact-induced pressure fields in Earth and Venus and their atmospheres. The radius of the impactor (a) is 5 km and the velocity (v) is 20 km/s. Shown are the pressure contours for the percentages listed in Figure 2a at various dimensionless times (tv/a). The maximum atmospheric pressures are indicated for each case (dynes/cm^2).

S31-25
ABS ONLY
167991

N94-20667

TAMBO QUEMADO: EXTRAORDINARY CONCENTRATIONS OF REE AND REFRACTORY TRACE ELEMENTS CAUSED BY ARTIFICIAL HEATING. E. Olsen (Geophys.Sci., Univ. of Chicago), I. Hutcheon (Geol. Planet. Sci., Caltech) & C. Moore (Dept. of Chem., Ariz.State U.)

Buchwald [1] examined samples of the IIIB iron Tambo Quemado (TAMQ) cut from the 130 kg main mass. He determined it had been artificially heated, at some time prior to being reported, in an attempt to obtain metal from it. Although the Widmanstätten structure appears relatively unaffected under macroscopic examination, microscopic study of etched sections reveals the effect of the heating. Taenite and plessite area boundaries are indistinct due to high temperature diffusion. Schreibersite, once present in significant amounts, has been melted. Schreibersites in the interior have resolidified in fine-grained eutectic textures surrounded by dark-etching metal rims supersaturated with phosphorus. Buchwald states that phosphate minerals were probably present originally, because graftonite, and its polymorph sarcopside (both essentially $Fe_3[PO_4]_2$), are common in irons of the IIIAB groups. Based on his metallographic study Buchwald estimates TAMQ was heated to 1000°C for about one hour.

An interior sample from TAMQ was examined in order to determine what effect this unintended heating "experiment" had upon the phosphate phases. It was considered unlikely that an interior sample within this large a meteorite would have had significant chemical communication with the terrestrial atmosphere during this short a heating time. Oxygen entering the interior would be buffered by metallic iron, and the results should be evident. Any observed changes could provide a baseline for interpreting unusual mineralogical or chemical features in the large number of IIIAB irons currently being studied by the authors of this abstract and their colleagues. An interior sample was collected from Arizona State Univ. sample ASU 605.6. It appeared to be a normal graftonite inclusion, ≈ 500 µm bleb contained in swathing kamacite. Back-scattered electron images of the polished section showed fragments (150 x 400 µm range) of graftonite (Phase 1 in Figs below) with irregular patches, 10 to 40 µm, of Phase 2 strung out in trains running through the length of the graftonite. Also, within the trains were numerous very small irregular grains, generally < 10 µm, of Phase 3, with very high back-scattered electron brightness. Grains of Phase 3 are contained within Phases 1 and 2. Electron microprobe analyses were made:

Phase	1	2	3
MgO	0.03	0.02	0.00
Al_2O_3	0.02	0.47	0.71
SiO_2	0.34	10.47	1.77
P_2O_5	39.91	25.00	9.78
CaO	0.28	0.00	0.00
TiO_2	0.00	0.00	0.12
FeO	60.02	65.01	89.12
Total	100.60	100.97	101.50

Phase 1 (Graftonite) $(Fe,Ca,Mg,Al)_3(Si,P)_2O_8$

Phase 2 (Silicophosphate) $Fe_{10}(Al_{0.09}P_{3.93}Si_{1.95})_6O_{24}$

Phase 3 (Phosphoran wüstite) ≈ $(Fe,Al,Ti,Si,P)_7O_8$

The phase relations in the system Fe-P-O (in the presence of metallic Fe) have been studied [2]. Solid phases 1 and 3 coexist in the subsolidus field below a 940°C eutectic. From the presence of phosphoran wüstite it is clear that a small amount of terrestrial oxygen entered the system during the heating, log $P(O_2) \approx -18$. Original graftonite in TAMQ melted, oxidized slightly and then recrystallized as graftonite and phosphoran wüstite. Graftonites in IIIAB irons ususally contain 0.02 to 0.04 wt% SiO_2. During the heating silica appears to have concentrated in the melted graftonite, increasing its silica content by about 10×, entering the phosphoran wüstite, and creating a new silicophosphate phase.

The abundances of rare earth elements (REE) and refractory trace elements (RTE) in the three phases in TAMQ were measured with the PANURGE ion microprobe [Figs. 1 & 2]. Phase 1 has a flat REE pattern with 1-2 × C1 abundances and a negative Eu anomaly. The pattern is similar to those measured in Ca-phosphates in chondrites [3,4] but at much lower REE abundances. The RTE abundances in Phase 1, except for Ti, are depleted relative to C1. Phase 3 has a LREE-enriched pattern with much higher abundances of LREE: La ≈ 20 × C1 and a C1-normalized La/Lu ratio of 10-20. Eu is strongly enriched at ≈ 120 × C1. The RTE abundances in Phase 3 are

TAMBO QUEMADO: Olsen E., Hutcheon, I. and Moore C.

also substantially enhanced relative to Phase 1 and decrease in abundance with increasing refractory character, from Ba ≈ 400 x C1 to Zr ≈ 3 x C1. The pronounced enrichments of Ba and Eu in phase 3 are accompanied by complementary depletions in Phase 1. Phase 2 contains the lowest REE abundances with a REE pattern very similar to that of Phase 3 but at abundances ≈ 10 times lower. It is possible Phase 2 contains essentially no REE and the data reflect very small, undetected inclusions of Phase 3 within Phase 2. The RTE abundance pattern of Phase 2 also mimics that of Phase 3, generally at lower abundances, although V, Sc and Ti levels are approximately equal in both phases. The relatively high abundances of REE and RTE in the TAMQ graftonite inclusion contrast sharply with the abundances of these elements measured in Fe-phosphates in other IIIAB irons. Ion probe analyses of graftonite and several associated phosphate phases have revealed very low REE and RTE concentrations, generally below 0.1 to 0.01 x C1; those results appear to confirm the argument that phosphates in IIIAB irons formed by oxidation of P dissolved in metal [5] with the phosphates inheriting the absence of lithophile elements in the metal source. High Ba has been found in one occurrence but without a satisfactory explanation.

Compared to phosphates in other IIIAB irons the abundances of the REE and RTE in the three phases of TAMQ are extraordinary. Unfortunately it was not possible to determine a mode to calculate bulk trace element concentrations because the sample chips do not represent the entire original inclusion. If the original inclusion was the same as phosphate inclusions analyzed in other IIIAB irons, *i.e.*, very depleted in both REE and RTE, then it is clear there has been a significant increase in both groups of elements in the graftonite inclusion during the heating "experiment". The source of these elements is a puzzle. One possibility is that temperature gradients in the heated mass caused these elements, in generally undetectable amounts in the original graftonite inclusions, to diffuse from graftonites in hotter volumes to those in cooler volumes. One difficulty with this arises from the manner of occurrence of phosphate inclusions in the metal host. The phosphates are commonly separated by large volumes of intervening metal, requiring diffusion of lithophile trace elements over distances of up to tens of centimeters.

The data from TAMQ, in particular the high and relatively uniform REE abundances in Phase 1 and the complementary distribution of Ba and Eu between Phases 1 and 3, serve as a warning. Natural reheating of a IIIAB iron, even at temperatures of only a few hundred degrees C for longer periods of time than in this "experiment", *i.e.* several hours, may lead to significant mobilization of trace elements. The resulting abundance patterns may strongly resemble those traditionally attributed to single nebular or parent body processes, leading the unwary to invalid conclusions. [Div. Contrib. 5227 (791)]

REFERENCES: [1] Buchwald, V.F.(1975) *Handbook of iron meteorites*, v.3, U.Calif. Press. [2] Trömel, G. & Schwerdtfeger, K. (1963) *Arch. Eisenhüttenwissen* **34**, 58. [3] Reed, S.J.B. & Smith, D.G.W. (1985) *Earth Planet. Sci. Lett.* **72**, 238. [4] Crozaz, G., *et al.* (1989) *Earth Planet. Sci. Lett.* **93**, 157. [5] Olsen, E. & Fredriksson, K. (1966) *Geochim. Cosmochim. Acta* **30**, 459.

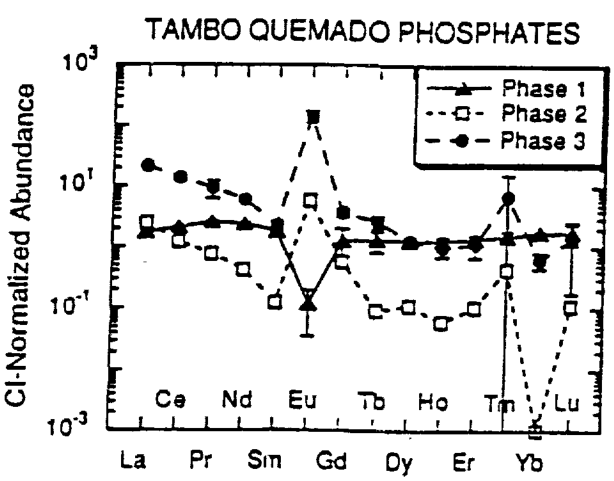


Fig.1

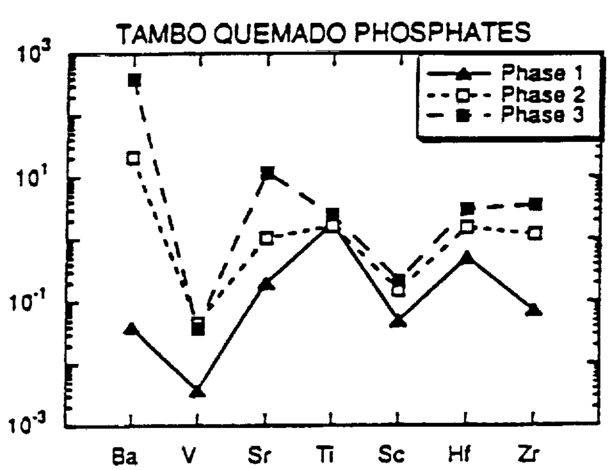


Fig.2

MODELLING THE GRAVITY AND MAGNETIC FIELD ANOMALIES OF THE CHICXULUB CRATER, C. Ortiz Aleman, Instituto de Geofisica, Ciudad Universitaria, Delgacion de Coyoacan, Codigo 04510, Mexico, D.F., Mexico; M. Pilkington, A.R. Hildebrand, W.R. Roest, R.A.F. Grieve and P. Keating, Geophysics Division, Geological Survey of Canada, 1 Observatory Crescent, Bldg. 3, Ottawa, Canada K1A 0Y3

The ~180-km-diameter Chicxulub crater lies buried by ~1 km of sediment on the northwestern corner of the Yucatán Peninsula, Mexico. Geophysical, stratigraphic and petrologic evidence support an impact origin for the structure and biostratigraphy suggests that a K/T age is possible for the impact (1). The crater's location is in agreement with constraints derived from proximal K/T impact-wave and ejecta deposits and its melt-rock is similar in composition to the K/T tektites. Radiometric dating of the melt rock reveals an age identical to that of the K/T tektites (2,3). The impact which produced the Chicxulub crater probably produced the K/T extinctions and understanding the now-buried crater will provide constraints on the impact's lethal effects. The outstanding preservation of the crater, the availability of detailed gravity and magnetic data sets, and the two-component target of carbonate/evaporites overlying silicate basement allow application of geophysical modelling techniques to explore the crater under most favourable circumstances. We have found that the main features of the gravity and magnetic field anomalies may be produced by the crater lithologies.

A cross section through the center of the Chicxulub crater was constructed for modelling purposes based on information from drill holes within the crater, seismic reflection profiles, the magnetic and gravity field anomalies and scaling from structural relations derived from other terrestrial craters. Density contrasts were assigned based in part on measurements on samples recovered from the crater. The resulting 2-dimensional field anomalies were calculated by interactive forward modelling using a program developed by W. Roest.

Figure 1 shows one modelled Bouguer gravity anomaly profile together with the observed anomaly. The density elements are based on the fallback breccia which includes a peak ring to account for the inner gravity low, an ~3-km-thick melt pool, megabreccia and a structural uplift underlying the melt pool, and an ejecta breccia on top of slumped blocks in the outer zone of collapse. This model uses geometry to account for the decrease in magnitude of the gravity anomaly towards the rim but this effect is more likely the consequence of decreasing density contrast with distance from the impact point due to decreased fracturing from the shock wave and/or decreased slumping. The model is non unique and even the handful of currently available density measurements are useful to constrain the results. A significant uplift of greater-density lower crust within the crater is precluded by the data although a weakly positive density contrast is permitted.

Figure 2 shows one modelled total magnetic field profile together with the observed anomaly. The magnetic elements are based on the structural uplift and the upper margins of the melt pool. The magnetic field anomaly is assumed to be due to remanence. The melt-pool anomalies are assigned a magnetization inclination of -41° and declination of 163°E based on the paleopole position and Yucatán Peninsula position at K/T time. This inclination is consistent with that reported in (3). The structural uplift is assumed to have a magnetization declination of ~90° E and inclination of ~30° based on the observed field. The ~80-km-diameter high-amplitude magnetic anomaly zone (Zone 1 of (4)) may be divided into two concentric zones. This distinction is clearer if the magnetic-field data are plotted after reduction to the pole.

Acknowledgements: We are grateful to Petróleos Méxicanos for allowing modelling of aeromagnetic data acquired for petroleum exploration and to PAIGH for supporting C. Ortiz.

References: (1) Hildebrand et al., 1991, Geology, 19: 867-871; (2) Swisher, C.C. et al., 1992, Science, 257: 954-958; (3) Sharpton et al., 1992, Nature, 359: 819-821; (4) Penfield and Camargo, 1981, SEG abs. 37-38; (5) Perrier and Quiblier, 1974, AAPGB 58: 507-528.

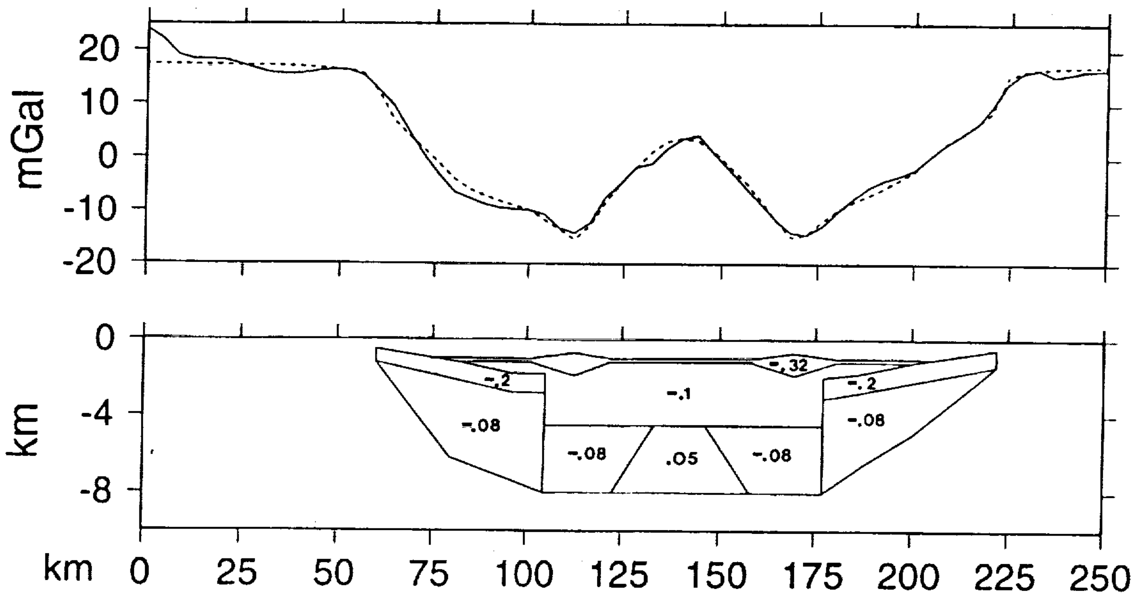


Figure 1: Bouguer gravity anomaly model of Chicxulub crater. Upper portion of diagram shows observed Bouguer anomaly along a near-central profile parallel to coastline with a regional gradient removed (Southernmost profile of two located on Figure 1 of Hildebrand et al. (1)). Solid line is observed anomaly; dashed line is calculated anomaly. Lower portion of diagram shows density elements chosen for Chicxulub crater together with density contrasts in g/cm^3. An 8 km depth limit was chosen for density contrasts based on assuming that lithostatic pressure would close porosity at this level (5). Note vertical exaggeration.

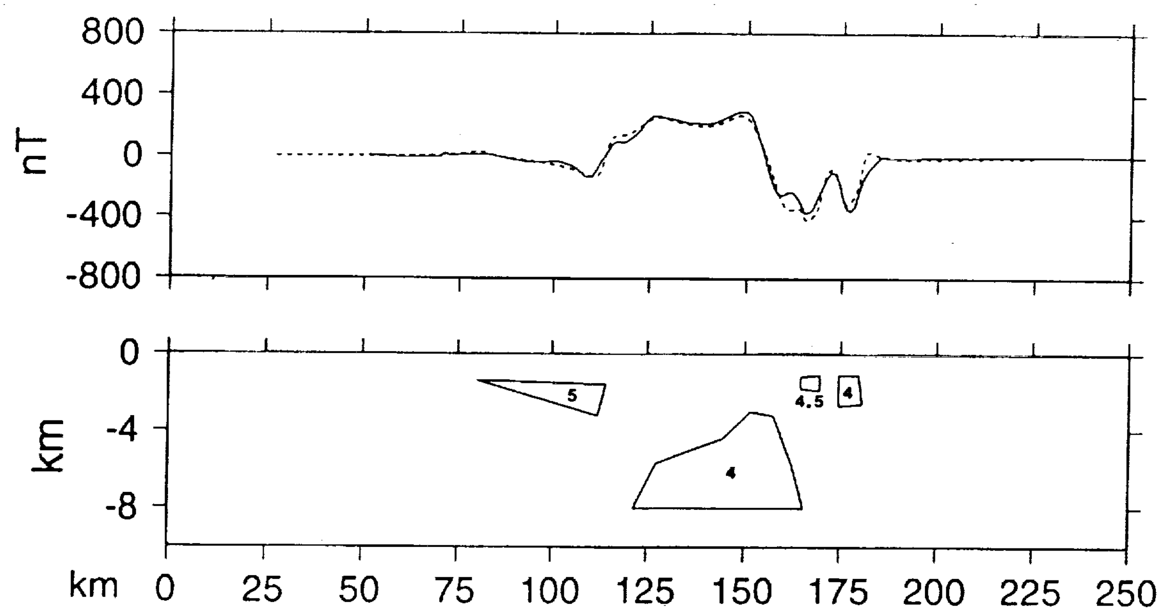


Figure 2: Total field magnetic anomaly model of Chicxulub crater. Upper portion of diagram shows observed magnetic field along same profile as in Figure 1. Solid line is observed field; dashed line is calculated anomaly. Lower portion of diagram shows magnetic bodies chosen for Chicxulub crater together with magnetization contrasts in A/m. Shallower bodies correspond to melt pool and deeper body to central structural uplift. Note vertical exaggeration.

533-25
ABS-ONLY

N94-20869

SELF DIFFUSION OF ALKALINE-EARTH IN Ca-Mg-ALUMINOSILICATE MELTS, EXPERIMENTAL IMPROVEMENTS ON THE DETERMINATION OF THE SELF-DIFFUSION COEFFICIENTS;

O. Paillat and G. J. Wasserburg, Lunatic Asylum, Div. of Geological and Planetary Sciences, California Institute of Technology, Pasadena CA 91125.

Experimental studies of self-diffusion isotopes in silicate melts often have quite large uncertainties when comparing one study to another. We designed an experiment in order to improve the precision of the results by simultaneously studying several elements (Mg, Ca, Sr, Ba), during the same experiment thereby greatly reducing the relative experimental uncertainties. Results show that the uncertainties on the diffusion coefficients can be reduced to 10%, allowing a more reliable comparison of differences of self-diffusion coefficients of the elements. This type of experiment permits us to study precisely and simultaneously several elements with no restriction on any element. We also designed an experiment to investigate the possible effects of multicomponent diffusion during Mg self diffusion experiments by comparing cases where the concentrations of the elements and the isotopic compositions are different. The results suggest that there are differences between the effective means of transport. This approach should allow us to investigate the importance of multicomponent diffusion in silicate melts.

As starting material we used a glass composed of 11.5 MgO, 12.5 CaO, 44 SiO_2 and 32 Al_2O_3 by weight %, close to the compositions used by Sheng *et al.* (1992) [1]. This glass was powdered and half of the batch was mixed with weighted amounts of oxides or carbonates doped with ^{25}Mg, ^{44}Ca, ^{84}Sr and ^{136}Ba. The other half of the batch was mixed with the same amount of oxides or carbonates of normal isotopic composition. The two batches were thus chemically homogeneous and isotopically different. The final concentration of BaO was 0.3 wt% and of SrO was 0.2 wt%. Samples were put in a vertical furnace at 1763 K (above the liquidus) for fifteen minutes. This type of self-diffusion experiment is a continuation of the study of Sheng *et al.* (1992) [1] and consists of using a diffusion couple in chemical equilibrium but isotopic disequilibrium. This has been extended to a melt-melt couple instead of a spinel-melt couple. Analyses of the quenched glass were done with the PANURGE ion probe, and the electron probe. Two traverses along the sample were done: first for Ca and Mg isotopes, then for Sr and Ba isotopes at the same points but with a higher primary beam current. Results from two traverses along the sample are shown in Fig. 1, the two profiles are very similar and seem to follow very well an error function law; thus no evidence of convection has been found. Moreover the fit of these profiles with an inv(erf), Fig. 2, are very good, and an estimation of the precision of the value of the slope is 10%. The value of the diffusion coefficients obtained from these fits are:

$D(cm^2/s) \times 10^6$	^{25}Mg	^{44}Ca	^{84}Sr	^{136}Ba
traverse #1	1.50	1.28	0.86	0.55
traverse #2	1.38	1.23		0.44

The differences between the coefficients for the different elements are several times larger than the precision and can be exploited with more confidence than if we had done separate experiments. The self-diffusion coefficients seem to vary linearly with the ionic radii of the element while there is a suggested relationship with $1/\sqrt{m}$ (m: atomic mass of the element) which is less clear. These interpretations will be investigated after we obtain the temperature dependence of the coefficients and the dependence on melt composition. In order to estimate the possible importance of multicomponent diffusion during self-diffusion experiments, we also designed an experiment in which only the ^{25}Mg concentration varies, but ^{24}Mg and ^{26}Mg concentrations are constant along the profile. This provides a small chemical gradient (10% of total Mg concentration variation compared to 100% variation of ^{25}Mg). The sample was held in the same furnace with the same time-temperature history as the previous experiment. We obtained a diffusion coefficient for ^{25}Mg of 1.0×10^{-6} cm^2/s, which is about 30% lower than the previous one. Fig. 3a shows that the two lines clearly cross, and that the slopes are different; this difference is believed to be significant. Moreover, the $^{24}Mg^+/^{30}Si^+$ ratio recorded during the analysis showed a variation along the profile, (Fig. 3b), which shows a sinusoidal trend in the region of the interface. This can hardly be due to ^{30}Si concentration variation, which is constrained to be fairly constant. Therefore this observation is interpreted as a variation of the ^{24}Mg concentration. Since the $^{24}Mg/^{26}Mg$ ratio is fairly constant along the profile, this suggests that ^{26}Mg should vary in the same way. These two independent observations can be consistently explained in terms of multicomponent diffusion between ^{24}Mg, ^{25}Mg and ^{26}Mg. Higher precision must be achieved on these observations to obtain a significant value for extra-diagonal term $D_{ij\,(i \neq j)}$. In summary, the approach used here appears to be applicable to essentially all chemical elements to determine their individual diffusion coefficients in a single experiment. We will attempt to carry these studies out below the liquidus and in the glass transition region if it is possible to eliminate

the problem of devitrification of the glasses at lower temperatures. Division Contribution 5240(803). References:

[1]Sheng Y.J., Wasserburg G.J. and Hutcheon I.D. (1992) *GCA 56*, 2535.

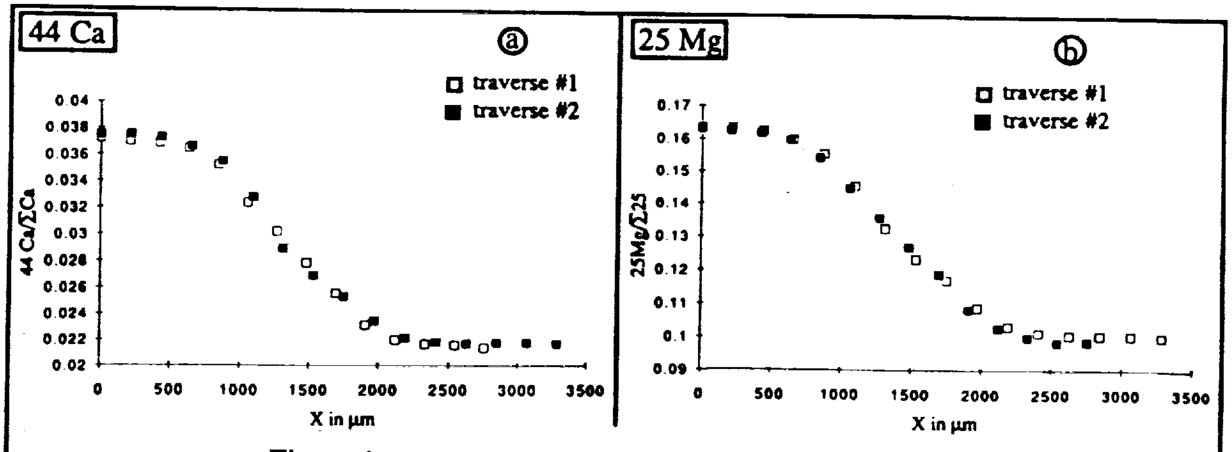


Figure 1 : Diffusion profile from 44Ca/40Ca (a) and 25Mg/24Mg (b) ratios

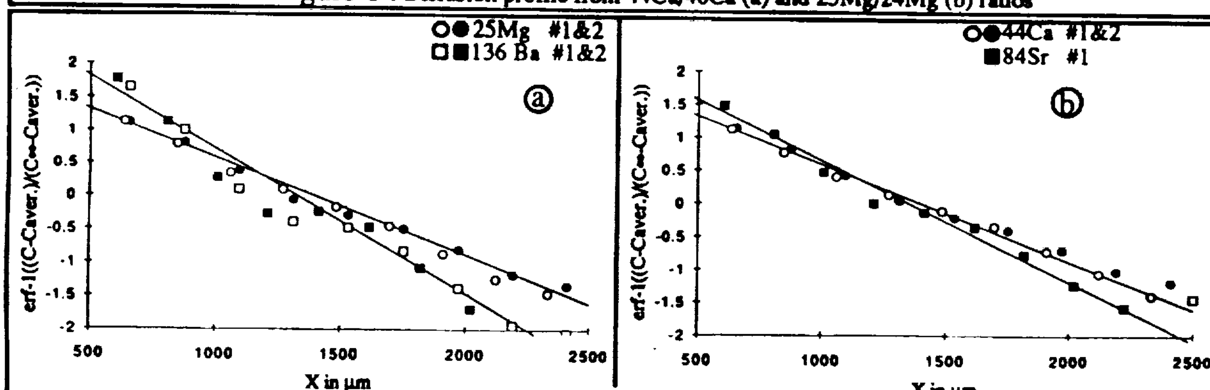


Figure 2 : Fit (lines) of the calculated inv(erf) versus x from data (symbols), showing the good precision (10%) on the slope (diffusion coefficent)

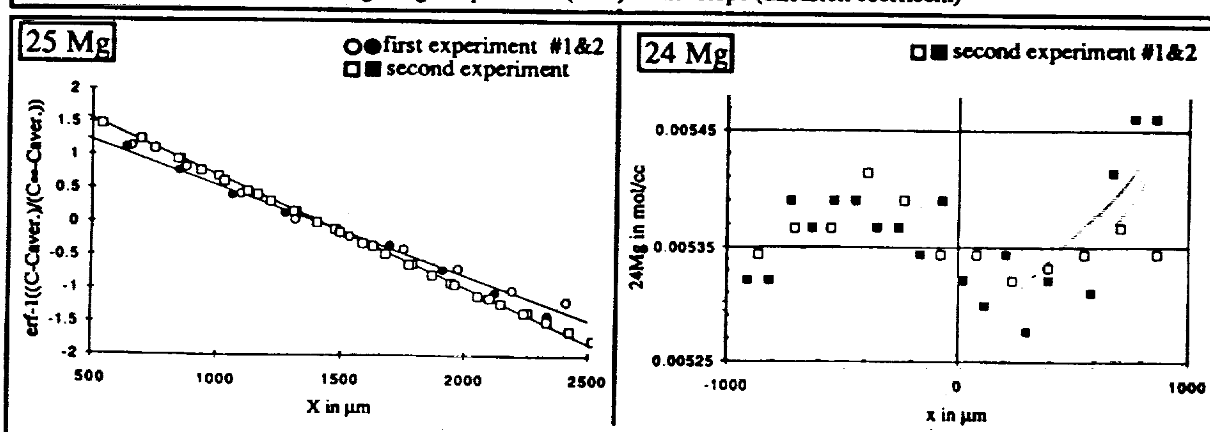


Figure 3

a : Fit of the calculated inv(erf) versus x for 25Mg : first experiment has constant total Mg concentration, second experiment does not have constant total Mg.

b : Variations of 24Mg concentration for the second experiment , it was nearly constant at the beginning of the experiment

534-25
ABS. ONLY

N94-20870

ORTHOPYROXENES AS RECORDERS OF DIOGENITE PETROGENESIS: MAJOR AND MINOR ELEMENT SYSTEMATICS. J.J. Papike, M.N. Spilde, G.W. Fowler, and C.K. Shearer; Institute of Meteoritics, Dept. of Earth & Planetary Sciences, University of New Mexico, Albuquerque, NM 87131-1126

INTRODUCTION. As a part of our research to better understand magmatic processes in the Eucrite Parent Body we have initiated an ambitious program of study of major, minor and trace elements in orthopyroxene from diogenites. This paper reports preliminary results for major and minor elements in orthopyroxenes for a suite of 13 diogenites: Aioun El Atrouss, ALH 84001, ALH A 77256, EET 87530, Ellemeet, Garland, Ibbenburen, Johnstown, Manegoan, Peckelsheim, Roda, Shalka, and Tatahouine. A companion paper by Shearer et al. [1] (this volume) reports new trace element data for ALH 84001, ALH A 77256, Ibbenburen, and Tatahouine. We have presently collected over 800 high quality pyroxene microprobe analyses for Si, Al, Ca, Na, Mn, Fe, Mg, Cr, and Ti. The chemical systematics observed for these orthopyroxenes reflect original magmatic mineral/melt partitioning plus later trapped liquid/mineral equilibration, subsolidus exsolution, and mineral/mineral metamorphic reactions. We have therefore avoided, at this point, any attempt to use statistical analysis to group (e.g. factor or cluster analysis [2, 3]) these orthopyroxenes chemically.

DISCUSSION. Fe/Mg systematics can be seriously affected by subsolidus equilibration with trapped liquid. The more disparate the Fe/Mg of the trapped liquid and OPX and the greater the amount of trapped liquid, the greater the shift in OPX Fe/Mg will be. This trapped liquid shift effect has been discussed with regard to terrestrial layered intrusions by Barnes [4] and Cawthorn et al. [5]. Figure 1 presents the Fe/(Fe+Mg)= X_{Fe} data for the 13 diogenites studied, ordered (upper left to lower right) in terms of increasing X_{Fe}. One assemblage in Rhoda is the most Mg-rich. Ellemeet has two populations X_{Fe} (0.20) and (0.27). The highest X_{Fe} values are found in Peckelsheim and Garland. The olivine diogenites (Sack et al [6]) require further comment. If the thirteen diogenites represent cumulates from magmatic systems, the olivine diogenites would be expected to display low X_{Fe} values. In fact one population of ALH 84001 has a value of (0.20). The second, more Fe-rich population (X_{Fe}=0.24) in ALH 84001 most likely reflects reaction between trapped melt and OPX. ALH A 77256 is even more annealed and it appears that its magmatic X_{Fe} has been erased. Thus in order to read the magmatic record recorded by OPX chemistry we will have to use elements with slower diffusion rates (e.g. REE [1]).

Figure 2 shows some interesting systematics in terms of Al vs Cr. A main trend occurs on the diagram with Peckelsheim, one assemblage of Garland (which is polymicht), and Ellemeet plotting on the low Cr, Al end and Manegoan, Johnstown, and Aioun El Atrouss plotting near the high Cr, Al end. The olivine diogenite ALH A 77256 falls off the trend at lower Cr values. Most OPX groups show rather smooth trends on this diagram with a positive slope; however, the slopes are different. The slopes of regression lines through the Al vs. Cr points range from 0.1 for ALH A 77256 to a high of .945 for Tatahouine. Note Tatahouine (tight group), ALH 84001, Ibbenburen, and ALH A 77256 which are highlighted on this diagram for comparisons to our companion study [1]. A range of Cr, Al concentrations can be found in single grains. Three mechanisms that could cause a decrease in Cr, Al abundances towards the rim of an OPX grain are: (1) co-crystallization of OPX and spinel, (2) a magmatic trend if Cr3+ and Al behave compatibly in OPX/melt partitioning, and (3) requilibration with trapped melt that has lower concentrations of Al and Cr relative to OPX.

Based on this study and our companion study, [1] it appears that: (1) olivine diogenites are cumulates, not restites [6], and (2) the diogenite suite appears to have crystallized from a series of chemically similar but distinct basaltic magmas.

References [1] Shearer C.K., Papike J.J. and Layne G.D. (1993) this volume. [2] Harriott T.A. and Hewins R.H. (1984) Meteoritics, 19, 15-23. [3] Berkley J.L. and Boynton N.J. (1992) Meteoritics, 27, 387-394. [4] Barnes S.J. (1986) Contrib. Mineral. Petrol., 93, 524-531. [5] Cawthorn R.G., Sander B.K. and Jones I.M. (1992) Contrib. Mineral. Petrol., 111, 194-202. [6] Sack R.O., Azeredo W.J. and Lipschutz M.E. (1991) G.C.A., 55. 1111-1120.

Acknowledgement This research was funded by NASA Grant NAG 9-497 (J.J. Papike, P.I.).

ORTHOPYROXENES FROM DIOGENITES: Papike et al.

Figure 1.

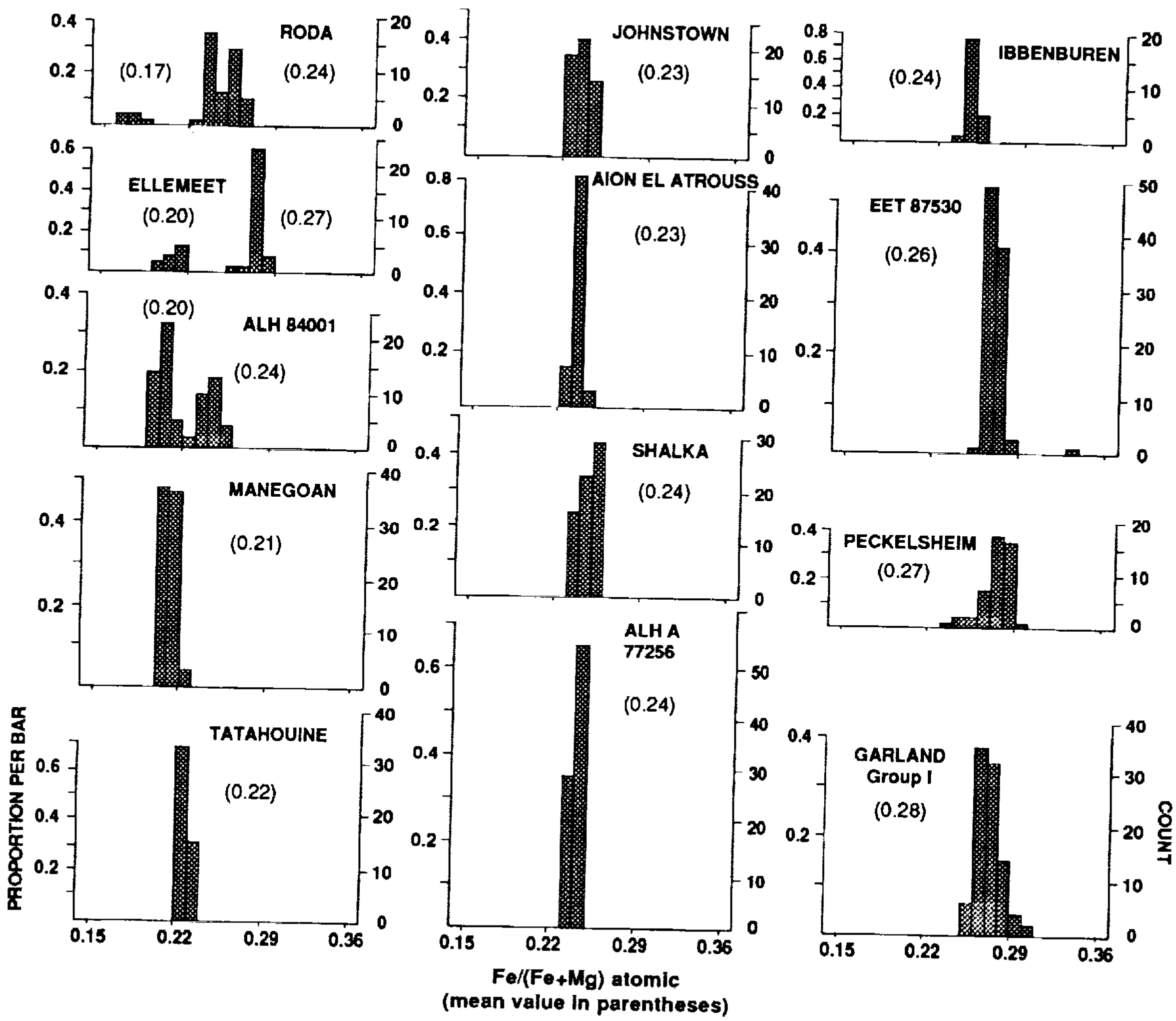
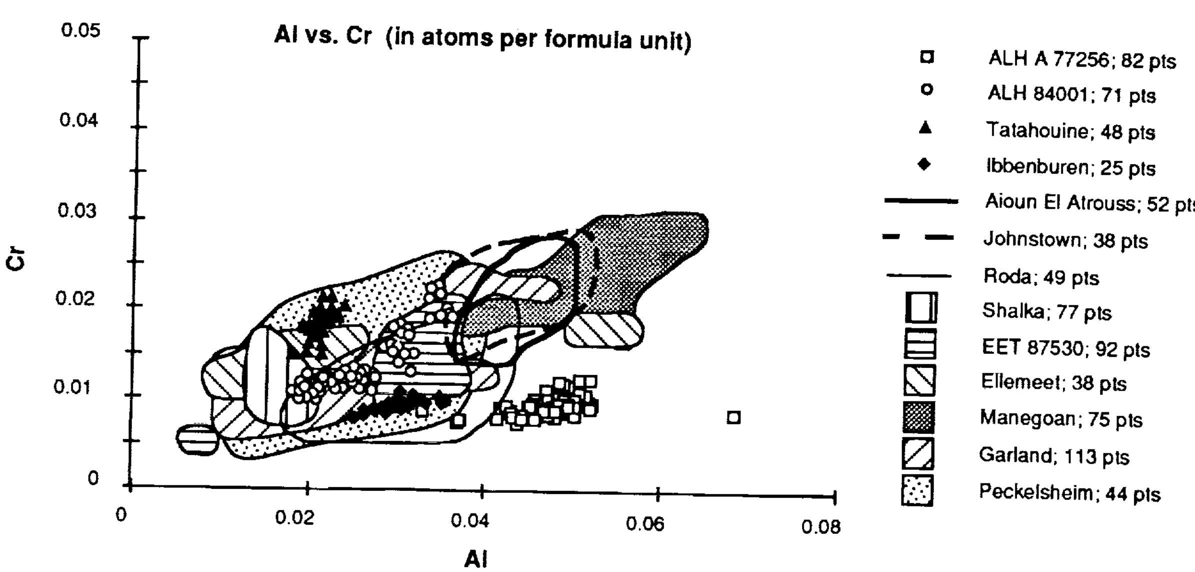


Figure 2.



S3S-11 ABS ONLY

N94-20671

167998 P-2

STRUCTURAL EVIDENCE FOR REORIENTATION OF MIRANDA ABOUT A PALEO-POLE

R. Pappalardo and R. Greeley, *Arizona State University, Tempe AZ, 85287.*

Summary: Two structural arguments support the premise that Miranda has reoriented with respect to Uranus over its geologic history. Orientations of major extensional and compressional features are consistent with a major satellite reorientation similar to that previously suggested based on cratering asymmetry. Furthermore, structures within Elsinore Corona provide supporting evidence that this reorientation took place about a paleo-pole located near (-75°, 80°), suggesting a second minor reorientation of Miranda.

Previous evidence for reorientation of Miranda: The distribution of small, fresh craters on Miranda shows an asymmetry consistent with predictions of leading/trailing cratering asymmetry [1,2], but the apex of motion suggested by the asymmetry is near the anti-uranian point, ~90° from the true apex. The observed crater distribution might have been produced by a reorientation that switched Miranda's *a* and *b* axes [1]. Furthermore, the location of Miranda's three coronae, near the south pole and the leading and trailing points of the satellite's motion, is consistent with their being negative mass anomalies whose origin caused satellite reorientation [2,3]. In discussions of possible reorientation, Miranda's rotation is assumed to be synchronous.

Structural evidence for a major reorientation: Figure 1 shows the pattern of tectonic deformation predicted for a 90° reorientation of a satellite about its pole, approximated as discreet events involving relaxation and growth of a tidal bulge [4]. Relaxation of a former bulge would result in longitudinally-oriented compression in a circular region within about 30° of the paleo-*a* (predicted present *b*) axis, accompanied by parallel extension within about 30° of the satellite pole. As the tidal bulge repositioned along the present a axis, longitudinally-oriented extension would occur there, with parallel over-the-pole compression predicted as well. Strike-slip faulting would be favored elsewhere across the satellite. Currently, the dimensions of Miranda's *a* and *b* axes differ by 6 km, about 2.5% of the satellite's mean radius [5]. Applying the observed axis dimensions to the method of [4], exchange of Miranda's *a* and *b* axes could produce differential stresses ~100 bar, enough to have caused deep lithospheric faulting [6].

The geology of Miranda (Fig. 2) can be compared to that predicted from reorientation. A major longitudinally-oriented ridge, probably compressional in origin, is observed along 210°, most prominent equatorward of 40° latitude. In the polar region, this ridge transforms into an extensional rift zone that forms the southern extent of Inverness Corona. Near the current *a*-axis is Verona Rupes, trending longitudinally, and prominent equatorward of 30° latitude. Extending poleward from Verona Rupes is an extensional band, rather than the predicted compressional features, ultimately linking with an extensional zone bounding Arden Corona. Propagation of more easily formed extensional features from Verona Rupes may have precluded formation of predicted polar compressional features; alternatively, discreet bulge relaxation and formation events may be too simple a model for the true reorientation stress field. Pre-existing structures certainly had a role in guiding the location and evolution of Verona Rupes as evidenced by the more ancient, mantled [2,7] tectonic terrace that parallels Verona to the west. Analogous cratered terrain deformation is not apparent in the present leading hemisphere of Miranda, but might be hidden by materials of Arden Corona.

The observed broad-scale cratered terrain tectonism is generally consistent with relaxation of a former bulge near 210° longitude and growth of the current tidal bulge along 0° longitude, corresponding to a ~45° satellite reorientation. The resulting deformation can be summarized as a westward (ccw) rotation of a single large plate containing present-day Silicia Regio and Elsinore Corona.

Initiation of major reorientation: An impact event has been invoked to account for the apparent satellite-wide mantling of Miranda [7] and may have initiated chaotic rotation and heating of the satellite [8]. If a basin created by a mantle-forming impact induced reorientation [7], and/or if chaotic rotation ensued, the distribution of fresh (post-mantling) craters necessitates a time lag be invoked before reorientation, during which mantling was completed and the asymmetric distribution of fresh craters developed with respect to the satellite's original orientation. It is more likely that diapirism related to corona formation triggered reorientation some time after the mantling event. This does not discount the possibility that an impact mantled Miranda; indeed, diapiric upwelling induced by basin relaxation may have initiated reorientation.

Structural evidence for a paleo-pole: We note that the 210° ridge-rift and the Verona rift systems meet not at Miranda's south pole, but near (-75°, 80°). This invites the suggestion that this location represents a paleo-pole about which reorientation took place. Further evidence for a paleo-pole comes from the orientation of ridges and troughs within the east-west trending Ridged Band of Elsinore Corona (Fig. 2).

MIRANDA REORIENTATION: Pappalardo, R. and Greeley, R.

Ridges and troughs of the Ridged Band were likely shaped by a combination of normal faulting and fissure extrusion along tectonically-induced trends, suggesting formation of Elsinore Corona above an upwelling mantle plume [9]. A diapiric "riser" model of corona formation [3,10] predicts hoop stresses about the center of upwelling that may account for the generally concentric form of the outer belts of Miranda's coronae and structures contained within. However, we believe the actual squared shape of each corona is likely due to superposition of a concentric stress field onto a pre-existing fracture pattern.

At the western and eastern extents of the Ridged Band, ridges and troughs show NW-SE and NE-SW trends, respectively, but through much of the band (longitudes 235° to 290°), structures trend nearly east-west. An east-west trending structural fabric can be understood as resulting from despinning in combination with moderate satellite expansion, with despinning fractures expected to be concentric to the satellite pole [11]. We have constructed great circles perpendicular to the trends of individual Ridged Band structures, expected to intersect at a center of concentricity if one exists.

Preliminary analysis shows that the great circle intersections scatter somewhat but concentrate near (-75°, 80°). This suggests that the Ridged Band's east-west structural fabric may be due to despinning not about the current satellite pole, but about the same paleo-pole of Miranda's major reorientation event, 65 km from the current pole location. A second, minor reorientation of Miranda is thus implied to account for the satellite's present orientation, perhaps resulting from late diapiric activity.

Conclusion: Structural evidence suggests that despinning and post-mantling reorientation of Miranda took place about a paleo-pole near (-75°, 80°). A second minor reorientation then brought Miranda to its current position with respect to Uranus. Reorientation was likely the result of corona formation and partial satellite differentiation involving diapirism. The major reorientation proposed here is somewhat different from that previously suggested on the basis of cratering studies [1], and Miranda's fresh crater distribution remains to be reexamined in this light.

[1] Plescia (1988), *Icarus* **73**, 442. [2] Greenberg *et al.* (1991), in *Uranus*, p. 693. [3] Janes and Melosh (1988), *JGR* **93**, 3127. [4] Melosh (1980), *Icarus* **43**, 334. [5] Thomas (1988), *Icarus* **73**, 427. [6] Pappalardo and Greeley, *LPSC Abstr. XXII*, 1021. [7] Croft and Soderblom (1991), in *Uranus*, p. 561. [8] Marcialis and Greenberg (1987) *Nature* **328**, 227; Dermott *et al.* (1988), *Icarus* **76**, 295. [9] Pappalardo and Greeley (1992), *LPSC Abstr. XXIII*, 1023. [10] McKinnon (1988), *Nature* **333**, 701. [11] Melosh (1977), *Icarus* **31**, 221.

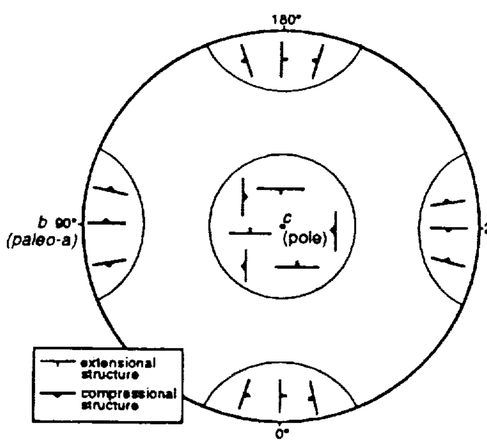


Figure 1.

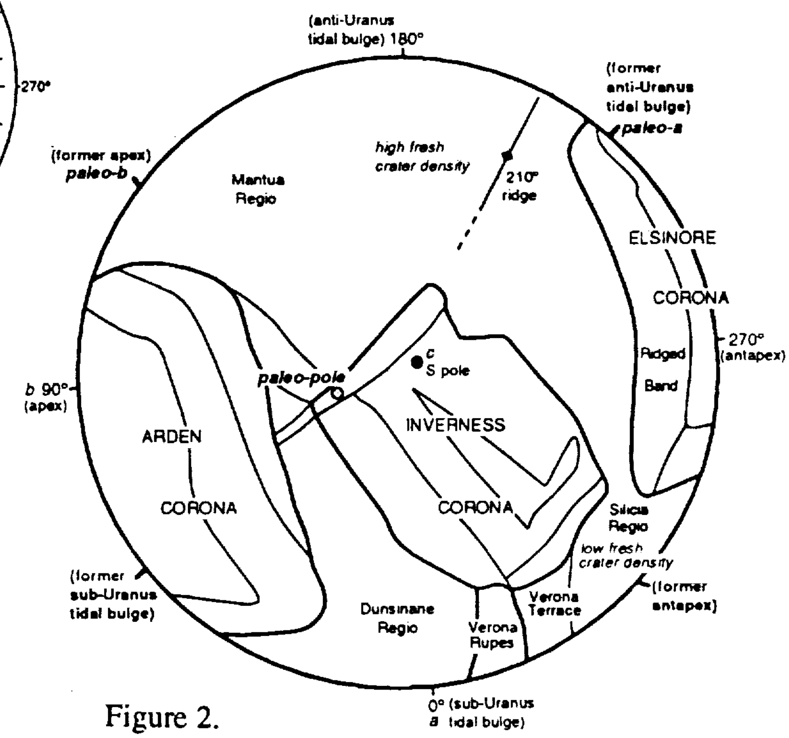


Figure 2.

FORMATION AND EVOLUTION OF RADIAL FRACTURE SYSTEMS ON VENUS. E. A. Parfitt and J. W. Head, Department of Geological Sciences, Brown University, Providence, RI 02912.

A survey of ~90% of the surface of Venus using Magellan data has been carried out to locate all radial fracture systems and to assess their association with other features such as volcanic edifices (1) and coronae (2,3). Squyres et al. (2) and Stofan et al. (3) have discussed the association of radial fracture features in relation to coronae features, our approach was assess the associations of all of the fracture systems. These fracture systems have two broad types of form - some fracture systems are associated with updomed topography, radiate from a point and have relatively uniform fracture lengths while others have a wider range of fracture lengths and radiate from the outer edge of a central caldera (4,5). Squyres et al. (2) and Stofan et al. (3) have interpreted both types of feature as reflecting tectonic fracturing resulting from uplift of the surface as a mantle plume impinges upon the crust. While it is true that a number of features are related to uplift and that such uplift will induce stresses consistent with radial fracturing we explore the possibility that these fractures are not exclusively of tectonic origin. Purely tectonic fracturing will tend to generate a few main fractures/faults along which most of the stresses due to uplift will be accommodated leading to the triple-junction form common for terrestrial updoming (6). Though this type of feature is observed on Venus (e.g., feature located at 34S86), the majority of radial fracture systems display much more intensive fracturing than this through a full 360°, this is difficult to explain by purely tectonic processes. The association of many of the fractures with radial lava flows leads us to interpret these fractures as reflecting dike emplacement, the form of the fractures being consistent with primarily vertical propagation from the head of a mantle plume. In the case of the second type of fracture system (those radiating from a central caldera) an even stronger case can be made that the fractures are <u>not</u> of tectonic origin. These features are not as commonly associated with updoming of the surface and where they are, the fractures extend out well beyond the edge of the topographic rise - an observation which is not consistent with the fractures being of tectonic uplift origin. Furthermore the fractures have a distribution of lengths (many short, fewer long) which is characteristic of dike swarms, and show direct associations with calderas and lava flows consistent with a volcanic origin. In addition, the longest fractures have a radial pattern only close to the center of the system but bend with distance to align themselves with the regional stress field - this behaviour is very difficult to explain on purely tectonic grounds but is a pattern commonly seen for terrestrial dikes (7). For these reasons we argue that many, if not the majority, of radial fracture systems found on Venus are the surface reflection of dike swarms (8), those associated with positive topography reflecting vertical emplacement and those radiating from calderas reflecting lateral propagation (4,5).

Classification Scheme

On the basis of both morphologic and topographic information we have developed a classification system for the radial fracture systems. This classification scheme consists of : **type 1** - radial fracture systems (novae) which may be associated with topographic highs but having no obvious edifice or caldera development and having no associated concentric fracturing; **type 2** - novae which are associated with coronae, divided into 2 classes - (a) novae contained within a corona and (b) long radial fractures extending from the outer edge of a corona; **type 3** - novae of complex form, usually found in association with tessera; **type 4** - radial fractures originating at the outer edge of a central caldera, which may have a limited number of lava flows but not enough to constitute a volcanic edifice; **type 5** - radial fractures associated with volcanic edifices - divided into three classes - (a) edifice with central novae, (b) edifices in which numerous lava flows are progressively covering up an earlier set of long radial fractures, and (c) edifices with a central caldera and interspersed radial fractures and flows; **type 6** - topographically high, flat-topped features with steep bounding scarps and fractures which radiate from a point on top of the 'plateau' outwards across the scarps, the fractures often feeding lava flows; **type 7** - central depressions which are considerably deeper than the feature is high and have fractures radiating from the outer edge of the depression.

Results

Using this scheme we have classified 188 radial fracture features on Venus. The most common association found is with coronae (33.5%), closely followed by volcanic edifices (27.7%) which, if the type 4 features are included (as these appear to be proto-edifices), give a total of 43.1% of the fracture systems being associated with volcanic edifices. There are ~20.2% of type 1 features, 16% type 3 complex features, 12.2% type 6 plateaus and 6.4% type 7 depressions (note that the total percentage is greater than 100% because some of the features are associated with more than one type of structure).

By looking in detail at the examples which we have classified as showing overlap between different types of

FORMATION AND EVOLUTION OF RADIAL FRACTURE SYSTEMS: E.A. Parfitt and J.W. Head.

By looking in detail at the examples which we have classified as showing overlap between different types of feature we have developed a preliminary evolutionary sequence for these features. Broadly speaking we have divided the features into 2 groups having somewhat different sequences of evolution. One sequence is broadly in keeping with the analyses of Squyres et al. (2) and Stofan et al. (3), and starts with updoming and fracturing of the surface as a mantle plume impinges on the crust. These updomes evolve along 2 (overlapping) paths, some updomes deform to form coronae and complex fracture features (type 3), while other updomes evolve into large volcanic edifices (type 5a). A number of features show a combined edifice/corona form which suggests that a spectrum of behaviours occur of which corona and edifice development are the endmembers. A number of the features however, show a different sequence of evolution which starts with the type 4 and 7 features which have central calderas and fractures radiating from the outer edge of the caldera. As mentioned above the type 4 features seem to reflect lateral dike emplacement from a central storage region. The fractures associated with type 4 and 7 features tend to be longer and of more variable length than those found for updoming (type 1). Type 5b/c volcanoes show similar predominance of relatively long fractures and type 5c edifices have central caldera and look very much like more developed examples of type 4 features. Thus we propose an evolution from type 4 and 7 structures into type 5c edifices. Later, formation of long fractures ceases and lava flows progressively cover all but the longest fractures and lead to type 5b edifice formation.

Discussion and conclusions

On the basis of the classification results we propose two sequences for the formation and evolution of radial fracture systems on Venus. In the first sequence the head of a mantle plume impinges on the lithosphere causing uplift, radial tectonic fracturing and formation of radial fractures by propagation of dikes vertically from the head of the plume. As the plume head thins and spreads, some features deform (9) to form coronae while others experience considerable volcanism which is sufficiently localised to allow edifice formation. The differences in evolution after uplift may have a number of causes. In particular edifice development entails the development of a central magma storage zone, and so coronae may form in areas where shallow storage in inhibited - possibly because of the lack of a neutral buoyancy level (10) or because the lithospheric thickness is somewhat greater than in the areas where volcanoes form.

In the second evolutionary sequence a shallow storage region has already formed and lateral dike propagation from this region dominates. These features show little or no evidence for an earlier stage of uplift, this may imply that the magma source in these regions is more limited (a smaller plume) or that the lithospheric thickness is greater than average and limits the amount of surface expression of the plume. In the early stages of formation the emplacement of long lateral dikes is common, the dikes rarely feeding lava flows suggesting that they propagated with a stable geometry as suggested by theoretical models (8). With time the length of the dikes decreases and they more commonly reach the surface feeding relatively short lava flows and allowing edifice development. The earlier long fractures are progressively covered-up as the volcano builds. This pattern of evolution is consistent with the gradual formation of a shallow magma reservoir and with a declining rate of magma production. Early rapid melt production allows the emplacement of long dikes but as the magma production rate falls and the shallow reservoir develops dike emplacement becomes more constrained and shorter dikes are emplaced which can generate flows of limited volume and length. This pattern of evolution is consistent with a mantle plume origin, in terrestrial hot spot areas like Hawaii and Reunion a similar pattern is observed in which melt production is initially great and declines with time allowing development of shallow magma reservoirs and edifice development (11,12). The key difference appears to be that on Earth the early stage of development is commonly associated with extensive flood basalt activity whereas on Venus the early stage seems to be largely intrusive. Further modelling studies should help us to understand this difference and to develop more complete models of both evolutionary sequences.

References

(1) Head, J.W. et al. (1992) J. Geophys. Res., 97, 13153-13197. (2) Squyres, S.W. et al. (1992) J. Geophys. Res., 97, 13611-13634. (3) Stofan, E.R. et al. (1992) J. Geophys. Res., 97, 13347-13378.(4) Parfitt, E.A. and Head, J.W. (1992) LPSC XXIII, 1029-1030. (5) Parfitt, E.A., Wilson, L. and Head, J.W. (1992) International Colloquium on Venus, 83-84. (6) Fahrig, W.F. (1987) Geol. Assoc. Canada Special Paper, 34, 331-348. (7) Muller, O.H. and Pollard, D.D. (1977) Pageoph, 115, 69-86. (8) Parfitt, E.A. and Head, J.W. (1992) LPSC XXIII, 1027-1028. (9) Janes et al. (1992) J. Geophys. Res, 97, 16055-16067. (10) Head, J.W. and Wilson, L. (1992) J. Geophys. Res., 97, 3877-3903. (11) Clague, D.A. et al. (1990) Earth and Plan. Sci. Lett., 98, 175-191. (12) Duncan, R.A. and Richards, M.A. (1991) Reviews of Geophysics, 29, 31-50.

THERMAL AND RHEOLOGICAL CONTROLS ON MAGMA MIGRATION IN DIKES: EXAMPLES FROM THE EAST RIFT ZONE OF KILAUEA VOLCANO, HAWAII; E.A. Parfitt[1], L. Wilson[1,2] and H. Pinkerton[2]. [1]Geological Sciences Department, Brown University, Providence, RI 02912, U.S.A. [2]Environmental Science Div., Lancaster University, Lancaster LA1 4YQ, U.K.

Abstract: Long-lived eruptions from basaltic volcanoes involving episodic or steady activity indicate that a delicate balance has been struck between the rate of magma cooling in the dike system feeding the vent and the rate of magma supply to the dike system from a reservoir. We describe some key factors, involving the relationships between magma temperature, magma rheology and dike geometry, that control the nature of such eruptions.

Background: The two longest-lived eruptions of Kilauea volcano this century were the 1969-1974 eruption at Mauna Ulu and the 1983-1990 eruption at Pu'u 'O'o and Kupaianaha. Both eruptions involved periods of episodic activity, in which a relatively high magma discharge rate episode would be maintained for about one day after an interval of up to about one month during which the discharge rate was very low or negligible. Both eruptions also involved periods when the discharge rate was nearly constant, but at a low rate which corresponded to the total magma mass erupted during one of the episodic cycles divided by the total duration of the cycle.

Magma flow in dikes to feed eruptions that continue for long periods can only take place when a delicate balance exists between the rate of cooling of the magma in the dike and the rate of supply of new magma to the dike from the magma reservoir. Various aspects of the cooling process have been considered by several authors, and conditions have been explored under which the mass flux of magma is likely to decrease with time as cooling through the dike walls dominates, or increase with time as heating, thermo-mechanical smoothing and possibly thermal erosion of the walls occurs or as viscous dissipation takes place [1-5] . These treatments draw a strong distinction between laminar and turbulent flow in the dike magma. Recently, it has been proposed that lateral heat transfer (due to advection caused by dike width irregularities and the presence of vertically migrating gas bubbles or crystals) can be efficient enough that a magma moving in a nominally laminar fashion in a dike may cool in a way much closer to that of a magma in turbulent motion [6]. This has strong implications for the variation, with distance from the source reservoir, of the mean magma temperature, the temperature profile across the dike, and the temperature of the interface between the magma and the dike wall.

The most elaborate calculations of this type so far have allowed only for the monotonic narrowing of a dike with distance from its magma source [6]. However, there is good evidence that the dike system feeding the long-lived Pu'u 'O'o-Kupaianaha eruption on Kilauea was formed by the linking together, by a new intrusion, of a small number of pre-existing dike segments which represented the still partly molten remains of earlier intrusions. This would have led to significant variations, with distance from the summit reservoir, of the width of the dike, and hence to significant spatial variations of the effects of cooling on the temperature profile [7].

Temperature (and, to a lesser extent, pressure) variations in a magma cause rheological changes, directly, by changing the structure of the liquid, and indirectly, when the composition of the liquid changes as crystals form. The presence of such crystals (and of any gas bubbles which form) is an additional major source of rheological variations. The rheological properties of a magma, which can be extremely non-Newtonian and time-dependent, determine the rate at which it will deform under a given shear stress and hence the velocity profile that will develop within a dike when magma is moving in it. The fact that a magma may possess a finite yield strength means that it may not flow at all unless the pressure gradient applied to it exceeds some threshold value.

Analysis: We have used the above considerations to calculate likely variations along a dike of the lateral profile of rheological properties. We find that episodic eruptions like that at the Pu'u 'O'o vent can be explained by a feedback system which operates as follows: Towards the end of an eruptive episode, the excess pressure in the summit reservoir becomes relatively low, due to transfer of magma from the elastically pressurised reservoir into the dike. As a result, the magma flow rate declines, and magma moving through some narrow part of the dike system near the vent end (i.e. furthest from the summit reservoir) cools sufficiently near its contact with the dike wall to develop a yield strength there. The shear stress near the wall (proportional to the pressure gradient acting along the dike and to the distance from the dike centre-line) is no longer great enough to cause shearing, and only magma in the central part of the dike is able to flow, thus reducing the total volume flux through the system.

Further decline in summit reservoir pressure causes the widths of the stagnant zones at the dike walls to increase, and enhanced cooling of the stationary magma causes its yield strength to increase and the boundaries between stationary and flowing magma to migrate even closer to the dike centre. Eventually the volume flow rate either

vanishes (if cooling causes a finite yield strength to exist everywhere across the narrow dike section), or becomes extremely small (if some magma motion still occurs in the warmest region around the middle of the dike); at this point, lava eruption at the vent ceases and a repose period begins.

The supply rate to the summit reservoir from the mantle now exceeds the magma loss rate into the dike. The summit reservoir pressure rises as it inflates, and the pressure gradient applied to the cooling magma in the narrow dike section also increases. This means that the shear stress increases at all points across the dike. The profile of this shear stress is linear, varying from a value of zero at the dike centre to a maximum value at the dike wall. The profile of the magma yield strength, however, will be very non-linear, increasing more rapidly near the wall than near the centre of the dike. As a result, shearing will first begin again, to start a new eruptive episode, at some intermediate point between the dike centre and edge. The rate at which the volume flux increases at the start of the episode may be very great, especially if the magma in the dike system has become completely stationary during the repose period. During this repose period, cooling of the unsheared magma will result in the formation of a three-dimensional network of interacting crystallites [8]. A high initial stress will be required to initiate movement of this thixotropic melt. However, once movement begins, field and laboratory measurements [9; 10] confirm that the static yield strength and high viscosities decrease rapidly. In addition, crystalline magmas are pseudoplastic. Consequently, their yield strengths and apparent viscosities decrease as the rate of shear increases. This will lead to an increase in velocity and volume flow rate with time even though the applied stress remains essentially constant (though in fact the onset of significant magma flow through the dike will rapidly reverse the trend of summit reservoir inflation into one of deflation as the new episode proceeds).

As fresh magma feeds through the narrow dike section, displacing the central part of the cooled magma which had developed a yield strength into an adjacent wider dike section, the still-stagnant magma nearest the dike wall will be reheated somewhat, and the boundary between flowing and stationary magma will migrate towards the dike wall. This, together with the fact that the displaced cool magma will now be moving through a wider dike section so that its yield strength will have a smaller effect on controlling the flow speed, means that the volume flux of magma through the system increases with time at first, even though removal of magma from the summit reservoir is decreasing the driving pressure gradient. Eventually, however, the declining summit reservoir pressure becomes the dominant factor; flow rate decreases, cooling in the narrow dike section becomes important again, a yield strength begins to develop near the dike wall, and the new eruptive cycle ends.

This process can be repeated many times (47 in the case of Pu'u 'O'o) before a combination of thermal and mechanical effects tends to increase preferentially the width of the narrowest section of the dike to the point where cooling, and the development of a yield strength near the wall, are no longer great enough to cause magma flow to cease when the summit reservoir has deflated to the point where inflow from the mantle is matched by outflow into the dike. At this point, the eruptive character changes to steady-state flow of magma through the system at a rate equal to that of the mantle supply: in the current Kilauea activity this corresponded to the movement of the eruption site to the Kupaianaha vent.

This steady-state condition may also persist for a long time; however, the progress of the Mauna Ulu eruption (and the most recent change of style of the current activity, coincident with the move of the eruption site from Kupaianaha to a location on the flank of the original Pu'u 'O'o cone) shows that it is possible for the eruption style to change back from steady-state to episodic. We infer that this is most likely to be triggered by a small decrease in the mantle supply rate.

Summary: the above scenario has been presented in qualitative terms. However, we have used it to model numerically a number of cycles of the Pu'u 'O'o activity, and find that the observed behaviour is reproduced well with dike section geometries that are consistent with geophysical evidence and with magma rheological parameters that are consistent with the measured properties of hawaiian basalts as a function of temperature. This work is currently being prepared for publication.

References.

[1] Delaney, P.T. and Pollard, D.D. (1982) Am. Jour. Sci., 282, 856-885. [2] Delaney P.T. (1987) pp. 31-46 *in* Mafic Dyke Swarms, Geol. Ass. Canada Sp. Pap. 34. [3] Bruce P.M. and Huppert H.E. (1989) Nature 342, 665-667. [4] Hardee H.C. (1987) pp. 1471-1486 *in* Volcanism in Hawaii, U.S.G.S. Prof. Pap. 1350. [5] Hulme, G. (1982) Geophysical Surveys, 5, 245-279. [6] Carrigan etc. (1992) J. geophys. Res. 97, 17377-17392. [7] Parfitt E.A. (1991) J. geophys. Res. 96, 10101-10112. [8] Pinkerton H.and Stevenson R.J. (1993) J. Volcanol. Geotherm. Res. (in the press). [9] Shaw H.R., Wright T.L., Peck D.L. and Okamura, R. (1968) Am. J. Sci. 266, 255-264. [10] Pinkerton H. and Norton G.E. (1993) LPS XXIV: this volume.

CONSTRAINTS ON THE RATE OF DISCHARGE AND DURATION OF THE MANGALA VALLES FLOOD. T. J. Parker and D. S. Gorsline, University of Southern California, Dept. of Geological Sciences, Los Angeles, CA 90089-0741.

Interest in Mangala Valles remains high within the planetary science community. This is justified because the survey mission images provide us with nearly complete coverage of the system at high resolution. Upcoming high resolution topography from the Mars Observer Laser Altimeter will enable the application of flood discharge models with an unprecedented level of detail.

Previous work on the Mangala Valles problem has relied on the available low resolution topography (1). This has limited the ability of workers to constrain discharge calculations to only within several-order-of-magnitude estimates. Local determinations of channel depths via shadow length measurements and photoclinometric profiling are much more accurate, but can only be applied to steep slopes (and/or low sun elevations) in the case of shadow measurements, or across relatively short distances (to avoid changes in albedo along asymmetric photoclinometric profiles).

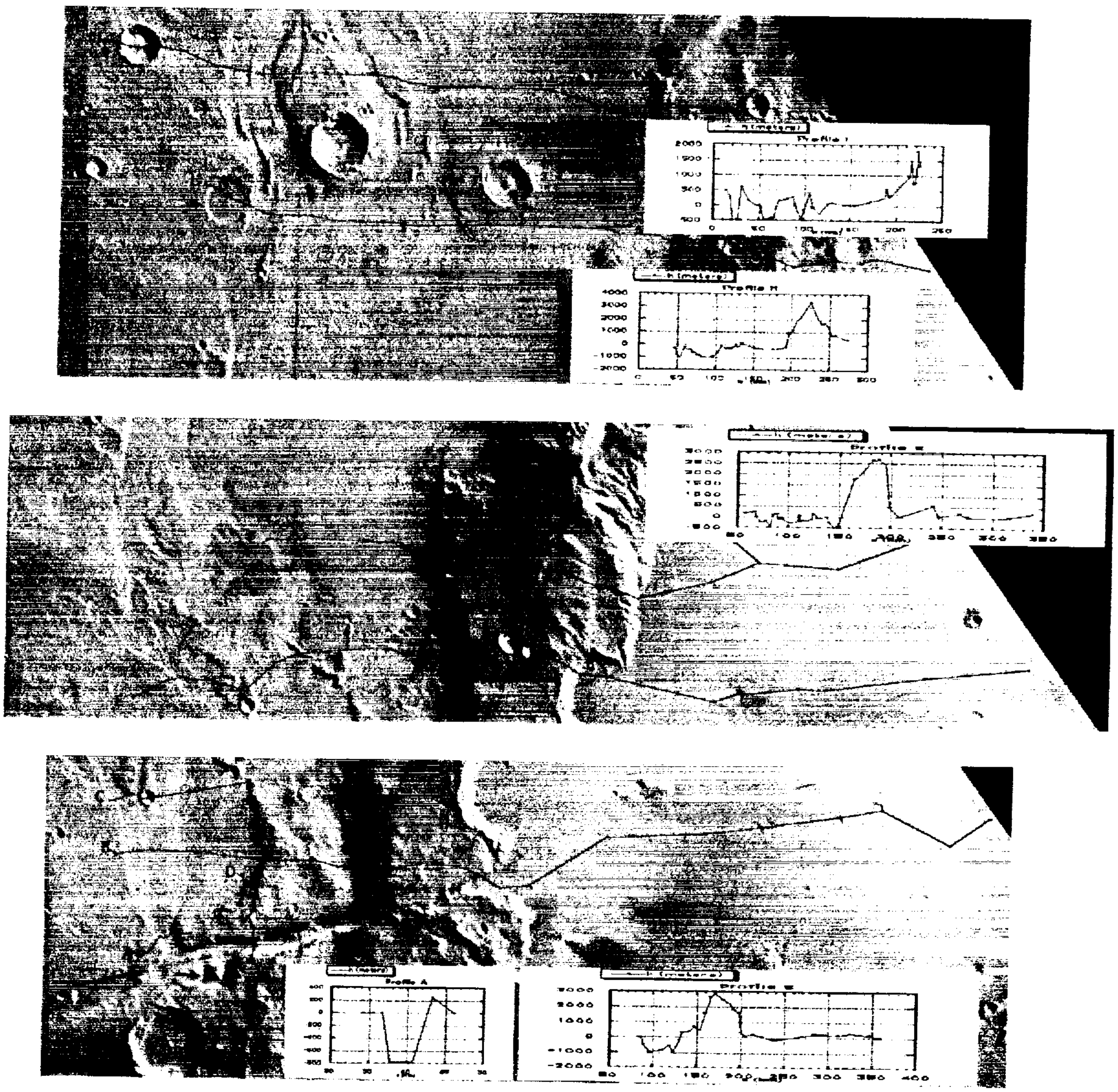
We are taking stereo parallax measurements from medium resolution Viking Orbiter images, which provide a valuable intermediate check of the topography between those measurements made thus far and the upcoming Mars Observer data. The images used are from orbits 034A and 637A, and cover Mangala Valles from the source graben in Memnonia Fossae to the beginning of the bifurcated reach (at 9.5°S lat., 151.5° lon.). These images are about 300m/pixel and 250m/pixel, respectively. Both sets of images were orthographically projected to 250m/pixel. The separation angle between left-right pairs is approximately 52°. This results in a vertical accuracy on the order of ±260m. Though this is still somewhat coarse, the channel relief is clearly resolved.

Preliminary profiles across Mangala Valles and the large topographic ridge to the east are shown on the following page. An east-west regional tilt that resulted from slight scaling differences in the digital data has been "removed" by visually estimating a regional datum on the stereo pairs. North-south variations in scale have not yet been adjusted for, so the zero datum for each profile was simply taken to be the high water line of the channel itself. Our depth measurement for the source breach of about 750m agrees reasonably well with values of 700-1000m determined from shadow measurements.

REFERENCE: (1) USGS Map I-2030, 1989.

CONSTRAINTS ON MANGALA VALLES FLOOD

Parker, T. J., and Gorsline, D. S.



339-91
ABS. ONLY

N94-20875

MIXING OF A CHEMICALLY BUOYANT LAYER AT THE TOP OF A THERMALLY CONVECTING FLUID: IMPLICATIONS FOR MANTLE DYNAMICS WITH APPLICATION TO VENUS. E.M. Parmentier and P.C. Hess, Department of Geological Sciences, Brown University, Providence, RI, 02906; C. Sotin, Laboratoire de Physique de la Terre et des Planètes, Bât. 509, Université de Paris-Sud, 91405, Orsay Cedex, FRANCE.

Partial melting to generate the crust of a planet can create a buoyant residual layer at the top of the mantle which may have important implications for episodic planetary evolution (1). However, the rate of mixing of such a chemically buoyant layer with a thermally convecting mantle is an important unresolved question. Except for a few laboratory and numerical studies designed to address questions related to convection in the Earth's mantle (2,3), previous studies (c.f. 4) have generally treated only the mixing of passive tracers. The inhibiting role of chemical buoyancy on mixing is intuitively obvious but not fully understood quantitatively. In this study we examine the dynamics of an intrinsically buoyant fluid layer at the top of a deeper, thermally convecting, infinite Prandtl number fluid that is heated from below.

Our two-dimensional numerical experiments are formulated using finite difference approximations for thermal convection (5) and a tracer particle method to treat the advection of intrinsic fluid properties (6). The usual finite difference approximations of advection introduces too much numerical diffusion to allow meaningful studies of non-diffusive mixing. Temperature and velocity fields were calculated with 65 and 129 grid points in the vertical and horizontal, respectively. Four tracer particles were used in each grid cell of the buoyant layer. Our numerical experiments consider a fluid in which the temperature initially increases linearly with depth. This fluid is confined to a region of aspect ratio two with periodic vertical boundaries and a prescribed temperature difference ΔT between top and bottom boundaries. An intrinsically buoyant layer with density contrast $\Delta\rho$ relative to the underlying fluid and of initially uniform thickness is prescribed along the top boundary of the fluid as shown in Figure 1 for time=0. We consider buoyant layer thicknesses 0.1 and 0.05 of the convecting layer thickness, both free-slip and no-slip boundaries, and a range of values of the buoyancy parameter $R=\Delta\rho/\rho_o\alpha\Delta T$ (3) where α is the coefficient of thermal expansion. Results for a thermal Rayleigh number (Ra) = 10^4 and free-slip boundaries for two values of R are shown in Figure 1. Here time is normalized by the usual conduction time scale. Mixing is indicated by the mean depth of the buoyant fluid as a function of the number of overturn times as shown in Figure 2. The overturn time is calculated as the time for fluid moving with mean vertical velocity to travel the perimeter of a convection cell.

Mixing occurs in two stages. First, as shown in Figure 1, the buoyant layer accumulates at sites of horizontal convergence above thermal downwellings. The second stage is the entrainment of these accumulations into the downwellings. For R=-0.333, the accumulations are not sufficiently buoyant to resist rapid viscous entrainment, while for R=-1 they are only gradually eroded by viscous stresses. Thinner buoyant layers mix more rapidly because they result in smaller more easily entrained accumulations. With no-slip boundaries mixing occurs more slowly because with less horizontal flow more time is required to create accumulations. Entrainement occurs while the accumulations are still growing. As for free-slip boundaries and for Ra values as large as 10^5, mixing is slow for $R\leq-1$.

Further work is needed for realistic application to planetary mantles. The results reported here will generally overestimate mixing. The strong temperature dependence of creep results in high viscosity within the thermal boundary layer at the top of the mantle and low viscosity at the base of thermal boundary layer where the mantle is close to (or at) its melting temperature. Both factors will inhibit the accumulation and entrainment of buoyant mantle. Time dependent thermal convection at higher Ra may also inhibit mixing if flow directions in the convecting fluid do not persist long enough to accumulate and entrain the buoyant layer.

References: (1) Parmentier and Hess, GRL 19, 2015, 1992. (2) Christensen, Phil. Trans. Roy. Soc. A328, 417, 1989. (3) Olson and Kincaid, JGR 96, 4347, 1991. (4) Kellogg, Ann. Rev. Planet. Sci. 20, 365, 1992. (5) Parmentier and Sotin, submitted to Geophys. J. Int., 1992. (6) Dupeyrat, Sotin, and Parmentier, LPSC 23, 319, 1992.

MIXING OF A CHEMICALLY BUOYANT MANTLE LAYER

E.M. Parmentier, P.C. Hess, and C. Sotin

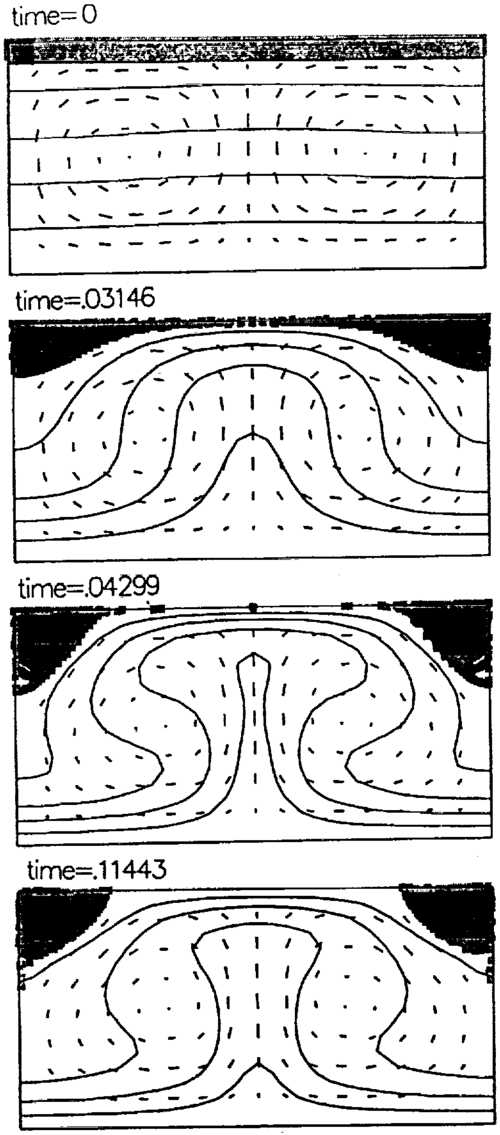
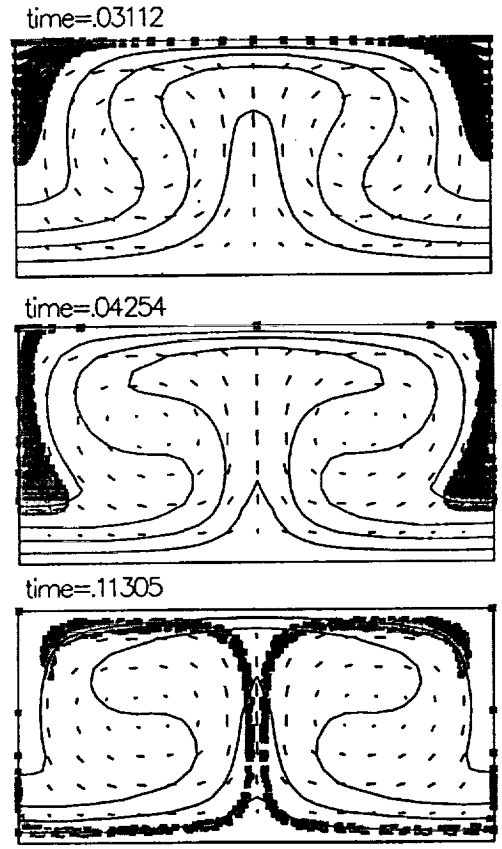


Figure 1. Numerical experiments with free slip boundaries and $Ra=10^4$ for values of the nondimensional density contrast R=-1 (left) and R=-0.333 (right). Intrinsically buoyant fluid is shown shaded, isotherms at equal fractions of the temperature difference across the layer are shown as solid lines, and the fluid velocity is shown by short solid lines.



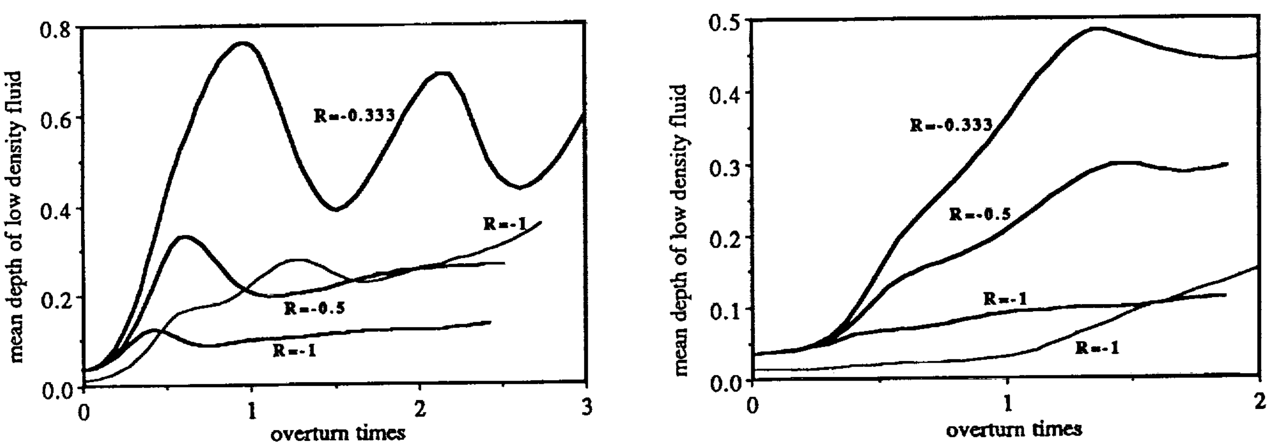


Figure 2. Mean depth of the low density fluid as function of time for free slip (left) and no-slip boundaries (right) derived from numerical experiments like those illustrated in Figure 1 for a range of R values.

340-25 ABS. ONLY

N94-20676 P-2

ABUNDANCE AND COMPOSITION OF SOLAR KR IN THE H3-H6 CHONDRITE ACFER111

Pedroni A., Max-Planck-Institut für Chemie, Abtlg. Isotopenkosmologie, Saarstrasse 23, 6500 Mainz, Germany

Summary: He/Ne, Ne/Ar and Ar/Kr abundance ratios of solar gases extracted by stepped heating (1), stepped oxidation (2) and stepped etching (3) of lunar and meteoritic regoliths are significantly lower than ratios measured directly or predicted by model estimates (4,5). Of these, the differences in the He/Ne and Ne/Ar ratios are explained to be owing to diffusive fractionation losses from the host minerals. In contrast, it remains controversial if the Ar/Kr and Kr/Xe ratios were fractionated prior to or after the implantation of the gases into the minerals. In the H3-H6 chondritic regolith breccia ACFER 111, measured He/Ne and Ne/Ar ratios appear to be of nearly unfractionated solar composition (6). The Ar/Kr ratio of ACFER 111, might thus be also unfractionated. We examined by stepped etching a metal sample of ACFER111 and obtained an average solar 36Ar/84Kr = 3150 ± 300 which is in agreement with the model predictions. The isotopic composition of solar Kr was observed to change in the course of the etching in a way very similar to that reported for lunar ilmenites by the Zürich group (3). This can be interpreted as a change of the mixing ratio of Solar Wind (SW) and Solar Energetic Particles (SEP). The isotopic composition of the SEP component obtained from our Kr data however, is distinct from that reported by the Zürich group(3).

Experiment: 314 mg of a magnetic fraction of ACFER 111 matrix, containing approximately 55% metal, was etched with a solution of citric acid in a high-vacuum extraction line similar to that in (3). The gases released were drawn off in 13 steps and analyzed mass spectrometrically. The experiment was stopped when ~70% of the metal were dissolved. From the etched residual we obtained by handpicking two >90% pure fractions of metal and silicate which where analyzed by total fusion. The concentration of solar neon in the residual silicates was only 17% lower than in the original sample, indicating that a large fraction of these silicates was not attacked by the acid. Nevertheless, the amount of cosmogenic 21Ne released by etching as well as the cosmogenic ratio 21Ne/38Ar = 3.1 are clearly higher and 3He/21Ne = 14.5 clearly lower than in pure metal and require some other mineral phase to be dissolved together with the metal. The ratios are consistent with the cosmogenic component from approximately 80% metal and 20% silicates.
Blank corrections were negligible for He,Ne and Ar. For Kr and Xe the corrections amounted to 2-10% in the first 8 steps but become more important (20-40%) at the end of the run. Approx 10% of all Kr and Xe is released in the final 5 steps.

Results He,Ne,Ar:
As etching proceeds, the isotopic composition of the released gases changes in a pattern similar to that observed previously in other regolithic materials (3). The isotopic compositions of solar He,Ne and Ar (Fig. 1) drift steadilily from values close to the Solar Wind (SW) in the first step, towards the composition interpreted previously as characteristic of Solar Energetic Particles (SEP). The 4He/20Ne ratio (Fig.2), initially 547, as in the Solar Wind (8), increases smoothly to a maximum of 680 ± 30, and then drops down to 533. The transient maximum reproduces well our previous results (6) and might reflect a difference of 20% in the 4He/20Ne ratios of SW and SEP. The solar gases ratio 20Ne/36Ar = 42.5 is constant to within ± 10% over the entire run.

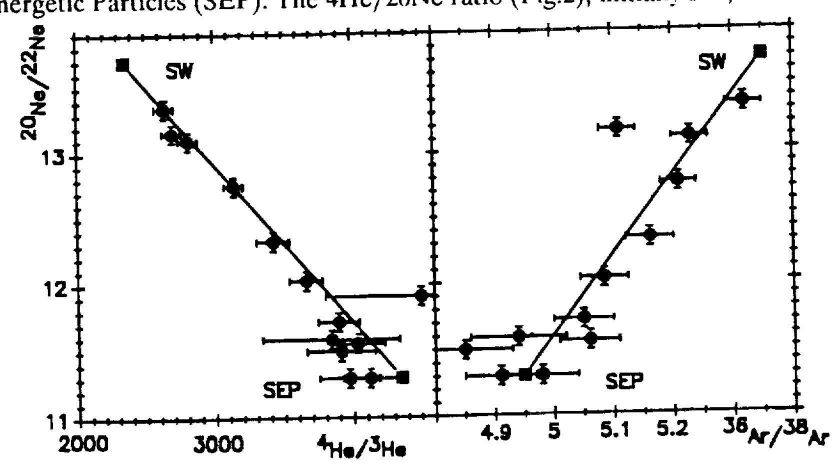


Fig.1. The isotopic composition of solar He (left panel) and Ar (right panel) calcuated for ACFER111 are compatible with SW (8) and SEP (3) compositions obtained previously.

Results Kr,Xe:
The isotopic composition of Xe is not solar (1). For the first three steps it is compatible with a mixture of Q-Xe (60-80%), atmospheric Xe (20-40%) and fission Xe (< 1,5%).

SOLAR KR: Pedroni A.

For later steps it is identical within experimetal error limits (±1%) to Q-Xenon, which implies that any atmospheric contamination cannot exceed 15%. The 84Kr/132Xe ratio was around 3.5 over the entire run, i.e. very much lower than the solar value of 20.7 (4). This suggests that most Xe is not of solar origin. The estimated amount of non-solar Kr (10-20% of total Kr), was obtained assuming all 132Xe to be planetary and (84Kr/132Xe)p=0.7. Solar-gas-free desert meteorite finds (7) may have 5>(84Kr/132Xe)>0.8, the estimated non-solar Kr might thus be somewhat underestimated, because of the unknown amount of atmospheric Kr present. For ACFER 111 bulk samples we measured (84Kr/132Xe)<1.5, which implies that the solar Kr might be overestimated by some 5-15%. Nevertheless, the (corrected) average ratio (36Ar/84Kr)sol=3150±300 is higher than measured for all lunar and meteoritic samples examined so far (1,2,3) and in excellent agreement with model estimates (4,5). Our data thus support the view that solar 36Ar/84Kr ratios measured for most regolith materials have been fractionated in situ and not by processes preceding the implantation of the gases into the host mineral. The isotopic compositions of solar Kr are variable, lie along the SW-SEP mixing lines reported previously by the Zürich group (3), and show a strong correlation to variations in solar He, Ne and Ar.

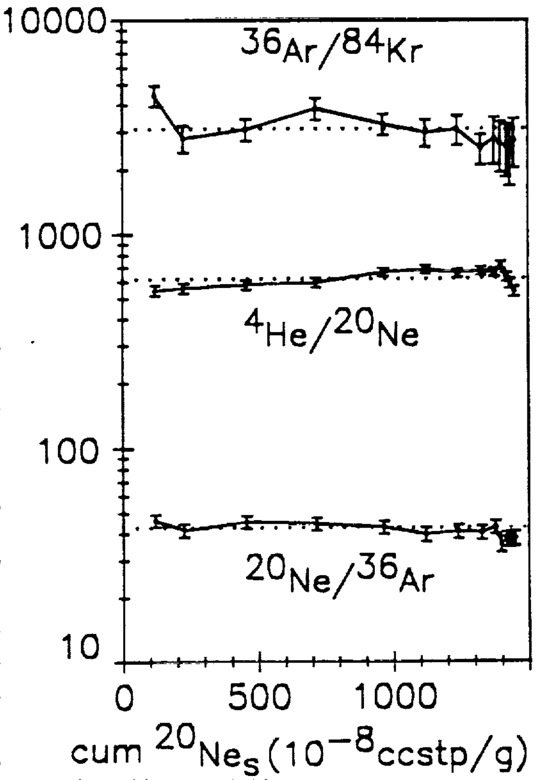


Fig.2. Elemental compositions calculated for solar gases in ACFER111. Dotted lines represents the average.

The SEP composition calculated from our Kr data, (82Kr : 83Kr : 84Kr : 86Kr)sep = 195±2 : 198±2 : 1000 : 317±3, is different from the composition given by the Zürich group, i.e. (82Kr : 83Kr : 84Kr : 86Kr)sep = 191 : 196 : 1000 : 323. This is particularly evident when Kr isotopic ratios are plotted vs. the 20Ne/22Ne ratios (Fig.3). We do not know the reason for this discrepancy. Corrections for the cosmogenic gases are negligible and assuming that the differences are due to admixture of air in our sample, would result in (36Ar/84Kr)sol>3800 which looks unresonably high.

References: (1) Marti K.(1969) Science 166, 1263-1265. (2) Frick U. et al. (1988) Proc. Lunar Planet. Sci. Conf. 18th 87-120. (3) Wieler R. et al. (1992) LPSC 23th, 1525-1526. (4) Anders E. and Grevesse N. (1989) Geochim. Cosmochim. Acta 53, 197-214. (5) Cameron A. G. W. (1982), Essays in Nuclear Astrophysics, 23-43 (Barnes C.A., Clayton D.D., and Schramm D.N. eds.) (6) Pedroni A. and Begemann F. (1992) Meteoritics 27, 273-274. (7) Scherer P. et al. (1992) Meteoritics 27, 314-315. (8) Bochsler P. (1987) Physica Scripta T18, 55-60.

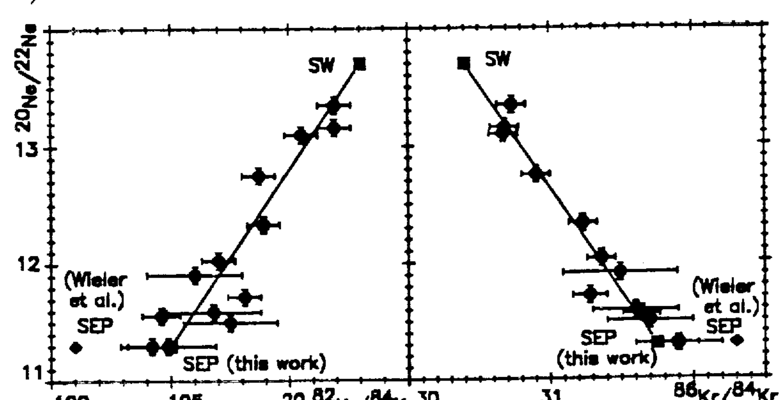


Fig.3. Correlation between Ne and Kr isotopic compositions (corrected for planetary and cosmogenic contributions) suggest a SW-SEP mixing line similar to that reported in (3). The SEP-endmember seems to have an isotopic composition differing from that in (3) however.

341-25
ABS ONLY
P. 2

N94-20677

FIRST DISCOVERY OF THE ORGANIC MATERIALS IN DEEP-SEA IRON COSMIC SPHERULE①; Peng Hanchang, First Institute of Oceanography, State Oceanic Administration, Qingdao 266003, P. R. China; Xu Peicang, Xian Institute of Geology and Mineral Resources, Xian 710054, P. R. China.

The dust impact mass analyser (PUMA) carried by the spacecraft Vega 1, Vega 2 and Giotto has provided the first direct measurements of the physical and chemical properties of cometary dust. The results indicate that most of the cometary dust particles are rich in light elements such as H, C, N and O, suggesting the validity of models that describe the cometary dust as including organic material (1, 2). Up to now, there were none find the orginic material from the deep-sea cosmic spherules. We have determined this materials from the deep-sea iron cosmic spherules collected from the North Pacific.

An iron cosmic spherule (382 um in diameter) was determined by the Laser Raman Microprobe. The Raman spectrum is showing in Figure 1.

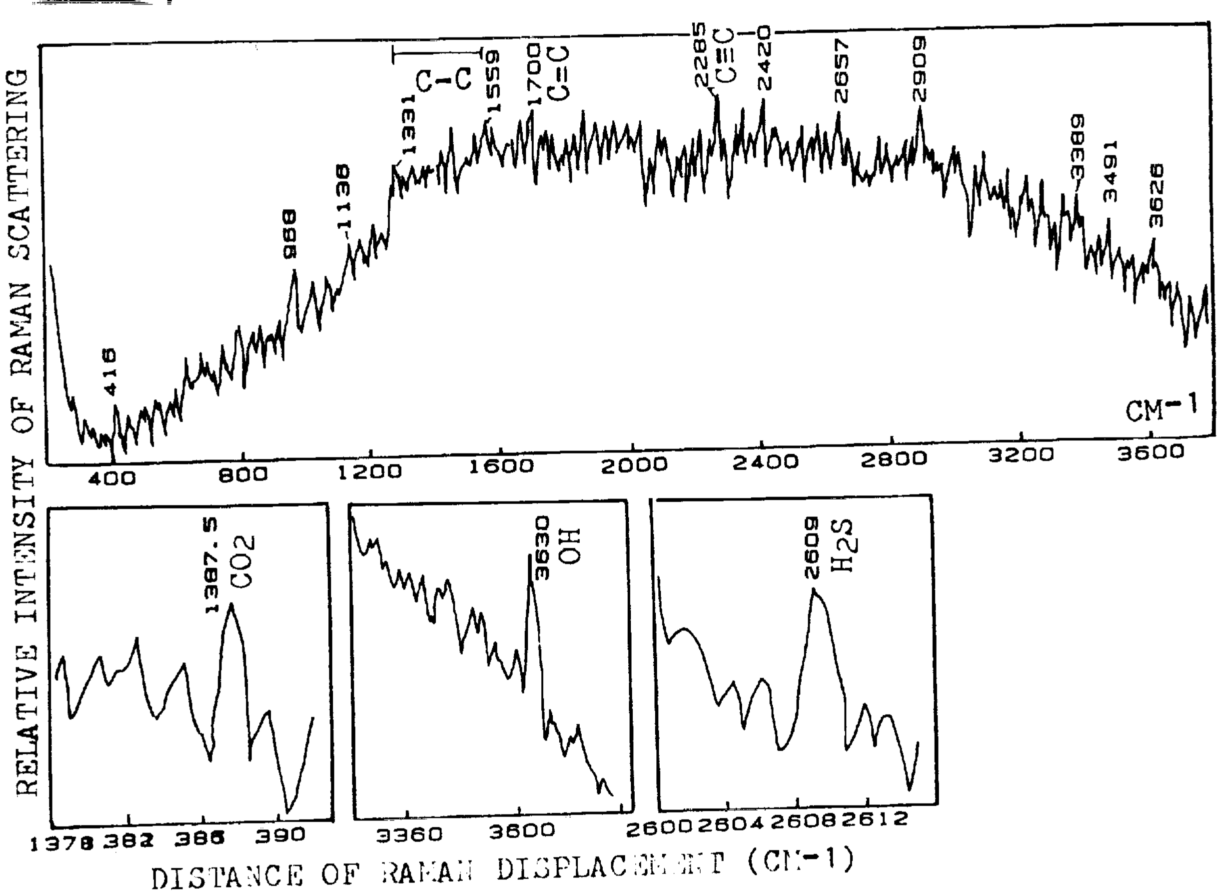


Fig. 1 Raman Spectrum of an Iron Cosmic Spherule

① The Project Supported by the National Natural Science Foundation of China, No. 49176263.

DISCOVERY OF ORGANIC MATERIALS IN COSMIC SPHERULE

Peng Hanchang and Xu Peicang

The following main molecules were contained in the iron cosmic spherule: the general molecules Al-O, which occurred at 416 cm^{-1} Raman displacement; Fe-Obr-Si, at 455 cm^{-1} Raman displacement; Fe-Fe, Fe-O and Fe-Ni, at 968 cm^{-1} Raman displacement; Si-Onb, at 1136 cm^{-1} Raman displacement; the nonfixiform C-C, which occurred at 1331-1559 cm^{-1} Raman displacement; C=C, at 1700 cm^{-1} Raman displacement; C≡C, at 2285 cm^{-1} Raman displacement; the organic molecule C-H-O, which occurred at 1300-3000 cm^{-1} Raman displacement and showed by the fluorescence spectrum in large area, and the volatile molecules CO_2, which occurred at 1387. 5 cm^{-1} Raman displacement; H_2S, at 2609 cm^{-1} Raman displacement and OH, at 3630 cm^{-1} Raman displacement.

This new research results indicate that the deep-sea cosmic spherules really contained the organic materials, suggesting some of the deep-sea cosmic spherules come from the comet. Perhaps this discovery is of important significance for exploring the origin of life on the early Earth.

References: (1) Kissel, J. et al., 1986, Composition of comet Hally dust particles from Vega observations, Nature, Vol. 321, 280-282. (2) Kissel, J. et al., 1986, Composition of comet Hally dust particles from Giotto observations, Nature, Vol. 321, 336-337.

C/O ATOMIC RATIOS IN MICROMETER-SIZE CRUSHED GRAINS FROM ANTARCTIC MICROMETEORITES AND TWO CARBONACEOUS METEORITES.

M. Perreau (LEM CNRS/ONERA, BP 72, 92322 Chatillon, France), C. Engrand, M. Maurette (C.S.N.S.M., Batiment 108, 91405 Orsay-Campus, France), G. Kurat and Th.Presper, (Naturhistorisches Museum, Postfach 417, A-1014 Wien, Austria).

Antarctic micrometeorites (AMMs) have similarities (but also differences) with primitive meteorites, such as unequilibrated mineral assemblages [1,2]. To further assess such similarities we have measured the carbon content of micrometeorites and meteorites (Orgueil and Murchison), as determined in a random selection of micrometer-size crushed grains, with an analytical transmission electron microscope. Such analyses yield the C/O atomic ratio, the major and minor elements contents, and the textural features of the grains on a scale of ≈100 nanometers. An important proportion of micrometeorites from both the 100-400 µm and the 50-100 µm size fractions contains much more carbon than CI chondrite Orgueil. The average C-content of all micrometeorites in these two size fractions amounts to ≈1.8xCI, and ≈0.8xCI, respectively (CI refers to the bulk C-content of Orgueil, of about 3.5% by weight). Carbon is usually not homogeneously distributed in the micrometeorite but is concentrated in C-rich grains. So far most of these grains are amorphous, and seem to be associated with an oxidized Fe-rich phase (possibly a variety of "dirty" magnetite). About 5% of them have the composition of "COPS", a phase additionnally enriched in O, P, and S [4].

Experimental

With a 20-30X binocular we preselect at random a family of dark/irregular particles, that are enriched in AMMs. Each particle is first splitted into several fragments. One fragment is polished, and examined with a SEM equiped with an EDS system, for a preliminary characterization. This way, all particles with chondritic compositions are identified and roughly classified as indicated elsewhere [1]. A second fragment of each chondritic particle is directly crushed onto a gold electron microscope grid held between two glass plates. The resulting micrometer-size crushed grains (embedded into the gold grid) are randomly analyzed with both the energy loss electron spectrometer (EELS) and the thin window EDX spectrometer of a 400 kV analytical transmission electron microscope (JEOL 4000FX). This procedure considerably minimizes carbon contamination, as shown by the analysis of single crystals of olivine, mounted and analyzed in the same way [3]. Chunks of Orgueil and Murchison with sizes of ≈100 µm were then processed and analyzed in a similar way.

C/O ratios on a microscale

In the Table we list individual EELS analyses of: Orgueil (15 grains); Murchison (6 grains); 8 AMMs from the 100-400 µm size fraction (109 grains), and 5 AMMs from the 50-100 µm size fraction (33 grains). Some preliminary analyses of the 100-400 µm size particleshave been already published [4]. In the Table we have included analyses of 3 new micrometeorites in this size range. No analysis of AMMs from the 50-100 µm size fraction was reported before. The value listed in the last column represents the mean value of the C/O ratio. In the Figure we report the EELS and the EDX spectra of a tiny "COPS" inclusions from AMMs No.91-32-11, showing a C/O ratio of 0.34.

Discussion

Thomas et al. [5] measured high carbon contents (0.5-7xCI) in ≈10 µm size chondritic IDPs, relying on a different technique (based on SEM analyses). We independently reported an average carbon content of ≈2xCI in a first selection of 100-400 µm AMMs [4], which well agrees with the new value inferred from the Table (≈1.8xCI). But here we observe a smaller value of the average C-content of 5 AMMs from the 50-100 µm fraction (≈0.8xCI). Such variations of the C-content in a large size range (≈10 up to ≈200 µm) are difficult to understand in term of either the loss of some pyrolizable C-rich material during frictional heating in the atmosphere (as described by classical modelings, that look more and more inappropriate), or ice, water [7,8] or atmospheric "weathering", which should somewhat be related to the settling time of the particles in the atmosphere.

Most C-rich grains in AMMs are amorphous. Carbon is frequently associated with high Fe and O contents, suggesting that the dominating C-rich species are a form of "dirty" magnetite, not observed yet in conventional meteorites (with the exception of the fusion crust of Murchison [6].Carbon is not associated with a single crystalline phase (SiC, diamond, carbonate, carbide). Only two amorphous C-rich grains composed only of carbon, were

observed (they were rejected from the Table on the suspicion that they might represent a terrestrial contamination). About 5% of the C-rich grains are in addition enriched in P and S, thus defining the "COPS" phase, more appropriately discussed in our companion paper [6]. SEM observation shows that the C-poor grains (such as 92-21-07) all originate from crystalline AMMs, mostly consisting of a few single crystals of olivine and pyroxene. Most fine grained unmelted AMMs, show high C-contents.

The average carbon content of >100 µm size AMMs is larger than the bulk content of Orgueil, quoted as the most carbon-rich meteorite so far. Moreover, in both the large and small AMMs size fractions an important proportion of the grains are definitively much richer in C-rich material than is Orgueil. Such feature could be taken as to suggest that micrometeorites of all sizes represent a new variety of primitive solar system objects not represented in the collection of meteorites. This conclusion is independently supported by studies of mineral compositions [2] and trace element contents of AMMs [7,8]. We shall extend these measurements to AMMs from the 25-50 µm size fractions, and in collaboration with J.L. Bada we expect to characterize soon the C-rich component of AMMs relying on the powerful technique of "Two Steps Laser Mass Spectrometry" [9].

Size	Samples	C/O ratios	Mean Values
100µm	Orgueil (2 samples)	1.24 1.18 1.00 0.50 0.58 0.28 0.21 0.19 0.04 0.03 0 0 0 0 0	0.35
	Murchison	0.60 0.33 0.18 0.16 0 0	0.21
100 to 400µm	91-32-04	2.17 1.91 1.03 1.03 0.97 0.97 0.68 0.50 0.48 0.40 0.45 0.21 0.13 0.07 0 0 0 0	0 0055
	91-32-05	3.13 2.63 1.72 1.39 1.37 1.20 1.09 0.96 0.90 0.81 0.72 0.69 0.67 0.65 0.20 0.06	1.14
	91-32-08	0.43	0.43
	91-32-09	2.44 2.31 1.90 1.39 1.24 1.13 0.97 0.81 0.78 0.73 0.30 0 0	1.08
	91-32-11	0.65 0.34 0.25 0.12 0.08 0.07 0 0 0 0 0 0 0	0.12
	91-32-12	1.22 0.98 0.78 0.46 0.19 0.02	0.61
	91-32-15	1.63 1.10 0.64 0.55 0.50 0.16 0.10 0.06 0.04 0.01 0.01 0 0 0 0	0.32
	91-32-18	0.25 0 0 0 0	0.05
50 to 100µm	92-21-01	0.58 0.48 0.07 0.04 0.01 0 0 0 0 0 0 0 0 0 0 0 0 0 0 0 0 0 0 0	0.05
	92-21-04	1.00 0.93 0.79 0.71 0.60 0.51 0.40 0.30 0.31 0.24 0.23 0.22 0.08 0.03	0.45
	92-21-05	0.69 0.60 0.21 0 0	0.3
	92-21-07	0 0 0 0 0	0
	92-21-16	1.25 1.19 0.72 0.70 0.63 0.55 0.44 0.42 0.33 0.26 0.19	0.61

Table : C/O ratios in primitive meteorites and micrometeorites

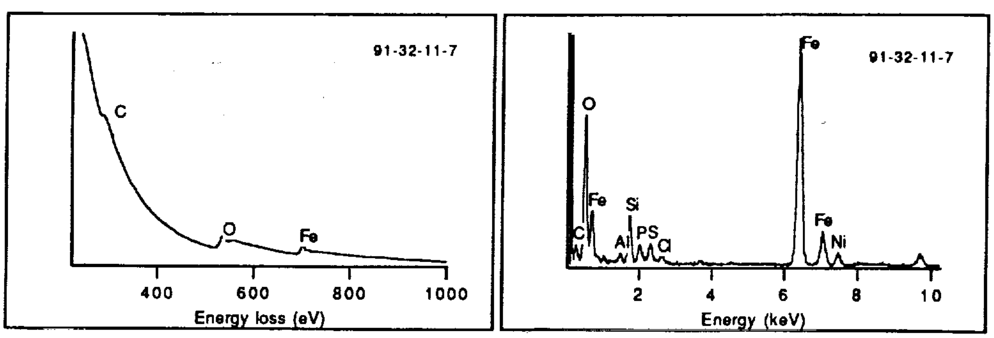


Figure : TEM analysis of a "COPS" inclusion

REFERENCES: [1] Maurette M., Olinger C.T., Christophe Michel-Levy C., Kurat G., Pourchet M., Brandstatter F., Bourot-Denisse M. (1991) *Nature 351*, 44; [2] Presper Th., Kurat G., Maurette M. (1992) *Meteoritics 27*, 246; [3] Maurette M., Bonny Ph., Brack A., Jouret C., Pourchet M., Siry P. (1990) *Lecture Notes in Physics 390*, 124; [4] Perreau M., Maurette M., Kurat G., Engrand C., (1992) *Meteoritics 27*, 274; [5] Thomas K. L., Keller L. P., Blanford G. E. and McKay D. S. (1992) *Meteoritics 27*, 296 ; [6] Engrand C., Maurette M., Kurat G., Brandstatter F., Perreau M. (1993) *this abstract volume*; [7] Presper Th. et al (1993) *this abstract volume*; [8] Kurat G., Koeberl C., Presper Th., Brandstätter F. and Maurette M. (1992), *Meteoritics 27*, 246; [9] Hahn J.H., Zenobi R., Bada J.L., Zare R. (1988) *Science 239*, 1523.

N94-20679

LAMELLAR OLIVINE IN THE DIVNOE ACHONDRITE: EVIDENCE FOR HIGH-PRESSURE EXSOLUTION?

M.I.Petaev, Harvard-Smithsonian Center for Astrophysics, Cambridge, MA, USA

The olivine-rich Divnoe achondrite contains numerous large olivine grains which have a lamellar or banded appearance in back-scattered electron images, caused by minor compositional differences. One such grain, viewed in transmitted light, displays a system of lamellae with the same orientation and scale as the compositional banding. The only process known to produce such structure and chemical variability in olivine grains is high-pressure transformations between α-, β- and γ-olivines, but in other meteorites and in experimental products the structure is ~ 100 times finer than the Divnoe lamella.

INTRODUCTION The meteorite Divnoe is an olivine-rich achondrite with subchondritic chemistry and mineralogy [1-4]. It has a coarse-grained granoblastic olivine groundmass with relatively large poikilitic patches of pyroxene and, rarely, plagioclase. The groundmass also contains areas of troilite- and/or metal-rich ol-px fine-grained lithology, having reactionary boundaries with the groundmass and different mineral chemistry [5]. Numerous µm- to mm-thick veins of troilite and, rarely, metal cross all the lithologies found in the meteorite.

The major silicate minerals display evidence of week to moderate shock metamorphism: wavy to blocky extinction in olivine, pyroxenes, and to a lesser degree, plagioclase; irregular, and, rarely, planar fractures in olivine and low-Ca pyroxene, often filled by troilite; strong planar fractures in high-Ca pyroxene. Some plagioclase grains display well-developed twinning, sometimes with diffuse boundaries between twins. No evidence of shock has been found in metal and troilite.

Olivine and pyroxenes display minor intergrain variations in composition [5] and complex zoning patterns.

OLIVINE STRUCTURE AND CHEMISTRY The most unexpected and intriguing result of this study was the discovery of fine µm-scale chemical variability in olivine grains in the rock whose textural and mineralogical characteristics suggest extensive recrystallization and slow cooling in the temperature range from ~ 1000°C to ~ 500°C and lower. In spite of this, in back-scattered electron images many if not all of olivine grains show a lamellar appearance, which seems to be crystallographically controlled (Fig. 1a), caused by minor chemical variations (Fig. 1b). The points on the graph are microprobe analyses made at the dark rounded spots seen in Fig. 1a. In some cases these fine-scale variations are superimposed on large-scale compositional zoning in olivine grains where they are in contact with pyroxene (Fig. 2). In all grains studied so far, the BSE variability is caused by differences in Fe/Mg ratio between lighter (Fe-rich) and darker (Fe-poor) lamellae. The range of variations in most of the microprobe scans done is less than 3 mol.% Fa; however, these points were equally spaced in the scans, not placed according to tones in the BSE images. To define more precisely compositional variability, the lightest, darkest, and some intermediate lamellae were analyzed in three olivine grains. Differences of 2.7, 3.0 and 3.2 mol.% Fa were found (Fig. 3), as well as a strong positive correlation between Fe and Mn, which was only detectable (>0.05 wt.%) minor element. Among several lamellar olivine grains studied by transmitted light, one was found to have 5 - 12 µm-thick lamellae (Fig. 4a) with the same orientation and thickness as the lamellae seen in back-scattered electron images (Fig. 4b). Several other grains with similar structure have been found in thin sections.

DISCUSSION The scale of structural and compositional variations found in Divnoe olivines has not been observed in terrestrial and other extraterrestrial olivines. Ferromagnesian olivines are generally understood to form an almost ideal solid solution between end members, and there is no reason to expect any exsolution to occur. Detailed structural studies of natural olivines has shown some preferred occupation of M1 sites by Fe at high temperatures [6 and references therein], but this would not promote exsolution.

Coexisting minerals with olivine stoichiometry and slightly different Fe/Mg ratios have been found in several highly shocked ordinary chondrites [7-11]. These grains are composed of isotropic polycrystalline aggregates of high-pressure olivine polymorphs - wadsleyite (β) and ringwoodite (γ) - and are characterized by compositional differences up to 8 mol.% Fa between coexisting phases. Some grains display ultrafine (up to 0.1 µm) lamellar structure (e.g. Fig. 2c in [11]), qualitatively similar to the structure of Divnoe olivine grains. Experimental [12 and references therein] and thermochemical [13] studies of the high-pressure transformations in olivine have shown that transformations at pressures of 100 - 160 kbar and temperatures of 800 - 1600 K result in substantial difference in Fe/Mg ratios between coexisting polymorphs. Lamellar structure was not found by [12] in their experimentally produced olivine polymorphs, but experimental studies of transformations between α, β and γ polymorphs of Mg_2SiO_4 at 150 kbars [14] did produce ultrafine (up to 0.01 µm) striated microstructure in β and γ phases similar to the structure observed in Divnoe olivine by transmitted light. This structure was interpreted by [14] to be a system of stacking faults that arises during the phase transformation. [14] also found lamellar intergrowths of β and γ phase, but the scale of the lamellae is even finer (~ 0.001 µm).

Thus, only process known to produce exsolution in olivine is high-pressure transformation between its polymorphs. The structural and compositional similarity between Divnoe olivine grains and the occurrences discussed above indicates that this could explain the Divnoe olivines. But what process was responsible for the transformations? Such high static pressures seem to be unrealistic for meteorites, and the presence of plagioclase in Divnoe limits the static pressure to less than ~ 30 kbars. The shock features recorded in Divnoe silicates are characteristic of shock pressure of 200 - 300 kbars, enough to produce transformations between α,

LAMELLAR OLIVINE IN DIVNOE: Petaev M.I.

β and γ polymorphs in olivine. The chemical variations between lamellae in Divnoe olivine are also comparable to those between olivine polymorphs in highly-shocked chondrites. However, the scale of exsolution is extremely coarse in Divnoe. In addition, lamellae with different compositions in Divnoe are composed only of the anisotropic α-polymorph of olivine. This discrepancy could be explained by low-temperature post-shock annealing which has erased shock features in metal and troilite, and transformed β and/or γ polymorphs to α without changing their compositions.

REFERENCES [1] Zaslavskaya N.I. et al. (1990) *Meteoritika*, **49**, 10-27 (*in Russian*) [2] Zaslavskaya N.I., Petaev M.I. (1990) *LPSC XXI*, 1369-1370 [3] Zaslavskaya N.I. et al. (1990) *LPSC XXI*, 1371-1372 [4] Petaev M.I. et al. (1990) *LPSC XXI*, 948-949 [5] Petaev M.I. (1993) *This volume* [6] Khisina N.R. (1987) *Subsolidus transformations in solid solutions of rock-forming minerals* M., Nauka, 206 p. (*in Russian*) [7] Binns R.A. et al. (1969) *Nature*, **221**, 943-944 [8] Smith J.V., Mason B. (1970) *Science*, **168**, 832-833 [9] Steele I.M., Smith J.V. *LPSC IX*, 1101-1103 [10] Putnis A., Price G.D. (1979) *Nature*, **280**, 217-218 [11] Price G.D. et al. (1979) *Contrib Miner Petrol*, **71**, 211-218 [12] Katsura T., Ito E. (1989) *JGR*, **94**, 15663-15670 [13] Akaogi M. et al. (1989) *JGR*, **94**, 15671-15685 [14] Brearley A.J. et al. (1992) *Phys Chem Minerals*, **18**, 343-358

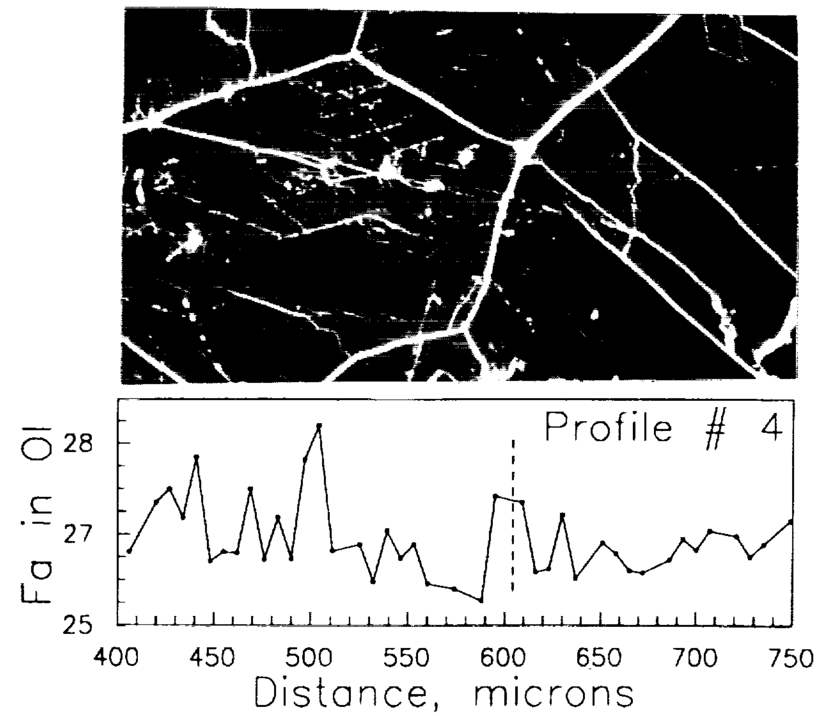


Fig. 1. Lamellae in Ol (top) and compositional variations between them (bottom).

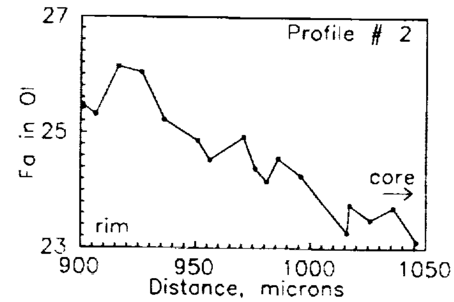
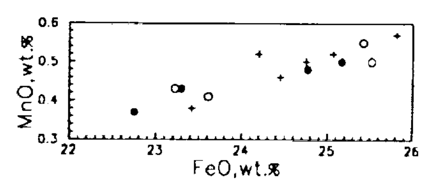


Fig. 2. Fine- and large-scale chemical variations in Ol.

Fig. 3. Fe-Mn correlation in lamellar Ol. Data on separate grains are shown by different symbols.



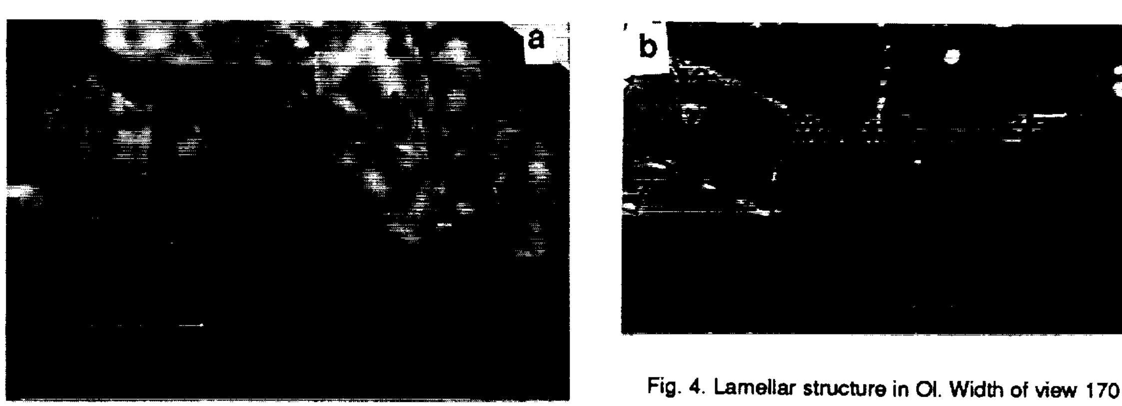


Fig. 4. Lamellar structure in Ol. Width of view 170 μm. **A** - transmitted light, **b** - BSE image.

OPAQUE-RICH LITHOLOGY IN THE DIVNOE ACHONDRITE: PETROLOGY AND ORIGIN

M.I.Petaev, Harvard-Smithsonian Center for Astrophysics, Cambridge, MA, USA

An opaque-rich lithology (ORL) makes up to ~9 vol.% of the Divnoe achondrite. It is characterized by enrichment of troilite and pyroxene compared to bulk Divnoe, the presence of tiny remnants of olivine in low-Ca pyroxene and low minor element concentrations in pyroxene. The ORL was formed by local reaction between gaseous sulfur and olivine in the Divnoe.

—INTRODUCTION The Divnoe meteorite is an olivine-rich achondrite with subchondritic chemistry and mineralogy [1-4]. It has a granoblastic coarse-grained olivine groundmass (CGL: coarse-grained lithology) with relatively large (2-10 mm) poikilitic patches (PP) of pyroxene and, rarely, plagioclase. The groundmass also contains an opaque-rich fine-grained lithology (ORL) which comprises ~9 vol.% of the meteorite, displays reaction boundaries with the groundmass, and differs in mineral chemistry from it. Numerous µm- to mm-thick veins of troilite and, rarely, metal cross all the lithologies found in the meteorite. The Divnoe itself appears to represent a sample of an igneous source region.

PETROLOGY The opaque-rich lithology has been found only within granoblastic CGL. It is often located at boundaries between olivine grains, or along preexisted cracks filled now by ORL. The types of occurrence of ORL vary from roughly equidimensional irregular areas ranging from tens to hundreds µm in size, to long (several mm) branching veins of varying thickness (100 - 900 µm). Sometimes ORL is associated with large metal or troilite grains. Texture of ORL depends upon its content of opaque minerals, changing from granoblastic to micrographic as the content of opaques and the troilite/metal ratio increases. The grain size of ORL rarely exceeds 100 µm, and varies from area to area from several µm to tens µm, being relatively constant within an area.

Major minerals are low-Ca pyroxene or, rarely, even two pyroxenes with slightly different compositions and very low birefringence; sulfide, usually troilite; metal; and olivine, the abundance of which varies considerably. Compared to the bulk meteorite, ORL is enriched in pyroxene and opaques (Table 1). Two modes of occurrence of olivine have been found in ORL: (1) relatively large anhedral grains similar in size to the other minerals, and (2) small relict grains inside pyroxene. The second type of olivine, characteristic for ORL, always shows reaction relations with the host pyroxene, implying a substitution of the latter for the former. In several cases, large anhedral olivine grains surrounded by pyroxene and opaque intergrowths, and small olivine relicts within pyroxene, display the same optical orientation. Opaque minerals also occur in two types of grains: (1) relatively large grains of metal and troilite, and (2) very small troilite grains along the boundaries between large grains of olivine and pyroxene inside ORL as well as at the boundary between ORL and CGL. The metal/sulfide ratio varies considerably, and, as a rule, the higher troilite content the higher the pyroxene/olivine ratio is in ORL. In two areas, where ORL is associated with large metal grains, it contains euhedral or subhedral whitlockite grains as a major mineral. The only grain of high-Ca pyroxene found is in such an area.

Characteristic of practically all occurrences of ORL is the presence of microcopy of it - finer-grained domains, even richer in opaques, inside ordinary ORL. These domains often concentrate at peripheries of ordinary ORL, near its boundary with olivine, and consist of pyroxene and sulfide, the latter comprising up to 70 % of the domains. The sulfide is often pyrrhotite. No olivine has been found in the micro-ORL.

The chemical composition of silicates in ORL differs slightly in major elements (Fig. 1) and considerably in minor (Fig. 2). Olivine and pyroxene are more magnesian then these minerals in CGL. The pyroxene in ORL is depleted in all minor elements relative to the pyroxene in PP. This appears to be a reason of very low birefringence of ORL pyroxene. The metal is often replaced by terrestrial oxides. Previous studies [1,3] revealed similar compositions of metal in CGL and ORL, with minor enrichment of ORL metal in Ni and Co. The troilite, phosphate, and high-Ca pyroxene are identical in composition to minerals in CGL.

ORIGIN The enrichment of ORL in opaques, especially troilite, and its variable but high pyroxene/olivine ratio, suggest the operation of a process involving redox reactions between silicate(s) and a reducing agent. In the case of Divnoe, such the reducing agent could be sulfur. Reaction between sulfur, with a fugacity was buffered by a troilite-metal assemblage in the source region, and CGL olivine at high temperature could results in the formation of pyroxene-troilite intergrowths associated with as yet unreacted olivine. This could occur during the final stages of partial melting when all other minerals except olivine and metal, were exhausted from a source region. In a microchambers represented now by ORL, reaction between olivine and gaseous sulfur resulted in the extraction of Fe_{2+} from the silicate and formation of troilite. The residual silicate assemblage had a lower (Mg+Fe)/Si ratio and, consequently, a lower melting temperature. Since the temperature was fixed, the decrease of (Mg+Fe)/Si resulted in increasing of melt/olivine ratio in the microchamber, with silicate melt being of pyroxenic composition.

OPAQUE-RICH LITHOLOGY IN DIVNOE: M.I.PETAEV

Simultaneously the amount of troilite increased, if sulfur was the only reducing agent. If another reducing agent, e.g. C-bearing gas species, played a role in this process, the amount of metal in the microchamber would increase. Such a melting event could also explain low minor element contents in pyroxene of ORL as a result of the dilution of the microchamber's melt with almost pure enstatite.

REFERENCES [1] Zaslavskaya N.I. et al. (1990) *Meteoritika*, 49, 10-27 (*in Russian*) [2] Zaslavskaya N.I., Petaev M.I. (1990) *21st LPSC*, 1369-1370 [3] Zaslavskaya N.I. et al. (1990) *21st LPSC*, 1371-1372 [4] Petaev M.I. et al. (1990) *21st LPSC*, 948-949

Table 1. Mineralogy of Divnoe lithologies (vol.%)

	Bulk*	PP-rich	ORL
Pyroxene	14.3	27.6	41
Olivine	74.6	57.9	32
Plagioclase	1.5	-	-
Opaques	9.5	6	13
ORL	-	8.5	14**

* Mineral norms converted to vol.%
** Very fine-grained ORL

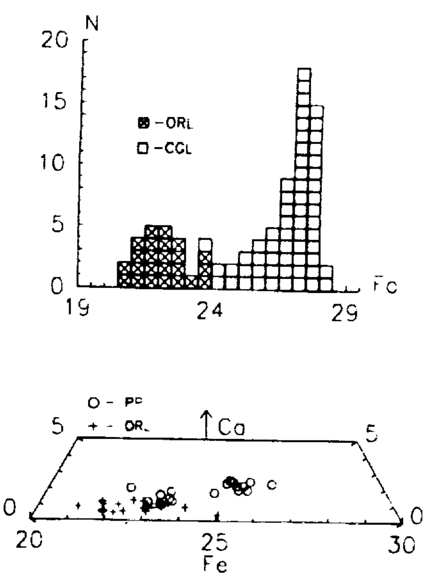


Fig. 1. Chemical variations in olivine (top) and pyroxene (bottom).

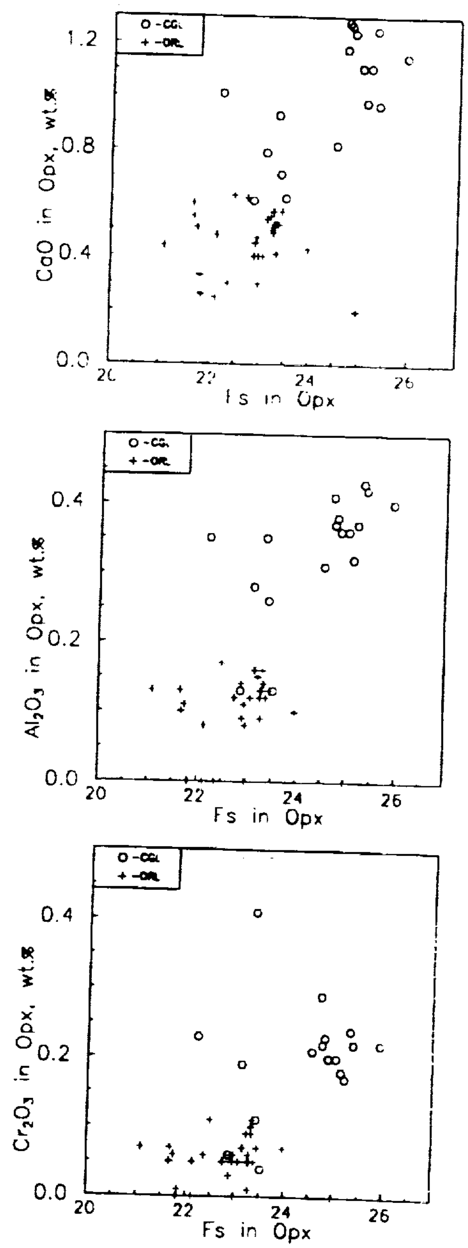


Fig. 2. Minor elements in low-Ca Px.

CHAUNSKIJ: THE MOST HIGHLY METAMORPHOSED, SHOCK-MODIFIED AND METAL-RICH MESOSIDERITE Petaev M.I.[1,2], Clarke R.S., Jr.[3], Olsen E.J.[4], Jarosewich E.[3], Davis A.M.[5], Steele I.M.[4], Lipschutz M.E.[6], Wang M.-S.[6], Clayton R.N.[4,5], Mayeda T.K.[5], Wood J.A.[1] 1 - Harvard-Smithsonian Center for Astrophysics, Cambridge, MA, USA; 2 - Vernadsky Inst. Geochem. Analyt. Chem., Russian Acad. Sci., Moscow, Russia; 3 - Smithsonian Institution, Washington, D.C., USA; 4 - Department of the Geophysical Sciences, University of Chicago, IL, USA; 5 - Enrico Fermi Institute, University of Chicago, Chicago, IL, USA ; 6 - Department of Chemistry, Purdue University, West Lafayette, IN, USA

The 1990 g Chaunskij meteorite was found in 1985 and classified as an anomalous ungrouped iron [1]. It contains ~10 vol.% mono- and polymineralic troilite-phosphate-silicate inclusions, microns to centimeters in size. In [2] we proposed its affinity with mesosiderites; here we present mineralogical, chemical and isotopic data establishing that Chaunskij is the most highly metamorphosed, shock-modified and metal-rich of the mesosiderites. The most striking manifestation of metamorphism in Chaunskij is the presence in it of a cordierite-bearing assemblage substituting for basalt lithology.

STRUCTURE AND MINERALOGY. Metal in Chaunskij displays mesosiderite structure, and shows unusually high levels of shock damage in the kamacite. Tetrataenite borders 5-10 µm wide enclose large regions of cloudy taenite, which, in turn, sometimes enclose martensitic regions. Much of the tetrataenite apparently has been disordered by shock. Schreibersite occurs as occasional very small precipitates at tetrataenite borders, and infrequently as larger masses at grain boundaries. Shock-affected troilite in moderately large globules (up to several mm) and rounded phosphate inclusions are irregularly distributed. Silicate areas in the polymineralic inclusions are, as a rule, irregular in shape. In larger inclusions, these areas are usually surrounded by phosphate rims.

Two dominant silicate lithologies have been found in the inclusions. One, making up a large inclusion (Fig.1), consists of a fine-grained (20-30 µm) aggregate of anhedral pyroxene, subhedral plagioclase laths and silica, minerals characteristic of HED meteorites and mesosiderites. Their compositions match those of mesosideritic pyroxene and plagioclase. Whitlockite is minor. Textures vary from microophitic or subophitic to xenoblastic, and are similar to the textures of highly-recrystallized and impact-melted mesosiderites such as Simondium and Hainholz [3]. This 'igneous' lithology contains relatively large (100 - 200 µm) porphyritic grains of pyroxene and (rarely) plagioclase having irregular edges, suggestive of reaction with the groundmass. Some of the porphyritic pyroxene grains have chromite-rich cores like those found in pyroxene phenocrysts in highly recrystallized mesosiderites [4]. The 'igneous' lithology also contains rare primary clasts enriched in Px, whose boundaries are almost unresolvable from the groundmass in transmitted light.

The second, 'metamorphic', lithology forms as separate small inclusions and as larger areas in intimate contact with the igneous lithology in the large inclusion (Fig.1). This lithology is a fine-grained (typically 30-50 µm) xenoblastic intergrowth of low-Ca pyroxene, whitlockite, and cordierite, with rare larger porphyritic grains of the first two minerals. Porphyritic pyroxene grain edges are generally irregular, indicative of reaction with the groundmasss. Plagioclase is present only as a rare accessory mineral.

Silicate areas also contain metal-phosphate veins and rare pockets or veins of impact glass saturated with Fe-Ni-S globules, mineral fragments, and clasts of the 'igneous' and 'metamorphic' lithologies. Minor minerals in both lithologies are SiO_2, kamacite, taenite, troilite, chromite, ilmenite and rutile. The chromite and ilmenite vary in MgO, MnO, and Al_2O_3 contents. Rare grains of pyrophanite, zircon, alabandite, native copper, stanfieldite, and a graftonite-farringtonite mineral are also present.

OXYGEN ISOTOPES. Oxygen isotope data for three different inclusions - one 'igneous' and two 'metamorphic' - plot on the same fractionation line, indicating fractionation during metamorphism (Fig.2). Data for the 'igneous' lithology falls exactly within the HED - mesosiderite field, leaving no doubt as to the mesosideritic affinity.

BULK CHEMISTRY. A chemical analysis of the large inclusion is shown in the Table 1, and REE contents of whitlockite and pyroxene by ion microprobe analysis are shown in Fig.3, along with the estimated bulk REE content. Recalculated to the silicate fraction only, the composition is very close to those of eucrites and mesosiderites except for minor enrichment in Al and depletion in Fe and Mn. The most important difference between Chaunskij and HED-Mes members is a large enrichment in P and volatile chalcophiles in Chaunskij. Table 2 shows that petrographic modes and chemical norms are in good agreement. Both major element and REE chemistry and bulk mineralogy point to a cumulate eucrite as the precursor of the silicate inclusions. This precursor was apparently slightly fractionated during the remelting event inferred by the structure of the 'igneous' lithology. Similar gabbroic clasts have been found in mesosiderites [5,6].

DISCUSSION. Mineralogical, chemical and O-isotopic data strongly suggest a relationship of Chaunskij to mesosiderites. However, the silicates in Chaunskij are not mixed as intimately with metal as those in mesosiderites,

THE CHAUNSKIJ MESOSIDERITE: M.I.Petaev et al.

but form discrete inclusions like those in irons with silicate inclusions. This is the only major difference between Chaunskij and known mesosiderites. Nevertheless, while Chaunskij formally corresponds to the 'irons with silicate inclusions' group on the basis of the proportion of metal and silicates, we classify it here as a metal-rich mesosiderite. Other differences between Chaunskij and mesosiderites fall on simple extensions of the mineralogical and chemical trends observed in mesosiderites. Prograde metamorphism, causing recrystallization of mesosideritic silicates and an increased content of phosphates, resulted in the formation of a true metamorphic cordierite-pyroxene assemblage in Chaunskij. In this sense, Chaunskij is the most metamorphosed member of the mesosiderites. The presence of impact glass in silicates and ε-structure in kamacite, atypical for mesosiderites, makes Chaunskij also the most shock-modified mesosiderite.

REFERENCES [1] The Meteoritical Bulletin (1988) *Meteoritics*, **23**, 171-173 [2] Petaev M.I. et al.(1992) *Meteoritics*, **27**, 276-277 [3] Floran R.J. et al. (1978) *Proc. 9th LPSC*, 1083-1114 [4] Floran R.J. (1978) *Proc. 9th LPSC*, 1053-1081 [5] Mittlefehldt D.W. (1979) *GCA*, **43**, 1917-1935 [6] Rubin A.E., Mittlefehldt D.W. (1992) *GCA*, **56**, 827-840

Table 1. Chemistry of inclusions

	Silicates	Bulk		
	wt.%			*ppm*
SiO_2	49.47	40.95	Co	244
TiO_2	0.42	0.35	Ga	5.99
Al_2O_3	14.00	11.59	Se	10.7
Cr_2O_3	0.57	0.47	Zn	8.31
FeO	14.04	11.62	Cd	6.01
MnO	0.36	*0.30*		*ppb*
MgO	9.70	8.03	Te	570
CaO	8.84	7.32	Ag	539
Na_2O	0.36	0.26	Au	81.8
K_2O	0.02	0.02	Sb	49
P_2O_5	2.26	1.87	Bi	10.6
H_2O^+		1.07	Tl	3.12
H_2O^-		0.28	In	0.83
Fe_{met}		2.26	Rb	727
Ni		1.80	Cs	45.5
Co		0.02	U	36.2
FeS		10.80		
C		0.02		
Total		99.01		
Fe_{tot}		17.87		

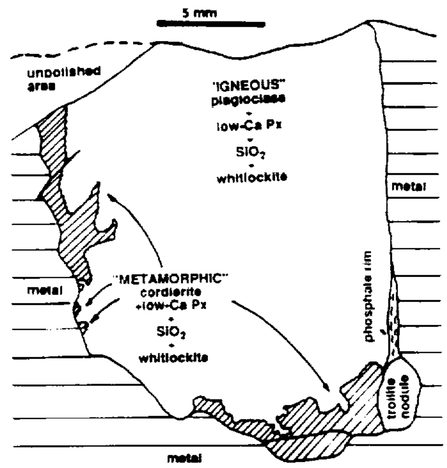


Fig. 1. Map of the large inclusion.

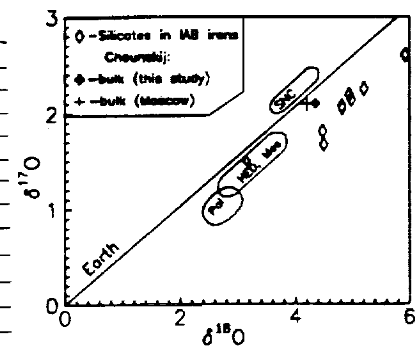


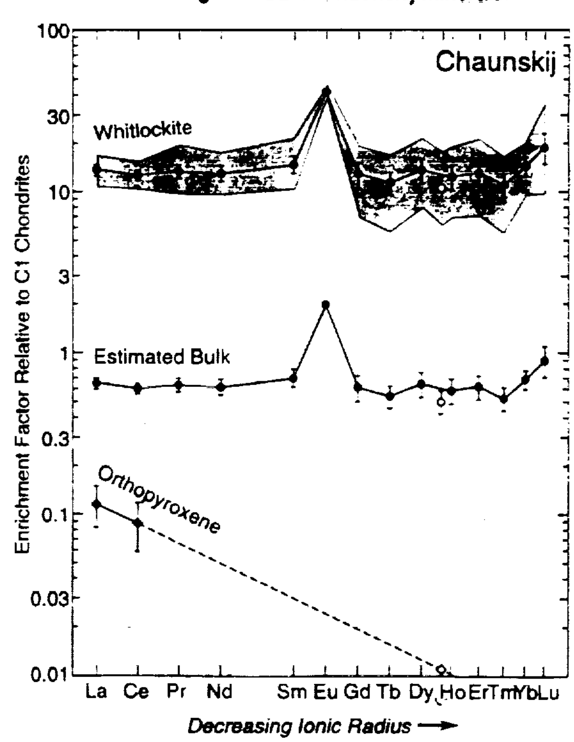
Fig. 2. Oxygen isotopes in the Chaunskij inclusions

Table 2. Mineralogy of inclusions (wt.%)

Mineral	Norms	Modes
Pyroxene	39.8	39
Plagioclase	29.5	29
Cordierite	3.5	6
Whitlockite	4.4	4
Silica	6.5	5
Chromite	0.7	1
Ilmenite	0.7	0.8
Metal	4.0	*
Troilite	10.8	15*

*Metal + troilite

Fig. 3. REE in Chaunskij minerals.



546-
ABS. ONLY

N94-20682

SPECTRAL REFLECTANCE STUDIES OF THE HUMORUM BASIN REGION; C.A. Peterson, B.R. Hawke, P.G. Lucey, G.J. Taylor, D.T. Blewett, Planetary Geosciences, SOEST, University of Hawaii, Honolulu, HI 96822; P.D. Spudis, Lunar and Planetary Institute, Houston, TX 77058.

SUMMARY. A portion of the mare-bounding (MB) ring of Humorum Basin is composed of pure anorthosite while other parts of the ring are composed of noritic anorthosite. An episode of mare volcanism emplaced basaltic units in the region northwest of the MB ring after the Humorum impact event. Subsequently, large impacts emplaced a veneer of highlands material atop the basalt flows. Some mare material could have been mixed with this highlands debris either by local mixing by secondary craters or by vertical mixing. Spectra for most other highlands units in the region indicate a noritic anorthosite lithology. Spectra of mare basalts in Mare Humorum and nearby mare flooded craters show relatively deep absorption bands due to the presence of abundant high-Ca pyroxene. An analysis of spectra for a small number of craters in the highlands west of the outer ring of Humorum reveals the presence of high-Ca pyroxene. This suggests the possible presence of an extensive gabbroic province.

INTRODUCTION. Humorum Basin is a large multiringed impact structure of Nectarian age located on the southwestern portion of the lunar nearside. The most complete ring is 440 km in diameter [1] and bounds Mare Humorum. A rimlike scarp almost twice as large (820 km) and resembling the Cordillera ring of the Orientale basin lies outside of this mare-bounding ring.

Many unresolved problems exist in this region. These include: 1) The composition of the highlands units surrounding the Humorum Basin; 2) The stratigraphy of the lunar crust in the Humorum target site; 3) The composition and extent of possible cryptomare deposits in the region; 4) The nature and origin of local light plains units; and 5) The distribution of pyroclastic deposits in the region. In order to address these issues, we have been conducting a variety of spectral studies of this portion of the lunar surface. The purpose of this paper is to present the results of an analysis of a large number of near-infrared reflectance spectra obtained for geologic units in the Humorum region.

METHOD. Near-IR reflectance spectra were obtained utilizing the University of Hawaii 2.24-m and 0.60-m telescopes at the Mauna Kea Observatory. The Planetary Geosciences indium antimonide spectrometer was used. This instrument successively measured intensity in each of 120 wavelengths covering a 0.6-2.5 μm region by rotating a filter with a continuously variable band pass. By using the f/35 oscillating secondary mirror on the 2.24-m telescope in its stationary mode, it was possible to collect spectra for relatively small areas (5-10 km). Differential atmospheric refraction limited such high-resolution observations to periods when the Moon was near zenith.

The lunar standard area at the Apollo 16 landing site was frequently observed during the course of each evening, and these observations were used to monitor atmospheric extinction throughout each night. Extinction corrections were made using the methods described by McCord and Clark [2]. These procedures produce spectra representing the reflectance ratio between the observed area and the Apollo 16 site. These relative spectra were converted to absolute reflectance utilizing the reflectance curve of an Apollo 16 soil sample. Analyses of pyroxene band positions and shapes as well as continuum slopes were made using techniques described by McCord *et al.* [3].

RESULTS AND DISCUSSION. At least a portion of the mare-bounding (MB) ring of Humorum is composed of pure anorthosite. Spectra were collected for Mersenius C (diameter=14 km), Liebig A (diameter=12 km), Liebig B (diameter=9 km), and the Gassendi E and K complex. These small impact craters expose fresh material from beneath the surface of massifs in the mare-bounding ring. These spectra exhibit either no "1 μm" absorption features or extremely shallow bands. Only very minor amounts of low-calcium pyroxene are present in the areas for which these spectra were obtained; an anorthosite lithology is indicated. The diameters of the areas for which spectra were obtained for Mersenius C and the Gassendi E and K complex varied from ~3 km to ~20 km. None of these spectra has a significant "1 μm" band. This indicates that anorthosite does not just occur on some small portion of the interiors of these craters; it is the dominant rock type in the ring massifs in this region.

While the northwestern part of the MB ring appears to be composed of pure anorthosite, spectra for other sectors of the ring indicate that both anorthosite and more pyroxene-rich material are present [4,5,6]. A spectrum of the east wall of the crater Vitello, located on the southern part of the MB ring, shows it also to be composed of pure anorthosite. However, the central peaks of Gassendi and

the craters Dunthorne (diameter=16 km), Loewy A (diameter=7 km) and others on or near the MB ring expose noritic anorthosite.

Several spectra were collected for an area with interesting spectral properties located to the northwest of the MB ring. The craters Gassendi G and F are both 8 km in diameter, and both exhibit partial dark haloes. Analysis of spectra obtained for areas of various sizes in this region has revealed details of the local stratigraphy. The spectrum of Gassendi F indicates the presence of major amounts of mare basalt with only minor amounts of highlands debris. The spectrum obtained for the center of the Gassendi G interior (aperture diameter=5 km) indicates the presence of mare basalt that is contaminated by a somewhat higher percentage of highlands material. In contrast, the spectrum of the dark halo immediately south of Gassendi G (aperture diameter=5 km) indicates that this area is composed almost totally of mature mare basalt. The spectrum obtained for a relatively large area (diameter=18 km) that included both the Gassendi G interior and the dark halo has spectral parameters that are intermediate between the other two spectra.

The spectral data have important implications for the stratigraphy of the Gassendi G and F target sites. A relatively thin highlands-rich surface layer overlies a mare basalt unit which occurs above a deposit of pure highlands material. Gassendi G fully penetrated the upper two layers and highlands debris is exposed on the crater interior. An episode of mare volcanism emplaced basaltic units in this region after the formation of the Humorum Basin. Subsequently, large impacts in the vicinity, such as those which formed Gassendi, Mersenius, and Letronne craters, emplaced a veneer of highlands atop the basalt flows. Some mare material could have been mixed with this highlands debris either by local mixing by secondary craters during ejecta emplacement or by vertical mixing due to small crater-forming impacts in the area.

One spectrum was obtained for Billy A, a 7-km impact crater that excavated material from the northwestern portion of the outer Humorum ring. Analysis of this spectrum indicated that noritic anorthosite is present in this segment of the outer ring. Spectra were also collected for a number of highlands units in the area surrounding Humorum. These include the craters Mersenius S, Billy D, Gassendi zeta, and Gassendi A. Analyses of the "1μm" band positions and shapes as well as continuum slopes indicate that these features exhibit many common spectral characteristics. These spectra indicate the presence of relatively fresh highlands rocks dominated by Fe-bearing plagioclase and Ca-poor pyroxene. Noritic anorthosite is the major rock type present in all of the areas for which these spectra were obtained. Our results are consistent with those of a recent CCD-imaging study of Gassendi crater presented by Chevrel and Pinet [7].

Spectra for regional pyroclastic deposits dominated by Fe^{2+} bearing glass are characterized by a broad absorption band centered longward of 1 μm [8,9]. We have obtained several spectra which support previous interpretations concerning the existence of a glass-rich regional pyroclastic deposit which mantles a substantial part of the southwestern portion of Mare Humorum between the west rim of Vitello crater and the crater de Gasparis [e.g., 8]. Localized pyroclastic deposits also occur inside the crater Mersenius and in the vicinity of Agatharchides.

Craters in Mare Humorum such as Gassendi J and Gassendi Y show the deep absorption band centered between 0.95 μm and 1 μm produced by the high-Ca clinopyroxene typical of mare basalts. Similar mare basalt signatures can be seen in the spectra of the mare flooded crater Billy as well as mare basalt covered regions to the north and east of the MB ring.

An intriguing area lies to the west of the outer basin ring. The crater Byrgius A and the southeast rim of the crater Prosper Henry expose highlands material, but their spectra indicate the presence of high-Ca pyroxenes. This marks a gabbroic, rather than a noritic, lithology. Other spectra in the region appear to show a component of high-Ca pyroxene as well. The spatial extent of this gabbroic province remains to be determined, and we are continuing our research in this area.

REFERENCES. [1] Wilhelms D.E. (1987) *U.S.G.S. Prof. Paper 1348.* [2] McCord T.B. and Clark R.N. (1979) *Publ. Astron. Soc. Pac., 91,* 571-576. [3] McCord T.B. *et al.* (1981) *J. Geophys. Res., 86,* 10883-10892. [4] Spudis P.D. *et al.* (1992) *Lunar Planet. Sci. XXIII,* 1345-1346. [5] Hawke B.R. *et al.* (1991) *Geophys. Res. Lett., 18,* 2141-2144. [6] Hawke B.R. *et al.* (1991) *Lunar Planet. Sci. XXII,* 539-540. [7] Chevrel S. and Pinet P.C. (1992) *Proc. Lunar Planet. Sci. Conf. 22nd,* 249-258. [8] Gaddis L.R. *et al.* (1985) *Icarus, 61,* 461-489. [9] Lucey P.G. *et al.* (1986) *Proc. Lunar Planet. Sci Conf. 16th,* D344-D354.

VENUS MAGMATIC AND TECTONIC EVOLUTION; R.J. Phillips[1] and V. L. Hansen[2]; 1. McDonnell Center for the Space Sciences and Department of Earth and Planetary Sciences, Washington University, St. Louis, MO 63130. 2. Department of Geological Sciences, SMU, Dallas, TX 75275.

Introduction. Two years beyond the initial mapping by the Magellan spacecraft, hypotheses for the magmatic and tectonic evolution of Venus have become refined and focussed. In this abstract we present our view of these processes, attempting to synthesize aspects of a model for the tectonic and magmatic behavior of the planet. The ideas presented should be taken collectively as an hypothesis subject to further testing. The quintessence of our model is that shear and buoyancy forces in the upper boundary layer of mantle convection give rise to a spatially and temporally complex pattern of strain in a one-plate Venusian lithosphere and modulate the timing and occurrence of magmatism on a global basis.

Boundary Layer Phenomena. Sources of magmatism and tectonism are related to boundary layers within the mantle. The ones with reasonable certainty we presume to exist are at the base of the mantle associated with core heat flux (lower boundary layer) and beneath the mechanical lithosphere (upper boundary layer). The former is responsible for major plumes that create topographic rises. The latter is responsible for storing significant potential energy related to both internal heating and heat flux from the core. Because internal mantle heating should be energetically more important than core heat flux, tectonic deformation of the lithosphere should be controlled dominantly by actions in the upper boundary layer. Since Venus lacks an asthenosphere, boundary layer flow stresses couple directly into the lithosphere [1].

Plumes transfer both buoyant and shear forces to the overlying lithosphere and are responsible for broad topographic rises, associated rifting, and large partial melting events leading to residual crustal plateaus [2]. Flow in the upper boundary layer provides shear forces as well as large buoyancy forces supplied by the downwellings associated with return flow to the mantle. This can be enhanced by detached lithosphere containing significant eclogite.

The surface of Venus does not participate in the flow of the upper boundary layer, and major tectonic plate boundaries do not exist. Topographic analogies of coronal trenches with terrestrial subduction zones [3,4] have led to hypotheses regarding the recycling of the Venusian lithosphere. However, geological predictions of the subduction model are not borne out by observation [5]. For example, pre-trench radial structures emanating from corona centers are found in places to be continuous across putative plate boundaries.

In-plane tectonic force supplied by the boundary layer to the overlying lithosphere is estimated from long-wavelength gravity data to be in places at least $5x10^{12}$ N/m [6]. This is equivalent, approximately, to the buoyant energy in a 100–km length of a 100–km–thick boundary layer if the average temperature contrast of the boundary layer with the convecting mantle "core" is 500 K. This magnitude of in-plane force will lead to significant crustal deformation: ductile flow in the lower crust and brittle failure in the upper crust. The tectonic style of mountain belts suggests that deformational forces are supplied largely from below and are not related to plate boundary phenomena as on Earth [7].

Widespread Magmatism. The global occurrence of dark-floored craters provides evidence that volcanism has been widespread in space and time on Venus [8]. Given the random global distribution of impact craters, this suggests that partial melt has been widely available in the Venusian interior. This in turn implies that passive magmatism is an important process on Venus. By the term "passive" we mean that partial melts or incipient partial melting conditions have existed widely in the subsurface at relatively shallow depths (certainly less than 100 kilometers) and that volcanism results when tectonic conditions permit access of

magmas to the surface, either directly or by pressure release partial melting of upwardly mobile subsolidus material.

Forces supplied by the upper boundary layer, and to a lesser extent plumes rising from the core-mantle boundary, give rise to a complex, time-varying history of strain in the lithosphere. Where the lithosphere is placed in significant tension, volcanism occurs at the surface and is associated with broad, diffuse regions of mantle upwelling. Volcanism is thus widespread, despite the fact that at present constructional volcanism is concentrated regionally [9]. Volumetrically, topographically subtler plains volcanism dominates, and, because of the strain modulation of the lithosphere, during any geological episode volcanism is active in only a limited number of regions on the planet. However, over longer periods (~ 1 Ga) volcanism has taken place in almost every region.

It is widely held that the volcanotectonic coronae are the direct result of active mantle plumes and that coronae and topographic rises are part of a size-continuum of the same process: plumes formed at the core-mantle boundary [e.g., 10]. In this view, chains of coronae can give rise to rifts. We adopt an alternative view given by Tackley and his colleagues [11,12]. Deep mantle plumes are not a universal explanation for Venusian volcanic features extending over a broad range of sizes. The formation of coronae involves Rayleigh-Taylor melt instabilities forming at depths of incipient partial melting. Such instabilities are initiated by vertical velocity perturbations, which are provided by horizontal lithospheric extensional events that are regional in nature and initiated from time to time in the global strain regime of the lithosphere. Thus coronae formation follows rifting in a passive manner.

Origin of topography and its support. Topography on Venus arises from crustal thickening, from thermal isostasy, and from dynamic support by mantle convection. Significant crustal thickening takes place by large-scale partial melting associated with lower boundary layer plumes, and, if subsolidus crustal flow takes place on geologically reasonable time scales, with downwelling of the upper boundary layer leading to shear thickening of the lithosphere [13]. These mechanisms lead to crustal plateaus, examples of which include Ovda, Thetis, Alpha, and Tellus regiones. Thickening of the crust results also from upwellings in combination with lateral variations in lithospheric rheology [14,15], as might be expected for the strength contrast of crustal plateaus with their surroundings. Isostatic support by thickened crust is responsible for at least partial support of many features.

Conclusions. Venus is different from Earth because of the strong effect of the upper convecting boundary layer on the overlying lithosphere [1]. The lack of divergent plate boundaries means that magmatism and tectonism are controlled by a distributed strain regime in the lithosphere [16], which in turn is largely influenced by the upper boundary layer of mantle convection.

References. [1] R.J. Phillips, *Geophys. Res. Lett.* **13**, 1141; (1986); [2] R.J. Phillips *et al., Science* **252**, 288 (1991); [3] D. McKenzie *et al., J. Geophys. Res.* **97**, 13,533 (1992); [4] D.T. Sandwell and G. Schubert, *Science* **257**, 766 (1992); [5] V.L. Hansen and R.J. Phillips, *Science*, submitted (1992); [6] R.J. Phillips, *J. Geophys. Res.* **95**, 1301 (1990); [7] V.L. Hansen and R.J. Phillips, this volume (1993); [8] R.J. Phillips *et al., J. Geophys. Res.* **97**, 15,923 (1992); [9] J.W. Head *et al., J. Geophys. Res.* **97**, 13,153 (1992); [10] E.R. Stofan *et al., J. Geophys. Res.* **97**, 13,347 (1992); [11] P.J. Tackley and D.J. Stevenson, *EOS* **72**, 287 (1991); [12] P.J. Tackley, D.J. Stevenson, and D.R. Scott, in Papers Presented to the International Colloquium on Venus, LPI Contribution No. 789, 123 (1992); [13] A. Lenardic, W.M. Kaula, and D.L. Bindschadler, *J. Geophys. Res.*, submitted (1992); [14] A.A. Pronin, *Geotectonics* **20**, 271 (1986); [15] R.E. Grimm and R.J. Phillips, *J. Geophys. Res.* **96**, 8305 (1991); [16] R.E. Grimm and S.C. Solomon, *J. Geophys. Res.* **94**, 12,103 (1989).

348-25 ABS. ONLY

N94-20884

POST-IGNEOUS REDISTRIBUTION OF COMPONENTS IN EUCRITES: Phinney W. C, Lindstrom D. J; NASA/JSC, Houston TX 77058, Mittlefehldt D. W, Martinez R. R; LESC, 2400 NASA Rd 1, Houston TX 77058

BACKGROUND: Evidence for redistribution of Fe and Mg in plagioclase of lunar and terrestrial samples during high-temperature metamorphism or very slow cooling has been described previously[1]. Redistribution of REEs in plagioclase of terrestrial anorthosites has also been demonstrated whereas lunar anorthosites do not appear to exhibit this effect[2]. Evidence for reequilibration between plagioclase and melts for some eucritic meteorites has also been provided on the basis of the extraordinary partition coefficients that are required to account for the contents of REEs and other components in separated plagioclases and their collateral whole rock eucrites[3]. Isotopic data show REE reequilibration between plagioclase, but not pyroxene, and phosphate in the meteorite Ibitira[4]. Because analyses of separated phases may be compromised by contaminants that could not be eliminated during separation, it is desirable to analyze individual mineral grains for their trace elements and utilize appropriate partition coefficients to test the reasonableness of calculated melts. Although microbeam analyses provide an excellent means for such analyses, sensitivity or interference problems may limit the range of elements and accuracy for such analyses. Therefore, we opted for another means of analysis.

TECHNIQUE: In our analyses *we utilize a microdrilling technique that removes 40 to 100μm diameter cores from mineral grains in thin sections analyzed by microprobe*. The cores are then analyzed by INAA using the technique of Lindstrom [5]. Three eucrites were selected for application of this analytical technique: monomict breccias Pasamonte and Stannern and unbrecciated EET90020. Pasamonte is among the most unequilibrated of the eucrites on the basis of zoning in pyroxenes and is considered to be an igneous rock not significantly affected by metamorphism[6]. Stannern has igneous texture but its pyroxenes indicate some reequilibration, although little, if any, recrystallization. EET90020 has a granulite texture and has been substantially recrystallized. Our sample of Pasamonte contains several clasts of different grain sizes ranging from glass to fine grained with diabasic texture containing lathy plagioclase, unexsolved pigeonite, and mesostasis. Cores were taken of the glass and from minerals and mesostases in six lithic clasts which normally allowed sampling of more than one phase per clast. Our sample of Stannern is also a breccia but with little difference in grain size between clasts and matrix. The plagioclase and pigeonite are blocky, twinned and exsolved and coexist with a bit of mesostasis. Cores were taken of plagioclase and pigeonite with no attempt to distinguish separate clasts. EET90020 is a granular mixture of twinned plagioclase and pigeonite having rather uniform size and many triple junctions. Several cores were taken of both phases. Both clear and cloudy grains of plagioclase and pyroxene were sampled in all three eucrites.

RESULTS: The results for REEs, Fe, and Mg in plagioclase and pyroxene are shown in Figs. 1 and 2. Because of small grain size in Pasamonte and Stannern, a few cores of plagioclase contain small amounts of pyroxene and vice versa. These results are not included in the figures. *The REE values in EET and Stannern are relatively consistent. The slopes for plagioclases in EET are significantly steeper than the more igneous-textured eucrites as also seen in terrestrial plagioclases[2]. Pyroxenes in EET have steeper light REE and flatter heavy REE patterns. The Fe and Mg in plagioclases of EET are lower and more consistent than those in Pasamonte and Stannern.* EET and Stannern have equilibrated pyroxenes with limited ranges in Fe/Mg. They are also quite homogeneous in compatible (Co, Cr) and incompatible (Sc, Sm) trace elements. EET is more homogeneous than Stannern, as expected based on its recrystallized texture. Pasamonte, on the other hand, shows variability in Fe/Mg and trace elements. We find a positive correlation of Fe/Mg vs Sc/Mg and Sm/Mg as expected for igneous zoning. Contrary to expectations we also find a positive correlation of Fe/Mg vs Cr/Mg and Co/Mg. At present, we do not understand the cause of the latter correlations. REE patterns for calculated melts for EET using recent partition coefficients[2, 7] are shown in Fig. 3. *The calculated melts are up to 40 times higher than whole rock values for igneous eucrites like Stannern and Pasamonte. Calculated melts for Stannern (Fig. 4) are also many times higher than for Stannern whole rock, and the pyroxenes produce higher values than plagioclase*. The small grain sizes of our Pasamonte sample allowed very few good analyses but the few usable values again produce calculated melts that are several times higher than Pasamonte whole rock. Previous analyses of minerals from eucrites[8] produce similar results. Basaltic and diabasic textured eucrites are believed to represent melt compositions[9] which requires that they were closed systems during crystallization. Thus, if igneous equilibrium is maintained, the melt REE patterns calculated from our mineral data should lie between whole rock (initial melt) and mesostasis (residual melt) patterns. We have mesostasis analyses only for Pasamonte and they lie within the calculated melts except for La in pyroxene. *The glass clast in Pasamonte is similar in both major and trace elements to Pasamonte whole rock values. The 5 samples of Pasamonte mesostases have REE patterns that are relatively flat, ranging from 15 to 100 times chondrites, but with large Eu depletions. The lowest two of these are broadly similar to*

Lakangaon and Nuevo Laredo which may be residual liquids [10]. Fe and Mg contents for calculated melts of EET using partition coefficients for plagioclase [11] are several times less than in igneous-textured eucrites as also seen in terrestrial and lunar recrystallized rocks[1]. *Pasamonte's calculated melts have Fe content about right but Mg is about 50% of what is expected. Stannern's calculated melts are scattered about the expected values.*

DISCUSSION: *Clearly the REEs, Fe and Mg in pyroxenes and plagioclases have been redistributed since their initial crystallization in all samples.* The very high content of REEs in some mesostases of Pasamonte provides a logical source for the increased REE contents in plagioclase and pyroxene, probably during equilibration with the mesostasis. The EET sample has ample textural evidence for extensive subsolidus recrystallization during which redistribution of components is expected. For Stannern and Pasamonte, however, their igneous textures suggest very little recrystallization. Thus, the redistribution must result from such causes as slow cooling accompanied by extensive reequilibration between melt and mesostasis, shock effects, or some combination of shock effects and a later heating. The fine-grained diabasic to ophitic texture in most eucrites seems to preclude slow cooling during initial stages of crystallization. The time and cause of the redistribution in these igneous textures requires further study and bears heavily on petrologic and isotopic interpretations of eucrites.

References: [1]Phinney 1991 Proc 21LPSC 29; 1992 LPS XXIII 1067 [2]Phinney & Morrison 1991 GCA 55 1639 [3]Phinney 1992 29thIGC abstr 639 [4]Prinzhofer et al 1992 GCA 56 797 [5]Lindstrom 1990 Nuc Ins Meth Phys Res A299 584 [6]Takeda & Graham, 1991 Meteoritics, 26 129 [7]McKay 1989 Rev Mineral 21 45[8] Stolper 1977 GCA 41 587 [9]Schnetzler & Philpotts 1969 Met. Res 206; Heavilon & Crozaz 1990 LPS XXI 487 [10]Warren & Jerde 1987 GCA 51, 713 [11] Phinney 1992 GCA 56 1885.

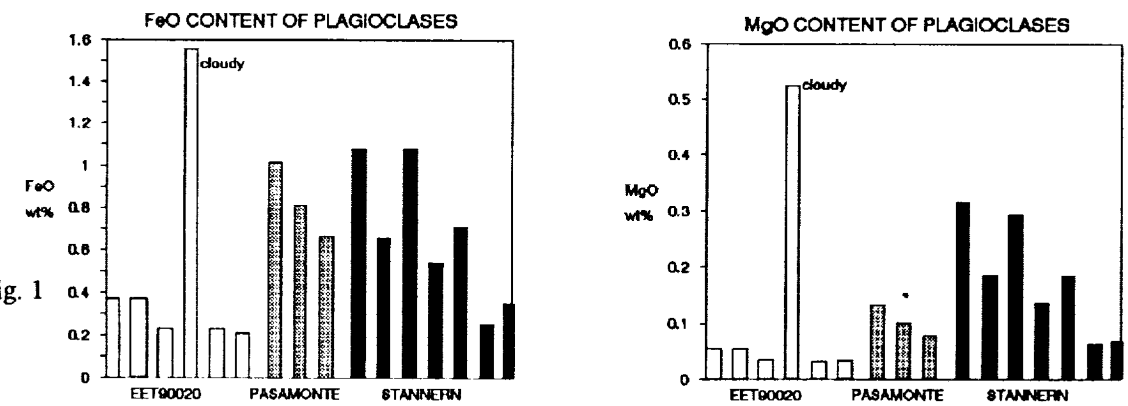


Fig. 1

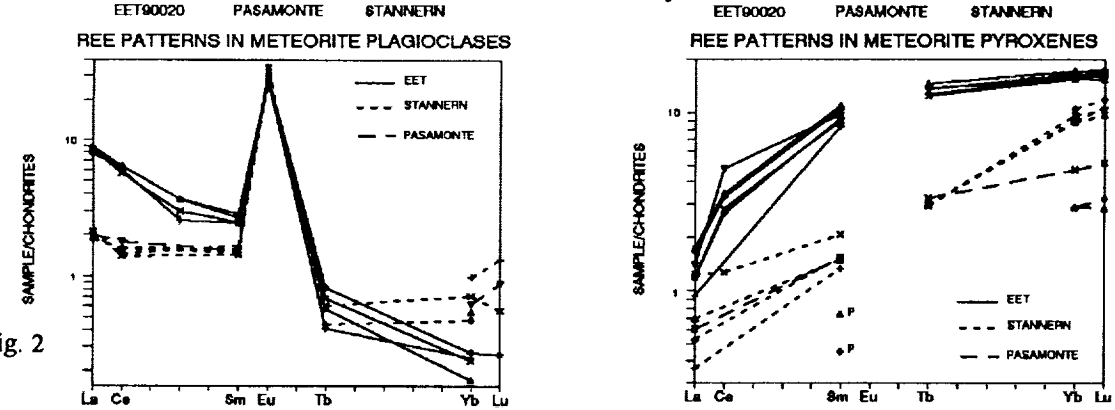


Fig. 2

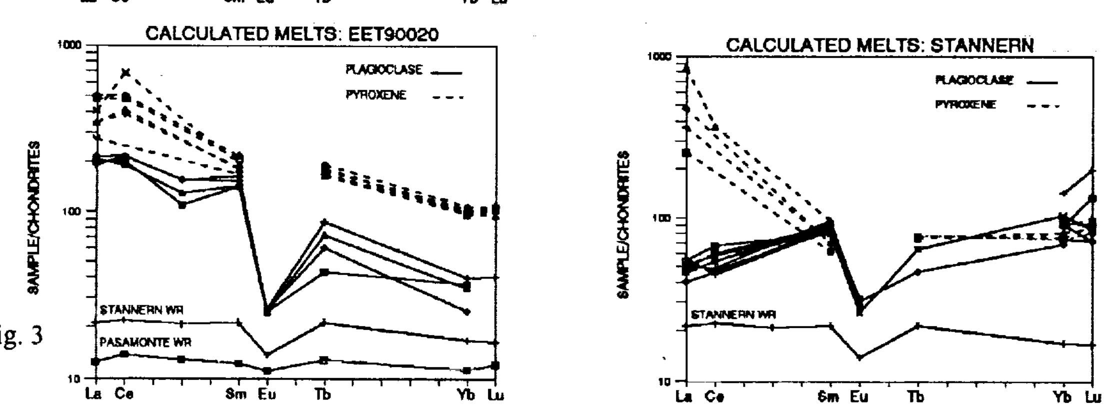


Fig. 3

WAVELENGTH DEPENDENCE OF LIMB-DARKENING OF MARS FROM VISIBLE AND NEAR-IR TELESCOPIC SPECTRAL IMAGING

E. Pierazzo and R.B. Singer, *Planetary Image Research Laboratory, LPL, University of Arizona.*

We are investigating the photometric properties of Mars using Earthbased telescopic spectral imaging obtained during 1988 [1]. Each spatial pixel consists of 300 spectral channels from 0.44 to 1.02 μm, calibrated to radiance factor (r_F) through a careful procedure involving standard star observations in 1988 and 1990 [2]. Calibrated data include 3 spectral images with solar phase angle (g) of 12° and 4 images with g of 4°. Pixels near the sub-Earth point have a spatial footprint of about 280x150 km. Preliminary work using Hapke photometric function [3,4,5] reveals a dependence of both single-scattering albedo and roughness parameter on wavelength. The former is in agreement with observed spectra of the martian surface, but the latter is unexpected.

Because of the instrumentation and observation method, individual slit exposures cannot simply be lined up to give an accurate spatial view of Mars. A photographic record of the slit position on Mars was made simultaneously with every CCD exposure at the telescope. Each slit position was then independently projected to a simple cylindrical map base and the data for that exposure resampled appropriately (Fig. 1). In addition to accurately determining latitude and longitude for each pixel, illumination (i) and emission (e) angles are calculated and added to the data base during this processing step. The resultant data base for g, i, e, and r_F as a function of wavelength is used for subsequent photometric modeling. Our initial objective is to characterize the limb-darkening of Mars as a function of surface albedo and wavelength. These data allow this analysis to be performed at high spectral resolution for the first time. For initial modeling data were averaged over five wavelength bands: Blue (0.438-0.478 μm), Green (0.53-0.578 μm), Red (0.618-0.678 μm), NIR (0.70-0.74 μm), and MIR (0.93-1.00 μm). Fig. 2 represents a typical slit profile of Mars' surface, given by a combination of limb-darkening and surface material characterization for the various spectral bands. The difference in profile from Blue to MIR is evident. The Hapke photometric function has been fit to the data base for these spectral bands. The constant phase angle, 4°, for the first image under analysis allowed us to reduce the number of parameters to be searched for in Hapke photometric function to two, as a result of the constant phase function P(g) and the constant opposition-effect function B(g). Existing information about the opposition-effect for the martian surface [6] allowed us to consider null the contribution to Hapke photometric function from the opposition-effect term.

A typical slit profile across Mars disk and the best fit for Hapke photometric function is plotted in Fig. 3, together with the best fit for the Minnaert photometric function, drawn for comparison. The result of the fit of Hapke photometric function to the data for the various spectral bands is reported in Fig. 4 for the single-scattering albedo and the roughness parameter vs. wavelength. The increase in single-scattering albedo from Blue to IR is consistent with the observed spectra of high- and low-albedo units (e.g. [7]). On the other hand, the inverse dependence of the roughness parameter with wavelength is unexpected for a surface, since the roughness effect is based on modeling the surface as unresolved facets (>> λ) tilted at various angles and should affect every wavelength in the same way [8]. Such behavior of the roughness parameter with wavelength is, then, indicating the presence of other effects that a simple Hapke photometric function cannot account for; one of these is due to the presence of the atmosphere that affects shorter wavelengths (Blue) more than longer ones (IR). Another effect is due to the bimodal character of the martian surface (bright and dark material) that is not taken into account in the Hapke photometric function. This effect is being investigated by applying the Hapke photometric function to dark and bright regions separately, and might be dealt with by generating a photometric function that combines Hapke photometric functions for dark and bright regions together.

One drawback of the Hapke photometric function for the determination of macroscopic roughness from telescopic data is the limited range of phase angle. A study of the geological interpretation of photometric surface roughness by Helfestein [9] shows that "reliable determination of photometric roughness from disk-integrated data or from disk-resolved photometric observations of geological features requires observations which extend from small phase angles out to phase angles above 90°". In particular, observations at high phase angles seem to provide the most important constraints for determination of the roughness parameter. However, even given a high uncertainty in the estimated values of the roughness parameter for our data, we believe that the general trend of the roughness parameter with wavelength is real and can provide the starting point for a further elaboration of the photometric function for Mars in which atmospheric effects are included.

[1] Singer R. et al., *Lunar and Planet. Sci,. XXI*, 413-414 (1990); [2] Miller J. et al., *Lunar and Planet. Sci., XXIII*, 911-912 (1992) [3] Hapke B., *J. Geophys. Res., 86*, B4, 3039-3054 (1981); [4] Hapke B., *Icarus 59*, 41-59 (1984); [5] Hapke B., *Icarus, 67*, 264-280 (1986); [6] Thorpe T. E., *Icarus, 49*, 398-415 (1982); [7] Singer R., *Adv. Space Res., V5*, #8, 59-68 (1985); [8] Helfestein P., Ph.D. Thesis, Brown Univ. (1986); [9] Helfestein P., *Icarus, 73*, 462-481 (1988).

Martian Limb-darkening; Pierazzo, E. and Singer, R.B.

Figure 1

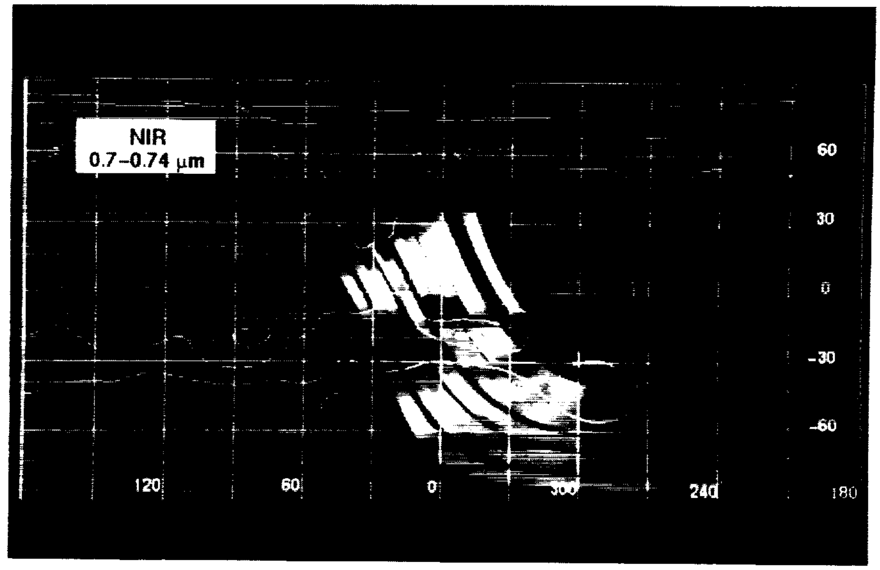


Figure 2

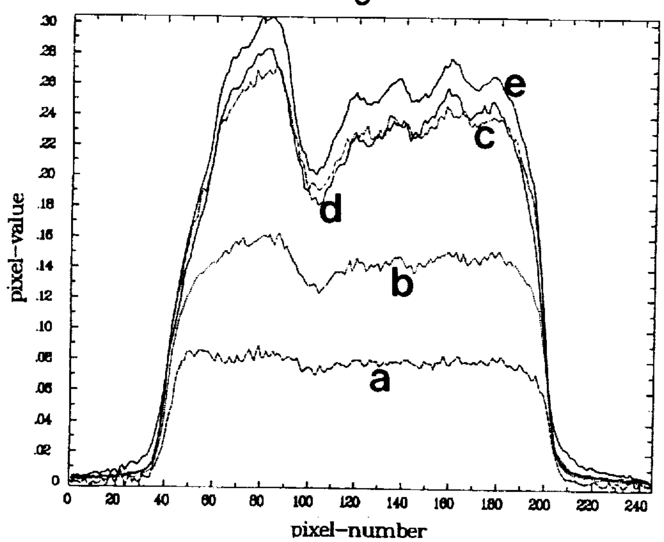


Figure 3

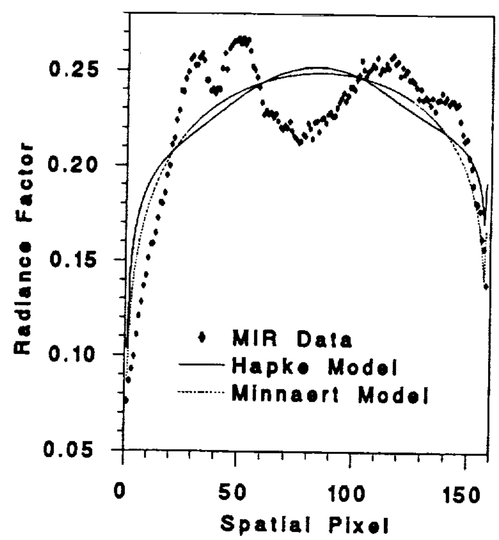


Figure 4

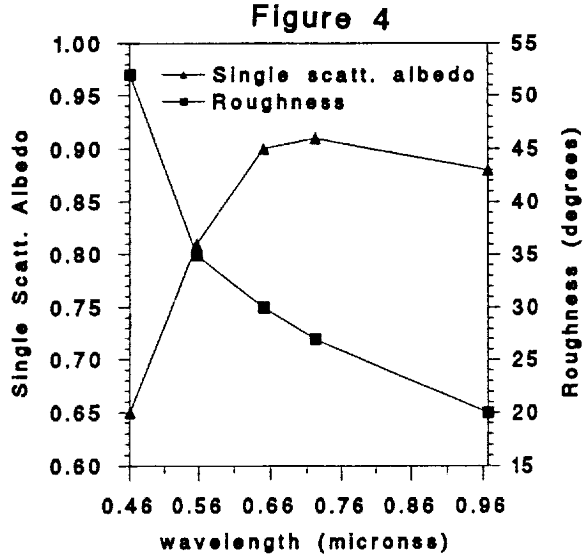


Fig. 1: Simple cylindrical map projection of Mars telescopic data (9/26/88).

Fig. 2: Slit profile from same Mars data for: a) Blue, b) Green, c) Red, d) NIR, e) MIR.

Fig. 3: Slit profile from same Mars data and best fit Hapke and Minnaert photometric functions.

Fig. 4: Single-scattering albedo and roughness parameter *vs.* wavelength for Hapke fit.

550-91
ABS ONLY

N94-20686

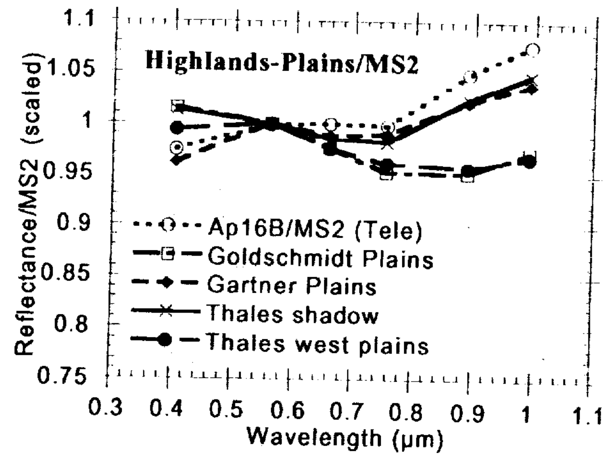
COMPOSITIONAL DIVERSITY OF THE LUNAR NORTH POLE: PRELIMINARY ANALYSES OF GALILEO SSI DATA. C. M. Pieters[1], M. Belton[2], J. W. Head[1], R. Greeley[3], A. McEwen[4], E. M. Fischer[1], J. M. Sunshine[1], K. Klaasen[5], J. Plutchak[1], G. Neukum[6], T.V. Johnson[5], and the SSI Team. [1]Brown University, Providence, RI, [2]Kitt Peak National Observatory, Tucson, AZ, [3]Ariz. State Univ. Tempe, AZ, [4]USGS, Flagstaff, AZ, [5]JPL, Pasadena CA, [6]DLR, Oberpfaffenhofen FRG.

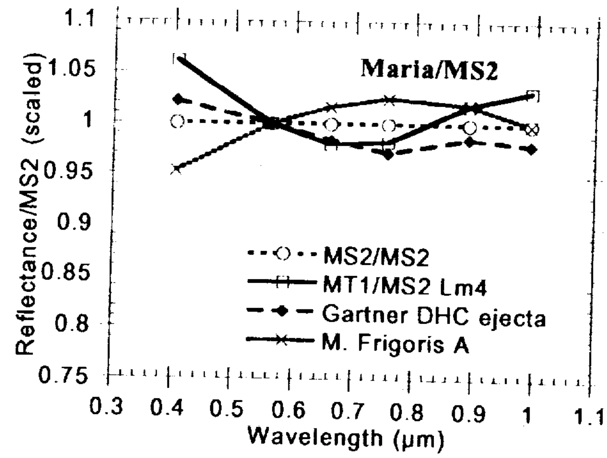
In December 1992 the Galileo spacecraft passed through the Earth-Moon system for its final gravity assist to Jupiter. The SSI camera obtained several 6-color mosaics of the lunar north polar region and the sunlit nearside and eastern limb at ~1.3km/pixel. Initial analyses have concentrated on the north polar areas to assess the composition of the crust in that region. Shown in the attached figures are representative 6-color calibrated SSI spectra (typically 5x5 pixels). Photometric corrections have not yet been applied, and all spectra are scaled to unity at 0.56 μm. The data were first calibrated relative to MS2, a standard area in Mare Serenitatis (18.7°N, 21.5°E), and the top four plots of highlands, highland craters, maria, and mare craters are displayed relative to MS2. SSI spectra of areas measured with telescopic data (mare MT1/MS2 and mare crater MSA/MS2) agree well with previous data, confirming that the calibration procedures and SSI data are spectrally accurate. The bottom three plots of craters/sun have been calibrated to reflectance using previously obtained telescopic spectra of Apollo 16/MS2 (shown with Highlands/MS2) and laboratory spectra of mature Apollo 16 soil (shown for reference with the Highland Craters/Sun). Although some variations in these spectra mimic previously observed spectra of lunar terrains (1, 2, 3, 4), several characteristics are unusual. Familiar and unfamiliar properties are observed in these northern latitudes and both types merit further investigation in their geologic context (e.g. 5).

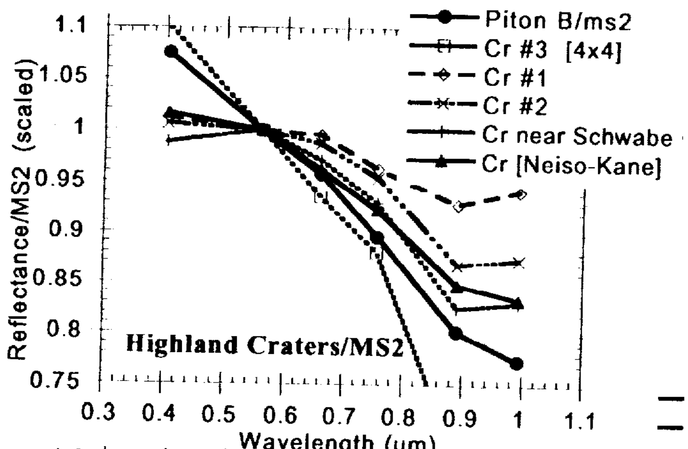
Highlands & Plains. To a first order the highlands and northern bright plains have characteristics similar to those of Apollo 16 soils implying a distinctly feldspathic and low iron composition. Extensive areas of plains around large northern Copernican craters such as Anaxagoras and Thales, however, have clearly been affected by the impact event (extending to four crater diameters from the rim). The spectral properties of these plains (Goldschmidt and Thales west) are peculiar in that they are not directly comparable to those of immature highland soils at small highland craters. Although these distinctive plains properties are clearly a cratering related effect (compare Thales west to nearby Thales shadow), it is currently not known whether they are due to compositional or physical effects.

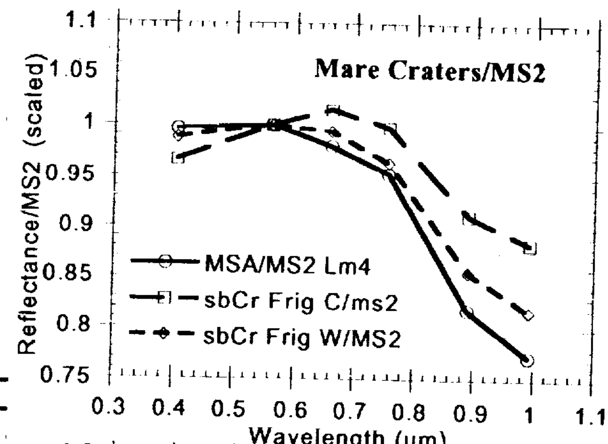
Maria and Mare Craters. SSI properties of mare materials are discussed by (6). In the north polar region extensive areas of Mare Frigoris exhibit properties similar to those studied previously (4,7), with the lowTi basalts more comparable to those of Luna 24 than those of Apollo 12. The Gartner DHC ejecta exhibits properties comparable to western intermediate Ti basalts (4). One mare crater at the easternmost edge of Frigoris (bottom plot) is unusual. Its brightness suggests a high feldspathic content, whereas it clearly has a 1 μm band center at wavelengths long even for maria, suggesting an usual mineralogy.

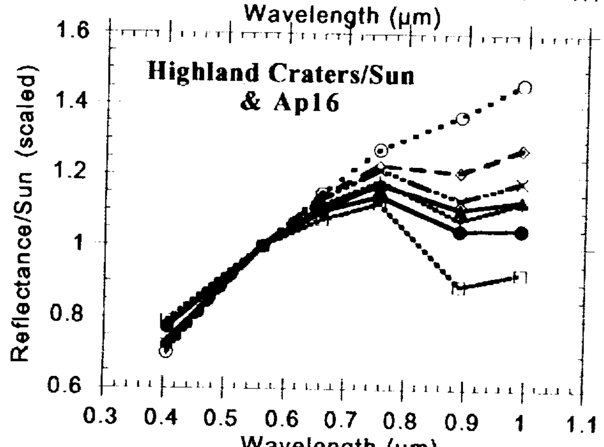
Highland Craters. Several small non-mare craters exhibit abundant mafic minerals. These craters exhibit great diversity in the strength and character of the ferrous 1 μm absorption, suggesting a range of mineral compositions, some of which may approach gabbroic compositions (e.g. Piton B and Cr [Neiso-Kane]). The high spatial resolution SSI data show that spectral contrast increases dramatically with spatial resolution for small features of freshly exposed material. Although mare craters have not yet been fully evaluated, the strongest lunar 1 μm band observed remotely to date is associated with a small unnamed crater in the Fra Mauro Formation (5) south of Anaxagoras (Cr #3). Compare the 2x2 pixel spectrum (corresponding to an area <3 km in diameter) to the 4x4 pixel spectrum (<6km).

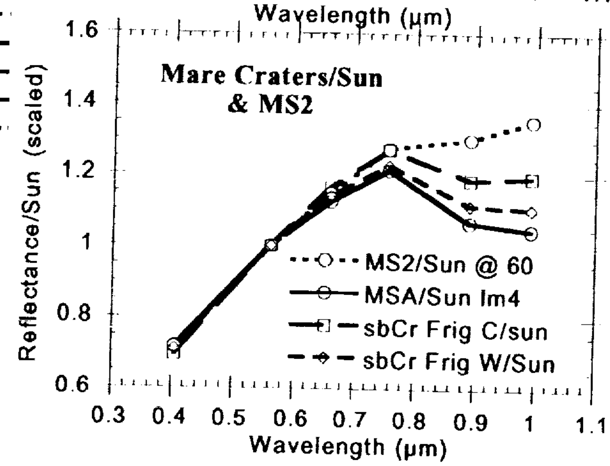


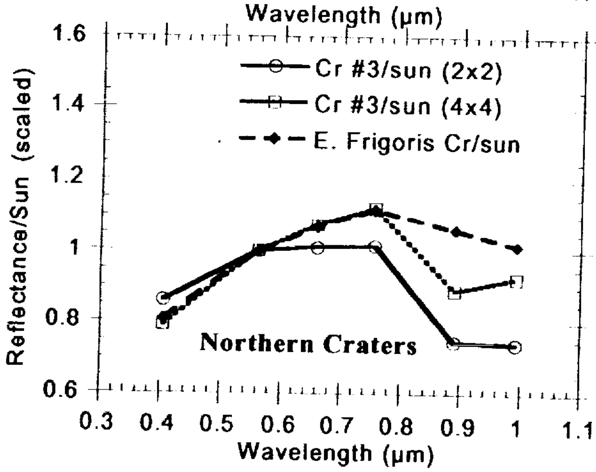












References. 1) Belton et al. (1992) *Science*, 255, 505; 2) McCord et al. (1972) *JGR*, 77, 1349; 3) Pieters (1977) *PLSC 8th*, 1037; Pieters (1986) *Rev. Geophys.*, 24, 557. 4) Pieters and McCord (1976) *PLSC7th*, 2677; 5) Luchitta (1978) *USGS MI*-1062; 6) Greeley et al. (1993) these volumes; 7) Whitford-Stark (1990) *PLPSC20th*, 174.

351-91
ABS. ONLY

N94-20687

OPTICAL EFFECTS OF SPACE WEATHERING ON LUNAR SOILS AND THE ROLE OF THE FINEST FRACTION.

C. M. Pieters[1], E. M. Fischer[1], O. D. Rode[2], A. Basu[3] [1]Brown University, Providence, RI, [2]Vernadsky Institute, Moscow, Russia, [3] Indiana University, Bloomington, IN

Background. Lunar soils represent a cumulative product of space weathering and as such they exhibit distinct optical alteration. In comparison to the optical properties of similar rock powders, lunar soils are darker, have weaker diagnostic absorption bands, and exhibit a characteristic red continuum slope between 0.3 and 4.5 μm. Well-developed (mature) lunar soils have a mean grain size of about 60 μm and may contain more than 50% agglutinates (complex, glass-welded aggregates) (1), which were previously believed to be the principal carriers of optical alteration resulting from space weathering (2). A detailed analysis of the spectral reflectance properties of the bulk soil, size separates, and agglutinate separates of several Apollo and Luna soils has been undertaken to evaluate the validity of the agglutinate paradigm for optical effects of space weathering. The data and results are summarized here which indicate that the finest fraction of natural lunar soils, rather than larger complex agglutinates, carries the principal effects of optical alteration.

Spectral Measurements and Sample Description. Bidirectional reflectance spectra were obtained using the small sample configuration of the RELAB facility, which accommodates 5-30mg of material. Spectra are displayed in Figures A - H with the labels for individual samples listed in order of brightness. Figures F and H are scaled versions of Figures E and G. Agglutinates were hand-picked from a > 250 μm separate of mature Apollo 11 soil 10084. For 10084, the bulk sample used for comparison is <250 μm. For all other samples, the bulk sample is < 1000 μm. Except for the smallest size fraction, all size fractions were wet-sieved. Size separates of the Luna samples were prepared at the Vernadsky Institute, Moscow. All samples are naturally occurring soils except for Apollo 16 regolith breccia 60019. A matrix rich area of this breccia (3) was selected for the particle size analyses illustrated in Figures G and H. The top spectrum in Figure E ("<25 from 45-75") is an artificial fine fraction prepared by grinding a 45-75 μm separate to <25 μm.

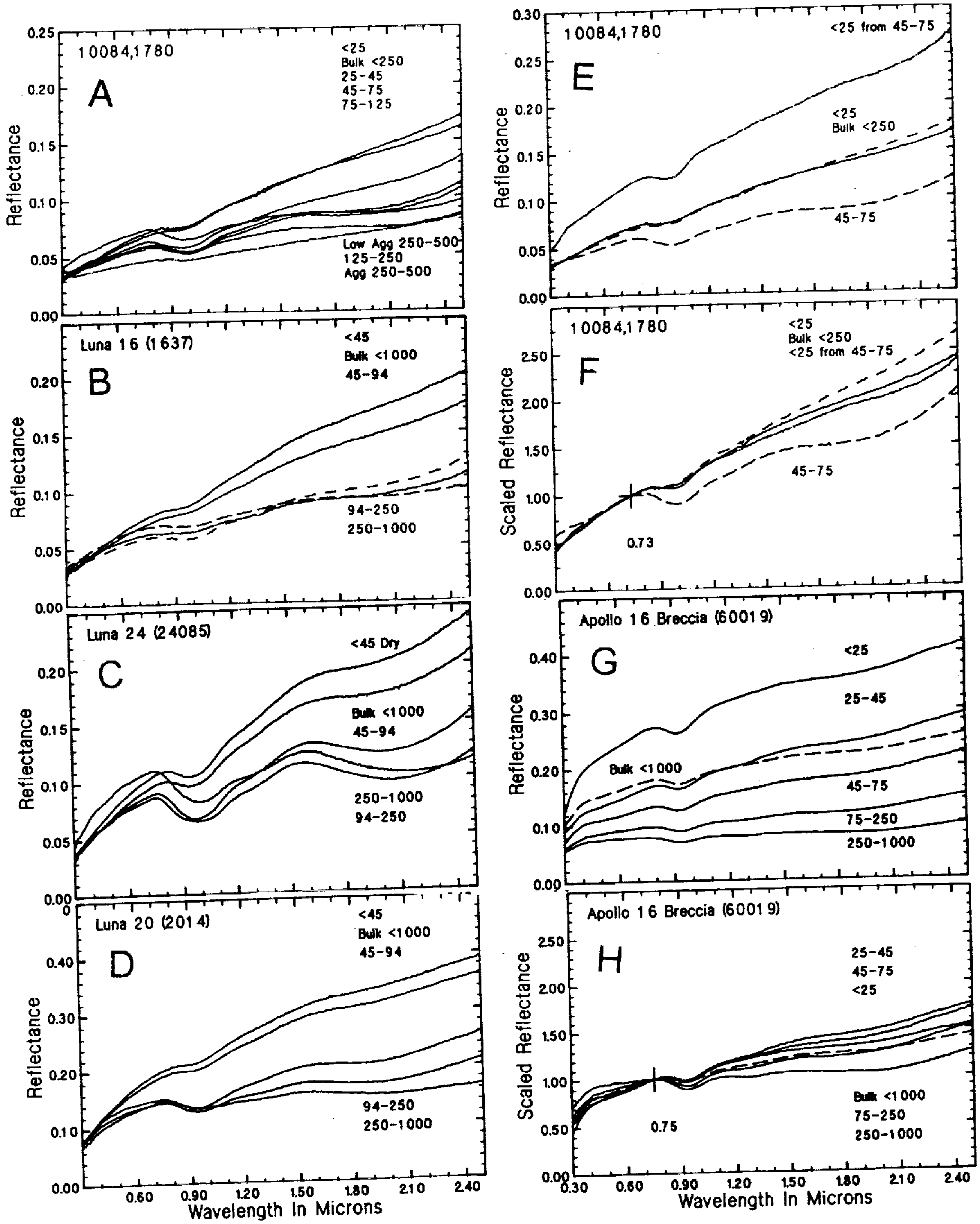
Discussion. The agglutinate separate of Figure A is dark, but does not exhibit a sufficiently steep red continuum to account for that observed for the 10084 bulk soil. Furthermore, each of the size fractions except the smallest have relatively strong absorption bands and also lack the red continuum although they are all agglutinate rich. It is the smallest size fraction that exhibits a steep continuum and weak absorption bands comparable to that of the bulk soil. Note that in the visible part of the spectrum all samples have similar albedos (the brightest sample is the low agglutinate separate 250-500 -- the remaining material after agglutinates were removed). Brightening normally associated with small particle size separates is not observed for this lunar soil. The same properties are observed for all Luna soil and soil separates (Figures B, C, D), even for the immature soil from Luna 24.

The carrier of the red continuum occurs principally in the finest fraction of lunar soils (this fraction may also dominate the strength of absorption bands). This character of the finest fraction is not a physical effect due to small particle size. Grinding an agglutinate-rich larger size separate of 10084 (Figures E, F) results in a sample that is too bright, has absorption bands too strong, and does not have a steep enough continuum to mimic the naturally occurring <25 μm size fraction. Also, in contrast to natural soils, the size separates prepared for regolith breccia 60019 exhibit the classical brightening with smaller particles, and the smallest fraction is not the reddest.

Conclusions. Agglutinate separates studied here are shown not to exhibit a sufficiently red-sloped continuum to account for the observed optical properties of mature soils. On the other hand, the finest size fraction analyzed (< 25 μm grain size), which constitutes ≤1/4 of the bulk lunar soil, is observed to be the principal carrier of the red continuum, and perhaps other optical alteration effects, for all lunar soils studied. The finest fraction thus appears to be preferentially affected by primary alteration products which suggests surface correlated weathering process(es). This suggests agglutinate formation, that is the physical process of creation and accumulation of dark aggregates of second generation soil particles, is not a principal requirement for optical alteration. A leading hypothesis for the cause of many of the observed optical alteration effects is the development of fine-grained metallic iron reduced from ferrous-bearing materials in the space weathering process (4). These are incorporated into agglutinates.

Acknowledgments. Support for this research from NASA grant NAG9-184 is gratefully acknowledged. RELAB is a multi-user facility supported under NASA Grant NAGW-748.

References: 1. Heiken et al., Eds. (1991) Lunar Sourcebook, Chapter 7, Cambridge. 2. Adams and McCord (1971) *Science, 171,* 567; ---(1973) *PLSC4th,* 163. 3. Pieters and Taylor (1989) *LPSC19th,* 115. 4. LPI Workshop on the Space Environment: Effects on the Optical Properties of Airless Bodies (November, 1992).



552-35
ABS. ONLY

N94-20888

MINMAP: AN IMAGING SPECTROMETER FOR HIGH RESOLUTION COMPOSITIONAL MAPPING OF THE MOON. C. M. Pieters[1*], J. W. Head[1#], T. B. McCord[2*] and the MinMap Team. [1]Brown University, Providence, RI, [2]SETS Technology Inc. and Univ. of HI, Honolulu, HI; #MinMap PI, *MinMap Deputy-PI.

MinMap has been selected by the Lunar Scout program to characterize and map the mineral composition of the Moon. The instrument will be built as a collaborative effort between Brown University, SETS Technology Inc., and Ball Aerospace Corp. MinMap is a visible to near-infrared imaging spectrometer that contains 192 spectral channels from 0.35 - 2.4 μm with signal to noise >200 and 256 cross-track spatial elements. The spectrometer design has a 6° field of view (FOV) and utilizes grating dispersive elements and two dimensional detectors (no moving parts). An "image cube" of data is produced that contains two dimensions of spatial information and one dimension of spectral information. All spectral channels and cross-track spatial elements are recorded simultaneously with spacecraft motion scanning the second spatial dimension. The high spectral resolution and continuous spectral range of MinMap are designed to measure the diagnostic absorption features of principal lunar minerals and their lithologic mixtures. Since the optical properties of lunar materials change in a regular manner upon exposure to the space environment, this spectral range is also quite sensitive to variations in exposure history (soil maturity). Nominal measurement strategy is to obtain full global data of the Moon at 180m/pixel from a 450km polar orbit during the first month or two of operation. A 100 km orbit is anticipated for the remaining part of a 1 year mission allowing higher resolution data (~80 m/pixel) to be obtained for targeted regions. MinMap exceeds LExSWG's measurement recommendations and will provide the highest spatial resolution compositional map of lunar rocks and soils currently planned for orbital missions. Since all spectral channels are co-registered and obtained simultaneously, "image cube" data swaths will be available for analysis almost immediately.

Global MinMap data are to be obtained from a ~450 km circular polar orbit rather than the nominal 100 km orbit traditionally used in LExSWG planning. There are several important reasons for this. First, it is highly desirable to have overlapping sequential data swaths. This minimizes the effort to produce a global mosaic since neighboring swaths have similar geometric properties. At 100 km, orbit spacing is 33 km at the equator requiring a FOV of 22° for orbit-to-orbit overlap. At an orbit of 450 Km, orbit spacing at the equator is 42.5 km requiring only about a 6° FOV for data overlap. Except near opposition at the equator, a 6° variation in phase angle across the data swath requires little correction. A second important reason for the global data to be obtained from a high orbit is orbit stability. The variations in orbit altitude due to variations in lunar gravity field are substantially less at the higher orbit (10% vs 50%), a highly desirable attribute for global mapping.

In terms of mineral characterization, the distinguishing feature of MinMap is that it is a spectrometer That is, it obtains contiguous spectroscopic information at high spectral resolution and high precision. Such spectroscopic data are required to identify key lunar minerals (pyroxenes, olivines, etc.) and to estimate their composition by the wavelength and shape of observed absorption bands (1, 2). Near infrared high spectral resolution measurements obtained with earth-based telescopes for lunar areas 3 - 20 km in diameter have quite successfully identified a

variety of lunar mineralalogies and rock types ranging from anorthosites to dunites (e.g., 3). Equally important, continuous spectroscopic data are required in order to assess the relative abundance of several minerals in a mixture when their absorption properties are superimposed. Several analytical approaches have been developed over the last few years to extract mineralogical information from complex or multicomponent spectra (e.g., 4, 5, 6) and these continue to improve. Subtle variations in absorption shape undetectable by visual inspection, for example, can be very important in compositional assessment (e.g. 7), but such small systematic variations require continuous spectral coverage for evaluation. In contrast, multi-spectral imaging (with fewer spectral channels) cannot characterize surface mineralogy, but with careful selection of channels can distinguish and map several compositional units.

MinMap operations and data management are designed to be extremely flexible in order to derive the maximum return within mission constraints on mass storage and downlink data rate. Specifically, several options will be programmed that select several cross-track elements to obtain full spectroscopic coverage (192 spectral channels) and a number of selected spectral channels for which full spatial coverage will be obtained. Full spectroscopic and full spatial coverage by MinMap produces data (uncompressed) at a rate of ~4Mbps for the high orbit and ~6Mbps for the low orbit. MinMap operation at full capacity will thus likely be reserved for selected targets of high interest to the scientific and exploration community. Full "image cube" data acquisition will be the normal operation plan for the low orbit, high resolution targeted data since it allows the most detailed compositional analyses. It is anticipated that the nominal mission plan for global coverage will allow 4 - 10 elements of full spectroscopic coverage nested in 20 - 40 spectral channels of full spatial coverage. In other words, the high orbit global data set will consist of global coverage at 180 m/pixel for up to 40 coregistered spectral channels with a N-S grid of full spectral resolution data spaced 4 - 11 km at the equator. This measurement strategy should provide an excellent assessment of lunar lithologies and provide a global basemap of principal compositional and maturity units.

The primary return from MinMap is an assessment of the global and regional mineral composition of the surface (spectroscopic information) in its naturally occurring geologic context (spatial information). This dataset provides key information in evaluating lunar resources, in site selection for robotic and/or human exploration, and for surface operations planning. Without question, the global assessment of lunar mineralogy provides fundamental information to address broad scientific issues such as the formation and evolution of the primordial lunar crust, volcanism and the thermal evolution of the Moon, and the transformation and dispersal of material in a major impact event. The MinMap Team is beginning to develop a list of targets for the high resolution detailed analyses and invite suggestions from the scientific community as the Lunar Scout program proceeds.

References: 1. Adams J. B. (1975) in *Infrared and Raman Spectroscopy of Lunar and Terrestrial Materials* (C. Karr, ed.), Academic, 91-116 2. Burns R. G. (1970) *Mineralogical Applications of Crystal Field Theory*, Cambridge, 224 pp. 3. McCord T. B. et al. (1981) *J. Geophys. Res., 86.*, 10883-10892; Pieters C. M. (1986) *Revs. Geophys., 24*, 557-578. 4. Hapke B. (1981) *J. Geophys. Res., 86.*, 3039-3054. 5, Mustard J. F. and Pieters C. M. (1987) *J. Geophys. Res., 92.*, E617-E626. 6. Sunshine et al, (1990) *J. Geophys. Res., 95.*, 6955-6966;, also, JGR submitted 7. Sunshine and Pieters (1993) Olivine Asteroids, these volumes

S53-25
ABS ONLY

N94-20689

VISIBLE - INFRARED PROPERTIES OF CONTROLLED LABORATORY SOILS. C. M. Pieters, J. F. Mustard, S. F. Pratt, J. M. Sunshine, and Andrew Hoppin, Brown University, Providence, RI

Introduction. Almost all surfaces available for remote observation consist of particulate materials, or soils. The distribution of mean particle sizes depend on the original material and physical and chemical processes that have acted on the surface over time. It is well known that the optical and infrared spectral properties of materials depends on the particle size (1, 2). There has been little detailed study, however, of natural soils, namely particulate materials with a range of particle sizes (3). Current models for intimate mixing (4) typically use an average particle size in calculations and are most successful when the particle size is constrained by known sieve fractions. Reported here are preliminary results of a study in which soils were prepared with a known composition and range of particle sizes. This discussion presents the overall visible to infrared properties of these synthetic soils and evaluates the mid-infrared properties. A companion paper (5) discusses the optical properties and information extraction from modeling lithologic mixtures.

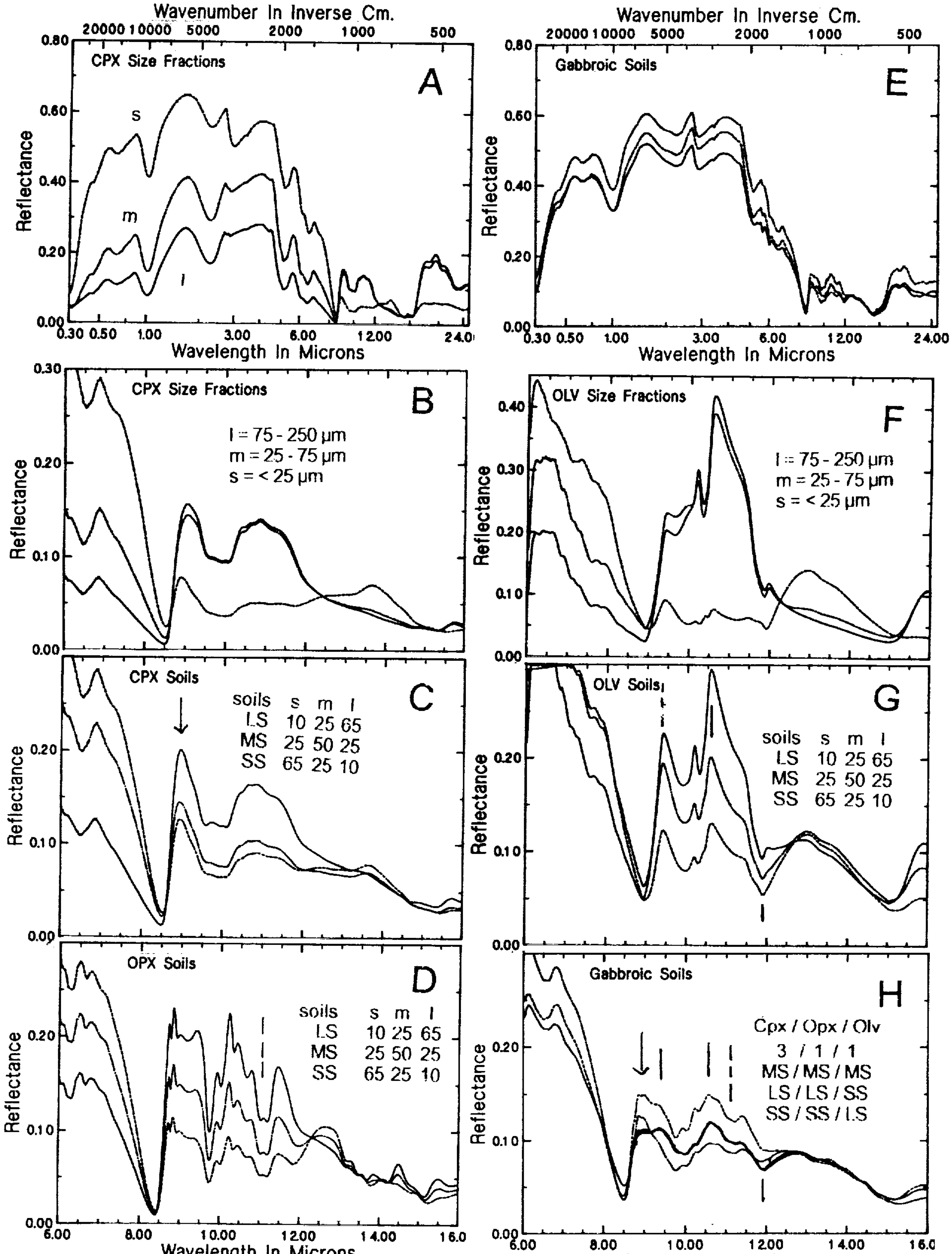
Experimental Procedure. Five minerals were prepared in different size fractions [s: <25μm, m: 25-75μm, l: 75-250μm], and mono-mineralic soils were prepared from these with three different distributions of particle sizes [large (LS), medium (MS), and small (SS)] (see description in 5). Initial experiments have focused on the mafic minerals clinopyroxene (Cpx), orthopyroxene (Opx) and olivine (Olv). Three multicomponent soils were prepared with the same "gabbroic" composition (Cpx:Opx:Olv = 3:1:1), but with distinctly different particle size distributions for each mineral constituent. Spectra of all samples were measured in the RELAB. The visible to near-infrared (0.3 - 2.5 μm) was obtained with the bidirectional spectrometer and the mid-infrared (2 - 25 μm) was measured under purged conditions using a Nicolet 740 FTIR. Composite spectra (0.3 - 25 μm) of the Cpx size separates and the Gabbroic soils are shown in Figures A and E. The remaining figures present the mid-infrared properties of mineral size fractions, mono-mineralic soils, and the gabbroic soils. The labels on each figure identify the size fraction, the percent of each size in the mono-mineralic soils, and the type of mono-mineralic soil used for each of the gabbroic soils. The order on the labels refer to the order of the spectra at 10 μm.

Discussion. In the visible to near-infrared, non-opaque materials become brighter with decreasing particle size and crystal field absorption features tend to become weaker. These properties can be seen in the Cpx size fractions of Figure A and are observed for all samples under study (see 5). For the strong fundamental absorptions in the infrared, however, some of these characteristics are reversed. Separates of large particles are typically brighter and have much stronger spectral contrast than their finer counterparts (Figures B and F). The "transparency feature," a peak noted for small particles by (6), is also seen near 13.5μm for Cpx and near 13mm for Olv. The mono-mineralic soils (Figures C, D, G) exhibit properties of both the large and small particles constituents. The soils with a higher abundance of small particles (SS) exhibit properties similar to those of the small size fraction (s) and those with a larger fraction of large particles (LS) exhibit properties generally similar to those of the larger particles (l), but no general rule applies to all parts of the spectrum. Small particles, for example, appear to have a stronger relative effect at the shorter wavelengths near 9 μm. At wavelengths near the "Transparency" peak, however, the spectra of all soils converge, suggesting this feature could be particularly useful in remote analyses. Since the "Transparency Feature" is predicted to decrease with decreasing atmospheric pressure (6), we will investigate this feature under a variety of atmospheric conditions (7).

Since large particles have stronger features due to Reststrahlen bands near 10μm than small particles, it was anticipated spectra of gabbroic soils that contained minerals with a larger size distribution (LS) would would be dominated by features of that mineral. The opposite is shown to be the case. Distinct features of these Cpx, Olv, and Opx are identified with arrows, lines, and dotted line, respectively, on figures C, G, D and H. Even though the proportion of minerals is the same for the gabbroic soils of Figure H, it is clearly the small particles that dominate the spectral properties. For example, for soil LS/LS/SS (the middle spectrum at 10μm), the Cpx and Opx features are the weakest and the Olv are the most prominent.

Acknowledgments. We are grateful for the support of NASA grant NAGW-28. RELAB is a multiuser facility supported by NASA grant NAGW-748. The infrared capabilities was provided by the Keck Foundation.

References. 1. Adams and Felice (1967) *JGR,72,* 5705, 2. Salisbury et al. (1992) *Infrared (2.1-25 μm) Spectra of Minerals,* 3. Pieters (1983) *JGR, 88,* 9534, 4. Hapke (1981) *JGR, 86,* 3039; Mustard and Pieters (1987) *PLPSC17th, JGR,* E617; Hiroi and Pieters, (1992) *PLPSC22d,* 313, 5. Mustard, Sunshine, Pieters, Pratt (these volumes), 6. Salisbury and Walters (1989) *JGR, 94,* 9192, 7. Bishop et al (1993) these volumes.



A COMPARISON OF CALCULATED AND MEASURED RHEOLOGICAL PROPERTIES OF CRYSTALLISING LAVAS IN THE FIELD AND IN THE LABORATORY.

Harry Pinkerton & Gill Norton, Environmental Science Division, Lancaster University, Lancaster LA1 4YQ, U.K.

Summary: Models of most magmatic processes, including realistic models of planetary lava flows require accurate data on the rheological properties of magma. Previous studies suggest that field and laboratory rheological properties of hawaiian lavas can be calculated from their physico-chemical properties using a non-Newtonian rheology model. The present study uses new measurements of the rheological properties of crystallising lavas to show that this is also true for lavas from Mount Etna. Rheological measurements on quenched Etna basalts were made in a specially designed furnace using a Haake Rotovisco viscometer attached to a spindle which has been designed to eliminate slippage at the melt-spindle interface. Using this spindle, we have made measurements at lower temperatures than other workers in this field. From these measurements, Mount Etna lavas are Newtonian at temperatures above 1120 °C and they are thixotropic pseudoplastic fluids with a yield strength at lower temperatures. The close agreement between calculated and measured rheology over the temperature range 1084 - 1125 °C support the use of the non-Newtonian rheology model in future modelling of planetary lava flows.

Introduction: At temperatures above 1150 °C, Hawaiian lavas are Newtonian, and at lower temperatures they approximate to Bingham materials (1). Since most basaltic lavas are erupted at, or below, this temperature, and since we are not aware of any rheological measurements on basaltic melts at temperatures below 1120 °C, one of our objectives was to acquire accurate rheological data in the temperature range at which basaltic lavas are erupted (1084-1125 °C). We also wished to determine whether there were significant differences between field and laboratory rheological measurements on Mount Etna, since Shaw and colleagues (1,2) found little difference between field and laboratory measurements on hawaiian lavas.

The rheological system used in this study is a concentric cylinder viscometer within a high temperature furnace which is similar to that developed independently by Spera et al. (3). Rheological measurements are performed using a Haake Rotovisco viscometer. Special spindles have been developed for sub-liquidus rheological measurements. These ensure that the spindles do not break during measurements, and they minimise the problems caused by slippage between the melt and spindle at high crystal concentrations. The viscometer was calibrated using standard soda-lime-silica float glass. Measured viscosities were within 5% of the supplied values at all measured temperatures, and thermocouple calibration confirm that temperature errors are ±2 °C.

Laboratory rheological measurements on a Mount Etna lava: Results presented here are based on two sets of measurements on lava collected during the 1983 eruption of Mount Etna (4). The lava was air-quenched from an eruptive temperature of 1095 °C. Controlled degassing in the laboratory was achieved by heating the powdered Etna basalt in the furnace at a temperature of 1145 °C. The lavas retained small crystal nuclei after heating in an Oxygen-free Nitrogen atmosphere at this temperature for 6 hours. During slow cooling from this temperature, the presence of these nuclei ensured rapid crystal growth rates. Consequently, our starting samples were similar in crystallinity to lavas which had cooled slowly in the field. Temperatures were raised at a rate of 10 °C /min to 1084 °C and a rheological measurement was made at this temperature and at temperature intervals of 5 °C up to 1125 °C. Thermal equilibrium within samples was attained at all temperatures by keeping the temperature constant at the required temperature for 60 minutes before making any measurement. We also made rheological measurements as the temperature was lowered to 1190 °C. Quenched samples confirm that the melts which were subjected to a heating cycle had a higher crystal content at any given temperature than those which had been cooled to this temperature.

Rheological results: Data from the laboratory rheological experiments are recorded as instrument torque vs. spindle rotation rate plots. Using the analytical procedure described by Spera et al. (3), the raw data are transformed to shear stress-shear strain rate relationships. The measurements, which have been analysed for strain rates in the range 0.3 to 5 s^{-1}, suggest that the 1983 Etna lava is Newtonian above 1120 °C. When the strain rate was very slowly reduced to zero, the lavas at temperatures below 1120 °C had yield strengths which varied systematically with temperature. The maximum yield strength recorded in the laboratory was 78 Pa at a temperature of 1087 °C. While the lavas are therefore Herschel-Bulkley models, their yield strengths are so low that they can be approximated as power law fluids ($r^2>0.95$) at temperatures below 1120 °C. The exponent in the power law equation decreases systematically from 1.00 above 1120 °C to 0.46 at 1084 °C.

Discussion of the rheological properties of Etna lavas: Post-rheological geochemical analyses of the sample quenched at 1097.5 °C show that the composition is not significantly different from that of the original

lava. In addition, the composition of the top of the sample is virtually identical to the composition of the bottom; this confirms that volatile-loss and crystal settling are not important on the time scale of these experiments. Viscous heating and crystal settling rates have been calculated, and they were negligible for the time scales and shear strain rates used in these experiments. In addition, calculations, supported by thin section analysis, confirms that migration of crystals and bubbles away from the spindle due to radial motion of the lava on shearing did not occur. Our measurements also indicate that, as previously found on Hawaii (1,2), the lavas are thixotropic at all temperatures measured. During the time interval between rheological measurements, the static yield strength increased; the magnitude of the regained yield strength is dependent on the time at rest. An additional complication arose because stirring induces crystallisation, especially at high degrees of supercooling; this leads to rheopectic behaviour, a dramatic increase in viscosity, and the development of a yield strength.

Because crystal growth rates are considerably slower than rates at which crystals melt, the crystal content on melting a lava at a given heating rate will generally be greater than in a sample which has been cooled to the same temperature at the same relatively rapid rate. This explains why the apparent viscosities of crystallising Etna lavas were larger in samples that have been heated than in those which have cooled (Fig 1). It also explains why the laboratory measurements on heating are close to those obtained in the field where the lavas have cooled slowly prior to eruption in a volatile-rich environment (Fig 1).

Comparison of measured and calculated rheological properties: The viscosities measured in this study are significantly higher than values calculated using the method of Shaw (5). This difference is due to changing chemistry of the melt during crystallisation, together with the hydrodynamic interaction effects caused by bubbles and crystals in the experimental sample. The factors controlling the development of a non-Newtonian rheology in crystallising melts have been reviewed recently (6,7), and it is accepted that basic melts can be approximated as Newtonian fluids at crystal concentrations below 25 vol%. At higher concentrations, lavas behave as pseudoplastic materials with a yield strength, and their shear stress-strain rate relationships can be calculated from the crystal sizes, shapes and size distributions.

In Fig 1, we show the calculated apparent viscosity of a supercooled Etna lava (lower dotted line); that of the residual melt during crystallisation (higher dotted line); and the calculated trends for 20% and 40% crystal content (upper dotted lines). Modelled crystal contents are similar to those of quenched samples heated to 1116 °C and 1098 °C respectively. The close agreement between theoretical and measured values of apparent viscosity in the field and in the laboratory (Fig 1) support the usefulness of the model which has been developed to calculate the rheological properties of lavas at sub-liquidus temperatures (6,7). This is the first stage in the development of finite element models which will predict the dimensions and advance rates of lavas from Mount Etna. Once these model is refined and tested, they can be used to refine existing models (e.g. 8,9) of planetary lava flows.

References: (1) Shaw HR (1969) J Petrol 10:510-535 (2) Shaw HR, Wright TL, Peck DL, Okamura R (1968) Am J Sci 266:255-264. (3) Spera FJ, Borgia A, Strimple J, Feigenson M (1988) J Geophys Res 93: 10273-10294. (4) Guest JE, Kilburn CRJ, Pinkerton H, Duncan A (1987) Bull volcanol 49:527-540. (5) Shaw HR (1972) Am J Sci 272:870-893. (6) Pinkerton H, Stevenson RJ (1992) LPS XXIII: 1079-1080. (7) Pinkerton H, Stevenson RJ (1993) J Volcanol Geotherm Res (in the press). (8) Baloga SM, Pieri DC (1986) J geophys Res 91:9543-9552. (9) Pinkerton H, Wilson L (1992) LPS XXIII: 1083-1084.

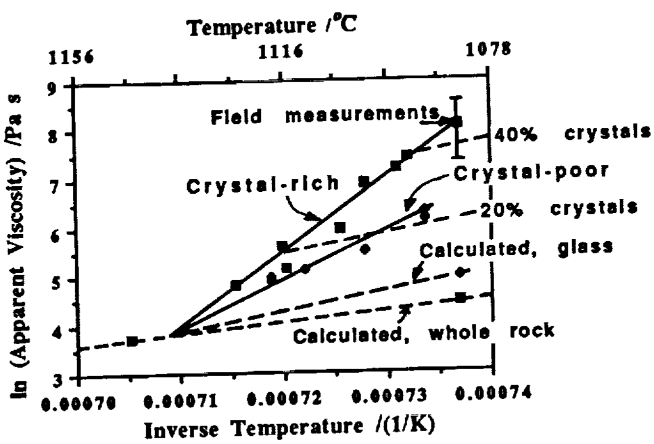


Figure 1 Apparent viscosity, at unit strain rate, of lavas from Mount Etna. Calculated trends are shown as dotted lines, and measured trends for the crystal-rich and crystal-poor lavas are shown as solid regression lines through measured data points.

N94-20691

MAGELLAN VERTICAL POLARIZATION RADAR OBSERVATIONS. Jeffrey J. Plaut, Jet Propulsion Laboratory, California Institute of Technology, MS 230-225, 4800 Oak Grove Drive, Pasadena, CA 91109.

Introduction

The Magellan high-gain radar antenna system was designed to transmit and receive signals in a pure linear polarization state. The nominal mapping configuration placed this linear polarization direction parallel to the surface of Venus, providing SAR image data in the HH polarization (horizontal transmit and receive) and radiothermal emission data in the H (horizontal - receive only) polarization. During Magellan's extended mission (cycles 2 and 3), two brief experiments were conducted in which the spacecraft was rotated 90 degrees along the axis of the antenna boresight, producing SAR data in the VV polarization and emission data in the V polarization. This study will focus on the SAR results from the first experiment, which included portions of the highly reflective Beta Regio highlands.

Theoretical models of polarimetric backscatter [1,2], along with experimental data from terrestrial surfaces, predict VV backscatter cross section values to be higher than HH values for most natural surfaces. Randomly polarized ("depolarized") backscatter from rough surfaces is expected in equal amounts for either incident polarization. Roughness differences will therefore be more pronounced in HH measurements than in VV, because the depolarized random component makes up a proportionately larger fraction of the HH backscatter. In addition, HH cross section values are observed to fall off more rapidly than VV values with increasing incidence angle. Slope-related backscatter differences will therefore be more pronounced in HH images. The small perturbation polarimetric scattering model also predicts higher VV to HH ratios for surfaces of high dielectric constant [2,3].

Data acquisition

The Magellan VV polarization data were obtained on orbits 3716-3719 and 4567-4574. The primary target of the first experiment was the highly reflective regions near the summit areas on Rhea and Theia montes, in Beta Regio. The center of the four-orbit swath crossed the equator at about 284 degrees longitude. Data acquisition was extremely successful for the first experiment. The second experiment, designed to image elevated regions in Ovda Regio, including a "festoon"-type lava flow [4], was less successful because of degradation of the spacecraft data transmission system. The center of the second swath crossed the equator near 95 degrees longitude.

For comparison of the HH and VV SAR images, small mosaics were constructed for areas likely to show differences. Inspection of these mosaics showed subtle differences between the polarizations in some areas. Difference images were constructed that directly displayed the

ratio of VV to HH backscatter cross sections. Best results were obtained using a median spatial filter on each image before calculating the cross section ratio image, to reduce the effects of speckle on the ratio determinations.

Results

Differences in HH and VV response were observed on several terrain types covered in the first experiment. The lowest backscatter areas, such as plains surfaces near impact craters (e.g. 45.5N, 282E; 13.0S, 286E) showed less contrast with the surroundings in the VV image, and therefore displayed a relatively higher VV/HH ratio than the surroundings. The most dramatic differences were observed in portions of the Beta Regio highlands showing enhanced Fresnel reflectivity and low emissivity. High VV/HH ratios are observed near the rift zone on the north flank of Theia Mons (27.0N, 282E) [5]. A VV/HH ratio of 2.6 dB is seen on an area with H polarization emissivity values ~0.55. The largest VV/HH anomaly, however, at 3.3 dB, is observed on an adjacent "dark summit" area [6] that has an H polarization emissivity of ~0.77. Along the southeastern flank of Theia Mons (24.0N, 282E), complex variations in VV/HH occur on overlapping lava flows within a low emissivity area. Although the magnitude of the VV/HH variations is small (1-2 dB), they are clearly correlated with geologic features and indicate variations in the physical properties of the lava flows. Possible causes for these scattering anomalies include differences in dielectric constant related to composition or density, or geometric elements at the surface of the flows that favor or discourage coupling of the impinging signals depending on the polarization orientation.

[This work was conducted at the Jet Propulsion Laboratory, California Institute of Technology, under contract with the National Aeronautics and Space Administration.]

References

1. Ulaby, F.T. et al. (1982). *Microwave Remote Sensing - Active and Passive*, vol. II.
2. vanZyl, J.J. et al. (1987). Radio Sci. 22, 529-543.
3. Campbell, B.A. et al. (1993), in preparation.
4. Moore, H.J. et al. (1992). JGR 97, 13,479-13,493.
5. Senske, D.A. et al. (1992). JGR 97, 13,395-13,420.
6. Pettengill, G.H. et al. (1991). JGR 97, 13,091-13,102.

ERUPTION HISTORY OF THE THARSIS SHIELD VOLCANOES, MARS:
J. B. Plescia, Jet Propulsion Laboratory, California Institute of Technology, Pasadena, CA 91109

The Tharsis Montes volcanoes and Olympus Mons are giant shield volcanoes (1). Although estimates of their average surface age have been made using crater counts, the length of time required to build the shields has not been considered. Crater counts (2, 3, 4, 5) for the volcanoes indicate the constructs are young; average ages are Amazonian to Hesperian (4). In relative terms; Arsia Mons is the oldest, Pavonis Mons intermediate, and Ascreaus Mons the youngest of the Tharsis Montes shields; Olympus Mons is the youngest of the group. Depending upon the calibration (5, 7), absolute ages range from 730 Ma to 3100 Ma for Arsia Mons and 25 Ma to 100 Ma for Olympus Mons. These absolute chronologies are highly model dependent, and indicate only the time surficial volcanism ceased, not the time over which the volcano was built.

The problem of estimating the time necessary to build the volcanoes can be attacked in two ways. First, eruption rates from terrestrial and extraterrestrial examples can be used to calculate the required period of time to build the shields. Second, some relation of eruptive activity between the volcanoes can be assumed, such as they all began at a specific time or they were active sequentially, and calculate a the eruptive rate. Volumes of the shield volcanoes were derived from the topographic/volume data of (7, 8).

Using known eruption rates, the time necessary to build the shields is illustrated in Figure 1. At one extreme, the eruption rate of the Imbrium flows (31500 $km^3\ yr^{-1}$ (10)) would build the volcanoes in tens of years. Although single flows might be erupted at such rates, it seems unlikely that the whole shield would be built at these rates. Such large rates have not been observed for terrestrial central vent volcanoes. In addition, an important aspect of large eruption rates for flood basalts is their extremely low viscosity which would not tend to favor shield building. A rate consistent with the Cretaceous super plume (30 $km^3\ yr^{-1}$ (10)) would result in construction times of a few hundred thousand years. These rates are associated with plumes that fed mid ocean ridges and produced oceanic basalt which is consistent with terrestrial shield building. Perhaps, the most relevant example comes from the long-term Hawaiian rate (0.1 $km^3\ yr^{-1}$ (11, 12)), because it represent a typical value for a central vent volcano. Using this rate, tens of millions of years are required to build the shields. Carr (13) originally estimated that Olympus Mons was built in 10^8 years assuming an eruption rate of 0.02 $km^3\ yr^{-1}$.

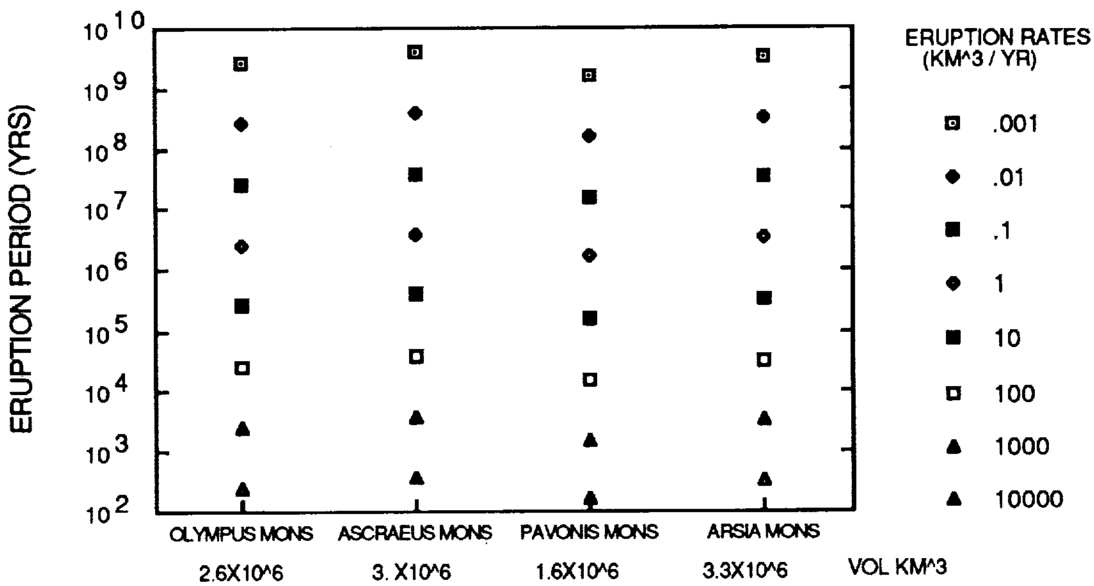
On the other hand, if one assumes that the volcanoes were built over periods of 10^8 to 10^9 years, such that they all began at the same time (e.g., 3.5 Ga) then the implied mean eruption rates are extremely low, 0.01 to 0.001 $km^3\ yr^{-1}$. Such low rates are not typical of terrestrial basaltic provinces; rather they usually occur for small volume constructs having silicic compositions. An additional problem with low eruption rates is maintaining the same conduit over long time periods for a central vent and producing a magma chamber large enough for caldera formation. Under extremely low eruption rates, maintaining an open conduit or a thermally weakened zone as a pathway from the mantle source would be difficult. The zone would cool over such long time scales and it might be expected that numerous, regionally distributed vents would occur, rather than a single vent. Additionally, under low magma production rates, it would be impossible to create the large magma chambers required to produce the observed caldera. Estimates of the volume of the Olympus Mons magma chambers are of the order 10^4 km^3 (14), which would require 10^6 - 10^7 years to fill at the lowest magma production rates. Under

these conditions, the magma would solidify before the chamber became large enough to produce a caldera. Thus, the presence of a caldera, which requires large magma chambers, in part constrains the magma production rates.

Assuming the shields are built over time spans of 10^7 - 10^8 years, the next question is why the absolute ages of the individual shields differ by 0.8 - 3 x 10^8 years, with each shield potentially being completed before volcanism at the next shield commenced. These age relations can be understood in the context of a model in which shield building results from mantle plumes.

It is becoming increasingly apparent in the study of flood basalt volcanism, that large eruptions occur over very brief intervals of time under very large eruption rates. The Columbia Plateau, Deccan and Siberian Traps all formed over only a few million years (15-18). Similarly, episodes of significantly increased sea floor spreading also occur (10). These volcanic episodes can be linked to large mantle plumes impinging upon the base of the lithosphere. As the plume rises through the mantle it ultimately encounters the base of the lithosphere, which acts as a barrier to further ascent. The plume then flattens out and high rate eruptions occur over a few million years.

In Tharsis, it can be proposed that each large shield marks the location of a ancient mantle plume which produced an intense, but relatively short lived pulse of volcanism. Early plumes were probably hotter or tapped different source regions such that the magmas were of very low viscosity and produced the large "sheet" flows that characterize the distal margins of Tharsis. Later plumes produced magmas that resulted in the construct of central vent volcanoes. Ultimately each of the plumes died out and volcanism ended.



References: (1) Greeley, R., and P. Spudis, 1981, Rev. Geophys. Space Phys. 19, 13. (2) Plescia, J. and R. Saunders, 1979, Proc. Lunar. Planet. Sci. Conf. 10th, 2841. (3) Tanaka, K., 1986, Proc. Lunar Planet. Sci. Conf. 17th, J. Geophys. Res., 91, E139. (4) Scott, D. and K. Tanaka, 1986, U. S. G. S. Misc. Inv. Map I1802-A. (5) Neukum, G. and K. Hiller, 1981, J. Geophys. Res., 86, 3097. (6) Soderblom, L., 1977, Impact and Explosion Crater, pp. 629. (7) Wu, S., unpublished manuscript, 8 pp. (8) Wu, S., et al., 1988, Abst. Lunar Planet. Sci. Conf. XIX, 1298. (9) Schaber, G., et al., 1976, Proc. Lunar Planet. Sci. Conf. 7th, 2783. (10) Larson, R., 1991, Geology, 19, 963. (11) Crisp, J., 1984, J. Volc. Geotherm. Res., 20, 177. (12) Dzurisin, D. et al., 1984, J. Volc. Geotherm Res., 21, 177. (13) Carr, M., 1973, J. Geophys. Res., 78, 4049. (14) Zuber M. and P. Mouginis-Mark, 1992, J. Geophys. Res., 97, 18295. (15) Renne, P. and A. Basu, 1991, Science, 253, 176. (16) Cambell, T., and R. Griffiths, 1990, Earth Planet. Sci. Lett., 99, 79. (17) Richards, M., et al., 1989, Science, 246 103. (18) White, R., and D. McKenzie, 1989, J. Geophys. Res., 94, 7685.

557-91
ABS ONLY.

N94-20693

GEOLOGY OF BIBLIS PATERA, ULYSSES PATERA, AND JOVIS THOLUS, MARS.

J. B. Plescia, California Institute of Technology, Jet Propulsion Laboratory, Pasadena, CA 91109

P. 2

There are a variety of constructional volcanic features in Tharsis[1]. These features range from Olympus Mons and the Tharsis Montes shields, to the small low shields and fissure eruptions that characterize much of the volcanic plains, to the smaller volcanic constructs in the northeast and western parts of Tharsis. Here, I describe the geology of the western group, which includes Biblis Patera, Ulysses Patera, and Jovis Tholus. Each of these volcanoes has had a unique, and complex geologic history.

BIBLIS PATERA: Biblis Patera is located at 2.3°N, 123.8°. The volcano is elongate in a northwesterly direction and has a large, faulted caldera complex. The flanks of the volcano and adjacent plains are characterized by lava flows, northwest-trending graben and troughs, and caldera-concentric graben and troughs. Biblis Patera is ~66 x 127 km with an oval 51 x 56 km caldera; the summit elevation is ~9 km, standing ~2 km above the surrounding plains [2]. The construct has an estimated volume of 8-22 x 10^3 km^3.

The caldera is characterized by numerous fault blocks surrounding the margin and a complex central floor that lies ~2 km below the rim. Several major graben lie just outside the caldera rim and several major fault blocks are contained with the caldera rim; the caldera has clearly expanded (~12 km) due to fault blocks dropping into the interior. The central floor exhibits a smooth annual region surrounding an area of ridged plains and a pit crater. The flank is characterized by a variety of volcanic and tectonic features - lava flows, pit craters, graben, and troughs. Two groups of faults occur, a northwest trending group cutting across the plains and the volcano, and a second group concentric about the caldera. The concentric graben are older. The flanks exhibits a radial texture that is interpreted to represent a myriad of lava flows. Several broad aprons of lavas flows also occur on the flank and appear to emanate from concentric fractures and channels. There are many similarity between the style of eruption exhibited by Biblis Patera and that of the Galapagos Islands shields [3].

ULYSSES PATERA: Ulysses Patera is located at 2.7°N, 121.3°W and stands ~2-3 km above the surrounding plain [2]; flank slopes are ~7° to 12°. The caldera floor is quite deep, lying 1.8 to 2.2 km below the caldera rim. The caldera has a void volume of ~5000 km^3, the total solid mass volume of the volcano is 7-16 x10^3 km^3.

The flanks of Ulysses Patera are characterized by a clearly defined radial texture, two huge impact craters and minor faulting. Locally on the flanks, individual lava flows (800 m wide) can be recognized, elsewhere the surface texture indicates lava flows extending down the flank from a central source (overflow from a completely filled caldera or a more localized source that subsequently collapsed into the caldera). The flanks are cut by north-northwest trending graben of variable width and age. Two large impact craters (15-30 km) also occur on the flanks. On the caldera floor, 15 low hills are observed. Based on their morphology, circular outline, and the presence of a central pit, they are interpreted to be cinder cones. Individual cones range from 300 - 1600 m in diameter; the summit craters are ~550 m in diameter; volumes are estimated to be ~0.1 km^3. Two shallow depression occur on the southwest floor of the caldera, they are a few km in diameter and have etched margins. These depressions are interpreted to be volcanic pit craters whose interiors were filled with molten lava. Crater counts indicate a paucity of craters <1000 m suggesting small diameter craters have been removed or buried. Aside from the relatively large caldera, Ulysses Patera appears to be a basaltic

shield. The presence of cinder cones on the floor suggest a limited amount of more highly evolved magma was erupted during the waning stages of volcanism.

JOVIS THOLUS: Jovis Tholus is centered at 18.3°N; 117.5°W; it is a low relief, volcano with gentle flank slopes of between 3 and 8°. The construct is dominated by a series of inset calderas which make up the largest fraction of the area . The caldera complex is offset to the southwest side. Total shield dimensions are ~77 km (e-wt) by 62 km (n-s); the caldera complex is ~44 x 34 km. The shield is embayed on all sides by younger Amazonian age volcanics. Total relief, relative to the surrounding plains, is probably ~2 km [2]. The total volume of Jovis Tholus is estimated to be ~2-5 x 10^3 km^3.

At least five episodes of caldera formation have occurred on Jovis Tholus. Caldera formation apparently migrated across the construct to the southwest. The caldera margins are cut by faults and have scalloped edges suggesting the coalescence of many caldera. The caldera volumes appear to increase with time, the youngest caldera being the largest. Caldera diameters are a few to more than 20 km across and depths relative to other caldera range from a few tens of meters to several hundred meters. Superimposed across the youngest caldera complex, and presumably marking the youngest volcanic activity, is a low shield. The shield covers a significant fraction of the caldera floor, measuring 17 x 21 km; an irregular vent 2.7 km x 560 m marks the summit. The total volume of the small shield is ~10^2 km^3. The flank of Jovis Tholus is rough and hummocky with a radial texture suggestive of flows just below the limit of resolution. Several troughs and pit chains, and graben cut the flanks of the volcano. The absence of small diameter craters on the flank of the volcano suggests that it has been resurfaced.

Crater counts for these volcanoes [4,5] indicate that Biblis Patera, Ulysses Patera, and Jovis Tholus are old in comparison to the large Tharsis shields, similar in age to the Elysium volcanoes, and younger than the patera of the southern highlands. As these volcanoes represent shield volcanism, as do the large Tharsis Montes shields, it suggests that a volcanic style in which low viscosity lavas were erupted from a point source to produce a volcanic construct was established during the earliest phases of geologic activity in Tharsis. The observation that Biblis Patera, Ulysses Patera, and Jovis Tholus, and the Uranius group to the northeast, are older than the Tharsis Montes shields, suggests that the style of volcanism changed with time. These early volcanoes were of small total volume and were probably built rapidly (~10^6 yrs). The source region was either cut off or rapidly depleted such that a large shield could not be built. The presence of the calderas suggests that significant magma chambers occurred in the near surface to allow collapse resulting in caldera formation. Despite the relatively large caldera size, it seems unlikely that these volcanoes are buried by more than a few hundred meters of lava around their flanks. Biblis Patera, Ulysses Patera, and Jovis Tholus all represent basaltic shield volcanoes.

References: [1] Greeley, R., and Spudis, P. , 1981, , Rev. Geophys. Space Phys., 19, 13. [2] U. S. Geological Survey, 1991, U. S. Geological Survey Miscellaneous Investigation Series Map I-2113. [3] Nordlie, B., 1973, Geol. Soc. Amer. Bull., 84, 2931. [4] Neukum, G., and Hiller, K., 1981, Martian ages, J. Geophys. Res., 86, 3097. [5] Plescia, J., and Saunders, R. S., 1979, Proc. Lunar Planet. Sci. Conf., 10th, 2841.

S5B-90 ABS. ONLY

N94-20694

GRAVITY INVESTIGATION OF THE MANSON IMPACT STRUCTURE, IOWA: J. B. Plescia, Jet Propulsion Laboratory, MS 183-501, Pasadena, CA 91109 P-2

The Manson crater, of probable Cretaceous/Tertiary age, is located in northwestern Iowa (center at 42° 34.44' N; 94° 33.60' W); a general review of the data available on the structure is presented in (1). A seismic reflection profile along an east west line across the crater and drill hole data (2,3) indicate a crater about 35 km in diameter having the classic form for an impact crater, an uplifted central peak composed of uplifted Proterozoic crystalline bedrock, surrounded by a "moat" filled with impact produced breccia and a ring graben zone composed of tilted fault blocks of the Proterozoic and Paleozoic country rocks. The structure has been significantly eroded. This geologic structure would be expected to produce a significant gravity signature and study of that signature would shed additional light on the details of the crater structure. A gravity study was undertaken to better resolve the crustal structure.

Gravity data for the Manson structure were originally collected by Holtzman (4). His data were collected on a 1 mile grid and extended out a few miles beyond the crater edge as it was understood at the time (5). It has since been recognized (1, 4) that the structure is more circular with a radius of 17.5 km, such that Holtzman's data extend only a short distance beyond the northwestern edge. In an attempt to better constrain the regional gravity field and to ensure areal coverage over the structure, additional data were collected.

The regional Bouguer gravity field is characterized by a southeastward decreasing field. Gravity values are about -64 mGal in the northwest and decrease to a low of about -75 mGal before rising up to as high as +20 mGal in the southeasternmost areas. Gradients range from <0.5 mGal/km to >10 mGal/km. To first order, the Bouguer gravity field can be understood in the context of the geology of the Precambrian basement. The high gravity at the southeast corner is associated with the mid-continent gravity high; the adjacent low to the northwest results from a basin containing low-density clastic sediments shed from the basement high. Modeling of a simple basin and adjacent high predicts much of the observed Bouguer gravity signature.

A gravity signature due to structure associated with the Manson impact is not apparent in the Bouguer data. To resolve the gravity signature of the impact, a series of polynomial surfaces were fit to the Bouguer gravity field to isolate the small wavelength residual anomalies. The residual gravity obtained after subtracting a 5th- or 6th-order polynomial seems to remove most of the regional effects and isolate local anomalies. Figure 1 illustrates the residual gravity after removal of a 5th-order polynomial surface.

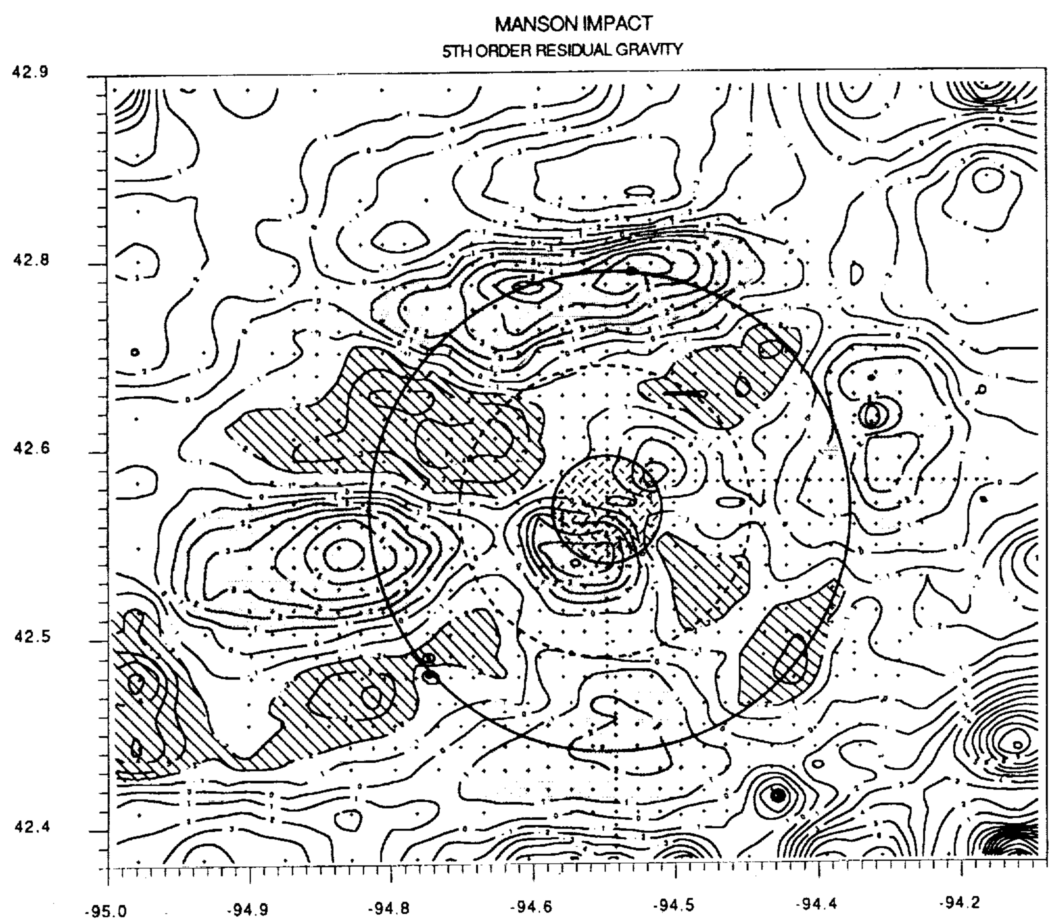
The pattern resolved in the residual gravity is one of a gravity high surrounded by gravity lows and in turn surrounded by isolated gravity highs. The central portion of the crater is characterized by two positive anomalies having amplitudes of about +4 mGal separated by a gentle saddle located approximately at the crater center. The highs extend out over an area larger than the region of shallow Proterozoic bedrock (1). Surrounding this central high is a ring of gravity lows of variable amplitude (-2 to -4 mGal). These lows correspond to both the moat and ring graben zones. In some areas they extend beyond the presumed crater rim. Locally surrounding the lows (to the north, south, east-northwest, and west-southwest) are isolated highs having amplitudes as great as +6 mgal. These highs geographically correspond to the position of the crater rim. Total gravity relief across the structure is >10 mGal.

The central high corresponds to uplifted Precambrian crystalline rock with densities of 2.5-2.7 g cm^{-3}; the surrounding lows are the result of the

breccia (density 2.1-2.6 g cm^{-3}); the highs along the margin may be due to uplift pieces of the Paleozoic limestone which has a high density (2.8 g cm^{-3}) or to variations in the density of the deeper crystalline basement. The amplitude of the anomalies on the southeast side are less than the amplitude of the anomalies to the northwest. When viewed in the context of an increase in the depth of the Proterozoic crystalline basement to the southeast, it suggests that the anomalies may be due to variations in the density of the basement rocks rather than the crater itself. It would appear that there is a gravity signature resulting from the crater, although it is subtle and to some extent overwhelmed by the signal from the variation in the Precambrian basement.

References: (1) Hartung, J. B., and Anderson, R. R., 1988, LPI Tech. Rept. 88-08, 32 pp. (2) Shoemaker, E. M., et al., this volume. (3) Anderson, R. R., and Hartung, J., Absts. 22nd Lunar Planet. Sci. Conf., 25-26. (4) Holtzman, A. F., 1970, Iowa. Master's Thesis, University of Iowa, Iowa City, 63 pp. (5) Hoppin, R. A., and Dryden, J. E., G. Geol. 66, 694-699, 1958.

Figure 1. 5th order residual gravity for Manson impact. Shaded areas have gravity > 1 mGal; striped areas have gravity < -2 mGal. Central stippled region indicates shallow Proterozoic crystalline rock (the central peak). Dashed line denotes boundary between moat and ring graben zones; solid outer line marks the inferred edge of the structure.



359-25 ABS. ONLY

N94-20695

P. 2

ELEVATED INITIAL $^{87}Sr/^{86}Sr$ IN ORDINARY CHONDRITE METAL;

F. A. Podosek[1], J. C. Brannon[1], C. Perron[2] and P. Pellas[2]; [1]McDonnell Center for the Space Sciences, Washington University, St. Louis, MO 63130, USA, [2]Laboratoire de Mineralogie du Museum, 75005 Paris, France.

The metal phase of ordinary chondrites has been found to contain a complex assemblage of non-metal phases [1], evidently formed when elements such as Si, Cr and P, originally dissolved in the metal, were subsequently oxidized and exsolved [1-3]. We have investigated the Rb-Sr isotopic system in samples of H-chondrite metal, finding small but nontrivial amounts of Sr, apparently concentrated toward the surface of metal grains, and characterized by pronounced excesses of ^{87}Sr relative to what would be expected for the normal chondrite age and the observed Rb/Sr ratio. The high $^{87}Sr/^{86}Sr$ in chondritic metal can plausibly account for the characteristically elevated initial $^{87}Sr/^{86}Sr$ found in ordinary chondrite phosphates [4], but it remains unclear when and where the metal experienced the high Rb/Sr environment needed to account for such high $^{87}Sr/^{86}Sr$.

We have previously reported Rb-Sr data [5] for separated metal from Dhajala (H3), Forest Vale (H4) and Estacado (H6). Here we report data for two size fractions (80-160 and 280-450 µm) of separated metal from the H4 chondrite Ste. Marguerite. These samples were etched twice (.5N HCl for one hour) before dissolution (6N HCl). Aliquots of the solutions were spiked for Fe, Ca and Rb + Sr. The results for Ste. Marguerite metal are presented in the Table; errors are two-sigma and elemental concentrations are stated in terms of total sample weight.

The concentrations of lithophile elements in chondritic "metal" are, as expected, quite low, but they are not trivial and in general they are well above analytical blank. Assuming metal concentrations of order 10%, the Sr observed in H3-H4 chondrite metal accounts for 1-3 permil of the whole rock inventory of Sr. The actual host phase of Sr in these samples is not known and is not well constrained by these analyses. We presume that the Sr, in particular, is probably not in solid solution in the metal phase but rather is concentrated in the other phases [1,3], notably phosphates, which are observed enclosed by the metal. It should be noted, however, that the Sr/Ca ratio in these samples is on average about an order of magnitude higher than that characteristic of phosphates extracted from bulk samples [4].

Although the number of samples studied is small, the available data are consistent with a trend in which Sr concentration in metal decreases with increasing metamorphic grade: the highest concentration is for Dhajala (H3), while Forest Vale (H4) and Ste. Marguerite (H4) have somewhat less and Estacado (H6) has very much (two orders of magnitude) less Sr.

Assuming that the sequential etches preferentially attack the surface regions of the metal, the Sr is inferred to be concentrated toward the surface, since it is disproportionately concentrated in the etch fractions. Such a trend was suggested by the Dhajala and Forest Vale data [5], and is evident for Ste. Marguerite, for which data on metal dissolution are available (see Table). This is not simply a matter of straightforward surface correlation, however, since in Ste. Marguerite metal the coarser fraction has a higher bulk concentration than the finer fraction. Concentration in the etch fractions is less prominent for Ca than for Sr, i.e. Sr/Ca is higher in the etches than in the residues.

In general, the H3-H4 metal samples have elevated initial $^{87}Sr/^{86}Sr$, i.e. on an Rb-Sr isochron diagram (see Figure) they plot above the characteristic chondrite isochron [6]. Elevation of initial $^{87}Sr/^{86}Sr$ is particularly pronounced in the H3-H4 etch fractions; it is less prominent to non-existent for the total dissolution residues and for the total metal in Estacado (H6).

Prior studies of the Rb-Sr system in ordinary chondrite phosphates [4] have revealed characteristic elevations of initial $^{87}Sr/^{86}Sr$ which are difficult to interpret chronologically if it is assumed that Sr now in phosphates was initially evolved in a bulk sample Rb/Sr environment. We can now make a plausible case that elevated initial $^{87}Sr/^{86}Sr$ in phosphates does not reflect bulk sample evolution but is rather an inheritance from chondritic metal, which is consistent with the scenario in which phosphates form by exsolution of oxidized P. Phosphates contain more Sr

than the metal, but their initial $^{87}Sr/^{86}Sr$ elevation is not as great, and the mass balance is nearly correct. For typical phosphate data [4] (initial $^{87}Sr/^{86}Sr \approx .6995$, [Sr] ≈ 70 ppm, 0.5% phosphates), phosphates contain on the order of 2×10^{-13} mole/g (total meteorite) excess ^{87}Sr. Again for ≈ 10% metal, the 280-450m fraction of Ste. Marguerite metal also contains of order 2×10^{-13}mole/g (total meteorite) excess ^{87}Sr. With allowance for likely loss of Sr from metal or metal-associated phases during sample preparation, and possibly higher levels of Sr in pre-metamorphic metal, it is not unreasonable to suppose that phosphate elevated initial $^{87}Sr/^{86}Sr$ in general reflects inheritance of excess ^{87}Sr from associated metal.

The connection with phosphate Sr, of course, does not address the issue of how the metal came to have such high $^{87}Sr/^{86}Sr$ in the first place. It is not plausible to imagine migration of radiogenic ^{87}Sr (unaccompanied by Rb) into the metal from the meteorite as a whole: this would run counter to the apparent trend of outward migration of Sr in response to metamorphism, and it would require unreasonably long times to generate such radiogenic Sr with typical bulk Rb/Sr (≈ 900 Ma for $^{87}Rb/^{86}Sr = 0.75$). Perhaps the metal has a close relationship with some high-alkali phase such as chondrule glass, but there are no observations relevant to such a suggestion. A more speculative suggestion is that metal may have reacted with relatively cool nebular gas, after removal of most (relatively refractory) Sr but before removal of (relatively volatile) Rb, in which the growth of $^{87}Sr/^{86}Sr$ could have been very rapid, but we have no basis for quantitative evaluation of such speculation.

REFERENCES. [1] Perron *et al.* (1990) *Meteoritics* **25**, 398, [2] Murrell & Burnett (1983) *GCA* **47**, 1999, [3] Perron *et al.* (1992) *Meteoritics* **27**, 275, [4] Podosek & Brannon (1991) *Meteoritics* **26**, 145, [5] Podosek *et al.* (1991) LPS XXII, 1081, [6] Minster *et al.* (1982) *Nature* **300**, 414.

Isotopic analyses of Ste. Marguerite "metal"

Sample	Fraction dissolved %	[Ca] ppm	[Rb] ppb	[Sr] ppb	$^{87}Rb/^{86}Sr$	$^{87}Sr/^{86}Sr$
		80-160μ (57 mg)				
Etch I (.5NHCl)	9.6	11	0.6	78	.0238±2	.70897±16
Etch II (.5NHCl)	7.6	5	0.3	6	.146±5	.71040±50
Dissolution (6NHCl)	82.8	48	2.3	52	.128±1	.70774±25
		280-450μ (173 mg)				
Etch I (.5NHCl)		19	0.7	138	.0143±1	.70993±4
Etch II (.5NHCl)		9	0.3	13	.064±1	.71446±34
Dissolution (6NHCl)		81	2.6	57	.132±1	.71158±25

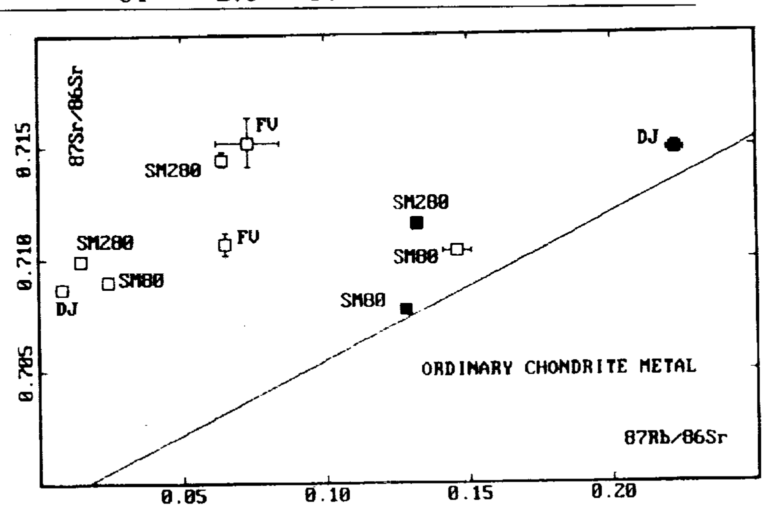


Fig.: Rb-Sr isochron diagram for ordinary chondrite metal. SM80 and SM280 are Ste. Marguerite size fractions (see Table); DJ is Dhajala and FV is Forest Vale [4]. Open symbols are etches, filled symbols are total dissolution after etching. Line is bulk chondrite isochron [6].

S60-91
ABS. ONLY
p-2

N94-20696

CRATER DESTRUCTION ON THE VENUSIAN HIGHLANDS BY TECTONIC PROCESSES; HOWARD A. POHN, U.S.GEOLOGICAL SURVEY, RESTON,VA AND GERALD G. SCHABER, U. S. GEOLOGICAL SURVEY, FLAGSTAFF, AZ

It is apparent that few, if any, craters as old, or highly modified as Imbrian craters on the surface of the moon are present on the Venusian highlands, or indeed anywhere on the planet's surface. Degraded craters such as those seen on the moon, Mercury, or Mars are conspicuously absent. Furthermore, virtually all the impact craters on the Venusian surface show modification only by extensional tectonics, whereas the Venusian highlands show modification by compression, strike-slip movement, and finally by extension. Presumably at an earlier time, the surface of Venus resembled the surfaces of the other inner planets. The relatively recent resurfacing event [1] that produced the plains units may be a mechanism for covering the older craters in the plains, but these vast outpourings of lava cannnot be invoked as a mechanism for covering the craters on the Venusian highlands. If the plains units had covered the highlands, the entire Venusian surface would appear to be as smooth as the plains units that are embayed by and, therefore, postdate the highlands. The last major tectonic events to affect the highlands such as those seen on Ovda Regio appear to be thrust faulting with consequent folding, followed by at least three episodes of strike-slip faulting and finally extensional faulting [2]. To test whether such tectonic movements could have destroyed highlands craters, a preliminary experiment was conducted by using a Lunar Orbiter mosaic (fig. 1, Lunar Orbiter IV-169-H1, Hevelius region) of the lunar uplands as an analog for the ancient Venusian highlands.

Four mechanical manipulations were performed on the mosaic. First a series of cuts was made, parallel to the scan directions (approximately east-west), with a spacing between cuts of 10 to 30 km. These strips were reassembled with an average overlap of 19 percent to simulate a group of southward-directed thrusts. The second manipulation was to offset the reassembled strips in an east-west direction by 5 to 30 km. This operation was intended to simulate a group of strike-slip faults that used the thrust fault surfaces in strike-slip movement. The third manipulation was to offset the newly assembled mosaic by a series of strike-slip faults oriented N. 45°E. with displacements of 10 to 30 km. A final mosaic (fig. 2) was produced by simulating a series of strike-slip faults with displacements of 5 to 30 km and a trend of N. 45°W.

Figure 2 shows that craters whose diameters are greater than 5-7 km have been largely destroyed. This diameter is not much larger than the minimum crater size of 2 to 3 km for craters observed on the Venusian surface. Any increase in the displacement of the mechanical manipulations, most particularly in the shortening caused by thrust faults, would bring the minimum size of preserved craters quite close to the observed dimension. Note also that the mechanical manipulations do not

CRATER DESTRUCTION BY TECTONIC PROCESSES: H.A. POHN AND G.G. SCHABER

simulate the considerable drag that would be caused by strike-slip faults, nor do they simulate the distortion at the leading edge of thrust faults. Although the magnitude of this drag and distortion associated with faults has yet to be determined, such effects would further reduce the maximum crater size on the Venusian highlands. It appears, from this preliminary experiment, that tectonic movements alone would be sufficient to destroy nearly all, if not all, of the craters on the Venusian highlands.

[1] Schaber, G. G. and nine others, (1992), JGR, 97, E8, 13,257-13,301
[2] Pohn, H. A. and Schaber, G. G., (1992), LPSC 23 pt. 3 p. 1095



Figure 1



Figure 2

LOW-ENERGY ION IMPLANTATION: LARGE MASS FRACTIONATION OF ARGON.

K.V. Ponganis, Th. Graf, and K. Marti, Dept. of Chemistry, University of California at San Diego, La Jolla, CA 92093-0317

Trapped argon acquired by low-energy implantation (≤ 100 eV) into solids is strongly mass fractionated (≥ 3%/amu). This has potential implications for the origin and evolution of terrestrial planet atmospheres.

The isotopic signatures of noble gases in the atmospheres of the Earth and other planets are considerably evolved when compared to signatures observed in the solar wind. The mechanisms driving the evolution of planetary volatiles from original compositions in the solar accretion disk are currently poorly understood. As Pepin stated, "The field bristles with models of one type or another, but none are without problems."[1]

Modeling of noble-gas compositional histories requires knowledge of fractionating processes that may have operated through the evolutionary stages. Since these gases are chemically inert, information on noble-gas fractionation processes can be used as probes. The importance of understanding these processes extends well beyond "noble-gas planetology."

The central issue to the origin and evolution of terrestrial planets' atmospheres is how, when, and from what sources did the accreting planetesimals get their gaseous elements. Volatile sources may include the gas phase of the solar nebula, the solar wind, comets and impacts by other bodies. Several mechanisms for the incorporation of planetary atmospheric gases have been proposed; some have been modeled in detail. One class of mechanisms, termed "non-fractionating" processes, includes: gravitational capture of nebular gases, solar-wind loading of accreting matter, and impact degassing of projectiles (comets, meteorites, asteroids). Another class, termed "fractionating" processes, includes: adsorption of gases on accreting grains, implantation of solar wind with sticking coefficients < < 1, ion bombardment in plasma interactions before or during accretion, giant impacts, Jeans' escape and hydrodynamic escape, and losses by non-thermal processes. Some of these mechanisms, such as adsorption, will fractionate only the elements.[2][3][4] Others will involve also isotopic fractionation: ion implantation from plasmas[5][6][7][8], gas sputtering[9], Jeans' escape and hydrodynamic escape.[1][2]

Fractionation mechanisms involving ion implantation have received scant attention possibly because Bernatowicz and coworkers concluded that the isotopic fractionation was too small to account for the large isotopic shifts of Xe observed in the terrestrial atmosphere.[8] On the other hand, Tombrello and coworkers observed significant isotopic shifts in sputtering processes, which were not predicted by theoretical models.[10] It is clear from these results that further examination of an ion implantation model and its related processes is needed. Ion implantation and gas sputtering may prove to be a viable process for fractionation in the origin of planetary atmospheres.

Recently, we have examined the ion implantation of argon onto a tungsten wire using a modified Bayard-Alpert device, which is a refinement of the one Bernatowicz and Hagee[8] used. We can degas the ion collector directly by resistive heating. Both the grid and the walls of the chamber are kept at ground. The filament is at -30 V relative to the grid. The ion collector is varied from -40 V to -100 V relative to the grid at ground. A metal canister encased the filament, grid and ion collector instead of glass, although all the feedthroughs are embedded in glass.

A modified static VG 5400 mass spectrometer was used for isotopic analyses. This instrument is fitted with both a Daly detector and Faraday detectors. The mass spectrometer is connected to an all-metal vacuum line that includes two getters, one of titanium sponge and one of SAES NP10. There is also a stainless-steel mesh frit.

The walls of the chamber were heated to 325°C for at least 12 hours before the procedural blanks were run. The grid and the ion collector were degassed several times prior to use.

Procedural blanks were run before every experiment and blank corrections are only significant at the lowest voltages. All ion implantation experiments were done for one hour while the reaction chamber was exposed to a getter. The free phase was collected on a liquid-nitrogen-cooled, stainless steel frit. The reaction chamber was then closed. To collect the trapped phase, the ion collector was brought to a white-hot temperature and remained at this temperature until all of the trapped gas was released.

To test the effect of temperature on ion implantation, the reaction chamber body was stabilized at 200°C before the experiment. The ion collector potential was set at -100 eV and as before the experimental run time was one hour. This result was compared with a -100 V experiment done in the usual manner.

In all experiments the amount of argon that initially entered the reaction chamber was known. Within error

Low Energy Ion Implantation, K.V. Ponganis et al.

limits all the gas was accounted for in either the trapped phase or the free phase.

Results for one-hour runs with -40 V to -100 V potentials on the ion collector are shown in Figure 1, and have been corrected for experimental blanks and mass discrimination.

Figure 1 reveals a large, uniform, ≥ 3% per amu, isotopic fractionation for implanted argon at the -50 eV potential. The trapped fraction here is about 6.6% of the original aliquot. At -100 eV, the trapping efficiency for argon increases to 38% while the isotopic fractionation for the trapped phase drops to 1% per amu. Isotopic mass balance was achieved between the trapped and free phases in all cases. Of course, mass balance assignments require that the isotopic fractionation of the trapped phase will drop to zero as trapping efficiency approaches zero.

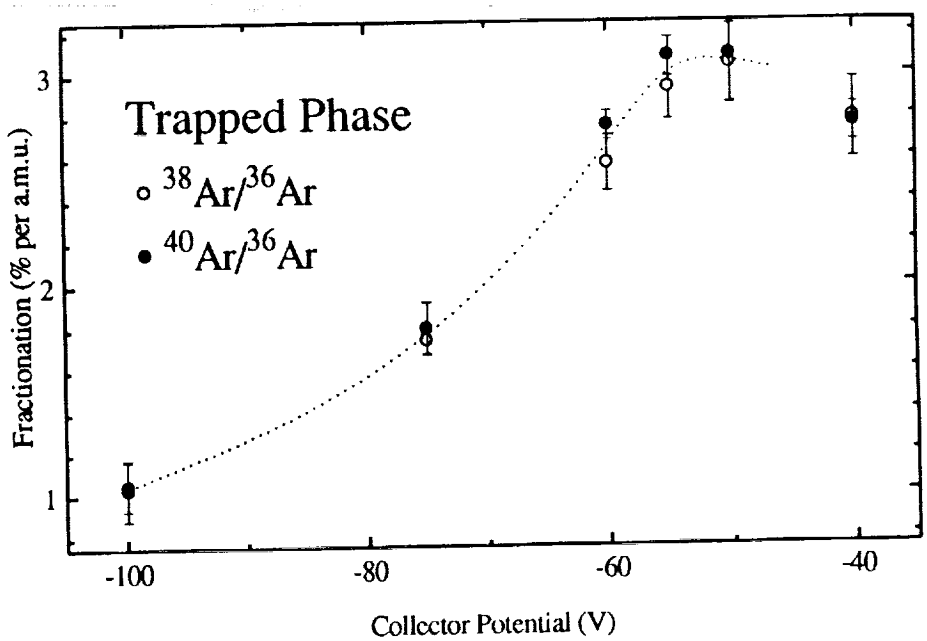


Figure 1: Mass fractionation of trapped argon as a function of ion collector potential with the filament at -30 eV and both the grid and walls at ground. At -50 eV, the trapped argon is 6.6% and at -100 eV, 38%. Mass fractionation is 3% per amu for -50 eV and 1% per amu for -100 eV.

The temperature dependence of argon ion implantation at -100 eV was studied in two experiments, with the ionization chamber initially at ambient temperature and at 200°C respectively before the ionization filament was turned on. The final temperature at the glass support for the feedthroughs was 73 °C in the former and 155 °C in the latter experiment. At 200°C the extent of argon trapping drops by a factor of five to (5.58 ± 0.05)% while the isotopic fractionation is at most only marginally increased to (1.32 ± 0.09) %/amu for $^{38}Ar/^{36}Ar$ and (1.26 ± 0.03) %/amu for $^{40}Ar/^{36}Ar$.

Although it is difficult to assign fractionation effects to either ion implantation, gas sputtering or diffusive loss after ion implantation in these experiments, it is obvious that significant isotopic fractionation is produced by low-energy ion implantation. One of these processes or a combination of them has potential implication for the isotopic evolution of planetary atmospheres. The magnitude of fractionation in other gases needs to be assessed.

References:

1. Pepin, R. O. (1992) Origin of noble gases in terrestrial planets in *Ann. Rev. Earth Planet Sci.* **20**, 389-430.
2. Niemeyer,S.and Marti,K (1981) *Proc. Lunar Planet. Sci. Conf.* **12**, 1177-1188.
3. Wacker, J.F. (1989) *Geochim. Cosmochim. Acta* **53**, 1421-1433.
4. Bernatowicz, T.J. and Podosek, F.A. (1986) *Geochim. Cosmochim. Acta* **51**, 1599-1611.
5. Frick, U., Mack, R. and Chang, S. (1979) *Proc. Lunar Planet. Sci. Conf. 10th; Geochim. Cosmochim. Acta Suppl.* **11**, 1961-1973.
6. Dziczkaniec, M., Lumpkin, G., Donohoe, K., and Chang, S. (1981) *Lunar Planet. Sci.* **XII**, 246-248.
7. Bernatowicz, T.J. and Fahey, A.J. (1986) *Geochim. Cosmochim. Acta* **50**, 445-452.
8. Bernatowicz, T.J. and Hagee, B.E. (1987) *Geochim. Cosmochim. Acta* **51**, 1599-1611.
9. Haff, P.K., Switkowski, Z.E. and Tombrello, T.A. (1978) *Nature* **272**, 803-804.
10. Weathers, D.L., Spicklemire, J. and Tombrello, T.A. (1992) submitted to *Nuc. Instr. Meth. B.*

N94-20698

GLOBAL BLACKOUT FOLLOWING THE K/T CHICXULUB IMPACT: RESULTS OF IMPACT AND ATMOSPHERIC MODELING; K.O. Pope, Geo Eco Arc Research, La Canada, CA 91011, A.C. Ocampo and K.H. Baines, Jet Propulsion Laboratory, Pasadena, CA 91109, and B.A. Ivanov, Institute for Dynamics of Geospheres, Russian Academy of Sciences, Moscow 117979.

Several recent studies have suggested that shock decomposition of anhydrite ($CaSO_4$) target rocks during the K/T Chicxulub impact would have ejected tremendous amounts of sulfur gas into the stratosphere (1-4). One of the many potential biospheric effects of this sulfur gas is the generation of a sulfuric acid (H_2SO_4) aerosol layer capable of causing darkness and severe disruption of photosynthesis for periods of years. In this paper we report the preliminary results of our modeling of shock pressures within the anhydrites and of light attenuation by the H_2SO_4 aerosol cloud. These models indicate that earlier studies over-estimated the amount of sulfur gas produced, but that more than enough was produced to extend global blackout conditions 4-6 times longer than the ~3 month predictions for silicate dust alone (5).

The exact size of the Chicxulub crater is not known, but the probable minimum is the 180 km diameter proposed by Hildebrand et al. (6) based on circular gravity anomalies. Pope et al. (7) suggest the crater diameter may be > 200 km, based on structural geology and hydrology. The Chicxulub crater may be a multi-ring basin with multiple ring fault systems and associated slump blocks. An inner ring, which has a diameter of 170 km, is demarcated by a semi-circular ring of sink holes that may correspond to the crater floor (7). Additional rings at greater diameters are suggested by the possible off-sets of Cretaceous strata (7).

Given the uncertainty of the size of the Chicxulub crater, we chose to model craters of 180 km and 300 km. These diameters correspond to transient crater diameters of 81 km and 126 km, based on the models of Croft (8) and Ivanov (9). For our model we assume a silicate bolide impacting at 20 km/s. When scaling laws are applied these diameters correspond to bolide diameters of 11 km and 19 km for the smaller and larger crater respectively. We used a model for a homogeneous stony target that is capable of tracing shock pressures in two dimensions. The average thickness of the sedimentary rocks that comprised the upper strata at Chicxulub in the Late Cretaceous was ~2.5 km, for which we estimate 60% was anhydrite and 40 % carbonate (3,7). Approximately 30 GPa of shock pressure is required for decomposition of these sedimentary rocks (10, 11). The model predicts that shock pressures would have exceeded 30 GPa within the sedimentary layer to a radius of 9.4 km from the center of impact for the small bolide and to 16.5 km for the large one. Based upon the predicted volume of vaporized sedimentary rock, we estimate that 2.7 or 8.2 x 10^{17} g of sulfur were vaporized for the two impact scenarios. These estimates are an order of magnitude less than some previous estimates (3,4).

We applied a radiative transfer model in the study of sunlight transmission through the proposed H_2SO_4 aerosol cloud generated by the Chicxulub impact. At this stage in our modeling we assume that most of the sulfur gas generated by the impact was ejected into the stratosphere, where it was globally distributed and rapidly

converted to H_2SO_4. The global H_2SO_4 stratospheric aerosol burden required to produce a global blackout is largely a function of particle radius and of the imaginary index of refraction (n_i), which is controlled by impurities in the aerosol. Global blackout is defined as an absorption optical depth (T_a) > 10 at a wavelength of 5000 A, which corresponds to total darkness. The true optical depth is much greater (~200) because absorption and multiple scattering occur.

Our model predicts that the amount of sulfur required for global blackout is a small percentage of the ejected sulfur mass predicted for the Chicxulub impact. Assuming a baseline sulfur ejection of 3 x 10^{17} g and 0.5 um diameter aerosols, ~0.3% of the ejected sulfur is required for global blackout for n_i = 0.03 (~7% of the value for soot); for n_i = 0.0025 (particles similar to volcanic dust) ~ 3% of the available sulfur is required. The two major factors controlling the duration of the blackout are particle sedimentation and coagulation, the latter of which causes rapid sedimentation when atmospheric loading is high and therefore limits the effects of large impacts (5). The model predicts a blackout duration of ~1.5 years for 0.5 um particles with n_i = 0.03, and ~1.0 year if n_i = 0.0025. These estimates represent minimum durations for the blackout event. Photosynthesis would be disrupted with an aerosol loading of about 5% of the blackout estimate, which could have lasted for 5-10 years.

In conclusion, our analyses show that global blackout is not very sensitive to our variable crater size estimates, and only a fraction of the sulfur produced need be converted to H_2SO_4 aerosol. The duration of the blackout is 4-6 times longer than that proposed for the dust alone (5), and therefore dramatic cooling of the surface and prolonged disruption of photosynthesis is indicated.

REFERENCES

(1) Brett, R. (1992), LPSC XXIII, 157-158.
(2) Perry, E.C., Winter, D.J, Sager, B., and Wu, B. (1992), LPSC XXIII, 1057-1058.
(3) Pope, K.O. and Ocampo, A.C. (1992), LPSC XXIII, 1097-1098.
(4) Sigurdsson H., D'Hondt, S., and Carey, S. (in press), Earth and Planet. Sci. Lett.
(5) Toon, O.B., Pollack, J.B., Ackerman, T.P., Turco, R.P., McKay, C.P., and Liu, M.S. (1982), GSA Spec. Paper 190, 187-200.
(6) Hildebrand, A.R., Penfield, G.T., Kring, D.A., Pilkington, M., Camargo Z., A., Jacobsen, S.B., and Boynton, W.V. (1991), Geology 19, 867-871.
(7) Pope K.O., Ocampo A.C., and Duller C.E. (1991), Nature 351, 105.
(8) Croft, S.K. (1985), Proc. Lunar Planet. Sci. Conf. XV, 828-842.
(9) Ivanov, B.A. (1989), LPSC XIX, 531-532.
(10) Florensky, C.P., Basilevsky, A.T., Ivanov, B.A. et al. (1983), Impact Craters on the Moon and Planets. Moscow, Nauka Press.
(11) O'Keefe, J.D. and Ahrens, T.J. (1989), Nature 338, 247-249.

563-47
ABS. ONLY

N94-20699

SCHOOLS OF THE PACIFIC RAINFALL CLIMATE EXPERIMENT, S.E. Postawko, Univ. of Oklahoma School of Meteorology/Ok. Space Grant Consortium, M.L. Morrissey, Oklahoma Climate Survey, Univ. of Oklahoma, G.J. Taylor and P. Mouginis-Mark, Planetary Geosciences/Hawaii Space Grant College

The SPaRCE program is a cooperative rainfall climate field project involving high school and college level students and teachers from various Pacific island and atoll nations. The goals of this program are both research and educational.

Climate change is one of our primary environmental concerns. Numerical models of the earth-atmosphere system have been developed in an effort to diagnose it's present state and predict future climate trends. These models require global observations of geophysical variables on a range of time and space scales. Perhaps the most required variable is rainfall. Unfortunately, rainfall observations are extremely sparse within the tropical oceans. Satellites, while offering excellent spatial coverage, must use algorithms to convert received radiance to rainfall. Thus, surface rainfall observations are required to test and validate satellite algorithms.

Climate change is of particular concern to people of the Pacific islands, due to the vulnerability of their islands to sea level changes.

The goals of the SPaRCE program are: 1) to foster interest and increase understanding among Pacific-area students and teachers of climate and climate change; 2) to educate the students and teachers as to the importance of rainfall in the Pacific area to climate studies; 3) to provide the students and teachers an opportunity of making a major contribution to the global climate research effort by collecting and analyzing Pacific rainfall data, and; 4) to incorporate collected rainfall observations into a comprehensive Pacific daily rainfall data base to be used for climate research purposes.

Schools participating in SPaRCE have received standard raingauges with which to measure rainfall at their sites. Students learned to site and use their raingauges by viewing a video produced at the University of Oklahoma. Four more videos will be produced which will include information on Earth's atmosphere, global climate and climate change, regional climate and implications of climate change, and how to analyze and use the rainfall data they are collecting. The videos are accompanied by workbooks which summarize the main points of each video, and contain concrete learning activities to help the student better understand climate and climate change. Following each video, interactive sessions are held with the students using the PEACESAT (Pan-Pacific Education And Communication Experiments by Satellite) satellite radio communication system.

At this time, approximately 12 schools, having a total of about 1000 students and teachers, are participating in the SPaRCE program. As long-term rainfall data are required for climate research, a specific aim of the SPaRCE program will be to ensure continuous raingauge measurements from year to year. It is hoped that the program can be expanded to include measurements of other climatological variables. So that schools in areas such as New Caledonia and French Polynesia may be included in this project, current plans call for all videos and workbooks to be translated into French.

564-91
ABS. ONLY

N94-20700

U-Pb ISOTOPIC AGES AND CHARACTERISTICS OF ANCIENT (>4.0 Ga) LUNAR HIGHLAND ROCKS;

W.R. Premo, U.S. Geological Survey, MS 963, Box 25046, Federal Center, Denver, CO 80225

A review of the present (and certainly sparse) U-Pb isotopic database for ancient (>4.0 Ga) lunar highland rocks indicates that both early-forming anorthosites and high-Mg suite rocks were formed from sources with a wide variety of $^{238}U/^{204}Pb$ (μ) values as early as 4.44 Ga. The U-Pb data from Apollo 16 anorthosites 67075, 60025, and 62337 [1,2] indicate source-μ values between ~35 and ~350; whereas values for high-Mg suite rocks are tentatively considered to be over 500 [3,4,5], similar to KREEP sources [6]. At present, I interpret the data to indicate that either early cumulates were formed slowly in a magma environment that allowed isotopic reequilibration or mixing over a long period of crystallization, or these cumulates formed from rapidly-evolving (both geochemically and isotopically) residual liquids. It is also possible that an early bombardment period played a role in the mixing process.

Four different decay schemes, K-Ar, Rb-Sr, Sm-Nd, and U-Pb, have predominantly been used for age determinations on lunar rocks. Each of these systems is not without problems when applied to lunar samples. In order for any single radiometric system to yield a primary crystallization age, it must remain closed from the time of crystallization until the present, without addition or loss of either parent or daughter isotopes. After many years of isotopic work, investigators have come to realize that most lunar samples (nearly all ancient highland samples) have been metamorphosed and their isotopic systematics disturbed [7]. U-Pb and Th-Pb isochron ages of lunar samples typically date metamorphic events [3]. Fortunately, there are two U-Pb systems that can be compared simultaneously in a concordia diagram to "look through" disturbances. This attribute of the U-Pb systems is most desirable when working with lunar samples, and helps to identify both the age of the rock and the age of the disturbance. A major drawback of this approach is the necessity for initial Pb corrections in order to calculate radiogenic Pb/U ratios [3]. Initial Pb compositions are typically defined by the y-intercepts on U-Pb and Th-Pb isochron diagrams, but because most U-Pb and Th-Pb isochrons for lunar samples are disturbed, the initial Pb values are undefined and therefore must be assumed. This situation has been confronted with norite 78235 [4] and troctolite 76535 [3]. A possible solution to the problem is to use an age (hopefully accurate), perhaps determined using one of the other dating techniques, and calculate the initial Pb values that produce the same age with the two U-Pb systems. Whereas this procedure relies on an accurate age for the rock, the resulting initial Pb information can be used to characterize the source magma as is done with initial Sr and Nd values, and can have important implications for models of the petrogenesis of lunar magma sources through time.

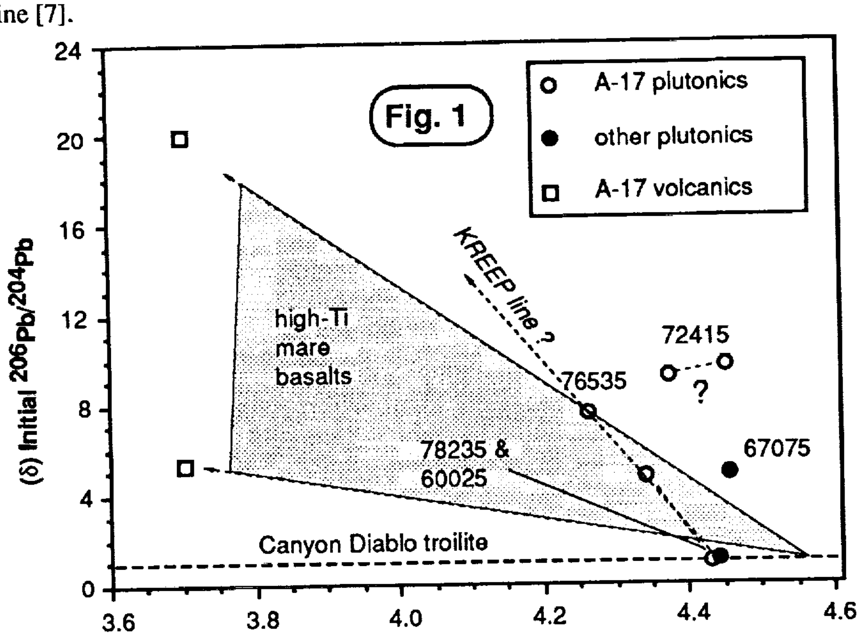
Because the various isotopic systems are disturbed differently during metamorphism, most samples yield conflicting ages when using the different dating schemes on the same sample. Whereas the discrepancy in ages is usually interpreted as a result of open-system behavior due to metamorphic disturbances that characterize lunar rocks, other factors may cause age disparity as well, including either the misuse of basic assumptions regarding the isotopic techniques (e.g. U-Pb), or a lack of understanding of lunar petrogenesis (isotopic closure ages vs. ages of crystallization), or a combination of these factors. One possibility that cannot be dismissed is whether the disparity in ages reflects very slow cooling and crystallizing of the parent magma, particular at depth in the lunar crust, and therefore the differences in isotopic closure temperatures of the various radiometric systems rather than the age of crystallization of the rock [4,7]. The isotopic data from ancient highland samples collected during the Apollo missions have many of these problems, so that at present investigators have only a very limited, reliable (as well as precise), isotopic database to work from. Interpretations on the magmatic ages and origins of at least the ancient highland rocks are therefore tentative at best.

Over the past five years we have analyzed Apollo 16 anorthosites 67075, 60025, and 62337 [1,2] and Apollo 17 high-Mg suite cumulates (troctolite 76535 [3], norite 78235 [4], and dunite 72415 [5]) in an effort to discover an earliest lunar Pb isotopic composition and accompanying U/Pb value, both of which may have important implications on our understanding of early lunar magmatic processes and evolution of a magma ocean. In general, U-Pb isotopic systematics are better behaved in the high-Mg suite rocks than in anorthosites that have shown evidence of mineral assemblages of mixed parentage [1,2,8]. Our results strongly suggest that plagioclase assemblages of the ferroan anorthosites, although geochemically uniform [8,9], are derived from isotopically different sources (μ = ~35 but up to ~350), but essentially during the same geologic event (formation of an outermost feldspathic crust) between 4.42 and 4.45 Ga [2,10]. Magnetic mineral assemblages, including olivines and pyroxenes, may or may not have crystallized at this same time. Most of the U-Pb isotopic evidence from magnetic mineral separates indicate that they are either derived from distinctly different liquids (isotopically speaking) than some of the plagioclase separates or formed at a younger time [2]. For example, one magnetic separate from anorthosite 60025, M-1, contains material that is younger than the plagioclase and may have been derived from a source with μ ~12 at 4.32 Ga.

U-Pb ISOTOPES OF ANCIENT LUNAR ROCKS: Premo, W.R.

The oldest high-Mg suite rocks are norite 78236 (assuming 4.425 Ga age) and dunite 72417 at ~4.45 Ga. These rocks are then followed by norite 77215 (~4.37 Ga), troctolite 76535 (~4.26 Ga), gabbronorite 73255 (~4.23 Ga), and norites 73215 and 78155 (~4.17 Ga), although the latter may not be primary ages. Accepting these minimum estimates, high-Mg suite formation appears to have continued from ~4.45 to ~4.15 Ga [7]. However, depending on the investigators interpretation of the isotopic age data, it is also possible to consider a much smaller magmatic interval. For example, we might question the Rb-Sr isochron age for dunite 72417, largely dependent on the mineral, olivine, previously noted to be highly altered and possibly isotopically unreliable or disturbed [5] in some of these samples. A "best guess" Pb-Pb age of ~4.37 Ga was reported by [5] for 72415. Conflicting Sm-Nd isochron ages of 4.43 and 4.34 Ga are not supported by other isotopic age results, resulting in some uncertainty of the true age of norite 78236 [7]. If we accept the younger age for this norite and assume that 73215 and 78155 are probably older than 4.17 Ga, then we find that most of the noritic-troctolitic (and probably dunitic) ages lie within a range of ~140 million years (4.37 to 4.23 Ga).

From these ages, we can construct Pb evolution curves for ancient lunar highland rocks as shown in Fig. 1. The initial $^{206}Pb/^{204}Pb$ (R) data is normalized ($\delta = R_m / R_{CD}$) to Canyon Diablo (CD) troilite ($\delta = 1$). The Pb isotopic data is too sparse and imprecise to make confident generalizations; however, the coherence of the data between anorthosite 60025 and norite 78236 would suggest that high-Mg suite rocks and ferroan anorthosites were both forming simultaneously during differentiation of the lunar magma ocean. Large uncertainties in the U-Pb data of 67075 and 72415 leaves these analyses in question, although an unpublished Sm-Nd internal isochron age of 4455 ± 140 Ma for 67075 indicates that it was also formed early. An interesting line of ascent is indicated by anorthosite 60025, norite 78235/6, and troctolite 76535, suggesting derivation from magma sources that are progressively evolving to higher $^{238}U/^{204}Pb$ and corresponding initial $^{206}Pb/^{204}Pb$ values, similar to the Sm-Nd KREEP line [7].



I tentatively suggest that either early cumulates were formed slowly in a magma environment that allowed isotopic reequilibration or mixing over a long period of crystallization, or these cumulates formed from rapidly-evolving (both geochemically and isotopically) residual liquids. It is also possible that an early bombardment period played a role in the mixing process.

References: [1] Premo W.R., Tatsumoto M., and Wang J.-W. (1988) Proc Lunar Conf 19th, pp. 61-71. [2] Premo, W.R. and Tatsumoto, M. (1993) U-Pb Isotopic Systematics of Anorthosite 60025. In Lunar and Planetary Science XXIV, pp. 00-11. Lunar and Planetary Institute, Houston. [3] Premo W.R. and Tatsumoto M. (1992) Proc Lunar Planet. Sci., v. 22, pp. 381-397. [4] Premo W.R. and Tatsumoto M. (1991) Proc Lunar Planet. Sci., v. 21, pp. 89-100. [5] Premo W.R. and Tatsumoto M. (1992) Lunar Planet. Sci. XXIII, pp. 1103-1104. [6] Tatsumoto M., Nunes P.D., and Unruh D.M. (1977) In The Soviet-American Conference on Cosmochemistry of the Moon and Planets (J.H. Pomeroy and N.J. Hubbard, eds.), pp. 507-523. NASA, Washington, D.C. [7] Nyquist, L.E. and Shih, C.-Y. (1992) GCA 56, 2213. [8] Premo W.R. and Tatsumoto M. (1989) Lunar Planet. Sci. XX, pp. 866-867. [9] Ryder, G. (1982) GCA 46, pp. 1591-1601. [10] Premo, W.R. and Tatsumoto M. (1992) abstract from the Apollo 17 Workshop, LPI, Houston, in press.

U-Pb PROVENANCE AGES OF SHOCKED ZIRCONS FROM THE K-T BOUNDARY, RATON BASIN, COLORADO;

W.R. Premo and G.A. Izett, U.S. Geological Survey, Denver Federal Center, Denver, CO 80225

P_2

U-Pb isotopic systematics from analyses of single zircons identify at least two provenance ages, ~575 Ma and ~330 Ma, for zircons from the impact layer of the K-T boundary, Raton Basin, Colorado. These data are a preliminary confirmation of results reported from the same layer [1]. The zircon provenance ages provide a unique signature for identification of the source crater since igneous rocks of these ages (or sedimentary rocks derived from them) must characterize part of the impact stratigraphy.

The K-T boundary interval in Western North America consists of a pair of thin claystone layers deposited in isolated coal swamps that extended from New Mexico to Alberta, Canada [1,2,3]. Both layers contain impact ejecta; the lower layer contains clay or phosphate pseudomorphs of tektites [4], and the upper layer contains a concentration of large shocked minerals and a major Ir anomaly [1,2,3]. These data, combined with the fact that the two layers are separated by a sharp contact, persuaded Izett [5] and Shoemaker and Izett [6] to conclude that the layers record two closely-spaced impact events. Altered tektites in the lower layer and large (0.65 mm) shocked minerals in the upper layer allegedly were derived from the Chicxulub and Manson impact events, respectively.

Heavy-mineral concentrates of the HF-insoluble residue from the upper layer in the Raton Basin contain zircon, tourmaline, garnet, allanite, epidote, and hornblende [1,3]. Krogh et al. [7] showed that the zircon crystals exhibit various types of shock effects, including multiple sets of shock lamellae and mosaicism. Our microscopic study of heavy-mineral concentrates from the upper K-T boundary layer shows that shocked zircons are most abundant at the Clear Creek North (CCN) site south of Trinidad, Colo. Mainly, the zircons are brown, opaque, and granular, but some are transparent and pale champagne in color. They typically are rounded crystals, 100-250-μm long. Several crystals are twinned and a few others have offset healed fractures. About 25 zircon crystals were studied optically; most show clear indications of shock metamorphism. From this group, we report U-Pb analyses from 4 zircons, including two euhedral crystals and two fragments that exhibited polycrystalline domains characterized by various degrees of transparency and color, probably reflecting variable-shock pressure. Zircon 1(40) was gray and opaque, whereas zircons 3(40) and 5(40) were translucent and light-brown to gray. In contrast, zircon 4(40) was translucent and yellowish-tan.

Table 1: U-Pb isotopic data of shocked zircons from the K-T boundary at CCN

Sample	Wgt. (μg)	U‡ (ppm)	Pb‡ (ppm)	$^{206}Pb/^{204}Pb$†	$^{206}Pb/^{238}U$§	$^{207}Pb/^{206}Pb$§	Age*
1(40) (whole grain)	9	1040	38	467 (0.133)	0.03291 (0.276)	0.05214 (0.258)	292
3(40) (whole grain)	4.5	650	62	354 (0.169)	0.07909 (0.284)	0.05886 (0.182)	562 ±4
4(40) (fragment)	4	460	40	299 (0.168)	0.06879 (0.431)	0.05905 (0.198)	569 ±4
5(40) (fragment)	6	820	48	281 (0.083)	0.05096 (0.293)	0.05792 (0.172)	527 ±4

‡ - The sample weights were determined using a Cahn 4100 electrobalance with an apparent minimum error of ~±0.35 μg, leading to minimum errors of ±4 to ±10% in these concentration values.

† - These values are raw data and not corrected for laboratory blank (12 pg total Pb: 206/204 = 18.57; 207/204 = 15.33; and 208/204 = 37.81) or mass fractionation (0.13 ± 0.05% per a.m.u.). Values in parentheses are two-sigma errors in percent). Instrumental biases were monitored through replicate analyses of NBS Pb Standard 983.

§ - Radiogenic values corrected for laboratory blank (12 pg total Pb), mass fractionation, and initial Pb (assuming Stacey & Kramer model Pb values at 65 Ma).

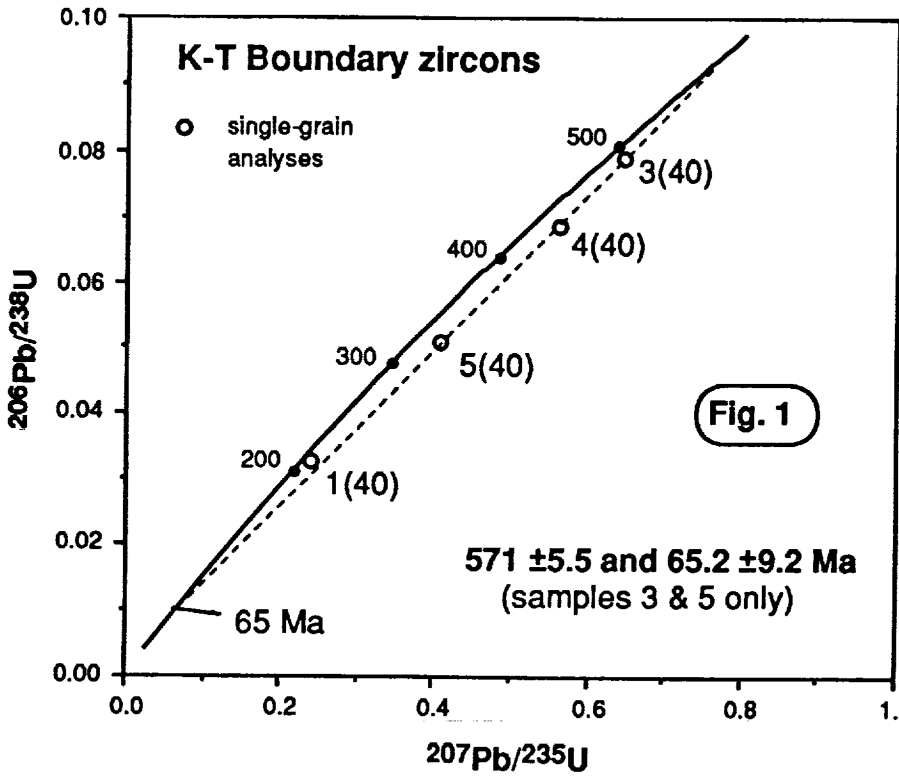
* - $^{207}Pb/^{206}Pb$ age in Ma. Errors are given at the 95% C.L.

Analytical methods used were the same as those given in [8], using the multi-sample, vapor-dissolution technique of Krogh [9]. All ages and errors are calculated using [10].

The U-Pb data (Table 1) of four analyses are neither concordant nor co-linear (Fig. 1). However, these zircons were shocked (and possibly annealed), transported, and deposited during (and possibly immediately just after) the K-T boundary impact event. Therefore, it is reasonable to assume that the impact event, which we know occurred at 65 Ma [11], may have incurred significant Pb loss in these grains. Three of the four data form an array between ~578 and 66 Ma, however, with very large errors. Sample 1(40), in contrast, yields a $^{207}Pb/^{206}Pb$ age of 292 Ma (~30% discordant). This analysis has an upper-intercept age of ~330 Ma, assuming a lower-intercept age of 65 Ma, which is similar to two of the fourteen analyses of [1]. Our other three data are similar to results from twelve of the fourteen analyses of [1] that yield concordia intercept ages of 65 ±3 Ma and 550 ±10 Ma. However, sample 4(40), which is petrographically different, lies just off our array and defines an upper-intercept age of 590 ±5

Ma, assuming a lower-intercept age of 65 Ma. This slight deviation outside of analytical precision is seen in at least two of the data of [1] and leads us to believe that there is a grouping of zircon ages between ~550 and 600 Ma, but apparently dominated by ages around 550 Ma [1]. Samples 3(40) and 5(40) are petrographically similar and yield a line that intersects concordia at 65.2 ±9.2 Ma and 571 ±5.5 Ma (dashed line; Fig. 1), nearly matching the results of 65.5 ±3 Ma and 559 ±5 Ma from four analyses of polycrystalline zircon grains [1].

Because these results scatter significantly beyond that allowed by analytical precision strongly suggests to us that the source of the shocked material in the upper layer of the K-T boundary in North America was composed of rocks (or sedimentary rocks derived from them) of several ages. Previously, the upper layer was thought to be ejecta from the Manson crater of central Iowa because of the abundance of shocked quartz and feldspar [4]. If this contention is true, then our zircon ages and those of [1] serve as a unique signature to match against the impact stratigraphy at the Manson site (a study to investigate the zircon contents of selected horizons at Manson is presently under way). Late Proterozoic, Paleozoic, and Mesozoic sedimentary rocks are a major part of the Manson impact stratigraphy [12] and many of these units, if not a mixture of them, could be the zircon source. Intuitively, it would appear that the impact stratigraphy at Manson should contain zircon populations at least partially derived from the surrounding Archean-Proterozoic shields, and the fact that none of the nineteen analyzed grains are older may suggest an alternative source crater.



Although reliable radiometric ages have not been reported for the Paleozoic basement at the Chicxulub impact site on the Yucatan peninsula of Mexico [13], it is probable that Pan-African (ca. 500-700 Ma) orogenic rocks or their metamorphic equivalents underlie the thick Cretaceous cover [14]. Similar zircons have been retrieved from the K-T boundary on Haiti. The present interpretation of two layers at most North American K-T boundary sites suggests two separate impact events; however, it is also possible that the shocked material in at least the upper layer was derived from different source rocks during simultaneous multiple impacting.

References: [1] Izett G.A. and Pillmore C.L. (1985) Geol. Soc. Am. Abstracts Prog. 17, p. 617. [2] Izett G.A. (1991) U.S. Geol. Surv. Open-File Rept. 87-606, 125p. [3] Izett G.A. (1990) Spec. Pap. Geol. Soc. Am. 249, 100 pp. [4] Izett G.A. (1991) J. Geophys. Res. 96, E4, pp. 20879-20905. [5] Izett G.A. (1991) EOS 72, p. 279. [6] Shoemaker E.M. and Izett G.A. (1992) Lunar Planet. Sci. 23, pp. 1293-1294. [7] Krogh T.E., Kamo S.L., and Bohor B.F. (1992) (abstract) in Sudbury 1992 Conference: Large Meteorite Impacts and Planetary Evolution, pp.44-45. [8] Premo W.R., Helz R.T., Zientek M.L., Langston R.B. (1990) Geology 18, pp. 1065-1068. [9] Krogh T.E. (1978) (abstract) in U.S. Geol. Surv. Open-File Rept. 78-701, pp. 233-234. [10] Ludwig K.R. (1987) U.S. Geol. Surv. Open-File Rept. 85-513, 47 p. [11] Izett G.A., Dalrymple G.B., and Snee L.W. (1991) Science 252, pp. 1539-1542. [12] Hartung J.B. and Anderson R.R. (1988) Lunar Planet. Sci. 19, pp. 455-456. [13] Hildebrand A.R. and Penfield G.T. (1990) (abstract). EOS 71, p. 1425. [14] Ramos E.L. (19??) in Geology of Mexico ??, pp. 257-282.

566-25 ABS. ONLY

N94-20702

p. 2

U-Pb ISOTOPIC SYSTEMATICS OF FERROAN ANORTHOSITE 60025;
W.R. Premo and M. Tatsumoto, U.S. Geological Survey, Denver, Co. 80225

Preliminary U-Pb isotopic data from separates of ferroan anorthosite 60025 confirm its antiquity at ~4.42 Ga. Three Pb-Pb isochron ages involving different sets of mineral separates vary by only 20 million years, but indicate derivation of the sets from isotopically distinct magma sources. If this anorthosite was a monomict cumulate product formed during the Moon's early primary differentiation stage, then residual liquids of crystallizing magmas were evolving isotopically, even at the cm-scale, over the duration of the crystallization period. Another explanation is that this sample is simply a polymict breccia and that the Pb isotopic results are a result of subsequent mechanical mixing of mineral assemblages from various cumulate piles formed coevally at ~4.42 Ga from isotopically distinct magma sources.

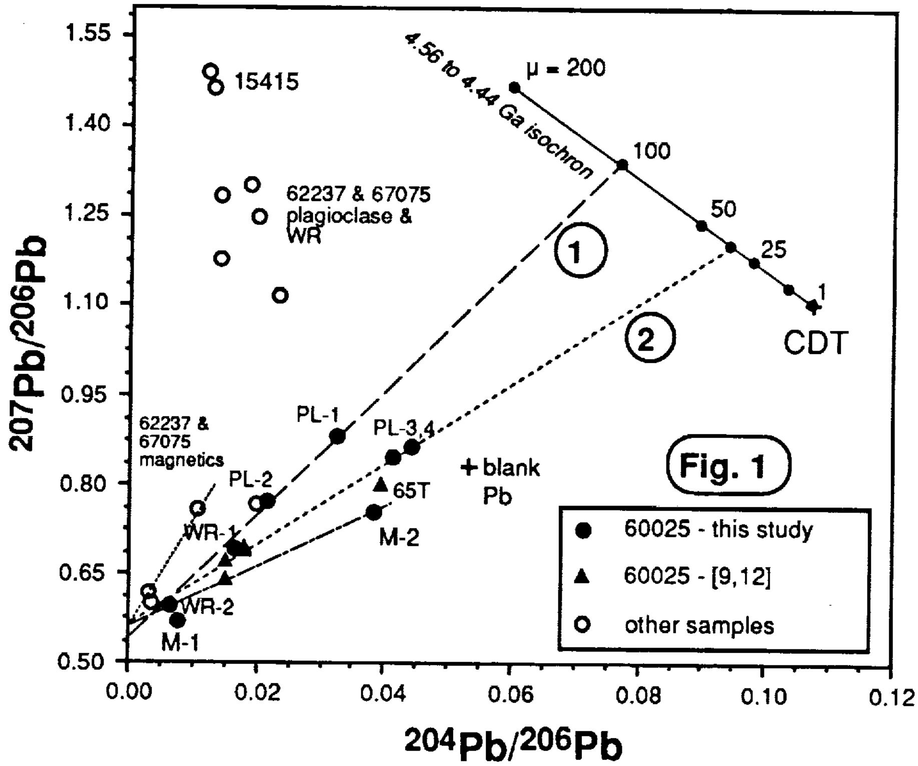
In our ongoing search for early lunar Pb isotopic compositions, we have analyzed Apollo 16 anorthosites 67075 and 62337 [1] and Apollo 17 high-Mg suite cumulates (troctolite 76535 [2], norite 78235 [3], and dunite 72415 [4]). The U-Pb isotopic systematics have been better behaved in the high-Mg suite rocks than in the anorthosites that have shown evidence of mineral assemblages of mixed parentage [1,5]. Our aim in analyzing anorthosite 60025 was to avoid or minimize this problem as it had been considered essentially monomict [6], although recent work by [7] has shown that not only is 60025 polymict, but shows textural evidence of at least two episodes of deformation. Of the five splits studied by [7], the four mineral splits appeared monomict, whereas the whole-rock split was considered polymict. Previous isotopic work indicated that this anorthosite was quite primitive [8], a claim that was apparently confirmed by the U-Pb isotopic age of 4.51 ±0.01 Ga on three plagioclase separates [9]. However, a Sm-Nd internal isochron age of 4.44 ±0.02 Ga was determined using plagioclase, olivine, and mafic mineral separates [10], creating some doubt about the anorthosite's true age. It was pointed out by [2] that the use of slightly evolved initial Pb values (corresponding to a source-μ value of ~ 35) to correct the U-Pb data of [9] can result in an U-Pb age of 4.44 Ga. The need to resolve the age and isotopic nature of this anorthosite is paramount to furthering our understanding of processes of ferroan anorthosite formation as well as the magmatic history of the early Moon.

Our analytical procedures are not very different than those used in [2,3]. The original subsample of three pieces weighed approximately 1.28 gm and was shaken in a sealed quartz vial until no further disaggregation occurred. The largest chip was removed and treated as a separate split (025C), and was further crushed, sieved, and magnetically split into four separates; hand-picked plagioclase (PL-3), a +150-μm, non-magnetic separate (PL-4), a -150-μm, non-magnetic separate (PL-1), and a magnetic separate (M-2). Two other chips from the shaking were analyzed as whole-rocks (WR-1 and WR-2). The remainder of the shaken material was considered loose matrix (025M) and was subsequently sieved and magnetically-split as well (a -150 μm, non-magnetic separate (PL-2) and a magnetic separate (M-1)). All of these fractions were subjected to alcohol washing and three dilute acid leachings (two HBr and one HNO_3) designed to remove terrestrial contamination and strip the grain surfaces of any adsorbed Pb component [11]. The Pb isotopic results from only the residues of these separates (washes and leaches will be analyzed soon) are shown in Figure 1 and compared to results from other anorthosites.

The residues (solid circles and triangles) of 60025 do not form an array, but are instead scattered inside of a triangle defined by CDT [13], anorthosite 15415 [14], and the radiogenic Pb composition of each separate, typically near 4.4 Ga (Fig. 1). However, three arrays or isochrons, defining ages ~4.41 to 4.43 Ga, can be constructed using the 60025 Pb data. PL-3 & 4 that represent the cleanest plagioclase separates from the large chip, 025C, lie on the same array as the three plagioclase separates from [9], yielding a $^{207}Pb/^{206}Pb$ age of 4431 ±15 Ma (short dashed line, marked 2). Another array, connecting PL-1 & 2 that are both very fine-grained plagioclase separates, one from the chip and the other from the loose matrix, defines a $^{207}Pb/^{206}Pb$ age of 4409 ±65 Ma (long dashed line, marked 1). The two magnetic separates, M-1 & 2, do not lie on either of these arrays, but plot below and indicate a younger age of 4316 ±65 Ma. An apparent isochron connects M-2 (from the chip), the mafic fraction from [9], and WR-2, yielding a $^{207}Pb/^{206}Pb$ age of 4422 ±10 Ma (94% prob. of fit; dot-dashed line). It is not obvious why these three separates should align so well, although M-2 and the mafic fraction of [9] are similar separates and WR-2, the larger of the two, may have contained a larger proportion of radiogenic-Pb-rich minerals. Nonetheless, it is possible that this array forms a pseudochron that just perchance defines the correct age. The two whole-rock separates, WR-1 & 2, plot between the plagioclase and magnetic separates, indicating that they are mixtures of the different Pb components.

Th U-Pb isotopic results (not shown) are not complete at present, but preliminary results from four of the separates indicate clear discrepancies in the use of initial Pb values from one separate to the next for correction of the U-Pb data. This problem appears to support our contention that these separates were derived from isotopically

U-Pb ISOTOPES OF ANORTHOSITE 60025: Premo, W.R. and Tatsumoto, M.



distinct sources. However, some consolation, the use of initial Pb values calculated assuming a source, single-stage Pb evolution between 4.56 and 4.44 Ga and a μ value of 35 (indicated by line #2) does produce a U-Pb concordia upper-intercept age of 4.433 Ga and a lower-intercept age of 230 Ma. Assuming this lower-intercept age as the time of some isotopic disturbance to all the material in 60025, an upper-intercept age of 4330 ±13 Ma is defined for the mafic fraction of [9] that agrees well with the Pb-Pb age of 4.32 Ga for M-1.

Our interpretation of these preliminary results is tentative at present, but the data would strongly suggest that plagioclase in 60025, although geochemically very similar [7], is derived from isotopically different sources (μ ~100 and μ ~35), but at essentially the same time (geologically speaking). The magnetic minerals may or may not be mixtures of 4.42 Ga and younger material. If some were formed at 4.42 Ga with the plagioclase, then they were derived from yet another isotopically distinct liquid (μ ~1). Certainly M-1 contains material that is younger than the plagioclase and may have been derived from a source with μ ~12 at 4.32 Ga. The variability in source-μ values is not uncommon for ancient (>4.0 Ga) lunar rocks [2,15]. An example is illustrated in Figure 1 with the magnetic separates from anorthosite 67075 that indicate a $^{207}Pb/^{206}Pb$ age of 4422 ±50 Ma and a source–μ value of ~250 that is clearly different than that of ~350 for 67075 plagioclase separates [1]. Although the source-μ values are different, the age is very similar to an unpublished Sm-Nd internal isochron age of 4.45 ±0.1 Ga for 67075. The same general pattern was obtained for separates from troctolitic anorthosite 62237 [1]. We tentatively suggest that either early cumulates were formed in a magma environment that allowed isotopic reequilibration or mixing over the duration of the crystallization period, or these anorthosites are mechanical mixtures of geochemically-similar, but isotopically different, mineral assemblages. Perhaps early bombardment played a role in the mixing process, although intuitively it would seem that later impacting events caused brecciation in this sample as is the rule in most lunar samples.

References: [1] Premo W.R., Tatsumoto M., and Wang J.-W. (1988) Proc Lunar Conf 19th, pp. 61-71. [2] Premo W.R. and Tatsumoto M. (1992) Proc Lunar Planet. Sci., v. 22, pp. 381-397. [3] Premo W.R. and Tatsumoto M. (1991) Proc Lunar Planet. Sci., v. 21, pp. 89-100. [4] Premo W.R. and Tatsumoto M. (1992) Lunar Planet. Sci. XXIII, pp. 1103-1104. [5] Premo W.R. and Tatsumoto M. (1989) Lunar Planet. Sci. XX, pp. 866-867. [6] Ryder, G. (1982) GCA 46, pp. 1591-1601. [7] James, O.B., Lindstrom, M.M., and McGee, J.J. (1991) Proc Lunar Planet. Sci., v. 21, pp. 63-87. [8] Papanastassiou, D.A. and Wasserburg, G.J. (1972) EPSL 17, pp. 52-?. [9] Hanan, B.B. and Tilton, G.R. (1987) EPSL 84, pp. 15-21. [10] Carlson, R.W. and Lugmair, G.L. (1988) EPSL 90, pp. 119-130. [11] Tatsumoto, M. (1970) Proc Lunar Conf 1st, pp. 1695-1612. [12] Tera, F. and Wasserburg, G.J. (1972) EPSL 17, pp. 36-51. [13] Tatsumoto, M., Knight, R.J., and Allegre, C.J. (1973) Science 180, pp. 1279-1283. [14] Tera F., Ray L.A., and Wasserburg G.J. (1972) in The Apollo 15 Lunar Samples (J.W. Chamberlain and C. Watkins, eds.), pp. 396-401. [15] Premo, W.R. and Tatsumoto M. (1992) abstract from the Apollo 17 Workshop, LPI, Houston, in press.

567-25
ABS. ONLY

N94-20703

THERMAL CONDUCTIVITY MEASUREMENTS OF PARTICULATE MATERIALS UNDER MARTIAN CONDITIONS

M.A. Presley and P.R. Christensen, Dept. of Geology, Arizona State University, Tempe AZ 85287

The mean particle diameter of surficial units on Mars has been approximated by applying thermal inertia determinations from the Mariner 9 Infrared Radiometer and the Viking Infrared Thermal Mapper data together with thermal conductivity measurements [1,2]. Several studies [e.g. 2,3,4] have used this approximation to characterize surficial units and infer their nature and possible origin. Such interpretations are possible because previous measurements of the thermal conductivity of particulate materials have shown that particle size significantly affects thermal conductivity under martian atmospheric pressures [e.g. 5,6,7]. The transfer of thermal energy due to collisions of gas molecules is the predominant mechanism of thermal conductivity in porous systems for gas pressures above about 0.01 torr [6]. At martian atmospheric pressures the mean free path of the gas molecules becomes greater than the effective distance over which conduction takes place between the particles. Gas particles are then more likely to collide with the solid particles than they are with each other. The average heat transfer distance between particles, which is related to particle size [8], shape and packing, thus determines how fast heat will flow through a particulate material.

The derived one-to-one correspondence of thermal inertia to mean particle diameter implies a certain homogeneity in the materials analyzed. Yet the samples used [5] were often characterized by fairly wide ranges of particle sizes with little information about the possible distribution of sizes within those ranges. Interpretation of thermal inertia data is further limited by the lack of data on other effects on the interparticle spacing relative to particle size, such as particle shape, bimodal or polymodal mixtures of grain sizes and formation of salt cements between grains. Furthermore, the thermal conductivities used in the derived correspondence were measured in a nitrogen-oxygen atmosphere (air) at room temperature. Temperature effects are expected to be minimal [11]. Thermal conductivities measured in a carbon-dioxide atmosphere are, however, consistently smaller than those measured in air by a small but significant amount (~7%) [9,10].

To address these limitations and to provide a more comprehensive set of thermal conductivities vs. particle size a linear heat source apparatus, similar to that of Cremers [12,13], was assembled to provide a means of measuring the thermal conductivity of particulate samples. In order to concentrate on the dependence of the thermal conductivity on particle size, initial runs will use spherical glass beads that are precision sieved into relatively small size ranges and thoroughly washed. All size ranges to be used have less than a 10 µm spread, except for the two largest samples (500-520 µm and 250-275 µm), and several samples have a spread of 5 µm or less. The total range of sizes to be examined is 10 µm to 500 µm.

Some of the preliminary data collected so far in the particle size analysis are plotted as thermal conductivity vs. pressure in Figure 1. The data fit a smooth curve with a deviation of less than 6%. Individual measurements appear to have a repeatability to within 7%, based on three duplicate measurements. These measures of inaccuracy are consistent with error analyses of the technique [14,15,16].

The thermal conductivity of 500-520 µm glass beads in carbon dioxide atmosphere are compared to previous data collected for similar grain sizes (Fig. 1): 470 µm glass beads [7] and 590-840 µm quartz sand [17]. The thermal conductivity vs. pressure trend measured in this study parallels that of the 470 µm glass beads, but with significantly lower values. This is expected in part because the 470 µm glass beads were examined under a nitrogen-oxygen atmosphere (air) and in part because the comparative method that was used to determine their thermal conductivity yields higher thermal conductivity values than any other method [6]. The trend for the quartz sand, however, has a much steeper slope than that of the glass beads for

pressures greater than around 0.5 torr. This deviation could simply be a peculiarity of the probe technique, which is known to be less accurate than the linear heat source method at low pressures [5,6]. Another possibility is that the steeper trend is caused by differences in the interparticle spacing of the samples, due either to a difference in grain shape (angular sand vs. spherical glass bead) or to a heterogeneity in sample particle size due to the rather wide range of grain sizes used in [17].

Some initial data from particle size mixing in this study should be ready for discussion at conference time and may help to shed some light on this question. The affects of the heterogeneity of samples will be examined by considering two component systems, varying the abundance of the fine component from 0 to 100% by 10%. In these experiments the 250 µm material will be the coarse fraction and the 75 µm material will be the fine fraction. Later runs will also be made on real eolian and fluvial sediments to determine the effects of natural distributions of particle sizes and to determine how these compare to the controlled set of experiments. This project will also examine the affect of particle shape by using angular grains (ground quartz), sieved and washed to the same size ranges as the glass beads, and platy clays. Salt encrusted samples will also be prepared in the lab in order to measure the effect of cements on the thermal conductivity of granular materials.

When complete this study will provide a refined correspondence of particle size to thermal conductivity at various pressures of carbon dioxide expected on the martian surface. The additional measurements on grain shape, heterogeneous mixtures and salts will provide additional information that would be necessary in the interpretation of the nature of surficial deposits using thermal data.

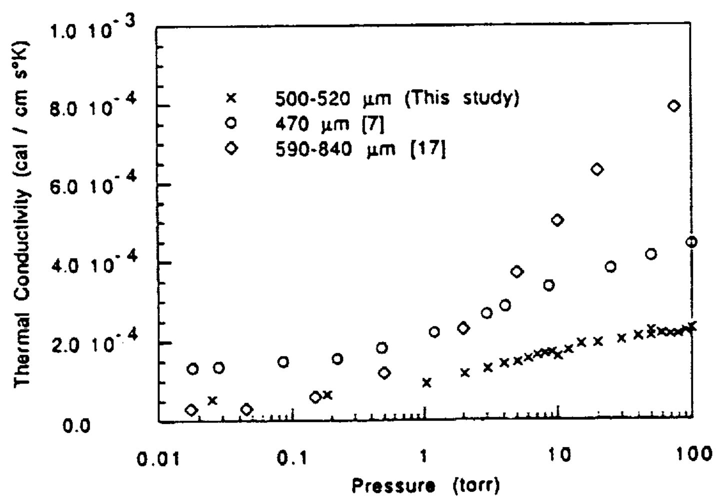


Fig.1: A comparison of effective thermal conductivity vs. pressure for glass beads analyzed in this study with that for glass beads [7] and quartz sand [17] analyzed in previous studies.

References: [1] Kieffer et al. (1973), *J. Geophys. Res.* **78**, 4291-4312. [2] Kieffer et al. (1981), *Proc. Lunar Planet. Sci. Conf.* **12B**, 1395-1417. [3] Presley and Arvidson (1988), *Icarus* **75**, 499-517. [4] Edgett and Christensen (1991), *J. Geophys. Res.* **96**, 22765-22775. [5] Wechsler and Glaser (1965), *Icarus* **4**, 335-352. [6] Wechsler et al. (1972), *Thermal characteristics of the moon*, pp. 215-241. [7] Masamune and Smith (1963), *I & EC Fund.* **2**, 136-143. [8] Schotte (1960), *AIChE Journal* **6**, 63-67. [9] Kistler (1935) *J. Phys. Chem.* **39**, 79-85. [10] Prins et al. (1950) *Physica* **16**, 379-380. [11] Fountain and West (1970), *J. Geophys. Res.* **75**, 4063-4069. [12] Cremers (1971), *Rev. Sci. Instr.* **42**, 1694-1696. [13] Cremers (1970), *ASME Proc. Symp. Thermophys. Prop. 5th.* 391-495. [14] Blackwell (1956), *Can. J. Phys.* **34**, 412-419. [15] Blackwell (1959), *J. Appl. Phys.* **25**, 137-144. [16] Scott et al. (1973), *Rev. Sci. Instrum.* **44** 1058-1063. [17] Woodside and Messmer (1961), *J. Appl. Phys.* **32**, 1688-1699.

368-90
ABS. ONLY
N94-20704

ELEMENTAL DEPLETIONS IN ANTARCTIC MICROMETEORITES AND ARCTIC COSMIC SPHERULES: COMPARISON AND RELATIONSHIPS

T. Presper, G. Kurat (Naturhistorisches Museum, Burgring 7, A-1014 Wien, Austria); C. Koeberl (Institut f. Geochemie, Universität Wien, Dr. Karl-Lueger-Ring 1, A-1010 Wien, Austria); H. Palme (MPI f. Chemie, Saarstraße 23, D-6500 Mainz, Germany) and M. Maurette (CSNSM, Bat. 108, F-91405 Campus Orsay, France)

Antarctic micrometeorites (MMs) and Arctic cosmic spherules (CSs) have bulk compositions comparable to those of chondritic meteorites. However, abundances of Na, Ca, Mn, Ni, Co, and S are commonly lower in MMs and CSs as compared to chondrites. Our SEM, EMP, and INAA studies suggest that these elemental depletions in unmelted MMs are likely to be due to leaching of soluble components from the MMs in the upper atmosphere and the melt ice water. Depletions in CSs appear to be mainly due to volatilization during melting in the atmosphere or to sampling bias during aggregate formation or parent rock break-up.

It was shown by several authors (e.g., /1-5/) that MM and CS abundance patterns display various exceptions from their more or less chondritic composition. Besides enrichments, which have been observed for volatile elements like K and Br (also observed in stratospheric interplanetary dust particles) and are currently explained by contaminations produced in the atmospheric E-Layer /6/, a variety of depletions are present. Unmelted, fine-grained phyllosilicate-bearing micrometeorites (PHs), which consist of a matrix-like material similar to that present in CI and CM chondrites, have depletions in Na, Ca, Ni, Co, S and often in Mg and Mn. The same holds for partially melted, scoriaceous particles (SCs). Completely melted CSs show depletions in Na, sometimes in Ca, and commonly in Ni and Co. Depletions of Na and also of Ni and Co tend to be stronger in CSs than in MMs. On the other hand larger depletions of Ca, Mg and Mn are observed in MMs. Both MMs and CSs have +/- flat chondrite normalized REE patterns. Volatile elements (such as Na and S) can be removed from CSs and SCs by volatilization during atmospheric entry while this cannot be the case for unmelted PHs. For CSs depletions in Ni and Co are suggestive of metal-silicate-fractionation. Such a process should yield Ir/Ni-ratios <CI. This is observed for some CSs but others and also some PHs even show Ir/Ni-ratios >CI. Alternatively Ni and Co depletions could be produced by loss of an Ir-free Ni-bearing phase which must have taken place before entry into the atmosphere. Probably this is a primordial pattern and resembles that observed in some chondrules /3,7/.

To understand depletions in Ca, Mg and Mn the Fe/Mn-ratios of MMs and CSs may give us a hint. Phyllosilicates in carbonaceous chondrites in equilibrium with carbonate (e.g., dolomite) are usually poor in Mn because Mn strongly partitions into the carbonates /8/. In contrast to CM and CI chondrites PHs have no detectable carbonates but display depletions in Ca, Mg and Mn. Mn-poor phyllosilicates in MMs can therefore indicate a former phyllosilicate-carbonate coexistence. We conclude that carbonates have been a part of the original mineral assemblage in PHs which have been lost by leaching /4/. Leaching could take place with sulfuric acid aerosols in the upper atmosphere or with melt water in ice. For CSs this leaching-model is unlikely because carbonates are destroyed during melting. However, carbonates or they breakdown products could have been lost due to ablation or by chance sampling of the precursor rock. Carbonates are not equally distributed in chondritic phyllosilicate matrices (like most sulfides) and therefore it depends on the part of the precursor grain that has been lost whether the final spherule has a chondritic Ca (Mg, Mn) abundance or not. Also, Ca (Mg,Mn)-enrichments can be produced this way. That most CSs were formed by melting of phyllosilicate precursors is evident in Fig. 1 where Fe vs. Mn contents are plotted. Crystalline, unmelted micrometeorites (XX), which consist mainly of anhydrous silicates such as pyroxene and olivine have low Fe/Mn-ratios (<65) while matrices of carbonaceous chondrites display higher ratios (≈ 75-200 /15/). Compositions of CSs straddle the chondritic ratio line indicating a derivation from variable mixtures of phyllosilicate, carbonates and anhydrous olivine and pyroxene.

A characteristic feature of CI and CM chondrites are veins of sulfates /11/. They are interpreted as in situ-formed reaction products of phyllosilicates with an aqueous medium on the chondrite parent body /9/. On Earth these compounds appear as efflorescences which cover the exposed surface of meteorites /e.g., 10/. We performed neutron-activation-analysis of such efflorescences from CI chondrite Orgueil. Results are given in the Table. Please note the high contents of Na and Ni. Fig. 2 shows CI-normalized patterns of siderophile elements of these efflorescences, in PHs and CSs. Orgueil efflorescences have a complementary pattern of MMs. Ni-sulfate has been verified in efflorescences by X-ray powder-diffraction. We also found Ni-rich sulfates covering grains of the CM chondrite Grosnaja. Such covers are not observed on MMs and cannot be expected on them because MMs have been exposed to melt ice water.

ELEMENTAL DEPLETIONS IN MICROMETEORITES: Presper, T. et al.

Depletions in Na, Co and Ni can be explained by leaching of sulfates which should have been a component of the original MMs (if the analogy to carbonaceous chondrites is correct). In this case iridium values remain chondritic as has been observed in many CSs and PHs. For unmelted PHs leaching of sulfates is a plausible process for loss of Na, S, Co and Ni (see also /14/ for elemental loss from weathered meteorites). A sampling fractionation of phyllosilicates and sulfates is also possible. Another aspect is that carbonaceous chondrites are not homogenous on the scale of a few hundred micrometers.

In summary, most compositional differences between MMs and carbonaceous chondrites can be explained by interaction processes between the micrometeoroids/-meteorites with the atmosphere and melt ice water. Another source of depletions is the biased sample set of MMs which probably does not fully represent the composition of the parent rock. Although there is an affinity to CI and especially to CM chondrites some differences remain in the composition of anhydrous silicate phases e.g., the higher FeO contents of olivines /12/ and pyroxenes and the high pyroxene olivine ratio /13/. This could indicate that the MM population may represent a new class of extraterrestrial matter not represented among the meteorite classes.

References: /1/ Klöck, W. et al. (1992), LPSC XXIII, 697 /2/ Koeberl, C. et al, 1992, LPSC XXIII, 709 /3/ Presper, T. & Palme, H (1991), Meteoritics 26, 386 /4/ Kurat, G. et al. (1992), Meteoritics 27, 246 /5/ Maurette, M. et al. (1992), LPSC XXIII, 861 /6/ Jessberger, E.K. et al. (1992), EarthPlanet.Sc.Let. 112, 91-99 /7/ Kurat, G. et al. (1985), LPSC XVI, 471 /8/ Brandstätter, F. et al. (1992), Meteoritics 27, 206 /9/ Richardson, S.M. (1978), Meteoritics 13, 141-159; Fredriksson, K. et al (1980), Meteoritics 15, 291.; Fredriksson, K. & Kerridge, J.F. (1988), Meteoritics 23, 35-44 /10/ Velbel, M.A. (1988), Meteoritics 23, 151-159 /11/ Zolensky, M. & McSween, H.Y. (1989) in Meteorites and their Parent Planets, Kerridge, J.F. et al. edts., 114-143, Univ. of Arizona Press /12/ Steele, I.M. (1992), Geoch. Cosmoch.Acta 56, 2923-2929 /13/ Presper, T. et al. (1992), Meteoritics 27, 278. /14/ Gooding, J.L. (1981), Proc. Lunar Planet Sci, 12B, 1105-1122. /15/ McSween, H.Y & Richardson, S.M. (1977), Geochim. Cosmochim.Acta 41, 1145-1161. /16/ Palme, H. (1988) in Reviews in modern Astronomy 1, 28-51, Klare, G. ed., Springer-Verlag.

Fig. 1: Fe vs. Mn in carbonaceous chondrite matrix and bulks of PHs, XX, SCs and CSs

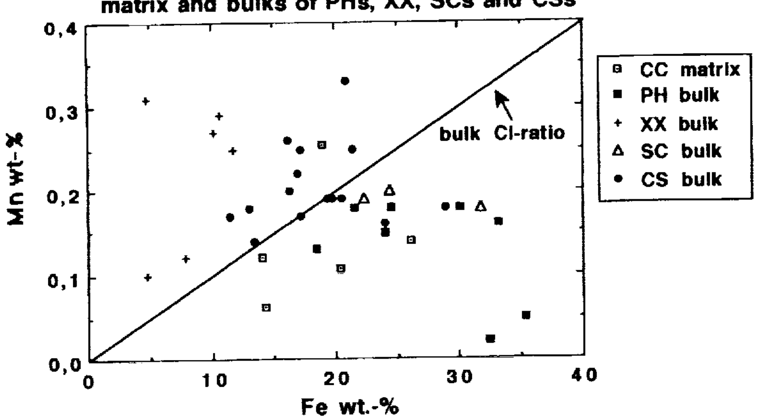


Fig. 2 Siderophile elements in PHs, CSs and efflorescences of Orgueil

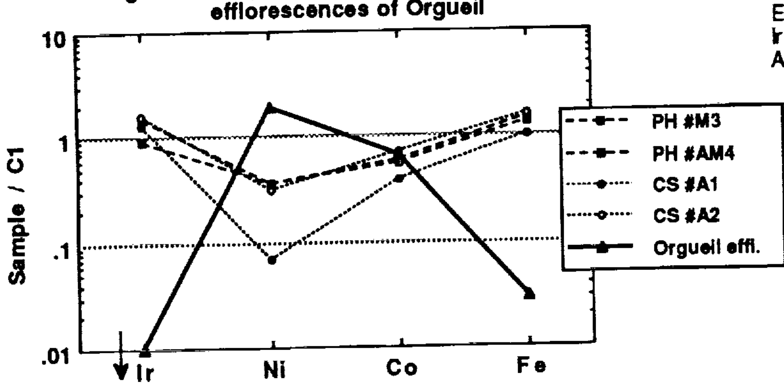


Table: Efflorescences of CI-chondrite Orgueil. INAA data. In paranthesis corrected data for contamination by ≈30% CI (Orgueil) chondritic material (based on Sc, Cr and Ir contents)

	ppm	*sample/ bulk CI /16/*
Na	6907 (7800)	1.38 (1.55)
K	230 (94)	0.44 (0.18)
Sc	1.9 (0)	0.32 (0)
Cr	828 (0)	0.31 (0)
Mn	887 (445)	0.49 (0.24)
Fe	6.3 % (0.6 %)	0.34 (0.03)
Co	390 (337)	0.78 (0.67)
Ni	1.78 % (2.06 %)	1.6 (1.9)
Zn	102 (0)	0.29 (0)
As	0.63 (0.05)	0.34 (0.03)
Se	11 (7.3)	0.58 (0.38)
Br	2.29 (1.69)	0.64 (0.47)
Sb	0.21 (0.25)	1.62 (1.92)
La	0.19 (0.05)	0.4 (0.1)
Sm	0.07 (0.03)	0.45 (0.19)
Eu	0.04 (0.03)	0.69 (0.52)
Ir	0.16 (0)	0.33 (0)
Au	0.06 (0.02)	0.43 (0.14)

369-91 ABS. ONLY N94-20705

GEOLOGIC MAPPING OF HARMAKHIS AND REULL VALLES REGION, MARS: EVIDENCE FOR MULTIPLE RESURFACING AND DRAINAGE EVENTS;

Katherine H. Price, Department of Geology & Geography, DePauw University, Greencastle, Indiana 46135.

P-1

Numerous mesas and irregular, channel-cut escarpments south of Harmakhis and Reull Valles suggesting at least two resurfacing events with subsequent periods of erosion are revealed from detailed geologic mapping of three adjacent 1:500,000-scale quadrangles (MTM-40262, -40267, -40272). Also, two distinct episodes of surface water runoff, each from different styles of water release, are evident [1]. Geologic mapping is based on 1:500,000-scale photomosaics of the Harmakhis vallis region, and is an outgrowth of preliminary regional geologic mapping on a 1:2,000,000-scale on the east rim of Hellas Basin [2].

Three plains units, formerly mapped together as the Channeled plains rim unit (Ah_5) [4], have been differentiated based on morphology and texture. The oldest unit is Hummocky material (AHh) which displays a mottled appearance and is dissected by numerous channels, some of which are dendritic. The irregular surface of moderate relief is probably volcanic material, and may represent relict topography or reworking of old (or exhumed) surface materials. Probable causes for the irregular surface texture, which may be contemporaneous with unit formation or more recent, include eolian processes (deflation or dunes) or partial collapse of water- or ice-rich deposits.

Superimposed on the AHh is the Smooth plains material unit (AHsp), which shows slight to moderate relief, and which is also etched by narrow, sinuous channels. Escarpments of AHh are incised by channels in places, and in other places form infacing windows on the Hummocky material below. Smooth plains materials are interperted to have been once more widespread as evidenced by the presumably retreating escarpments which delineate the unit. The third and youngest plains unit is the Mesa materials (AHm). Mesas have irregular outlines, smooth surfaces, range in size from less than one km to approximately 70 km in width, and are found in the southern half of the mapped area. Mesa materials are interpreted as erosional remnants of a once more widespread sedimentary (probably windblown) deposit.

Outflow channels originating south of Hadriaca Patera, appear to have their sources in collapse depressions within 40 km of each other in the highlands of Promethei Terra. Harmakhis extends southwest toward Hellas basin, and Reull extends southeast. Harmakhis transects an older dendritic drainage network (on MTM -40267) whose morphology suggests a water source either from precipitation or from drainage of a large body of water [1]. Portions of the dendritic network show topographic inversion, which are interpreted as the result of several episodes of channeling and infilling of a more resistant material [1,3].

REFERENCES. [1] Price,K.H. (1992) *Lunar Planet. Sci. Conf., XXIII,* 1107. [2] Crown,D.A., Price,K.H. and Greeley,R. (1990) *Lunar Planet. Sci. Conf., XXI,* 252-253. [3] Crown, D.A., Price,K.H. and Greeley,R. (1992) *Icarus*, 100, 1-25. [4] Greeley,R. and Guest,J.E. (1987) *USGS Map I-1802-B.*

Some Deformation Trends and Topographic Characteristics of Tesserae on Venus

Maribeth Price and John Suppe
Dept. of Geological and Geophysical Sciences, Princeton University, Princeton, NJ 08544

Abstract: Mapping of dominant trends of deformation and topographic analysis of tesserae reveal that 1) consistent patterns of deformation exist between individual tesserae; 2) regional deformation associated with coronae and rifts commonly overprints tesserae fabrics; 3) normalized area frequency plots of tesserae display a strongly bimodal distribution between -70 to 70 degrees latitude; and 4) the relief at tessera margins is relatively constant and independent of tessera elevation. We are continuing to expand these observations and test their implications for the formation of tesserae and for global models of deformation on Venus.

Introduction: Tesserae are complexly deformed, usually steep-sided highlands which cover approximately 10-20% of the planet Venus [1]. Others have mapped individual tessera regions in detail, including Alpha and Tellus Regio, and agree that tesserae are at least partially the result of compression [2,3]. We have started to map and analyze large-scale occurrence patterns and deformation fabrics on a global scale, to uncover additional clues to tessera formation which may not be apparent when they are studied as individual regions.

Observations: We have mapped tessera boundaries and sketched the most obvious large-scale deformation fabrics both inside and outside tessera blocks discernible on C2 (twice compressed) MIDRs. The fabrics, although often complex, commonly show coherent patterns when viewed globally. Consistent trends occur between some adjacent tessera blocks up to 900 km apart as seen in examples in several locations (figure 1, a,b,c,d). In tessera groups showing ring-like or arcuate outcrop patterns [3], fabric trends usually are consistent within the group; sometimes they parallel the curve (e), but may also cut across it (f). These observations suggest a shared history between some groups of tessera, especially the ring and arcuate types which might be collapsed and extensively embayed remains of previously intact tessera. However, dominant fabrics in tesserae often result from fractures associated with nearby coronae or rifts which continue into the tessera block, overprinting previous fabrics (g,h). Hence tesserae deformation structures must be considered to possibly have formed over a wide range of ages and conditions, and do not necessarily reflect a discrete process which formed the tessera. Detailed mapping of structures both within and without tesserae will be necessary to provide constraints for models of their formation.

Areally, tesserae are strongly concentrated at equatorial and near-polar latitudes, in addition to being concentrated between 0-150 degrees longitude [3]. Tessera normalized areas, binned by latitude between -70° and 80° (figure 2), exhibit a strongly bimodal distribution characterized by asymmetric peaks near the equator and the high northern latitudes. It has been suggested that poleward convergence in the northern hemisphere is causing compressional deformation expressed as north-trending fold belts, producing a geometric increase in fold belt area with latitude [4]. This bimodal distribution of tesserae is quite different, and we must begin to consider ways to include the tessera terrain in our model of global organization of tectonic deformation on Venus [4,5].

Analysis of the topographic characteristics of tesserae using compressed 20 km resolution altimetry data from Magellan reveals several intriguing observations. Relief at the margins of most tesserae seems to be essentially independent of the elevation of the surrounding plains. We have constructed 258 topographic profiles over the margins of tesserae from 70° to -70° latitude, and plotted the mean elevation of the tessera edge versus the mean elevation of the surrounding plains (figure 3). An analogous plot for fold belt toes and crests reveals a strongly linear trend with slope ≈ 2, and it has been suggested that factors affecting the depth to the brittle-plastic transition are controlling fold belt relief [6]. In contrast, most tessera points fall between the fold belt trend and the line of no relief (slope = 1), but a significant number appear to plot closer to the fold belt trend, especially in Fortuna and Tellus Tesserae and Ovda Regio. Whatever process which is proposed to control fold belt relief could have important implications for tesserae relief. We are currently examining these data in greater detail to discover additional clues to the factors affecting relief of compressional features on Venus.

References: [1] Ivanov, M.A. (1992) LPSC XXIII:2, pp. 581-582. [2] Bindschaedler, D.L. et al. (1992) JGR 97:E8, pp. 13563-13578. [3] Bindschaedler, D.L. and Tatsumura, M.J. (1992) LPSC XXIII:2, pp. 103-104. [4] Bilotti, F., Connors, C. and Suppe, J. (1992) Int'l Colloquium on Venus, 10 (abs). [5] Bilotti, F., Connors, C. and Suppe, J. (1993), this issue. [6] Suppe, J. and Connors, C. (1992) JGR 97:E8, pp. 13545-13562.

Some Deformation Trends and Topographic Characteristics of Tesserae on Venus
Maribeth Price and John Suppe

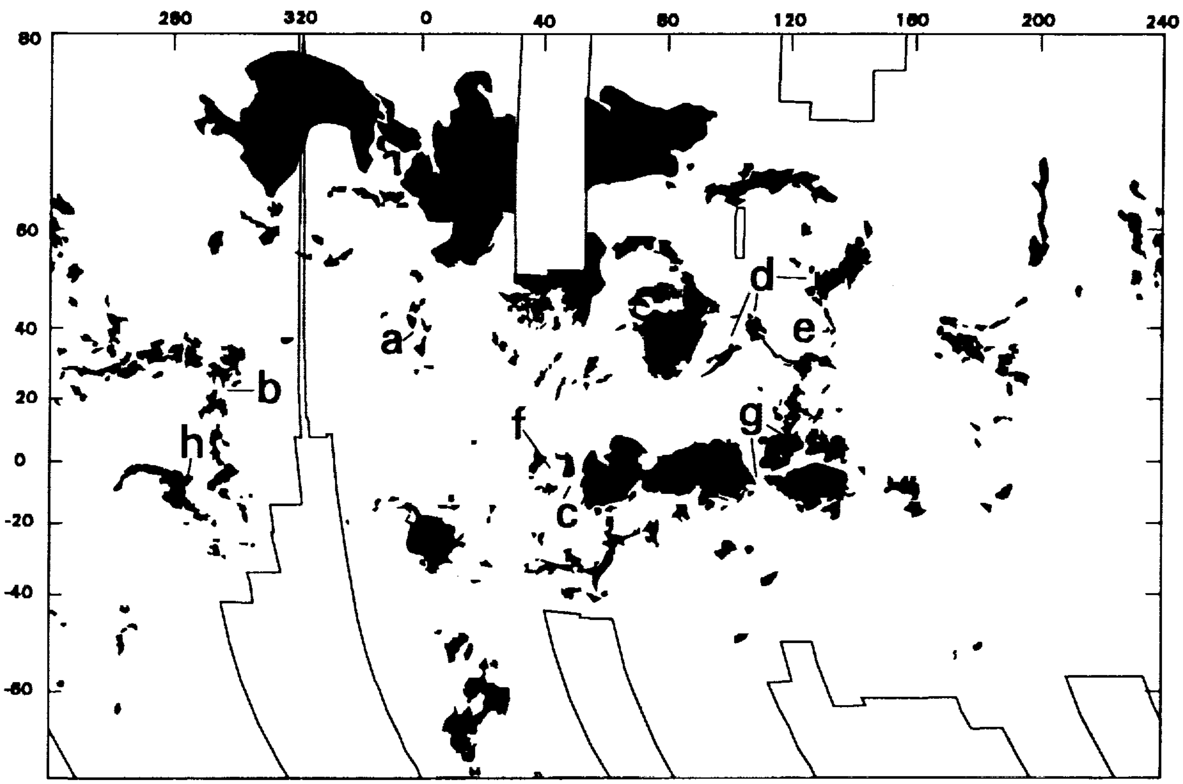


Figure 1. Global map of tesserae (black) as mapped from C2 MIDRs. Letters refer to features discussed in the text. Boxed white areas are data gaps.

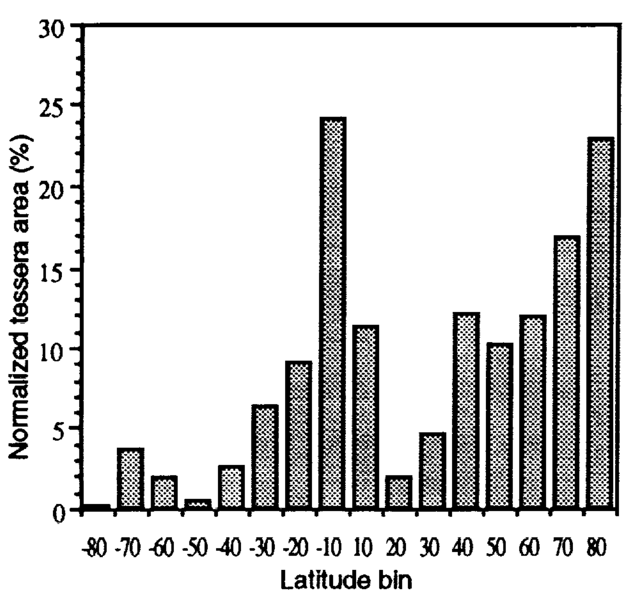


Figure 2. Normalized area histogram of tesserae binned by latitude. Areas of no C2 SAR coverage were subtracted from the total area in each bin before normalizing.

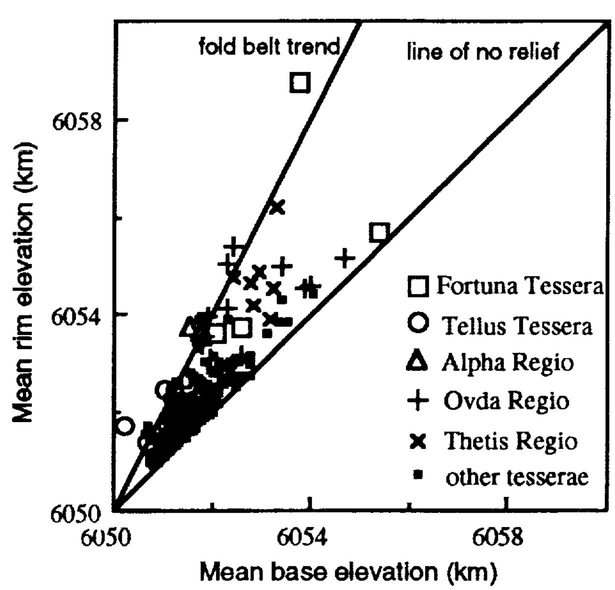


Figure 3. Observed relationship between elevation of tesserae rims and elevation of the surrounding plains. Notice that the relief is fairly constant (0-1 km) and does not vary with mean base elevation, with a few interesting exceptions.

S71-91
ABS. ONLY
168031
N94-20707

Studying Venus using a GIS Database

Maribeth Price and John Suppe
Dept. of Geological and Geophysical Sciences, Princeton University, Princeton, NJ 08544

Abstract: A Geographic Information System (GIS) can significantly enhance geological studies on Venus because it facilitates concurrent analysis of many sources of data, as demonstrated by our work on topographic and deformation characteristics of tesserae. We are creating a database of structures referenced to real-world coordinates to encourage the archival of Venusian studies in digital format and to foster quantitative analysis of many combinations of data. Contributions to this database from all aspects of Venusian science are welcome.

Introduction: The extended Magellan Mission has provided a wealth of high-quality data, the study of which will advance the understanding of planetary geologic and tectonic processes for many years. Making best use of this resource requires the ability analyze many combinations of data, including observed tectonic features and their characteristics, topography, gravity, and emissivity. One way to accomplish this, called georeferencing, is to register all data and observations to real-world coordinate axes. Once data are registered, it becomes possible to easily convert them into different map projections, plot them at virtually any scale or resolution, and combine them with other registered data for display and analysis. A computer system which performs such operations is called a geographic information system, or GIS. We have been using a GIS for our studies of structural geology and tectonics on Venus, enabling us to analyze and interpret our findings with greater speed, accuracy, and flexibility than traditional methods. It is our aim to establish a georeferenced database of geologic and tectonic features for use by all scientists working on Venus.

Discussion: The implementation of a GIS database is rapidly becoming the standard way of georeferencing observations and data to solve many geological and engineering problems on Earth, and we are creating one for Venus. Features currently being mapped and entered in the database include fold belts, rifts, wrinkle ridges, and tesserae. We have automated the process of reading the SAR images into our GIS format, so features are mapped directly on displayed MIDRs for greatest accuracy. If greater resolution is required, we digitize maps made on mylar overlays on MIDR photoproducts. Attributes pertaining to structures, such as latitude and longitude, orientations, areas, lengths, widths, spacings, extension or shortening, relief, and tectonic setting, are included where appropriate. We are also converting altimetric, radiometric, and gravity imagery into GIS format for quantitative analysis of these properties with respect to the mapped features. Working with combined data sets in an integrated spatial analysis environment is much more powerful and productive than looking at each data set individually. We have begun to incorporate additional data, such as coronae [1] and volcanic features [2], provided by other research groups, and plan to establish and periodically update a data library accessible over the Internet computer network, utilizing a standard format easily transported to other GIS platforms. We strongly encourage other groups to use and contribute to this database.

Several examples of our current work will serve to demonstrate the facility of GIS as a tool for analyzing combinations of data--in this case SAR, altimetry, and geologic interpretation. This work was done using the GIS ARC/INFO [3]. First, we calculated the normalized area of tesserae terrain present within 10-degree latitude bins. With GIS the process was quick and simple. The tessera outlines were mapped digitally on twice compressed SAR MIDRs, compiled and projected into a common equal-area projection, and then geometrically intersected with latitude lines. The tessera area and total area of C2-SAR coverage were then summed for each bin [figure 2 in Price & Suppe, this issue].

In the second example we determined if a linear relationship between relief at tessera margins and the basal elevation exists, as has been demonstrated for fold belt relief [5]. We digitized 258 profile lines across tessera margins and split them into base and crest sections where they intersected the tessera outlines. Then a 20 km resolution global altimetry image was used to calculate the mean elevation along the base and crest sections of the profile (figure 1). The method was improved by masking pixels with high topographic slope from the image, in order that values from the steep margins are not included in the calculations.

Third, we created a global image of altimetry inside tesserae which emphasizes global and local topographic patterns (figure 2). When displayed behind a map of deformation trends (in progress), it will facilitate the recognition of significant patterns which may provide clues about the formation of tesserae.

Conclusions: We are using GIS to analyze fold belts, rifts, wrinkle ridges, and tessera, and vouch for its utility for structural and tectonic studies. We are creating an Internet-accessible database to foster GIS analysis of Venus, and we encourage contributions from all aspects of Venus science. For further information contact maribeth@wanda.princeton.edu.

References: [1] Stofan, E. et al. (1992), JGR 97:E8, pp. 13347-13378. [2] Head J. et al. (1992), JGR 97:E8, pp. 13153-13198. [3] ARC/INFO © Environmental Systems Research Institute, Inc., Redlands, CA. [5] Suppe, J. and Connors, C. JGR 97:E8, pp. 13545-13562.

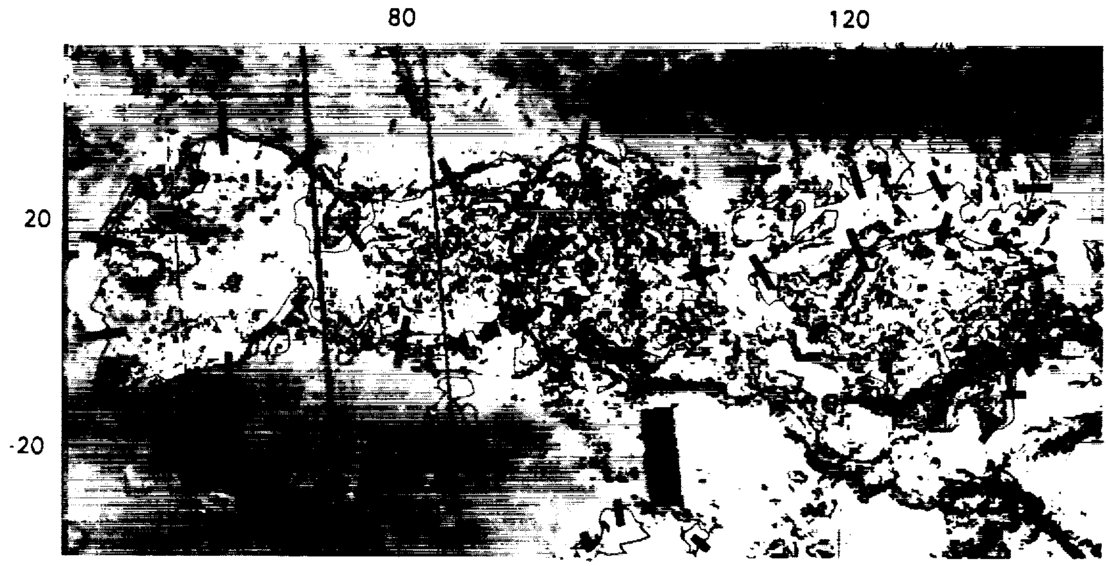


Figure 1. Altimetry of Aphrodite Terra (low elevation dark, high white) with high slopes masked in black. The thin lines are mapped tesserae outlines; the thick line segments are topographic profile lines; and the rectangular black patches are data gaps. The masked image was used to calculate mean elevations for the profiles inside and outside the tesserae.

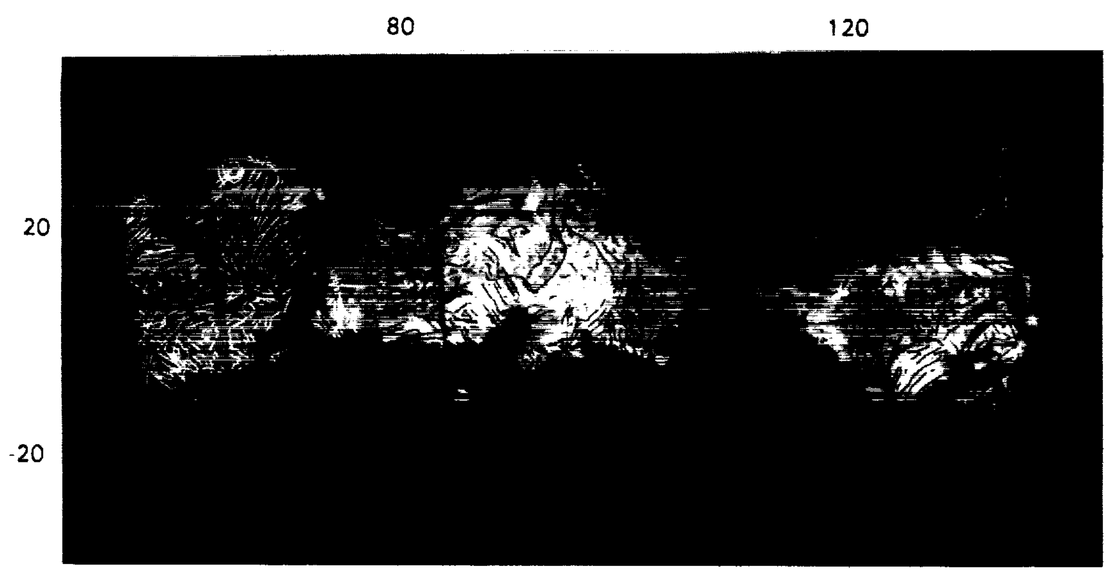


Figure 2. Map of Aphrodite Terra showing the dominant deformation trends of tesserae displayed over altimetry with non-tesserae masked in black. Trends were digitized on C1 (once compressed) digital MIDRs and compiled into a common projection for display. Lines are shown in both white and black for clarity only, no classification is implied.

S72-90
ABS. ONLY.

N94-20708

OXYGEN ISOTOPIC RELATIONSHIPS BETWEEN THE LEW85332 CARBONACEOUS CHONDRITE AND CR CHONDRITES.

M. Prinz[1], M. K. Weisberg[1], R.N. Clayton[2] and T.K. Mayeda[2]. (1) Dept. Mineral Sci., Amer. Museum Nat. Hist., New York, NY 10024. (2) Enrico Fermi Inst., Univ. Chicago, Chicago, IL 60637.

LEW85332, originally described as a unique C3 chondrite [1], was shown to be a C2 chondrite with important linkages to the CR clan (CR chondrites, ALH85085, Acfer 182) [2]. An important petrologic aspect of LEW85332 is that it contains anhydrous chondrules and hydrated matrix, and new oxygen isotopic data on chondrules, matrix and whole rock are consistent with the petrology. Chondrules fall on the equilibrated chondrite line (ECL), with a slope near 1, which goes through ordinary chondrite chondrules. This contrasts with the CR chondrule line which has a lower slope due to hydrated components. LEW85332 chondrules define a new carbonaceous chondrite chondrule line, parallel to the anhydrous CV chondrule line (CCC), consistent with the well-established concept of two oxygen isotopic reservoirs. Matrix and whole rock fall on the CR line. The whole rock composition indicates that the chondrite is dominated by chondrules, and that most of them contain light oxygen similar to that of anhydrous olivine and pyroxene separates in the Renazzo and Al Rais CR chondrites.

INTRODUCTION. CR chondrites have been studied extensively [3] and it has been shown that the oxygen isotopic compositions of chondrules, matrices and whole rocks fall on a CR mixing line with a slope near 0.7. Since all anhydrous chondrules in ordinary and carbonaceous chondrites fall on lines with a slope near 1 (Fig. 2), indicative of two oxygen isotopic reservoirs, the CR chondrules indicate an additional oxygen source. This has been considered to be water since the CR chondrules are hydrated to varying degrees. It has been shown that LEW85332 is a member of the CR clan because it has significant chemical similarities to the CR group (e.g., oxygen and nitrogen isotopic compositions), although it does have different petrologic characteristics [2]. The chondrules are smaller (average, 170 μm) than in CR chondrites (up to 1cm), but more importantly they are anhydrous. However, the matrix which occurs interstitially, as clasts and as chondrule rims, is hydrous [2,4]. Matrix consists of phyllosilicates (mainly saponite and serpentine) and magnetite framboids. Thus, the purpose of this study was to extract chondrules and matrix from LEW85332 in order to measure their oxygen isotopic compositions and determine the oxygen reservoirs of the anydrous chondrules as compared to the hydrous matrix. In this way it would be possible to determine the pre-hydration oxygen isotopic composition of the related CR chondrules.

RESULTS. Oxygen isotopic data are presented in Table 1 and Figs. 1 and 2. Whole rock data were presented earlier [2], but because the sample is weathered a second sample was HCl-washed and analyzed; both data points are presented. The HCl-washed sample did not move the analysis in the usual direction for weathered Antarctic samples, i.e., parallel to the terrestrial fractionation line; perhaps an indigenous component was removed. Chondrules C1, C3 and C5 represent single chondrules, whereas C4 is a composite of 3 smaller chondrules; thus 6 chondrules are represented. The surprising result is that not only do they fall on a line with a slope near 1 (as predicted), but that they fall on the ECL line (Fig. 1). Ordinary chondrite chondrules also fall on this line [5] (Fig. 2), and thus LEW85332 chondrules fall on an extrapolation of the ordinary chondrite chondrule line, towards lighter oxygen, and two overlap with ordinary chondrite chondrules. This line is parallel to the anhydrous carbonaceous chondrite chondrule (CCC) line. Seventeen chondrules from CR chondrites [3] are also shown in Fig. 2 and they fall on a line with a slope < 1 (near 0.7). Since the LEW85332 chondrules fall on a slope~1 line (ECL line), it is inferred that the pre-hydrous alteration CR chondrule line probably also had a slope close to 1, similar to the LEW85332 trend. This is somewhat supported by the anhydrous olivine and pyroxene separates (Fig. 1), probably derived from chondrules. They contain lighter oxygen than that in the CR chondrules, and are similar to the LEW85332 whole rock and some of the chondrules. A single matrix sample was extracted, and it falls on the CR mixing line (Fig. 1), indicative of its hydrous nature.

Thus, LEW85332 contains anhydrous chondrules whose oxygen isotopes fall on a slope 1 line (same as ordinary chondrite chondrules) indicative of two oxygen isotope reservoirs, and the matrix falls on the CR line (slope 0.7) which contains hydrous components representing a third oxygen isotopic source (water). The whole rock composition falls near the intersection of these two lines. Anhydrous phases in CR chondrules may also fall on a slope 1 line. The coexistence of anhydrous chondrules and hydrated matrix in LEW85332 (as well as in Acfer 182 and ALH85085) highlights the problem of nebular vs. parent body hydrous alteration.

References: [1] Rubin, A.E. and Kallemeyn, G.W. (1990) Meteoritics 25, 215-225. [2] Prinz, M. et al. (1992) Meteoritics 27, 278-279. [3] Weisberg, M.K. et al. (1993) The CR (Renazzo-type) carbonaceous chondrite group and its implications, GCA, in press. [4] Brearley, A. (1992) LPSC XXIII, 155-156. [5] Clayton, R.N. et al. (1991) GCA 55, 2317-2337.

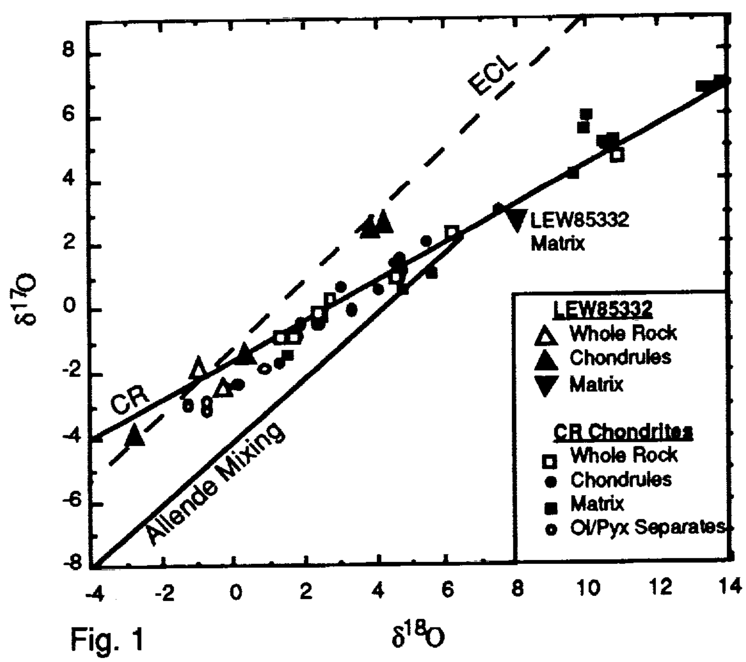


Fig. 1

Table 1. Oxygen isotopic compositions of LEW85332 whole rock, chondrules and matrix.

	$\delta^{18}O$	$\delta^{17}O$
Whole Rock	-0.92	-1.93
Whole Rock (HCl)	-0.23	-2.54
Chondrules		
C1	4.31	2.54
C3	-2.76	-3.98
C4 (3 chondrules)	0.36	-1.52
C5	3.89	2.39
Matrix	8.06	2.54

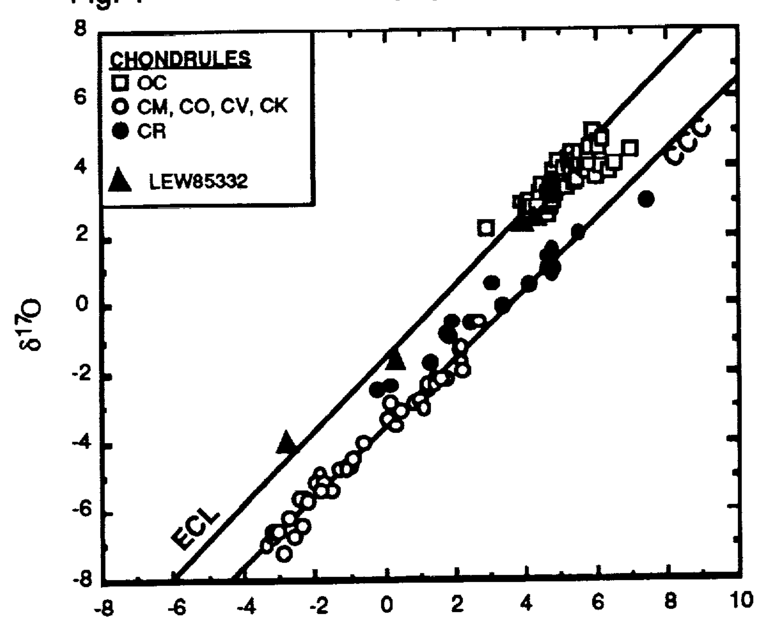


Fig. 2

IMPACT DISTURBANCE OF THE VENUS ATMOSPHERE

A.A.Provalov and B.A.Ivanov, Institute for Dynamics of Geospheres, Russian Academy of Sciences, Moscow, 117979

Summary. Experimental simulations of the atmosphere-surface interaction during the high-velocity impact are presented. At Venus an atmospheric vortex, generated with impact, may interacts with a local wind. Some of surface features, observed at Magellan images may be related with the simulated effect.

Introduction. A laboratory simulation of the passage of a high velocity body through the atmosphere has begun at the Explosion Branch of Schmidt Institute (now the Institute for Dynamics of Geospheres) several years ago. The effect of a long distance soil transport has been observed [1]. An atmospheric toroidal vortex originated around a zero point was discussed as a possible mechanism of this near-surface non-ballistic soil transport [2]. Here we present some new results of the experimental investigation of this effect.

1. Special experiments to visualize an impact-induced vortex has been carried out. As in our previous experiments the detonation of the long (0.9 m) and thin (3mm) line HE charge of PETN above the surface of an aluminum sheet with a sand layer has been used to simulate an impact disturbance of the atmosphere.

Fig. 1 (a-c) demonstrates a vortex origin for a vertical downward detonation. Times after the detonation are 0.1 s (a), 0.3 s (b) and 0.7 s (c). One may see the vortex formation near the surface. The vortex does not form when the detonation propagated upward from the surface. So the vortex origin is a consequence of an interaction between the downward gas flow and a solid surface.

The scaling of this effect to the natural conditions is a rather complex problem. For the first approximation we have chosen as characteristic parameter of the event the energy transferred to the atmosphere per unit length of a projectile trajectory, q_L, (or an explosive energy per unit length of a HE line charge), the velocity of a projectile, V (the detonation speed), the characteristic height of an atmosphere, H (the HE charge length), an atmospheric pressure, p, and sound velocity, c. These values may be used for a comparison of any two events, being combined in nondimensional parameters: the Mach number $M=V/c$, the characteristic length $L=(q_L/p)^{.5}/H$. Comparing with these parameters one may conclude that the described experiment simulate the early stage of the impact on Venus for a projectile with a diameter of 2.3 km and a velocity of 8 km/s.

For laboratory continuous the time scale of a vortex spreading is about 1 s. The Reinolds number for the vortex is about 10^5, so the vortex seems to be a turbulent one. Using the time scale comparison with the same parameters the real time scale for the Venusian impact is about 50,000 s or 13 hours. We are not yet sure for this estimate, but it is interesting to look at the possible consequence. For a near surface wind velocity of 1 m/s a down-wind vortex displacement is about 50 km. So the final shape of the dust deposits transported by the vortex seems to be affected with a local wind direction. It would be very interesting to analyze a possible connection of this effect with a parabola phenomenon on Venus.

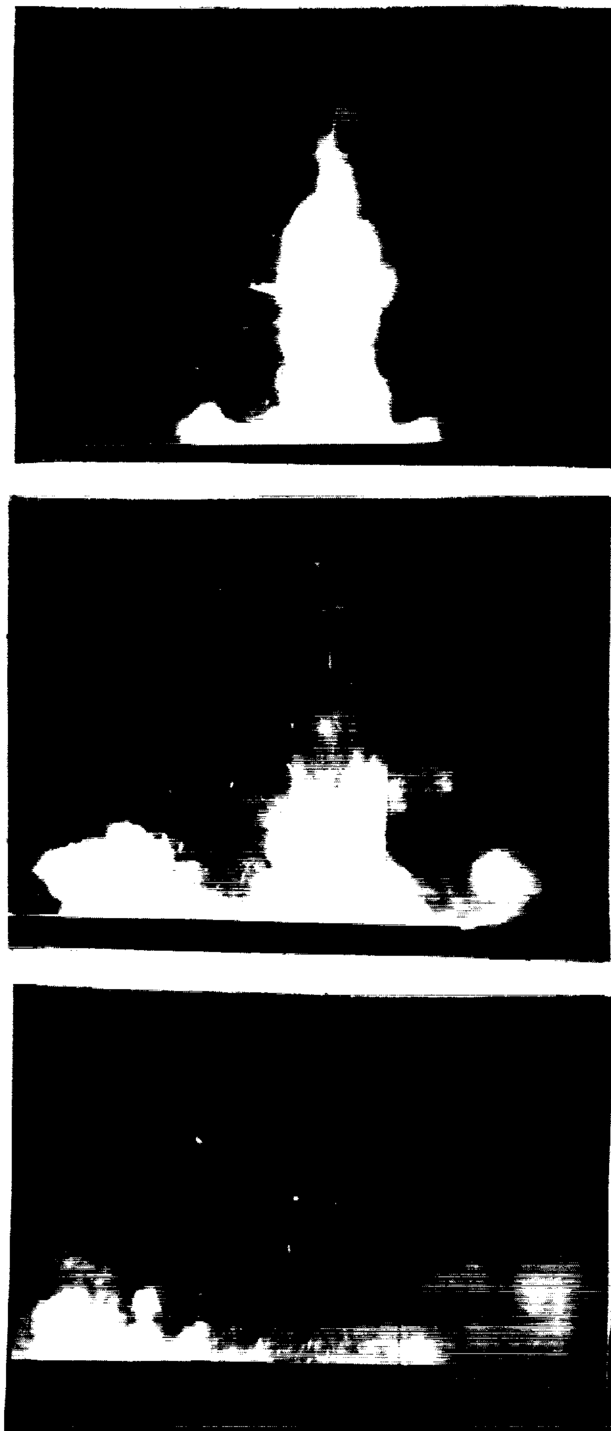
2. Experiments to simulate an oblique impact has been carried out with an HE charge inclined at 45^o to the surface. Fig 2 (a-c) shows the target surface with low profiles sand strips. Frames demonstrate the initial configuration (a), the moment 0.034 s after detonation (b) and a final picture (c). Sand particles under the charge begin to move from the point of impact to periphery (b). The final picture (c) show that later part of these particles change the direction of motion, being finally displaced forward. Special side framing has revealed the formation of a vortex, which moves downrange with 3 to 5 m/s. This velocity is about 0.001 of the particle velocity in the charge which allow to estimate displaced mass of air.

Conclusions. Conducted experiments revealed two phenomena which may be observed on Venus: (i) a long lived near surface vortex may interact with an down wind atmospheric motion, and (ii) a complex time history of the soil particles displacement for an oblique impact. Experiments should be continued.

IMPACT DISTURBANCE... A.A.Provalov and B.A.Ivanov

References. 1. Provalov A.A. and B.A.Ivanov.(1992). *LPSC XXIII*, p. 1115-1116. 2. B.A.Ivanov, I.V.Nemchinov, V.A.Svetsov, A.A.Provalov, and V.M.Khazins (1992) Impact cratering on Venus: Physical and mechanical models. *J. Geophis. Res.*, V. 97, No. E10, pp. 16167-16181.

Fig.1 (top to down: a, b, c) Fig2. (a, b, c) (top to down: a, b, c)



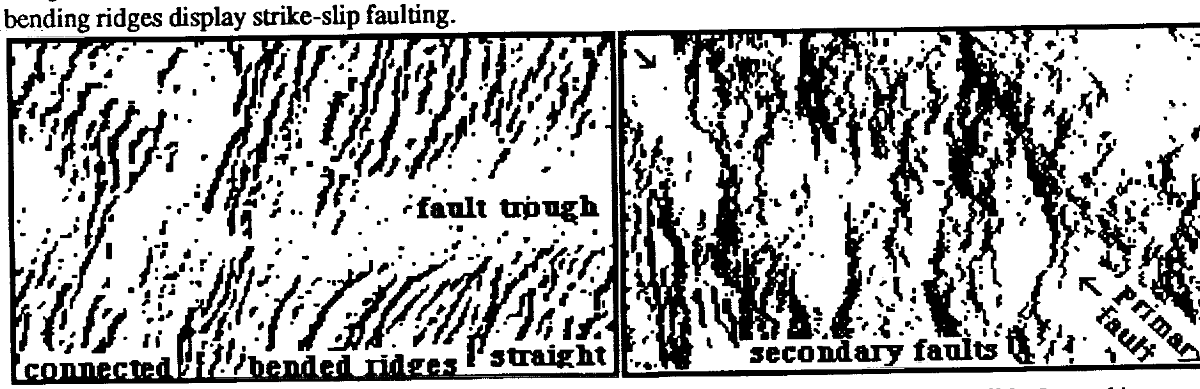


CHOCOLATE TABLET ASPECTS OF CYTHEREAN MESHKENET TESSERA; J. Raitala, Deptartment of Astronomy, University of Oulu, 90570 Oulu, Finland; e-mail: jouko@hiisi.oulu.fi

Meshkenet Tessera structures were mapped from Magellan data and several resemblances to chocolate tablet boudinage were found. The complex fault sets display polyphase tectonic sequences of a few main deformation phases. Shear and tension have contributed to the areal deformation. Main faults cut the 1600 km long Meshkenet Tessera highland into bar-like blocks which have ridge and groove patterns oriented along or at high angles to the faults. The first approach to the surface block deformation is an assumption of initial parallel shear faulting followed by a chocolate tablet boudinage. Major faults (a) which cut Meshkenet Tessera into rectangular blocks have been active repetitively while two progressive or superposed boudinage set formations (b, c) have taken place at high angles during the relaxational or flattening type deformation of the area.

Chocolate tablet boudinage is caused by a layer-parallel two-dimensional extension resulting in fracturing of the competent layer. Such structures, defined by two sets of boudin neck lines at right angles to each other, have been described by a number of authors (e.g. Ramberg, 1955; Ramsay, 1967; Casey et al., 1983; Ghosh, 1988). They develop in a flattening type of bulk deformation or during superposed deformations where the rock is elongated in two dimensions parallel to the surface. This is an attempt to describe and understand the formation and development of structures of Meshkenet Tessera which has complicate fault structures.

Western Meshkenet Tessera has several parallel and conjugate fault directions. Offsets along NW-SE faults indicate their deformation by conjugate NE-SW faults. In the south faults have also a N-S orientation while the eastern faults have both conjugate NE-SW and NW-SE orientations. **Middle Meshkenet** Tessera is cut into few blocks offsetted along the faults. Some arcuate faults have parallel ridge-groove counterparts indicating horizontal displacements. In places young ridges cross main fault troughs. Western N to NNE ridges cross NW-SE faults. Gabie Rupes is parallelled by long NW-SE ridges and faults. **Eastern Meshkenet** Tessera is cut by fault systems. The NW, WNW and ENE faults and ridges characterize wedge-shaped tessera blocks which are bordered by wide E-W troughs in the south. Ridges also cross major troughs, bend beside the trough or match on opposite sides of the trough. While connected ridges indicate late ridge development the bending ridges display strike-slip faulting.



The surface at Meshkenet is sandwich-like and displays two-dimensional structures, possibly formed in a suitably oriented brittle layer with a relaxation of flattening bulk deformation from tensional strain in the underlying matrix. **Primary main** faults may have been generated by independent faulting. **The ductile** flow in the underlayer may then have been caused either by layer-normal compression or gravity relaxation of the topographic height. The boudinaging of Meshkenet Tessera could have taken place by action of viscous force acting from below. Tessera areas represent elevated surface units on a planet the surface temperature of which is close to the Curie point. The high surface temperature together with high lithospheric temperature gradient results in thin brittle crustal or lithospheric units over mobile layers, or asthenosphere. The brittle plate units may have floated on the underlying viscous matrix layers which have sticked firmly to the plate and caused effective viscous drag to it. The initiation and evolution of resulted fractures lets us trace evidences of the fracturing mechanism, the viscous drag and make comparisons to the laboratory experiments (Ghosh, 1988).

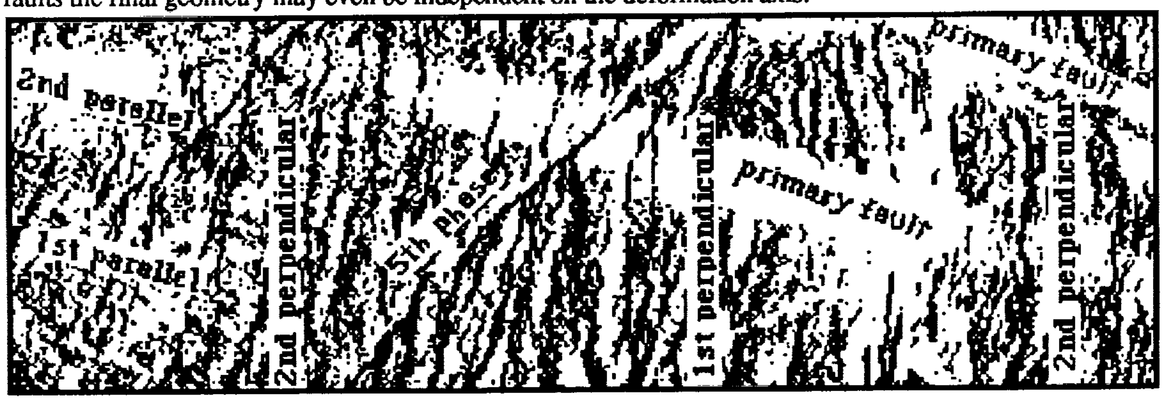
A certain fracture set may be formed perpendicular to the long axis of a bar-like plate independent to the orientation of the maximum extension. This set is entirely controlled by the plate geometry, not by the actual stress direction. The matrix flow opens caps between the parallel boudins and breaks them into rectangular fragments along the development of fractures perpendicular to the bars. With progressive deformation tensional

CHOCOLATE TABLET OF MESHKENET TESSERA: Raitala, J.

fractures are later formed at perpendicular to the first set. In relaxational or flattening deformation this second set is independent of extensional direction but at right angles to the first faults. Along superposed deformation of chocolate tablet boudinage long, narrow first boudins are cut by second generation boudinage structures despite of the orientation of the strain directions, resulting in two sequences of orthogonal fractures (Ghosh, 1988).

Previous faults cause parallel and perpendicular fractures, i.e. longitudinal and transverse boudins. With lineation roughly perpendicular to the maximum tensile stress the longitudinal fractures are generated first. With lineation roughly parallel to the maximum tensile stress the first fractures are either longitidinal or transverse ones depending on the strength of the plate and the ratio of the two tensile stresses (Ghosh, 1988).

The crossing boudinage sets may have generated either during a progressive deformation or unrelated superposed deformations. Progressive deformation allows some analysis of the stress field while in the second case only some aspects of stresses are evident. All previous or additional structures further complicate the situation and make the interpretation more difficult. Boudinage in narrow oblique rectangular plates with uniaxial extension produces secondary boudins perpendicular to the first boudin axis. In the case of previous faults the final geometry may even be independent on the deformation axis.



The two fracture sets on the Meshkenet Tessera blocks may indicate that the surface-parallel strain rates have been rather directed than equal in all directions. The long dividing and shorter perpendicular faults are necessary not simultaneous but may display either progressive faulting or superposed deformation (Ghosh, 1988): **With continuing** tension and long first boudins the local medium tensile stress along the bars may become large enough to break long boudins and the two fractures form in successive alternative steps resulting in a complex boudinage faulting in two cross-cutting directions. **A pre-existing** lineation may also modify the boudinage development by decreasing the strength of the surface plate and resulting in the first extension fracture set while the second fracture set developes at right angles to it. **Successive** unrelated deformation phases may cause that neither of the sets are indicative for the strain even if the produced two fault boudin axis are at right angles to each other. This is the case with first long and narrow bars or a uniform second phase over the whole area. The second faults are mostly defined by the first set. **Simultaneous** fracturing might play a role within an individual block with a large underlayer deformation before any fracturing.

Meshkenet Tessera has cross-cutting faults similar to the chocolate tablet boudinage modified by pre-existing faults. The development of the fractures has been caused by two-dimensional boudinage with certain pre-boudinage faulting. Meshkenet Tessera was originally faulted with the boudin axes running parallel to the faults and the neck lines at a high angle to the faultsm The srain rate may have been different parallel and perpendicular to the faults. Relaxation or flattening deformation was able to produce tensional fractures in one direction while the ductile flow across caused alternative compression-extension structures. Pre-existing faults and fault-induced lineation may have favoured boudins along the lineation over those across it, even if the maximum extension is not normal to the lineation. Although Meshkenet Tessera has effective fault-parallel fractures also perpendicular ones are well-developed indicating at least a two-phase boudinage formation.

References: Ramberg, H., 1955, J. Geol. 63: 512-526; Ramsay, J. G., 1967, Folding and Fracturing of Rocks, McGraw-Hill; Casey, M., Dietrich, D. and Ramsay J. G., 1983, Tectonophysics 92: 211-239; Ghosh, S. K., 1988, J. Structural Geol., 10: 541-553.

S75-91
ABS ONLY

168035
N94-20711

RIDGE BELT -RELATED SCARPS AND TROUGHS: COMPRESSIONAL CRUSTAL BENDING ON VENUS; J. Raitala, T. Törmänen, K. Kauhanen and T. Tokkonen, Department of Astronomy, University of Oulu, Oulu, Finland; e-mail: jouko@hiisi.oulu.fi, terhi@hiisi.oulu.fi

Cytherean ridge arcs resulted in crustal shortening in places with either the strongest compression or weakest surface layers. Arcuate scarps on or close to the edge of the ridge arcs were compressional fronts formed by overthrust over or subduction of adjacent lowland.These ridge arcs became wider due to the propagation of new ridge formation close to previous one(s). As this process repeated itself with time, the crust became thicker and the foreland was bent either due to the excess load, overthrust or subduction event.

The Salme Dorsa arc measures 100 km in width and 600 km in length. It consists of a horseshoe-like set of ridges and grooves on a gently sloping lowland. The westward arcuate ridge belt indicates lateral compressional stresses and crustal deformation from SE against the southern Ishtar Terra foreland plain. The trough on the western side of the ridge belt and tensional grabens close to the crest of the bulge to the west of the trough are due to the crustal bending and indicate effects of the load and thrust. Compression and relative movement from southeast against and over the foreland planitia have resulted in ridge belt, trough and bulge formation. The load- and/or stress-induced bending of the uppermost crust allows some estimations of the uppermost elastic lithosphere thickness.

Repeated folding and thrust faulting of surface layers due to compression are indicated by four more ridge belts located close to Salme Dorsa indicate. The northeasternmost one has short ridges located in troughs. The west-opening arcuate ridge belt interlocks with the Salme Dorsa horseshoe. To the south of Salme Dorsa are the prominent N-S ridges of Ausra Dorsa. The NE-SW ridges of the northern Sigrun Fossae zone parallel the border of Ishtar Terra just to the south of Salme Dorsa. In addition to the distinct ridge belts, there are numerous small mare ridges in the planitia areas.

The eastern ridge annulus of Tusholi Corona has topographically high compressional ridges and a deep scarp along the eastern edge. The eastward facing Tusholi scarp gives an impression that the movement of the ridge belt relative to the lowlands has been to the east. Compressional overthrust, subduction or a mere surface load by the weight of the Tusholi massif as the crust thickened during compression have resulted in trough formation in front of the eastern scarp. This trough has been partly filled by the flows from the crater Lafayette. This eastern trough together with adjoining crustal bulge bending closely resembles that of Salme Dorsa.

To the north of Lakshmi Planum the scarps (Uorsar Rupes) are described to have been caused by series of repetitive overthrusts (Head, 1990, Head et al. 1990). They parallel the highland edge rising stepwise from the low northern planitia up to Freya Montes. Similar structures are also found to the north of Maxwell Montes. Their formation mechanism may be

COMPRESSIONAL CRUSTAL BENDING ON VENUS; Raitala, J., Törmänen, T., Kauhanen, K. and Tokkonen, T.

roughly the same as that of the ridges in the Salme and Tusholi areas. A foreland trough is found in front of the northward scarps which thus display the compression and load edges of the topographically high terrains over northern lowlands.

Sel-anya Dorsa is cross-cut by Fortuna Tessera terrain at 75°N, 80°E. It presents an another example of movements of northern Ishtar Terra where an edge scarp cuts through the N-S ridges of Sel-anya Dorsa. The ridge belt has some parallel lineaments on the tessera indicating the relative northward movement of tessera or tessera formation.

Audra Planitia is bordered in the south and southwest by a 1200 km long and up to 200 km wide arcuate ridge belt, which has a low-lying eye-shaped small plain between two ridge belt branches. The ridge belt formation has postdated formation of the ridges within Audra Planitia (Törmänen and Raitala, 1992). The ridge belt has a steep north-facing scarp rising 1 to 1.6 km higher than Audra Planitia. The eye-shaped plain is bounded by two similar scarps the southern scarp being steeper and higher than the northern one. Its surface continues exactly the topographic trend of Audra Planitia and there is a linear foredeep just north of the southern scarp as is also the case within the larger plain. Compression, crustal shortening and under/overthrusting have been important deformation events. The main ridge belt structures have formed in underthrusting and crustal shortening in NE-SW direction. Underthrusting has moved to the NE resulting in formation of the remnant eye-shaped plain. The ridge belt, being a deformed compressional zone, has also bent the crust in its deformation direction either due to the load and/or overthrust.

Ridge belt -related scarps presented above have resulted in crustal compression. Arcuate scarps may thus be seen as compressional fronts formed by overthrust over adjacent lowland or by lowland subduction in places where crustal plates moved against or over each other. Overthrust-subduction and load bent the uppermost surface layers of the lowland. The foredeep trough became wider due to the propagation of the process. The trough can be seen as a synclinal depression next to the compressional massif load. As the process proceeded with time the foreland crust was bent more and resulted in tensional graben formation along or on an adjacent anticlinal bulge on lowland side of the trough.

References: Head, J.W., 1990, Geology 18:99-102. Head, J.W. et al. 1990, GRL 17: 1337-1340. Törmänen, T. and Raitala, J., 1992, LPSC XXIII: 1441-1442.

S76-92 ABS. ONLY N94-20712 P-2

SCR NEON & ARGON IN KAPOETA FELDSPAR: EVIDENCE FOR AN ACTIVE ANCIENT SUN.

M. N. Rao, D. H. Garrison[1], and D. D. Bogard (NASA Johnson Space Center, Houston, TX 77058; [1]also Lockheed-ESC).

Abstract: From etched feldspar size-fractions of Kapoeta, we determine a significant excess of cosmogenic ^{21}Ne and ^{38}Ar over that produced by galactic cosmic rays. This excess component is attributed to early production by energetic solar protons and suggests that the energetic proton flux from the ancient Sun was several hundred times more intense than that of the contemporary Sun.

Introduction: In stepwise temperature extractions of samples from oriented lunar rocks 61016 and 68815, we previously demonstrated a depth-dependent component of SCR Ne and Ar, which, in feldspar, is clearly distinct in Ne isotopic composition from GCR Ne [1,2; Fig. 1]. (We use the terms SCR and GCR to denote nuclear components produced *in situ* by energetic solar protons and galactic cosmic rays, respectively, and SW and SF (sometimes referred to as SEP) to denote solar wind and energetic solar components, respectively, *implanted* into grain surfaces.) In an earlier study, we reported evidence for excess ^{21}Ne and ^{38}Ar in pyroxene and feldspar minerals of the dark (solar gas-rich) phase of Kapoeta howardite compared to the light (gas-poor) phase [3]. This excess SCR component was attributed to early, *in situ* production by energetic solar protons.

Our Kapoeta study was repeated with a different sample having clearly defined dark and light phases. (Data from both sample sets are reported, Table 1.) We prepared 100-150 mg feldspar size separates of 35-125 μm and 125-200 μm (dark phase) and 35-200 μm (light phase). These were chemically etched to remove the surficially-sited SW. Noble gases were extracted by step-wise heating and analyzed by standard mass-spectrometric techniques [1].

Isotopic Evidence for an SCR Component: Ne data from Kapoeta feldspar separates are plotted in a 3-isotope diagram in Fig. 1. In the 500-600°C extractions 68-81% of the total ^{21}Ne was released; 16-28% was released in the 1000-1200°C extractions; and only 3-4% percent was released at 1600°C. A solar-implanted (SF) $^{20}Ne/^{22}Ne = 11.5 \pm 0.2$ was defined by an ordinate-intercept plot of the four analyzed samples; a similar ratio of 11.6 ± 0.2 was defined by ordinate-intercept plots of Kapoeta pyroxene separates [3]. A pure GCR composition has been defined by several previous studies, including [1]. The filled diamond symbol (Fig. 1 inset) denotes the mixed SCR+GCR composition defined for near-surface (<2 mm) samples of 61016 lunar anorthosite [1]. A similar SCR+GCR composition was given by 68815 [2]. Surface samples of 61016 plotted between this composition and the implanted component, whereas deeper samples (2-25 mm) plotted between this SCR+GCR component and a pure GCR component at the greatest depth [1,2,3].

The Ne isotopic data from Kapoeta feldspar behave similarly to that from 61016 and 68815 [1,2] and indicates a contribution from SCR as well as SF and GCR. The 61016 data [1] demonstrated that differences in shielding cause variations in the net SCR+GCR isotopic composition. Since the four analyzed Kapoeta samples represent an assemblage of solar proton irradiated grains from different shielding depths, the distribution of isotopic data shown in Fig. 1 likely indicate SCR/GCR mixing ratios ranging from that seen in 61016 to pure GCR. Compared to near-surface samples of the two lunar rocks, these Kapoeta samples also show a larger proportion of implanted solar gas. The concentration of this implanted component varies among samples due to different degrees of etching. In addition, only ~15% of the grains in Kapoeta were irradiated by energetic solar particles [4,5], whereas 100% of the grains experienced GCR irradiation. While isotopic deviations from the SF-GCR tie-line are clearly observed in the temperature data, the factors mentioned above make the SCR Ne component difficult to isotopically characterize.

Concentrations of SCR Component: Using the lever rule, the relative concentrations of SF and cosmogenic (SCR+GCR) components are calculated from the total Ne and Ar concentrations for each sample (Table 1.). Cosmogenic ^{21}Ne concentrations range from 60 to 94% of the total and vary only a few percent for different assumed cosmogenic $^{21}Ne/^{22}Ne$ ratios between 0.7 and 0.8 (Fig. 1). Cosmogenic ^{38}Ar concentrations range from 28 to 72% of the total measured. The SCR concentration in these feldspar separates are calculated as follows: We assume both dark and light phases of Kapoeta contain comparable amounts of GCR Ne and Ar, while only the dark phase contains an excess component. Subtracting the cosmogenic ^{21}Ne and ^{38}Ar concentrations in the light phase from those in the dark phase yields the excess (Table 1) which we attribute to SCR production.

Since the dark phase contains only ~15% SF-irradiated grains [4,5], the derived SCR ^{21}Ne and SCR ^{38}Ar concentrations need to be correspondingly corrected to determine an SCR exposure age. The average SCR

^{21}Ne concentration, corrected to 100% irradiated grains, is 5.3 x10^{-8} cm^{3}STP/g. This value is similar to the SCR ^{21}Ne content of 5.6 x10^{-8} cm^{3}STP/g reported for 10 SF-irradiated feldspar grains from Kapoeta [6; Fig. 1 inset]. The SCR ^{38}Ar concentration in our dark-phase, feldspar samples, corrected to 100% irradiated grains, is 5.4 x10^{-8} cm^{3}STP/g. An excess ^{38}Ar concentration of 2.2 x10^{-8} cm^{3}STP/g was reported by [6]. Using SCR production rates determined for feldspar [1], and correcting for SCR irradiation at 3 AU rather than 1 AU, we calculate apparent SCR ^{21}Ne and ^{38}Ar exposure ages of ~1500 Myr and ~500 Myr, respectively, for the irradiated Kapoeta grains. Other evidence [8] indicates maximum residence times of the silicate grains on surfaces of meteorite parent bodies of ~1 My, which conflicts with the very long apparent surface exposure ages derived here. The GCR exposure ages calculated from the light phase of Kapoeta are 2.8 Myr for ^{21}Ne and 2.5 Myr for ^{38}Ar using production rates reported by [9]. These values are close to the 3 Myr GCR exposure ages for ^{53}Mn determined from both light and dark phases of Kapoeta by [10].

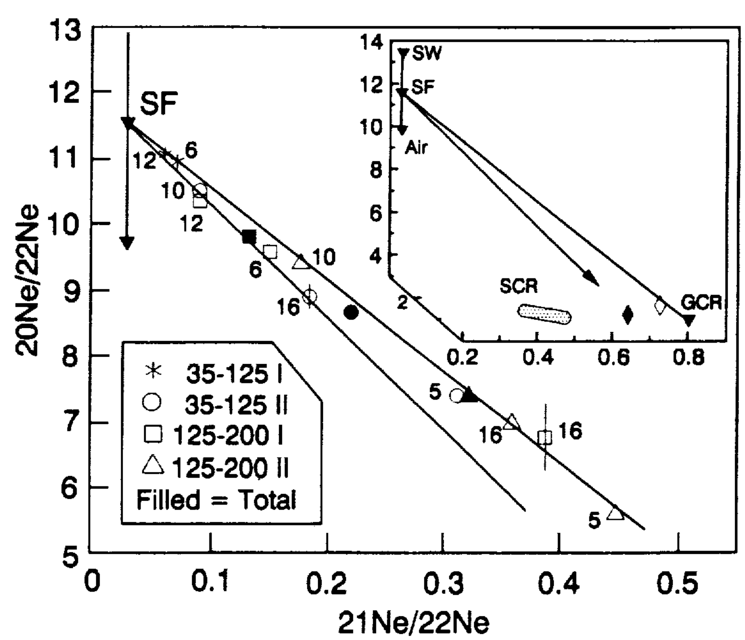
Early Solar Irradiation: Only two obvious explanations exist for the very large calculated SCR exposure ages for Kapoeta. Either the dark phase contains an extra GCR component not present in the light phase [7], or Kapoeta experienced an early solar particle irradiation with a much higher flux than the average solar flux over the past ~4 Gyr [6]. We believe that the first explanation is unlikely because figure 1 indicates that the excess Ne in Kapoeta dark feldspar has an isotopic composition unlike that produced by GCR, but consistent with Ne produced by energetic solar protons as demonstrated on the lunar surface [1]. Furthermore, the expected SCR ^{21}Ne concentration produced from ~1 Myr of exposure to a contemporary flux of solar protons at 3 AU should be <1% of the GCR ^{21}Ne measured in Kapoeta and should not be detectable. Yet, SCR and GCR concentrations determined in this study are comparable. On the other hand, if some grains in Kapoeta dark-phase were irradiated during an early, energetic phase of the Sun [6] at ~500-1000 times the contemporary flux of solar energetic particles, then a surface residence time on the Kapoeta parent body of only ~1 Myr would be sufficient to produce the observed excesses. We favor this latter explanation, which requires that the ancient Sun was highly active, emitting a proton flux of several hundred times the present SCR flux.

References: [1] Rao et al. (in press) *J. Geophys. Res.*; [2] Garrison et al. (1993) *LPSC 24* (abs); [3] Rao et al. (1990) *LPSC 21* (abs), 993; also, Rao et al. (1991) *J. Geophys. Res. 96*, 19321; [4] Brownlee & Rajan (1973) *Science 182*, 1241; [5] Price et al. (1975) *Proc. LPSC 6th*, 3449; [6] Caffee et al.(1987) *Ap. J. Lett 313*, L31; [7] Weiler et al. (1989) *G.C.A 53*, 1441; [8] Housen et al. (1979) *Icarus 39*, 317; [9] Hohenberg et al. (1979) *Proc. LPSC 9th*, 2311; [10] Goswami and Nishiizumi (1982) *LPI Tech. Rep. 82-02*, 44.

Fig 1. Three-isotope Ne correlation plot for temperature extractions (open symbols) and summed data (closed symbols) of etched grain-size separates of Kapoeta feldspar. Numbers indicate extraction temperatures in 100°C. Uncertainties are within the symbols, except where shown. Theoretical SCR field determined for lunar feldspar [1]. Filled diamond = 61016 [1]; Open diamond = Kapoeta irradiated grains reported by [6].

Table 1. Cosmogenic concentrations, x10^{-8} cm^{3}STP/g, in etched feldspar size fractions from dark and light phases of Kapoeta. Previous (I) and present (II) analysis of each size fraction are shown. Estimated uncertainties are ~±10%. [a]Total cosmogenic; [b]Dark phase excess.

Kapoeta Feldspar	[^{21}Ne] Total[a]	Excess[b]	[^{38}Ar] Total[a]	Excess[b]
Dark:				
35-125μm$_I$	1.21	0.70	1.25	0.74
35-125μm$_{II}$	1.16	0.65	1.40	0.89
125-200μm$_I$	1.40	0.89	1.29	0.78
125-200μm$_{II}$	1.42	0.91	1.34	0.83
Light:				
35-200μm$_I$	0.54		0.51	
35-200μm$_{II}$	0.48		0.51	



577-23
ABS. ONLY

N94-20713

COSMOGENIC-RADIONUCLIDE PROFILES IN KNYAHINYA: NEW MEASUREMENTS AND MODELS*; R. C. Reedy[1], J. Masarik[1], K. Nishiizumi[2,3], J. R. Arnold[2], R. C. Finkel[4], M. W. Caffee[4], J. Southon[4], A. J. T. Jull[5], and D. J. Donahue[5]; 1. Los Alamos National Laboratory, Los Alamos, NM 87545. 2. Univ. California, La Jolla, CA 92093. 3. Present address: Univ. California, Berkeley, CA 94720. 4. Lawrence Livermore National Lab., Livermore, CA 94551. 5. Univ. Arizona, Tucson, AZ 85721.

Cosmic-ray-produced nuclides measured in samples taken from known locations on a big slab of the large (R≈45 cm) L5-chondrite Knyahinya [1] provide good depth-*vs.*-concentration profiles to develop and test models for the production of cosmogenic nuclides in meteorites [*e.g.*, 2,3,4]. We report new profiles for ^{10}Be, ^{26}Al, ^{36}Cl in metallic and non-magnetic phases of 8 documented samples from Knyahinya and for ^{14}C in bulk samples from 7 Knyahinya samples. These new measured profiles are very similar to profiles calculated with particle fluxes from the LAHET Monte Carlo production and transport code system and with cross sections for major reactions.

Samples and Measurements. Our samples are from 8 locations on the same big slab of Knyahinya used by [1] for their measurements. The chlorine content of one sample was determined by M. Honda and M. Ebihara [priv. comm.] to be 50 parts-per-million by weight. One set of 8 samples was separated into metallic and non-magnetic phases, and major target elements in each phase were measured by atomic absorption spectrometry. The metallic phases contained ~0.2% silicates. Be, Al, and Cl were chemically separated, and ^{10}Be, ^{26}Al, and ^{36}Cl were measured at Livermore by accelerator mass spectrometry (AMS). Measured concentrations as a function of depth from the pre-atmospheric surface determined by [1] are shown in Figs. 1–3, except for ^{26}Al in the metallic phase, which is being measured. The ^{10}Be and ^{26}Al in our non-magnetic samples agree well with the same radionuclides measured by [1] in bulk samples. A set of 7 samples was analyzed at Tucson for their ^{14}C contents using AMS, and results are shown in Fig. 4.

The profile for ^{10}Be in the metallic phase decreases slightly from the surface to the center. The profile for ^{36}Cl in the metallic phase is fairly flat, similar to that measured for ^{36}Cl in metallic phases from other chondrites, and the measured concentrations are the same as those in most other chondritic metal [*e.g.*, 5]. The other profiles show a decrease in concentration with decreasing depth for depths $\lesssim$20 cm and a flat profile nearer the center.

Model and Calculated Production Rates. Our calculations are based on Los Alamos LAHET Code System (LCS) [6], which is a system of coupled Monte Carlo computer codes that treats the relevant physical processes of particle production and transport. This code system is discussed in [7,8] and is very similar to that used by [4]. An isotropic GCR irradiation by 4.8 protons/cm^2/s, corresponding to the GCR primary particle spectrum averaged over a typical solar cycle, of a sphere with a radius of 45 cm (160 g/cm^2) and Knyahinya's bulk composition was simulated, and neutron and proton fluxes were calculated for concentric shells with 2.5-cm thickness. Production rates for spallogenic nuclides were calculated with these particle fluxes and cross sections for neutron- and proton-induced reactions on major target elements. The proton-induced cross sections are mainly experimental ones used to model nuclide production by solar protons. The cross sections for energetic neutrons are ones used previously at Los Alamos for GCR production in the Moon and meteorites and usually have been adjusted to fit measured data, such as done for ^{36}Cl [5]. Rates for the ^{35}Cl(n,γ)^{36}Cl neutron-capture reaction were calculated directly by LCS. Statistical errors in the calculated particle fluxes were less than 5%.

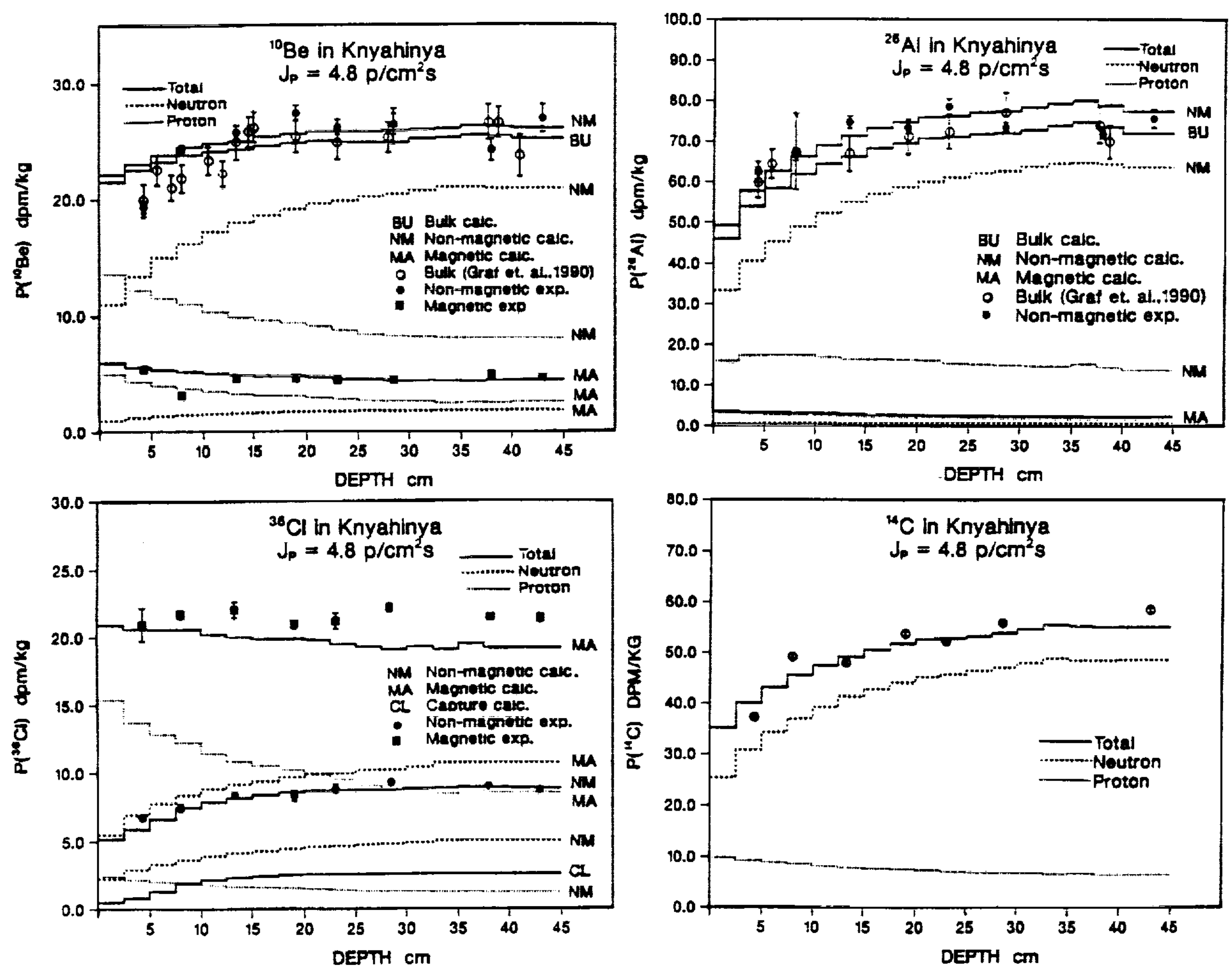
The production rates calculated with LCS are shown as the lines in Figs. 1–4, with production by secondary energetic neutrons and by primary and secondary protons shown as well as the total rate. For ^{36}Cl in the non-magnetic samples, an additional line shows production by the ^{35}Cl(n,γ)^{36}Cl reaction for 50-ppm chlorine. For ^{10}Be and ^{26}Al, the total production rates calculated for bulk samples also are shown. Our calculated production rates for ^{26}Al in bulk Knyahinya samples are similar to those calculated by [4]. In metal, ^{26}Al is calculated to be ~3 dpm/kg.

Comparison of Measured and Calculated Activities. For ^{14}C in bulk samples, there is good agreement (~ 10%) of the calculated production rates with the measured activities, with energetic-neutron production dominant. For ^{10}Be and ^{26}Al, the calculated production rates agree within about ±10% of the measured concentrations, except for an unusually low value for ^{10}Be in one metallic sample. For bulk and non-magnetic samples, production by energetic neutrons dominates for ^{10}Be and ^{26}Al, whereas high-energy particles, mainly protons, dominate their production in metal. The production rates in bulk samples are slightly lower than for non-magnetic samples

because of the lower rates for the metal in the bulk samples.

For ^{36}Cl in the metallic phase, the calculated production rates in deeper samples are less than the measured activities. The difference in measured to calculated activities parallels the calculated rates by energetic neutrons, suggesting that the cross sections estimated by [5] for ^{36}Cl made from Fe and Ni by high-energy neutrons are too low at lower energies. Our calculations for ^{36}Cl in metal from St. Severin are also similarly low. Production of ^{36}Cl by high-energy particles is very important in metallic samples. In non-magnetic samples, the calculated and measured ^{36}Cl activities and profiles agree well, within ~10%. The calculations indicate that pure spallogenic ^{36}Cl in the non-magnetic phase would have a fairly flat profile and that it is production of ^{36}Cl by the capture of thermal neutrons that causes most of the observed increase in activity near the center relative to that near the pre-atmospheric surface.

References: [1] Graf Th. *et al.* (1990) *Geochim. Cosmochim. Acta*, **54**, 2511. [2] Graf Th. *et al.* (1990) *Geochim. Cosmochim. Acta*, **54**, 2521. [3] Reedy R.C. (1991) *Meteoritics*, **26**, 387. [4] Michel R. *et al.* (1991) *Meteoritics*, **26**, 221. [5] Nishiizumi K. *et al.* (1989) *PLPSC-19*, 305. [6] Prael R.E. and Lichtenstein H. (1989) *Los Alamos Report LA-UR-89-3014*. [7] Masarik J. and Reedy R.C. (1992) *Meteoritics*, **27**, 256. [8] Masarik J. and Reedy R.C. (1993) *This Conference.*
* Work supported by NASA and done at LANL and LLNL under the auspices of the US DOE.



Figs. 1–4. Measured and calculated activities of ^{10}Be, ^{26}Al, ^{36}Cl, and ^{14}C in samples from Knyahinya are shown as functions of depths from the pre-atmospheric surface. The ^{14}C is from bulk samples, as are results by [1] shown for ^{10}Be and ^{26}Al. Other activities were for separated metallic or non-magnetic phases. If not shown, experimental errors are smaller than the symbol. Calculated rates are shown as lines for production by energetic neutrons and protons as well as total rates in the phases measured. Calculations for the neutron-capture production of ^{36}Cl in non-magnetic samples and for total production of ^{10}Be and ^{26}Al in bulk samples are also shown.

578-46
ABS. ONLY

N94-20714

KALKKOP CRATER, EASTERN CAPE - A NEW IMPACT CRATER IN SOUTH AFRICA;
[1]W.U. Reimold, [2]F.G. Le Roux, [3,4]C. Koeberl, and [4]S.B. Shirey, [1]Econ. Geol. Res. Unit, Univ. of the Witwatersrand, P.O. Wits 2050, Johannesburg, R.S.A.; [2]Geol. Surv. of South Africa, P.O. Box 1774, Port Elisabeth 6000, R.S.A.; [3]Inst. of Geochemistry, Univ. of Vienna, Dr.-Karl-Lueger-Ring 1, A-1010 Vienna, Austria; [4]Dept. of Terr. Magn., Carnegie Institution, 5241 Broad Branch Road, N.W., Washington, D.C. 20015, U.S.A.

Reimold et al. [1] suggested that the 640 m diameter Kalkkop crater, at 32°43'S/24°34'E in the Eastern Cape Province (South Africa), could possibly be of impact origin. This idea was based on the circularity of this structure, its regional uniqueness, lack of recent igneous activity in the region, and descriptions of drillcore [2,3] indicating that the crater is not underlain by a salt dome and is partially filled with a breccia layer of a thickness which would agree with the dimensions expected for an impact structure of this size. Unfortunately the old drillcore was no longer available for detailed study, and in the absence of sufficient surface exposure only drilling could provide the evidence needed to solve the problem of the origin of Kalkkop. For this reason and to study the crater fill from a paleoenvironmental point of view, the S. African Geological Survey decided to sponsor a new research drilling project at the Kalkkop site. We are now able to present first petrographic and isotopic results from Kalkkop drillcore studies confirming, without doubt, that this crater is of impact origin.

The Kalkkop drilling project was to comprise a vertical borehole into the center and a second, steeply inclined borehole from outside of the rim towards the crater center. To date, the central borehole has been sunk to a depth of 151.8m, where drilling was temporarily suspended. However, it is known from [2] that the fractured/brecciated basement will only be reached at ca. 213m depth. The stratigraphic record obtained so far consists of 89.3 m crater sediment (finely laminated limestone with a few mm- to cm-wide debris flows) that is underlain by breccia. This breccia (Fig.1) appears very similar to suevite from other impact structures. Fresh melt or glass fragments have not been found yet - the whole breccia layer is strongly wheathered; but inclusions, interpreted as altered 'flaedle' or glass particles were repeatedly observed in thin sections. It is therefore justified to apply the term suevite to the Kalkkop breccia. The 3 examples of Kalkkop breccia shown in Fig. 1 show strong differences in clast population and texture on a m-scale. Clasts are either shale or sandstone, derived from the Middleton Formation (Lower Beaufort Group, Karoo Sequence). Below ca. 140 m, clast sizes increase to >1 m. Several strongly fractured shale clasts broke on gentle prodding to reveal shatter cone-like fractures (Fig. 2a,b) with apices pointing in many different directions with regard to the orientation of the borehole. It is believed that these 'fractures' are the result of interference of the strong cleavage/lamination of the shale with cratering-induced microjoints.

A visit to Kalkkop revealed that the structure is raised a few m above the surrounding Beaufort sandstone plains, because the limestone crater fill is capped by a very resistant calcrete layer. Exploration trenches dug close to the rim and limited outcrop along the crater rim indicate shallow (4-20°), inward dips for the limestone (Fig. 3a,b). Where limestone and rim sandstone can be studied in contact, the sandstone stands vertical. It is strongly deformed by narrow-spaced, vertical, radial joints (Fig. 3c). A few m from this locality, the sandstone dips at 10° towards the crater center and is possibly overturned.

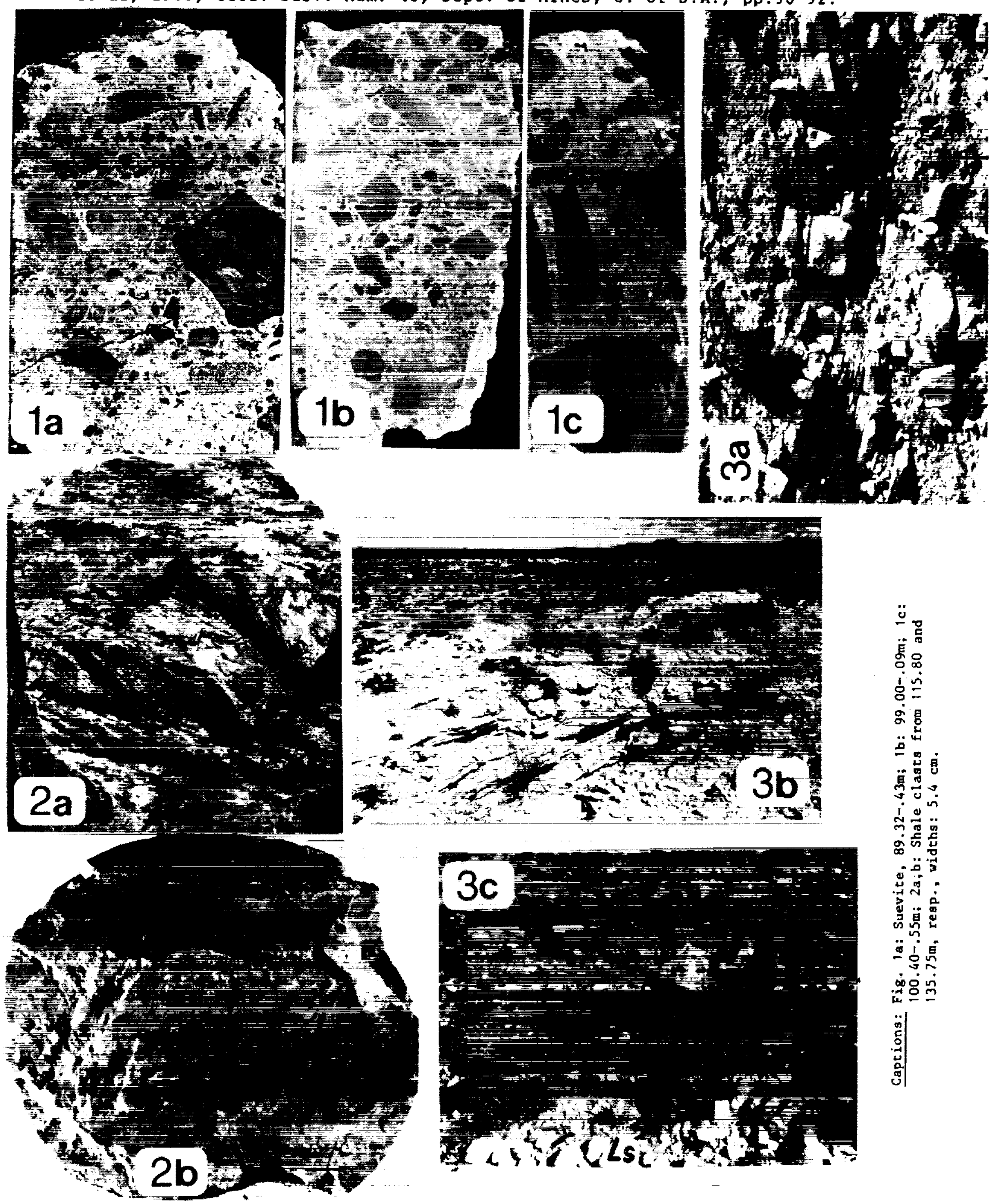
Numerous quartz grains with planar deformation features (PDFs) in up to 6 orientations per grain were detected. In addition, partially isotropic quartz grains, frequently with relics of densely spaced PDFs, and a few alkali feldspar grains with PDFs were observed. The total amount of probable (altered, but still recognisable) melt breccia and glass fragments is estimated at <<1% of the total breccia volume. However, the much larger Ries crater does not contain much melt breccia either, and it was argued that this could be caused by sedimentary targets. At the top of the breccia layer a series of mm-thick gritty layers were found and interpreted as debris off the crater rim. However, the lowest one contains a high amount of sulfide droplets and many shocked grains and could represent a fallout layer.

Negative thermal ionization mass spectrometry was used to measure the concentrations and isotopic abundances of Os and Re in selected samples of Kalkkop sandstone, shale and suevite. The $^{187}Os/^{186}Os$ ratios are a new powerful tool to detect the presence of a meteoritic component in impact melts, even at very low abundances (cf. Koeberl and Shirey, this volume). The sandstone has Os and Re abundances of 0.019 ppb and 0.033 ppb, resp., a $^{187}Os/^{186}Os$ ratio of 7.65 and a $^{187}Re/^{186}Os$ ratio of 73. The shale yielded Os and Re abundances of 0.027 and 0.090 ppb, and $^{187}Os/^{186}Os$ and $^{187}Re/^{186}Os$ ratios of 7.69 and 147, respectively. These values are fairly typical for old crustal rocks. The suevite, however, showed Os and Re abundances of 0.189 and 0.062 ppb, and $^{187}Os/^{186}Os$ and $^{187}Re/^{186}Os$ ratios of 1.79 and 16.1. The low $^{187}Os/^{186}Os$ ratio, in comparison with the high, crustal target rock ratios,

is unambiguous proof of a meteoritic component in the suevite. This component is also supported by the 7-10 times higher Os content in the suevite, compared to target rocks. In **conclusion, petrographic and isotopic studies have provided unequivocal proof of an impact origin for the Kalkkop crater.**

Acknowledgements: The support of the Director of the Geological Survey of South Africa is gratefully acknowledged. C.K. and S.B.S. are supported from the Austrian FWF Project. No. P9026-GEO and the NSF Project. EAR-9218847.

Refs.: [1] Reimold et al., 1992, LPSC XXIII, 1141-1142; [2] Blignaut et al., 1948, Geol. Surv., U. of S.A., Expl. of sheet No. 166, pp.17-22; [3] Haughton et al, 1953, Geol. Surv. Mem. 45, Dept. of Mines, U. of S.A., pp.90-92.



Captions: Fig. 1a: Suevite, 89.32-.43m; 1b: 99.00-.09m; 1c: 100.40-.55m; 2a,b: Shale clasts from 115.80 and 135.75m, resp., widths: 5.4 cm.

577-90
ABS ONLY

16 N94-20715

MICROMETEORITE DYNAMIC PYROMETAMORPHISM: NONSTOICHIOMETRIC CLINOENSTATITE (CLEN).

Frans J.M. Rietmeijer, Department of Earth and Planetary Sciences, University of New Mexico, Albuquerque, NM 87131, USA.

Polymorphs of enstatite are common phases in many meteorites. They contain clues on their formation and the thermal evolution of their host rock which includes shock metamorphism. Rare, micron-sized, CLEN whiskers and thin platelets in chondritic porous micrometeorites were interpreted as solar nebula condensates that remained unaffected during atmospheric entry flash-heating [1]. This CLEN formed by (1) protoenstatite (PEN) inversion whereby the surface energy of the micron-sized PEN crystals aided the OREN-CLEN transformation or (2) by metastable growth [1]. Ca-poor, Mg,Fe-pyroxene with unequilibrated, intraparticle, Mg/(Mg+Fe) distributions occur in most chondritic micrometeorites [2, for a recent review]. These distributions are a parent body signature that survived dynamic pyrometamorphism [3] because the duration of the thermal spike during atmospheric entry is too short [4] but this conclusion does not consider the ultrafine grain size of micrometeorites. The maximum temperature and duration of the heating event will depend on the kinetic energy and entry angle of the incoming micrometeorite. But lacking detailed petrological data for an individual particle, its thermal profile during atmospheric entry can not be deduced from its mass alone as a function of entry angle [5]. In order to constrain dynamic pyrometamorphism in unmelted micrometeorites I have determined the petrological composition and silicate mineralogy [5] in non-chondritic micrometeorites L2005T13, L2005E40 and L2006A28.

RESULTS. All three particles are coarse-grained with sulfide and silicate grains that are on average between ~0.5 and 1.5 μm, in size. Particle L2005T13 has no distinct iron-oxide rim but Fe-oxide grains that are up to several hundreds of nanometers in size, are scattered along the periphery. Mostly euhedral CLEN single-crystals are elongated along the *a* crystallographic axis. They are up to 1.7 x 0.28 μm, in size with a subequant *bc* cross-section of about 250 x 550 nm. Particles L2005E40 and L2006A28 predominantly consist of Fe,Ni-sulfides. They have a polycrystalline maghemite rim that is distinctly associated with the Fe,Ni-sulfides. This rim is 85-125 nm thick on L2005E40 and much thicker, 220-340 nm, on L2006A28. Both particles have ultrafine-grained (< 100 nm in size), polycrystalline, domains among the coarse sulfide grains. These domains contain rounded and subhedral CLEN, nonstoichiometric Mg-rich olivine and Ca-poor pyroxene, Fe,Ni-sulfides and (probably) iron-oxide nanocrystals in an amorphous matrix. Subhedral CLEN single-crystals in L2005E40 (up to 300 x 220 nm in size) have hollow crystal faces. CLEN in L2006A28 occurs as rounded crystals up to ~75 nm, in size embedded in polycrystalline domains with an almost (CI-) chondritic composition.

CLEN. High-resolution lattice imaging of pyroxene single-crystals in L2005T13 show a disordered phase with CLEN field widths indicating the PEN tranformation. The average of 15 single-crystal electron diffraction patterns along different major zone axes yield: *a* (Ä) = 10.9 (± 7.5%), *b* (Ä) = 9.9 (± 6%), *c* (Ä)= 5.9 (± 10%) and β = 111.5° (range 110-113°). These data are consistent with the High-CLEN polymorph. CLEN is chemically pure with a structural formula $Mg_{(2-x)}Si_{(2+0.5x)}O_6$ where X = 0.0 - 0.465 (L2005T13) and X is up to 1.3 in L2005E40. There appears to be a correlation between CLEN single-crystal size and the value for X, whereby X increases with decreasing size.

DISCUSSION. The Fe,Ni-sulfide compositions and associate maghemite rims in particles L2005E40 and L2006A28 suggest dynamic pyrometamorphic temperatures up to 1463K [5]. The Fe,Ni-sulfide compositions in L2005T13 suggest temperatures up to ~1173K [cf. 6]. This lower temperature seems consistent with dispersed iron-oxide grains rather than a distinct rim. This temperature in L2005T13 is ~100° below the OREN-PEN transition at 1273K and suggests that PEN did not form during atmospheric entry flash-heating. Citing earlier observations of enstatite in micrometeorites [1], I assume that the PEN-CLEN transformation also predates atmospheric entry heating. This interpretation is consistent with the relic nature the CLEN

grains in L2005E40 and L2006A28. The interrelationships among the enstatite polymorphs as a function of temperature, pressure and shear stress are still open to debate. Unique enstatite polymorph relationships may not exist due to the (probably) small differences in free energy of the polymorphs. It is possible that (sub)micron high-CLEN is a stable polymorph above 1353K in between the PEN and OREN fields, or metastable low-CLEN instead of OREN [7].

The origin of nonstoichiometric CLEN is enigmatic as there is no MgO or forsterite intimately associated with this pyroxene which excludes reactions such as
(i) $Mg_2Si_2O_6 + (0.5x)\ SiO_2 = Mg_{(2-x)}Si_{(2+0.5x)}O_6 + (x)\ MgO$, or

(ii) $(1+0.5x)\ Mg_2Si_2O_6 + (0.5x)\ SiO_2 = Mg_{(2-x)}Si_{(2+0.5x)}O_6 + (x)\ Mg_2SiO_4$.
There is also no evidence for pyroxene melting either which excludes quenching of a fractionated enstatite-SiO_2 melt.

CONCLUSION. Nonstoichiometric enstatite reflects conditions unique to dynamic pyrometamorphism, *viz*. ultrahigh heating and cooling rates. The high rate of atmospheric entry heating may not be conducive to Mg-rich silicate melting in micrometeorites up to ~30 μm in size. I submit that ultrafast diffusion in these (superheated?) silicates determines their behaviour during dynamic pyrometamorphism. The CLEN compositions delineate a reaction: $Mg_2Si_2O_6 + (0.5x)\ Si = Mg_{(2-x)}Si_{(2+0.5x)}O_6 + (x)\ Mg$. The enthalpy of nonstoichimetric pyroxene in the reaction is probably higher than for CLEN. Diffusion rates in pyroxenes are not well-known but experimental and calculated cation interdiffusion rates in Ca-poor pyroxenes are on the order of 10^{-11} - 10^{-12} $cm^2\ sec^{-1}$ at ~1350K [8]. In this case, magnesium diffusion along the c-axis of CLEN in L2005T13 occurs in ~5 sec. This result by no means constrains the dynamic pyrometamorphism event but it indicates that the proposed mechanism is not impossible.

If ultrafast diffusion produced the nonstoichiometric high-CLEN compositions in these particles, it defines a thermal regime that is much higher than that inferred from Fe,Ni-sulfide compositions in L2005T13. It is not inconsistent with the high pyrometamorphic temperatures in L2005E40 and L2006A28 [5]. Local gas phase ratios, silicate-sulfide distributions, mineral reaction rates and the time-temperature profile of atmospheric entry heating will critically determine the ultimate dynamic pyrometamorphic mineralogy. Whilst models of atmospheric entry heating predict temperatures high enough to melt silicate/Fe,Ni-sulfide particles of ~30 μm in size, there is very little evidence for melting in at least four of these particles.

The results suggest that the thermal models might need revision [5]. Or, the four particles on collectors L2005 and L2006 that sa,pled the stratosphere at the same time are fragments of a micrometeorite that had already slowed down considerably. Hence, the fragments did not reach the high pyrometamorphic temperatures that they would have experienced individually.

REFERENCES. [1] Bradley JP, 1983, *Nature* **301**, 473; [2] Rietmeijer FJM, 1992, In *Research Trends in Mineral.* (J Menon, ed), Council Sc. Res. Integration, India, in press; [3] Klöck W *et al.*, 1990, *LPS* **XXI**, 637; [4] Keller LP *et al.*, 1992, *LPS* **XXIII**, 675; [5] Rietmeijer FJM, 1993, *LPS* **XXIV**, companion abstract; [6] Kullerud G *et al.*, 1969, *Econ. Geol. Monograph* **4**, 323 (Wilson HDB, ed); [7] Schwab RG & Schwerin M, 1975, *N. Jb. Mineral. Abh.* **124**, 223; [8] Rietmeijer FJM, 1983, *Contrib. Mineral. Petrol.* **83**, 169.
This work is supported by NASA grant NAG 9-160.

N94-20716

MICROMETEORITE DYNAMIC PYROMETAMORPHISM: OBSERVATION OF A THERMAL GRADIENT IN IRON-NICKEL SULFIDE.

Frans J.M. Rietmeijer, Department of Earth and Planetary Sciences, University of New Mexico, Albuquerque, NM 87131, USA.

Dynamic pyrometamorphism describes the mineralogical changes in a micrometeorite that occur in response to flash-heating during atmospheric entry. Mineral reactions during this event will be endothermic and act as local sinks for thermal energy which delays a uniform temperature distribution in decelerating micrometeorites [1]. The most common pyrometamorphic reaction is formation of magnetite nanocrystal decorations on Mg,Fe-silicate grains [2] and magnetite [3,4] or (partial) maghemite rims [5]. Constituent silicates also respond to this thermal event and show formation of olivine-maghemite symplectites and growth of garnet [1] and partial laihunitisation [4]. In continued effort to constrain dynamic pyrometamorphism of unmelted interplanetary dust particles (IDPs), I determined the mineralogical composition, and Fe,Ni-sulfide chemistry, in the sulfide-rich particles L2005C39, L2005E40 and L2006A28 using a JEOL 2000FX analytical electron microscope equipped with a TN5500 energy dispersive spectrometer for *in situ* microanalysis [1,5]. Sulfide compositions in these three IDPs are distinctly different from those in silicate-rich particle L2005T13 [6] which might suggest a delicate balance of the fO_2/fS_2 ratios during dynamic pyrometamorphism.

RESULTS. In a Fe-Ni-S (at%) diagram the sulfide compositions in L2005C39, L2005E40 and L2006A28 form a distinct cluster between stoichiometric pyrrhotite (FeS) and $Fe_{7+x}S_8$ (~46 at% Fe) with rare grains between 40-45 at% Fe. Pyrrhotite in L2005C39 and L2006A28 is Ni-free but it contains 2-10 at% Ni in L2005E40. The latter also also contains Ni-rich sulfides with compositions mostly in the monosulfide solid solution field of the Fe-Ni-S diagram and rare pentlandite. The Ni-rich sulfides have almost constant Fe/Ni atomic ratios. The similarity of variations in (Fe+Ni)/S and Fe/Ni ratios among these three IDPs support that they followed comparable time-temperature (T-t) paths during dynamic pyrometamorphism.

Most sulfide grains in these IDPs contain randomly distributed domains that show mottled or striated textures. These textures are related to the presence of nanocrystalline iron-oxide inclusions. The density of iron-oxide domains tends to increase towards the sulfide grain boundary, particularly in the grain area along the pre-entry micrometeorite surface which is the location of a maghemite rim.

I have reported a layered texture in sulfur-rich parts underlying a partial maghemite (γ-Fe_2O_3) rim on IDP L2005T12 [5]. I here describe a layered texture in sulfide grains of L2004E40 adjacent to the maghemite on this particle. The density of randomly distributed iron-oxide domains in the interior part of the sulfide grains increases dramatically and concentrate in a well-defined zone. This zone is about 55-70 nm wide and parallel to the particle surface (Z1). Towards the surface of the IDP, Z1 is overlain by a 140-180 nm wide zone of vesicular sulfides (Z2). The Z1/Z2 interface is well-defined. Adjacent to Z1 the vesicules are small and round and are limited in number. Their number increases sharply towards the interface of Z2 with the maghemite rim. Simultaneously, the vesicule size increases and they develop negative crystal shapes at the contact with the 85-125 nm thick maghemite rim.

DISCUSSION. The maghemite rim, vesicular sulfides (Z2) and iron-oxide nanocrystals (Z1) in L2005E40 delineate dynamic pyrometamophism that included melting, loss of sulfur, and diffusion and oxidation of Fe,Ni-sulfides. To understand the observations it is important that (1) iron self-diffusion in iron-sulfides is very rapid, ~10^{-5} cm^2 sec^{-1} at 1250K, which is many orders of magnitude faster than sulfur diffusion [7] and (2) in IDPs mineral reactions occur at the nanometer scale. Ferous sulfides accommodating ferric iron have the compound formula $Fe^{2+}_{1-3\delta}Fe^{3+}_{2\delta}\square_{\delta}S$, where $\square$ denotes an iron vacancy and δ is the iron deficit; δ is up to 0.25 close to the melting temperature of 1463K [7]. Pyrrhotite compostions, $Fe^{2+}_{1-3\delta}Fe^{3+}_{2\delta}\square_{\delta}S$ (or "po") in this IDP are consistent with a reaction FeS + $0.5O_2$ = "po" + FeO to describe iron diffusion and

oxidation in the sulfides. In ZI δ reaches ~0.25, viz. $Fe^{2+}_{0.25}Fe^{3+}_{0.5}\square_{0.25}S$. Using a best estimate (best guess) for the free energy of "po" (δ = 0.25), the equilibrium oxygen fugacity at 1300K is calculated at 3.45 x 10^{-15} atm. At 1300 K this value is in the wüstite field off the I/W buffer curve. I submit that Z1 was formed at ~1300K. Oxidation of FeO to maghemite took place at higher fO_2 above the hematite/magnetite buffer curve probably during the downward part of the dynamic pyrometamorphic T-t path. An estimate of the oxidation temperature depends on the dT/dt path during micrometeorite cooling and which is unknown. Using the standard US Atmosphere-1976 to estimate fO_2 at the altitude where IDPs reach their rest velocity (~80 km), maghemite probably formed below ~1175K.

Vesicular sulfide in Z2 is evidence for boiling off of sulfur gas. The increase in density and size of these vesicules towards the particle surface is consistent with a temperature increase from the Z1/Z2 interface to the Z2/maghemite rim interface. Desulfurisation of "po" (δ = 0.25) follows a reaction $2FeS + 3/2O_2 = \gamma\text{-}Fe_2O_3 + 2S(g)$ (or S_2) which is endothermic below 525°C. The endothermic nature of this type of reaction at low temperature will make this reaction favorable during kinetically-controlled dynamic pyrometamorphism. The pyrrhotite melting temperature is reached at the Z2/maghemite rim interface. Thus, I calculate a thermal gradient of at least 163K over a distance of 140-180 nm between the Z1/Z2 and Z2/rim interfaces. The temperature in the un-reacted sulfide underlying Z1 was less than 1300K; possibly as low as ~900K as might be inferred from the presence of rare sulfide grains (pre-heating relics) with 40-45 at% Fe [8]. If the estimate is correct the flash-heating thermal gradient in this IDP was 563K over a distance of 195-250 nm. The gradient observed in IDP L2005E40, 0.9 - 2.25 °K nm^{-1}, is much steeper than a gradient of 0.014 °K nm^{-1} calculated for a 100 μm diameter micrometeorite using a thermal diffusivity of 1 x 10^{-10} m^2 sec^{-1} [9].

CONCLUSION. Although survival of layer silicates might indicate heterogeneous temperature distributions in IDPs [9], their unscathed survival in flash-heated IDPs is controlled by the kinetics of the dehydration reactions [10]. Thus, this first observation of a thermal gradient in an unmelted IDP is important because it shows that the asumption of a uniform internal IDP temperature during atmospheric entry is not correct. This assumption is made when modelling the atmospheric entry temperatures as a function of particle mass, velocity and entry angle [9]. It is known that the value for the thermal diffusivity in these models critically determine the calculated temperature distribution. At low values a thermal gradient might be established [9]. The present data show that either probable thermal diffusivity values are < 1 x 10^{-10} m^2 sec^{-1}, which may be unrealistic [9], or endothermic mineral reactions are critical in management of the thermal budget in unmelted IDPs during dynamic pyrometamorphism.

REFERENCES [1] Rietmeijer FJM, 1992, *LPS* **XXIII**, 1151; [2] Fraundorf P, 1981, *GCA* **45**, 915; [3] Germani MS *et al.*, 1990, *EPSL* **101**, 162; [4] Keller LP *et al.*, 1992, *LPS* **XXIII**, 675; [5] Rietmeijer FJM, 1992, *LPS* **XXIII**, 1153; [6] Rietmeijer FJM, 1993, *LPS* **XXIV**, companion abstract; [7] Condit RH *et al.*, 1974, *Oxid. Met.* **8**, 409; [8] Kullerud G *et al.*, 1969, *Econ. Geol. Monograph* 4, 323 (Wilson HDB, ed); [9] Szydlik PP & Flynn GJ, 1992, *Meteoritics* **27**, 294; [10] Rietmeijer FJM, 1991, *Meteoritics* **26**, 388.

This work is supported by NASA grant NAG 9-160.

WAVELENGTH DISPERSIVE ANALYSIS WITH THE SYNCHROTRON X-RAY FLUORESCENCE MICROPROBE M. L. Rivers[1], K. S. Thorn[1], S. R. Sutton[1], K. W. Jones[2], and S. Bajt[1]; [1]Department of the Geophysical Sciences and Center for Advanced Radiation Sources, The University of Chicago, Chicago, IL 60637; [2]Department of Applied Science, Brookhaven National Laboratory, Upton, NY 11973.

A wavelength dispersive spectrometer (WDS) was tested on the synchrotron x-ray fluorescence microprobe at Brookhaven National Laboratory. Compared to WDS spectra using an electron microprobe, the synchrotron WDS spectra have much better sensitivity and, due to the absence of bremsstrahlung radiation, lower backgrounds. The WDS spectrometer was successfully used to resolve REE L fluorescence spectra from standard glasses and transition metal K fluorescence spectra from kamacite.

Introduction: The synchrotron x-ray fluorescence (SXRF) microprobe [1-3] has proven to be a valuable tool for trace element cosmochemical and geochemical research permitting analyses down to the parts-per-million level for many elements with a spot size of less than 10 mm. Existing SXRF microprobes are using energy dispersive detectors (EDS), either Si(Li) or intrinsic Ge diodes. Such detectors have the advantage of collecting the entire fluorescence spectrum at once and can also be positioned to collect a relatively large solid angle. However, EDS detectors suffer from several significant problems: (1) energy resolution at Fe K_α is about 150 eV, roughly 60 times the natural line width; (2) the maximum count rate is about 20,000 counts/second in the entire spectrum; (3) low-energy background due to scattering and incomplete charge collection in the device is significant. These limitations preclude trace element analyses in the presence of a major concentration of a high atomic number element: for example, trace elements studies zircon ($ZrSiO_4$) and Cr and Ti analyses in minerals with more than a few percent Fe or Mn. The poor energy resolution also prevents the measurement of L-shell fluorescence from trace rare-earth elements in samples with significant concentrations of first-row transition elements. Wavelength dispersive spectrometers (WDS), based upon Bragg diffraction from a bent crystal, have several distinct advantages over EDS detectors. The resolution at Fe K_α is better than 10 eV, only 4 times the natural line width. This resolution permits the analysis of rare-earth elements and also lowers the background thereby improving detection limits to the 0.1 ppm range. Also, the WDS spectrometer only detects a single energy at any time so it is possible to measure trace elements in the presence of intense fluorescence of a major element.

Experimental: A model WDX-3PC wavelength dispersive spectrometer from Microspec Corporation (Fremont, CA) equipped with LiF(220), LiF(200), PET and TAP analyzing crystals was used. Two proportional counters were included, a thin-window, argon-filled flow counter and a sealed xenon counter arranged in tandem geometry. A remotely adjustable slit (0-2.5 mm) just in front of the flow counter was used to control the trade-off between energy resolution and count rate. The spectrometer was temporarily installed for testing on beamline X-19C under the following conditions: white light, 25 μm beam size, 20 m from the source, 55 cm of air and 50 μm of Al in the incident beam, single bunch operations, 70 mA average ring current. A variety of standard samples were analyzed to determine sensitivities, peak/backgrounds, and other important perfomance benchmarks.

Results: X-ray fluorescence spectra of Fe metal and Zn metal obtained with both the SXRF microprobe and the electron microprobe showed that the synchrotron spectra have much lower backgrounds due to the absence of bremsstrahlung radiation. Using a 0.25 mm exit slit rather than a 1mm slit on the spectrometer reduced the count rate by a factor of 3 but improved the resolution by a factor of 2, from 21 to 11 eV (FWHM). High energy resolution is desirable in cases of very close spectral overlaps.

Spectra for kamacite from IAB iron meteorites (Odessa and Canyon Diablo) are shown in figure 1. The upper spectrum was collected on X-26A with a Si(Li) detector, while the lower one was collected on X-19C with the WDS spectrometer. The WDS detector completely resolved Co and Cu K fluorescence peaks which suffer severe overlap in the Si(Li) spectrum. Galium and Ge are present in these samples at about 70 and 260 ppm, respectively. One of the most difficult sets of elements to analyse using the Si(Li) detector at X-26A are the rare-earth elements (REE). The difficulties arise from the large number of closely spaced L fluorescent lines (4 major lines per element), the fact that REE almost always occur together, and the overlaps with the K fluorescent

lines of the first-row transition elements. Figure 2 shows spectra of synthetic glasses doped with several REE. Note that in almost all cases the WDS detector has completely resolved the lines, while there are often severe overlap problems with the Si(Li) detector. These results suggest that the WDS detector will permit routine analysis of REE on the X-26A microprobe.

Spectra of a standard anorthite glass showed that the count rate at low energy (e.g., Ca at 3.69 keV) was much lower using the WDS detector than it was on X-26A using the Si(Li) detector. Absorption along the longer air path in the incident beam at X-19C can partly but not entirely explain this difference. Other possible effects that are being investigated include absorption in the poorly-characterized Be entrance window on the spectrometer and decreased spectrometer efficiency at lower energy (higher Bragg angles).

Future Directions: The WDX-3PC spectrometer will be installed permanently on the SXRF microprobe on beamline X-26A during Spring, 1993, and will be mounted such that the existing Si(Li) detector can be used simultaneously. This combination of detectors should greatly enhance the utility of the microprobe: the Si(Li) detector will be used for the ``big picture" since it collects the entire spectrum at once, while the WDS spectrometer will be used to obtain maximum sensitivity for a particular element, and in cases where spectral overlaps exist. The experimental conditions at X-26A are much more favorable than those used for the tests reported here on beamline X-19C. The X-26A conditions are as follows: white light or monochromatic light, 8 micron beam size, 9 meters from the source, 3 cm of air in the incident beam, 25 bunch operations, 150 mA average current. The countrate reduction due to the smaller beam size on X-26A will be almost exactly offset by the shorter distance to the source and the higher ring currents. In addition, the incident beam filtering will be greatly reduced. Thus, we expect the count rates at X-26A to be comparable to those obtained in these tests except at low energy where we expect much better sensitivity.

Acknowledgments: This research was supported by the following grants: NSF EAR89-15699 (MLR), NASA NAG9-106 (SRS), DOE-E&G DE-FG02-92ER14244, Chemical Sciences Division, Office of Basic Energy Sciences, US DOE under Contract No. DE-AC02-76CH00016.

References: [1] Rivers M. L., et al. (1992) in X-ray Microscopy III, Springer-Verlag, 212-216. [2] Flynn, G. J., and Sutton, S. R. (1990) Proc. 20th Lunar Planet. Sci. Conf., 335-342. [3] Jones, K. W. and B. M. Gordon (1989) Anal. Chemistry 61, 341A-356A.

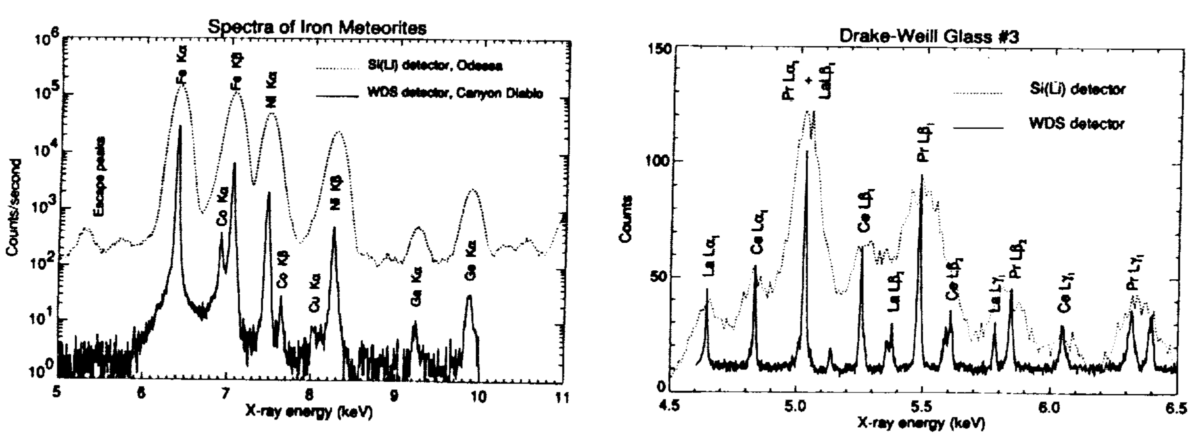


Figure 1: XRF spectra of IAB iron meteorites done using a Si(Li) detector at X-26A and the WDS spectrometer at X-19C. The Co and Cu peaks are well resolved in the WDS spectrum, while they are completely overlapped in the Si(Li) spectrum. The Si(Li) spectrum was filtered with 170 μm Al to reduce the Fe count rate and was collected for 10 minutes. The WDS spectrum was collected for 37 minutes, but the time on each peak was only about 15 seconds.

Figure 2: Spectra of synthetic glasses which contain several percent rare-earth elements. Si(Li) spectrum was collected for 100 seconds on X-26A using a 200 μm Kapton filter to reduce the Ca count rate. The REE peaks are well resolved in the WDS spectrum whereas the Si(Li) spectra suffer from severe overlap. The WDS spectrum was collected for 1000 seconds.

582-91
ABS ONLY

SUBDUCTION ON THE MARGINS OF CORONAE ON VENUS: EVIDENCE FROM RADIOTHERMAL EMISSIVITY MEASUREMENTS. C.A. Robinson, Harvard-Smithsonian Center for Astrophysics, Cambridge MA 02138.

Retrograde subduction has been suggested to occur at three coronae on Venus: Latona, Artemis and Eithinoha [1]. Using the mineralogical arguments of [2] to explain surface emissivity, a study of radiothermal emissivity of Venus coronae [3] has shown that emissivity changes associated with Latona, Artemis and Ceres imply the same crustal movements predicted by the subduction model of [1].

Emissivity (e) varies with altitude (a) on Venus: at low altitudes e is nearly constant at ~0.85, then at an altitude around 6055-km planetary radius (the critical altitude (c.a.) [2]) e decreases abruptly to values as low as ~0.35. One explanation for this first-order a/e trend is that weathered material at high altitudes has a greater dielectric constant (~20) than that at low altitudes (5-10) owing to a higher proportion of electrically conductive minerals within the dry host rock (~7% at high altitudes compared with ~3% at low altitudes) [2,4]. Deviations from this first-order trend can be simply explained by the absence of weathered material at high altitudes in some settings, owing to volcanic or tectonic activity that has occurred so recently that weathering has not had time to create the low-e mineralogy [5,6]; instances of this can be detected by constructing a/e scatter plots (e.g. Fig. 1).

At Latona the features of the a/e plot (Fig. 1) crucial to this discussion are the points within the areas labelled A, B and C. The points which make up area A come from measurements in the inner wall of the N and NW rim of Latona, and the two intermediate-altitude low-e regions come from measurements that embrace the inner SE rim (B) and the trench outboard of the rim (C; Figs. 2 and 3). Assuming the anomalous low-e material was produced at higher altitudes where its mineralogy is stable [2], then its presence at low altitudes now can be explained by recent tectonic movement of crustal material downwards and in a southeasterly direction. These activities must have taken place at a rate faster than that of weathering in order to retain the anomalous emissivity signatures, and so may be continuing to the present day. This interpretation of tectonic activity at Latona is the same as that predicted by the subduction model of [1] which proposes that subduction may be occurring along the margins of the SE sector of Latona. [1] also suggest that extension should take place in the corona interior in order to accommodate the subduction; such extension could explain the downward movement of the low-e material at the inner N and NW rim by tensional tectonics.

At Artemis an important second-order deviation from the first-order a/e trend is that e decreases by only 10% along the NE rim compared with the 30-50% decrease usually observed above the c.a.; the NE rim of Artemis reaches 6057.9 km which is 2.9 km higher then the average c.a. recorded by [2]. This suggests that formation of weathered material is incomplete over this part of the rim which would indicate that it has been uplifted recently at a rate comparable to that of weathering. Uplift of the rim is expected in the subduction model for Artemis of [1], owing to compressive forces that result from subduction into the trench outboard of the rim.

Ceres was not included in the study of [1], but results from the study of [3] indicate it has experienced tectonic movements similar in nature to those at Latona. At the NNW rim the first-order a/e trend is observed since low-e material is found at high altitudes, but on the SSE rim deviations from the first-order trend are observed: low-e material is found in the low-altitude trench outboard of the rim, and high-e material is found at high

altitudes. Assuming the low-e material originally formed at high altitudes, this observation can be explained by recent tectonic movements of crustal material downwards and in a southeasterly direction, possibly by subductive forces similar to those described for Latona. On the other hand [1] suggested that subduction might have occurred at Eithinoha, but there is no evidence in the emissivity dataset to support this. However, this cannot be taken to exclude tectonic activity at Eithinoha. Eithinoha reaches a maximum altitude of 6053.6 km, and therefore if tectonism has taken place it probably would have done so entirely beneath the c.a. and so would not leave evidence in the emissivity dataset in the form of weathered material.

References: 1. Sandwell, D.T., and G. Schubert (1992) *Science* 257, 766. 2. Klose, K.B. et al. (1992) *J. Geophys. Res.* 97, 16353. 3. Robinson, C.A., and J.A. Wood (1993) in preparation. 4. Pettengill, G.H. et al. (1982) *Science* 217, 640. 5. Robinson, C.A., and J.A. Wood (1992) *Icarus*, submitted. 6. Pathare, A. (1992) B.S. thesis, Harvard University.

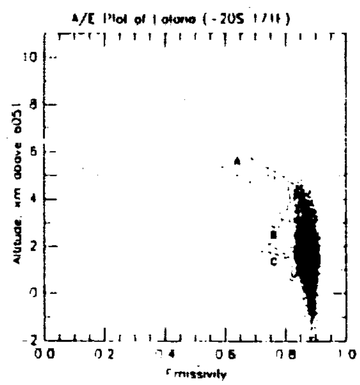


Figure 1. A/e plot of Latona. A: these points come from measurements of the inner N and NW rim. B: these points come from measurements of the SE rim. C: these points come from measurements of the trench outboard of the SE rim.



Figure 2. SAR image of Latona taken from C1MIDRs 15S163 and 30S171 (D:-16°S, 167.5°E; E: -25.5°S, 175°E), showing the location of the NW rim (A), the SE rim (B) and the trench outboard of the SE rim (C). North is to the top of the photograph. Latona measures ~600 km from east to west.

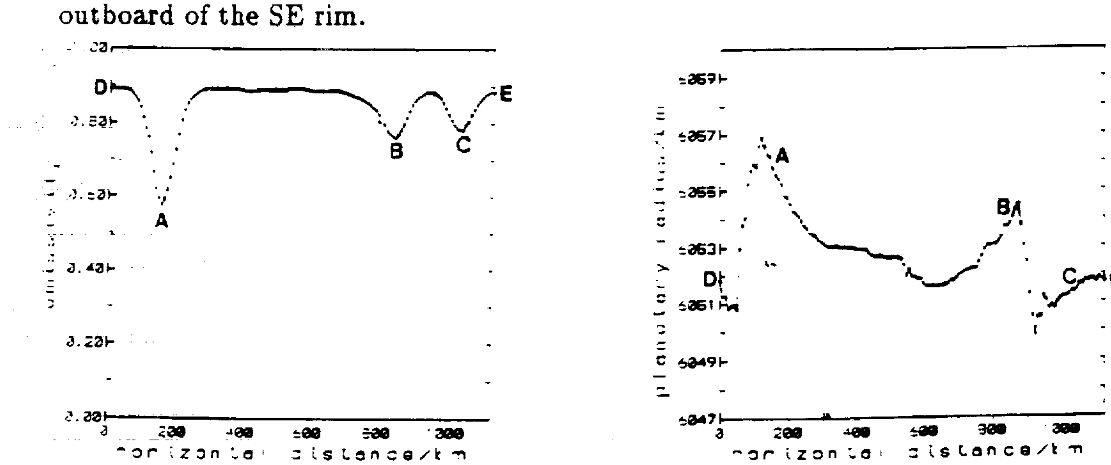


Figure 3. Altimetry and emissivity profiles across Latona (D: -16°S, 167.5°E; E: -25.5°S, 175°E). A: NW rim. B: the SE rim. C: the trench outboard of the SE rim. A, B and C correspond to traverses through the 3 anomalous fields labelled in Fig. 1.

PRELIMINARY RESULTS FROM MARINER 10: HIGH RESOLUTION IMAGES OF THE MOON . Mark S. Robinson[1], B. Ray Hawke[1], Kay Edwards[2], Paul G. Lucey[1], Beth E. Clark[1], [1]*Planetary Geosciences, University of Hawaii, Honolulu, Hawaii, 96822.* [2]*U.S. Geological Survey, Flagstaff, Arizona, 86001.*

In November of 1973 the Mariner 10 spacecraft acquired high resolution images of both the Earth and the Moon as it began its voyage to Venus and then Mercury [1]. The best images had a resolution of ~1 km and were taken from an unusual viewpoint, above the lunar North Pole. At this time the Moon was illuminated such that the eastern limb, including ~30° of the farside, was visible. Two high resolution mosaics were acquired during this period which provide excellent views of regions of the Moon poorly seen from the Earth. These include the Frigoris, Humboldtianum, Marginis, and Smythii regions. These images also covered expanses of highlands not visible from the Earth. These data were unique in that they were the only useful robotic spacecraft images of the Moon; and they remained so until December of 1990 when the Galileo spacecraft made its first encounter with the Moon [2]. We have acquired these Mariner 10 lunar images and are currently using them in conjunction with Earth-based telescopic spectra as well as Apollo and Lunar Orbiter photographic data to investigate the nature of deposits comprising the Northeast Nearside of the Moon (NEN, [3]). These Mariner 10 frames have proved useful for photogeologic, photometric, and photoclinometric (R. Kirk) analyses; they have also been used in support of the second Galileo lunar encounter of December 1992 (see other abstracts this issue [4]).

Our initial work on these high resolution frames includes a sequence of 10 clear filter images that compose a mosaic centered at 70°N 95°E (see Fig. 1). To make these images useful for interpretation we first radiometrically and then geometrically calibrated each frame. During the actual lunar encounter an anomaly in the spacecraft resulted in a lower than expected vidicon temperature; -10° C [1]. Prelaunch calibration tests of the two vidicon imaging systems onboard the spacecraft revealed that one of the cameras (camera A, odd numbered frames) exhibited a sensitivity nonuniformity instability at the lunar encounter temperature [5]. Camera B (even numbered frames) was stable at this temperature. We currently are investigating the calibration of the A frames by comparing regions of overlap with the B frames. Our radiometric calibration includes dark current removal and a nonuniformity/nonlinearity correction based on a scheme we derived from examination of both prelaunch calibration frames and frames shuttered after launch. The details of this radiometric calibration closely follows the procedure outlined in [6].

Recalculation of both the Mariner 10 spacecraft position and camera pointing angles during the lunar encounter was recently performed at the Rand Corporation [7]. We used these new camera angles to determine the geometry of each image at the time of acquisition to calculate latitude and longitude for each pixel within a frame. We corrected for electronics induced geometric distortion in the images by accounting for reseau movement in the images relative to their measured nominal positions on the vidicon [8]. These steps are necessary to geometrically reproject the frames for mosaicking. To test the accuracy of the pointing geometry we compared a calculated limb position based on the new geometry with the actual limb in the images and found that the fit was best on the central nearside (~2 pixels) and worsened around the farside (~20 pixels). The source of this error is undetermined at this point

We have constructed a preliminary normalized albedo map of the NEN region from 4 frames (PICNOs 2660, 2661 ,2667, 2668). The calibrated images were

transformed to relative albedo using a Hapke function [9]. Based on the experience of Galileo Lunar images from 1990, the Hapke parameter Θ was adjusted from 20 to 5 to correct for over-brightening at high latitudes [10]. Examination of seam boundaries between frames indicate that the top left and right corners of the camera A frames are too bright; this being consistent with the prelaunch calibration. We found that selective masking of these areas results in a qualitatively acceptable match. Future work will quantify these results and determine if portions of the A frames are useful for photometric analysis. Our analysis of this preliminary map indicates: 1) Some portions of the "light plains" deposits [11] east and north of Mare Frigoris exhibit unusually low albedo, compatible with mare units. Mare volcanism in this region may have been more extensive than has previously been thought. 2) New albedo data confirm the existence of dark mantle deposits in the NEN region. 3) Localized pyroclastic deposits occur in the interior of Gauss crater; additional analysis may reveal the presence of dark mantling units.

REFERENCES: [1]Dunne, J.A. and Burgess, E. 1978. *NASA SP 424*. [2]Belton et al., 1991. *Science*,255, 570-576. [3]Hawke, B.R. 1992 *Bull AAS*, 24, 1027. [4]Belton, M.J.B. et al., this volume. [5]Benesh and Morrill, 1973 *JPL Doc* 615-148. [6]Robinson et al. 1992, *JGR*, 97, 18265-74. [7]M. Davies, personal comm., 1992. [8]PICS manual 1990. [9] Helfenstein, P. and Veverka, J., 1987, Icarus 72, 342-357. [10]Alfred McEwen, personal communication, 1992. [11]Luchitta, B.K., 1978, *USGS Map I-1062*.

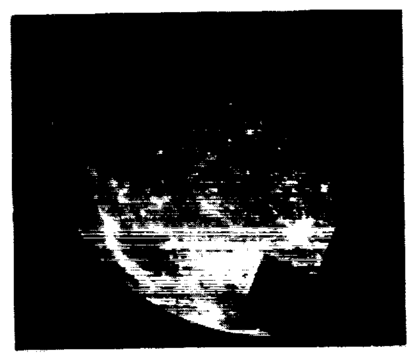


Figure 1. Mariner 10 digital mosaic of the lunar north pole region (orthographic projection, 1.1 km/pixel). The center of the mosaic is 70°N 95°E. This mosaic is very useful for comparison with the recently acquired Galileo SSI image data; LUNMOS04, 67°N 70°E [4]. Mare Humboldtianum is near the center of the disc, while Mare Crisium is the large circular feature near the lower left limb.

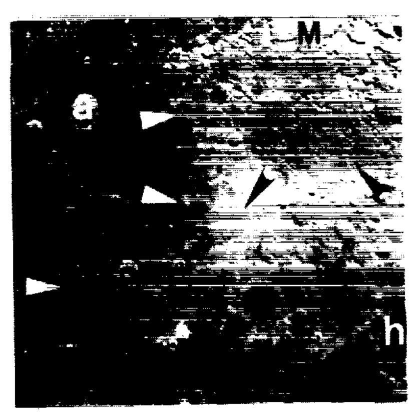


Figure 2. High resolution albedo map of the NEN region of the Moon. The Mariner 10 frames that comprise this mosaic were normalized with a Hapke photometric function [9] . Arrows indicate extensive light plains deposits [11], a = Aristoteles, h = Mare Humboldtianum, M = Meton. UL corner of mosaic 37.4° N 0.1° E; LL 19.1° N 38.1° E; UR 80.8° N 30.7° E; LR 47.2° N 82.8° E.

Acknowledgements: The U.S.G.S., Flagstaff, Arizona, provided PICS which was essential to this study. We thank R. Kirk for photoclinometric assistance.

CHRONOLOGY, ERUPTION DURATION, AND ATMOSPHERIC CONTRIBUTION OF APOLLINARIS PATERA, MARS. M.S. Robinson[1], P.J. Mouginis-Mark[1], J.R. Zimbelman[2], S.S.C. Wu[3]. [1]Planetary Geosciences, SOEST, University of Hawaii, Honolulu, HI, 96822. [2]CEPS National Air and Space Museum, Smithsonian Institution, Washington, D.C. 20560. [3]Astrogeology Branch, U. S. Geol. Survey, Flagstaff, AZ, 86001.

INTRODUCTION: Geologic mapping from Viking image data of the Martian volcano Apollinaris Patera has allowed identification of 6 major events that have shaped its current morphology. Derivation of new topographic data has allowed accurate estimates of the volume of erupted products from which estimates of an eruption duration are presented for the edifice and its corresponding atmospheric water contribution.

For this study topographic data were acquired using stereophotogrammetric (Viking picnos 603A42, 639A92) techniques [1] in both profiling and contouring modes (1 km contour). The profiling mode results in a more precise measurement than the contouring mode, but is limited in its areal coverage. The contour data are used in a more general sense to provide synoptic coverage for the volcano. These new stereophotogrammetric measurements constrain the topography to an accuracy of ~800 m vertically and ~1000 m horizontally. Conversion of the derived contour map to a raster-based digital elevation model (DEM) was done by a growing contours interpolation. An ambiguity arises in this volume calculation due to an uncertainty regarding the actual base of the volcano relative to the pre-existing topography. Thus, the volume estimate was bracketed by using the 100 m and the 750 m elevations, which generally correspond to the lower and upper portions of the circumferential basal scarp, respectively. The resulting volumes are 103,000 km^3 and 97,000 km^3; therefore the total volume of Apollinaris Patera is estimated to be ~100,000 km^3.

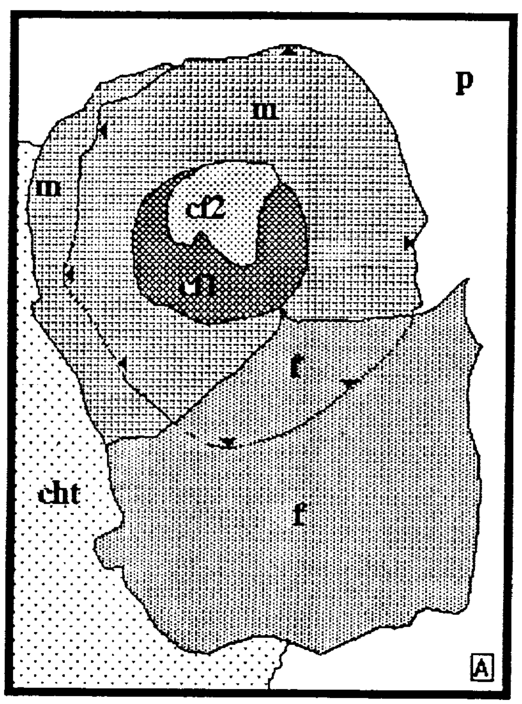
CHRONOLOGY: For this study the volcano is mapped into 4 distinct units (Fig. A); the main edifice (m), the outer caldera (cf1), the distinct fan (f) that occurs on the southern flank, and the inner caldera (cf2) [see also 2,3]. We propose the following 6 stage chronology for Apollinaris Patera (Fig. B): **1)** emplacement of the main edifice (m), largely by explosive activity, **2)** formation of the basal scarp, either by tectonic or erosive processes, **3)** erosion of valleys on the main flanks (f), **4)** formation of the outer caldera (cf1), with infilling, **5)** emplacement of the fan materials (f), dominantly by effusive activity, **6)** and finally, formation of the inner caldera (cf2), with lava flooding (cf2). These divisions are not temporally sharp, but may be gradational in some cases (see Fig. B). For instance, basal scarp formation may have commenced during the latter part of stage 1, while eruption of the materials comprising the fan may be related to intra-caldera activity of stage 4. Formation of the neighboring chaotic material occurred throughout much of the lifetime of the volcano.

ERUPTION DURATION: Typical effusion rates of terrestrial volcanic eruptions are in the range 10^{-3} to 10^{-2} km^3 yr^{-1} [4] from which a plausible range of activity for Apollinaris Patera is estimated, excluding periods of repose, from 10^7 to 10^8 yrs. To constrain further this estimate it is assumed that, to a first order, the rate of eruption at Apollinaris Patera is similar to that of the Hawaiian Hot Spot. The oldest seamount in the Hawaiian-Emperor chain has an age of 65 x 10^6 years and the total volume of the chain is estimated to be 10^6 km^3 [5]. Therefore, the average rate of eruption for the Hawaiian-Emperor Chain is 1.5 x 10^{-2} km^3 yr^{-1} (including periods of repose), which roughly corresponds with the upper rate from Crisp. This Hawaiian-Emperor rate must be considered a lower limit due to removal of an unknown amount of material by erosion. Therefore, our smaller duration estimate (10 x 10^6 years) seems more reasonable.

ATMOSPHERIC CONTRIBUTION: Assuming a density of 2000 kg m^{-3}, which is reasonable for analogous terrestrial deposits, the total mass of material erupted is 2 x 10^{17} kg. Thus a total mass of 2 x 10^{15} kg is predicted for the water vapor released into the atmosphere assuming a reasonable value of 1 wt % for the released water content of the parent magma [6]. This estimate may be substantially low due to the input of non-juvenile water resulting from the interaction of groundwater/ice during

phreatomagmatic eruptions. From the volume calculation and our estimate of eruption duration, approximately 10^7- 10^8 kg yr^{-1} (assuming 1 wt %) of water vapor was added to the Martian atmosphere; for comparison the current total Martian atmospheric water budget is estimated to be about 10^{12} kg [7]. Along with water vapor, it is likely that other gases, such as CO_2 and SO_2, were also released in amounts similar to water, and they also would have an important control on climate [8,9]. Based on these estimates, outgassing from Apollinaris Patera must have had a significant effect on local climate, if not global climate.

REFERENCES: [1]Wu, S. S. C., Elassel, A. A., Jordan, R., and Schafer, F. J. 1982. *Planet. Space Sci.*, 30, 45-55. [2]Scott, D.H, Morris, E.C., and West, M.N. 1978. *US Geologic Survey Map I-1111.* [3]Scott, D.H. and Dohm J.M. in press USGS Map I-2351 [4]Crisp, J.A. 1984. *J. of Volcan. and Geotherm. Res.*, 20, 177-211. [5]Clague, D.A. and Dalrymple, G.B. 1987. U.S. Geological Professional Paper 1350, v. 1, 5-54. [6]Greeley R. 1987. Science, 236, 1653-54 [7]Jakosky, B.M. and Farmer, C.B. 1982. *J. Geophys. Res.*, 87, 2999-3019, [8]Postawko, S.E., Fanale, F.P., and Zent, A.P. 1988. *LPSC XIX*, 943-944. [9]Plescia, J.B. and Crisp, J. 1991. *MSATT LPI Tech Rep 92-02*, 115 - 116.



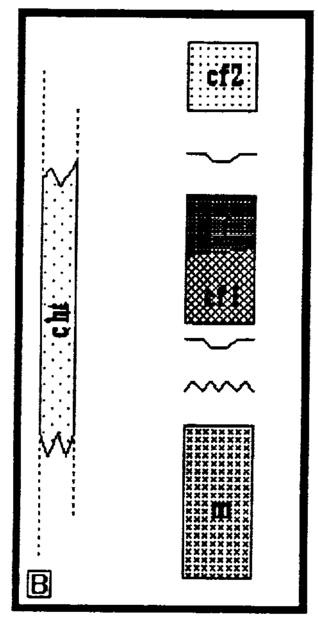


Fig. A. Sketch geologic map indicating the division of Apollinaris Patera into four units (m = main edifice, cf1 = outer caldera, f = fan deposit, cf2 = inner caldera). Unit cht is chaotic terrain and unit p is a simplification of plains units genetically unrelated to Apollinaris Patera. **Fig. B** shows the chronology of events that have resulted in the present morphology of the volcano. Initially unit m was emplaced, then basal scarp and valley formation (jagged line) occurred. Next, outer caldera formation (broken line) with subsequent infilling (cf1), fan (f) emplacement, possibly as a result of late stage overflow from cf1 deposits, and finally inner caldera formation (broken line) with infilling by ponded lava deposits (cf2). Triangles indicate basal scarp, dotted where inferred. Formation of the chaotic terrain adjacent to the volcano both preceded and followed emplacement of the fan materials. Unit cf1 is about 80 km E-W, north is to the top.

Acknowledgements: The U.S.G.S., Flagstaff, Arizona, provided the Planetary Image and Cartography System (PICS) software which was essential to this study. Portions of this work were supported by a Smithsonian Institution Graduate Fellowship. S. Rowland and B. Clark (both Univ. Hawaii) provided helpful input to this work.

168045 N94-20721 p. 2

THE MANSON IMPACT CRATER: ESTIMATION OF THE ENERGY OF FORMATION, POSSIBLE SIZE OF THE IMPACTING ASTEROID OR COMET, AND EJECTA VOLUME AND MASS; D.J. Roddy and E.M. Shoemaker, U.S. Geological Survey, Flagstaff, AZ 86001; R.R. Anderson, Iowa Department of Natural Resources-Geological Survey Bureau, Iowa City, IA 52242-1319

A research program on the Manson impact structure has substantially improved our knowledge of the detailed features of this eroded crater [1]. As part of our structural studies, we have derived a value of 21 km for the diameter of the final transient cavity formed during crater excavation. With this information, we can estimate the energy of formation of the Manson crater and the possible size of the impacting asteroid or comet. In addition, we have estimated the near- and far-field ejecta volumes and masses.

High-speed impact produces a transient cavity that expands rapidly outward from the penetration path of the projectile. After the transient cavity has reached its maximum size, its uplifted rim begins to collapse inward, and the crater floor starts to rebound. In large craters, the rim collapses to form a structurally complex set of down-dropped blocks (referred to as terrace terrane in [1]). These blocks normally move downward and inward to produce a final collapsed crater substantially larger than the transient cavity. The contact between the down-dropped block nearest the crater center and the chaotic crater breccia on the crater floor marks the approximate final position of the wall of the transient cavity. The wall is transported slightly inward during collapse.

Our estimate of the present position of the transient cavity wall at Manson is based on interpretation of a seismic reflection profile provided by Amoco. This interpretation is supported by new drill core data acquired along this east-west radial. Drill holes in adjacent blocks in the terrace terrane penetrated down-dropped Upper Cretaceous strata and crater ejecta stacked in inverted stratigraphic sequence. The distance from the west edge of the westernmost downdropped block that is recognizable along the seismic profile is about 10.5 km $\pm$ 1 km east of the center of the crater. The center refers to the 35-km-diameter crater formed by collapse; the position of the lip of the collapsed crater has been established by study of cuttings from numerous water wells supplemented by two seismic reflection profiles.

Analysis of fault displacements recognized in the Amoco seismic reflection profile suggests that inward migration of the transient cavity wall during collapse was negligible. In estimating the energy of formation of the crater, we adopt 21 km as the maximum diameter of the transient cavity. This value implies enlargement of the crater during collapse by a factor of ~1.7, substantially larger than the collapse factor of 1.3 adopted as an average value by [2] but smaller than the factor suggested by formulas given in [3].

The energy of formation of the Manson crater was calculated from energy scaling by using two different approaches. In the first approach, we utilized a numerical computer simulation of the vertical impact of a 10-km-diameter asteroid into continental crust [4]. The kinetic energy of the projectile (density = 2.5 gm cm^{-3}, velocity = 20 km sec^{-1}) in this calculation was 6.2x10^7 Mt, and the resulting transient cavity was estimated to be ~90 km (Table 1). To obtain the energy of formation of the much smaller Manson crater, the following energy scaling relation was used,

$$\frac{E_M}{E_A} = \left[\frac{D_{Mtc}}{D_{Atc}}\right]^{3.4} , \qquad (1)$$

where E_M = energy of formation of the Manson crater, E_A = kinetic energy of the 10-km asteroid in the numerical simulation, D_{Mtc} = diameter of the Manson transient cavity, and D_{Atc} = diameter of the transient cavity resulting from the 10-km asteroid impact. The energy estimated for the special case of vertical impact at Manson is 4.4x10^5 Mt. In the general case, the impact will not be vertical, and a correction should be made for an elevation angle of impact less than 90°. This correction, given our present understanding of impact mechanics, is uncertain; moreover, the actual impact angle is unknown. For small-scale laboratory experiments, Gault [5] found the following empirical relationship,

$$D_i = D(\sin i)^{2/3}, \qquad (2)$$

where D_i is the diameter of a crater formed by impact at elevation angle i, and D is the diameter of a crater formed by a projectile of the same kinetic energy impacting at vertical incidence. Gault later suggested that the exponent in equation (2) should be reduced to 1/3 for large craters [6], but no formal treatment has been given for this relationship. As an upper bound for the most likely energy for oblique impact at Manson, we adopt equation (2) and i = 45°, the most probable impact angle for an isotropic flux of impactors. The energy estimated for oblique impact is 10x10^5 Mt (Table 1), about twice as high as for vertical impact.

In the second energy scaling approach, we used the formula

$$E=\left[\frac{D_{Mtc}}{K}\right]^{3.4}\frac{\rho_t}{\rho_a}, \qquad (3)$$

as modified from [2] where E = energy of crater formation, K = 0.56 km (Mt)$^{-1/3.4}$, ρ_a = 1.8 gm cm^{-3}, ρ_t = 2.4 gm cm^{-3}. The constant K in equation (3) is based on the 78-m diameter Jangle U nuclear crater [2]; it yields the same estimate of energy of formation for Meteor Crater, Arizona (1.2 km in diameter) as obtained by numerical computer simulations for vertical impact (i.e., ~15Mt) [7]. Solution of equation (3) for Manson gives an energy of 2.9x10^5 Mt for vertical impact (Table 1), about 35% less than that obtained from equation (1) in the first approach. This difference is indicative of the likely errors of the estimates. Correcting for oblique impact, we find a maximum likely energy of 6.4x10^5 Mt using equation (3) in the second approach.

The size of an asteroid or comet that could have formed Manson can be estimated from the formula for kinetic energy, with various assumptions about densities and velocities of the impacting body (Table 1). For the asteroid we used a density of 2.5 gm cm^{-3} and a velocity of 17.8 km sec^{-1}; for the comet we used a density of 1.0 gm cm^{-3} and a velocity of 57.7 km sec^{-1}. The velocities are the respective rms impact velocities weighted by probability of collision for Earth-crossing asteroids and for long-period comets [8].

Also listed in Table 1 are estimates of the masses and volumes of the near-field and far-field ejecta from Manson. These estimates have been derived by scaling of results from the numerical simulation of the 10-km-diameter asteroid impact. Materials ejected above the tropopause are taken to be "far-field" ejecta.

For purposes of comparison, we have also calculated energies, projectile sizes, and masses and volumes of ejecta for the 180-km diameter Chicxulub crater in Yucatan, by using the same scaling techniques applied here to the Manson crater (Table 1). A crater collapse factor similar to that observed at Manson was assumed for the Chicxulub crater. The far-field ejecta from Chicxulub are about 150 times greater in volume and mass than from Manson.

References: [1] Anderson, R.R. et al., 1993, this volume. [2] Shoemaker, E.M., 1983, Ann. Rev. Earth and Planet. Sci., 11, 461-494. [3] Melosh, H.J., 1989, Impact Cratering, A Geologic Process, Oxford Univ. Press, N.Y., 245 p. [4] Roddy, D.J. et al., 1987, Int. J. Impact Eng., 5, 525-541. [5] Gault, D.E., 1983, The Moon, 6, 32-44. [6] Gault, D.E., 1974, in Greeley R., and Schultz, P., eds., A Primer in Lunar Geology, Ames Research Center, NASA, Mountain View, Calif. [7] Roddy, D.J. et al., 1980, Lunar Planet. Sci. Conf. Proc., 11th, 2275-2308. [8] Shoemaker, E.M. et al., 1990, Geol. Soc. America Spec. Paper, 247, 155-170.

Table 1. Measured and estimated crater diameters and estimated energies of crater formation, asteroid and comet projectile diameters, and ejecta volumes and masses for the Manson and Chicxulub craters. Values (~) are calculated estimates. All values listed in the asteroid impact numerical simulation are calculated except for the asteroid diameter (initial parameter).

	D_{cc} km	D_{tc} km	E_v Mt (ergs)	E_o Mt (ergs)	Asteroid Diameter Vert. km	Asteroid Diameter Oblq. km	Comet Diameter Vert. km	Comet Diameter Oblq. km	Ejecta Near-fld km^3 (tons)	Ejecta Far-fld km^3 (tons)
Manson	35	21	~4.4x10^5 ~(1.9x10^{28})	~10x10^5 ~(4.2x10^{28})	~2.0	~2.7	~1.3	~1.7	~1040 ~(2.5x10^{12})	~166 ~(4.0x10^{11})
			~2.9x10^5 ~(1.2x10^{28})	~6.4x10^5 ~(2.7x10^{28})	~1.8	~2.4	~1.1	~1.5		
Chicxulub	180	~110	~12x10^7 ~(5.2x10^{30})	~27x10^7 ~(1.1x10^{31})	~13.6	~17.4	~8.4	~10.8	~150,000 ~(3.6x10^{14})	~24,000 ~(5.7x10^{13})
			~8.1x10^7 ~(3.4x10^{30})	~18x10^7 ~(7.6x10^{30})	~11.8	~15.4	~7.3	~9.6		
Asteroid Impact Numerical Simulation	~150	~90	~6.2x10^7 ~(2.6x10^{30})	--	10.0	--	--	--	~85,000 ~(2.0x10^{14})	~13,500 ~(3.2x10^{13})

D_{cc} = diameter of collapsed crater
D_{tc} = diameter of transient cavity
E_v = energy of crater formation with vertical impact, given in megatons TNT equivalent (Mt) and (ergs)
E_o = energy of crater formation with 45° oblique impact, given in megatons TNT equivalent (Mt) and (ergs)

COMPARATIVE HYPSOMETRIC ANALYSIS OF BOTH EARTH AND VENUS TOPOGRAPHIC DISTRIBUTIONS: P. Rosenblatt[1], P.C. Pinet[1], E. Thouvenot[2]; [1]UPR 234/GRGS/OMP, 14, Av. E. Belin, 31400 Toulouse, France; [2]CNES, 18, Av. E. Belin, 31400 Toulouse, France. p. 2

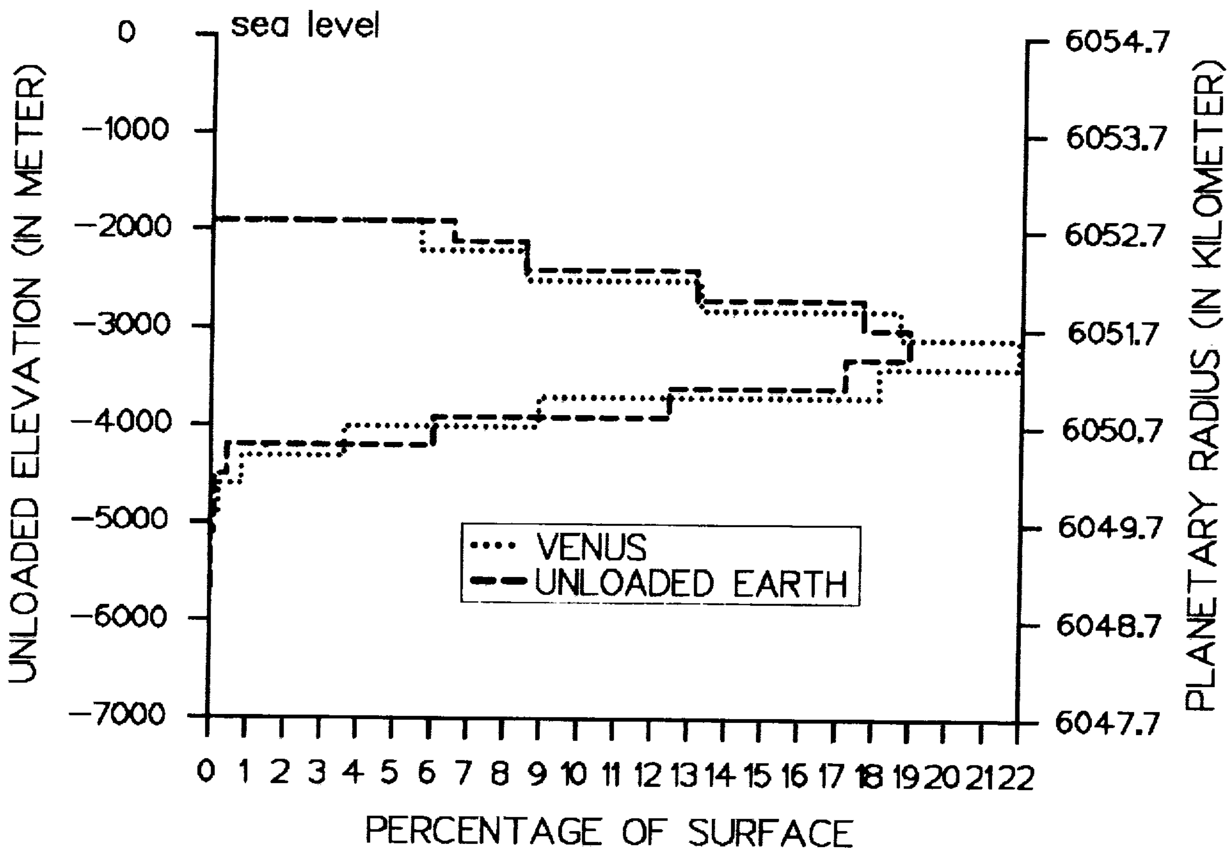
Previous studies [1,2,3,4] have compared the global topographic distribution of both planets by means of differential hypsometric curves. For the purpose of comparison, the terrestrial oceanic load was removed [2,4] and a reference baselevel was required. It was chosen on the basis of geometric considerations.and reflected the geometric shape of the mean dynamical equilibrium figure of the planetary surface in both cases. This reference level corresponds to the well-known sea level for the Earth; for Venus, given its slow rate of rotation, a sphere of radius close to the mean, median and modal values of the planetary radii distribution was considered and the radius value of 6051 km arbitrarily taken [1] These studies were based on the low resolution (100x100 km2) coverage of Venus obtained by the Pioneer Venus altimeter [1] and on the 1°x1° terrestrial topography [3,5]. But, apart from revealing the distinct contrast existing between the Earth's bimodal and the strong Venus' unimodal topographic distribution, the choice of such a reference level is inadequate and even misleading for the comparative geophysical understanding of the planetary relief distribution.

The present work reinvestigates the comparison between Earth and Venus hypsometric distributions on the basis of the high-resolution data provided, on one hand, by the recent Magellan global topographic coverage of Venus' surface [6], and on the other hand, by the detailed NCAR 5x5' grid topographic database currently available for the Earth's surface [7]. For both datasets, the spatial resolution is considered to be on the order of 10x10km2 with a vertical accuracy estimated around 50 to 100 m.

For the Earth, the oceanic bathymetry is unloaded from the water column weight. The study of the cumulative hypsometric curve for both planets reveals, as noted earlier, that there exists a domain of elevation for which the relationship between elevation and cumulative area percentage is linear. On Earth, it corresponds to the oceanic domain and is a consequence of the seafloor spreading process occurring on Earth. Under some conditions regarding the uniformity of seafloor spreading velocity and plate consumption by subduction with plate age [8], it is possible to use, on a global scale, cumulative area in place of plate age, and then to express the basic linear depth to square root of age relationship, arising from cooling boundary layer theory, in terms of depth to square root of cumulative area relationship, i.e. $h=f(\sqrt{S})$.

The cut-off thresholds, for which the hypsometric terrestrial distribution departs, in such a graph, from the linear trend , are -1950m and -3920m. Calculation of the mean depth of the whole system of mid-oceanic ridges, for the water unloaded topography, gives -1900m, with a standard deviation 470 m. Consequently, the upper threshold corresponds to the mid-oceanic ridge mean depth value while the lower one is related to the depth from which the seafloor is older than 80-90Ma [8]. For Venus, the upper threshold found is the planetary radius of 6052.8 km, the lower limit is 6051km, and the linear domain comprises around 80 % of the mapped surface. The geophysical meaning of the topographic level of the mid-oceanic ridges depth, in terms of thermal lithospheric structure, is that it represents the planetary level at which the thermal lithospheric thickness tends towards zero. It is of interest to note that, in an attempt to account for the venusian relief in terms of thermal isostasy, a venusian planetary radius of 6053 km has been proposed,

under plausible geophysical assumptions, as a theoretical estimate of the surface elevation of the unbounded asthenosphere [9].
If on this ground, the upper threshold of the linear domain for the curves h=f(√S) is taken as a reference level for the Earth and Venus differential hypsometric curves, then one notes that the oceanic peak and the venusian peak of the distribution do coincide very closely. If, in addition, a correcting factor taking into account the different relative surface partitioning existing for the planetary topography distributed below and above the reference threshold is applied, then the hypsometric distributions (300m interval class) of a terrestrial ocean-like planetwide topography (T1) and a low elevation (below 6052.8 km) Venus-like planetwide topography (T2) are very similar both in terms of modal distribution and amplitude (see figure), the distance between the mean and modal values being about 100m and the peak symmetry rather pronounced, in both cases.
This is somewhat at variance with the previous analyses [e.g., 9] based on a significant departure of the shape of these two peaks.



References: [1] Masursky H., Eliason E., Ford P. G., McGill G.E., Pettengill G.H., Schaber G.G., and Schubert.G. (1980) *JGR, 85,* 8232. [2] Head, J. W., Yuter S.E., and Solomon S.C. (1981) *Am. Sci., 69.* 614. [3] Mc Gill G.E., Warner J.L., Malin M.C., Arvidson R.E., and Eliason E. (1983) *University of Arizona Press, Tucson,* 69.[4] Sharpton, V.L., and Head, J.W. (1985) *JGR 90, B5, 3733* [5] Gates, W. L., and Nelson A.B. (1975) *Rep. R-1277-1-ARPA, Rand Corp. Santa Monica, Calif,* 140.[6] Ford P. and Pettengill G.H. (1992) *JGR 97,* 13,103. [7] ETOPO5 Database, *NGDC, Boulder Colo.* [8] Parsons B.(1982)*JGR, 87,* 289. [9] Morgan and Phillips (1983) *JGR, 88,* 8305.

587-91
ABS ONLY
N94-20723

Derivation of the Midinfrared (5.0-25.0μm) Optical Constants of Hydrous Carbonate and Sulfate. Ted L. Roush and James B. Orenberg (San Francisco State Univ. & NASA Ames Research Center), and James B. Pollack (NASA Ames Research Center)

BACKGROUND: There is ample theoretical and observational evidence suggesting liquid water was once stable at the surface of Mars [*e.g.* 1, 2, 3, 4]. Because water is essential to the evolution of life [5], it is important to understand the types of environments in which the liquid water was present. For example, if water were present early in Mars' history, then this raises the possibility that biological activity may have evolved only to eventually become extinct as liquid water became scarce. Alternatively, if liquid water were stable only later in Mars' history, then it becomes problematic to envision mechanisms by which biological activity evolved and remained viable without water until more favorable conditions existed. Even without biological activity, atmospheric carbon dioxide dissolved in water can assist the chemical weathering of primary igneous minerals producing common secondary phases such as hydrates, carbonates and sulfates [*e.g.* 4]. While the identification of hydrates, carbonates, and sulfates on Mars cannot provide direct evidence of biological activity, it can provide significant information regarding the presence and duration of an environment that would support the presence of liquid water at the surface. The specific mineralogy of these secondary phases can provide insight into the environments of their formation [6]. For example, slow precipitation that occurs in large standing bodies of water, *e.g.* oceans or lakes, commonly results in the formation of calcite, magnesite, dolomite, siderite, and rhodochrosite [6]. Rapid precipitation that occurs in ephemeral bodies of water, *e.g.* hypersaline lakes or playas, can result in the formation of all of the above phases as well as aragonite, vaterite, hydrated carbonates, alkali carbonates, bicarbonates, and other poorly ordered phases [6].

Absorption features identified in recent near-infrared spectra of Mars have been interpreted as being due to bicarbonate and bisulfate located in the mineral scapolite [7]. Spectral data returned by the Mariner 6 and 7 spacecraft have been interpreted as remaining consistent with the presence of hydrated carbonates [8]. Additionally, airborne thermal infrared spectra of Mars have been interpreted as implying the presence of carbonates, sulfates and hydrates [9]. Modeling of the thermal infrared data relied upon the optical constants of calcite anhydrite and a mixture of water in basalt because of their availability [9]. The derived abundances of carbonate and sulfate were 1-3% and 10-15% by volume [9]. However, the observed complexity and positions of the bands suggested other carbonate-, and sulfate-bearing species [9]. We have already derived optical constants for hydrous and anhydrous silicates [10] and we now apply these techniques to the derivation of the optical constants of hydrous carbonate and sulfate.

EXPERIMENTAL: A suite of carbonate and sulfate samples were collected from mineralogical supply houses. All of these samples were initially investigated using standard transmission spectroscopy techniques that involved dispersing a small amount of the sample in a KBr pellet. The transmission spectra of all samples were acquired and the carbonate and sulfate that provided the best comparison to the bands seen in the thermal infrared spectra of Mars were selected as a sub-set for derivation of their optical constants. The carbonate was

dypingite with the structural formula $Mg_5(CO_3)_4(OH)_2 \bullet 5H_2O$ [11] and the sulfate was fibroferrite, having the structural formula $Fe^{3+}(OH)SO_4 \bullet 3\text{-}5H_2O$ [12]. Because these samples consisted of fragile fine-grained masses that are not suitable for preparing polished surfaces, pressed pellets of the pure materials were prepared, similar to the clays previously studied [10]. The Fresnel reflectances of these tablets were measured (relative to aluminum mirror) using a Fourier transform infrared (FTIR) spectrometer and standard attachment at 4 cm^{-1} resolution from 4000 to 400 cm^{-1} (2.5-25.0μm). As with our previous work for clays [10], we rely upon dispersion analysis to describe the real (n) and imaginary (k) indices of refraction as the contributions due to a sum of classical oscillators.

$$n^2 - k^2 = \epsilon_\infty^2 + \sum_{i=1}^{n} \frac{4\pi\rho_i\lambda^2(\lambda^2 - \lambda_i^2)}{(\lambda_i^2 - \lambda^2)^2 + \Gamma_i^2\lambda^2} \tag{1}$$

$$2nk = \sum_{i=1}^{n} \frac{4\pi\rho_i\lambda^3\Gamma_i}{(\lambda_i^2 - \lambda^2)^2 + \Gamma_i^2\lambda^2} \tag{2}$$

where $4\pi\rho_i$, Γ_i, and λ_i are the strength, width, and central wavelength of each oscillator, and ϵ_∞ is the high frequency dielectric constant. Fresnel's equations for non-normal incidence were used to relate n and k to the near-normal reflectance measured in the laboratory. Nonlinear least squares techniques were used to minimize the differences between the calculated and observed spectra. Results of the analyses for dypingite and fibroferrite will be presented.

REFERENCES: [1] Pieri, D.C. (1980) *Science*, **210**, 895. [2] Squyers, S.W. (1989) *Icarus*, **79**, 229. [3] Baker, V.R. *et al.* (1992) *Mars*, Univ. Arizona Press, 493. [4] Fanale, F.P. *et al.* (1992) *Mars*, Univ. Arizona Press, 1135. [5] McKay, C.P. *et al.* (1992) *Mars*, Univ. Arizona Press, 1234. [6] Gaffey, S.J. (1989) *LPSC XX*, 323. [7] Clark, R.N. *et al.* (1990) *JGR*, **95**, 14,463. [8] Calvin, W.M. & T.V.V. King (1990) *LPSC XXI*, 153. [9] Pollack *et al.* (1990) *JGR*, **95**, 14,595. [10] Roush *et al.* (1991) *Icarus*, **94**, 191. [11] Raade, G. (1970) *Am. Mineral.*, **55**, 1,457. [12] Palache *et al.* (1951) *Dana's System of Mineralogy, 7th Ed.*, v.II, 614, New York, Wiley

ACKNOWLEDGEMENTS: This research is supported by grant NAGW-2212 of the NASA Planetary Geology & Geophysics Program and RTOP 199-70-22-11 of the NASA Exobiology Program.

EUHEDRAL METALLIC-Fe-Ni GRAINS IN EXTRATERRESTRIAL SAMPLES.

Alan E. Rubin, Institute of Geophysics and Planetary Physics, University of California, Los Angeles, CA 90024, USA.

Metallic Fe-Ni is rare in terrestrial rocks, being largely restricted to serpentinized peridotites and volcanic rocks that assimilated carbonaceous material. In contrast, metallic Fe-Ni is nearly ubiquitous among extraterrestrial samples (i.e., meteorites, lunar rocks and interplanetary dust particles). Anhedral grains are common. For example, in eucrites and lunar basalts, most of the metallic Fe-Ni occurs interstitially between silicate grains and thus tends to have irregular morphologies. In many porphyritic chondrules, metallic Fe-Ni and troilite form rounded blebs in the mesostasis because their precursors were immiscible droplets. In metamorphosed ordinary chondrites metallic Fe-Ni and troilite form coarse anhedral grains. Some of the metallic Fe-Ni and troilite in meteorites and lunar rocks has also been mobilized and injected into fractures in adjacent silicate grains where local shock-reheating temperatures reached the Fe-FeS eutectic (988°C). In interplanetary dust particles metallic Fe-Ni most commonly occurs along with sulfide as spheroids and fragments.

Euhedral metallic Fe-Ni grains are extremely rare. Several conditions must be met before such grains can form: (1) grain growth must occur at free surfaces, restricting euhedral metallic Fe-Ni grains to systems that are igneous or undergoing vapor-deposition; (2) the metal±sulfide assemblage must have an appropriate bulk composition so that taenite is the liquidus phase in igneous systems or the stable condensate phase in vapor-deposition systems; and (3) metallic Fe-Ni grains must remain undeformed during subsequent compaction, thermal metamorphism and shock. Because of these restrictions, the occurrence of euhedral metallic Fe-Ni grains in an object can potentially provide important petrogenetic information. Despite its rarity, euhedral metallic Fe-Ni occurs in a wide variety of extraterrestrial materials. Some of these materials formed in the solar nebula; others formed on parent body surfaces by meteoroid impacts.

Chondrules. Euhedral metallic Fe-Ni grains have been reported in rare chondrules where they crystallized during chondrule formation. Such chondrules probably cooled slowly enough near the crystallization temperature of metallic Fe-Ni to allow formation of euhedral grains instead of spheroidal blebs.

Olivine phenocrysts. Housley [1] reported curvilinear trails of tiny (2 μm) crystals of awaruite (Ni_3Fe) within an olivine grain from a porphyritic olivine chondrule in the Allende CV3 chondrite. The euhedral metallic Fe-Ni grains may have crystallized from the chondrule melt directly onto the surface of the growing olivine; euhedral morphologies developed because of the large difference in surface energy between the crystallizing metallic Fe-Ni and the surrounding silicate-rich liquid.

Opaque nodules. Within an Allende porphyritic olivine chondrule, Rubin [2] found a large (290x510 μm) opaque nodule comprised (in vol.%) of 9% euhedral awaruite grains (typically 35-65 μm), 85% magnetite, 5% pentlandite and 1% merrillite. Haggerty and McMahon [3] had suggested that such magnetite-rich nodules formed by subsolidus oxidation of pre-existing kamacite-rich nodules. However, this model was rejected because of the lack of petrographic evidence for the factor-of-2 increase in molar volume expected when kamacite changes into magnetite [2]. It seems more likely that oxidation occurred in the nebula prior to chondrule formation. During chondrule melting, immiscible magnetite-rich melt droplets developed within the silicate droplet; in this particular chondrule, taenite with 71 wt.% Ni was the sole liquidus phase and developed euhedral morphologies as it crystallized. After the chondrule cooled below ~500°C the taenite transformed into awaruite.

Interplanetary dust particles (IDPs). M.E. Zolensky (personal communication, 1993) has observed rare unrecrystallized chondritic IDPs containing 0.01-0.03-μm-size euhedral kamacite grains associated with troilite (or pyrrhotite), and, in some cases, with enstatite, diopside, forsterite, feldspathic glass and/or amorphous pyroxene. Although some chondritic IDPs have been significantly reheated, the friability of the euhedral-kamacite-bearing assemblages suggests that they were not. It seems likely that these euhedral kamacite grains are nebular condensates that formed when the nebula cooled below 1063°C (the 50%-condensation temperature of Fe at 10^{-4} atm; [4]).

Vugs. Euhedral low-Ni kamacite grains occur within vugs in highly recrystallized Apollo 14, 15 and 16 lunar breccias [5]. Such grains exhibit trapezohedral, cubic, tetrahexahedral, octahedral and dodecahedral faces. They formed by vapor deposition of Fe onto silicate grain surfaces. An analogous

case occurs in the Farmington L5 impact-melt breccia (and a few other ordinary chondrite breccias as well). Vugs within Farmington contain elongated prismatic and (probably) trapezohedral kamacite grains attached to a silicate substrate [6]. Calculations indicate that, after S, Fe is among the most abundant condensible vapor components in a gas generated by vaporization of lunar basalt or chondritic material [6,7]. This suggests that the Fe was probably derived from reduction of FeO in mafic silicates that were vaporized during shock events.

Ivanov [8] reported several 350-μm-size euhedral metallic Fe-Ni grains with 11.7-12.0 wt.% Ni, 0.54-0.68 wt.% Co and 0.63-0.68 wt.% P inside a 2-mm-diameter vug within the CR2-like lithology of Kaidun (i.e., Kaidun I). The vug itself is located within a fracture. The high Ni and Co contents of these euhedral metal grains place them close to the positively correlated Co-Ni trends of metallic Fe-Ni in CR chondrites [9]. Most CR metal grains with high Co and Ni probably formed in the nebula at low temperatures when metallic Fe reacted to form FeO or FeS [9]; however, the occurrence of the euhedral metal grains within a vug indicates that these grains probably condensed after an impact event caused vaporization of normal CR metal in the Kaidun regolith.

Lunar glass. Glass [10] reported the occurrence of about 25 ~4-μm-size octahedral crystals of kamacite with ~6 wt.% Ni situated along a plane within a 230-μm-diameter pale green glass spherule from Apollo 11 sample 10084. He also found similar octahedral metallic Fe-Ni crystals in two glass particles from sample 12057. Frondel *et al.* [11] reported 5-μm-sized octahedral crystals of metallic Fe in a glass fragment from Apollo 11 fines; isolated subhedral metallic Fe crystals reported in these fines may have been detached from glass surfaces. The relatively high Ni/Fe ratio in the metal reported by Glass [10] is similar to that in chondrites and, although not definitive, is consistent with the metal having been a meteoritic contaminant rather than having been formed by reduction of FeO from mafic silicates. It seems likely that these glass particles formed by impact melting lunar basaltic material and that the metal initially formed immiscible droplets. Von Engelhardt *et al.* [12] suggested that during cooling of the glasses the temperature remained near that of the crystallization temperature of Fe long enough to allow the growth of a single crystal from each immiscible metal droplet.

Impact-melt rock clasts. I report here the discovery of a 65x107 μm grain of euhedral tetrataenite (ordered FeNi) attached to a similarly sized grain of troilite within a 4x6-mm-size impact-melt rock clast in the Jelica LL6 chondrite breccia. The clast consists principally of olivine, orthopyroxene, diopside and plagioclase forming a hypidiomorphic-granular texture; minor phases include metallic Fe-Ni, troilite and chromite. After impact-melting, immiscible metallic-Fe-Ni-troilite droplets formed within the silicate melt. At ≥1200°C, while the surrounding silicate was still partly molten, taenite (the liquidus phase in many of the isolated metal-troilite droplets) began to crystallize. In one such droplet, taenite with ~50 wt.% Ni crystallized with a euhedral morphology. Troilite nucleated at one edge of this grain and began to crystallize at ~870°C. At ~460°C the taenite transformed into disordered FeNi; at 320°C the metal phase underwent an ordering reaction and formed tetrataenite.

A 60-μm euhedral metallic Fe-Ni grain found in the Sena H4 chondrite breccia [13] was also plausibly derived from an impact-melt rock clast.

References: [1] Housley R.M. (1981) *Proc. Lunar Planet. Sci. Conf.* **12B**, 1069-1077. [2] Rubin A.E. (1991) *Amer. Mineral.* **76**, 1356-1362. [3] Haggerty S.E. and McMahon B.M. (1979) *Proc. Lunar Planet. Sci. Conf.* **10**, 851-870. [4] Wasson J.T. (1985) *Meteorites: Their Record of Early Solar System History*, Freeman, New York. [5] Clanton U.S., McKay D.S., Laughon R.B. and Ladle G.H. (1973) *Proc. Lunar Sci. Conf.* **4**, 925-931. [6] Olsen E.J. (1981) *Meteoritics* **16**, 45-59. [7] Naughton J.J., Hammond D.A., Margolis S.V. and Muenow D.W. (1972) *Proc. Lunar Sci. Conf.* **3**, 2015-2024. [8] Ivanov A.V. (1989) *Geokhimya* no. **2**, 259-266. [9] Lee M.S., Rubin A.E. and Wasson J.T. (1992) *Geochim. Cosmochim. Acta* **56**, 2521-2533. [10] Glass B.P. (1971) *J. Geophys. Res.* **76**, 5649-5657. [11] Frondel C., Klein C., Ito J. and Drake J.C. (1970) *Proc. Apollo 11 Lunar Sci. Conf.*, 445-474. [12] Von Engelhardt W., Arndt J., Müller W.F. and Stöffler D. (1970) *Proc. Apollo 11 Lunar Sci. Conf.*, 363-384. [13] Jedwab J. (1972) *Meteoritics* **7**, 537-546.

S89-91
ABS ONLY

N94-20725

NAMED VENUSIAN CRATERS; Joel F. Russell and Gerald G. Schaber, U.S. Geological Survey, 2255 N. Gemini Dr. Flagstaff, AZ 86001

Schaber et al. [1] compiled a database of 841 craters on Venus, based on Magellan coverage of 89% of the planet's surface. That database, derived from coverage of approximately 98% of Venus' surface, has been expanded to 912 craters, ranging in diameter from 1.5 to 280 km [2]. About 150 of the larger craters were previously identified by Pioneer Venus and Soviet Venera projects and subsequently formally named by the International Astronomical Union (IAU).

A few of the features identified and named as impact craters on Pioneer and Venera images have not been recognized on Magellan images, and therefore the IAU is being requested to drop their names. For example, the feature known as Cleopatra is officially named as a patera, although it is now generally accepted that Cleopatra is a crater [1]. Also, the feature Eve, which has been used to define the prime meridian for Venus, was erroneously identified as an impact feature, but its true morphology has not been determined from Magellan images.

The Magellan project has requested the IAU to name hundreds of craters identified by Magellan. At its triennial General Assembly in Buenos Aires in 1991, the IAU [3] gave full approval to names for 102 craters (table 1) in addition to those previously named. At its 1992 meeting, the IAU's Working Group for Planetary System Nomenclature, which screens all planetary names prior to formal consideration by the General Assembly, gave provisional approval to names for an additional 239 Venusian craters. These names will not be formally approved until the next IAU General Assembly in 1994; however, provisionally approved names may be used in publications if their provisional status is indicated. Another 62 crater names submitted to the IAU for approval will be voted on at the 1993 meeting of the Working Group for Planetary System Nomenclature.

Altogether, the crater names submitted to the IAU for approval to date number about 550, a little more than half of the number of craters identified on Magellan images. The IAU will consider more names as they are submitted for approval. Anyone--planetary scientist or layman--may submit names; however, candidate names must conform to IAU rules. The person to be honored must be deceased for at least three years, must not be a religious figure or a military or political figure of the 19th or 20th century, and, for Venus, must be a woman.

All formally and provisionally approved names for Venusian impact craters, along with their latitude, longitude, size, and origin of their name, will be presented at LPSC, and will be available as handouts.

References: [1] Schaber, G.G., and nine others (1992) *J. Geophys. Res., 97, E8*, 13,257-13,301; [2] Schaber and Chadwick, this conference; [3] International Astronomical Union (1991) Proceed. 21st Gen. Assembly, Buenos Aires, 1991: *Trans. Internat. Astron. Union, 21B*, 357-363.

Table 1. Venusian crater names approved by the IAU in 1991.

Name	lat	long
Adivar	8.9N	75.9E
Aglaonice	26.5S	339.9E
Agnesi	39.5S	37.8E
Agrippina	33.2S	65.6E
Alcott	59.5S	354.5E
Al-Taymuriyya	32.9N	336.2E
Amalasthuna	11.5S	342.4E
Amaya	11.3N	89.3E
Amenardes	15.0N	54.1E
Andami	17.5S	26.5E
Anicia	26.3S	31.3E
Annia Faustina	22.1N	4.6E
Astrid	21.4S	335.5E
Aurelia	20.3N	331.8E
Avviyar	18.0S	353.6E
Badarzewska	22.6S	137.2E
Ban Zhao	17.2N	146.9E
Barrera	16.6N	109.3E
Barton	27.4N	337.5E
Bassi	19.0S	64.6E
Behn	32.5S	141.8E
Blixen	59.9S	145.6E
Bonnevie	36.1S	126.8E
Boulanger	26.5S	99.3E
Bourke-White	21.2N	147.9E
Bridgit	45.3S	348.9E
Buck	5.7S	349.6E
Budevska	0.5N	143.0E
Callas	2.4N	26.9E
Callirhoe	21.3N	140.6E
Carreno	3.9S	16.1E
Carson	24.2S	344.1E
Chapelle	6.4N	103.8E
Cori	25.4N	72.7E
Cunitz	14.5N	350.9E
Cynthia	16.7S	347.5E
Danilova	26.4S	337.3E
de Beauvoir	2.0N	96.1E
De Lalande	20.3N	354.9E
Deloria	32.0S	97.0E
Devorguilla	15.3N	3.9E
Erxleben	50.9S	39.4E
Ferber	26.4N	13.0E
Ferrier	15.8N	111.3E
Festa	11.5N	27.2E
Flagstad	54.3S	18.9E
Frank	13.2S	12.9E
Fredegonde	50.6S	93.1E
Geopert-Meyer	59.8N	26.8E
Germain	38.0S	63.6E
Greenaway	22.9N	145.0E
Guilbert	57.9S	13.6E
Halle	19.8S	145.4E
Hellman	4.8N	356.2E
Henie	52.0S	145.8E
Hepworth	5.1N	94.6E
Himiko	19.0N	124.2E
Holiday	46.7S	12.8E
Horner	23.4N	97.7E
Hua Mulan	86.8N	337.7E
Huang Daopo	54.2S	165.2E
Hwangcini	6.3N	141.7E
Joliet-Curie	1.6S	62.5E
Kartini	57.8N	333.0E
Kollwitz	25.2N	133.6E
Lachappelle	26.7N	336.5E
Lehmann	44.1S	39.1E
Li Qingzhao	23.7N	94.5E
Lullin	23.1N	81.0E
Manzolini	25.7N	91.2E
Marie Celeste	23.5N	140.2E
Marsh	63.7S	46.6E
Mead	12.5N	57.2E
Merian	34.5N	76.2E
Millay	24.4N	111.1E
Mona Lisa	25.6N	25.1E
Mu Guiying	41.2N	80.7E
Nemcová	5.9N	125.1E
Nijinskaya	25.8N	122.5E
O'Connor	26.0S	143.8E
Parra	20.5N	78.5E
Piaf	0.8N	5.2E
Recamier	12.5S	57.9E
Riley	14.0N	72.3E
Roxanna	26.5N	334.6E
Samintang	39.0S	80.6E
Saskia	28.6S	337.2E
Scarpellini	23.2S	34.6E
Simonenko	26.9S	97.5E
Stein	30.0S	345.5E
Stuart	30.8S	20.2E
Vigier Lebrun	17.3N	141.1E
von Siebold	52.0S	36.7E
Wilder	17.4N	122.4E
Woolf	37.7S	27.1E
Xantippe	10.9S	11.7E
Xiao Hong	43.6S	101.7E
Zhu Shuzhen	26.5S	356.5E

S90-90
ABS. ONLY

N94-20726

A CARBON AND NITROGEN ISOTOPE STUDY OF CARBONACEOUS VEIN MATERIAL IN UREILITE METEORITES: S.S. Russell, J.W. Arden*, I. A. Franchi, and C.T. Pillinger, Dept. Earth Sciences, Open University, Milton Keynes, MK7 6AA, U.K. *Dept. Geological Sciences, Parks Rd, Oxford OX1 3PR, U.K.

The ureilite meteorite group is known to be rich in carbon (*e.g.* Vdovykin, 1970) in the form of graphite/diamond veins that are associated with planetary type noble gases (Weber *et al.*, 1971). This paper reports preliminary data from a systematic study of the carbon and nitrogen isotopic composition of this carbonaceous vein material. A previous study (Grady *et al.*, 1985) focused on the whole rock signatures and reported that the carbon inventory appeared to be dominated by the graphitic/diamond intergrowths whereas the nitrogen was clearly composed of several distinct components, including one that that was isotopically light, possibly associated with the carbonaceous material. Recent studies (*e.g.* Russell *et al.*, 1992; Gilmour *et al.*, 1992; Yates *et al.*, 1992) have demonstrated that diamonds in the solar system formed in many different environments. C and N measurements from ureilitic diamond made in a similar way would be a useful addition to this overall study. The methods used for isolating diamonds of possible presolar origin from primitive meteorites are equally applicable to the processing of carbon bearing components in the ureilite meteorite group so that their stable isotopic composition can be determined.

Herein we discuss conjoint C and N stepped combustion measurements made on crushed whole rock ureilite samples that have been treated with 1M HCl/9M HF to dissolve silicates and free metal. In addition, two samples have been further treated with oxidising acids to leave a diamond rich residue. The results to date are presented in table 1. The major release of both carbon and nitrogen was between 600° and 900°C. The carbon isotopic composition for six samples varied between 0 and -5‰, in accordance with the results presented for bulk ureilites by Grady *et al.*, 1985. The nitrogen release patterns were similar for all the samples so far analysed; $\delta^{15}N$ values varied from around 0‰ for the low temperature steps, (which could represent an input from terrestrial contamination), to a ^{14}N enriched value of typically of -100 to -120 ‰ (-83‰ for Nilpena), released at temperatures >600°C; figure 1. This enrichment in ^{14}N suggests that the carbonaceous material may represent an early condensate that has preserved a primitive isotopic signature, and is distinct from nitrogen within other meteoritic diamond sources. The C/N ratios of the four HF/HCl insoluble residues (which are dominated by graphite) and the two diamond concentrates all fall between 1000 and 1500, so that at present we cannot say whether there is any difference between the two carbon bearing components. Isotopically light nitrogen exists in both graphite and diamond, in contrast to the noble gases, which are thought to be

C & N IN CARBONACEOUS MATERIAL FROM UREILITES: RUSSELL ET AL

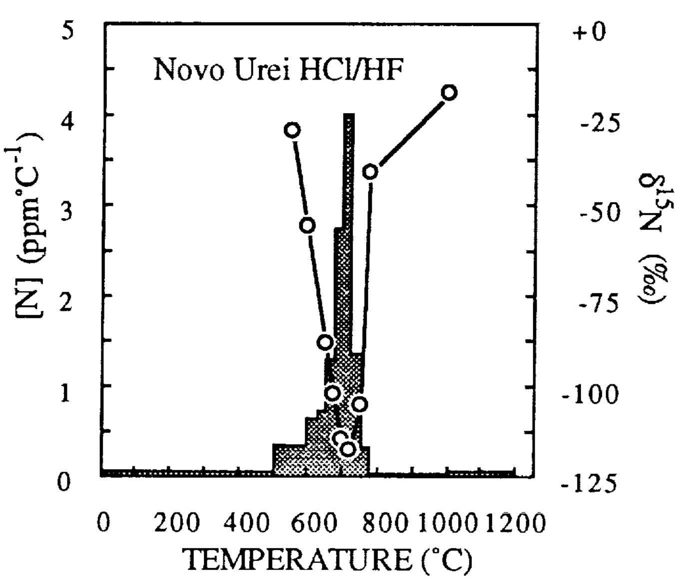
concentrated in the diamond phase (*e.g.* Gobel *et al.*, 1978).

The noble gas signature of carbon in ureilites has been compared to that of "phase Q" (Ott *et al.*, 1985). Light nitrogen may also be present in phase Q thus providing a further link between these two primitive components. Data for ^{36}Ar, ^{38}Ar and ^{40}Ar can now be obtained conjointly to the nitrogen and carbon information to determine whether the light nitrogen correlates with the enrichment in ^{36}Ar that is representative of a planetary noble gas signature (Weber *et al.*, 1975), and thus determine whether the ^{14}N enrichment may be linked to this distinctive noble gas pattern of the ureilitic carbonaceous material.

Table 1

Meteorite	Residue	$\delta^{15}N$ (mean)	$\delta^{15}N$ (min)	$\delta^{13}C$ (mean)	C/N
Novo Urei	HF/HCl	-110‰	-118.1±0.5‰	-4.4‰	1580
Y 790981	HF/HCl	-80‰	-111.3±0.3‰	-2.2‰	1410
Y 74123	HF/HCl	-104‰	-115±5.0‰	-1.1‰	1140
Nilpena	HF/HCl	-74‰	-83±5.0‰	-4.8‰	1460
Y 791538	Diamond	-94‰	-112±4.0‰	-5.0‰	1516
Novo Urei	Diamond	-86‰	-104±5.0‰	-1.8‰	1060

Figure 1



References: Russell *et al.*, (1992) Science **256**, 206. Gilmour *et al.*, (1992) Science, **258,** 1624. Yates *et al.*, (1992) Meteoritics **27,** 309. Weber *et al.*, (1971) Earth Plan. Sci. Lett. **13,** 205. Vdovykin (1970) Space Sci Rev. **10** 483. Grady *et al.*, (1985) Geochim. Cosmochim. Acta **49**, 903. Weber *et al.*, (1975) Earth Plan. Sci. Lett. **29**, 81. Gobel *et al.*, (1978) JGR **83,** 855. Ott *et al.*, (1985) Lunar Plan. Sci. Lett. **XVI**, 639.

Acknowledgements: Financial support was provided by SERC. The authors are grateful to to following who kindly donated samples for this study: Uli Ott of the Max Planck Institute für Chemie, Mainz; L. Semjenova and A. V. Fisenko, of the Vernadsky Inst. Moscow; and H. Kagi, of the University of Tsukuba, Ibaraki, Japan.

S91-25
ABS. ONLY
N94-20727

C-O VOLATILES IN APOLLO 15 AND APOLLO 17 PICRITIC GLASSES.

Malcolm J. Rutherford, Dept. Geological Sciences Brown University, Providence RI. and Robert A. Fogel, Dept. Mineral Sciences, American Museum of Natural History, New York, NY

Summary: A15 and A17 primitive picritic glasses have been examined by FTIR for the presence of dissolved C-O species to determine the role of C-O gasses in driving lunar fire-fountains. A15 green and yellow glasses were extensively studied and found to be free of dissolved C species down to FTIR detection limits (10-100 ppm; species and sample specific). Preliminary data on A17 orange glasses are similarly devoid of FTIR detectable C-O species. Re-analyses of the C-O driving mechanism theory for mare volcanism demonstrates the need to determine the fO_2 of the lunar interior; the factor that most critically determined the role of C gasses in the fire-fountaining events. Oxygen fugacities equivalent to IW-0.5 and above imply dissolved $CO_3^=$ in the primitive glasses at levels above FTIR detection. fO_2's below IW-0.5 imply concentrations of $CO_3^=$ below FTIR detection. Recent data suggesting lunar mantle fO_2's of IW-2 or less, strongly mitigate against finding FTIR measurable dissolved $CO_3^=$, consistent with the findings of this study.

Introduction: A15 and A17 picritic lunar glasses are considered to be the products of lunar fire-fountaining [e.g., 1] and are amongst the most primitive lunar materials. Their source region may have been as deep as 400 km [2] and may possibly have consisted of undifferentiated lunar material [3]. The usefulness of these glasses in understanding lunar evolution and composition is dependent upon the theory that these glasses are primitive melting products of the lunar interior that were injected into the lunar atmosphere by fire-fountaining. The fire-fountaining process is, thus, central to understanding the origin of these glasses. Likewise, the magmatic behavior of volatiles is central to understanding the origin of these glasses since lunar fire-fountaining is thought to have proceeded by the degassing of fluids [e.g., 3,4].

It has been proposed [4,5] that CO and CO_2 were the dominant fluid species driving lunar fire-fountaining. The theory holds that CO and CO_2 were generated by the oxidation of reduced-C and were dissolved within the melt. Resultant degassing upon magmatic ascent drove the fire fountains. Evidence in support of this mechanism includes the auto-reduction behavior of 74220 orange glass, an analysis implying the presence of CO-rich gas trapped in a green glass vesicle [6], and carbon-rich coatings on some of the glass spheres [e.g., 7]. The theory merits further investigation because of the important implications of the model and because C-O species and abundances have not been directly analyzed in primitive glasses.

Analytical: 28 green glass and 5 yellow glass spherules from samples 15426 and 15427, and 2 orange glass spherules from sample 74220 were examined by micro-FTIR. Sample preparation and analyses follow that of [8] and [9]. It was found that some glasses could be examined for the presence of C-O species without resorting to sectioning. The ten samples that were examined without FTIR sectioning were first ultrasonified in acetone and ethanol to remove particulate matter adhering to the surfaces. Several samples contained bubbles varying in size from 5 to 15 µm. These were also examined by micro-FTIR using appropriate spectral subtraction techniques.

Results: The entire spectrum from 5000 to 1000 cm^{-1} was examined for dissolved volatiles. The following vibrational regions were given particular scrutiny: molecular CO_2 at 2350 cm^{-1}, molecular CO at 2160 cm^{-1}, carbonyl (2125-1700 cm^{-1}) and carbonate (1700-1300 cm^{-1}). *Both pure and subtraction spectra were examined and found to be devoid of all C species consistent with our initial findings [9].* Spectra of vesicles trapped in glass spherules appear to be devoid of a gas signature. Although the possibility of post-quench escape of trapped gasses must be entertained, cracks connecting the vesicles to the exterior of the spherules were not found. At least in some cases, vesicles may be contraction phenomena and may never have contained trapped fluids. Vapor filled vesicles have yet to be unequivocally identified in any lunar glasses although data implying so do exist [6].

Discussion: We have previously discussed several interpretations for the absence of IR-detectable C in these lunar glasses [9]; however, considering recent developments, the following interpretation appears most likely.

Within the resolution of FTIR it has been determined that CO does not dissolve in basaltic liquid [10]. The limiting factor for the dissolution of $CO_3^=$ in basalt is the fugacity of CO_2 and its solubility is described by the relation: $X_{CO_2} = 0.492 \cdot f_{CO_2}$ [10]. The implications of this data for

lunar fire-fountaining are considerable. The crucial factor controlling the conversion of CO into CO_2 is oxygen fugacity. This can be seen from the reaction, $CO + 1/2O_2 = CO_2$. Since fCO_2 controls the solubility of C in the melt, CO merely acts to dilute the fluid and decrease fCO_2, thereby decreasing $CO_3^{=}$(melt). Moreover, since the fO_2 of an isothermal graphite saturated C-O gas is dependent upon pressure, the pressure at which oxidation of graphite and the formation of gas begins is critically dependent upon the fO_2 of the basaltic liquid/source region.

At high pressures, the graphite-C-O gas oxidation surface occurs at oxygen fugacities that are too high for the lunar interior. Carbon in the form of graphite would have existed stably and not reacted to form gaseous oxides since the fO_2 of the lunar interior is *under the graphite surface.* As the magma ascends and pressure decreases a critical depth will be reached at which the fO_2 of the melt matches that of the graphite oxidation surface. It is at this depth and pressure (P_{crit}) that formation of a gas phase begins. Since the solubility of $CO_3^{=}$ depends upon the CO_2 fugacity alone, the composition of the fluid at P_{crit} determines whether FTIR detectable amounts of $CO_3^{=}$ will be present. To determine this pressure, the fO_2 of the melt/source must first be known.

Although no consensus exists, the fO_2 of lunar basalts is thought to be ≈ IW-1.0 [11,12]. Intrinsic oxygen fugacity measurements (IOF) of lunar materials range from IW+0.2 to IW-1.0 [4,5]. Recently, it has been suggested that the lunar interior is as reducing as IW-2.5 [13]. To determine the implications of these estimates vis-a-vi the critical pressure at which graphite oxidizes, and through it the concentration of $CO_3^{=}$(melt), we have calculated P_{crit} and the solubility of $CO_3^{=}$ in basaltic liquids at various lunar mantle fO_2's (Table). A green glass liquidus of 1420°C + $3.33 \cdot 10^{-3}$(°C/bar)·P(bar) [14], was assumed. Additionally, it was assumed that the Henry's Law constant for $CO_3^{=}$ in basaltic melt does not change (or changes little) with T above 1200°C [15]. Lower T would push P_{crit} and X_{CO_2} to values even lower than those listed in the table. It is interesting to note that even at fO_2's within the lower end of the IOF measurements, X_{CO_2} (Melt) is below FTIR detection. Note also that P_{crit} yields a maximum $CO_3^{=}$; gas-melt re-equilibration at lower pressures would lower $CO_3^{=}$.

Log fO_2 (ΔIW)	P_{crit} (bars)	X_{CO_2} (Melt) (ppm)	FTIR Detectable
+0.2	2610	620	Y
0.0	2060	370	Y
-0.5	1140	100	Y
-1.0	630	30	N?
-1.5	350	9	N
-2.0	200	3	N

Recent experimental studies [e.g., 16,17] on the distribution of siderophile trace elements between basalt and silicate minerals suggest that the fO_2 of the lunar interior may well have been even lower than the lowest IOF measurements and closer to IW-2.0 or IW-2.5 [13]. These studies have shown that at low fO_2 substantial amounts of certain transition metals can dissolve in silicate melts in the metallic valance state (e.g., Ni^0); thus, D's change such that elements normally olivine and orthopyroxene compatible behave incompatibly. This has been proposed as the cause for the positive correlation of Ni /Co with normally incompatible trace elements such as REE's [13]. A lunar mantle fO_2 closer to IW-2.0 would be consistent with our findings.

A lunar interior of low fO_2 (IW-1.0 to IW-2.5) implies that: a) lunar fire-fountains could not have been driven by the exsolution of dissolved $CO_3^{=}$ within magmatic liquids; their concentrations are too low and, b) if lunar fire-fountains were driven by C-O-rich gasses it most likely occurred via the breakdown of graphite carried up by the ascending magma. A positive aspect of the low P_{crit} for graphite oxidation determined here is that the physically difficult processes of keeping gas bubbles within the magma for tens to hundreds of miles within the lunar interior are somewhat mitigated. A P_{crit} of 200 bars (Log fO_2 =IW-2.0) corresponds to a lunar depth of 4 km. By comparison, a lunar interior at an fO_2 of IW would begin to oxidize graphite at a depth of 42 km.

References: [1] Heiken et al. (1974) GCA 38, 1701-1718; [2] Longhi (1992) PLPSC 22, 343-353; [3] Delano (1986) Or. Moon, 231-247; [4] Sato (1979) PLPSC X 311-325; [5] Sato (1976) PLPSC VII, 1323-1344; [6] Fredericks et al. (1991) LPSC XXII 409-410; [7] McKay & Wentworth (1992) LPI T.R. 92-09, 31-36; [8] Fogel & Rutherford (1990) Am. Min. 75, 1311-1326; [9] Fogel & Rutherford (1992) LPSC XXIII, 377-378; [10] Pawley & Holloway (1992) EPSL 110, 213-225; [11] Delano (1990) LPSC XXI 278-279; [12] Longhi (1992) GCA 56, 2235-2251; [13] Steele et al. (1992) GCA 56, 4075-4090; [14] Green & Ringwood (1973) EPSL 19, 1-8; [15] Pan et al. (1991) GCA 55, 1587-1595; [16] Colson (1992) Nature 357, 65-68; [17] Ehlers et al. (1992) GCA 56, 3733-3743.

FORMATION OF THE LOW-MASS SOLAR NEBULA

T.V. Ruzmaikina (Lunar and Planetary Laboratory, The University of Arizona, Tucson, and Schmidt Institute of Earth Physics, Moscow), I.V. Khatuncev (Institute of Cosmical Research, Moscow), and T.V.Konkina Schmidt Institute of Earth Physics, Moscow)

The reconstruction of the solar nebula by adding losted volatiles (mostly H and He) to restore solar composition results in the minimum mass about 0.01 to 0.07 $M_\odot$ and angular momentum $3 \cdot 10^{51}$ g cm^2/s. Opaque for the thermal IR-radiation circumstellar disks around many of T Tau stars have mass between 10^{-2} to $10^{-1} M_\odot$ and radius between 10 to 10^2 AU. Angular momentum of such disks is ranging from 10^{51} to a few 10^{52} g cm^2/s. Even more extended disks have a comparable angular momentum, if they have a low mass. Thus a keplerian disk about HL Tau, those mass is estimated as ~ 0.1 $M_\odot$, has the angular momentum about 10^{53} g cm^2/s, provided that its radius is about 10^3 AU (and remarkably less if only internal region of the radius 10^2 AU is a keplerian disk). The last possibility assumes that the velocity distribution in the HL Tau envelope should be interpreted as the nonaxially symmetric infall, instead of keplerian rotation. The angular momentum of the order of 10^{52} to 10^{53} g cm^2/s could be typical for a dense core of solar mass (or a central region of a larger core in the molecular cloud) if rotation of the core has been braked before the start of the hydrodynamical collapse. Therefore, a value of the order of 10^{52} g cm^2/s is a reasonable low limit of the angular momentum of presolar nebula.

Low-mass-disks appear around T Tauri stars, even as young as 10^5 yrs, and disk parameters do not depend on the stellar age while the stars are younger than $3 \cdot 10^6$ yrs. These data seems imply, that formation of the low- mass extended circumstellar disk is related mainly to the first few 10^5 yrs. The time-scale of accretion (infall) of the molecular cloud core material onto the forming star and disk has the same order of magnitude for the cloud with the temperature $T \simeq 10$ K. It implies that the formation of the low-mass disk occurs during the stage of infall, and further its evolution is slowing down by an orders of magnitude, plausibly $\lesssim 10^{-7}$ $M_\odot$/yr. (The last value is supported also by the spectral energy distribution of T Tauri stars, which could be reproduced, assuming additional energy from disk accretion with the rate $\dot{M} \sim 10^{-7}$ to 10^{-8} $M_\odot$/yr.) Actually, the rate of the disk accretion could be even smaller because a dust floating in the upper, optically thin parts of the disk atmosphere, can include into IR-luminosity.

In this paper we study an accretional stage of the formation and early evolution of the solar nebula with relatively small angular momentum (10^{52} to $5 \cdot 10^{52}$ g cm^2/s). We investigate the evolution of the disk and its vertical structure, particularly the shock front between disk and infalling material. Calculations start at a moment when a low-mass star-like core (containing several percent of the total mass) surrounded by small embryo disk have been formed at the center of the presolar nebula and the bulk of mass remained in the envelope. The forming solar nebula is approximated as a thin viscous disk surrounded by accreting envelope. The distribution of a temperature in the infalling envelope is determined by solving spherically symmetric equations of radiative transfer. As the energy source we take into account all energy released within centrifugal radius of the infalling matter. The turbulent energy dissipation, radiation of the opaque envelope and the shock front are considered as a heat sources for the estimation of a temperature distribution in the disk. The final thickness of the disk and its shape are taken into account when the rate of inflow of new material into the disk is studied. The shape of the disk is identified with a shape of the shock between the disk and accreting envelope, there it exists; and with the surface at which density of the infalling gas is equal to the density in the disk otherwise. We consider the evolution of the radius and mass of the disk, distribution of temperature and the mass flux through the disk, shape and intensity of the shock produced by falling gas at the surface of the disk. A core has a radius $R_c = 3 \cdot 10^{11}$ cm, and exchange of the mass between disk and core are taken into account. Distribution of the specific angular momentum in the accreting envelope is assumed to be similar to that either in homogeneously rotating (Ω_0 =const) cloud with a homogeneous density ρ_0 =const or with $\rho_0 \propto r^{-2}$. It is supposed that the gas is falling under the action of the gravity of the core and rotation of the envelope. Self-gravity of the cloud and the gravity of the disk are neglected. The effect of the gravity of a low mass disk onto the accretion is estimated by Ziglina and Ruzmaikina (1991,*Astr.Vestnik*,25,53). The accretion is supposed to be a spherically symmetric at a sonic point at radius is $r_s \simeq GM/c_s^2$ (where G is the gravitational constant, M is the core mass, and c_s is the

sound speed in the accreting gas), i.e., $r_k \ll r_s$. Being surrounded by the accreting envelope, a forming disk has a well defined radius. A radiative shock front divides the disk and infalling gas. As the proper boundary condition at the edge of the disk we take zero thickness of the disk, i.e. $z_D = 0$ at $R = R_D$, and find that near the edge

$$z_D{}^2 = 2\int_R^{R_D} \left(\frac{R}{1+F(R)}\right) dR,$$

where $F(R_D) = \frac{R_D^2}{HD^2} - \frac{3}{4}$, and H_D is the thickness of the homogeneous atmosphere in the disk. The equation determining the shape of the shock front, is integrated numerically from the disk edge inside, checking at every grid point if $v_\perp > c_s$. When the shock disappear we continue by solving equation of equality of the density in the infalling gas, to the density in the disk, and checking condition for the repeated appearance of the shock.

We run a set of models with the initial mass of the presolar cloud $M_0 = 1.1$ M$_\odot$, and the angular momentum $J_0 = 1 \div 5 \cdot 10^{52}$ g cm^2/s, with the constant rate of infall $\dot{M} = 10^{-5}$M$\odot$, and effective (turbulent) viscosity $\nu = \nu_0\sqrt{M_c R_{AU}}$, where M_c is the core mass in units of the solar mass, and R_{AU} is the radial distance in AU, and ν_0 ranges between 0.1 to $10 \cdot 10^{15}$ cm^2/s.

Figures 1 to 3 show evolution of the surface density, radial velocity in the disk, and the shape of the disk for the model with $J_0 = 2 \cdot 10^{52}$ g cm^2/s, and $\nu_0 = 3 \cdot 10^{15}$ cm^2/s; curves a), b), and c) correspond to the core mass 0.1, 0.5, and 1 M$_\odot$. It is assumed that the gas falling onto the disk slides to its centrifugal radius without exchange of the angular momentum with disk. Fig. 3 shows also distribution of the Mach number for the normal component of the infall velocity; the shock exist in the regions where Mach > 1— at the edge of the disk and in the vicinity and within centrifugal radius R_k which is < 1 AU for this model. While the shock occupies a relatively small part of the surface, a significant fraction of falling in matter comes through it, and can be reprocessed. The heating of the outer part of the disk by the shock wave makes IR-spectrum of the disk more flat, and plausibly could explain effect, observed for some T Tauri stars, — a "slow" decrease with the distance from the star of the disk's effective temperature. Fig.4 shows the dependence of the disk mass on the mass of core (growing protosun).

Parameters of the disk to the end of infall are similar to the parameters of the reconstructed solar nebula and disks about solar type T Tauri stars. Further investigation is neeeded to study instabilities associated with infall, and their efficiency in supporting of turbulence or other mechanisms of the angular momentum transport.

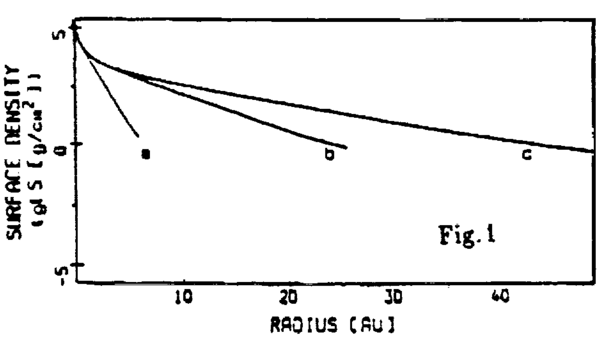


Fig. 1

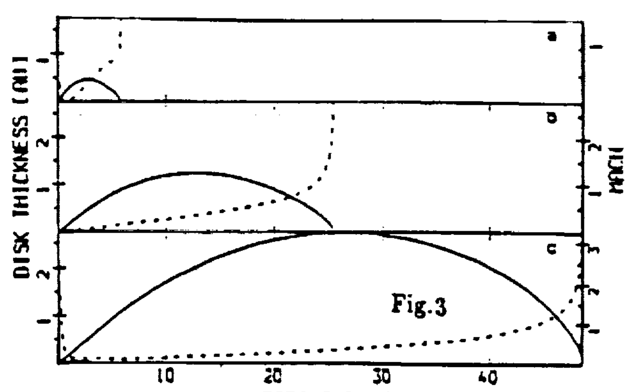


Fig.3

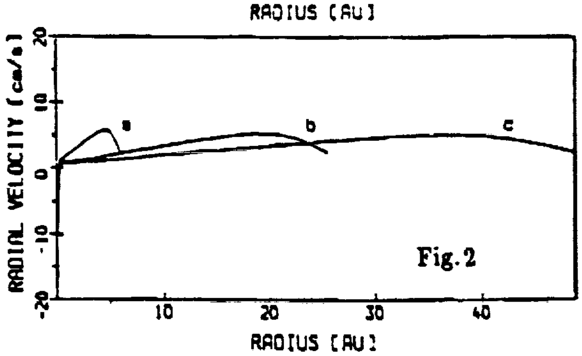


Fig. 2

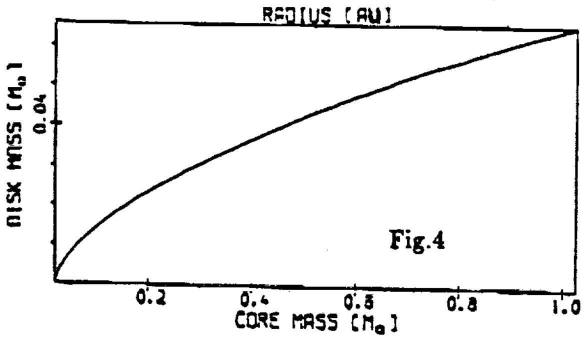


Fig.4

ASTEROID COLLISIONS: TARGET SIZE EFFECTS AND RESULTANT VELOCITY DISTRIBUTIONS; Eileen V. Ryan (Planetary Science Institute)

To study the dynamic fragmentation of rock and to simulate asteroid collisions, we use a two-dimensional, continuum damage numerical hydrocode which models two-body impacts. This hydrocode monitors stress wave propagation and interaction within the target body, and includes a physical model (Grady and Kipp (1) fragmentation theory) for the formation and growth of cracks in rock. With this algorithm we have successfully reproduced fragment size distributions and mean ejecta speeds from laboratory impact experiments using basalt, and weak and strong mortar as target materials (see (2) and (3)). Using the hydrocode we have determined that the energy needed to fracture a body has a much stronger dependence on target size than predicted from most scaling theories. In addition, velocity distributions obtained indicate that mean ejecta speeds resulting from large-body collisions do not exceed escape velocities.

We used the hydrocode to examine the dependence of fragmentation outcome on target size. Specifically, we analyzed how the size of the target body influences the amount of specific energy needed to fracture it. The critical specific energy Q^*, defined as the energy necessary to fragment a body such that the largest remaining fragment contains half the original target mass, is recorded as target size is varied from 10 cm to 1000 km in diameter. This size range covers both the strength regime, where material bonds dominate the fracture process, and the gravity regime, where the incoming stress pulse must overcome gravitational self-compression in addition to material bonds to initiate damage. We modeled three materials, basalt, and weak and strong cement mortar, all having different material strengths. Previously, scaling theories had used data from only basalt laboratory experiments to infer a size dependence, and it remained unknown what effect material type would introduce. The hydrocode uses no scaling approximations in its simulations, it computes the fragmentation outcome for each target size. Impact velocity was kept constant for this size-dependence study to isolate only the effect of target size (i.e., mass).

The hydrocode results (Figure 1) clearly show that energy scaling does not work— Q^* is indeed dependent on target size. Q^* decreased with increasing target size in the strength regime with slopes of 0.43, 0.59, and 0.61, for basalt, strong mortar, and weak mortar, respectively. These values are much steeper than the 0.24 slope-dependence predicted for basalt targets by Housen and Holsapple (4) nominal strain rate scaling theory. The decrease in Q^* in this regime is due to the fact that strain rate is also decreasing, making the bodies weaker and easier to fragment. The slopes for weak and strong mortar ar steeper than that of basalt, as these materials have larger strain rate exponents associated with them. In the gravity regime, Q^* increases with increasing target size, with a slope equal to $\sim$2.6 for all three materials. This is once again steeper than the 1.7 slope dependence predicted from Housen and Holsapple scaling theory. The fact that Q^* is independent of material type in the gravity regime confirms that it is gravitational compressive pressures and not material bonds that govern fracture in this region.

The first data on how ejecta velocity distributions vary with target size was also obtained using the hydrocode, and Figure 2 displays the results obtained for basalt. Mean fragment speeds tend to follow the Q^* versus target size curve: the more energy put into the collision, the higher the average velocities. A surprising result is that for large bodies, not enough energy is being transferred to the ejecta in the form of kinetic energy for them to overcome escape velocity and disperse. This implies that many large Solar System bodies could be gravitationally reaccumulated rubble piles.

ASTEROID COLLISIONS: TARGET SIZE EFFECTS, E.V. Ryan

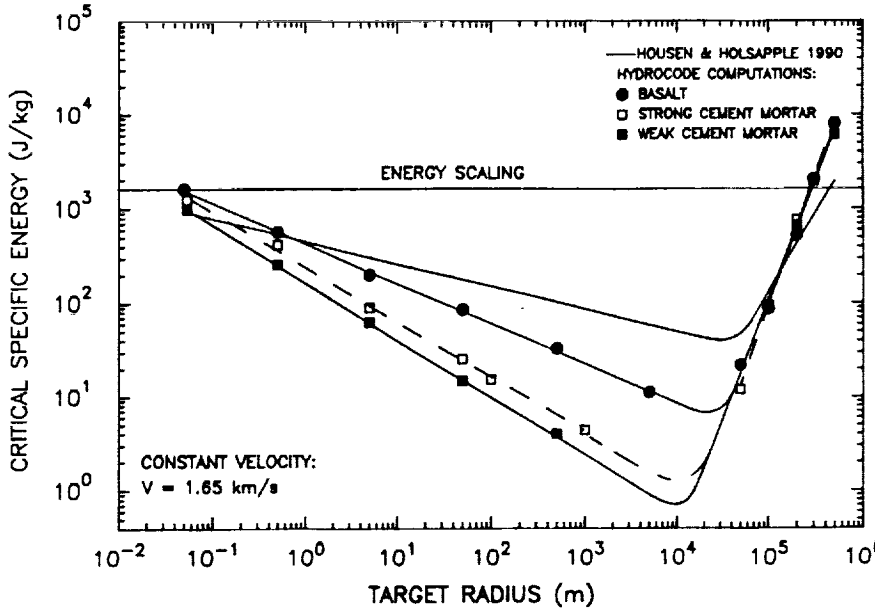


Figure 1: Hydrocode results for the dependence of critical specific energy Q^* on target size for basalt, and weak and strong cement mortar. Housen and Holsapple's (4) nominal scaling law for basalt (solid curve) and energy scaling for basalt (solid line) are also shown. Impact velocity is kept constant at 1.65 km/s.

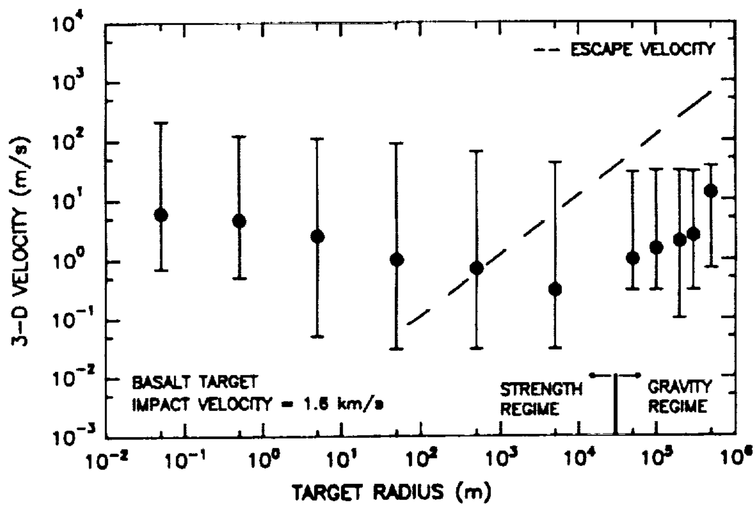


Figure 2: Mean ejecta speeds (solid circles) as a function of target size for the collisional disruption of basalt. Error bars are used to indicate the range of velocities found at each target size. Escape velocity is indicated by the dashed line.

References: (1) Grady, D.E., and M.E. Kipp (1980), *Int. J. Rock Mech. Min. Sci. Geomech. Abstr.* **17**, 147-157. (2) Melosh, H.J., E.V. Ryan, and E. Asphaug (1992), *J. Geophys. Res.* **97**, 14735-14759. (3) Ryan, E.V. (1992), Ph.D. Thesis, University of Arizona. (4) Housen, K.R. and K.A. Holsapple (1990), *Icarus* **84**, 226-253.

DETECTABILITY OF CRYSTALLINE FERRIC AND FERROUS MINERALS ON MARS: Donald E. Sabol Jr. (Department of Geological Sciences, University of Washington, Mail Stop AJ-20, Seattle WA 98195), James F. Bell III (NASA/Ames Research Center, Mail Stop 245-3, Moffett Field CA 94035), and John B. Adams (Department of Geological Sciences, University of Washington, Mail Stop AJ-20, Seattle WA 98195)

Introduction: Telescopic and spacecraft spectroscopic and geochemical data have been used to constrain the surface mineralogy of Mars and to yield clues about past and present Mars surface weathering/alteration scenarios [1,2]. Based primarily on their visible to near-IR reflectance properties, several terrestrial iron-bearing minerals have been either identified on Mars or proposed as Mars spectral analogs. Among these are crystalline hematite, pyroxenes, as well as poorly crystalline materials like nonophase hematite and palagonite [e.g., 3-6]. Other iron-bearing minerals include (but not limited to) nontronite, magnetite, jarosite, and goethite, have been proposed as Mars surface constituents based on Viking Lander measurements or geochemical modeling [e.g., 7-9]. If present on Mars, these materials likely appear as spectral mixtures at the coarse spatial resolution of remotely sensed data. The detectability of any of these components must be evaluated relative to the other (background) components with which they occur. The primarily goal of this study is to determine how much of any given mineral would have to be present for it to be detectable in remotely-sensed data. Here, the detectability of iron-bearing minerals ("target spectra") was evaluated using detection threshold analysis (DTA), an analytical technique based on spectral mixture analysis [10].

Methods: DTA is used to predict target detectability (at a given confidence level) under given conditions of target-background spectral contrast and system noise. Two general cases are considered in DTA: 1) Continuum Analysis - the target is treated as a spectral endmember where the "detection threshold" is the smallest fractional abundance of the target that can be measured above system noise, and 2) Residual Analysis - the target, which is not included as an endmember, is detected as deviations of the observed mixed spectrum (including the target) from spectral mixtures of "background" endmembers.

Two sets of background spectra were used: 1) nanophase hematite and magnetite ("pure" phases of iron bearing minerals), and 2) palagonite and lunar basalt (natural materials composed of mineral composites). Spectra of nine target minerals were examined: hematite, goethite, enstatite, hypersthene, diopside, pigeonite, epidote, jarosite, and nontronite. Because the spectral signatures due to iron were primarily of interest, we used high resolution spectra (183 bands) between 0.402 μm and 1.392 μm. Signal-to-noise ratios(SNR) of both 20/1 and 80/1 as well as a confidence level of 90% were used for determining detection thresholds. Because these materials could be expected to occur as both macroscopic and intimate mixtures on Mars, both linear and non-linear mixing (single-scattering-albedo) models were used.

Results: Overall, continuum analysis shows that very little of each of these target minerals is needed to detected within our modeled background, even when the data are noisy. At a SNR of 20/1 the thresholds ranged from 2% to 11% , while at an 80/1 SNR the thresholds were reduced to between 1% and 6.5% (Figure 1). Detection thresholds in residual analysis, which vary by wavelength, ranged from being undetectable to as low as 8% (Figure 2). For most of the minerals examined, residual detectability was highest between 0.4 μm and 0.6 μm. Minerals that have a weaker Fe^{3+} crystal field absorption at 0.4 μm were more detectable in this wavelength region than those with stronger absorptions because they had higher spectral contrast with the background, which also had strong absorptions at the lower wavelengths. Generally, the minerals the have weaker Fe^{3+} crystal-field bands were more detectable when they were modeled as spectral endmembers than when they were detected in the band residuals

Conclusions: This study indicates that under ideal conditions (i.e., hyperspectral, high-resolution; high solar illumination; no calibration errors) relatively low abundances of crystalline iron-bearing minerals can be detected in spectral mixtures with known background materials. Future refinement of this work will include: 1) accounting for the spectral variability of each mineral (including phase angle and particle size effects), 2) more complex combinations

of spectral components, 3) selection of bands that optimize detection of these minerals, and 4) extension to image analysis of Mars using telescopic and spacecraft data.

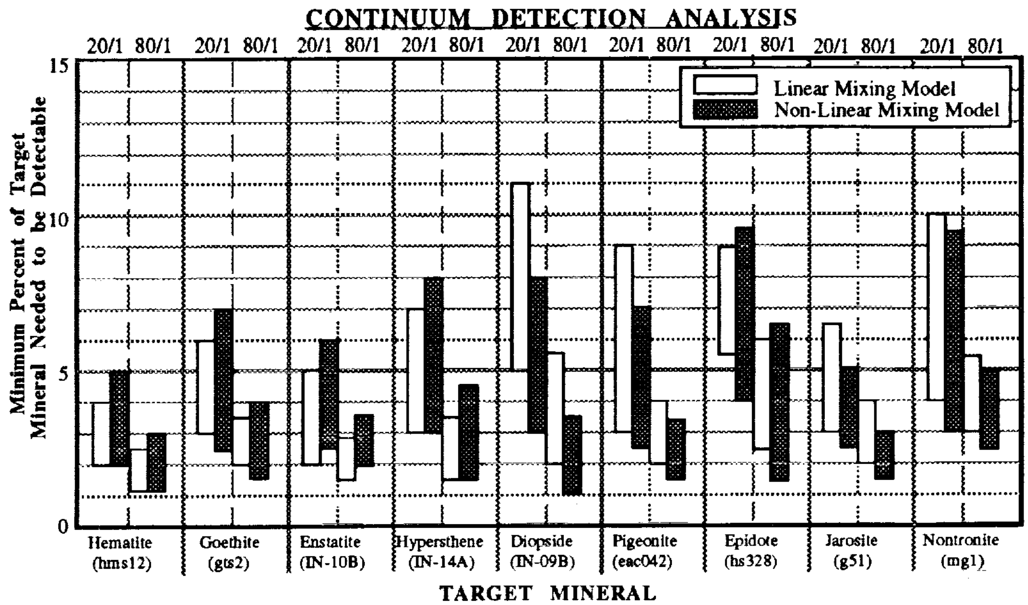


Figure 1: Continuum detection thresholds for a suite of iron-bearing minerals in a background composed of Basalt (LS-CMP-001) and Palagonite (PN9_20). The range of detection thresholds for each mineral varies with the fractions of the background. The results for both linear and non-linear models are shown at both 20/1 and 80/1 signal-to-noise ratios.

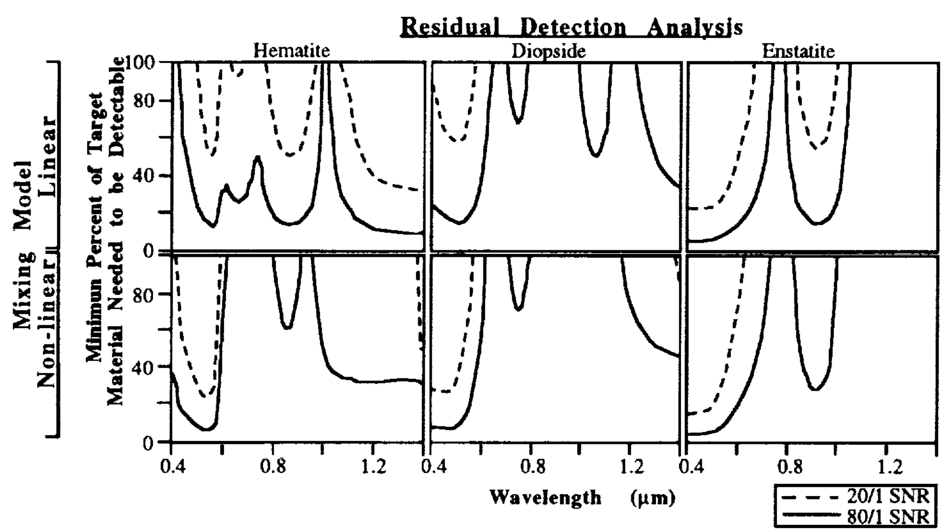


Figure 2: Residual detection thresholds for hematite, diopside, and enstatite in the same background as in figure 1.

References: [1] Bell J.F. III et al. (1991) LPI-MSATT Tech Report 92-04, 2. [2] Bell J.F. III et al. (1992) LPSC XXIII, 81. [3] Bell J.F. III et al. (1990) JGR, 95, 14447. [4] Singer R.B. et al. (1979) JGR, 84, 8415. [5] Morris R.V. et al. (1989) JGR, 94, 2760. [6] Bell J.F. III et al. (1993) JGR, in press. [7] Toulmin P. et al. (1977) JGR, 82, 4625. [8] Pollack J.B. et al. (1977) JGR, 82, 4479. [9] Burns R.G. (1987) JGR, 92, E570. [10] Sabol D.E. Jr. et al (1992) JGR, 97, 2659.

Distribution of Small Volcanic Cones on the Surface of Venus by Size and Elevation: Implications for Differential Deposition of Volcanic Features; Sahuaro High School Astronomical Research Class[1], Tucson, AZ, J. F. Lockwood, teacher, Evergreen High School Research Class[2], Vancouver, WA, Mike Ellison, teacher, Advisors: J. Johnson, G. Kamatsu , (Lunar and Planetary Laboratory, University of Arizona, Tucson AZ 85721)

Introduction: It appears that volcanic features are not evenly distributed on the surface of Venus (3). Head et. al.(4,5) theorizes that the sparcity of volcanic features in the lowlands may be due to an altitude dependant inhibition of volatile exsolution and the resulting production of neutural buoyancy zones sufficient to form magma reservoirs and favoring flood lavas at lower elevation. The astronomy research classes of Evergreen and Sahuaro High Schools surveyed a cross- section of different elevation topography to investigate size and distribution of small volcanic cones by elevation.

Observations: Student researchers at Sahuaro High School in Tucson, Arizona and Evergreen High School in Vancouver, Washington, measured and located small volcanic cones (1 to 20 km) in sixteen FMIDRS taken from five Venus Magellian Mosiacked Image Data set. These FMIDRS are located in a strip from 60 degrees north to 10 degrees south latitude and 272 degrees to 295 degrees longitude.

The volcanic cones were located and measured by using the x and y coordinates found in the NIH Image 1.44 Program. The computer cursor was centered on the caldera of the cone and the x and y coordinates were recorded. The following formulas were utilized to convert the pixel values into degree values:

latitude= min. latitude+((max. latitude-min. latitude)/1024)* y coordinate

longitude= min. longitude+((max. longitude-min. longitude)/1024)* x coordinate

The minimum and maximum latitudes and longitudes are those of each of the fifty-six frames contained within an FMIDR. They were supplied by the labels for each frame.

The diameters were also measured in pixels along their x and y axes, averaged, and converted into kilometers by multiplying the pixel value by the resolution of the image (.075 kilometers per pixel).

In order to find the elevation of the cones, the latitude and longitude of each cone were converted back into x and y pixel values that corresponded to the GXDR Elevation and Altimetry Disk. To obtain the x coordinate, the minimum longitude for the elevation images were subtracted from the longitude of each cone, then multiplied by the longitude resolution of the elevation image. The longitude resolution of the image is acquired by dividing 1024 by the difference of the maximum and minimum longitudes. To obtain the y coordinate, the minimum latitude for the elevation image was subtracted from the latitude of each cone, then multipled by the latitude resolution, 1024 divided by the diference between the maximum and minimum latitudes of the elevation image.

Then the elevations were found, again using the NIH Image 1.44 Program, and were added to the minimum planetary radius, 6,040,000 m, and converted into kilometers.

The graphs of Cone Elevation vs. Cone Diameter, Cone Diameter Distribution, and Cone Elevation Distribution were then plotted.

Results: Figure One plots the diameter of the 6200 cones found in the sixteen FMIDRS against their elevation. Even though the data is too scattered to realistically fit a line to it, when a linear curve fit is applied to the data, a slightly increasing slope--about four percent--is evident, suggesting that as the elevation increases, the diameter of the cones increases slightly as well. The curved fit line centers close to the four kilometer diameter level.. The distribution of volcanic cone diameters is shown in Fig. 2. Forty-two percent of the 6200 cone sample fell in the two to four kilometer diameter bins. The graph peaks at the two kilometer bin with 690 cones and has a gaussian-like distribution down to the ten kilometer bin.

The sixteen FMIDR sample represents about one percent of the Venusian surface area between 65 N and 65 S latitudes. Given one data set is a rough approximation of the various topographic levels on Venus, we project that the number of small volcanic cones may range from 600,000 to one million in number if the polar regions are included.

Figure 3 shows the distribution by elevation produced by this sampling area. For lower elevations, the number of cones increases through the first four bins. But for middle to high elevation bins, the graph appears to contradict the result predicted by Head et.al. (4,5), in that small volcanic cones seem to occur more in plateau areas, as opposed to highland regions. We feel that the negative slope produced by this graph is due primarily to a significant lack of processed data above an elevation of 6052 km.. Although the

Distribution of Small Volcanic Cones: Sahuaro, Evergreen H.S. Astronomical Research Classes

gaussian nature of the curve produced does provoke some interest, we cannot make any firm interpretations from this graph because of the paucity of data collected in highland regions where the theory put forth by Head et. al. 1992 predicts most of these small cones will be found. Future efforts will center on including many more FMIDRS, particularly those in regions above 6052 km in elevation. Many high school classes from different parts of the United States will process and collate this data

[1] Kathryn J. Arbeit, Shela M. Barker[a], Jeanine Y. Bashir, Jennifer E. Bodzioch, Dawn L. Brown, Kelly R. Charles, Amanda S. Doimas, Maury R. Friend, Laura B. Glennie[a], Malea S. Hainstock, John C. Holman[a], Joshua Kaufer, Jeffrey W. Keippel[a], Lezlie D. King, Kristina Y. Lovio, Michael C. McGinley[a], Jeffrey A. Parker, Christina H. Philips, Michael C. Prosser, Michael J. Safford[a], Joann R. Snyder[a], Christopher T. Spears, Stacy L. Wiens.

[2] Kyle A. Gerlach, Benjamin M. Hjelm, Miles J. Penner, Shane E. Stone

[3] Saunders, S., et. al., 1992, *JGR*, vol. 97, no. E8, pp. 13067-13090.

[4] Head, J., et. al., 1992, *JGR*, vol. 97, no. E8, pp. 13153-13197.

[5] Head, J., Wilson, L., 1992, *JGR*, vol. 97, no E8, pp. 3877-3903.

[a] Principal investigator

Fig. 1- Cone Elevation vs. Cone Diameter

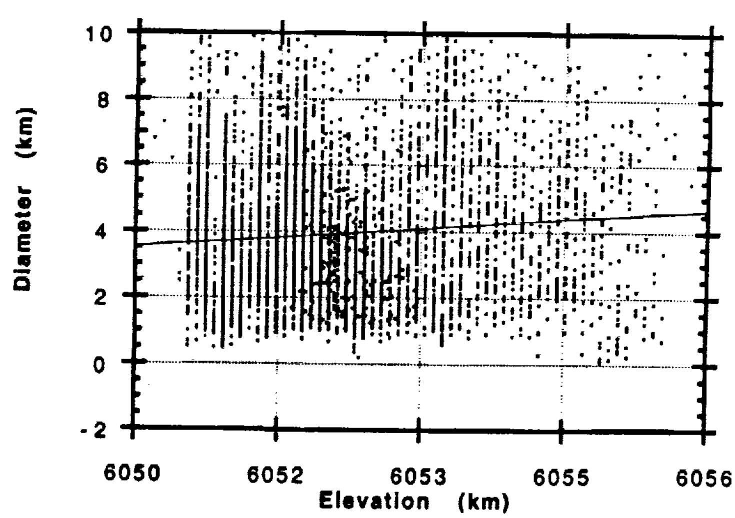


Fig. 2- Cone Distribution By Diameter

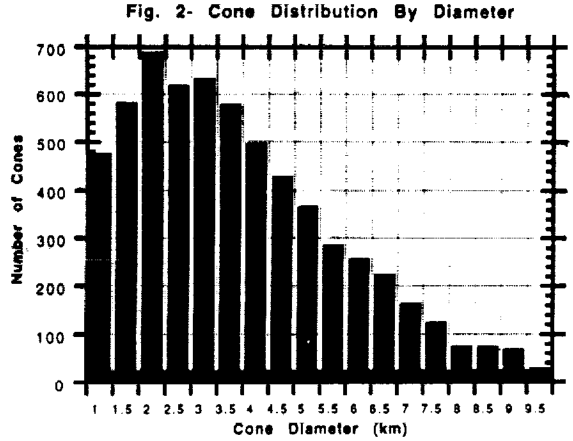
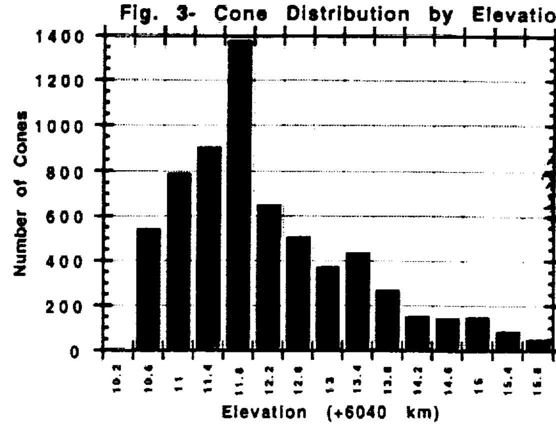


Fig. 3- Cone Distribution by Elevation



VENUS PANCAKE DOME FORMATION: MORPHOLOGIC EFFECTS OF A COOLING-INDUCED VARIABLE VISCOSITY DURING EMPLACEMENT;
S.E.H. Sakimoto[1] *and M.T. Zuber*[1,2], [1]Department of Earth and Planetary Sciences, The Johns Hopkins University, Baltimore, MD 21218, [2]Geodynamics Branch, NASA/Goddard Space Flight Center, Greenbelt, MD 20771.

The distinctive steep-sided "pancake" domes discovered in the Magellan images of Venus have morphologies that suggest formation by a single continuous emplacement of a high viscosity magma [1]. A resemblance of the venusian domes to—much smaller—terrestrial rhyolite and dacite volcanic domes has prompted some authors to suggest that the domes on Venus also have high silica compositions [1, 2] and thus high viscosities. However, viscosity is a function of crystallinity as well as silica content in a magma, and thus increases as a result of magmatic cooling. To investigate the effect of a cooling-induced viscosity increase on dome morphology, we are modeling the domes as radial viscous gravity currents that cool during emplacement.

The spreading of radial viscous gravity currents has been previously discussed and solved for constant viscosities using a similarity solution approach [3, 4]. If the dome emplacement is modeled as the release of a fixed fluid volume, the cooling-induced viscosity is primarily a function of time, and may be approximated as

$$\nu = k t^{\beta}$$

where ν is kinematic viscosity, k is a constant, t is time, and β is a constant ≥ 0. Figure 1 illustrates viscosity functions for $\beta=0$ (constant viscosity), $0<\beta<1$, $\beta=1$(linear viscosity with time), and $\beta>1$(Magmatic viscosities [5]). For this fixed volume release, time-dependent viscosity case, an approach similar to Huppert's yields a similarity solution valid only for the range $\beta<1$. However, the similarity solution is a good indication of the behavior of the general solution as β increases from the constant velocity case of $\beta=0$ through the $0<\beta<1$ range of the similarity solution and towards the $\beta>1$ range of realistic magmatic viscosity functions. In general, as $\beta \to 1$ for $t \to \infty$, flow velocity $\to 0$, and it is reasonable to expect that, in the full solution, the flow would halt in a finite, β-dependent time that is only weakly dependent on composition. If this is the case, the Venus dome morphologies might be the result of the cooling process rather than the initial composition.

A solution of the flow problem for all β is in progress and is obtained by numerically solving the nonlinear partial differential equation

$$\frac{\partial h}{\partial t} - \frac{1}{3}\frac{g}{\nu} r^{-1} \frac{\partial}{\partial r}\left(r h^{3} \frac{\partial h}{\partial r} \right) = 0$$

for flow height as a function of radius and time where h is flow height, t is time, r is radius, g is acceleration of gravity, and ν is viscosity. A full solution to the problem couples the viscosity as an explicit function of temperature predicted by a exterior convection-interior conduction cooling model of the flow during emplacement. An approximate solution may be obtained by using a time-dependent viscosity function determined by a fit to empirical cooling data (e.g.[5]). If the results from the approximate solution follow the general trend illustrated in table one, then the viscosity change resulting from cooling during emplacement will be a significant factor in emplacement and final morphology of volcanic features such as the venusian "pancake" domes, and the composition of the domes will not be uniquely determined by their final morphology

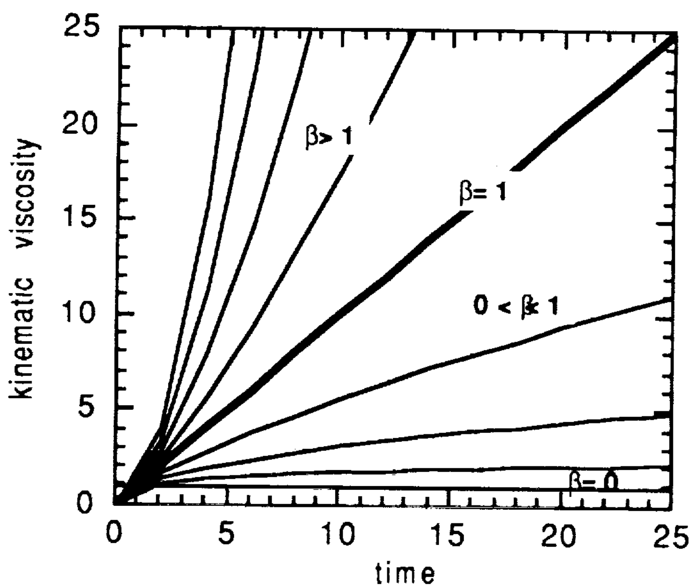
References:[1] Pavri, B., Head, J. W., et al., *J. Geophys. Res.*, **97**, 13445-13478, 1992. [2] McKenzie, D., Ford, P. G., et al., *J. Geophys. Res.*, **97**, 15967-15976, 1992. [3] Huppert, H. E., Shepard, J. B., et al., *J. Volcanol. Geotherm. Res.*, **14**, 199-22, 1982. [4] Huppert, H. E., *J. Fluid Mech.*, **121**, 43-58, 1982. [5] Murase, T. and McBirney, A. R., *Geol. Soc. Am. Bull.*, **84**, 3563-3592, 1973.

VENUS PANCAKE DOME FORMATION: Sakimoto, S.E.H. et al

Table 1. viscosity function shapes and flow behaviors for the variable time dependent viscous radial gravity flows described in the text.

Viscosity function shape	β value	Flow behavior as $t \to \infty$
Constant	$\beta = 0$	Flow spreads indefinitely
Concave downward	$0 < \beta < 1$	Flow decelerates
Concave downward	$\beta \to 1$	Flow velocity $\to 0$ as $t \to \infty$
Linear	$\beta \geq 1$	Similarity solution breaks down
Concave upward	$\beta > 1$	Flow will stop (predicted results)

Figure 1. Time dependent kinematic viscosity functions of the form $\nu = k t^{\beta}$ where the function shape and flow behavior are related as described in table 1, the units are any compatible set of viscosity and time units, and the magmatic viscosities are in the region where $\beta > 1$ (see text).



S97-25
ABS. ONLY
N94-20733
168057

THERMAL INFRARED REMOTE SENSING AND KIRCHHOFF'S LAW: I LABORATORY MEASUREMENTS; J. W. Salisbury, A. Wald, and D. M. D'Aria, Johns Hopkins University

With the near-term prospect of thermal infrared spectroscopic measurements of martian surface materials by Mars Observer, it has become important to understand the emissivity behavior of materials, especially particulate materials. Perhaps the most fundamental question to be answered is the extent to which such materials follow Kirchhoff's Law [1] under less than ideal conditions.

Kirchhoff's Law is typically stated in its simplest form (for opaque materials without wavelength or directional subscripts) as E=1-R, where E and R are emissivity and reflectance, respectively. However, this Law, as originally conceived, applies only to samples in thermal equilibrium with their surroundings-- i.e.., the sample is isothermal and at the same temperature as the background to which it radiates. Most laboratory measurements of emissivity only approach this condition and it never applies in remote sensing applications. In particular, the background is often much cooler than the radiating sample, and this has led to a long controversy about the applicability of Kirchhoff's Law under such conditions. It has also led to field and laboratory emissivity measurement techniques that use some form of the "emissivity box" approach, which surrounds the sample with a background as close as possible to the sample temperature [2,3]. However, clear theoretical arguments have been made that a "freely radiating" sample (i.e. sample independent of an environmental radiation field) will still follow Kirchhoff's Law, if the sample material obeys the Boltzmann distribution [4], resulting in Planckian emission.

However, non-Planckian emission behavior can occur in particulate materials when a thermal gradient is induced and the bulk sample no longer obeys the Boltzmann distribution. This is best illustrated for remote sensing purposes by laboratory measurements of the spectral emissivities of fine particulate samples under simulated lunar environmental conditions [5]. Here, the lack of interstitial gas molecules results in very slow heat transfer between grains by conduction across the small asperity points of contact, compared to the more rapid convective heat transport when gas is present. Under such conditions, a cold skin of particles can develop over a warmer interior (the solid state greenhouse effect) [5]. The net result is increased spectral contrast and distortion of the spectral curve compared to directional hemispherical reflectance measurements. In short, Kirchhoff's Law does not apply because of the non-Planckian source function of the emitted radiation. Although the thermal gradient is less severe in a fine particulate sample under terrestrial or even martian conditions, where interstitial gas provides convective heat transport, no measurements have been made to determine the exact extent to which Kirchhoff's Law may still be applied. Thus, there is uncertainty about the extent to which laboratory measurements of directional hemispherical reflectance can be used to predict emissivity simply because of the presence of thermal gradients.

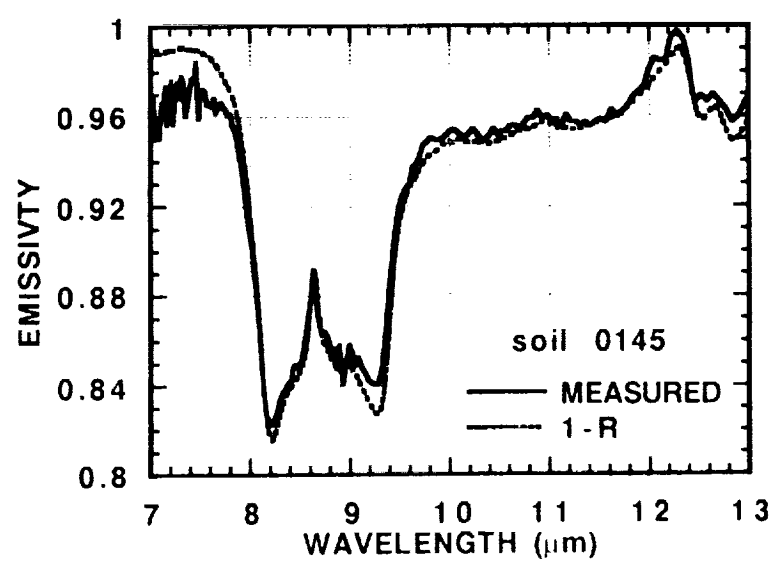
Theoreticians are fond of using simple examples in their arguments, such as large solid surfaces, where geometrical optics hold and scattering is not important [4]. However, geometrical optics do not hold for particulate samples with grain size $\leq \lambda$, and absorption efficiencies in this case can exceed unity [6], implying a possible violation of Kirchhoff's Law. Further, individual particles in a geological sample may

have a highly complex interaction with radiation. The ultimate in complex samples may be soils in which the larger, opaque (in the reststrahlen bands) quartz grains are coated with a semi-transparent layer of tiny, optically thin particles of clay and quartz. The particulate nature of these soils enhances scattering, and the combination of opaque grains with semi-transparent coatings results in an extremely complex radiative transfer problem. Such particulate samples are also more likely than solid samples to develop thermal gradients when radiating to a cooler background, due to their low thermal conductivity. Thus, such samples provide a severe test of Kirchhoff's Law.

In our initial experiments, we have heated soil samples in air on a hot plate in the laboratory to a much higher temperature (~50° C) than the room temperature background. Spectral emissivity was measured as described in [7], except the known emissivities (determined from reflectance) of both the primary and secondary Christiansen features were used, instead of assuming an emissivity of unity at these wavelengths. This measured emissivity was compared to directional hemispherical reflectance measured as described in [8]. As shown in the figure below, spectral emissivity calculated from reflectance is very close to measured emissivity, despite noise in the emissivity curve due primarily to atmospheric water vapor. In fact, measured and calculated emissivity agree within better than 1%, which is within our estimated experimental error of 2% with such noisy emission data obtained under high humidity conditions. Thus, despite the complexity of the sample and the marked temperature difference between sample and background, Kirchhoff's Law can still be used to predict emissivity from laboratory measurements of reflectance.

A subsequent paper will address similar comparisons made in the field under realistic remote sensing conditions.

REFERENCES: [1] Nicodemus, F. E., 1965, Ap. Op., 4, 767-773. [2] Buettner, J. K., and Kern, C. D., 1965, JGR, 70. 1329-1337. [3] Nerry, F., Labed, J. and Stoll, M. P., 1990, JGR, 95, 7045-7054. [4] Baltes, A. P., 1976, Progress in Optics XIII, 3-25. [5] Logan, L. M., Hunt, G. R., Salisbury, J. W., and Balsamo, S. R., 1973, JGR, 78, 4983-5003. [6] Van de Hulst, 1057, Light Scattering by Small Particles, Wiley, N Y, 470 pp. [7] Salisbury, J. W., 1990, Proceedings IEEE Remote Sensing Symp., 3, 1775-1778. [8]Salisbury, J. W. and Walter, L. S., 1989, JGR, 94, 9192-9202.



168258 N94-20734 2

MAGELLAN AT VENUS: SUMMARY OF SCIENCE FINDINGS; R.S. Saunders, E.R. Stofan, J.J. Plaut, and D.A. Senske, Jet Propulsion Laboratory, Calif. Institute of Technology, Pasadena, CA 91109

This paper gives a brief summary of the principal science findings of the Magellan mission and plans for future data acquisition. This includes high resolution gravity data from a nearly circular orbit and atmospheric drag and occultation experiments. The Magellan science results represent the combined effort of more than 100 Magellan investigators and their students and colleagues. More complete discussions can be found in the August and October, 1992 issues of the *Journal of Geophysical Research, Planets* [1]. The Magellan mission's scientific objectives were (1) to provide a global characterization of landforms and tectonic features; (2) to distinguish and understand impact processes; (3) to define and explain erosion, deposition, and chemical processes; (4) to model the interior density distribution. All but the last objective, which requires new global gravity data, have been accomplished, or we have acquired the data that are required to accomplish them.

To meet these objectives, synthetic aperture radar imaging and altimetry were acquired over nearly 99% of the planet. Several kinds of images were obtained in order to provide the best interpretation of the landforms. For the first 243 day cycle, one Venus rotation, an incidence angle, or look-angle, profile was used that maximized the image resolution and overall quality everywhere along the orbit. This profile caused the incidence angle to vary from about 15° over the north pole to 45° at the equator. In the first cycle we mapped 83% of Venus, more than meeting the primary mission objectives. In the second mapping cycle, mapping was restricted in order to control spacecraft temperature. Image data were obtained at a constant incidence angle, and looking to the right (toward the west) in the opposite direction from cycle 1. Also, in cycle 2, some of the major gaps were filled with the same incidence angle profile as used in cycle 1. In cycle 2, we also conducted a successful test of a stereo mode in which we imaged at a slightly different angle than in cycle 1. The stereo was so useful that it was decided to devote much of the third mapping cycle to acquiring stereo images. All of the radar image data were processed at JPL in a complex flow that begins at the DSN stations at Goldstone, Madrid, and Canberra. In addition to images and altimetry, Magellan also acquired radiometer data whenever images were obtained [2]. The radiometry samples the radio emission of the surface at the radar wavelength. Emissivity varies from place to place because of variations in surface properties. Gordon Pettengill (MIT) is Principal Investigator of the radar team. William Sjogren (JPL) and Georges Balmino (CNES, France) are PIs for the gravity experiments.

Imaging was terminated at the end of the third cycle and gravity data are being acquired during cycle 4 by pointing the antenna toward Earth during the part of the orbit that we previously were mapping and recording the radio signal. From this signal we extract the slight accelerations of the spacecraft as it orbits Venus and convert these accelerations into gravity maps that tell us about density variations in the interior.

Summary of principal Magellan science findings

The rotation period of Venus was refined to 243.0185 ± 0.0001 days and the north pole direction, in J2000 coordinates, has been refined to right ascension $272.76° \pm 0.02°$ and declination $67.16° \pm 0.01°$. The mean radius was refined to 6051.84 km, with the lowest point

6048.0 km and the highest point 6062.57 km [3].

Volcanism was established as the dominant surface process on Venus [4]. Volcanism is broadly distributed, not completely random, but not forming linear patterns as on Earth where major volcanic activity tends to occur along plate boundaries. Image analysis reveals thus far 556 shield fields, 274 volcanoes 20-100 km, 156 volcanoes, 100 km, 86 calderas (not on shields), 259 arachnoids, 53 lava flow fields, 200 sinuous lava channels, 145 steep-sided domes (pancakes) [4]. Over 360 coronae and corona-like features have been identified [5].

Tectonics is a major process [6], with evidence for extension and compression. Steep slopes, up to tens of km in extent, and 20°-30° provide evidence of active tectonics. Deformation is more distributed than on Earth. Shear zones are seen in complex ridged terrain. Trench topography resembles terrestrial subduction. An extensive equatorial zone of fractures is among the most recent tectonic features.

More than 900 impact craters 1.5 km to 280 km have been identified [7,8]. There appears to be a globally random distribution yielding an average surface age of about 500 my. Both bright and dark splotches appear to be shock signatures. Most craters are unmodified. Bright and dark E-W oriented parabolic halos are associated with about 20% of craters [9].

Surface processes and surface properties [10,11,12] investigations yield more than 8000 mapped wind streaks with directions consistent with Hadley circulation. Possible dune fields have been identified and there is widespread evidence of landslides [13]. Anomalous left-right reflectivity behavior indicates unusual surface reflectivity behavior possible caused by asymmetric shapes. Anomalous low emissivity in elevated regions has been confirmed [2].

Major questions about Venus remain unresolved, pending acquisition of new data and further analysis of existing data. Interpretation of the impact crater population suggests a major secular change in the rate or style of resurfacing [7], but the details or even the reality of this change, whether catastrophic, cyclical, local or global scale is unknown. High-resolution global gravity data will help address some of the unresolved issues concerning the generation, support, and relaxation of topography.

References: [1] R.S. Saunders *et al., J. Geophys. Res.*, **97**, E8, 13,067, 1992; [2] G.H. Pettengill *et al.*, J. Geophys Res., **97**, E8, 13,091, 1992; [3] M.E. Davies *et al., J. Geophys. Res.*, **97** ,E8, 13,141, 1992; [4] J. W. Head *et al., J. Geophys. Res.*, **97**, E8, 13,153, 1992; [5] E.R. Stofan *et al., J. Geophys. Res.*, **97**, E8, 13,347, 1992; [6] S. C. Solomon *et al., J. Geophys. Res.*, **97**, E8, 13,199, 1992; [7] G.G. Schaber *et al. J. Geophys. Res.*, **97**, E8, 13,257, 1992; [8] R.J. Phillips *et al., J. Geophys. Res.*, **97**, E10, 15,923, 1992; [9] D.B. Campbell *et al., J. Geophys. Res.* [10] G.L. Tyler *et al., J. Geophys. Res.*, **97**, E8, 13,115, 1992; [11] R.E. Arvidson *et al., J. Geophys. Res.*, **97**, E8, 13,303, 1992; [12] R. Greeley *et al., J. Geophys. Res.*, **97**, E8, 13,319, 1992; [13] M.C. Malin, *J. Geophys. Res.*, **97**, E10, 16,337

Acknowledgements: This work was performed, in part, at the Jet Propulsion Laboratory, California Institute of Technology, under contract with NASA.

S99-70
ABS. ONLY
168059
N94-20735

PRELIMINARY ESTIMATION OF TAGAMITE COOLING CONDITIONS (PUCHEZH-KATUNKI ASTROBLEME, RUSSIA).

L.Sazonova, V.Feldman, N.Korotaeva. Moscow State University., Russia.

The velosities and initial temperatures of crystallization from super-heated shocked melts have been estimated as a result of the investigation of the structures and mineral association in impact melt rocks of Puchezh-Katunki astrobleme. The dependence of the these parameters vs. the body thickness of impact melt rocks have been found.

Impact melt rocks of Puchezh-Katunki astrobleme are represented by thin dikes and veins in gneisses and amphibolites. The thickness of such formations ranges from few sm to few m (more seldom few tens of meters). Sometimes these impact melt rocks include shocked rock and mineral fragments of the target (from few % to few tens of %). Their texture ranges from glassy to fine crystalline. In crystalline impact melt rocks there are Pl-lathes, Cpx and Opx grains (small, often skeletal).

Pl is of needle and long-prism form (length to some tens of mkm, width to ten mkm). Pl is often zonate. Its composition changes from $An_{52.5}Ab_{45.5}Or_2$ in the nucleus to pure Ab in the range. The zonation sometimes is reverse. Thus in the sample B-3035 Pl composition changes from $An_{21.0}Ab_{77.0}Or_2$ in the nucleus to $An_{38.9}Ab_{57.9}Or_{3.2}$ in the range. Such phenomenon may be caused by either Pl nuclei albitization or by Pl crystallization around tiny nonmelted relicts of the target rock Pl. Cpx and Opx are of long-prizm face- ore edge-skeletal forms and zonate as a rule. The crystal length reaches 30 mkm, the width - few mkm. The succession of Cpx and Opx crystallization may be different even in a single thin section. Sometimes Cpx forms fine grains and Opx grows around it in needles. Sometimes a reverse picture is observed. Such phenomenon shows non-equilibrium of impact melt crustallization as a whole. Sometimes Cpx and Opx grows closely into each other which shows simultaneity of their crystallization. Cpx composition ranges: in nuclei - $En_{55-39}Fs_{22-14}Woll_{47-23}$; in

PRELIMINARY ESTIMATION...

Sazonova L., Feldman V., Korotaeva N.

ranges - $En_{49-33}Fs_{30-14}Woll_{44-27}$. Opx composition ranges from Fs_{27} in the nucleus to Fs_{41} in the range. Impact melt rock cooling velosities were estimated by Lofgran diagram [1] (by Ti and Al content in Cpx). Initial crystallization temperatures of impact melts were defined with two-pyroxen thermometer [2]. The preliminary estimations of impact melt rock cooling conditions of Puchezh-Katunki astrobleme allowed us to state: 1. the cooling velosity of impact melts from thin dices (~1 m thin) and from edge parts of thicker dices is $\geq 10^{o}C$/hour (group I); 2. cooling velosity of impact melts from the central parts of the relatively thick dikes (~ 5 m thickness and more) is ~ $4^{o}C$/hour (group II). The initial crystallization temperatures of impact melts of group I are ~ 1350-1400^{o}C, group II - 1100-1200^{o}C. Thus we may assume non-equilibrium impact melt crystallization of Puchezh-Katunki astrobleme melts. The comparison of impact melt rocks of Puchezh-Katunki, Zhamanshin and Boltysh astroblems allows us to make a row in which there is a connection between the body thickness and the impact melt cooling conditions. The initial impact melt crystallization temperature of thick Boltysh body (~ 200 m thickness) was estimated by us as ~ 800^{o}C [3], and the first liquidus phase (spinel) in Zhamanshin thin jet fragments, bombs, lapilli, splashes (thickness in first tens of sm) appears at 1800^{o}C [4].

[1] Physics of magmaqtic processes. Princton.(1980); [2] L.Perchuk and J.Rjabchikov (1976). Compositional relations in mineral systems. (in Russian); [3] L.Sazonova, V.Feldman, N.Korotaeva (1989). LPSC XX; [4] V.Feldman (1990). Petrology of impactites (in Russian).

VENUS' IMPACT-CRATER DATABASE: UPDATE TO ~98% OF THE PLANET'S SURFACE;

Gerald G. Schaber and David J. Chadwick, U.S. Geological Survey, Flagstaff, AZ 86001.

p-2

A total of 912 impact craters between 1.5 and 280 km in diameter have now been identified on about 98% of Venus' surface (Fig. 1). This total includes an additional 71 craters (mostly in the southern hemisphere) not in the crater inventory given in Schaber et al. [1] for 89% of the planet (Table 1). (Extrapolated to 100% of the surface, the inventory should consist of 930 craters >1.5 km in diameter.) The total crater inventory for 98% of the planet is only slightly larger (912 versus 882) than that extrapolated from the inventory of 135 craters when only 15% of the planet had been mapped by Magellan [2]. The remarkably consistent density of about 2.02 impact craters per 10^6 km^2 emphasizes the completely random nature of the crater population's distribution [1,2]. About 400 craters recognized from Magellan mapping have been assigned names [3].

References: [1] Schaber, G.G. and 8 others (1992) *J. Geophys. Res.*, *97*, 13,257-13,301; [2] Phillips, R.J., and 6 others (1992) *J. Geophys. Res.*, *97*, 15,923-15,948; [3] Russell, J. and Schaber, G.G., this volume.

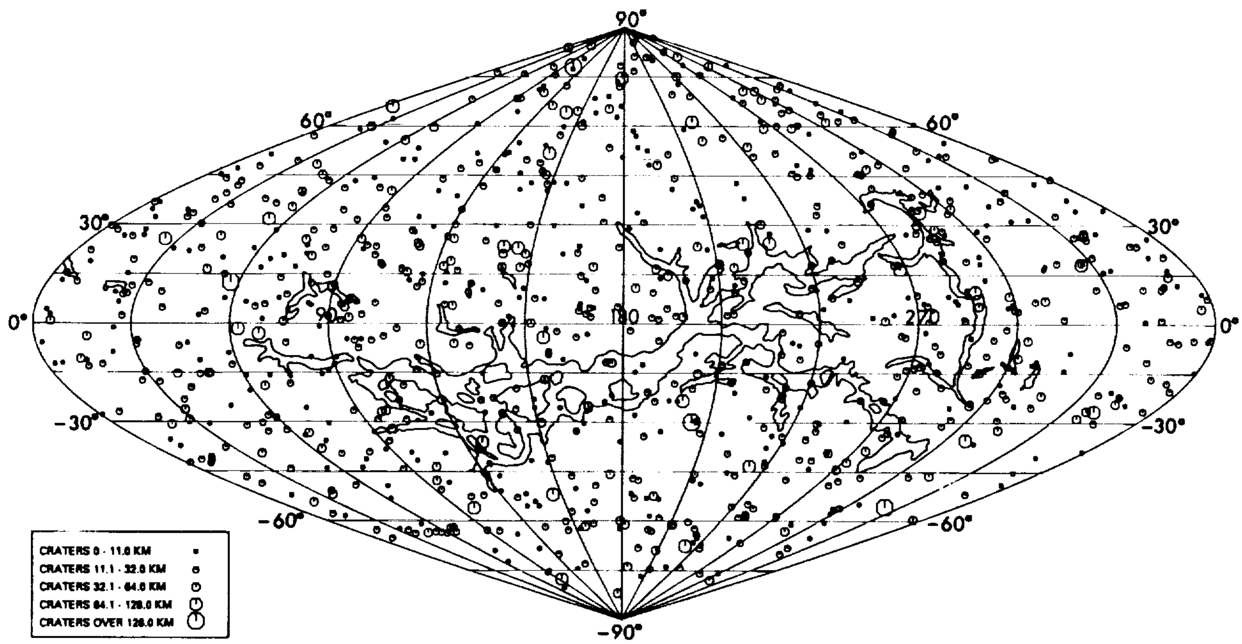


Figure 1 - Sinusoidal Equal-Area map of Venus showing impact crater distribution on ~98% of the planet (only the southernmost region was not covered by Magellan). Gray areas indicate major fracture belts.

Table 1 - Impact craters identified subsequent to the crater inventory of 89% of Venus' surface given in Schaber et al. [1]. (Listed crater names not yet formally approved by the International Astronomical Union.)

Name	Latitude	Longitude	Diam. (km)
	62.6	40.5	105
	44.25	73.65	10
	40.3	105.8	5
	38.7	114.7	5
	37.7	350.1	3
Miriam	36.5	48.2	15
Bernhardt	31.6	84.5	25
	27.8	108.1	8
	13.25	112.8	4

	1.5	69.89	6.5
Makola	-3.75	106.5	18
	-4.65	95.4	2.5
Blanche	-8.55	157.05	18
	-9.3	157.0	13
	-11.85	275.25	5.5
	-15.05	135.6	8.5
Jhirad	-16.75	105.55	50
	-18.85	109.2	11
Cline	-21.8	317.0	40
Fukiko	-23.25	105.7	15
	-23.29	132.9	12.5
	-23.65	173.97	5
WuHou	-25.4	317.4	30
Judith	-29.1	104.5	18
Lida	-29.15	94.5	14
	-29.5	108.1	8
von Paradis	-32.2	314.8	36
Nevelson	-35.2	307.75	75
	-36.30	312.6	10
	-39.4	109.95	2
	-39.5	69.0	11
	-43.8	70.25	9
	-46.15	314.75	40
	-46.45	306.4	13
	-49.2	55.5	13
	-52.3	15.1	10
Lazarus	-52.8	127.2	25
	-53.3	61.8	10
	-54.8	305.25	10
	-55.4	135.4	5
Vesna	-60.30	220.4	17
	-60.45	304.8	10.5
	-61.0	53.5	6
Gretchen	-61.05	212.3	19
Ichikawa	-61.6	156.4	36
Megan	-61.75	130.6	17.5
	-61.9	70.9	12
Lucia	-62.1	67.8	17
	-62.4	153.0	7
Durant	-62.3	227.5	23
Melanie	-62.75	144.3	16
Sartika	-63.4	67.1	28
Berggolts	-63.4	53.0	31
Danute	-63.5	56.5	14
Rand	-63.75	59.5	27
	-64.2	232.2	12
	-65.1	234.1	10
	-65.1	315.9	10
	-66.5	234.2	8
	-67.5	230.0	90
	-68.1	315.1	12
	-69.0	72.0	10
	-69.9	319.6	12
	-72.3	66.0	8
Giliani	-72.9	142.0	27
Leonard	-73.8	186.0	37
Weick	-74.2	244.	21
	-75.75	88.00	9
	-76.7	204.8	8
Hurston	-77.65	94.5	65
	-80.2	78.0	5
Bickerdyke	-82.0	170.8	39

S/01-91
ABS. ONLY
N94-20737

LOCAL TOPOGRAPHY OF MARS AND ITS RELATIONSHIP TO SURFACE WEATHERING PROCESSES; M. W. Schaefer, University of Maryland, College Park, MD (currently at Goddard Space Flight Center, Greenbelt, MD)

There is a growing body of evidence in favor of the importance of aqueous sedimentary processes on Mars. It is important to understand the role that surface weathering processes have played in the development of the present morphology of the Martian surface. Such an understanding is important not only for its relevance to the study of volatile sources and sinks on Mars through time, but also for its relevance to Martian geologic and tectonic history. Digital topography is an important part of geologic and geomorphic studies, useful in distinguishing between different lithologies and between different types of weathering. Preliminary work is underway to develop tools for the analysis of the Mars Observer topography data set.

Many authors have supported models of Martian geological evolution that assume an early warm, wet period in its history [1-5], and contain such things as a lake in Valles Marineris [6-8], an ocean in the northern plains [9-12], and inorganically precipitated carbonate deposits [13]. Such elements are likely to have had a significant influence on the geomorphology of the areas of the planet in which they occurred. In some cases, particularly northward of the crustal dichotomy boundary, and in the great canyons of Valles Marineris, chemical weathering and erosional processes may have obscured the effects of tectonics and meteorite impacts. This is especially true if these regions do indeed contain sedimentary deposits of one sort or another, as has been postulated [14-15].

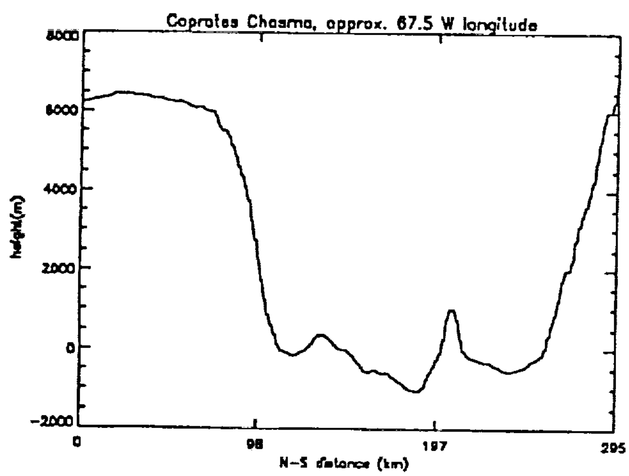
Starting in the fall of this year, the Mars Observer Laser Altimeter will begin sending back to Earth data on the topography of Mars that is of a higher quality than most of the topography data available for the Earth. This data will be invaluable, not only for understanding global and large-scale regional processes and landforms on Mars, but also for the study of local and smaller-scale regional processes and landforms. Digital topography is an important part of geologic and geomorphic studies, useful in distinguishing between different lithologies and between different types of weathering. Digital topography data may be used to study a wide variety of local and regional-scale landforms, including valleys, sand dunes, lava flows, landslides, and slopes [15]. Topography data are also essential to the analysis of spectral response patterns, especially in areas of high topographic relief. Geomorphic classification can be significantly improved by the addition of topographic information [16].

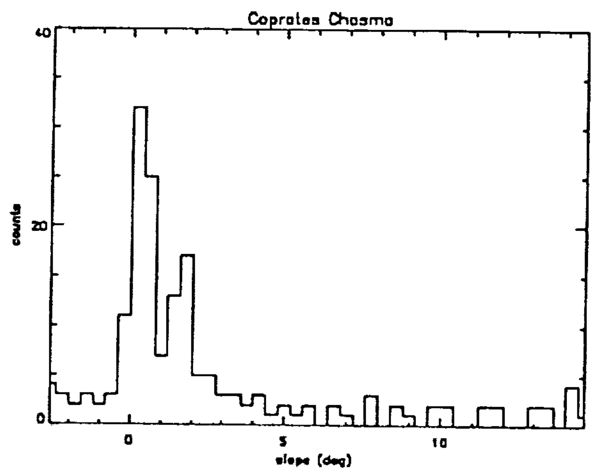
Preliminary work is underway to develop tools for the analysis of the Mars Observer topography data set. One method of quantitative analysis of topographic profiles that will be used is slope statistics [17]. Slope-angle statistics, in the form of frequency distributions of slopes, may be used both in the determination of rock type: under similar climatic conditions, different rock types will have different peak frequencies of slope; and in the determination of process: given a similar geology, such processes as landslides, soil slips, and solifluction will have different

characteristic slopes [18]. A trial of this method has been made using the USGS USGS digital elevation model of Mars.

As an example, here is a topographic profile Coprates Chasma, in the eastern end of the Valles Marineris. The resolution is about 1 kilometer. The south (left) wall, especially, displays a simple s-shape, in appearance a classic simple catena (soil-covered slope). This shape indicates an evolved slope, probably debris-covered, with physical transport of material, not chemical weathering, controlling the recession of the slope.

Some specific questions that will be addressed when the Mars Observer data become available include: Is the present topography of Mars consistent with the presence of an eroded sedimentary terrain (particularly in the northern plains)? Can the canyons of the Valles Marineris system be used as a 'window' into the subsurface geology of Mars? What can the topography of the canyon walls and floor tell us about the materials of which they are made? To what extent are the signatures of tectonic processes in the region north of the crustal dichotomy boundary obscured by weathering and sedimentation?





[1] Carr, M.H., *The Surface of Mars*, Yale University Press, New Haven, Conn., 1981. [2] Carr, M.H., *Icarus, 68*, 187, 1986. [3] Fanale, F.P., *Icarus, 28*, 179, 1976. [4] Pollack, J.B., J.F. Kasting, S.M. Richardson, and K. Poliakoff, *Icarus 71*, 203, 1987. [5] Rossbacher, L.A., and S. Judson, *Icarus 45*, 39, 1981. [6] Nedell, S. S., Squyres, S. W., and D. W. Anderson, *Icarus 71*, 409, 1987. [7] McKay, C.P., and S.S. Nedell, *Icarus 73*, 142, 1988. [8] Spencer, J. R. and F. P. Fanale, *J. Geophys. Res. 95*, 14301, 1990. [9] Parker, T.J., D.M. Schneeberger, D.C. Pieri, and R.S. Saunders, *Reports of the Planetary Geology and Geophysics Program – 1986, NASA Tech. Memo., TM-89810*, 319, 1987a. [10] Parker, T.J., D.M. Schneeberger, D.C. Pieri, and R.S. Saunders, *Reports of the Planetary Geology and Geophysics Program – 1986, NASA Tech. Memo., TM-89810*, 322, 1987b. [11] Parker, T.J. and R.S. Saunders, *MEVTV Workshop on Nature and Composition of Surface Units on Mars, LPI Tech. Rep. 88-5*, 100, Lunar and Planet. Inst., Houston, Tex., 1988. [12] Schaefer, M. W., *J. Geophys. Res. 95*, 14291, 1990b. [13] McGill, G.E., *Lunar Planet. Sci, XVI*, 534, 1985. [14] Lucchitta, B.K., H.M. Ferguson, and C. Summers, *Proc. Lunar Planet. Sci. Conf. 17th, Part 1, J. Geophys. Res. 91*, suppl., E166, 1986. [15] *Processes Branch, Earth Science and Applications Division, NASA Headquarters.* Lunar and Planetary Institute, Houston. 64 pp. [16] Franklin, S.E. (1990) *Computers and Geosciences* 16, 1003. [17] Small, R. J., and M. J. Clark, *Slopes and Weathering*, Cambridge University Press, Cambridge, 1982. [18] Gerrard, J., *Rocks and Landforms*, Allen and Unwin, London, 1988.

ABS. ONLY N94-20738

p. 2

DIAPIRS & CANTALOUPES: LAYERING AND OVERTURN OF TRITON'S CRUST;

P. Schenk, Lunar & Planetary Institute, Houston, TX; M.P.A. Jackson, Bureau of Economic Geology, Univ. of Texas, Austin, TX

It has recently been proposed that cantaloupe terrain formed as a result of instability and overturn (i.e., diapirism) of Triton's crust [1]. Morphologic evidence implicates compositional layering within Triton's crust as the driving mechanism for this overturn. Here, we review the morphologic evidence for this origin and evaluate some of the implications.

GEOLOGY

Cantaloupe terrain is comprised of well over 100 individual structural cells 25-40 km wide. Cells are elliptical to kidney-shaped in planform, and although closely spaced, they are interfering and do not crosscut each other. They most closely resemble the structural patterns observed in terrestrial diapirs such as salt domes (e.g., in the Great Kavir [2]), granitoid batholiths (e.g., in the Pilbara Block, W. Australia [e.g., 3]), and experimental centrifuge diapirs [2]. Diapirs are driven by density inversions in the crust resulting from either compositional or thermal induced density contrasts or both. Two geologic units have been identified in the structural cells; the rough central area or core (unit A), and the smoother annulus (unit B) surrounding the core. A third geologic unit, C, forms the matrix between the cells and may be the youngest unit. Unit C is comprised of numerous parallel ridges 20%-50% darker and 300-800 higher than the cell units. The first two units were stratigraphically lowest, having risen and pierced the overlying unit. All three units appear to be comprised of rheologically and compositionally distinct materials, indicating that compositional layering of the crust is the more likely cause of diapirism on Triton, although thermal convection may also be important.

STRATIGRAPHY

Evidence for diapirism on Triton opens a window into the crustal structure and stratigraphy. In simple systems, spacing between cells is related to the thickness of the overlying unit by a factor of ~2.6 [4]. Cell spacing averages 47 km, indicating a thickness of ~20 km for the denser overlying unit. Also, it is generally the case that the total thickness of all layers involved in the overturn is approximately on the order of the mean spacing of the diapirs, which implies a total thickness of 40-50 km. From a maximum formation time of ~2 b.y., we estimate a maximum crustal viscosity [4] of $<10^{22}$ Pa•s.

Many of the ridges in the matrix unit parallel cell margins; others form complex subparallel sigmoidal patterns reminiscent of fold belts on Earth. These are interpreted as forming from the buckling of relatively thin layer(s) of mechanically anisotropic material. As a first approximation, we use buckling theory [e.g., 4], where the wavelength of the folding is related to the thickness of the layer, to estimate the thickness of the surface unit. For a wavelength of ~3 km for the ridges, the estimated thickness of the buckled layer is 35-45 meters. The wavelength is also dependent on the viscosity contrast and usually decreases (by as much as a factor of 2) from the initiation wavelength as buckling progresses. Thus, we suggest that the thickness of the dark surface layer is probably between 35 and 100 meters. At this point, however, we stress that in our analyses we have assumed the crust was isothermal. The viscosities of most ices are highly temperature dependent [e.g., 5]. Hence our viscosity and thickness estimates should be considered approximate as more sophisticated analyses are being pursued.

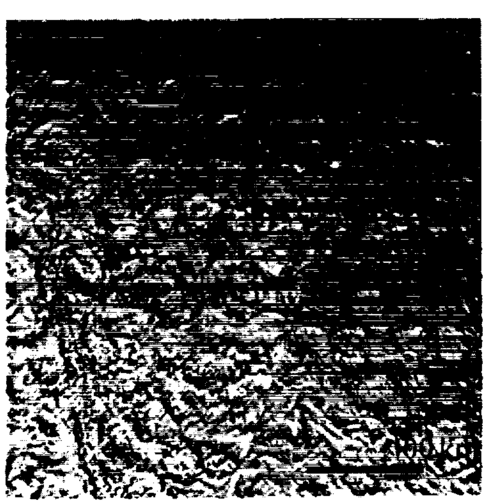
In principal, the less dense cores of the diapirs should be elevated above the denser

intercellular matrix. While crumpling could initially produce a thickened zone of accumulated material, equilibrium should eventually be restored. Our preferred interpretation is that the thin buckled surface unit is both more viscous and less dense relative to underlying portions of unit C. This encouraged buckling and discouraged downward drag on this thin surface unit. The bulk of the 20-km-thick overlying unit C would be denser than the cell units A & B, however. Complete piercing of the matrix by the cell units and of the outer unit B by unit A implies that these structures are mature or advanced diapiric structures. Spacing and widths of diapir cells in cantaloupe terrain increase northward, which may indicate a thickness change. Many cells in the northern portion of cantaloupe terrain have partially merged, suggesting they may form a diapiric canopy structure [2].

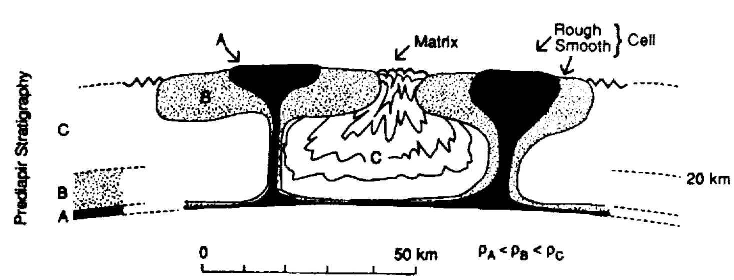
ORIGINS OF LAYERING

Diapirism appears to have been one of the first major events recorded in the crust that was regenerated following global melting [e.g., 6]. This overturn exposes compositional layering, including formation of a density inversion, in Triton's crust which may contain a record of the reconstruction of Triton's crust. At least three distinct layers have been identified to date. Although we are unable, as yet, to unambiguously identify the composition of these layers, they probably include layers composed of ice phases other than (and some denser than) water ice. The maximum crustal viscosity estimate ($<10^{22}$ Pa•s) is consistent with a bulk crustal composition dominated by H_2O, NH_3, or CO_2 [5, 7, 8] ices phases (or possibly simple hydrocarbons that may also be present [9]). Triton may have possessed a thick volatile rich atmosphere during the period of global melting [6, 10]. Among the consequences of this episode may have been the deposition or concentration of CO_2, NH_3, or simple organic compounds on the surface, either volcanically or through atmospheric condensation. Whatever the composition, the evidence of compositional layering in the crust is important evidence of the complexity of Triton's evolution.

[1] Schenk, P., & M.P.A. Jackson, *Geology*, in press, 1993. [2] Jackson, M.P.A., et al., *Geol. Soc. Am. Memoir 177*, 1990. [3] Hickman, A., in *Archean Geology*, Geol. Soc. Austr., p. 57, 1981. [4] Turcotte, D., & G. Schubert, *Geodynamics*, Wiley & Sons, 1982. [5] Kirby, S., et al., *J. Phys. C*, 48, 227, 1987. [6] McKinnon, W., EOS, 73, 190, 1992. [7] Durham, W., et al., pers. comm. [8] Clark, B., & R. Mullins, *Icarus*, 27, 215, 1976. [9] Shock, E., & W. McKinnon, *Icarus*, in press, 1993. [10] Lunine, J., & M. Nolan, *Icarus*, 100, 221, 1992.



Canteloupe Terrain



Cross-section of Triton's crust

GEOLOGY OF THE SOUTHERN HEMISPHERE OF TRITON: NO POLAR CAP; P. Schenk, Lunar & Planetary Institute, Houston, TX; J.M. Moore, NASA Ames, Moffett Field, CA

The bright southern hemisphere, comprising Uhlanga Regio, is perhaps the most poorly understood geologic province on Triton. The entire bright southern hemisphere has been described as a bright polar 'cap' [1], implying a seasonal origin, or as a permanent geologic terrain distinct from the equatorial terrains [2]. Also, thermal models have predicted seasonal migration of frosts and ices from the presently sun-lit south latitudes to the dark northern latitudes [e.g., 3]. The distribution of frosts and geologic history of this region must be determined observationally. We reexamine the geology of this terrain with the goal of answering these questions.

MACULAE Uhlanga Regio consists of two major terrain types: bright spotted terrain (bs), and bright streaked terrain (bst) located mostly south of -50°. Bright spotted terrain occurs in a band between roughly 10° S and 45° S and consists of two geologic units: relatively dark spots (maculae) and relatively bright intervening material. Broad diffuse bright and dark streaks are also located in this terrain. Maculae are sharply defined and bulbous to ameboid in shape. Most are between a few and 50 km in size and are very smooth at kilometer scales. Digitate lobes extend from many maculae. Relief of this terrain is extremely low. Relative topography between bright and dark units is unknown because stereo separation is only 12°, insufficient for discrimination on low relief terrains. Relative ages of bright and dark units are also ambiguous.

We consider two possible origins for construction of maculae. Maculae may result from sublimation and mass wasting. In this hypothesis, plains-forming darker material has been eroded to produce scarp-bounded topographic lows, which were later infilled with bright material. A variant of this hypothesis is that the darker material is a thin layer that is being removed to reveal an underlying substrate of brighter material. The best analog for this mechanism is that proposed for formation of the etched and pitted terrain of the south polar region of Mars [4]. An interstitial volatile material within the deposit sublimates or is released resulting in loss of cohesion or mechanical strength, followed by ground and slope collapse, pitting, and scarp retreat.

Alternatively, maculae may be deposits or the product of an unusual volcanic mechanism. A possible morphologic analog is the bulbous-shaped floor mounds in the interior of the D-shaped 'caldera' *Ina* in Lacus Felicitatis on the Moon [5]. These smooth-textured mounds are a few hundred meters across and only 5 to 25 meters high. Small spots, which appear to be oblong pits, have been identified on several maculae. These resemble small pits on many of the floor mounds of Ina. Unfortunately, the origin of the Ina mounds is somewhat unclear. It is unlikely, that these lunar features are the result of sublimation and mass-wasting. Strain and El-Baz [r] conclude they are probably volcanic extrusions. Their size and morphology suggest they may be small volumes of low-viscosity material extruded onto flat terrain at a slow rate.

STRATIGRAPHY The bright material between the dark maculae is not uniform in albedo or texture. The bright unit is often brightest near maculae margins but tends to decrease in brightness southward, resulting in decreased contrast between the two units. Two prominent craters 10 & 11 km across are partially buried beneath the bright deposit; in one crater the central peak is just barely visible. A linear graben with raised rim (extending from the dark equatorial

plains) is also partially obscured by bright material. Dark maculae material avoids these two crater rims but partially buries the graben. These relationships suggest that both the dark maculae and bright materials are superposed on an ancient, partially exposed crust. If younger, bright material could have infilled depressions between the dark maculae. Contacts between bright and dark material are sharp, implying that any infilling may be volcanic. Although the emplacement mechanisms remain uncertain, the observations are consistent with independent evidence in cantaloupe terrain [6] that the upper crust of Triton is layered.

Two lines of evidence indicate these terrains are perennial over geologic time scales. Several global scale lineaments, similar to those found in equatorial terrains, cross this terrain. Also, seven relatively pristine impact craters have been identified within this terrain. The pristine crater population on Triton is strongly concentrated toward the apex of orbital motion. Within this distribution, however, the crater population appears to be random. Given the relatively low resolution and foreshortened viewing geometry and high local sun angles under which the southern terrain was imaged, the pristine crater population is consistent with an age that is not grossly younger than the equatorial terrains.

SOUTH POLAR REGION South of ~50° S, the geology changes rather abruptly to a more coarsely textured, geologically complex terrain, known as bright streaked terrain (bst). This terrain appears to be topographically rough. Numerous discrete geologic units are traceable. Most prominent are isolated smooth bright units, some of which have a flow-like morphology and may be topographically confined. Several global-scale lineaments also cross into this poorly viewed terrain. Poor viewing geometry makes interpretation difficult. Photometric studies are also underway to assist clarify the geology of the southern hemisphere.

[1] Smith, B., et al., *Science*, 246, 1422, 1989. [2] Moore, J., & J. Spencer, *Geophys. Res. Lett.*, 17, 1757, 1990. [3] Stansberry, J., et al., *Geophys. Res. Lett.*, 17, 1773, 1990. [4] Sharp, R, *J. Geophys. Res.*, 78, 4222, 1973. [5] Strain, P. & F. El-Baz, *Proc. 11th Lunar Planet. Sci. Conf.*, 2437, 1980. [6] Schenk, P., & M.P.A. Jackson, *Geology*, in press, 1993; this volume.



Bright spotted terrain of Triton. Scene is ~ 500 km across. Partially buried craters and graben are visible (arrows).

S164-91
ABS. ONLY
168064
N94-20740

3-D MOONS: THE VOYAGER STEREO ATLAS OF THE OUTER SOLAR SYSTEM; P. Schenk, Lunar and Planetary Institute, Houston, TX; J. M. Moore, NASA Ames, Moffett Field, CA

Comprehension and analysis of geologic features on any planet is enhanced manyfold by a clear perception between albedo and topography. On many of the icy satellites significant albedo contrasts due to mixtures of dark rocky and bright icy materials can be associated with topographic features. Subtle topographic features can be masked by albedo variation and under high solar illumination albedo and topography can be difficult to separate. To this end we are compiling an atlas of stereo image pairs of the outer solar system based on Voyager imaging for the investigation of various geologic problems and for general use.

For the icy satellites, general perceptions of topography are usually gleaned from shape-from-shading information in the images processed by the human brain (i.e., visual inspection). With few exceptions, actual topography has been measured on a spot-by-spot basis using shadow heights or photoclinometry [1-3], or along limb profiles (where geographic context may be unavailable) [4]. Shadow heights are limited to regions within ~10° of the terminator and images with resolutions better than ~ 1 km/pixel. Photoclinometric scans can be used more widely but are subject to a variety of errors, primarily uncertain assumptions of uniform scene albedo or poorly understood photometry. Stereoscopic analysis, where available, has the potential for greatly expanding topographic perception.

Stereo imaging of selected icy satellites has already been used on occasion to some advantage. Examples include Miranda, Ariel [5, 6], Triton [7] and even Europa [8]. Quality stereo coverage exists for portions of eight icy satellites, including Miranda, Ganymede, Iapetus, Dione, and others, as well as Io. Up to 30% of the surface areas of some of these bodies can be viewed stereoscopically. Limited coverage may exist for at least six other icy satellites and perhaps several of the irregular satellites. The satellites with the best stereo coverage and resolution are Rhea, Miranda, Ariel, and Io; all satellites with especially prominent topography.

Format and Problems

No one map projection is ideal for stereo images that cover large fractions of curved surfaces. Stereo pairs are being constructed of images reprojected to a common orthographic map projection in order to minimize aspect-ratio distortion. For primary targets, such as Miranda, global-scale scenes covering nearly an entire hemisphere, as well as smaller-scale scenes providing optimum viewing of selected targets, have been constructed. Other map projections are being evaluated. Selected stereo pairs of varying targets, viewing geometries and resolutions will be on display via LPI's Tektronix stereo monitor for viewing and evaluation.

The Voyager mission plan did not specifically include targeted stereo coverage. As a result, the quality of stereo coverage is uneven. As viewing geometry changed, resulting in stereo capabilities, imaging resolution often changed significantly, as did local sun angle. These effects varied with encounter geometry and satellite characteristics, primarily orbital period. (In contrast, lighting geometry did not change at all between the two Mercury Mariner 10 encounters,

eliminating this problem.) Also, changes in phase angle often resulted in changes in overall brightness of the scene, necessitating cosmetic corrections to produce similar brightness levels in both pair elements. This was achieved using a 301x301 pixel high-pass filter. Inherent topographic relief also affects stereo discriminability. On Callisto and Ganymede, for example, relief rarely exceeds 1.5 km [2]. Therefore, wider stereo divergence was required for relief to be detectable than on satellites such as Miranda were relief sometimes exceeded 5 km [4]. As a result of these factors, selection criteria for most stereo pairs included a minimum 15° angular convergence, and a maximum factor of 2 difference in the resolution between images.

Stereo Height Determination

Methodology to determine local height variations is similar to that employed for terrestrial air photos. Because the scale of satellite topography is significantly less than the flyby distances for Voyager (factoring in angular separation), the formal errors associated with height determinations can be greater than 50%, and in many cases renders the resulting values meaningless. Prominent exceptions include Miranda, Ariel, Rhea, etc., where formal errors (depending on scene location) can be as low as a few percent.

Work in progress

Craters: Many satellites are heavily cratered. Preliminary analysis of stereo pairs has already confirmed earlier measurements of crater depths and peak heights on Rhea, as well as general conclusions that extensive terracing is absent on most of these satellites [1]. Stereoscopic study also confirms the existence of prominently raised rims on icy satellites, which was difficult to demonstrate using photoclinometry [2]. Stereo is also being employed to map the structure detail of large impact features on Ganymede, including several penepalimpsests (e.g., Nidaba), and the multi-ring structures Gilgamesh and Valhalla and the W. Equatorial Basin. Using the extensive stereo coverage of Rhea, we are also mapping the putative multi-ring structures reported on that satellite [9].

Tectonics and volcanism: On many of the satellites, volcanism and tectonism has deformed the surface. Stereo is being used to map and investigate the topography of graben and other geologic structures. It has already been useful in mapping Miranda's coronae [6]. Stereo is also being used to investigate the geology and structure of volcanic vents on Io, both active (circa 1979) and inactive. Because of complex albedo patterns, stereo is the only means of mapping local topographic relationships on Io (although coverage is spotty). Haemus Mons and other prominent Ionian mountains are also stereo candidates. Stereo mapping of the outer solar system will open new avenues of investigation and enhance our understanding of geologic processes in these diverse, complex bodies.

[1] Schenk, P., *J. Geophys. Res.*, 94, 3813, 1989. [2] Schenk, P., *J. Geophys. Res.*, 96, 15635, 1991. [3] Jankowski, D., & S. Squyres, *Science*, 241, 1322, 1988. [4] Thomas, P.C., *Icarus*, 73, 427, 1988. [5] Wu, S., et al., *Lunar Planet Sci. XVIII*, 1110, 1987. [6] Croft, S., & L. Soderblom, in *Uranus*, Univ. Arizona Press, p. 561, 1991. [7] Schenk, P., & M.P.A. Jackson, *Geology*, in press, 1993; this volume. [8] Schenk, P., *NASA TM-86247*, 1984. [9] Moore, J., et al., *J. Geophys. Res.*, 90, suppl., C785, 1985.

S105-90
ABS. ONLY

N94-20741

Iridium in sediments containing large abundances of Australasian microtektites from DSDP hole 758B in the Eastern Indian Ocean and from DSDP hole 769A in the Sulu Sea. Gerhard Schmidt, Lei Zhou and John T. Wasson, Institute of Geophysics and Planetary Physics, University of California, Los Angeles, CA 90024, USA.

Excess Ir found in sediments at the Cretaceous/Tertiary (K/T) boundary and in other (e. g., Pliocene) sediments from deep sea drilling cores is widely interpreted as evidence of major impact events [1,2]. The Australasian tektites originated in an impact event ~0.77 Ma ago; microtektites have been found in deep-sea sediment cores from throughout the Indian Ocean, the Philippine Sea, and western Pacific Ocean, but Ir has not been previously reported in these horizons. The deep-sea record of tektites is of particular interest, because in contrast to most continental occurrences, the stratigraphy preserves the original depositional position. Recently several cores having exceptionally high contents of Australasian microtektites have been investigated, Glass and Wu [3] found shocked quartz associated with the microtektites. We used neutron activation to determine concentrations of Ir and other elements in two cores bearing microtektites [4,5], one from Deep Sea Drilling Project (DSDP) hole 758B in the Eastern Indian Ocean and one from DSDP hole 769A in the Sulu Sea (near Mindanao, Philippines). The sedimentation age for the microtektite layers in core 758B lies between 0.73-0.78 Ma [6] and agrees well with the mean laser-fusion $^{40}Ar/^{39}Ar$ age of Australasian tektites of 0.77±0.02 Ma by Izett et al. [7]. We are able to resolve a small positive Ir enhancement in 758B. Core 769A shows too much scatter to allow resolution of an Ir peak.

The dominant lithology of core 758B consists of alternating layers of light nannofossil ooze with clay and foraminifers and layers of dark clayey nannofossil ooze with foraminifers; three discrete ash layers with volcanic glass, record explosive volcanism in the northeastern Indian Ocean [8]. The dominant lithology of Site 769A consists of thin- to thick-bedded nannofossil marl with foraminifers and foraminiferal nannofossil marl. Minor thin beds of volcanic ash and turbidites of foraminiferal ooze are also present within the unit. The marl contains clay, abundant nannofossils and planktonic foraminifers, scattered benthic foraminifers, volcanic glass, and varying amounts of siliceous biogenic material [9]. These cores have high sedimentation rates, as required to reduce the background level of Ir due to cosmic dust. The linear sedimentation rate for the investigated interval in core 758B is 1.1 cm ka^{-1} [10] and in core 769A 11 cm ka^{-1} [3], much higher than a typical sedimentation rate of 0.03 cm ka^{-1} in central North Pacific cores [11].

Our standard sample size was 1 cm^3 of wet sediment. We analyzed 27 samples from depths of 9.6-12.4 meters below the sea floor (mbsf) from 758B and 23 samples at 60.6-65.4 mbsf from 769A . In the Eastern Indian Ocean core 758B our chemical analyses show small (factor of 3) enrichments in the Ir-content of the pelagic clay layer containing the microtektites. On the basis of a dry sediment bulk density of 0.77 g cm^{-3} [10], we calculate a net Ir fluence of 1.9 ng cm^{-2} over the interval from 10.4 to 11.4 m depth based on an estimated background level of 0.100 ng/g Ir. For comparison, the Ir fluence in the K/T boundary is ~70 ng cm^{-2}, 37 times higher. In the Sulu Sea core a small Ir peak was associated with the microtektites but other Ir enhancements were also present, seemingly associated with layers of volcanic ash.

Acknowledgements. This work was partially supported by NSF grant EAR 91-19065. Additional fellowship support for Gerhard Schmidt was provided from NATO.

References: [1] Alvarez L. W. et al. (1980) Science, 208, 1095-1108. [2] Kyte F. T. et al. (1980) Nature, 288, 651-656. [3] Glass B. and Wu J. (1992) LPSC XXIII, 415-416. [4] Schneider D. A. et al. (1992) EPSL 111, 395-405. [5] Smit J. et al. (1991) Proc. ODP, Sci. Res., 121, 489-503. [6] Farrell J. W. and Janecek T. R. (1991) Proc. ODP, Sci. Res., 121, 297-355. [7] Izett G. A. and Obradovich J. D. (1992) LPSC XXIII, 593. [8] Dehn J. et al. (1991) Proc. ODP, Sci. Results, 121, 273-295. [9] Desprairies A. et al. (1991) Proc. ODP, Sci. Results, 124, 489-503. [10] Leg 121 Shipboard Scientific Party, Site 758 (1989) Initial Rep. DSDP, 121, 359-453. [11] Kyte F. T. and J. T. Wasson (1986) Science, 232, 1225-1229.

PRESSURE VERSUS DRAG EFFECTS ON CRATER SIZE

R. M. Schmidt, Boeing Defense and Space Group, M/S 87-60, Seattle WA 98124

The topic of atmospheric effects on crater formation is very complex because it includes not only pressure effects on excavation, but also drag effects on ejecta placement. Experiments have to be designed very carefully to allow isolation of the two phenomena. Historically, numerous investigators (Johnson *et al.*, 1969; Herr, 1971; Schultz and Gault, 1979; Holsapple, 1980; and Schultz, 1992) have shown an influence of atmospheric pressure. However none have identified the scaling that correctly isolates pressure from drag effects. On-going work (Housen and Schmidt, 1990; Housen,*et al.*, 1992; and Schmidt *et al., 1992)* in explosive cratering has produced scaling paradigms for deeply buried explosive charges where drag effects are negligible. Here it was found that increased pressure caused significant induced strength effects that impeded crater excavation. The effect is more pronounced with increasing burial depth and less pronounced with increased yield.

In the case of impact cratering, equivalent burst depth tends to be small, and atmospheric effects are expected to be primarily drag induced. Figure 1 is a plot of gravity scaled cratering efficiency versus atmospheric pressure, divided by lithostatic pressure for one impactor radius, for Flintshot sand with relatively large grain size, on the order of 500µ. Here we calculate negligible drag effect and attribute the decrease in cratering efficiency to pressure domination. However note the pressure exponent is quite small, on the order of 0.040 with a standard deviation of 0.007. The value for the gravity exponent alpha from this same regression is 0.49. Also shown are three tangent-below explosion data points which also agree with the weak pressure dependence seen for impact.

The data points denoted by the letter "s" are from Schultz (1992). These are variable pressure impacts fired into his S1 sand (no. 140-200). Note the strong departure from the regression based upon the Flintshot data points. This is suspected to be strength or cohesion domination, since he used five different gases with various densities to demonstrate absence of drag effects. To confirm this supposition, two impacts were made into a comparable sand, F-140. One at 1G that can be seen right in with the Schultz data as expected (see shaded "star" symbol). The second was launched at 500G to eliminate strength and as can be seen lies right on the regression curve to the gravity data. Small-scale 1G experiments are almost always fraught with undesired strength effects.

Since firing projectiles into a high pressure atmosphere is difficult, if not impossible, shallow buried explosive experiments were designed to explore the pressure-drag regime applicable to impact cratering. These experiments incorporated a pressure/vacuum chamber mounted on a centrifuge that allows independent variations in gravity and pressure. Drag was varied by using different sand grain sizes and different gases as suggested by Schultz (1992). This allowed experiments to be conducted at fixed scaled drag or at fixed scaled pressure. The tests have to be conducted at high gravity to eliminate or minimize material strength effects. Figure 2 is a contour plot of crater size versus scaled drag and scaled pressure. As can be seen crater size diminishes in the direction of the upper right hand of the plot. Reading the symbol, this contour is on the order of a 1km impactor on Venus with a block size of 1 meter. This trend agrees with observations by Phillips *et al.* (1990) reporting no craters smaller than 3 km dia.

Herr, R. W. (1971) Effects of atmospheric-lithostatic pressure ratio on explosive craters, *NASA TR-R-366*.

Holsapple, K. A. (1980) Equivalent depth of burst for impact cratering, *Proc. LPSC 11th*, 2379-2401.

Holsapple K. A. and Schmidt R. M. (1987) Coupling parameters in cratering mechanics, *J. Geophys. Res.* 92(B7), 6350.

Housen, K.R. and R.M. Schmidt, (1990)Atm pressure effects on craters from deeply buried explosives, *EOS*, 71, 6, 258.

Housen, K. R *et al.*, (1992) D. O. B. scaling and critical depth of burst for cratering, *DNA-TR-92-24*.

Johnson, S. W. *et al.*, (1969) Gravity and atm pressure effects on crater formation in sand, *J. Geophys. Res.*, **74**, 4838.

Phillips, R. J. *et al.*, (1991) Impact craters on Venus: Initial analysis from Magellan, Science, 252, No. 5003, 288.

Schmidt, R. M .*et al.*, (1992) Pressure/strength effects in cratering. *EOS*, 73, 43, 324.

Schmidt, R. M. (1992) Experiments to investigate atmospheric effects on crater size, *Lunar Planet. Sci. XXIII*, 1221-1222.

Schultz, P. H. and D.E. Gault (1979) Atmospheric effects on Martian ejecta emplacement, *J. Geophys. Res.*, **84**, 7669.

Schultz, P. H. (1992) Atmospheric effects on cratering efficiency, *J. Geophys. Res.*, **97**, E1 975-1005.

PRESSURE VERSUS DRAG EFFECTS ON CRATER SIZE: Schmidt, R. M., Boeing Co.

Fig. 1. Regression to Ottawa Flintshot data to get pressure effects

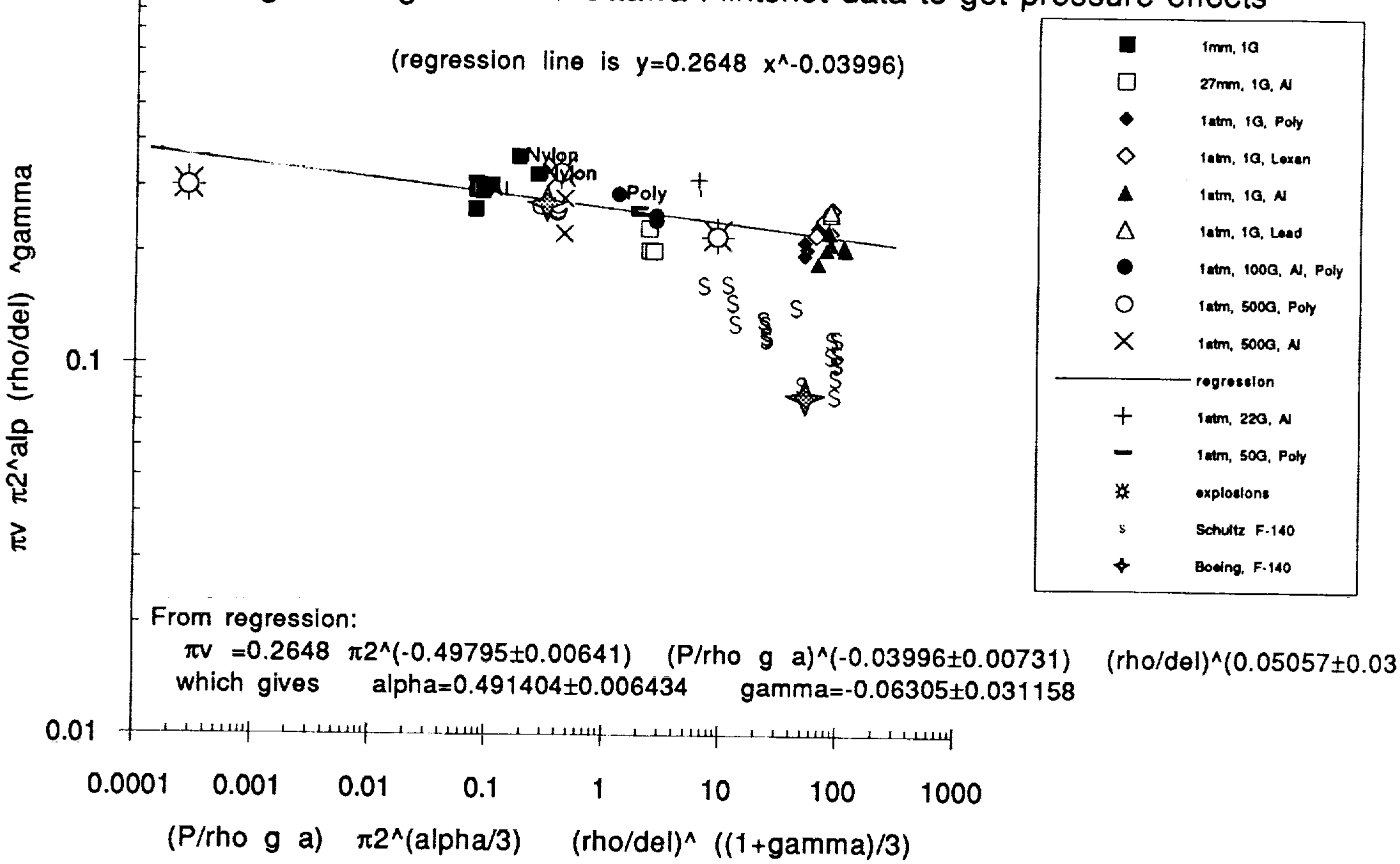
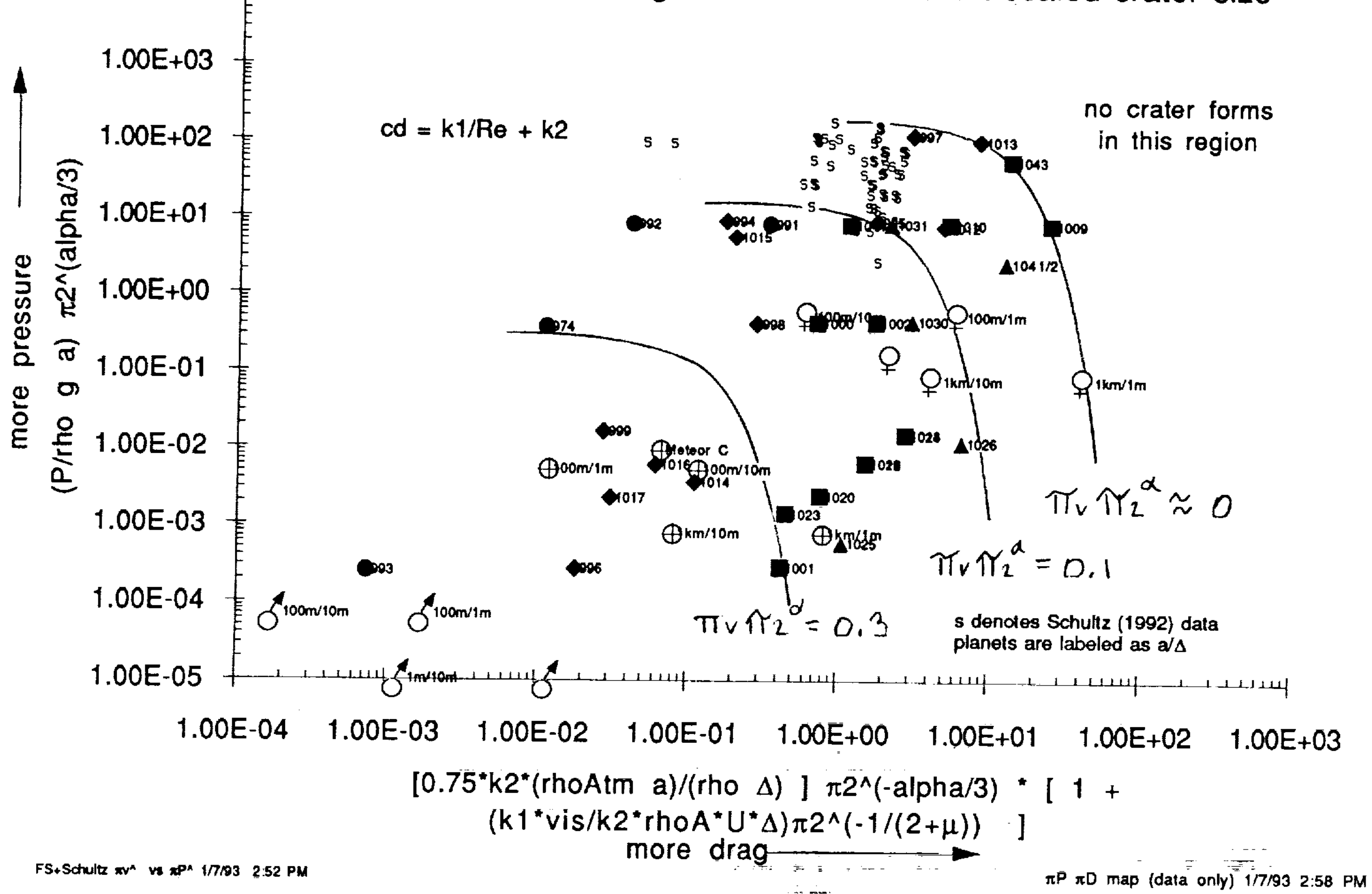


Fig. 2. Plot showing contours of constant scaled crater size



S107-91
ABS ONLY N94-20743
P-2

Searching for Ancient Venus. Peter H. Schultz, Department of Geological Sciences, Brown University, Providence, RI 02912.

The cratering record on Venus provides one of the few available remote chronometers for establishing relative age. Because the dense atmosphere shields the surface from smaller impactors, the most statistically significant fraction of the cratering record is incomplete at best and indeterminate at worst. Larger craters represent survivors of entry but occur too infrequently for delineating statistically significant ages on a local scale (1). This contribution reconsiders processes affecting the statistical cratering record and argues that the globally averaged age approaches 2-3*by* with isolated relict surfaces dating back to 3-4*by*.

Global Crater Production Curves: The cumulative power-law function for the global cratering record on Venus exhibits a segment that resembles, at first glance, a crater production curve (1). Consequently, initial studies often assume that a direct comparison can be made, after adjustments for flux and scaling differences. The statistically significant portion of the global cratering curve, however, represents a very narrow window (factor of two in size from 50km to 100km) limited at small sizes by atmospheric shielding effects and loss processes. Uncertain regional geologic histories (2), visible effects of enhanced crater enlargement for craters larger than 100km (3), and statistical uncertainty of small numbers lessen the confidence at large sizes. This narrow range of diameters may yield a production-like slope, but its slope may have little significance. The Apollo 17 site on the Moon also exhibited a production-like slope and indicated that this site would provide some of the youngest basalt samples (4), yet the returned sample ages were among the oldest (5). Enhanced degradation of small craters in a thick particulate surface layer and an insufficient counting area at large sizes accounted for this incorrect estimate (6,7). Yet, the correct relative age could have been easily predicted from simple embayment relations with adjacent maria, thereby underscoring the importance of understanding the local geologic context, stratigraphy, and operative processes - - as well as statistical significance.

Although the tangent of the Venus global curve with a lunar calibration curve can yield a minimum average age, such an approach implicitly assumes that the relative impactor flux and crater scaling relations are reasonably well understood. But the dense atmosphere of Venus introduces significant scaling effects by changing the shape (8) and effective density (9) of the impactor and by arresting lateral crater growth (3). Laboratory experiments clearly demonstrate that crater diameter is largely controlled by impactor size, while at a given velocity depth can be controlled somewhat independently by impactor density for a given target (9). If no other processes operate, an aerodynamically flattened impactor (8) will increase crater diameter for a given mass striking a gravity-controlled particulate target, whereas an aerodynamically streamlined impactor (3,10) will decrease crater diameter. In natural materials with strength, however, gravity-controlled growth requires shock-preconditioning the target into a near-strengthless medium. If impactor velocity has been reduced significantly (6km/s), gravity scaling laws become inappropriate.

Laboratory experiments also reveal that a dense atmosphere introduces both static and dynamic pressure effects (3,11). Even though the total excavated crater mass greatly exceeds the displaced atmospheric mass, crater ejecta leave the cavity within a relatively thin wall (i.e., curtain), thereby substantially decreasing the mass per unit area at any given time (3). At laboratory scales, dynamic pressure effects can reduce cratering efficiency by an order of magnitude (3). Dynamic forces acting to retard outward advance of the base of the curtain are transmitted hydrostatically to the cratering flow field. This can be illustrated experimentally by using a plate positioned just above the surface with a hole to allow passage of the impactor. Ejecta striking the plate spray outwards without returning to the cavity, but interactions with the plate reduce cratering efficiency similar to observed atmospheric effects. Because craters grow non-proportionally (i.e., continuously changes shape by first growing downward, then outward), atmospheric dynamic pressure prematurely arrests lateral growth as shown in Figure 1. The process of arrested lateral growth can be modeled analytically as a cylinder expanding with a constant velocity and constant thickness (3) or numerically using variable thickness and decreasing velocity once subsonic (12), both approaches being consistent with experimental results. Scaling to Venus can be justified since outward crater growth is subsonic for most of the latter stages of crater growth and since atmospheric blast effects appear to be offset from crater excavation (3). This approach reveals that excavation craters on Venus could be reduced by as much as a factor of two. This process is consistent with observations of more pronounced rim heights and greater depths than expected(1,13), particularly once empirically adjusted for gravity (14). If correct, the minimum average age from the global crater inventory approaches 2-3 *by*, in contrast with previous estimates of 0.5-1.5*by* (1).

Crater Preservation States: Craters on Venus seem to be in remarkably similar states of preservation (1). This observation has been used to argue that catastrophic global resurfacing has reset the cratering chronometer(15) or that the surface preserves a record of catastrophic bombardment (16). But similar preservation states of radar-bright ejecta facies may not indicate a common maximum age but resistance to weathering and or very weak erosional processes in order to produce the obvious range of expected morphologies found on the other planets.

Searching for Ancient Venus. Peter H. Schultz

The formation of an impact crater in an atmosphere must generate an intense atmospheric response due to the outward kinematic interactions with the ejecta curtain and containment of the vapor cloud (3,11). As a result, emplacement of the inner ejecta will be accompanied by intense winds and vortices with velocities (100m/s - 400m/s) sufficient to winnow and entrain smaller (<meter scale) ejecta, leaving behind a blocky lag surface for the inner facies and creating turbidite-like, run-out flow of smaller (radar-dark) materials. If winds are the primary erosional agent on Venus, then the inner facies will be archived unless winds of comparable magnitude occur again while the outer deposits provide Venus with a local reservoir of particulates

Impact-generated wind storms may represent one of the principal erosional agents on Venus. Such storms can be inferred from laboratory experiments and from the geologic record (3,17). For example, radar-bright and -dark wind streaks associated with the crater Carson are interpreted as the consequence of upper level winds deflected by the expanding, impact-generated, vapor cloud (3). Equally important, however, is the radar-bright, lineated zone extending westward from Carson and eroding ejecta and run-out flow deposits of the crater Aglaonice (600km away from Carson). This scour zone is interpreted as the trail of the late-stage thermal disturbance initially created by Carson but subsequently dragged westward by the strong winds aloft. Other craters with a wide range of preserved facies exhibit evidence for similar impact-generated windstorms (3,17). The widespread occurrence of other wind streaks could represent more gentle, less intense circulation patterns (18,19) or the final stages of impact-generated disturbances far from the source. Conversely, the absence of similar effects around all craters underscores a true continuum of degradational states, in contrast with the perception of a catastrophic flux.

Identifying Ancient Terrains: Relict ancient terrains on Venus should be characterized by the following features: spatial clustering of relatively large craters with different impact trajectories in a common geologic/tectonic setting; evidence for a wide range of preservation states of the outer radar-dark facies; mantling of crater interiors by radar-dark materials; and occurrence in a radar-dark regional setting. The last characteristic should result from the long-term accumulation of smaller size impact debris and accretion of failed entries (estimated to contribute about 1-10m over the last 3*by*), and perhaps pyroclastics. The general absence or poorly expressed craterless radar-bright blast haloes (indicative of a thinly veneered regolith) should be another consequence of this long-term depositional history. With these criteria, the "Crater Farm" and a region near Atla Regio are proposed to represent islands in time dating back to at least 3*by*. These regions are intermediate in elevations (i.e., have not been low-lying depositional traps) and are notably deficient in volcanic centers (20,21). The dramatic contrast between this surface and our perception of ancient terrains from other planets simply reflects the long-lived atmospheric shield on Venus, her depositional (rather than erosional) history of its ancient surfaces, and perhaps the relative inefficiency of cratering under the dense atmosphere.

1. Phillips, R.J. *et al.* (1991) *Science 252*, 288-296. 2. Saunders, R.J. *et al.* (1991) Science 252, 249-251. 3. Schultz, Ph.H. (1992) *J. Geophys. Res. 97*, E10, 16, 183-16, 248. 4. Scott, D.H. *et al.* (1972) *U.S. G. S. Misc. Geol. Inv. Map*, I-800. 5. Taylor, S.R. (1982) *Planetary Science: A Lunar Perspective*, Lunar and Planet. Sci. Institute. 6. Lucchitta, B.K. and Sanchez, A.G. (1975) *Proc. Lunar. Planet. Sci. 6th*, 2427-2441. 7. Schultz, Ph.H. *et al.* (1977) *Proc. Lunar Planet. Sci. 8th*, 3539-3564. 8. Melosh, H.J. (1981) *In Multi-Ring Basins*, pp. 29-35, Pergamon, New York. 9. Schultz, P.H. and Gault, D.E. (1985) *J. Geophys. Res. 90*, 3701-3732. 10. Ivanov, B.A. *et al.* (1992) *J. Geophys. Res. 92*, No. E10, 16,167-16,181. 11. Schultz, P.H. (1992) *J. Geophys. Res. 97*, 975,1006. 12. Schultz, P.H. (1990) *Int. J. Impact. Engin* (in press). 13. Basilevsky, S. and Ivanov, B.A. (1990) *Geophys. Res. Letts.*, 175-178 14. Herrick, R. (1992) Analysis of the Impact Cratering Record on Venus (PhD Thesis), Southern Methodist University, Dallas. 15. Schaber, G.G. *et al.* (1992) *J. Geophys. Res. 97*, E8, 13,257-13,301. 16. Bills, B. (1992) Lunar and Planet. Sci. XXIII, 99-100. 17. Schultz, P.H. (1992) *Int. Colloq. in Venus*, LPI Contrib. No. 789, 104-106. 18. Arvidson, R. *et al.* (1991) *Science 252*, 270-275. 19. Greeley R., *et al.* (1992) *J. Geophys. Res. 92*, 13,319-13,346. 20. Crumpler, L. *et al.* (1992) *Int. Colloq. in Venus*, LPI Tech. Contrib. 789, p. 25. 21. Head, J.W. *et al.* (1992) *J. Geophys. Res. 97*, No.E8, 13, 153-13, 197.

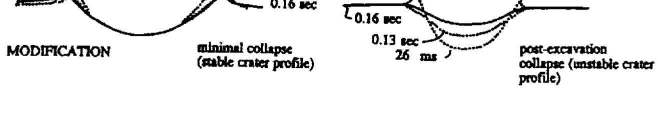


Fig 1. Atmospheric effects on crater growth from quarter space laboratory impact experiments. Atmosphere retards outward growth of curtain because it behaves as an impermeable plate. Craters in non-cohesive sand form a deep bowl-shaped transient cavity resembling an early stage of growth in a vacuum (left). The transient profile collapses in sand (bottom right) but is preserved in compacted pumice (3,17).

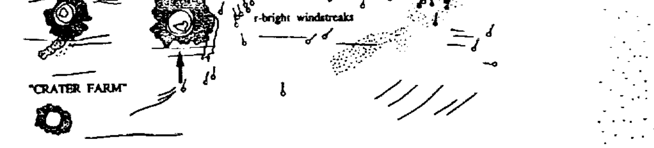


Fig. 2 Effect of impact-generated windstorm created by formation of the crater Carson (middle right). Downrange fireball is carried westward by winds aloft creating a radar-brightened surface (stipple) and scouring ejecta deposits of Aglaonice. Radar-bright winds streaks, scour zones, and radar-dark streaks represent superposition of gradually decreasing winds through time. Different impact directions (arrows) and angles indicate separate impact events. This area is proposed to be an ancient relict of Venus.

S108-46
ABS. ONLY
N94-20744

Impactor Control of Central Peak and Peak-Ring Formation. Peter H. Schultz, Department of Geological Sciences, Brown University, Providence, RI 02912.. D.E. Gault, Murphys Center of Planetology, Murphys, CA

Introduction: The relation between the depth and diameter of excavation for impacts typically is assumed to be proportional. Such an assumption is consistent with the constant aspect ratio (diameter: depth) observed for simple craters found in a wide range of planetary settings (1,2) and crater-scaling laws derived from laboratory experiments (e.g., 3,4). Although complex craters exhibit evidence for floor uplift and rim collapse of a transient profile, they are typically thought to resemble initially smaller, simple crater (5,6). At large scales, however, early-time processes consume a greater fraction of crater growth (7) and the assumption of late-time equivalence of energy release as a point source becomes inappropriate. We propose instead that crater diameter, depth, and impactor penetration represent separable dependent variables that underscore the fundamental difference between impact and point-source explosion excavation process. An important consequence of this perspective is that central pits, peaks, and rings may represent contrasting target responses to impactor penetration and could provide an important indicator of impactor dimensions..

Declaration of Independence: Crater aspect ratios from laboratory experiments are not constant, whether in gravity-controlled particulate targets (9,10) or non-porous strength-controlled targets (11). Three simple experiments dramatize how lateral crater growth (diameter) can be independent of penetration (depth). First, a 0.635 cm-thick aluminum plate was buried at different depths in a No. 24 sand target and impacted with a 0.635 cm-polyetheline sphere at 2km/s in a vacuum. If lateral growth reflects the total energy coupled to the particulate target, crater diameter should increase as the burial depth of the plate decreases. Instead, crater diameter (normalized to impactor size) remains nearly constant until the burial depth approaches 2 projectile diameters when crater diameter decreases. Hence crater diameter is simply controlled by the energy coupled at first contact and shock rarefaction from the free surface (8).

A second experimental series impacted a ridged particulate target obliquely. Ridges with faces comparable in size to the impactor were oriented perpendicular to the trajectory. An oblique impact (30°) into a smooth surface produces a crater with diameter scaling as $(v^2 \sin^2\theta/rg)^{2/3}$, whereas an oblique impact into the ridged surface is largely independent of angle. This result again underscores the importance of both the energy coupled at first contact and the fate of impactor ricochet.

A third series examined the parameters controlling the size and formation of "penetration pits" in solid, ductile targets by hypervelocity impactors. Penetration pits represent an inflection in crater profile correlated with a distinct transition between lateral and downward flow. Penetration depth (p) is often cited as crater depth and can be expressed as $(p/L)(\delta t/\delta p)^{1/3} \sim (\delta_p v^2/Y_t)^{\beta/3}$ where L indicates impactor length, δ the density for target (t) or projectile (p), and Y_t target strength (12). The diameter of the pit (x_o) depends simply on impactor diameter (2r), target/impactor density ratio ($\delta t/\delta p$), impactor velocity (v) and target sound speed (c_t) as shown in Fig. 1:

$$(x_o/2r)(\delta_t/\delta_p)^{1/3} \sim (v/c)^{\mu}$$

where μ is an exponent characterizing the pressure-decay law as derived in (13) and discussed further in (14). If $v\sin\theta > c_p$, experiments reveal that the dimensions of x_o (perpendicular to the trajectory) do not depend on impact angle in contrast with earlier conclusions (15). Comparisons with numerical codes (16,17) reveal that x_o corresponds approximately to the diameter of the deformed impactor when the shock detaches laterally. Such experiments reveal that the diameter of the penetration zone depends simply on impactor diameter for a given mach number (i.e., independent of target strength in contrast with diameter or depth). Consequently, pit diameter relative to crater diameter increases as impact angle decreases.

These three experiments reveal that crater diameter, depth, and penetration exhibit separable dependences. Moreover, resisting forces acting on crater diameter (strength or gravity) can act independently of maximum penetration depth. This is further illustrated by three other studies. First, dynamic atmospheric pressure can restrict lateral crater growth in particulate targets without affecting crater depth (18,19). Second, impacts by low-density debris clouds into particulate targets produce craters with diameters following scaling laws for high-density, solid impactors but depths controlled by impactor density (10). Third, experiments involving gravity-controlled particulate and strength-controlled ductile targets reveal a systematic effect of impactor penetration time on diameter/depth for hypervelocity impacts (11).

Impactor Control: Schultz P.H. and Gault, D.E.

Discussion and Implications: For small hypervelocity impactors at laboratory scales, the transfer time of energy/momentum from impactor to target (10μs) is a small fraction of the time for crater formation (10-100ms). As a result, late-stage growth can consume signatures of penetration and produce a simple crater with a nearly constant aspect ratio. Such a profile is not diagnostic of strength-controlled growth but only the validity of the point-source approximation. As the time for energy/momentum transfer comprises an increasing significant fraction of growth at large scales, the penetration phase becomes more evident and persists to later times. This phenomenon is also documented in computational experiments as an inflection in the growing crater profile but is often masked by allowing late-stage growth to "coast" to a more symmetrical form (17). Survival of the zone of maximum penetration depends on material properties and its size relative to the impactor. Large, low velocity impactors (>6km/s) produce a compressed penetration zone only slightly larger than the projectile, whereas very high velocity objects produce a much larger zone relative to the projectile. If the over-all limit of this zone follows the simple experimental relation where $x_o \sim r(v/c)^{\mu}$, as indicated above, then target response may not affect dimensions significantly but could affect the morphology. It is proposed that central pits, peak pits, peaks, and peak rings are contrasting manifestations of this common zone.

Three simple tests at planetary scales are consistent with this suggestion. First, central peak or peak ring diameter normalized to an impactor diameter calculated from scaling relations should remain approximately constant for a given impact angle over a limited range of crater diameters. Second, crater size normalized to observed peak ring diameter should decrease with decreasing impact angle. Third, craters formed by oblique impacts (<20°) should exhibit central peaks offset uprange corresponding to point of maximum coupling and breaching downrange due to impactor failure and ricochet. All three tests have been successfully tested for Venus where the preserved cratering record allows recognizing impact angle but also can be documented on the Moon and Mercury (14).

If the diameter of central relief features in craters simply depends on $(v/c)^{\mu}(\delta p/\delta t)$, then existing crater scaling relations can be recast in terms of an observable quantity with best guesses for average impact velocity, target sound velocity, and density ratio for different planets with different gravitational fields (Fig. 2). Such a strategy reveals that a.) normalized crater diameter approximately scales as $\pi_2^{-1/6}$ consistent with expectations; b.) central peaks and peak rings for different planets collapse into a single relation for reasonable values of impactor velocity and target properties (excluding highly oblique impacts and multi-ring basins); c.) peaks and peak rings for a given planet are part of progression; d.) the onset diameter for peaks and peak rings for different planets depends on both target (g) and impactor (r/v) properties; and e.) the ubiquitous occurrence of central pits on Mars are consistent with lower velocity impactors (<14 km/s) comprising 2/3 of its population.

1. Pike, R.J. (1980) U.S. Geol. Survey Prof. Paper 1046-C. 2. Cintala, M.J. *et al.* (1971) Proc. Lunar and Planet. Sci. 8, 3409-3425. 3. Schmidt, R.M and Holsapple, K. (1982) *In Geol. Soc. Amer. Sp. Pub. 190*). 4. Schmidt, R.M. and Housen, K. A. (1987) *Int. J. Impact Engin.*, *5*, 543-560. 5. Grieve *et al.* (1977) In *Impact and Explosion Cratering* (D.J. Roddy *et al.*, eds), pp. 791-814, Pergamon, New York. 6. Melosh, H.J. (1982) *J. Geophys. Res. 87*, 371-380. 7. Schultz, P.H. *et al.* (1991) In *Multi-ring Basins*, pp. 181-195, Pergamon, NY. 8. Holsapple, K.A. and Schmidt, R.M. (1987) *J. Geophys. Res. 92*, 6350-6376. 9. Schultz, P.H. and Gault, D.E. (1985) *Lunar and Planet. Sci. XVI*, 742-743. 10. Schultz, P.H. and Gault, D.E. (1985) *J. Geophys. Res. 90*, 3701-3732. 11. Schultz, P.H. (1988) In *Mercury* (F. Vilas *et al.* , eds), pp. 274-335, U. Arizona Press, Tucson. 12. Herrmann, W. and Wilbeck, J. S. (1987) *Int. Jour. Impact. Engin.*, 5, 307-322. 13. Holsapple, K. (1987) Int. Jour. Impact *Engin. 5*, 343-356. 14. Schultz, P.H. (1992) *J. Geophys. Res. 97*, E10, 16,183-16,249. 15. Schultz, P.H. and Gault, D.E. (1992) *Int. Conf. on Large Meteorite Impacts and Planet. Eval.*, LPI Contrib. No. 790, 64-65 16. Roddy, D.J. *et al.* (1980) *Proc. Lunar Planet. Sci. Conf. 11th*, 2275-2308. 17. Orphal, *et al.* (1980), *Proc. Lunar. Planet. Sci. 11th*, 2309-2323. 18. Schultz, P.H. (1992) *J. Geophys. Res. 97*, 975-1005. 19. Schultz, P.H. (1993) *Int. Jour. Impact Engin.* (in press).

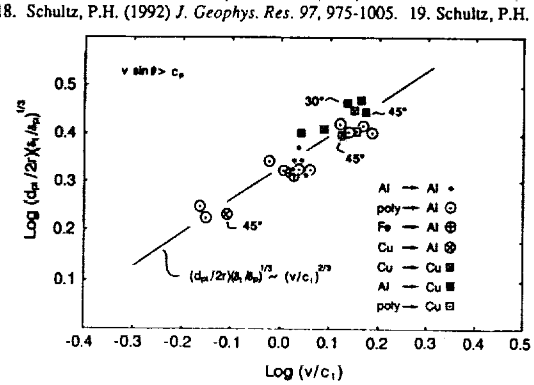


Fig. 1 Central penetration pit (dpt) normalized to impactor (2r) diameter produced by impacts into solid aluminum (Al) and copper (Cu) targets as a function of mach number (v/ct) in the target. Pit diameter is independent of impact angle provided that the vertical velocity component is greater than the sound speed of the impactor. Hence, size of the penetration zone may provide an indicator of the impactor dimensions.

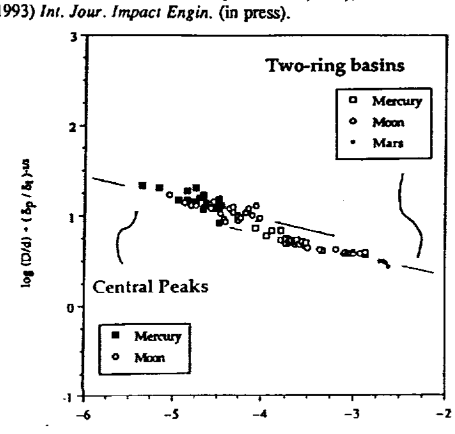


Fig. 2 Crater diameter (D) normalized to estimated impactor diameter (d) as a function of the gravity-sealing parameter $\pi_2 = gr/v^2$. Impactor diameter is based on the assumption that the central peak and peak-ring diameters represent contrasting target responses to impactor penetration zone. For central peaks, assumed impact velocities are 16 km/s and 40 km/s for the Moon and Mercury, respectively; for peak rings, impact velocities are 14, 16 and 32 km/s for Mars, Moon, and Mercury, respectively. Vertical offset of peaks and peak rings probably indicate additional processes, e.g., collapse.

Further Analyses of Rio Cuarto Impact Glass. Peter H. Schultz[1], T.E. Bunch[2], C. Koeberl[3], and W. Collins[1], [1]Department of Geological Sciences, Brown University, Providence, RI 02912; [2]Space Sciences Division, NASA-AMES, Moffett Field, CA 94035; [3]Inst. Geochemistry, U. Vienna, A-1010 Vienna, Austria

Initial analyses of the geologic setting (1,2,3), petrology (4), and geochemistry (5) of glasses recovered from within and around the elongate Rio Cuarto (RC) craters in Argentina focused on selected samples in order to document the general similarity with impactites around other terrestrial impact craters and to establish their origin. Continued analysis has surveyed the diversity in compositions for a range of samples, examined further evidence for temperature and pressure history, and compared the results with experimentally fused loess from oblique hypervelocity impacts. These new results not only firmly establish their impact origin but provide new insight on the impact process.

Variety in Glass Compositions: Results of electron microprobe analyses of impactites from five different locations are shown in Figure 1a. The various oxides are referenced to averaged values for clear interstitial glass within bulk loess which has been heated to 1168°C for 30 minutes (at one atmosphere) and quickly quenched (FL-1168). Loess heated to 939°C for 3 hours failed to fuse the sample, whereas a sample heated to 1335°C for 3 hours produced a clear glass with only a few remaining large quartz and small zircon grains left undigested (FL-1335). As shown in Figure 1a, compositions of vesicle-poor, drop-shaped green impactites (VPD) most closely resembled loess fused at higher temperatures (FL-1335). Because of the long melting times, no inferences about the temperature history of RC impactites can be made directly. However, the experiments show that higher temperatures tend to deplete MgO relative to FL-1168 as observed in the homogeneous impactite samples. Other samples show even greater relative depletion of MgO with additional losses of FeO, MnO and CaO, while Figure 1b illustrates the range of oxide compositions for glasses within a single sample. In addition to the relative CaO loss exhibited by the dense, black glass matrix, relative CaO enhancement is observed in glass comprising an outer red zone. Such chemical variations may reflect dilution of bulk loess by quartz (5) or selective melting of certain mineral phases while leaving others undigested.

An earlier report described some characteristics of low to medium grade impact-formed Rio Cuarto impactites (4). Here we report shock features consistent with higher grade (>50 Gpa) impactites. Heterogeneously melted samples (≈2-6 cm) that show prominent flow lines similar to those in some tektites have shock features that range from reduced birefringence and planar elements in quartz and feldspars (<40 Gpa; ref 6) to the presence of mono- and polymineralic glasses, decomposition of zircon to baddeleyite + SiO_2 and magnetite to quenched melts, diaplectic phases and vesicular, shock-formed fusion, among others. These indicators suggest pressures > 50 Gpa for formation(6). The presence of such a wide range of P-T conditions in small samples is probably due to the very strong P-T heterogeneities characteristic of rocks as porous as loess (7) and the application of mechanical shear heating as well as shock heating from oblique impacts (8). Rapid quenching, however, is necessary in order to preserve observed heterogeneities, flow patterns (Schlieren), immiscible blebs, and minimal reaction rims. Such melt histories of the RC glasses are typical of glasses produced by impacts, rather than other natural phenomena (e.g., 6,).

Experimental Impactites: Hypervelocity impacts into bulk loess were performed with the NASA Ames Vertical Gun Range (AVGR) for comparison with the Rio Cuarto glasses. The experiments used 0.635cm aluminum and pyrex spheres impacting at 5.5km/s with an angle of 15°. Five types of impact glasses were recovered: striated (sheared) yellow glass, tubular clear glass, blocky yellow glass, vesiculated glass, and microspheres (both hollow and solid). The oxide compositions of the first three types of impact glasses are shown in Figure 2a, again normalized to FL-1168. The last two could not be analyzed because of the thin (<10μ) membrane walls, but energy dispersive spectra confirmed their loess provenance. Figure 2a reveals that the striated and tubular glasses were essentially identical with the exception of MnO, but they differed significantly from the blocky lithified loess glass. The latter sample may have contained contamination from the aluminum impactor or polishing material. When the possible TiO_2 and Al_2O_3 enhancements are removed (with corrections to the totals), the blocky yellow glass oxide distribution resembled the Rio Cuarto impactites (Fig. 1a). The sheared/tubular glasses, however, exhibited an oxide distribution closely resembling the reddish zone of the impactite in Figure 1b, except they also exhibited a pronounced depletion in the abundances more volatile oxides, Na_2O and K_2O.

Rio Cuarto Impact Glass. Schultz, *et al.*

Discussion: The oxide distributions exhibited by the experimentally impacted loess generally correspond to those observed in the Rio Cuarto glasses except that the experimental glasses are more depleted in the highly volatile fractions (Na2O and K2O). This difference may reflect replenishment of this fraction by resorbed K-feldspars, a significant component of the Argentine loess (9), or the small size of the experimental impact glasses which allows greater volatile loss. These alternatives are consistent with the oxide distribution along a seam in an RC impactite that widens into a cavity containing free loess. While the average clear glass matches the distributions in Figure 1a with elevated K2O and depleted CaO, the fused portion of the seam matches the distribution in Figure 2a.

Impactites subjected to higher pressure and temperatures (hence launched at higher velocities) should provide a more direct analog for the AVGR glasses . Five small (1-2cm) green, vesicular glasses found at a distance of about 500km from the Rio Cuarto site have been analyzed and exhibit very similar oxide distributions (Fig. 2b). In this case, the various glasses (including the AVGR sample) have been referenced to the homogeneous drop-shaped impactites (VPD) found at Rio Cuarto, rather than the heated/fused bulk loess. These samples exhibit remarkable similarity to the AVGR glass.

Concluding Remarks: The range in major element distributions of the Rio Cuarto impactites generally resemble the composition of bulk loess heated to high temperatures for long times, yet exhibit clear evidence for rapid heating to much higher temperatures and quenching. Moreover, impactites are found that resemble the quickly heated and quenched glasses produced in laboratory impact experiments. In spite of obvious differences in the effects of heating times, such comparisons underscore the extreme pressure/heating conditions of formation unique to the impact process. The excellent preservation state and diversity of recovered impact glasses as a function of distance from Rio Cuarto should provide unique insight into the impact process at low angles. We gratefully acknowledge use of the Keck Microprobe Facility at Brown and assistance of J. Devine for portions of this effort.

1. Schultz, P.H. and Lianza, R. (1992) *Nature 355*, 234-237. 2. Schultz, P.H. *et al.* (1992) *Lunar and Planet. Sci. XXII*, 1237-1238. 3. Grant, J. and Schultz, P.H. (1992) *Lunar and Planet. Sci. XXII*. 4. Bunch, T.E. and Schultz, P.H. (1992) *Lunar and Planet. Sci. XXIII*, 179-180. 5. Koeberl, C. and Schultz (1992) *Lunar and Planet. Sci. XXII*, 707-708. 6. Stöffler, D. (1972) *Fortschr. Min. 49*, 50-130. 7. Kieffer, S.W. (1971) *J. Geophys. Res. 76*, 5449-5503. 8. Schultz, P.H. and Gault, D.E. (1990) In *Geol. Sp. Paper 247* (V.L. Sharpton and P.D. Ward, eds), pp. 239-261. 9. Teruggi, M.E. (1957) *J. Sedim. Petrol.* 27, 322-332.

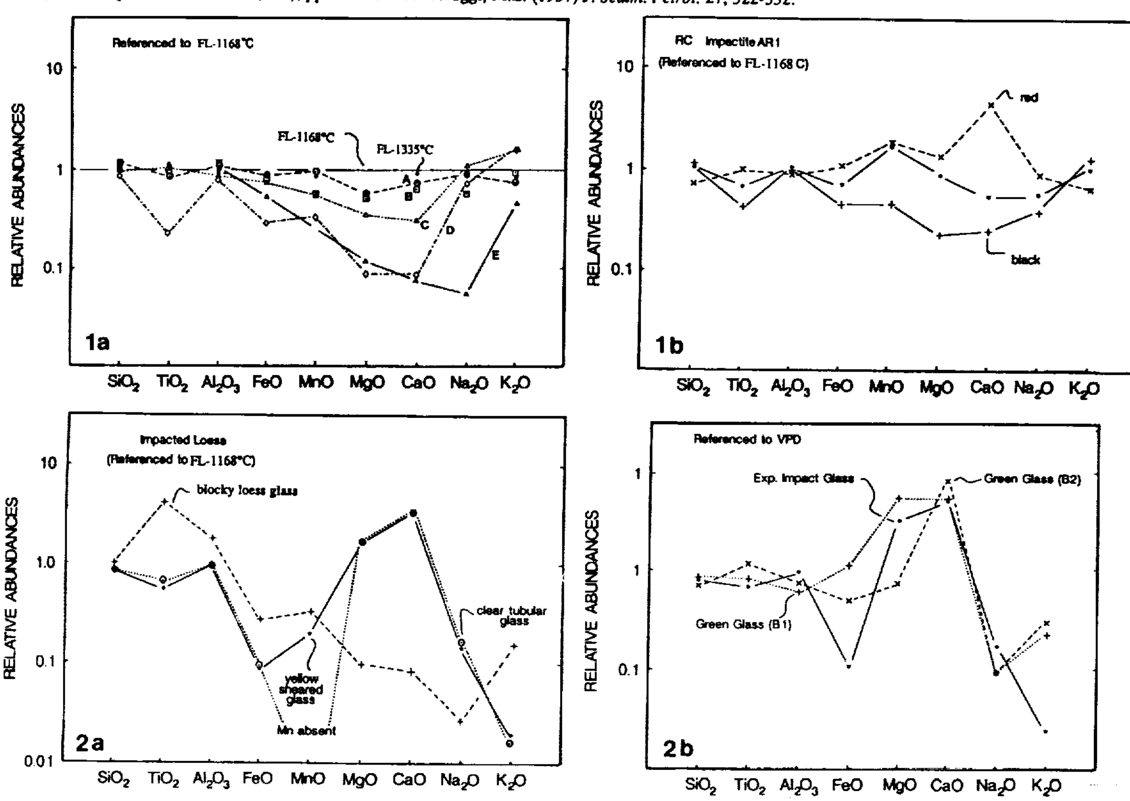


Fig. 1 (Top). Comparison of impactites referenced to bulk loess heated and fused at 1168°C. Fig. 1a shows different impactites including experimental impact glass produced from impact into loess at 15° (sample E). Fig. 1b shows typical range of composition in a single sample. Fig. 2 (bottom) compares experimentally produced impact glass of different morphologies using the AVGR. The blocky glass resembles lower temperature/pressure impactites shown in Fig. 1a after correction for containmants (sample E) . The striated glass resembles possible RC impactites found at much greater distances (samples B1, B2 in Fig. 2b). The examples in Fig. 2b have been normalized to a drop-shaped impact (VPD; sample A in Fig. 1a).

C_2, CN AND DUST IN COMET WILSON (1987VII); **R. Schulz, M. F. A'Hearn, Department of Astronomy, University of Maryland, P. V. Birch, C. Bowers, M. Kempin, R. Martin, Perth Observatory, Bickley, Western Australia**

Column density profiles in C_2, CN as well as in blue and red continuum (BC and RC) were constructed from two-dimensional images of the coma of Comet Wilson (1987VII). Our analysis showed that the continuum profiles decrease with the nuclear distance ρ as $1/\rho$. From the C_2 and CN profiles we determined the parent and the daughter lifetimes as well as the production rates in terms of the vectorial model.

The dynamically new comet Wilson (1987VII) was observed with the 24" Planetary Patrol Telescope at Perth Observatory, Australia, pre as well as post perihelion in April and May, 1987. Coma images were obtained with the University of Maryland's CCD camera system (field of view 9'.5 × 15', resolution 1".8) in several different spectral ranges using the photometric filter set of the International Halley Watch (IHW). Additionally, CCD images of selected standard stars for narrowband photometry of comets [1] were taken with the same filters. This is a report on the analysis of the post perihelion observations taken in C_2 and CN as well as blue and red continuum.

All images were bias subtracted, flat fielded, sky subtracted and normalized to counts per second. The standard stars were used to convert the cometary images into absolute fluxes by applying the calibration procedures and parameters, established for the IHW [2]. The underlying continuum in the emission band images was two-dimensionally approximated and subtracted, using the observations in blue and red continuum, which leads to a more accurate continuum correction with regard to spatial variations in the different components. For the conversion into column densities we assumed a constant g-factor for C_2 [3]. The g-factors for CN [4] were adapted to the actual heliocentric distances and velocities of the comet. The fluxes in the continuum images were converted into radiation powers (erg s^{-1} $Å^{-1}$), which are independent of the geocentric distance and therefore facilitate a comparison between the profiles observed on different dates.

The application of several well working structural enhancement techniques [5] to the images revealed no prominent features (e.g. jets) in the coma. Therefore, mean radial column density profiles, constructed by averaging around the nucleus, lead to a satisfactory representation of the intensity distribution as a function of nuclear distance ρ. Fig. 1 shows a typical example for the resulting mean radial profiles of the emission band and the continuum images. The radial continuum profiles (Fig. 1c and 1d) are in good agreement with the expected $1/\rho$ law for the decrease of brightness as a function of nuclear distance. In case of the C_2 and the CN (Fig. 1a and 1b) the circles reflect the column density profiles of the original images (no continuum subtraction), while the dots represent the column density profiles, constructed after a two-dimensional continuum subtraction. The continuum corrected profiles were used to determine lifetimes and production rates by fitting the Festou vectorial model [6] to them. The solid line in Fig. 1b shows the fit for the CN column density profile of May 4th, 1987. All post perihelion CN profiles could be well fitted under the assumption of steady state conditions for the CN production rate. With an adopted parent velocity of v_p = 1 km/s the best fits were obtained for a lifetime of the CN parent of τ_p = (30500 ± 1000) s and a lifetime of the CN radical of τ_d = (432000 ± 8000) s (r_H = 1 km/s). Tab. 1 gives the CN production rates corresponding to a CN velocity of v_d 1.2 km/s. The comparison with HCN production rates [7] shows that the CN production is significantly higher. Therefore, HCN cannot be the only parent molecule of the CN in Comet Wilson.

Tab. 1 CN production rates (v_d = 1.2 km/s) of Comet Wilson during its post perihelion phase.

Date / 1987	May 02	May 03	May 04	May 05	May 17
Q_{CN} / 10^{26} s^{-1}	3.5 ± 0.1	3.6 ± 0.1	2.6 ± 0.1	2.5 ± 0.1	2.2 ± 0.1

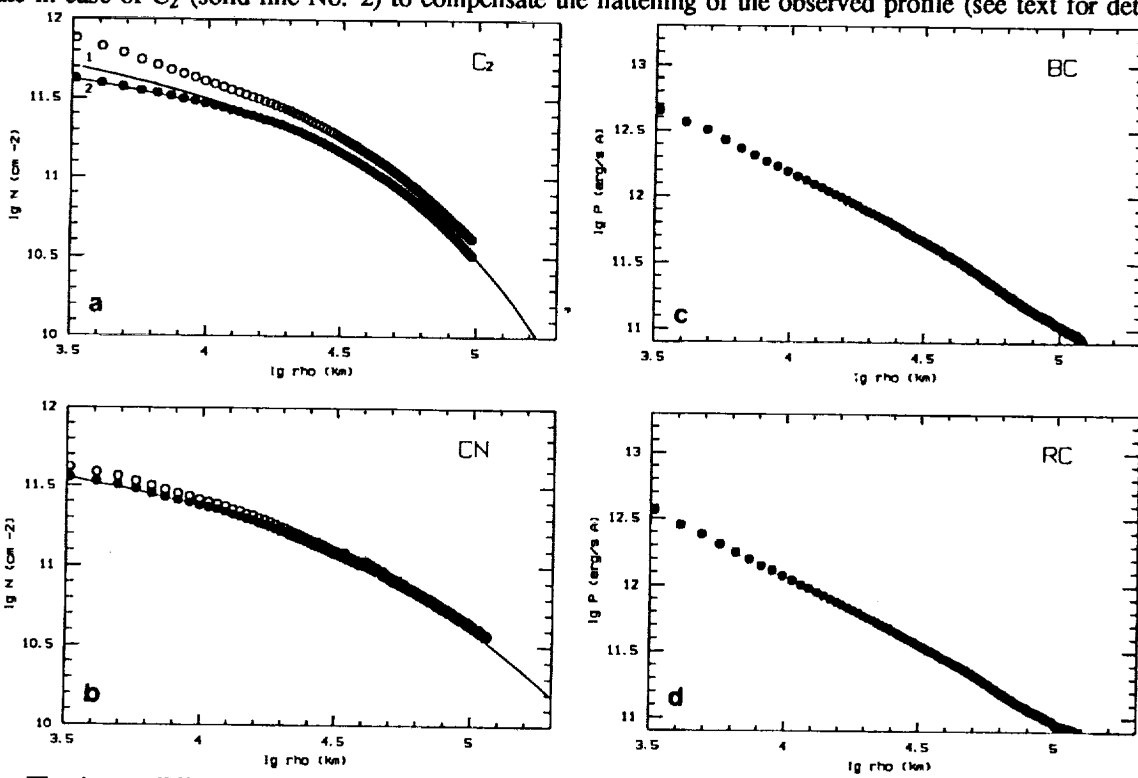
In case of C_2 the inner part of the column density profiles could not sufficiently be fitted by the conventional use of the vectorial model. The observed C_2 profile in Fig. 1a (dots) is much flatter in the inner part of the coma than the best fit of a steady state vectorial model (solid line 1). To compensate this flattening, we decreased the C_2 production rate in the vectorial model for the past 0.25 days by a factor of 1.5. This is a simple trick to easily simulate functions of the C_2 production rate, which are not known, but in any case different from those reflecting the production in conventional photolytic models. The best fit to the observed profile, using this trick to accomodate the flattening of the C_2 profiles, is shown in Fig. 1a as solid line 2. The parent and daughter velocities were set to v_p = v_d = 1 km/s. The best fitting lifetimes τ (r_H = 1 AU) and production rates Q are listed in Tab. 2.

C_2, CN AND DUST IN COMET WILSON (1987VII): Schulz R. et al.

Tab. 2 The fitting parameters for the C_2 profiles. Q_1: production rate for steady state conditions; Q_2: values, to which Q_1 has to be reduced, Δt: time, for which this has to be done to compensate the profiles' flattening.

Date	$\tau_p / 10^3 s$	$\tau_d / 10^3 s$	$Q_1 / 10^{26} s^{-1}$	$Q_2 / 10^{26} s^{-1}$ (Δt / days)
02.05.1987	35	65	4.3	3.2 (0.30)
03.05.1987	38	65	4.7	4.0 (0.25)
04.05.1987	35	65	4.8	3.2 (0.25)
06.05.1987	40	70	5.5	4.5 (0.15)
12.05.1987	39	80	5.0	2.8 (0.10)
14.05.1987	34	65	4.7	3.2 (0.30)
17.05.1987	41	65	4.8	3.7 (0.20)
Average	37.4 ± 2.9	67.9 ± 6.1	4.8 ± 0.4	3.5 ± 0.6 (0.22 ± 0.08)

Fig. 1 Mean radial profiles of Comet Wilson's coma in C_2, CN, BC and RC on May 4th, 1987. In case of C_2 and CN the circles represent the profiles of the original images, while the dots show the column density profiles after continuum correction. The CN and C_2 profiles were fitted by the vectorial model, assuming steady state conditions for the production rates (solid line for CN, solid line No. 1 for C_2), as well as a temporally altered production rate in case of C_2 (solid line No. 2) to compensate the flattening of the observed profile (see text for details).



The impossibility to fit the flat shape of the C_2 profiles in terms of a vectorial model indicates that the source function of C_2 is not sufficiently represented by an exponential law. On the other hand we find a C_2 profile resulting from modeling of chemical reactions [8], which is too flat to fit the observations. However, the knowledge of the source function of C_2 is totally necessary to draw conclusions on precursor molecules. We therefore need a coma model that combines both assumptions and allows to vary the contribution of each separately.

[1] Osborn,W.H. et al. (1990) Icarus 88, 228.
[2] A'Hearn, M.F. & Vanysek V. (1989) App. IHW-Archive of Obs. of Giacobini-Zinner, Ed. Z. Sekanina, JPL
[3] A'Hearn, M.F., Birch, P.D., Feldman, P.D., and Millis, R.L. (1985) Icarus 64, 1
[4] Schleicher, D.G. (1983) Thesis, Dep. of Physics and Astronomy, Univ. of Maryland, 108–110
[5] Schulz, R. (1991) Proc. 3rd ESO/ST-ECF Data Analysis Workshop, p. 73
[6] Festou, M.C. (1981) A&A 95, 69
[7] Crovisier, J. et al. (1990) A&A 234, 535
[8] Biermann, L., Giguere, P.T., and Huebner, W.F. (1982) A&A 108, 221

STRENGTH AND DEFORMATION PROPERTIES OF BASALTIC LAVA FLOWS ON PLANETARY SURFACES, **Richard A. Schultz**, Mackay School of Mines, University of Nevada, Reno, NV 89557–0138.

Introduction and Results.

Basaltic rocks are thought to constitute a volumetrically significant rock type on the Moon, Mercury, Mars, and Venus, in addition to the Earth. Spacecraft images of surfaces with known or suspected basaltic composition on these bodies, particularly on Venus, indicate that these rocks have been deformed in the brittle regime to form faults and perhaps dilatant cracks, in addition to folding and more distributed types of deformation [1].

Predictions of brittle fracture or other type of deformation are made by comparing calculated stresses from a tectonic model to some criterion for rock strength. Common strength criteria used in the planetary science literature for near-surface deformation include a Griffith tensile-strength criterion for intact rock [2], a Mohr envelope for intact basalt [3], and a brittle strength envelope based on Byerlee's law of rock frictional resistance [4,2,5].

However, planetary terrains of basaltic composition consist of much more than just intact basaltic rock. The aggregate basaltic material, termed the "rock mass," consists of both the intact rock and the associated fractures, faults, lithologic contacts, and other discontinuous surfaces [e.g., 6]. A basaltic rock mass is the relevant material for which strength properties must be defined and calculated model stresses must be compared to this material in order to more accurately predict brittle deformation [7]. For example, the various strengths of a rock mass are less than that of intact material of the same composition. This means that tectonic models which compare stresses to intact failure strengths overestimate the stresses required for fracture, and so underestimate the extent and magnitude of brittle deformation predicted in these models. On the other hand, rock mass shear strength can be greater than that predicted from Byerlee's law. The concept of rock mass strength is central to many engineering design studies in which calculated stresses are used to predict brittle fracture, and this experience indicates that brittle strength envelopes which assume properties for intact rock (Griffith parabolas) or sliding along a single, continuous surface (Byerlee's law) inadequately characterize the tensile, compressive, and shear strengths of rock masses.

The criterion adopted here to relate stresses to rock mass fracture is that defined for large-scale engineering projects by *Hoek and Brown* [8]. This criterion is based on a Griffith-type curve for tensile normal stress and a concave downward curve for compressive normal stress, and it is the only available criterion that explicitly considers the weakening effects of discontinuities within the rock mass on the stress state required for fracture. This criterion has been embraced by the geotechnical community for the design and construction of large engineering projects in fractured rock such as basalt [9].

Using the Hoek-Brown criterion, the strength of basalt may be approximated by

$$\sigma_1 = \sigma_3 + \sqrt{m\sigma_c\sigma_3 + s\sigma_c^2} \quad (1)$$

in which σ_1 and σ_3 are the greatest and least principal stresses at fracture, σ_c is the unconfined compressive strength of intact basalt, and m and s are empirical parameters that reflect the degree of block interlocking and fracturing of the rock mass. For intact rock, $s = 1$, and for pervasively fractured rock, $s = 0$. The parameter m decreases with the degree of fracturing or blockiness of the rock mass. Using representative values of $m = 4.9$ for a jointed basaltic rock mass [6], $s = 0.0021$, and $\sigma_c = 262$ MPa, the strength envelope for basaltic lava flows written using the principal stresses is

$$\sigma_1 = \sigma_3 + \sqrt{1{,}284\sigma_3 + 144} \quad (2)$$

The tensile strength of basalt whose strength is characterized by equation (1) can be obtained from

$$T_0 = \frac{\sigma_c}{2}\left(m - \sqrt{m^2 + 4s}\right) \quad (3)$$

The predicted tensile strength T_0 of the basaltic rock mass obtained using these values of σ_c, m, and s is –0.1 MPa, or nearly zero. This value contrasts with the average tensile strength of intact basalt of about –18 MPa listed in the literature.

The Hoek-Brown criterion can be recast into a depth-dependent strength envelope for brittle deformation of the rock mass. Comparison of this envelope with the standard one based on Byerlee's law indicates that a basaltic rock mass is stronger in both extension and compression than might be supposed.

Deformability properties of rocks and rock masses before bulk failure occurs are typically described by a modulus and Poisson's ratio. Young's modulus is used for rocks that respond elastically to stress. In contrast, the deformation modulus describes the often inelastic deformation properties of a fractured rock mass and is obtained from the slope of the stress-strain curve measured during an in situ field test. This modulus is invariably less than the Young's modulus for intact rock of the same composition and mineralogy. Poisson's ratio for a basaltic rock mass is somewhat larger than that for unfractured intact basalt. Typical values of these parameters are given in Table 1.

The deformation properties of a basaltic rock mass in the near-surface environment of Venus are of particular interest given abundant evidence for faulting and folding of near-surface rocks there [1]. The strength parameters discussed above are appropriate for rock material deformed under ambient pressure (~0 MPa) and temperature (20°C) conditions. These parameters must be modified for application to Venus. In particular, the deformation modulus appears to increase with temperature, perhaps by as much as a factor of two at 450°C; the other parameters may be reduced slightly for this temperature. Estimates of the strength parameters for Venus are listed in Table 1.

Conclusions.

Strength properties of basaltic rocks presented here differ significantly depending on the scale of observation. This well-known effect [e.g., 10,11] is incorporated into the empirical brittle strength envelope defined by *Hoek and Brown* [8]. This rock mass envelope is generally intermediate between the envelope for intact rock (Modified Griffith criterion) and that for the frictional resistance of a through-going surface (Byerlee's law); the latter two end-member approaches provide imprecise estimates of the strengths of a basaltic rock mass under compression or extension.

An important finding of the present work is the marked reduction in strength parameters for a basaltic rock mass relative to the intact material under the same conditions. For example, tensile strength of the rock mass is reduced to nearly zero, uniaxial compressive strength is reduced by an order of magnitude, and the modulus is reduced by a factor of two relative to intact basalt for conditions of ambient temperature and no confining pressure. These reference values and associated strength envelopes should provide better estimates of rock mass strengths for use in planetary tectonic modeling of near-surface deformation on any of the terrestrial planets.

Table 1. *Strength Parameters for Basaltic Rocks on Planetary Surfaces*

Parameter	Intact	Rock Mass	Venus Rock Mass
Young's modulus, GPa	73	–	–
Poisson's ratio	0.25	0.3	0.3
Deformation modulus, GPa	–	20	~40
Tensile strength, MPa	–18	~0.1	~0.1
Compressive strength, MPa	262	12	<12
Cohesion, MPa	66	4.5	4

References. [1] Solomon et al., *JGR, 97,* 13,199–13,255, 1992. [2] Tanaka and Golombek, *Proc. Lunar Planet. Sci. Conf., 19th,* 383–396, 1989. [3] Smrekar and Solomon, *JGR, 97,* 16,121–16,148, 1992. [4] Melosh, *Proc. Lunar Sci. Conf., 7th,* 2967–2982, 1976. [5] McGovern and Solomon, *Lunar Planet. Sci., XXIII,* 885–886, 1992. [6] Bieniawski, *Engineering Rock Mass Classifications,* Wiley, 1989. [7] Hoek, *Géotechnique, 33,* 187–223, 1983. [8] Hoek and Brown, *J. Geotech. Eng., 106,* 1013–1035, 1980. [9] Pan and Hudson, in *Rock Mechanics and Power Plants,* Balkema, 95–103, 1988. [10] Barton, in *Scale Effects in Rock Masses,* Balkema, 31–55, 1990. [11] Scholz, *The Mechanics of Earthquakes and Faulting,* Cambridge, 1990.

5112-91
ABS. ONLY

N94-20748

MARS: NEW EVIDENCE FOR ORIGIN OF SOME VALLES MARINERIS LAYERED DEPOSITS;
David H. Scott, U.S. Geological Survey, Flagstaff, AZ 86001

The discovery of layered deposits in the walls of a deep trough in Lunae Planum [1] has implications for the origin of similar-appearing deposits in some canyons of Valles Marineris. Although layering is visible in the competent, cliff-forming upper walls of the canyons, the dissimilarity in appearance between canyon walls and soft rounded hills of layered deposits on canyon floors, as well as their contrasting patterns of erosion, has been considered strong evidence that their modes of origin were different. Most workers agree that the wall rocks are volcanic flows derived from fissure vents and other volcanic sources in the region [2-5]. However, several hypotheses have been advanced to account for the softer-appearing stratified floor deposits. Chief among them is the proposal that the floor deposits are waterlaid sediments that accumulated in large lakes within the canyons and include materials eroded from canyon walls, eolian deposits, and subaqueous volcanic eruptives [2,6,7,8].

The trough on the Lunae Planum plateau is about 1000 m deep and exposes eight light and dark layers (Fig. 1). No stratigraphic break is visible in the walls of the trough, which probably consist of a sequence of lava flows and interbedded pyroclastic materials that form the ridged plains geologic unit. These lava flows cover the surface of Lunae Planum and are Hesperian in age [1,4]; an alternate interpretation [9] places the lower part of the layered material in the Noachian Period.

The interbedded volcanic materials closely resemble layered deposits that form a hill in Juventae Chasma (Fig. 2) more than 1500 km to the south; in both places the attitude, thickness, and albedo contrasts of layers appear to be similar, although more individual beds are exposed in the 2000-m-deep Juventae Chasma [10]. Although many investigators have favored lacustrine deposition for the layered deposits in the canyons of Valles Marineris, others have considered that deep filling of the canyons was improbable [11], or that residence times of water were insufficient to account for thick accumulations of sedimentary material [12]; they interpreted the layered deposits to be remnants of the adjacent plateau material (which at Juventae Chasma consists of ridged plains lava flows and possibly older volcanics of Late Noachian age [4,13]). This interpretation is now supported by the layering found in the lava flows of Lunae Planum. It is especially applicable to Juventae Chasma, where streamlined blocks within chaotic terrain on the relatively shallow chasma floor attest to a short duration of ponded water.

<u>References</u>
[1] Scott D.H. (1991) U.S. Geol. Survey Map I-2208. [2] McCauley J.F. (1978) U.S. Geol. Survey Map I-897. [3] Scott D.H. and Carr M.H. (1978) U.S. Geol. Survey Map I-1083. [4] Scott D.H. and Tanaka K.L. (1986) U.S. Geol. Survey Map I-1802-A. [5] Tanaka K.L. (1986) Proc. Lunar and Planet. Sci. Conf. 17, 139-158. [6] Lucchitta B.K. (1982) NASA TM-85127, 233-234. [7] Nedell S.S., Squyres S.W., and Anderson D.W. (1987) Icarus, 70, 409-441. [8] Peterson C. (1981) Proc. Lunar and Planet. Sci. Conf. 12, 1459-1471. [9] Tanaka K.L. and Chapman M.G. (1992) Proc. Lunar and Planet. Sci. Conf. 22, 73-83. [10] U.S. Geol. Survey (1988) Map I-1208. [11] Malin M.C. (1976) Ph.D thesis, Calif. Inst. Tech., Pasadena, 176 p. [12] Scott D.H. and Witbeck N.E. (1983) NASA TM-86246, 298-300. [13] Witbeck N.E., Tanaka K.L., and Scott D.H. (1991) U.S. Geol. Survey Map I-2010.



Figure 1. Trough on Lunae Planum plateau. Light and dark layers probably lava flows and pyroclastic material in the ridged plains geologic unit.



Figure 2. Hill in Juventae Chasma, a large collapse depression in Lunae Planum. Hill forms spur extending from base of canyon wall, consists of ridged plains unit.

C-5

5/13-90 ABS ONLY N94-20749

POST-METAMORPHIC BRECCIATION IN TYPE 3 ORDINARY CHONDRITES: E.R.D. Scott, T.J. McCoy, and K. Keil, Planetary Geosciences, Department of Geology and Geophysics, SOEST, University of Hawaii, Honolulu, HI 96822. p-2

Type 3.1-3.9 ordinary chondrites can be divided into two kinds: those in which the compositions of chondrule silicates are entirely consistent with metamorphism of type 3.0 material [1-3], and those in which the compositional heterogeneity appears to be too extreme for in situ metamorphism [4]. We present petrologic data for three LL3 chondrites of the second kind, Ngawi, ALH A77278 (both type 3.6) and Hamlet (type 3.9), and compare these data with results for the first kind of LL3-4 chondrites [1]. Given that chondrules form in the nebula and that metamorphic equilibration occurs in asteroids, our new data imply that Ngawi, A77278, Hamlet and many other type 3 ordinary chondrites [4] are post-metamorphic breccias containing materials with diverse metamorphic histories: they are not metamorphic rocks or special kinds of 'primitive breccias' [5]. We infer also that metamorphism to type 3.1-3.9 levels produces very friable material that is easily remixed into breccias and lithified by mild shock. Thus, petrologic types and subtypes of chondrites indicate the mean metamorphic history of the ingredients, not the thermal history of the rock. The metamorphic history of individual type I or II, porphyritic chondrules in type 3 breccias is best derived from olivine and pyroxene analyses and the data of McCoy et al. [1] for unbrecciated chondrites. The new chondrule classification scheme of Sears, DeHart et al. [6, 7] appears to provide less information about the original state and metamorphic history of individual porphyritic chondrules and should not replace existing classification schemes.

Olivine compositions in type IA and IIA chondrules. The detailed study of mineral compositions and zoning in type IA and IIA chondrules in LL3.0 [2, 3] and LL3.3-5 [1] chondrites and the analogous petrologic and theoretical studies of CO3 chondrites [9, 10] give us considerable confidence that we can identify mineral compositions in these chondrite types that are inconsistent with metamorphic equilibration in type 3 chondrites. Figures 1a and 1b show how the mean olivine compositions in 31 type IA and 28 type IIA chondrules vary with the metamorphic subtype in type 3-4 chondrites that show no evidence for post-metamorphic brecciation [1]. The corresponding data for ALHA 77278 (Fig. 1c and d) and Ngawi (Fig. 1e and f) show vastly greater scatter than shown by Parnallee, although all three are nominally LL3.6 chondrites. We suggest that the compositional data in Ngawi and ALH A77278 scatter because these chondrites are breccias composed of at least four distinct types of material including type 3.0, 3.3, 3.6, and 4 material; subtype uncertainty is ±0.2. The compositional zoning of olivine within individual chondrules in these chondrites is also consistent with this origin. Analogous data for Hamlet suggest it is largely type 3.8-4 material with a small amount of type 3.6 material.

Other petrologic evidence. Metallographic cooling rates. Data for taenite grains in the type 3 chondrites studied by McCoy et al. [1] plot coherently on Wood plots indicating cooling through 400 °C at rates of 1-1000 °C/Myr [11]; there are insufficient taenites in Semarkona to derive a metallographic cooling rate. Our data for taenite grains in Ngawi, A77278 and Hamlet plot incoherently, although individual grains are zoned consistently with slow cooling. We infer that taenites in these chondrites cooled at rates of 10-1000 °C/Myr in different locations prior to lithification, as suggested for many fragmental and regolith breccias [12, 13]. Clasts. We found several type 3.9-5 chondritic clasts in Ngawi; Sears et al. [14] infer from CL studies that there are also type 3.1 clasts in Ngawi. An equilibrated clast has been described in Hamlet [15], but none have been found in A77278. Matrix rims on chondrules. In Ngawi and A77278, there is a good relationship between the petrologic subtype of individual chondrules inferred from the data in Fig.1 and the nature of the matrix rim around the chondrule [16]. Thus type 3.0 chondrules have Semarkona-like, opaque matrix rims, type 3.6-4 chondrules have recrystallized matrix rims like those in Parnallee and Bo Xian, and type 3.3 chondrules are intermediate in nature.

Discussion. The diversity of olivine compositions in Ngawi and A77278 cannot be due simply to the differing response of their chondrules to metamorphism. Sears et al. [17, 6] suggest that chondrules in Dhajala and other type 3 chondrites show diverse degrees of equilibration because

TYPE 3 ORDINARY CHONDRITE BRECCIAS: SCOTT et al.

the mesostasis of unequilibrated chondrules was more resistant to devitrification. We did not find any relationship between mesostasis texture and olivine heterogeneity to support this hypothesis. We infer that the three LL chondrites that we have studied are precisely analogous to the fragmental and regolith breccias of higher mean petrologic type [e.g., 12, 13]. The only difference is that the type 3 breccias have a lower abundance of clasts and clastic material in their matrices and have generally not previously been recognized as breccias. We infer that this is due to the difficulty in recognizing brecciation in chondrites [8], that metamorphism produces friable type 3 material, and that the breccias were lithified by shock. Except for Ngawi, which contains solar-wind gases [18], we cannot preclude the possibility that mild metamorphism (to <300 °C) occurred after final lithification. By calling these rocks post-metamorphic breccias, we only imply that lithification of the breccias occurred after peak metamorphic temperatures had been reached.

References: [1] McCoy T.J. et al. (1991) GCA *55*, 601; [2] Jones R.H. and Scott E.R.D. (1989) Proc. 19th LPSC, 523; [3] Jones R.H. (1990 GCA *54*, 1785; [4] Scott E.R.D. (1984) Smithson. Contrib. Earth Sci. *26*, 73; [5] Scott E.R.D. and Taylor G.J. (1981) LPI Tech. Rept. 82-02, 130; [6] Sears D.W.G. et al. (1992) Nature *357*, 207; [7] DeHart J.M. et al. (1992) GCA *56*, 3791; [8] Scott E.R.D. et al. (1985) Proc. 16th LPSC, JGR Suppl. *90*, D137; [9] Scott E.R.D. and Jones R.H. (1990) GCA *54*, 2485; [10] Jones R.H. and Rubie D.C. (1991) EPSL *106*, 73; [11] McCoy T.J. et al. (1990) LPS XXI, 749; [12] Scott E.R.D. and Rajan R.S. (1981) GCA *45*, 53; [13] Taylor G.J. et al. (1987) Icarus *69*, 1; [14] Sears D.W.G. et al. (1991) Proc. LPS *21*, 493; [15] Fodor R.V. and Keil K. (1978) Sp. Pub. UNM Inst. of Met. *19*, 11; [16] Huss G.R. Keil K., and Taylor G.J. (1981) GCA *45*, 33; [17] Sears D.W.G., Sparks M.H., and Rubin A.E. (1984) GCA *48*, 1189; [18] Schultz L. and Kruse H. (1989) Meteoritics *24*, 155. This work was partly supported by NASA grants NAG 9-454 and NAGW-3281.

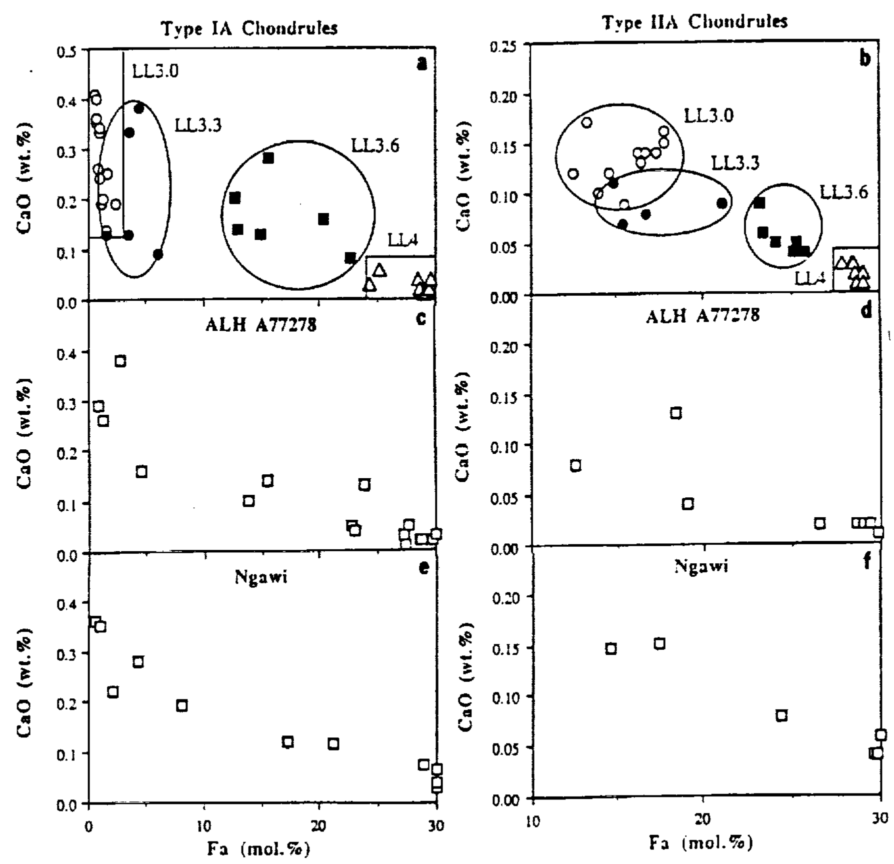


Fig.1. Mean compositions of olivine in type IA and IIA chondrules. (a) and (b) show data for Semarkona (LL3.0) and three LL3-4 chondrites (ALH A81251, Parnallee, and Bo Xian) that appear to have formed by simple metamorphism of Semarkona-like material; data from [1-3]. Our corresponding data for ALH A77278 (c and d) and Ngawi (e and f) show a wide scatter implying that these chondrites which are nominally type 3.6, like Parnallee, are actually breccias composed of at least four kinds of ingredients of type 3.0, 3.3, 3.6 and 4.

ABS. ONLY N94-20750

CATHODOLUMINESCENCE OBSERVATIONS OF *IN SITU* AQUEOUS DESTRUCTION OF CHONDRULES IN THE MURCHISON CM CHONDRITE.

Derek W.G. Sears, Paul H. Benoit, Lu Jie and Andrew S.R. Sears. Cosmochemistry Group, University of Arkansas, Fayetteville, AR 72701.

A low-power cathodoluminescence (CL) mosaic of a 1x2 cm section of the Murchison CM chondrite contains chondrules of two types, one containing olivines with red CL, and thought to be the equivalent of group A chondrules of Sears et al. (1992), and one without observable CL, probably equivalent of their group B chondrules. Both types of chondrule contain dust mantles with a characteristic uniform red CL due to very fine-grained forsterites, but the mantles of group A chondrules have complex internal structure and are much thicker than the relatively thin rims on group B chondrules. The variety of internal textures and the progressive integration of the objects with the surrounding matrix suggests to us that these features are large group A chondrules in the process of being destroyed by aqueous alteration. Prior to aqueous alteration, group A chondrules in CM chondrites were larger than group B chondrules, which is contrary to the situation in ordinary chondrites and were apparently destroyed more rapidly than group B chondrules by aqueous alteration.

Introduction. Aqueous alteration played an important part in the history of CI and CM chondrites affecting most of the minerals present and probably lowering the bulk Fe/Si of the matrix and the decreasing the chondrule/matrix ratio[1-3]. Most of the aqueous alteration clearly occurred on the parent body [4,5], although there have been some recent suggestions that minor alteration occurred prior to accretion, perhaps in the nebula. Similar to the matrix, although perhaps slightly more coarse-grained, are fine-grained rims around chondrules (sometimes termed "dust mantles", "halos", "accretionary rims")[4,6,7], which are widely thought to be the result of the accretion of nebular dust prior to the aggregation of the meteorite. Being dependent on both texture and composition, low-powered CL mosaics enable a novel and widescale assessment of the mineralogical and textural properties of meteorites[9,10] which is complementary to the other techniques. Like many little-metamorphosed chondrites, the CL properties of Murchison are dominated by the distribution and grain size of forsterites (generally $\leq 5\ \mu m$ in size and <3 mol% FeO, since higher levels quench the CL), although occasionally calcic glasses cause regions of yellow CL.

Two groups of chondrules. The CL reveals essentially two kinds of chondrule in Murchison. About 35% (by number) consist of circular or elliptical objects with no CL and which stand out sharply against the profusion of fine-grained forsterite grains in their dust mantles and matrix. Purely on the basis of CL, these appear to be the equivalents of the group B chondrules observed in type 3 ordinary chondrites[11,12]. The remaining chondrules are large objects which display varying degrees of integration with the matrix. They contain forsterites which are sometimes large ($\sim 100\mu m$) and euhedral, and sometimes of moderate size (say, $10\text{-}50\mu m$), with bright red CL indicative of <2wt% FeO and are often surrounded by areas of dark red CL indicative of 2-4wt% FeO. We suspect that this is due to the original igneous zoning. In that they contain essentially Fe-free olivine, these chondrules resemble the group A chondrules of ordinary chondrites, differing only in the frequent absence of a Ca-rich mesostases of bright yellow CL. The destruction of chondrule mesostasis and its conversion to phyllosilicates ("spinach") has often been observed [e.g.13], and we suggest that the loss of CL reflects this process. Thus we suggest that these chondrules are the aqueously altered equivalents of group A chondrules[11,12].

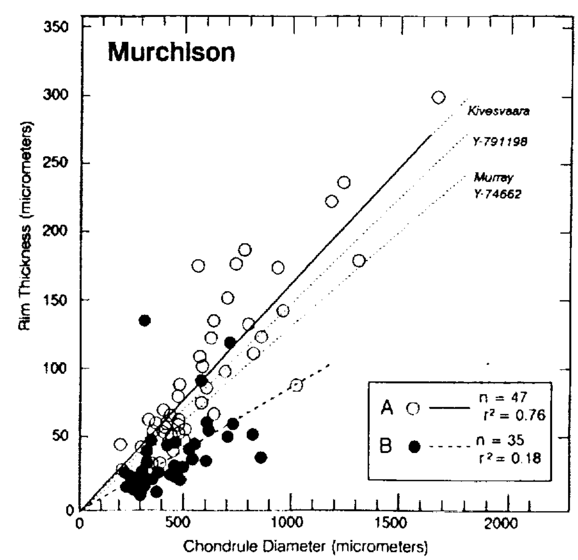


Fig. 1. Plot of chondrule 'rim' thickness against the diameter of the chondrule being 'rimmed' as measured in mosaics of the cathodoluminescence (the data points, 'group A' are those which show CL, i.e. contain Fe-free olivine, and 'group B' without CL, i.e. >2wt% FeO in the olivine). The dotted lines refer to data from BSE images for four CM chondrites[6].

Comparisons of the features around group A and group B chondrules. The major distinction between the fine-grained circular features around group A chondrules and the fine grained rims around group B chondrules is their thickness. The thickness of the fine-grained diffuse 'rim-like' features around group A

chondrules is much greater than the group B rims (Fig. 1). It is also apparent from Fig. 1 that group A chondrules tend to be larger than group B chondrules in Murchison, whereas in the Semarkona (type 3.0) ordinary chondrite, the reverse is true. Rims on chondrules in four CM chondrites have thicknesses up to ~250 μm on ~1.4 mm diameter chondrules[6], so that the thickness-diameter trends are comparable to those of the present group A chondrules. In comparison, the thickness/diameter ratio of the rims on B chondrules is significantly smaller than that of group A chondrules and they are apparently not represented in Metzler *et al.*'s data determined from mosaics of BSE images, although 35% of the chondrules in Murchison are group B. Apparently, group B chondrules and their mantles have been largely unsampled in previous studies, perhaps because they do not stand out as well as the group A chondrules in BSE images.

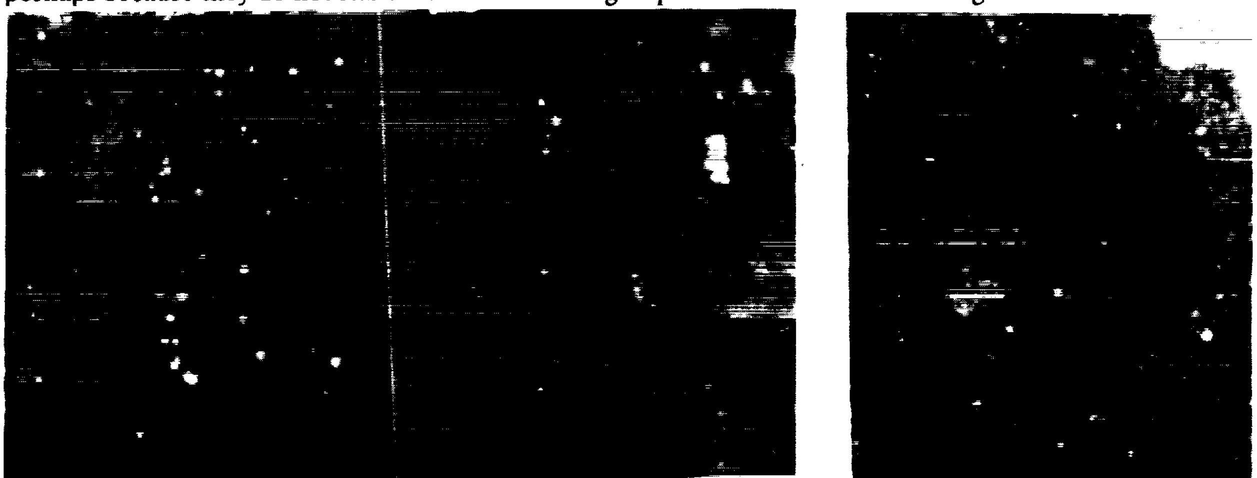


Fig. 2. Photograph of the cathodoluminescence of group A (left) and group B (right) chondrules in Murchison. White and light grays are areas of red CL produced by forsterite, darker gray is olivine with $\geq$2wt% FeO. Both chondrules contain thin rims, but in the case of the group A chondrule there is also a mantle extending further into the chondrule of lower grain density. (1 cm is 200 μm).

All chondrules in Murchison have a group B-like rim of bright red, low-Fe olivine but, in the case of the group A chondrules, this rim forms the outermost shell of the mantle (Fig. 2). The thickness of these outermost rims appear to follow the group B trend (Fig. 1) and their outlines in section are usually circular. The contact between the mantle and the object being mantled in group A chondrules, on the other hand, is often highly irregular with numerous embayments (Fig. 2) and, furthermore, their outermost rim is often somewhat more diffuse than the rims of group B chondrules such that group A chondrules often appear to be intergrown with the matrix.

Discussion. There are clearly differences between the mantles of group A and B chondrules in Murchison. It is possible that these differences reflect differences in the dust accretion history of the two groups, accretion of nebular dust often being discussed as an origin for chondrule mantles[4,7,8]. However, we would suggest that the mantle is the product of *in situ* aqueous alteration. The textures observed in CL images of group A chondrules are more suggestive of an aqueous alteration front than they are of pristine mantled chondrules. In this case, the differences in the mantles on A and B chondrules are related to differences in alteration susceptability and hence to differences in chondrule group chemistry[11,12]. If this is the case, we are observing the process described by McSween[1] and Tomeoka and Buseck[2] whereby chondrules are destroyed by aqueous alteration and the alteration products added to the matrix.

Summary of observations. (i) Murchison contains two groups of chondrules (A and B, 65 and 35% n/n, respectively) which are analogous to those of the primitive ordinary chondrites, (ii) unlike the ordinary chondritic chondrules, A chondrules tend to be larger than B chondrules, (iii) all Murchison chondrules have a thin mantle containing brightly luminescent Fe-poor olivine, but (iv) only the A chondrules have complex thick mantles similar to those described by Metzler *et al.* (1992).

1. McSween H.Y. (1979) *Rev. Geophys. Space Phys.* **17**, 1059-1078. 2. Tomeoka K. *et al.* (1989) *Proc. NIPR Sym. Antarct. Meteor.* **2**, 221-234. 3. McSween H.Y. (1987) Geochim. Cosmochim. Acta 51, 2469-2477. 4. Bunch T.E. and Chang S. (1980) Geochim. Cosmochim. Acta 44, 1543-1577. 5. DuFresne E.E.. and Anders E. (1960) Geochim. Cosmochim. Acta 26, 1085-1114. 6. Metzler K. *et al.* (1992). *Geochim. Cosmochim. Acta* **56**, 2873-2897. 7. King T.V.V. and King E.E.. (1981) *Icarus* **48**, 460-472. 8. Zolensky M.E. *et al.* (1981) *Lunar Planet. Sci.* **XIX**, 1327-1328. 9. Sears D.W.G. *et al.* (1989) In *Spectroscopic characterization of minerals and their surfaces* (ed. L.M. Coyne, *et al.*), 190-222. 10. Sears D.W.G. *et al.* (1991) *Proc. NIPR Symp. Antarct. Meteor.* **4**, 1745-1805. 11. Sears D.W.G. *et al.* (1992) *Nature* **357**, 207-210. 12. DeHart J.M. *et al.* (1992) *Geochim. Cosmochim. Acta* **56**, 3791-3807. 13. Fuchs L.H., Olsen E. *et al.* (1973) *Smithson. Contrib. Earth Sci.* **10**, 39pp. (Supported by NASA grant NAG 9-81).

5/15-92 ABS. ONLY N94-20751 p-2

DIFFUSIVE REDISTRIBUTION OF WATER VAPOR IN THE SOLAR NEBULA REVISITED; William D. Sears, Department of Planetary Science, University of Arizona, Tucson, AZ 85721

Stevenson and Lunine [1] presented a model for enhancing the abundance of solid material in the region of the solar nebula at the water condensation point. This was used to provide a means to produce a much more rapid formation of Jupiter than the standard solar nebula models. However they underestimated the drag induced sun-ward radial drift of the planetesimals of interest. Reanalysis reveals that these particles would spread over the inner solar system and might influence the formation of the asteroids.

The basic concept in [1] is to use a diffusive redistribution of water vapor from the inner part of the solar nebula out to the point where the temperature drops low enough to form ice. Stevenson and Lunine used simple but reasonable models for the growth of ice grains and a cold finger model for the diffusive redistribution. They found that micron sized particles grow in days and after about a hundred thousand years particles approach $1cm$.

They then used Weidenschilling's [2] results for radial drift of large particles to argue that $100m$ particles will decouple from the turbulent gas and remain in the area of the condensation zone. These would then form the basis of larger planetesimals and would eventually form Jupiter. They gave values for the radial drift of $1cm/s$ and a drift in 10^5 years of order $0.1AU$.

This appears to have been done with Weidenschilling's $1AU$ data. Therefore the solar nebular parameters used in [1] were re-applied to Weidenschilling's [2] model at $5AU$. Some additional nebular parameters which were required for this exercise but not provided in [1] were taken from Wood and Morfill [3]. This resulted in a radial drift of $16cm/s$ which corresponds to a radial motion of $3.3AU$ in 10^5 years. This is much greater than the value used in [1] and has the effect of spreading the proto-planetesimals throughout the inner solar system.

The effect of newer drag laws and the complete, and therefore hopefully self-consistent, simple nebular model of Wood and Morfill [3] was also investigated. The newer drag law given in Hood and Horanyi [4], was compared with the Epstein drag law used by Weidenschilling, which are both valid for the same size and velocity regions. It was assumed that the grain was at the same temperature as the surrounding nebula. The results are shown in the figure.

The two drag laws produce only slightly different results, and those are limited to the small particle region. However, the different nebular model produces a radial drift approximately ten times as large, mostly due to the pressure gradient differences. If this model is more correct then the $100m$ particles would move over $30AU$ inward in 10^5 years, calculated the same way as the above drifts. Obviously this is an unrealistic result as the sun is only $5AU$ away.

There are several implications of these results. The foremost of these is that Stevenson and Lunine's rapid formation of Jupiter would most likely not take place since the larger radial drifts at $5AU$ would spread out the proposed planetesimals. Therefore the requisite increased surface particle density would not materialize to provide the runaway growth of a solid core. Another model which explains the existence of this gaseous planet must be found.

Other possible effects of this mechanism are also of interest. If the grains drift sun-ward again after they decouple from the gas, then they will heat up. This will cause evaporation. This is a mechanism for moving water vapor back inside the condensation zone and form a kind of "back pressure" to the diffusion of vapor into the condensation zone in the first place. Since it is unlikely that all of the ice will return to the vapor phase, the remainder may well have formed parts of the present day asteroids.

Finally, Stevenson and Lunine's model of the depletion of water vapor inside the condensation point has other implications for the formation of the asteroids. Reduced water vapor would reduce

the formation of metal hydrates directly from the nebula, though the solid particles which have moved inward may provide local areas of enhanced water availability. Also, since water is the primary form of oxygen in the inner solar nebula, any decrease would decrease the carbon to oxygen ratio, possibly to the point where there is more carbon than oxygen. This would have a large effect on the formation of organic compounds.

ACKNOWLEDGMENT.
Parts of this work were supported by a grant from the NASA Origins of Solar Systems program to Jonathan Lunine.

REFERENCES.

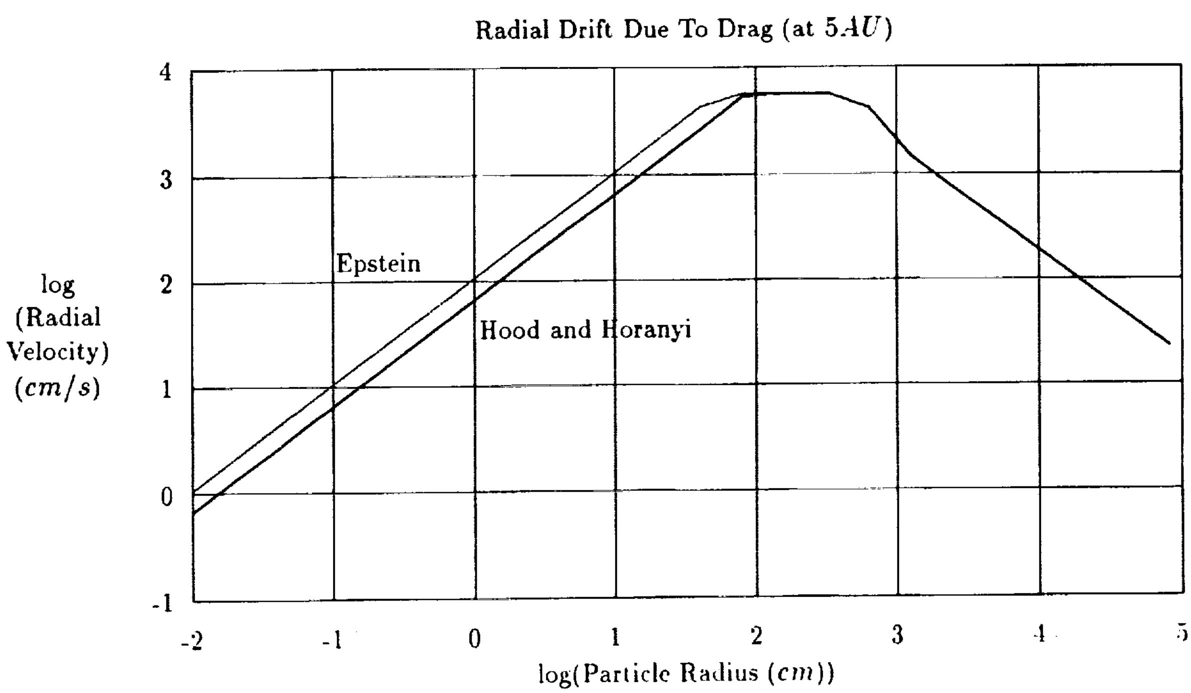
[1] Stevenson, D.J. and Lunine, J.I. (1988) *Icarus, 75*, 146-155.

[2] Weidenschilling, S.J. (1977) *Mon. Not. R. Astr. Soc., 180*, 57-70.

[3] Wood, J.A. and Morfill, G.E. (1988). In *Meteorites and the Early Solar System*, eds. J.F. Kerridge and M.S. Matthews, pp. 329-347.

[4] Hood, L.L. and Horanyi, M. (1991) *Icarus, 93*, 259-269.

FIGURE.



S116-90 ABS. ONLY

N94-20752

LUNAR BASALT METEORITE EET 87521: PETROLOGY OF THE CLAST POPULATION. A.S.Semenova, M.A.Nazarov, and N.N.Kononkova. Vernadsky Institute of Geochemistry and Analytical Chemistry, Moscow 117975, Russia

The Elephant Moraine meteorite EET 87521 was classified as a lunar mare basalt breccia which is composed mainly of VLT basalt clasts [1-3]. Here we report about our petrological study of lithic clasts and monomineralic fragments in the thin sections EET 87521,54 and EET 87521,47,1 prepeared from the meteorite. The results of the study show that EET 87521 consists mainly of Al-rich ferrobasalt clasts and olivine pyroxenite clasts. The bulk composition of the meteorite can be well modelled by mixing of these lithic components which appear to be differentiates of the Luna 24 basalt melt. KREEP and Mg-rich gabbro components are minor constituents of EET 87521.

Results. The lithological components of EET 87521 are lithic clasts (1-4 mm) and monomineralic fragments (0.1-1.5 mm) which are cemented by a shock glass. The glass makes up nearly 10% of the studied samples. The ferrobasalt clasts and olivine pyroxenite clasts are dominant in EET 87521. No highland fragments were identified.

Ferrobasalts have a relative coarse-grained ophitic texture and consist of feldspar (An 86-92), olivine(Fo 2-16), and pyroxene of ferroaugite (Wo 33-40, Fs 45-52) and sub-ferroaugite (Wo 17-25, Fs 47-61) compositions(Fig). Accessories are ilmenite, silica and troilite. These ferrobasalt fragments exhibit large compositional variations: feldspar 24-74; pyroxene 10-66; olivine 0-10, silica 0-13 (vol.%). Average composition of 5 ferrobasalt clasts (SiO_2 49.4; TiO_2 .26; Al_2O_3 18.35; Cr_2O_3 .09; FeO 13.13; MnO .14; MgO 3.33; CaO 14.51; Na_2O .72; K_2O .06; wt.%) was calculated on the basis of modal data and mineral compositions.

Olivine pyroxenites are fine-grained rocks as compared to the ferrobasalts. They show an equigranular texture and contain 57-75% of pyroxene, 18-26% of olivine, and 2-17% of feldspar. Ilmenite and troilite are minor phases. Mineral compositions in the pyroxenites are close to those in the ferrobasalts, but feldspar in these rocks is characterized by a limited compositional range (An 91-92). Average composition of 2 pyroxenite clasts is: SiO_2 47.1; TiO_2 .49; Al_2O_3 2.18; Cr_2O_3 .16; FeO 33.84; MnO .45; MgO 5.51; CaO 10.28; Na_2O .03; K_2O .02 (wt.%).

Monomineralic fragments of olivine, pyroxene and feldspar are most abundant in EET 87521. Ilmenite (0.5-2.5 wt.% of MgO) and Al-Ti-chromite fragments are present in very minor quantity in the breccia. Compositions of some monomineralic silicate fragments are similar to those of the silicate phases in the lithic clasts. However some pyroxene and olivine fragments are rich in Mg and plot outside the field of the lithic clasts (Fig). Some monomineralic fragments show a more sodic feldspar (An 68-73, Or 3-4), which were not found in the lithic clasts.

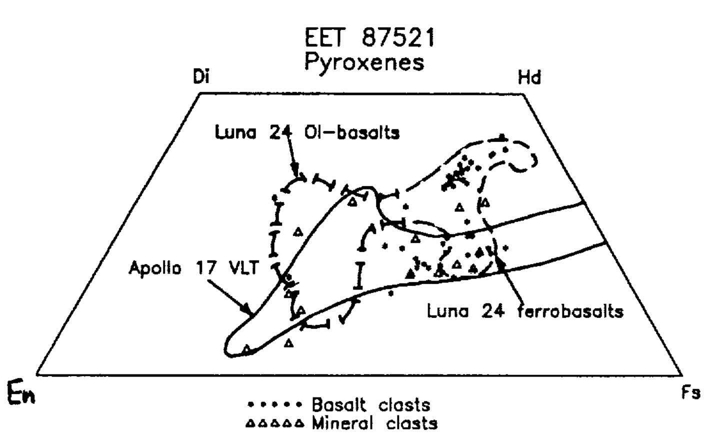
Discussion. This study demonstrates that the ferrobasalts and the olivine pyroxenites are main lithological components in the

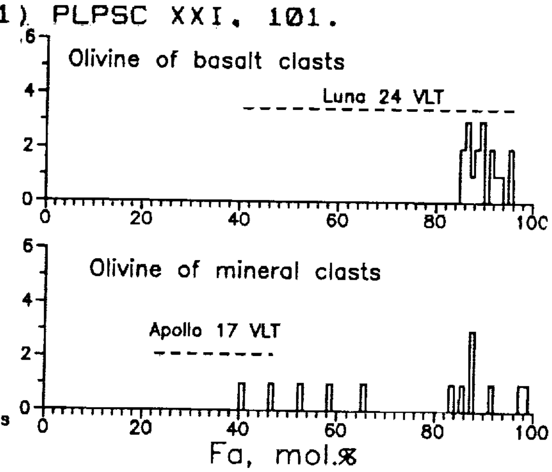
EET 87521 breccia. The bulk composition of the breccia [2] can be well modelled by mixing of the ferrobasalt (65%) and the olivine pyroxenite (35%) that supports the petrological observations. Some deviations from this model can be explained by a contribution of a few percents of Mg-rich olivine and ilmenite which are present in EET 87521 as monomineralic fragments. The EET 87521 ferrobasalt is much higher in Al and lower in Fe, Mg and Ti when compared to the Luna 24 VLT basalt. However in chemical and mineral compositions the EET 87521 ferrobasalt is close to the cristobalite gabbro 24170 described in the Luna 24 soil [4]. The EET 87521 olivine pyroxenites were not found in Luna 24 samples. These rocks resemble the Luna 24 metabasalts in their texture, but they are much higher in olivine and pyroxene relative to the metabasalts. Because the bulk composition of EET 87521 is close to that of the Luna 24 VLT basalt and can be approximated by mixing of the ferrobasalt and the olivine pyroxenite, we suggest that the main EET 87521 lithologies can be complementary cumulates formed from the Luna 24 VLT magma. The fine-grained, equigranular texture of the pyroxenites assumes that the rocks underwent a thermal metamorphism after their crystallization.

Additional components of the EET 87521 breccia can be inferred from the chemistry of the monomineralic fragments and mixing model calculations. The Mg-rich olivine and pyroxene fragments as well as the Al-Ti-chomite grains can be derived from a Mg-rich cumulate. The olivine gabbro, found in the Luna 24 soil [4], have a similar mineral chemistry and, hence, this rock can be a source for these monomineralic grains. The Na-rich feldspar grains cannot be related also to VLT basalts containing a less sodic plagioclase. These grains could be derived from KREEP or quartz monzodiorite rocks which have the same feldspar compositions [5-7]. A contamination of EET 87521 with a KREEP material has been suggested from trace element data [1,2].

Acknowledgments: We are grateful to Dr. M.Lindstrom and to the Meteorite Working Group for the opportunity to study this very interesting meteorite.

References: [1] J.S.Delaney et al.(1990) 15 Symp. on Antar.Met.,116; [2] M.M.Lindstrom et al.(1991) LPSC XXII,817; [3] P.H.Warren and G.W.Kallemeyn (1989) GCA 53, 3323-3330; [4] L.S.Tarasov et al. (1977) PLSC 8th, 3333-3356; [5] D.T.Vaniman and J.J.Papike (1980) PLSC, 271-337; [6] U.B.Marvin et al. (1991) PLPSC XX, 119; [7] B.L.Jolliff (1991) PLPSC XXI, 101.





S//7-25
ABS. ONLY N94-20753
p. 2

MAGNETIC PROPERTIES AND MÖSSBAUER ANALYSES OF GLASS FROM THE K-T BOUNDARY, BELOC, HAITI; F. E. Senftle and A. N. Thorpe, Howard University; L. May, A. Barkatt, M. A. Adel-Hadadi, and G. S. Marbury, The Catholic University of America; G. Izett, U. S. Geological Survey; H. Sigurdsson, University of Rhode Island; F. J.-M. R. Maurasse, Florida International University.

The experimental magnetic susceptibility, the temperature-independent component of the magnetic susceptibility, the magnetization, and the Curie constant have been measured for a number of specimens of glass from the K-T boundary found at Beloc, Haiti, and the results are compared with those of similar measurements of tektites. Because the Fe^{3+}/Fe^{2+} ratio is needed to calculate the magnetic parameters, Mössbauer spectroscopic measurements were also made. The data were consistent with the classification of the Beloc glasses as tektites.

Prior to magnetic measurements, the specimens were well cleaned in acid and ultrasonically scrubbed. Initially, five of the specimens were large enough to measure individually and the effects of surface contamination on the susceptibility were found to be negligible relative to those of the bulk volume of the sample. The experimental values of the Curie constant, magnetization, and the total magnetic susceptibility fall within the known range observed for tektites. However, the temperature-independent component of the magnetic susceptibility is generally a little higher than that found for tektites [1].

Beloc glass is often considered to be the same as tektite glass [2], but the previously reported Fe^{3+}/Fe^{2+} ratio of 0.7 [3] is substantially larger than that found for tektites. Accordingly, the values of the magnetic properties mentioned above were calculated using methods which have been found to be satisfactory for calculating the magnetic properties of tektite glass [1]. Calculations made on this basis using the reported Fe^{3+}/Fe^{2+} ratio of 0.7 do not compare favorably with the experimental data. However, if continuously smaller ratios are arbitrarily used in the calculations, the calculated values of the magnetic properties approach the experimental values. The reported Fe^{3+}/Fe^{2+} ratio was therefore suspected to be too high.

To check the above possibility, the Fe^{3+}/Fe^{2+} ratio of the five large normally cleaned specimens of Beloc glass was determined by Mössbauer spectroscopy. The Fe^{3+}/Fe^{2+} ratio was found to be 0.039 ± 0.018. The sample was then chemically analyzed and found to contain 3.75 percent total iron. Using these new data, the magnetic parameters were recalculated. The results compared quite well with the experimental values.

Subsequently, two collections of small glass beads were obtained from the same site in Haiti. One sample of small beads of glass was cleaned in the usual way using acid and ultrasonic scrubbing. Even after substantial cleaning, small amounts of smectite were found in microscopic pockets and indentations on the surface. To remove any oxidized iron in the outer layer of glass which may have been altered [3], the second sample was similarly cleaned except it was also heavily etched in HF to remove the surface layer to reveal the core glass. Both the normally cleaned and core glass samples were measured by Mössbauer spectroscopy. The first sample yielded a Fe^{3+}/Fe^{2+} ratio of 0.34 ± 0.02 while the core glass had a ratio of 0.025 ± 0.003, a value close to that of tektite glass.

Using the new ratio, the calculated and experimental values agree quite well. Apparently, the presence of small amounts of smectite, which contains ferric iron, or the presence of ferric iron in the outer layers of the glass beads, is sufficient to substantially increase the Fe^{3+}/Fe^{2+} ratio. When these sources of ferric iron were removed, a true value of the

Fe^{3+}/Fe^{2+} ratio of the core glass was obtained in the Mössbauer spectroscopy measurements. Magnetic measurements of the etched glass also showed the low Fe^{3+}/Fe^{2+} ratio to be valid.

The Haiti glasses are known to exhibit a considerable chemical variability [4,5]. Thus the variable Fe^{3+}/Fe^{2+} ratio of different glass spherules, and also possibly of cores and outer layers of the glass particles, may in part reflect this general chemical variability, and thus a real variation in oxidation state. This requires further study on a larger number of samples.

It was concluded that, based on its oxidation state and the magnetic properties, the Beloc glass can be considered to belong to the same type of glass as tektites. The only difference between Haitian glass and conventional tektites was the observation that the temperature-independent component of the magnetic susceptibility is a little higher than that found for tektites, while the other magnetic parameters, including the Fe^{3+}/Fe^{2+} ratio, are within the ranges found for tektites. The temperature-independent magnetic susceptibility has been ascribed to submicroscopic metallic iron in tektites [6,7]. If the slightly higher temperature-independent susceptibility is due to a slightly higher concentration of metallic iron in Beloc glass than in other tektites, then one can consider the Beloc glass as being essentially the same as normal tektite glass with a slightly higher concentration of metallic iron.

References

[1] Thorpe, A. N. and Senftle, F. E. (1964) Geochim. Cosmochim. Acta, *28*, 981-94.

[2] Izett, G. A., Dalrymple, G. B. and Snee, L. W. (1991) Science, *252*, 1539-42.

[3] Oskarsson, N., Steinberg, M., Pradel, P., Helgason, O., Sigurdsson, H., and D'Hondt, S. (1991) Lunar Planet Sci., *22*, 1009.

[4] Sigurdsson, H., D'Hondt, S., Arthur, M. A., Bralower, T. J., Zachos, J. C., Fossen, M., and Channell, J. E. T. (1991) Nature, *349*, 482-487.

[5] Koeberl, C. and Sigurdsson, H. (1992) Geochim. Cosmochim. Acta, *56*, 2113-2129.

[6] Senftle, F. E. and Thorpe, A. N. (1959) Geochim. Cosmochim. Acta, *17*, 234-47.

[7] Senftle, F. E., Thorpe, A. N., and Lewis, R. R. (1964) J. Geophys. Res., *69*, 317-324.

RIFTING AT DEVANA CHASMA, VENUS: STRUCTURE AND ESTIMATION OF THE EFFECTIVE THICKNESS OF THE ELASTIC LITHOSPHERE, D. A. Senske, Jet Propulsion Laboratory, California Institute of Technology, Pasadena, CA 91109.

To understand the relationship between extension and sites on Venus interpreted to be associated with mantle upwelling, the characteristics of the northern part of Devana Chasma in Beta Regio are examined. The structure of this rift is compared to that of terrestrial continental rifts. To ascertain the degree to which the lithosphere at Beta might be thinned, estimates of lithospheric thickness are calculated using a plate flexure model. These values are compared to those determined for other parts of the planet (1, 2, 3).

Northern Devana Chasma falls along a N-S strike, covering a distance of 650 km between Theia Mons and Rhea Mons (Fig. 1). The rift crosses two major units: (1) radar-dark plains that contain numerous local volcanic centers, and (2) tesserae, an elevated, complexly deformed terrain. Small shields (diameters of 2- to 5-km) and their deposits make up a large portion of the plains, suggesting that the most recent episode of plains emplacement on this part of Beta is associated with local volcanic centers. Near 31.5° N, Devana intersects a region of tesserae that is irregular shaped in plan view. The lack of infilling of the rift by rock debris and volcanic material makes it possible to map pre-rift structure between the major border faults. In several locations, these faults strike obliquely to the tesserae fabric, indicating that the tesserae are not being formed by rifting, but are being disrupted by it.

The style of rifting varies along the length of Devana Chasma. Three zones (Fig. 1) are identify in a south to north direction, beginning North of Theia Mons and ending to the North of Rhea Mons. Within the first zone, the rift contains two distinct troughs separated by a major horst. The entire zone of deformation, including both troughs, averages 227 km wide. The second zone, is made up of a single trough (average width of 177 km), is asymmetric, and forms a half graben. The western side of the rift is bound by two major scarps separated by a distance of 60- to 85-km. Topography data show that the region between the faults is rotated in a counter clockwise direction by as much 1.5°. The third section of the rift lies completely within and deforms a unit of tesserae. Along this section, Devana is narrowest (average width of 139 km) and is a single trough that is asymmetric.

Comparison to terrestrial rifts. Previous analyses have likened Devana Chasma to terrestrial continental rifts (4). To assess the similarity and differences between extensional zones on Venus and Earth, the structure of terrestrial rifts are compared to northern Devana.

Terrestrial continental rifts are typically segmented into series of en echelon basins (i.e., Baikal, Rio Grande, and East African rifts (5, 6, 7, 8)). In cross section, they are half graben with the throw on one fault being substantially greater than that on the others. At the East African rift, the sense of asymmetry typically alternates between basins with the major border fault switching from one side of the rift to the other between consecutive basins.

Devana Chasma possesses some similarities to its terrestrial counterparts. Along part of its length, the rift is asymmetric, forming a half graben with the main border fault located on the western side of the rift. Unlike terrestrial rifts that are made up of interconnected basins, Devana is a single trough. Also, unlike a number of terrestrial rifts, the major border fault does not switch back and forth between opposite sides of the rift.

Rift segmentation is thought to be related to reactivation of pre-existing zones of weakness in the crust (9), reorientation of stress fields during individual episodes of rifting (10), and rift propagation (11). Devana is in general not segmented. Map patterns show that northern Devana and its internal structure are oriented parallel to the fabric within the tesserae on the east flank of the highland. On the basis of its distribution and stratigraphic relationships, tesserae is suggested to underlie a greater part of Beta (12). If this is the case, then the N-S strike of Devana may be controlled by pre-existing structure. If rift segmentation is caused by the reorientation of stresses, then the continuous linear nature of Devana may indicate that extension has persisted along an E-W trend for much of the rift's history.

Flexural Model of Flanking Rift Structure. To examine the properties of the subsurface at Beta, topography profiles of the uplifted rift flanks are used to evaluate a model of lithospheric flexure at Devana. The results of this analysis provide an estimate of the effective thickness of the elastic part of the lithosphere. To constrain this thickness, the concave structure of the rift flanks is matched by calculating the deflection of a thin plate due to the mass deficit at the rift.

Two profiles striking perpendicular to Devana are modeled. The first profile is located within a unit of tesserae, just to the North of Rhea Mons (Fig. 2). Models with plate thicknesses of 30- to 40-km provide good fits to the structure of the eastern flank. The fit for the western flank is not as well constrained, with approximately 1- to 2-km of residual topography present. The western border fault in this area is associated with a part of the rift that is an asymmetric half graben. If this fault penetrates to a great depth, then a broken plate model may be more appropriate. The second profile, to the North of Theia Mons, crosses the part of Devana where two distinct troughs are present (Fig. 2). The flanking structure is best fit by a plate with a thickness of 20- to 30-km. Plates with greater thicknesses also provide good fits to the observed topography, suggesting that the values calculated here may represent a lower bound on the thickness of the elastic layer.

Conclusions. Extensional deformation at Beta is restricted to the 139- to 227-km wide zone of rifting at Devana. Evidence showing a lack of large-scale offset of features suggests that extension is limited and is interpreted to be actively driven by dynamic processes in the mantle. Plate flexure models indicate effective lithospheric thicknesses comparable to those at coronae (35- to 40-km) (2) and substantially greater than those at Freyja Mons (11- to 18-km) (1) and Juno Dorsa (8- to 20-km) (3). The implication for thicknesses obtained here suggests that in comparison to the low land plains (2, 3), the lithosphere at Beta may not be substantially thinned. Depending on its composition, a thick lithosphere may act as a barrier, preventing the upward migration of magma. This might explain the lack of volcanic deposits within Devana. If relatively large amounts of magma are not reaching the surface, then much of the domical structure of topography may be the result of intrusion, underplating and dynamic uplift by the plume rather than volcanic construction.

References: (1) Solomon, S. C. and J. W. Head, *Geophys. Res. Lett.*, 17, 1393-1396, 1990. (2) Sandwell, D. T. and G. Schubert, *J. Geophys. Res.*, 97, 16069-16083, 1992. (3) Evans, S. A., *et al.*, *Inter. Colloq. on Venus*, 30-32, 1992. (4) McGill, G. E., *et al.*, *Geophys. Res. Lett.*, 8, 737-740, 1981. (5) Logatchev, Y. A. *et al.*, *Tectonophysics*, 94, 223-240, 1983. (6) Kelly, V. C., in Rio Grande Rift: Tectonics and Magmatism, pp. 57-70, AGU, Washington, D.C., 1979. (7) Bosworth, W., *et al.*, *Eos Trans.*, 577-583, 1986. (8) Ebinger, C., *Tectonics*, 8, 117-133, 1989. (9) McConnell, R. B., *Geol. Soc. Am. Bull.*, 83, 2549-2572, 1972. (10) Ebinger, C., *Geol. Soc. Am. Bull.* 101, 885-903, 1989. (11) Bosworth, W., *Nature*, 316, 625-627, 1985. (12) Senske, D. A., *et al.*, *Geophys. Res. Lett.*, 18, 1159-1162, 1991.

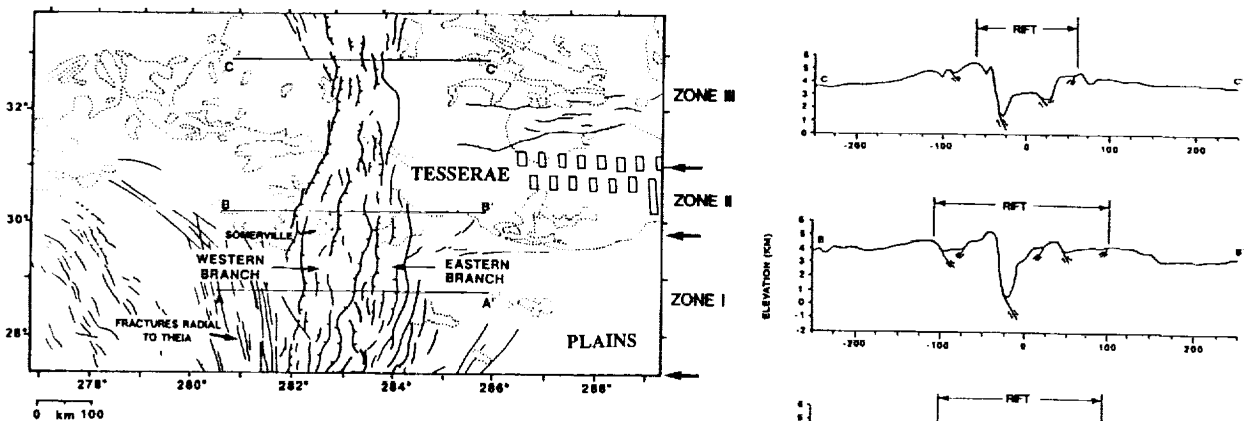


Fig. 1 Map showing fault patterns and variability in structure along the strike of Devana Chasma. The rift crosses two units, radar-dark plains and tesserae (outlined by the dotted pattern).

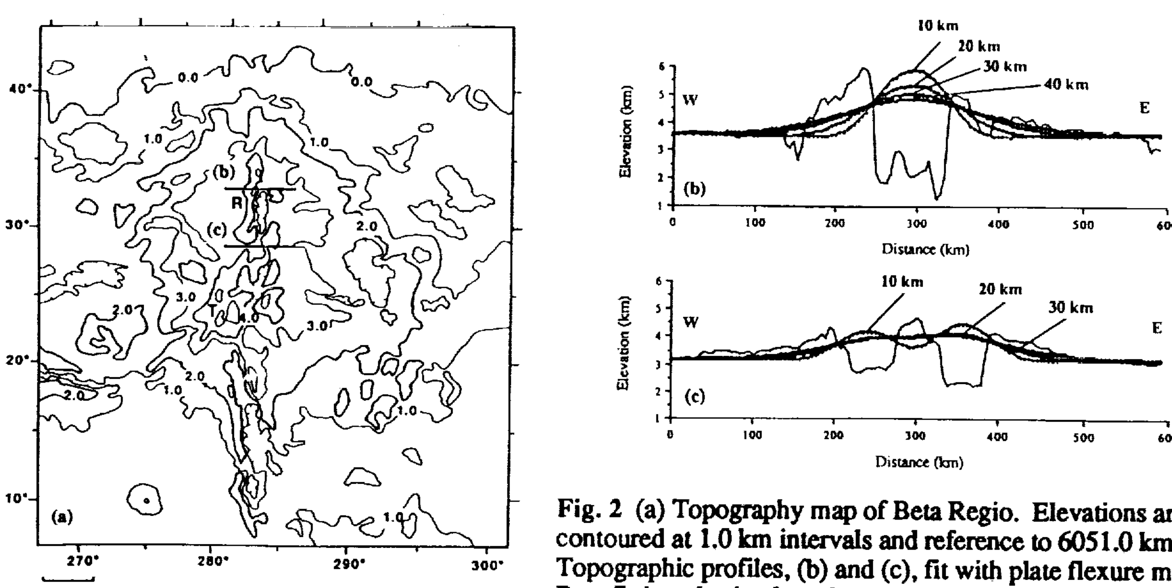


Fig. 2 (a) Topography map of Beta Regio. Elevations are contoured at 1.0 km intervals and reference to 6051.0 km. Topographic profiles, (b) and (c), fit with plate flexure models. Best fitting elastic plates have thicknesses of 20- to 40-km.

VOLCANIC RISES ON VENUS: GEOLOGY, FORMATION, AND SEQUENCE OF EVOLUTION, D. A. Senske[1], E. R. Stofan[1], D. L. Bindschadler[2], and S. E. Smrekar[1], [1]Jet Propulsion Laboratory, California Institute of Technology, Pasadena, CA, 91109, [2]Dept. of Earth and Space Sciences, UCLA, Los Angeles, CA 90024.

Introduction. Large centers of volcanism on Venus are concentrated primarily in the equatorial region of the planet and are associated with regional topographic rises. Analysis of both radar images and geophysical data suggest that these uplands are sites of mantle upwelling [1-6]. Magellan radar imaging provides a globally contiguous data set from which the geology of these regions is evaluated and compared. In addition, high resolution gravity data currently being collected provide a basis to assess the relationship between these uplands and processes in the planet's interior. Studies of the geology of the three largest volcanic highlands (Beta Regio, Atla Regio, Western Eistla Regio) show them to be distinct, having a range of volcanic and tectonic characteristics [1]. In addition to these large areas, a number of smaller uplands are identified and are being analyzed (Bell Regio, Imdr Regio, Dione Regio (Ushas, Innini, and Hathor Montes), Themis Regio). To understand better the mechanisms by which these volcanic rises form and evolve, we assess their geologic and geophysical characteristics.

Characteristics of Major Centers of Volcanism. The geologic characteristics of the volcanic rises are shown in Table I. On the basis of the relative contributions of tectonism and volcanism, four classes of features are established. The first class contains extensive arrays of rifts that converge on highlands (Beta Regio and Atla Regio). These extensional belts are part of a system of global-scale deformation zones [7]. Geophysical data show Beta and Atla to have large geoid to topography ratios (GTR's), indicating apparent depths of compensation (ADC) in excess of 250 km [2, 4]. Significant differences between these uplands include the distribution of coronae and presence of tesserae. Coronae and tesserae are abundant at Beta but are not present at Atla. The second class of features are distinguished by the presence of large volcanoes (Western Eistla Regio, Dione Regio, Imdr Regio) with rifting being a less significant process. Compared to Beta and Atla, Western Eistla is compensated at a shallower depth (ADC ~ 200 km [6]), suggesting that the plume may be closer to the surface. Tesserae make up only a minor part of these areas with coronae being significant at Western Eistla. The third class of highlands are characterized almost exclusively by large-scale volcanism forming edifices and coronae (Bell Regio). Unlike the other rises, Bell lacks evidence for zones of rifting. On the basis of it's GTR, Bell is interpreted to be compensated at depth similar to Western Eistla [2]. The final class of rises is characterized by coronae that are interlinked or connected by linear extensional belts (Themis Regio) [8]. Due to its location in the southern high latitudes, gravity data obtain by the Pioneer Venus Orbiter (PVO) were not of sufficient resolution to determine an ADC for Themis. Likewise, ADC's have not been calculated for Dione and Imdr Regiones.

Interpretations. On the basis of geophysical and stratigraphic relationships, we suggest that the range of geologic characteristics may represent different stages in the evolution of a plume. This sequence is characterized by: (1) updoming and extension forming major rift zones (Beta and Atla). The larger GTR at Beta may indicate that it is in an earlier stage of formation relative to Atla; (2) a period where the plume is at a shallower depth with surface geology dominated by edifice construction and rift infilling (Western Eistla, Dione, Imdr); (3) continued edifice construction and relaxation of volcanoes, forming coronae (Bell Regio). Compressional ridges along eastern part of the corona, Nefertiti, in Bell Regio are interpreted to have formed by relaxation of a large volcano [8]. Within the framework of this model, Themis appears to be anomalous. In comparison to the large highlands, its formation may be related to the presence of smaller scale mantle instabilities [8]. Because of the insufficient resolution of PVO gravity data, GTR's have not been calculated for number of the volcanic rises. Data currently being collected by Magellan and those proposed to be collected when the spacecraft orbit is circularized will greatly improve estimates of ADC for structures at high latitudes. These data will provide a stronger basis for linking surface geology to dynamic processes in the Venus mantle.

References: [1] Senske *et al.*, *J. Geophys. Res.*, 13395-13420, 1992. [2] Esposito, P. B. *et al.*, *Icarus*, 51, 448-459, 1982. [3] Bindschadler *et al.*, *J. Geophys. Res.*, 97, 13495-13532. [4] Smrekar S. E. and R. J. Phillips, *EPSL*, 107, 582-597,1991. [5] Kiefer, W. S. and B. H. Hagar, *J. Geophys. Res.*, 91, 403-419, 1991. [6] Grimm, R. E., and R. J. Phillips, *J. Geophys. Res.*, 97, 16035-16054, 1992. [7] Schaber, G. G., *GRL*, 499-502, 1982. [8] Stofan *et al.*, *J. Geophys. Res.*, 97, 13347-13378, 1992.

VOLCANIC RISES ON VENUS: Senske, D. A. et al.

TABLE I: CHARACTERISTICS OF MAJOR VOLCANIC RISES

Feature	Primary Processes	GTR*	Maximum Height of Rise (km)	Contribution of volcanism	Presence of coronae	Presence of Rifts	Presence of Tesserae	Regional Setting
I. Rift Dominated								
Beta Regio	Rifting & uplift >> volcanism	31	3.0	Low/moderate	Along periphery	3 major rifts	Major	Rift junction
Atla Regio	Rifting > volcanism	23	~4.0	High	None	5 major rifts	None	Rift junction
II. Volcano Dominated								
W. Eistla Regio	Volcanism > rifting	~19	2.0	High	Central part of highland	1 rift	Minor	Plains
Dione Regio	Volcanism > rifting	?	1.0	High	None	Moderate	Minor	Plains
Imdr Regio	Volcanism ~ rifting	?	0.5-1.0	Moderate	None	Moderate	Minor	Plains
III. No Rifts								
Bell Regio	Volcanism > uplift	21	1.5	High	Central part of highland	None	Minor	Plains
IV. Corona Dominated								
Themis Regio	Coronae >> uplift & rifting	?	0.5-1.0	Low/moderate	Corona chain	Moderate	None	Rift/corona chain

* From Smrekar and Phillips, Earth and Planet. Sci. Letters, 107, 582-597,1991

MOLECULAR EQUILIBRIA AND CONDENSATION SEQUENCES IN CARBON RICH GASES;

C. M. Sharp, Commissariat a L'Energie Atomique, Centre de Etudes, de Limeil-Valenton, France F94195, G. J. Wasserburg, Lunatic Asylum, California Institute of Technology, Pasadena, CA

Chemical equilibria in stellar atmospheres have been investigated by many authors. Lattimer, Schramm and Grossman [1] presented calculations in both O rich and C rich environments and predicted possible presolar condensates. A recent paper by Cherchneff and Barker [2] considered a C rich composition with PAHs included in the calculations. However, the condensation sequences of C bearing species have not been investigated in detail. In a carbon rich gas surrounding an AGB star, it is often assumed that graphite (or diamond) condenses out before TiC and SiC. However, Lattimer et al. [1] found some conditions under which TiC condenses before graphite. We have performed molecular equilibrium calculations to establish the stability fields of C(s), TiC(s), and SiC(s) and other high temperature phases under conditions of different pressures and C/O. The preserved presolar interstellar dust grains so far discovered in meteorites are graphite, diamond, SiC, TiC [3,4,5,6] and possibly Al_2O_3 [7]. A striking study of the internal morphology of a few of these grains by Bernatowicz et al. [5] showed that in some cases TiC crystals are found inside of graphite spherules. There is a suggestion that this information could be used to infer the conditions of their formation. Following Sharp [8], a solar mixture was used with the 20 most abundant elements, except carbon which was allowed to vary. Following Sharp and Huebner [9] calculations were performed between 2000 and 1250 K for C/O ratios between 1.02 to 2.00 and for pressures between 0.05 and 500 dyne/cm^2. Equilibria were calculated both with and without condensed species included. The most abundant species were generally in good agreement with those of Cherchneff and Barker [2]. As virtually all oxygen is bound in CO, it is convenient to define the fraction of carbon that is not in CO but is taken up by species y, $f^{y}_{(C)-CO} \equiv \nu_{Cy} n_y/(n_{(C)} - n_{CO})$ where n_y and n_{CO} are respectively the number densities of y and of CO and $n_{(C)}$ the total abundance of carbon in all species and phases and ν_{Cy} is the stoichiometric coefficient of carbon in y. Figure 1 is a plot of the log of these fractions (>1%) against 1000/T at C/O = 1.122 and P = 0.05, 50 and 500 dyne/cm^2 (where $n_{(C)} = 1.6 \times 10^8$cm^{-3} at 2000 K and 0.05 dyne/cm^2), with condensation included (solid curves) and neglected (dashed curves), and with the condensation temperatures of graphite, SiC and TiC indicated by vertical dotted lines. The curves showing the fractions in condensates are labelled C and SiC. Of particular interest is that, except just below its condensation temperature, the curve for graphite follows closely that of C_2H_2 when condensation was neglected. We believe that in most regions graphite condensation is governed by the reaction $C_2H_2 \rightleftarrows 2\,C(s) + H_2$ (i.e. C_2H_2 is converted to graphite or diamond) with an equilibrium constant $K(T) = \ln\ P_{H_2}/P_{C_2H_2}$. Insofar as $P_{H_2}/P_{C_2H_2}$ is approximately constant, then the condensation of graphite is independent of temperature. The temperature shifts in the graphite condensation curves with increase in C/O mostly result from an increase in the partial pressure of C_2H_2 by the factor [(C/O) - 1] due to increases in the amount of free carbon since (O/H) has been held constant. For the cases of TiC(s) and SiC(s) we believe that their condensation is governed by the reaction $C_2H_2 + 2Ti(Si) \rightleftarrows 2TiC\ (SiC)(s) + H_2$. Insofar as $P_{C_2H_2}/P_{H_2}$ is constant and as P_{Ti}/P_{H_2} is constant up till condensation, there is a strong dependence of condensation temperature on total pressure. The stability fields are shown in Figure 2. For simplicity we have shown the TiC and SiC condensation curves for C/O = 1.29 as they shift only slightly over the total range of C/O investigated. It can be seen that TiC always condenses before SiC. For a given C/O value, high pressures favor TiC condensation over graphite. For P < 500 dyne/cm^2 graphite is the first phase to condense at C/O = 1.51. At lower C/O values the stability region of TiC expands to give TiC condensing before graphite. We note that the ratio of condensed C to SiC is ~5 at C/O = 1.122 at ~ 1400 K. This is increased with substantially higher C/O ratios. Substantial Si is in the gas phase as SiO and SiS. We also investigated the nitrogen fractions. As expected, most remaining nitrogen after N_2 (by far the most abundant species) is HCN and CN at 2000 K. However of particular interest at high pressures and low temperatures, the condensate AlN plays an important role and below about 1400 K for all pressures considered, a significant fraction of the remaining nitrogen is in PN in spite of the low abundance of

phosphorous. No Al or N compounds were identified that condensed in the same high T region as SiC or TiC. AlN always appears to condense at 1368 K for all C/O > 1 at 500 dyne/cm^2 and disappears at 1200 K. TiN is the first condensing species for C/O ~ 0.98. We infer that the Al and N in interstellar SiC and graphite must be in solid solution. Division Contribution 5228(792).

References: [1]Lattimer J., Schramm M. and Grossman L. (1978) *Ap. J. 218m*, 230. [2]Cherchneff I. and Barker J.R. (1992) *Ap. J. 994*, 703. [3]Amari S., Anders E., Virag A., and Zinner E. (1990) *Nature 345*, 238. [4]Lewis, R., Tang, M., Walker, J, Anders, E. and Steele, E. 1987, *Nature 326*, 160. [5]Bernatowicz T., Amari S., Zinner E. and Lewis R. (1991) *Ap. J. 373*, L73. [6]Zinner E., Tang M. and Anders E. (1987) *Nature 330*, 730. [7]Huss G.R., Hutcheon I. D., Wasserburg G.J. and Stone J. (1991) *LPSC XXIII*, 563. [8]Sharp C.M. (1992) *Highlights of Astronomy, Trans XXIst I.A.U. General Assembly, v. XX*, Kluwer Academic Publishers. [9]Sharp C.M. and Huebner W.F. (1990) *Ap. J. Suppl. Ser., 72*, 417.

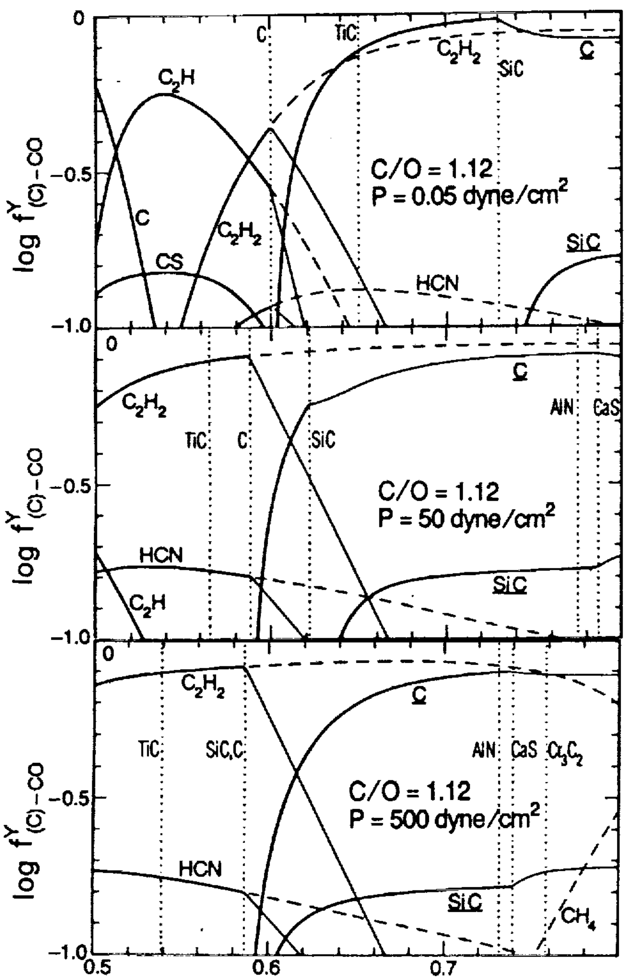


Figure 1. 1000/T with T in K

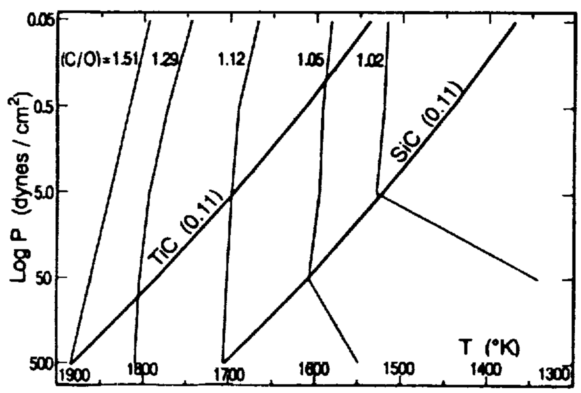


Figure 2.

Fig. 1. The fraction of total carbon that is not in CO is plotted vs 1/T for equilibrium condensation at C/O = 1.12 at three different pressures. Species without bars are in the gas phase, species with bars are condensed phases (C, SiC). The dashed curves are the values without condensation. Vertical dotted lines indicate condensation of a phase. Note that at 500 dyne/cm^2 SiC and graphite condense at the same temperature. Fig.2. Condensation temperature as a function of pressure. The curves labelled TiC(0.11) and SiC (0.11) are the condensation curves for these phases at C/O = 1.29. These curves are not sensitive to C/O. The curves with C/O ratios indicated are the graphite condensation curves. These are not strongly pressure dependent except in the neighborhood of C/O ≈ 1 where competing reactions interfere. Note the appearance of SiC before graphite for high D, low C/O.

S121-46 ABS. ONLY

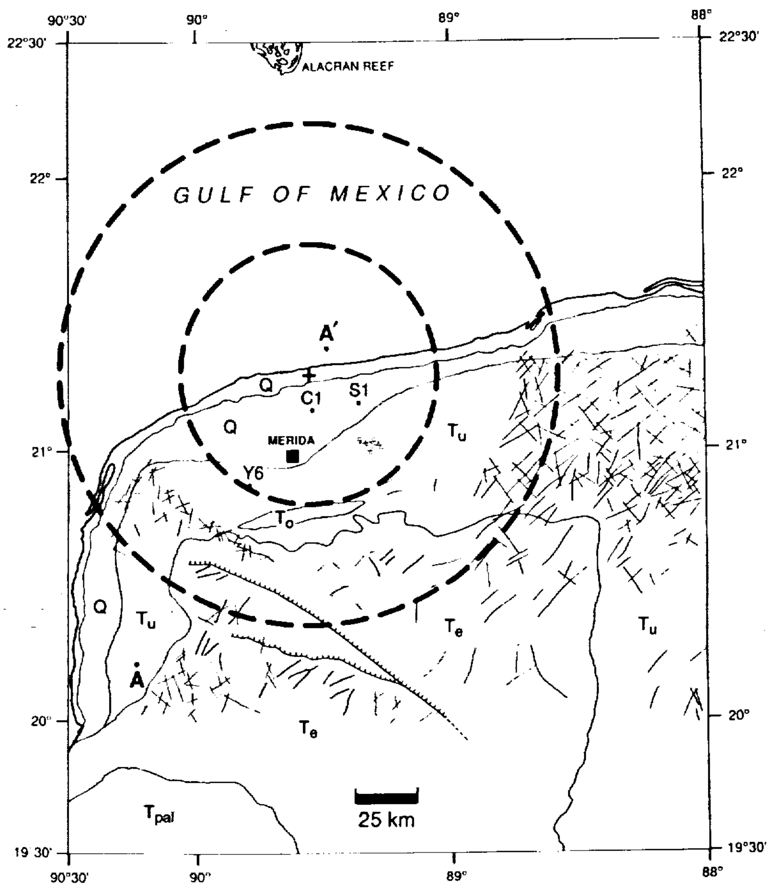
N94-20757

p. 2

CHICXULUB IMPACT BASIN: GRAVITY CHARACTERISTICS AND IMPLICATIONS FOR BASIN MORPHOLOGY AND DEEP STRUCTURE; Virgil L. Sharpton[1], Kevin Burke[2], Stuart A. Hall[2], Scott Lee[1], Luis E. Marín[3], Gerardo Suarez[3], Juan Manuel Quezada-Muñeton[4], and Jaime Urrutia-Fucugauchi[3], [1]*LPI, 3600 Bay Area Blvd., Houston TX 77058 (713-486-2111),* [2]*Dept. of Geosciences, University of Houston, Houston TX 77004, Instituto de Geofisica,* [3]*UNAM, Mexico City, Mexico 04510,* [4]*Gerencia de Exploración, Petróleos Mexicanos, Marina Nacional 329, Mexico City, Mexico 11311.*

The K-T-aged Chicxulub Impact Structure **[1-4]** is buried beneath the Tertiary carbonate rocks of the Northern Yucatán Platform *(Figure 1)*. Consequently its morphology and structure are poorly understood. Reprocessed Bouguer (onshore) and Free Air (offshore) gravity data over Northern Yucatán *(Figure 2)* reveal that Chicxulub may be a 200-km-diameter multi-ring impact basin with at least three concentric basin rings.

Figure 1: Surface Geology and Basin Rings of Chicxulub Multi-ring Basin, Yucatán. Inner circle: peak ring; outer circle: rim location.



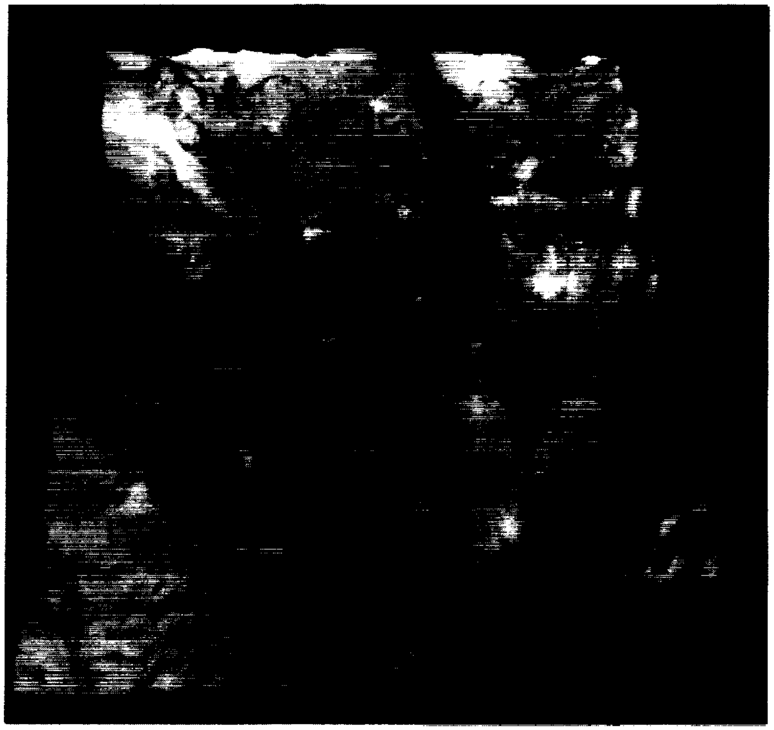
Ring Spacing and Basin Size: The positions of these rings follow the $\sqrt{2}$ spacing rule derived empirically from analysis of multi-ring basins on other planets, indicating that these rings probably correspond to now-buried topographic basin rings **[5]**. A forward model *(Figure 3)* of the gravity data along a radial transect from the southwest margin of the structure (A-A'; *Figure 1)* indicates that the Chicxulub gravity signature is compatible with this interpretation. We estimate the basin rim diameter to be 204 ± 16 km and the central peak ring diameter (D) is 104 ± 6 km. This ring assignment places the highly magnetic zone of **[1]** within the central ring (central uplift), and the weakly magnetic zone inside the basin rim, suggesting that the magnetic source is related to deep rocks uplifted and melted in the center of the structure. Steep gravity gradients located 25-40 km inside the rim could mark the outward extent of relatively deep basin excavation and deformation. Segments of an intermediate ring (D = 150 ± 16 km) are evident in *Figure 2* just inside the steep gradients.

Deep Structure: Figure 2 further reveals that the weak concentric expression in the northwest quadrant of the basin is not due to post-impact truncation along an E-W fault as previously proposed **[2,6]** but instead may be caused by the superposition of the crater signature onto an older linear gravity high extending ~N-S through the basin. Because this linear feature is not disrupted we believe its source resides deep within the crust, and may be affected by the impact only near the crater center. During the Jurassic, the Yucatán block moved rapidly away from the U.S Gulf Coast along an anticlockwise, southward path (*e.g.,* **[7-9]**). Consequently this feature

may have resulted from earlier crustal thinning or incipient rifting associated with the opening of the Gulf of Mexico, or it could be a feature inherited from the assemblage of Pangea.

Chicxulub Basement Age and KT Boundary Implications: The pre-rift position of Yucatán, against the *Florida Escarpment* and south of the *Suwannee-Wiggins Suture Zone* **[8,9]** indicates that the basement under Chicxulub is Pan-African Terrane (*e.g.*, **[9,10]**), like the crystalline basement of the Florida Peninsula (*i.e.*, 500 ± 150 Ma). The major linear features in gravity and magnetic data covering the Yucatán Platform, such as the *Alacrán High* and the *Vallodolid Low* (*e.g.*, **[11]**) are concordant with features in Florida. Furthermore, samples of crystalline basement recovered from offshore NE Yucatán in DSDP Leg 77 Holes 537 and 538A have ^{40}Ar-^{39}Ar metamorphic ages of ~500 Ma **[12]**. Consequently, the 550 Ma U-Pb ages of zircons from the *upper* member of the KT boundary layer in the Western US **[13]** may implicate Chicxulub rather than Manson in the formation of this layer.

Figure 2: Perspective view of gravity data for region shown in *Figure 1*. Viewing and lighting are toward North. Gravity values range from -20 to +50 MGal.



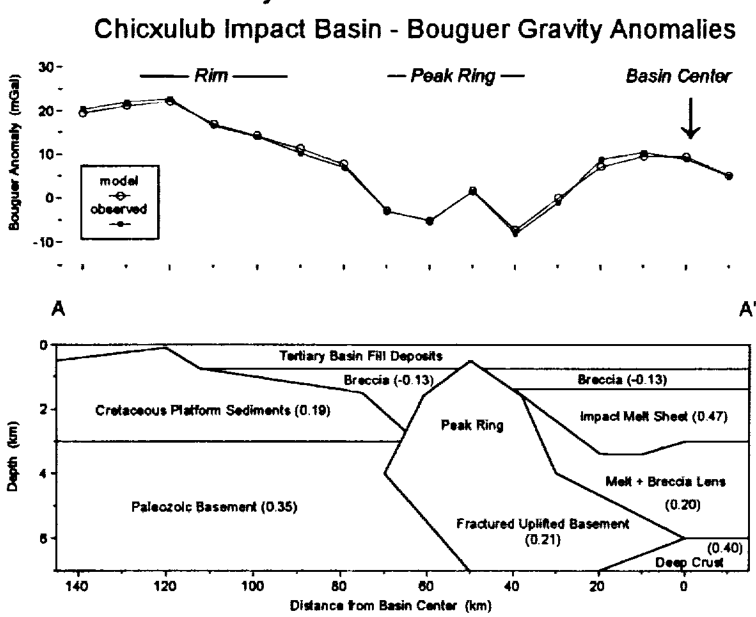


Figure 3: Forward model of radial gravity profile (A-A'; *Figure 1*) of Chicxulub Impact Basin. Numbers in parentheses show $\Delta\rho$ used in modeling. Stratigraphy is consistent with drill core data.

References: **[1]** Penfield, G.T. and Camargo, A. *SEG 51st Ann. Mtg Tech. Prog.*, 37 (1981). **[2]** Hildebrand, A.R. *et al. Geology 19*, 867-871 (1991). **[3]** Swisher, C.C., *et al. Science 257*, 954-958 (1992). **[4]** Sharpton, V.L. *et al. Nature 359*, 819-821 (1992). **[5]** Spudis, P.D. and Sharpton, V.L. *(this volume)*. **[6]** Hildebrand, A.R. *et al. LPSC XXIII*, 539-540 (1992). **[7]** Pindell, J.L. *Tectonics 4*, 1-39 (1985). **[8]** Burke, K. *Ann. Rev. Earth Planet. Sci. 16*, 201-230 (1988). **[9]** Hall, S.A. and Najmuddin, I. *GSA Absts. Prog. 24:1*, 14 (1992). **[10]** Smith, D.L. *Tectonophysics 88*, 1-22 (1982). **[11]** Garcia-Abdeslem, J. *Ph.D. Thesis*, U. Oregon, 120 p. (1990). **[12]** Dallmeyer, R.D. in *Init. Repts. DSDP, 77*, 497-504 (1984). **[13]** Krough, T.E. *et al. Internat. Conf. on Large Meteorite Impacts and Planet. Evol.*, 44 (1992).

5/22-91
ABS. ONLY

N94-20758

BASALTIC MAGMATISM ON THE MOON. A PERSPECTIVE FROM VOLCANIC PICRITIC GLASSES. P-2

C.K. Shearer and J.J. Papike, Institute of Meteoritics, Department of Earth and Planetary Sciences, University of New Mexico, Albuquerque, New Mexico 87131-1126.

Introduction. It is widely accepted that basaltic magmas are products of partial fusion of peridotite within planetary mantles [1]. As such they provide valuable insights into the structure and processes of planetary interiors. Those compositions which approach primary melt compositions provide both a clearer vision of planetary interiors and a starting point at which to understand basaltic evolution. Within the collection of lunar samples returned by the Apollo and Luna missions are homogeneous, picritic glass beads of volcanic origin [2,3,4]. These glass beads provide a unique perspective concerning the origin of mare basalts, the characteristics of the lunar interior and processes culminating in the in the early differentiation of the moon. In this presentation, we report our ion microprobe derived trace element data from all picritic glasses previously identified [3]. We place this trace element data and literature isotopic and experimental data on the picritic glasses within the framework of mare basaltic magmatism.

Analytical Procedures. Electron microprobe techniques and criteria established by Delano [3] were used to identify picritic glasses of volcanic origin. Glasses were identified from all the Apollo landing sites. The glasses were than analyzed for REE, Ba, Sr, V, Cr, Ti, and Zr using ion microprobes. Most of these analyses were accomplished using the ion microprobe at Woods Hole Oceanographic Institute (WHOI). Additional glass analyses were performed at the ion microprobe facility at the University of New Mexico.

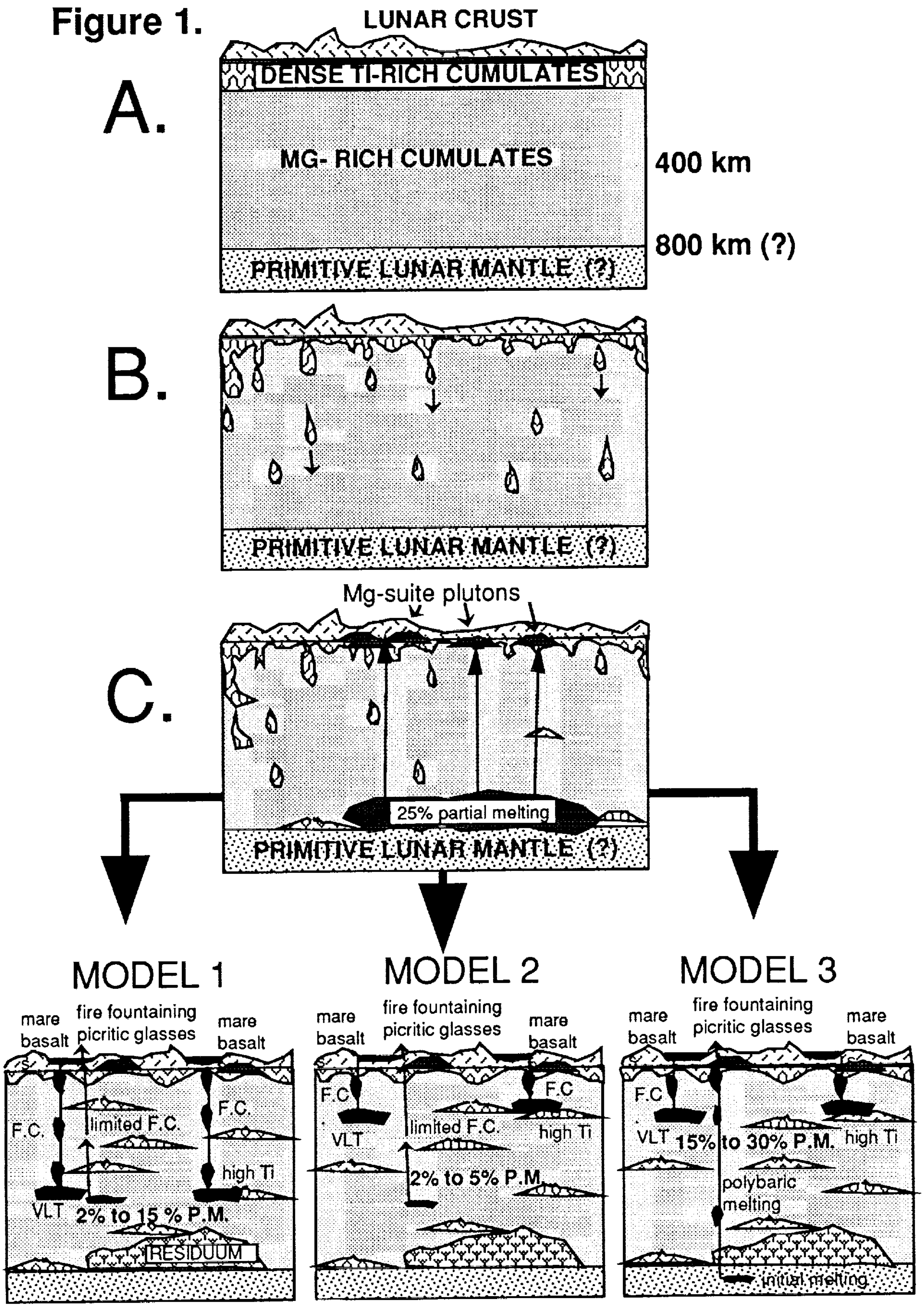
Results. The trace element data on the glass beads illustrate a wide diversity of trace element characteristics. For example, the lunar glasses show a wide range in REE pattern shape and concentration [5]. Like the crystalline mare basalts, all picritic glasses have a consistent negative Eu anomaly. Unlike the crystalline mare basalts, there is a limited correlation between the extent of the Eu anomaly and overall REE concentrations. Trace element differences among the various glasses suggests that a KREEP component was incorporated into their mantle source. This implies large scale mixing of the "Lunar Magma Ocean" derived cumulate pile. Several lines of evidence are consistent with the view that the picritic glasses are derived from mantle sources that are compositionally distinct from the sources for crystalline mare basalts. These are: (1) parallel, but no common, liquid lines of descent; (2) chemical differences between picritic glasses and the more primitive crystalline mare basalts; (3) experimental studies indicate the picritic glasses are multiply saturated at depths greater than that of the mare basalts [6]; (4) differences in Pb isotopic data [7,8]; and (5) the mode of eruption (i.e. fire fountaining) indicates a somewhat more volatile-rich source for the picritic glasses.

Discussion. Our suggested models for the generation of lunar picritic magmas and their relationship to mare basalts are illustrated in Figure 1. These models include the evolution of the mantle source for the lunar basalts (A-C) and possible models for the generation of lunar basalts (1-3). The stages of mantle evolution are **A.** Formation of cumulate pile and lunar crust through the crystallization of a lunar magma ocean. The depth of the cumulate pile and the existence of an unprocessed, primitive lunar mantle is unknown. **B.** Development of gravitational instability due to sinking of late-stage Ti-rich cumulates through less dense Mg-rich cumulates at subsolidus conditions. Various cumulate lithologies were transported to depths greater than 300 km. **C.** Partial melting of the lower cumulate pile to generate Mg-suite plutons. Possible melting models for the generation of mare basaltic magmas include: (1) Partial melting of heterogeneous lunar mantle at depths greater than 300 Km. Picritic magmas represented by glass beads were erupted to the surface with limited fractional crystallization. Mare basalts were produced by 15-30% fractional crystallization of similar (but not identical) picritic magmas. (2) Picritic magmas represented by the glass beads are generated at depths greater than 400 Km in volatile enriched (relative to the mare basalt source) heterogeneous mantle. Mare basalts are fractional crystallization products of picritic magmas generated at depths of less than 400 Km. (3) Mare basalts represent products of fractional crystallization of picritic magmas generated at depths of less than 400 Km. The picritic magmas represented by the glass beads represent polybaric melting [6]. Initial melting began at depths of at least 1000 Km [6]. A primitive (or less processed) mantle component and cumulate mantle components were melted during this polybaric process.

References. [1] Bowen (1928) The evolution of igneous rocks, 334p [2] Meyer et al. (1975) Proc. LPSC 6, 1673-1699 [3] Delano and Livi (1981) GCA 45, 2137-2149 [4] Delano (1986) Proc. LPSC 16, D201-D213 [5] Shearer and Papike (1993) GCA in review [6] Longhi (1992) GCA 56, 2235-2252 [7] Tera and Wasserburg (1976) LS VII, 858-860 [8] Tatsumoto et al. (1987) Proc. LPSC 17, E361-E371.

Acknowledgment. This research was funded by NASA Grant NAG-497 (J.J. Papike, P.I.)

Figure 1.


LUNAR CRUST
A.
DENSE TI-RICH CUMULATES
MG- RICH CUMULATES
400 km
800 km (?)
PRIMITIVE LUNAR MANTLE (?)
B.
PRIMITIVE LUNAR MANTLE (?)
Mg-suite plutons
C.
25% partial melting
PRIMITIVE LUNAR MANTLE (?)
MODEL 1
mare basalt
fire fountaining picritic glasses
mare basalt
F.C.
limited F.C.
F.C.
high Ti
VLT
2% to 15 % P.M.
RESIDUUM
MODEL 2
mare basalt
fire fountaining picritic glasses
mare basalt
F.C
F.C
VLT
limited F.C.
high Ti
2% to 5% P.M.
MODEL 3
mare basalt
fire fountaining picritic glasses
mare basalt
F.C
VLT
15% to 30% P.M.
high Ti
polybaric melting
initial melting

5123-25 ABS ONLY

N94-20759

P. 2

ORIGIN OF THE APOLLO 15 VERY LOW TI GREEN GLASS. A PERSPECTIVE FROM THE COMPOSITIONAL DIVERSITY IN THE VERY LOW TI GLASSES. C. K. Shearer and J.J. Papike. Institute of Meteoritics, Department of Earth and Planetary Sciences, University of New Mexico, Albuquerque, New Mexico, 87131-1126.

Introduction. The very low Ti green glasses from the Apollo 15 site have intrigued scientists for over 20 years. Their primitive composition has been used to understand magmatic processes and the structure of the moon. The compositional variability observed in the Apollo 15 glass population has long been a point of debate. Initial studies did not recognize the compositional diversity in the glasses. Stolper et al. [1] documented the major element variability and concluded it could not be produced by magmatic processes and therefore concluded that these glasses must be of impact origin. Subsequent studies confirmed a volcanic origin for the glass population and attempted to elucidate magmatic processes to account for its compositional variability. Models that have been proposed for these glasses include (1) the crystallization of single or multiple phases (olivine, pyroxene, Fe metal, immiscible sulfide) [e.g., 2,3], (2) the incompatible behavior of Ni and Co during multiple phase crystallization at extremely low fO2 [4], and (3) magma or source mixing [5,6,7]. All of these models have problems. Type (1) models appear not to be consistent with recent trace element studies on the glasses [7], model (2) is dependent on the debatable incompatible behavior of Ni and Co, and in models of type (3) the origin and nature of mixing models are somewhat unconstrained. This study compares the Apollo 15 green glasses with the very low Ti picritic glasses from other landing sites.

Analytical Procedures. Electron microprobe techniques and criteria established by Delano [3] were used to identify the very low Ti glasses of volcanic origin. Glasses were identified from the Apollo 11, 14, 15, 16 and 17 landing sites. The glasses were than analyzed for REE, Ba, Sr, V, Cr, Ti, and Zr using ion microprobes. Most of these analyses were accomplished using the ion microprobe at Woods Hole Oceanographic Institute (WHOI). Additional glass analyses were performed at the ion microprobe facility at the University of New Mexico. The ion microprobe is a microbeam technique which allows analysis of individual electron microprobe spots on a glass bead and multiple analyses of a single bead. In addition, this technique is not hampered by weighing errors, equating microprobe spots with bulk analysis, and contamination by deposits on bead surfaces or in cracks as is the case with INAA techniques.

Results. Fig. 1 illustrates the relative major element relationships among the more Mg-rich members of each suite of glasses (TiO_2 = 0.25 to 1.10 wt. percent). As illustrated in numerous major [1,2] and trace element [4,5,6,7] studies of the A-15 green glasses, MgO is (+) correlated to SiO_2. Co is (+) correlated to incompatible elements such as REE, Y, Zr, and Ba (Fig. 2) [5,6,7]. Fig. 2 compares the very low Ti glasses from the Apollo 11,14,16, and 17 sites with the Apollo 15 glasses. In these plots of incompatible elements versus Co, the Apollo 11, 16 and 17 glasses plot near the Apollo 15 glasses. The Apollo 14 glasses define a compositional range that far exceeds that observed in the Apollo 15 glasses. These compositional similarities and differences are also reflected in a plot of Sr versus Ba (Fig. 3).

Discussion. The Co versus incompatible element diagrams (Fig. 2) illustrates several points. (1) The compositional range observed in the very low Ti glasses far exceeds that of the Apollo 15 glasses. This wide range in composition cannot be accounted for by fractional crystallization or partial melting under any extreme P or fO2. This indicates that compositional heterogeneity in the lunar mantle accounts for the variability in the glass population. Therefore, compositional heterogeneity in the mantle can account for the variability observed in the Apollo 15 glasses. (2) There are two different types of trajectories in Fig. 2 (A and B). A is a result of the incorporation of a KREEP component either through assimilation or during melting (Fig. 3). B may be a mixing trajectory resulting from local compositional variability in the cumulate pile due to the sequence of crystallization, the amount of intercumulus melt, and the extent of reequlibration between the trapped melt and crystals. As illustrated in Fig. 4, these variables may result in the co-linearity of compatible and incompatible elements.

Conclusions. The wide range in trace element characteristics exhibited by the very low Ti glasses from the various Apollo landing sites indicates that the lunar mantle is itself variable and can yield a wide range of compositionally distinct very low Ti picritic magmas. Therefore, it is not surprising that the compositional variability observed in the Apollo 15 Green glass is a result of mantle inhomogeneities.

References. [1] Stolper et al. (1974) LS V, 749-751 [2] Delano (1979) Proc. LPSC 10, 275-300 [3] Grove (1981) Proc. LPSC 12B 935-948 [4] Steele et al. (1992) GCA 56, 4075-4090 [5] Delano (1986) Proc. LPSC 16,D201-D213 [6] Ma et al. (1981) Proc. LPSC 12B 915-933 [7] Galbreath et al (1990) GCA 54, 2565-2575

Acknowledgement. This research was funded by NASA Grant NAG-497 (J.J. Papike, P.I.)

A15 GREEN GLASS. C.K. Shearer and J.J. Papike

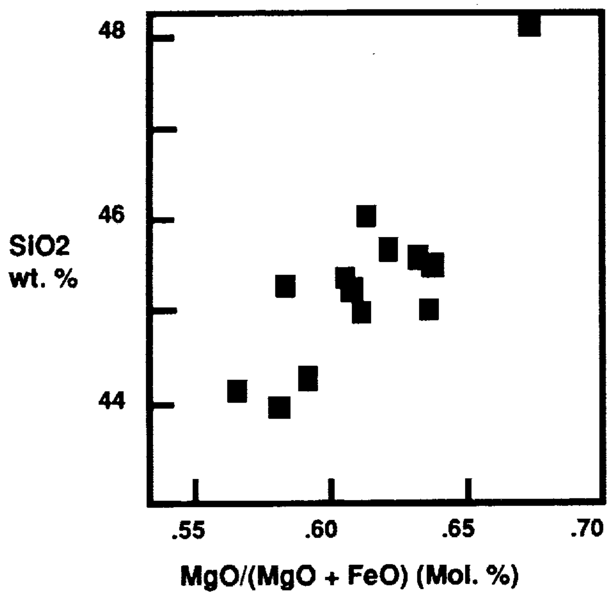


Figure 1. Plot of SiO2 wt% versus MgO/(MgO+ FeO) (Mol.%) for the more Mg glasses of the various very low Ti glass suites.

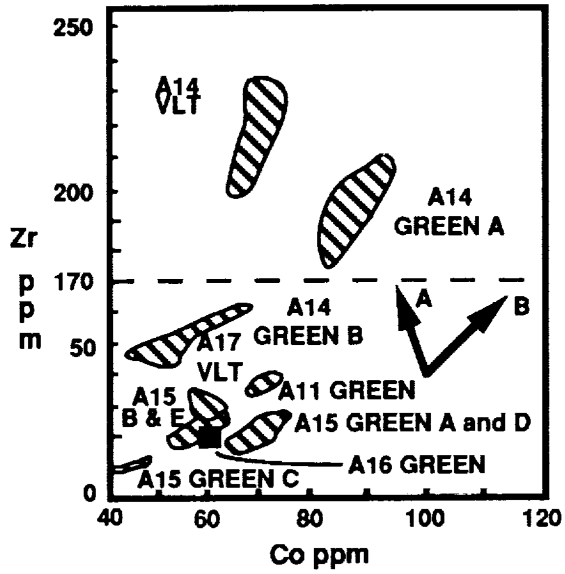


Figure 2. Plot of Zr versus Co for the very low Ti picritic glasses.

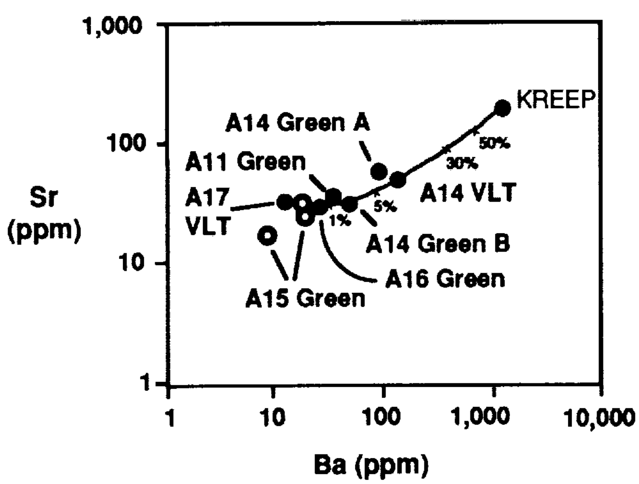


Figure 3. Plot of Ba versus Sr for the very low Ti picritic glasses. A mixing line between A15 glasses and KREEP is superimposed on diagram.

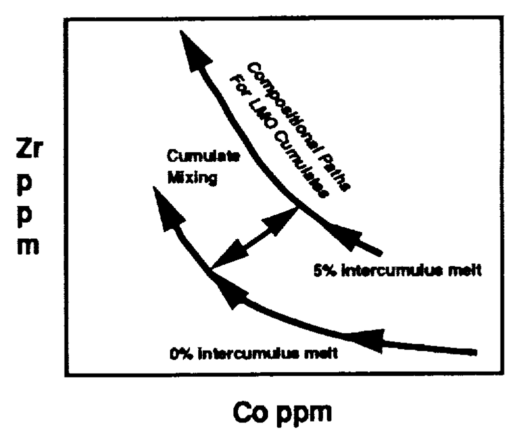


Figure 4. The diagram illustrates highly simplified evolutionary paths for two end-member cumulate sources with differing amounts of intercumulate melt. Mixing between these two hypothetical cumulates have the potential to produce hybrid mantle sources. Upon melting, these sources may produce basalts with the compositional variability exhibited by the A15 glasses.

ORTHOPYROXENES AS RECORDERS OF DIOGENITE PETROGENESIS: TRACE ELEMENT SYSTEMATICS. C.K. Shearer, J.J. Papike, and G.D. Layne. Institute of Meteoritics, Department of Earth and Planetary Sciences, University of New Mexico, Albuquerque, New Mexico, 87131-1126.

Introduction. Eucrite, howardite, and diogenite members of the achondrites are considered, by many, to be genetically related. Therefore, each provide a piece of the puzzle for reconstructing magmatic processes on the eucrite parent body (EPB). The relationship between eucrites and diogenites can be viewed within the context of two distinctly different models: (1) fractional crystallization and (2) partial melting. In fractional crystallization models [1,2,3] eucrites and diogenites represent a complementary continuum of planetary fractional crystallization products in which the diogenites represent crystal accumulations during the crystallization of eucritic magmas at shallow to deep levels in the EPB. Alternatively, experimental studies may be interpreted as indicating eucrites represent peritectic partial melts of a primitive, chondritic EPB mantle [4]. Within this type of model, the diogenites are also generally considered to be cumulates; however, their petrogenetic relationship to the eucrites is less clear. Sack et al. [5] proposed that the olivine diogenites represent residua from the partial melting events that produced eucritic liquids. Initial trace element studies of orthopyroxene (OPX) are consistent with this model [6,7]. However, this trace element modeling of the olivine diogenites is nonunique. As a further test of these models, we (1) analyzed OPX from cumulate diogenites to compare with the olivine diogenite data, (2) improved ion microprobe analytical techniques for the analysis of elements critical to our interpretations, and (3) selected more relevant Kds for OPX-eucritic melt [8,9].

Analytical Procedures. OPX from 13 diogenites were analyzed for major and minor elements using the JEOL electron microprobe (EMP) at the University of New Mexico (UNM). These results are reported by Papike et al. [10]. We selected 2 cumulate diogenites (Tatahouine, and Ibbenburen) to compare with the olivine diogenites (ALH A77256, ALH 84001) [5, 6, 7]. Points documented with the EMP were analyzed for trace elements with a Cameca IMS 4f ion microprobe. The ion microprobe is located on the UNM campus and is operated under a UNM-Sandia National Laboratories cooperative agreement. The OPX were analyzed for REE (La, Ce, Nd, Sm, Eu, Dy, Er, Yb), Cr, V, Sr, Ti, Zr, and Nb. We were able to improve on previously reported ion microprobe analyses of OPX in olivine diogenites [6,7] by increasing both primary beam current and peak counting times. In addition, we noted that the quality of the analyses were also improved by the denser and more stable primary O^- beam of the Cameca 4f.

Results. As demonstrated by EMP analyses [10; Figure 2], the OPX generally show an increase in Al and a decrease in Cr in the sequence Tatahouine => 84001 => Ibbenburen => 77256. Within individual pyroxene zoning profiles and among the four analyzed diogenites, the concentration of incompatible trace elements in OPX is (+) correlated to Al content. C1 chondrite normalized REE patterns are LREE depleted relative to HREE. LREE are typically less than 0.1 x C1 chondrite whereas HREE are between 0.4 and 1.0 x C1 chondrite (Fig. 1). All patterns have negative Eu anomalies. Zr and Ti concentration in the OPX range from less than 0.1 ppm to 5.0 ppm and 400 ppm to 1000 ppm, respectively. Both Ti and Zr show a positive correlation with Al content.

Discussion. The trace element data presented in Figs. 1 and 2 may be interpreted as indicating that the diogenites and olivine diogenites are part of a continuum (accumulation of crystals during fractional crystallization) rather than representing two separate processes (melting versus crystallization). Based on the REE patterns for the OPX and the most relevant Kds available for opx-eucritic melt [8,9], calculated basaltic melts in equilibrium with these OPX have a rather flat REE pattern between 8 and 14 x C1 chondrite. These calculated REE melt patterns are parallel to and of similar concentration to the non-cumulate eucrites. The LREE (La, Ce) in these patterns are somewhat more variable, a consequence of the relatively larger analytical error at these low concentrations. Superimposed on Fig. 2 are batch and fractional melting trajectories for OPX in residua from a hypothetical EPB mantle. The four diogenites plot along either a fractional melting trajectory (4-12 % melting) or a batch melting trajectory (5-90% melting). In that the olivine-

absent diogenites cannot represent residua because of their OPX dominant mineralogy [1,2,3,4,5], the trajectory as defined by the OPX must represent accumulation of OPX +/- olivine. Calculated melt compositions in equilibrium with these OPX indicate a wide range of eucritic melt compositions.

Conclusions. The lower diffusion rates in OPX of selected trace elements such as REE, Ti, and Zr (compared to Fe and Mg) [10] allow a better interpretation of the role of diogenites in EPB magmatism. The diogenites thus far analyzed (including the olivine diogenites) appear to define a compositional continuum that most likely is a result of the accumulation of crystals during the fractional crystallization of several compositionally similar but distinct eucritic melts. The eucritic melts from which the diogenites originated appear to exceed the compositional variability thus far documented in non-cumulate eucrites.

References. [1]Mason (1967) GCA, 31, 107-115 [2] Bunch (1975) Proc. L.P.S.C., 6th, 469-492 [3] Grove and Bartels (1992) Proc. L.P.S.C. 22, 437-445 [4] Stolper (1977) GCA, 41, 587-611 [5] Sack et al (1991) GCA, 55,1111-1120 [6] Shearer and Papike (1992) LPSC XXIII,1279-1280 [7] Shearer and Papike (1992) Goldschmidt Conf., A-100 [8] McKay et al. (1987) GCA 50, 927-937 [9] Jones and MaKay (1992) EOS 73, 607 [10] Papike et al (1993) this volume.

Acknowledgements. This research was funded by NASA Grant NAG-497 (J.J. Papike, P.I.). The SIMS data was collected in the UNM/SNL Ion Microprobe Facility; a UNM-SNL cooperative venture.

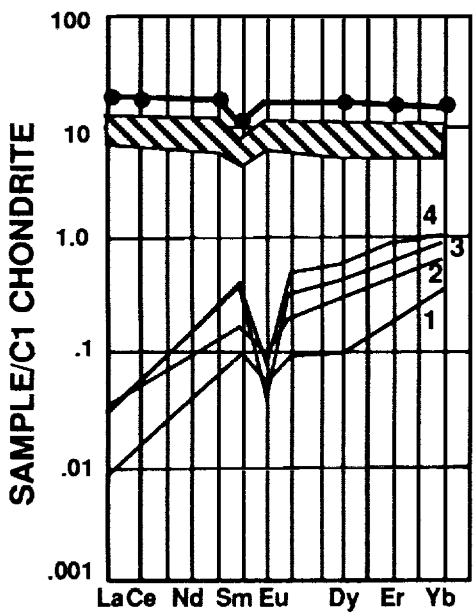


FIGURE 1. Tatahouine (1), 84001 (2), Ibbenburen (3), and 77256 (4). The shaded region is the calculated melt composition in equilibrium with OPX. Data points represent Stannern for comparison.

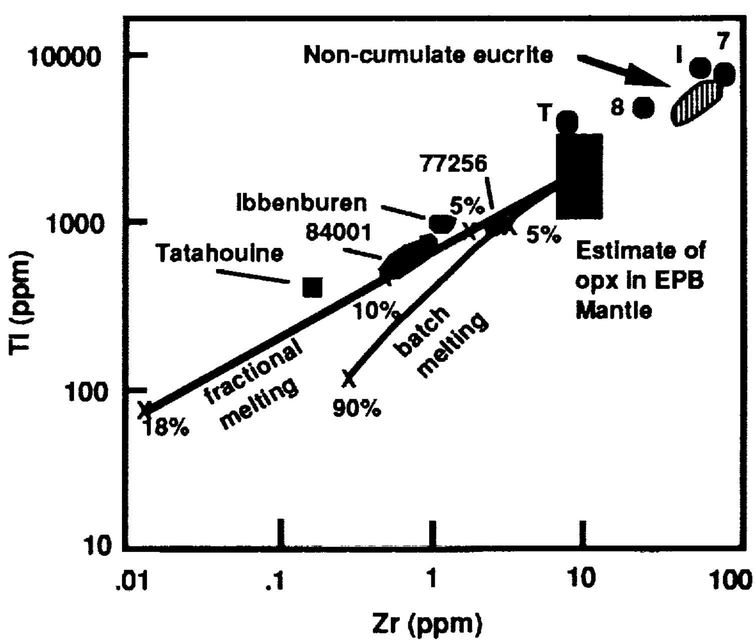


FIGURE 2. Ti (ppm) and Zr (ppm) for orthopyroxenes analyzed in this study. Also included in the figure are an estimate of the EPB mantle opx, composition field for non-cumulate eucrites, calculated batch melting and fractional melting trajectories, and estimates of basaltic melt in equilibrium with the orthopyroxenes (T= Tatahouine, 8=84001, I=Ibbenburen, 7=77256).

COMBINED BACKSCATTER MÖSSBAUER SPECTROMETER/X-RAY FLUORESCENCE ANALYZER (BaMS/XRF) FOR EXTRATERRESTRIAL SURFACES; T.D. Shelfer, E.L. Wills, D.G. Agresti, M.M. Pimperl, M.H. Shen, Department of Physics, University of Alabama at Birmingham, Birmingham, AL 35294, R.V. Morris, Code SN2, NASA Johnson Space Center, Houston, TX 77058, and T. Nguyen, Lockheed Engineering and Sciences Co., Houston, TX 77058.

Introduction. We have designed and tested a prototype combined backscatter Mössbauer spectrometer and x-ray fluorescence analyzer (BaMS/XRF). A space qualified instrument based on this design would be suitable for *in-situ* use on planetary missions to the surfaces of the Moon (Artemis and lunar outpost), Mars (MESUR), asteroids, or other solid solar system objects. The BaMS/XRF instrument is designed to be capable of concurrent sample analyses for the mineralogy of iron-bearing phases and elemental composition without the need for sample preparation.

BaMS/XRF Instrument. For this proof-of-concept prototype design we have split the instrument into two separate logical units: the probe unit and body unit. The probe unit contains a miniature (~20 g) Mössbauer drive [1], ^{57}Co source, collimator, PIN diode radiation detector, and the detector preamplifier and amplifier circuitry all mounted to an aluminum chassis as shown in figure 1. The body unit is a portable 80386-33MHz computer with a multichannel analyzer card (Nucleus PCA-II-4k) and the Mössbauer drive feedback circuitry mounted internally. With this arrangement, all that is needed to perform both analytical techniques (Mössbauer and XRF) is to present the unprepared sample (soil, rock, etc.) to the source/detector end of the probe unit.

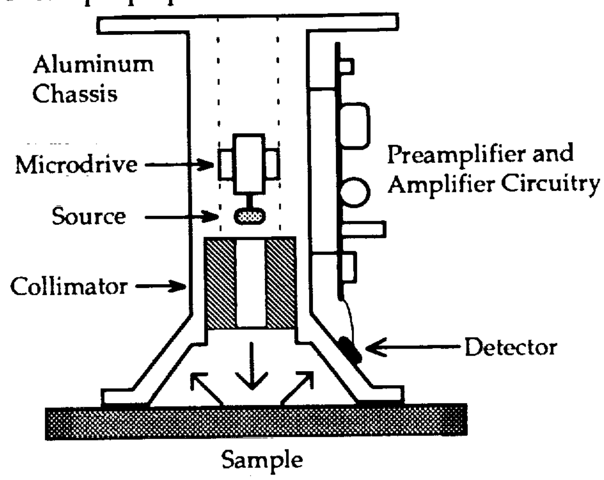


Figure 1. Probe unit schematic design.

Results and Discussion. The completed BaMS/XRF prototype instrument has been tested with a variety of standard Mössbauer and XRF samples. In particular, the BaMS capability has been applied to a Martian infrared spectrum analogue soil, Hawaiian palagonite PN9 [2]. Figure 2 shows a comparison between a transmission Mössbauer spectrum of PN9 and the backscatter spectrum obtained with the BaMS prototype. The general structure of the backscatter spectrum shows the central doublet and additional resonance to its right; however, the quality of the spectrum suffers due to the relatively weak ^{57}Co source used (~15 mCi vs ~50 mCi for the transmission spectrum) and the small solid angle of backscattered radiation collected by the single PIN diode (2.8% of the total 2π solid angle). Under these conditions (~100 hr collection time) the long-term drifts of the initial drive circuitry employed leads to a loss of resolution in the spectrum. The final BaMS design will include a stronger source (≥ 100 mCi), an array of backscatter detectors (~75% of total solid angle), and improved detector and drive circuitry which should result in a backscatter spectrum of adequate quality in ~30 minutes.

To test the XRF capabilities of the instrument, a variety of pure metal foil samples were analyzed at room temperature (~20 °C) by placing the foils on an aluminum target at the source/detector end of the BaMS/XRF probe head. The pulse height spectrum for each was taken for a preset length of time and stored. A blank (aluminum) spectrum was then subtracted from the foil spectrum to remove the noise contributions. The difference spectra for a number of metal foils (ranging in atomic number from Z=29 to Z=82) are shown in figure 3. Figure 4 is a pulse height spectrum of the ^{57}Co source taken with the PIN diode at 12 °C. To improve the range and sensativity of the XRF capability, the flight instrument might include several higher resolution radiation detectors or shutter in different excitation sources. Cold extraterrestrial temperatures will also improve the resolution of the PIN diode/preamplifier detector system.

A similar instrument development program is underway in Europe [3].

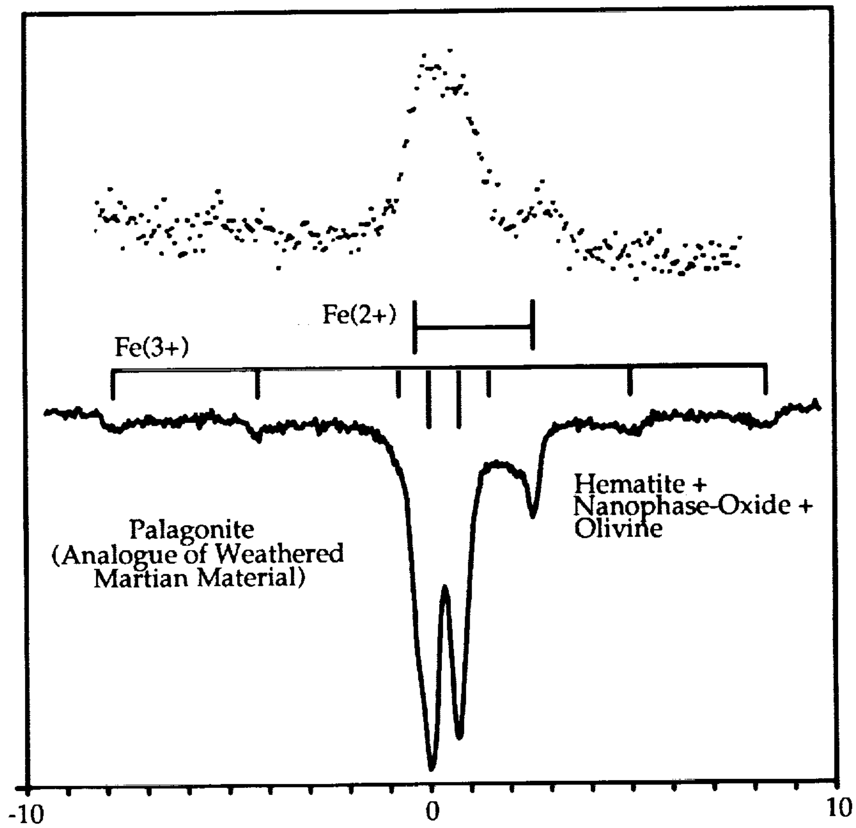


Figure 2. Transmission and backscatter Mössbauer spectra of PN9.

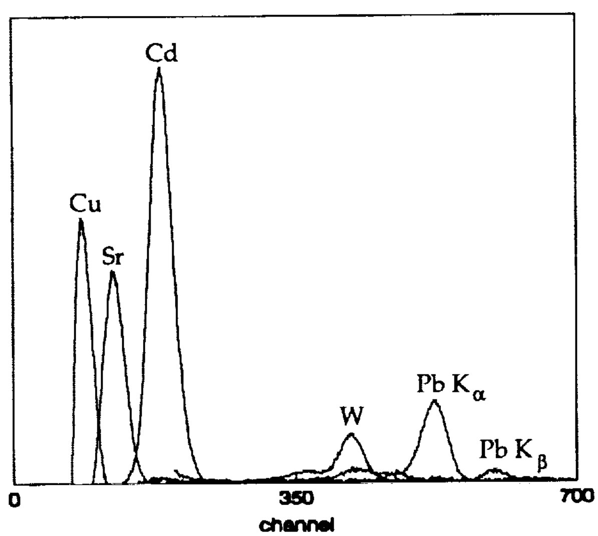


Figure 3. K x-ray difference fluorescence spectra.

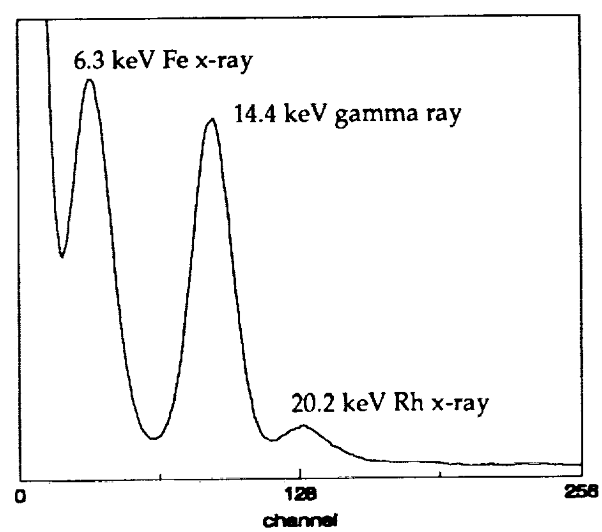


Figure 4. ^{57}Co PHA spectrum using PIN diode.

References: [1] Shelfer *et al.* (1992) *Lunar Planet. Sci. XXIII*, 1283; [2] Morris *et al.* (1989) *Lunar Planet. Sci. XX*, 723; [3] Klingelhöfer *et al.*(1992) *Hyperfine Interactions*, *71*, 1449.

S126-91
ABS ONLY

N94-20762

P-2

THE ROUGHNESS OF THE MARTIAN SURFACE: A SCALE DEPENDENT MODEL.

M. K. Shepard, E. A. Guinness, and R. E. Arvidson, McDonnell Center for the Space Sciences, Washington University, St. Louis, MO 63130.

In the coming decade, several lander missions to Mars are planned (e.g., MESUR Pathfinder, MESUR). One of the dangers facing planners of these missions is the rough topography observed at both Viking Lander sites. Both landing sites are ubiquitously covered with meter-scale boulders. Objects of this size pose obvious threats to soft landers, especially at Mars where the distance from Earth causes prohibitive time lags between the transmission of commands and feedback from the spacecraft. An obvious solution is to scout for a "smooth" site prior to the landing. However, the best resolutions realizable on current and future missions (i.e., Mars Observer) are on the order of several meters. Even at this scale, boulders of 1-2 meters in size are unresolvable. Additionally, the amount of time and spacecraft resources required to search even a small area of the planet are unrealisitic given other mission objectives. An alternative is to determine the "roughness" of the surface at a subpixel scale using bidirectional reflectance observations. Much larger areas of the planet can be searched and much of the search can easily be automated.

The morphology of the martian plains observed by the Viking Landers is physically simple. The surface is covered with a layer (approximately flat lying) of aeolian sediment from which numerous outcrops of bedrock and boulders protrude. This morphology, while simple, will be difficult to characterize from orbit using traditional bidirectional reflectance models (i.e., Hapke (1)) for two reasons. First, modeling the surface as facets with gaussian or exponential slope distributions is not realistic given the morphology described above. Second, the roughness parameter is an "average" of the roughness at scales ranging from the wavelength of light being scattered to the pixel size of the observation (2). Thus, there is no definite scale of roughness that can be extracted from the Hapke roughness parameter. Using the concepts of geometric and boolean models developed by several workers (3,4,5) we have developed a model for the bidirectional reflectance of a surface morphology comparable to that observed at the Viking Lander sites. The model assumes that the surface is flat layer of sediment partially covered by rock, similar to the model of Christensen (6). The model is capable of extracting the proportion of boulders, a measure of the average boulder aspect ratio, and a quantitative estimate of average boulder size. The reflectance of each pixel is modeled as the linear sum of three endmembers: surface, boulder, and shadow, weighted by the observed fraction of each endmember. The bidirectional reflectance of each endmember is assumed to be Lambertian for simplicity, although more complex functions could be used. The reflectance of a pixel made up of these endmembers is then:

$$r = A_b{*}r_b + A_s{*}r_s + A_{sh}{*}r_{sh} \qquad \text{(eq. 1)}$$

where r is the radiance factor as defined by Hapke (7), A_b is the fractional area of the pixel area covered by boulders, r_b is the radiance factor of the boulder material, A_s and r_s are the corresponding quantities for the surface not covered by boulders or shadows, and A_{sh} and r_{sh} are the values for the area covered by shadow. The sum of the areas is forced to 1.0. Utilizing the work of Strahler and Jupp (6), we derived the following expression for A_s:

$$A_s = \exp -[\, A_m(1+hwr{*}\tan(i)) + A_m(1+hwr{*}\tan(e)) - O(i,e,\Delta ø)\,] \qquad \text{(eq. 2)}$$

where

A_s = fractional area of visible and illuminated surface

$A_m = -\ln(1-A_b)$, here called the model area of boulders

hwr = the height to width ratio of the boulder, e.g., 1.0 for a sphere or cube

i = incidence angle, e = emission angle
$\Delta\phi$ = relative azimuth between incidence and emission vectors
$O(i,e,\Delta\phi)$ = the fractional overlap between viewing and illumination shadows.

Equation (2) assumes that the boulders are randomly placed on the surface and that no two boulders overlap. Assuming values for the radiance factor of the surface, shadows, and boulders, the average height-to-width ratio (hwr) of boulders, and the proportion of the surface covered by boulders, it is possible to solve for the proportion of the surface in shadow and in sunlight from equation (2) and the radiance factor of the pixel from equation (1) for any illumination and viewing geometry. Given a minimum of 2 observations of the same area under different lighting and viewing geometries, it is possible to solve for hwr and A_b simultaneously in a least squares solution. Given observations from at least three more viewing geometries, it is theoretically possible to also solve for r_b, r_s, and r_{sh}. The utility of equation (2) has been confirmed with computer simulated surfaces.

Currently, the model assumes a unimodal distribution of boulders. To determine the average size of the subpixel boulders requires multiple pixels of an area in which each pixel can be assumed to be covered by approximately the same number and size of boulders. Qualitatively, one can reason that the smaller the boulders are with respect to the pixel, the smaller the variance in radiance factor from pixel to pixel. Similarly, the larger the boulder size with respect to the pixel, the greater the interpixel variance. Again, computer simulations confirm this reasoning.

The model was tested on a terrestrial surface analogous to the martian plains - a portion of the Lunar Lake playa, Nevada, approximately half covered by cobble size basalt fragments (8). This area was one of several sites extensively studied during the Geologic Remote Sensing Field Experiment (GRSFE) (8) and was imaged by the Advanced Solid-State Array Spectroradiometer (ASAS) (9). ASAS is an airborne instrument which acquires multiple emission angle observations of the surface and has pixels 4.25 m in size (cross-track). Data were acquired at incidence angles of 17°, 18°, 61°, and 65°. The data considered here were taken at a wavelength of 0.65 µm. The radiance factors of the endmembers were independently known from other ASAS and portable spectrometer measurements. Atmospheric effects were ignored in this study based upon results from earlier work (10). Model results for cobble surface cover are within 10% of the best estimates of surface cover made by ground observations. Additionally, the model indicates that the average basalt cobble size is < 5% of the pixel size and that the average height-to-width ratio (hwr) is < 0.5, both in excellent agreement with ground observations. Current and future work involves applying this model to high resolution images obtained by the Viking orbiters and later by the Mars Observer Camera.

(1) Hapke, 1986, Icarus, 67, 264-280.
(2) Helfenstein, 1986, Icarus, 73, 462-481.
(3) Li and Strahler, 1985, IEEE Trans. Geosci. Remote Sens., GE-23, 705-721.
(4) Jupp et al., 1988, IEEE Trans. Geosci. Remote Sens., 26, 463-473.
(5) Strahler and Jupp, 1990, Remote Sens. Environ., 34, 153-166.
(6) Christensen, J. Geophys. Res., 87, 9985-9998.
(7) Hapke, 1981, J. Geophys. Res., 86, 3039-3054.
(8) Arvidson et al., 1991, Archive of Geologic Remote Sensing Field Experiment Data, Release 1.0, NASA Planetary Data System, Jet Propulsion Laboratory, Pasadena, CA.
(9) Irons et al., 1991, IEEE Trans. Geosci. Remote Sens., 29, 66-74.
(10) Guinness et al., 1991, Geophys. Res. Lett., 18, 2051-2054.

CHRONOLOGY OF LUNAR GRANITE 12033,576: RESETTING OF Rb-Sr AND K-Ca ISOCHRONS; C.-Y. Shih, H. Wiesmann and D. H. Garrison, Lockheed Engineering and Science Co., 2400 NASA Road 1, Houston, TX 77058; L. E. Nyquist and D. D. Bogard, NASA Johnson Space Center, Houston, TX 77058.

Lunar granite 12033,576 is a subsample of the "large" (~1 g) felsite 12033,507 which was identified from a collection of 4-10 mm particles from the 12033 soil sampled from the north rim of Head Crater in the eastern part of Oceanus Procellarum. Discordant ages of ~3.6, ~0.8, ~3.9 and ~2.2 Ga for this lunar granite were obtained, respectively, by the K-Ca, ^{39}Ar-^{40}Ar and U-Pb zircon methods in previous studies and by the Rb-Sr method in this study. Assuming the granite crystallized ~3.9 Ga ago (zircon age), and was shocked by meteoritic impacts at 0.8 Ga ago (^{39}Ar-^{40}Ar age), the intermediate apparent ages by the Rb-Sr and K-Ca methods can be interpreted as reset by diffusion of the parent and daughter nuclides. The Rb-Sr age is less resistant to resetting than the K-Ca age, but more resistant than the ^{39}Ar-^{40}Ar age.

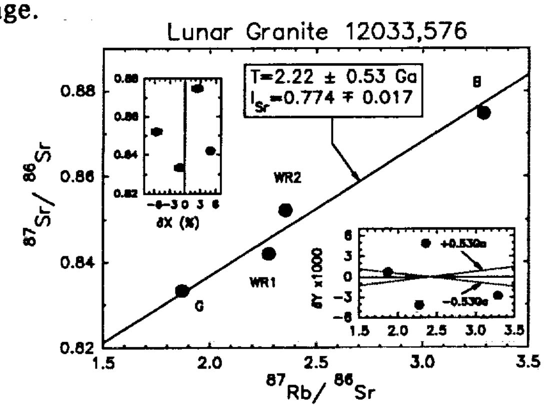


Figure 1. Rb-Sr mineral isochron of granite 12033.

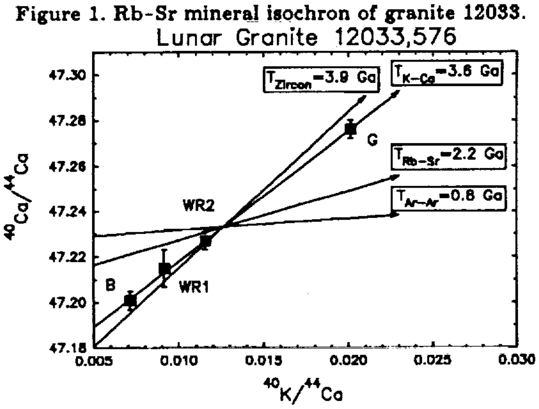


Figure 2. Discordant ages for granite 12033,576, shown on the K-Ca isochron diagram.

<u>Rb-Sr mineral isochron for granite 12033,576:</u> Rb and Sr isotopic data for this subsample of large felsite 12033,507 [1] were obtained with procedures described in [2]. Two bulk samples, WR1 and WR2, and two mineral separates, G and B, handpicked from the whole rock sample crushed to <149 μm were analysed. G is a gray feldspar-rich sample and B is a dark sample containing brownish glasses of possible shock origin [1] as well as mafic minerals. K-Ca isotopic data for these samples yield a well-defined isochron age of 3.62±0.11 Ga [3]. Rb-Sr isotopic results are reported here for the same samples, and do not define a good isochron (Fig. 1). The best-fit line for the disturbed Rb-Sr system yields a young and imprecise age of 2.22±0.53 Ga (2σ) and a high initial $^{87}Sr/^{86}Sr$ of 0.774±0.017 (2σ) using the York program [4]. Both K-Ca and Rb-Sr ages are younger than the upper concordia intersection age of 3.898±0.010 Ga obtained from the U-Pb data for zircons [5]. All these ages are considerably older than the ^{39}Ar-^{40}Ar age of 800±15 Ma, interpreted as the age of Copernicus, determined from an aliquot of the bulk sample [6]. The high initial $^{87}Sr/^{86}Sr$ and $^{40}Ca/^{44}Ca$ values for the granite indicate that both the Rb-Sr and K-Ca isochrons could have been partially reset by the Copernicus impact. If so, the crystallization age for this granite could be significantly older than the K-Ca isochron age and probably close to the U-Pb zircon age of ~3.9 Ga, but not older than the K-Ca model age of ~4.2 Ga.

<u>Diffusion model for resetting internal isochrons:</u> Discordant ages for the granite are summarized in a K-Ca isochron diagram (Fig. 2). Assuming that the granite crystallized at ~3.9 Ga and underwent shock metamorphism at 800 Ma, fractional exchanges (loss or gain), F(Sr) and F(Ca), of ^{87}Sr and ^{40}Ca, respectively, by diffusion in partially reset isotopic systems can be defined as $F=(R_{3.9}-R_t)/(R_{3.9}-R_{0.8})$ where R is $^{87}Sr/^{86}Sr$ or $^{40}Ca/^{44}Ca$ for points on isochrons representing ages of 3.9 Ga, 0.8 Ga and the observed age t at a given parent/daughter ratio. Thus defined, F is given by the relative degree of isochron rotation, and can be calculated by a lever rule [7]. The calculated F(Sr) and F(Ca) for mineral separates B

AGE OF LUNAR GRANITE 12033,576: Shih C.-Y. et al.

and G are 0.58-0.60 and 0.18-0.16, respectively. These values can be used to calculate the diffusion parameter $\alpha=(Dt/a^2)^{1/2}$ for Sr and Ca, using procedures analogous to those developed by [8] for the diffusion of Ar. The results for α(Ar), α(Sr) and α(Ca) are >0.8, ~0.2 and ~0.05, respectively, as presented in Fig. 3. The three solid lines represent the anticorrelation between diffusion time and diffusion coefficient for the three isotopic systems: K-Ar, Rb-Sr and K-Ca. Petrographic evidence suggests that the granite had experienced a shock-related thermal event at ~700°C [1]. The D/a^2 value for the K-Ar system at this temperature is determined from an Arrhenius diagram of temperature release ^{39}Ar data to be $\sim10^{-6}$ sec^{-1}. This temperature and D/a^2 value correspond to an Ar diffusion time of several days needed to totally reset the K-Ar chronometer. The Rb-Sr and K-Ca isotopic data indicate that diffusion in the Rb-Sr and K-Ca system is, respectively, ~10x and ~400x slower than in the K-Ar system. These differences are in good agreement with the relative values of experimentally determined diffusion coefficients for Sr and Ca in granitic melts recommended by [9]. At 700°C, it would have required months to totally reset the Rb-Sr system in the granite, and years to toally reset the K-Ca system.

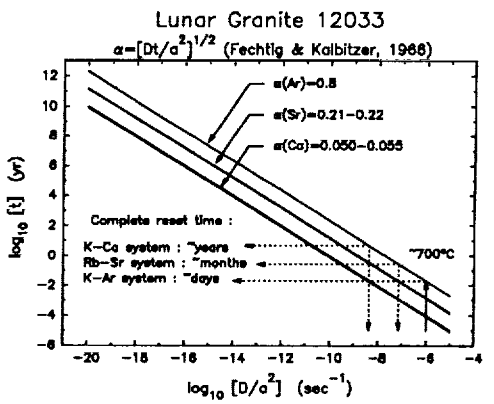


Figure 3. Diffusion time (t) vs. parameter (D/a^2).

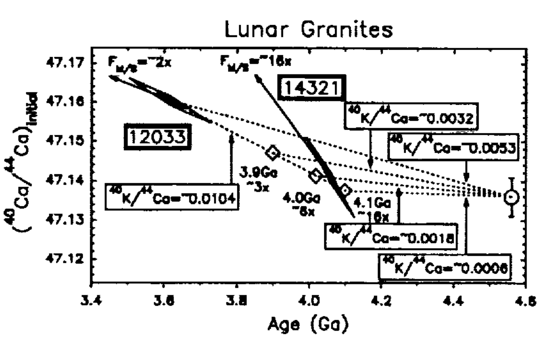


Figure 4. Age vs. I(Ca) for lunar granites.

Crystallization age and petrogenetic implications: Ages and initial $^{40}Ca/^{44}Ca$ ratios of lunar granites 14321 and 12033 [3,10] are represented by error parallelograms in Fig. 4. Dotted lines represent $^{40}K/^{44}Ca$ growth curves. For a simple two-stage model, the $^{40}K/^{44}Ca$ ratio in the source of granite 14321, which has concordant ages [10,11], was calculated to be ~0.0018, similar to values found for quartz monzodiorites [12-14], suggesting large K/Ca fractionations ($F_{M/S}$~16x) during granite formation. Large enrichments of K/Ca can be produced by silicate liquid immiscibility (SLI) processes [*e.g.* 15,16]. The $^{40}K/^{44}Ca$ ratio calculated for the source of granite 12033 formed at the K-Ca isochron age of 3.6 Ga is so high that it either must have been derived from an already granitic source, or have assimilated a large amount (~40%) of ancient granitic materials prior to its crystallization. Assuming a similarly large $F_{M/S}$~16x for this granite as for 14321, the 12033 granite could have been derived from a low K/Ca source similar to that for granite 14321 ~4.1 Ga ago in a plutonic environment perhaps associated with the parental magma of some Mg-suite rocks.

References: [1] Warren P. H. et al., (1987) PLPSC 17th, E303-E313. [2] Nyquist L. E. et al. (1990) GCA 54, 2195-2206. [3] Shih C.-Y et al. (1992) LPS XXIII, 1289-1290. [4] York D. (1966) Can. J. Phys. 44, 1079-1086. [5] Meyer C. Jr. et al., (1989) LPS XX, 691-692. [6] Bogard D. D. et al. (1992) LPS XXIII, 133-134. [7] Nyquist L. E. et al. (1979) 43, 1057-1074. [8] Fechtig H. and Kalbitzer S. (1966), In Potassium Argon Dating (ed. O.A. Schaeffer and J. Zaehringer), Springer-Verlag New York Inc., 66-106. [9] Jambon A. (1982) JGR 87, B-13, 10797-10810. [10] Shih C.-Y et al. (1992) GCA (submitted). [11] Shih C.-Y et al. (1985) GCA, 49, 411-426. [12] Ryder G. (1976) EPSL 29, 255-268. [13] Marvin U.B. et al. (1991) PLPSC 21st, 119-135. [14] Jolliff B. L. (1991) PLPSC 21st, 101-118. [15] Watson E. B. (1976) Contrib. Mineral. Petrol. 56, 119-134. [16] Longhi J. (1990) PLPSC 20th, 13-24.

ABS. ONLY 168088
N94-20764

THE CHONDRITE MIHONOSEKI - NEW OBSERVED FALL; Masako Shima, National Science Museum, A. Okada, Institute of Physical and Chemical Research, K. Nagao, Institute for Study of the Earth Interior, Okayama University

On December 10, 1992, 21:00 hours Japanese standard time, a stone weighing 6.385kg, struck the two-storied house in Mihonoseki-machi, Yatsuka-gun, Shimane-ken, Japan, 35°34.1' N., 133°13.2' E. By petrographical and mineralogical examination and rare gas analysis, the meteorite was classified as L6 chondrite. The chondrite is rather small preatmospheric size, ($^{22}Ne/^{21}Ne$=1.180, extremely low ^{60}Co activity) and shocked feature is not distinct. Cosmic-ray exposure ages obtained from ^{3}He, ^{21}Ne and ^{38}Ar are 61m.y.,and ^{40}K-^{40}Ar age is 4.41b.y. Measurements of cosmogenic radioactive nuclides, and chemical analyses are now proceeding.

Circumstances of fall: During thunderstorm, something accompanied with heavy sound attacked the roof of two-storied house. The owner of the house, Mr. M. Matsumoto, his wife and a visitor(lady) sitting in the kitchen, believed that the house was struck by lightning, but around the house, nothing was happened. A few hours later, he found that the roof was broken so rain come through the hall, and mud was spread on the floor of the room in 2nd floor. On the next day evening, his wife found a stone which was passing from the roof through under-ground. On December 12, information brought through the member of local amateur astronomers association and journalists in local branch offices to S. Murayama and M. Shima, separately.

There are many eye-witnesses of fire-ball of the meteorite. Those are reported from Wakayama, Osaka, Hyogo, Okayama and Hiroshima prefectures, and Shikoku Island. Among those, two in Hiroshima reported separately the exact time as 20:58 and 20:59, when they watched fire-ball. As preliminary results, S. Nakano, one of the member of amateur astronomer association, calculated that fire-ball entered to the earth from south-west with an incidence angle 20°.

Texture: Mihonoseki shows a distinct, recrystallized structure under the microscopic observation of the thin section in the transmitted light. Chondrules, 0.4-1.0 mm in diameter, are

all present as relicts, buried in the well-crystallized matrix. The chondrule-matrix boundaries are scarcely discernible in the granulated matrix. In the relict chondrules composed of barred and granulated orthopyroxene and olivine crystals, the interstices between the phenocrysts are filled with well-developed, clear feldspar grains. Olivine grains show a slight undulose extinction and fractured appearances, but the deformed texture of Mihonoseki seems to be low-graded in degree.

Minerals: Olivine and orthopyroxene are the most abundant minerals both in the matrix and chondrule relicts. Ca-rich pyroxene are present rimming the orthopyroxene grains in the relict chondrule. Although Mihonoseki shows a highly recrystallized strucrute, a few grains of clinobronzite still remain in the matrix. Interstitial feldspar crystals are common in the matrix and chondrule relicts, and often enclose minute chromite and pyroxene grains. Main opaque minerals are metallic nickel-iron and troilite, and the metal phase appears more abundant than the sulfide. In both phases, shock-metamorphosed features such as Neumann structure and recrystallization are not observed under the microscope.

Rare gases: The results of measurements of rare gases are listed in following Tables:

Table 1. rare gas concentrations($10^{-8}cm^3STP/g$) and isotopic ratios of He, Ne and Ar.

^4He	$^3He/^4He$	^{21}Ne	$^{22}Ne/^{21}Ne$	$^{20}Ne/^{22}Ne$
2190	0.0424(4)	15.5	1.180(4)	0.8086(15)
^{36}Ar	$^{38}Ar/^{36}Ar$	$^{40}Ar/^{36}Ar$	^{84}Kr	^{132}Xe
2.42	0.981(8)	2586.7(2.7)	0.0265	0.0182

Table 2. Cosmic ray exposure ages(m.y.) and ^{40}K-^{40}Ar age(b.y.).

^3He age*	^{21}Ne age*	^{38}Ar age**	^{40}K-^{40}Ar age***
59	61	63	4.41

* Production rates by Eugster(1988)
** Production rate by Schultz *et al.*(1991).
***: Concetntration of K was assumed to be 850ppm.

Acknowledgement: Authors are indebted to Mr. M. Matsumoto for allowing us to use the chondrite for research immidiately after the fall.

* Eugster, G.C.A.52,1649-1662(1988). **: Schultz *et al.*,G.C.A.55, 59-66(1991)

S129-12

NBS. ONLY 168089

N94-20765

CLEMENTINE: AN INEXPENSIVE MISSION TO THE MOON AND GEOGRAPHOS; Eugene M. Shoemaker, U.S. Geological Survey, Flagstaff, AZ 86001, and Stewart Nozette, SDIO/TNI, The Pentagon, R 1E167, Washington, D.C. 20301-7100.

The Clementine Mission, a joint project of the Strategic Defense Initiative Organization (SDIO) and NASA, has been planned primarily to test and demonstrate a suite of lightweight sensors and other lightweight spacecraft components under extended exposure to the space environment. Although the primary objective of the mission is to space-qualify sensors for Department of Defense applications, it was recognized in 1990 that such a mission might also be designed to acquire scientific observations of the Moon and of Apollo asteroid (1620) Geographos. This possibility was explored jointly by SDIO and NASA, including representatives from NASA's Discovery Program Science Working Group, in early 1991. Besides the direct return of scientific information, one of the benefits envisioned from a joint venture was the development of lightweight components for possible future use in NASA's Discovery-class spacecraft. In January 1992, SDIO informed NASA of its intent to fly a "Deep Space Program Science Experiment," now popularly called Clementine; NASA then formed an advisory science working group to assist in the early development of the mission.

The Clementine spacecraft is being assembled at the Naval Research Laboratory, which is also in charge of the overall mission design and mission operations. Support for mission design is being provided by the Goddard Space Flight Center and by the Jet Propulsion Laboratory. NASA's Deep Space Network will be utilized in tracking and communicating with the spacecraft. Following a recommendation of the COMPLEX committee of the Space Science Board, NASA will issue an NRA and appoint a formal science team in early 1993.

Clementine is a 3-axis stabilized, 200 kg (dry weight) spacecraft that will be launched on a refurbished Titan-IIG. One of the goals has been to build two spacecraft, including the sensors, for $100M. Total time elapsed from the decision to proceed to the launch will be two years. Main features of the mission timeline are (1) launch on January 24, 1994; (2) insertion into an eccentric 5-hour lunar polar orbit on February 21, after 2-1/2 phasing loops, (3) escape from lunar orbit on May 3; and (4) injection into a transfer trajectory to Geographos on May 27, following two Earth flybys and one lunar flyby. Clementine will encounter Geographos on August 31, 1994, in a fast flyby at a nominal miss distance of 100 km. Clementine's complement of instruments of principal interest to the scientific community includes an ultraviolet/visible (UV/Vis) CCD camera, near-infrared and long-wavelength infrared imaging systems, and a combined high-resolution CCD camera-laser ranging system (LIDAR) [1]. The Lawrence Livermore National Laboratory is in charge of development and calibration of these instruments.

The mission is designed to obtain complete coverage of the Moon with the UV/Vis and near infrared cameras in 11 wavelength bands with centers distributed from 0.30 to 2.78 microns. Ten of these bands were selected by the advisory science working group to obtain optimum lithologic discrimination using the available number of filter wheel positions. Phase angles will range from 0° to 28° near the lunar equator and up to 90° near the lunar poles. Periselene has been set at 400 km; it will be shifted from 30° N latitude to 30° S latitude during the comprehensive imaging phase of the mission. Resolution (pixel size) at periselene will be ~100 m in the UV/Vis images and ~150 m in the near-infrared images. The LIDAR camera will take long strings of images with 5-m pixel size and also range measurements with about 40-m range resolution at intervals of about 1 km along the sub-spacecraft track.

Clementine will approach Geographos from the dark side, at a phase angle of 140°. The spacecraft will be programmed to lock on the asteroid while passing from the dark to the sunlit side at high speed and close range. Maximum pixel size will be about 30 m with the UV/Vis camera, 40 m with the near- infrared camera, and roughly 1 m with the LIDAR camera. The long-wavelength infrared camera will obtain images of both the dark and sunlit sides with a maximum pixel resolution of about 8 m.

The plan for management of the scientific data acquired by Clementine is to prepare the data in usable form and to distribute them as quickly as feasible to the scientific community on CDs through NASA's Planetary Data System [2]. The total data set from a fully successful Clementine mission, when uncompressed, will be comparable in volume to the data from the first cycle of the Magellan mission to Venus. These data should provide the basis for the next giant step in our understanding of the geology of the Moon [3] and of one member of the family of Earth-crossing asteroids.

References: [1] Lucey, P.G. (1993) *LPSC XXIV*, this volume; [2] McEwen, A.S. (1993) *LPSC XXIV*, this volume; [3] Spudis, P.D. and Lucey, P.G. (1993) *LPSC XXIV*, this volume.

RESEARCH PROGRAM ON THE MANSON IMPACT STRUCTURE, IOWA: E.M. Shoemaker and D.J. Roddy, U.S. Geological Survey, Flagstaff, AZ 86001 and R.R. Anderson, Iowa DNR Geological Survey Bureau, Iowa City, IA 52242-1319.

At or near the end of the Cretaceous, at least two large impact events occurred in the western hemisphere [1,2,3]. One impact formed the 180-km diameter Chicxulub crater on the northern tip of the Yucatan peninsula. Another formed the 35-km diameter Manson structure in western Iowa. Several lines of evidence, including the chemical and isotopic composition of glass found in the K/T boundary layer at sites in the Gulf of Mexico and Caribbean region [4,5,6], the regional variation in thickness and the size of spherules in the K/T boundary layer [7,8,9], and indications at and near the boundary of disturbance and deposition of beds by giant waves in the Gulf of Mexico [10,11], point to Chicxulub as a major source of K/T boundary material, including a lower layer of clay at K/T boundary sites in western North America. The size, abundance, and mineral and lithic composition of shocked grains from an upper K/T boundary layer found at western North American sites, on the other hand, point to Manson as a possible source crater [7]. More than one impact seems to be indicated by the K/T boundary stratigraphy in western North America [12], and present constraints on the age of the Manson structure suggest that it, as well as Chicxulub, may be a K/T boundary crater [1].

Multiple craters produced over a relatively short interval of time are much more likely to have been formed by impact of comets rather than by impact of asteroids. Among likely mechanisms that could have produced multiple craters at or near the time of the K/T boundary are 1) splitting of a comet shortly before impact with Earth (impacts may have been spaced over about an hour), 2) fragmentation of a very large, Sun-grazing, periodic comet to form a compact stream of comets that intercepted the Earth's orbit (impacts may have been spread over about a century), and 3) perturbation of the Oort comet cloud by a passing massive object to form a comet shower in the inner solar system (impacts may have been spread over about a million years). Only in the first two cases are the impacts likely to have been close enough in time to contribute to the observed K/T boundary layers. All mechanisms could have produced many more than two craters. In the first case, the craters would be confined largely to one hemisphere of the Earth, whereas in the second and third cases, the craters could be very broadly distributed over the Earth.

Research programs were initiated in the U.S. Geological Survey and the Iowa Department of Natural Resources, Geological Survey Bureau (IDNR-GSB) to elucidate the relationship of the Manson impact event to the K/T boundary. Primary goals were to determine the size, structure, and precise age of the Manson crater and to determine whether Manson ejecta are represented among the shocked mineral and lithic grains in the upper K/T boundary layer in western North America. In 1991, the USGS and IDNR-GSB joined in a cooperative project to drill the Manson structure. Drilling is required to investigate the geology of the structure, because it is concealed beneath Pleistocene glacial drift. Priority targets for the drill were the impact melt sheet and a possible post-crater lake-bed sequence that was thought to occupy part of the crater floor. Precise isotopic ages and possible traces of the impactor were sought from the melt sheet; it was hoped that study of the postulated post-crater lake-bed sequence might yield a tightly constrained biostratigraphic and magnetostratigraphic age of the crater. Additional objectives of the drilling were to obtain a broad picture of the structure of the crater, and to investigate the pre-crater Cretaceous stratigraphy and the shock and post-shock processes that have affected the crater.

The Manson project was expanded in 1992 into a multidisciplinary research effort funded by the USGS, IDNR-GSB, the National Science Foundation, the Department of Energy, and the National Aeronautics and Space Administration. This effort is a component of the interagency Continental Scientific Drilling Program. The current investigator team includes:

R.R. Anderson, IDNR-GSB (crater structure and Cretaceous stratigraphy)
R.A. Black, Univ. Kansas (high-resolution seismic profiles)
L.J. Crossey, Univ. New Mexico, (post-impact hydrothermal alteration)
C.T. Foster, Univ. Iowa (petrology)
B.M. French, NASA (shock metamorphism)
W.D. Gosnold, Univ. N. Dakota (heat flow)
J.B. Hartung, IDNR-GSB (crater structure and petrology)
G.A. Izett, USGS (petrology of melt sheet and shock metamorphism)

M.J. Kunk, USGS (isotopic age determination and ejecta characteristics)
J.M. Mikesell, USGS (in-hole geophysical logging)
D.J. Nichols, USGS (palynology)
J.B. Plescia, JPL (gravity survey)
H.N. Pollack, Univ. Michigan (heat flow)
M.K. Reagan, Univ. Iowa (petrology)
R.L. Reynolds, USGS (magnetic properties of core)
D.J. Roddy, USGS (cratering processes, shock metamorphism, and petrology)
J.G. Rosenbaum, USGS (magnetic properties of core)
E.M. Shoemaker, USGS (crater structure and paleomagnetism)
N.M. Short (shock metamorphism)
M.B. Steiner, Univ. Wyoming (paleomagnetism)
B.J. Witzke, IDNR-GSB (crater structure and stratigraphy of target rocks)
P.K. Zeitler, LeHigh Univ. (isotopic age determination)

Drilling was completed in December 1992 and returned about 1200 m of NX core from twelve holes with about 95% core recovery. Many of the drill sites are close to a seismic reflection line that extends eastward from the center of the crater to the rim. The seismic reflection profile, provided by Amoco, served to guide siting of holes planned for exploration of different structural terranes in the crater. A brief overview of the rocks cored and the broad structure of the crater is given in the accompanying abstract by Anderson et al. [13]. Initial reports by many of the other investigators will also be presented at the conference.

A complex impact melt sheet was encountered on the flank and possibly in the center of the central uplift. An intensive search using several holes failed to discover any early post-crater lake beds; the evidence now available from drilling suggests that the Manson structure has been too deeply eroded for early post-crater sediments to have been preserved. A distinctive and somewhat unanticipated feature of the Manson structure is the presence of debris flows and landslide blocks, composed chiefly of Upper Cretaceous shales, that mantle most the interior of the crater, including parts of the central peak. The mechanisms of emplacement of the landslide debris remain to be determined. Landsliding appears to have been due to prompt collapse of the crater rim. Both ejecta and a substantial part of the bedrock Cretaceous section of the rim probably were sources of the slide materials.

The drill core is being split. Half will be archived at the USGS Core Research Center, Denver, Colorado, and will be available for continued research. The other half will be archived at the IDNR-GSB core facility, Iowa City, Iowa. Qualified investigators who are interested in working on the core should contact one of the authors.

References.
[1] Kunk, M.J., et al. (1989) *Science, 244*, 1565-1568.
[2] Swisher, C.C., et al. (1992) *Science, 257*, 954-958.
[3] Izett, G.A., (1991) *Science, 252*, 1539-1542.
[4] Izett, G.A., (1991) *J. Geophys. Res., 96*, 20879-20905.
[5] Sigurdsson, H., et al. (1991) *Nature, 349*, 482-487.
[6] Premo, W.R. and Izett, G.A. (1992) *Meteoritics, 27*, 413-423.
[7] Izett, G.A. (1990) *Geol. Soc. Am. Spec. Paper 249*, 100 p.
[8] Hildebrand, A.R. and Boynton, W.V. (1990) *Science, 248*, 843-846.
[9] Hildebrand, A.R., et al. (1991) *Geology, 19*, 867-871.
[10] Smit, J., et al. (1992) *Geology, 20*, 99-103.
[11] Alvarez, W., et al. (1992) *Geology, 20*, 697-700.
[12] Shoemaker, E.M. and Izett, G.A. (1992) *LPSC XXIII*, 1293-1294.
[13] Anderson, R.R., et al. (1993) this volume.

S131-46
ABS ONLY
168091
N94-20767

PETROGRAPHY OF SHOCK FEATURES IN THE 1953 MANSON 2-A DRILL CORE.

N.M. Short, Penn State University - Hazleton Campus, Hazleton, PA 18201 and D.P. Gold, Penn State University, University Park, PA 16802.

Drilling of Nx core in late 1953 into an anomalous zone of disturbed rocks northwest of Manson, Iowa disclosed presence of extensive breccias including crystalline rocks brought to the surface from depths of 4 km or more [1]. Hole 2-A penetrated breccias dominated by leucocratic igneous and metamorphic lithologies, later interpreted to be part of a general ringed peak complex within a 35 km wide impact structure produced about 65 Ma ago. Proof of this origin was given in 1966 [2,3] by NMS through recognition of shock metamorphic features in 2-A materials during a cursory examination of samples provided by R.A. Hoppin, University of Iowa. A detailed study of this material now underway has revealed that most breccia clasts in 2-A show abundant and varied evidence of shock damage, including extensive planar deformation features (PDF) in quartz, K-feldspar, plagioclase, and a pyroxene and varying degrees of isotropization and incipient melting in feldspars.

In 1966 22 samples from 17 intervals at depths between 30 and 96 m (from the top 58% of the core taken to a depth of 145 m) were collected. Sampling was biased towards recovery of large or distinctive clasts but matrix binder accompanies 18 of these samples. At least 80% of rock fragment clasts consist of igneouslike rocks (mostly granodiorites) containing crystals (from 2 to 10+ mm) of quartz, plagioclase (mainly oligoclase), some microcline, and biotite (5-25% by volume). Biotite schists, two types of diorite, and a fine-crystalline rock (which may be a phyllite derived from a shale protolith) comprise most of the remaining lithologies. The matrix varies from dominance of fine sized rock fragments and single (disaggregated) quartz and feldspar grains, and mica shreds to a similar mixture in which a possible molten phase now crystallized acts to hold particles together; chlorite is common in the matrix and replacement calcite may be present. Nearly every larger clast and many of the matrix fragments show conspicuous signs of shock damage (excepting sample M-318, in which only a few quartz fragments contain some PDFs; its black matrix is anomalous). These effects are described below in terms of mineral categories:

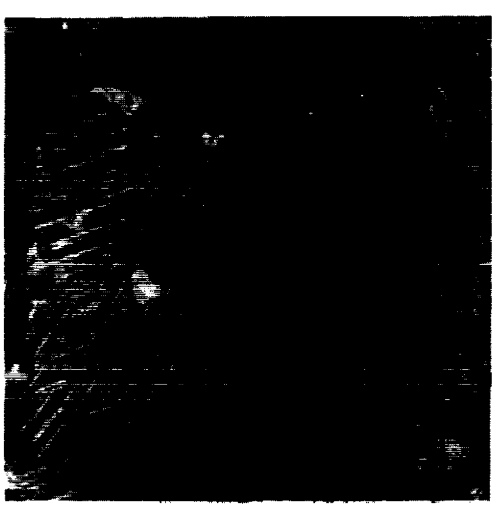
Quartz: The most diagnostic characteristic of shocked Manson crystalline rocks in the abundant and often unusual development of PDFs in most quartz crystals/grains. Many grains contain at least 3 and up to 8 sets of generally close-spaced PDFs; preliminary measurements indicate $\omega\{10\bar{1}3\}$ and $\pi\{10\bar{1}2\}$ are common (determination of crystal plane orientation, in progress, will be presented at the Conference). The predominant mode of PDF occurrence in the granodioritic clasts, and in most quartz matrix fragments, is associated with a pervasive alteration whose identity is under investigation. Individual crystals appear in plane transmitted light to have an orange-brown color related to extremely tiny specks of unknown identity; in reflected light, these crystals have a cloudy grayish translucent tone. Under cross-polarizers, this coloring effect replaces the normal gray to yellow birefringence of quartz with shades of deep reddish-brown. As the effect intensifies, the PDFs become more obscured until a stage is reached in which they seem to "disappear" as the quartz undergoes incipient isotropization. Where the brown color is less intense, individual PDFs often appear "decorated" with the specks. While this coloration is found in most quartz that occurs as single crystals or a cluster of several, some of these larger entities (which normally display undulatory extinction) have few such specks.

A second mode in these leucocratic rocks is that of an area that looks like a single crystal but is composed of tens to hundreds of small, anhedral quartz crystals of varying orientation, giving rise to a granoblastic or mortarlike texture (smaller rock fragments in the matrix with this texture resemble quartzite but are probably disaggregated from their granodioritic parents). We speculate that this stainlike coloration is due to an iron-rich clay mineral that formed in the "vulnerable" shocked quartz after the impact event. Examination of quartz-bearing rocks from 23 other impact craters has failed to duplicate this degree of discoloration (only Steen River [Canada] material shows similarities); we believe this effect is a signature "unique" to Manson and thus may afford a diagnostic criterion for correlating it to K-T boundary shocked quartz. Examples of undecorated and decorated PDFs are shown below.

Feldspars: PDFs form as low density, broadly spaced patches to continuous, contiguous (resembling fine polysynthetic twins) sets in plagioclase not showing twinning. Albite-twins show close-space sets arranged either normal or en echelon to the twin plane. PDFs form intermittently in parts of microcline grid twinning. PDFs occur in poikolitic quartz in feldspar and rarely in minute quartz in myrmekite. More highly shocked feldspars display fractures (offsetting twins), undulatory extinction, and breakdown through incipient isotropization into irregular patches and blebs that form complex light-dark extinction patterns during stage rotation. Some crystals in a sample appear to have been briefly melted, with internal flow bands. Rarely, maskelynite stage isotropization develops. Alternate albite twins are selec-tively altered to secondary minerals, as though converted to glass. A diorite clast contains feldspar glass recrystallized spherulitically.

Dark Minerals: Biotite is notably kinked in some samples; at higher shock levels its cleavage traces disappear and it may decompose to a brown phase with black (magnetite?) inclusions. Enstatite in the diorite clast develops fine polysynthetic twins resembling PDFs.

[1] Hartung J.B. and Anderson R.R. (1988), LPI tech. Rpt. 88-08, 32 pp
[2] Short N.M. (1966), J. Geol. Educ., v. 14, #4, 149
[3] Short N.M. and Bunch T.E., Shock Metam, Nat. Mat., Mono Book, 255





^{60}FE AND THE EVOLUTION OF EUCRITES.

A. Shukolyukov and G. W. Lugmair, Scripps Inst. of Ocean., Univ. of Calif. San Diego, La Jolla, CA 92093-0212.

We have recently presented evidence for the existence of live ^{60}Fe in the early solar system [1-3]. This evidence comes from the observation of 2.4 to 50 ε unit (1 part in 10^4) relative excesses of ^{60}Ni ($^{60}Ni^*$) measured in samples from the eucrite Chervony Kut (CK). These isotopic excesses have been produced by the decay of the now extinct short-lived radionuclide ^{60}Fe ($T_{1/2}$ = 1.5 Ma). Because CK originates from a planetesimal which was totally molten and its high Fe/Ni ratio is due to a planet-wide Fe - Ni fractionation during metal-silicate segregation, the presence of the ^{60}Fe decay product indicates the large scale abundance of ^{60}Fe in the early solar system and its presence during differentiation of this planetesimal. The observed variable ^{60}Ni excesses in different bulk samples and mineral separates (and their washes) from CK can only be understood if some ^{60}Fe was still alive at the time when basaltic magma had solidified on the eucrite parent body. The lack of a correlation between $^{60}Ni^*$ and the respective Fe/Ni ratios in different mineral fractions from CK indicates a metamorphic remobilization of Ni after essentially all ^{60}Fe had decayed. However, $^{60}Ni^*$ from three bulk samples from different locations within the meteorite appears to correlate reasonably well with the respective Fe/Ni ratios. If we regard this correlation as an isochron then its slope yields a $^{60}Fe/^{56}Fe$ ratio of (3.9±0.6) x 10^{-9} and an initial $^{60}Ni^*$ of 3.2±0.9 ε units at the time of crystallization of CK [3]. Estimates based on these values and a ~10 Ma time interval between CK solidification and formation of the earliest condensates in the solar system followed by rapid accretion of planetary bodies indicate that the decay of ^{60}Fe could produce sufficient heat to melt these planetesimals. If ^{26}Al was present on a planetary scale as ^{60}Fe and at abundances close to values observed in Allende inclusions [4] then melting of small early formed planets is inevitable.

As an attempt to further explore the $^{60}Fe-^{60}Ni$ isotope system as an early solar system chronometer we studied another noncumulate eucrite, Juvinas (JUV) (sample USNM 1051), which belongs to the same subgroup as CK [5]. In contrast to CK, JUV is generally more brecciated, contains clasts, and has more than a century longer terrestrial residence time. Several samples of matrix, ranging from 130 to 500 mg, from two clasts (CL A and B) and several H_2O, methanol, and HCl washes have been analyzed for Ni isotopic composition and Fe/Ni ratios. Most importantly, clear evidence for the decay of ^{60}Fe was found in all unwashed and washed samples. As in CK, Ni is very heterogeneously distributed within the meteorite: Ni concentrations in unwashed bulk samples vary from 1.2 ppm up to 10.7 ppm. However, there are important differences between JUV and CK. In JUV, the ^{60}Ni excesses in bulk samples range from ~1.6 to ~8 ε units (up to 40 ε in CK) while the spread in Fe/Ni ratios is similar. $^{60}Ni/^{58}Ni$ ratios in H_2O and 1.8N HCl washes are all very close to the normal terrestrial value (Fig. 1) while the washes of CK samples have $^{60}Ni^*$ close to the initial ratio (+3 ε) obtained from a CK bulk sample isochron. If JUV and CK originate from the same parent body, which is most likely, the JUV samples should not have any $^{60}Ni/^{58}Ni$ ratios lower than the initial ratio found in CK. Moreover, 30 to 60% of the total Ni in the washed samples was found in the H_2O (and methanol) washes. Thus, the normal Ni isotopic composition of the large amount of readily removable Ni could most plausibly be explained by contamination of JUV during its terrestrial exposure, consistent with other observations [6]. However, introduction of normal Ni at

^{60}FE IN EUCRITES: Shukolyukov A. and Lugmair G. W.

some time in its pre-terrestrial history (e.g. brecciation event) cannot be excluded.

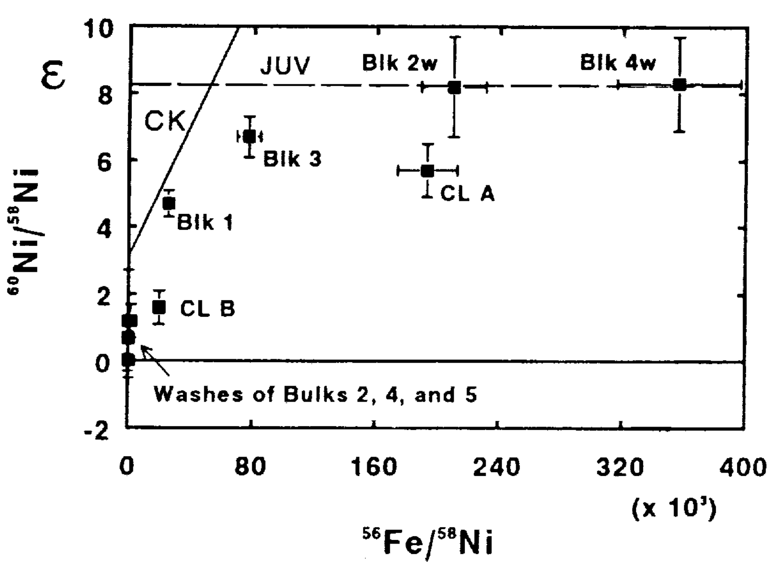
So far two washed bulk samples, Bulk 2 and 4, have been analyzed. Although their very high Fe/Ni ratios are different, they have the same $^{60}Ni^*$ of ~8ε (Fig. 1). $^{60}Ni^*$ in all unwashed samples are distinctly lower. Thus, it is reasonable to assume that these low $^{60}Ni^*$ values are due to contamination with normal Ni. Since the cleaned matrix samples with the highest Fe/Ni ratios have the same $^{60}Ni^*$ a line through these two points has a slope of ~0 and an initial $^{60}Ni^*$ of ~8.3 ε units. This implies that all ^{60}Fe had decayed at the time when JUV crystallized. If we assume that JUV and CK were produced by similar degrees of partial melting then the intercept of the two 'isochrons' (Fig. 1) yields a good approximation for their total rock $^{56}Fe/^{58}Ni$ ratios of $5x10^4$. From this we calculate that JUV has crystallized at least 5 Ma after CK. This time difference suggests a deeper burial for JUV than for CK.

The new estimate for the total rock Fe/Ni ratio also affords a better approximation for the $^{60}Fe/^{56}Fe$ ratio ($6.3x10^{-9}$) at the time of parent body differentiation and the time difference (δT ≈ 1.1 Ma) until CK formed, in good agreement with our earlier upper limit of 1.4 Ma [3]. If some Fe/Ni fractionation occurred during partial melting of the CK source, a conservative upper limit for δT of 3 to 4 Ma can be estimated. Regardless of the precise conditions, a short time interval of 1 to 4 Ma between core formation and solidification of CK is indicated.

References: [1] A. Shukolyukov and G. W. Lugmair (1992), *LPSC 23*, 1295. [2] ___ (1992), *Meteoritics*, 27, 289. [3] ___ (1993), *Science*, in press. [4] T. Lee, D.A. Papanastassiou, G.J. Wasserburg (1976), *GRL*, 3, 109. [5] P.H. Warren and E.A. Jerde (1986), *GCA*, 51, 713. [6] H. Palme and W. Rammensee (1982), in Proc. Lun. Planet. Sci. Conf. 12, *GCA*, Suppl. 16, 949.

We thank G. MacPherson for sample USNM 1051.

Figure 1: Relative $^{60}Ni/^{58}Ni$ excesses ($^{60}Ni^*$) from the decay of ^{60}Fe in the Juvinas (JUV) eucrite, expressed in ε units ($1x10^{-4}$). H_2O and HCl washed bulk (Blk) samples are indicated by (w). All washes have $^{60}Ni^*$ close to zero, suggesting contamination with normal (terrestrial) Ni, which appears to have affected the clasts (CL A, B) as well. The dashed line (marked JUV) through the data points corresponding to the washed samples has zero slope which indicates closure of the ^{60}Fe-^{60}Ni system after ^{60}Fe had totally decayed. The solid line (marked CK) shows the Fe-Ni 'isochron' for Chervony Kut (CK) which yields $^{60}Fe/^{56}Fe$ = $3.9x10^{-9}$ at the time of closure of the ^{60}Fe-^{60}Ni system in CK. From this we calculate a formation time interval for CK and JUV of ≥5 Ma. The time between core formation on the eucrite parent body and CK crystallization is 1 to 4 Ma.



S133-91
ABS ONLY

N94-20769

Geoid, Topography, and Convection-Driven Crustal Deformation on Venus;
Mark Simons[1], Bradford H. Hager[1], and Sean C. Solomon[2], [1]Department of Earth, Atmospheric, and Planetary Sciences, Massachusetts Institute of Technology, Cambridge, MA 02139, [2]Department of Terrestrial Magnetism, Carnegie Institution of Washington, Washington, DC 20015.

Introduction. High-resolution Magellan images and altimetry of Venus reveal a wide range of styles and scales of surface deformation [1] that cannot readily be explained within the classical terrestrial plate tectonic paradigm. The high correlation of long-wavelength topography and gravity and the large apparent depths of compensation suggest that Venus lacks an upper-mantle low-viscosity zone [2-5]. A key difference between Earth and Venus may be the degree of coupling between the convecting mantle and the overlying lithosphere. Mantle flow should then have recognizable signatures in the relationships between the observed surface topography, crustal deformation, and the gravity field [6,7]. Therefore, comparison of model results with observational data can help to constrain such parameters as crustal and thermal boundary layer thicknesses as well as the character of mantle flow below different Venusian features. We explore in this paper the effects of this coupling by means of a finite element modelling technique.

Model. The crust and mantle in the models are treated as viscous fluids. We solve both the equations of motion and the heat equation at each time step using a modified version of the two-dimensional, Cartesian finite-element program ConMan [8]. Our formulation assigns material properties to each element and explicitly tracks the free surface topography and the crust-mantle interface by letting the grid deform with time in a semi-Lagrangian fashion. This procedure permits variation in the crustal buoyancy as well as specific crustal and mantle rheologies that can depend on composition, temperature and stress. In addition to the flow field, the stress field in the lithosphere, the surface topography, and the resulting geoid are readily calculated. The model domain is a square box. We impose free-slip boundary conditions on the bottom and side walls, with no flow through these walls. The top of the box is a true free surface, so there is no need to derive surface topography from vertical stresses on the top of the box. We investigate two classes of models. In the first class flow is dominated by concentrated upwelling (Figure 1a), and in the second class flow is dominated by concentrated downwelling (Figure 1b). We vary the initial crustal and thermal boundary layer thicknesses as well as the effect of crustal and mantle viscosities that are either constant, temperature-dependent, or fully non-Newtonian.

Results. In all of our models, convection produces horizontal compressional stresses in lithosphere above downwelling mantle and extensional stresses in lithosphere above upwelling mantle. As the convective vigor increases so does the magnitude of the stress. In models with constant-viscosity mantle overlain by a constant-viscosity crust, stress in the crust reaches values in excess of 100 MPa in less than 100 My. We find that the rate of increase in compressive stress decreases with increasing crustal viscosity. This is because the stronger the crust, the more the development of the convective instability in the mantle driving the deformation is impeded. We also find that the magnitude of the peak compressive stress achieved above the downwelling increases with higher viscosities and/or with thinner initial crustal layers; the stronger the crustal lid, the more are tractions from mantle convection supported in the crust. Since force balance on the crust requires that shear tractions integrated along the base be balanced by normal tractions integrated through its thickness, the thinner the crust, the larger the horizontal stresses.

Both analytical models [9,10] and our numerical models of convection-induced crustal flow indicate that the amplitude and sign of the topography are time- and rheology-dependent. In general, possible responses of the crust to mantle flow can be divided into three categories. The first involves little, if any, crustal flow, and topography results mainly from the transmission of normal tractions induced by density contrasts within the mantle. The second possible regime involves substantial crustal flow, with geologically rapid thickening over convective downwelling and thinning over convective upwelling. In this regime the effects of crustal thickness variations dominate the topography. A third possible regime lies between the first two, with "in phase" deformation on short time scales and crustal flow on longer time scales. A strong mantle lithosphere tends to shield the crust from convective shear tractions, and topography results mainly

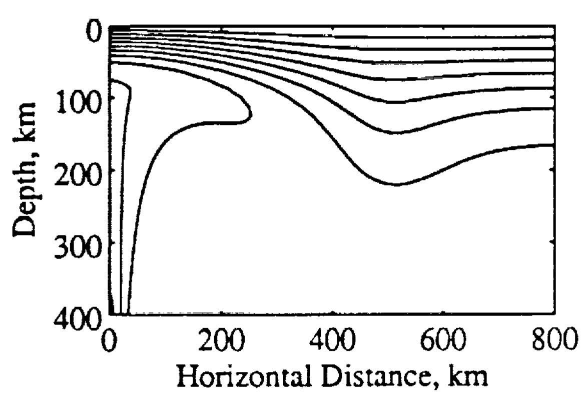
from the transmission of convective normal tractions. A relatively weak lower crust facilitates crustal deformation, and the isostatic effects of crustal thickness variations dominate the topography.

Consideration of geoid-to-topography ratios (GTRs) can restrict the regime of crustal response appropriate for Venus. The distribution of estimated GTRs for several highland regions on Venus is bimodal with two clusters around 10 and 25 m/km [5]. The positive correlation of long-wavelength gravity and topography implies that there are no major regions that have negative GTRs. To keep the GTRs positive, the geoid must follow the surface topography in sign at all times. Although the regime of negligible crustal flow can correctly predict both the sign and magnitude of the GTRs, it does not account straightforwardly for the crustal deformation (i.e., flow) inferred from observations of tectonic features, and particularly areas of extensively deformed terrain, on Venus.

In contrast to the regime of negligible flow, that of time-dependent crustal flow generates topography that changes sign. Over a mantle downwelling, the topography is negative in the early stages of deformation and positive in the later stages of deformation; the converse holds over a mantle upwelling. During the transitional period the topography goes through zero, the geoid does not go through zero, and the GTR is unbounded; this singularity is not observed on Venus.

In the absence of a mechanism by which the sign of the geoid anomaly mimics that of the topography over a given upwelling or downwelling, only the regime of rapid crustal flow is plausible. In the case of mantle downwelling this would also require that the lower mantle be more viscous than the upper mantle in order to produce the required positive geoid anomalies. This layering of viscosity structure has already been shown to hold for the Earth, where the observed geoid highs over regions of mantle upwelling and regions of mantle downwelling are best explained by the presence of a strong lower mantle [11,12]. The large positive GTRs and the presence of large shield volcanoes in certain highland regions on Venus, such as Beta Regio and Eistla Regio, are best explained as areas of mantle upwelling [5,13,14]. The regime of rapid crustal flow predicts crustal thinning over the upwelling. However, the partial melting and ensuing volcanism and crustal plutonism expected over such regions may outweigh the effects of crustal thinning on the surface topography and thus also yield positive GTRs [15].

References. [1] S. C. Solomon et al., *Science, 252*, 297, 1991; [2] W. S. Kiefer et al., *Geophys. Res. Lett.*, *13*, 14, 1986; [3] B. G. Bills et al., *J. Geophys. Res.*, *92*, 10, 1987; [4] R. J. Phillips et al., *Science, 252*, 651, 1991; [5] S. E. Smrekar and R. J. Phillips, *Earth Planet. Sci. Lett.*, *107*, 587, 1991; [6] R. J. Phillips, *Geophys. Res. Lett.*, *13*, 1141, 1986; [7] R. J. Phillips, *J. Geophys. Res.*, *95*, 1301, 1990; [8] S. D. King et al., *Phys. Earth Planet. Inter.*, *59*, 195, 1990; [9] D. L. Bindschadler and E. M. Parmentier, *J. Geophys. Res*, *95*, 21, 1990; [10] H. Schmeling and G. Marquart, *Geophys. Res. Lett*, *17*, 2417, 1990; [11] M. A. Richards and B. H. Hager, *J. Geophys. Res*, *89*, 5987, 1984; [12] B. H. Hager, *J. Geophys. Res*, *89*, 6003, 1984; [13] R. E. Grimm and R. J. Phillips, *J. Geophys. Res.*, *96*, 8305, 1991; [14] R. E. Grimm and R. J. Phillips, *J. Geophys. Res.*, *97*, 16035, 1992; [15] R. J. Phillips et al., *Science, 252*, 651, 1991.



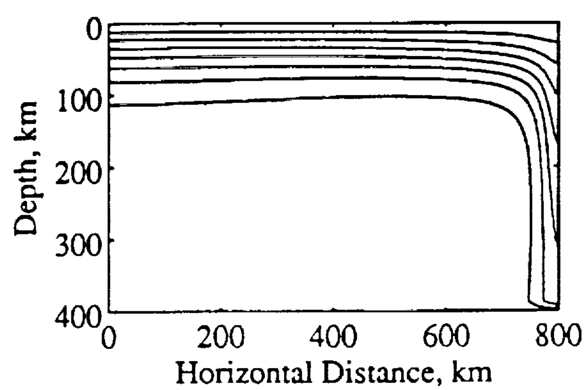


Figure 1. Temperature contours for the (a) upwelling and (b) downwelling models. The box is 800 km in the horizontal dimension and 400 km in the vertical. Top and bottom temperatures are fixed at 500 °C and 1250 °C, respectively. Contour interval is 100 °C.

5134-90 ABS ONLY N94-20770

PETROGRAPHY AND ORIGIN OF REFRACTORY INCLUSIONS FROM THE MURRAY AND MURCHISON C2 CHONDRITES; S.B. Simon[1], L. Grossman[1,2] and A. Hsu[3]. [1]Dept. of Geophysical Sciences, The University of Chicago, 5734 S. Ellis Ave., Chicago, IL 60637. [2]Enrico Fermi Institute, The University of Chicago, 5640 S. Ellis Ave. [3]Illinois Math and Science Academy, Aurora, IL 60506.

Abstract. By freeze-thaw disaggregation we have recovered a total of 47 refractory inclusions. New discoveries include a hibonite-pyroxene spherule from Murray; a $CaAl_4O_7$-bearing spherule from Murchison; and a Sc-fassaite-bearing ultrarefractory inclusion from Murchison.

Freeze-thaw disaggregation, combined with density separation and hand-picking as described by [1], is a proven method for recovering rare objects from carbonaceous chondrites. This method is especially effective on C2's due to their porosity, and typically results in the discovery of new types of refractory inclusions [*e.g.*, 2, 3, 4]. Because few refractory inclusions from Murray have been described, we studied this meteorite, although only a small amount of material (730 mg) was available for disaggregation. Many refractory inclusions from Murchison have been described [2-6], and we disaggregated a larger amount (~18 g) of Murchison in an attempt to find new types of refractory inclusions, especially corundum-bearing ones.

Murray. Five refractory inclusions were recovered. Two are spinel-pyroxene objects, with interiors composed of Mg-, Al-spinel with many void spaces and trace amounts of perovskite, and rims of aluminous diopside. One object is like the "nodular" type previously found in Murchison [3] while the other is a spherule. One inclusion is best classified as a spinel-hibonite aggregate [4], with ragged hibonite laths 10-20 μm long and much void space, perhaps formed by dissolution during secondary alteration. It does not have a continuous spinel rim like SH-6 [4] but, like SH-6, spinel is present only at the edges of the inclusion and appears to be replacing hibonite. One spinel-hibonite spherule [4], MY92L9, was found in Murray. It is kidney-shaped, 200 × 125 μm, and consists of 20 μm-long hibonite (~2.3 wt % TiO_2, 1.0 wt % MgO) laths and blades in a matrix of spinel, with many void spaces and rare grains of perovskite. Many of the hibonite laths are perpendicular to the rim of the inclusion, consistent with nucleation on the edge of a cooling droplet. Unlike the Murchison inclusions separated by MACPHERSON et al. [3, 4], but similar to those described by MACDOUGALL [5], this inclusion is completely enclosed in a rim of Fe-rich phyllosilicate. Outward from this layer in MY92L9 is a sequence (only partially retained) of aluminous diopside, enstatite and pure diopside. MACDOUGALL [5] also observed outer layers of pure diopside and inner layers of Fe-silicate on hibonite-bearing spherules, but did not report finding enstatite.

The most unusual inclusion among the Murray samples is MY92S3, a hibonite-pyroxene spherule like one in Y791717 (CO3) [7]. The Murray sample is ~70 × 60 μm in size and consists of several isolated hibonite laths (<10 μm across and 10-25 μm long) enclosed in a silicate matrix. The laths are not oriented at high angles to the rim as in MY92L9. Sample MY92S3 consists of 14.4% hibonite (2.4% TiO_2, 1.1% MgO) and 85.6% pyroxene (6.4% MgO, 28.5% Al_2O_3, 37.1% SiO_2, 25.8% CaO and 2.2% TiO_2). This composition is also similar to that of the glass in a Lancé hibonite-glass spherule [8], but the material in MY92S3 consists of 2-3 optically birefringent crystals and has pyroxene stoichiometry (as does the material in Lancé), with four cations (including one Ca) per six oxygen ions. The pyroxene in MY92S3 has a very high CaTs ($CaAlAlSiO_6$) component (~59.3 mole %). This is not a stable pyroxene composition [9] and must have formed metastably, probably due to rapid cooling. The bulk composition of MY92S3 is spinel-saturated, not hibonite-saturated, and plots in the Sp+An+L field when projected from spinel onto the anorthite-gehlenite-forsterite plane [10], but neither spinel nor anorthite are present in the sample. Although rapid cooling can delay anorthite crystallization [11], this is probably not the case for spinel. The absence of spinel and presence of hibonite suggest that at least some of the hibonite is relict. This spherule may have formed by heating of a hibonite-, silicate (probably Al-diopside)-bearing object to a temperature high enough to melt all of the silicate and some of the hibonite. Upon rapid cooling, the liquid, enriched in Al due to the melting of hibonite, crystallized to a metastable pyroxene. A problem with this model is that we have not observed any other inclusions composed exclusively of hibonite and pyroxene that would represent a likely (unmelted) source. Hibonite always occurs with spinel, and spinel could not be melted completely without hibonite melting completely unless it was finer grained and less abundant than hibonite.

Murchison. We recovered 42 refractory inclusions. Of these, 18 are spinel-pyroxene objects, 17 are spinel-hibonite spherules (or fragments thereof), and five are simply hibonite plates ± attached alteration products, such as calcite. One of the spinel-hibonite spherules, M92B6, is unusual in that it contains an ~10 μm-wide mantle of spinel, an ~20 μm-thick inner zone of spinel + hibonite laths (5.1 wt % TiO_2, 3.3% MgO) and a core of $CaAl_4O_7$ + perovskite. This is the first report of $CaAl_4O_7$ from Murchison. Bulk trace element abundances for this inclusion, determined by INAA, are reported in [12]. In thin section, the sample is a wedge-shaped piece of a spherule whose original radius was ~85 μm. This does not include the rim sequence, which consists of monomineralic layers of melilite (~$Åk_5$), anorthite and aluminous diopside outward from the spinel mantle. The melilite and anorthite layers are each ~2-5 μm thick and the pyroxene layer is ~10 μm thick. The silicate rims on this SiO_2-free, unaltered inclusion were either deposited upon the spherule in different physico-chemical regimes within the solar

nebula, or formed by metasomatic reaction of the spherule with the gas, as has been suggested for some Allende inclusions [13]. If we now ignore these layers and the perovskite and normalize the bulk composition to 100% $CaO+MgO+Al_2O_3$, the result is 6.0, 18.4 and 75.6 wt %, respectively. According to the phase equilibria of this system [14, 15], a liquid of this composition should begin crystallizing spinel at ~2100°C and continue until the spinel-hibonite cotectic is reached at ~1750°C. These phases should be joined by $CaAl_4O_7$ at ~1700°C [16]. The textural relationships of the phases in the inclusion are thus consistent with this crystallization sequence, assuming sequential crystallization, from the outside inward, by cooling from the surface of a liquid droplet. The round shape of the inclusion also supports a liquid origin. Substitution of Mg+Ti into hibonite lowers its melting point [3], so taking into account the TiO_2 in the system and the 5 wt % TiO_2 in the hibonite in M92B6, the above liquidus temperatures could be lowered by ~150°C (proportional to a 230°C depression in hibonite with 7 wt % TiO_2 [3]). Even so, assuming that all the hibonite in M92B6 crystallized from a liquid would require a temperature of at least 1600°C, perhaps the highest temperature yet inferred for a refractory inclusion. MACPHERSON et al. [3] reported a SiO_2-free, spinel-, hibonite-, perovskite-bearing inclusion from Murchison, BB-2, in which, based on the inclusion's bulk composition and the relevant phase equilibria, $CaAl_4O_7$ should have, but did not, crystallize after spinel + hibonite. They attributed the absence of $CaAl_4O_7$ in that inclusion to the presence of TiO_2, which presumably stabilized Ti-, Mg-bearing hibonite at the expense of $CaAl_4O_7$ [3]. The sample we studied has virtually the same CaO, MgO and Al_2O_3 contents as BB-2, but less TiO_2 (0.9 *vs.* 3 wt %) and does contain $CaAl_4O_7$. This supports the conclusion of [3] that the presence of TiO_2 expands the stability field of hibonite at the expense of $CaAl_4O_7$. This effect may account for the rarity of the latter phase in refractory inclusions.

Another unique inclusion, M92HIB11, is half of a spherule that was originally ~80 μm in diameter. It consists of numerous grains of Mg-, Al-spinel, mostly ~5 μm across, and perovskite, mostly <5 μm across (but one grain is ~10 × 6 μm), enclosed in Sc-, Ti-rich pyroxene. Ranges of six electron probe analyses of this pyroxene are: 1.7-5 wt % MgO; 24.8-27.5% Al_2O_3; 21.2-26.9% SiO_2; 21.5-24.0% CaO; 4.6-10.7% Sc_2O_3; 9.2-16.8 TiO_2^{tot} (all Ti as TiO_2); ~1.5% ZrO_2; 0.5-0.7% V_2O_3; and 0.1-0.5% FeO. This composition is similar to that of a Sc-rich fassaite reported by DAVIS [16] in an ultrarefractory inclusion (OSCAR) in Ornans, but the pyroxene in M92HIB11 has less Sc_2O_3 and more TiO_2^{tot} than that in OSCAR [17]. Perovskite in M92HIB11 contains ~1.6 wt % Y_2O_3, compared to 5.9% in the OSCAR perovskite [17]. Based on strong depletion of LREE relative to HREE with little isotopic mass fractionation, DAVIS [pers. comm.] has concluded that OSCAR is an ultrarefractory condensate, rather than a volatilization residue. Preliminary ion probe analyses indicate that M92HIB11 has a chondrite-normalized REE pattern similar to that of OSCAR and is therefore also an ultrarefractory inclusion.

Another unusual inclusion is M92HIB9, an oval-shaped, 100 × 65 μm object consisting of ~90 vol % Mg-, Al-spinel with many small (up to 10 μm) inclusions of perovskite and gehlenite. Most of the gehlenite is in the interior of the inclusion and several of the grains are near the rim. If the object crystallized from a liquid, it would have begun to crystallize spinel at about 2100°C and would have continued to do so until the spinel-gehlenite cotectic was reached at 1527°C [16]. This sequence should yield an inclusion with a thick spinel mantle and a small, gehlenite + spinel core, and this is essentially what is observed.

We also recovered two blue hibonite crystals that are large enough (~80 μm across) for investigation of zoning trends with the electron probe. In both grains analyzed, MgO and TiO_2^{tot} increase from core to rim. On an atomic basis, there is a slight excess of Ti over Mg. Equal proportions would be expected from the coupled substitution $Ti^{4+} + Mg^{2+} \rightleftarrows 2Al^{3+}$. The "excess" Ti is probably in the form of Ti^{3+}, which can substitute directly for Al^{3+}. Our analyses indicate that, in both samples, the Ti^{3+}/Ti^{4+} ratio remains constant and that ~15% of the Ti is Ti^{3+}. This is at the high end of the range (2-15%) observed in synthetic blue hibonite [18] but a little lower than that (23%) detected in a blue hibonite from a Murchison spinel-hibonite inclusion [18].

This work, in which we sampled a fairly large (and presumably representative) group of inclusions, provides further evidence that refractory inclusions in C2 chondrites represent higher-temperature assemblages than those in C3 chondrites; that new types of inclusions remain to be discovered; and that freeze-thaw disaggregation combined with density separation and hand-picking is an efficient way of finding these inclusions. Corundum is very rare.

REFERENCES: [1] G.J. MACPHERSON et al. (1980) *LPS XI*, 660-662. [2] M. BAR-MATTHEWS et al. (1982) *GCA 46*, 31-41. [3] G.J. MACPHERSON et al. (1983) *GCA 47*, 823-839. [4] G.J. MACPHERSON et al. (1984) *PLPSC 15*, C299-C312. [5] J.D. MACDOUGALL (1979) *EPSL 46*, 1-6. [6] T.R. IRELAND (1988) *GCA 52*, 2827-2839. [7] K. TOMEOKA et al. (1992) *Meteoritics 27*, 136-143. [8] T.R. IRELAND et al. (1991) *GCA 55*, 367-379. [9] H.-Y. YANG (1975) *Proc. Geol. Soc. China 18*, 48-58. [10] E. STOLPER et al. (1982) *GCA 46*, 2159-2180. [11] G.J. MACPHERSON et al. (1984) *J. Geol. 92*, 289-305. [12] S. YONEDA et al. (1993) This volume. [13] G.J. MACPHERSON et al. (1981) *PLPSC 12*, 1079-1091. [14] G.A. RANKIN and H.W. MERWIN (1916) *Amer. Chem. Soc. J. 38*, 568-588. [15] R.G. BERMAN (1983) Ph.D. thesis, U. Brit. Columbia. [16] M.R. RAO (1968) *J. Am. Ceramic Soc. 51*, 50-54. [17] A.M. DAVIS (1984) *Meteoritics 19*, 214. [18] J.R. BECKETT et al. (1988) *GCA 52*, 1479-1495.

5135-91
ABS. ONLY

N94-20771

SCATTERING BY VENUS' SURFACE; R.A. Simpson, G.L. Tyler, M.J. Maurer, E. Holmann, and P.B. Wong, Center for Radar Astronomy, Stanford University, Stanford, CA 94305-4055

During 1992 Magellan altimetry echoes were processed to yield scattering functions $\sigma_0(\phi)$ over near-nadir angles $\phi \leq 10°$ from some 2000 Venus orbits [1]. SAR image strips acquired simultaneously at oblique angles were also reduced to give scattering functions but over a few degrees of incidence angle in the range $15 \leq \phi \leq 45°$. By sorting, the altimetry and SAR results can be combined to give composite scattering functions for much of Venus' surface. The data in hand should allow definition of such composite functions for 70-80% of Venus at resolutions of 20 km — approximately one million separate functions.

Figure 1 is an example of a composite scattering function from Magellan observations southeast of Alpha Regio. The surface is one of the smoothest found on Venus from analysis of the altimetry echoes; the data at small incidence angles match an expression derived by Hagfors [2] for scattering by a gently undulating surface with gaussian height distributions and an exponential autocorrelation function. The Hagfors free parameter can be interpreted as an rms surface slope $C^{-1/2}$ on the order of 0.9°.

Scattering at angles greater than 30° is likely to be dominated by mechanisms other than mirror-like reflection from properly oriented surface facets. Thus, it is not surprising that the radar cross section derived from the corresponding image strip does not fall on the Hagfors curve. Small scale structure, irregularities, and inhomogeneities in the regolith likely are responsible for the enhancement over the Hagfors prediction. Achieving a satisfactory interpretation of oblique backscatter results within the context of the gently undulating surface seen at near nadir may be possible through integration of numerical modeling techniques with more conventional analysis methods. If so, the link between radar remote sensing observations and sound geologic interpretation will be strengthened.

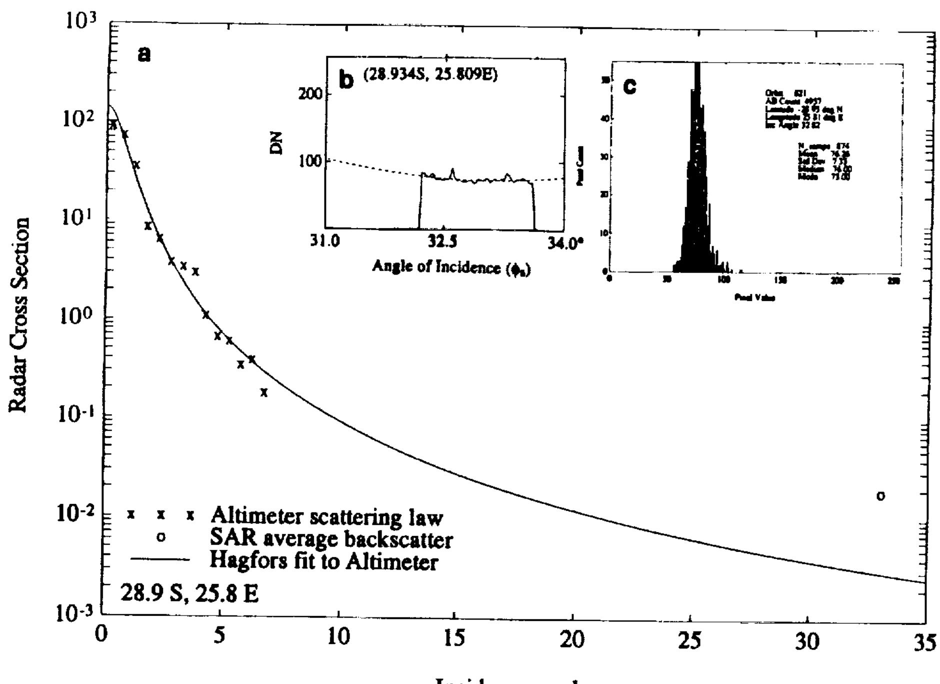


Figure 1. Composite Venus backscatter function derived from Magellan data (a). Results of altimetry inversion are indicated by "x"; the best Hagfors function fit is given by the solid line. A single point "o" represents the mean SAR backscatter. Detail on the SAR scattering vs. angle is shown in (b); a histogram of pixel values is shown in (c).

[1] G.L. Tyler, R.A. Simpson, M.J. Maurer, and E. Holmann (1992), *JGR*, *97*, 13115.
[2] T. Hagfors (1964), *JGR*, *69*, 3779.

VENUS GRAVITY: NEW MAGELLAN LOW ALTITUDE DATA; W.L. Sjogren, A.S. Konopliv, and N. Borderies, Jet Propulsion Laboratory California Institute of Technology, Pasadena, CA 91109; M. Batchelder, Telos Aerospace Systems, Pasadena, CA 91107; J. Heirath, R.N. Wimberly, Sterling Software, Palo Alto, CA 94303

Acquisition of a new high quality gravity data set has begun which presently covers one third of the Venusian longitude. Better spatial resolution is obtained from a 60th degree and order spherical harmonic solution. Plans for aerobraking in May 1993 into a near circular orbit will provide excellent data for higher latitudes regions.

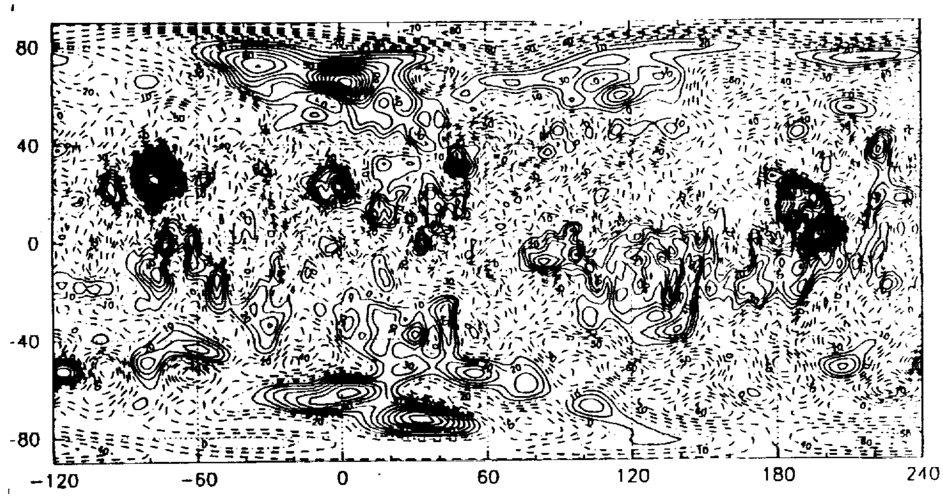
On September 24, 1992 the Magellan spacecraft lowered its periapsis altitude to 180 km and a new high quality gravity data set was initiated. It will require some 243 days before 360°of longitude coverage is obtained (≈ May 24, 1993). These new data are at X-Band frequencies and produce a data quality which is a factor of 10 better than previous S-Band data from Pioneer Venus Orbiter. Typical X-Band 10 second Doppler data have a 0.1 mm/sec noise level where as the old S-Band data were near 1.0 mm/sec. This is primarily due to the reduced effect of space plasma at X-Band frequency. When line-of-sight acceleration profiles are extracted from these data, they reveal additional details that were previously lost, such as the crater, Mead. We have made some very preliminary analyses on this crater to check its isostatic state. However we find that detailed surface topographic modeling is necessary to account for rim deposits that cancel the crater deficit. Additional altimetry profiles of the eastern rim are necessary and are being analyzed at this time.

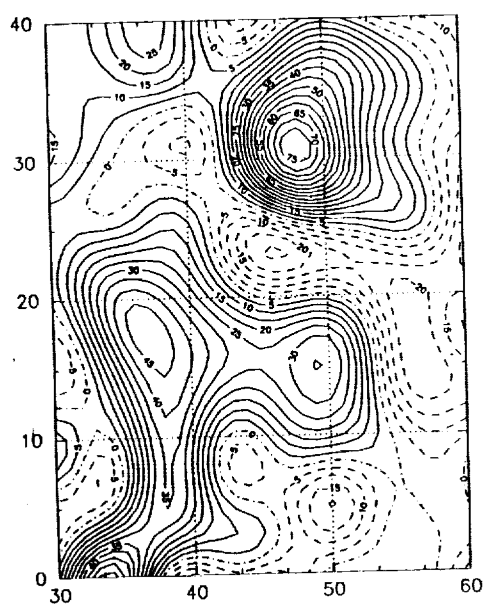
We have also packed these new data into a 60th degree and order spherical harmonic model that reveals definite refinement over the longitudes from 330°E to 100°E. Gravity contours are shown in figure 1. There is definite separation of the Laskmi and Maxwell Montes anomalies and peak amplitudes for Gula, Bell, Sappho and Alpha have increased. Figure 2a,b shows the improvement over Bell Regio where previously there was only S-Band data. The new peaks in the contours correspond very closely to the detailed altimetry from MGN. The Heng-O Coronae at +2N latitude, 5W longitude is revealed as a slight positive anomaly centered more over the circular coronae rather than the southern high topography as was indicated at the December American Geophysical Union meeting in San Francisco. This became evident when the Kaula apriori constraint, that provides numerical stability for high order fields, was removed and therefore only the data controlled the mapping of the anomaly locations (fig. 3). As a result, resolution in the high latitudes was completely lost but the mid-latitudes, 40N to 10S, were clearly defined and uncontaminated by the constraint. This result just further reinforces the need to have a near circular orbit for Magellan, so there will be no need to apply Kaula's constraint. There presently is a plan to do this with an aerobraking period for 70 days after May 24, 1993. We would then acquire gravity data for another global coverage period where the high latitudes would be at near uniform resolution with the equatorial region.

The research described in this article was carried out at the Jet Propulsion Laboratory, California Institute of Technology, Pasadena, CA under contract to the National Aeronautics and Space Administration.

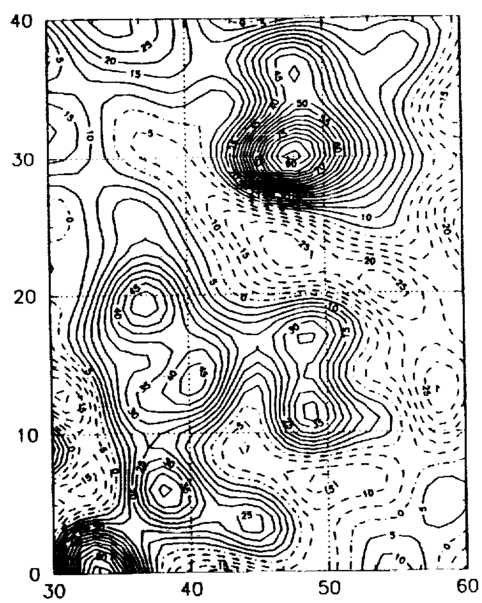
MAGELLAN LOW ALTITUDE DATA: W. L. Sjogren et al.

Fig 1 Venus Gravity (PMG60A with Kaula constraint, data to Dec 13, 1992) 10 milligal contours at the surface





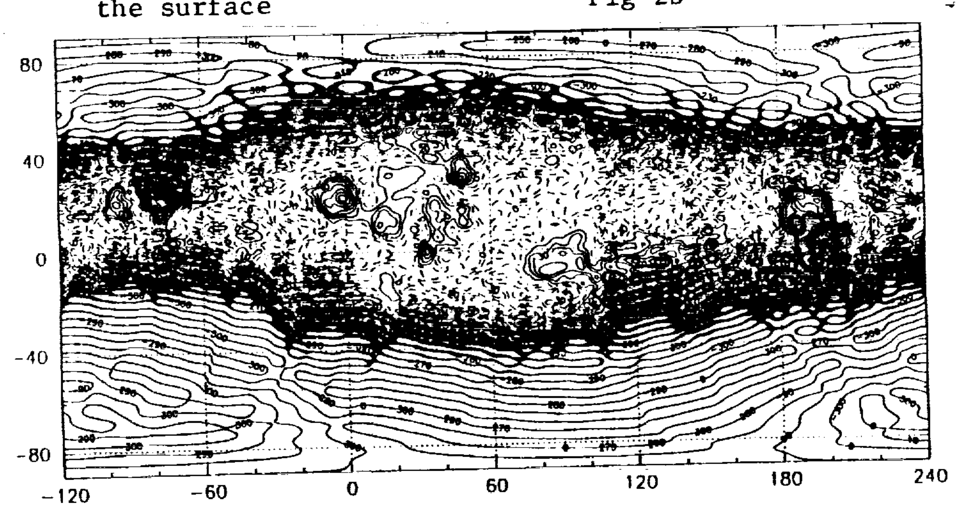
Gravity Bell Regio PVO data (50F solution) 5 milligal contours at the surface
Fig 2a



Gravity Bell Regio MGN data (60A solution) 5 milligal contours
Fig 2b

Fig 3

Venus Gravity same as Fig 1 No Apriori Constraint



SIZE DISTRIBUTIONS AND AERODYNAMIC EQUIVALENCE OF METAL CHONDRULES AND SILICATE CHONDRULES IN ACFER 059. **William R. Skinner,** Department of Geology, Oberlin College, Oberlin, OH 44074, and **James M. Leenhouts,** Department of Hydrology, University of Arizona, Tucson, AZ 85721.

The CR2 chondrite Acfer 059 is unusual in that original droplet shapes of metal chondrules are well preserved. We determined separate size distributions for metal chondrules and silicate chondrules; the two types are well sorted and have similar size distributions about their respective mean diameters of 0.74 mm and 1.44 mm. These mean values are aerodynamically equivalent for the contrasting densities, as shown by calculated terminal settling velocities in a model solar nebula. Aerodynamic equivalence and similarity of size distributions suggest that metal and silicate fractions experienced the same sorting process before they were accreted onto the parent body. These characteristics, together with depletion of iron in Acfer 059 and essentially all other chondrites relative to primitive CI compositions, strongly suggests that sorting in the solar nebula involved a radial aerodynamic component and that sorting and siderophile depletion in chondrites are closely related.

Chondrule diameters were determined by direct measurements of major and minor dimensions taken from enlarged photographs of six thin sections cut from the same orientation on a single piece of Acfer 059. The apparent diameter in thin section was obtained from the average of the two orthogonal dimensions. Most chondrules are almost circular or are slightly flattened (elliptical) as seen in thin section. A total of 64 metal chondrules, 412 silicate chondrules, and 19 "composite chondrules" (consisting of major proportions of both metal and silicate) were measured. The "composite chondrules" were not plotted nor otherwise considered in this study. Figure 1 shows the apparent size distributions of metal chondrules and silicate chondrules as measured in thin section; note that standard deviations for these two populations are quite small. Sorting is actually better than is indicated by the distribution seen in thin section [1], so that adjusted distributions of actual diameters would plot with steeper slopes. The size of

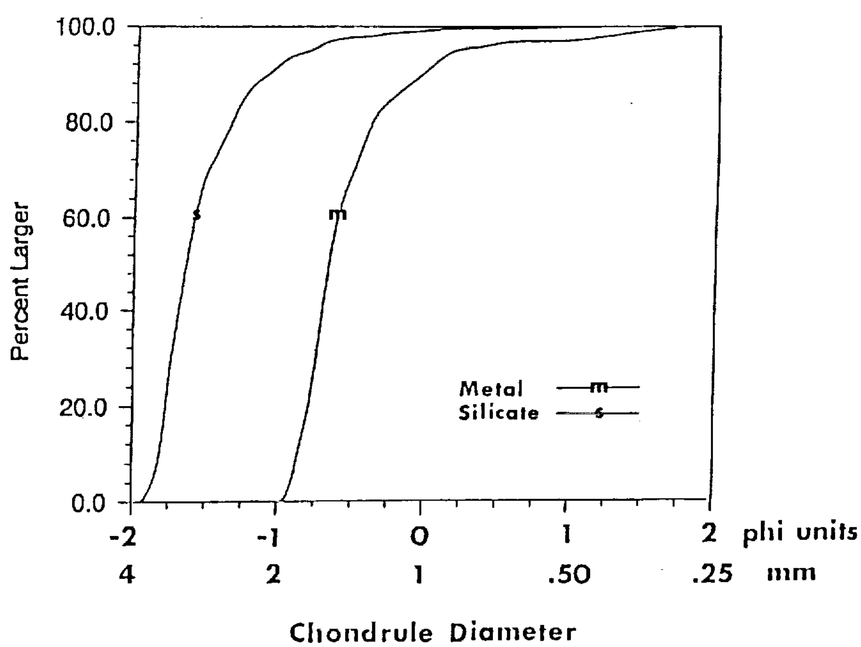


Figure 1. Apparent size frequency distributions of metal chondrules (n=64, std. dev. = 0.32) and silicate chondrules (n=412, std. dev. = 0.58) measured in six thin sections of Acfer 059.

the largest object in each distribution would remain the same, but smaller diameters would be shifted to larger values. The adjusted mean diameters are 0.74 mm for metal chondrules, 1.44 mm for silicate chondrules, and 1.84 mm for "composite chondrules" (1.251 times the apparent mean diameters [1]).

Many of the silicate chondrules, especially the larger ones, exhibit an agglomerated or accretionary habit and contain small metal inclusions; metal is also commonly attached to their perimeters. Metal chondrules generally have original droplet shapes; terrestrial weathering has partly converted some metal to iron oxides, but the original chondrule outlines are easily discerned. Metal content of Acfer 059 is about 10 vol% [2].

The size distributions determined here reveal a high degree of size sorting of both metal chondrules and silicate chondrules. The distributions about their respective mean values are similar for the two populations as shown by the nearly parallel curves in Figure 1. Aerodynamic terminal velocities of spherical objects falling in a model solar nebula were calculated for the two mean sizes using estimated densities of 7.8 gm/cc for metal chondrules and 3.76 gm/cc for silicate chondrules. The latter figure include 10% metal inclusions in the silicate chondrules based on a visual estimate. Calculated terminal velocities are 515 cm/sec for the mean metal chondrule (diameter 0.74 mm) and 504 cm/sec for the mean silicate chondrule (diameter 1.44 mm). These values are virtually identical, strongly supporting an interpretation that the two types of chondrules were sorted aerodynamically at the same time.

The intimate association of metal chondrules and silicate chondrules having metal inclusions seems to indicate that both metal and silicate chondrules formed in the same high temperature event. Chemical similarity of metal chondrules and metal included in silicate chondrules in Renazzo [3] supports this hypothesis. It has been shown for ordinary chondrites that silicate chondrules were formed in a wider size range than that represented in the accreted chondrites [4]. The present study indicates that a wide range of metal and silicate chondrules that formed in a high temperature event (or events) were later sorted into the narrow size ranges observed here. The size ranges of silicate and metal chondrules produced by chondrule-forming events are not known, but it is possible that the same process that sorted chondrules also produced a silicate/metal fractionation. This would account for the depletion of iron and other siderophile elements in chondrites relative to CI compositions [5].

Simple models for parent body formation that consider only vertical settling of particles to the nebular midplane do not explain the overabundance of chondrites with siderophile depletion and the extreme rarity of those with excess metal (and even these rare types, e.g. ALH 85085, were most likely extensively processed on the parent body [6] and may have acquired their metal-rich character after accretion). Strictly vertical settling models should produce abundant metal-enriched chondrites as well as metal-depleted ones, which are not observed. Models that include a radial transport component in the sorting mechanism thus seem to be indicated and could account for transport of the missing metal to regions other than those zones of the asteroid belt from which sampled meteorites are derived.

The correlation in this study between the size sorting of metal and silicate fractions strongly suggests that sorting and siderophile depletion in chondrites are closely connected. It also supports the view that aerodynamic drag is an important process in the preaccretionary history of all chondrites.

Acknowledgment: We wish to thank David New for providing the thin sections used in this study.

References: [1] Hughes D.W. (1978) EPSL 38, 391-400. [2] Bischoff A. et al. (1992) Meteoritics 27, 204. [3] Zanda B. (1991) LPS XXII, 1543-1544. [4] Skinner W.R. and Leenhouts, J.M. (1991) Meteoritics 26, 396. [5] Larimer J.W. and Wasson J.T. (1988) in Meteorites and the Early Solar System, (Kerridge J.F. and Matthews M.S., eds.), 416-435. [6] Brearley A.J. (1990) LPS XXI, 123-124.

S138-91
ABS. ONLY N94-20774

GMM-1: A 50^TH DEGREE AND ORDER GRAVITATIONAL FIELD MODEL FOR MARS; *D.E. Smith*[1], *F.J. Lerch*[1], *R.S. Nerem*[1], *M.T. Zuber*[2,1], *G.B. Patel*[3], *S.K. Fricke*[4], and *F.G. Lemoine*[1,5], [1]Laboratory for Terrestrial Physics, NASA/Goddard Space Flight Center, Greenbelt, MD 20771, [2]Dept. of Earth and Planetary Sciences, Johns Hopkins University, Baltimore, MD 21218, [3]Hughes-STX Corp., Lanham, MD 20706, [4]RMS Technologies, Inc., Landover, MD 20785, [5]Astronomy Department, University of Maryland, College Park, MD 20742.

Knowledge of the gravitatational field, in combination with surface topography, provides one of the principal means of inferring the internal structure of a planetary body. The highest resolution gravitational field for Mars published thus far [1] was derived from Doppler tracking data from the Mariner 9 and Viking 1 and 2 spacecraft and is complete to degree and order 18 corresponding to a half wavelength resolution of approximately 600 km. This field, which is characterized by a spatial resolution that is slightly better than that of the highest resolution (16x16) topographic model [2], has been utilized extensively in analyses of the state of stress and isostatic compensation of the Martian lithosphere [*e.g.*. 3-5]. However, the resolution and quality of current gravity and topographic fields are such that the origin and evolution of even the major physiographic features on Mars, such as the hemispheric dichotomy and Tharsis rise, are not well understood.

We have re-analyzed the Viking and Mariner data sets and have derived a new gravitational field, designated GMM-1 (Goddard Mars Model-1). This model is complete to spherical harmonic degree and order 50 with a corresponding (half wavelength) spatial resolution of 200-300 km where the data permit. In contrast to previous models, GMM-1 was solved to as high degree and order as necessary to nearly exhaust the attenuated gravitational signal contained in the tracking data. This was possible in part due to the use of a least squares collocation solution technique [6], which stabilized the behavior of the solution at high degree and order where correlation and data sensitivities become problematic. The extension of the model to high degree and order significantly reduced errors resulting from spectral leakage coming from the omitted portion of the gravitational field beyond the limits of the recovered model. GMM-1 has a higher spatial resolution than previous iterations of the model [7,8], and in addition is fully calibrated to give a realistic error estimate from the solution covariance.

The data set consisted of 265 orbital arcs representing over 1100 days of S-band Doppler tracking data from the Mariner 9 and Viking 1 and 2 spacecraft, collected by the Deep Space Network between 1971-1978. In total over 215,000 total observations were included in the solution. The data were processed using the GEODYN/SOLVE orbit determination programs, which have previously been used in the derivation of a series of Goddard Earth gravity models, GEM, [*e.g.* 8,9] and have been adapted for the analysis of planetary tracking data [10].

The gravitational potential at spacecraft altitude was represented in spherical harmonic form as

$$V_M(\bar{r}) = \frac{GM_M}{r} \sum_{l=0}^{N} \sum_{m=0}^{l} \left(\frac{r_M}{r}\right)^l P_{lm}(\sin\phi)\ [C_{lm}\cos m\lambda + S_{lm}\sin m\lambda]$$

where $\bar{r}$ is the position vector of the spacecraft in areocentric coordinates, r is the radial distance from the center of mass of Mars to the spacecraft, ϕ and λ are the areocentric latitude and longitude of the spacecraft, r_M is the mean radius of the reference ellipsoid of Mars, GM_M is the gravitational constant for Mars, P_{lm} are the normalized associated Legendre functions of degree l and order m, C_{lm} and S_{lm} are the normalized spherical harmonic coefficients which were estimated from the tracking observations, and N is the maximum degree representing the size (or resolution) of the field. The gravitational force due to Mars which acts on the spacecraft corresponds to the gradient of the potential, V_M. The origin of the field was taken to be the center of mass of Mars, which required that C_{00}=1 and C_{10}=C_{11}=S_{11}=0.

To determine the field, orbits were computed for each arc by estimating from the tracking data the initial state vector of the spacecraft, along with the atmospheric drag, solar radiation pressure, and Doppler tracking biases. After the solutions were iterated to convergence, information equations were created for each arc by evaluating the partial derivatives of the observations with respect to the arc parameters and gravity coefficients along each arc. The gravitational field was then found by adding together the information

equations for each arc and solving the resulting linear system. The dominant error sources in the model are the uncertainties in the spacecraft orbits, which are affected by the tracking coverage as well as the assumed models of atmosphospheric drag and solar radiation pressure, and unmodeled spacecraft perturbations [10]. We imposed *a priori* constraints on the model using weights based on Kaula's Rule [11] rescaled to Mars, which causes poorly observed (usually high degree and order) coefficients to tend towards zero, but has little effect on coefficients that are well sensed by the tracking data [8,9].

Free air gravity anomalies calculated at the surface from the model are plotted in Figure 1. As for previous models, the gravity anomalies correlate well with principal features of Martian topography. The model also shows a greater dynamic range of power in both the gravity anomaly field and the geoid. Probable reasons for the significant improvement achieved over previous fields include: increased computational capabilities; the application of collocation and optimum data weighting techniques in the least squares inversion for the field; and the use of longer arcs (days vs. hours) than used previously for Viking low altitude data made possible by improved force and measurement models.

The near-circular, polar orbit of the Mars Observer spacecraft, now enroute to Mars, will allow considerable improvement of the Martian gravitational field, with the greatest improvement occurring at high latitudes far removed from the Mariner 9 and Viking 1 and 2 periapsis latitudes. This gravity field, in combination with topography derived from from the Mars Observer Laser Altimeter [13], will allow detailed analyses of Mars' internal structure and mechanisms of compensation of surface topography.

References: [1]Balmino, G. et al. (1982) *JGR, 87,* 9735. [2]Bills, B.G. and A.J. Ferrari (1978) *JGR, 83,* 3497. [3]Banerdt, W.B. et al. (1982) *JGR, 87,* 9723. [4]Willemann, R. J. and D.L. Turcotte, (1982) *JGR, 87,* 9793. [5]Sleep, N. and R.J. Phillips (1985) *JGR, 90,* 4469. [6]Lerch, F.J. et al. (1979) *JGR, 84,* 1979. [7]Smith, D,E. et al. (1990) *EOS Trans. Am. Geophys. Un. 71,* 1427. [8]Zuber, M.T. et al. (1991) *Lunar Planet. Sci. Conf. XXII,* p. 1581, Lunar Planet. Inst., Houston. [8]Marsh, J.G. et al. (1988) *JGR, 93,* 6169. [9]Marsh, J.G. et al. (1990) *JGR, 95,* 22043. [10]Smith, D.E. et al. (1990) *JGR, 95,* 14115. [11]Kaula, W.M. (1966) *Theory of Satellite Geodesy,* 124 pp., Blaisdell, Waltham. [12]Tyler, G.L. et al. (1992) *JGR, 97,* 7759. [13]Zuber, M.T. et al. (1992), *JGR, 97,* 7781.

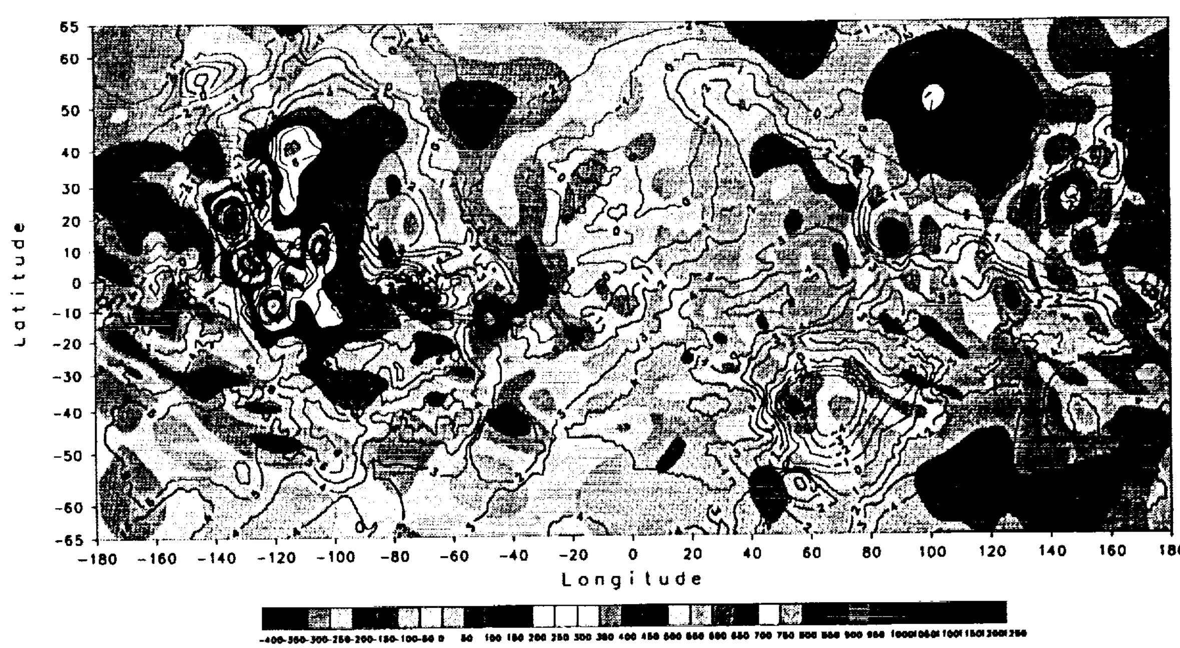


Figure 1. Free air gravity anomalies at the surface computed from Goddard Mars Model-1 (GMM-1) to spherical harmonic degree and order 50. The contour interval is 50 mgals. Also shown is the topographic field with a 1-km contour interval.

3139-91 ABS ONLY N94-20775

RESPONSE OF THE TOPOGRAPHY AND GRAVITY FIELD ON VENUS TO MANTLE UPWELLING BENEATH A CHEMICAL BOUNDARY LAYER;

Suzanne E. Smrekar[1] and E. Marc Parmentier[2], [1]California Institute of Technology, Jet Propulsion Laboratory, Pasadena, CA, 91109; [2]Department of Geological Sciences, Brown University, Providence, RI, 02912.

Introduction. The long wavelength correlation of the gravity and topography and the large apparent depths of compensation (~150-300 km) for large highland regions on Venus require significant differences between the interior structure of Earth and Venus. The morphology, geologic history, and large apparent depths of compensation for many highlands have been interpreted to indicate areas of mantle upwelling [e.g. 1,2]. A large apparent depth of compensation at a mantle upwelling is generally interpreted to indicate the base of the thermal boundary layer of convection. A boundary layer thickness of 150-300 km implies that the interior of Venus is presently much colder than Earth and thus tectonically less active. The recent Magellan mission has provided contradictory evidence regarding the present level of tectonic activity on Venus, prompting considerable debate [3,4]. In this study, we investigate the possibility that a chemical boundary layer acts together with a thermal boundary layer to produce large apparent depths of compensation, or, equivalently, large geoid-to-topography-ratios (GTRs). The crust of a planet forms through partial melting of mantle material. Both the melt and the residuum are lower in density than unmelted (or undepleted) mantle. In the absence of vigorous plate tectonics, a thick layer of buoyant residuum, or depleted mantle, may collect beneath the lithosphere. In this scenario, the thermal lithosphere need not be usually thick and cold to match the GTRs. Cooling of the depleted layer may lead to overturn of the upper mantle and episodic resurfacing with time scales on the order of 300-500 MY, consistent with the resurfacing age of Venus [5].

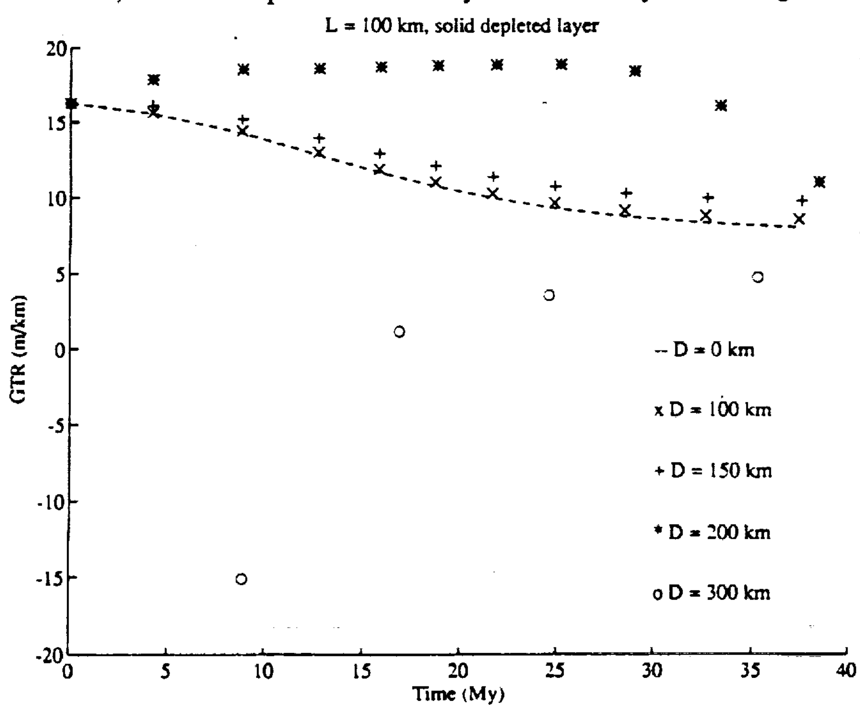
Models. We model an upwelling plume using an axisymmetric finite element code to describe flow and a finite difference solution for the temperature and depletion. The finite element code employs linear quadralateral elements and a direct gaussian elimination solver, which is stable for large viscosity contrasts. The grid contains 40x40 finite elements and 80x80 finite difference elements. The vertical grid spacing is irregular to permit higher resolution in the upper portion of the box, with 1/2 of the elements located into the upper 1/4 of the box. Viscosity decreases exponentially by three orders of magnitude from the surface to a depth a L, which corresponds to the thermal lithosphere, and is constant below this depth. The mantle upwelling is specified at the axis of symmetry by a region of high temperature 7 finite elements in radius by 10 finite elements high. Scaling parameters are $r=1600$ km, $\mu=10^{21}$ Pa s, $dT=200°C$, $\rho=3300$ kg/km^3, $g=8.87$ m/s^2, $\alpha=3\times10^{-5}$ °C^{-1}, $K=10^{-6}$ m^2/s, where r is the radius (and the height) of the box, μ is the viscosity in the interior, dT is temperature difference between the plume and the normal mantle, ρ is the mantle density, g is the acceleration of gravity, α is the coefficeint of thermal expansion, and K is the thermal diffusivity. Depletion in the chemical boundary layer, D, is equal to 20%, typical of residuum from basaltic volcanism. Depletion by 20% is equivalent to the density change resulting from a 500°C increase in temperature. Note that these models do not yet include the effect of melting; the depleted layer is assumed to have formed prior to the start of modeling.

Results. In the absence of a depleted layer, the gravity signal is made up of the gravity due to the topography, which is always the same sign as the topographic relief, and the negative contribution due to the low density material in the upwelling. A buoyant, depleted mantle layer effects the gravity and topography above a rising plume in several ways. The ascent of the rising plume is stalled if the buoyant layer is less dense than the plume. As compared to the case with no depleted layer, the GTR is higher because the low density upwelling is farther from the surface and does not have as large an effect on the gravity. If the strength of the upwelling is great enough to thin the depleted layer locally, the topography above the thinned region becomes negative. More dense mantle material replaces the buoyant, depleted layer, loading the surface. In the early stages of evolution, the positive contribution from the thinned, depleted layer can outweigh the negative contribution from the negative topography, producing slightly positive gravity and slightly negative gravity and thus a negative GTR (see below). Lastly, secondary convection cells may arise as a result of the gradients in depletion and temperature. Such cells are likely to have a minor but complex effect on the GTR.

The time evolution of the GTR above an upwelling is shown in Figure 1. The high viscosity lid extends to 100 km and the thickness of the depleted mantle layer (depletion = 20%) varies. For the case with no depleted layer, the GTR decreases with time as the low density thermal upwelling nears the surface, causing the gravity to decrease. Although the increase in topographic relief produces a more positive contribution to the geoid, overall the geoid is reduced relative to the uplift. The GTR differs only modestly from the D=0 case when the thickness of the depleted layer extends to the same, or a somewhat greater, depth (see Figure 1). When D=2L, the GTR increases substantially above the D=0 km case. For the first several tens of millions of years, the upwelling does not significantly penetrate the depleted layer. As thinning occurs, the GTR approaches that of the D=0 case, and will probably continue to decrease. Extensive thinning occurs in the D=300 km case, causing the topography to rapidly become negative above the upwelling. The D=300 km case thins more readily than the D=200 km case because it extends farther below the stablizing thermal lithosphere and because it encounters the plume when less diffusion of the temperature anomaly has occurred.

Conclusions. These results have important implications for the evolution of highlands on Venus. A continuing debate is whether the observed variations in highland properties represent different stages of evolution or different formation conditions [6]. Using these models, we are likely to be able to match the observed properties of large highlands through a combination of differences in evolutionary stage and depleted layer thickness. As an example, Beta Regio, which has a GTR much larger than those of other highlands, may represent an area where the depleted layer is thicker than normal. Such an interpretation may be consistent with its relative dearth of volcanism [7] if the thick depleted layer reduces pressure release volcanism. Highlands with somewhat lower GTRs may have thinner depleted layers. Coronae in these highlands, such as Nerfertiti on the flank of Bell Regio, may form through secondary convection in the depleted layer. Finally, plains regions may represent more evolved areas where the chemical and/or thermal boundary layers are thinned. This model is not unlike a prior model for thermal topography proposed for Venus [7], but may be able to explain more of the details of the tectonic and volcanic history of venusian highlands.

Future work includes trying to fit the observed topography, gravity, and stress patterns observed at individual highlands, determining more precisely the time scales and density contrasts at which thinning of the depleted mantle layer and secondary convection occur, and incorporating melting into the models. This latter task is likely to have a significant impact on the GTR. Melting will lead to volcanism at the surface, which will both increase the relief and load the surface, and will replenish the buoyant mantle layer, making thinning more difficult.



References. [1] S.E. Smrekar and R.J. Phillips, *EPSL*, *107*, 582, 1991; [2] W.S. Kiefer and B. H. Hager, *Geophys. J. Int.*, *108*, 198, 1992; [3] G.G. Schaber et al., *JGR*, *97*, *E8*, 13,257, 1992; [4] R.J. Phillips et al., *JGR*, *97*, *E10*, 15,923, 1992; [5] E.M. Parmentiter and P.C. Hess, *GRL*, *19*, 2015, 1992; [6] D. Senske et al., this volume, 1993; [7] P. Morgan and R.J. Phillips, *JGR*, *88*, 8305, 1983.

Figure 1. The geoid-to-topography ratios for a plume rising beneath a chemical boundary layer, D, and a thermal boundary layer, L, are shown as a function of time. The geoid-to-topography ratios are calculated at an elevation of 300 km for ease of comparison to venusian values.

5140-46 ABS ONLY

N94-20776

PRIMARY DIFFERENTIATION IN THE EARLY EARTH: Nd AND Sr ISOTOPIC EVIDENCE FROM DIAMONDIFEROUS ECLOGITES FOR BOTH OLD DEPLETED AND OLD ENRICHED MANTLE, YAKUTIA, SIBERIA

Gregory A. Snyder, Eric A. Jerde, and Lawrence A. Taylor, Univ. of Tennessee, Knoxville, TN 37996; **Alex N. Halliday,** Univ. of Michigan, Ann Arbor, MI 48109; **Vladimir N. Sobolev and Nickolai V. Sobolev;** Siberian Branch, Russian Academy of Sci., Novosibirsk, Russia; **Robert N. Clayton and Toshiko K. Mayeda,** Univ. of Chicago, Chicago, IL 60637; **Peter Deines,** Penn State Univ., University Park, PA 16802.

Ancient, stable, continental cratons possess thick, subcontinental-lithosphere mantle "keels" which favor particularly the emplacement of diamondiferous kimberlites, and included peridotites and eclogites [1-5]. These refractory mantle samples of the roots provide hard constraints on the theories of formation, growth, and evolution of these cratons. Xenoliths containing only primary garnet and clinopyroxene (eclogites), although rare in most kimberlites, can retain the geochemical signatures of their parent protoliths (e.g., subducted oceanic crust, ancient mantle; [6,7]), thus offering the opportunity to address mantle processes which may have taken place at earlier times in the Earth's history. In fact, it has been postulated [8], 1984) that some eclogites are residues from the accretion of the early Earth. Nd and Sr isotopic data are presented which may be interpreted as evidence of an early (> 4 Ga) mantle differentiation event.

The kimberlites of Yakutia are located both marginal and central to the Siberian craton, and a wide variety of xenoliths are present within them (e.g., [9]). The Siberian mantle samples have received little attention in the western world, largely because suitable suites of Yakutian samples have not been readily available. Importantly, there is evidence that metasomatism of the Siberian lithosphere has been considerably less intense or extensive than for the Kaapvaal craton [10]. Therefore, it should be considerably easier to elicit the igneous/metamorphic histories of Siberian kimberlitic xenoliths. One of the notable features of the Siberian eclogites is the common appearance of diamonds, especially in the Mir and Udachnaya pipes [10]. In all, eight eclogite samples (eight garnet separates and eight clinopyroxene separates) have been analyzed to date on the Udachnaya pipe, seven from our group (one [11]).

Nd-Sr ISOTOPIC DATA AND AGE INFORMATION -- Sr isotopes in ultra-pure clinopyroxene separates yield measured $^{87}Sr/^{86}Sr$ in the range of 0.70150 to 0.70311. These separates have lower Rb/Sr ratios ($^{87}Rb/^{86}Sr$ = 0.00135 - 0.0946) than coexisting garnet. Garnet separates yield more variable $^{87}Sr/^{86}Sr$ (0.70207 - 0.71162), reflecting wide-ranging $^{87}Rb/^{86}Sr$ (0.00466 - 1.75) due to the incompatibility and low abundances of both Rb and Sr ($\leq$ 0.4 ppm and $\leq$ 5 ppm, respectively). Mineral ages for samples U-25 and U-281 are variable -- 482 $\pm$ 12 Ma and 110 $\pm$ 8 Ma, respectively -- but, bracket the suspected age of the kimberlite (~340 Ma; [11]). Two other Rb-Sr mineral "isochrons" are formed from samples U-86 and U-5. It is granted that these "isochrons" show a much smaller spread in Rb/Sr ratios (and are not indicated on Fig. 1) and are therefore less robust than the other isochrons. U-86 indicates a similar, albeit older, age to the other samples (593 $\pm$ 44 Ma). However, sample U-5 indicates a late-Archean-early Proterozoic "age" of 2528 $\pm$ 340 Ma.

Measured $^{143}Nd/^{144}Nd$ in clinopyroxene separates vary from 0.51134 to 0.51867 and correlate with the $^{147}Sm/^{144}Nd$ (0.0941 - 0.257; Fig. 1). The garnets yield $^{147}Sm/^{144}Nd$ ratios of 0.353 to 0.944 and $^{143}Nd/^{144}Nd$ from 0.51205 to 0.52059. In contrast to mineral separates from eclogites of South Africa, these mineral separates always yield positive slopes, thus allowing the interpretation of "age" information (Fig. 1). Without exception, these rocks have so far yielded Phanerozoic ages -- in fact, ages which approximately point to the time of emplacement of the host kimberlite. These mineral ages range from 214 $\pm$ 11 Ma to 570 $\pm$ 17 Ma with an average of 390 $\pm$ 80 Ma (MSWD = 255). Exclusion of the highest value and the lowest value yields virtually the same average age of 389 $\pm$ 4 Ma (MSWD = 35), but with a much higher precision.

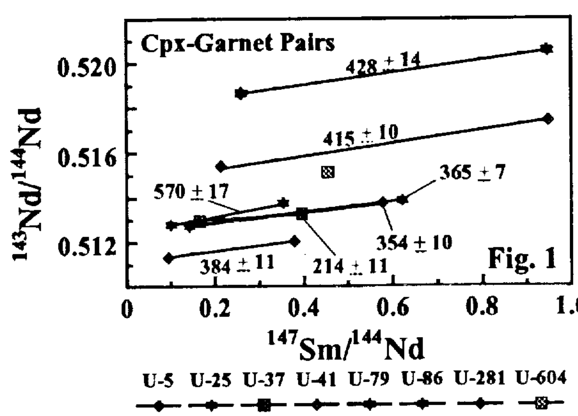


Fig. 1

RECONSTRUCTED WHOLE-ROCK ISOTOPIC EVOLUTION -- The actual whole-rocks contain various alteration minerals which elevate the large ion lithophile elements (such as Rb and the REE). Therefore, reconstructed whole-rock compositions were used in determining model ages. Typically, clinopyroxene is subordinate to garnet in the samples analyzed and comprises 15-58% of the total rock. Obviously, whole-rock reconstructions involve a considerable amount of uncertainty. However, many samples contain pyroxene and garnet that are both LREE-depleted, though to different degrees based upon the accepted modal mineral abundances. Depleted mantle [12] Nd model ages vary widely, and one sample (U-25) does indicate a late Archean/early Proterozoic protolith. All but two samples (U-25 and U-86) indicate at least two-stage histories (Fig. 2; plus the Obnazhënnaya [labeled Ob] samples from [13]). Three such samples (U-37, U-41, and U-79) converge at 2.2 - 2.7 Ga (Fig. 2). A fourth sample (U-5) also converges at this age range and is unique in exhibiting the most enriched signature of any of the samples yet analyzed (present-day ε_{Nd} of -20). Furthermore, this enrichment in U-5 is reflected in both the clinopyroxene and the garnet (which, although LREE-depleted, is the least depleted of any of the garnets analyzed). Varying the proportions of garnet and clinopyroxene in the reconstructed whole-rock may change the slope of

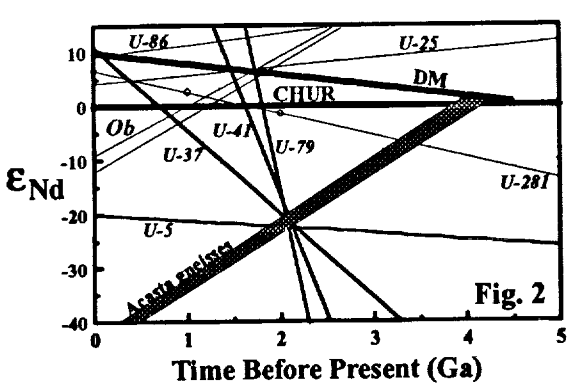


Fig. 2

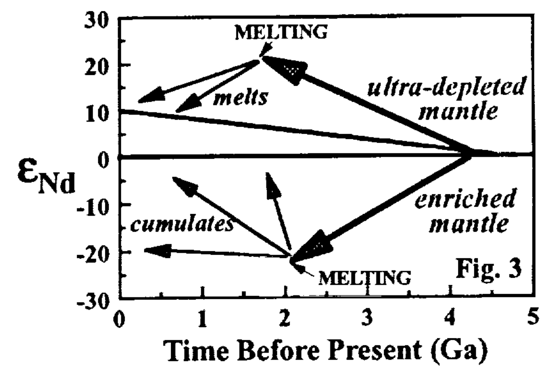
the evolution array for this sample from negative to positive, but no reasonable reconstruction will allow this array to intersect the depleted mantle evolution line or the CHUR line. Therefore, **this sample alone points unequivocally to an old, enriched component.**

Although old enriched mantle is difficult to constrain, the evolution of early enriched Archean crust has been studied in great detail. In Fig. 2, we have also plotted an evolutionary array for some of the oldest enriched crust on Earth, the Acasta Gneisses [14]. Note that this enriched material intersects the four depleted eclogite xenoliths at approximately 2.2 Ga.

EVIDENCE OF OLD (> 4 Ga?) DEPLETED AND ENRICHED RESERVOIRS IN THE EARTH – With this isotopic reconnaissance of the Yakutian samples, we have formulated a working model for the evolution of these eclogites. Samples U-86 and U-25 indicate *LREE-enriched* whole-rock reconstructions. Sample U-281 is one of the few intermediate samples (i.e., the whole-rock may just as likely be LREE-depleted or LREE-enriched, depending upon the proportions of garnet and clinopyroxene in the original rock). The four samples that converge at an ε_{Nd} of -20 at 2.2 Ga actually show depleted LREE signatures. It is somewhat confusing, but **those samples which indicate a long-lived enriched mantle protolith are now LREE-depleted,** whereas **those samples which may indicate an old depleted mantle protolith are LREE-enriched.**

Garnets in the three LREE-enriched samples (U-86, U-25, and U-281) also contain by far the highest abundances of Cr, which is consistent with a link to depleted mantle peridotites. Garnets in the four samples converging at 2.2 Ga contain vanishingly small amounts of Cr (< 0.04 wt.% Cr_2O_3), consistent with their origin as *partial melts (enriched) of primitive mantle leaving a peridotitic residue (depleted).* This differentiated part of the mantle was then melted at 2.2 Ga leaving an eclogitic residue which was depleted. Furthermore, these four convergent samples exhibit more evolved clinopyroxene compositions (Mg#s = 72-87) than those in the samples which are derived from mantle peridotites (Mg#s = 89-91). This is also consistent with the four convergent samples being derived from a differentiated portion of the mantle. Samples U-25, U-86, and U-281 could have been derived from a residue which was depleted early in Earth's history, whereas the four convergent samples (LREE-depleted) would represent the *residue from re-melting of the complementary enriched component* at 2.2 Ga.

SUMMARY – The final working model for genesis of eclogites from the Udachnaya kimberlite is illustrated in Fig. 3: (1) an **early mantle differentiation** event occurred prior to 4 Ga, whereby a chondritic source was melted yielding an **enriched basaltic partial melt** and a **depleted peridotitic residue.** Evidence of an old ultra-depleted mantle beneath the Siberian platform is suggested by two garnet peridotite xenoliths from the Mir pipe which yield ε_{Nd} values of +23 at 1.7 Ga and 0.9 Ga [15]. (2) These two complementary reservoirs then diverged with time until, **at about 2 to 2.2 Ga, both were again melted;** a) partial melts from the melting of the **depleted peridotite source gave rise to the *LREE-enriched* eclogites** (U-25, U-86, and U-281) and b) the **enriched source was depleted at this time** (2 - 2.2 Ga). Either the basaltic mantle component was finally transformed to eclogite and this led to its depletion, or more likely, the **melting of the enriched source was initiated at 2.2 Ga, which left a very depleted eclogitic residue** which gave rise to the *LREE-depleted* eclogites (U-5, U-37, U-41, and U-79).



Extremely low measured $^{87}Sr/^{86}Sr$ values, as well as reconstructed whole-rock model ages, provide evidence for the antiquity of the Yakutian eclogite protoliths and point to a mantle origin for all samples. To date there is **little evidence for the involvement of a crustal component in these eclogites** ($\delta^{13}C$ values [-3.15 to -6.78 for 21 samples; one yields -1.32] in diamonds do not indicate a crustal (biogenic) component, as well as $\delta^{18}O$ mineral values [5.0-7.0] which appear to be mantle only) which is in contrast to eclogites from South Africa which do indicate the involvement of oceanic crust. Complex histories for both LREE-enriched and LREE-depleted eclogites indicate that eclogite xenoliths from the same pipe may reflect grossly different geneses (*"It appears that eclogites found in diamond pipes may possess a multiplicity of origins and, when correctly interpreted, may provide guides to fractionation processes which have occurred within the mantle."* – A.E. Ringwood, [16]), and may further suggest that layering in the mantle occurs on very small scales. Continued studies of eclogites from other Yakutian pipes are underway with the hope of obtaining a better understanding of the earliest differentiation of the mantle beneath Siberia.

REFERENCES: [1] Anderson, D.L. (1981) *Science 213*, 82-89; [2] Anderson, D.L. (1989) Theory of the Earth, 366 pp.; [3] Harte, B. (1986) *4th Int'l Kimberlite Conf.*, abstr., 224-227; [4] Finnerty, A.T. & Boyd, F.R. (1987), Mantle Xenoliths, 381-402; [5] Boyd, F.R. (1989) *EPSL 96*, 15-26; [6] Taylor, L.A. & Neal, C.R. (1989) *J. Geol. 97*, 551-567; [7] Neal, C.R. et al. (1990) *EPSL 99*, 362-379; [8] Jagoutz, E. et al. (1984) *LPSC XV*, 395-396; [9] Sobolev, N.V. & Nixon, P.H. (1987) Mantle Xenoliths, 159-165; [10] Sobolev, N.V. (1977) Deep-seated Inclusions in Kimberlites..., 304 pp.; [11] Jagoutz, E. (1986) *4th Int'l Kimberlite Conf*, abstr., 265-266; [12] Goldstein, S.L. et al. (1984) *EPSL 70*, 221-236; [13] McCulloch, M.T. (1989) Kimberlites & Related Rocks, Vol. 2, 864-876; [14] Bowring, S.A. et al. (1990) Origin of the Earth, 319-343; [15] Zhuravlev, A.Z. et al. (1991) *Geokhimiya 7*, 982-994; [16] Ringwood, A.E. (1975) Composition and Petrology of the Earth's Mantle, 618 pp..

S141-91 ABS ONLY

N94-20777

CHRONOLOGY AND GENESIS OF HIGH-Ti MARE VOLCANISM: MELTING OF COGENETIC DEPLETED AND ENRICHED RESERVOIRS

Gregory A. Snyder, Lawrence A. Taylor, and Alex N. Halliday* Dept. of Geol. Sci., Univ. of Tennessee, Knoxville, TN 37996; * Dept. of Geol. Sci., Univ. of Michigan, Ann Arbor, MI 48109.

An understanding of the chronology and petrogenesis of volcanic rocks is paramount to unravelling the complexities of the composition and structure of the mantle of the Moon. High-Ti mare basalts represent the best-sampled suite of lunar volcanic rocks and likely represent melts of the uppermost mantle of the Moon. Compiled Nd and Sr isotopic data for high-Ti basalts, combined with weighted average ages determined by various techniques yield a complex melting history for the high-Ti mantle source. Melting occurred during three distinct episodes (3.84 Ga, 3.75-3.69 Ga, and 3.56 Ga) separated by hiatuses of 100 Ma or more. The first episode included the melting of a relatively trapped liquid (KREEPy)-rich source beneath the A-11 landing site. Later melting of this source produced magmas which were relatively trapped liquid-free at the A-11 site. Synchronous melting at the A-17 landing site produced magmas with variable proportions of this evolved trapped liquid component. The final phase of volcanism occurred at the A-11 site and invoved the assimilation of an evolved "neuKREEP" component. Continued melting of a similar source, which was nearly exhausted of its ilmenite component, beneath the A-12 landing site may have lead to production of magmas parental to the A-12 ilmenite basalts.

Nd and Sr ISOTOPIC DATA FOR HIGH-Ti BASALTS -- Data from all high-Ti basalts (Apollo 11 and Apollo 17 landing sites) display a broad scatter in initial Nd and Sr isotopic composition as shown in Figure 1 [1,2,3,4,5]. Basalts from Apollo 11 generally plot with less radiogenic Nd compared with those from Apollo 17. Although Apollo 11 Group B1 basalts have ε_{Nd} values that are similar to Apollo 17 A, B1, and C basalts, these groups are distinct in Sr isotopic composition. These variations in initial Nd and Sr isotopic compositions have led previous workers to postulate that the basalts were derived from separate sources and have been used as evidence of heterogeneity in the lunar upper mantle [4]. Though this interpretation seems quite adequate, it is difficult to reconcile with the view that the lunar upper mantle was a simple system which crystallized early and has not been subject to later mixing and recycling processes. Furthermore, this interpretation, which includes a myriad of different sources, does not explain the homogeneity in mineralogy and major-element chemistry for these rocks.

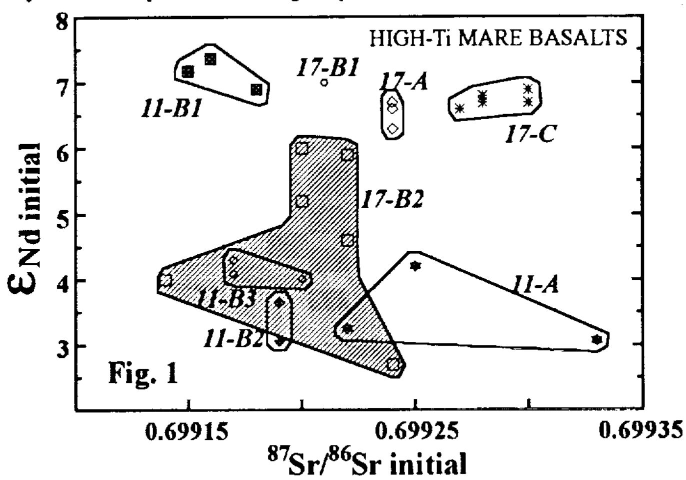


Fig. 1

FORMATION OF COGENETIC ENRICHED AND DEPLETED RESERVOIRS -- Implicit in current understanding of the location of terrestrial enriched and depleted reservoirs is the notion that they are spatially separated. The depleted reservoir on Earth is situated in the upper mantle, and the complementary enriched reservoir is located in the crust. However, Earth reservoirs are continually being modified by recycling driven by mantle convection. The Moon is demonstrably different from Earth in that its evolution was arrested relatively early -- effectively within 1.5 Ga of its formation [1]. It is possible that crystallized trapped liquids (from the late stages of a magma ocean) have been preserved as LILE-enriched portions of the lunar mantle. This would lead to depleted (cumulate) and enriched (magma ocean residual liquid) reservoirs in the lunar upper mantle. There is no evidence for significant recycling from the highlands crust back into the mantle. Therefore, reservoirs created at the Moon's inception may have remained intact for over 4.0 Ga.

It is generally believed that for less than the first 0.2 Ga of its history, the Moon differentiated into a small Fe-rich core, an olivine-rich lower mantle, and a differentiated magma ocean [6]. This outer magma ocean, or magmasphere, progressively crystallized to form the upper mantle of the Moon and, once plagioclase became a liquidus phase, its anorthositic crust. The crystallization of the magmasphere likely led to layering of the upper mantle and included phases, such as ilmenite, late in its differentiation. The adcumulate portion of the lunar upper mantle would be LREE-depleted and contain relatively low abundances of the incompatible elements.

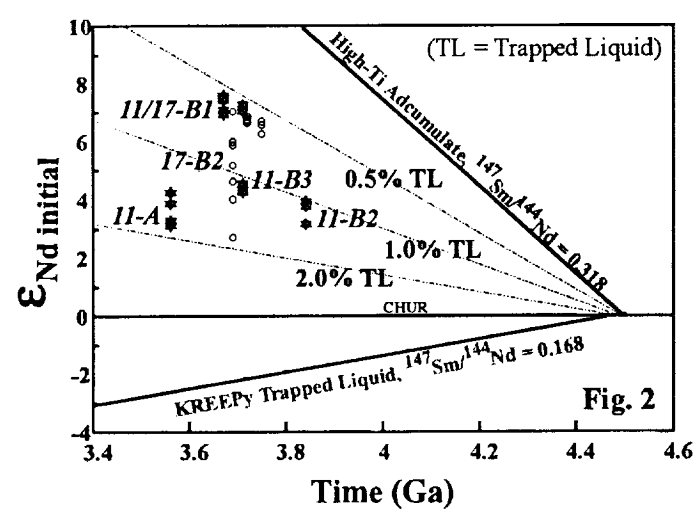


Fig. 2

The residual liquid magmasphere became more evolved with time, leading to enrichment in the LILE. This LILE-enriched liquid could have been trapped in variable, yet small, proportions and effectively "metasomatized" the relatively LILE-depleted crystallizing mafic cumulate. In this way, adjacent regions or layers of the mantle could maintain mineralogic and major-element homogeneity while exhibiting heterogeneities in their trace elements. The LILE-enriched, trapped liquid end-member of the source is represented by residual liquid after 95% crystallization of the LMO (as per Snyder et al.[7]). The isotopic and trace-element composition of this KREEPy liquid component may be represented by KREEP basalt sample 15382 (Rb=16 ppm, Sr=195 ppm, $^{87}Sr/^{86}Sr$ (3.84 Ga)= 0.70115; Sm=31 ppm, Nd=112 ppm, ε_{Nd}(3.84)= -3; [8, 9]). The cumulate portion of the source is modelled as a cpx-pigeonite-ilmenite-olivine perfect adcumulate (Rb=0.01 ppm, Sr=4.16 ppm, Sm=0.631 ppm, Nd = 1.2 ppm, again as per [7]) that has an extremely elevated ε_{Nd} (+8 at 3.84 Ga) and the lowest Sr initial ratio (0.69910) at 3.84 Ga. The Nd isotopic evolution of both end-member components with time is shown if Fig. 2. However, it is not likely that these two components remained distinct over a period of 500 Ma, when the interior of the Moon

was still hot [10]. Recrystallization of the cumulate-trapped liquid pile could have occurred yielding a source which was heterogeneous in trace elements on the scale of meters. Due to the low Sm/Nd ratio of the trapped liquid relative to the cumulate, those portions of the mantle which contained a larger proportion of this component would evolve with more enriched isotopic signatures.

After an extended period of evolution (e.g., > 0.5 Ga), earliest melting of the trapped liquid-cumulate pair would likely affect regions which were relatively enriched in the LILE (containing heat-producing elements U, Th, and K). Therefore, those regions which trapped the largest proportion of residual LMO liquid would melt first. Melts of these regions would exhibit relatively enriched isotopic signatures (Fig. 2). Later melting would tap regions with less trapped liquid and would yield more isotopically depleted melts. Obviously, the degrees of enrichment and depletion of the melts are highly dependent upon the proportion of trapped liquid and the extent of melting of the cumulate + trapped-liquid pile. However, the trapped liquid component is LILE-enriched (generally by at least an order of magnitude over the mafic cumulate) and would have originally consisted of low-temperature melting phases that would readily remelt. Therefore, even a small proportion (e.g., 1 %) in the cumulate pile will greatly affect the isotopic signature of initial derived melts. However, because of its small proportion, the trapped liquid would have a lesser effect (inversely proportional to the degree of melting) on the major-element composition of the melt.

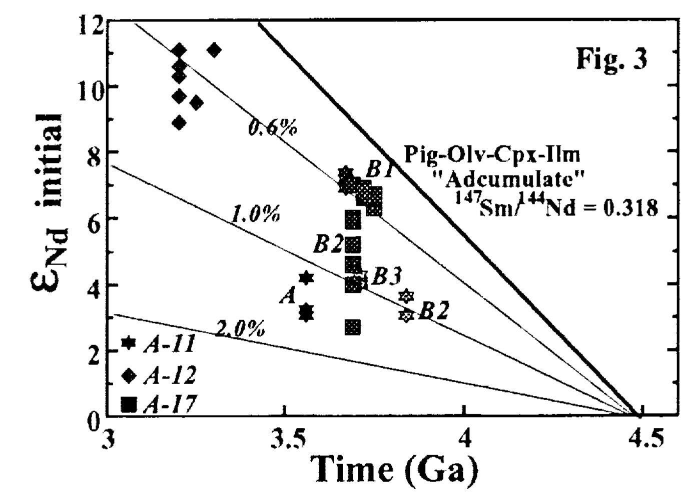
Similar calculations to discern the proportion of KREEP in these basalts were performed by Hughes et al. [11] and Paces et al. [4]. Both groups concluded that small percentages (generally <1%) of a Rb, Sr, and REE enriched component, with high Rb/Sr and low Sm/Nd ratios, are required to explain the compositions of parental magmas for the high-Ti basalts. However, both groups envisioned this component as distal to the cumulate source and added to the source prior to its fusion, but not cogenetic with its inception – approximately 4.4 Ga ago.

MELTING HISTORY OF THE LUNAR UPPER MANTLE – With this model in mind and utilizing both K-Ar and Sm-Nd ages which have been determined by previous workers, including our group, we can suggest an overall scenario for high-Ti basaltic volcanism on the Moon:

1) 3.84 Ga = relatively KREEPy trapped liquid portion of source melted, yielding A-11 B2 (and D?) basalts.
2) 3.75 Ga = melting of relatively trapped liquid-free portion of mantle yields A-17 A basalts.
3) 3.72 Ga = continual melting of trapped liquid-free cumulate leads to A-17 C basalts.
4) 3.71-3.67 Ga = A-11 B3 and B1 basalts produced; **volumetrically most significant**; high-Ti volcanism ceases (?) at A-11 landing site.
5) 3.69 Ga = KREEPyest portion of mantle beneath A-17 site melted yielding A-17 B2 basalts.
6) 3.56 Ga = neuKREEP-rich A-11 A basalts extruded (see Jerde et al., this volume).

Finally, there was volcanic activity at 3.2 Ga at the Apollo 12 landing site ages which was relatively high-Ti in tenor. Apollo 12 ilmenite basalts may represent the final known melting of this cumulate source, after it had been nearly exhausted of its ilmenite and trapped liquid components.

The Apollo 12 ilmenite basalts do indicate a source which is even more depleted than the high-Ti basalts (Fig. 3). The extension of the same or a similar high-Ti source beneath the western portion of the lunar near-side hinges on the identification of older high-Ti basalts near the Apollo 12 landing site. Such high-Ti basalt rocks have not been found in the Apollo 12 collection. However, ultraviolet/visible spectral imaging of Oceanus Procellarum (within which the Apollo 12 landing site is located) by the *Galileo* spacecraft has indicated the presence of wide-spread high- to low-Ti basaltic flows in the basin [12]. Also, studies of Whitaker color-difference photographs of the lunar near-side led Charette et al. [13] to classify one of the stratigraphically oldest mare units in the basin as high-Ti in character.



SUMMARY – The interpretation of cogenetic depleted and enriched reservoirs in the Moon is the consequence of events unique to the Moon. First, the late-stage, LREE- and Rb-enriched residual liquid from a crystallizing LMO was trapped in variable and small proportions in the depleted upper mantle cumulates. A lack of recycling in the lunar environment would allow these reservoirs to diverge along separate isotopic evolutionary paths. This portion of the mantle would remain undisturbed for > 0.5 Ga, prior to being melted to form the oldest high-Ti mare basalts. The isotopic character of the melts would be controlled by the degree of melting, as the least radiogenic reservoir would be melted first – i.e., that portion of the cumulate containing the greatest proportion of trapped liquid would melt first. The range in Sr and Nd isotopic ratios seen in basalts from Mare Tranquillitatis (Apollo 11) is due to melting of a clinopyroxene-pigeonite-ilmenite-olivine cumulate layer with variable proportions of trapped intercumulus liquid. Types B2 and B3 basalts were melted from a portion of the cumulate layer with intermediate amounts of trapped KREEPy liquid. Type B1 basalts from both Apollo 11 and 17 are melted from a "near-perfect" adcumulate portion of this layer. Type A basalts may have been extruded from a vent(s) near the Apollo 17 landing site [14] and could, therefore, represent melting of a similar source, albeit with the added complexity of neuKREEP assimilation.

REFERENCES: [1] Nyquist, L.E. and Shih, C.-Y. (1992), *GCA 56*, 2213-2234; [2] Papanastassiou, D.A. et al. (1977), *PLSC 8th*, 1639-1672; [3] Unruh, D.M. et al. (1984) *PLPSC 14th*, B459-B477; [4] Paces, J.B. et al. (1991), *GCA 55*, 2025-2043; [5] Snyder, G.A. et al. (1993) *EPSL*, submitted; [6] Agee, C.B. and Longhi, J., editors (1992), Workshop on the Physics & Chemistry of Magma Oceans from 1 bar to 4 Mbar, LPI Tech. Rept. 92-03, 79 pp.; [7] Snyder, G.A. et al. (1992), *GCA 56*, 3809-3823; [8] Nyquist, L.E. (1977), *Phys. Chem. Earth 10*, 103-142; [9] Lugmair, G.W. and Marti, K. (1978), *EPSL 39*, 349-357; [10] Warren, P.H. et al. (1991), *JGR 96*, 5909-5923; [11] Hughes, S.S. et al. (1989), *PLPSC 19th*, 175-188; [12] Sunshine, J.M. et al. (1992), *LPSC XXIII*, 1387-88; [13] Charette, M.P. et al. (1974), *JGR 79*, 1605-1613; [14] Jerde, E.A. et al. (1992), *GCA*, submitted.

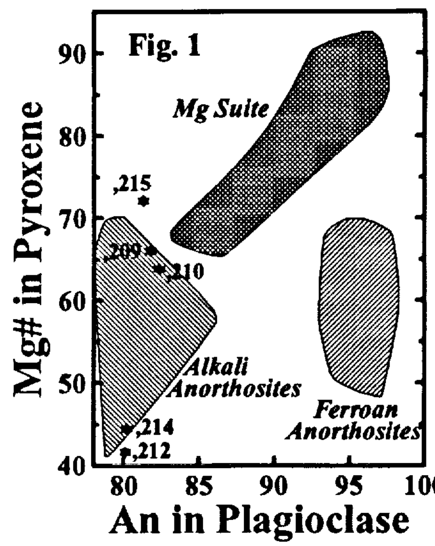
GEOCHRONOLOGY AND PETROGENESIS OF THE WESTERN HIGHLANDS ALKALI SUITE: RADIOGENIC ISOTOPIC EVIDENCE FROM APOLLO 14

Gregory A. Snyder and **Lawrence A. Taylor**, Dept. of Geological Sciences, University of Tennessee, Knoxville, TN 37996-1410; **Alex N. Halliday**, Dept. of Geological Sciences, University of Michigan, Ann Arbor, MI 48109.

Several rocks of alkalic affinity, from the western highlands of the Moon, have been analyzed for their Nd and Sr isotopic compositions. One sample yields a Sm-Nd mineral isochron of 4110 + 41 Ma. This age, in conjunction with U-Pb zircon ages on two other alkalic rocks from the Apollo 14 landing site [1], suggests a distinct western highlands alkalic "event" which was approximately 100 Ma in duration. Since the last dregs of the lunar magma ocean likely crystallized prior to 4.3 Ga, this alkalic "event" may have included the re-melting of evolved plutons or the remobilization of urKREEP trapped liquid from upper mantle cumulates.

Alkalic lithologies such as granites and felsites have been known from the Moon since the earliest days of the Apollo lunar sample returns [2]. However, not until 1977 [3] were alkali-rich rocks recognized from typical highlands suites such as ferroan anorthosites (FAN) and norites and Mg-suite rocks. In the intervening years several other alkali suite samples have been discovered and characterized, mostly through labor-intesive breccia pull-apart studies of clasts and analyses of coarse-fine fractions of soils. We will speculate on the origins of this suite of lunar highlands rocks.

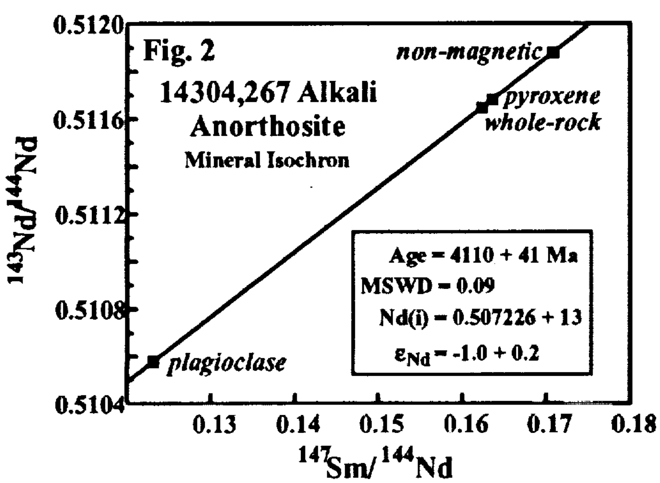
MINERALOGY AND PETROLOGY OF THE HIGHLANDS ALKALI SUITE - - To be considered part of the **alkali suite** from the lunar highlands, only samples which are determined to have attained this character through primary igneous differentiation will be included. Criteria for inclusion in the alkali suite include evolved (elevated) large-ion lithophile elements (LILE) in the whole-rock chemistry combined with evolved mineral chemistry (plagioclase, An < 90; pyroxene, En < 70). Samples which exhibit evolved LILE chemistry in conjunction with FAN-type (An_{91-97}) or Mg-suite-type (En > 70) mineral chemistry are considered to have attained that signature via metasomatism. Obviously, designation as monomict and pristine (or "quasipristine"; in short, endogenous) are also prerequisites for inclusion in the alkali suite. Several "new" clasts were analyzed from breccia 14304. These clasts of alkali anorthosites and a gabbro have plagioclase, pyroxene and olivine compositions consistent with an alkalic affinity (Fig. 1).



GEOCHRONOLOGY AND ISOTOPE GEOCHEMISTRY OF ALKALI SUITE ROCKS Nd and Sr isotopes are reported on three separate clasts of alkali anorthosite from Apollo 14 breccia 14304 (Table 1).

Table 1: Rb-Sr and Sm-Nd isotopes from crustal rocks and mineral separates at Apollo 14

Sample	Rb	Sr	$^{87}Rb/^{86}Sr$	$^{87}Sr/^{86}Sr$	$^{87}Sr/^{86}Sr_{(4.1\ Ga)}$	Sm	Nd	$^{147}Sm/^{144}Nd$	$^{143}Nd/^{144}Nd$	$\varepsilon_{Nd(T)}$
14304,267	3.090	471.3	.01896	.700306+11	0.69917	7.01	26.1	0.16237	0.511648+7	-1.2
"residue"	4.964	93.74	.1532	.708647+11		10.7	37.8	0.17079	0.511880+8	
cpx	9.082	1052.7	.02495	.700657+10		12.8	47.2	0.16361	0.511683+9	
plag	1.141	553.9	.00595	.699448+11		1.54	7.55	0.12311	0.510580+10	
14304,270	24.03	178.1	.3910	.722780+13	0.69928	32.7	117	0.16966	0.511848+7	-1.0
14304,272	17.99	184.9	.2818	.717431+12	0.70049	41.6	149	0.16839	0.511814+7	-1.0

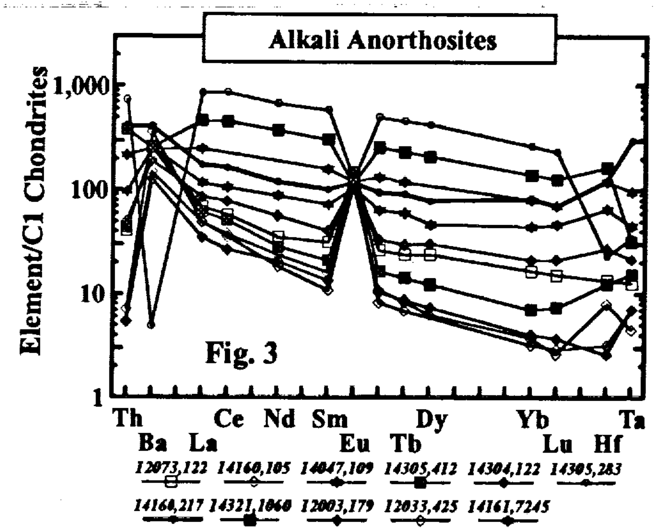


One clast is moderately enriched in Rb and the REE (,267) whereas the others exhibit extreme enrichment for lunar rocks. In an attempt to achieve an age for this alkalic event in the western lunar highlands, isotopic analyses of minerals in sample 14304,267 have also been performed (Table 1). A four-point Sm-Nd "mineral" isochron, including whole-rock, plagioclase, clinopyroxene, and a non-magnetic picking residue yields an age of 4110 + 41 Ma (Figure 2). The initial ε_{Nd} (relative to CHUR) from this line is -1.0. To date, no radiogenic isotopic analyses of alkali gabbronorites/norites have been performed.

In a study of zircons from various lunar rock types, Meyer et al. [1] achieved precise ages for two Apollo 14 rocks of alkalic highlands affinity: alkali anorthosite 14321,16 and mg alkali gabbronorite 14066,47 yielded ages of 4028 ± 6 Ma and 4141 ± 5 Ma, respectively. **These two ages bracket the age obtained for 14304,267 (4110 ± 41 Ma) presented herein and suggest an alkalic "event" of approximately 100 Ma duration on the**

western limb of the Moon. However a single zircon age on an alkali gabbronorite from the Apollo 16 landing site (eastern limb of the Moon) yielded an age of 4339 $\pm$ 5 Ma and points to the chronologically continuous Moon-wide nature of alkalic magmatism.

ORIGIN OF WESTERN HIGHLANDS ALKALI SUITE -- **Alkali anorthosites** are distinguished from other highlands rocks by exhibiting relatively elevated LILE (La = 30-1000x C1 chondrites compared to 1-10 x C1 chondrites for FAN) along with evolved mineral chemistry including plagioclase and pyroxene compositions of An_{86-72} and En_{70-40}, respectively (Figure 1). A total of eighteen alkali anorthosites (sensu lato, > 85% plagioclase) have been described and analyzed from the Moon , however only eleven have been analyzed for the REE (Figure 3; Apollo 12 and 14 sites: [4-13]). Only one known alkali anorthosite has been described from the eastern highlands (15405,181; [14]).



The actual composition of the original liquid from which the alkali anorthosites fractionated was KREEP-like. Some samples, noteably 14160,217, 14305,283, and 14321,1060, contain significant whitlockite. Warren et al. [13] stated that the presence of whitlockite in an anorthosite may complicate its interpretation. However, Snyder et al. [15] have contended that the whitlockite may be representative of the trapped liquid. Late-stage trapped liquids (mesostases) in basalts often contain Ca-phospates including whitlockite.

The lowest REE rock, 14160,105, is "absolutely pure plagioclase, except for one 90x30 μm grain of augite" [4], and can be classified as a nearly perfect adcumulate. Assuming this sample is indeed pure plagioclase, the liquid in equilibrium with this mineralogy can be readily calculated using the mineral/melt partition coefficient relation. Snyder et al. [15] have shown that this equilibrium liquid has LREE abundances which are approximately 1000x C1 chondrites. The pattern is similar to that for high-K KREEP, but has abundances which are a factor of two higher. However, this calculated liquid is similar to the "Super-KREEP" quartz monzodiorite (QMD) 15405c quoted in Warren et al. [13] from Ryder [16]: $(Ce/Lu)_n$ = 2.64, Sm = 93 ppm. This liquid is also similar to recently reported analyses of QMD (14161,7069) from the Apollo 14 site [17].

As pointed out by previous workers (and summarized in [13]), the evidence continues to mount for a relationship between KREEP and the alkali anorthosites. It has been postulated that QMD is the final crystallization product of a KREEP basalt magma [18]. Snyder et al. [15] postulated that the alkali anorthosites are plagioclase cumulates from this late-stage Super-KREEP residual liquid with variable proportions of the liquid trapped in the rock. QMD (similar to 14161,7069) melt can be considered the parental liquid for the alkali anorthosite suite. Alkali anorthosites indicate generally <20% trapped intercumulus KREEPy (QMD) liquid [15].

However, the age of the alkali anorthosites (at least that from samples 14321,16 and 14304,267 -- 4028 Ma and 4110 Ma, respectively) obviates their direct derivation from a residual liquid of the lunar magma ocean, as this early magma ocean could not have persisted beyond 4300 Ga ago. Instead, the parental liquid must be a later melt of the crystallized products of residual KREEPy magma ocean. Evidence that these rocks are indeed melts of a KREEP source rock (original urKREEP residuum?) is found in the initial $^{143}Nd/^{144}Nd$ of the three alkali anorthosites analyzed in this study. The initial ε_{Nd} y-intercept of the mineral isochron is -1.0, indistinguishable from KREEPy rocks at this time.

SUMMARY -- Radiogenic isotopic data from Apollo 14 suggest a relationship between alkali anorthsites and KREEP. A Sm-Nd mineral isochron for 14304,267 indicates an age of 4110 + 41 Ma which is bracketed by two zircon ages of alkali suite rocks from Apollo 14 (4028 + 6 Ma and 4141 + 5 Ma; [1]). This indicates that alkali anorthosites were formed after crystallization of the lunar magma ocean. However, alkali anorthosites may represent remelted portions of differentiated plutons or precipitates from remobilized urKREEP.

REFERENCES: [1] Meyer, C. et al. (1989) *LPSC XX*, 691-692; [2] Brown, G.M. et al. (1972) *Proc. 3rd Lunar Sci. Conf.*, 141-157; [3] Warren, P.H. and Wasson, J.T. (1977) *Proc. Lunar Sci. Conf. 8th*, 2215-2235; [4] Warren, P.H. and Wasson, J.T. (1980) *Proc. Lunar Planet. Sci. Conf. 11th*, 431-470; [5] Warren, P.H. et al. (1981) *Proc. Lunar Planet. Sci. Conf. 12th*. 21-40; [6] Warren, P.H. et al. (1983) *Proc. Lunar Planet. Sci. Conf. 13th*, A615-A630; [7] Warren, P.H. et al. (1983) *Proc. Lunar Planet. Sci. Conf. 14th*, B151-B164; [8] Hunter, R.H. and Taylor, L.A. (1983) *Proc. Lunar Planet. Sci. Conf. 13th*, A591-A602; [9] Shervais, J.W. et al. (1983) *Proc. Lunar Planet. Sci. Conf. 14th*, B177-B192; [10] Shervais, J.W. et al. (1984) *Proc. Lunar Planet. Sci. Conf. 15th*, C25-C40; [11] Goodrich, C.A., et al. (1986) *Proc. Lunar Planet. Sci. Conf. 16th*, D305-D318; [12] Warren, P.H. et al. (1987) *Proc. Lunar Planet. Sci. Conf. 17th*, E303-E313; [13] Warren, P.H. et al. (1990) *Proc. Lunar Planet. Sci. Conf. 20th*, 31-59; [14] Lindstrom, M.M. et al. (1988) *Proc. 18th Lunar Planet. Sci. Conf.*, 169-185; [15] Snyder, G.A. et al. (1992) *Proc. Lunar Planet Sci. 22*, 399-416; [16] Ryder, G. (1985) Catalog of Apollo 15 Rocks. NASA Publ. 72, 1296 pp.; [17] Jolliff, B.L. (1991) *Proc. Lunar Planet. Sci. 21*, 101-118; [18] Ryder, G. (1976) *Earth Planet. Sci. Lett. 29*, 255-268.

5143-91
ABS ONLY

N94-20779

MAGNESIAN ANORTHOSITES FROM THE WESTERN HIGHLANDS OF THE MOON: ISOTOPE GEOCHEMISTRY AND PETROGENESIS

Gregory A. Snyder and **Lawrence A. Taylor,** Dept. of Geological Sciences, University of Tennessee, Knoxville, TN 37996; **Alex N. Halliday,** Dept. of Geological Sciences, University of Michigan, Ann Arbor, MI 48109

Breccias from the Apollo 14 landing site have provided a wealth of information on the genesis of the lunar highlands. Various pristine rock-types have been discovered in relative abundance, including rare ferroan anorthosites, and alkali-suite and magnesian-suite rocks (e.g., [1-3]). Mineral-chemical and radiogenic isotopic data are reported here for a newly discovered Mg-suite anorthosite from Apollo 14, sample 14303,347. Meyer et al. [4] reported U-Pb zircon analyses of Mg-suite highlands rocks from the western limb of the Moon. We have compiled these ages and generated a weighted average age of **4211 + 5 Ma; some 200 Ma younger than ferroan anorthosites**. Utilizing this age for Mg-anorthosite 14303,347, our data results in an initial ε_{Nd} value of -1.0 and initial $^{87}Sr/^{86}Sr$ of 0.69915. Based on trace-element, isotopic, and mineral-chemical data, the western highlands Mg-suite is interpreted to be crustal precipitates of a picritic magma, which assimilated KREEPy trapped liquid from upper-mantle cumulates during its transport to the crust.

MINERALOGY AND PETROLOGY OF ANORTHOSITE 14303,347 -- Clast 14303,347 consists of approximately 95% coarse-grained plagioclase and 5% olivine in a brecciated matrix. Plagioclase composition varies from $An_{93.0}$ to $An_{95.5}$, and olivine composition varies from $Fo_{86.6}$ to $Fo_{88.0}$. The composition of olivine is a clear indication that this sample is not a ferroan anorthosite, but an anorthosite of the Mg-suite (Figure 1) as defined by Lindstrom et al. [3].

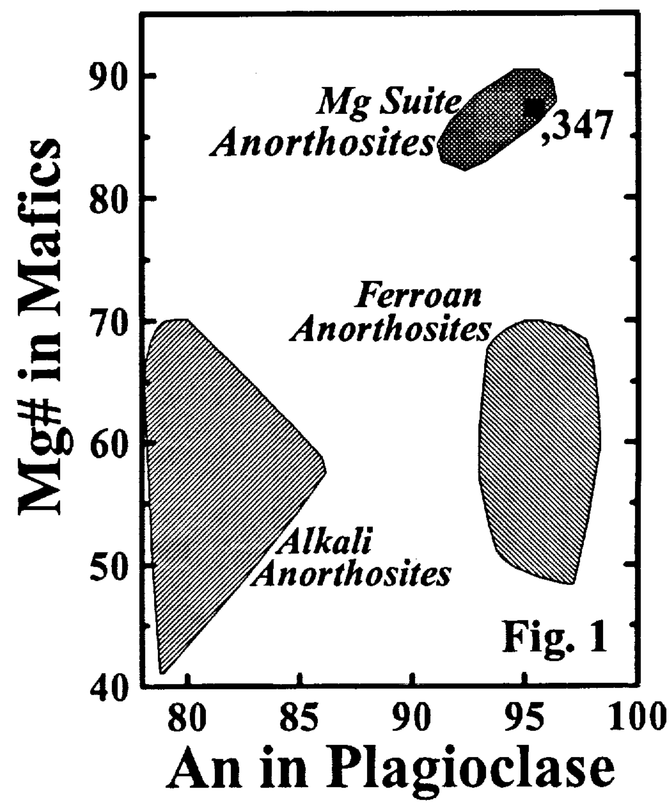


Fig. 1

Nd AND Sr ISOTOPIC RESULTS FOR Mg-SUITE ANORTHOSITE 14303,347

A total of six magnesian anorthosites have been analyzed from the western lunar highlands. Of these, only the one presented herein has been analyzed for Nd and Sr isotopic composition. The measured Sm-Nd ratio for anorthosite 14303,347 is similar to that measured for lunar KREEP. It must be pointed out that this observation, in and of itself, does not necessitate a relationship with KREEP. This is simply an artifact of the partitioning behavior of plagioclase, such that the slope of the LREE in plagioclase is identical to KREEP. Nd and Sr isotopic initial ratios for 14303,347 (Table 1) are consistent with this anorthosite being derived from an enriched portion of the Moon.

Table 1: Rb-Sr and Sm-Nd isotopes of Mg-Suite Anorthosite 14303,347

Rb	Sr	$^{87}Rb/^{86}Sr$	$^{87}Sr/^{86}Sr$	$^{87}Sr/^{86}Sr_{(i)}$	Sm	Nd	$^{147}Sm/^{144}Nd$	$^{143}Nd/^{144}Nd$	$\varepsilon_{Nd(i)}$
0.494	257	0.00556	0.699492+13	0.69915	12.3	44.0	0.16825	0.511792+6	-1.0

PETROGENESIS OF WESTERN HIGHLANDS ANORTHOSITES -- Based on mineral chemistry alone, three distinct types of anorthosites have been determined from the Moon: (1) Ferroan Anorthosites -- uncommon in the western highlands; (2) Magnesian Anorthosites -- of which there are only six recognized from the western highlands; and (3) Alkali Anorthosites -- the most common type in the western highlands (eighteen have been recognized). Fields for these anorthosite types are indicated in Fig. 1.

Based on primitive plagioclase compositions (An_{92}-An_{96}), more-evolved mafic-mineral compositions, and an age of 4.44 $\pm$ 0.02 Ga [5], ferroan anorthosites are thought to be flotation cumulates from the lunar magma ocean. Due to their mineral compositions and trace-element contents, alkali anorthosites are likely cumulates from an evolved quartz-monzodiorite (QMD) liquid [6,7]. An age of 4110 $\pm$ 41 Ma for alkali anorthosite 14304,267 [7] obviates a direct relationship to the lunar magma ocean and is consistent with the QMD parent being a re-melt of an evolved pluton or remobilized KREEP. However, magnesian anorthosites are more difficult to explain.

MAGNESIAN ANORTHOSITES -- Magnesian anorthosites exhibit mineral chemistry consistent with their derivation from a primitive source (picrite?), but have trace-element contents consistent with an evolved parentage. REE contents vary widely, but in all cases, the REE are at least an order of magnitude higher than those in ferroan anorthosites [3]. A compilation of U-Pb zircon ages for Apollo 14 Mg-suite rocks (14305,91:norite = 4211 $\pm$ 5 Ma; 14306,150:troctolite = 4245 $\pm$ 75 Ma; 14306,60:gabbronorite = 4200 $\pm$ 30 Ma; [4]) yield a weighted average age of 4211 $\pm$ 5 Ma (MSWD = 0.54). **Therefore, the Mg-suite is demonstrably younger than the ferroan anorthosites and also must have crystallized some 200 Ma after magma ocean solidification.** However, the enriched Nd isotopic signature for anorthosite 14303,347 (ε_{Nd} = -1.0) obviates its derivation from depleted mantle cumulates alone (which would have exhibited *positive* ε_{Nd} values at 4.2 Ga). Therefore, the Mg-suite could represent re-melted portions of the Moon's deep interior which have been contaminated (metasomatized?) by an enriched component.

As indicated by Lindstrom et al. [3], it is likely that these Mg-anorthosites, and indeed, the whole Apollo 14 Mg-suite, are mixtures of a primitive Mg-rich magma and urKREEP. A primitive picritic magma, possibly derived from the lower mantle, would have been relatively hot and could have assimilated a small amount of KREEPy trapped liquid from the interstices of upper mantle cumulates during transport to the lunar crust. A troctolitic cumulate from this picritic magma would then have an evolved incompatible element chemistry while still exhibiting primitive mineral compositions.

REFERENCES: [1] Shervais, J.W. et al. (1983), *PLPSC 14th*, B177-B192; [2] Shervais, J.W. et al. (1984) *PLPSC 15th*, C25-C40; [3] Lindstrom, M.M. et al. (1984), *PLPSC 15th*, C41-C49; [4] Meyer, C. et al. (1989), *LPSC XX*, 691-692; [5] Carlson, R.W. and Lugmair, G.W. (1988), *EPSL 90*, 119-130; [6] Snyder, G.A. et al. (1992), *PLPS 22*, 399-416; [7] Snyder, G.A. et al. (1993), *LPSC XXIV*, this volume.

3144-91
ABS. ONLY
168154
N94-20780

DIFFERENTIATION OF MAGMA OCEANS AND THE THICKNESS OF THE DEPLETED LAYER ON VENUS; V. S. Solomatov, and D. J. Stevenson (Division of Geological and Planetary Sciences, 170-25, California Institute of Technology, Pasadena, CA 91125, U.S.A.)

Various arguments suggest that Venus probably has no asthenosphere and it is likely that beneath the crust there is a highly depleted and highly viscous mantle layer which was probably formed in the early history of the planet when it was partially or completely molten [*Kaula*, 1990; *Head et al.*, 1992; *Parmentier and Hess*, 1992]. Models of crystallization of magma oceans suggest that just after crystallization of a hypothetical magma ocean the internal structure of Venus consists of a crust up to about 70 km thickness, a depleted layer up to about 500 km and an enriched lower layer which probably consists of an undepleted "lower mantle" and heavy enriched accumulates near the core-mantle boundary.

Partial or even complete melting of Venus due to large impacts during the formation period [*Kaula*, 1979; *Benz and Cameron*, 1990; *Melosh*, 1990; *Wetherill*, 1990] eventually results in differentiation [*Agee and Waker*, 1988; *Herzberg and Gasparik*, 1991; *Abe*, 1990]. However, the final result of such a differentiation can vary from a completely differentiated mantle to almost completely preserved homogeneous mantle depending on competition between convection and differentiation: between low viscosity ("liquid") convection and crystal settling at small crystal fractions or between high viscosity ("solid") convection and percolation at large crystal fractions [*Solomatov and Stevenson*, 1992a,b,c]. The model is following. After the melting event, cooling and crystallization of a magma ocean is due to convection driven by the temperature difference between the hot magma and a relatively cool surface. The surface of Venus radiates as a black body or can be covered by a dense steam atmosphere creating a greenhouse effect. The initial depth of the magma ocean is assumed to be from a few hundreds kilometers to the bottom of the mantle. The equilibrium multiphase thermodynamics of magma ocean assumes three-component ideal mixture between olivine and pyroxenes (upper mantle) or between perovskite and magnesiowüstite solid solution (lower mantle). Rheology is newtonian and coincides with the rheology of dense suspensions (or with the rheology of solids at large crystal fractions). Convection is described in terms of multiphase thermodynamics and rheology with a correction for rotation.

The structure of the magma ocean consists of a completely molten uppermost layer, a layer consisting of melt and the first solid phase, a layer consisting of melt and the first two solid phases and so on. The lowest layer is purely solid, although the complete solidification could be reached somewhere in the middle of the lower mantle. In the absence of differentiation and chemical layering, the convective flow passes through all the regions that causes crystallization and melting cycles in the moving magma. During the crystallization the number and size of the crystals is determined by kinetics. A kinetic model of this process together with calculation of subsequent Ostwald ripening estimates crystal sizes depending on the convective velocities and the kinetic parameters.

DIFFERENTIATION OF VENUS; V. S. Solomatov and D. J. Stevenson

There are three regimes of differentiation: no differentiation (sedimentation is completely compensated by re-entrainment); differentiation is controlled by a competition between crystal settling and turbulent or laminar remixing; differentiation is catastrophic in the sense that all the crystals settle down or float because the heat flux from the magma ocean is unable to remove the heat dissipating from sedimentation.

There are three pronounced critical periods for differentiation – the uncertainties in kinetics are so large that other intermediate cases occupy only a small space in the parameter range. Already in the very beginning of crystallization, the differentiation could be catastrophic that results in a complete "ideal" fractional crystallization. This happens, for example, if the crystals grow to 1 cm size. If this period is passed, the second critical period occurs when the "wet" adiabats drop below liquidus everywhere. Now, the time for ripening is several orders of magnitude larger because it is controlled not by the curculation time scale but by the time scale of the complete crystallization. The last critical moment occurs when the crystal fraction beneath the surface reaches some critical value 0.3 – 0.7. At this point, the partially molten region extends to pressures 5-10 GPa. It differentiates via melt expulsion by compaction forming a crust and a depleted layer. Stratification occurs in any case. However, in the first case, the entire mantle is differentiated and the mantle consists of 4-5 chemically different layers. The depleted layer beneath the crust could be up to 500 km. In two other cases, the differentiation is limited mostly by the upper mantle. The minimum thickness of the depleted layer is about 100 km. However, such a thin layer implies a small degree of differentiation and a small chemical density difference, and as a result the stratification is convectively unstable. Although it is still an open question, we beleive that the difference from the crystallization of a terrestrial magma ocean (likely to result in a small degree of differentiation) could be due to the volatile content. This works in several ways: composition of the early atmosphere can change the cooling rate and convective velocities by several orders of magnitude; the crystal growth rate can be changed by 1-2 orders of magnitude and the viscosity of magmas is also very sensitive to volatiles.

References. Abe, Y., in *Workshop on the Physics and Chemistry of Magma Oceans from 1 bar to 4 Mbar*, pp. 9-10, Lunar and Planetary Institute, Houston, 1992. Agee, C. B., and D. Walker, *Earth Planet. Sci. Lett., 90*, 144-156, 1988. Benz W. and Cameron A. G. W. (1990) In *Origin of the Earth*, 61-67, Oxford Univ. Press, New York. Kaula, W. M., *Geophys. Res. Lett., 17*, 1401-1403, 1990. Head, J. W., et al., in *Papers Presented to the International Colloquium on Venus*, 45-47, August 10-12, Pasadena, 1992b. Herzberg, C., and T. Gasparik, *J. Geophys. Res.*, 96, 16,263-16,274, 1991. Melosh H. J. (1990) in *Origin of the Earth*, p. 69-83, Oxford Univ. Press, New York. Newsom H. E. and S. R. Taylor (1989) Nature, 338, 29-34. Parmentier, E. M., and P. C. Hess (abstract), in *Papers Presented to the International Colloquium on Venus*, 85-87, August 10-12, Pasadena, 1992. Solomatov V. S. and D. J. Stevenson (1993a,b,c) *J. Geophys. Res.*, in press. Wetherill, G. W., *Ann. Rev. Earth Planet. Sci., 18*, 205-256, 1990.

S45-91
ABS. ONLY

N94-20781

A Tectonic Resurfacing Model for Venus; Sean C. Solomon, Department of Terrestrial Magnetism, Carnegie Institution of Washington, Washington, DC 20015.

Two remarkable aspects of the population of impact craters on Venus are that craters at all sizes are indistinguishable from a random population [1] and that the vast majority of craters have not been significantly modified by tectonic strain or by volcanic flows external to the crater rim [1,2], despite evidence from Magellan images that volcanic [3] and tectonic [4] features are widespread on Venus. One interpretation of these observations [2] is that most of the surface dates from the end of a catastrophic global resurfacing event that ceased about 500 My ago, and that the small fraction of craters volcanically embayed or modified by deformation indicates that volcanic and tectonic activity subsequent to that time has been at much lower levels. An alternative model, in which resurfacing occurs episodically in patches a few hundred kilometers in extent and there is a wider spectrum of surface ages, also appears to be consistent with the characteristics of impact craters on Venus [1]. A number of potential mechanisms for catastrophic resurfacing of Venus have been proposed, ranging from geologically sudden convective destabilization of the global lithosphere [5,6] to strongly time-dependent heat flux and melt generation in the underlying mantle [7-9]. In most of these geophysical models, resurfacing occurs implicitly or explicitly by volcanism. We explore here the hypothesis that, at least in the geologically recent history of Venus, the primary resurfacing mechanism has been tectonic deformation rather than volcanism. We show how such a hypothesis provides at least as good an explanation of a wide range of observations as do volcanic resurfacing models. Finally, we explore the implications of the tectonic resurfacing hypothesis for the controversy over the recent resurfacing history of the planet.

Key Observations. Any model for resurfacing on Venus should be consistent with the following observations: (i) The average crater retention age of the surface is about 500 My [1,2,10]. (ii) As noted above, the distribution of craters of all sizes is not distinguishable at high confidence from that of a random population [1]. (iii) Only about 5% of the craters are embayed by volcanic flows exterior to the rim [1,2]. (iv) About one third of the craters have been deformed subsequent to the impact event [2]; for approximately 10% of the craters the post-impact deformation has been extensive [1,2]. (v) There is some tendency for modified craters to be located in areas of low crater density [1]. (vi) There is a weak inverse correlation between crater density and radar backscatter; i.e., smooth plains have some tendency to be more densely cratered than radar-bright regions of high topography and/or high roughness [1]. (vii) The most common radar-bright regions on Venus are the intensely deformed complex ridged terrain, or tessera, that make up large areas of many highland regions [11] and occur pervasively as small exposed inliers in many lowland plains units [4]. (viii) Deformation on Venus tends to be broadly distributed rather than concentrated into narrow zones as on Earth; Venus lacks a global system of tectonic plates [4]. (ix) Topography and gravity are strongly correlated at long wavelengths [12]; many major features have a large gravity-to-topography ratio (GTR) and apparent depth of compensation [13]. (x) Evidence for tectonic activity substantially more recent than 500 My ago, in addition to the large number of deformed craters, includes the great relief and steep slopes of the mountain belts and plateau scarps of Ishtar Terra and of the equatorial chasm systems [4, 14] and elevation profiles indicating differential vertical movements along major channels [15]. (xi) Evidence that the crust and upper mantle of Venus may be stronger than predicted by simple extrapolation from Earth and the 450 K greater surface temperature include the apparently unrelaxed depths of impact craters [2] and large values of elastic lithosphere thickness derived from flexural models of topographic profiles across the margins of coronae [16]. (xii) The ^{40}Ar abundance of the Venus atmosphere is a factor of 4 less than that on Earth as a fraction of planet mass [17], suggesting that any widespread outgassing such as might accompany large-scale overturn of the global lithosphere [5,6] or upper mantle [8] was restricted to times significantly earlier than 500 My ago [18]. (xiii) While episodes of widespread volcanism at a flux greater than the long-term average for the planet have been documented for Mars [19] and Earth [20], none of the other terrestrial planets have been subjected to a global volcanic resurfacing event over the last 4 Gy.

Tectonic Resurfacing Hypothesis. An important difference between Venus and all of the other terrestrial planets is its high surface temperature. Characteristic time scales for ductile deformation

a-6

of crustal and mantle material are known to vary exponentially with reciprocal temperature, so for a given thermal gradient and stress field, high rates of flow are expected to be reached at much shallower levels on Venus than on other terrestrial planets. The large values of GTR and apparent depth of compensation on Venus have been taken as evidence that Venus lacks an asthenosphere or upper mantle low-viscosity channel and that mantle convective stresses couple strongly to the overlying lithosphere [21]. In the absence of plate tectonics, these stresses should give rise to lithospheric strains that are broadly coherent over large regions. For a sufficiently weak lower crust, rates of lower crustal deformation and consequently of surface strain can be high.

Prior to the era of Venus history now preserved, therefore, if the surface temperature was comparable to that at present, the higher heat flow associated with early planetary cooling and enhanced levels of radiogenic heat production and a mantle convective vigor at least that of the present should have led to geologically rapid rates of crustal deformation over most, if not all, of the surface. Such an era would have been characterized by a nearly global extent of complex ridged terrain and few impact craters sufficiently undeformed as to be recognizable from surface images. At some point in the evolution of Venus, however, heat flow will decline to levels sufficiently low that the ductile strength of the lower crust will increase rapidly with small increments of additional cooling. Subsequent to that transition, which might appear to be rapid relative to the geological record, rates of deformation will be substantially less, and both volcanic deposits and impact craters will persist for long intervals with at most modest deformation of landforms. The observations enumerated above are consistent with this hypothesis if this transition from rapid to modest rates of surface strain accumulation occurred about 500 My ago.

Implications for Resurfacing History. The tectonic resurfacing hypothesis leads to some simple predictions that are germane to the resurfacing controversy. If Venus were laterally uniform in both crustal thickness and heat flow, then the transition in surface strain rates would occur with global synchroneity. That is, there would be a rapid change on a planetary scale from high rates of resurfacing to low rates, as is called for by the catastrophic resurfacing model [2], although no true catastrophe - and certainly no global outpouring of magma - is involved. While the assumption of uniform crustal thickness and heat flow is unreasonable, the unimodal hypsometric distribution for Venus suggests that a large fraction of the Venus surface may not depart greatly from this assumption; i.e., an apparently "catastrophic" change is not a bad first approximation. Departures from a globally uniform change in resurfacing rates are to be expected, however. In particular, highland regions, whether they owe their elevations primarily to greater than average crustal thickness or to enhanced temperatures at depth, should persist as regions of high strain rate long after the rate of deformation in lowland plains regions has dropped to modest levels. Lowlands should thus be preferred sites for the preservation of relatively undeformed volcanic deposits and impact craters, as is observed [1,3,4].

Conclusions. The hypothesis that most resurfacing on Venus has occurred by tectonic rather than volcanic processes can account for many of the important characteristics of the planet. The unusual cratering record on Venus is seen in this light to be a consequence primarily of the atmospheric greenhouse and the effect of the high surface temperature on the rheology of the crust. The hypothesis leads to the view that the resurfacing history should contain elements of both the "catastrophic" and "episodic" scenarios for crater removal, with approximately coeval stabilization of lithosphere beneath plains regions but more recent tectonic activity concentrated in highlands.

References. [1] R.J. Phillips et al., *JGR, 97*, 15923, 1992; [2] G.G. Schaber et al., *JGR, 97*, 13257, 1992; [3] J.W. Head et al., *JGR, 97*, 13153, 1992; [4] S.C. Solomon et al., *JGR, 97*, 13199, 1992; [5] E.M. Parmentier and P.C. Hess, *GRL, 19*, 2015, 1992; [6] D.L. Turcotte, *Eos Trans. AGU, Fall Suppl., 73*, 329, 1992; [7] J. Arkani-Hamed and M.N. Toksöz, *PEPI, 34*, 232, 1984; [8] V. Steinbach and D.A. Yuen, *GRL, 19*, 2243, 1992; [9] J. Arkani-Hamed, *Eos Trans. AGU, Fall Suppl., 73*, 332, 1992; [10] E.M. Shoemaker et al., *LPS, 22*, 1253, 1991; [11] D.L. Bindschadler et al., *GRL, 17*, 171, 1990; [12] W.L. Sjogren et al., *JGR, 88*, 1119, 1983; [13] S.E. Smrekar and R.J. Phillips, *EPSL, 107*, 582, 1991; [14] S.E. Smrekar and S.C. Solomon, *JGR, 97*, 16121, 1992; [15] V.R. Baker et al., *JGR, 97*, 13421, 1992; [16] D.T. Sandwell and G. Schubert, *JGR, 97*, 16069, 1992; [17] T.M. Donahue and J.B. Pollack, in *Venus*, p. 1003, Univ. Ariz. Press, 1983; [18] T. Matsui and E. Tajika, *LPS, 22*, 863, 1991; [19] K.L. Tanaka et al., PLPSC 18th, 665, 1988; [20] R.L. Larson, *Geology, 19*, 547, 1991; [21] R.J. Phillips, *GRL, 13*, 1141, 1986.

THE "MISSING" IMPACT CRATERS ON VENUS; D. H. Speidel, Dept. Geol., Queens College, CUNY, Flushing, NY 11367

The size-frequency pattern of the 842 impact craters of Venus measured to date [1] can be well described (across four standard deviation units) as a single log normal distribution with a mean crater diameter of 14.5 km. This result was predicted in 1991 [2] on examination of the initial Magellan analysis [3]. If this observed distribution is close to the real distribution, the "missing" 90% of the small craters and the "anomalous" lack of surface splotches [4] may thus be neither missing nor anomalous.

The cummulative frequency curve of impact crater diameters (Fig.1) illustrates a familiar pattern: the crater diameter size-frequency relationship can be described as approximating a power law in the large sizes. For diameters below about 50 km, the deviation from this power law increases as the diameter decreases, producing the knee or rollover effect displayed. When the individual size-frequencies are plotted however, the pattern seductively appears to approximate a normal distribution.

By using probability graphs [5], the diameters of 842 craters of Venus can be well described by the straight line in Fig. 2 for all but the largest 1% and the smallest 1% of the diameters -- a range of 4 standard deviation units around the mean. But what is the relationship of the OBSERVED to the REAL?

It could be coincidence that a steadily increasing number of smaller and smaller craters starting at about 50 km diameter have been destroyed in the exact proportion necessary to give an apparent log normal distribution. It is to be expected that the dense atmosphere of Venus has strongly affected the production of craters, selectively screening the greater amount of smaller craters. The surface "splotches", assumed to be produced by air blasts from disintegrating impactors [1,4], could be evidence of such atmospheric screening. But the 367 splotches tabulated [4] are nowhere near enough in observed number for the expected power law distribution. Where are the several thousand that would be produced instead of 16 km craters? The approximately 10,000 instead of 8 km craters? They are not observed in anywhere near the number expected if the size-frequency power law holds. The number of splotches is not, however, inconsistent with the observed log normal size distribution of craters.

I think that the missing craters and missing splotches can be satisfactorily explained by accepting that the observed distribution approximates the real one, that it is not the craters that are missing but the impactors. What you see is what you got. The implication that Venus crossing impactors would have the same type of log normal distribution is consistent with recently described distribution for terrestrial craters and Earth crossing asteroids [6].

MISSING VENUS CRATERS: Speidel D. H.

References. [1] Schaber, G.G et al, 1992, J. Geophys. Res, **97**, E8, 13257-13301. [2] Speidel, D.H., 1991, GSA Abstracts with Programs Annual Meeting, A474-475. [3] Phillips, R.A. et al, 1991, Science, **252**, 288-297. [4] Soderblom, L.A. et al, 1992, LPS XXIII, 1329-1330. [5] Sinclair, A.J., 1976, Application of Probability Graphs in Mineral Exploration, Assoc. Explor. Geochemists. [6] Speidel, D.H., 1993, manuscript.

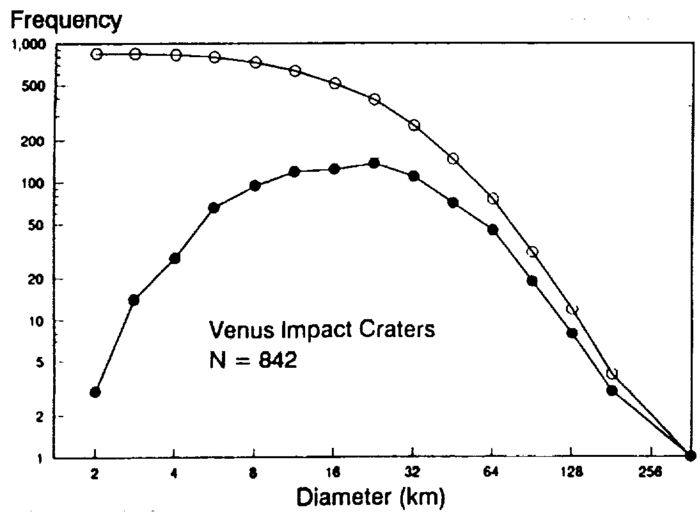


Fig. 1. Size-frequency of Venus impact craters. Cumulative values are open circles. Individual bin values are solid circles. Data from [1]

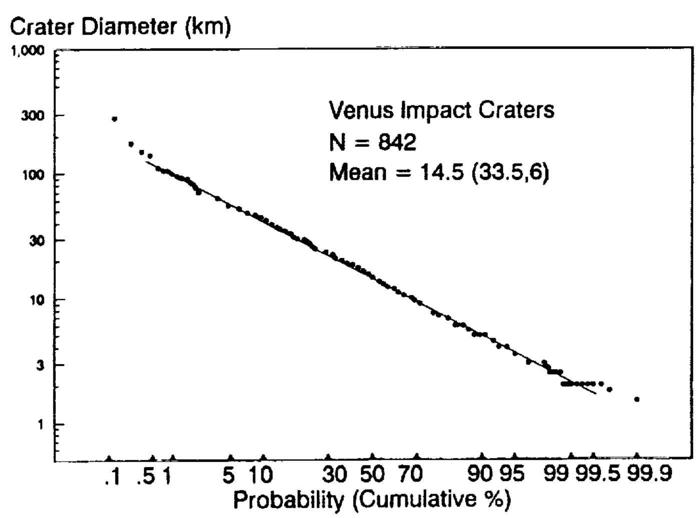


Fig. 2. Probability distribution of Venusian impact craters. Data from [1]. Mean (+/- 1s) is measured from the straight line at 50 (16,84) cumulative percent values. This distribution covers 89% of Venus' surface.

S147-46
ABS. ONLY

N94-20783

DELIMITATION OF TERRESTRIAL IMPACT CRATERS VIA PSEUDOTACHYLYTIC ROCK DISTRIBUTION. *John G. Spray,*
Department of Geology, University of New Brunswick, Fredericton, New Brunswick, Canada

The determination of the shape and size of terrestrial impact craters is problematic, yet is critical to understanding cratering mechanics and for scaling bolide mass, volume and impact velocity with crater size and target response (1). The problem is particularly difficult in older geological terrains (e.g. Precambrian) which are more likely to have suffered post-impact deformation and hence distortion of the original structure and/or where weathering may have partly removed or obscured its original shape. Traditionally, a number of features are used to assist us in determining the shape and size of an impact structure. These include (a) the occurrence of faults, especially those disposed concentrically relative to the crater: the outermost ring faults being interpreted as indicating a viable minimum diameter and (b) the development of so-called breccias (2), some of which are also associated with faults (e.g. the Sudbury Breccia developed within the target rocks of the Sudbury Struture of Ontario, Canada). "Breccia" is not a satisfactory term because a number of breccia-types exist at impact sites (e.g. fall-back breccias and in-situ brecciated target material).

Of relevance to crater diameter determination is the recognition of discrete zones of fault- and shock-related pseudotachylyte (3). Pseudotachylyte is a rock type comprising a fine-grained, usually dark matrix containing clasts of minerals and/or rock derived from the country rock target material. Its origin is normally attributed to high-speed slip (including vibration) along a slip surface (i.e. fault) or to the passage of a shock wave through the host material. The clasts can occur as angular fragments (i.e. like a breccia), but are more commonly developed as rounded to sub-rounded fragments. Significantly, the scale of these pseudotachylytes can range from sub-millimetre thick veinlets to dyke-like bodies up to 1 km or more thick. It is the latter, larger occurrence which has been referred to as "breccia" (4). The smaller-sized occurrence is generally not recognized in the field, nor is it traditionally associated with its larger counterpart.

Recognition of the different types and dimensions of pseudotachylyte occurrences at impact sites is important. Small-scale pseudotachylyte development should not be automatically attributed to pre- or post-impact faulting unrelated to impact. For example, many impact structures contain basement rocks that are pervaded by thin (< 1 mm thick) pseudotachylyte veins that are clearly unrelated to any obvious endogenically-generated fault. Such pervasive zones are common at the margins of the melt sheets in the vicinity of overturned lithologies. The development of densely veined zones of pseudotachylyte may be the result of

rebound and transient crater collapse. Also, the presence of pseudotachylyte at the extremities of the structure can be used as an important indicator of crater size.

References

(1) Melosh, H.J., 1989. Impact cratering. A geological process. Oxford Monographs on Geology and Geophysics, no.11, Oxford University Press, U.K., 245 p.
(2) Lakomy, R., 1990. Distribution of impact induced phenomena in complex terrestrial impact structures: implications for transient cavity measurements. Lunar and Planetary Sciences Conference, XXI, p. 676-677.
(3) Spray, J.G., 1992. A physical basis for the frictional melting of some rock-forming minerals. Tectonoophysics, v. 204, p. 205-221.
(4) Stöffler, D., Bischoff, L., Oskierski, W., and Wiest, B., 1987. Structural deformation, breccia formation, and shock metamorphism in the basement of complex terrestrial impact craters: implications for the cratering process, in: Deep Drilling in Crystalline Rock, edited by Boden,A., and Eriksson, K.G., New York, Springer-Verlag, p. 277-297.

S148-91 ABS. ONLY

N94-20784

CONTRIBUTIONS OF THE CLEMENTINE MISSION TO OUR UNDERSTANDING OF THE PROCESSES AND HISTORY OF THE MOON

Paul D. Spudis[1] and Paul G. Lucey[2] 1. Lunar and Planetary Institute, Houston TX 77058 2. University of Hawaii, Honolulu HI 96822

The Clementine mission [1] will provide us with an abundance of information about lunar surface morphology, topography, and composition, permitting us to infer the history of the Moon and the processes that have shaped that history. This information can be used to address fundamental questions in lunar science and allow us to make significant advances towards deciphering the complex story of the Moon. The Clementine mission will also permit a first-order global assessment of the resources of the Moon and provide a strategic base of knowledge upon which future robotic and human missions to the Moon can build.

What we want to know about the Moon Goals for the scientific exploration of the Moon have recently been articulated [2]. We need to understand the internal evolution of the Moon, including both physical and chemical effects. An intense magmatic history has resulted in a complex, heterogeneous crust and a global inventory of these compositions and their spatial distributions will permit us to determine what processes have operated and the intensities and durations of such processes. The Moon preserves a record of cosmic bombardment in Earth-Moon space and we can use the lunar surface as a natural laboratory to study physics of the impact process, the cratering flux for the last 4 Ga, and to probe the crust at depth by using large craters and basins as natural "drill-holes" into the Moon. The regolith contains information on both the underlying bedrock geology and also the irradiation history of the Moon. We can thus use the lunar regolith as a probe of solar and galactic history. All of these studies improve our understanding of global properties and processes, important constraints on modes of lunar origin.

Where does the Clementine mission fit in? The pressing need for global mapping of the Moon, by a variety of remote-sensing techniques, has been stressed repeatedly in every lunar science report for the last 20 years (e.g., [2,3]). The Clementine mission begins this task. Global mapping of the Moon is one element of a scientific strategy for lunar exploration. Such a strategy includes additional sensing from orbit, surface networks and automated rovers, reconnaissance sampling of carefully selected targets, and detailed human exploration of complicated geological sites [2]. Clementine will obtain the first global digital image data set for the Moon. The imaging sensors are equipped with a variety of filters [4] that have been selected to optimize the geologic value of the multi-spectral data. Topographic profiles derived from LIDAR laser altimetry will greatly improve our knowledge of the global figure of the Moon. Although not carrying X-ray or gamma-ray instruments for chemical mapping, significant chemical information can be obtained from multispectral imaging data (e.g., Ti abundance from ratio of 415/750 nm; [5,6]). It is important to view the Clementine mission in the proper perspective; while not completely satisfying our scientific needs for lunar global mapping, the mission is an impressive beginning towards obtaining such a data set.

Clementine will map the Moon in 11 spectral bands in the visible and near-IR [4]; although surface resolution of the image data varies because of the spacecraft's elliptical orbit, the average resolution will be about 200 m/pixel. The LIDAR instrument will take topographic profiles by taking 100 m spot ranging measurements of about 50 m precision at 2 km intervals; the 5-hour orbital period of the spacecraft ensures that adjacent orbital profiles will be spaced by about 2.5° of longitude (about 70 km at the chosen perilune latitudes of ± 30°). In addition, the LIDAR imager will obtain selected high resolution images (6-15 m/pixel), either as long contiguous strips in a single color or shorter, multi-color images, in up to 4 colors [4]. A thermal IR imager will obtain selected broadband images in the 8000-10,000 nm region at about 70 m/pixel resolution.

What will Clementine data tell us about the Moon? After the Clementine mission, we will possess the data needed to construct a global digital image model (DIM) of the Moon. These data are augmented by: 1) a set of topographic profiles (depending upon the efficacy of the ranging laser, topographic coverage may be nearly complete for the middle latitude band (± 60°) of the Moon); and 2) a geodetic control net for the whole Moon that, when tied to the Apollo data, should permit knowledge of the true positions of lunar surface features in inertial space to within a few hundred meters. Moreover, the framing cameras take data

CLEMENTINE AND LUNAR SCIENCE: Paul Spudis and Paul Lucey

sequentially and some stereo may be possible from overlapping images. Thus, maps of the Moon made from Clementine data will enable studies of regional history and permit us to decipher the processes of volcanism, tectonism, and impact that have shaped lunar history. In a supporting mode, the global DIM will serve as a base to overlay other data; the geological context of the multi-spectral data must be understood to interpret such data properly.

From the combined visible and near-IR cameras, we will have a global color map that we can interpret in terms of the distribution of rock types. At a minimum, we will be able to recognize and discriminate between the absence of mafic minerals (pure feldspar), and the presence of orthopyroxene, clinopyroxene, and olivine, as has been done for the near side of the Moon from Earth-based data (e.g., [7]). Thus, we can distinguish, on a global basis, the distribution of anorthosite, "noritic" rocks, olivine-bearing rocks (dunites and troctolites), and gabbros. For mare deposits, visible color mapping can classify the mare in terms of Ti abundance [5], an element that can be used to estimate the distribution of solar-wind hydrogen, an important lunar resource [8].

Combined with our knowledge of cratering and the use of basins as probes of the crust, these data will permit us to reconstruct the composition and petrologic structure of the crust in three dimensions. We can address the question of the existence of a magma ocean [2,9], the nature of Mg-suite magmatism, the history and extent of ancient KREEP and mare volcanism [9], the compositional diversity of mare units, and the effects of cratering on the composition of the lunar surface. Topographic data from the LIDAR ranger combined with spectral information will allow us to model and understand the dynamics of large impacts, e.g., the problem of depth of excavation for basin-sized impacts [10].

With high-resolution data from the LIDAR imager, we can study surface processes and compositions in greater detail. Many mare units display significant heterogeneity and color imaging from the Clementine LIDAR can map different color units, some of which are perhaps related to individual mare flows. Images of crater walls and central peaks can not only provide high-resolution compositional data, but permit us to better understand the geological setting and processes that have affected given regions, information that may prove critical to the proper interpretation of the regional compositional information. Finally, the high resolution imaging can be used to make detailed geological studies of areas of high scientific interest.

Conclusion The Clementine mission is a boon to the study of the geological processes and history of the Moon. Not an end unto itself, this mission is an important first step in our renewed effort to explore the fascinating and complex story of our nearest planetary neighbor.

References [1] Shoemaker E.M. and Nozette S. (1993) this vol. [2] LEXSWG (1992) *A Planetary Science Strategy for the Moon*, NASA JSC-25920, 26 pp. [3] COMPLEX (1991) *Update to Strategy for Exploration of the Inner Planets*, NAS-NRC Press, 47 pp. [4] Lucey P.G. (1993) this vol. [5] Charette M.P. *et al.* (1974) *JGR* **79**, 1605 [6] Johnson J.R. *et al.* (1991) *GRL* **18**, 2153 [7] Pieters C.M. (1986) *Rev. Geophys.* **24**, 557 [8] Spudis P.D. (1992) *LPI Tech. Rpt.* **92-06**, 47 [9] Spudis P.D. *et al.* (1986) *Status and Future of Lunar Geoscience*, NASA SP-484, 54 pp. [10] Spudis P.D. and Hawke B.R. (1987) *LPS* **XVIII**, 942

S; 49-91
ABS ONLY

IMPACT BASINS ON VENUS AND SOME INTERPLANETARY COMPARISONS

Paul D. Spudis and Virgil L. Sharpton, *Lunar and Planetary Institute, Houston TX 77058*

Impact is one of the many processes that have shaped the surface of Venus [1-3]. The largest impact craters, basins, are important features affecting the evolution of the terrestrial planets [4]. Because Venus has an atmosphere, a gravity similar to Earth's, and a surface target with a high geothermal gradient, venusian basins provide an important comparative set of data to test our ideas about basin-forming impacts and their geological effects on the evolution of the crusts of the terrestrial planets.

Spacing of basin rings: The evidence from Venus The spacing of concentric rings has long been thought to be an important constraint on ring origin specifically and the basin-forming process in general [4-7]. Comparative study of multi-ring basins on the Moon, Mercury, and Mars has shown that ring spacing is constant and independent of planet size, target conditions, or position in the Solar System [7]. Rings of the well preserved Orientale basin on the Moon are spaced at a constant factor of $\sqrt{2}$, i.e., the diameter of each ring is $\sqrt{2}$ times the diameter of the ring lying just inside of it [5,6,8]. This relation was subsequently affirmed not only for all other multi-ring basins on the Moon, but also those on other terrestrial planets [7]. Although it was previously held that two-ring basins follow a different spacing law [6], subsequent analysis has shown that the ratio of inner peak ring to basin rim diameter for these features is 1:2 [7]. The $\sqrt{2}$ spacing rule thus accounts for these features as well if the rule is re-stated as "observed rings are spaced at integer powers of $\sqrt{2}$, or $D_n = (\sqrt{2})^N D$, where N is an integer" [7].

The $\sqrt{2}$ spacing should hold for terrestrial impact basins, but the eroded or buried nature of most of these features precludes rigorous statistical analysis [9]. However, Venus is Earth-like in its basic characteristics and displays several basins having nearly pristine surface morphology. Schaber et al. [3] found that for a set of 33 basins and large craters on Venus, multi-ring basins and two-ring basins followed the $\sqrt{2}$ spacing rule while protobasins [7] followed trends similar to those seen for these large craters on the other planets [3]. We independently mapped the rings of 10 venusian basins (Fig. 1) and likewise find that the spacing of basin rings on Venus is well described by the $\sqrt{2}$ factor. Moreover, our analysis confirms that two-ring basins on Venus are well described by the 1:2 ratio, as in [7], interpreted here as a subset of the general $\sqrt{2}$ spacing rule. Protobasins (craters having a peak and peak-ring; [10]) on Venus follow morphometric trends different from either two-ring or multi-ring basins. An example is Yblochkna (48°, 195°), a protobasin that displays both ring and peak (cf. [11]) and has a rim/ring ratio of 2.8, identical to the mean value found for venusian protobasins (2.8 ± 1.0; [3]) and similar to protobasins on other terrestrial planets (3.3 ± 0.6; [7]).

Our analysis supports the concept that basin rings on Venus are spaced according to the same systematics as basin rings on the other planets [3,7]. Although scatter is seen in the statistical sample [11], as it is for all terrestrial planet basins [7], we are impressed more with the similarity than the diversity of the spacing of venusian basin rings. Such regularity imposes stringent constraints on models of ring genesis [4,7]. Models of ring formation that call upon special conditions of the impact target to control ring formation (such as crustal layering [12] or lithospheric thickness [13]) are not supported by a constant spacing of rings on many bodies of widely varying environments and surface conditions.

Venusian multi-ring basins: Pristine analogs to degraded terrestrial structures Active geological processes on Earth rapidly modify and remove the original surface expression of impact craters, but in many cases, such processes provide invaluable access to crater substructure. Reconstruction of the original crater morphology via comparison with pristine craters on the smaller terrestrial planets is hindered by incomplete knowledge of how such variables as gravity, target properties, and atmosphere affect the cratering process and resulting landform. Venus is earth-like in terms of gravity, atmosphere, and lithospheric thickness. Consequently, the craters and basins of Venus, being both abundant and having pristine morphology, are potentially a Rosetta Stone for deciphering the cratering process on the Earth [14].

The largest impact basins recognized on the Earth are the Sudbury basin, Vredefort Dome, and Chicxulub basin. Sudbury and Vredefort are heavily modified by erosion and tectonic deformation; Chicxulub is virtually pristine, but is buried beneath a 1 km thickness of carbonates. Sudbury, in particular, provides excellent exposure of the interior and vertical structure of a large terrestrial impact basin.

IMPACT BASINS ON VENUS: Paul Spudis and Virgil Sharpton

Moreover, the recent concept that the igneous complex of Sudbury is a differentiated impact melt sheet [15] can be tested through comparative studies of basins of comparable size on Venus. Chicxulub can provide complementary information on and insight into unmodified terrestrial basin structure and morphology. Recent analysis of gravity data over Chicxulub structure suggests that it is a 200 km diameter multi-ring basin [16]. The spacing of the Chicxulub basin rings expressed in the *gravity* data conform to the √2 rule derived solely from the study of the *topographic* rings of planetary basins on Venus and elsewhere (Figure 1; [7]). The best planetary analog to both Sudbury and Chicxulub is the 170 km diameter multi-ring basin Isabella on Venus. We are currently using the complementary sources of information provided by Sudbury, Chicxulub, and Isabella to reconstruct a more complete picture of the formation of multi-ring basins on the terrestrial planets.

References [1] Ivanov B. *et al.* (1986) *PLPSC* **16**, *JGR* **91**, D414 [2] Phillips R. *et al.* (1991) *Science* **252**, 288. [3] Schaber G. *et al.* (1992) *JGR* **97**, 13257 [4] Spudis P. (1993) *Geology Multi-ring Basins*, Cambridge Univ. Press [5] Hartmann W. and Kuiper G. (1962) *Commun. LPL* **1**, Univ. Ariz., 55 [6] Hartmann W. and Wood C. (1971) *Moon* **3**, 3 [7] Pike R. and Spudis P. (1987) *Earth Moon and Planets* **39**, 129 [8] Fielder G. (1963) *Nature* **198**, 1256 [9] Pike R. (1985) *Meteoritics* **20**, 49 [10] Pike R. (1982) *NASA TM* **85127**, 117 [11] Alexopoulus J. and McKinnon W. (1992) *Venus Colloq.*, LPI Contr. **789**, 2 [12] Hodges C. and Wilhelms D. (1978) *Icarus* **34**, 294 [13] Melosh J. (1989) *Impact Cratering*, Oxford Univ. Press [14] Sharpton V. (1992) *Conf. Large Body Impacts*, LPI Contr. **790**, 65 [15] Grieve R. *et al.* (1991) *JGR* **96**, 22753 [16] Sharpton V. *et al.* (1993) this volume.

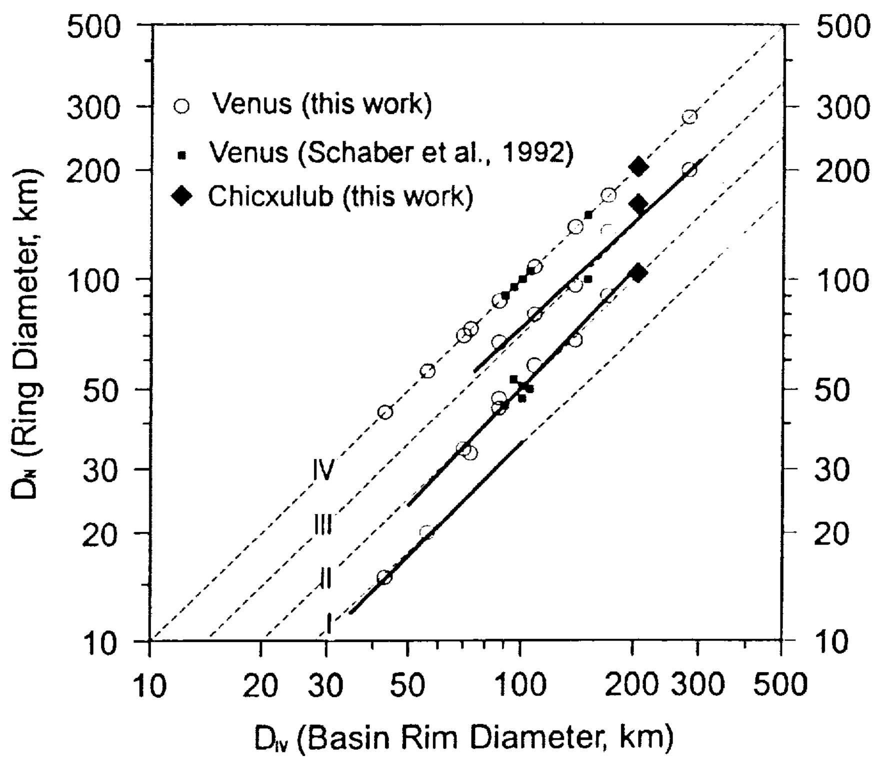


Figure 1. Plot of observed rings (D_N: D_{IV}, D_{III}, D_{II}) against main basin rim (D_{IV}), after convention used by [7], for 16 basins and protobasins on Venus. Open circles our data, solid squares from [3], and solid diamonds are rings observed in gravity data for terrestrial Chicxulub crater [16]. Top line is ring IV (basin rim) plotted against itself; linear least-squares fits (solid black lines) and model (√2) values (dotted lines) shown for intermediate (III), peak (II), and innermost rings (I), after [7].

S150-91
ABS. ONLY

N94-20786

p. 2

GEOLOGY AND DEPOSITS OF THE SERENITATIS BASIN

Paul D. Spudis[1], B. Ray Hawke[2], Paul G. Lucey[2] 1. Lunar and Planetary Institute, Houston TX 77058. 2. Planetary Geoscience, SOEST, Univ. Hawaii, Honolulu HI 96822.

The Serenitatis basin is prominent on the near side of the Moon, just east of Mare Imbrium. Originally thought to be one of the oldest lunar basins, re-interpretation of both geological relations and Apollo 17 isotopic data suggest instead that Serenitatis is one of the youngest basins, having formed in the Nectarian Period about 3.87 Ga ago [1]. As part of our continuing effort to understand the geology of multi-ring basins on the Moon and to use basins as probes of the deep lunar crust [2], we here report results for the Serenitatis basin. Our examination of Serenitatis was stimulated in part by a new effort to re-examine the geology of the Apollo 17 landing site [3].

Geology of Serenitatis Basin Deposits The interior of the Serenitatis basin is extensively flooded by mare basalt and there are no exposures of geological units analogous to those contained within other basins. Presumably, a basin impact melt sheet underlies the basalts of Mare Serenitatis, and the terra surrounding the inner basin mare may be discontinuously mantled by the distal margins of such a melt sheet; this is postulated to have happened at the Apollo 17 landing site. The highlands east of the central Serenitatis basin are composed of two main terrain types: rugged massifs that are crudely aligned along basin-concentric circles and a knobby terrain that has been called informally the Sculptured Hills [1,4]. Rugged massifs form two distinct rings outside the flooded interior of the basin. The intermassif regions are undulating terra that has both rough and smooth facies. The hummocky intermassif deposits are gradational with the Sculptured Hills unit. All of these terra units are found near the Apollo 17 landing site.

Most investigators interpret the Sculptured Hills as an analog to the knobby, Montes Rook Formation of the Orientale basin [4,5]. In this view, the Sculptured Hills are primary ejecta from the Serenitatis basin, deposited between the main topographic rim and the intermediate rings of the basin. A key relation not consistent with a Serenitatis origin for the Sculptured Hills unit is its superposition on the rims of post-Serenitatis basin craters, such as Le Monnier and Littrow [6]. The Sculptured Hills occurs throughout the eastern rim of the Serenitatis basin and may be polygenetic, in part composed of Serenitatis ejecta where it grades into hummocky, intermassif deposits and partly Imbrium ejecta where it is gradational with radially lineated terrain found inside the main rim of Serenitatis.

The heavily cratered eastern rim of the Serenitatis basin may be a product of extensive secondary cratering from the Imbrium basin [1]; these craters are sometimes overlain by the Sculptured Hills and related highland units. Some of the large craters in the eastern Serenitatis rim region (e.g., Littrow) may be Imbrium secondaries that were formed contemporaneously with the deposition of distal ejecta from Imbrium [7]. Thus, in contrast to basin units at Orientale, all of which underlie post-basin craters, highland units on the eastern rim of Serenitatis may both underlie and overlie large, post-basin craters, producing ambiguous stratigraphy.

Ring System of the Serenitatis Basin Serenitatis displays at least four distinct rings. The inner (Linné) ring (410 km diameter) is not expressed by massifs, but its presence is inferred by the circular arrangement of mare ridges within the central basin. The ring that borders the mare is composed of rugged massifs and basin-facing scarps and is approximately 620 km in diameter. This ring passes through the Montes Taurus east of the basin and just west of the Apollo 17 landing site and intersects the northern Apennines of the Imbrium basin. Most workers [1,4,5,7] agree that the main topographic rim of Serenitatis is defined by highland scarps and isolated massifs as well as the "Vitruvius Front", a well-defined platform southwest of the Apollo 17 site, is about 920 km in diameter and corresponds to the Cordillera ring of Orientale. That no textured ejecta are evident in association with this basin ring may result from the extensive obliteration of Serenitatis ejecta by the effects of the impact forming the Imbrium basin.

Outside the main basin rim, two additional rings are evident, with diameters of 1300 and 1880 km, respectively [7,8]. Parts of these rings can actually be traced inside the Apennine ring of the Imbrium basin, helping to constrain the size of the transient cavity for that basin [2]. The rings of the Serenitatis basin display a crudely polygonal outline that reflects interaction with topography both older and younger than the basin. The Vitruvius ring is missing where the Serenitatis basin intersects the Tranquillitatis basin in the

south and is truncated by the Apennines of the Imbrium basin to the west. In addition, the Vitruvius ring becomes highly irregular northeast of the central basin and a tangential structure is evident near the crater Atlas.

Composition of Serenitatis Basin Deposits The composition of highland deposits associated with the Serenitatis basin appears to be more mafic than is typical for other basins we have studied [2]. Orbital chemical data indicate a low-alumina composition, noticeably less feldspathic (Al_2O_3 = 20 wt.%) than typical lunar highlands (Al_2O_3 = 26 wt.%) [9]. Such a chemical composition suggests that Mg-suite noritic rocks and polymict, highland basaltic compositions dominate the deposit. Earth-based spectra indicate that the Taurus-Littrow region, the highlands in Montes Haemus (southwestern basin rim), and terrain north of Mare Serenitatis all contain anorthositic norite. The interior of the crater Menelaus shows noritic anorthosite, but significantly more mafic compositions also occur within and near this crater [10]. Many of the highlands areas contain contaminating mixtures of post-basin mare volcanics, both basalts and pyroclastics; however, some ancient basaltic debris is probably included within the Serenitatis ejecta [6,7].

The Apollo 17 site is near large massifs that are probably close to, if not making up, the rim of the basin transient cavity [1,4,5]. Two classes of impact melt breccias from the Taurus massifs are the poikilitic and aphanitic impact melts [6]. The poikilitic melts are LKFM in composition, form a tight compositional cluster, and have been postulated to represent the impact melt sheet of the Serenitatis basin [11]. The aphanites are also LKFM, but show diffuse chemical grouping and diverse clast populations [6]; this may indicate that they come from a different large impact event [6], but others hold that the aphanites are also from the Serenitatis basin impact [1,4,7,12]. Clastic debris from the site is almost exclusively Mg-suite norites, troctolites, and dunites (in accord with the orbital chemical data [9]), but the ferroan suite is represented by granulitic breccias of unknown precursors. Several chips have been proposed as pristine ferroan rocks from the site [13], but such samples are extremely small and may be unrepresentative pieces of larger samples of uncertain provenance and origin.

Discussion The impact that formed Serenitatis basin probably occurred 3.87 Ga ago [1] and excavated a large fraction of the crustal column in this region of the Moon [7,14]. The main rim diameter of Serenitatis is 920 km; thus, Serenitatis is a basin nearly identical in size to Orientale [4]. On the basis of our previous results for Orientale and other lunar basins [2], we estimate that the Serenitatis basin had a transient cavity diameter of about 500-600 km, a maximum depth of excavation of 55-60 km, and an excavated volume of about 7.5×10^6 km^3 [7]. In contrast to Orientale, where the average pre-impact crustal thickness was about 100 km [15], the crustal target in this region of the Moon was on the order of 60-70 km thick [15]. Thus, the maximum excavation depth of Serenitatis nearly reached the lunar mantle and a significant amount of lower crustal material may make up the basin ejecta. Consistent with this concept, the Serenitatis ejecta appears to be more mafic than other lunar basin deposits. The impact melt sheet of the Serenitatis basin was sampled at the Taurus massifs at the Apollo 17 landing site; it is unclear whether multiple events are represented by the Apollo 17 impact melts. We will continue to acquire new spectral data of Serenitatis basin deposits to better characterize its ejecta and to constrain models of basin excavation.

References [1] Wilhelms D.E. (1987) *USGS Prof. Paper* **1348** [2] Spudis P.D. *et al.* (1984) *PLPSC* **15**, *JGR* **89**, C197; (1988) *PLPSC* **18**, 155; (1989) *PLPSC* **19**, 51; (1989) *LPS* **XX**, 1042; (1992) *LPS* **XXIII**, 1345 [3] Ryder G., Schmitt H.H., and Spudis P.D., eds. (1992) *LPI Tech. Rpt.* **92-09** [4] Wolfe E.W. *et al.* (1981) *USGS Prof Paper* **1080** [5] Head J.W. (1979) *Moon and Planets* **21**, 439; (1992) *LPI Tech. Rpt.* **92-09**, 15. [6] Spudis P.D. and Ryder G. (1981) *PLPSC* **12A**, 133 [7] Spudis P.D. (1993) *Geology of Multi-ring Basins*, Cambridge Univ. Press [8] Pike R.J. and Spudis P.D. (1987) *Earth Moon and Planets* **39**, 129 [9] Spudis P.D. and Hawke B.R. (1981) *PLPSC* **12B**, 781 [10] Hawke B.R. *et al.* (1992) *LPI Tech. Rpt.* **92-09**, 14. [11] Simonds C.H. (1975) *PLSC* **6**, 641 [12] James O.B. *et al.* (1978) *PLPSC* **9**, 789 [13] Warren P. *et al.* (1991) *PLPSC* **21**, 51 [14] Dence M.R. *et al.* (1976) *PLSC* **7**, 1821 [15] Bills B. and Ferrari A.J. (1976) *PLSC* **7**, frontispiece.

S/51-91
ABS ONLY

N94-20787

EARTH-BASED MEASUREMENT OF LUNAR TOPOGRAPHY USING DELAYED RADAR INTERFEROMETRY; N.J.S. Stacy and D.B. Campbell, National Astronomy and Ionospheric Center and Dept. of Astronomy, Cornell University, Ithaca, New York 14853.

Radar interferometry has been applied to radar mapping of the surface of Venus to resolve the ambiguity in the backscatter from the areas with the same delay-Doppler coordinates [1]. For observations of the Moon these points are usually isolated by the small extent of the area illuminated by the radar beam so interferometric techniques can be used to determine a third dimension to the location of the radar backscatter [2]. Recent observations of Sinus Iridum (45.1°N, 31.0°W) using the Arecibo Observatory S-Band radar system (12.6 cm wavelength) in April and August 1992 have yielded a pair of images viewed with a very small 0.0420° difference in incidence angle. These images can be used as a delay interferometric pair and have been correlated to generate phase fringes that are related to topography. The spatial resolution of the images are 18 m in delay and 33 m in cross range (Doppler). The anticipated topographic resolution once the phase fringes have been unwrapped is approximately ±10 m.

In 1972 Zisk [3, 4] used the Haystack radar system with a nearby communications antenna as an interferometer with a baseline of 1.2 km to map the Alphonsus-Arzachel region on the Moon at a pixel resolution of 1–2 km and height accuracy better than 500m. In such an interferometric experiment one antenna transmits a signal to the Moon and both antennas simultaneously receive the echo. Two complex (as in magnitude and phase) delay-Doppler images of backscatter cross section are processed from the two receive signals. The interferometric information is contained in the phase difference between individual pixels, estimated from the phase in the complex product of one image with the complex conjugate of the second image.

Recent Arecibo Observatory S-Band radar observations of the Lunar surface have resulted in several images with spatial resolutions better than 40 m. Unfortunately due to the design of this radar system the main antenna can not receive the Lunar echo because of the small round trip time so the auxiliary antenna, previously used with the main antenna for interferometric observations of Venus, is used as the receiving antenna. An alternative to having two antennas simultaneously receive the same echo is to image the same area twice with a small difference in viewing geometry. This two pass method of radar interferometry, which we refer to as "delayed interferometry", has been successfully used with data from SAR systems orbiting the Earth such as Seasat [5] and the Shuttle Imaging Radar B (SIR-B) [6]. The constraint on the viewing geometry difference can be defined in terms of a viewing geometry correlation function [7],

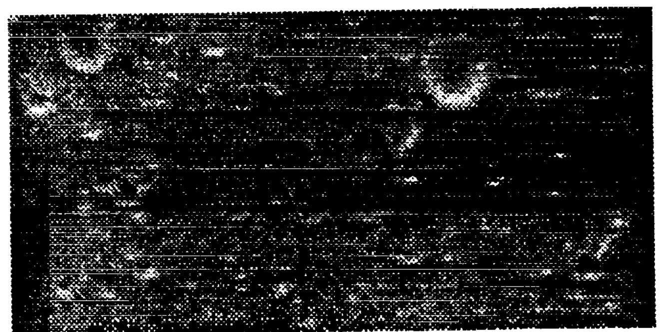
$$\rho_{\text{view}}(\Delta\theta) = 1 - \frac{2\,\delta_{\text{sr}}}{\lambda\,\tan\theta_i}\,\Delta\theta \qquad (1)$$

where δ_{sr} is the slant range resolution and θ_i is the incidence angle so $\delta_{sr}/\tan\theta_i$ is the height of the range resolution projected onto a plane orthogonal to the Earth–Moon vector. If $\Delta\theta$ is zero then the two images have been viewed with exactly the same geometry and there will be no decorrelation due to viewing geometry and there will also be no topographic information. If $\Delta\theta = \lambda\,\tan\theta_i/2\,\delta_{sr}$, the two-way beam width of the projection of the range pixel, then the data in the two images are decorrelated and the phase difference will have no topographic information. For the high resolution S-Band Lunar observations the slant range resolution is 15 m so the maximum viewing geometry difference is 0.24 $\tan\theta_i$ degrees. Such a small difference in viewing geometry requires a very close alignment of the Earth–Moon system. Since observations of the Moon from Arecibo Observatory are restricted to the period in each month when the Moon is above the equator and the period each day when the Moon is near zenith there are a limited number of observation times with closely repeated geometries. A careful examination of the Lunar 1992 ephemeris found three opportunities where the viewing geometry was less than the viewing decorrelation limit. Data was successfully acquired for one of these opportunities in April and August for a 200 km by 400 km area centered on Sinus Iridum at 45.1°N, 31.0°W. Twenty four minutes of data from each observation were processed using a new focused delay-Doppler technique to images of complex radar backscatter. The preliminary results from correlation of two 512 by 512 pixel regions is shown in Figure 1. The incidence angle of the observation is 57° so the projected height of the range resolution is approximately one tenth the fringe spacing. The regular spacing of the phase fringes indicates that this is a relatively flat region of the Moon. The phase

fringe can be seen to deviate around the 2 km crater in the upper right part of the image indicating that the rim of this crater may be 300 m higher than the surrounding terrain.

References

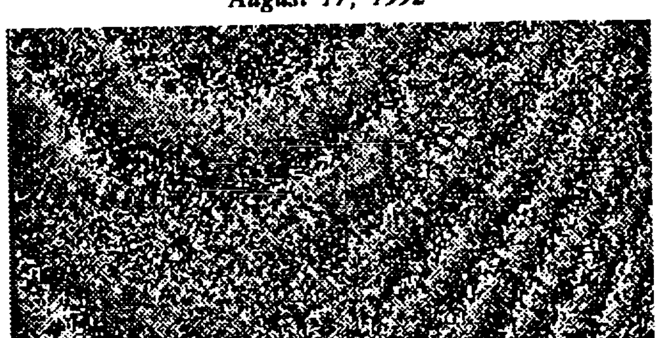
[1] Rogers A.E.E. and Ingalls R.P. (1969), *Science*, **165**, 797–799. [2] Shapiro I.I. et al., (1972), *Science*, **178**, 939–948. [3] Zisk S.H., (1972), *The Moon*, **4**, 296–306. [4] Zisk S.H., (1972), *Science*, **178**, 977–980. [5] Goldstein R.M. et al., (1988), *Radio Sci.*, **23**, 713–720. [6] Gabriel A.K. and Goldstein R.M., (1988), *Int. J. Remote Sensing*, **9**, 857–872. [7] Zebker H.A. and J Villasenor J., (1992), *IEEE Trans. Geosci. Remote Sensing*, **30**, 950–959.



April 29, 1992



August 17, 1992



Interferometric Phase Fringes

Figure 1: Images of the delay-Doppler backscatter and interferometric fringes in the center of the April and August Sinus Iridum data sets. Each image is corresponds to an area on the Moon approximately 17 km by 9.2 km. The original image resolution is 18 m in delay and 33 m in Doppler. The two backscatter images have been averaged by a factor of 4 in delay and 2 in Doppler to 72 m by 66 m pixels to reduce speckle noise. A phase ramp with period of 9.5 pixels has been removed from the phase image which was then averaged by a factor of 4 in range and 2 in Doppler to reduce noise.

S152-90
ABS-ONLY

N94-20788

FE/MN IN OLIVINE OF CARBONACEOUS METEORITES. Ian M. Steele, Dept. of Geophysical Sciences, 5734 S. Ellis Ave., Chicago IL 60637. P-2

Olivines in primitive meteorites show a range of Fe/Mn both within one grain and among grains suggesting that they have recorded changing conditions during or after growth. Because olivine should be an early forming phase, Fe/Mn is used here to infer these earliest conditions. Initial Fe/Mn in cores of isolated, euhedral forsterite in both C2 and C3 meteorites ranges from 25 to 35 but differs at grain edge. Murchison (C2) forsterites show Fe/Mn approaching 1.0 at the grain edge while Ornans Fe/Mn is near 60 at grain edge. These values are lower than the matrix Fe/Mn for both meteorites and the distinct difference in zoning profile indicates different processes operating during and after grain growth.

The Fe/Mn of bulk samples from a particular source such as the Moon is near constant. Individual samples show variation suggesting that there is some fractionation of Mn from Fe. Minerals have their individual ranges of Fe/Mn which has been used to recognize different types of olivine within one meteorite (1). Extreme values of Fe/Mn below 1.0 occur in forsterite from some IDPs, UOC matrix (2) and C1 meteorites (3). There are apparently no detailed studies of Fe/Mn variation within single olivine grains.

Forsterite grains in C2 and C3 carbonaceous chondrites show complex zoning and the nearly pure forsterites (Fo> ~99.5) have high levels of some minor elements including Ti, Al, V and Sc (4). There is disagreement on the original source of these grains and both chondrule (4) and vapor (5) growth have been proposed. In addition, there is clear evidence that diffusion has affected the outer margins but in some cases the whole grain. Within the cores, the FeO range is limited and if growing under constant conditions the Fe/Mn should be near constant as there is little fractionation of Mn from Fe by forsterite and there are apparently no co-crystallizing phases as evidenced by a lack of common inclusions in the forsterites. These observations are now followed by analyses of isolated olivine grains in C2 and C3 meteorites.

Plots of FeO vs Fe/Mn are given below (Fig. 1a,b) for scans from interior to edge of isolated grains in Murchison (C2) and Ornans (C3O). The FeO values clearly show a wider range in the Ornans grain and the trend for Fe/Mn with increasing FeO (from interior to edge) is distinctly different from that of Murchison. Because the Mn level is near the detection level of the electron microprobe in the interior of both grains, Fe/Mn shows wide scatter for low FeO concentrations. To obtain accurate Fe/Mn at low Mn concentrations, special analyses were made with counting times 300sec on both peak and background giving a Fe/Mn of 24 and 35 in Murchison and Ornans olivine cores, respectively. The Murchison trend shows a decrease in the Fe/Mn from 24 to near 1.4 at the grain edge where MnO and FeO have values of about 0.6 and 0.8 wt%, respectively. The Ornans grain is very different where Fe/Mn increases to values of about 60, similar to values for Allende (5).

The enrichment of Murchison forsterite in Mn (Fig. 2) and the low Fe/Mn at the grain edge is reminiscent of the published data for some matrix olivines in Semarkona (UOC) (2) where olivines were reported with up to 1.0 wt% MnO and Fe/Mn of 0.5, but not as extreme as some IDP forsterites (2). These chemical trends are additional evidence of a relationships among several types of extraterrestrial olivines found in micrometeorites, C1 and C2 meteorites, UOC matrix, and IDPs (5). In addition, the interior trace element abundances of forsterites are indistinguishable in all extraterrestrial material suggesting a common origin (6).

While the increase in both Fe and Mn at the grain edges can be attributed to diffusion of a more Fe,Mn rich reservoir, the Fe/Mn is not the same as the core and does not match that of the present matrix with an Fe/Mn over 100. Diffusion of Fe is known to be more rapid than Mn (7) and diffusion alone would also give a higher Fe/Mn toward the grain interior which is not observed for Ornans. Thus for Ornans, diffusion from a reservoir intermediate in Fe/Mn and contemporaneous progressive growth is invoked to explain the chemical trends. The extreme Mn enrichment in Murchison forsterite edges suggests an environment very different from that in which the grain interior grew and unlike the present surrounding matrix. A Mn enriched reservoir suggested by these data is not represented by other recognized extraterrestrial material. The oxygen isotope composition of Ornans forsterite is similar to that of Allende forsterite and different from the bulk meteorite, indicating no direct relation to matrix (C2 forsterite oxygen has not been measured). The observations are consistent with an initial assemblage of homogeneous olivine grains which then followed two diverse chemical paths possibly due to reaction with an inhomogeneous nebula. The distinctly different Fe/Mn trends are most easily explained by a variation

FE/MN IN OLIVINE OF CARBONACEOUS CHONDRITES: Steele, I.M.

in the oxidation state of Fe where the Ornans grains show both an increase in FeO and an increase in Fe/Mn indicating progressively more oxidizing conditions. Based on O16-rich oxygen of several Fe-rich matrix grains, some of the matrix probably was formed during growth of the larger forsterite grains. The Murchison grains show only a marginal increase in Fe and a decrease in Fe/Mn indicating a low concentration of oxidized Fe and a competition between Fe and Mn during growth resulting in both a weak enrichment in FeO under reducing conditions such that the oxidized Fe was removed from the system and effectively decreasing the Fe/Mn of its reservoir. Like the C3 meteorites some matrix grew under the same conditions and has been recognized within the matrix of Semarkona.

Both the observations and proposed mechanism of growth require an inhomogeneous nebula in which at least two chemical/isotopic paths were followed. This was followed by mixing of the components (at least represented by matrix) but not of the coarser fraction. The inhomogeneity of the nebula is represented in chemistry, oxidation state, and oxygen isotopic composition.

References: (1) Kimura and Ikeda (1992) Proc. NIPR Sympos. on Antarctic Meteorites 5, 74-119. (2) Klöck et al. (1989) Nature 339, 126-128. (3) Steele (1992) GCA 56, 2923-2929. (4) Jones (1992) GCA 56, 467-482. (5) Steele (1986) GCA 50,1379-1396. (6) Steele and Smith (1986) LPS XV, 822-823. (7) Morioka (1981) GCA 45, 1573-1580.

Acknowledgements: NASA NAG 9-47 and NAGW 2272 for support.

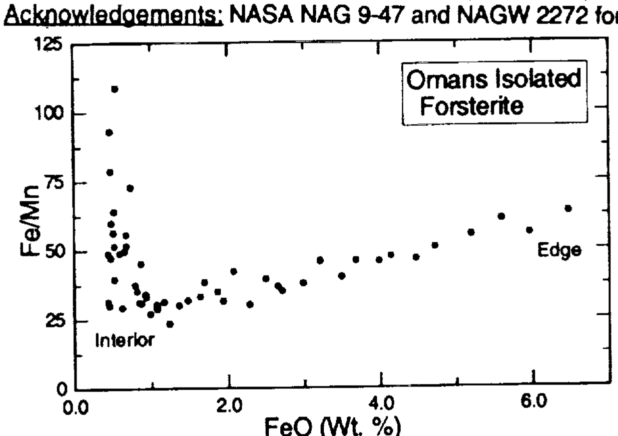


Fig. 1a. Variation of Fe/Mn as function of FeO in Ornans isolated forsterite. Because FeO increases from interior to edge, the FeO is a function of distance from edge. Mn is very low in interior giving large scatter shown for FeO<0.7%. Detailed analyses show the the Fe/Mn in the interior as near constant with a average value of 35. Toward the edge the Fe/Mn increases to 60.

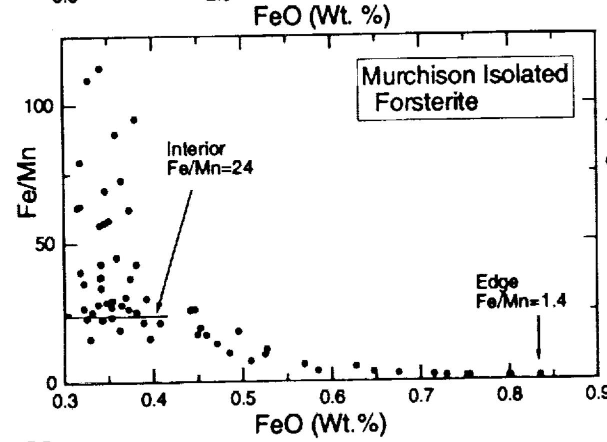


Fig. 1b.Variation of Fe/Mn as function of FeO in Murchison isolated forsterite. In contrast to 2a, The Fe/Mn decreases to values near 1.0 at grain edge from an internal value near 24.

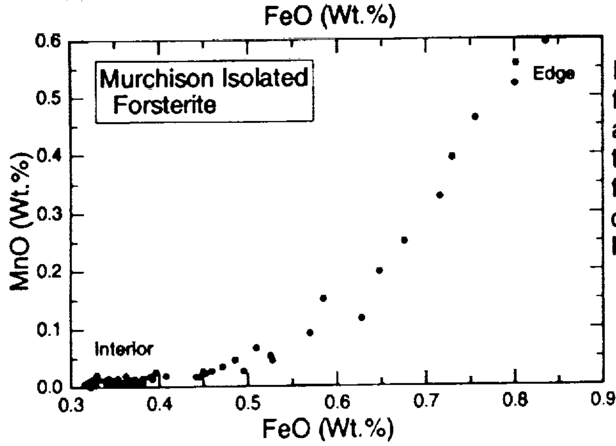


Fig. 2. MnO vs FeO for isolated Murchison forsterite. FeO is near constant in the interior and increases near the edge. MnO is very low in the interior and increases toward edge but at a faster rate than FeO. The edge MnO is comparable to values found in forsterites in many IDPs (2).

5153-46
ABS ONLY

N94-20789

p. 2

TWO-POLARITY MAGNETIZATION IN THE MANSON IMPACT BRECCIA.

M.B. Steiner, Dept. Geology/Geophysics, Univ. of Wyoming, Laramie, WY 82071 and E.M. Shoemaker, U.S. Geol. Survey, Flagstaff, AZ 86001

Preliminary paleomagnetic study of the impact breccia matrix and clasts has produced surprising results: nearly antipodal normal and reversed polarity magnetic vectors are observed in different portions of the core. Near-antipodal magnetizations within a segment of matrix, and within individual samples rule out core inversion as the explanation of the dual polarity. In both the dense and the sandy matrix breccias, the magnetizations of clasts and matrix within the same core segment are identical; this negative 'conglomerate test' indicates that magnetization originated after impact.

Paleomagnetic study of the Manson Impact Structure is an attempt to refine the Ar^{40}/Ar^{39} age (65.7±1 m.y. [1]) that suggests Manson to be a Cretaceous-Tertiary boundary impact. Refinement is possible because the boundary occurs within a reversed polarity interval (29R) of only 0.5 m.y. duration. The two breccia types in the Manson structure were both examined, one of a very dense matrix and apparently partially melted, and the breccia stratigraphically below it of granular or "sandy" chloritic matrix. Samples were taken from the matrixes and a wide variety of clast compositions, including granite, diabase, gneiss, amphibolite, and melted granite. Currently, measurements have been made on 22 samples, using 30-35 steps of either alternating field (AF) or thermal demagnetization.

Samples display either a dominantly reversed or normal polarity magnetization, but vectors of both polarities are observed within most of the samples. The dominant magnetization is held between 250° and 570°C and decays linearly to the origin of orthogonal axes plots; the opposite polarity magnetization is commonly observed as a vector removed, below 250° or above 570°C, and also as the vector remaining at heating steps above 570°C. One sample, a diabase clast, particularly clearly displays both of the near-antipodal polarities both at low and at high temperatures. Most of the samples, regardless of dominant polarity, display two unblocking temperatures: 250°C and 500°C.

AF demagnetization shows the removal at fields ≤10 mT of vectors of the opposite polarity to that of the remanence observed at high fields. Above 10mT, the remanence of both polarities decay univectorially to the origin. Both AF and thermal demagnetization of samples of the same clast or matrix piece give the same directions for magnetizations held between 250-570°C and above 10 mT within a sample. The inclinations observed are steeper than the Cretaceous inclination for the site (64°): normal inclinations average +80°, and reversed, -76°. The Iowa site has had no geologic events subsequent to this impact, hence no obvious mechanism for remagnetization in the Tertiary. Tertiary inclinations at this site would lie between only 61° and 71°, hence the steep inclinations may represent unaveraged secular variation.

MANSON DUAL POLARITY: Steiner M. B. and Shoemaker E. M.

The dense matrix breccia has entirely normal polarity dominant magnetizations, with reversed polarity seen as removed vectors both at low and high temperatures, as the vector remaining at some steps above 570°C, and as the vector removed by low field AF demagnetization. The sandy matrix breccia samples display a dominant magnetization that is either of normal or reversed polarity depending on the depth in the core. Of six core segments examined, the magnetization polarity of three is normal, two reversed, and one normal interrupted by a small interval of reversed polarity. The opposite polarity vector is observed as the vector removed during both types of demagnetization (at both high and low temperatures), and both polarities are alternately observed as the remanent vector during thermal demagnetization of the diabase clast mentioned earlier. Normal and mixed polarity were found 60 m deeper in this breccia by an earlier study [3].

At this preliminary stage of the study, the only definitive evidence of which polarity may represent the earliest magnetization is the fact that the hottest material has a normal polarity dominant magnetization (although only 3 core segments thus far have been studied). Rock-magnetic and mineralogic studies currently in progress will assist in resolving this question.

The data indicate that either a reversal of the geomagnetic field has been recorded or the core mineralogy includes a self-reversing magnetic mineral. Self-reversal seems the less likely explanation because the two polarities are observed in both matrix and clasts, and in a wide variety of clast compositions.

Several possibilities could explain a magnetic field record of normal and reversed polarity near the Cretaceous-Tertiary boundary: 1) Manson may be younger or older than the K/T boundary. The boundary is thought to lie in the middle of marine magnetic anomaly 29R, and these data may suggest that Manson is closer to the upper or lower boundary of 29R. (If so, this may suggest that the K/T event was a comet shower.) 2) Large impacts have been speculated to cause excursions or reversals of the geomagnetic field; although Manson is not large enough, if it is associated with the Chicxulub impact, this explanation might be tenable. 3) A later heating event (e.g., hydrothermal) may have occurred after impact, occurring sufficiently later in time that the field had changed polarity. 4) A hitherto unknown short normal polarity event may have occurred at the K/T boundary, a suggestion already advanced by Lerbeckmo [2].

References: [1] Kunk M. J., et al (1989) Science, v. 244, 1565. [2] Lerbeckmo J. F. (1991) in Joint meeting of IGCP Projects 216, 293, 303, Aug. 28-30, 1991, Calgary, Alberta, Canada, 48. [3] Cisowski S. M. (1988) in Lunar and Planetary Science XIX, pp. 188-189.

N94-20790

MULTIELEMENT ANALYSIS OF INTERPLANETARY DUST PARTICLES USING TOF–SIMS; **T. Stephan,**[1,2,3] **W. Klöck,**[2] **E. K. Jessberger,**[3] **H. Rulle,**[1] **and J. Zehnpfenning;**[1] [1]Physikalisches Institut der Universität Münster, Wilhelm–Klemm–Straße 10, D–4400 Münster, Germany; [2]Institut für Planetologie der Universität Münster, Wilhelm–Klemm–Straße 10, D–4400 Münster, Germany; [3]Max–Planck–Institut für Kernphysik, Postfach 103980, D–6900 Heidelberg, Germany.

Sections of three stratospheric particles, U2015G1, W7029*A27, and L2005P9, respectively, were analyzed with TOF–SIMS (Time–Of–Flight Secondary–Ion–Mass–Spectrometry) continuing our efforts to investigate the element distribution in IDPs with high lateral resolution [1] ($\sim 0.2\ \mu$m), to examine possible atmospheric contamination effects [2], and to further explore the abilities of this technique for element analysis of small samples. The samples, previously investigated with SXRF (synchrotron X–ray fluorescence analysis) [3,4], are highly enriched in Br (Br/Fe: 59 × CI, 9.2 × CI, and 116 × CI, respectively). U2015G1 is the IDP with the by far highest Zn/Fe–ratio (81 × CI) ever reported in chondritic particles [3].

Secondary ion images of all three samples were obtained by rastering the sample with a 30 keV Ga^+ primary ion beam. Positive and negative secondary ions were measured successively, different ion species with the same polarity simultaneously. For a more quantitative analysis selected areas of the sample were analyzed more extensively. To calculate element ratios from the detected ion signals, SIMS sensitivities for a number of elements were determined. Fig. 1 shows the results of a TOF–SIMS analysis of a homogeneous glass standard (Lunar Analog Glass). The resulting sensitivities are comparable with those in the literature [5] and were used to calculate the element ratios shown in Fig. 2.

U2015G1 consists of two well separated units. From previously reported analysis of the sample we classified these as fine–grained ($\sim$ 20 nm) Fe–oxide intergrown with an presently unidentified hydrous phase and more coarse–grained (μm) smectite–like phyllosilicate [1]. We found the halogens strongly concentrated in the fine–grained material. This was interpreted as a result of an interaction of halogen–containing aerosols with individual Fe–rich grains [1]. During the present analysis $\sim 3\ \mu$m of the particle were sputtered away and most of the halogens were lost supporting the assertation that they are concentrated in a small region of the particle. Especially no Br was left for a quantitative analysis. Zn, which had not been measured in the previous study, is highly concentrated in a few at present mineralogically unidentified regions of the particle, 0.5 – 1 μm in diameter, respectively. No correlation with halogens was found. This leads to the

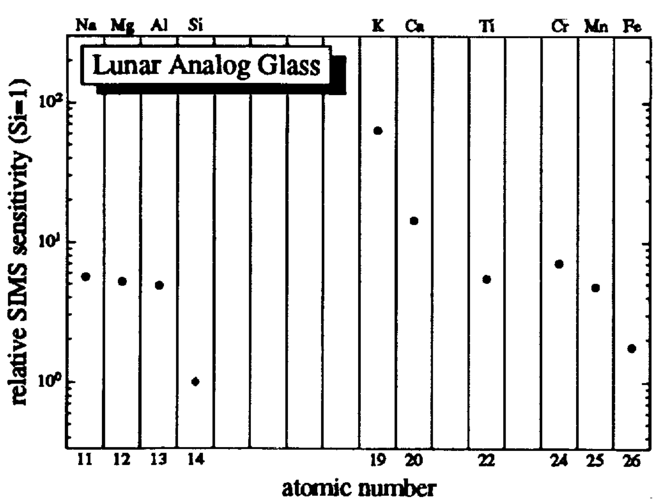


Figure 1: Relative SIMS sensitivities for positive secondary ions relative to Si. The sensitivities were determined by a TOF–SIMS measurement of a glass standard (Lunar Analog Glass) with well known composition.

interpretation that, if the Zn enrichment is a result of contamination, the incorporation process is completely different from that for the halogens, or, more likely, Zn in the particle is pristine and the enrichment is a result of a, on a μm–scale, inhomogeneous distribution of Zn in solar system material. The results of our analysis of element ratios for particle U2015G1 is shown in Fig. 2. A highly undulating abundance pattern with deviations from chondritic ratios up to a factor of 54 is apparent.

W7029*A27 shows CI abundances within a factor of 2 for most elements (Fig. 2). No Br rich phase was obvious in our section of the particle.

The section of **L2005P9** we analyzed was contaminated during sample handling with terrestrial material mainly consisting of Na, K, Ca, and Cl. Besides this contamination our TOF–SIMS analysis yields chondritic abundances for most elements (Fig. 2). Br was found only in the contamination. The extremely high Br content reported by [4] has vanished as with the other IDPs, and was neither found in the contamination nor in the extraterrestrial particle.

The fact that extreme Br–enrichments are *present* initially in whole rock studies and are *absent* in subsequent detailed analyses with high spatial resolution deserves further studies but in any case demonstrates that Br is distributed highly inhomogeneously and is therefore possibly not indigenous to the IDPs.

References: [1] Stephan T. *et al.* (1992) *Meteoritics 27*, 292. [2] Jessberger E. K. *et al.* (1992) *EPSL 112*, 91. [3] Sutton S. R. and Flynn G. J. (1988) *Proc. 18th LPSC*, 607. [4] Thomas K. L. *et al.* (1992) *LPS XXIII*, 1427. [5] Lange G. *et al.* (1986) *LPS XVII*, 456.

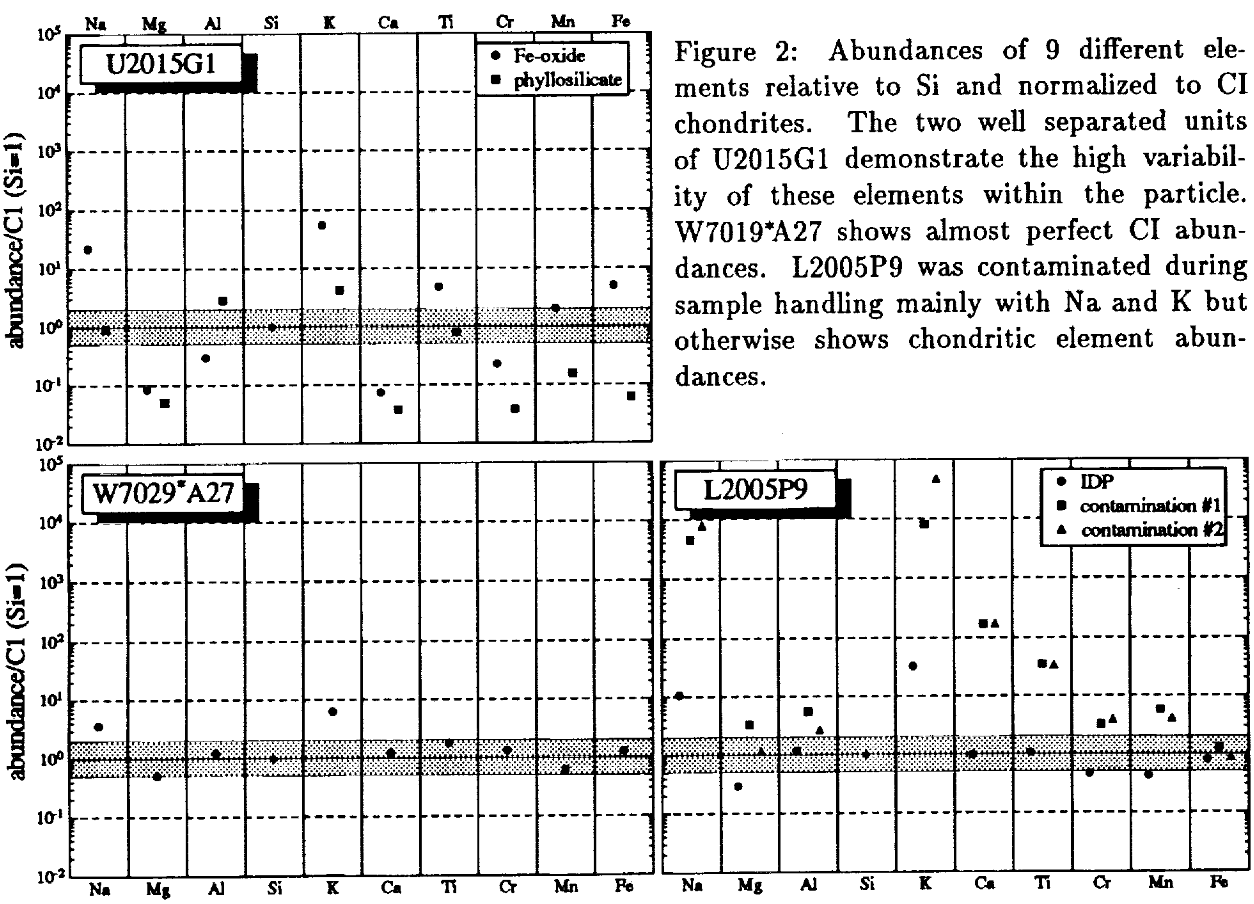


Figure 2: Abundances of 9 different elements relative to Si and normalized to CI chondrites. The two well separated units of U2015G1 demonstrate the high variability of these elements within the particle. W7019*A27 shows almost perfect CI abundances. L2005P9 was contaminated during sample handling mainly with Na and K but otherwise shows chondritic element abundances.

S155-92 ABS. ONLY

-168-115

N94-20791

MAGNETICALLY CONTROLLED SOLAR NEBULA T. F. Stepinski, Lunar and Planetary Institute, 3600 Bay Area Blvd., Houston, TX 77058, and M. Reyes-Ruiz, Dept. of Space Physics and Astronomy, Rice Univ., Houston, Texas

It is widely believed that a primordial solar nebula, the precursor of the Sun and its planetary system, could be best described in terms of an accretion disk. Such an accretion disk is thought to be turbulent, and it is usually imagined that turbulent viscosity *alone* provides a torque responsible for the structure and the evolution of the nebula. However, it was found [1,2] that an MHD dynamo operating in a turbulent nebula can contemporaneously produce magnetic fields capable of significantly altering or even dominating the total torque. Thus, it seems that no model of a viscous solar nebula is complete without taking magnetic fields into consideration.

It was demonstrated [2] that there are usually two distinct regions of nebular disk where a dynamo can operate: the inner region, where the magnetic field couples to gas due to relatively high thermal ionization, and the outer region, where this coupling is achieved due to nonthermal ionization. Most models also show the existence of an intermediate region, "the magnetic gap," where neither thermal nor nonthermal sources can produce enough ionization to provide the necessary coupling between the magnetic field and the gas. The location and width of the gap change substantially from one model to another. At present, we can only estimate the strength of a generated magnetic field. It seems that a large-scale magnetic field is likely to be in the equipartition with the turbulent kinetic energy; however, the intense magnetic fluctuations may greatly exceed this equipartition strength on short time and length scales.

To show how a dynamo-generated magnetic field changes the structure of a viscous nebula, we consider four nebula models extensively discussed in [2]. All four models are described by the dimensionless strength of turbulent viscosity, α_{ss}, equal to 0.08 and obtained from the turbulent closure model [3]. Model I nebula is characterized by $\dot{M} = 10$; there is no magnetic gap and the magnetic field is generated everywhere in the nebula. Model II nebula is characterized by $\dot{M} = 1$; there is a magnetic gap between 2.3 AU and 4.5 AU. Model III nebula is characterized by $\dot{M} = 0.1$; there is a magnetic gap between 0.8 AU and 4 AU. Model IV nebula is characterized by $\dot{M} = 0.01$; magnetic fields cannot be maintained anywhere in the nebula. Here $\dot{M}$ is an accretion rate measured in 10^{-6} solar masses per year. We have found the physical quantities describing the state of the nebula, such as temperature, T, disk's half-thickness, h, its density, ρ, and surface density, σ_s, by solving the standard, steady-state, "thin-disk" set of equations [4]. Two of those standard equations have to be modified to take into account the presence of magnetic fields. The first is the equation of hydrostatic equilibrium, which in the presence of magnetic field is

$$h = \frac{C_s}{\omega}\left(1+\frac{1}{\beta}\right)^{1/2} \tag{1}$$

where C_s is the sound velocity, ω is the Keplerian angular velocity, and $\beta = P_g/(B^2/8\pi)$ is the ratio of gas pressure to magnetic pressure. Second, we have to take into consideration that in addition to turbulent viscous stress there is also the Maxwell stress due to magnetic fields permeating the nebula. We can incorporate the effect of magnetic stress by defining the "effective" dimensionless strength of turbulence α_{eff} (see [2]) and use it instead of α_{ss} in the standard set of "thin-disk" equations. This effective coefficient can be expressed as

$$\alpha_{eff} = \alpha_{ss}\left(1+\frac{2}{\beta\alpha_{ss}^{1/2}}\right) \tag{2}$$

Generally speaking, the presence of magnetic fields results in a cooler nebula, with smaller surface density. The nebula half-thickness is about the same as in models without any magnetic fields. Fig. 1 shows the radial dependence of nebular surface density for models I to IV described above. In those calculations $\beta = 1$ has been assumed, except in magnetic gaps, where a very large value of β was assumed to model the absence of a magnetic field.

MAGNETICALLY-CONTROLLED SOLAR NEBULA T. F. Stepinski and M. Reyes-Ruiz

As expected, magnetic fields with their associated stresses comparable to gas pressure ($\beta = 1$) are dynamically very important, and completely control the structure of the nebula. Surface density in the regions of the nebula pervaded by magnetic fields drops by a factor of about 7 in comparison with the same model but without any magnetic field. This is because magnetic stress raises the effective viscosity, allowing more efficient removal of angular momentum. Within "magnetic gaps" turbulent viscosity is the sole source of stress; consequently those regions have enhanced surface densities. This enhancement can be as much as an order of magnitude relative to what would be expected if magnetic fields had pervaded the entire nebula. For weaker fields ($\beta > 1$) the results are qualitatively the same; however, departures from the standard, non-magnetized nebula structure are relatively smaller.

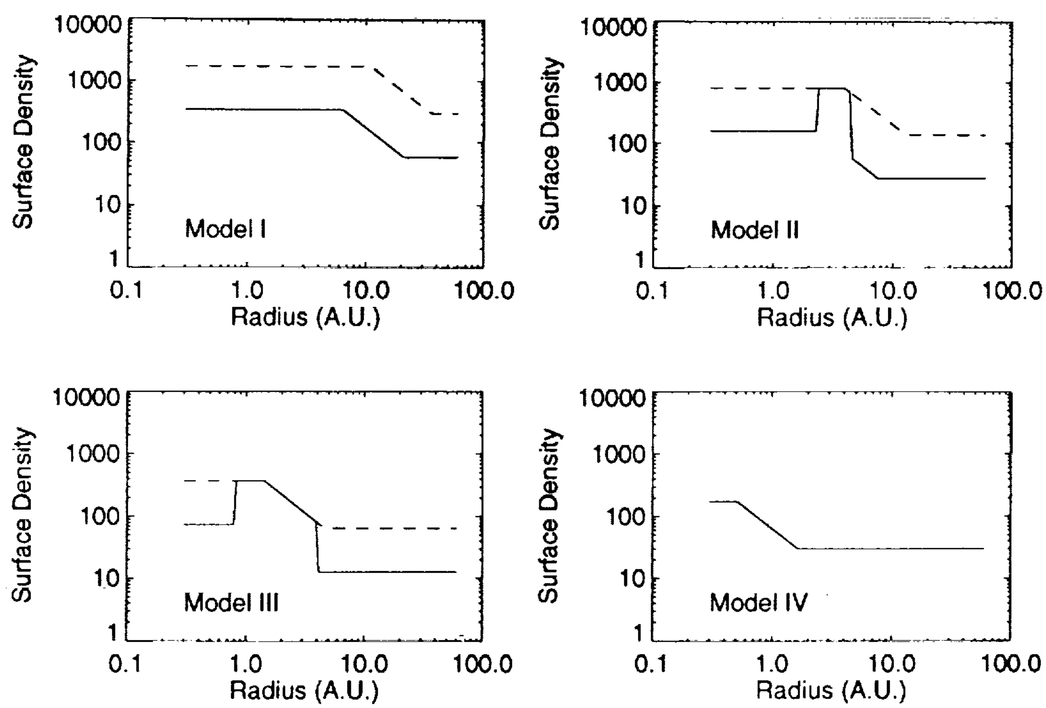


Figure 1. - Values of surface density (in g cm^{-2}) as functions of radial distance from the protosun for four different models of the solar nebula. Solid lines correspond to solutions with a magnetic field, and dashed lines correspond to solutions without a magnetic field.

In summary, the present calculations reveal basic aspects of the influence of magnetic fields on the structure of the viscous solar nebula. Further work will explore the possible influence of those fields on the nebula evolution and the process of planetary formation.

References: [1] Stepinski, T.F. (1992) *Icarus*, **97**, 130; [4] Stepinski, T.F., Reyes-Ruiz, M., and Vanhala, H.A.T. (1993) submitted to *Icarus*; [3] Dubrulle, B. (1992) *Astron. Astrophys.*, **266**, 592; [4] Shakura, N.J. and Sunyaev, R.A. (1973) *Astron. Astrophys.*, **24**, 337.

S156-91
ABS. ONLY

N94-20792

EXPECTATIONS FOR THE MARTIAN CORE MAGNETIC FIELD;

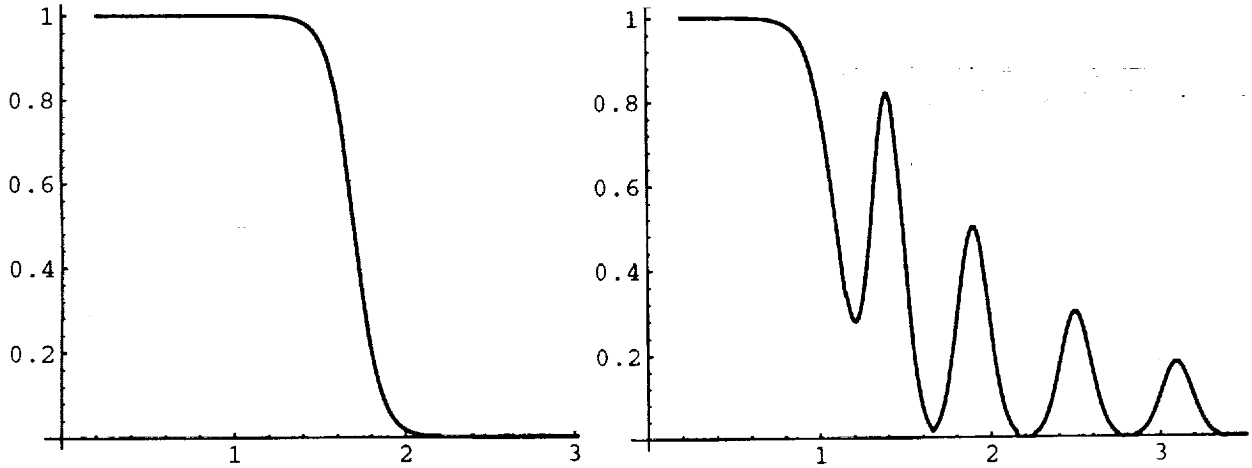
D.J. Stevenson, Caltech 170-25, Pasadena CA 91125

p. 2

In the traditional view of planetary magnetism, a planet either has a core dynamo (Earth, Jupiter, Saturn, Uranus, Neptune, maybe Mercury) or does not (Mars, Venus, Moon...) I argue that this view is simplistic in two respects. First, mantle convection in terrestrial planets is invariably at high enough Rayleigh number that it is time variable; this leads to the intermittent arrival of mantle "cold fingers" at the core-mantle boundary, promoting at least local core convection and dynamo action even when the planetary core is stably stratified on average. Thus, I predict an *intermittent dynamo regime* in addition to the simple dynamo-on (Earth) and dynamo-off regimes. Second, the mantle convection-driven horizontal temperature gradients just below the core-mantle boundary can lead to unstable flows that will convert thermoelectric or electrochemical toroidal fields into externally detectable poloidal fields, even when a dynamo is not possible. It is likely that Mars possesses an interesting core magnetic field of the latter kind, complex but with a dipole that might be approximately aligned with the rotation axis and a surface field of a few to tens of gammas.

Background. As I have argued for many years [1] , the principal issue governing the existence of a dynamo in terrestrial planet cores is the existence of core convection rather than some more restrictive criterion based on the subtleties of magnetohydrodynamics. According to this view, Mars does not possess a dynamo because the heat flow from the core is less than that which can be carried by conduction along an adiabat. The core is then stably stratified, and unable to provide the vertical fluid motions necessary for dynamo generation. Since the heat flow was larger in the past, Mars would once have had a dynamo [2], perhaps for the first billion years or so. This picture makes sense if Mars does not develop an inner core (since such a development will lead to compositional convection which should drive a dynamo). This in turn requires a fairly sulfur-rich core (though still about a factor of two less sulfur than cosmic abundance relative to iron). The alternative of a completely frozen core is unrealistic given our current understanding of mantle rheology, even allowing for the possible presence of water. Thus the conventional picture for Mars suggests an Earth like field early in its history followed by a very abrupt switch to a field that is purely crustal (near surface permanent magnetism).

New Ideas. The error in the conventional picture lies in its very simplistic view of a smooth, thermally uniform core-mantle boundary (CMB). In fact, overlying mantle convection is certainly time variable and capable of generating significant CMB topography on Earth (e.g.[3]), and is expected to be time variable even at the somewhat lower Rayleigh number appropriate to Mars, based on 3D spherical convection simulations[4,5]. The heat flow out of the core is dictated by the overlying mantle ...delivery of cold material to the CMB from above is what allows the core to cool. Moreover, the core heat flow is small compared to the total mantle heat flow so even modest fluctuations in the mantle heat flow can be big fluctuations for the core. There are two consequences of this viewpoint: First, one must think of the core heat flow not as a monotonically decreasing function as geologic time progresses (with the dynamo switch-off defined as the instant at which this heat flow equals the conduction along an adiabat) , but as the sum of this secular trend together with "noise" whose characteristic amplitude may approach the secular term and whose fluctuation time scale is that of mantle convection.



In both figures, the vertical axis is a nominal field strength (based on the available energy; unity may correspond to a few tenths of a gauss surface field though with a large uncertainty). The horizontal axis is time in billions of years since planet formation. The LHS figure is a conventional model based on simple thermal evolution calculations with a dynamo shut-off at about 1.7 Ga. The RHS figure is the new model with CMB heat flow fluctuations comparable to the secular heat flow; it shows several "events " of field shut-down and resuscitation extending out to 3 Ga. or beyond. But it is unlikely that this intermittent phase extends to the present day.

Non-Dynamo Models. The most likely non-dynamo sources of core magnetic field are both associated with the non-uniform CMB. They are the thermoelectric[6] and electrochemical fields[7] associated with emfs that drive currents through the outermost core and lowermost mantle. In both cases the fields directly created are toroidal and hence not externally detectable. However, any source of circulation in the outermost core can create some poloidal field, in accordance with the formula $B_p \approx R_m B_T$ where B_p is the poloidal field, B_T is the toroidal field and R_m is the magnetic Reynolds number for the circulation. The latter comes from instabilities of the thermal wind flow, predicted on the basis of a Richardson number criterion [8,9]. These flows are predicted to occur even when the outermost core has a sub-adiabatic temperature gradient . There is considerable uncertainty in the numerical values but possible values are B_T =10 to 100γ, R_m =0.03 to 0.3 and the predicted (observable) B_p = 0.3 to 30γ. Values in the upper part of this range are detectable by Mars Observer. This field would have a spherical harmonic complexity similar to that of topography at the CMB, but the importance of low order harmonics in the geoid together with the effects of True Polar Wander and the Coriolis effect on the core flows favors a roughly spin-axis aligned dipole.

References. [1] Stevenson, D.J. Rep. Prog. Physics **46**, 555 (1983) . [2] Stevenson, D.J. *et al* , Icarus **54** 466 (1983). [3] Young, C.J. and Lay, T. Ann. Rev. Earth Planet. Sci. **15** ,25 (1987). [4] Schubert,G. *et al* J. Geophys. Res. **95** 14105 (1990). [5] Tackley, P. J. *et al* ,submitted to Nature. [6] Stevenson, D.J. Earth Planet. Sci. Lett. **82** ,114 (1987). [7] Stevenson, D.J. EOS **72**, 133 (1991). [8] Hathaway, D. *et al* , Geophys. Astrophys. Fluid Dyn. **13** 289 (1979). [9] Stevenson, D.J. Geophys. J. Roy. Astron. Soc. **88** ,311(1987).

S157-90
ABS. ONLY

N94-20793

P. 2

VOLATILE LOSS FROM ACCRETING ICY PROTOPLANETS;

D.J. Stevenson, Caltech 170-25 , Pasadena CA 91125.

A large self-gravitating body does not easily lose significant mass because the escape velocity is much larger than the sound speed of atmosphere-forming species under ambient thermal conditions. The most significant exceptions to this are giant impacts or impact jetting by fast-moving projectiles[McKinnon, *Geophys. Res. Lett.* **16**, 1237(1989)]. A very small object (e.g. a comet) also does not easily lose significant volatile mass upon formation because the energy release associated with its accretion is so small. (It can however lose a great deal of mass if it is subsequently moved closer to the Sun.) I argue that there is an *intermediate mass range* (corresponding to bodies with radii of ≈300-800 km) for which the ambient steady-state mass loss is a maximum. By ambient, I mean those conditions pertaining to the formation region of the body. By steady state, I mean to exclude infrequent traumas (giant impacts). The existence of a preferred intermediate mass arises through the competition of growing gravitational containment and growing energy release by accretion; it corresponds typically to $GM/(Rc_s^2) \approx 2$ to 4, where M is the protoplanet mass of radius R, and c_s is the sound speed. Several factors determine the amount of volatile loss in this vulnerable zone during accretion but in general the loss is a substantial fraction of the volatiles, sometimes approaching 100%. *The principal implication is that bodies larger than a few hundred kilometers in radius will not have a "primitive" (i.e. cometary) composition.* This is relevant for understanding Triton, Pluto, Charon and perhaps Chiron.

Accretional Heating and Volatile Loss. When a protoplanet accretes material, most of the infalling material hits the surface at velocities only slightly in excess of escape velocity. The resulting temperature rise in the subsurface of the body is

$$\Delta T \approx 5\varepsilon (R_2)^2 \ \ K$$

where ε is an efficiency factor (plausibly 0.2-0.3 at low temperatures) and R_2 is the radius of the body in units of 100km. This would seem like a very small temperature rise but even a few degrees can be important in the outermost solar system where highly volatile constituents such as CO,N_2 and CH_4 are of considerable interest.(This is principally what I mean by volatiles in this paper.) The *surface* temperature of the protoplanet is much less affected if it is determined by radiative equilibrium, including insolation and the much smaller gravitational energy input (even if the latter is supplied on a timescale of a million years or less). Indirectly, the surface is affected because volatiles released by accretional heating in the subsurface can migrate up to the surface, forming a reservoir for atmosphere formation. This surface layer may actually be *less* stable than the material from which it was derived (clathrate, amorphous water ice or adsorbed on fine-grained water ice surfaces) since it has accumulated as a bulk surface deposit that is much more than a monolayer in thickness (i.e. it would have similarity to the *present* surface of Triton.) It is perhaps more relevant to ask how much volatile icy material can be mobilized by the subsurface heating: this is determined by a latent heat (of sublimation or clathrate breakdown or whatever) which is probably very low to judge by the activity of fresh comets at very large heliocentric distances. The fraction f of mobilized material per gram of accreted material is given by

$$f \approx 0.02\varepsilon(R_2)^2/L_2$$

where L_2 is the latent heat in units of 100cal/g (a nominal value that is somewhat less than for H_2O sublimation yet more than for sublimation of the ices in question).

VOLATILE LOSS BY ACCRETION Stevenson, D.J.

Solar insolation can then ensure the final escape provided the gravitational containment is not too great. The ability to escape is characterized by the parameter

$$\lambda \equiv GM/Rc_S^2 \approx 0.11(\mu/28)(R_2)^2/T_2$$

where μ is the molecular weight of the species in question and T_2 is the temperature in units of 100 K. Roughly speaking, the escape of volatiles is then given by

$$dM_{vol}/dt \approx \mathrm{Min}[\ f dM/dt, 4\pi R^2 P_{vap} e^{-\lambda}/3c_S, \pi R^2 \delta S/(GM/R)]$$

where Min[....] means the smallest of the expressions contained within, M_{vol} is the volatile mass that leaves , dM/dt is the accretion rate , P_{vap} is the vapor pressure of the species in question, S is the solar constant and δ is the fraction of the insolation available for driving escape. The last term inside Min[...] is relevant since there is an energy limit to the amount of material that can escape the body. The expression for evaporation flux assumes an isothermal atmosphere but allows for an escape that proceeds from an exobase that is not necessarily coincident with the physical surface. In practice there is a mixture of volatile species and some interesting fractionation effects can arise. Clearly there are many parameters in play here but it is obvious that the smallest (i.e relevant) of the expressions in the square brackets is necessarily the first at low mass (since it tends to scale as R^4 while the second scales as R^2 and R^0 respectively) and necessarily the second or third at high mass (because they are bounded above by something independent of R, unlike the first.) The radius where loss is greatest is dependent on many variables but it is typically in the range 300-800km. For those cases where a substantial fraction of insolation is used to promote escape (a fairly readily achievable circumstance) most of the volatiles mobilized (the parameter f above) do in fact escape until λ becomes substantially larger than unity.

Other Considerations. I have also considered the role of the nebula streaming by a growing protoplanet. Despite the fact that the wind is greater than the sound speed of relevant volatiles or the escape velocity (for most of the mass range of greatest interest), the very low density of the nebula at Uranus orbit or beyond greatly limits the ability of the nebula to promote the escape of volatiles. "Giant" impacts (any impact with a body of order 0.1 the mass of the protoplanet or more) can obviously be important for both differentiation (preferential loss of the most volatile material) and bulk loss (changing the ratio of total ice to total rock?)

Conclusions. (1) It is not correct to think that bodies in excess of a few hundred kilometers in radius will have the mean composition of the smaller bodies from which they accumulated. There will be preferential loss of the most volatile constituents as a continual wind during accretion (and perhaps beyond, depending on the final mass). (2) The fraction of the total volatile loss (here meaning CH_4 and anything more volatile) is dependent on many variables, some of which are poorly known and others of which will have varied from object to object. But this fraction is usually in the range of a few percent to over 90%. (3) It follows that it is not correct to use cometary or primitive solar nebular condensate compositions as the starting point for structural and evolutionary models of Triton, Pluto, Charon....even aside from traumas that these bodies may have experienced.

S158-25 ABS. ONLY

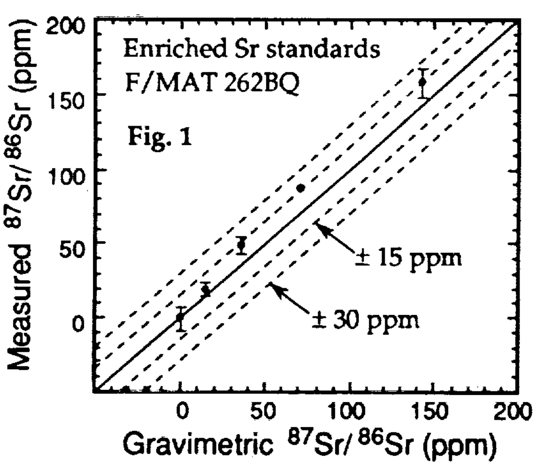
N94-20794

FINE RESOLUTION CHRONOLOGY BASED ON INITIAL $^{87}Sr/^{86}Sr$; B. W. Stewart, D. A. Papanastassiou, R. C. Capo, and G. J. Wasserburg, The Lunatic Asylum, Division of Geological and Planetary Sciences, Caltech, Pasadena, CA 91125

It has been recognized that small variations in initial $^{87}Sr/^{86}Sr$ (Sr_I), can provide a fine scale relative chronology for the chemical fractionation of materials with low Rb/Sr from parent reservoirs with high Rb/Sr. Similarly, Sr_I, as determined for low Rb/Sr phases in meteorites, may permit a fine resolution chronology of the recrystallization or metamorphism of planetary materials [1,2]. For the establishment of a primitive $^{87}Sr/^{86}Sr$ chronology, it is important to search for samples with extremely low Rb/Sr for which the *measured* $^{87}Sr/^{86}Sr$ is below BABI, in which case the primitive nature of the Sr can be directly established. Using the measured Rb/Sr to calculate an initial $^{87}Sr/^{86}Sr$ can introduce substantial uncertainty if the Rb-Sr systems are disturbed [1-3]. We report $^{87}Sr/^{86}Sr$ in plagioclase from silicate pebbles from the Vaca Muerta mesosiderite on which we have reported ^{147}Sm-^{143}Nd and ^{142}Nd correlations [4]. For the purpose of cross-calibration with our previous work we have performed extensive new measurements on Angra dos Reis and on anorthite from Moore County, which have very low Rb/Sr and primitive $^{87}Sr/^{86}Sr$ [1,5]. The instrumental development in the late sixties [6] permitted resolution in $^{87}Sr/^{86}Sr$ of 1 ϵu. For the work reported here we used the newer generation multiple Faraday cup, simultaneous ion beam collection instrumentation (Finnigan 262 BQ). As in the earlier work [1], we used gravimetric standards, of known enrichment in $^{87}Sr/^{86}Sr$, to establish instrumental resolution in $^{87}Sr/^{86}Sr$. The present standards range from 0.15 to 1.45ϵu (15 to 145 ppm) in $^{87}Sr/^{86}Sr$. We have demonstrated a resolution in $^{87}Sr/^{86}Sr$ of better than 20 ppm (see Fig. 1), which represents a factor of five improvement over our earlier work [1]. For the new data we quote uncertainties of 0.20 ϵu (20 ppm in $^{87}Sr/^{86}Sr$); internal (within a run) $2\sigma_M$ uncertainties are 9-14 ppm. Additional Sr standards used are NBS (NIST) 987 and seawater Sr. In prior work we established a whole rock isochron for eucrites with a well defined initial $^{87}Sr/^{86}Sr$ labelled BABI [1]. Subsequent extensive work on Moore County plagioclase, in conjunction with the lunar work on Luna 16 samples, showed Sr_I in Moore County to be 0.9 ϵu below BABI [7]. Angra dos Reis total rock measurements demonstrated that Angra dos Reis had both *measured* and Sr_I distinctly more primitive than BABI, with Sr_I, labelled ADOR, being 2 ϵu below BABI [5]. This was confirmed on larger samples of Angra dos Reis [8], by measurements on unleached total rock samples and on handpicked phosphate crystals. Work on Allende CAI provided the most primitive *measured* $^{87}Sr/^{86}Sr$ of -3.0 ϵu, relative to BABI, and labelled ALL; correction for *in situ* ^{87}Rb decay yielded Sr_I=-3.2 ϵu from BABI [3]. Based on samples with extremely low Rb/Sr, the current range in primitive Sr_I is 3 ϵu. This range corresponds to a time interval of differential evolution of 20 Ma in chondritic parent reservoirs or to about 10 Ma in a solar Rb/Sr reservoir [1,3,8]. This restricted range in Sr_I has been identified now for nearly two decades, and includes the initial $^{87}Sr/^{86}Sr$ for the moon, clasts from the Kapoeta achondrite and angrites from Antarctica [9,10]. By contrast, Sr_I well above BABI have been measured for phosphates in chondrites and in a silicate inclusion in an iron meteorite and correspond to much later formation or re-crystallization events, of the order of 100 Ma [2,11,12]. The primitive $^{87}Sr/^{86}Sr$ data obtained in this laboratory are shown in Figure 2. New data are shown as full symbols; earlier data are shown as open symbols. For the new data, it is clear that only the plagioclase from Vaca Muerta Pebble 12 and Angra dos Reis total rock and phosphate samples have *measured* $^{87}Sr/^{86}Sr$ that are below BABI (dashed horizontal line). The plagioclase from the other Vaca Muerta pebbles and from Mt. Padbury are within +1 ϵu of BABI and indicate primitive $^{87}Sr/^{86}Sr$ in these samples. The Sr_I values for Vaca Muerta pebbles, calculated from the plagioclase data range from -1.02±0.21 to -1.62±0.30 ϵu, clearly in the range between BABI and ALL. The Sr_I values calculated from the whole rock data (not shown, because measured values are slightly more radiogenic) and the plagioclase data for the Vaca Muerta pebbles do not agree within each pebble and clearly indicate disturbed systems. This further emphasizes the need for separates with extremely low Rb/Sr and measured $^{87}Sr/^{86}Sr$, and that Sr_I, obtained by assuming an age, need not be meaningful. To the extent that the Vaca Muerta and Mt. Padbury silicates have measured $^{87}Sr/^{86}Sr$ very near BABI, it is clear that all these low Rb/Sr planetary materials were fractionated from any high Rb/Sr parent within a few million years. For Moore County plagioclase we confirm a measured value close to BABI and calculate Sr_I below BABI by 0.64±0.12 ϵu. For Angra dos Reis there is good agreement between the new (including a leached sample) and old data reported from this laboratory, except for the new analysis of phosphate. The measured $^{87}Sr/^{86}Sr$ for this sample agrees with the measured values of the total rock samples and, within the larger errors, of the earlier phosphate analyses. However, the new phosphate analyzed has an extremely low $^{87}Rb/^{86}Sr$ (0.00006) and high Sr (2200 ppm); this results in essentially no correction for *in situ* ^{87}Rb decay, so that there is a significant difference in Sr_I calculated (by assuming an age of 4.56 AE) from this phosphate and from all other Angra dos Reis data shown. This indicates disturbed Rb-Sr

systematics or an analytical problem with the phosphate analysis, which requires further attention. Recently Lugmair and Galer [13] presented precise Sr data for Moore County plagioclase and leached total rock samples of Angra dos Reis. These workers have found that Sr_I (for T=4.56 AE) for Moore County plagioclase and for Angra dos Reis are indistinguishable and concluded that there was some question about our value of ADOR. Detailed comparison with [13] shows that the *measured* values for Angra dos Reis total rock samples and Moore County plagioclase are in good agreement between the laboratories when normalized using the NBS 987 data. This places the reason for the difference in Sr_I between the two laboratories on the differences in $^{87}Rb/^{86}Sr$. The present results show that there is indeed a problem about the propriety of extrapolating to Rb/Sr=0 to obtain Sr_I. From our new data on Angra dos Reis an extrapolation along a zero-age line is indicated; this yields an upper limit for the Sr_I of Angra dos Reis of 0.87 εu below BABI. We conclude that our previous value for ADOR of 2.1 εu below BABI is not justified, as there appears to be a recent disturbance of the Rb-Sr system. Since the ALL value is not subject to uncertainty due to extrapolation, we conclude that the range in $^{87}Sr/^{86}Sr$ from ALL to BABI still provides a narrow window for primitive Sr and for the early fractionation and separation of planetary materials, within about 20 my. The extent to which a specific sequence can be established in this time interval remains uncertain and depends on the identification of samples with effectively no Rb and with primitive $^{87}Sr/^{86}Sr$. We believe that there is also a need to readdress the extent to which BABI is well defined, using the more refined precision currently available.

References. 1. Papanastassiou D.A.& Wasserburg G.J. (1969) *EPSL 5*, 361; 2. Wasserburg G.J., Papanastassiou D.A., Sanz H.G.(1969) *EPSL 7*, 33; 3. Gray C.M., Papanastassiou D.A. & Wasserburg G.J.(1973) *Icarus 20*, 213 & Podosek F.A., Zinner E.K., MacPherson G.J., Lundberg L.L., Brannon J.C. and Fahey A.J. (1991) *GCA 55*, 1083; 4. Stewart B.W., Papanastassiou D.A., Wasserburg G.J.(1993) this abstract volume; 5. Papanastassiou D.A.(1970) *PhD Thesis*; 6. Wasserburg G.J., Papanastassiou D.A., Nenow E.V. & Bauman C.A.(1969) *RSI 40*, 288; 7. Papanastassiou D.A. & Wasserburg G.J.(1972) *EPSL 13*, 368; 8. Wasserburg G.J., Tera F., Papanastassiou D.A. & Huneke J.C. (1977) *EPSL 35*, 294; 9. Lugmair G.W., Galer S.J.G. & Loss R.(1989) *LPSC XX*, 604; 10. Nyquist L.E., Wiesmann H., Bansal B., Shih C.-Y. & Harper C.L. (1991) *LPSC XXII*, 989; 11. Sanz H.G., Burnett D.S. & Wasserburg G.J. (1970) *GCA 34*, 1227; 12. Podosek F.A. and Brannon J.C.(1991) *Meteoritics 26*, 145; 13. Lugmair G.W. and Galer S.J.G.(1992) *GCA 56*, 1673. Contribution #5230(794). Work supported by NASA, NAG 9-43.



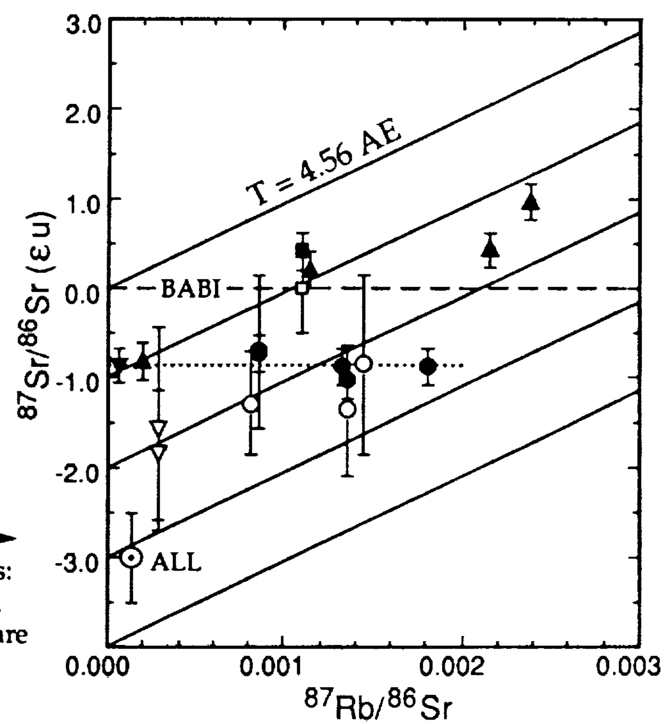


Fig. 2 ⟶
Sr evolution diagram, with symbols as follows: ▲ mesosiderite plag; ● ADOR TR; ▼ ADOR phos; ■ Moore County plag. Filled symbols are 262BQ data, open symbols are Lunatic I data.

5/69-90
ABS ONLY

N94-20795

Sm-Nd SYSTEMATICS OF SILICATE INCLUSIONS IN IRON METEORITES: RESULTS FROM CADDO (IAB); Brian W. Stewart, D. A. Papanastassiou, and G. J. Wasserburg, The Lunatic Asylum, Division of Geological and Planetary Sciences, California Institute of Technology, Pasadena, CA 91125

The timing of events leading to the formation of silicate-rich and metal-rich regions in planetesimals remains an important problem in the study of planetary formation and differentiation in the early solar system. The IAB irons are especially important as they are considered to represent a magmatic differentiation series [1]. Iron meteorites present a particular challenge for chronological studies, due to the relative paucity of phases serving as hosts for radioactive parent-daughter nuclides. Recent work using the Re-Os system, following on the pioneering work by Herr *et al.* [2] and Luck and Allegre [3], appears promising, but investigations up to now have concentrated on whole rock isochrons. Silicate clasts enclosed within iron meteorites can provide information about the chronology and thermal history of irons. Extensive work on Rb-Sr, K-Ar, and I-Xe has been reported on silicate inclusions in iron meteorites [4-9]. We report the initial results from our Sm-Nd study of an inclusion within the Caddo IAB iron, the first Sm-Nd isotopic study of a silicate clast embedded within an iron meteorite. Our results include measurements of the standard long-lived ^{147}Sm-^{143}Nd ($\bar{\tau}$ = 152 AE) system, as well as the shorter-lived ^{146}Sm-^{142}Nd ($\bar{\tau}$ = 0.149 AE) system, which has been shown to be very useful in deciphering the history of the early solar system [10-15]. The Caddo silicate clast was described by Palme *et al.* [16], who kindly provided us with a major part of the inclusion. The inclusion is coarse-grained, consisting predominantly of olivine, clinopyroxene, and plagioclase, with lesser amounts of orthopyroxene, Fe-Ni metal, sulfide, and phosphate. The relatively large grain size (up to 3 mm) and 120° grain boundaries suggest extensive metamorphism at high temperature. Based on study of a thin section, there is evidence for metal invading along grain boundaries in some regions of the inclusion, suggesting that the Fe-Ni metal was molten when the silicate clast was incorporated. Metamorphic recrystallization may have occurred during this event.

We obtained a mineral separate of plagioclase by heavy liquid and magnetic separation techniques and a clinopyroxene separate by hand-picking prior to density separations. Samples used for Sm-Nd were lightly leached in cold 2.0 N HCl for 10 minutes prior to dissolution in order to remove any surface weathering products and adhering phosphate. We measured Sm and Nd concentrations and isotopic ratios of ^{142}Nd/^{144}Nd and ^{143}Nd/^{144}Nd on samples of plagioclase (PL) and clinopyroxene (CPX); the results are given in Table 1. The Sm and Nd concentrations and fractionation are consistent with the ion probe measurements of Palme *et al.* [16]. CPX, by virtue of its high abundance and REE concentrations, is the dominant carrier of the REE in this inclusion. PL has an extreme LREE enrichment, with an $f^{Sm/Nd}_{CHUR}$ value of -0.76 relative to chondrites, while CPX has a nearly chondritic Sm/Nd ratio. The LREE enrichment in PL has led to a very low measured ε_{143} value of -88.0 εu. The correlation of the ^{143}Nd/^{144}Nd and ^{147}Sm/^{144}Nd ratios defines a slope corresponding to an age of 4.41±0.03 AE, with an initial ε_{143} of -2.6±0.3 εu (Figure 1). This "age" should be regarded with caution until further data are obtained to establish more than a two point-two phase correlation. For PL, the ε_{142} value of -2.4 εu is the lowest ever measured, thus providing an upper limit on the solar system initial ε_{142} value. This is consistent with the extreme Sm/Nd fractionation and Sm depletion in this separate. The ^{142}Nd/^{144}Nd-^{147}Sm/^{144}Nd correlation defines a slope corresponding to ^{146}Sm/^{144}Sm(I) = 0.0099±0.0021, and an initial ε_{142} of -3.2±0.5 εu (Figure 2). This initial ^{146}Sm/^{144}Sm ratio is higher than would be expected for the ^{147}Sm-^{143}Nd age; we believe the short-lived ^{146}Sm-^{142}Nd system provides a more reliable fine scale chronology than the long-lived system. The large deviation

of the plagioclase Sm/Nd ratio from the chondritic value allows calculation of a model $^{146}Sm/^{144}Sm$ value (RM_{CHUR}) for the time at which the mineral was isolated from a chondritic source. RM_{CHUR} is given by $\varepsilon_{142}/(354.3 \cdot f^{Sm/Nd}_{CHUR})$, which for PL yields a value of $^{146}Sm/^{144}Sm = 0.0089 \pm 0.0013$. These ^{146}Sm-^{142}Nd data clearly show that the Caddo silicate inclusion formed or underwent high temperature metamorphism early in solar system history, probably within the first 50 m.y. In Table 2, we compare the Caddo Sm-Nd results with mesosiderite data obtained in this laboratory [13,14]. Inferred initial $^{146}Sm/^{144}Sm$ ratios of mesosiderites are generally lower than the value reported here for Caddo, and initial ε_{142} values are higher. These results suggest that mesosiderites have had an extended thermal history, probably due to intense bombardment near the surface of their parent body, while the Caddo iron quenched below Sm-Nd closure temperature 20-70 m.y. earlier. Insofar as Caddo is representative of IAB irons, we now have a basis of directly comparing the ages of these planetary metal segregates by direct dating of both silicate and metal phases. It appears that core segregation on planetesimals took place very early in solar system history.

References. [1] Wasson J.T. *et al.* (1980) *Z Naturforsch 35a*, 781 [2] Herr W. *et al.* (1961) *Z Naturforsch 16a*, 1053; [3] Luck J.M. & Allegre C.J. (1983) *Nature 302*, 130; [4] Wasserburg G.J. *et al.* (1965) *Science 150*, 1814; [5] Burnett D.S. & Wasserburg G.J. (1967) *EPSL 2*,397; [6] Bogard D.D. *et al.* (1968) *EPSL 3*, 275; [7] Sanz H.G. *et al.* (1970) *GCA 34*, 1227; [8] Niemeyer S. (1979) *GCA 43*, 843; [9] Niemeyer S. (1979) *GCA 43*, 1829; [10] Lugmair G.W. & Marti K. (1977) *EPSL 35*, 273; [11] Jacobsen S.B. & Wasserburg G.J. (1984) *EPSL 67*, 137; [12] Prinzhofer A. *et al.* (1989) *Ap J 344*, L81; [13] Stewart B.W. *et al.* (1991) *LPSC XXII*, 1333; [14] Prinzhofer A. *et al.* (1992) *GCA 56*, 797; [15] Stewart B.W. *et al.* (1992) *LPSC XXIII*, 1365; [16] Palme *et al.* (1991) *LPSC XXII*, 1015. We thank H. Palme for providing the material for this study. Supported by NASA (NAG9-43). Division Contribution No. 5241(804).

Table 1. Sm-Nd results from Caddo silicate inclusion.

	Weight (mg)	Sm (ppm)	Nd (ppm)	$^{147}Sm/^{144}Nd$	$f^{Sm/Nd}_{CHUR}$	ε_{143}	ε_{142}
Clinopyroxene	24.2	3.5	10.0	0.202	0.028	0.7 ± 0.4	0.4 ± 0.3
Plagioclase	76.1	0.031	0.40	0.0470	-0.761	-88.0 ± 0.4	-2.4 ± 0.4

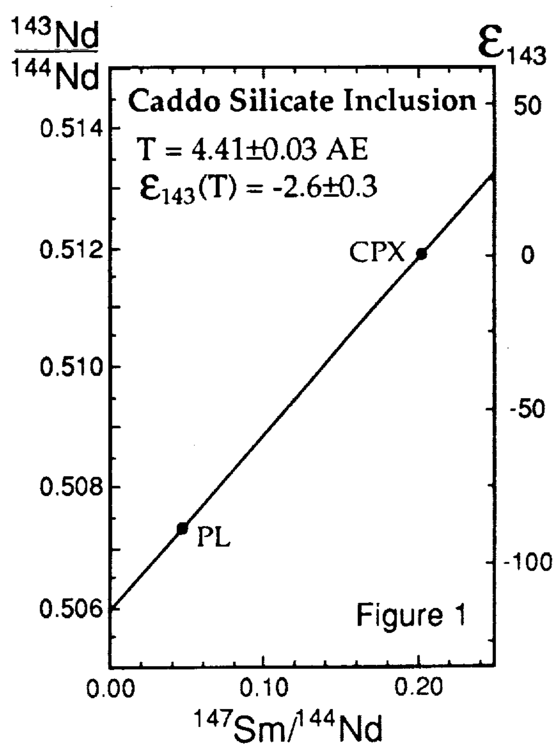


Figure 1

Table 2. Caddo and mesosiderite Sm-Nd data .

Sample	^{143}Nd age (AE)	$^{146}Sm/^{144}Sm(I)$	$\varepsilon_{142}(I)$
Caddo	**4.41**	**0.0099**	**-3.2**
Vaca Muerta p. 5	4.42	0.0042	-1.6
Vaca Muerta p. 12	4.48	0.0058	-0.1
Vaca Muerta p. 16	4.48	0.0059	-1.6
Mt. Padbury	4.52	0.0059	-1.9
Morristown	4.47	0.0075	-2.1

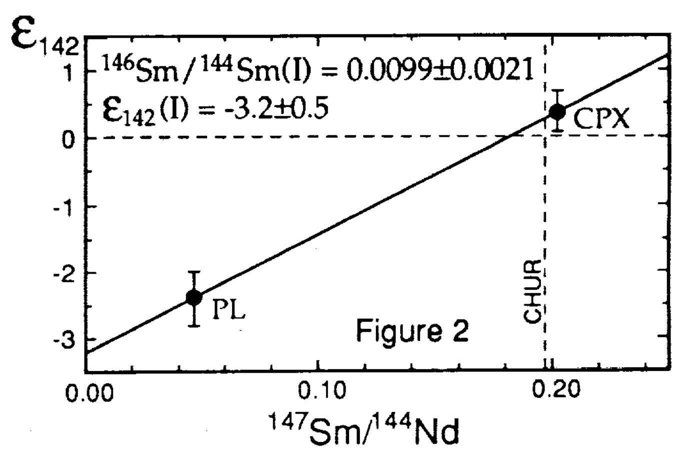


Figure 2

S160-91
ABS. ONLY

N94-20796

PARGA AND HECATE CHASMATA, VENUS: STRUCTURE, VOLCANISM AND MODELS OF FORMATION, Ellen R. Stofan, Jet Propulsion Laboratory, California Institute of Technology, Pasadena, CA 91109; Victoria E. Hamilton, Department of Geology, Occidental College, Los Angeles, CA 90041; Kristen Cotugno, Department of Geology and Geography, University of Massachusetts, Amherst, MA 01003.

Linear zones of deformation in the equatorial zone of Venus characterized by extension and volcanism have previously been identified in Pioneer Venus and Arecibo data [1, 2]. Two of these zones, Parga and Hecate Chasmata, are seen in Magellan data to be characterized by systems of fractures along which lie numerous coronae and corona-like features. The relationship between tectonic deformation, corona formation and volcanism in Parga and Hecate Chasmata is examined using Magellan image and altimetry data. We examine several hypotheses for the origin of these zones, including extension and upwelling [2, 3] and delamination or subduction [2, 4]. In a companion abstract [5], we examine a section of Hecate Chasma in detail.

Hecate and Parga Chasmata extend to the northeast and southeast, respectively, from Atla Regio. Atla is a junction from which the four 'arms' of Ganis, Parga, Hecate, and Dali Chasmata radiate [6]. Parga Chasma is a zone over 10,000 km long extending to the southeast of Atla Regio. Its southern termination is at Themis Regio, a small (<1000 km across, 0.5-1.0 km high) highland region characterized by coronae, volcanic edifices, and rifting. Hecate Chasma is a complex 8000 km long zone of linear features and coronae between Atla Regio and Asteria Regio. Neither system is a well-defined rift system such as Devana Chasma. Instead, they are complex branching networks with several discontinuous offsets along the main trend. The region between Parga, Hecate, and Devana Chasmata is characterized by a high concentration of volcanic features [7].

Tectonic characteristics. Linear features along Parga and Hecate are dominantly graben which occur in broad, diffuse zones or narrow, highly concentrated, parallel groups of troughs and fractures. The narrow, intense zones of fracturing are generally located where a trough is particularly well-expressed, and the lineaments tend to correspond well with the topographic depressions. In regions where the graben and fractures form broad diffuse groups, the faulting and fracturing is not restricted to the troughs and frequently cuts across them. Some ridge features interpreted to be compressional in origin are located within both systems. These include low, widely-spaced wrinkle ridges along with more closely-spaced ridges within the annuli of some coronae.

Five types of coronae and corona-like features are identified along Parga and Hecate. These include Asymmetric, Double Ring, Radial/Concentric coronae and Radial corona-like features and arachnoids. In addition to the over 75 features that can be reliably classified as coronae and corona-like features [3], a large number of arcuate segments and highly subdued features are identified that may be remnants of coronae. In some places, it is possible to identify superposition relationships between adjacebnt coronae. In addition, some features appear to be nearly covered by volcanic material associated with the trough systems. The circular features along both Hecate and Parga superpose and are cut by graben and faults, indicating that deformation and corona formation has overlapped in time.

Volcanic Characteristics. Along the length of Parga and Hecate Chasmata, numerous types of volcanic features are identified including flows, edifices and domes. Flows originate at the margins or from the interior of coronae and corona-like features, from edifices and domes, and from fractures along the trough systems. Volcanism typically appears to be the most recent event, with flows embaying coronae, infilling portions of the troughs, and covering fractures. In several locations along both Hecate and Parga, however, flows have been fractured by subsequent tectonic activity.

Models of Origin. Three possible models of origin are considered for the origin of Parga and Hecate Chasmata. (1) Hotspot model. The zones may represent a hotspot track, similar to the Hawaii-Emperor seamount chain [2, 3]. This model is not favored, due to the lack of evidence for large-scale plate motions on Venus [8]. Features along a hotspot track would be expected to

PARGA AND HECATE CHASMATA, VENUS: E.R. Stofan *et al.*

show a systematic progression in age, indicated by changing morphology of the coronae consistent with the stages of coronae evolution [3, 9-11]. (2) Extension and upwelling. The trough systems are major zones of extension, along which diapiric upwellings form coronae and corona-like features [2, 3]. This model is consistent with the abundance of extensional features, the faulting and rifting in Parga and Hecate Chasmata, and the proposed origin for coronae and coronae -like features as sites of upwelling [3, 9-11]. (3) Delamination or subduction. Parga and Hecate may represent zones along which subduction and/or delamination are occurring [2, 4]. Subduction has been suggested on the basis of the curvature and the asymmetry of topographic profiles in places along both systems [4]. Major asymmetries exist in both relatively linear zones of fracturing and along the rims of some coronae [5]. Asymmetric topographic profiles at coronae are also consistent with gravitational relaxation of the feature [9], and rifing [5].

The general morphology and topography of Parga and Hecate Chasmata are most consistent with major zones of extension along which diapiric upwellings form coronae and corona-like features. Relative age relationships between tectonic features, volcanism and corona formation indicate that these processes have overlapped in time, with abundant late-stage volcanism. Further detailed mapping and analysis of the morphology and temporal relationships between features in these regions is ongoing, and will hopefully lead to a better understanding of the formation and evolution of the complex equatorial zone of Venus.

Acknowledgements. This work was conducted at the Jet Propulsion Laboratory, California Institute of Technology under contract from the National Aeronautics and Space Administration. VEH and KC gratefully acknowledge the support of the NASA Planetary Geology Undergraduate Research Program.

REFERENCES [1] G. Schaber, *GRL, 9*, 499, 1982.; [2] E.R. Stofan, J.W. Head and D.B. Campbell, *LPSC XVI*, 825, 1984.; [3] E.R. Stofan *et al., JGR, 97*, 13, 347, 1992.; [4] D.T. Sandwell and G. Schubert, *JGR, 97*, 16,069, 1992. [5] V.E. Hamilton and E.R. Stofan, *LPSC XXIV*, this volume.; [6] D.A. Senske *et al., JGR, 97*, 13, 395, 1992.; [7] J.W. Head *et al., JGR, 97*, 13, 153, 1992.; [8] S.C. Solomon *et al., JGR, 97*, 13, 199, 1992.; [9] E.R. Stofan and J.W. Head, *Icarus, 83*, 216, 1990.; [10] E.R. Stofan *et al., JGR, 96*, 20, 933, 1991.; [11] S.W. Squyres *et al., JGR, 97*, 13, 611, 1992.

LINEAR STRUCTURES ON THE SMALL INNER SATELLITES OF SATURN, Philip J. Stooke, Department of Geography, University of Western Ontario, London, Ontario, Canada N6A 5C2 (stooke@vaxr.sscl.uwo.ca).

Shape modelling methods developed for non-spherical worlds were applied to four satellites of Saturn, Prometheus, Pandora, Janus and Epimetheus, resulting in the first detailed shaded relief maps of their surfaces. Ridges and valleys are described with their implications for satellite history and asteroid 951 Gaspra. They probably result from fracturing during break-up of parent bodies and/or later large impacts. Prometheus and perhaps Gaspra may be coated with debris from parent body fragmentation as well as more recent regolith.

These four satellites are covered by relatively few useful images (3 or 4 views each), so the shapes are imperfectly known and positions of features on maps may be wrong by up to a few tens of degrees in some areas (worst where a feature is seen only near a limb). Nevertheless, these shape models (refs **1-5**) are more useful than the previous triaxial ellipsoid models (e.g. **6**). The maps reproduced in refs **3**,**4** and **5** are the only detailed maps yet published, and despite remaining shortcomings they offer the best chance yet to examine global structures.

Prometheus (Fig. 1) is very elongated and appears unexpectedly smooth in the one high resolution image. It resembles Gaspra in having a few small sharp craters and subdued depressions suggestive of a mantled appearance. Three parallel ridges run across its north polar region, the largest (middle) one 100 km long (70% of the length of the satellite). A possible faint depression crosses the leading side at about 90° longitude, and may continue as a groove or chain of depressions where it meets the set of parallel ridges near the north pole. Two large depressions, possibly craters, occur at either end of the leading side (longitudes 12° and 160°).

Pandora is heavily cratered, with several large craters and others down to the limit of resolution. The surface must be old. No linear features are visible in the 25% of the satellite clearly imaged.

Janus (Fig. 2) is the largest (diameter 200 km) and roundest of the four satellites. A complex of bright linear markings near longitude 30° may be artifacts of the smeared image covering this area, or rims of large craters. The only obvious linear ridge runs from 20° north, 350° west to 10° north, 290° west, separating two major facets. It may be a relic of the original shape of Janus as its parent body broke up. The surface is heavily cratered so any such break-up must have been ancient. The other linear features are large crater chains. Several occur in the Voyager 2 image where their linear walls might be interpreted as faults. The component craters are large and shallow, more like the lunar Vallis Rheita than Catena Davy. More are seen in the Voyager 1 transit image. The chains (or parts of them) might be artifacts of smearing (**7**), but other craters appear relatively unsmeared and a groove-like chain seen at high sun in the transit image is clearly visible as a chain of depressions near the terminator in the Voyager 2 frame. These two groups of crater chains are seen in different images and appear unconnected until mapped globally, when they appear to radiate from an otherwise unremarkable region near 30° south, 260° west.

Epimetheus (Fig. 3) has the highest resolution coverage among these satellites, 1.6 km/pixel on parts of the trailing side. It has a unique topographic data set, six images of the shadow of the F Ring crossing its surface. The portion of the ring casting the shadow was assumed linear and the shape model was adjusted until the ring shadows appeared linear from the direction of the sun. The shape of the trailing side of Epimetheus is better known than any other part of the inner satellite system. The surface is heavily cratered. Several linear markings, some certainly grooves or valleys, are visible in Voyager 1 images, another in a Voyager 2 image. Some appear on an unpublished map by P. Thomas (personal communication), but a prominent valley in the high-sun region of the best images has never been described previously. The F Ring shadows are roughly parallel to it and may have hindered its identification. The valley is 100 km long, 20 km wide through most of its length, widening at its eastern end. The depth is not usefully constrained, though photometry may help. It runs from 30° south, 30° west across the prime meridian to 30° south, 290° west. A prominent ridge of about the same scale runs along 10° north over a similar range of longitudes.

Prometheus, Epimetheus and Janus have more linear features than have been acknowledged before. The most plausible mechanism for their formation is impact damage, possibly enhanced by tidal effects as orbits evolve. Damage may be caused by impacts creating craters large in relation to the size of the satellite (e.g. Stickney on Phobos) - e.g. depressions on the leading side of Prometheus or craters like Pollux or that at 20° south, 50° west on Epimetheus. No suitable crater has been found on Janus, but a limb depression at 40° north, 25° west is a possibility. Damage may also result from the fragmentation event which ejects a satellite from a parent body - the pristine 'new' satellite may be heavily fractured. If subsequent cratering does not entirely obliterate the old fractures or tidal effects reactivate old fractures, a 'cratered graben' may result, looking like some of the apparent crater chains on Janus.

Prometheus appears oddly smooth in the best image. It may be young, formed by a recent (ring-forming?)

fragmentation event, but Pandora has an older surface and cannot be its sibling. On the other hand, Prometheus has many depressions which might be heavily mantled craters, in which case it could be as old as Pandora but mantled by ejecta, perhaps from the largest leading side depression (30° north, 160° west) or from a ringlet like the F Ring which collapsed onto the surface of the satellite as orbits evolved. These explanations would not work for Gaspra which looks similar (much Prometheus ejecta could be re-accreted from Saturn orbit) , but a third could accomodate both bodies: most of the debris is from the fragmentation event which presumably formed each body, the equivalent of late low velocity ejecta which forms a crater rim or falls back into the crater on a larger body but could be accreted onto the larger fragments during parent-body breakup. The premise that fragmented bodies are initially dust-free and only acquire a regolith by subsequent cratering may need to be re-examined.

REFERENCES: (1) Stooke, P.J., 1986. Proc. 2nd Int. Symp. Spatial Data Handling, pp. 523-536. (2) Stooke, P.J. and Keller, C.P., 1990. Cartographica **27**: 82-100. (3) Stooke, P.J., 1992. "The topography of Epimetheus", Earth, Moon, Planets (submitted). (4) Stooke, P.J., 1992. "The shapes and surface features of Prometheus and Pandora", Earth, Moon, Planets (submitted). (5) Stooke, P.J. and Lumsdon, M.P., 1992. "The topography of Janus", Earth, Moon, Planets (submitted). (6) Yoder, C.F., Synnot, S.P. and Salo, H., 1989. Astron. Journ. **98**: 1875-1889. (7) Thomas et al., 1983. J. Geophys. Res. **88**: 8743-8754.

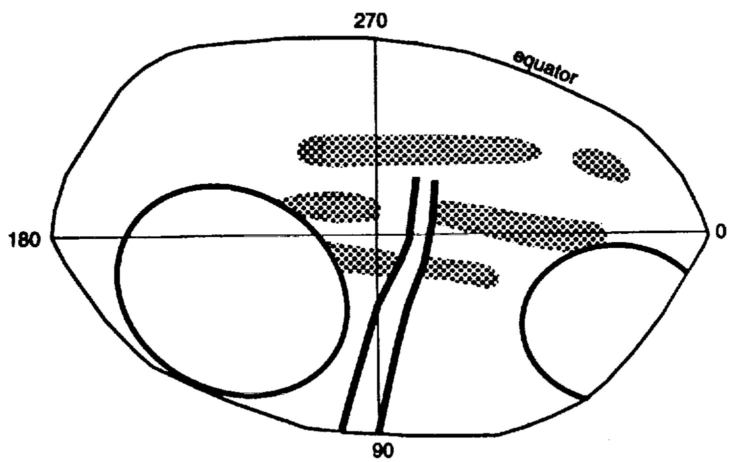


Figure 1. Major features, north side of Prometheus. Pattern: ridges; double line: valley; loops: depressions. Base is an equal area projection (ref. 4). Outline is convex hull of equator.

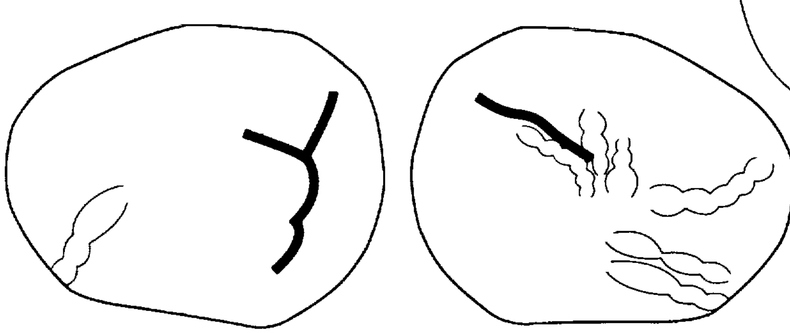


Figure 2. Non-crater features of Janus. Heavy lines: ridges (Y shape is very uncertain); scalloped lines: crater chains. Conformal projections centred on equator (ref. 5), trailing side at right. Outline is convex hull.

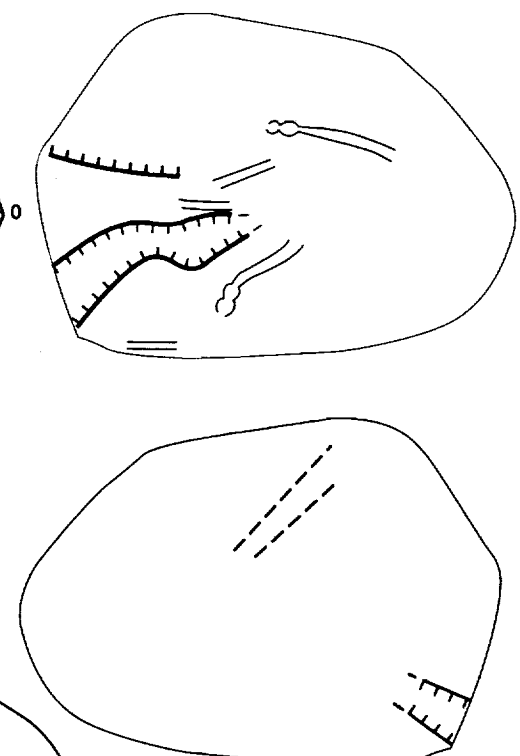


Figure 3. Non-crater features of Epimetheus. Heavy lines - scarps (ticks downslope); light lines - grooves (scalloped where they resemble crater chains); dashes - possible grooves. Conformal projections (ref. 3), trailing side at top. Outline is convex hull.

5162-46
ABS. ONLY

N94-20798

THE AGE OF THE PRETORIA SALTPAN IMPACT CRATER, SOUTH AFRICA.

p. 2

Dieter Storzer[1], Christian Koeberl[2], and Wolf Uwe Reimold[3]. [1]*Laboratoire de Mineralogie, Museum Histoire Naturelle, 61 rue Buffon, F-75005 Paris, France;* [2]*Institute of Geochemistry, University of Vienna, A-1010 Vienna, Austria;* [3]*Economic Geology Research Unit, Department of Geology, University of the Witwatersrand, Johannesburg 2050, South Africa.*

The Pretoria Saltpan impact crater, situated about 40 km NNW of Pretoria, South Africa, has a diameter of about 1.13 km. The structure was formed in 2.05 Ga Nebo granite of the Bushveld Complex. The impact origin of the crater was recently established by the discovery of characteristic shock-metamorphic features in breccias found in drill cores at depths >90 m. Impact glass fragments were recovered by standard magnetic separation techniques and handpicking from the melt breccias. As no reliable crater age was known so far, several hundred sub-millimeter-sized glass fragments were studied for fission tracks. The results show that the Saltpan impact crater has an age of 220±52 ka, which is in agreement with field geological observations.

The Pretoria Saltpan crater is located at 25°34'30" S and 28°04'59" E, about 40 km north-northwest of Pretoria, South Africa. The structure has a rim-rim diameter of 1130 m, with a maximum rim elevation over the present crater floor of 119 m. The rim is generally about 60 m above the surrounding plains. When first described by geologists, the crater was interpreted as being of volcanic or cryptovolcanic origin (e.g., Wagner [1]). The first to suggest that the structure was the result of a meteorite impact was Rohleder [2] in 1933. The impact theory was also supported by studies of intense structural deformation at the crater rim [3]. The observation of some rocks of clearly volcanic origin in the crater rim (e.g., trachytes, lamprophyre dikes) was taken as evidence for a volcanic origin of the crater [4]. Also, Fudali et al. [5] interpreted their gravity data and field observations as inconsistent with an impact origin. However, recent field studies [6] proved beyond any doubt that these volcanics are a feature of the regional geology and not related to the cratering event. The first firm evidence for an origin by impact was found in drill core samples taken from a depth of >90 m. Reimold et al. [7,8] found shock-metamorphosed quartz and feldspar with one or more sets of planar deformation features (PDFs), diaplectic quartz and feldspar glass, melt breccias, and impact glass fragments.

The age of the crater remained, however, problematic. The structure is relatively fresh in appearance (minimum erosion), similar to Meteor Crater in Arizona, only covered with vegetation. The crater was formed in 2.05 Ga Nebo granite of the Bushveld Complex. Fig. 1 shows a geological map of the crater area. The crater rim is partly covered by Karoo grit, which is overlain by fragmental granitic breccia. Altered carbonatite or trachyte veins are exposed in the rim. Milton and Naeser [3] obtained zircon and apatite fission-track ages of 1.9±0.4 and 0.6±0.09 Ga for carbonatite samples. K-Ar and Rb-Sr biotite ages for lamprophyre samples range from 1.3 to 1.4 Ga [7,9]. These old ages are not in agreement with field evidence and the erosional state of the crater. A late Pleistocene crater age of ca. 200,000 years was suggested [e.g., 8] through extrapolation of accumulation rates based on ^{14}C dating of upper lacustrine sediments.

Samples recovered from the drill core provided an excellent opportunity to obtain a more reliable age. Fig. 2 shows a cross-section of the crater stratigraphy as obtained from the borehole. 90 m of lacustrine sediments are underlain with a 53 m thick unit of unconsolidated fragmental breccia consisting of granitic sands intercalated with fractured granite boulders (5 cm to 1.5 m in size). Below the breccia, strongly fractured Bushveld granite was encountered. Within the melt breccia, glass fragments and spherules were found. The fragments are translucent, greenish, or brownish in color, and contain abundant schlieren. Most of those glasses have compositions that are very similar to the host granite [8], as shown, for example, by the rare earth element (REE) pattern (Fig. 3). Others are compositionally similar to the main mineral components of the Nebo granite or mixtures thereof.

A large number of these glass fragments were separated from the melt breccias by standard magnetic separation techniques and handpicking. The glasses were then mounted, polished, and etched for fission track analysis. A total of 456 glass fragments on 7 mounts were studied for fossil tracks, and one mount with 91 particles was irradiated with an integral thermal flux of $1.65.10^{15}$ n/cm², yielding 420.87±7.87 induced tracks/mm². The measurements were done using techniques similar to those described before (e.g., [10]), although complications were introduced by the abundance of schlieren and inhomogeneous distribution of uranium in the Saltpan glasses. The

AGE OF THE SALTPAN IMPACT CRATER, SOUTH AFRICA: Storzer, D. et al.

results are summarized in Table 1. The mean fission track age of the Saltpan crater determined from granitic impact glasses, is 220±52 ka. The 1 σ standard deviation of the mean fission track age is composed of the statistical counting errors of the number of fossil tracks (±23%) and thermal neutron induced tracks (±1.9%) and the determination of the neutron flux (±5%). This age is in excellent agreement with the preservation state of the crater and extrapolated ^{14}C results for lacustrine sediments.

References: [1] Wagner, P.A., The Pretoria Saltpan, Geol. Surv. South Africa Mem. 20, 136 p., 1922. [2] Rohleder, H.P.T., Geolog. Magazine 70, 489-498, 1933. [3] Milton, D.J., and Naeser, C.W., Nature, Phys. Sci., 299, 211-212, 1971. [4] Feuchtwanger, T., unpubl. B.Sc. Hon. thesis, Univ. Witwatersrand, 41 pp, 1973. [5] Fudali, R.F., Gold, D.P., and Gurney, J.J., J. Geology, 81, 495-507, 1973. [6] Brandt, D., and Reimold, W.U., this volume, 1993. [7] Reimold, W.U., Koeberl, C., Kerr, S.J., and Partridge, T.C., Lunar Planet. Sci. XXII, 1117-1118, 1991. [8] Reimold, W.U., Koeberl, C., Partridge, T.C., and Kerr, S.J., Geology, 20, 1079-1082, 1992. [9] Partridge, T.C., Reimold, W.U., and Walraven, F., Meteoritics, 25, 396, 1990. [10] Koeberl, C., and Storzer, D., Proc. 2nd Intern. Conf. Natural Glasses, Prague, 207-213, 1988.

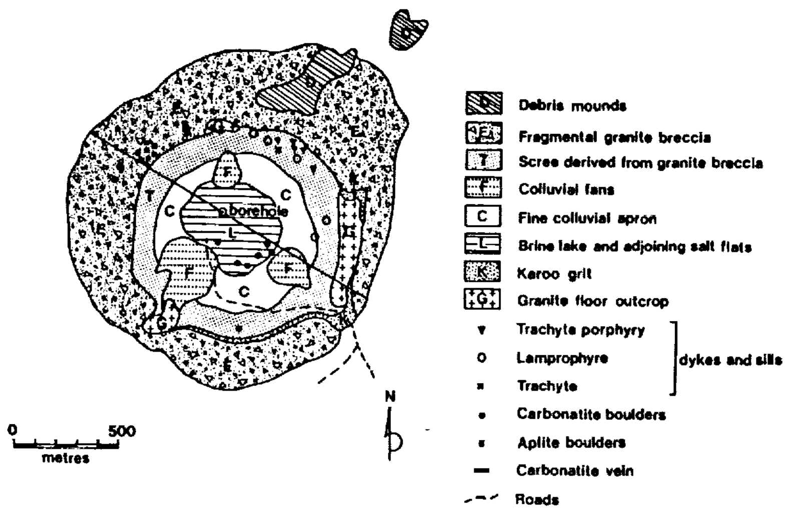


Fig. 1: Geology of the Pretoria Saltpan crater, after [8].

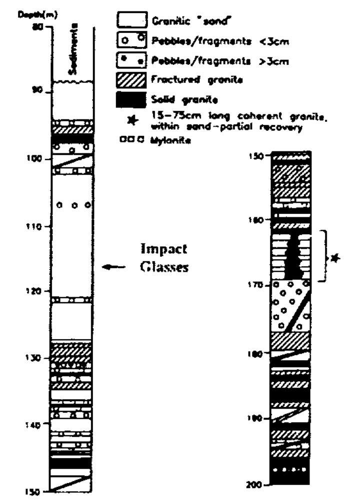


Fig. 2: Schematic stratigraphy of Saltpan borehole [8]. The impact glass samples were taken from a depth of 116-118 m.

Table 1. Fission track age of impact glass from the Saltpan crater. The glass fragments were separated from drill core samples from a depth of 116-118 m.

Section No.	No. of particles	Area scanned[a]	D_s[b]	Age [ka]
10	83	3.61	0.55	107±76
11	59	2.70	1.85	361±161
12	27	1.76	1.14	222±157
13	87	3.24	1.54	301±135
14	52	1.74	0.58	112±112
15	91	2.72	1.10	215±124
16	57	1.06	0.94	183±183
Total		16.83	1.13±0.26	220±52

[a]in mm^2; [b]Density of fossil tracks per mm^2

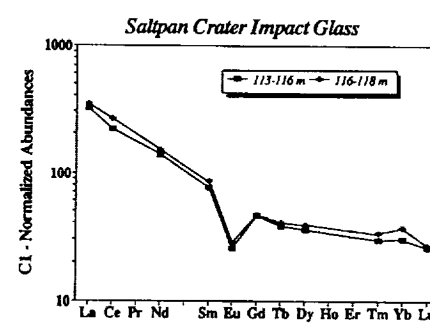


Fig. 3. REE abundance pattern of impact glass fragments.

N94-20799
168123
p-2

THE ROLE OF CO_2 IN WEATHERING REACTIONS AND THE PRESENCE OF S_2 ON VENUS: IMPLICATIONS FOR THE PYRITE STABILITY FIELD

D'Arcy W. Straub, Department of Earth, Atmospheric and Planetary Sciences, Massachusetts Institute of Technology, Cambridge, MA 02139.

Introduction: The stability of pyrite has become the focal point of study since regions of low radio thermal emissivity were detected during the Pioneer Venus and Magellan radar mapping missions of Venus. Thermodynamic calculations and experimental studies have been performed assuming CO_2 is a major contributor to the weathering of sulfides [1,2], as CO_2 is the major gas species in the Venusian atmosphere. The purpose of the present study, however, is to demonstrate that CO_2 is a non-reactive gas and that a minor species, S_2, is the most important gas in determining whether pyrite is stable in the high radar reflectivity regions.

Kinetic studies have suggested that pyrite and pyrrhotite are capable of being oxidized by CO_2. In the first study [1], pyrrhotite was shown to react with 99.95% pure CO2 at 524-787°C via the following reaction:

$$3\ Fe_7S_8 + 76\ CO_2 \rightarrow 7\ Fe_3O_4 + 76\ CO + 24\ SO_2. \qquad (1)$$

In a related study [2], 99.95% pure CO_2 was reacted with pyrite, which produced mixtures of pyrrhotite and magnetite. In neither study, the relevant oxygen fugacity was not reported. In one of our previous studies [3], "pure" CO_2 was also used to study the behavior of pyroxenes heated in a CO_2 rich atmosphere. The < 30 ppm O_2 present as a contaminant, however, destroyed the simulation of the Venusian atmosphere (where $f_{O_2}<10^{-21}$) and caused the oxidation of the pyroxenes. By analogy, the "pure" CO_2 used in the sulfide stability studies probably contained O_2 as a contaminant, with the O_2, and not CO_2, being responsible for the oxidation of pyrite and pyrrhotite.

To determine whether pyrite and pyrrhotite are susceptible to oxidation by CO_2, pyrite and pyrrhotite samples were heated at 475°C with $NaHCO_3$, which thermally decomposes to NaOH and CO_2. By using the decomposition of $NaHCO_3$ to release CO_2, an uncontaminated source of CO_2 can be produced.

Experimental Results: Pyrite and pyrrhotite samples (~100mg) were placed in evacuated cells with $NaHCO_3$. The amount of $NaHCO_3$ used (~0.50mg) was equivalent to that which would produce slightly less than 1 atm. pressure in the cell. This amount of $NaHCO_3$ would also produce enough CO_2 to ensure that at least 10% of the iron sulfide would be oxidized if all of the CO_2 was consumed. After 30 days at 475°C, the reactions were terminated. The remains of the $NaHCO_3$ were dissolved in water. The pH was > 11, confirming the production of NaOH from the thermal decomposition of $NaHCO_3$. The sulfides were analyzed by Mössbauer spectroscopy, and in each case, no oxidation product was observed, whether it be magnetite, in the case of pyrrhotite, or magnetite and/or pyrrhotite, in the case of pyrite.

Discussion: The results indicate that CO_2 is not as effective at oxidizing pyrite and pyrrhotite as the earlier studies may have lead one to believe. The reason for this is that although CO_2 has

PYRITE STABILITY ON VENUS: Straub, D.W.

the highest mixing ratio in the Venusian atmosphere, it is not the gas responsible for oxidizing the minerals. For example, the following reaction could be proposed to occur on Venus:

$$2\ Fe_3O_4 + CO_2 \rightarrow 3\ Fe_2O_3 + CO. \quad (2)$$

Here, CO_2 is the oxidizing gas, but in reality, it is the O_2 that is oxidizing the magnetite via the following mechanism:

$$CO_2 \rightarrow CO + \tfrac{1}{2}\ O_2 \quad (3)$$

$$2\ Fe_3O_4 + \tfrac{1}{2}\ O_2 \rightarrow 3\ Fe_2O_3 \quad (4)$$

As is well known, whether Fe_3O_4 is oxidized is ultimately dependent upon the oxygen fugacity. Hence, from the above equations, the role of O_2 is to be an oxidizing agent, the role of CO is to be a reducing agent, and the role of CO_2 is to buffer the O_2 and CO. It should also be noted that at 740K, ΔG=+76 kJ and ΔG=-143 kJ for reactions (2) and (4), respectively.

Another reaction of interest concerns the production of COS:

$$3\ FeS_2 + 2\ CO + 4\ CO_2 \rightarrow Fe_3O_4 + 6\ COS. \quad (5)$$

Reaction (5) is reported to occur spontaneously [4], but this is in contradiction with ΔG=+264 kJ at 740K. A spontaneous reaction (ΔG=-614 kJ at 740K), and one which takes into account the true oxidizing agent, is as follows:

$$3\ FeS_2 + 6\ CO + 2\ O_2 \rightarrow Fe_3O_4 + 6\ COS. \quad (6)$$

For reaction (6) at 740K, $K_{eq}=2.1\times10^{43}$. If f_{CO}~40 ppm and f_{COS}~0.3 ppm, then at equilibrium $f_{O_2}\sim9\times10^{-29}$. Because the f_{O_2} of the Venusian atmosphere is approximately 8 orders of magnitude higher, the f_{O_2} of Venus dictates that magnetite, and not pyrite, is the stable phase, although the rate at which pyrite is weathered to magnetite is unknown.

Other investigators [5] have argued that reaction (5) does not adequately describe the Venusian atmosphere, and that the reaction of importance, which forms pyrite is:

$$Fe_3O_4 + 6\ SO_2 + 16\ CO \rightarrow 3\ FeS_2 + 16\ CO_2. \quad (7)$$

This reaction may occur (ΔG=-1231 kJ at 740K), but gaseous sulfur, a more important gas in the Venusian atmosphere in regard to pyrite stability, is being overlooked. For pyrite to be stable, a minimum f_{S_2} must be maintained, and is illustrated by the following reaction:

$$FeS_2 \rightarrow \tfrac{1}{2}\ S_2 + FeS. \quad (8)$$

At 740K and 700K, the f_{S_2} must be 6×10^{-6} and 4×10^{-7}, respectively for pyrite to be stable [6]. Initial kinetic studies, in which pyrite is placed in an evacuated tube with Ag foil, suggest that the formation of pyrrhotite and Ag_2S is extremely rapid at 740K. The importance of reaction (8) cannot be ignored. If a minimum f_{S_2} is not maintained, S_2 will rapidly diffuse from the pyrite, *regardless of any atmospheric composition*. A mixing ratio reported for S_2 of 20 ppb [7], which is well below the required minimum f_{S_2} for pyrite stability, raises doubts that FeS_2 is the mineral responsible for the high radar reflectivity at high elevations on Venus.

References: [1] A.H. Treiman & B. Fegley, Jr., *Lun. Planet. Sci.*, **XXII**, 1409 (1991); [2] B. Fegley, Jr. & A.H. Treiman, *Bull. Amer. Astron. Soc.*, 22, 1055 (1990); [3] D.W. Straub & R.G. Burns, *Lun. Planet. Sci.*, **XXII**, 1928 (1991); [4] B. Fegley, Jr., A.H. Treiman & V.I. Sharpton, *Proc. Lun. Planet. Sci.*, 22, 3 (1992); [5] K.B. Klose, J.A. Wood & A. Hashimoto, *JGR*, 97, 16,353 (1992); [6] P. Toulmin & P. Barton, *Geochim. Cosmochim. Acta*, 28, 641 (1964); [7] N. San'ko, *Cosmic Res.*, 18, 437 (1980); [8] Research supported by NASA grant NAGW-2220.

S164-91
ABS. ONLY

N94-20800

P. 2

THE STABILITY OF OXYAMPHIBOLES: EXISTENCE OF FERRIC-BEARING MINERALS UNDER THE REDUCING CONDITIONS ON THE SURFACE OF VENUS

D'Arcy W. Straub and Roger G. Burns, Dept of Earth, Atmospheric and Planetary Sciences, Massachusetts Institute of Technology, Cambridge, MA 02139.

Introduction: An enigma of Venusian mineralogy is the suggestion that Fe^{3+}-bearing minerals exist under the reducing conditions of the Venusian atmosphere. Analysis of the spectrophotometric data from the Venera 13 and 14 missions, combined with the laboratory reflectance spectral measurements of oxidized basalts at elevated temperatures, led to the suggestion that metastable hematite might exist on Venus [1]. Heating experiments at 475°C when f_{O_2}~10^{-24}, demonstrated that the hematite to magnetite conversion is rapid, indicating metastable hematite is not present on Venus [2]. In addition to hematite, several other ferric oxide and silicate minerals have been proposed to occur on Venus, including laihunite or ferrifayalite [3], Fe^{3+}-bearing tephroite, oxyamphiboles [4], and oxybiotites [4]. Heating experiments performed on these Fe^{3+}-bearing minerals under temperature-f_{O_2} conditions existing on Venus suggest that only oxyamphiboles and oxybiotites may be stable on the surface of Venus.

Experimental Procedure: To simulate the appropriate redox conditions of the Venusian atmosphere, a Ni/NiO solid buffer was used. The Ni/NiO buffer, when heated to 475°C in an evacuated quartz cell, provides an f_{O_2} of approximately 10^{-24} [5]. The Ni/NiO buffer and mineral samples were wrapped in separate silver foil sheets. After heating periods of 1-30 days, the samples were quenched and analyzed by Mössbauer spectroscopy.

Results: The laihunite (25% Fe^{3+}) and the tephroite (16% Fe^{3+}) samples were each shown to have all of their Fe^{3+} reduced to Fe^{2+} when heated with the Ni/NiO buffer at 475°C for 7 days and 14 days, respectively. Conversion of the Fe^{3+} in these olivines to Fe^{2+} is demonstrated by the Mössbauer spectra of laihunite, illustrated in figure 1.

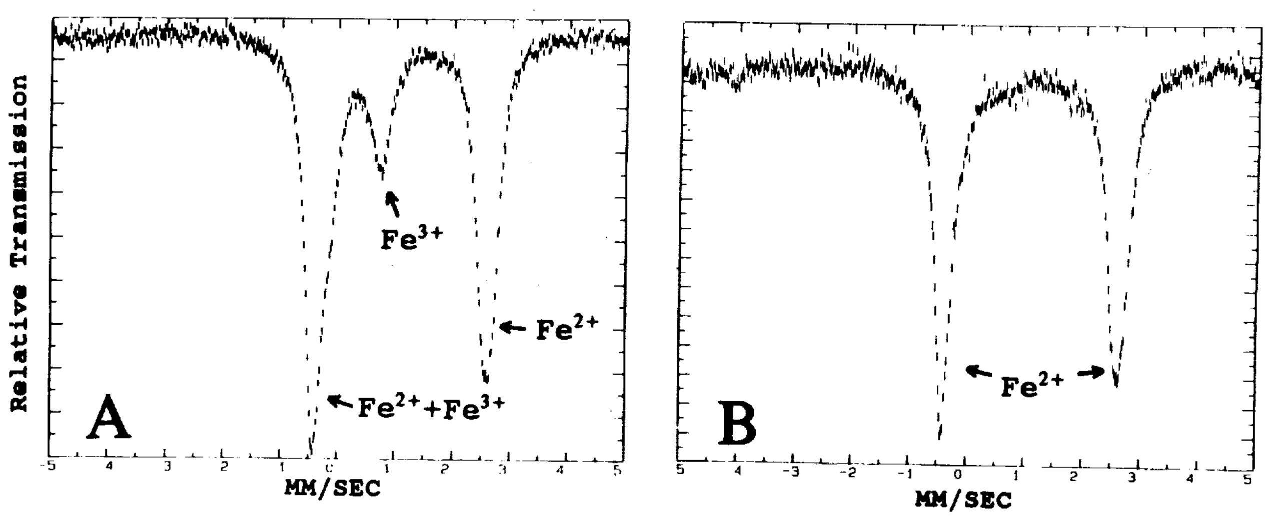


Figure 1: Laihunite before (A) and after (B) heating with Ni/NiO.

Heating experiments performed with a variety of amphiboles, including glaucophane, actinolite, hornblende, and kaersutite, indicated that Fe^{3+} ions initially present in the amphiboles are stable under Venusian surface conditions, where T~475°C and f_{O_2} < 10^{-21}. For example, the Mössbauer spectra illustrated in figure 2 of hornblende before and after heating for 28 days show that virtually none of the Fe^{3+} has been reduced (cf. laihunite in figure 1). In a related experiment, hornblende was first heated in air for 20 minutes at 700°C to oxidize most of the Fe^{2+} ions, after which the oxidized sample was heated at 475°C with the Ni/NiO buffer for 7 days. The Mössbauer spectra of these reaction products, illustrated in figure 3, show that Fe^{3+} ions remain in the oxidized hornblende when heated under the reducing conditions of the Ni/NiO buffer.

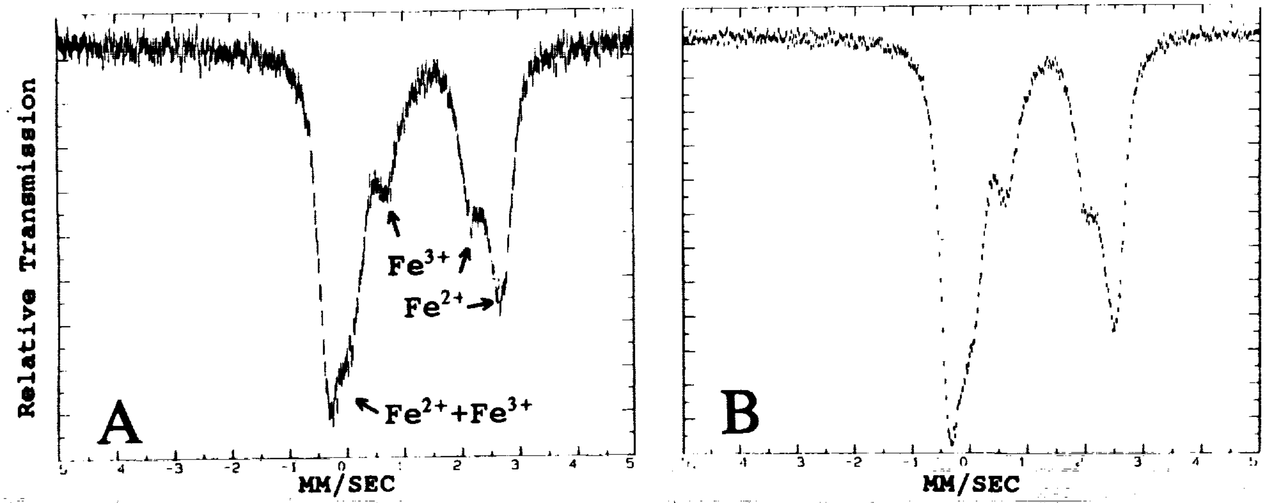


Figure 2: Hornblende before (A) and after (B) heating with Ni/NiO.

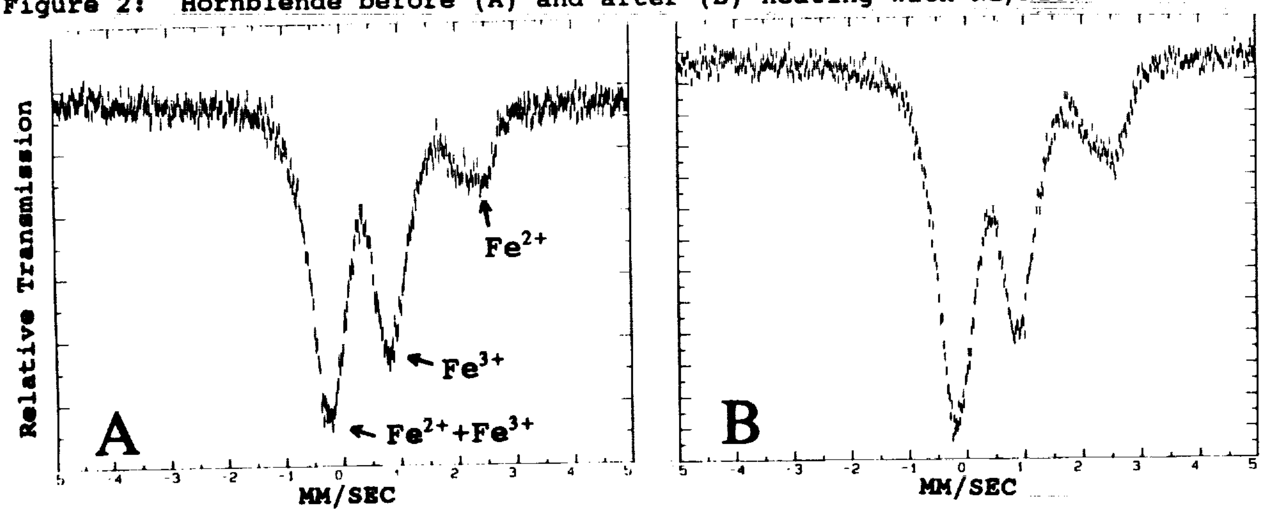


Figure 3: Oxidized hornblende before (A) and after (B) heating with Ni/NiO.

Discussion: The stability of Fe^{3+} in the oxyamphiboles may be explained by the intracrystalline redox reaction

$$Fe^{2+} + OH^{-} \rightarrow Fe^{3+} + O^{2-} + \frac{1}{2}H_2.$$

The Fe^{3+} and O^{2-} ions remain in the crystal structure as a result of this dehydrogenation reaction. Thus, no oxygen is added to the amphibole. This contrasts with the laihunite and hematite in which reduction, when heated with the Ni/NiO buffer, proceeds by diffusion of oxygen atoms from their crystal structures. The amphiboles lack this "excess" oxygen and cannot be reduced with the Ni/NiO buffer. Preliminary studies show that oxybiotites, which also can be formed by the removal of hydrogen during intracrystalline redox reactions, are also stable when heated at 475°C with the Ni/NiO buffer. These results also conform with phase equilibrium diagrams for iron-bearing calcic amphiboles and oxybiotites [6], which indicate that they have stability fields within ranges of temperatures, oxygen fugacities and atmospheric pressures existing on the Venusian surface.

References: [1] C.M. Pieters *et al.*, *Science*, **234**, 1379 (1986); [2] D.W. Straub & R.G. Burns, *Lun. Planet. Sci.*, **XXIII**, 1375 (1992); [3] B. Fegley, Jr., A.H. Treiman & V.I. Sharpton, *Proc. Lunar Planet. Sci.*, **22**, 3 (1992); [4] R.G. Burns & D.W. Straub, *Intern. Colloq. Venus, LPI Contrib. No. 789*, p.15 (1992); *EOS, Trans. Amer. Geophys. Un.*, **73**, 332 (1992); [5] D.H. Lindsley, *Rev. Min.*, **III**, L-61 (1976); [6] H.P. Eugster & D.A. Wones, *J. Petrol.*, **3**, 82 (1972); [7] Research supported by NASA grant NAGW-2220.

N94-20801

Parabolic Features and the Erosion Rate on Venus;

Robert G. Strom, Dept. of Planetary Sci., Univ. of Arizona, Tucson, AZ 85721

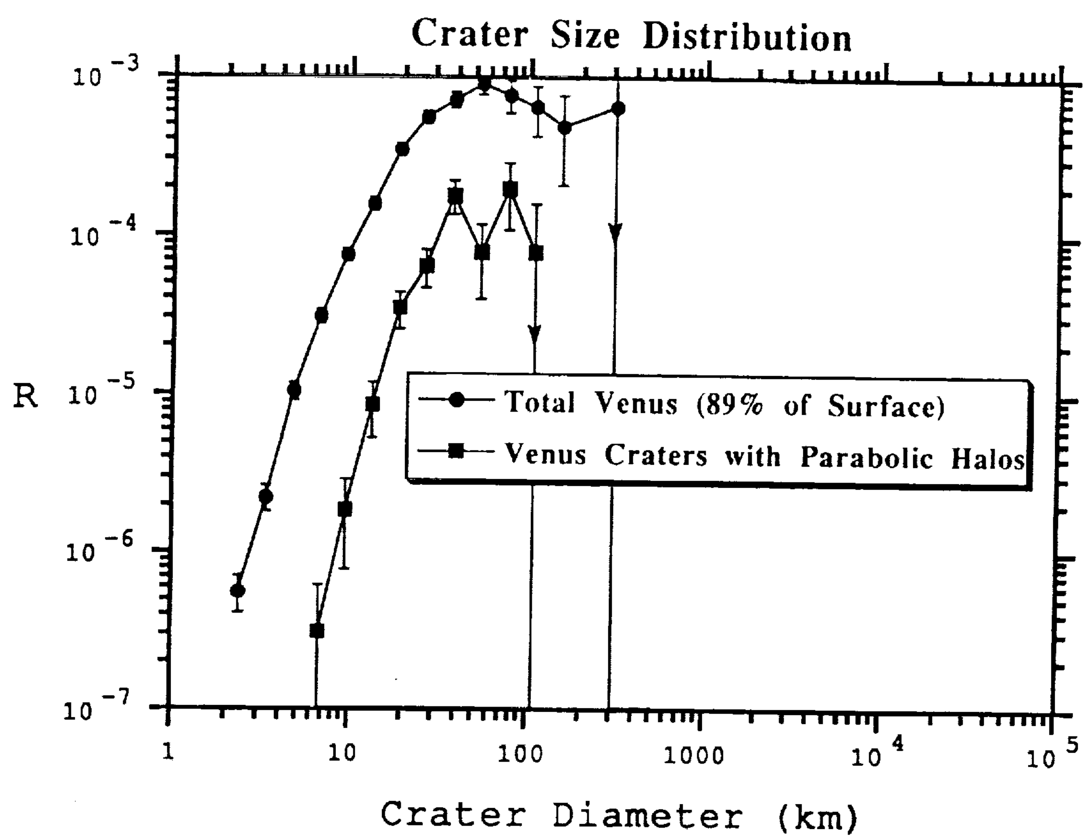
The impact cratering record on Venus consists of 919 craters covering 98% of the surface. These craters are remarkably well preserved, and most show pristine structures including fresh ejecta blankets (1). Only 35 craters (3.8%) have had their ejecta blankets embayed by lava and most of these occur in the Atla-Beta Regio region; an area thought to be recently active (1). Parabolic features are associated with 66 of the 919 craters (2). These craters range in size from 6 to 105 km diameter (2). The parabolic features are thought to be the result of the deposition of fine-grained ejecta by winds in the dense venusian atmosphere (2,3). The deposits cover about 9% of the surface and none appear to be embayed by younger volcanic materials (2). However, there appears to be a paucity of these deposits in the Atla-Beta Regio region (2), and this may be due to the more recent volcanism in this area of Venus. Since parabolic features are probably fine-grain, wind-deposited ejecta, then all impact craters on Venus probably had these deposits at some time in the past. The older deposits have probably been either eroded or buried by eolian processes. Therefore, the present population of these features is probably associated with the most recent impact craters on the planet. Furthermore, the size/frequency distribution of craters with parabolic features is virtually identical to that of the total crater population (Fig. 1). This suggests that there has been little loss of small parabolic features compared to large ones, otherwise there should be a significant and systematic paucity of craters with parabolic features with decreasing size compared to the total crater population. Whatever is erasing the parabolic features apparently does so uniformly regardless of the areal extent of the deposit. The lifetime of parabolic features and the eolian erosion rate on Venus can be estimated from the average age of the surface and the present population of parabolic features.

The average age of the surface is estimated to be 330 million years, but could be as young as 200 million years or as old as 700 million years based on the uncertainty in the estimated asteroid crater production rate (1). Since 66 of the 919 craters have parabolic features and the average age of the surface is 330 million years, then the average lifetime of parabolic features is about 24 million years, but could be as short as 14 million years or as long as 50 million years. This suggests that the eolian erosion, particularly for unconsolidated material, or burial rate on Venus is extremely low compared to the Earth or Mars. Campbell, et al. (2) estimate that the thickness of the parabolic deposits is from several to tens of centimeters thick, possibly 0.16 to 3 meters. If the deposits average about 3 meters thick

Strom, R.G., **Erosion Rate on Venus**

then the maximum possible erosion rate is about 0.21 meters/million yearsand the minimum rate is about 0.06 meters/millionyears. On the other hand, if the deposits are only 0.16 meters thick, then the maximum possible erosion rate is only about 0.01 meters/million years and the minimum rate is about 0.003 meters/million years. These low erosion or burial rates make it unlikely that eolian processes on Venus have been important in shaping its surface.

References: (1) Schaber, G.G. *et al.*, JGR-Planets, **97**, 13,257-13,301, 1992; (2) Campbell, D.B. *et al.*, JGR-Planets, **97**, 16,249-16,277, 1992; (3) Vervack, R.J., and Melosh, H.J., Geophys. Res. Lett., **19**, 525-528, 1992.



5166-91
ABS ONLY

N94-20802

TRITON'S CRATERING RECORD AND ITS TIME OF CAPTURE.

R.G. Strom and S.K. Croft, Lunar and Planetary Lab., Univ. of Arizona, Tucson, AZ 85721

P. 2

Recent impact crater counts on the Voyager 2 high resolution images of Triton have resulted in a more accurate crater size/frequency distribution down to about 3 km diameter. These counts reveal a size/frequency distribution characterized by a differential -4 slope. This is consistent with the observation that there are no craters larger than 27 km diameter on the 20% of Triton viewed at resolutions capable of detecting them. A -4 slope is deficient in large craters and at the very low crater density on Triton no craters larger than about 30 km are expected on just 20% of the satellite.

The Triton size distribution is significantly different from the differential -3 slope of the fresh crater population on Miranda (Fig. 1), but both show leading/trailing asymmetries (1,2, 3). Since Miranda is in prograde orbit this crater population is probably due to objects in heliocentric orbit, i.e., comets. If this crater population is due to comets, then the significantly different crater population on Triton is probably due to some other population of impacting objects. The most likely origin of these objects is planetesimals in planetocentric orbits. Because Triton is in retrograde orbit, objects in prograde planetocentric orbits will also produce a leading/trailing asymmetry. If the Triton craters are largely the result of objects in planetocentric orbit, then where are the comet craters that should be there if they have a differential -3 distribution function as inferred from the Miranda fresh crater population? The most likely answer is that they are there, but at such a low density that they can not be distinguished from the planetocentric population. An upper bound on this density can be estimated by determining the density of a crater population with a differential -3 slope (the comet distribution inferred from Miranda) where no craters larger than 27 km would be expected on the 20% of Triton viewed by Voyager at resolutions sufficient to detect them. This density is at the density of the largest crater (27 km) shown in Fig. 1. At this density the number of craters in size bins greater than 27 km is less than 1 for a -3 distribution function. Fig. 2 shows the observed size distribution, the upper limit of the hypothetical comet crater size distribution, and the difference between the observed and the hypothetical comet crater populations. The "difference" curve is not appreciably different from the observed curve.

Shoemaker (1) estimates that at Triton the comet crater production rate for craters >10 km diameter is 8.4×10^{-15} km^{-2} yr^{-1}. If we assume that the "comet" curve shown in Fig. 2 represents the maximum number of comet craters that could be present on 20% of the surface, then the number of craters greater than 10 km diameter is less than half the number observed, and the maximum average surface age is about 600 million years. This age is not changed significantly by scenarios invoking an early massive atmosphere on Triton (10).

Because of its retrograde orbit and high inclination to Neptune's equatorial plane (21°), Triton is thought to have been captured by Neptune, possibly following a collision with a regular satellite(4). The collision-capture hypothesis is thought to be more plausible than others, e.g., gas drag (9), because (a) the Neptune satellite system is the only one in the outer Solar System that has just one major satellite, and it is in a retrograde and highly inclined orbit, (b) Nereid has an unusually large semimajor axis and eccentricity, and (c) all other minor regular satellites are interior to Triton. The capture process would probably produce a highly eccentric orbit that would evolve by tidal dissipation to its present near circular orbit. During the capture process it could have caused Nereid to acquire its peculiar orbit (4). The estimated time to evolve from an eccentric orbit to its present orbit is about 400 million years (4). As the orbit circularized, Triton would sweep up pre-existing satellites. During this time tidal dissipation would have heated Triton, leading to large scale melting. This may have resulted in the global volcanism and large scale resurfacing observed on Triton.

Triton's Time of Capture: Strom, R.G. and Croft, S.K.

In this scenario, the cratering record is largely the result of the final sweep up of objects in prograde planetocentric orbits after circularization of the orbit and cession of internal activity. Neried and the present satellites interior to the orbit of Triton may be all that remains of the satellites of Neptune prior to the capture event (4). Since all unambiguous impact craters are relatively fresh (there are no degraded or partially embayed craters) and the sweep up time for planetocentric objects is very rapid, the cession of widespread resurfacing must have been relatively abrupt. The maximum time at which Triton was captured is then the age of the surface estimated from inferences of the maximum density of comet impacts, plus the time to circularize Triton's orbit and cession of widespread volcanic activity. If all of the above reasoning is correct, then this capture event occurred roughly about 1 billion years ago with probably a large, but unknown, uncertainty.

The capture of Triton by collision or with a previously existing satellite of Neptune gas drag probably requires that it took place near the end of the accretion of Neptune in order for there to be a sufficient number of planetesimals or sufficiently high gas densities in the vicinity to make capture plausible (4). The accretion time scale for Neptune is highly uncertain, with numerical models suggesting formation times as short as 5×10^6-10^8 years (5,6) to many billion years (7,8). However, even those that indicate runaway accretion only accrete about 1/10 the mass of Neptune in 2×10^5 years (5). The rest takes much longer. If the capture event of Triton took place about 1 billion years ago, then it suggests that Neptune finished its accretion rather late in Solar System history.

References: (1) Smith, B. *et al.*, Science, **246**,1422-1449, 1989; (2) Strom, R.G. *et al.*, Science, **250**, 437-439, 1990; (3) Greenberg, R. et al., Uranus, Univ. Ariz. Press, 693-735, 1991; (4) Goldreich, P. *et al.*, Science, **245**, 500-504, 1989; (5) Lissauer, J.J., Icarus, **69**, 249-265, 1987; (6) Greenberg, R. *et al.*, Icarus, **59**, 87-113, 1984; (7) Safronov, V.S., NASA TTF-677, 1972; (8) Wetherill, G.W., Annu. Rev. Astron. Astrophys. **18**, 77-113, 1980; (9) McKinnon, W.B., Nature, **311**, 355-358, 1984; (10) Lunine, J.I. and Nolan, M.C., Icarus, in press.

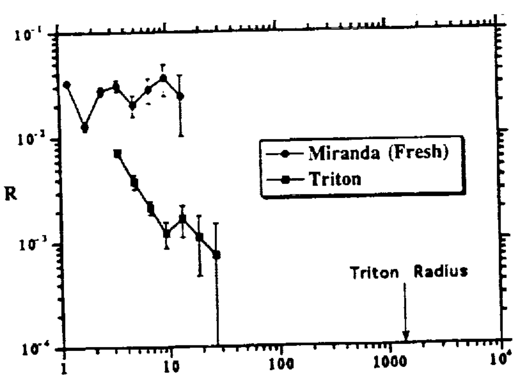


Fig. 1. "R" plot of the size distribution of the fresh crater population on Miranda and Triton.

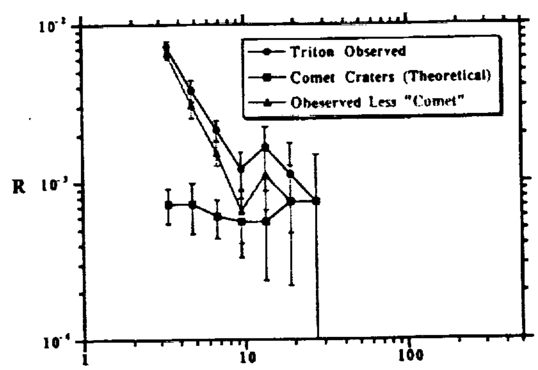


Fig. 2. "R" plot of the size distribution of Triton craters, the maximum hypothetical comet craters that could be present, and the difference between the hypothetical and observed curves.

S167-91
ABS ONLY

N94-20803

ARE PLINIAN TYPE ERUPTIONS POSSIBLE ON VENUS ?

p. 2

Seiji Sugita[1,2] and Takafumi Matsui[2], [1]Department of Geological Sciences, Brown University, Providence RI 02912; [2]Department of Earth and Planetary Physics, University of Tokyo, Tokyo, Japan.

Calculations of dynamics of eruption plumes in the Venusian atmosphere reveal the following results: I) Conditions for a convective eruption column are very limited on Venus with required magma temperatures higher than 1100°K. Otherwise pyroclastic flows form. II) Once a convective eruption column is established, it may extend as high as about the tropopause (~60km). III) Critical eruption velocities for a convective eruption column as a function of temperature and gas content of magma may provide a useful tool for estimating interior condition of Venus, including its volatile inventory.

Introduction; Volcanism is a major process to transport volatile from mantle of a planet to its surface (degassing) as well as heat and mass, all of which affect planetary evolution. For example, after completion of planetary accretion, volcanism is the dominant continuous degassing process for all the terrestrial planets. Explosive volcanism is a very important process for mantle degassing due to its high magma gas content. Consequently, eruption styles and the controlling physical processes need to be understood.

Recent satellite and terrestrial ground-based observations suggest existence of explosive volcanism on Venus [1, 2, 3, 4] even though explosive volcanism is very difficult to occur on Venus due to its high atmospheric pressure [5, 6]. The purpose of this study is to investigate dynamics of explosive eruption on Venus and the relation between eruption conditions such as gas content and temperature of magma and eruption velocity, and eruption styles such as Plinian type and pyroclastic flow type.

Model of Eruption Plume; A one-dimensional, steady state, single phase, fluid dynamical model of the eruption column takes into account the vertical structure of the Venusian atmosphere and changes in specific heat of gas as a function of temperature change with altitude. It is assumed that eruption smoke is an ideal gas, and that pressure and temperature are locally in equilibrium. Under these assumptions, equations for mass conservation, momentum conservation, and energy conservation, and equation of state for an ideal gas are combined and solved. Prandtl's jet theory [7] is used to describe turbulent entrainment of ambient air into the eruption column. The temperature profile of Venus atmosphere is given by a first order Simpson function modified from [8]

Numerical Results; We carried out numerous calculations using a fourth-order Runge-Kutta scheme. Figure 1 shows distinct contrasts in column height between pyroclastic flow cases (small column height) and stable convective eruption column cases (large column height). The bulk density in the eruption column is much higher than the ambient air at the vent. But the density decreases rapidly due to air entrainment by turbulence. If the density becomes less than the ambient air before vertical velocity in the eruption cloud becomes zero, the cloud rises buoyantly until its thermal energy is exhausted. This represents a stable eruption column [9]. Otherwise, a pyroclastic flow is formed, whose height is controlled by its initial momentum.

Height of a stable convective column is higher than on the Earth [9]. There are two reasons for this: I) The thermal gradient of Venusian troposphere (~60km) is almost adiabatic for CO_2, which is the dominant component in the Venus atmosphere [10]. On Earth, the thermal lapse rate in the atmosphere is considerably smaller than the dry adiabat of air because of the condensation of H_2O. II) The height of the tropopause is much larger on Venus than on Earth.

Conditions for a stable convective eruption column depend on initial temperature T_o, initial gas mass fraction n_o, initial eruption velocity U_o, and vent diameter D. Figure 1 shows the dependence of column height on these parameters. The abrupt change in column height indicates the transition from a pyroclastic flow to a stable convective eruption column. Higher temperatures, higher gas ratios, higher eruption velocities, and smaller vent diameters favors a stable convective eruption column. A smaller vent prevents an eruption column from collapsing because it entrains air more efficiently. Higher gas ratio and smaller vent diameters decrease the heights of stable convective eruption columns because of smaller mass discharge rates, which have a positive correlation with column height [11].

The transition from a pyroclastic flow to a stable convective eruption column is so abrupt that a critical velocity for each set of T_o, n_o, and D can be defined. The definition of the critical velocity $U_{cr}(T_o, n_o, D)$ is that an eruption column collapse occurs with an initial velocity smaller than U_{cr} under the condition that initial temperature, initial gas ratio, and vent diameter are T_o, n_o, and D, respectively. Critical velocity U_{cr} becomes smaller with higher initial temperature, initial gas content, and smaller vent diameter (Figure 2). The absolute value of the critical velocity is much larger than on the Earth [9] because the temperature of ambient air on Venus

ARE PLINIAN TYPE ERUPTIONS POSSIBLE ON VENUS ? S. Sugita and T. Matsui

is much higher, thereby reducing thermal buoyancy of the eruption cloud. A stable convective eruption column is barely formed with an initial temperature less than 1100°K.

Implication; Eruption velocity U_e can be determined theoretically if temperature and composition of magma and geometry of conduit and magma chamber are known [12], although the real nature of an eruption is very complicated. For a given vent diameter D, the eruption velocity U_e should be larger for larger temperature T_o and gas mass fraction n_o of magma [12], while U_{cr} is smaller for larger T_o and n_o. Therefore, the surface of U_e in U-T-n space and that of U_{cr} must intersect. This line depends on D, which can be determined from observations. Thus, if the vent radius of a volcano and eruptive styles can be established (i.e., pyroclastic flow or Plinian style), temperature and gas content of the magma beneath the volcano can be constrained.

Since the atmosphere of Venus is presently extremely hot, it is impossible for the familiar volatiles such as H_2O and CO_2 to condense. Therefore, it is highly probable that volcanic gas of Venus is juvenile [5]. Plinian type eruption on Venus could be evidence for a very volatile rich Venusian interior, since the explosive volcanism on the Earth is mainly induced by recycled water from the hydrosphere.

References; [1] Wenrich, M. L. and R. Greeley, *LPSC*, **23**, 1515-1516, 1992; [2] Ivanov, M. A. *LPSC*, **23**, 577-578, 1992; [3] Moore, H. J., J. J. Plaut, P. M. Schenk, and J. W. Head, *JGR*, **97**, 13479-13493, 1992; [4] Esposito, T. W., *Science*, **223**, 1072-1074, 1984; [5] Head, J. W. and L. Wilson, *JGR*, **91** 9407-9446, 1986; [6] Head, J. W. and L. Wilson, *JGR*, **97** 3877-3903, 1992; [7] Prandtl, L., *Essentials of Fluid Mechanics* 1954; [8] Young, R. E. et al., *J. Atmos. Sci.*, **44**, 2628-2639, 1987; [9] Woods, A. W., *Bull. Volcanol.* **50**, 159-191, 1988; [10] Seiff, A. et al. *Venus*, Hunten D. M. et al. eds., University of Arizona Press, 215-279, 1983; [11] Morton, B. R. et al., *Proc. R. Soc., London Ser.* **A234**, 1-23, 1956; [12] Wilson, L. and J. W. Head, *JGR*, **86**, 2971-3001, 1981;

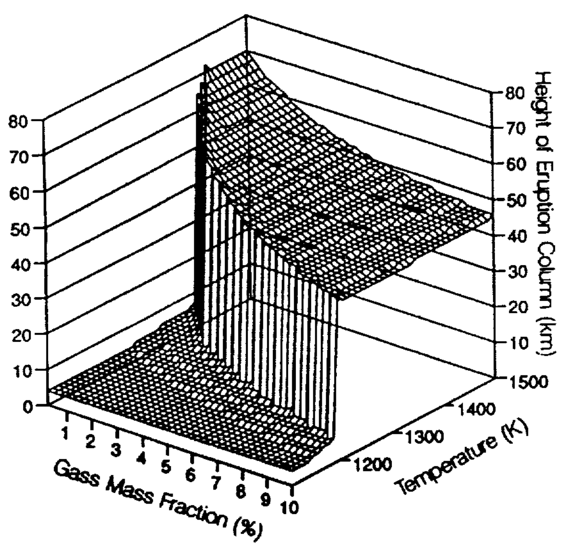


Fig. 1 Maximum height of eruption column as a function of initial temperature and gas mass fraction of magma. Initial velocity and vent diameter is 300m/s and 50m, respectively.

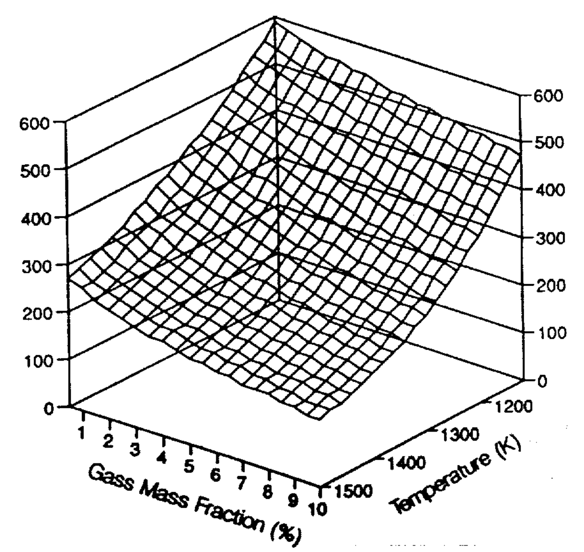


Fig. 2 Critical velocity necessary to form a stable convective eruption column as a function of initial temperature and gas mass fraction. Vent diameter is 50m. Note that direvtion of axis of temperature is reverse from Fig. 1.

S168-25
ABS. ONLY

168128

N94-20804

IMPLANTATION OF NITROGEN: EFFECTS OF HYDROGEN AND IMPLANTATION ENERGY;

Naoji Sugiura, Dept. of Earth and Planetary Physics, Univ. of Tokyo, Japan Tsuneji Futagami and Siro Nagai, Japan Atomic Energy Res. Inst., Japan

To solve the questions on solar nitrogen in lunar soils, i.e. variation in isotopic composition and apparently high retentivity compared with rare gases, nitrogen implantation experiments were conducted. At the Meteoritical Society Meeting in Copenhagen, we presented the results of stepped combustion of implanted nitrogen in ilmenite and olivine[1]. The degassing behavior of nitrogen (and also Ar) was quite different from that observed in the case of lunar soils. 1) Extraction temperatures are higher (>1100 C for ilmenite and 1500 C for olivine) than that for lunar soils. 2) Both nitrogen and Ar seem to be retained at the same efficiency. Therefore, additonal experiments were conducted to make degassing behavior of nitrogen more close to that observed in the case of lunar soils.

The experimental condition and the results of all the combustion experiments are summarized in the table. The samples of the new series of experiments are named by two digit numbers. For these samples, due to technical problems, nitrogen and hydrogen were accelerated as molecules. But this should not cause any difference compared with previous experiments, because as soon as the molecules enter the crystals they are expected to be dissociated into atoms. In many cases, the extraction of gases are not complete because heating to above 1200 C (or 1500 C) is not easy with our extraction systems. This is the reason that the recovery rates are given as lower limits. Implantation dose was estimated by monitoring ion current, and thus may have a relatively large error (>10 %). A recovery rate higher than 100% is attributable to this uncertainty of the implantation dose. Following features are observed.

1) In all experiments, degassing of nitrogen correlates well with that of Ar. (This is observed in the release pattern as a function of temperature of combustion.)
2) Presence of hydrogen promotes degassing at lower temperatures from olivine but not from ilmenite.
3) Presence of He slightly promotes degassing at lower temperatures in the case of olivine but does not affect the degassing from ilmenite.
4) Implantation energy affects the degassing temperature only slightly within the experimental range of implantation energy (from about 1KeV to 75KeV in the case of nitrogen). Nitrogen implanted at 0.9KeV is degassed mainly at 1000 C while nitrogen implanted at 75KeV is degassed at 1100 C from ilmenite. It seems that the degassing from ilmenite is mainly controlled by the oxidation process.
5) Retentivity (or recovery rate) of nitrogen and Ar are similar and at least one half of the implanted atoms seems to be retained.
6) The result for the H_2O_2 treated sample confirms that the gases are present very close to the surface.

IMPLANTATION OF NITROGEN:Sugiura N. et al.

Comparing the above results with those obtained from lunar soils, the following can be said.

1) Degassing temperatures (from 600 C to 1200 C) of nitrogen from lunar soils are yet slightly lower than that observed here in the case of olivine (the lowest main release temperature is 800 C) and much lower than that in the case of ilmenite (the lowest main release temperature is 1000 C). Since presence of hydrogen promote degassing at lower temperatures, additional presence of carbon may help lowering the degassing temperature further. Judging from the weak dependence of release temperature on implantation energy, low energy lunar wind probably can not explain the difference in the release temperature.

2) In the present experiments retentivity of nitrogen and Ar are rather similar both in ilmenite and in olivine, while in the case of lunar soils nitrogen is nearly one order of magnitude more abundant than Ar. At the moment there is no possibility of explaining this difference as due to the difference in implantation efficiency for these gases. It seems that either the abundance ratio of nitrogen to Ar of the solar wind was different or there was an additional source of nitrogen.

[1] Sugiura N., Futagami T., Zashu S. and Nagai S. (1992) Meteoritics, 27, 293.

	Sample	Gas species	Energy	Dose	Peak Temp.	Recovery
1			(KeV)	(1E14/cm2)	(C)	(%)
2	Ilmenite#1	He	20	110	1000	10
3		Ar	200	2.2	1000	>63
4		N	75	2.1	1000	>56
5	Ilmenite#2	Ar	200	2.2	1100	>85
6		N	75	2.2	1100	>70
7	Ilmenite#3	N	75	2.1	1100	>69
8	Ilmenite#6	N	20	2.1	1100	>41
9	Olivine #1	He	20	110	-	-
10		Ar	200	2.2	>1200	>18
11		N	75	2.1	>1200	>18
12	Olivine #2	Ar	200	2.2	1500	>48
13		N	75	2.2	1500	>62
14	Olivine #2,H2O2	Ar	200	2.2	-	0
15		N	75	2.2	-	0
16	Olivine #6	N	20	2.1	1400	>42
17	Ilmenite #11	H2	2	1000	-	-
18		Ar	40	2	1200	>56
19		N2	30	2.2	1200	>46
20	Ilmenite #12	H2	2	1000	-	-
21		Ar	1.5	5.7	1000	>42
22		N2	0.9	3.0	1000	>40
23	Olivine #11	H2	2	1000	-	
24		Ar	40	2.2	800	109.3
25		N2	30	2.2	800	71.5

Determining the Composition of Olivine on Asteroidal Surfaces. Jessica M. Sunshine and Carle M. Pieters, Department of Geological Sciences, Box 1846, Brown University, Providence, RI, 02912.

Olivine has been remotely identified as a major component on many S- and A-type asteroids based on qualitative analyses of broad absorption features near 1.0 μm in their telescopic reflectance spectra. Laboratory studies have shown that this diagnostic olivine absorption feature is composed of three individual absorption bands resulting from electronic transitions of Fe^{+2} in distorted M1 and M2 sites [*e. g.* 1]. Both the overall absorption feature [1,2] and each of the individual absorption bands are also known to vary systematically as a function of olivine composition [1,3]. Thus, it should be possible to remotely determine the composition of olivine present on the surfaces of the various olivine-rich asteroids. However, extrapolation of laboratory studies to compositional interpretation of asteroid spectra is complicated by several factors: observational noise; lower spectral resolution; compositional heterogeneities (including the presence of other phases such as pyroxenes and/or metal); and the effects of alteration processes.

In order to address such complex problems, a quantitative approach to spectral analysis, the modified Gaussian model (MGM) was developed by Sunshine *et al.* [4] which deconvolves spectra into their constituent absorption bands. The MGM, a refinement of the Gaussian model, more accurately adheres to the physical processes involved in electronic transition absorptions. Under the MGM, each spectrum is modeled in log reflectance and energy as a sum of absorption bands superimposed onto a baseline or continuum. Each absorption band is described by three model parameters (center, width, and strength) which can be interpreted and used to infer composition [4,5,6,7]. One of the strengths of the MGM is that it allows compositional information to be extracted directly from measured spectra and is therefore complementary to other approaches to modeling asteroid spectra which require the use of meteorites and/or terrestrial samples as spectral analogs.

A quantitative understanding of the properties of olivine absorptions was established by using the MGM to analyze a laboratory suite of spectra spanning a full range of olivine compositions. The MGM model fit to a Fo97 olivine spectrum is shown, as an example, in **Figure 1**. Initial analysis of the entire suite of olivine spectra reveals several relationships among the absorption band parameters as a function of both composition and absorption site [3]. The solid lines in **Figure 2** illustrate that the centers of each of three primary olivine absorption bands shift towards longer wavelengths with increasing iron content at a rate determined by the absorption site (M1 vs. M2). Subsequent analyses indicate that the widths and relative strengths of the olivine absorptions are also controlled by the absorption site and vary systematically with composition. These systematic variations reveal inter-relationships among the band parameters that can be used to establish rigorous bounds on acceptable values for absorptions in olivine spectra.

The analysis of laboratory spectra also provides criteria for evaluating the results of MGM modeling of the spectra of olivine-rich asteroids. For example, the best model fit to the spectrum of 246 Asporina [8] (*i. e.* the minimum mathematical solution) is found to be inconsistent with laboratory results. As illustrated in **Figure 2** (unconstrained data), the bands centers derived for each of the three primary olivine absorptions each imply a different Fo# for the asteroid, clearly a physically unrealistic result. Although there is insufficient information in the spectrum of 246 Asporina to obtain a reasonable solution, one can successfully model the spectrum by explicitly including the laboratory definitions of olivine absorption bands as constraints on the fitting process. Two endmember solutions to 246 Asporina are tested: one using band widths and relative strengths typical of fosteritic olivines; and one using widths and strengths of fayalitic olivines. Both of these solutions appear to adequately model the spectrum of 246 Asporina (**Figures 3** and **4**), yet lead to very different values of absorption band centers. The derived band centers can be compared to laboratory results and used to discriminate between the two solutions. As indicated on **Figure 2**, in order to satisfy both the data and the fayalitic constraints, the

fayalitic model results in band centers that are physically unreasonable and completely at odds with a fayalitic compositions. In contrast, the fosteritic solution yields band centers that are fully consistent with a fosteritic composition. Thus, MGM analysis strongly suggests that the olivine component of 246 Asporina is distinctly fosteritic. Further refinements on the Fo# of 246 Asporina will be undertaken. In addition, the spectra of other olivine-rich asteroids will be examined to evaluate the compositional diversity among the olivine-rich asteroid population.

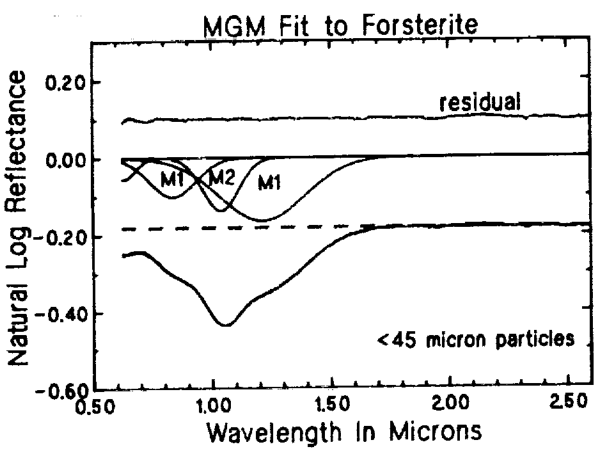


Figure 1: MGM fit to laboratory forsterite (Fo 97) consisting of three primary absorptions (denoted by their site assignments), superimposed onto a continuum (dashed line). The residual error between the modeled spectrum and actual spectrum (top line) is offset 10% for clarity.

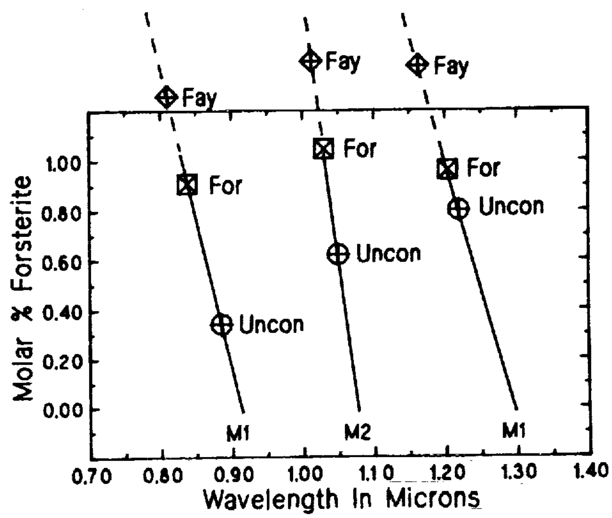


Figure 2: Band centers of primary olivine absorptions as a function of composition. Solid lines represent best fits to the suite of 18 laboratory spectra. Symbols are derived band centers resulting from MGM modeling of 246 Asporina: Unconstrained Model, Fosteritic Model (**Figure** 3), and Fayalitic Model (**Figure** 4).

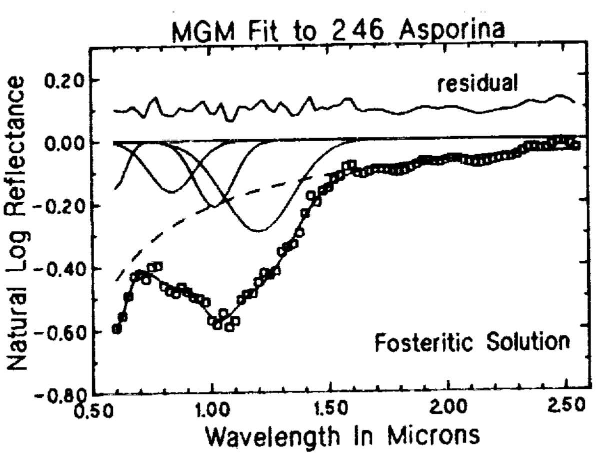


Figure 3: MGM model to 246 Asporina using band widths and relative band strengths that are typical of fosteritic olivines. Lines are as in Figure 1.

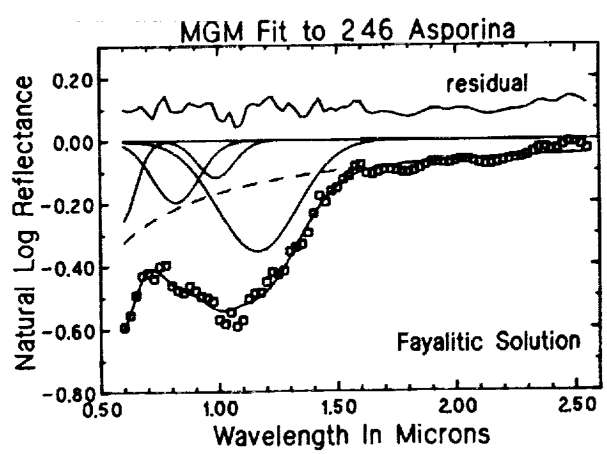


Figure 4: MGM model fit to 246 Asporina using band widths and relative band strengths that are typical of fayalitic olivines. Lines are as in Figure 1.

References:

[1] Burns, *Am. Min.*, 1608-1632, 1970.
[2] King and Ridley, *J.G.R.*, 11,457-11,469, 1987.
[3] Sunshine and Pieters, *LPSC XXI*, 1263-1264, 1990.
[4] Sunshine *et al.*, *J.G.R.*, 6955-6966, 1990.
[5] Sunshine and Pieters, *J.G.R.*, submitted.
[6] Sunshine and Pieters, *LPSC XXII*, 1361-1362, 1991.
[7] Mustard, *Am. Min.*, 345-358, 1992.
[8] Cruikshank and Hartmann, *Science*, 281-282, 1984.

Acknowledgments: Support for this research, a NASA Graduate Student Fellowship to J.M.S. and NASA grant NAGW-28, are greatly appreciated. The authors would like to thank T. Hiroi and J.F. Bell for providing easy access to the spectrum of 246 Asporina and T. King for the use of her Kiglipait olivine spectra in our suite of olivine spectra.

5170-91
ABS. ONLY

N94-20806

p. 2

DISCOVERY VENERA SURFACE - ATMOSPHERE GEOCHEMISTRY EXPERIMENTS MISSION CONCEPT; Yu. A. Surkov[1], J. W. Head[2], R. Kremnev[3], K. T. Nock[4], and the Discovery Venera Team. [1]Vernadsky Institute, Moscow, 117975, Russia, [2]Dept. Geological Sciences, Brown University, Providence, R.I. 02912 USA, [3]Babakin Center, Moscow Russia, [4]Jet Propulsion Lab, Pasadena CA.

SCIENTIFIC GOALS AND OBJECTIVES - The phenomenal increase in our understanding of Venus provided by the Magellan Mission has raised a series of focused, fundamental scientific questions about the geochemistry of the surface of Venus, the nature of the lower atmosphere, and the relationship of the lower atmosphere and surface. First, surface geochemical measure-ments from the Venera/Vega spacecraft showed that widely spaced regions of the venusian plains are made of basalts; thus basalts are significant and may be the only component of the venusian crust. But we lack information on the composition of several key elements of Venus geology: 1) Tessera terrain (which may be outcrops of continental-like non-basaltic crustal material) and steep-sided domes/festoons are promising candidates for non-basaltic geochemically evolved material. The composition of the lower part of the Venusian crust is unknown: however, ejecta from large venusian craters provides us with the possibility of sampling this material on the surface; 2) Bulk chemistry (structure and dynamics) of the venusian atmosphere are known. The altitude profiles of water vapor content and minor admixtures relevant to redox conditions in the lower atmosphere(< 20 km altitude) remain uncertain. Lack of that knowledge means that we don't understand the fine chemical structure of the main mass of the Venusian atmosphere; 3) Thermodynamic models predict that igneous materials on the surface of Venus should react with gases of the venusian atmosphere. But because the water vapor content and redox conditions in the lower atmosphere are not well known, we don't understand the nature of venusian weathering: oxidation, sulfatization, carbonatization, hydration. The answers to these questions are critical to the understanding of Venus, the most Earth-like of the terrestrial planets.

THE CONCEPT: The primary goal of the Discovery Venera Surface-Atmosphere Geochemistry Experiments (SAGE) Mission is to acquire the data to address these fundamental questions. The concept is to launch a Venera-class lander to a designated target of high scientific interest on the surface of Venus with instruments to measure lower atmosphere constituents and surface geochemistry and mineralogy, as well as to investigate surface geology. The core of this mission would involve the utilization of mature and flight-proven spacecraft hardware and experiment concepts from the Soviet Venera lander program, with some experiments modified to take advantage of recent technological developments. Discovery Venera can be repeated at appropriate intervals to explore a variety of environments on Venus and our analysis of launch opportunities shows that widespread and representative areas of the surface of Venus are accessible. The Discovery cost envelope is met through the availability of low-cost Russian spacecraft hardware and mission design experience.

THE INSTRUMENTS: Scientific goals of the mission will be met by measurements using four instruments:

1. Optical Atmospheric Spectrometer: This will obtain vertically resolved profiles of the key atmospheric gases (H2O, HDO, SO2 H2S, OCS, and CO) in the lower atmosphere. The instrument will be based on flight heritage of the Venera spectrometer. It will implement an F/1.5 dual arm grating approach. The first arm covers 0.8 to 1.20 mm, the second, 2.25 to 2.2 mm; l/Dl=1000. The instrument will collect measurements looking both up and down. Mass: ~ 12 kg, Power: ~12W.

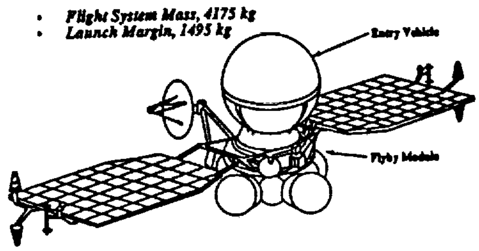
2. Imaging Spectrometer: This will provide a closeup view of the targeted terrain, obtain spectra of soil and rock and provide us with an understanding of what kind of material (soil, rocks) other surface measurements are related to. The instrument utilizes proven Venera F/2 camera optics and scanning system as a telescope for the imaging spectrometer. There is an option to add a beamsplitter and fly both the Russian TV camera and Imaging Spectrometer. Mass: ~11 kg, Power: ~8W.

3. Neutron Probe and Gamma Ray Spectrometer: This will work in two regimes: 1) passive, measuring abundances of K, Th and U from their natural gamma irradiation and 2) active, measuring bulk composition of the surface material from gamma irradiation due to nuclear interaction with free neutrons generated by a Pulsed Neutron Generator. The instrument utilizes commercial petroleum industry technology (Schlumberger GSO/PMT) and Russian Vega CsI/PMT. It utilizes also proven Vega deployment technology. Mass: ~27 kg, Power: 30W average.

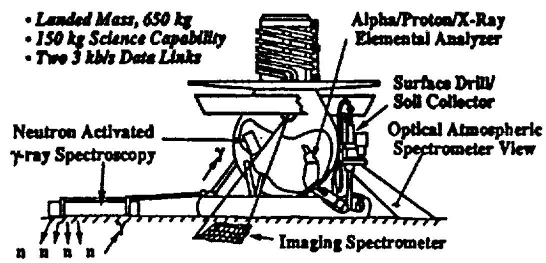
4. Alpha-Proton-X-ray Elemental Analyzer, which will measure elemental composition from C through Ni of a sample taken by the sampling device from a depth of 10 mm. The instrument utilizes Venera/Vega technology for sample acquisition and technological developed for the Phobos and Mars 94 APX instruments. Mass: ~6 kg, Power: ~1W.

EXPECTED SCIENCE RESULTS:

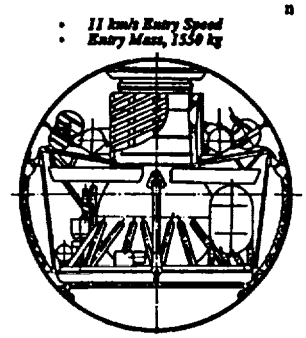
•Major and trace element geochemistry of the target (e.g., tessera, festoon) material.
  - Determine rock type/implications for igneous petrology.
  - Understand whether Venus crust is composed of basalts only or is compositionally bimodal.
•Key components of lower atmosphere.
  - Redox conditions and water vapor content in lower atmosphere.
•IR spectra and chemistry of surface material.
  - Mineralogy of surface material: Surface weathering.
•Closeup view of the target region (e.g., tessera, festoon) landscape.
  - Character of surface processes in non-plain area.



Modified Phobos Flyby Module



Venera/Vega Lander



Venera/Vega Entry System

DISCOVERY VENERA TEAM:

James W. Head III
Principal Investigator
Department of Geological Sciences
Brown University

Yuri Surkov
Deputy Principal Investigator
Vernadsky Institute
Russian Academy of Sciences

Co-Investigators and Collaborators:

Roald Kremnev, Director
Babakin Center

Heinrich Wanke
Max Plank Institute

Alexander T. Basilevsky
Vernadsky Institute

Jack Trombka
Goddard Space Flight Ctr.

Steve Squyres
Cornell University

Vasily Moroz
Inst. for Space Res.

Bruce Fegley
Washington University

Arnold Selivanov
Inst. for Space Devices

Peter Englert
San Jose State Univ.

John Mustard
Brown University

Ray Arvidson
Washington University

David Crisp
Kerry Nock
Ellen Stofan
R. Stephen Saunders
Jet Propulsion Lab.

Ronald Greeley
Arizona State Univ.

Tom Donahue
University of Michigan

S171-25
ABS. ONLY

N94-20807

p-2

X-RAY MICROPROBE DETERMINATION OF CHROMIUM OXIDATION STATE IN OLIVINE FROM LUNAR BASALT AND KIMBERLITIC DIAMONDS

S. R. Sutton, S. Bajt, M. L. Rivers, and J. V. Smith; Department of the Geophysical Sciences and Center for Advanced Radiation Sources, The University of Chicago, Chicago, IL 60637;

The synchrotron x-ray microprobe is being used to obtain oxidation state information on planetary materials with high spatial resolution. We report initial results on chromium in olivine from various sources including laboratory experiments, lunar basalt and kimberlitic diamonds. The lunar olivine was dominated by Cr^{2+} whereas the diamond inclusions had Cr^{2+}/Cr^{3+} ratios up to about 0.3. The simpliest interpretation is that the terrestrial olivine crystallized in a more oxidizing environment than the lunar olivine.

Introduction: The oxidation states of minor and trace elements in minerals provide important clues on the physio-chemical history of the planets. Petrogenetic models generally assume oxygen fugacities based on indirect evidence. Since many of these assumptions involve low oxidation states that can stabilize reduced species, a technique that can directly measure valences could provide valuable constraints. The x-ray absorption near edge structure (XANES) technique used with the synchrotron x-ray microprobe, in principle, allows oxidation state determinations on individual co-existing phases in conventional rock thin sections. We report initial results on chromium in olivine from various sources including laboratory experiments, lunar basalt and kimberlitic diamonds.

Samples and Standards: Various reference materials were analyzed to establish the systematics of the Cr K XANES as a function of oxidation state. These materials were principally silicates but also included chromium metal (Cr^0) and potassium chromate (K_2CrO_4; Cr^{6+}). A suite of alkali borosilicate glasses (Savannah River Laboratory glass frit 131) was synthesized under various controlled oxygen fugacities by H. Schreiber (Virginia Military Institute). The oxidation states of Cr in these glasses were determined previously by conventional chemical procedures and optical spectrophotometry [1]. Three chromium-doped, synthetic forsterite standards (kindly supplied by G. Rossman, Caltech) contained either Cr^{2+} (GRR 1690), Cr^{3+} (Ito Forsterite), or Cr^{4+} (GRR 1587).

Lunar olivine grains from mare basalt 15555 were analyzed. The analyzed grains (5 olivines and 4 pyroxenes) were part of conventional thin sections mounted on pure silica slides. The olivine showed normal zoning with higher Mg in the cores than the rims. Fo numbers (100*Mg/(Mg+Fe)) of the XANES-analyzed regions ranged from Fo 56 to Fo 68 (electron microprobe analyses by J. Delaney, Rutgers U.).

The diamond inclusions (100-300 μm) derived from three kimberlite regions - Premier and Koffiefontein (South Africa; kindly supplied by J. Harris, U. of Glasgow) and Kalimantan (Asia; kindly supplied by H. Meyer, Purdue U.). The Kalimantan olivine was an exposed inclusion and was analyzed while still embedded. The South African olivines were extracted from the diamonds and mounted individually for analysis. Each inclusion was analyzed with the electron microprobe to determine Cr content (200-800 ppm) and verify mineralogical identification. Fo numbers ranged from Fo 93 to Fo 97 (electron microprobe analyses by I. Steele, Univ. of Chicago, and H. Meyer).

Analytical Techniques: The synchrotron x-ray fluorescence microprobe on beamline X26 at the National Synchrotron Light Source (Brookhaven National Laboratory, NY) was used in its normal configuration [see e.g., 2-4] with the addition of a silicon (111) channel-cut monochromator on the incident radiation. A relatively large beam size of about 100-200 μm was used because of the trace level Cr contents of the olivine. XANES spectra were obtained by scanning the incident beam energy from just below to just above the Cr K absorption edge and recording the Cr K_α count rate at each incident energy. The detector was a Si(Li) energy dispersive instrument with an area of 30 mm^2 mounted at 90^o to the incident beam (i.e., incident and takeoff angles = 45^o). Cr K_α count rates were optimized by adjusting the distance between

the sample and the detector. The geometry of the apparatus limits the minimum sample-to-detector distance (i.e., largest collection angle) to about 1 cm corresponding to a solid angle of about 0.25 sr. A total energy scan of about 100 eV was typically made in 300 steps (0.3 eV/step) with each step counted for between 1 and 30 live seconds depending on the Cr content of the sample. Energies were defined relative to the energy of the prominent pre-edge peak in the XANES spectrum of chromate (Cr^{6+}). The Cr K XANES spectra typically contained three peaks: an isolated pre-edge peak, a bump on the absorption edge rise, and the edge crest, analogous to features observed in Fe XANES by Waychunas et al. [5]. Derivatives of the XANES spectra were used to determine the relative energies of these spectral features. XANES spectra of the reference materials (i.e., materials with Cr in known oxidation state) were used to determine the energy dependence of the edge position and resonance features and this information was used to infer Cr oxidation states in the lunar and kimberlitic olivine.

Results: Spectral features in the reference materials showed a good correlation with known oxidation state . Comparison of these data with those for the olivine indicate that Cr in the lunar olivine is predominantly divalent whereas the Cr in the diamond inclusions contains both Cr^{2+} and Cr^{3+} with the latter dominant [6]. For the diamond inclusions, the chromium in the Kalimantan inclusion was predominantly trivalent whereas a larger divalent component was present in the Premier and Koffiefontein olivine. Our first attempt to quantify the divalent content in these inclusions used a series of computational mixtures of XANES derivatives of the divalent and trivalent reference forsterites. The South African diamond inclusion spectra most closely match the theoretical spectrum with Cr^{3+} and Cr^{2+} in 2:1 proportions.

Discussion: These initial chromium oxidation state determinations on olivine from lunar basalt and terrestrial kimberlitic diamonds indicate that divalent chromium is a ubiquitous component of olivine crystallized under reducing conditions. The simplest explanation of the Cr speciation in 15555 is that the mare magma source originally contained Cr^{2+} and Cr^{3+} and that these species were preferentially incorporated into olivine and pyroxene, respectively. This conclusion implies that either the olivine D values for Cr^{2+} under lunar conditions are greater than suggested by laboratory partitioning studies [e.g., 7,8] or, more likely, the melt was dominated by divalent chromium at the time of olivine crystallization (caused, for example, by spinel crystallization). The diamond inclusions studied had Cr^{2+}/Cr^{3+} ratios up to 0.3. The obvious interpretation is that the terrestrial olivine crystallized in a more oxidizing environment than the lunar olivine [8]. However, additional research needs to be done to verify this conclusion.

MicroXANES has great potential for tackling planetary petrogenesis but more work is needed to refine the quantification of mixed valences. Particularly important are XANES analyses on synthetic olivine crystallized under controlled redox conditions. The present results suffer from several complications. First, the olivines have greatly different Fe contents and the effect on XANES spectra of Fe content needs to be studied in detail. Second, some and perhaps all of the olivines studied contain Cr-bearing micro-inclusions, notably, chromite. Smaller, more intense x-ray beams are needed to avoid these inclusions. And, third, the synchrotron beam is a linearly polarized x-ray source and XANES spectra depend somewhat on crystal orientation [9]. Polarization experiments will be pursued to study this effect.

Acknowledgments: This research was supported by the following grants: NASA NAG9-106 (SRS), NSF EAR89-15699 (MLR), and Chemical Sciences Division, Office of Basic Energy Sciences, US DOE under Contract No. DE-AC02-76CH00016.

References: [1] Schreiber, H., et al. (1984) Comm. Amer. Ceram. Soc. 1984, 67, C106-C108. [2] Flynn, G. J., and Sutton, S. R. (1990) Proc. 20th Lunar Planet. Sci. Conf., 335-342. [3] Jones, K. W. and B. M. Gordon (1989) Anal. Chemistry 61, 341A-356A. [4] Rivers M. L., et al. (1992) in X-ray Microscopy III, Springer-Verlag, 212-216. [5] Waychunas, G. A., et al. (1983) Phys. Chem. Minerals 13, 31-47. [6] Sutton, S. R., et al. (1992) Geochim. Cosmochim. Acta in press. [7] Schreiber H. S. and Haskin L. A. (1976) Proc. Lunar Sci. Conf. 7th, 1221-1259. [8] Hanson, D. Z., and Delano, J. W. (1992] Lunar Planet. Sci. XXIII, 481-2. [9] Waychunas, G. A., and Brown, G. E., Jr. (1990) Phys. Chem. Miner. 17, 420-430.

MICROANALYSIS OF IRON OXIDATION STATE IN IRON OXIDES USING X-RAY ABSORPTION NEAR EDGE STRUCTURE (XANES) S. R. Sutton[1], J. Delaney[2], S. Bajt[1], M. L. Rivers[1], and J. V. Smith[1]; [1]Department of the Geophysical Sciences and Center for Advanced Radiation Sources, The University of Chicago, Chicago, IL 60637; [2]Department of Geology, Rutgers University, New Brunswick, NJ.

An exploratory application of x-ray absorption near edge structure (XANES) analysis using the synchrotron x-ray microprobe was undertaken to obtain Fe XANES spectra on individual sub-millimeter grains in conventional polished sections. The experiments concentrated on determinations of Fe valence in a suite of iron oxide minerals for which independent estimates of the iron speciation could be made by electron microprobe analysis and x-ray diffraction.

Introduction: The valence states of transition metals are of fundamental importance in many cosmo- and geochemical systems. In particular, a vast body of literature exists relating the ratio of ferric to ferrous iron to the geological environment. Iron may occur in both ferrous and ferric states in important rock-forming minerals (e.g. pyroxene, amphiboles, micas, feldspars, and oxide minerals). Minerals that can simultaneously accept both Fe^{2+} and Fe^{3+} are particularly valuable as these minerals directly provide constraints on the oxygen fugacity of the environment in which they equilibrated. The limited availability of extraterrestrial samples suitable for conventional techniques for ferrous/ferric ratio determination (such as Mössbauer and wet chemistry) has inhibited the study of valence states. Models of lunar and achondrite petrogenesis generally assume particular oxygen fugacities based on indirect evidence. Since many of these assumptions involve low oxidation states that can stabilize reduced species of Ti and Cr (Ti^{3+} and Cr^{2+}) as well as Fe^0 and Fe^{2+}, a technique that can directly measure these valences could provide valuable constraints on these models. We report here an exploratory application of x-ray absorption near edge structure (XANES) analysis [1] using the synchrotron x-ray micrprobe to obtain Fe XANES spectra on individual sub-millimeter grains in conventional polished sections. Previous microXANES studies have included Cr in lunar olivine [2], Cr in diamond inclusions [3], and Fe in plagioclase [4]. The experiments reported here concentrated on Fe valence in a suite of iron oxide minerals for which independent estimates of the iron speciation could be made by electron microprobe analysis and x-ray diffraction.

Samples: Magnetite crystals consisted of Rutgers University Geological Museum specimens, commercial samples and the NMNH magnetite microprobe standard. The Fe^{3+} standard was a hematite (Fe_2O_3) powder pressed into a pellet with boric acid as a binder. The magnetites provide a particularly useful test of the ability of microXANES to determine ferrous/ferric ratios. Although, magnetite is theoretically Fe_3O_4 with $Fe^{2+}/Fe^{3+}=0.5$, natural samples can deviate significantly from this ideal ratio either by substitution of other spinel end-members or by alteration. Of the seven magnetites studied here the maximum observed substitution was about 10% (mol.) ulvöspinel (Fe_2TiO_4). Only two samples were essentially unaltered (NMNH standard from Minas Gerais, Brazil; and the Mineville, NY magnetite) and these were used as pure magnetite standards. All other magnetites and the commercial "Fe_3O_4" analytical grade reagent were significantly altered (as determined by XRD) containing predominantly either hematite (Fe_2O_3) or an iron oxyhydride phase. The Fe^{2+}/Fe^{3+} ratio of these magnetites was therefore significantly higher than that of an ideal magnetite.

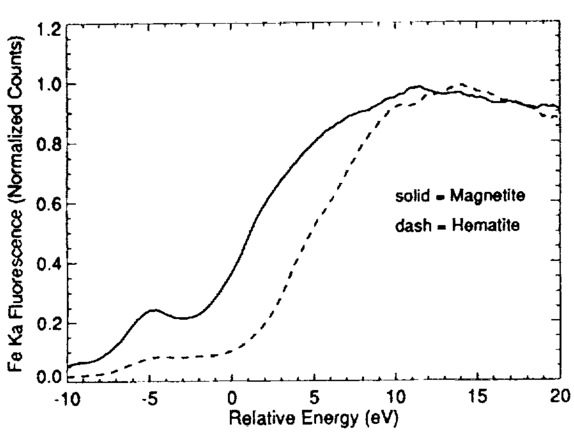
Analytical Techniques: The synchrotron x-ray fluorescence microprobe on beamline X26 at the National Synchrotron Light Source (Brookhaven National Laboratory, NY) was used in its normal configuration [see e.g., 5-7] with the addition of a silicon (111) channel-cut monochromator on the incident radiation. A beam size of about 50 μm was used. XANES spectra were obtained by scanning the incident beam energy from just below to just above the Fe K absorption edge and recording the Fe K_α count rate at each incident energy. The detector was a Si(Li) energy dispersive instrument with an area of 30 mm^2 mounted at 90^o to the incident beam (i.e., incident and takeoff angles = 45^o). Fe K_α count rates were reduced to sufficiently low levels (~5000-7000 cps) by increasing the sample to detector distance to about 25 cm and adding a 3 mm detector aperture. A total energy scan of about 100 eV was made in 300 steps (0.3 eV/step) with each step counted for between 1 and 5 live seconds. Energies were defined relative to the energy of the half-height of the Fe metal absorption edge.

Results: The hematite and unaltered magnetite XANES spectra are shown in figure 1. The general form of these spectra are consistent with those reported by Waychunas et al. [8]. Derivatives of the XANES spectra were used to determine the energies and relative intensities of the XANES spectral features. Four peaks were present in the derivative spectra at relative energies of -7, 1, 4, and 7 eV (figure 2). The unaltered magnetite spectra were dominated by the pre-edge peak at -7 eV and a peak at 1 eV. The hematite spectrum also contained the pre-edge peak but was dominated by peaks at 4 and 7 eV instead of the 1 eV peak seen in the magnetite spectra. Also shown in figure 2 is a representative derivative spectrum for the altered magnetities. As expected, the intensities of the peaks in the altered magnetite spectrum are intermediate to those of the two standards. Qualitatively, the XANES spectra suggest that the altered magnetites are roughly equal mixtures of magnetite and hematite. Work is in progress to quantify the Fe^{2+}/Fe^{3+} ratio in these crystals.

Conclusions: MicroXANES has great potential for tackling lunar, meteoritic and terrestrial petrogenesis. It may, for example, eventually be possible to determine f_{O_2} from Fe^{2+}/Fe^{3+} ratios after careful studies of crystals grown under controlled conditions. In principle, such determinations should be possible on zones of individual crystals. The chemical states of other elements such as Ti, V, Mn, and Ni should also be measurable using microXANES.

Acknowledgments: This research was supported by the following grants: NASA NAG9-106 (SRS) and NAG9-104 (JSD), NSF EAR89-15699 (MLR), DOE-E&G DE-FG02-92ER14244 (JVS), and Chemical Sciences Division, Office of Basic Energy Sciences, US DOE under Contract No. DE-AC02-76CH00016.

References: [1] Bianconi A. (1988) in X-ray Absorption, eds. D. C. Koningsberger and R. Prins, volume 92 in Chemical Analysis, Wiley, NY. [2] Sutton, S. R., et al. (1992) Geochim. Cosmochim. Acta in press. [3] Sutton, S. R., et al. (1992) EOS, Trans. Amer. Geophys. Union 73, p. 651. [4] Delaney J. D., et al. (1992) Lunar Planet. Sci. XXIII, 299-300. [5] Flynn, G. J., and Sutton, S. R. (1990) Proc. 20th Lunar Planet. Sci. Conf., 335-342. [6] Jones, K. W. and B. M. Gordon (1989) Anal. Chemistry 61, 341A-356A. [7] Rivers M. L., et al. (1992) in X-ray Microscopy III, Springer-Verlag, 212-216. [8] Waychunas, G. A., et al. (1983) Phys. Chem. Minerals 13, 31-47.



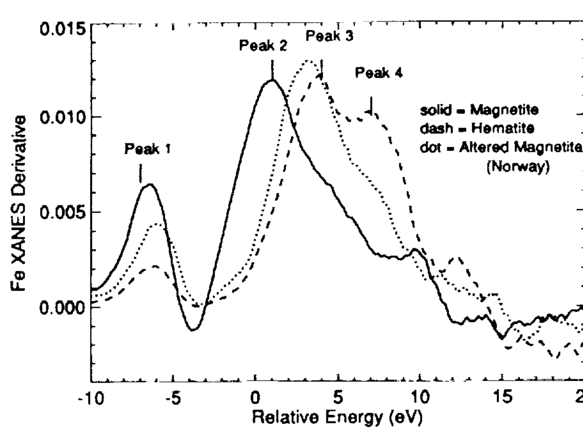


Figure 1: Fe K XANES spectra for unaltered magnetite (Fe^{2+}/Fe^{3+} = 0.5; solid line) and hematite Fe^{2+}/Fe^{3+}=0; dashed line). The shift in edge energy is due to the difference in oxidation state.
Figure 2: Derivatives of the spectra in figure 1 plus that of an altered magnetite (dotted line). The derivative spectra consist of 4 peaks which vary in intensity.

SPH MODELLING OF ENERGY PARTITIONING DURING IMPACTS ON VENUS

T. Takata and T. J. Ahrens. Division of Geological and Planetary Sciences, California Institute of Technology, Pasadena, CA 91125.

P. 2

Impact cratering of the Venusian planetary surface by meteorites was investigated numerically using the Smoothed Particle Hydrodynamics (SPH) method. Venus presently has a dense atmosphere. Vigorous transfer of energy between impacting meteorites, the planetary surface, and the atmosphere is expected during impact events. We have concentrated our investigation on the effects of the atmosphere on energy partitioning and the flow of ejecta and gas.

The SPH method is particularly suitable for studying complex motion, especially because of its ability to be extended to three dimensions [1,2,3,4]. In our simulations, particles representing impactors and targets are initially set to a uniform density, and those of atmosphere are set to be in hydrostatic equilibrium. Target, impactor, and atmosphere are represented by 9800, 80, and 4200 particles, respectively. A Tillotson equation of state for granite is assumed for the target and impactor, and an ideal gas with constant specific heat ratio is used for the atmosphere. Two dimensional axisymmetric geometry was assumed and we modelled normal impacts of 10km diameter projectiles with velocities of 5, 10, 20, 40 km/s, both with and without an atmosphere present.

The resulting flow fields show that the atmospheric gas and entrained target particles above the crater move upward at close to the escape velocity of Venus, whereas a strong radial horizontal gas flow along the surface is observed around the crater at lower altitudes [fig.1], in agreement with the previous work of Ivanov *et al.*[5] and Roddy *et al.*[6]. Coupling to the atmosphere is strong, because the size of the impactor is comparable to the scale height of the atmosphere ($\sim$ 15km). Not only ejecta, but a large amount of the atmospheric gas is accelerated to escape velocity. Because of the surrounding high gas pressure, however, the upward flow of the target particles at the bottom of the ejecta curtain is slower than in the no atmosphere case. These results qualitatively agree with experimental data [7].

The transfer of the kinetic energy of the impactor to the atmosphere continues after the impact. Approximately 10% of the kinetic energy is transferred directly from the impactor to the atmosphere [fig.2,3]. In the case of low impact velocity (5km/s), a greater fraction of the impact energy is partitioned into internal energy of the impactor and atmosphere than in the high impact velocity case (40km/s). When the atmosphere is present, the ratio of the internal energy of the impactor to that of the target is slightly smaller than in the case of vacuum [fig.3]. This may imply that the direct energy transfer from the impactor to the target is more efficient with an atmosphere.

In conclusion, impact cratering in the presence of an atmosphere can modify the energy partitioning among impactor, planetary surface, and atmosphere. For 10km diameter impactors, the Venusian atmosphere obtains $\sim$10% of the impact energy directly. This quantity is more than twice as large as for the earth (<5% [8]).

Acknowledgements ; Research supported by NASA. We appreciate the use of the CRAY Y-MP at JPL for these calculations.

MODELLING OF IMPACT CRATERING : Takata T. and Ahrens. T.J.

References ; 1. Gingold R.A. & Monaghan J.J.(1977) *Month. Not. Astr. Soc.*, 181, 375. 2. Benz W., Slattery W.L., & Cameron A.G.(1986) *ICARUS*, 66, 515. 3. Pongracic H.(1988) Monash Univ. Ph.D. Thesis. 4. Cloutman L.D.(1990) Lawrence Livermore Lab. Report, UCRL-ID-103698. 5. Ivanov B.A. *et al.*(1992) *JGR*, 97,16167. 6. Roddy D.J. *et al.*(1992) Int. Col. on Venus, abstract, Pasadena. 7. Schultz P.H.(1992) *JGR*, 11623. 8. O'Keefe J.D. and Ahrens T.J.(1982) *GSA special paper*, 190, 103.

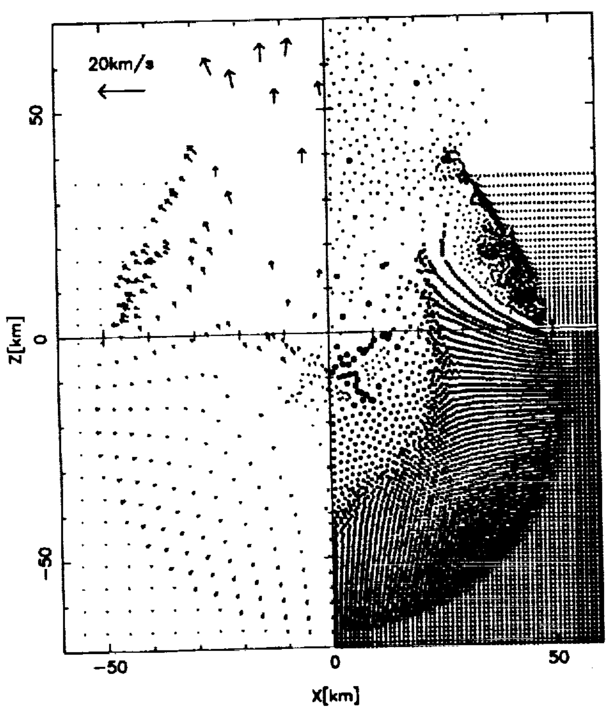


Fig.1. The particle positions (X>0) and velocities (X<0) for an impact on the Venusian surface with an atmosphere at t=7.7s after the impact. The impactor size is 10km and the impact velocity is 20km/s. The large, medium, and small dots represent the particles of the impactor, the target, and the atmosphere, respectively.

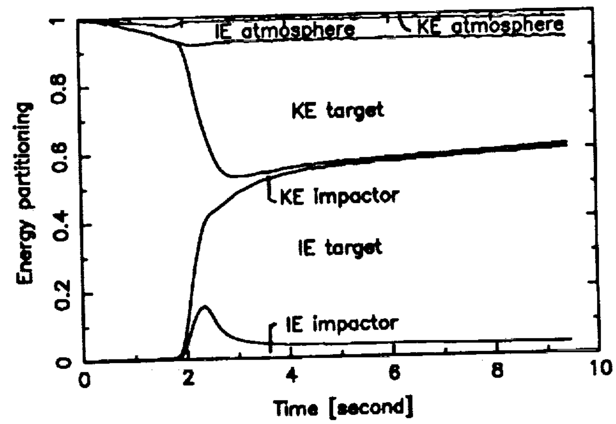


Fig.2. Energy partitioning (fraction of total) as a function of time in the same case as Fig.1. t=0 is set when the meteorite is at the altitude of 40km. The energy is normalized by the initial energy of the impactor. KE and IE denote kinetic and internal energy, respectively.

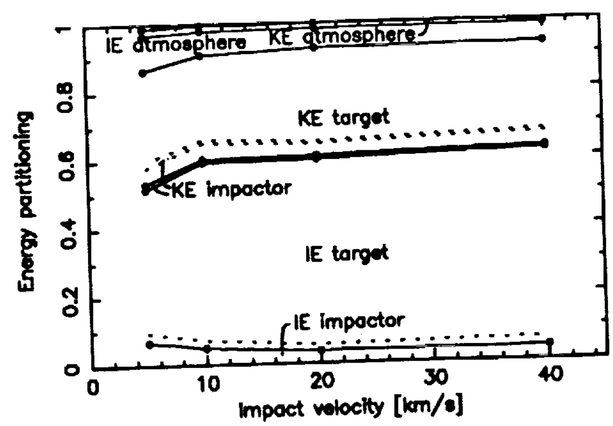


Fig.3. Final energy partitioning (fraction of total). Solid and dotted lines represent cases with and without atmosphere, respectively.

5174-25
ABS. ONLY

N94-20810

HYDROTHERMAL ALTERATION EXPERIMENTS OF OLIVINE WITH VARYING Fe CONTENTS: AN ATTEMPT TO SIMULATE AQUEOUS ALTERATION OF THE CARBONACEOUS CHONDRITES;

Koichi Takatori[1], Kazushige Tomeoka[2], Katsuhiro Tsukimura[3] and Hiroshi Takeda[1]; [1]Mineralogical Inst., Univ. of Tokyo, Tokyo 113, Japan, [2]Dep. of Earth Sciences, Kobe Univ., Kobe 657, Japan, and [3]Mineralogy Div., Geological Survey of Japan, Tsukuba 305, Japan.

Hydrothermal alteration experiments of olivine powder with several Fe/Mg ratios were carried out under acidic and neutral conditions, and TEM observations were made on the run products. Well-developed tubular crystals of serpentine (chrysotile) were synthesized from Fo100 under both acidic and neutral conditions, and from Fo92 and Fo80 under acidic condition. Abundance and size of chrysotile apparently depend on the Fe contents of olivine, i.e. with increasing Fe contents, less and smaller chrysotile was formed. Acidity of the solution plays an important role for the formation of chrysotile. Platy and fibrous crystals of phyllosilicate, probably serpentine, were obtained from Fo50 and Fo20 treated under acidic condition, which are most similar to the phyllosilicates in the CI and CM chondrites. Framboidal aggregates of Fe-rich grains (presumably Fe-hydroxide) were formed from Fa100 and Fo20, but no phyllosilicate was formed from Fa100.

INTRODUCTION

Carbonaceous chondrites are thought to be the most primitive surviving materials from the early solar system. However, some types of chondrites, CI and CM types in particular, show abundant evidence of aqueous alteration, suggesting that aqueous alteration was probably a common process in the early solar system. Nevertheless, physico-chemical conditions under which the alteration occurred are still poorly known. In order to better understand the conditions, experimental studies would be the most promising approach. Olivine is the major constituent of the carbonaceous chondrites and the most common precursor to the phyllosilicates, and olivine in the carbonaceous chondrites is characterized by its wide range of Fe/Mg ratios. As a first step to experimentally simulate the aqueous alteration in the carbonaceous chondrites, we conducted hydrothermal experiments of olivine having various Fe/Mg. ratios under neutral and acidic conditions. The experimental products were observed by a transmission electron microscope (TEM). The purposes of this study are: (1) to know whether there are differences among alteration products formed from olivine of different Fe contents, (2) if there are, to know how different they are and what causes the differences, and (3) to compare the experimental products with the materials in the CI and CM chondrites and to infer the physico-chemical conditions that governed the alteration processes in the carbonaceous chondrites.

EXPERIMENTAL METHODS

Powder samples of natural olivine (San Carlos, ~Fo_{92}) and synthesized olivine (Fo_{100}, Fo_{80}, Fo_{50}, Fo_{20}, and Fa100) were prepared for our experiments. These olivine samples were examined by XRD and SEM-EDS, and it was confirmed that they have no chemical zoning or inclusions. Olivine samples (~50mg each) were sealed in gold tubes with 200 μl of pure water or 1N-HCl, then heated in autoclaves at 400°C and 500 bars for 1 week (Fo_{100} and Fa_{100} with 1N-HCl were treated for 2 weeks). Run products were examined by a JEOL JEM-100CX TEM operated at 100 kV.

RESULTS

Fo_{100} with 1N-HCl (2 weeks)

Abundant straight, needle-like tubular crystals of serpentine (chrysotile) and Mg-Si-rich amorphous material were formed from Fo_{100}. The tubes are 50~80 nm in diameter and 1000~3000 nm in length and have a tubular form. Olivine grains were almost completely consumed to form chrysotile. No other materials were found.

San Carlos olivine (Fo_{92}) with 1N-HCl (1 week)

Tubular crystals of chrysotile and Mg-Si-rich amorphous material were formed, similar to the products from Fo_{100}. A remarkable feature is that numerous needle-like tubes grow radially from each olivine grain, showing an appearance of sea urchin; the texture is quite similar to that obtained by Yada and Iishi [1], who treated natural olivine (Fo_{91}) under 0.3N-HCl at 300 and 400°C and at 700 bars. The chrysotile tubes are slightly finer than those formed from Fo_{100}.

Fo_{80} with 1N-HCl (1 week)

Tubular crystals of chrysotile and Mg-Si-rich amorphous material were formed from Fo_{80}. This result is basically the same as those of the former two runs, but the chrysotile crystals obtained from this run are slightly finer (30~80 nm in diameter). Furthermore, some tubes are curved, while those formed from Fo_{100} and San Carlos are all straight.

Fo_{50} with 1N-HCl (1 week)

No tubular crystals were formed from Fo_{50}. Instead, platy, fibrous serpentine-like phyllosilicate (~1 µm in length) and membranous Mg-Si-rich amorphous material were formed. The phyllosilicate occurs in packets of platy grains.

Fo_{20} with 1N-HCl (1 week)

Platy, fibrous crystals of phyllosilicate were formed from Fo_{20}. Their crystallinity is lower than that of the phyllosilicate formed from Fo_{50}. A minor amount of framboidal aggregates (100~200 nm in diameter) of small Fe-rich grains occur. Electron diffraction patterns of the Fe-rich grains show broad powder rings, suggesting that they are poorly crystallized Fe-hydroxide. Olivine grains were almost completely decomposed and converted into phyllosilicate, Fe-rich grains and amorphous material.

Fa_{100} with 1N-HCl (2 weeks)

No phyllosilicate-like material was formed from this sample. Instead, abundant aggregates (20~200 nm in diameter) of Fe-rich grains (Fe-hydroxide?) and minor silica-rich amorphous material were formed. Olivine grains were almost completely consumed.

Fo_{100} with pure water (1 week)

Tubular and conical crystals of chrysotile were formed From Fo_{100} under the neutral condition, but they are not so abundant as those in the run products treated with 1N-HCl. Conical crystals were formed only under the neutral condition. Probably because of its lower crystallinity, chrysotile is unstable under a focused electron beam and rapidly decomposed.

Fo_{80} with pure water (1 week)

No tubular crystals were formed from Fo_{80} under the neutral condition. Note the contrast between this run's products and those obtained from the same starting material under the acidic condition. Filmy phyllosilicate-like material of low crystallinity was formed, and membranous nuclei of phyllosilicate-like material grew from the surface of olivine grains; the latter appears to indicate the initial stage of serpentinization of olivine.

DISCUSSION & CONCLUSIONS

The present experiments reveal that extensive aqueous alteration occurred in all of the runs and that there are remarkable differences among the alteration products formed from olivine of different Fe contents. Well-developed straight, tubular crystals of chrysotile as well as Mg-Si-rich amorphous material were formed from Fo_{100}, Fo_{92}, and Fo_{80}. The amounts and sizes of produced materials apparently depend on the Fe contents of olivine in this compositional range (Fo_{100-80}); the amount and size of chrysotile decrease, while the amount of Mg-Si-rich amorphous material increases with increasing Fe contents.

From Fo_{50} and Fo_{20}, no such tubular crystals were obtained, instead abundant fibrous and platy crystals of serpentine and membranous material were formed. The serpentine formed from Fo_{50} commonly shows curved and contorted layers, exhibiting very complex textures. The textures are most similar to those of serpentine in the CI and CM chondrite matrices [2,3 and 4].

Another interesting products are aggregates of Fe-rich grains (probably Fe-hydroxide) obtained from very Fe-rich olivine (Fo_{20} and Fa_{100}). The texture is strongly reminiscent of the framboidal aggregates of magnetite that commonly occur in the CI chondrites. In the CI and CM chondrites, Fe-hydroxide and magnetite commonly coexist with phyllosilicates, and they are believed to be by-products of aqueous alteration [2 and 5]. Although, at present, we are not certain yet how the aggregates of Fe-rich grains and the framboidal magnetite are related, the present study provides evidence that Fe-hydroxide is a by-product of aqueous alteration of particularly Fe-rich olivine.

Differences between the products formed under the acidic condition and neutral condition are quite remarkable. No chrysotile was formed from Fo_{80} under the neutral condition, while abundant chrysotile was formed under the acidic condition. From Fo_{100}, chrysotile was formed under both acidic and neutral conditions, but more and larger crystals were formed under the acidic condition. These results indicate that acidic conditions are very effective for the formation of serpentine.

REFERENCES

[1] Yada,K. and Iishi,K. (1977) *Amer. Mineral.* **62**, p.958-965. [2] Tomeoka, K. and Buseck, P.R. (1988) *Geochimica et Cosmochimica Acta* **52**, p.1627-1640. [3] Barber, D.J. (1981) *Geochimica et Cosmochimica Acta* **45**, p.945-970. [4] Tomeoka, K. and Buseck, P.R. (1985) *Geochimica et Cosmochimica Acta* **49**, p.2149-2163. [5] Kerridge, J.F., MacKay, A.L. and Boynton, W.V. (1979) *Science* **205**, p.395-397.

MINERALOGY AND COOLING HISTORY OF MAGNESIAN LUNAR GRANULITE 67415;
Hiroshi Takeda and Masamichi Miyamoto, Mineralogical Institute, Faculty of Science, University of Tokyo, Hongo, Tokyo 113, Japan

We investigated Apollo granulite 67415 by mineralogical techniques to gain better understanding of cooling histories of lunar granulites. We estimated cooling rates from chemical zoning of olivines in magnesian granulitic clasts by computer simulation of diffusion processes. The cooling rate of 10 degrees C/yr obtained is compatible with a model of the granulite formation, in which the impact deposit was cooled from high temperature or annealed, at the depth of about 25 m beneath the surface.

Our previous mineralogical studies of lunar granulites [1], granulitic clasts in lunar meteorites and highland breccias [2] showed that granulites are common lithologies of the ancient highlands and their cooling rates are 0.3 to 3°C/day. In this study we investigated cooling rates of magnesian granulite 67415, which was well characterized [3], but not available in our previous study. We measured CaO chemical zoning profiles of olivines in 67415 with an electron probe microanalyzer (EPMA JCXA-733) to estimate the cooling rates of granulitic clasts by the same computer method as previously used [1].

The polished thin section (PTS) of 67415,14 was supplied from NASA. Four large granulitic clasts (GR1-GR4) are present in the PTS; GR1 (2.6x1.5 mm in size) contains rounded olivine crystals (up to 0.4 mm in diameter) and minor orthopyroxene and augite in granoblastic plagioclase. GR2 (1.3x0.96 mm) is similar to GR1, but the mafic silicates are thinner in GR3 and GR4 than those in GR1, and the grains are connected. 67415,14 is classified as a monomict cataclastic noritic anorthosite and consists of abundant angular mineral fragments and a few lithic clasts in a matrix of very fine-grained crushed material [3]. Lithic clasts have annealed plutonic textures and consist of polygonal plagioclase crystals (up to 1 mm) with scattered rounded olivine crystals. Some crystals are joined together to form an aggregate of two to three crystals.

The mafic silicates in GR1 are mostly olivine (Fa_{23}), and minor orthopyroxene ($Ca_3Mg_{78}Fe_{19}$) and augite ($Ca_{43}Mg_{48}Fe_9$). Plagioclase compositions range from An_{91} to An_{92}. The zoning profiles of olivine were obtained by point analyses along a line form core to rim of a crystal. The enrichment of CaO was detected along the rims towards plagioclase, but not towards the olivine to olivine grain boundaries.

The method to estimate cooling rates and burial depths is the same as that used for the previous study [1,4,5]. Mg/Fe ratios of olivines in 67415 are constant, but Ca zoning with Ca enrichment towards the rim has been detected (Fig. 1). The temperature of equilibration estimated from coexisting orthopyroxene and augite chemistries [8] is about 1000°C. We calculated cooling rates from 1000°C based on the following two mechanisms (Case I and II) for the formation of zoning as:

(I) The zoning profiles were assumed to have been established during crystallization. During subsequent annealing process, the Mg-Fe zoning is homogenized but the Ca zoning is not. This can be explained by the fact that the diffusion coefficient of Ca in olivine is smaller than that of Fe in olivine [6,7]. The cooling rate to homogenize the Mg-Fe zoning in olivines is slower than about 200°C/yr and the cooling rate to preserve the Ca zoning is faster than 1°C/yr. In this case, we can give only ranges of cooling rate.

COOLING HISTORY OF GRANULITE 67415: Takeda H. and Miyamoto M.

(II) Ca distribution was uniform (CaO ~0.04 wt %) when olivine was crystallized. Then, Ca zoning was produced by diffusion of Ca into olivine from the surrounding plagioclase during thermal metamorphism. An approximate cooling rate can be determined uniquely. 10°C/yr gives best fit for the observed profile (Fig. 1). This cooling rate corresponds to a burial depth of 25 m for a rock-like material (thermal diffusivity=0.004 cm^2/s) and 1 m for a regolith-like one (0.00001 cm^2/s). Mg-Fe homogenization is taken place at this cooling rate by a process considered in Case I, if Mg-Fe zoning was initially present. The assumption on the CaO content at the interface between olivine and plagioclase, which gives best fit for the observed profile is supported by the partition coefficient (k) between olivine and plagioclase. k of oliv. /plag. are the same as our previous work [e.g., 9]. The CaO content of plagioclase of 67415 is 18 wt %.

Textures of 67415 is granulitic but more coarse-grained and look like a pultonic rock. The facts suggest that this granulite was formed by thermal annealing of a more igneous textured rock than impact heated breccias, which were parts of a hot ejecta blanket. Since no Ca enrichment or depletion at the rim of an olivine joined together were detected, Case II is more likely process to produce the CaO zoning. The estimated burial depth by our calculation implies that the GR1 clast in 67415 was cooled from high temperature or annealed about 25 m beneath the surface.

We thank NASA for the sample and Dr. T. Ishii and the Ocean Research Inst. of University of Tokyo for the EPMA, and Mrs. M Otsuki for her technical assistance.

REFERENCES: [1] Takeda H., Miyamoto M. and Mori H. (1992) Lunar Planetary Science XXIII, 1405-1406. [2] Takeda H., Miyamoto M., Mori H., Wentworth S. J. and McKay D. S. (1990) Proc. Lunar Planet. Sci. Conf. 20th, 91-100. [3]) Lindstrom M. M. and Lindstrom D. J. (1986) Proc. Lunar Planet. Sci. Conf. 16th, D263-D276. [4] Miyamoto M. (1987) Lunar and Planetary Science XVIII, pp.651-652. [5] Miyamoto M., McKay D. S., McKay G. A., and Duke M. B. (1986) J. Geophys. Res., 91, 12804-12816. [6] Buening D. K. and Buseck P. R. (1973) J. Geophys. Res., 78, 6852-6862. [7] Morioka M. (1981) Geochim. Cosmochim. Acta, 45, 1573 -1580. [8] Lindsley D. H. and Anderson D. J. (1983) Lunar Planet. Sci. Conf. 13th, A887-A906. [9] Yurimoto H. and Sueno S. (1984) Geochem. Journ., 18, 85-94.

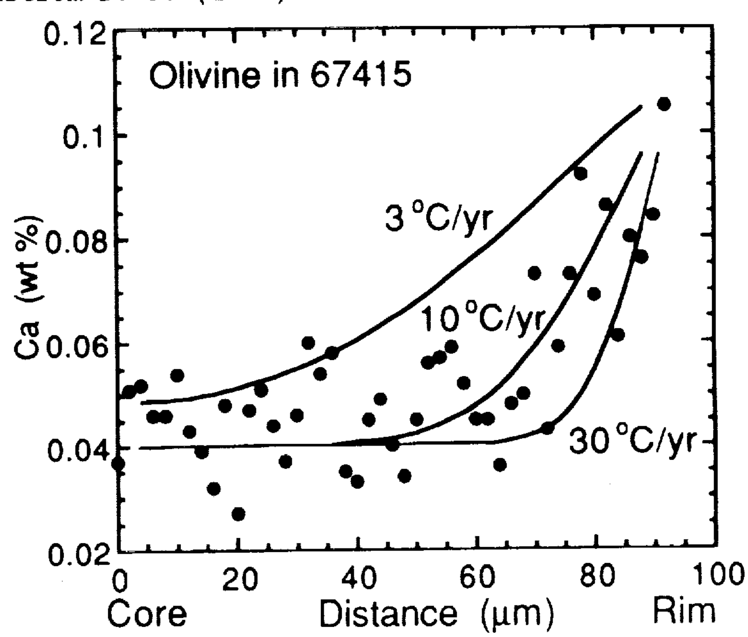


Fig. 1 Olivine chemical zoning profiles from core to rim of weight percent CaO (solid circles)

S176-90 ABS. ONLY

N94-20812

Ti-BEARING OXIDE MINERALS IN LUNAR METEORITE Y793169 WITH THE VLT AFFINITY; Hiroshi Takeda, Tomoko Arai and Kazuto Saiki, Mineralogical Inst., Faculty of Science, Univ. of Tokyo, Hongo, Tokyo 113, Japan.

Lunar meteorite, Yamato 793169 previously classified as a VLT mare basalt contains considerable amounts of Ti-bearing oxides in the mesostasis area (2 vol. %). Mineralogical study of these oxides revealed that they are isolated grains of ilmenite, ulvöspinel and chromite, which are formed at the last stage of crystallization. Ti/(Ti+Al+Cr) and Cr/(Cr+Al) versus Fe/(Mg+Fe) variations of these phases are not in the same trends as in the low Ti pigeonite basalts of Apollo 12 and 15 in spite of its higher TiO_2 contents.

Among four lunar meteorites proposed to be samples of mare regions of the Moon, EET87521 and Y793274 are breccias rich in lunar mare components [1-3], but Y793169 and A881757 are crystalline rocks composed of Fe-rich pigeonite and plagioclase with affinity to the VLT basalts [4], despite their higher bulk TiO_2 contents than the limit for VLT [5].

We investigated polished thin sections (PTS) Y793169,51-3 and A881757,51-4 (Asuka-31) supplied by the National Institute of Polar Research (NIPR). Both samples were allocated as parts of two consortium studies [6]. Mineral chemistries and textures were examined by an electron probe micro-analyzer (EPMA) and scanning electron microscope (SEM), JEOL 840A with X-ray chemical map analysis (CMA) utilities. Modal abundances of minerals in Y793169 were obtained from colored back scattered electron (BSE) image of SEM for a particular mineral by a computer and by point analysis for minerals with a similar BSE intensity.

The Y793169,51-3 PTS is a crystalline subophitic basalt with Fe-rich pyroxene, plagioclase and dark mesostasis portions. Mineralogy and petrography have been reported as a part of the consortium study [6]. Modal abundances of minerals are: pyroxene 56 vol. % (Mg-rich 34 %, Fe-rich 22 %), plagioclase 42 %, ilmenite 1 %, ulvöspinel 1 %, fayalite, chromite and silica mineral (<0.1 %). Although this basalt has been classified as a VLT basalt [4], the amounts of ilmenite and ulvöspinel in the mesostases are fairly large (ca. 2 vol. %). The bulk composition computed from the modal abundance data and their average mineral compositions gives 1.8 wt % TiO_2. The Cr-Ti-Fe spinels found in the mesostases in Y793169 are chromite and Cr-bearing ulvöspinel. Ulvöspinel is as important as ilmenite for higher concentration of TiO_2 than VLT. Chemical variations of ulvöspinel and chromite in Y793169 are compared with the Apollo and Luna spinels [7].

Our previous study showed that crystallization trends of zoned pyroxenes in Y793169 and A881757 are similar to those of the the VLT basalts but are different from known mare basalts including Apollo 12 and 15 low-Ti basalts [7], in spite of their higher TiO_2 concentration (TiO_2 for A881757 is 2.5 wt. %) [5] than previously known and the presence of fair amounts of ilmenite (or ulvöspinel) of these two rocks. Although A881757 is classified as a VLT basalt, abundant dark mesostasis portions contain fair amounts of ilmenite (6 vol. %) [4]. The Apollo 12 and 15 pigeonite basalts contain large phenocrysts of pigeonite in fined-grained matrices of pyroxene and plagioclase [7]. Among the groups, 12064 shows texture and pyroxene chemical zoning trend comparable to those of Y793169 [7]. The Ti/(Ti+Cr) versus Fe/(Fe+Mg) trend of Y793169 and A881757 pyroxenes are intermediate between the Apollo 15 basalts and the Apollo 17 VLT basalts [6].
The characterization of their bulk chemistries in the TiO_2 versus Mg/(Mg+Fe)

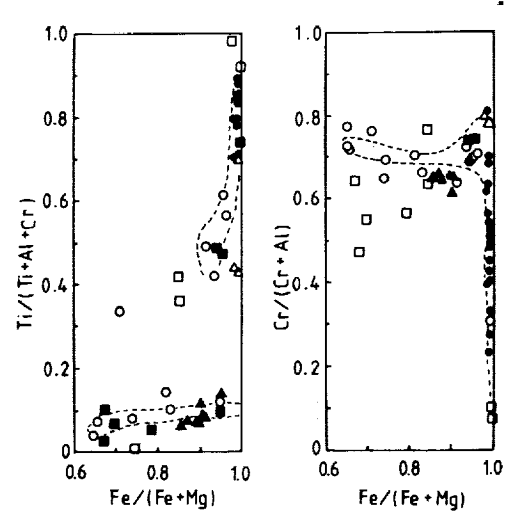
diagram indicates that these two rocks plot closer to the VLT field than to the low-Ti basalts [9].

The Ti/(Ti+Cr+Al) versus Fe/(Fe+Mg) variation (Fig. 1) of Y793169 indicates that the Y793169 spinel trends represent only very last stage of the local differentiation of the mare basalt. The Cr/(Cr+Al) versus Fe/(Fe+Mg) trend (Fig. 1) has some resemblances to Apollo 12 ilmenite basalts and feldspathic basalts [7], but the Cr/(Cr+Al) ratios of Y793169 are little lower than those of the Apollo 12 low-Ti basalt, and the Y793169 trend represents only for that of the Fe-rich end. It is to be noted that the low-Ti basalt trends represent those of core to rim variation during crystal growth, whereas the Y793169 trends are shown by the coexisting three Ti-bearing phases, precipitation of which took place at the last stage of the small-scale differentiation. Mineralogy of Y793169 and A881757 suggests the term VLT or low-Ti basalt may not be appropriate for such basalts.

We are indebted to NIPR for the consortium samples, and to Drs. P. H. Warren, J. S. Delaney, T. Ishii, K. Nishiizumi, K. Misawa and K. Yanai for discussion. We thank T. Ishii, E. Yoshida, O. Tachikawa, K. Hashimoto, M. Ohtsuki and M. Hatano for their technical assistances.

REFERENCES: [1] Delaney J. S. (1989) Nature, 345, 889-890. [2] Warren P. H. and Kallemeyn G. W. (1989) Geochim. Cosmochim. Acta, 53, 3323-3330. [3] Takeda H., Saito J., Mori H., Yanai K. and Kojima H. (1991) Proc. NIPR Symp. Antarct. Meteorites, 4, 3-11. [4] Yanai K. (1991) Proc. Lunar Planet. Sci. 21, 317-324. [5] Warren P. H. and Kallemeyn G. W. (1992) Abstr. 17th Symp. Antarctic Meteorites, 113, Tokyo, NIPR. [6] Takeda H., Arai T. and Saiki K. (1992) Ibid, 109-112. [7] Pipike J. J., Hodges F. N., Bence A. E., Cameron M. and Rhodes J. M. (1976) Rev. Geophys. Space Phys., 14, 475-540. [8] Yanai K. and Kojima H. (1991) Proc. NIPR Symp. Antarct. Meteorites, 4, 70-90. [9] Koeberl C., Kurat G. and Brandstätter F. (1992) Abstr. 17th Symp. Antarctic Meteorites, 219-222.

Fig. 1. Ti/Ti+Al+Cr and Cr/(Cr+Al) vs. Fe/(Fe+Mg) variation diagrams for spinels from major mare basalt groups [4,7], and Y793169. Solid circles: Y793169 ulvöspinel, solid triangle: Y793169 chromite; open triangles: EET87521 and A881757; open squares: Apollo 11 and 17; open circles: Apollo 12 and 15 (dotted lines for pigeonite basalts); and solid squares: Apollo 14 and Luna 16.



5172-90
ABS. ONLY

N94-20813

p. 2

A NEW ANTARCTIC METEORITE WITH CHROMITE, ORTHOPYROXENE AND METAL WITH REFERENCE TO A FORMATION MODEL OF S ASTEROIDS; Hiroshi Takeda, Kazuto Saiki Mayumi Otsuki, Mineralogical. Inst., Faculty of Science, Univ. of Tokyo, Hongo, Tokyo 113, Japan and Takahiro Hiroi, SN3, NASA Johnson Space Center, Houston, Texas 77058.

Mineralogy of a unique meteorite from Antarctica, EET84302 and the related primitive achondrites has been studied to gain better understanding on relationship between S asteroids and this meteorite group. EET84302 consists of metal-rich (M) region with metal filling interstices of silicate grains of orthopyroxene (Opx), olivine Fa_8, plagioclase An_{24}, and augite (Aug), chromite-rich (C) region with major chromite and Opx, and silicate-rich (S) region with mainly Opx. This is the first example of chromite-rich achondrite. Distribution of three areas (C, M, S) are in line with a proposed model of primitive achondrites and S asteroids.

Since reflectance spectra of some members of primitive achondrites combined with those of iron meteorites, resemble those of the S asteroids [1], there is an expectation that S asteroids are modified products of chondrites [2]. The trends of the variations in their mineral assemblages are in line with those of the S asteroids [2]. Hiroi et al. [1] proposed a stony-iron model of S asteroids, which assumes that a few domains of various primitive achondrites are embedded in iron matrix.

Polished thin sections (PTS) of EET84302,19 and ALH81187,16 have been supplied from Meteorite Working Group (MWG). A previously studied PTS of EET84302 was similar in both texture and mineralogy to silicate inclusions in some iron meteorites [3]. We have studied PTS EET84302,19 by electron probe microanalyzer (EPMA) and scanning electron microscope (SEM). The reflectance spectra of EET84302 showed a weathering problem and has not been used to match with those of S asteroids [1].

EET84302,19 is an Opx-rich meteorite with their grain boundaries filled with complex veins and amoeboid grains of opaque minerals (Fig. 1). One third of the PTS (C area) is richer in chromite and its grains are interconnected to form a domain of chromitite with rounded inclusions of silicates (Opx). Another area is richer in metal (M area), but their amoeboid grains are isolated. In the middle of two distinct areas, there is a silicate rich area (S) similar to metal-poor lodranite MAC88177 [2]. In a transitional zone, two joined amoeboid grains of opaque minerals have a sharp boundary between metal and chromite (Fig. 1). Modal abundances of minerals of EET84302,19 are: Opx 49 vol.%, olivine 4 %, plagioclase 6 %, Aug 0.7 %, whitlockite 0.2 %, chromite 23 % and metal 14 %.

The Opx crystals in EET84302 often have dusty cores similar to those in shock recrystallized diogenite (Y74013-type) [4]. The chemical compositions of Opx $Ca_{2.4}Mg_{89.6}Fe_{8.0}$ is more reduced than those of lodranites [2], and their Ca contents decrease towards the rims $Ca_{1.2}Mg_{91.5}Fe_{7.3}$. No exsolution was detected in Opx or Aug optically. Their compositions give the last equilibrated temperature of 1050-800°C [5]. ALH81187 is acapulcoite showing dusty appearance induced by shock reduction. Their mg numbers Mg X 100/(Mg+Fe) mol % is lower than those of Y75274 and Y8002 [6,7].

The silicate minerals closer to the C area are mostly Opx, but an area closer to the M area contains more olivine, plagioclase and augite than S. The plagioclase compositions range from An_{21} to An_{24}, but they are still within the Ca-richer end of the compositional variations of a shock

recrystallized LL7 chondrite [8]. The chromite compositions are Mg-rich $(Mg_{0.56}Fe_{0.42}Mn_{0.02})(Cr_{1.66}Al_{0.33})O_4$. The metal grains contain Ni 5 to 6 wt%, Co 0.5-0.6 %, and rarely includes ellipsoidal grains of a (Ni,P)-rich mineral (ca. Fe_2NiP).

A chromite-Opx assemblage is found in diogenites [4], but the texture of chromite is different. It is to be noted that amoeboid shapes of metal and chromite are nearly identical (Fig. 1). The texture suggests that these opaque minerals were formed by migration of materials through grain boundaries. We admit that there is no experimental phase relation to support the idea, but the materials may be supplied as Fe-Ni-S eutectic melt with Cr and P or Cr may be supplied as primitive liquid or a melt rich in Cr_2O_3.

As origin of chromitites, a few models of chromite formation have been proposed. Near absence of olivine in the C area favors the formation of chromite from olivine and Cr-rich melt as (Private comm., Z. Johan, 1992):

$$MgFeSiO_4 + Cr_2O_3 = FeCr_2O_4 + MgSiO_3$$

Kimura et al. [7] suggested that chromites in winonaites may have crystallized from a sulfide-metal liquid under reducing conditions. By a mechanism proposed by Irvine [9], the concentrated chromite is precipitated from chromite-saturated liquid when this liquid is blended with earlier liquid of the same type. The heterogeneous distribution of the C, M, S areas is in line with our proposed model of S asteroids [1,2]. Evidence of migration of materials through grain boundaries and the presence of dusty cores as in the shock recrystallized chondrites and diogenites is in accordance with a formation model of primitive achondrites by heating due to planetesimal scale collision in addition to the decay of ^{26}Al [2].

We thank MWG for the meteorite samples. Drs. Z. Johan, H. Ozawa, T. J. McCoy, J. Saito, T. Ishii and Profs. M. Miyamoto and K. Keil for discussions and Mr. H. Yoshida, O. Tachikawa, Mrs. K. Hashimoto and M. Hatano for technical assistance.

REFERENCES: [1] Hiroi T., Bell J. F., Takeda H. and Pieters C. M. (1993) Icarus, in press. [2] Takeda H., Saito J. and Hiroi T. (1992) Proc. Japan Academy, 68, Ser B, 115-120. [3] Mason B. (1986) Antarctic Meteorite Newsletter, 9, No.3, p. 18. [4] Takeda H., Mori H and Yanai K. (1981) Mem. Natnl. Inst. Polar Res. Spec. Issue, 20, 81-99. [5] Lindsley D. H. and Anderson D. J. (1983) Proc. Lunar Planet. Sci. Conf. 13th, A887-906. [6] Nagahara H. (1992) Proc. NIPR Symp. Antarct. Meteorites, 5, 191-223. [7] Kimura M. et al. (1992) Ibid 5, 165-190. [8] Takeda H., Huston T. J. and Lipschutz M. E. (1984) Earth Planet. Sci. Lett. 71, 329-339. [9] Irvine J. N. (1977) Geol. 5, 273-277.

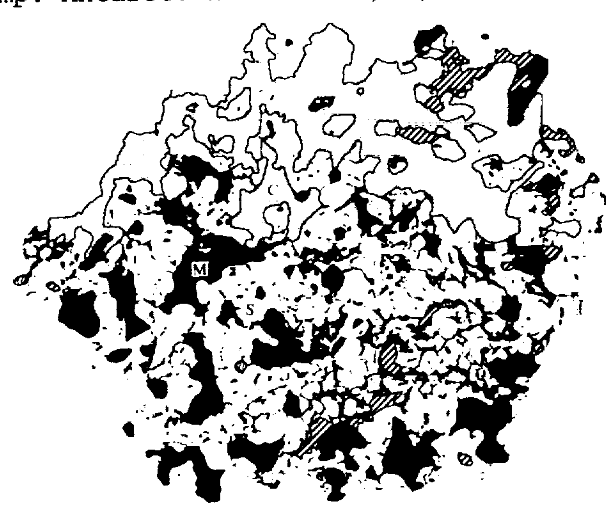


Fig. 1. Image processed PTS photograph of EET84302,19. Width is 8.3 mm. Note inhomogeneous distribution of C (chromite), S(Opx etc.) and, M(metal) areas. Unmarked striped portion is oxidized metal.

C-7

5178-91 ABS ONLY N94-16938 N94-20814 2

EXTENSIONAL HISTORY OF MARS' THARSIS REGION; **Kenneth L. Tanaka** and **D. John Chadwick**, U.S. Geological Survey, 2255 N. Gemini Dr., Flagstaff, Ariz., 86001

Summary. Graben structures in the outer part of Mars' Tharsis region follow calculated stress patterns that are based on Tharsis topographic and gravity anomalies and flexural response of the lithosphere [1, 2]. However, Tharsis extension is not evenly distributed—most extension is concentrated in the Alba, Tempe, Valles Marineris, and Syria-Thaumasia volcanotectonic provinces [3]. Our preliminary results suggest that the overall extension of Tharsis *produced by loading* is about 8 km (based on the assumption that the Sirenum province exemplifies the overall extension of Tharsis), whereas the *total* circumferential extension of the Tharsis region *estimated thus far* is about 33 km (we have not made an estimate for the Syria-Thaumasia province, and evidence in some other areas may be buried). We conclude that local tectonism, possibly caused by intrusion and passive and active rifting, produced most of the extension in the Tharsis region.

Regional extension. In Sirenum, extension produced by the flexural response to the Tharsis load appears to be the major and perhaps sole cause of graben formation [1, 2]. Because we do not have detailed morphometric data for the Sirenum grabens, we assume that extension is roughly proportional to graben width. This approach is based on work at Alba Patera [4], where the average extension for smaller grabens (<3 km wide) is about 22 m/km of graben width. At Sirenum, 29 grabens (all but one <3 km wide) occur about 2,500 km from the center of Tharsis. These grabens have a total width of 43.5 km, which yields nearly 1 km of extension. Extrapolating to the entire circumference of Tharsis results in 8 km of total extension, or a strain of about 4 to 6 x 10^{-4} (depending on distance from the center of Tharsis).

Extension by province. Of the eight Tharsis provinces (Fig. 1), three—Olympus, Elysium, and Tharsis Montes—are mostly covered by Amazonian rocks. The remaining five appear to have a structural record that is sufficiently preserved for estimates of extension to be made. For these (with the exception of the complex Syria-Thaumasia province) we indicate estimates of extension extracted or inferred from other work. Not surprisingly, the province with the greatest estimated extension is Valles Marineris, where the large grabens in its central area indicate a total extension of at least 16 km (possibly exceeding 30 km, depending on the dip of major graben-bounding faults [5, 6]). Subtracting the extension produced by Tharsis in this province (2 km) and the local strain produced by the passive uplift of Valles Marineris (1 km [5]) results in at least 13 km of extension that must be due to some other mechanism such as active rifting. At Alba Patera, a morphometric analysis of grabens along lat 35° N. [4] indicates that total extension is ~8 km. No comprehensive extensional strain measurements have been made for Tempe Terra. However, visual inspection of southwestern Tempe suggests that its grabens have size and density distributions nearly identical with those of Alba Patera. We therefore assign the same value of extension to Tempe as determined for Alba; both greatly exceed the estimated regional extension (Fig. 1).

Implications for Tharsis extensional history. Most Tharsis faults radiate from its center [7], which demonstrates the influence of regional stress on structural orientations. However, the grabens of the Sirenum province have been dated as Late Hesperian and perhaps Early Amazonian [8], which may indicate that the period in which grabens were produced by flexural response of the Tharsis load began in the Late Hesperian [1]. Also, a few grabens of Early and Middle Amazonian age [7], possibly produced by regional stress, radiate from Tharsis Montes. Elsewhere in Tharsis, most regional extension is not identified because of burial or the dominance of local structure. On broad Lunae Planum, in the northern part of the Valles Marineris province, extensional structures are absent, perhaps due to local compressional stress exerted during the formation of Valles Marineris to the south [2].

Our work indicates that Tharsis can be viewed as a region of warm, weak lithosphere in which mantle plumes or heat sources were concentrated; significant extensional strain developed both locally and regionally due to intrusion and passive and active rifting. Further detailed

morphometric analysis, particularly in the Sirenum and Syria-Thaumasia provinces [9], is necessary for a more precise and complete assessment of Tharsis extensional history.

References cited. [1] Banerdt, W.B., et al., 1992, *Mars*, UA Press, Tucson, ch. 8, p. 249-297. [2] Tanaka, K.L., et al., 1991, *JGR 96*, 15,617-15,633. [3] Tanaka, K.L., and Dohm, J.M., 1989, *LPI Tech. Rept. 89-04*, p. 79-81. [4] Plescia, J.B., 1991, *JGR 96*, 18,883-18,895. [5] Chadwick, J. and Lucchitta, B.K., *this volume*. [6] Schultz, R.A., 1991, *JGR 96*, 22,777-22,792. [7] Scott, D.H., and Dohm, J.M., *PLPSC 20*, 487-501. [8] Tanaka, K.L., and Chapman, M.G., *JGR 95*, 14,315-14,323. [9] Tanaka, K.L., and Dohm, J.M., *this volume*.

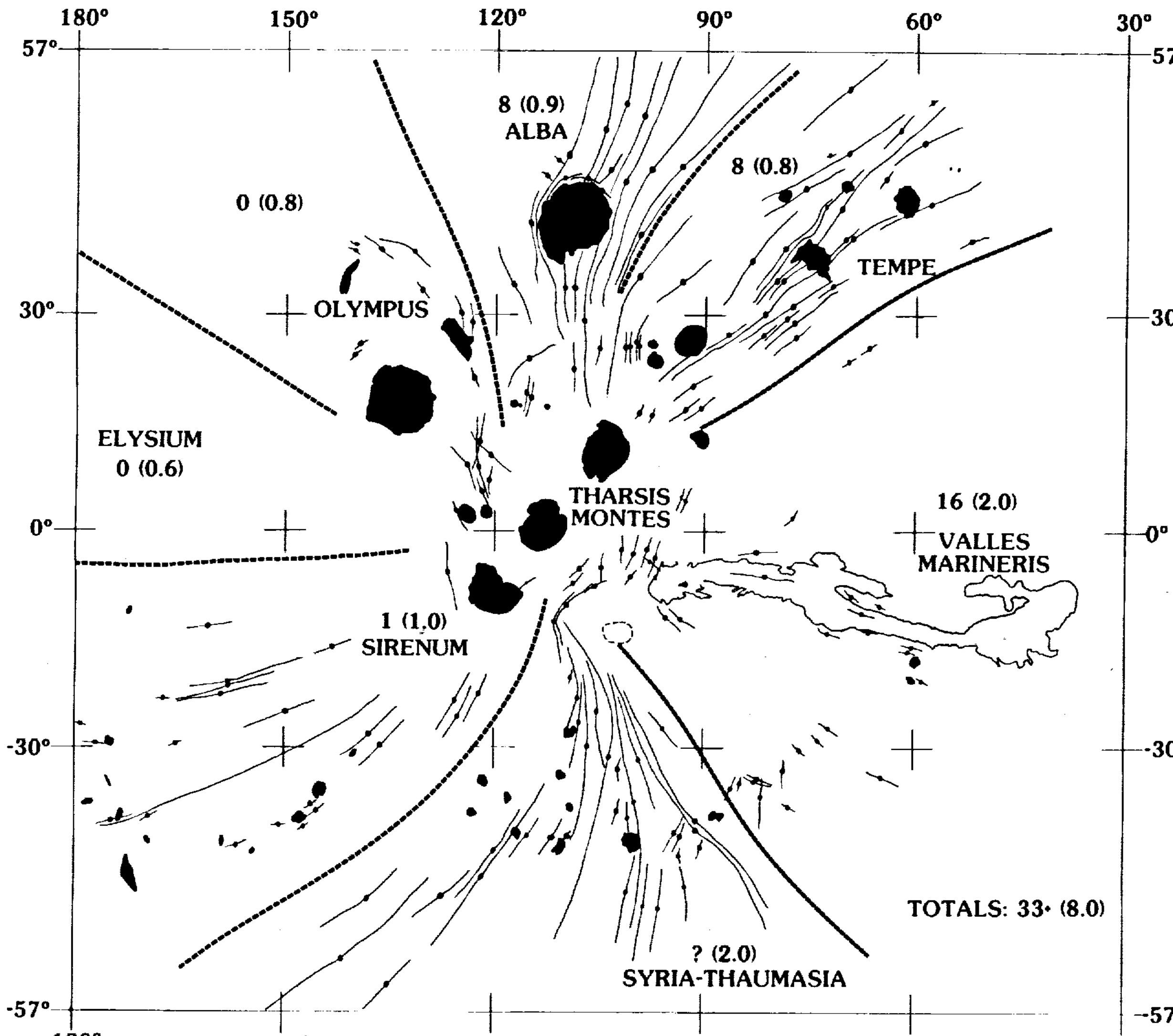


Figure 1. Map of the Tharsis region of Mars showing individual volcanotectonic provinces (modified from [3]). Heavy dashed lines separate the seven provinces radiating from the eighth, Tharsis Montes. Solid areas are volcanoes; lines with balls are grabens. Solid line outlines Valles Marineris trough system. Compare estimated circumferential extensional strain in each province (in km) with model-based regional calculations of extensional strains (in parentheses).

N94-20815

COMPLEX STRUCTURE OF THE THAUMASIA REGION OF MARS;

Kenneth L. Tanaka and **James M. Dohm**, U.S. Geological Survey, 2255 N. Gemini Dr., Flagstaff, Ariz., 86001

Introduction. The Thaumasia region was the first center of Tharsis tectonism [1, 2], and it is the most complex and poorly understood [2]. We are therefore compiling a geologic map of the entire Thaumasia region (lat 15° to 50° S., long 50° to 115°) at 1:5,000,000 scale. This region is mostly made up of the Thaumasia plateau, which includes the high plains of Syria, Sinai, and Solis Plana and surrounding highlands; the highlands are fractured by Thaumasia, southern Claritas, Coracis, Melas, and Nectaris Fossae. Our preliminary structural analysis of the most complexly faulted area in the region (the central part, at lat 30° to 45° S., long 80° to 100°) indicates that, unlike other regions of Mars, Thaumasia has undergone extensive deformation by both small- and large-scale extensional and compressional structures (Fig. 1). These results indicate that the early (Noachian) style of tectonism commonly involved lithospheric-scale deformation, in contrast to most younger tectonism (which mainly affected the upper parts of the crust above mechanical discontinuities); this difference may be due to a weaker (and thus more readily deformable) early lithosphere in this region.

Small-scale structure (Fig. 1A). Narrow grabens (mostly <5 km across) probably reflect deformation of the upper few kilometers of the crust above shallow mechanical discontinuites [3]. Claritas Fossae include northwest-trending Noachian and Early Hesperian grabens that dissect rugged terrain in the western part of the central Thaumasia region; these grabens appear related to Syria Planum-centered faulting [4]. Some grabens extend southward and southeastward, splaying out into two main groups; the north-trending Thaumasia Fossae make up the western group that cuts Lower Hesperian plains material that embays the Thaumasia plateau. A few grabens of Claritas Fossae cut the Upper Hesperian lava flows of the Syria Planum Formation that embay the northern part of the Thaumasia highlands [see also 4]; thus, older grabens of Claritas having similar trends may have been reactivated as well. Coracis Fossae include narrow, north-trending, Noachian (and perhaps Early Hesperian) faults in the eastern part of the area shown in Fig. 1; wider grabens (5 to 10 km across) may be bounded by secondary faults mentioned below. Scattered northeast-trending grabens farther west appear to be part of the same fault pattern.

Wrinkle ridges have been attributed to buckling of upper crustal layers decoupled from the lower lithosphere [5] or to thrust-faulting of the entire lithosphere [6]. A belt of wrinkle ridges, possibly formed during the Early Hesperian, flanks the south edge of the Thaumasia plateau.

Large-scale structure (Fig. 1B). High-relief, mostly east-trending ridges and scarps of Noachian to Early Hesperian age, particularly along the edge of the Thaumasia plateau, are associated with wrinkle ridges and truncated impact craters. The ridges and scarps are part of the proposed Thaumasia fold belt that wraps around the south half of the Tharsis region; the belt is proposed to have formed by periodic lithospheric-scale folding and thrust faulting [7]. Broad (15- to 50-km-wide), irregular, mostly north-trending grabens of Coracis Fossae reflect lithospheric rifting [3]. They cut Noachian and Lower Hesperian rocks and may be partly filled by Upper Hesperian volcanic material; subsequently, parts of the graben floors have failed, resulting in deep, enclosed depressions.

Conclusion. The complex tectonic history of the Thaumasia region resulted from multiple local and regional lithospheric stresses. The prevalent lithospheric-scale deformation observed may be a consequence of a relatively thin, weak lithosphere of early Mars. Through further geologic mapping and structural analysis, we will attempt to (1) reconstruct in detail the sequence of deformation in the Thaumasia region, (2) interpret development of thin- and thick-skinned styles of deformation, and (3) identify the sources of tectonic stresses.

References cited. [1] Frey, H., 1979, *JGR 84*, 1009-1023. [2] Plescia, J.B., and Saunders, R.S., 1982, *JGR 87*, 9775-9791. [3] Banerdt, W.B., et al., 1992, *in* Mars, Univ. Ariz. Press, ch. 8. [4] Tanaka, K.L., and Davis, P.A., 1988, *JGR 93*, 14,893-14,917. [5] Watters, T.R., 1991, *JGR 96*, 10,236-10,254. [6] Golombek, M.P., et al., 1991, *PLPSC 21*, 679-693. [7] Tanaka, K.L., and Schultz, R.A., *this volume*.

THAUMASIA REGION OF MARS: Tanaka, K.L., and Dohm, J.M.

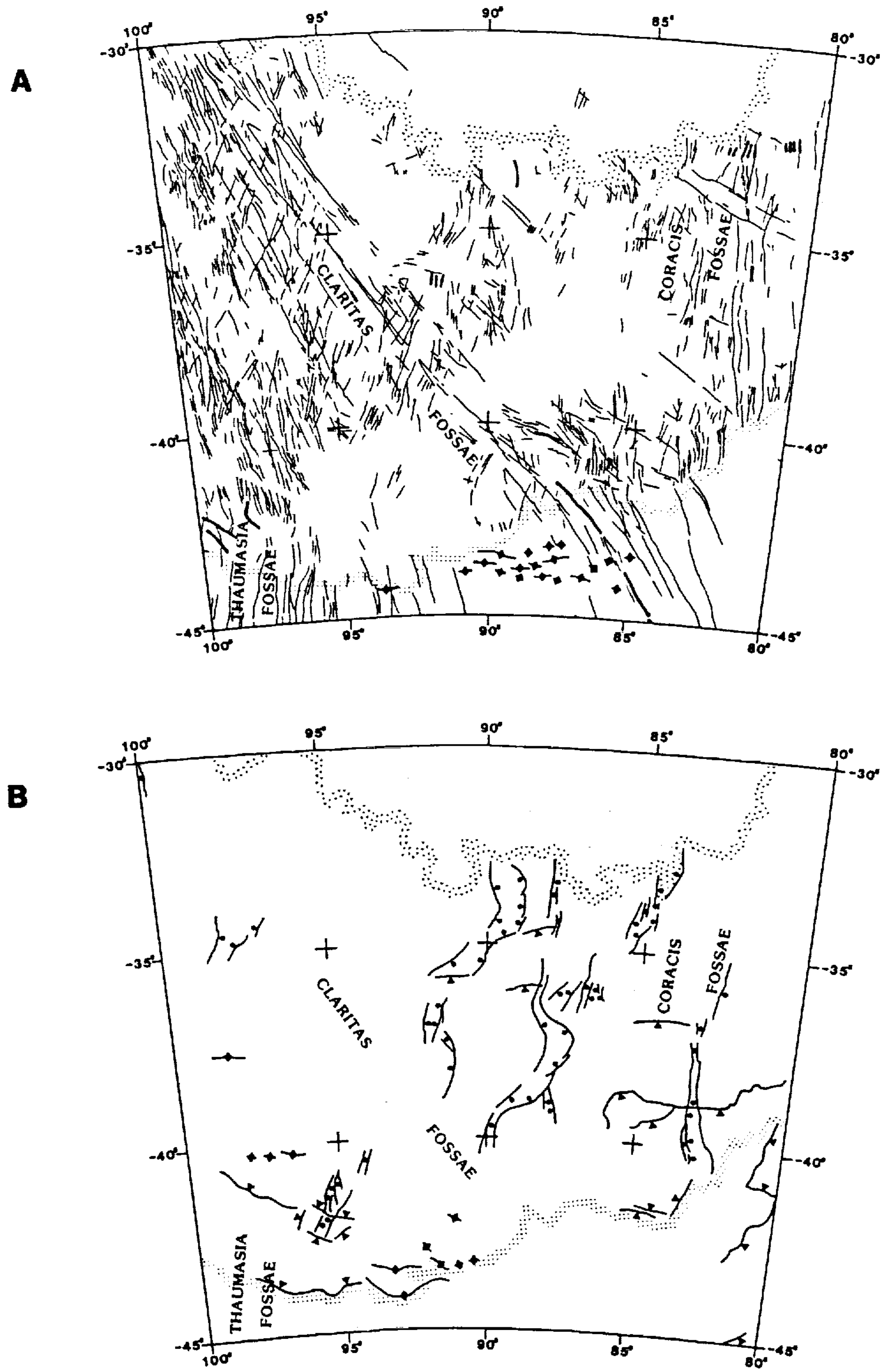


Figure 1. Structural maps of central Thaumasia region. Stippled line in north is contact between Syria Planum Formation and Thaumasia highlands; stippled line in south is edge of Thaumasia plateau. *A*, Small-scale structures: grabens <5 km wide shown by thin lines, grabens 5 to 10 km wide by thick lines, wrinkle ridges by lines with diamonds. *B*, Large-scale structures: normal faults bounding broad grabens (bar and ball on down-thrown side), high ridges (lines with diamonds), and scarps (barbs on upper flank).

LARGE, ANCIENT, COMPRESSIONAL STRUCTURES ON MARS; **Kenneth L. Tanaka**, U.S. Geological Survey, Flagstaff, Ariz., and **Richard A. Schultz**, Mackay School of Mines, University of Nevada, Reno, Nev.

Overview. Our search for large compressional structures similar to the Coprates rise reveals that the rise is part of a group of about three dozen structures (here named the "Thaumasia fold belt") that encircles the southern part of the Tharsis region. Similar structures are scattered over Mars. All appear to be Noachian or Early Hesperian in age, suggesting that lithospheric-scale buckling was a common form of early Martian compressional deformation.

Coprates. The Coprates rise, a broad, north-trending, asymmetric ridge (higher on the east) south of Valles Marineris, is 900 km long and 2 to 4 km high. The rise is recognized as a tectonic structure that has resulted in tilted rock layers [1-3]. Watters [3] noted from radar profiles that the rise is flanked by broad ridges, which he suggested may be periodic lithospheric folds having a spacing of about 400 km. Similar periodic spacings have been noted for ridge systems on Earth, and the spacings appear to be proportional to lithospheric thickness [4, 5]. Our work agrees with this fold interpretation and also indicates that the folding was asymmetric (east-vergent) and took place during the Late Noachian and possibly Early Hesperian [6, 7].

Other large compressional structures on Mars. Our conclusions for the Coprates rise have raised a related question: Do other large lithospheric folds or compressional structures (formed by thrust faulting) occur on Mars? To answer this question, we searched for ridges and scarps larger than those typified by wrinkle ridges. Furthermore, because large ridges and scarps can also be produced by normal faulting or impact, we looked for associated evidence for compression, such as tilted rock layers, truncated or shortened impact-crater rims, and large or multiple wrinkle ridges. Also, the relative age and geologic context of an individual feature may indicate that it is part of a group of large compressional features.

Results. A group of structures that includes the Coprates rise and other large ridges and scarps interpreted to be formed by compression forms a broad semicircle centered at Syria Planum that extends from the east end of Valles Marineris to the Memnonia region (Fig. 1). Because most of the structures are aligned with the edge of the Thaumasia plateau, we name the group the "Thaumasia fold belt." Other associated ridges extend west into the Sirenum and Memnonia regions and southeast toward Argyre Planitia. Although the Thaumasia fold belt generally coincides with the pattern of wrinkle ridges that surrounds the Tharsis region, it differs from this pattern in detail. For example, the belt does not extend into Lunae Planum, where wrinkle ridges are also abundant.

Additional compressional structures occur in other highland and lowland regions (Fig. 1). At Phlegra Montes, Amenthes Rupes, and Eridania Scopulus, compression is indicated by closely spaced wrinkle ridges and high scarps that locally truncate or shorten impact craters. In contrast, at Mareotis Fossae, a compressional origin for the ridges is uncertain, because broad ridges are dissected by deep troughs and irregular scarps.

All or most of the features interpreted to be large compressional structures appear to be Noachian to Early Hesperian in age; many are embayed by Lower Hesperian ridged plains material or other Hesperian (or younger) plains materials. Their antiquity suggests that conditions for their formation were more favorable on early Mars, when the lithosphere was warmer and thinner and when global and Tharsis compressions were greatest [8]. Perhaps, because of thickening and hardening of the lithosphere, the mode of compression later gave way to periodic thrust faulting or thin-skinned folding that resulted in wrinkle ridges [9, 10].

Our understanding of and ability to interpret properly these compressional features can improve with more detailed study of the features themselves and their relations with other similar features and tectonic centers. Moreover, improved topographic data provided by Mars Observer is likely to reveal more candidate structures and perhaps broad patterns of lithospheric deformation.

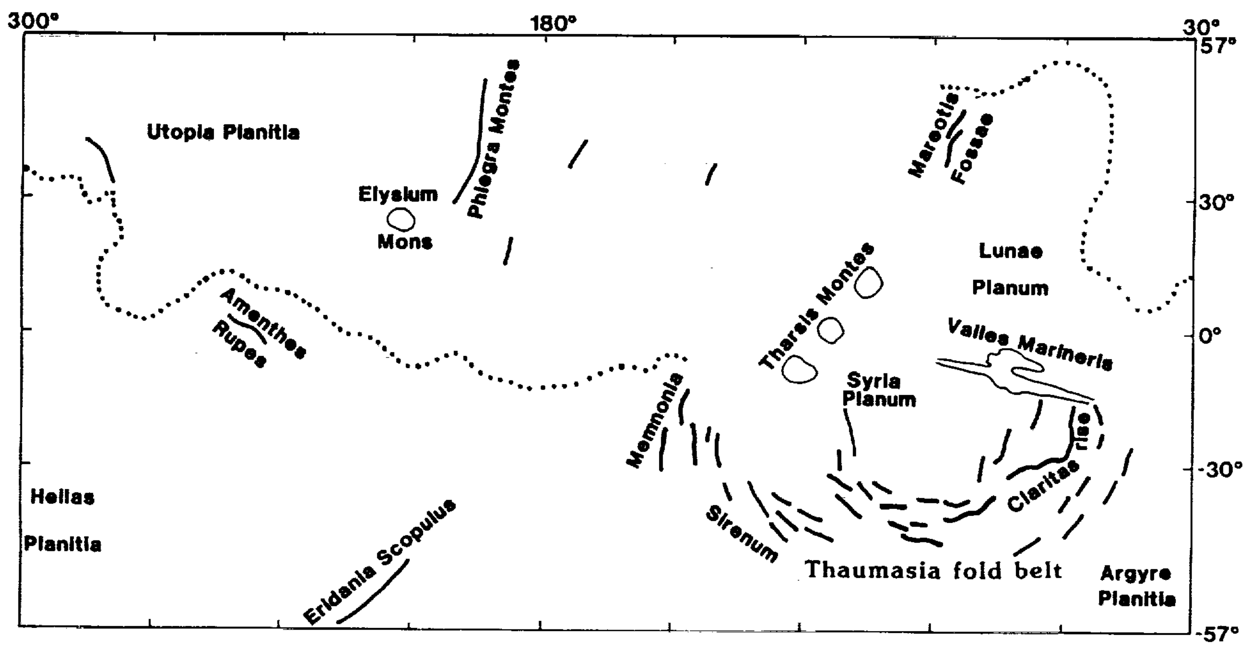


Figure 1. Large compressional structures on Mars. Approximate highland/lowland boundary indicated by dotted line. Note that most structures surround southern Tharsis region, forming Thaumasia fold belt.

References cited.
[1] Plescia, J.B., et al., 1980, *NASA TM 81776*, 68-70.
[2] Saunders, R.S., et al., 1980, *NASA TM 81776*, 74-76.
[3] Watters, T.R., 1987, *NASA TM 89810*, 481-483.
[4] Weissel, J.K., et al., 1980, *Nature, 287*, 284-291.
[5] Martinod, J. and Davy, P., 1992, *JGR, 97*, 1999-2014.
[6] Tanaka, K.L. and Schultz, R.A., 1991, *LPSC 22 Abstracts*, 1379-1380.
[7] Schultz, R.A. and Tanaka, K.L., 1992, *LPSC 23 Abstracts*, 1245-1246.
[8] Tanaka, K.L., et al., 1991, *JGR 96*, 15,617-15,633.
[9] Golombek, M.P., et al., 1991, *PLPSC, 21*, 679-693.
[10] Watters, T.R., 1991, *JGR 96*, 10,236-10,254.

N94-20817 p. 2

DETERMINATION OF PARAMETERS FOR HYPERVELOCITY DUST GRAINS ENCOUNTERED IN NEAR-EARTH SPACE: William G. Tanner[1], Carl R. Maag[2], W. Merle Alexander[1], and Patricia Sappenfield[1]; [1]Baylor University Space Science Laboratory, Department of Physics, Waco, Texas 76798; [2]Science Applications International Corporation, Glendora, California 91740.

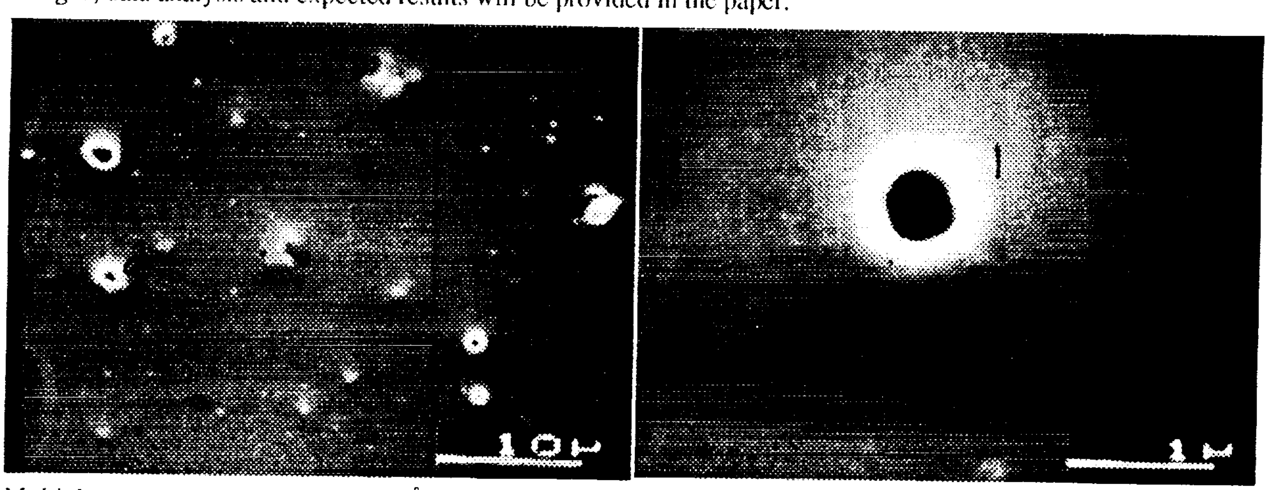
INTRODUCTION: The authors have been primarily interested in the determination of the population of micrometeoroids and space debris and have sought to interpret the hole size in a thin film or in a micropore foam returned from space with theoretical calculations describing the event. In order to augment the siginficance of the theoretical calculations of the impact event, an experiment designed to analyze the charge production due to hypervelocity impacts on thin films also produced data which described the penetration properties of micron and sub-micron sized projectiles. The thin film penetration sites in the 500Å and 1000Å aluminum films were counted and a size distribution function was derived. In the case of the very smallest dust grains, there were no independent measurements of velocities like that which existed for the larger dust grains ($d_p \leq 1\ \mu m$). The primary task then became to assess the relationship between the penetration hole and the particle diameter of the projectile which made the hole. The most promising means to assess the measure of the diameters of impacting grains came in the form of comparing cratering mechanics to penetration mechanics. Future experimentation will produce measurements of the cratering as opposed to the penetrating event. Particles encountered by surfaces while being flown in space will degrade that surface in a systematic manner even when the impact is with small hypervelocity particles, $d_p \leq 10\ \mu m$. Though not to a degree which would precipitate a catastrophic failure of a system, the degradation of the materials comprising the interconnected system will occur. It is the degradation of the optical systems and the subsequent embrittlement of other materials that can lead to degradation if not to failure. It is to this end that research has been conducted to compare the primary consequences for experiments which will be flown to those which have been returned.

EXPERIMENT DESIGN: Thin film experiments flown on the U. S. Space Shuttle (STS) have produced data which substantiate theoretical calculations describing the penetration dynamics associated with hypervelocity thin film perforations. A nine-month measurement of the Space Debris and Meteoroid population is being made by an experiment on-board the EuReCa 1 spacecraft and will be returned for examination in April 1993. The nine-month exposure of the thin film experiments to Low-Earth Orbit (LEO) will produce data which will allow further characterization of the Space Debris and Meteoroid population as well as the effect that population has on materials. Systems exposed to the extreme environment of LEO can avoid catastrophic failures only if the materials which compose them can provide a "shield" against the effects of continuous hypervelocity impacts. The size distribution of the objects a surface will encounter in LEO has not been adequately characterized, especially for that portion of the distribution which contains the highest number of objects, i.e., the smallest. To obtain *in situ* data depicting the size distribution of these objects in LEO, several experiments have been designed and successfully flown in the Science Applications International Corporation (SAIC) Interim Operational Contamination Monitor (IOCM) aboard STS-32, STS-44, and the Particle Impact Experiment (PIE) aboard STS-46 and STS-52 . Each of these shuttle secondary experiments have been scheduled for flight on STS-53 (PIE) and STS-63 (IOCM). As a result of experimental activities associated with Carl Maag's IOCM and PIE payloads, an opportunity to participate in the ESA's European Retrievable Carrier (EuReCa 1) was provided for a nine-month exposure at 525 km for similar experiments. The small-size micrometeoroid and space debris population has received little attention, and few experiments have been devoted to the measurement of these abundant dust grains. In order to supply data for both theoretical and experimental research, the EuReCa 1 experiment includes an intact capture system which will non-destructively decelerate small Space Debris and Meteoroid grains. The detection and collection of Space Debris and Meteoroids will improve knowledge concerning the size distribution of the cosmic dust grain complex and will provide parameters for larger body break-up models. The main theoretical thrust of research remained to establish a relationship for the 500Å films now being flown on EuReCa 1. Together with calculations produced by a hydrodynamic computer program (Sandia National Laboratory's CTH) and experiment data generated by use of an electrostatic dust accelerator (University of Kent at Canterbury, UK), a hole size relationship for hypervelocity thin film penetration can be developed which will aid in the interpretation of the data returned by the EuReCa 1 experiments. The results of the calibrations will then be used to assess the size of grains which perforated the 500Å film and were decelerated in the micropore foam. Preliminary analysis concerning theoretical limits for intact capture of Space Debris and Meteoroids in micropore foam will also be compared with previous laboratory studies of foam penetration.

COMPUTER SIMULATIONS: Results of both two-dimensional (2D) and three-dimensional (3D) computer simulations of the hypervelocity impact events which penetrate the STS and the EuReCa 1 thin films have reported[1].

A relationship between the particle diameter, D_p, and the diameter, D_h, of the hole created in a 500 Å aluminum thin film (T_f) and micropore foam (T_m) for relevant particle and target parameters has been derived and has been compared with empirical equations. That relationship will be used to analyze *in situ* data of the thin film experiments flown in LEO, and to determine the size distribution of grains which penetrate the thin films and are captured intact in the micropore foam. Few laboratory hypervelocity impact experiments have investigated the mechanisms of ejecta creation. Consequently, a significant uncertainty attends predictions of the effects high-speed ejecta can have on surfaces lying near the site of a hypervelocity impact. For this reason, the effect on materials which will be incorporated into the design of future Earth-orbiting vehicles needs to be investigated by exposure to long-duration space flight conditions. To this end an experiment was developed and flown as part of the TICCE experiment on the EuReCa 1 payload. This experiment has provided the opportunity to assess a wide range of dynamics of ejecta created by hypervelocity impacts on various substrates. The existing experimental data suggest that an oblique angle hypervelocity impact can create much more ejecta particles than do normal incidence impacts, and that the velocity distribution of these ejecta particles will be skewed toward higher values. Therefore, ejecta created in oblique impacts will transfer a significant portion of the impactor's kinetic energy to the surrounding structures. In order to examine this phenomenon further, the authors saw a need for an experiment which could capture hypervelocity ejecta so that an ejecta size and velocity distribution might be derived from a non-destructive study. The effects which a variation in the density of the substrate might have on ejecta production is also being investigated. Eulerian and smooth particle hydrodynamic computer programs will assist in establishing the theoretical parameters for the full regime of impact events from ultra thin film penetrations to semi-infinite targets composed of mixed material systems, viz., metallic surface evaporated onto a substrate.

SCIENCE OBJECTIVES: The primary objectives of the experiment are to: 1) Examine the morphology of primary and secondary hypervelocity impact craters. Primary attention will be paid to craters caused by ejecta during hypervelocity impacts on different substrates, e.g., gold, aluminum, palladium, copper, carbon, and at different angles of incidence, viz., 45°, 30°, 15°, 0°; 2) Determine the size distribution of ejecta by means of witness plates and collect fragments of ejecta from craters by means of momentum sensitive micro-pore foam. With an established ejecta size distribution via witness plates and with the determination of total momenta of each ejected particle, a velocity distribution by angle will be derived; 3) Assess the directionality of the flux by means of penetration hole alignment [above each cell, a 500 Å aluminum thin films will be placed. Particles larger than 0.3 µm ($\rho_{Al2O3} \sim 3.8$ g/cm^3) and 2.0 µm ($\rho_{IDP} \sim 1.0$ g/cm^3) will penetrate 500 Å of film]. Theoretical work using Sandia Laboratory's CTH "hydro" code[2] will be performed to assess the lower bound on the mass which could cause a penetration hole of the thousand angstroms of aluminum thin film; 3) Attempt to capture, intact, the particles which perforated the thin film and entered the cell. Capture medium will consist of both previously flight tested micro-pore foams and Aerogel. The foams have different latent heats of fusion and accordingly, will capture particles over a range of momenta. Aerogel will be incorporated into the cells to determine the minimun diameter that can be captured intact. A complete description of all experiment designs, data analysis and expected results will be provided in the paper.



Multiple penetrating impacts on 1000Å aluminum film used in the University of Kent at Canterbury expeiments.

REFERENCES:[1] Tanner *et al.* (1992), International Journal of Impact Engineering, in press; [2] J. M. McGlaun, S.L. Thompsom, M.G. Elrick (1990), International Journal of Impact Engineering, Vol. 10.

N94-20818

TUMULI AND TUBES: TEACHING SCIENTIFIC TECHNIQUES; Michelle J. Tatsumura, G.J. Taylor, and P.J. Mouginis-Mark, Planetary Geosciences, Dept. Geology & Geophysics, SOEST, University of Hawaii, Honolulu, HI 96822

Planetary and space science is the best way to teach basic chemistry, physics, and math. Einstein once said that "man is drawn to the mysterious and it is from that that we achieve true art and science." Planets and the processes that shape them are especially mysterious and fascinating to students, young and old, and because of this planetary geology kindles interest that draws them further into the world of science. At the very least, they are engaged enough to learn how science works, a key ingredient in scientific literacy. This paper describes a project involving field measurements on Kilauea volcano, Hawaii, by a Geology 101 honors class.

In Hawaii, we are blessed with spectacular, active, accessible, and relatively safe basaltic eruptions. The study of volcanoes, the landforms they produce, and the processes that operate on and in volcanoes, combined with the study of volcanoes on other planets, is an excellent way to link aspects of Hawaiian geology to the planets.

During the past year we have taken advantage of our setting to organize a NASA field workshop for junior investigators and senior graduate students, made field trips and planetary volcanism the centerpieces of our annual Summer Workshop for Teachers, and led a field trip around Kilauea Volcano during the Challenger Center Faculty Development Conference, held on the island of Hawaii last summer. We are presently planning an activity for the honors Geology 101 class (all undergraduates) at the University of Hawaii. Our goal is to give them some hands on experience working on a field project and applying what they've learned to planetary volcanoes. The work will include qualitative observations and quantitative measurements on volcanic lava flows. Follow-up activities will involve data analysis. The trip requires planning (at least 3 months before hand) everything from accommodations and insurance to the actual activities we will be doing. Our goal is to stimulate interest and awareness in the students' surroundings, in this case, our volcanoes, and to include planetary applications and how studies of terrestrial geology greatly aids studies of the other planets. We plan two studies, both of which are active research projects being conducted by the authors. These projects are described below.

Tumuli in pahoehoe flow fields. Work being done by MJT for her masters' thesis focuses on lava flow emplacement mechanisms via the study of tumuli in lava flows in Hawaii and on Venus and Mars. It has yet to be explained why tumuli form where they do and how their distribution and sizes relate to ground slope. These results may shed some light on the subsurface plumbing system of pahoehoe lava flow fields. The work involves measuring strike and length of the tumulus' longest axis, width, the amount of dilation or opening of the axial cleft, plus any other notable characteristic of the tumulus. These data in turn will be used as a tool for analysis by way of graphing, charting, and describing the features studied eventually to provide some qualitative and marginally quantitative statements about tumuli and what may have caused them to form in their present locations (Fig. 1). We hope that data such as air photography, SIR-B, Magellan, and Viking photographs can be utilized in studying remote areas where field work on tumuli is impossible. Comparative studies with the remotely sensed data combined with ground field work in Hawaii may provide insight into lava flow emplacement processes on other volcanoes on Venus and Mars as well as remote volcanoes on Earth.

Lava tube cross-sectional areas. GJT has been studying the fractal properties of lava tube systems [Taylor G.J. (1992) *EOS* **73**, p. 648]. This work has shown that the cumulative number of tubes is a power-law function of tube cross-sectional area (Fig. 2). Many more measurements are needed, however, so the undergraduates in the Geology 101 honors course will be able to contribute in a significant way to this study. Students will make measurements in the field of tube width and height, photograph each tube for later measurement of cross-sectional area, and make other appropriate observations of each tube. Furthermore, analysis of the data

will involve use of logarithms, the concept of binning data (how many categories of tube size?), and practice in plotting graphs and testing for linearity.

These activities are scientifically useful, educationally sound, and accomplish several goals. The first, to address a specific scientific problem, consider explanations that satisfy the question, to practice making observations and taking notes, and finally, to get them out into the field and getting hands-on experience with things most people only see in postcards. The students learn more specifically about volcanoes, the complexity of pahoehoe lava flow fields, and get a glimpse of science works. The trip is scheduled for February 19 through February 21, 1993 and results of the trip will be presented at the LPSC meeting in March.

Acknowledgments. This work was supported by NASA grant NAGW 2955 (MJT and PJMM).



Fig. 1. Drawing of a typical tumulus in Hawaii. Widths at the base ranges from 1-10's of meters. The students will be undertaking a project that involves measurements of lava tubes and tumuli on the Big Island of Hawaii.

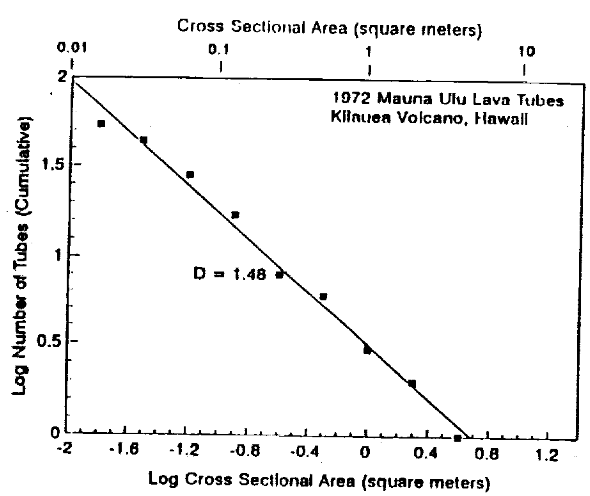


Fig. 2. Plot of the number of lava tubes of a given cross-sectional area or larger, versus cross-sectional area. Straight line (R^2=.98) indicates a power-law (hence fractal) relation. Acquiring and plotting data like these and testing for linearity is manageable and useful task for students in freshman geology.

5183-80
ABS ONLY

- 168143
N94-20819

SPARKING YOUNG MINDS WITH MOON ROCKS AND METEORITES.

G. Jeffrey Taylor[1] and Marilyn M. Lindstrom[2] [1]Hawaii Space Grant College, Planetary Geosciences, University of Hawaii, Honolulu, HI 96822 [2]SN2 Johnson Space Center, Houston, TX 77058

What could be more exciting than seeing pieces of other worlds? The Apollo program left a legacy of astounding accomplishments and precious samples. Part of the thrill of those lunar missions is brought to schools by the lunar sample educational disks, which contain artifacts of six piloted trips to the Moon. JSC is preparing 100 new educational disks containing pieces of meteorites collected in Antarctica. These represent chunks of several different asteroids, that were collected in one of the most remote, forbidding environments on Earth. These pieces of the Moon and asteroids represent the products of basic planetary processes (solar nebular processes, initial differentiation, volcanism, impact), and, in turn, these processes are controlled by basic physical and chemical processes (energy, energy transfer, melting, buoyancy, etc.). Thus, the lunar and meteorite sample disks have enormous educational potential.

We are developing new educational materials to accompany the disks. Present materials are not as effective as they could be, especially in relating samples to processes and to other types of data such as spectral studies, photogeology. Furthermore, the materials are out of date. We will be producing new background materials for teachers, assembling slide sets with extensive captions, and devising numerous hands-on classroom activities to do while the disks are at a school and before and after they arrive. The classroom activities will be developed by teams of experienced teachers working with lunar and meteorite experts.

Background information. Each disk will be accompanied by a booklet that provides essential background information to teachers. John Wood is writing the meteorite booklet. These booklets will be written for a general audience and will convey the scientific importance and excitement of the Moon, asteroids, and meteorites. They will integrate what we find out from sample studies with information from other sources, such as photogeologic studies of the Moon. Each booklet will also discuss future possibilities, such as lunar bases and asteroid mining.

Slide sets. Photos can make a subject come alive. Our slide sets will be accompanied by lucid captions that describe interesting features and the main message of each slide. The sets will tell the same basic story as the booklets, but in a more pictorial way. Slides also provide the opportunity to explore planetary connections. For example, lava channels on the Moon (such as Hadley Rille) can be compared with lava channels on the Earth. We hope to convert the slides to video format because video players are more common in schools than are projectors, and because many teachers feel more comfortable letting experts explain each slide, rather than relying on the captions.

Classroom activities. This is the heart and soul of the project. We will assemble groups of experienced elementary, middle, and high school teachers (six in Texas and ten in Hawaii) to help devise hands-on activities. Our goal is to use the sample disks as starting points for the exploration of planetary processes. For example, examination of the basalt samples in the disks leads to experiments in volcanic eruptions and the nature of volcanoes on Earth. The emphasis will be on experiments; there will be no crossword puzzles or find-the-hidden-word exercises. There will, however, be ideas for creative writing (e.g.,suppose a big meteorite hit the Earth?), history (e.g., early exploration of Antarctica), and social studies (e.g., what type of government should there be at a lunar base?). The essential ingredient in this part of the project is the partnership between scientists and teachers. Each brings different knowledge and experience to the enterprise, and it helps forge solid relationships for future educational projects.

Final product. We will produce separate publications for lunar samples and meteorites. Each document will contain the background material (the booklet described above), the activities organized in units (e.g., volcanism, impact), and hints for using the activities effectively. Although independent, the two publications will refer to ideas and activities in the other and will be organized and laid out in similar ways. The sample disks, slides sets and booklets will be distributed as educational packages to schools by the Teacher Resource Centers at various NASA centers.

N94-20820

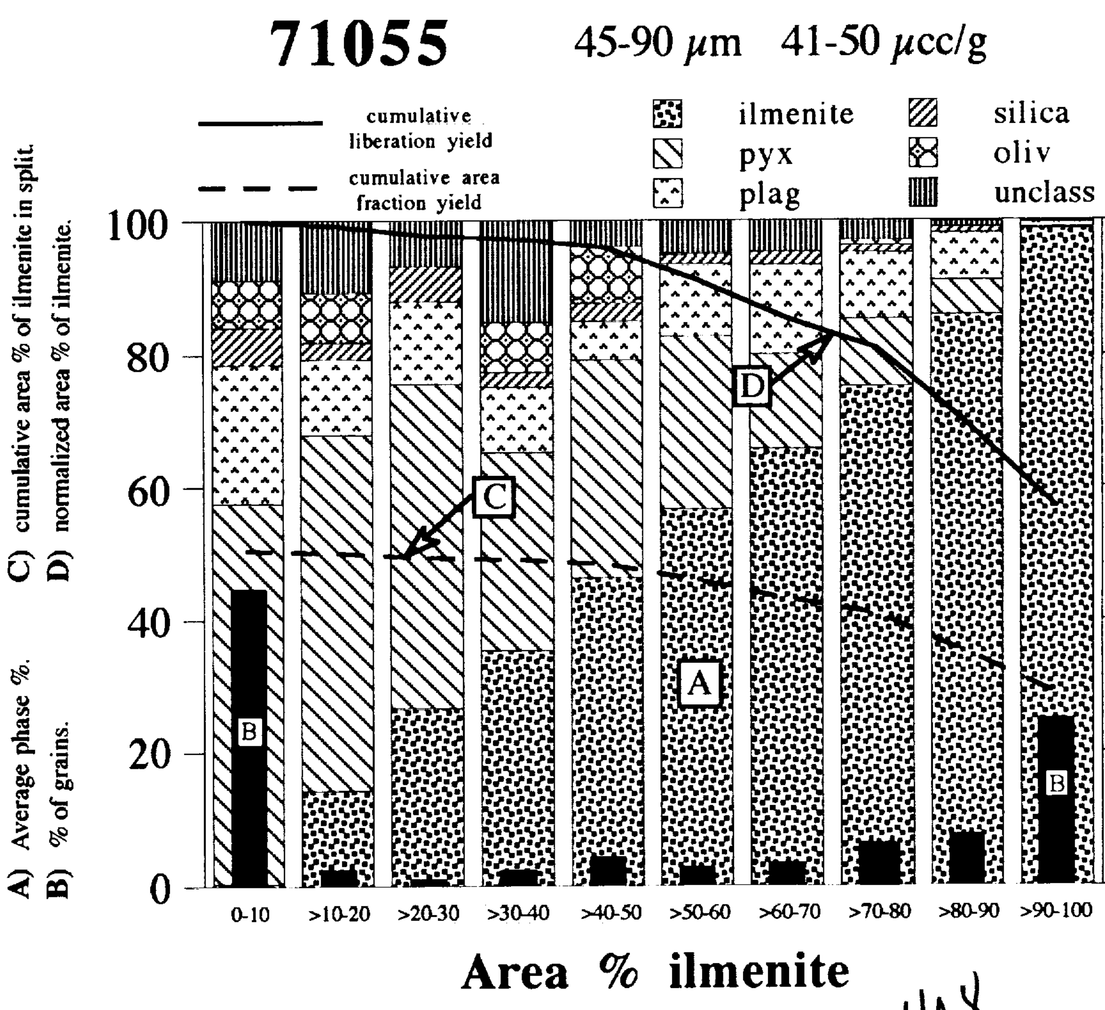
p. 2

EVALUATION OF LUNAR ROCKS AND SOILS FOR RESOURCE UTILIZATION: DETAILED IMAGE ANALYSIS OF RAW MATERIALS AND BENEFICIATED PRODUCTS.

Lawrence A. TAYLOR[1], John G. CHAMBERS[1], Allan PATCHEN[1], Eric A. JERDE[1], David S. McKAY[2], John Graf[2], and Robin R. ODER[3]. 1 = Planetary Geosciences Institute, Dept. of Geol. Sci., Univ. of Tennessee, Knoxville, TN 37996; 2 = Mission Sci. & Tech. Office, Code SN14, Johnson Space Center, Houston, TX 77058; 3 = EXPORTech Co., Inc., New Kensington, PA.

The rocks and soils of the Moon will be the raw materials for fuels and construction needs at a lunar base. This includes sources of materials for the generation of hydrogen, oxygen, metals, and other potential construction materials. For most of the bulk material needs, the regolith, and its <1cm fraction, the soil, will suffice. But for specific mineral resources, it may be necessary to concentrate minerals from rocks or soils, and it is not always obvious which is the more appropriate feedstock. Besides an appreciation of site geology, the mineralogy and petrography of local rocks and soils is important for consideration of the resources which can provide feedstocks of ilmenite, glass, agglutinates, anorthite, etc. In such studies, it is very time-consuming and practically impossible to correlate particle counts (the traditional method of characterizing lunar soil petrography) with accurate modal analyses and with mineral associations in multi-mineralic grains. But x-ray digital imaging, using x-rays characteristic of each element, makes all this possible and much more (e.g., size and shape analysis). In this paper, we demonstrate an application of beneficiation image analysis, in use in our lab (Oxford Instr. EDS and Cameca SX-50 EMP), to study mineral liberation from lunar rocks and soils.

The high-Ti basalt studied was lunar sample 71055 [12.8 wt% TiO_2], which we reported on last year [1]. This rock is a fine-grained, vesicular, subophitic to ophitic, olivine-bearing ilmenite basalt composed of ilmenite [20 vol%; with traces of ulvöspinel], clinopyroxene [42%], olivine [3%], plagioclase [29%], tridymite [5%], and traces of troilite (FeS), Fe metal, and apatite. Ilmenite forms skeletal blades with amoeboid rims, mostly 0.2-0.3 x 1-3 mm. It also occurs as discrete subhedral to euhedral grains, 0.1-0.4 mm across.. Rock chips of this basalt were lightly crushed in a "shatterbox", sieved into size fractions >150, 90-150, 45-90, 20-45, and <20 μm, and then magnetically separated with a Frantz Isodynamic



Separator, instrumented for both separations and magnetization measurements. A polished grain mount was prepared from a 5-10 mg portion of each magnetic split from the size fractions. Grains were characterized and counted using reflected- and transmitted-light optical microscopy. In addition, X-ray image analysis on our Cameca SX-50 EMP of portions of each grain mount has resulted in a plethora of data which have been applied to this study of beneficiation, with primary interest in the mineral ilmenite. Below, we present some of the results of this image analysis and thereby demonstrate the power of the application of such analysis to studies of size, shape, mineral associations, modal mineralogy, etc. for the resource evaluation of lunar rocks and soils.

MINERAL LIBERATION ANALYSIS: As an illustration of the power of these analyses, we have applied them to a grain mount of the 45-90 µm size split of ground basalt 71055, more specifically, that sample with a magnetic susceptibility of 41-50 µcc/g. Figure 1 illustrates the results from the modal/association portion of the analysis of this sample. This figure will be explained in some detail to provide an understanding and appreciation for the power of these image analyses.

Figure 1 is a composite of four graphs, A-D. The X-axis is divided into intervals each based upon the area % of ilmenite (since this is a 2-dimensional analysis) of the particles on this grain mount. That is, in the bin labeled >70-80, each grain has 71-80 area % ilmenite.

The **A portion of the figure** refers to the shaded bars of the diagram, which are the area % of different minerals in each bin. Note that the area % of ilmenite matches the label at the bottom of each bin. These shaded columns give the area % of each mineral in the "average" grain within the bin. For example, within the >40-50 area % ilmenite bin, the grains average 46 area % ilmenite, 33 % pyroxene, 5.9 % plagioclase, 2.7 % silica (tridymite), 8.5 % olivine, and 3.9 % unclassified. In reality, the unclassified region contains troilite, native Fe, apatite, cracks, and portions of grain edges which were unclassifiable; each is small in area % and the amounts were lumped together as "unclassified".

The **B portion of the figure** designates the percentages of the grains relative to the total grain population which have a certain area % ilmenite, that is, are within a particular bin. For example, the >90-100 area % ilmenite bin contains about 25 % of the total grains in the sample. It should be noted that about 45 % of the grains have 0-10 area % ilmenite; that is, almost half of the particles are essentially free of ilmenite. These observations indicate that the grinding process did a reasonably good job of liberating ilmenite from the silicates. This same magnetic susceptibility sample at a finer grain size would obviously show even a better separation.

The **C curve on the figure refers to the Cumulative Area Fraction Curve**. This curve shows the percentage of the total area of all grains that is ilmenite in a bin and those bins above it (i.e., to the right). For example, in the >90-100 area % ilmenite bin, the ilmenite represents about 30 % of the total grain area of all bins; that is, 30 % of the total area of all grains analyzed is ilmenite in grains composed of 90-100 % ilmenite. Further, in the >50-60 area % ilmenite bin, the curve is at 46% meaning that 46% of the total area of all grains is ilmenite in grains with 50-100 area % ilmenite (i.e., all bins above it [to the right], hence the name cumulative). Since the curve is cumulative, the highest point on the curve is equal to the area % of ilmenite in the sample -- that is, the modal % of ilmenite. The importance of this curve is that it illustrates the principle that although only 26% of the particles analyzed were >90-100 % ilmenite, the ilmenite constitutes about 30% of the total area analyzed. That is single-grain ilmenite makes up 30 modal % of the sample.

The **D curve on the figure refers to the Cumulative Liberation Yield Curve** which illustrates the area % which a bin, plus those above it (i.e., to the right), represents of the total amount of ilmenite in the sample. For example, approximately 55% of all ilmenite in this sample is located in the >90-100 area % bin. This curve is simply the normalized area % of ilmenite in each bin and those bins above it. This curve is interesting because one can see that over 80% of the ilmenite in this sample is in grains composed of >70 % pure ilmenite.

SUMMARY OF MODAL % ILMENITE AND MINERAL ASSOCIATIONS: Figure 1 should not be over-interpreted since it is data from only one of many grain mounts of a particular size range and magnetic susceptibility. However, some interesting speculations are possible. There exist two modes of particles: 25% with 90-100% ilmenite and 45% with 0-10% ilmenite. About 30% of the particles are intermediate in their ilmenite content (i.e., 10-90%). If the liberation was absolutely complete, these two modes would total almost 100%, and the intermediate grains would not exist, but this is not the case here. Therefore, the grinding did not completely liberate the ilmenite. Perhaps even more important is the observation that the magnetic separation failed to effectively separate the near-clean ilmenite grains from those with less than 10% ilmenite and made up large of pyroxene and olivine (78%). The degree of liberation will undoubtedly be better at finer grain sizes, but the separation of pyroxene and ilmenite grains may remain about the same. However, in this one grain mount studied, over 85% of the ilmenite particles are >70 area % ilmenite.

MORPHOLOGICAL MEASUREMENTS: In addition to accurate modal analyses and mineral association determinations, the imaging software allows many morphological measurements to be made on individual grains and compared to each other. Some of the parameters include aspect ratio (length/width), area, perimeter, hydraulic radius (area/perimeter). The hydraulic radius, which is analogous to the inverse of the well-known surface area/volume ratio, is a parameter which is important to producing feedstock for processes which are based upon surface-controlled reactions. Certain processes of ilmenite and glass reduction for oxygen production may apply here. Also, these measurements could prove important in attempts to compare two high-Ti basalts which have ilmenite of approximately the same size but with markedly different shapes (e.g., skeletal vs. blocky vs. bladed/needle-like) and mineral associations.

CONCLUSIONS: In essence, this prototype of x-ray image analysis, demonstrated above, will be extremely useful in correlating ilmenite morphology, size, and modal abundance in the raw material (rock or soil) with the nature and amount of clean, single-grained ilmenite produced by various beneficiation schemes. This is the very nature of mineral liberation studies.

REFERENCES: [1] Taylor, L.A., et al., 1992, Magnetic beneficiation of hihg-Ti mare basalts: Petrographic analyses, LPSC XXIII, 1415-1416.

S185-91
ABS. ONLY

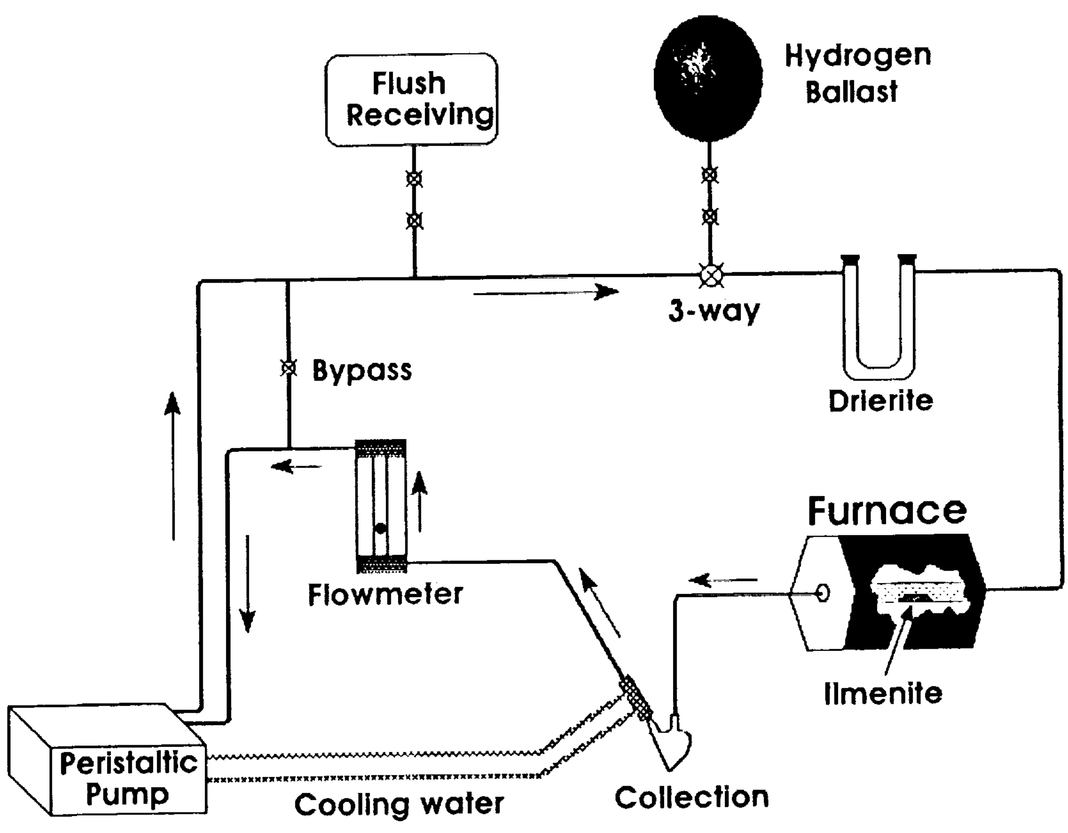
N94-20821

PRODUCTION OF O2 ON THE MOON: A LAB-TOP DEMONSTRATION OF ILMENITE REDUCTION WITH HYDROGEN. Lawrence A. TAYLOR[1], Eric A. JERDE[1], David S. McKAY[1], Michael A. GIBSON[2], Christian W. KNUDSEN[2], and Hiroshi KANAMORI[3]. 1 = Planetary Geosciences Institute, Dept. of Geological Sciences, Univ. of Tennessee, Knoxville, TN 37996; 2 = Carbotek Development Laboratories, Houston, TX 77084; 3 = Shimizu Corp., Space Projects Office, Tokyo, Japan.

Estimates of the costs of transporting materials from Earth to the Moon are around $25,000 per pound. Therefore, it is imperative that we learn to utilize the resources on the Moon to partially offset these "astronomical" expenses The production of oxygen on the Moon utilizing indigenous materials is crucial to the establishment and development of an autonomous lunar colony. Besides obvious biologic needs, this lunar liquid oxygen (LLOX) could result in tremendous cost savings on fuel for effective transportation systems, particularly with its export to low-Earth orbit. Over 20 different process concepts have been proposed and evaluated for the production of oxygen from lunar materials [1-3]. Simplicity, low energy, easily attainable feedstock, and low resupply mass are the keywords for the process(es) which will ultimately be selected for the initial production of oxygen on the Moon. One of these schemes, which has received considerable study to date, is the ***hydrogen reduction of ilmenite.*** In fact, Carbotek, Inc. (Houston, TX) has patented an ilmenite, hydrogen-reduction technique involving a three-stage, fluidized-bed process for the production of LLOX [4]. This abstract explains a lab-top demonstration unit of the basic concepts of this oxygen generation process that has been constructed by our group at the University of Tennessee. It utilizes many of the principles which must be addressed in designing an effective production plant for operation on the Moon.

The fundamental equation that most easily explains the chemistry of this process is:

$$FeTiO_3 + H_2 = Fe + TiO_2 + H_2O; \qquad H_2O \text{ (electrolysis)} = H_2 + 1/2O_2$$



Hydrogen reacts with ilmenite to produce native iron (i.e., zero-valence) and titanium oxide and water, which is electrolytically split to form oxygen and hydrogen, which is recycled. Oxygen is then cryogenically liquified to make LLOX. The amount of LLOX that can be obtained by this process is greater than 10 wt% of the ilmenite reactant. Actually, it can be several percent more, since the TiO_2 is effectively reduced to a less oxygen-rich titanium oxide species.

In addition, it should be possible to process the Fe + TiO_2 product and effectively liberate the Fe for recovery as an additional by-product. It is anticipated that the initial hydrogen will be brought from Earth; however, it is possible that little additional hydrogen make-up (i.e., resupply mass) will be necessary from Earth. This assumption is based upon the establishment of a ready source of hydrogen on the Moon. Lunar soil contains abundant hydrogen (50-100 ppm), and other solar-wind particles, which have impinged upon, penetrated slightly (<200Å), and are lightly held on the surfaces of each soil particle [5]. In fact, lunar ilmenite in the soil acts as an effective "sink" for solar-wind particles, and this ilmenite can contain up to 0.1 wt%. This ilmenite-hydrogen in itself will supply about 10% of the mass needed for complete reduction. If a lunar soil is used for feedstock with little real beneficiation, additional hydrogen input will be realized from the surfaces of the various silicate mineral and glass particles. In fact, a resupply need of 10-20% should be entirely offset by this solar-wind input.

A schematic flow diagram of our lab-top demonstration model is given in Fig. 1. We want to emphasize the simplistic, self-contained nature of this unit. The ilmenite feedstock (pure $FeTiO_3$ with only Fe^{2+}) is placed into the silica-glass tube within the furnace. The system is flushed of air by use of a **balloon of H_2** and the switching of valves while the H_2 is flowing such that the air and H_2 is collected in a flush-receiving bladder. A fresh balloon with about 3 liters of H_2 is attached to the system and stable hydrogen circulation is measured by a calibrated flowmeter. A **peristaltic pump** has two functions: 1) to pump cooling water to the condenser on the out port of the pear-shaped collection flask; and 2) to effectively circulate the H_2 (and H_2O) gas through the system.

The furnace is turned on and reaches 1000°C is about 0.5 hours. The circulating H_2 reduces the ilmenite, forming water vapor that is also carried along with unreacted H_2. The water vapor is either a) condensed out into the pear-shaped flask or b) scrubbed out by absorption into the drierite in the U-tube. In reality, a portion of the H_2O vapor stays as gas, thereby decreasing the effectiveness of the H_2 reduction process (the H_2O causes an increase in fO_2 of the reducing gas). This illustrates an extremely important concept that must be well-addressed in the actual lunar production plant, namely the efficiency of the extraction of H_2O from the system. The kinetics of the ilmenite reduction depend directly upon the H_2/H_2O ratio in the reducing gas -- the higher the ratio, the faster and more complete the reduction. If the mole fraction of H_2O in the gas stream passing over the sample exceeds about 10% at 1000°C, the reaction will be at equilibrium and further reduction will stop. Consequently, it is extremely important to keep the H_2O mole fraction low in the reacting gas.

Using about 20 gm of pure ilmenite as our charge, it was possible to obtain almost 1 cc of condensed H_2O. The remainder of the H_2O produced was absorbed by the drierite, which could be seen to get a pinkish color, particularly at the leading side of the U-tube. In 1.5 hours from the start of the demonstration (about 1 hour at temperature), the ilmenite was observed to be >95% reduced. The kinetics of reduction are fast even in the presence of the small amount of H_2O in the reducing gas. Of course, the kinetics are not as fast as when an open system is used with pure H_2 [6]. The balloon supply of H_2 decreased by about 2 liters, the amount that was converted to H_2O.

We have constructed a "science-fair-like", lab-top demonstration unit for the reduction of ilmenite by hydrogen. We have stressed the self-contained, simplistic design of the entire system, with a total hardware cost of <$1000. It should be possible to make a similar unit into a compact flight package, for Artemis (?), for *in situ* experimentation on the Moon.

REFERENCES: **[1]** Taylor, L.A. & Carrier, W.D., 1992, in Engr., Constr., & Oper. in Space III, ASCE Publ., 752-762; **[2]** Taylor, L.A. & Carrier, W.D., 1992, *AIAA Jour.*, v. 30, no. 12, 2858-2863; **[3]** Taylor, L.A. & Carrier, W.D., 1993, in Resources in Near-Earth Space, U of Ariz. Press, in press; **[4]** Gibson, M.A., Knudsen, C.W., & Roeger, A., 1990, in Engr., Constr., & Oper. in Space II, ASCE Publ., 357-367; **[5]** Taylor, L.A., 1990, in Engr., Constr., & Oper. in Space II, ASCE Publ., 68-78; **[6]** Allen, C.C., Gibson, M.A., Knudsen, C.W., Kanamori, H., Morris, R.V., Keller, L.P., and McKay, D.S., 1992, LPI Tech. Rept. 92-09, Part 1, 1-2.

5186-91 ABS. ONLY

168146

N94-20822

THE Mg-SUITE AND THE HIGHLAND CRUST: AN UNSOLVED ENIGMA

Stuart Ross Taylor[1], Marc D. Norman[2] and Tezer M. Esat[3]
1. Department of Nuclear Physics, Australian National University, Canberra, Australia
2. Planetary Geosciences, SOEST, University of Hawaii, Honolulu HI 96822 U.S.A.
3. Research School of Earth Sciences, Australian National University.

Most of the rocks returned from the highlands are polymict breccias, pulverized by the massive bombardment. However, some monomict breccias with low siderophile element contents are considered to be "pristine" rocks that represent the original igneous components making up the highland crust. Three principal pristine constituents make up the lunar highland crust: ferroan anorthosites, the Mg-suite and KREEP.

Ferroan anorthosite, typically coarsely crystalline with cumulate textures, is the single most common pristine highland rock type, making up probably 80% of the highland crust. The pristine clasts in lunar meteorites are mostly ferroan anorthosites. The major component (95%) is highly calcic plagioclase, typically An_{95-97} with a pronounced enrichment in Eu (Eu/Eu* ~50). Low-Mg and low-Ca pyroxene is the next most abundant mineral, but the mafic minerals are usually minor constituents in this dominantly monomineralic feldspathic rock.

An age of 4440 ± 20 m.y. has been obtained for the Apollo 16 anorthosite 60025 [1] and this is taken to represent the crystallization of ferroan anorthosites from the lunar magma ocean and the flotation of the feldspathic highland crust as "rockbergs." Alternatively, this date represents the "isotopic closure age" during cooling of the crust. Their old age, primitive $^{87}Sr/^{86}Sr$ ratios, uniform composition, Eu enrichment, presence of large massifs of pure (<3% mafics) anorthosite [2] and their global extent all combine to suggest that the ferroan anorthosites crystallized from a magma ocean.

KREEP originated as the final 2% or so melt phase from the crystallization of the magma ocean [3] and is strongly enriched in those "incompatible" trace elements excluded from the major mineral phases (olivine, orthopyroxene, clinopyroxene, plagioclase, ilmenite) during crystallization of the bulk of the magma ocean. This residual phase was the last to crystallize, at about 4360 m.y. and apparently pervaded the crust, with which it was intimately mixed by cratering. Its presence tends to dominate the trace element chemistry of the highland crust. Extreme REE enrichment up to 1000 times the chondritic abundances are known.

The Mg-suite comprises norites, troctolites, dunites, spinel troctolites and gabbro-norites [4]. Some are granulites, possibly from deep within the crust. These rock types are characterized by higher, and so more primitive Mg/Mg+Fe ratios compared to the ferroan anorthosites. They have a range in ages from about 4.43 b.y. down to about 4.17 b.y. although the older limit may be 4.37 b.y. The crucial point is that available data suggest that typical ages are 100-200 m.y. younger than those of the ferroan anorthosites.

The Mg-suite is petrographically distinct from the older ferroan anorthosites and does not appear to be related directly to the crystallization from the magma ocean. It makes up a minor, but signicant proportion (perhaps 20%) of the highland crust. It has two distinct and contradictory components in terms of conventional petrology. It is Mg-rich, commonly with Mg#>90 and so primitive in terms of igneous differentiation, but also contains high concentrations of incompatible elements, typical of highly evolved or differentiated igneous systems. The Mg-suite rocks typically contain REE at 15 to 100 times chondritic. The REE patterns are parallel to those of KREEP and ferroan anorthosites [5]. This KREEP signature does not represent post-crystallization contamination of Mg-suite plutons by KREEP, but was present in the magma from which the Mg-suite crystallized.

The contradictory characteristics of the Mg-suite suggest an origin by mixing of these two distinct components, one primitive to account for the major elements (particularly the high Mg/Fe), and the other evolved to account for the trace element characteristics. The source of the highly evolved component is clearly KREEP. The source of the "primitive" Mg-rich

component is less clear. Conventional theories propose that the Mg-suite arose as separate plutons which intruded the crust as separate igneous intrusions. However, all Mg-suite rocks have parallel REE patterns [5], a characteristic compatible with mixing, but not expected to occur with such regularity in multiple separate igneous intrusions. Furthermore, it is of interest that the Mg-suite contains Mg-rich orthopyroxene, a mineral that is lacking in mare basalts.

Clearly the Mg-suite sources were distinct from those of the mare basalts. During crystallization of the magma ocean, Mg-rich minerals, (e.g. olivine and orthopyroxene) are among the first to crystallize and accumulate on the bottom of the magma chamber, in this case at depths exceeding 400 km. It is sometimes suggested that massive overturning has occurred to bring these within reach of the surface [6]. The isotopic systematics of the mare basalts show that their source regions were solid by 4400 m.y. The only melt remaining was the residual KREEP liquid, which solidified by 4360 m. y. Thus the magma ocean had completed crystallization by 4400 m.y. with only the minor KREEP component remaining liquid until about 4360 m.y. so that the lunar interior was mainly solid at the time of the formation of the Mg-suite. It seems difficult to envisage a massive overturning of the upper 400 km of the lunar interior after 4400 m.y. Other arguments have been advanced for only localized overturning during crystallization of the magma ocean [7].

There is no obvious internal source of energy for remelting early refractory Mg-rich cumulates. Subsequent melting to produce mare basalts took place in more differentiated cumulates and produced lavas with a different mineralogy, without the primitive and evolved characteristics of the Mg-suite. The total amount of mare basalt melt was probably about 0.1% of lunar volume. The melting, fueled by variable amounts of K, U and Th trapped in the cumulates, occurred over a period exceeding 1 b.y. in over 20 separate locations and was essentially trivial on a Moon-wide scale.

The Mg-suite, constituting at least 20% of the highland crust, or 2% of the Moon, has a volume about 20 times that of the mare basalts, and was produced in less than 20% of the time that the Moon took to produce the mare basalts. It requires a major energy source.The problems with the Mg-suite are thus to provide both a large volume of a primitive component (taking the evolved component as KREEP) and a source of energy to produce a magma.

We argue that large-scale overturning of the lunar mantle is unlikely to produce the voluminous and compositionally distinct magmas required to produce the Mg-suite. If the primitive compositions cannot come from the interior, perhaps they came from above. The giant impact hypothesis for lunar origin provides a ring of debris of primitive lunar composition from which the Moon accreted. Sweepup of some leftover objects at relatively low velocities following the formation of the lunar crust might result in mixing of whole Moon compositions with the residual KREEP liquid and with some remelted ferroan anorthosite. Such early impacts at about 4.3 b.y. into hot crust might differ significantly from later basin-forming events in cold crust (e.g. Imbrium, Orientale; note that gravity anomalies are confined to young basins and that the old highlands are in isostatic equilibrium). The resulting magmas could then pond beneath the ferroan anorthositic crust and subsequently intrude the crust. The amount of material added to the Moon need amount only to about 2% of lunar volume. Such a model can account for the mineralogy of the Mg-suite, with orthopyroxene and plagioclase, for the old ages (but younger than the accretion of most of the Moon) and provide both the primitive "whole Moon" component and a sufficient energy source.The production of igneous-textured rocks like 14310 may also be expected.

[1] Carlson, R. W. and Lugmair, G. W. (1988) *Earth Planet. Sci. Lett.* **90**, 119.
[2] Belton, M. J. S. et al. (1992) *Science* **255**, 570.
[3] Taylor, S. R. and Jakes, P. (1974) PLC 5,1287.
[4] see Warren, P.H. *Amer. Mineral.* (in press) for a review of pristine samples.
[5] Taylor, S. R. and Koeberl, C. (1992) *Meteoritics*, **27**, 295.
[6] Ryder, G. (1991) *Geophys. Res. Lett.* **18**, 2065.
[7] Snyder, G. A. and Taylor, L. A. (1992) *Antarctic Meteorites Symposium* **17**, 114.

S387-90
ABS. ONLY

168147

N94-20823

THE SAND BAG MODEL OF THE DISPERSION OF THE COSMIC BODY IN THE ATMOSPHERE

A. V. Teterev
Belorussian State University, Minsk, Belarus

I. V. Nemchinov
Institute for Dynamics of Geospheres, Moscow, Russia

The strength of the extraterrestrial bodies depends on their structure, composition, dimensions and the history of this body but usually is low enough. So the fragmentation of the body due to aerodynamic stresses [2] begins at sufficiently large heights above the surface of the Earth.

The process of fragmentation and dispersion of the fragments usually is studied by the hydrodynamic [1-3] or even gasdynamic [4-5] models. If the fragmentation process begins due the initial cracks and faults of the body, or this body consists of large boulders glued by ice the strength of these boulders after fragmentation remains higher than the aerodynamic stresses exerted at the remaining part of the body. We suppose that fragmentation occurs at initial moment $t = 0$ at some height z_0 above the surface of the air, these fragments remain solid. We do no take into account the possibility of further fragmentation during the remaining part of the trajectory. If the number of these parts is large enough and their size is small in comparison to the initial radius of the body than we can use the sand bag model proposed in [6] in qualitative form.

The quantitative sand bag model used in our computer simulation is as follows. There is a number N of fragments loosely packed in the sand bag, N is large in comparison to unity. For instance, in the computations the results of which are presented in this paper $N = 9 \cdot 10^5$, the initial radius of the sand bag $R_0 = 100$ m, the size of the stony boulders $R_0 = 1$ m and their density $\rho_0 = 2.7$ g/cm^2, the shape of the boulders is spherical, and they do not interact directly between each other.

The motion of the fragments or of the boulders (we call them particles) is governed by the set of simple ordinary differentially equations.

Keeping in mind the uncertainties of the initial stage of fragmentation we have supposed that all the particles have the same size. For the motion of the air we use the equations of gas dynamics and take into account the energy release due to the motion of the particles with the respect to the air. As we have supposed that the initial size of the particles is large enough (boulders with the mass ~ 10^4 kg) the effects of evaporation and ablation are small.

The particles are decelerated by the air and the decrease of their kinetic energy leads to the increase of the internal

energy of the air. Due to these processes the shock wave in the air isformed, the density and the velocity of the air before and between the boulders is changing and thus the motion of the airis coupled to the motion of the particles.

The results for z_0 = 10 km, initial velocity of the particles V = 50 km/sec, and the initial ratio of the volume of the boulders to the whole volume of the sand bag 0.9 are presented. It was assumed that at the initial stage of fragmentation all the particles in the spherical sandbag have attained radial velocities proportional to the their distance from the center of the sphere and the maximum velocity is 0.3 km/sec which is less than the estimates [1] of the lateral velocities [1] due to the aerodynamic forces in the stage of fragmentation and initial separation of the fragments. The shape of the sand bag becomes conical and some of the boulders leave the main volume of the sand bag into the trail, similarly to the gas dynamic simulations [5]. But the main number of the boulders exhibit collective behavior. At the moment 0.2 sec just before the impact the diameter of the sandbag reached 400 m and the its thickness remained 200 m. So the average density before the impact decreases 4 times in comparison to the initial density. The average velocity of the particles in the sand bag and of the sand bag as a whole has slightly decreased but much less than in the case of the fluid volume with the same cross section without the pores when the drag increases proportionally to the area of the cross section. The distances between the boulders is still not large enough and the single bow shock wave which encloses them has not been dissolved into separate bow shock waves yet.

References:

1. Melosh H.J. Impact cratering: a geological process. Oxford University Press, N.Y.,Claderon press, Oxford (1989).
2. Grigorian S.S. Cosmic Research (Kosmicheskie Issledovaniya), 17, 875 (1979).
3. Ivanov B.A. Proc. Lunar. Planet. Sci. Conf. 19, LPSI, Houston, 535, 1988.
4. Korobeinikov V.P., Chushkin P.I., Shurshalov L.V. Solar system research, 25, 242 (1990).
5. Ivanov B.A., Nemchinov I.V., Svetsov V.V., Provalov A.A., Khazins V.M., Phillips R.J. J. Geophys. Research, V 97, № E 10, 16167-16181 (1992).
6. Öpic E.J. Physics of meteor flight in the atmospheres Interscience, N.Y., (1958).

S/88-90
ABS. ONLY

N94-20824

p. 2

ATMOSPHERIC BREAKUP OF A SMALL COMET IN THE EARTH'S ATMOSPHERE

A. V. Teterev, N. I. Misychenko, L. V. Rudak
Belorussian State University, Minsk, Belarus

G. S. Romanov, A. S. Smetannikov
Institute of Heat and Mass Transfer, Belarus

I. V. Nemchinov
Institute for Dynamics of Geospheres, Moscow, Russia

The aerodynamic stresses can lead to the deformation and even to destruction of the meteoroids during their flight through the atmosphere [1]. The pressure at the blunt nose of the cosmic body moving a very high speed through the dense layers of the atmosphere may be much larger than the tensile or the compressive strength of the body. So the usage of the hydrodynamics theory is validated. The estimates [1] show that the transverse velocity of the substance of the body U is of the order of $(\rho_a / \rho_o)^{1/2}V$, where V is the velocity of the body and ρ_o is its density, ρ_a is the density of the atmosphere. The separation of the fragments is larger than the diameter of the body D if $D < D_c = 2H \sqrt{\rho_a/\rho_o}$, where H is the characteristic scale of the atmosphere. For an icy body one obtains U = 1/30 V and critical diameter D_c = 500 m. The process of the disintegration of the body is still not fully understood and so one can use the numerical simulation to investigate it. Such simulations where conducted for the Venusian atmosphere [2] and the gaseous equation of state of the body was used. For the Earth atmosphere for the velocity V = 50 km/s the pressure at the blunt nose of the body is 25 kbar, and is of the order of bulk modulus of compressibility of the water or ice. So we used the realistic EOS of water in tabular form. We assume the initial shape of the body to be spherical and the initial diameter D_o of the body is 200 m and so it is smaller than the critical diameter D_c [1]. The initial kinetic energy of the icy body is equivalent to the energy of the explosion 1200 Mt of TNT. The results of the simulation of the deformation of the body during its vertical flight through the atmosphere and during its impact into the ocean are presented. At the initial moment t = 0

ATMOSPHERIC BREAKUP OF A SMALL COMET: Teterev A.V. et al.

the center of the body was assumed to be at the hight z_0 = 12.5 km. At t = 0.05 sec the instability at the surface of the body predicted in [3] is initiated and at t = 0.15 sec this surface was sufficiently corrugated. A special numerical code used to follow the deformation of such contact surface which allows the areas of one substance which are not connected to main bulk of this substance to be formed in another. It also allows to dissolve these areas when their size diminishes to the size of the interval of the numerical grid.

The outer surface of the body becomes conical as in [2] but at t = 0.20 sec conical cavern near the axis of the body is also formed. The pressure in this cavern is higher than at the outer surface of the body and this causes the outward motion of the walls of this cavern. At the moment t = 0.245 sec just before the impact the diameter of the body reaches 280 m and the back surface of the body is ruptured and the body becomes a hollow shell with a thin rod at the axis. This shell intrudes into the ocean. These stages of the impact resembles the so called swarm impact of a porous (0.1 g/cm^3) icy body [4]. But the hollow shape of the impactor causes the implosion process and the formation of large bubbles in the rising water plume at t = 0.5 sec. At the moments t = 0.8 sec and later one can see the formation of the instability of the water surface which is presumably caused by the air moving behind the blast shock wave along the surface.

The process of the dispersion of the body increase the diameter of the zone of the impact, decreases the average density of the impacting body and diminishes the mechanical effect of the impact.

REFERENCES:1. Melosh H.J. Impact cratering: a geological process. Oxford Univ. Press, N.Y. Claredon Press, Oxford (1989). 2. Ivanov B.A., Nemtchinov I.V., Svetsov V.V., Provalov A.A., Khazins V.M., Phillips R.J. Impact cratering on Venus: Physical and mechanical models. J. Geophys. Res., V.97, № E 10, 16167-16181 (1992). 3. Ivanov B.A. Simple hydrodynamic model of atmospheric breakup of hypervelocity projectiles. In Proc. Lunar Planet. Sci. Conf., 19, Lunar Planet. Sci. Inst. Houston, 535 (1988). 4. O'Keefe J.D., Ahrens T.J. Cometary and meteorite swarm impact on planetary surfaces. J. Geophys. Res. B., V.87, 6668-6680 (1982).

S189-46
ABS. ONLY

N94-20825

ORIGINAL SIZE OF THE VREDEFORT STRUCTURE, SOUTH AFRICA; A.M. Therriault,[1,2] A.M. Reid,[1] and W.U. Reimold;[3] [1]Department of Geosciences, University of Houston, Houston, TX 77204, USA; [2]presently at: Department of Geology, McMaster University, Hamilton, Ontario, L8S 4M1, Canada; [3]Economic Geology Research Unit, at the Department of Geology, University of the Witwatersrand, P.O. Wits 2050, Johannesburg, South Africa.

The Vredefort structure is located approximately 120 km southwest of Johannesburg, South Africa, and is deeply eroded. Controversies remain on the origin of this structure with the most popular hypotheses being: 1) by impact cratering about 2.0 Ga,[e.g. 1,2,3] 2) as a cryptoexplosion structure about 2.0 Ga,[e.g. 4,5] and 3) by purely tectonic processes starting at about 3.0 Ga and ending with the Vredefort event at 2.0 Ga.[6,7] In view of recent work in which the granophyre dikes are interpreted as the erosional remants of a more extensive impact melt sheet, injected downward into the underlying country rocks,[8,9] the impact origin hypothesis for Vredefort is here adopted.

In order to estimate the original dimensions of the Vredefort impact structure, it is assumed that the structure was initially circular, that its predeformation center corresponds to the center of the granitic core, and that the pre-Vredefort geology of the area prior to approximately 2.0 Ga ago is as suggested by Fletcher and Reimold,[10] Figure 4, p.229.

The spatial relationship between shock metamorphic effects, the shock pressures they record, and the morphological features of the crater have been established for a number of large terrestrial craters.[e.g. 11,12,13,14,15] The principles of crater formation at large complex impact structures, comparable in size to Vredefort, have also been established, although many details remain unresolved.[e.g. 16,17] An important conclusion is that the transient crater, which is formed directly by excavation and displacement by the shock-induced cratering flow-field (i.e., the particle velocity flow field existing in the region of the transient crater but behind the initial outgoing shock front), is highly modified during the late stage processes. The original transient crater diameter lies well within the final rim of the crater, which is established by structural movements during late-stage cavity modification.

Using current knowledge of impact cratering processes and following a treatment similar to that given by Grieve and co-workers[18] for the Sudbury Structure, an estimate of the transient crater diameter of the Vredefort structure can be made using the radial position of shock metamorphic effects and the location of outliers of the Transvaal cover rocks at Vredefort. Correction for the large amount of erosion implied over the Vredefort area, larger than at most other terrestrial impact structures, is added to the transient crater dimensions estimated.

At Vredefort, the present location of the limit of shatter cone formation at 26-37 km from the outer edge of the granitic core suggests a transient cavity diameter, at the present level of erosion, of 92-114 km (Table I). Shock-produced microscopic planar features in quartz occur out to a distance of about 13 km from the edge of the core.[3] The outermost planar features developed at Vredefort record shock pressures of at least 6 GPa, according to. Grieve and co-workers.[3] Shock pressures in this range occur at approximately 0.7 the radius of the transient cavity.[19] This would yield an estimate of about 94 km for the diameter of the transient crater at Vredefort, at the present level of erosion (Table I). The outliers of downfaulted Transvaal sediments north of the Vredefort structure[20] also provide a constraint on transient crater dimensions. In eroded complex craters, such as Manicouagan, West Clearwater and Charlevoix, outliers of original cover rocks occur outside the transient crater rim but within the final structural rim. The downfaulted outliers of Transvaal rocks occur at 50-60 km from the outer edge of the granitic core and give an estimated transient crater rim diameter of less than 140-160 km (Table I).

These three spatial estimates constrain the original diameter of the transient crater of the Vredefort structure between 114-140 km (Table I) at the level of present erosion. The final rim diameter of the Vredefort crater, using the same approach as Grieve and co-workers employed to reconstruct the original dimensions of the Sudbury Structure,[18] is then calculated to be 175-280 km, for the present level of erosion (Table II).

McCarthy and co-workers[20] estimated erosional depth of the Vredefort structure at between 5 and 10 km. The estimate of about 8 km of erosion above Vredefort, based on the impact cratering model described in the accompanying paper,[21] thus appears to be reasonable. Using this latter estimate, an additional 8 km of crust above the present level of erosion at Vredefort is worked into the calculations and yields an adjusted estimated transient cavity diameter of about 125-150 km and an adjusted final crater diameter of 192-300 km (Table I and II).

An impact structure of this size would have a complex, probably multiring form.[22] Complex impact structures are characterized by uplifted target rocks in their central areas. The occurrence of an apparent dome of granitic rocks in the core of the Vredefort structure, about 40-56 km in diameter, and representing a 36 km section of crustal rocks[23] is in agreement with uplifting of the target rocks. The exposure of granulite facies rocks, and thus rocks from considerable depths, in the center of the core is expected from the suggested size of the Vredefort structure. Using the relation $D_{cp} = 0.22\ D$,[24] where D_{cp} is the diameter of the central peak, the final crater diameter (D) of the Vredefort structure is estimated to have been 180-255 km at the present level of erosion. After adjustment for the amount of erosion that has occurred over the Vredefort area, these latter values are in agreement with the previous estimates of 192-300 km for the final crater diameter of the Vredefort structure. A maximum structural uplift (SU) of 20-32 km for a structure like Vredefort is determined using the relation $SU = 0.06\ D^{1.1}$,[25] where D is the final crater diameter and units are in kilometers, here D = 192-300 km. This estimated uplift is

in agreement with Hart and co-workers[23] who found that the overturned section of crystalline basement is approximately 25 km thick.

Recently, modeled gravity profiles across the Vredefort Dome have been interpreted to indicate a 100 km wide uplift,[26] which is about twice the diameter of the core of the Vredefort structure. Using this value for D_{cp} in the equation $D_{cp} = 0.22\ D$, the final crater diameter of the Vredefort structure would be estimated at 455 km. This latter diameter estimate, although perhaps too high, would indicate that the high-end values of our 192-300 km estimates best represent the final crater diameter of the Vredefort structure about 2.0 Ga ago.

References: **(1)** Dietz, R.S. (1961) *J. Geol. 69*, 499-516. **(2)** French, B.M. and Nielsen, R.L. (1990) *Tectonophysics 171*, 119-138. **(3)** Grieve, R.A.F., *et al.* (1990) *Tectonophysics 171*, 185-200. **(4)** Bucher, W.H. (1963) *Am. J. Sci. 261*, 597-649. **(5)** Nicolaysen, L.O. and Ferguson, J. (1990) *Tectonophysics 171*, 303-315. **(6)** Colliston, W.P. (1990) *Tectonophysics 171*, 115-118. **(7)** Corner, B., *et al.* (1990) *Tectonophysics 171*, 46-61. **(8)** Therriault, A.M. (1992) M.Sc. thesis (unpubl.). **(9)** Therriault, A.M. and Reid, A.M. Paper presented at the conference: Sudbury 1992 - Large Meteorite Impacts and Planetary Evolution. **(10)** Fletcher, P. and Reimold, W.U. (1989) *S. Afr. J. Geol. 92*, 223-234. **(11)** Dressler, B.O. (1990) *Tectonophysics 171*, 221-228. **(12)** Lakomy, R. (1990) *Lunar and Planet. Sci. XXI*, 676-677. **(13)** Robertson, P.B. (1975) *Geol. Soc. Am. Bull. 86*, 1630-1638. **(14)** Robertson, P.B. and Grieve, R.A.F. (1977) *Impact and Explosion Cratering*, 687-702. **(15)** Stöffler, D., *et al.* (1988) *Deep Drilling in Crystalline Bedrocks, i*, 277-297. **(16)** Schultz, P.H. and Merrill, R.B. (1981) *Multi-ring Basins, Proc. Lunar Planet. Sci. 12A*, 295pp. **(17)** Melosh, H.J. (1989) *Impact Cratering A Geologic Process*, 245pp. **(18)** Grieve, R.A.F., *et al.* (1991) *J. Geophys. Res. 96*, 22753-22764. **(19)** Dence, M.R. (1972) *Spec. Pap. Geol. Assoc. Can. 10*, 7-18. **(20)** McCarthy, T.S., *et al.* (1990) *S. Afr. J. Geol. 93*, 1-4. **(21)** Therriault, A.M., *et al.* (1993) this volume. **(22)** Stöffler, D., *et al.* (1989) *Meteoritics 24*, 328. **(23)** Hart, R.J., *et al.* (1991) *Tectonophysics 192*, 313-331. **(24)** Pike, R.J. (1985) *Meteoritics 20*, 49-68. **(25)** Grieve, R.A.F., *et al.* (1981) *Multi-ring Basins, Proc. Lunar Planet. Sci. 12A*, 37-57. **(26)** Reimold, W.U., and Wallmach, T. (1991) *S. Afr. J. Sci. 87*, 412-417. **(27)** Croft, S.K. (1985) *Proc. Lunar Planet. Sci. Conf. 15th*, 828-842.

Table I: Estimates of the diameter of the transient cavity (D_{tc}) of the Vredefort structure, South Africa.

Observation	Max. radial distance from the outer edge of the core, km	Constraint from other structures	Estimated D_{tc}, km
Shatter cones	26-37	$< D_{tc}$	92-114
Planar deformation features in quartz	13	$0.7D_{tc}$	94
Transvaal outliers	50-60	$> D_{tc}$	140-160

Table II: Estimates of the diameter of the final crater rim (D) of the Vredefort structure, South Africa.

Relationship	Source	Estimated D, km
$D_{tc} = 0.5\text{-}0.65\ D$	Grieve et al., 1981[24]	175-300
$D_{tc} = 1.23\ D^{0.85}$	Croft, 1985[27]	206-285
$D_{tc} = 0.57\ D$	Lakomy, 1990[12]	200-263

For D_{tc} = 114-150 km

5190-46
ABS. ONLY

N94-16815 N94-20826 p.2

ORIGIN OF THE VREDEFORT STRUCTURE, SOUTH AFRICA: IMPACT MODEL; A.M. Therriault,[1,2] A.M. Reid,[1] and W.U. Reimold;[3] [1]Department of Geosciences, University of Houston, Houston, TX 77204, USA; [2]presently at: Department of Geology, McMaster University, Hamilton, Ontario, Canada; [3]Economic Geology Research Unit, at the Department of Geology, University of the Witwatersrand, P.O. Wits 2050, Johannesburg, South Africa.

A model is presented for the evolution of the Vredefort structure, based on reasoned constraints on the original size of the Vredefort structure from observational data[1] and comparison with other terrestrial impact craters. The models for complex craters (ring and multi-ring basins) of Croft,[2] Grieve and co-workers,[3] and Schultz and co-workers,[4] were used to reconstruct the Vredefort impact event, using a final crater diameter of 300 km, as estimated by Therriault *et al.*[1] The sequence of events (stages 2-5) is illustrated diagramatically in Figures 1-4.

Stage 1 - Initial penetration: A meteorite with a possible SSE-NNW trajectory strikes the surface of the earth near the location of the present town of Vredefort, South Africa. At impact, a shock wave is generated and transmitted to the target rocks and back into the impacting body. The generated shock wave accelerates material radially away from the point of impact. With relaxation of the extreme shock pressures, increasing volumes of both target and projectile are vaporised, melted, and fractured. During this stage shatter cones and pseudotachylite rocks are produced.

Stage 2 - Excavation and compression (Fig. 1): Maximum growth of the excavated and transient cavities are reached in this stage by excavation and displacement of material along the transient cavity walls in a radial growth pattern. Very little of the transient cavity volume is actually due to compression of target materials because once the primary shock wave has detached from the flowfield, pressures quickly equilibrate to small values.[2] The primary shock wave decays to an elastic wave and travels outside the transient cavity. Fracturing continues via tensile stresses and cataclastic deformation in the diverging flow. Melted and brecciated material (granophyre rocks and granite breccia in the Inlandsee Leucogranofels[5]) rest beneath the maximum penetration of the projectile.[3] The ejecta sheet (not recognized at present in the Vredefort area) consists of material at many levels of shock metamorphism.[4]

Stage 3 - Dynamic rebound and uplift (Fig. 2): A central uplift of granitic rocks is initiated before the formation of the hinge zone,[2] and before achievement of maximum radial growth. The rebound begins from the lower walls of the transient cavity, trapping a portion of the transient cavity floor and portions of the central down-driven cone.[2] Excavation continues with turbulent flow driving material inward and upward under the crater, and surface material outward over the transient crater rim.

Stage 4 - Maximum radial growth and collapse (Fig. 3): After reaching the apices of their trajectories, all material uplifted by the impact moves downward under the influence of gravity: ejecta falls back, an overheightened and physically unstable uplift collapses with overthrusting and stacking strata, peripheral blocks settle downward and inward, and the highly fractured transient cavity wall and rim collapse into the annular trough of the transient crater around the central uplift. The excess volume is accommodated on the flanks of topographic ring peaks close to the diameter of deep excavation, D_e.[3] Due to its dynamic and highly fragmented state, the rim of the transient crater is probably lost as a distinct structure during collapse. Ejecta, melt, breccia and small blocks of the hinge zone and upper transient crater wall tumble down, mix together and ultimately accumulate on the flanks of the uplift, into fractures, and in the peripheral depression (granophyre dikes as melt filling fractures). At increasing distances from basin center, kinetic energies are smaller and the collapse is more orderly. The rim region will continue to collapse dynamically in larger blocks until a radius is reached where the fracture density is small enough that internal friction and energy loss can overcome the effects of gravitational and dynamical stresses. Structural displacements in the final basin are strongly upward at basin center and at shallow depths. For basins sufficiently large relative to the local crustal thickness, a significant upwelling of dense mantle material below the central uplift is expected.

Stage 5 - Final crater form (Fig. 4): The central uplift collapses to below original surface and further deepening of the peripheral depression occurs.

After deposition of post-impact fallback material (no longer present in the Vredefort area) and prior to the deposition of the Karoo sedimentary cover (Carboniferous to Permian), erosion of about 8 to 10 km is necessary to concur with the present form of the Vredefort structure (Fig. 4). The actual erosion level opens a rare window to the deeper structure of a complex (multi-ring?) impact crater, exposing rocks found below the level of the impact melt sheet, and possibly at, or below, the crater floor. Among others exposed are disturbed target rocks, breccias (as one of the pseudotachylite types), and remnants of the impact melt occurring as fracture fills (in this case the granophyre dikes).

In the case of the Vredefort structure, the observations diagnostic of shock and thus of impact are shatter cones in the collar and basement rocks[6,7,8] and microscopic planar deformation features (although anomalous[9]) in quartz grains of the country rocks and in clasts within the granophyre dikes.[10] Other features found in Vredefort and consistent with impact include the occurrence of coesite and stishovite;[11,12,13,14] a component of circularity to the entire structure; circumferential ring fractures and sets of folds centered around the Vredefort granitic core;[15] and the uplift and exposure of granulite facies rocks, i.e., the Inlandsee Leucogranofels terrain, in the center of the structure.[16]

ORIGIN OF THE VREDEFORT STRUCTURE: IMPACT MODEL: Therriault, A.M. *et al.*

The Vredefort structure has been subjected to approximately 2 Ga of erosion,[16] which has resulted in the removal of the original crater structure and all exterior deposits. Only small amounts of the interior deposits, including parts of the impact melt sheet (the granophyre dikes) and breccias (pseudotachylite veins and dikes, granite breccia in the Inlandsee Leucogranofels) have been preserved within the Vredefort structure.

References: **(1)** Therriault, A.M., *et al.* (1992) this volume. **(2)** Croft, S.K. (1981) *Multi-ring Basins, Proc. Lunar Planet. Sci.12A,* 207-225. **(3)** Grieve, R.A.F., *et al.* (1981) *Multi-ring Basins, Proc. Lunar Planet. Sci. 12A,* 37-57. **(4)** Schultz, P.H., *et al.* (1981) *Multi-ring Basins, Proc. Lunar Planet. Sci. 12A,* 181-195. **(5)** Dressler, B.O. and Reimold, W.U. (1988) Global Catastrophes in Earth History. An Interdisciplinary Conference on Impacts, Volcanism and Mass Mortality, 42-43. **(6)** Hargraves, R.B. (1961) *Trans. Geol. Soc. S. Afr. 64,* 147-161. **(7)** Manton, W.I. (1965) *Ann. N.Y. Acad. Sci. 123,* 1017-1049. **(8)** Simpson, C. (1981) *J. Geophys. Res. 86,* 10701-10706. **(9)** Grieve, R.A.F., *et al.* (1990) *Tectonophysics 171,* 185-200. **(10)** Therriault, A.M. (1992) M.Sc. thesis (unpubl.). **(11)** Martini, J.E.J. (1978) *Nature 272,* 715-717. **(12)** Martini, J.E.J. (1991) *Earth Planet. Sci. Let. 103,* 285-300. **(13)** McHone, J.F. and Nieman, R.A. (1988) *Meteoritics 23,* 289. **(14)** Halvorson, K. and McHone, J.F. (1992) *Lunar Planet. Sci. XXIII,* 477-478. **(15)** McCarthy, T.S., *et al.* (1990) *S. Afr. J. Geol. 93,* 1-4. **(16)** Hart, R.J., *et al.* (1991) *Tectonophysics 192,* 313-331. **(17)** Simpson, C. (1977) M.Sc. thesis (unpubl.). **(18)** Hart, R.J., *et al.* (1990) *Chem. Geol. 82,* 21-50.

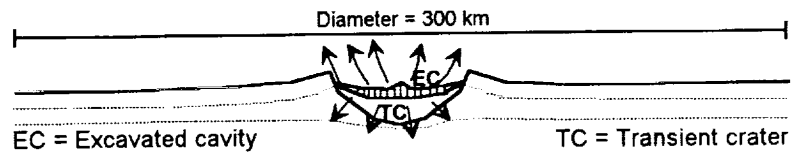


Figure 1: Excavation/Compression

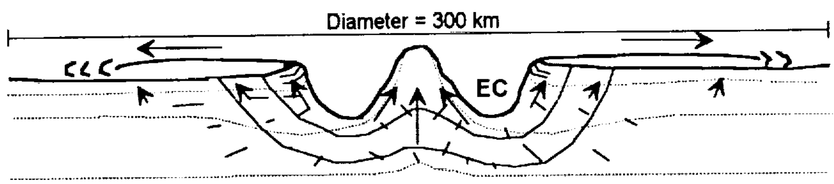


Figure 2: Uplift (excavation)

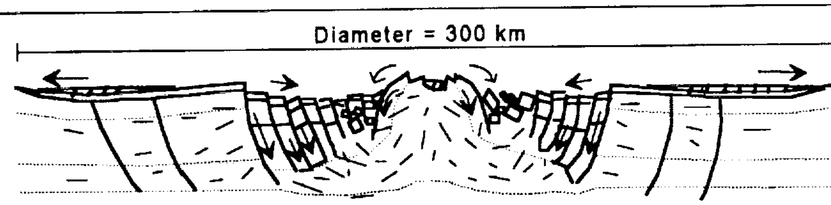


Figure 3: Collapse

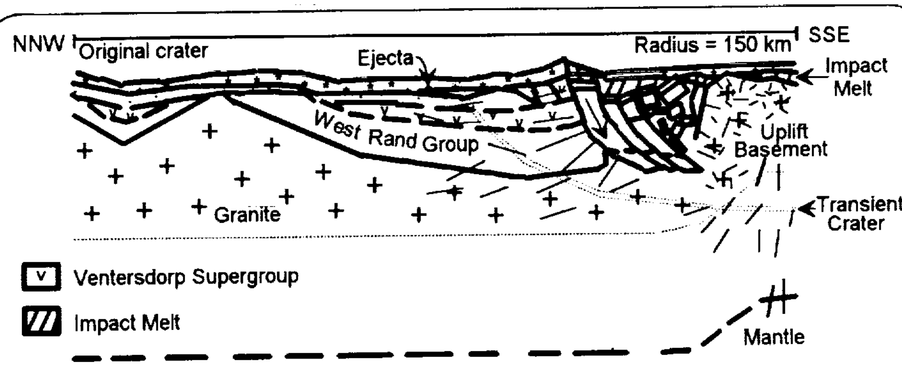


Figure 4: Final crater prior to erosion

3191-70 ABS. ONLY

N94-20827

SYNOPTIC OBSERVATIONS OF NEAR SURFACE PROCESSES OF AN INSOLATED ICE-DUST BODY UNDER SPACE CONDITIONS: THE CASE OF KOSI 9 AND 10; K. Thiel[1], G. Kölzer[1], E. Lorenz[2], H. Kochan[3], J. Gebhard[4], and E. Grün[4]; [1]Abteilung Nuklearchemie, Univ. Köln, Zülpicher Str 47, D-5000 Köln 1, FRG, [2]DLR Berlin-Adlersdorf, FRG, [3]DLR Köln-Porz, FRG, [4]MPI für Kernphysik, Postfach 10 39 80, D-6900 Heidelberg, FRG.

The recent experiments of the Comet Simulation Project, KOSI 9 and KOSI 10 for the first time yielded synoptic results of physically correlated phenomena near the surface of insolated porous ice dust mixtures (90% H_2O, 10% olivine, 0.1% fine dispersed carbon, sample mean density 0.40 ± 0.01 g/cm^3) under space conditions. Correlations were observed e.g. between (a) grain size of emitted dust and dust mantle formation, (b) surface avalanches and local surface temperature, and (c) lateral variations of the surface temperature and the thickness of the dust mantle at the end of the experiment. The dynamic surface processes and the observed structural parameters of the dust mantle and the emitted mineral residues are discussed in view of real comets.

The relevant near surface phenomena were recorded by means of improved diagnostics which is based on the instruments already successfully employed in the previous KOSI experiments, including: Thermoresistors (1), optical (2) and IR cameras (3), gas measuring devices (4), and ice/dust detectors and dust collectors (5-7). After the experiments the sample was off-line studied with respect to albedo (8), mechanical hardness (9), structure, stratigraphy, and composition changes (10-11).

Synoptic data acquisition was achieved by radio controlled computer clocks (based on the German time standard at Braunschweig) allowing synchronization of the various diagnostics to better than 0.1 s. The main topics of interest during the two facility experiments included dust mantle formation and dust emission activity (KOSI 9) and synoptic *in-situ* observation of single dust particles and gas-dust interaction (KOSI 10).

The KOSI 9 simulation experiment for the first time allowed to observe the reactivation of an inactive ice/dust body that had formed a shielding dust mantle (12). Three insolation periods of 8, 11.5, and 12 hrs were chosen, separated by dark phases of 15.25 and 12.25 hrs. The insolation phases included high intensities of 1.4 solar constants for 1, 6, and 6.5 hrs. The recovered sample after ~60 hrs of experiment exhibited a weakly coherent dust mantle of 1...4 mm thickness that allowed to prepare polished sections for off-line structural investigations.

The KOSI 10 experiment that was finished only in November/December 1992 yielded new results particularly on the interrelation of mantle thickness, gas emission and gas-dust interaction on a time scale of 1 s at a time resolution of 20 ms. Test particles hitting the surface under 45° partly removed the dust mantle by mechanical forces and caused an enhanced gas flow, obviously due to the reduced mantle thickness. This was concluded from the different gas dust interaction of

test particles approaching the surface before and after impact of the bulk test material. These observations are of special interest in view of meteoroid impact events on cometary nuclei. Unlike KOSI 9 the final thickness of the dust mantle in the KOSI 10 experiment was only 0...2 mm due to a comparatively short duration of the experiment and a high intensity insolation of 1.6 solar constants at the end of the simulation run. A detailed discussion of the most recent experimental data is in progress.

References

(1) Benkhoff, J. and T. Spohn (1991), Geophys. Res. Lett. 18, 261-264.
(2) Kochan, H. et al. (1991), Geophys. Res. Lett. 18, 273-276.
(3) Lorenz, E. et al., in prep.
(4) Hesselbarth, P. et al. (1991,) Geophys. Res. Lett. 18, 269-272.
(5) Thiel, K. et al., (1990), Proc. 20th Lunar Planet. Sci. Conf., 389-399, Lunar and Planetary Institute, Houston.
(6) Thiel, K. et al., (1991,) Geophys. Res. Lett. 18, 281-284.
(7) Mauersberger, K. et al., (1991), Geophys. Res. Lett. 18, 277-280.
(8) Oehler, A. and G. Neukum (1991), Geophys. Res. Lett. 18, 253-256.
(9) Thiel, K. et al., (1989) NASA Special Publication, Milpitas 1989.
(10) Thiel, K. et al. (1991), Proc. 21st Lunar Planet. Sci. Conf., 579-589, Lunar and Planetary Institute, Houston, and: Geophys. Res. Lett. 18, (1991) 281-284.
(11) Hsiung, P. and K. Roessler (1990), Lunar and Planetary Science XXI, 538-539, Lunar and Planetary Institute, Houston.
(12) Grün, E. et al. (1993), JGR-Planets, submitted for publication.

S192-90 ABS ONLY

N94-20828

p-2

COMETARY INTERPLANETARY DUST PARTICLES? AN UPDATE ON CARBON IN ANHYDROUS IDPS

K.L.Thomas [1], L.P. Keller[2], G.E. Blanford[3], and D.S. McKay[2]
[1]Lockheed C-23, Nasa Rd.1, Houston, TX 77058 [2]NASA/JSC SN, Houston, TX 77058
[3]University of Houston Clear Lake, Houston, TX 77058

Introduction

Chondritic anhydrous interplanetary dust particles (IDPs) are widely considered to be the most pristine samples available for the study of the early solar system because of their primitive mineralogy, chemistry, and isotopic characteristics. Previously, we quantitatively analyzed anhydrous IDPs for light elements and found that these particles have significantly higher bulk carbon abundances than known chondritic meteorites [1]. We have also identified a relationship between carbon abundance and silicate mineralogy which, in general, shows that particles dominated by pyroxenes have a higher carbon abundance than those dominated by olivines. Particles containing equal amounts of olivine and pyroxene show a range of carbon contents and can be grouped with either the pyroxene- or olivine-dominated particles based on their carbon abundance. We have suggested that high carbon pyroxene-rich IDPs are derived from cometary sources [1].

In this study, we have determined bulk compositions and mineralogy of four additional IDPs; one particle has the highest carbon abundance reported in IDPs or any other chondritic material, with the possible exception of the carbon-rich Halley particles.

Methods

Our procedures and extensive analytical checks for quantitative SEM EDX light element analysis are described in detail elsewhere [1]. Following the chemical analysis, the IDPs were embedded in epoxy, thin sectioned using an ultramicrotome, and examined in the TEM.

Results and Discussion

Four IDPs have been added to the data set: L2006P2, L2006B21A, L2005W13, and L2006B23. L2006P2 has bulk carbon abundance of ~4 wt.% and is composed predominantly of olivine (Fo 20-90) with minor enstatite, magnetite and Fe-Ni sulfides (~3-7 wt.% Ni). L2006B21A is a high carbon IDP (~15 wt.% C) which is dominated by low Ca pyroxene grains. A partial magnetite rim is present; olivines are ~Fo 65-70. Both of these IDPs follow the relationship between carbon abundance and silicate mineralogy determined previously for anhydrous IDPs [1].

L2005W13 is a unique IDP because it is composed of two mineralogically and chemically distinct lobes. One lobe is composed of sulfide, enstatite, and olivine (Fo 40-60) grains, while the other lobe is dominated by a Si-rich glassy matrix surrounding tiny crystals <10 nm in size. Both lobes have partial magnetite rims indicative of atmospheric entry heating [2]. SEM EDX measurements indicate that L2005W13 has a carbon abundance of 8 wt.%. However, one of our major assumptions for quantitative carbon analysis is that the carbon is homogeneously distributed throughout the particle. The mineralogical heterogeneity of L2005W13 suggests that the carbon may not be homogeneously distributed throughout both lobes. Since this particle is mineralogically atypical for anhydrous IDPs, we have not included it in our modeling of carbon abundance and mineralogy.

L2006B23 is an ~ 15 um fragment of a group of particles comprising cluster 14 from collection surface L2006. All elements (relative to Si) are chondritic within a factor of two with the exception of Na (7xCI) and C (~13.5xCI). The bulk carbon content of L2006B23 is ~46 wt.%. Examination in the TEM confirms that the particle is dominated by amorphous carbonaceous material. Several sub-micrometer sized fine-grained aggregates also occur similar to those observed in other anhydrous IDP [3]. These aggregates contain numerous FeS and FeNi (kamacite) grains, typically ~5 nm in diameter (ranging from 1-50 nm) embedded in a Si-rich

matrix. Sulfide grains are generally coarser grained than the kamacite; Ni ranges from ~1.5-11.5 wt.%. Grains of forsteritic olivine, on the perimeter of the fine-grained aggregates, are 100-200 nm in size. Like L2005W13, this particle is not included in our modeling because carbonaceous material is the dominant phase and anhydrous silicates are a minor component (<20 vol.%). Of the 15 IDPs studied, only these two particles, L2005W13 and L2006B23, do not fit our model.

Two related IDPs (L2006B15 and L2006B20), from the same cluster as L2006B23, have been analyzed by others using various techniques. Synchrotron X-ray Fluorescence (SXRF) measurements of L2006B15 show that its CI normalized Zn/Fe ratio is 0.27 which indicates that this particle has undergone little or no atmospheric heating (G. Flynn, pers. comm.). Another fragment of the cluster (L2006B20) was heated to determine ^{4}He amounts and ^{4}He release temperatures. These measurements indicate that L2006B20 is definitely an extraterrestrial particle which has undergone little atmospheric heating (A. Nier, pers. comm.).

We have proposed that the high carbon, pyroxene-rich anhydrous IDPs are strong candidates for cometary dust particles. Although we do not exclude the possibility that some carbon-rich IDPs could be derived from asteroids in the outer belt (*e.g.*, P and D asteroids), the abundance of carbonaceous material relative to silicate material is poorly constrained for these asteroids. On the other hand, the olivine-dominated, low carbon IDPs are probably derived from asteroids [1]. The distribution of carbon abundances in the mixed mineralogy particles indicates that this group may contain representatives from either asteroidal or cometary sources. If true, then the low carbon anhydrous IDPs are derived from very primitive sources unlike the carbonaceous chondrites but perhaps resembling the fine-grained material in unequilibrated ordinary chondrites (*e.g.*, Semarkona).

Implications

SXRF and ^{4}He measurements indicate that fragments related to L2006B23 are either unheated or only mildly heated. The lack of heating effects suggests that the entry velocity for this cluster was low, of the same magnitude as dust derived from asteroidal sources [4]. The abundant carbonaceous material and fine-grained aggregates in L2006B23 are incompatible with any known meteorite group. Infrared spectra from anhydrous IDPs containing abundant fine-grained aggregates show similarities to some cometary dust [5]. The compositional and mineralogical data indicate a cometary source for L2006B23. However, cometary particles are generally believed to arrive at the Earth's atmosphere with high velocities. If L2006B23 is truly a cometary particle, then the ^{4}He and SXRF data indicate it arrived at a low velocity. Calculations by [6] show that there are comets with low eccentricities and perihelia > 1.5 AU which should contribute low velocity particles to the stratospheric IDP population.

References: [1] Thomas K.L. *et al.*, (1993) *GCA*, In press. [2] Thomas K.L. *et al.*, (1992) *LPSC 23*, 1427. [3] Bradley J.P. (1993) *LPSC*, this volume. [4] Flynn G.J. (1989) *Icarus*, 287. [5] Bradley J.P. *et al.*, (1992) *Astrophys.J.*, *394*, 643. [6] Blanford G.E. (1993) *LPSC*, this volume.

MAGELLAN MISSION PROGRESS REPORT; Thomas W. Thompson and Magellan Flight Team, Jet Propulsion Laboratory, California Institute of Technology, Pasadena, California

The Magellan spacecraft was launched from Cape Kennedy on May 4, 1989 and was inserted into orbit around Venus on August 10, 1990. The Magellan spacecraft carries a radar instrument that makes synthetic aperture radar (SAR) images of the surface, measures the altitude of the Venusian surface directly below the spacecraft, and obtains radiometric observations of the surface. Radar and radiometric observations of the Venusian surface commenced on September 15, 1990 and continued until September 15, 1992. Gravity observations began on 24 September 1992 and will continue until late May 1993. The radar observations have produced SAR images and surface topography for 99 percent of the surface. These radar observations support the objective of improving the knowledge of the geological history of Venus by analysis of surface morphology and the processes that control them. The gravity observations that are being conducted now support the Magellan objective of improving the knowledge of the geophysics of Venus, principally its density distribution and dynamics. Also, Magellan has generated more digital planetary image data than all previous planetary missions.

During the two years of radar observations, Venus rotated three times under the orbit defining the first 3 mission cycles. The first mission cycle from 15 September 1990 until mid-May 1991 emphasized the acquisition of radar data with images from the left side of the spacecraft. Since periapsis is near 10-degrees north, the first mission cycle imaging from the North Pole to as far south as possible. Some 84 percent of the surface was observed in this first mission cycle. At the end of this first mission cycle, the large unimaged areas were at the south pole and from longitudes of 30 to 50 degrees. During October and November 1990, Venus went through a Superior Conjunction phase when radar observations were not conducted because the Sun interfered with communications between Earth and the Magellan Spacecraft.

The second mission cycle from mid-May 1991 until mid-January 1992 emphasized the filling of these two large gaps. To image the South Pole the spacecraft was rotated and radar observations were made of areas on the right side of the orbit. Also, an Orbit Trim Maneuver (OTM) was conducted at the beginning of cycle 2 to interleave the altimeter footprints for cycles 1 and 2 in the equatorial areas of Venus. (The altimeter footprint of 10 kilometers undersamples the near-equatorial regions because the orbit-to-orbit spacing at the equator is 22 kilometers. The second mission cycle suffered from overheating. Thermal evasions by pointing the large antenna toward the Sun decreased the data downlink to Earth. However, about half of Venus was imaged and cumulative coverage rose to 94 percent at the end of second mission cycle. Unfortunately, a downlink transponder failure late in mission cycle 2 curtailed observations in the third mission cycle.

The third mission cycle was conducted from mid-January until mid-September 1993. Radar observations were once again from areas from the left side of the orbit. A Stereo Test in mid-Cycle 2 showed that Magellan could produce images equivalent to terrestrial stereo photographs from aircraft by reimaging areas observed earlier in Cycle-1 with different look directions. The transponder failure forced the use of a previously degraded back-up unit. However, about 25 percent of the surface was observed with a geometry that complemented those of the first mission cycle. In addition, the last large gap was imaged when the Ushas,

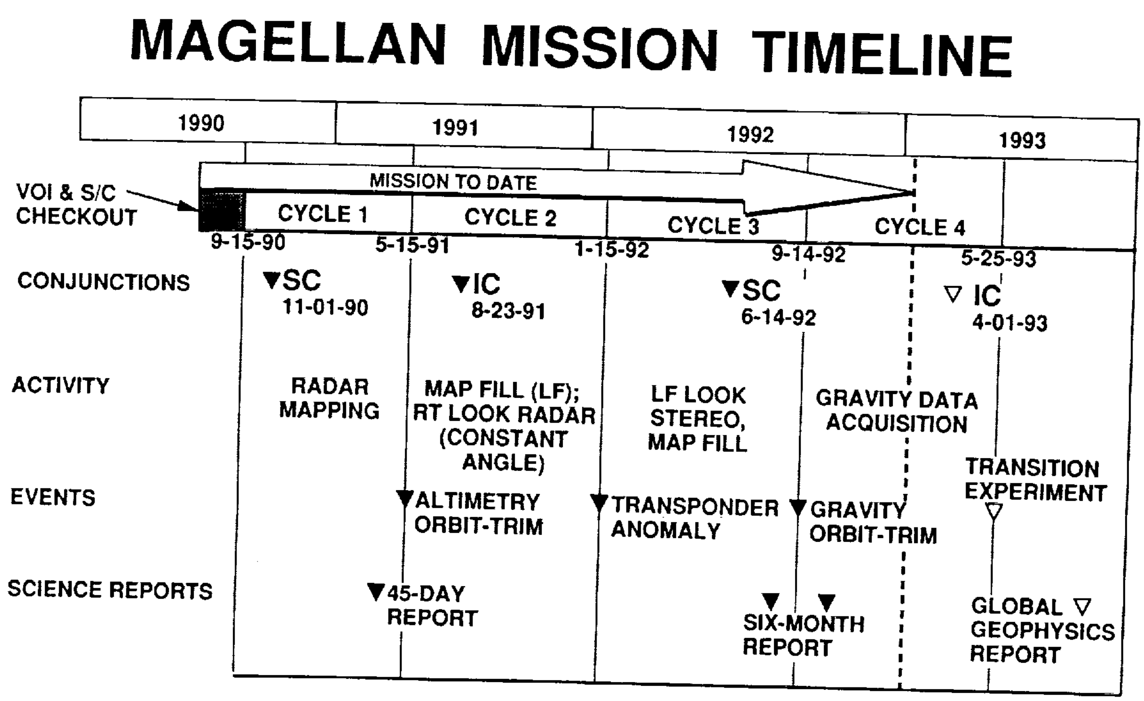
MAGELLAN MISSION REPORT: Thompson, T.W., et al.

Inni, and Hathor volcanoes were observed at the end of mission Cycle-3. Cumulative coverage rose to 99 percent of the surface at this mission cycle. (Figure 1.)

The radar was turned off so the large antenna could be used for gravity observations in the fourth mission cycle, which commenced in mid-September 1992 and continues today. Another Orbit Trim Maneuver (OTM) was performed on 16 September 1992; it lowered periapsis from 275 km to 184 kilometers to provide better lateral resolution of the gravity observations. This fourth mission cycle will continue until late-May 1993. The Magellan Project is currently planning limited aerobraking during the summer of 1993.

Magellan radar products are available as analog photographs and as digital compact disks (CD-ROMs) at the National Space Science Center (NSSDC) at the Goddard Space Flight Center in Greenbelt, Maryland. Over 1000 radar mosaics are available. In addition, altimetry and radiometry products produced by MIT and cartographic products produced by the USGS are available.

Figure 1.



DISCHARGE RATES IN MA'ADIM VALLIS, MARS. G. D. Thornhill, D. A. Rothery, J. B. Murray, Dept. of Earth Sciences, Open University, Walton Hall, Milton Keynes, UK, T. Day, A. C. Cook, J-P Muller, J. C. Iliffe, Dept. of Photogrammetry and Surveying, University College London, Gower St., London, UK.

Introduction. A digital elevation model (DEM) of a small part of the Martian channel Ma'adim Vallis has been produced using the Frankot and Chellappa shape-from-shading algorithm [1]. Software developed by the Dept. of Photogrammetry and Surveying at University College London uses this technique to extract slope information from the grey levels of image pixels. This technique has been applied to a Viking Orbiter image of part of Ma'adim Vallis, and measurements of the channel depth and bed-slope of a channel incised into the floor of Ma'adim Vallis have been made. These results have been used to calculate order of magnitude estimates for discharge rates through the channel. The maximum values calculated are three orders of magnitude less than those for N. Kasei Vallis [2], and are similar to values cited for the Missoula floods [3]. However, when more realistic values of the water depth are used, discharge rates comparable with those for the Mississippi River result [4].

Ma'adim Vallis

This channel is approximately 700 km long and 15-25 km wide, and is situated at 182°W, 20°S, in the Aeolis quadrangle of Mars. An inner channel, incised on the floor of Ma'adim Vallis, is clearly visible near mouth of the main channel, just before it debouches into the150 km diameter crater Gusev. This evidence for a secondary channel forming episode is supported by the irregular blocks occurring where the channel flows into Gusev which have been interpreted [5] to be the remnants of a debris lobe deposited by earlier water flow. A subsequent flood event, which also formed the inner channel, partially eroded this sedimentary deposit, according to Schneeburger [5]. He suggests this may have occurred when water ponded in Gusev breached the northern crater rim and drained away, changing the base level. Paired terraces further upstream may also provide evidence of multiple flooding episodes.

The area covered by the DEM includes part of the inner channel, and it is discharge rates through this that have been calculated.

Methodology

The shape-from-shading software uses an iterative procedure, with initial gradient estimates which are improved by minimising the differences between the observed grey levels, and those predicted by calculations based on the orientation of the sun, and a theoretical photometric function (e.g., Lambertian or Minnaert). The gradients are then projected to form an integrable surface, with the minimisation being carried out on the adjustments required to produce a continuous surface. This procedure is repeated, until a user-defined number of iterations is reached. The effects of surface reflectance and atmospheric scattering are allowed for by using two reference grey levels, one for the lowest grey-level, representing values of areas of the image in shadow, and a second one representing level terrain (based on the modal grey-level, assuming that the image contains large flat areas with uniform grey levels).

Results

The resulting DEM was used to find the depth and bed slope of the channel. The hydraulic radius is the cross-sectional area divided by the wetted perimeter, and is equivalent to the mean depth for channels much wider than deep. For this section of the channel, the hydraulic radius is 52m; the bed-slope is measured at 0.012 (0.7°). The discharge rates are calculated using equations adapted for Mars by Komar [4], using a range of Manning coefficients (from which dimensionless drag coefficients are derived) similar to those used by Robinson and Tanaka [2] . The results of these calculations are shown in Table1.

These values are three orders of magnitude lower than those calculated for N. Kasei Vallis by Robinson and Tanaka [2], which is due to the much smaller channel dimensions in the Ma'adim Vallis case. Also, the general morphology of the channel and surrounding area does not show the characteristic features associated with the larger outflow channels, such as streamlined bed-forms and scouring, so lower discharge rates and a less catastrophic mode of formation would be expected.

However, as the assumption of brim-full flow provides only a maximum estimate, similar calculations were carried out for lower water depths, with a mid-range Manning coefficient. These

results are given in Table 2, and show the effect of water depth on the final discharge rate calculated.

Table 1. Discharge Rates as a function of Manning coefficient for brim-full flow.

n (Manning Coefficient)	Cf (Drag Coefficient)	u (Velocity) (ms^{-1})	Q (Discharge rate) (m^3s^{-1})
0.015	5.9×10^{-4}	62.2	7.1×10^6
0.02	1.1×10^{-3}	46.6	5.3×10^6
0.025	1.6×10^{-3}	37.3	4.2×10^6
0.03	2.4×10^{-3}	31.1	3.5×10^6
0.035	3.2×10^{-3}	26.6	3.0×10^6

Table 2. Discharge Rate as a Function of Depth

Mean depth (m)	u (Velocity) (ms^{-1})	Q (Discharge rate) (m^3s^{-1})
52	37.3	4.2×10^6
25	23.0	1.1×10^6
10	12.5	7.2×10^4
5	7.9	1.3×10^4

Discussion

These preliminary calculations demonstrate the influence of both the Manning coefficient, and thus the drag coefficient, and the assumed water depth on calculations of discharge rate. Thus it will be important in future to attempt to constrain these two factors as closely as possible. Producing detailed DEMs of other parts of this channel will indicate how typical the depth and slope values of this section are, and the implications of changes in these values along the length of the channel can be examined. More extensive and precise topographic data will become available with the MOLA experiment, which will allow improved estimates of maximum channel depths and bed-slopes for some areas of Mars. Using estimates for the discharge rates, further work can be done to calculate theoretical filling times for Gusev, and comparisons with the possible volumes of ground-water or ice available in the source regions may allow for the necessity or otherwise for hydrological recycling to be established.

References

[1] Frankot R. T. and Chellappa R. (1988) IEEE Trans. Pattern Analysis and Machine Intell., 10(4), 439. [2] Robinson M. S. and Tanaka K. L. (1990) Geology, 18, 902. [3] Baker V. R. (1973) Geol. Soc. Am. Spec. Pap. 144. [4] Komar P. D. (1979) Icarus, 37, 156. [5] Schneeburger D. M. (1989) Lun. Plan. Sci. XX, 964.

OBJECTIVE DETERMINATION OF IMAGE END-MEMBERS IN SPECTRAL MIXTURE ANALYSIS Stefanie Tompkins, John F. Mustard, Carle M. Pieters, Donald W. Forsyth, Dept. Geol. Sci., Box 1846, Brown University, Providence, RI 02912

Introduction: Spectral mixture analysis has been shown to be a powerful, multifaceted tool for analysis of multi- and hyper-spectral data (1, 2). The essence of the first phase of the approach is to determine a set of image end-members that best account for the spectral variance in an image cube within a constrained, linear least squares mixing model. The selection of the image end-members is usually achieved using *a priori* knowledge and successive trial and error solutions to refine the total number and physical location of the end-members. However, in many situations a more objective method of determining these essential components is desired. We approach the problem of image end-member determination objectively by using the inherent variance of the data. Unlike purely statistical methods such as factor analysis, this approach derives solutions that conform to a physically realistic model.

Damped Least Squares Model: The underlying assumption of spectral mixture analysis is that each pixel on the surface is a physical mixture of several components, and the spectrum of the mixture is a linear combination of the end-member reflectance spectra. The spectral variability of a scene is thus modeled as a linear combination of a small number of image end-members. The fundamental equations of spectral mixture analysis are:

$$\sum_b r_b f_{ib} = \sum_b . \sum_i r_b f_{ib} + \sum_b E_b \quad \text{and} \quad \sum_i F_i = 0$$

where F_i is the fractional abundance of end-member i in the pixel, R_b is the total reflectance of the pixel in band b, r_{ib} = the reflectance of end-member i in band b, and E_b is the residual error in band b. In a typical spectral mixing analysis, the end-members are prescribed and the fractional abundances and errors are then calculated for each pixel. A two-dimensional graphical representation of mixture analysis is shown in Figure 1. The image end-members (indicated by squares) should reside as close as possible to the boundaries of the data cloud. Fractions that are >1.0 or <0.0 occur for data points that lie outside the region defined by the end-members, and cannot be entirely eliminated no matter how well chosen the image end-members.

Consider, instead, an approach where the end-member spectra are not prescribed, but are treated as unknowns along with the fractional abundances. The model equations are the same as stated above, but because F_i and r_{ib} are both unknowns, they must be solved non-linearly. The approach we have chosen employs a damped least squares non-linear inversion technique as presented by (3). In short, a starting model is provided (a suite of possible end-member spectra, estimated fractional abundances, and the image data to be modelled). Constraints on the solutions are imposed as additional equations (i.e. fractions must sum to 1.0) or as allowable deviations from the starting model (damping of solutions). Both the starting model and the constraints are based on *a priori* knowledge. Each successive iteration of the equations results in a calculated change to the previous model that will reduce the error of the fit. These changes are incorporated and the inversion is run successively until a prescribed error threshold is surpassed. The model results are therefore intimately guided by the inherent spectral variability of the data, the magnitude of the damping, and the constraints imposed on the solutions. The calculated end-member spectra are driven to better bound the data cloud. This is shown in Figure 1 (new end-members indicated by circles). The effects in a spectral sense are illustrated conceptually in Figure 2 (initial end-member spectra are shown by solid lines and calculated end-members by dashed lines). Although the new end-member spectra are not necessarily identical to any pixel spectrum (they can lie outside the data cloud), they provide the best mathematical fit to the whole data set and are determined using a model which is based on a physically realistic description of the surface. One might think of these as *virtual end-members*.

Preliminary Results: This model was developed and refined on a test data set where the end-members and their abundances are known perfectly. This data set provides a working template for establishing the necessary conditions under which the best solution can be derived. The model

successfully reproduces the true end-member spectra in the test data sets for a variety of initial conditions, provided that the model is minimally constrained. An additional step in spectral mixture analysis is determining the optimum number of end-members. Using the test data set, model solutions for fewer than and greater than the correct number of spectral end-members were analyzed. When too few end-members were used, the solution failed to meet the original constraints on the model. The residual error steadily declined as the number of end-members increased until the optimum number was reached; thereafter, the improvement in error was statistically insignificant. Thus, the evolution of error and successful satisfaction of model constraints as a function of the number of end-members can be used to threshold the optimum solution. We continue to use the artificial data sets to develop a better understanding of the model, and establish limits on the amount of *a priori* information that is needed to calculate the true end-member spectra.

The model is now being applied to 8-band CCD images of the lunar crater Bullialdus (4). This requires some restructuring of the program due to the increased number of spectral channels and pixels; however, the model is the same. The starting model is guided by previous investigations (4, 5). Initial results on small data sets within the image show generally the same results as were obtained with the traditional mixing approach, but provide a much lower rms error and only very rare occurrences of superpositive (>100%) or negative abundances. In mixing models, the best image end-members can be considered those that best describe the data cloud (Figure 1), for all bands simultaneously. As was found with the test data, the nonlinear inversion defines virtual end-members that are outside the data cloud, while still providing a physically reasonable solution.

One of the strengths of spectral mixture analysis is the ability to calibrate raw data to reflectance by linking the image end-members to reference end-members from a spectral library. This can be especially advantageous when using data from systems with poorly defined characteristics or areas lacking well characterized reference end-members. Though this can lead to non-unique solutions for the reference end-members, common sense and geologic context help govern the choice of library end-members to which the image end-members are calibrated. The data inversion approach presented here may confer a distinct advantage for proceeding to the calibration stage. The virtual end-members are thought to be more spectrally pure than the image end-members, thereby reducing the number of non-unique solutions. Future work will involve testing this type of calibration using the Bullialdus images, as well as further constraining the mixture model.

References: (1) Adams et al. (1986) *J. Geophys. Res.*, 91: 8098-8112. (2) Smith et al. (1990) *Remote Sens. Env.*, 31: 1-26. (3) Tarantola and Valette (1982) *Rev. Geophys. Space. Phys.*, 20: 219-232. (4) Tompkins et al. (1992) LPSC 23: 1435-1436. (5) Pieters, (1991) *Geophys. Res. Let.*, 18: 2129-2132.

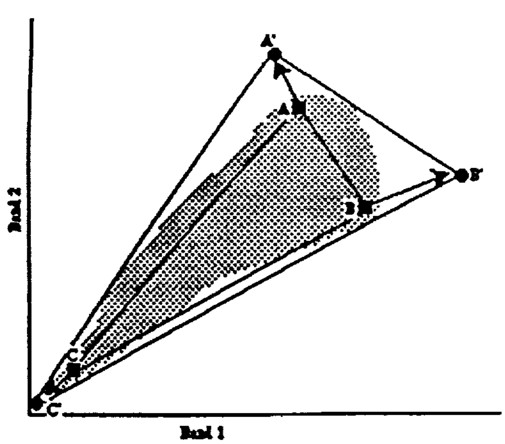


Figure 1: A, B, and C indicate image end-members. A', B', and C' are the model-derived end-members.

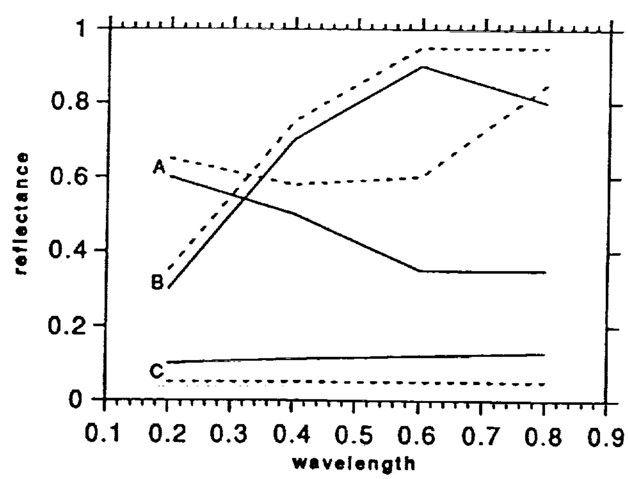


Figure 2: Solid lines represent image end-member spectra. Dashed lines are model-derived virtual end-members.

5196-91
ABS. ONLY

N94-20832

P. 2

DISTRIBUTION AND GEOLOGIC HISTORY OF MATERIALS EXCAVATED BY THE LUNAR CRATER BULLIALDUS Stefanie Tompkins, Carle M. Pieters, John F. Mustard, Dept. Geol. Sci., Box 1846, Brown University, Providence, RI 02912

Introduction: The crater Bullialdus is a 61 km, Eratosthenian-age impact crater located on the western edge of Mare Nubium. Previous analysis of the spatial distribution of materials in the area using nine telescopic near-infrared spectra suggested a possible three-layer structure prior to the impact event: two shallow gabbroic layers and one deeper noritic layer (from a potential depth of 5.5 km) (1). The initial interpretation of this stratigraphy was that Bullialdus may have tapped a layered mafic pluton, such as have been invoked to explain the existence of Mg-suite rocks (2). High-spatial resolution CCD images of Bullialdus were analyzed to better map the spatial distribution of the observed lithologies, and to assess the plausibility of the pluton interpretation.
Data Processing: CCD images were obtained with a Thomson CCD camera mounted on the 2 m telescope (F/D = 25) of the Pic du Midi Observatory. Image dimensions were 194 pixels by 281 lines. Eight spectral images were used at 0.40, 0.56, 0.73, 0.91, 0.95, 0.98, 0.99, and 1.02 µm. Images taken at 0.73 µm and longer wavelengths were calibrated to telescopic spectra (1) using an empirical line method (3). Images obtained at 0.40 and 0.56 µm were calibrated using similar Galileo image data (4) but the accuracy of these spectral calibrations may be lower due to the lower DN values and spatial resolution for Galileo. A linear mixing model was initially used to evaluate the distribution of spectroscopically distinct materials across the crater. In this approach (5, 6), small areas thought to represent distinct lithologies are chosen within the image. The spectral properties of these representative "end-members" are combined in a least-squares mixing algorithm to provide the best fit for each pixel within the image. (For a discussion of objectively identifying and characterizing end-members, see (7)). Images mapping the fractional abundance of each end-member show their spatial distribution. These fractional abundances are constrained to sum to 1.0 for each pixel, and the average fitting error is less than 2%. Surface units can be mapped based on the relative proportion of materials present. Shown in Figure 1 is a map of the distribution of lithologic units based on the spectral mixture model results. Calibrated spectra of end-members are shown in Figure 2.
Discussion: Analysis of the fraction images clearly indicates the western portion of the central peaks (End-member 1) as a localized unit within the crater. From the previously obtained near-infrared spectra (1), the central peaks are interpreted to be anorthositic norite. The remainder of the peaks and part of the floor are a distinctly different unit (End-member 2), with a shallower 1-µm absorption. This distinction can be clearly seen in the end-member spectra (Figure 2). End-member 2 is interpreted to be a second noritic unit, but with a lower abundance of pyroxene relative to plagioclase than End-member 1, comparable to noritic anorthosite. The spatial resolution of the near-infrared spectra is much lower than for the CCD images, and the noritic spectrum identified by (1) was a mixture of these two end-members. End-member 3 includes both wall and rim material, interpreted to be gabbroic in composition (1), with a longer wavelength 1-µm absorption and a relatively immature spectral slope. The small difference in absorption band positions observed previously between the wall and rim near-infrared spectra (1) is not detectable within the spectral range of the CCD images. Relative freshness of the gabbroic materials is distinguished by End-member 4 (associated with the low-albedo area surrounding the crater). This end-member appears to represent mature, well developed gabbroic soils, with the same long wavelength 1-µm absorption as End-member 3, and a redder slope than the other end-members.
Stratigraphy: The surface distribution of materials can be combined with a knowledge of impact cratering dynamics (e.g. 8) and general lunar history (9) to predict the pre-impact stratigraphy beneath Bullialdus. Figure 3 presents a possible cross-section. From top to bottom, the stratigraphic units are: a thin layer (250-500 m) of mare basalt (10), Imbrium and Humorum ejecta (total thickness estimated to be less than 600 m) (11), two types of gabbroic material, and two types of noritic material (noritic anorthosite and anorthositic norite). The upper two layers are inferred from geologic context, but are not observed from the spectral data. The central peak end-members appear to be confined to their respective halves of the crater floor. There are several interpretations for these two central peak units. If the central peaks were derived from the

same depth, their compositional distinction suggests that the two units either were one continuous layer with a lateral change in composition, or that they occurred as two dipping layers. A graben has been mapped that occurs along the contact between the two central peak noritic compositions (12). This graben suggests the central peak compositions occurred separately and would support a model with two separate layers. The direction of dip is not clear, however: the observed distribution could be caused be eastward dipping layers with End-member 2 above End-member 1, or westward dipping layers with 1 above 2.

Possible Interpretations and Implications: The existence of pre-impact layered units with distinct mafic mineral compositions is clear, but the origin of these layers is not uniquely determined. The original layered mafic pluton theory is still viable, although such a pluton would have to post-date or survive the basin-forming events of the area. Another possibility is that the gabbroic material seen at Bullialdus is derived from basalt from older flows within Mare Nubium that pre-date the Humorum and Imbrium basin-forming events, and that the noritic central peaks are sampling the Nubium Basin floor. Alternatively, the geologic setting at Bullialdus provides a possible source for a large differentiated melt sheet. Investigations of the Sudbury Impact indicate that a differentiated impact melt sheet could form within a large impact crater (e.g.13). Bullialdus lies near the center of the 420-km-diameter pre-Nectarian Western Nubium Basin (9, 10). As the Western Nubium Basin could have had a melt sheet approximately 3.5 km thick, a layered mafic body may well exist beneath Bullialdus of an origin similar to that hypothesized for Sudbury. If a differentiated impact melt sheet or pluton was formed in the Nubium Basin, layered sequences could be expected at other basins. A more detailed study of craters in a similar geologic context to Bullialdus (e.g. Copernicus) should be undertaken to examine this possibility.

References: (1) Pieters, C.M. (1991) *Geophys. Res. Let.*, 2129-2132. (2) Warren (1985) *Ann. Revs. Earth Plan. Sci.*, 13201-13240. (3) Edvidge (1988) JPL Pub. 88-38: 97-101. (4) Pieters et al., submitted to *J. Geophys. Res.* 1992. (5) Adams et al. (1986) *J. Geophys. Res.*, 91: 8098-8112. (6) Smith et al. (1990) *Remote Sens. Env.*, 31: 1-26. (7) Tompkins et al., submitted this volume, 1993. (8) Melosh (1989) *Impact Cratering*, 245 pp. (9) Wilhelms (1987) *The Geologic History of the Moon*, 302 pp. (10) DeHon (1979) *Proc. Lun. Sci. Conf. 10th*, 2935-2955. (11) McGetchin et al. (1973) *Earth Plan. Sci. Let.*, 226-236. (12) Trask and Titley (1966) *Geo. Map of the Pittatus Region of the Moon.* (13) Grieve et al. (1991) *J. Geophys. Res.*, 96: 22753-22764.

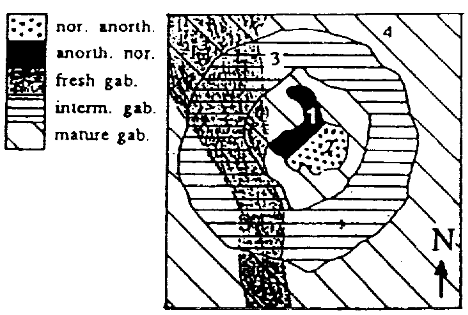


Figure 1: Map of lithologic units seen in spectral mixture model results for the 61 km crater Bullialdus. Numbers indicate location of spectra shown in Figure 2.

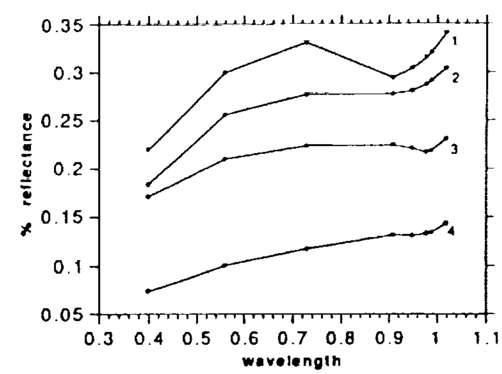


Figure 2: End-member spectra (for locations see Figure 1).

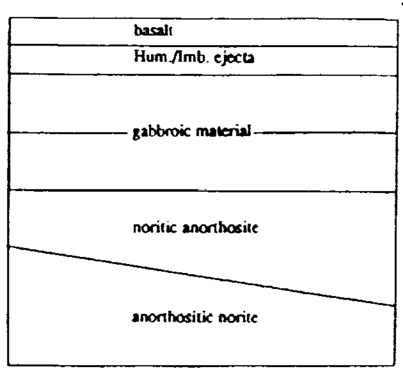


Figure 3: Cross section of possible pre-impact stratigraphy.

CORE FORMATION BY GIANT IMPACTS: CONDITIONS FOR INTACT MELT REGION FORMATION. W. B. Tonks and H. J. Melosh, University of Arizona, Tucson, AZ 85721

Among the many effects of high-speed, giant impacts is widescale melting that can potentially trigger catastrophic core formation. If the projectile is sufficiently large, the melt pools to form an intact melt region. The dense phase then segregates from the melt, forming a density anomaly at the melt region's base. If the anomaly produces a differential stress larger than a certain minimum, it overcomes the mantle's long-term elastic strength and rapidly forms a core. We previously showed that giant impacts effectively trigger core formation in silicate bodies by the time they grow to the mass of Mercury and in icy bodies by the time they grow larger than Triton (Tonks and Melosh 1991, 1992 a, b). In order for this process to be viable, an intact melt region must be formed. We now examine conditions under which this occurs in more detail than previously published.

Experience with observable terrestrial craters indicates that the portion of the melt that is not excavated from the crater, referred to here as the "retained melt", does not form an intact melt region, but is either incorporated in the breccia lens of simple craters or forms a relatively thin surface sheet in complex craters. This is because the melt volume is only a small fraction of the crater's volume. The melt does not significantly affect crater collapse or other modification processes. This is the realm observed in the very largest terrestrial and lunar craters. The melt region formed an annulus approximately 2 km thick around the center of the ~100-150 km Sudbury structure (Grieve, 1991). If the material in which Sudbury was formed had been previously undifferentiated, a layer of dense material would probably be found at the base of this annulus, although certainly not enough to trigger planetary differentiation. Crater scaling relationships imply that as the crater size increases, melt becomes an ever larger fraction of material displaced to form the crater. In craters formed by giant impacts, melt dominates the material that is displaced to form the crater, perhaps even extending below the transient crater's boundary. Melt dominates the crater collapse process, because of its low viscosity. In this case, melt pools to form the intact melt region necessary for dense phase segregation even after crater collapse. There is an obvious transition between these two conditions. The transition is continuous; melt begins pooling in structures as "small" as Sudbury.

Determining a criterion for intact melt region formation is a difficult task. If the melt radius is equal to the crater radius, the crater is formed entirely within the melt region. In this case, it seems obvious that melt completely dominates the crater collapse and pools to form an intact melt pond. However, this is too conservative. The dominance of melt in regulating crater collapse depends on the displaced melt fraction, which we define as the fraction of melt in the material displaced (but not excavated) from the crater. The larger the displaced melt fraction, the lower the effective viscosity of the mixture and the more important melt is in determining the modification flow regime. If the displaced melt fraction is small, melt forms a surface sheet as in Sudbury. If the displaced melt fraction is >50%, the fluid flow mechanism is viscous flow of a liquid rather than solid state or acoustically fluidized flow. There is also a spatial effect-melt is concentrated where excavation streamlines are nearly radial (near the crater's symmetry axis). As the melt region becomes a larger fraction of the crater volume, the remaining displaced solids are located along the crater sides where the streamlines flow upward and outward. This concentrates solids near the surface and causes the bulk of the melt to remain as a body. Because melt dominates modification flow if the displaced melt fraction is > 0.5, this is a plausible criterion for intact melt region formation. Another plausible criterion is if the melt region extends below the transient crater's bottom. If so, some melt pools to form an intact melt region.

We combined the relationship of shock pressure to the shock and particle velocities (the 2nd Hugoniot equation), the linear shock-particle velocity equation to get shock pressure as a function of particle velocity only, and the empirical power law relationship between particle velocity and distance to estimate the shock pressure as a function of distance. This was inverted to determine the radial distance as a function of shock pressure. If the complete shock melting pressure is known, it can be used to compute the radius of the complete melt region. Likewise, the radius to any degree of partial melting can also be computed in the same way. We used the

INTACT MELT REGION FORMATION: W. B. Tonks and H. J. Melosh

ANEOS equation of state to determine the complete and partial melting shock pressures. The melt region's radius depends critically on the projectile's radius.

Once the melt region's radius is known, its geometry determines the melt volume. We used two different geometric models: the hemispherical model, in which the melt region is a hemisphere, and the truncated sphere model, in which the melt region is spherical, but truncated at the planet's surface. Reality lies somewhere between these two extremes.

The crater and excavated melt volumes are found by using the Maxwell Z model (Maxwell, 1977) to determine geometry of the excavated region. We used pi scaling theory (Schmidt and Housen, 1987) to estimate the relationship between projectile diameter, mass, and crater volume. The melt region's radius grows faster with projectile diameter than does the crater radius, causing melt to become increasingly important with increasing projectile mass.

We computed the displaced melt fraction as a function of planet mass for three different projectile/planet mass ratios. Figure 1 was computed for silicate planets; Figure 2 was computed for icy bodies. The displaced melt fraction grows to 0.5 by the time a silicate planet's mass lies between the mass of the Moon and Mercury. Likewise, the displaced melt fraction grows to 0.5 by the time an icy body's mass lies between the mass of Triton and Europa. The precise mass at which the displaced melt fraction grows to 0.5 depends, of course, on the projectile/ planet mass ratio. The smallest ratio shown here is 0.001, sufficient to form a crater approximately 3,000 km in diameter on Earth. If the projectile/ planet mass ratio is smaller, the planet must be larger for the displaced melt fraction to be > 0.5.

Although a precise criterion for intact melt region formation is difficult to define, these calculations illustrate that an intact melt region does not form in very small planets, even if struck by giant impacts. Silicate planets must be at least the mass of the Moon (and probably closer to the mass of Mercury) before an intact melt region forms. Icy bodies must be larger than Triton (and probably closer to the mass of Europa) before an intact melt region forms. This is about the same mass range where we determined that giant impacts trigger core formation in these bodies simply assuming that the intact melt region forms. This work supports our earlier suggestion that giant impacts trigger core formation in silicate bodies larger than the mass of Mercury and in icy bodies larger than Triton. It also suggests that the projectile must be a significant fraction of the planet's mass (>~1%) to trigger core formation in this mass range. Smaller projectiles do not form intact melt regions until the planet grows much larger. Giant impacts do not trigger core formation on smaller bodies because the planet's gravity is too weak to generate the minimum differential stress and because intact melt regions are not formed.

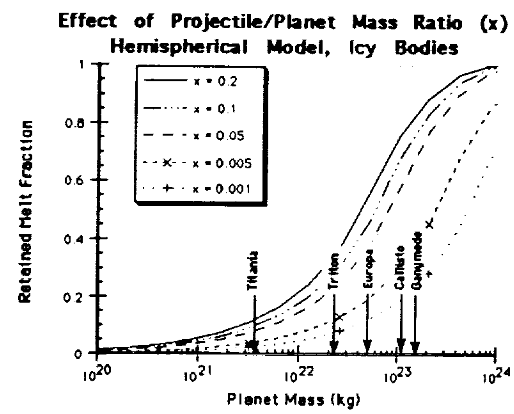


Figure 1

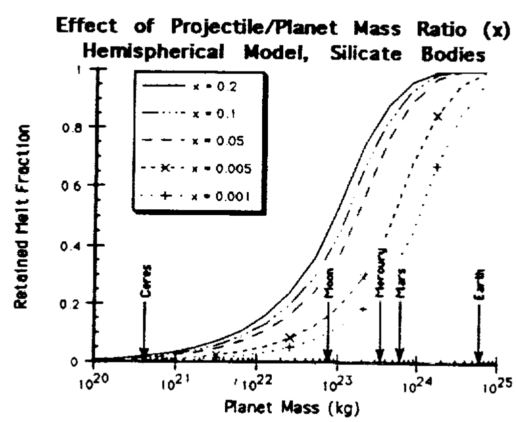


Figure 2

References: Grieve, R. A. F., D. Stöffler and A. Deutsch (1991) *J. Geophys. Res.*, *96 (E5)*, **22**,753-22,764; Maxwell, D. E. (1977) *Impact and Explosion Cratering*, ed. Roddy, Pepin and Merrill, 1003-1008; Schmidt, R. M. and K. R. Housen (1987) *International Journal of Impact Engineering*. **5**, pp. 543-560;.Tonks, W. B. and H. J. Melosh (1991.) *Lunar and Planetary Science XXII*, 1405-1406; Tonks, W. B. and H. J. Melosh (1992a) *Icarus*, **100**, in press; Tonks, W. B. and H. J. Melosh (1992b) *EOS, Trans. AGU*, 27 Oct, 1992, 323.

5198-90
ABS. ONLY

168158

N94-20834

U-Th-Pb, Sm-Nd, and Ar-Ar Isotopic Systematics of Lunar Meteorite Yamato-793169. Noriko Torigoye,[1] Keiji Misawa,[1*] G. Brent Dalrymple,[2] and Mitsunobu Tatsumoto[1]; [1] U.S. Geological Survey, MS 963, P. O. Box 25046, Denver, CO 80225. [2] U.S. Geological Survey, MS 937, 345 Middlefield Rd., Menlo Park, CA 94025

U-Th-Pb, Sm-Nd, and ^{40}Ar-^{39}Ar isotopic studies were performed on Yamato (Y)-793169, an unbrecciated diabasic lunar meteorite whose chemical composition is close to low Ti (LT) and very low-Ti (VLT) mare basalts [1]. The isotopic data indicate that the meteorite was formed earlier than 3.9 Ga from a source with low U/Pb and high Sm/Nd and was disturbed by a thermal event at 751 Ma. Due to the small sample size (104 mg), a plagioclase crystal and glass grains were handpicked for Ar analysis, leaving four fractions for the U-Th-Pb and Sm-Nd studies; a fine-grained fraction (<63 μm; Fine) and three medium-grained fractions (63-150 μm). Medium-grained fractions were divided by density; a heavy fraction (ρ>3.3) consisting mainly of pyroxene (PX1), a lighter fraction (ρ<2.8)) consisting of plagioclase (PL), and a middle density fraction (predominantly pyroxene; PX2). The fractions were washed with acetone and alcohol, and then leached in 0.01 HBr and 0.1N HBr in order to remove any terrestrial Pb contamination. Analysis of the HBr leaches revealed that this meteorite was heavily contaminated with terrestrial Pb during its residence in Antarctic ice.

The residues of leached PX1 and PL exhibited the most radiogenic Pb compositions ($^{206}Pb/^{204}Pb$ values up to 125). The Pb isotopic composition is less radiogenic compared to Apollo mare basalts, but similar to Luna 24170 VLT basalt [2]. The three most radiogenic residues indicate a Pb-Pb age of 3916 ± 90 Ma (Fig.1). The Sm-Nd data for the four fractions yield an internal isochron age of 3470 ± 180 Ma and an initial $^{143}Nd/^{144}Nd$ value of 0.50841 ± 29 (Fig. 2). The $^{40}Ar/^{39}Ar$ age spectrum (Fig.3) for plagioclase is typical of a system disturbed by shock-induced heating, wherein the apparent ages increase with increasing temperature, except during the last 3 increments. The high temperature fractions show ages between 3.9 and 4.3 Ga, but without a plateau. The total fusion age of the glass is 751 ± 4 Ma, which is close to the age obtained from the lowest temperature fraction of plagioclase. Although we cannot define the age of this diabase exactly, our preferred interpretation is that this lunar meteorite was formed earlier than 3.9 Ga and was disturbed by a thermal event at 751 Ma.

If the Sm-Nd age (3.47 ± 0.18 Ga) represents the crystallization age of this lunar meteorite, the age is comparable to ages between 3.3 and 3.6 Ga for most LT and VLT mare basalts. The old Pb-Pb age may be an artifact of terrestrial Pb contamination, still remaining in the residues. However, the apparent Ar-Ar ages from the high temperature fractions strongly indicate a formation age for this meteorite older than 3.9 Ga, so it is apparent that the Sm-Nd age was disturbed by the later thermal event. If this was the case, the formation age of this meteorite may be older than most LT and VLT basalt, and similar to the age obtained from another lunar VLT-like meteorite, Asuka 881757 [3]. By applying a Pb isotopic single-stage evolution model between 4.56 and 3.9 Ga to the data, the source $^{238}U/^{204}Pb$ (μ) value is estimated to be as low as 10. This value is also similar to that obtained from Asuka 881757 [3] and much lower than those obtained for many Apollo mare basalts. The ε_{Nd} value of 5.8 (T=3.47 Ga) for Y-793169 is higher than 3.2 (T=3.3 Ga) for lunar 24170 [4] but lower than 7.3 (T=3.87 Ga) for Asuka-881757 [3] suggesting that the source for Y-793169 is different from that for Asuka-881757 and Luna 24170 VLT basalt. The low μ and high ε_{Nd} values for Y-793169 suggest that the meteorite was derived from a source with low U/Pb and high Sm/Nd in the deep lunar mantle.

* Present address: National Institute of Polar Research, Tokyo 173, Japan.

References: [1] Yanai, K. and Kojima, H. (1991) *Proc. NIPR. Symp. Antarct. Meteorites*, **4**, 70-90. [2] Unruh, D. M. and Tatsumoto, M. (1978) in *Mare Crisium: The view from Luna 24*, G.C.A., *Suppl*. **9**, Pergamon, pp. 689-694. [3] Misawa, K., and Tatsumoto, M. (1992).. Lunar Planet. Sci. Conf. XXIII, 917-918. [4] The Lunatic Asylum (1978) in *Mare Crisium: The view from Luna 24*, G.C.A., *Suppl*. **9**, Pergamon, pp. 657-678.

Fig.1a

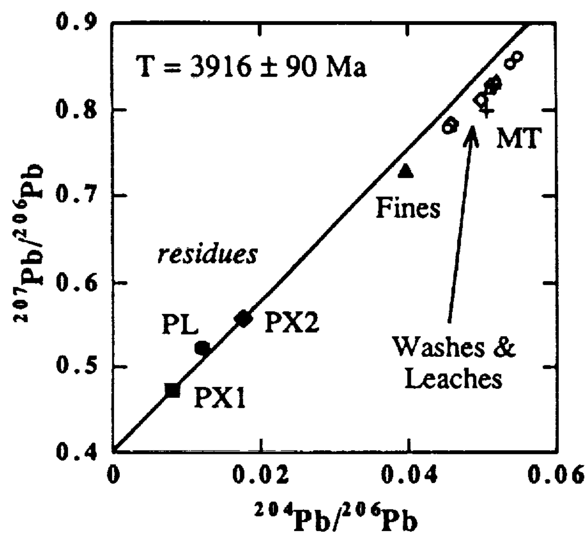
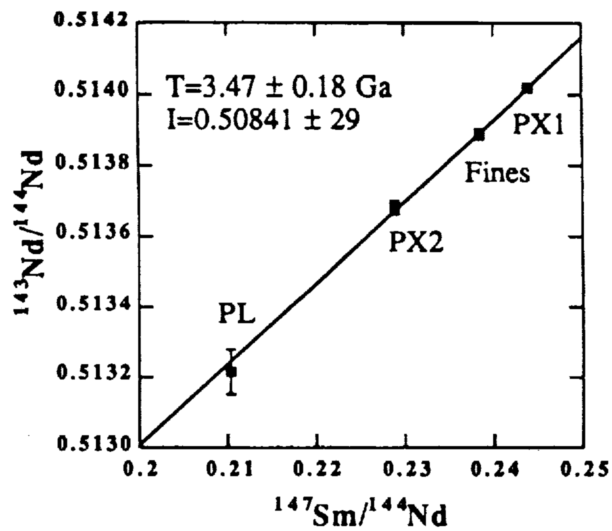


Fig.2



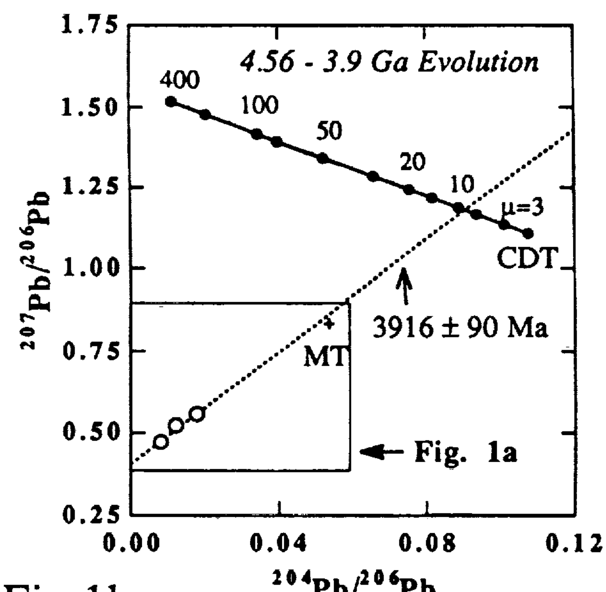


Fig.1b

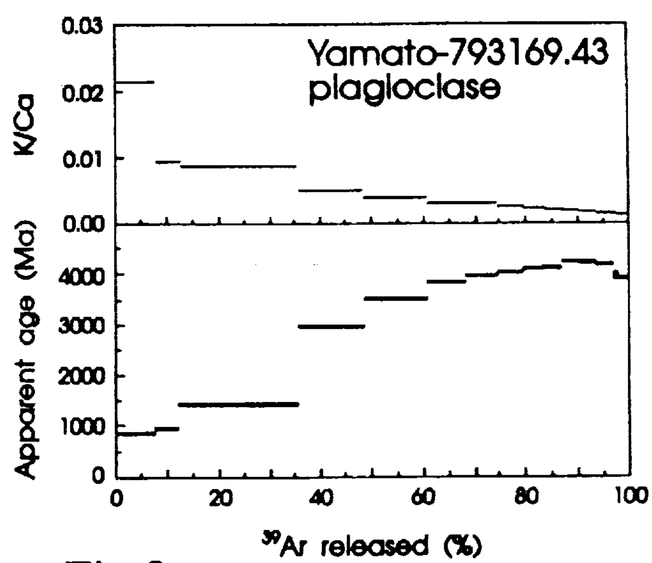


Fig.3

Fig.1(a) $^{204}Pb/^{206}Pb$ vs. $^{207}Pb/^{206}Pb$ diagram for Yamato 793169. The age is calculated from the line fit by three radiogenic residues (PX1, PX2, and PL). MT (+); modern terrestrial Pb. (b) A Pb isotopic evolution model for the source for Yamato 793169. The data indicate the source-μ value of 10. CDT; the Pb isotopic composition of Cañon Diabro troilite. Fig. 2. $^{147}Sm/^{144}Nd$ vs. $^{143}Nd/^{144}Nd$ diagram for the residues of Yamato 793169. Fig. 3. Ar-Ar age spectrum and K/Ca ratios for a plagioclase crystal (0.250mg) from Yamato 793169 were measured by laser incremental-heating. The total gas age is 3257 ± 8 Ma.

S199-91
ABS. ONLY

N94-20835

P 2

COMPLEX RIDGED TERRAIN -RELATED RIDGE BELTS ON VENUS: GLOBAL DISTRIBUTION AND CLASSIFICATION;

T. Törmänen, Department of Astronomy, University of Oulu, SF-90570 Oulu, Finland

56 features were identified in a global survey of complex ridged terrain (CRT) -related ridge belts. Nonrandom aerial distribution was observed with all of the CRT-related ridge belts located to the north of 20°S and increasing in number towards the north. In the equatorial highlands the only concentration of CRT-related ridge belts occurs along N and NE Ovda Regio and western Thetis Regio. Major areas of CRT devoid of related ridge belts (Beta , Phoebe, Alpha Regiones, and northern Lada Terra) are regions dominated by rifting, fractures, coronae, and volcanic features. A noticable concentration of ridge belts is located within a region 20°S-80°N,0°-150°E. Three classes of CRT-related ridge belts were defined: 1) Ridge belts directly in contact with CRT margins, 2) Ridge belts located apart from the CRT boundary, but whose shape and strike are affected by CRT, and 3) Ridge belts terminating against a margin of CRT. There does not appear to be any relation between ridge belt class and type of CRT margin. Some of the class 2 and 3 belts of the 20°S-80°N,0°-150°E region seem to be continuations of adjacent elongated blocks of CRT and could reflect the hypothesized basement of tessera-like material. Majority of class 1 and 2 ridge belts within this region parallel N or NE boundaries of large CRT plateaus or arc-like arrangements of tesserae. These relationships show that this region has been dominated by compressional stresses oriented perpendicular to the CRT boundaries, in N-S/NE-SW direction.

Introduction. Deformational belts on Venus were first identified from Venera 15/16 and Arecibo radar images [1-3]. Magellan radar images revealed that deformational belts fall into three morphological classes [4]. Class 2 belts, i.e. ridge belts [4] are generally thought to be results of compression and shortening [e.g. 4-8], probably fold-and-thrust belts [7,8]. It was earlier noticed that many ridge belts are associated with areas of complex ridged terrain (CRT, also called tessera) [1,7-9]. Plains ridge belts [6], general characterictics, distribution, and formation mechanisms of ridge belts [7,8,10] have been previously studied based on the Magellan data. In this paper we present the first results of an independ-ent global survey of CRT-related ridge belts and propose a classification scheme based on geometric relations between ridge belts and CRT areas. CRT-related ridge belts were mapped using the following criteria: 1) deformational belts domi-nated by ridges (fractures or grooves may be a minor component), 2) location adjacent to areas of CRT, and/or 3) belt formation and shape clearly affected by the presence of nearby CRT.

Aerial distribution. 56 CRT-related ridge belts were mapped from Magellan cycle 1 and 2 C1-MIDRs (all cycle 2 C1-MIDRs were not available for mapping). Identified ridge belts are shown on the map in Fig. 1 (marked with small arrows). A nonrandom distribution of CRT-related ridge belts is observed. 48 (86%) of the identified CRT-related ridge belts are located on the northern hemisphere and only 8 (14%) on the southern hemisphere. There are no CRT-related ridge belts south of 20°S within the mapped area. These results confirm an earlier observation that CRT-related ridge belts are concentrated to the northern hemisphere [7,10].This can be partly explained by the fact that blocks of CRT are more numerous on the northern hemisphere [11], and therefore there are more suitable areas for the CRT-related ridge belts. The number of CRT-related ridge belts and their normalized surface area increase towards the north [10].

In the equatorial highlands the only concentration of CRT-related ridge belts occurs along the northern and north-eastern margins of Ovda Regio and western Thetis Regio (Fig. 1). Large areas around western Aphrodite Terra are deformed by an extensive system of dense swarms of fractures [4,12]. These extensional fractures are youngest tectonic features in the region [4,12]. Extensional stress regime has prevented large-scale ridge belt formation in the area, and fracturing may have also destroyed most of the possible older ridge belts.

There are only a few CRT-related ridge belts in Beta and Phoebe Regiones, and none were identified around CRT areas of Alpha Regio and northern Lada Terra. In both Beta and Phoebe CRT areas have been deformed by large rift zones and sets of fractures and embayed by lavas [e.g. 5,13,14]. Numerous volcanic features are found on the plains surrounding these CRT plateaus [15]. Compressional features of any kind are not common outside CRT in this region. Any signs of earlier compression along the CRT boundaries may have been destroyed by later tectonics and/or covered by lavas. Although there are no CRT-related ridge belts around Alpha Regio and northern Lada Terra, there are compressional ridge belts on nearby plains [4-6]. The lack of CRT-related ridge belts may be connected to the presence of large coronae and associated fracturing and volcanism. More than half of all mapped CRT-related ridge belts and largest part of surface area covered by them are located within a region bounded by latitudes 20°S and 80°N and longitudes 0° and 150°E. This region corresponds to the "0°-150°" cluster of tesserae, excluding Alpha Regio and CRT blocks south of 20°S, identified in [11]. This region contains majority of the CRT boundaries and thus most of the possible locations for CRT-related ridge belts.

Classification. Based on the observations of locations the ridge belts and their relations to CRT three classes of CRT-related ridge belts were defined: 1) Ridge belts directly in contact with CRT margins. More than half (~32) of all identified CRT-related ridge belts belong to this class. They are typically curving belts of even width composed of paral-lel, closely-spaced curving or linear ridges. Ridge widths vary from a few hundred meters to several kilometers and lengths from few kilometers to several 10s of kilometers. Their topography may be very pronounced (heigths varying from a few hundred meters to several kilometers [7]) or they may be very hard to distinguish from Magellan altimetry data. Typical examples of these belts are the steep-sloped, almost 2 km high [7,16] ridge belt adjacent to NE Laima Tessera at 59°N, 60°E and the belt along northeastern Ovda Regio at 6°N,105°E. 2) Ridge belts located apart from the CRT boundary, but whose shape and strike are clearly affected by CRT (~20 belts). These belts include several ridge belts which are part of the large northern fan of plains ridge belts [1,2], e.g. a ridge belt at 68°N,230°E. Other belts of class 2 may be connected to groups of class 1 belts (e.g. at 7°N,112°E) or occur alone near a CRT block. Preliminary analyses do not show major differences in ridge belt or ridge morphology or dimensions between members of two classes. Future work will include more detailed studies of morphologies of ridge belts of classes 1 and 2 and possible refinement of the classification. 3) Ridge belts striking in a large angle and terminating against a margin of CRT. This class has only 4 identified members (triangles in

Fig.1). The belt located at 49°N,130°E differs from the other three: It appears to continue the trend of a distinct structure, a large N-S trough, of the CRT.

Observations and implications of ridge belt - CRT relations. There does not apper to be any relation between ridge belt class and type of CRT margin. Belts of classes 1 and 2 occur along both types of CRT margins: em-bayed and scarp-like [11]. Some of the class 2 and 3 belts within the 20°S-80°N,0°E-150°E region seem to be continua-tions of adjacent partly embayed elongated blocks of large arcuate CRT areas. These ridge belts could reflect the hypothe-sized basement of tessera-like material [11]. Majority of class 1 and 2 ridge belts within this region are located parallel to northern or northeastern boundaries of large CRT plateaus or arc-like arrangements of tesserae. These relationships show that this region has been dominated by compressional stresses oriented perpendicular to the CRT boundaries, and that dominant stress directions were N-S/NE-SW. Class 1 belts located NE of Tellus Regio, NE/E of Ovda Regio and some belts west of Thetis Regio parallel large ridges of the linear ridged terrain unit of CRT [4,17]. The belt ridges are smaller than the CRT ridges, but have very similar morphological characteristics with them. Ridges have been recognized to be the oldest structures within CRT [e.g. 17-19]. The presence of younger, but morphologic-ally similar ridges adjacent to these CRT ridges may give clues to the formation and/or deformation of CRT.

References. [1] Barsukov, V.L. et al. (1986) *JGR*, **91**, D378-D398.; Basilevsky, A.T. et al. (1986) *ibid.*, D399-D411. [2] Frank, S. & Head, J.W. (1990) *Earth, Moon, and Planets*, **50/51**, 421-470. [3] Senske, D.A. et al. (1991) *ibid.*, **55**, 97-161. [4] Solomon, S.C. et al. (1992) *JGR*, **97**, 13199-13255. [5] Solomon, S.C. et al. (1991) *Science*, **253**, 297-312. [6] Squyres, S.W. et al. (1992) *JGR*, **97**, 13579-13599. [7] Suppe, J. & Connors, C. (1992) *ibid.*, 13545-13561. [8] Connors, C. & Suppe, J. (1992) *Workshop on Mountain Belts on Venus and Earth*, 10-12. [9] Head, J.W. (1990) *Earth, Moon, and Planets*, **50**, 391-408. [10] Bilotti, F. et al. (1992) *Int. Colloq. on Venus*, 10-12. [11] Ivanov, M.A. et al. (1992) *Lunar Planet. Sci. XXIII*, 581-582. [12] Michaels, G.A. et al. (1992) *ibid.*, 903-904. [13] Stofan, E.R. et al. (1989) *Geol. Soc. Am. Bull.*, **101**, 143-156. [14] Senske, D.A. et al. (1991) *GRL*, **18**, 1159-1162; Senske, D.A. et al. (1992) *JGR*, **97**, 13395-13420. [15] Head, J.W. et al. (1992) *ibid.*, 13153-13197. [16] Törmänen, T. & Raitala, J. (1992) *Lunar Planet. Sci. XXIII*, 1441-1442. [17] Bindschadler, D.L. et al. (1992) *JGR*, **97**, 13495-13532. [18] Bindschadler D.L. & Head, J.W. (1991) *ibid.*, **96**, 5889-5907. [19] Törmänen, T. (1992) *Int. Colloq. on Venus*, 125-127.

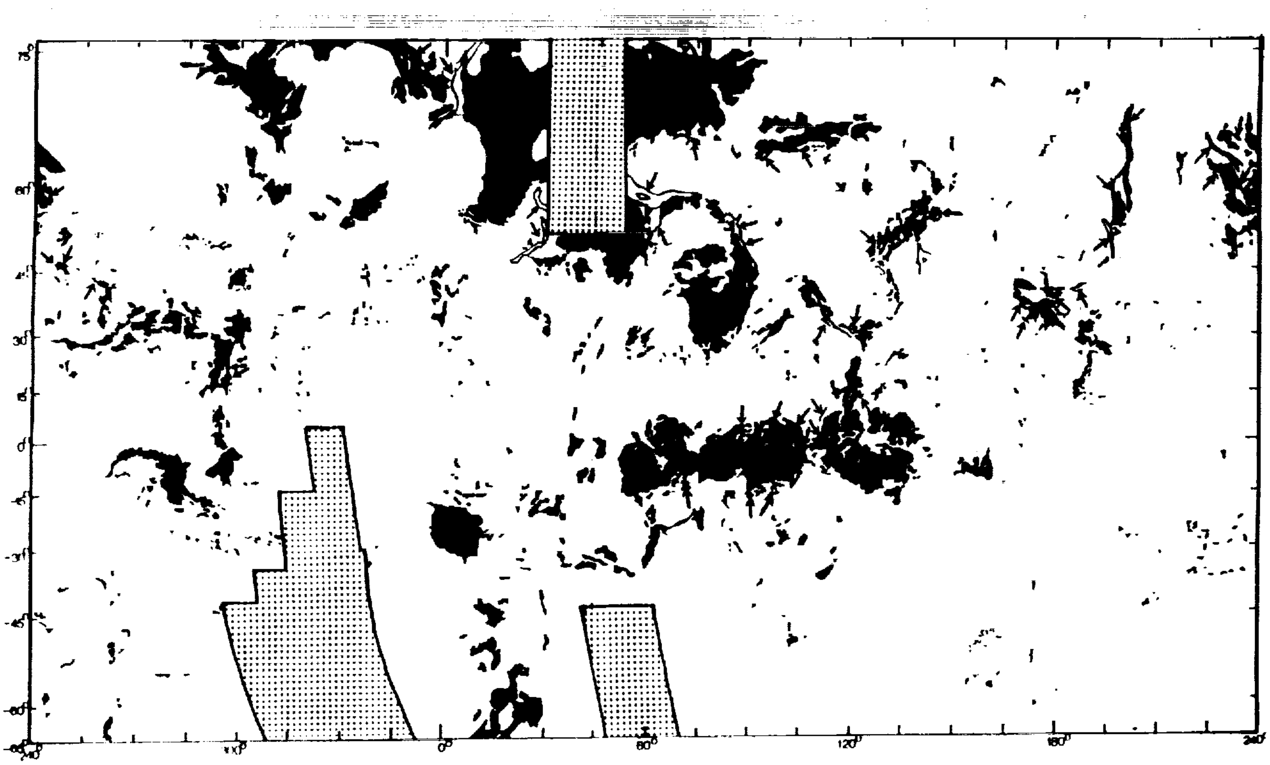


Fig. 1. Distribution of CRT-related ridge belts. Small arrows and triangles point to features. Base map modified from [11].

S200-90 ABS. ONLY

N94-26836

THE PARENT MAGMA OF THE NAKHLA (SNC) METEORITE: RECONCILIATION OF COMPOSITION ESTIMATES FROM MAGMATIC INCLUSIONS AND ELEMENT PARTITIONING. A.H. Treiman, C-23, Lockheed Engineering and Sciences Co., 2400 NASA Rd 1. Houston TX 77258.

The composition of the parent magma of the Nakhla meteorite has been difficult to determine, because it is a cumulate rock, enriched in olivine and augite relative to a basalt magma. A parent magma composition is estimated here from electron microprobe area analyses of magmatic inclusions in olivine [1]. This composition is consistent with an independent estimate based on the same inclusions [2], and with chemical equilibria with the cores of Nakhla's augites (recalculated after [3]). This composition reconciles most of the previous estimates of Nakhla's magma composition, and obviates the need for complex magmatic processes [4]. Inconsistency between this composition and those calculated by [5] suggests that magma flowed through and crystallized into Nakhla as it cooled [6].

The Nakhla meteorite is one of the SNC group, inferred to be igneous rocks from the Martian crust. Nakhla is a cumulate rock, enriched in augite and olivine compared to basaltic magma [4-8]. The composition of Nakhla's parental magma is of great importance for Martian petrology and mantle geochemistry, but has proved difficult to determine [2,3,5]. Magmatic inclusions, the remnants of magma trapped within solid phases, are abundant in Nakhla's olivines and provide another method of estimating Nakhla's parental magma [2,9].

INCLUSIONS Thin sections of Nakhla used here included two from the Harvard Mineralogy Museum and 22 serial sections from the Smithsonian Institution. The magmatic inclusions in Nakhla's olivines have been described by [1,2,9], and consist of augite rich in Al and Ti, granitic glass, feldspars, Fe-Ti-Cr oxides, and phosphates. Adjacent to the host olivines are rinds of augite + Fe-Ti-Cr oxide only.

PARENT MAGMA COMPOSITION Bulk compositions of 24 magmatic inclusions (20 and 350 μm diameter) in Nakhla olivines were obtained by rastered-beam EMP analysis. Projected from olivine composition, inclusions larger than 50 μm diameter have essentially the same composition, suggesting that these larger inclusions represent fair samples of host magma, and that these inclusions sampled a single parent magma. The average of these analyses was corrected for the proportion of host olivine included in the analytical volumes, and the difference between the true volume proportion of rind and the proportion actually analyzed. To retrieve the composition of the magma originally entrapped in the inclusions, this corrected average inclusion (Table) composition was modified by Fe/Mg exchange and addition of olivine to have: FeO/MgO in equilibrium with the core augites; and both augite and olivine on its liquidus. This calculated inclusion magma composition, NK93 (Table, Figure), also has Al_2O_3/TiO_2 and Na_2O/TiO_2 abundance ratios consistent with the geochemistry of the SNCs [10].

OTHER ESTIMATES OF PARENTAL MAGMA COMPOSITIONS

Magmatic Inclusions of [2]. The same magmatic inclusions studied here were recently investigated by phase analyses (EMP) and a linear least squares minimization method [2]. That parent magma composition, NK3, contains much more FeO and MgO than NK93, but projects from OL(ivine) to essentially the same point as NK93 (Table, Figure). From the liquidus boundaries of [11], NK3 appears to have olivine as its sole liquidus phase. Other than olivine content, the most significant difference between the two compositions is that NK3 has more than 3 times the Ti of NK93. It is possible that the least squares method has insufficient constraints on Ti abundances.

Element Distributions. Augite/basalt partition coefficients for major and minor elements were used by [3] to calculate a parent magma, N (Table, Figure). Unfortunately, the augite composition used had half the Al_2O_3 of more recent analyses ([4], unpubd. data). Recalculation following [3] yielded N' (Table, Figure); within the uncertainty of the partition coefficients, N' is identical to NK93.

Mass Balance. Assuming that Nakhla formed as a closed system of cumulus grains and intercumulus parental magma, [5] calculated the composition of that magma by mass balance on bulk and mineral compositions for a range of proportions of intercumulus magma. Those calculation have been redone correcting errors and using revised mineral compositions, with the resultant compositions (A'-E', Figure) now constrained to have augite and olivine on their liquidi. B' has the proper MgO/FeO. These compositions are inconsistent with NK93, N', and NK3, suggesting that Nakhla probably was not closed during crystallization, but was affected by infiltration metasomatism [6].

CONCLUSIONS A parental magma composition for Nakhla estimated from magmatic inclusions in olivine are consistent with that estimated from major and minor element abundances in augite. This consistency suggests that Nakhla's olivines and augites grew from a single parental magma with composition like NK93. Multiple parent magmas or xenolithic olivine [12] are not required. The failure of calculations of [5] to yield the same composition suggests that Nakhla was not a closed system after crystal accumulation.

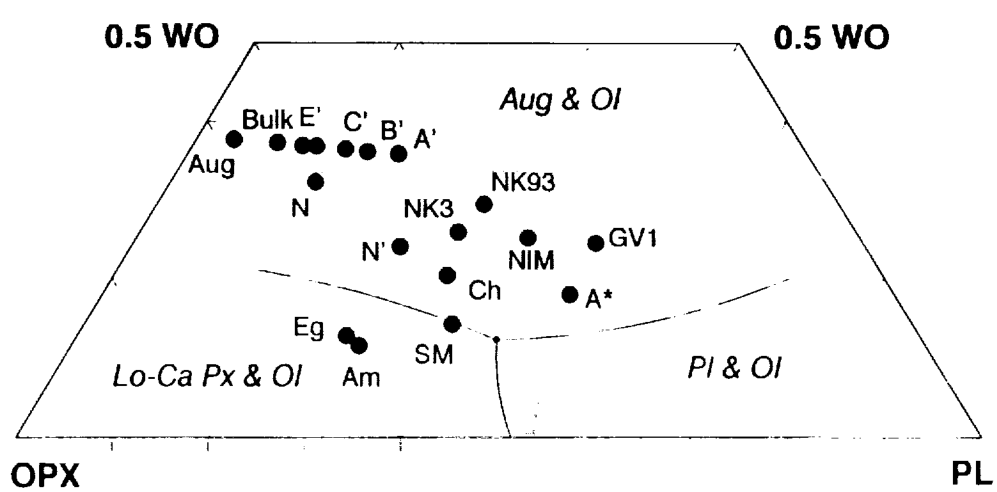
I am grateful to J.H. Jones and J. Berkley for their many helpful suggestions. J. Wood, B. Holmberg, G. McKay, and V. Yang assisted with EMP analyses. Support was from an NRC Senior Fellowship.

[1] Treiman A. (1993) GCA, sub. [2] Harvey R. & McSween H.Jr. (1992) EPSL 111, 467. [3] Longhi J. & Pan V. (1989) Proc. LPSC 19th, 451. [4] Treiman A. (1990) Proc. LPSC 20th, 273. [5] Treiman A. (1986) GCA 50, 1061. [6] Berkley J. et al. (1980) Proc. LPSC 11th, 1089. [7] Bunch T. & Reid A. (1975) Meteor. 10, 303. [8] Harvey R. & Mcsween H.Jr. (1992) GCA 56, 1655. [9] Treiman A. (1992) LPS XXIII, 1447. [10] Treiman A. et al. (1986) GCA 50, 1071. [11] Longhi J. (1991) Am. Mineral. 76, 785. [12] Stolper E. & McSween H.Jr. (1979) GCA 43, 1475. [13] McSween H.Jr. et al. (1988) LPS XIX, 766. [14] Johnson M. et al. (1991) GCA 55, 349.

Table. Nakhla's Magmatic Inclusions and Estimated Parent Magmas

	Avg.Incl.	NK93	NK3	N'
SiO_2	53.7	50.2	45.8	50.5
TiO_2	1.1	1.0	3.1	1.4
Al_2O_3	10.2	8.6	7.2	6.8
Cr_2O_3	0.1	0.1	n.g.	0.1
FeO	10.8	19.1	26.2	21.9
MnO	0.2	0.4	n.g.	0.4
MgO	3.9	4.0	5.7	4.3
CaO	14.0	11.9	10.4	13.0
Na_2O	1.5	1.2	0.8	1.2
K_2O	3.3	2.8	1.4	0.3
P_2O_5	0.8	0.7	n.g.	n.g.

Figure. Inferred parental magma compositions for SNCs. Projection in oxygen units from OL(ivine) and liquidus boundaries from [11]. Proposed nakhlite parent magmas are: NK93 here, [1]; NK3, GV1 and average NIM [2]; A' through E' [1] after [5]; N [3]; N' [1] calculated as in [3]. Also shown are Nakhla bulk and average of Nakhla core augite (AUG) compositions. Other proposed SNC magma compositions are: SZ, Shergotty and Zagami [12]; Eg, EETA79001 and Ch, Chassigny [3]; Am, ALHA77005 [13]; A*, Chassigny [14].



S201-90
ABS-ONLY

N94-20837

p. 2

INTACT CAPTURE OF HYPERVELOCITY PARTICLES ON SHUTTLE

P. Tsou[1], D. E. Brownlee[2], & A. L. Albee[3]
[1]Jet Propulsion Laboratory, [2]University of Washington, [3]California Institute of Technology

The capability for capturing micrometeoroid analogs intact through laboratory simulations in passive underdense media offers a valuable tool for cosmic dust research [Tsou 1984, Tsou 1990, Tsou 1992]. However, no amount of laboratory simulations can replace actual space experiments due to the technical inability to launch high fidelity analogs of micrometeoroids in ground laboratories and then reliably simulating high hypervelocities (greater than 7 km/s). Fluffy composite micrometeoroid analogs tend to break up and have not survived laboratory launches at beyond 4 km/s, however, a new technique of launching cluster analogs was developed for the two-stage light-gas gun at NASA Ames Vertical Gun Range [Tsou 1988]. Plasma drag or electrostatic accelerators may be able to achieve higher speeds than two-stage light-gas guns but only with very limited projectile compositions and may result in severe projectile deformation [Tsou 1990]. Consequently, a space demonstration of intact capture has been sought since 1983. This abstract reports initial results from our STS-47 flight, which carried the first Shuttle Sample Return Experiment (SRE) with silica aerogel capture media, September 1992.

EXPERIMENT Five thermal insulated end covers for the Shuttle Get Away Special (GAS) Program payload canisters were modified to hold capture cells. These end covers were placed on top of the GAS payload canisters and were designed to replace standard covers. Each modified cover is 57.6 cm in outer diameter, and contained twenty-one 10 cm x 10 cm capture cells as shown in Figure 1.

The clear silica aerogel capture cells were about 1 cm thick and had densities in the range of 20 mg/ml. Each of the aerogel capture cells was cast individually in the desired dimensions but eight of the corner cells had to be rounded to fit into the cover as seen in Figure 1. To minimize launch vibration damage, each capture cell was edge-wrapped with a thin layer of space approved polyamide foam to fit snugly. Due to structural requirements, the actual active surface area for each cell was 9 cm x 9 cm minus the corners, making a net total of .165 m^2 of surface exposed for each SRE.

The primary payload on STS-47 was the Japanese Spacelab, "Fuwatto" (weightlessness). The GAS bridge is mounted in the aft of the Shuttle payload bay. The intact capture SRE was in the eighth position of the bridge, closest to the aft wall of the Shuttle payload bay (Bay 12), on the port side. The top of the capture surface was about mid-height of the Shuttle payload bay. As the Shuttle payload bay door opened, SRE's field of view was limited most by the Shuttle's tail with about a 75° acceptance angle and about 45° from the back edge of the Japanese Spacelab. The field of view from the starboard and port sides was essentially a full 180°. The SRE was covered during the GAS payload integration process only.

STS-47 was an extended 9 day mission from September 11 through September 19, 1992. The cruising altitude was 300 - 304 km at a 28.5° inclination. The Shuttle's tail was pointed at Earth while its right wing pointed in the velocity vector; consequently, the orientation of the SRE was normal to the ram direction, facing space in the plane perpendicular to Earth's radius. The total 'space' exposure time is estimated to be approximately 170 hours.

RESULTS All twenty-one aerogel cells were returned without any apparent damage under optical inspection at 192X. Upon initial examination, there were at least four large hypervelocity particles captured in three of the cells. Ample evidence of the notorious Shuttle payload bay contamination has also been captured intact on these cells. Initial optical in situ examination of the captured hypervelocity particles has been carried out. Particle extraction followed by chemical and structural analyses is in process.

The track morphology of the captured particles reveled a typical carrot-shaped track pointing to a particle lodged at the tip of the track as shown in Figure 2. One of

these tracks is 1.5 mm long, with the maximum diameter of 50 um indicating a hypervelocity capture in the range of 6-8 km/s. The primary particle at the tip of the track is estimated to be about 10 - 20 um in size. Two smaller particles split off during capture at 1.1 mm with an estimated size of 5 - 10 um and 1 um, respectively.

The second and third hypervelocity captures appear similar to the first and have carrot tracks next to each other as shown in Figure 3. The track length of the second capture is 2.1 mm long with a maximum diameter of .14 mm. The second primary particle is estimated to be 30 - 40 um. The third capture track is 1.4 mm long and 100 nm in maximum diameter. The third primary particle is estimated to be 5 um in diameter. Based upon the capture track morphology and the splitting of the projectile, these three particles are characteristic of silicate particles rather than space debris.

The fourth hypervelocity capture was substantially different from the other three captures having a considerably larger carrot track with significant radial cracking, similar to bullet holes in window glass as shown in Figure 4. Radial cracking is characteristic of impacts in very high density aerogel. The entry hole is about 70 um. This particle is more likely a large piece space debris traveling at high speeds.

FINDINGS Silica aerogel capture cells survive the Shuttle launch and reentry and incontrovertibly capture hypervelocity particles intact. The large hypervelocity particle flux for this SRE is estimated to be 2.5 to 3.5 (10 - 30 um) per m^2, per day.

ACKNOWLEDGMENT The assistance of Douglas Buettner in making the aerogel cells is gratefully recognized. The efficient GAS staff is greatly appreciated. This work was carried out in part by the Jet Propulsion Laboratory, California Institute of Technology, under NASA contract.

REFERENCE Tsou, P., et al, LPSC 15 (1984), Tsou, P., et al, LPSC 19 (1988), Tsou, P., et al, LPSC 21 (1990) and Tsou, P., et al, LPSC 23 (1992).

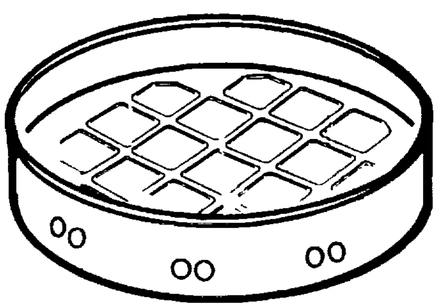


Figure 1. GAS SRE



Figure 2. Track 1

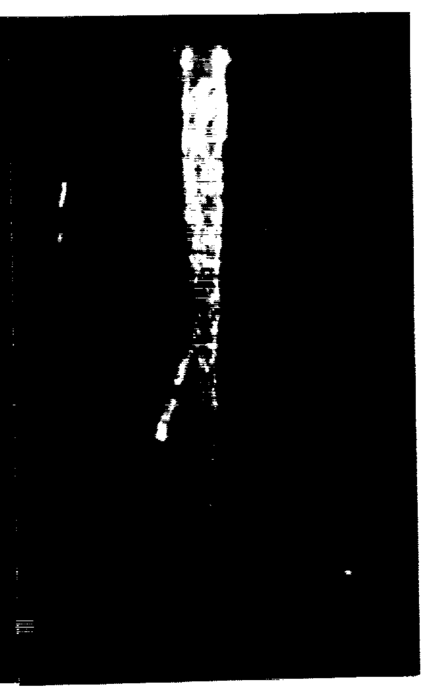


Figure 3. Track 2 & 3

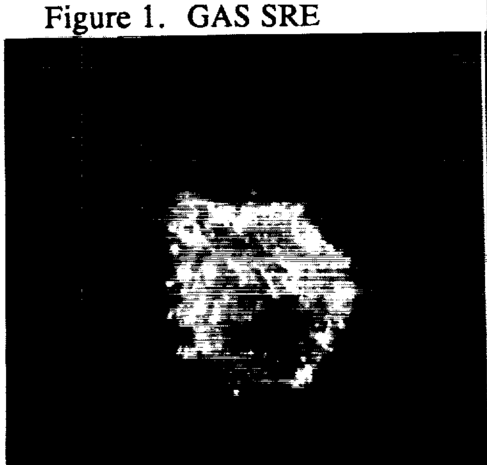


Figure 4. Capture Track 4

S202-91
ABS ONLY

N94-20838

p. 2

PHOTOGEOLOGICAL ANALYSIS OF EUROPAN TECTONIC FEATURES; B. R. Tufts, Dept. of Geosciences, University of Arizona, Tucson, AZ 85721

Preliminary photogeological analyses of the Pelorus Linea and Sidon Flexus regions of Europa were conducted to explore the proposal by Schenk et al that lateral motion of crustal blocks has occurred in a "rift zone" including possible strike-slip, tension fracturing, and geometric plate rotation about an Euler pole [1]. (Figs. 1 and 2) These analyses revealed features interpreted as tensional structures and block rotation in a strike-slip regime consistent with the Schenk et al hypotheses and implied the presence of at least two stages of crustal deformation consistent with a chronology developed by Lucchitta et al [2]. Confirmation of regional scale Euler pole rotation was ambiguous however. Up to 80 kilometers of possible extension was identified in the rift zone; to accommodate this, "cryosubduction" is speculatively proposed here as a mechanism for recycling Europan "ice lithosphere [1]."

The cumulative width of wedge-shaped bands included in the rift zone was measured [8] and plotted versus distance from the inferred rotation pole. (Figs. 2,3) Three sharp decreases in the total width were noted. These occur roughly where certain triple bands cross the rift zone suggesting that the bands are structural features that predate and influence the zone. While the curve hints at one or more sinusoidal relationships consistent with rotation geometry, given the low photographic resolution and the preliminary nature of this examination the question of whether the observations represent *coherent regional* rotation *modified* by crosscutting structures or instead imply *independent local* rotations *separated* by these structures is unanswered by this analysis.

The rift zone and neighboring areas were examined for local structures that suggest lateral motion. Parallelogram-shaped features in the rift zone and near Libya Linea (Fig. 4) resemble "pull-apart basins," a tensional structure found in terrestrial strike-slip settings (Fig. 5) [3]. One of these may exhibit reactivation of a possible bounding triple band. Lineations crossing curvilinear features were seen to be slightly offset implying rotation of rounded blocks, possibly associated with regional shear.

Inferred extension represented by the 80 km maximum cumulative band width in the rift zone must be compensated in some way. Presumably, in the context of the hypothesized mobile ice shell and underlying ocean [1], the relatively light (ice I) Europan lithosphere would be unlikely to subduct into denser ocean water or brine. However, depending on rheology, cryosubduction of Europan ice lithosphere might occur in two ways, obviating the need for theorized global expansion [4]. Compression could bring about simple pressure melting of ice I at block boundaries or could be accommodated by local thickening of the ice shell, forming ridges [1,2,5] and below-water keels as with terrestrial sea ice. Depending on P-T conditions, melting of the ice keels might occur putting meltwater into the aqueous aesthenosphere. Remaining overlying ridges would sink, restoring Europa's low-relief topography. Whenever the ice shell cracked, water would fill the gap and freeze, completing the cycle.

References: [1] Schenk, P. and Seyfert, C.(1980) EOS Trans. AGU 61, 286; Schenk, P.(1984) NASA TM-86247, 3-111; Schenk, P., and McKinnon, W.(1989) Icarus, 79, 75-100. [2] Lucchitta, B.K., and Soderblom, L.A. and Ferguson, H.M. (1981) Proc. Lunar Planet. Sci. Conf. 12B, 1555-1568; Lucchitta, B.K., and Soderblom, L.A. (1982) Satellites of Jupiter, 521-555. [3] Harding, T.P., Vierbuchen. R.C., and Christie-Blick, N.(1985) SEPM Spec.Pub. no. 37, 51-78. [4] Smith, B.A. et al (1979b) Science 206, 927-950; Finnerty, A.A. et al, (1981) Nature (London) 289, 24-27. [5] Nolan, M.C. and Greenberg, R.(1990) in print. [6] Cox, A., and Hart, R.(1986). [7] Chase, C.(1991) personal communication. [8] USGS map, Je-3; Je 5M 0/180 CM (1985). [9] USGS map, Je-3, Je 5M 0/180 AN.(1984).

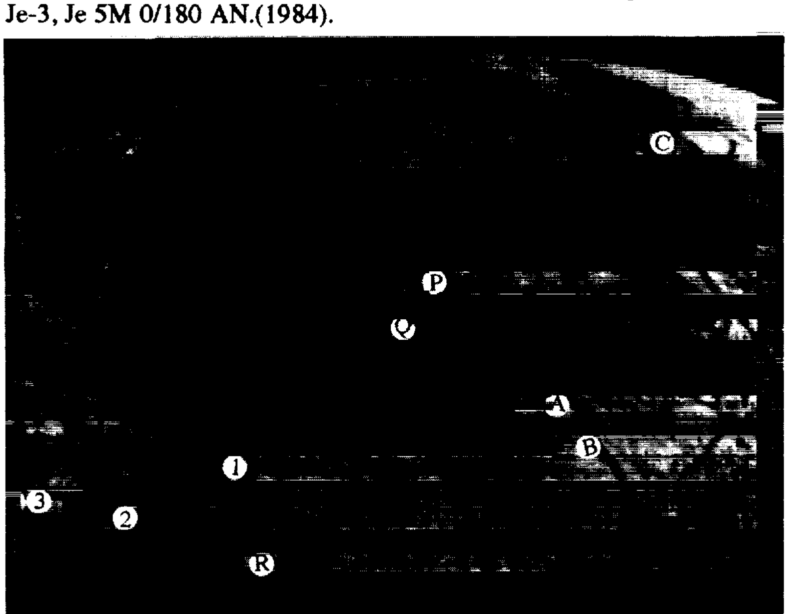
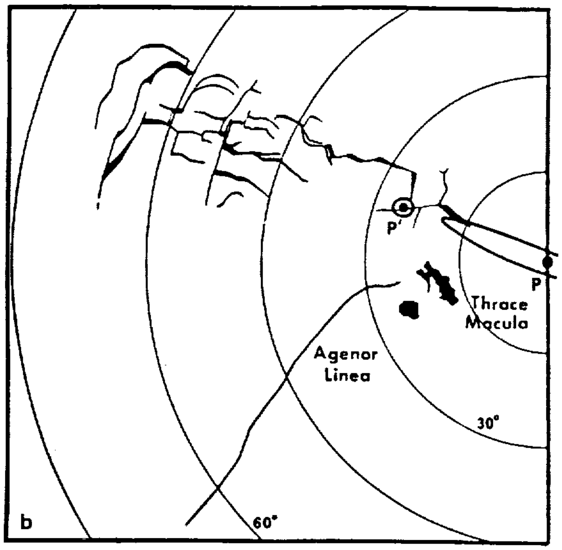


Fig. 1. The Pelorus Linea region of Europa containing the rift zone proposed by Schenk et al [1}, and showing triple bands Pelorus Linea (A), Echion Linea (B), and Argiope Linea (C) [9]. Features P,Q, and R resemble terrestrial "pull aparts." [3) Lineations bounding the ends of feature R are sharpest where differential motion would be predicted, suggesting reactivation. The northern such lineation may be a triple band. Lineations crossing curvilinear features show slight right-lateral offset at points 1,2, and 3. North is to the right. (NASA photograph)



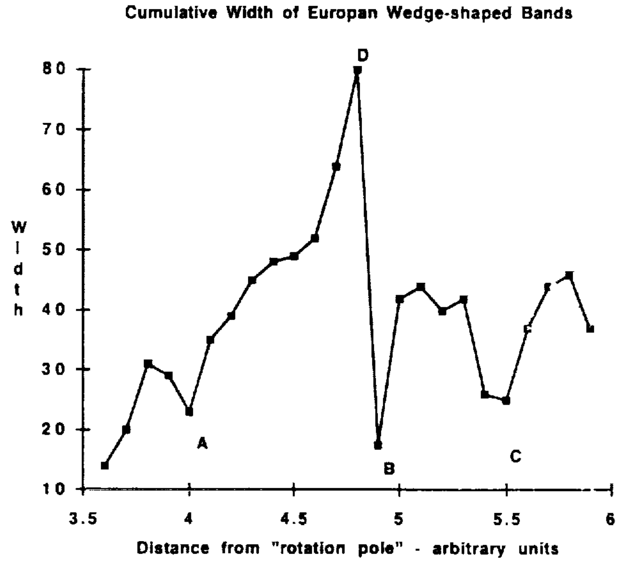


Fig. 2, above left. The cumulative width of "wedge-shaped bands" included by Schenk in the "rift zone" was measured parallel to small circles centered at the proposed Euler pole (P) and plotted against distance from that pole [1]. In terrestrial plate tectonic settings plates rotating about an Euler pole show a velocity proportional to the sin of the angular distance from the pole [6]. Breaks in the pattern suggest the presence of a transform fault [7]. On Europa, cumulative width of the wedge-shaped bands must be taken as a proxy for velocity in the absence of a rotation velocity indicator like paleomagnetic stripes. North is up. (After Schenk and McKinnon, 1989)

Fig. 3, above right. Total spreading (km) measured along individual small circles is plotted against the surface distance (in arbitrary units) between the small circles and the Euler pole, spanning the rift zone. The breaks in the curve suggest changes in the kinematics of rotation at those points, i.e. a change in rotation poles and the presence of a structure. Prominent NE-SW trending triple bands including Pelorus Linea (A), Echion Linea (B), Argiope Linea (C) seem to cross the rift zone at points roughly corresponding to the width drops; occasionally, they truncate individual wedge-shaped bands at those points. This possible relation of triple bands with a change in "rift zone" kinematics is consistent with Schenk et al's division of the rift zone into southeast and northwest portions [1] although the results here also suggest additional structural complexity. The strong initial rise in the curve is consistent with rotation about a nearby Euler pole. However, the remaining pattern does not clarify whether the apparent crosscutting structures modified a broad rotation pattern or simply separated smaller ones. The lack of measured band width near the pole raises questions about pole location or measurement technique.

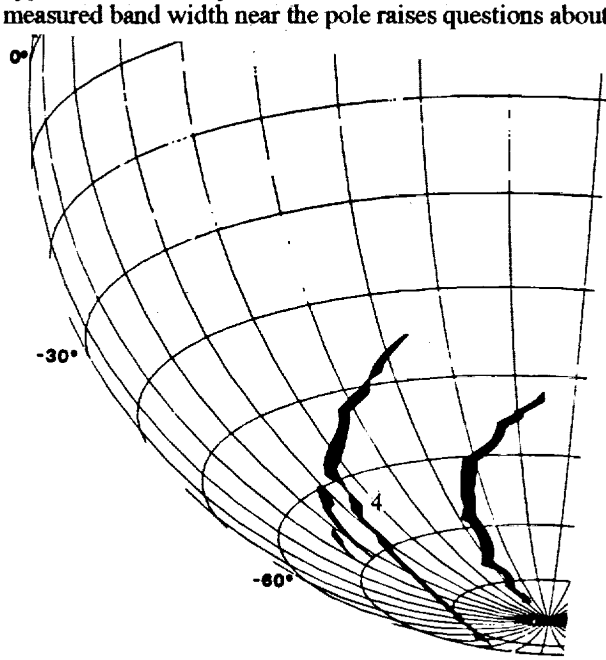
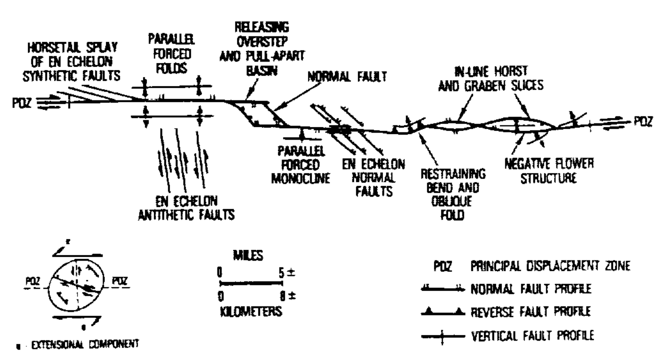


Fig. 4, left. A parallelogram-shaped feature can be seen at point 4 on a branch of Libya Linea. North is up. (After Lucchitta and Soderblom, 1982)

Fig. 5, below. Structures, including "pull-aparts," found in certain terrestrial strike-slip systems. (After Harding, Vierbuchen and Christie-Blick, 1985)



S263-91
ABS. ONLY

N94-20839

IS THERE UNIFORMITARIAN OR CATASTROPHIC TECTONICS ON VENUS?

Donald L. Turcotte, Department of Geological Sciences, Cornell University, Ithaca, NY 14853

The distribution and modification of craters on Venus favors a near global, volcanic resurfacing event about 500 Myrs ago [1,2]. Such an event indicates that the tectonic evolution of Venus has been catastrophic rather than uniformitarian.

The creation of a global, single-plate lithosphere on Venus about 500 Myrs ago can explain a variety of tectonic features on Venus that are not consistent with the thin lithosphere required by a uniformitarian hypothesis. A lithosphere on Venus that has thickened for 500 Myrs has a present thickness of about 300 km whereas steady-state heat loss from Venus requires a mean lithospheric thickness near 40 km. A thick lithosphere on Venus can support the high plateaus (elevations of 3-4 km) and mountain belts (up to 9 km) using the same isostatic compensation concepts applicable to the earth. If a thick lithosphere is thinned by a mantle plume, elevation is caused by thermal isostasy. The elevation due to the thinning of a 300 km thick lithosphere is about 3 km. Thus the domal elevation of Beta Regio [3] can be explained by the same mechanism responsible for the elevation of the Hawaiian Swell. While the broad highland plateaus on Venus may be associated with thermal isostasy, the mountain belts in Ishtar Terra clearly cannot be. The high topography of Freyja Montes is almost certainly associated with underthrusting and the likely compensation mechanism is Airy isostasy associated with a thickened crust [4]. With a density contrast Δ, of 500 kg m^{-3} an elevation of 9 km requires a crustal thickening of about 70 km. With a thick lithosphere there is no difficulty in supporting such a thick crust.

Unlike on earth, gravity anomalies correlate with high topography on Venus. Large positive gravity anomalies are directly associated with Beta Regio and Aphrodite Terra. These features are at least 75% compensated but the associated gravity anomalies are much larger than those found on the earth. For compensated topography, the geoid-topography ratio (GTR) is a measure of the associated gravity anomaly. Smrekar and Phillips [5] have obtained GTRs for elevated regions on Venus. They find that Beta has the highest value with a GTR = 31±2 m/km. An explanation for the high topography on Venus must also be able to explain the large associated gravity anomalies. Thermal isostasy with a 300 km thick lithosphere gives GTR=20 m/km.

With a stable thickening lithosphere the heat flux to the surface is less than the heat generated within Venus, thus the mean interior temperature will increase. The rate of increase is about 100°K/Gyr. Although such an increase appears to be small, it can have a profound influence on the rates of plume generation and volcanism in a planetary interior.

Another major feature that is unique to Venus are the coronae [6,7]. These are quasi-circular features, 100-2600 km in diameter, with raised interiors and elevated rims, often with annular troughs. McKenzie et al. [8] have argued that the perimeter of several large coronae on Venus, specifically Artemis, Latona, and Eithinoha, resemble terrestrial subduction zones in both platform and topography. Artemis chasma has a radius of curvature similar to that of the South Sandwich subduction zone on the earth. Sandwell and Schubert [9] have shown that the morphology of several coronae are in good agreement with the lithospheric flexure models that have been successful in explaining the sea floor morphology at ocean trenches on this planet. Their fluxural profiles yield elastic lithosphere thicknesses of 37 km for Artemis, 35 km for Latona, 15 km for Eithona, 40 km for Heng-O, and 18 km for Freyja. At depths of 15-35 km the temperatures in a stable, 500 Myr old lithosphere are 840-960°K, these are reasonable values for the base of an elastic lithosphere.

The propagation of a near circular subduction zone could lead to the destruction of the global lithospheric plate in one relatively short subduction episode. This could lead to a period of global surface volcanism and high heat flow that would cool the interior of Venus. Eventually the lithosphere would stabilize and thicken by conduction. This episode of catastrophic subduction of a thick lithosphere followed by a period of extensive volcanism is consistent with many Magellan observations. Parmentier and Hess [10] have suggested that episodic convection (subduction) is associated with a stable depleted layer on Venus.

Arkani-Hamed and Toksoz [11] suggested that the vigor of mantle convection decayed sufficiently that the lithosphere permanently stabilized 500 Myrs ago. The principal point to be made is that the stabilizing and thickening of a global lithosphere for 500 Myrs can explain the high topographic, the associated gravity anomalies, and the apparent thick elastic lithospheres which cannot be explained by a thin lithosphere.

[1] Schaber G.G., Strom R.G., Moore H.J., Soderblom L.A., Kirk R.L., Chadwick D.J., Dawson D.D., Gaddis L.R., Boyce J.M. and Russell J. (1992) *JGR 97*, 13,257.

[2] Strom R.G., Arkani-Hamed J. and Toksoz M.N. (1992) *Lunar Planet. Sci. XXIII*, 1379.

[3] Solomon S.C., Smrekar S.E., Bindschadler D.L., Grimm R.E., Kaula W.M., McGill G.E., Phillips R.J., Saunders R.S., Schubert G., Squyres S.W. and Stofan E.R. (1992) *JGR 97*, 13,199.

[4] Voder Bruegge R.W. and Head J. W. (1991) *Geology 19*, 885.

[5] Smrekar S.E. and Phillips R.J. (1991) *EPSL 107*, 582.

[6] Stofan E.R., Sharpton V.L., Schubert G., Baer G., Bindschadler D.L., James D.M. and Squyres S.W. (1992) *JGR 97*, 13,347.

[7] Squyres S.W., Janes D.M., Baer G., Bindschadler D.L., Schubert G., Sharpton V.L. and Stofan E.R. (1992) *JGR 97*, 13,611.

[8] McKenzie D., Ford P.G., Johnson C., Parsons B., Sandwell D., Saunders S. and Solomon S.C. (1992) *JGR 97*, 13,533.

[9] Sandwell D.T. and Schubert G. (1992). Subduction on Venus, *Science 257*, 766.

[10] Parmentier E.M. and Hess P.C. (1992) *Lunar Planet. Sci. XXIII*, 1037.

[11] Arkani-Hamed J. and Toksoz M.N. (1984) *PEPI 24*, 232.

N94-20840

IMPACT-INDUCED DEVOLATILIZATION OF $CaSO_4$ ANHYDRITE AND IMPLICATIONS FOR K-T EXTINCTIONS: PRELIMINARY RESULTS.

James A. Tyburczy, Department of Geology, Arizona State University, Tempe, AZ, 85287-1404, and Thomas J. Ahrens, Seismological Laboratory, California Institute of Technology, Pasadena, CA 91125

The recent suggestions that the target area for the K-T bolide may have been a sulfate-rich evaporite and that the resulting sulfuric acid-rich aerosol was responsible for the subsequent cooling of the Earth and the resulting biological extinctions [1,2, but see 3 for a contrasting view] have prompted us to experimentally examine the impact-induced devolatilization of the sulfate minerals anhydrite ($CaSO_4$) and gypsum ($CaSO_4 \cdot 2H_2O$). Here we report preliminary results for anhydrite. Up to 42 GPa peak shock pressure, little or no devolatilization occurs, consistent with chemical thermodynamic calculations. Calculation of the influence of the partial pressure of gas species on impact-induced devolatilization suggests that an even greater amount of sulfur than that proposed by Brett [1] could have been released to the atmosphere by an impact into a sulfate-rich layer.

Solid recovery, impact-induced devolatilization experiments were performed on the Caltech 20 mm gun using vented, stainless steel sample assemblies [4,5]. To enhance recovery of solid products after the shock, the sample was sandwiched between Zn discs. The anhydrite shock equation of state results of Simakov et al. [6] were employed. Post-shock analysis consisted of thermogravimetric analysis (TGA) in a He atmosphere to 1500°C and powder X-ray diffraction. During TGA of anhydrite, loss of sulfate begins at about 800°C and is complete by about 1200°C.

In experiments to date, up to 42 GPa peak shock pressure, little or no devolatilization of the anhydrite occurs (Figure 1). For comparison, peak shock pressures for incipient devolatilization of serpentine, calcite, and Murchison carbonaceous chondrite are about 20 GPa [4,5,7]. The greater difficulty of devolatilization of anhydrite relative to serpentine and calcite is consistent with thermodynamic calculations of the stability of these minerals [8].

Decomposition of anhydrite will occur according to the following reaction:

$$CaSO_4 \leftrightarrow CaO + SO_2 + 1/2\ O_2$$

Under standard state conditions ($P_{SO_2} = P_{O_2} = 1$ bar), this reaction proceeds to the right ($\Delta G < 0$) at temperatures greater than 1846 K. However, under conditions in which the gas pressures are less than 1 bar, the reaction proceeds to the right at lower temperatures. For example, for $P_{O_2} = 0.2$ bar and $P_{SO_2} = 10^{-4}$ bar the equilibrium temperature is 1270 K. Using the shock entropy method of estimating impact-induced devolatilization, and including the effects of gas pressure [5] we have calculated the shock pressures required for devolatilization under each of these gas atmospheres (Figure 1). For $P_{SO_2} = P_{O_2} = 1$ bar, incipient devolatilization occurs at about 48 GPa shock pressure and complete devolatilization occurs at about 107 GPa. For $P_{O_2} = 0.2$ bar and $P_{SO_2} = 10^{-4}$ bar, incipient devolatilization occurs at about 37 GPa, and complete devolatilization occurs at about 92 GPa. Our experimental results are consistent with these calculations, but do not cover a sufficient shock pressure range to prove their validity.

These calculations suggest that impact-induced devolatilization of anhydrite occurs at shock pressures sufficiently low that significant amounts of sulfur could have been injected into the atmosphere upon impact into a sulfate-rich evaporite environment. Consideration of the influence of partial pressure of gaseous species on the impact-induced devolatilization indicates that the total amount of sulfur released to the atmosphere could be greater than the 2×10^{17}g calculated by Brett [1].

IMPACT DEVOLATILIZATION OF ANHYDRITE: **Tyburczy J. A. and Ahrens T. J.**

References: [1] Brett, R., *Geochim. Cosmochim Acta, 56,* 3603, 1992. [2] Sigurdsson, H., D'Hondt, S., and Carey, S., *Earth Planet Sci. Lett, 109,* 543, 1992. [3] Blum, J. D., and Chamberlain, C. P., *Science, 257,* 1104-1107, 1992. [4] Lange, M. A., Lambert, P., and Ahrens, T. J., *Geochim. Cosmochim Acta, 49,* 1715-1726, 1985. [5] Tyburczy, J. A., and Ahrens, T. J., *J. Geophys. Res., 91,* 4730-4744, 1986. [6] Simakov, G. V. M. N., Pavlovskiy, N. M., Kalashnikov, N. G., and Trunin, R. F., *Izv. Phys. Solid Earth, 8,* 488-492, 1974. [7] Tyburczy, J. A., Frisch, B., and Ahrens, T. J., *Earth Planet Sci Lett., 80,* 201-207, 1986. [8] Robie, R. A., Hemingway, B. S., and Fisher, J. R., *U. S. Geol. Survey Bull 1452,* 1979.

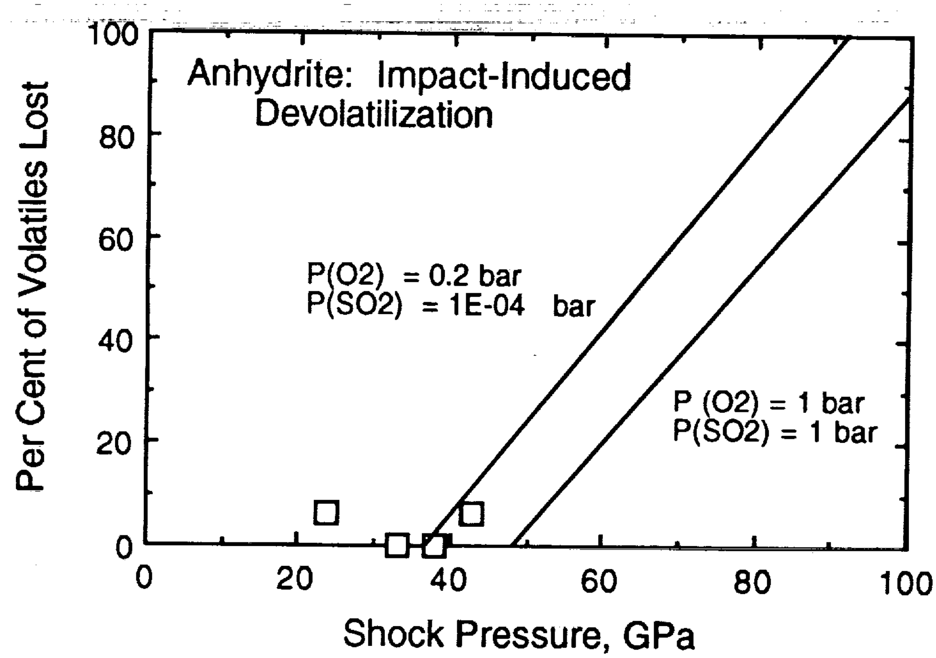


Fig. 1: Impact-induced devolatilization of anhydrite. Open squares; experimental results from this study. Solid lines; calculated devolatilization using shock entropy method assuming different gas compositions.

MEASUREMENTS OF THE DIELECTRIC PROPERTIES OF SIMULATED COMET MATERIAL AS PART OF THE KOSI 10 EXPERIMENT

S. Ulamec*, H. Svedhem*, H. Kochan+
*Space Science Department of ESA, P.O. Box 299, 2200 AG Noordwijk, the Netherlands
+DLR Institut für Raumsimulation, P.O. Box 906058, D-5000 Köln, FRG

The dielectric constant ε of the snow-mineral-mixture used for the comet simulation in the German KOSI 10 experiment was measured in the radio frequency range from 2 to 4 GHz. The traditional microwave bridge method was used, but instead of using a waveguide, that contains the sample material, small $\lambda/4$ antennas were used as sensors. A change in the dielectric properties indicates a change in density and/or composition, respectively. The method is presented as an analytical tool for measuring such density or composition changes during alternation snow-dust materials.

The KOSI (determined from the German: Kometen Simulation) experiments, performed in the Space Simulator of the DLR/Institut für Raumsimulation, during the last years have revealed many processes that presumably take place on comets [1]. So far, modifications of the internal structure could be identified only during the post-experiment inspection via hardness tests. It was the aim of the KOSI 10 and KOSI 10a experiments to emphasize on a synoptic detection of events like particle emission or crust formation. The composition of the KOSI 10 sample material was an ice-mineral mixture with about 10% of mineral (olivine) content.

An excellent method to investigate the change of the density of the probe material during its exposure to the artificial sun *in situ* is to do it via the measurement of the dielectric constant. The traditional method to determine ε, by using a microwave-bridge to measure the transmission and the reflection factor of the sample material for electromagnetic waves in the radio frequency range, had to be modified, since the commonly used practice to fill the sample material into a waveguide was not compatible with the need for *in situ* measurements during the simulation experiment.

Instead of the waveguide, small antennas were placed inside the sample container and their resonance frequency (which is dependent on the dielectric constant of the surrounding material) was determined by using both a sweep oscillator and a swept amplitude analyzer. The antennas were $\lambda/4$ groundplane structures, as shown in figure 1. They were placed in distances of about 2.5 cm and 9 cm underneath the surface of the "comet".

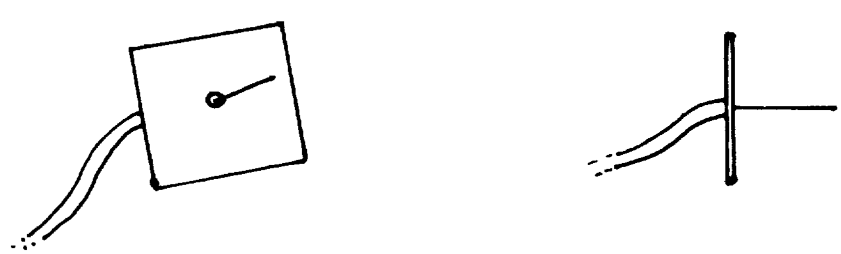


Figure 1: *Sketch of the used $\lambda/4$ antenna*

DIELECTRIC PROPERTIES OF COMET MATERIAL: S. Ulamec et al.

The dielectric constant of snow (which means a porous mixture of ice, and eventually liquid water and dust) depends on the fraction and distribution of all of these components. However, the most important parameters (in absence of liquid water) to influence ε, are the density as well as the dust content; the grain size and shape exerts a much smaller influence. The effect on ε caused by changing these parameters has been studied both theoretically and experimentally for terrestrial snow [2-4]. Figure 2 shows the dielectric constant of terrestrial snow as a function of density (Tiuri et al. 1984).

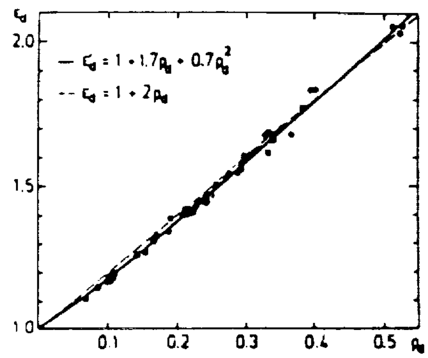


Figure 2: *Real part of dielectric constant as a function of density [Tiuri et al. 1984]*

The measurements of the dielectric constant of the sample material during the KOSI experimental runs have shown that there was little or no increase of the density. Even though a crust formed, the density of the materials appeared not to have been modified within the measurable range. This indicates that the crust formation is mainly based on a structural change, at least in this specific case. The KOSI 10 sample which was radiated for 6 hours showed an extremely slight density increase while in case of KOSI 10a (4 hours) there was no detectable change at all.

The described method will be used as a reference tool to characterize the stage of sintering of other comet-analogue samples, that are to be used for testing Rosetta[1] hardware; in specific the drilling system.

[1] Grün E., Benkhoff J. and Gebhard J. (1992); Past, present and future KOSI comet simulation experiments; *Ann. Geophysicae 10*, p.190-97

[2] Nyfors E. (1982); On the Dielectric Properties of Dry Snow in the 800 MHz to 13 GHz Region; *Helsinki University of Technology, Radio Laboratory Report*

[3] Tiuri M., Shivola A., Nyfors E. and Hallikainen M. (1984); The Complex Dielectric Constant of Snow at Microwave Frequencies; *IEEE Jour. of Oceanic Eng.*, Vol. OE-9(5)

[4] Ulamec S. (1992); Dielectric Constant of Simulated Comet Material; Proceedings of the 7. Kometenwerkstatt; Neustadt; in print

[5] *Rosetta - A Comet Nucleus Sample Return Mission*; ESA-SP-1125, 1991

[6] *Physics and Mechanics of Cometary Material*; ESA-SP-302, 1991

[1] planned Comet Nucleus Sample Return mission

S206-91
ABS ONLY

N94-20842

GEOLOGY OF GALILEO REGIO QUADRANGLE, GANYMEDE; James R. Underwood, Jr., Department of Geology, Kansas State University, Manhattan, KS 66502, Ruggero Casacchia, Instituto di Astrofisica Spaziale, Reparto di Planetologia, Viale dell'Universita 11, 00185 Roma, Italia, Alex Woronow, Department of Geosciences. University of Houston-Main Campus, Houston, TX 77204, and Michael J. Teeling, Groundwater Technology, Inc., 80 Holtz Drive, Checktowaga, NY 14225

Galileo Regio quadrangle, including most of Galileo Regio, contains two basic geologic units: older dark, furrowed, and heavily cratered material and younger light, grooved, relatively less-cratered material. Dark material dominates, the light material occurring to the W and SW in about five percent of the quadrangle. Dominant structural features, of uncertain origin, are the NW-trending arcuate furrows and associated orthogonal and oblique furrows in the dark material; grooves in the light material are not as well-ordered nor as intensely developed as elsewhere on Ganymede. Fifteen palimpsests, located partly or totally in the quadrangle and representing the period when the crust became sufficiently strong to record impact events, are subdivided into three relative-age classes, as are the numerous impact craters, some of which are dome, moat, and rampart-like. Galileo Regio is believed to have formed when, because of cooling, differentiation, and expansion, the thin, weak, icy lithosphere broke into blocks and light material filled the space between, or overspread those blocks that subsided, or both. Grooves formed in most of the light material and both light and dark material were cratered by impact, the most recent of which created bright-ray craters, the youngest features visible in the quadrangle.

Introduction: Ganymede has been interpreted to be a mixture of silicate material and water ice, based on its low mean density, 1.94 gm/cm^3, and its reflectance spectra (1); absorption spectra indicate that water ice, together with small amounts of oxidized iron-bearing minerals, constitute most of the surface material (2). Theoretical studies suggest that Ganymede is a differentiated body with a rocky core and a water-ice mantle and lithosphere (3). Voyager I and II spacecraft provided images of Galileo Regio quadrangle that have resolutions between 0.5 and 2.0 km/pixel (4), and the following summary is based on geologic mapping on an airbrush base map (scale c. 1:5,000,000) prepared from those images.

Dark Material: The most conspicuous features of the dark material are the NW-trending arcuate furrows and associated orthogonal and oblique furrows (4,5,6,7,8). Image resolution does not permit the discrimination between an exogenic origin (e.g. impact) or an endogenic origin (e.g. arching owing to an upwelling mantle plume) for the furrows. None of the furrows has craters >10 km superposed, so the furrows must have formed after the lithosphere was brittle enough to fracture but before it was strong enough to preserve larger craters (6). Scattered patches of smooth, dark material occur marginal to such topographic features as furrows and crater rims. The increase in abundance of this material equatorward suggests that the lithosphere may have been thinner there during the emplacement of the smooth, dark material (6).

Light Material: Light material along the western margin of the quadrangle is part of Ur Sulcus, and that along the southern boundary is part of Nippur Sulcus. Boundary grooves, distinct double-walled depressions, separate the dark and light material in most places, and in places the dark material seems to be topographically higher (9). In at least two places in the quadrangle, light material appears to be spreading over dark material as it subsides. Nowhere in

the quadrangle do well-developed, complex groove sets and systems, interpreted to have formed from some combination of tensional fracturing and ice volcanism (10, 11, 12, 13), occur as they do elsewhere on Ganymede.

Crater-Palimpsest Material: Palimpsests 100-400 km in diameter occur partly or totally in this quadrangle and are classified into three classes of relative age: ancient, old, and young palimpsest material. Young palimpsests have associated fields of secondary craters and ejecta deposits that are designated pitted palimpsest material. Palimpsests are among the oldest crater forms on Ganymede and postdate the furrows in the dark material.

Crater Material: Craters exhibit a wide range of form that is size related: those of <20 km diameter have central peaks; those 20-40 km in diameter have central pits; those >40 km in diameter have terraces and most have domical floors. Three relative-age classes of craters occur: highly degraded, slightly degraded, and bright. Several chains of secondary craters, a few kilometers to about 100 km long, occur; distinctive crater types are dome, moat, and martian-like rampart craters. Both bright- and dark-ray craters occur in the quadrangle. Numerous craters are polygonal in plan, probably reflecting control by the regional fracture patter.

Geologic History: The earliest events in Ganymede's history, accretion and heavy bombardment, are not represented by surface features. The first recorded event was the formation of dark material or of the material constituting the irregular but subdued surface on which the dark material lie. Cooling of the body eventually strengthened the lithosphere such that it could preserve a record of furrow formation and of meteorite impact >10 km in diameter. Earlier and larger impact events are represented by palimpsests; subsequent and smaller events by the spectrum of craters of varied size and degree of degradation. Following the formation of the dark material and the system of furrows, global expansion accompanying differentiation fractured the lithosphere, allowing the emplacement of light material, possibly by a system of convection cells in the mantle. Subsequently, much of the light material was fractured, probably by extensional stress systems. Young palimpsests formed after the light material; bright-ray craters are the youngest features recognizable on the planet. Surface processes currently active on Ganymede are occasional meteorite impact, mass wasting, and ablation, the result either of ion sputtering or of thermal migration of water, or both.

References: (1) Pilcher et al., Science, 178, 1087-1089, 1972. (2) Clark R. N. et al. in Burns, J. M. and Matthews, M. S., eds., Satellites, Univ. Arizona Press, 437-491, 1986. (3) Consolmagno, G. J. and Lewis, J. S. in Gehrels, T. A., ed., Jupiter, Univ. Arizona Press, 1035-1051, 1976. Cassen, P. M. et al. in Morrison, D., ed., Satellites of Jupiter, Univ. Arizona Press, 93-128, 1982. (4) Smith, B. A. et al., Science, 204, 951-972, 1979a. Smith, B. A. et al. Science, 206, 927-950, 1979b. (5) Shoemaker E. M. et al. in Morrison, D. ed., Satellites of Jupiter, Univ. Arizona Press, 435-520, 1982. (6) Casacchia, R. and Strom, R. G., JGR, 89, B419-B428, 1984. (7) Murchie, S. L., PhD dissertation, Brown Univ., 331 p., 1988. (8) Murchie, S. L. and Head, J. W., USGS Misc. Inv. Map I-1966 (Jg-4), 1989 (9) Lucchitta, B. K., USGS Misc. Inv. Map (Jg-7), in press. (10) Lucchitta, B. K., Icarus, 44, 481-501, 1980. (11) Squyres, S. W., PhD dissertation, Brown Univ. in NASA Tech. Memo. 84412, 356 p., 1981. Squyres, S. W., Geophys. Res. Lett., 7, 593-596, 1980. (12) Parmentier, E. M. et al., Nature, 295, 290-293, 1982. (13) McKinnon, W. B. and Parmentier, E. M. in Burns, J. A. and Matthews, M S., eds., Satellites, Univ. Arizona Press, 718-763, 1986.

REVERSE POLARITY MAGNETIZED MELT ROCKS FROM THE CHICXULUB IMPACT STRUCTURE, YUCATÁN PENINSULA, MEXICO; Jaime Urrutia-Fucugauchi[1], Luis E. Marín[1], Virgil L. Sharpton[2], Juan Manuel Quezada[3]; [1]*Instituto de Geofisica, Universidad Nacional Autonoma de Mexico, Del. Coyoacan 04510 D.F., Mexico.* [2]*Lunar and Planetary Institute, 3600 Bay Area Blvd., Houston, TX 77058.* [3]*Gerencia de Exploracion, Petróleos Mexicanos, Marina Nacional 329, 11311 D.F. Mexico*

We report further paleomagnetic data for core samples of melt rock recovered in the Petróleos Mexicanos (PEMEX) exploratory wells within the Chicxulub structure, northern Yucatan peninsula, Mexico. A previous report by *Sharpton et al. (1992)* has shown that the rocks studied contain high iridium levels and shocked breccia clasts, and an ^{40}Ar-^{39}Ar age of 65.2 ± 0.4 Ma. The geomagnetic polarity determined for two samples is reverse (R) and was correlated with chron 29R that includes the K/T boundary. Our present analysis is based on two samples from each of three clasts of the melt rock from PEMEX well Y6-N17 (1295 to 1299 m b.s.l.). This study concentrates on the vectorial nature and stability of the remanence (NRM), the magnetic mineralogy and remanence carriers (i.e., the reliability and origin of the record) and on the implications (correlation with expected paleolatitude and polarity).

The relative orientation of the drill core samples with respect to the horizontal is known. Samples were stable under alternating field (AF) and thermal treatments, and after removal of a small component they exhibited single-vectorial behaviour. The characteristic remanence inclinations show small dispersion and a mean value (-43°) in close agreement with the expected inclination and paleolatitude (derived from the North American apparent polar wander path). Isothermal remanence (IRM) acquisition experiments, Lowrie-Fuller tests, coercivity and unblocking temperature spectra of NRM and saturation IRM, susceptibility and Q-coefficient analyses and the single-component nature indicate a dominant mineralogy of iron-rich titanomagnetites with single or pseudo-single domain states. The stable characteristic magnetization may be interpreted as a result of shock heating of the rock at the time of formation of the impact structure and its polarity, age and paleolatitude are consistent with a time about the K/T boundary.

References: Sharpton, V.L., Dalrymple, G.B., Marín, L.E., Ryder, G., Schuraytz, B.C., and Urrutia-Fucugauchi, J. *Nature 359*, 819-821, 1992.

S208-90
ABS ONLY

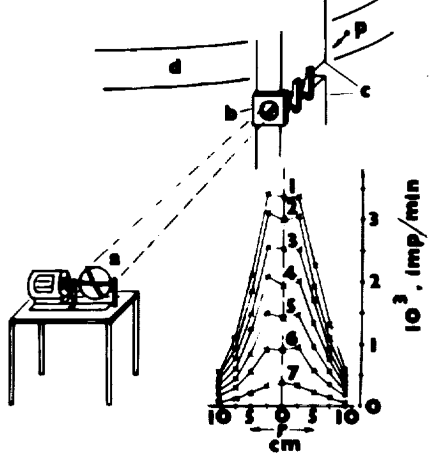
N94-20844

ON MODELLING NUCLEAR REACTIONS IN METEORITES; G.K.Ustinova and A.K.Lavrukhina, Institute of Geochemistry and Analytical Chemistry, Russian Academy of Sciences, Moscow 117334, Russia

An original method of experimental modelling depth distribution of radionuclides in sphere thick targets irradiated by protons in 4π-geometry on JINR (Dubna) synchrocyclotron is described. Some results are presented.

At present a new wave of works on the experimental modelling nuclear reactions in meteorites by irradiating thick targets on accelerators emerged, which is conditioned by the appearance of more perfect methods of measuring radioactivity, making it possible to enhance the precision of modelling, as well as by the interest in more subtle regularities, e.g., the effects of cosmic ray modulation, isotopic anomalies, etc.. Among the features of these works, the tendency is observed to an experimental simulation of isotropic irradiation of targets in 2π- and 4π-geometry. In connection with this, we would like to pay attention to an original method elaborated and used by us on JINR (Dubna) synchrocyclotron /1,2/.

The target is chosen as an iron sphere, having a radius of 10 cm, that is the optimal size for development of nuclear cascades in iron; besides, just for small meteorites the uncertainties of all the theoretical methods of the modelling are the greatest. The sphere, revolving about two mutually perpendicular axes with the speed of 18 RPM, was installed at ~6 m from the exit of the proton beam from the synchrocyclotron chamber (see Figs.1 and 2). An iron core along the diameter of the sphere contained 9 sets of iron and aluminium plates separated by iron inserts. The iron plates of 18 mm diameter and ≤ 1 mm thickness were made of armco-iron (impurity 0.16%): the aluminium plates of the same diameter



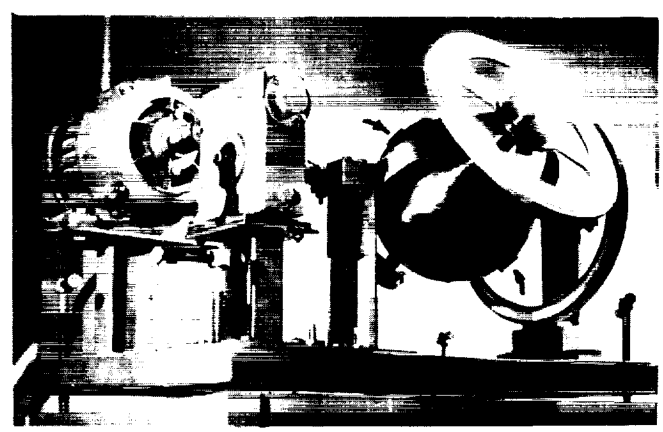


Fig.1- Scheme of the experiment (a is target; b is magnetic lens; c are nozzles of electromagnet at exit of proton beam p from the synchrocyclotron chamber d); the graph shows the distribution of induced activity along the diameter after the end of irradiation at: 3d 4h (1); 3d 12h (2); 4d 4h (3); 5d 6h (4); 7d 3h (5); 10d 5h (6), and ~25d (7); r is a distance from the center.
Fig.2- The target (the arrows point to the core with specimens).

PRECEDING PAGE BLANK NOT FILMED

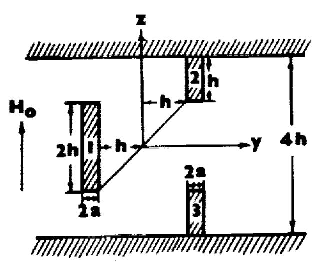


Fig.3- Principal scheme of the magnetic lens (1,2 and 3 denote iron bars in the magnetic field H_0 of electromagnet.

were made of spectral pure foil (99.9%) of 0.25mm thickness. Each of the sets consisted of 3 Al plates, 2 Fe and 3 more Al ones. The border of each 3 Al plates served for protection from recoil nuclei from iron and for compensation of recoil nucleus loss from the middle Al plates, in which the Na-24 radioactivity was measured.

The sphere was irradiated with the expanded beam of 660 MeV protons. The expansion of the beam was performed by the magnetic lens installed between nozzles of the electromagnet at the exit of the beam from the synchrocyclotron chamber (see Fig.1). The additional gradient of magnetic field (~539 oersted/cm) is created by three iron bars: one bar is 400 x 65 x 10 mm and two others are 400 x 32.5 x 10 mm (Fig.3). The aperture of the lens is 2h=65 mm, and its focal length is 2 m. At the distance of 6 m from the exit of the beam its initial elliptic cross section of 5 x 10 cm was transformed by the lens into the circular eddy spot with the outer ring of 20 cm in diameter (the shape and position of the spot were recorded by photoplates). While revolving about two mutually perpendicular axes, the surface of the sphere was irradiated isotropically with the intensity of $I_0 = I_p/16\pi$ $cm^{-2}s^{-1}sr^{-1}$, where I_p is the average intensity of the proton beam at the location of the target, as measured by the monitor (a screen of Al foil and the reaction Al-27(p,3pn)Na-24). The intensity ranged in the limits of $(5.3-7.6)\cdot10^8$ $cm^{-2}s^{-1}$ for different expositions which duration was 1.5-4 h. As seen from the graph in Fig. 1, the curves of induced activity display clear symmetry about the center of the sphere, which visually proves the isotropy of irradiating its surface.

Depth distribution of radionuclides inside the sphere together with the curves calculated by the analytical method /2,3/ are demonstrated in Fig.4. The quantitative agreement of the theory with the experiment is observed on all depthes except for ≲ 2 cm near the surface due to some leakage of particles. However, the high ablation of meteorites while passing through the earth atmosphere, entirely overlaps the leakage zone.

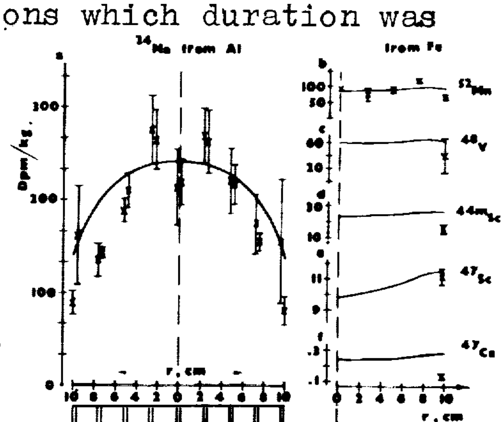


Fig.4-Depth distribution of radionuclides within the sphere (a is Na-24 in Al plates; under the graph a scheme of their disposition along the diameter is shown; b,c,d,e, and f are Mn-52, V-48, Sc-44m, Sc-47, and Ca-47 in Fe plates, successively; r is the distance from center).

References [1] Lavrukhina A.K. et al. Atomic Energy (Russian) 34(1973)23. [2] Lavrukhina A.K., Ustinova G.K. Meteorites as probes of cosmic ray variations. Moscow: Nauka(1990). [3] Lavrukhina A.K., Ustinova G.K. Proc. LPSC 9th (1978)2399.

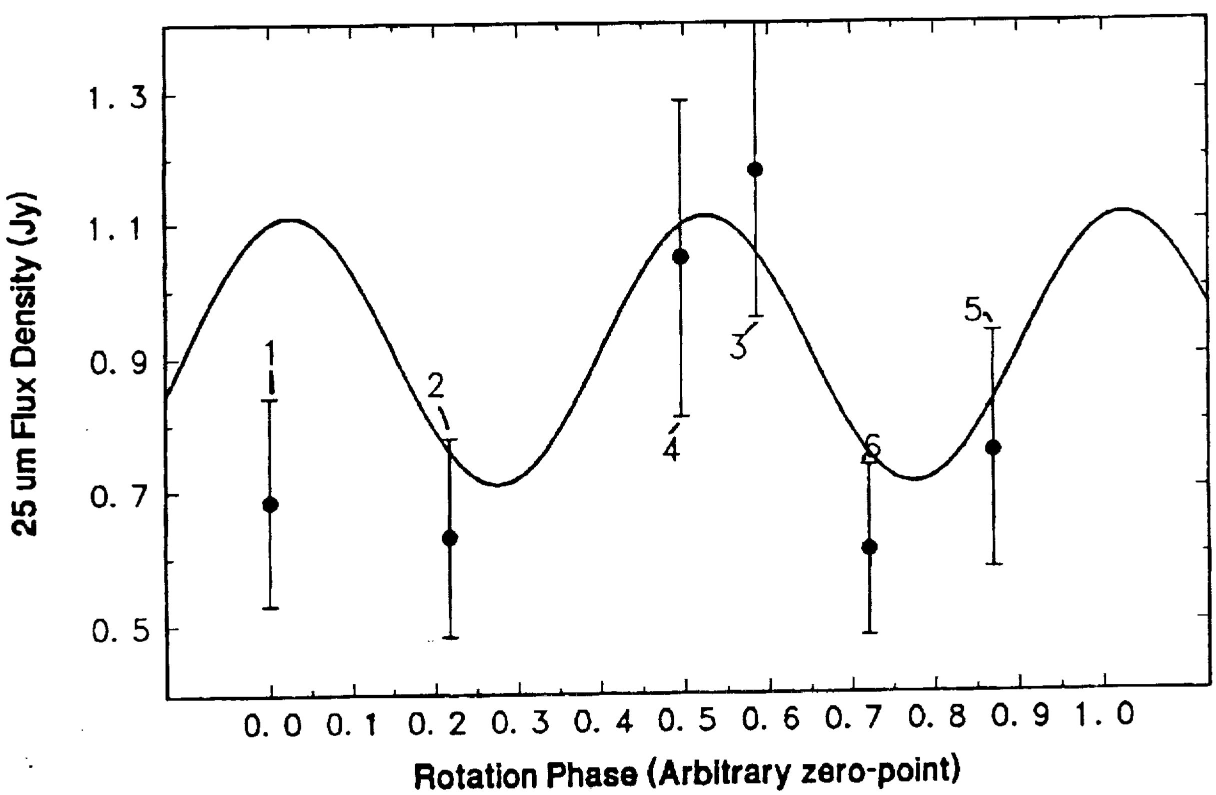
S209-90 ABS. ONLY.

N94-20845

IMPS ALBEDO AND DIAMETER FOR ASTEROID 243 IDA; G. J. Veeder, Jet Propulsion Laboratory and E. F. Tedesco, Mission Research Corporation

243 Ida is the second asteroid target of the Galileo mission. The Infrared Astronomical Satellite (IRAS) detected Ida several times during its 1983 sky survey. The IRAS Minor Planet Survey (IMPS) yields a total of 13 usable observations during 6 sightings of Ida [1]. These data result in a geometric visual albedo of 0.24 and a mean diameter of 28 km for Ida. The IMPS catalog updates and extends the IRAS Asteroid and Comet Survey [2,3] through asteroid number 4679. File versions of IMPS final products will be available from the National Space Science Data Center (NSSDC). The input for IMPS processing includes updated visual absolute magnitudes and orbital elements for each asteroid. H and G are 9.94 and 0.15 for Ida. IMPS also includes a correction for low flux densities (less than ~1 Jansky). In the case of Ida, 3 observations at 12μm, 6 at 25μm and 4 at 60μm were considered acceptable for analysis. Most of these do have flux densities less than 1 Jansky with a value of approximately 5 for their estimated SNR. The 25μm observations as plotted in the figure are consistent with the variation expected for the cross section of Ida with rotation. Ida is a main belt asteroid with an S taxonomic classification [4,5]. The spectra of S asteroids tend to be dominated by pyroxene [6,7] with visual albedos from 0.1 to 0.3 [8]. The IMPS average albedo of 0.24 ($\pm$0.07) for 243 Ida is in the upper range observed for S asteroids.

IMPS Results for 243 Ida



IMPS ALBEDO AND DIAMETER FOR 243 IDA: Veeder G. J. and Tedesco E.F.

REFERENCES:[1] Tedesco E. F. and Veeder G. J. (1993) *IRAS Minor Planet Survey*, in press. [2] *IRAS Asteroid and Comet Survey* (1986) JPL D-3698 (D. Matson, ed.) Jet Propulsion Laboratory, Pasadena. [3] Matson D. L., Veeder G. J., Tedesco E. F. and Lebofsky L. A. (1989) In *Asteroids II* (R. P. Binzel, T. Gehrels and M. S. Matthews, eds.), pp. 269-281. U. Arizona Press, Tucson. [4] Tholen D. J. (1989) In *Asteroids II* (R. P. Binzel, T. Gehrels and M. S. Matthews, eds.), pp. 1139-1150. U. Arizona Press, Tucson. [5] Barucci M. A., Capria M. T., Coradini A. and Fulchignoni M. (1987) *Icarus, 72*, 304-324. [6] Gaffey M. J. and McCord T. B. (1979) In *Asteroids* (T. Gehrels, ed), pp. 688-723. U. Arizona Press, Tucson. [7] Gaffey M. J., Bell J. F. and Cruikshank D. P. (1989) In *Asteroids II* (R. P. Binzel, T. Gehrels and M. S. Matthews, eds.), pp. 98-127. U. Arizona Press, Tucson. [8] Tedesco E. F., Williams J. G., Matson D. L., Veeder G. J., Gradie J. C. and Lebofsky L. A.(1989) In *Asteroids II* (R. P. Binzel, T. Gehrels and M. S. Matthews, eds.), pp. 1151-1161. U. Arizona Press, Tucson. This work was supported by the Air Force Phillips Laboratory.

ARE THE Cδ LIGHT NITROGEN AND NOBLE GASES LOCATED IN THE SAME CARRIER? A.B. Verchovsky, S.S. Russell and C.T. Pillinger, The Open University, Walton Hall, Milton Keynes MK7 6AA, U.K., A.V. Fisenko and Yu. A. Shukolyukov, Vernadsky Institute of Geochemistry and Analytical Chemistry, Russian Academy of Sciences, Moscow 17975, Russia.

Light nitrogen and the HL family noble gas components of Cδ appear to be separable by high resolution pyrolysis experiments. Thus Cδ is not an homogeneous material and probably consists of debris of many stars. The question of whether the N and Xe(HL) actually reside in different carriers continues to be addressed.

It is well known that Cδ which was identified as nanometer sized diamonds (1) contains isotopically anomalous elements, in particular noble gases including Xe(HL) (2) and its family and light nitrogen ($\delta^{15}N$ down to –350‰) (3). Before the true nature of Cδ was recognised it was easy to suppose that the Xe(HL) and light nitrogen were located in the same carrier (3). However, recognition that light nitrogen in diamond from different samples varies by greater than a factor of six (4) compared to Xe(HL) fluctuations of *ca.* 20% (5) makes such an assumption questionable. On the basis of simple arithmetic logic, the Xe and nitrogen cannot be absolutely co-located. The average diamond grain consists of only about 1000 - 2000 atoms of carbon; one grain among a few x 10^6 contains an atom of Xe(HL) whilst 5 - 30 atoms of light nitrogen are the typical number which need to be in every diamond grain to account for observed concentrations. If some grains are devoid of N, the others have to have a higher N concentration. Even if we were able to analyse an individual grain of the diamond for noble gases and nitrogen we would be faced with the monumental task of locating the one amongst 10^6 identical grains containing the Xe atom to examine its nitrogen content. The problem can be simplified to some extent if instead of Xe, He which is 10^4times more abundant is assumed to be a member of the HL family. Attempts to fractionate the separate carriers might be attempted using He and N as guiding indicators but even experiments of this nature are for the future. Faced with apparently insoluble problems, we have returned to an investigation we last used in our original efforts to find isotopically light nitrogen (3), that is to compare release patterns of the different components during stepped pyrolysis and combustion.

The main Cδ noble gas component - Xe(HL) and associated He, Ne, Ar and Kr(H) are released during combustion in the range 400 - 600°C with a maximum of 600°C (5). Pyrolyses are carried out with much larger temperature increments but $^{136}Xe/^{132}Xe$ ratios only reach a value indicative of the release of Xe(HL)of about 0.6 in fractions liberated above 1050C; the maximum release of gas with this isotopic composition is usually from 1250° to 1450°C with some still being liberated at over 1500°C (6). The release of light nitrogen with $\delta^{15}N$ = –350‰ is very precisely defined by stepped combustions on a number of samples carried out at 10°C temperature intervals; the maximum yield is never in excess of 550°C and usually at 490 - 500°C. In contrast to the noble gases above, pyrolysis experiments on Efremovka and Cold Bokkeveld using 50°C increments, reveal that significant evolution of light nitrogen commences at temperatures around 750°C, reaches a peak in the 1000 - 1050°C step, and is completely off by 1350°C. Interestingly, we note that the carbon which constitutes the diamond only begins to significantly degrade after the 1100 - 1150°C step, once nitrogen has gone and heavy noble gases are just beginning to become labile. We conclude that nitrogen and Xe(HL), including its cohorts Ne-A2, Ar and Kr(H) can be decoupled by pyrolysis by between 200 - 400°C.

ARE THE C_δ LIGHT NITROGEN ....Verchovsky *et al.*

It is difficult to explain the (~300°C) difference in the nitrogen and the noble gases released during pyrolysis by simple diffusion effects. Nitrogen is presumed to be chemically bonded in the diamond structure, therefore intuitively it ought to be released at higher temperatures than inert gas with nearly the same mass, for example, Ne implanted into lattice spaces in a minute crystal. It is possible that migration of N through the lattice is somehow facilitated but exactly why this should be easier than diffusion through open space is unclear. Monitoring of CO_2 during the pyrolysis experiments did not show any significant amount of carbon in association with the nitrogen release. The kinetics governing the aggregation of singly substituted N defects in diamond is reasonably well understood (7), but provides no clues. Complete degassing of nitrogen from type IaA and IaB terrestrial diamonds requires heating to in excess of 2200°C (8). On the other hand there is practically no difference between release of the noble gases heavier than helium during pyrolysis (6).

One explanation of the observation might be that the light nitrogen is located in diamonds with a systematically smaller grain size than those hosting Xe(HL) and associated noble gases. Practically no difference in the noble gases and the nitrogen release patterns are observed during stepped combustion but these experiments have still not been performed with sufficient temperature resolution in the case of the former. Combustion may not be capable of decoupling the N and noble gases because during burning diamond aggregates of many small grains may behave similar to bigger individual diamonds. During mass wasting combustion, big grains actually become smaller. Overall the small and the big diamond grains may be oxidised at the same time and in the same temperature range. The presence of the diamond aggregates possibly does not seriously affect the diffusion rate of the species from individual grains. Another hypothesis we have to consider is that the nitrogen carrier exists as a separate entity. If all the light nitrogen was in a nitride, for arguments sake Si_3N_4, then assuming an approximately similar grain size to diamond requires less than 1% of the crystals to be the N carrier; a 1% interloper within nanometer sized diamond would be difficult to spot either microscopically or by elemental analysis. We have speculated elsewhere (9) concerning the possibility of CN groups on material such as carbyne intergrown with the diamond; these are attractive for a number of reasons not least their abundance in molecules observed in the circumstellar envelope of AGB stars.

References:
1. Lewis R.S. *et al.* (1987), Nature **326**. 2. Lewis R.S., Scrinivasan B. and Anders E. (1975), Science **190**, 1251. 3. Lewis R.S. *et al.* (1983), Nature **305**, 767. 4. Russell S.S. *et al.* (1991), Science **254**, 1188. 5. Verchovsky *et al.* (1993), (in preparation); 6. Huss R.R. and Lewis R.S. (1993), Meteoritics (submitted). 7. Evans T. and Qi Z. (1982). Proc. Roy. Soc. A. **381**, 159. 8. Woods G.S. *et al.* J. Phys. Chem. Solids (1990) **51**, 1191. 9. Gilkes K.W.R. *et al.* (1993) submitted to Science.

C-8

S211-91 ABS. ONLY

N94-20847

p. 2

NUMERICAL MODELING OF IMPACT EROSION OF ATMOSPHERES: PRELIMINARY RESULTS; A. M. Vickery, Lunar and Planetary Laboratory, The University of Arizona, Tucson, AZ 85721

It is clear from the great diversity of atmospheres among the terrestrial planets that their formation and evolution must have depended on a balance among a number of different processes. One of these processes is atmospheric erosion by impacts, which may have been particularly effective on Mars [1] The reason is that geomorphic evidence on Mars suggests that this planet had, early in its history, a dense enough atmosphere to sustain active precipitation over geologically significant periods of time [2]. Analytic calculations indicate that neither the projectile entering the atmosphere nor the main crater ejecta can cause the lose of significant amounts of atmosphere [3,4]. The vapor plume that is formed, however, expands rapidly as its internal energy is converted into kinetic energy, and may blow off the overlying atmosphere. A model of this part of the impact/atmosphere interaction predicts Mars could have lost a substantial early atmosphere by impact erosion alone [5]. Although our more detailed calculations, which took into account the anisotropy of the atmosphere with respect to zenith angle, show that the process isn't quite as effective, they still indicate the probability of substantial atmospheric loss from Mars[6]. In this abstract, I discuss the first results from 2-D hydrocode runs. These include two runs which make most of the same simplifying approximations as the analytic models, in order to compare the analytic and numerical results directly, and one run (as yet incomplete) that models the full impact.

The calculations described below use the 2-D hydrocode CSQ, with the ANEOS equation of state program. I have started a calculation that follows the impactor as it traverses the atmosphere and then impacts the solid planet. The projectile and target are composed of dunite, and the 1 km diameter projectile approaches the planet at 15 km/s. The atmosphere in this calculation, and in the simpler ones discussed below, is composed of pure CO_2, which is modeled as a perfect gas. The atmosphere is isothermal, with a temperature of 298 K and a surface pressure of 1 bar. The gravitational acceleration is 3.72 m/s^2, that of Mars. This calculation is extremely difficult to keep stable, requiring small time steps and frequent regridding. After 2 months of working on the problem, the calculation has been carried out to a simulated time of 2 seconds. At this time, the shock wave generated by the passage of the impactor through the atmosphere is expanding outward more-or-less cylindrically, and the shock wave in the target is expanding approximately hemispherically (See figure 1). A crater is beginning to form, and some ejecta is being thrown out, but the calculation has not yet proceeded to the point of following the expansion of the expected vapor plume.

As it became apparent that doing the full-up calculation would take a long time, I decided to start a series of much simplified calculations. The plan is to run models of increasing complexity and verisimilitude, and thereby understand the what factors are important for impact erosion. The first such runs model the expansion of a hemisphere of highly shocked dunite into an exponential atmosphere that overlies a rigid substrate -- essentially the approximation made in the analytic studies. It is assumed that the projectile and an equal mass of target are shocked to the highest pressures given by the planar impact approximation. The initial temperature, pressure, and density of the shocked material are determined from the Hugoniot. generated by ANEOS. This material is assumed to start as a hemisphere at rest, and is allowed to expand into the overlying atmosphere, described above. If this material were expanding into a vacuum, theory suggests that it should achieve a mean velocity of 7.5 km/s, with a maximum velocity at the leading edge 2 - 3 times as great.

The first set of results from the simplified problem are for the impact of a 1-km diameter projectile, whose mass is much less than that for catastrophic atmospheric blow-off, as indicated by the analytic models. The evolution of the plume was followed for roughly 18 seconds of problem time, as it expands to nearly 45 km (3 scale heights). The striking thing about these results is that the plume is subject to a Rayleigh-Taylor type instability and begins to break up and mix with the atmosphere at very early stages (figure 2). The velocity in some

atmosphere; it is clear that this material does not have sufficient momentum to approach the theoretical limiting velocity or to maintain velocities greater than escape velocity. The second such run increased the mass of the vapor plume by a factor of 100, although it is still much less than required for catastrophic blowoff, with all other parameters the same. This calculation followed the expansion for ~ 7 seconds, with the shock front reaching upward to about 50 km and to about 40 km along the "planetary surface". This quasi-elliptical shape is an expected consequence of the density gradient in the atmosphere, which is largest in magnitude directly upward. As for the smaller plume, Rayleigh-Taylor instabilities develop, but are not as pronounced. The time-averaged velocity of the leading edge of the plume is ~ 7.5 km/s in the upward direction and ~ 6 km/s in the horizontal direction. Thus one predicts the loss of some atmosphere in this case, even though the impactor mass is much less than the threshold for catastrophic blow-off.

REFERENCES: 1. Cameron, A.G.W., *Origin of the Atmospheres of the Terrestrial Planets.* Icarus, 1983. **56**: p. 195-201. 2. Baker, V.R. and J.B. Partridge, *Small Martian Valleys: Pristine and Degraded Morphology.* J. Geophys. Res., 1986. **91**(B3): p. 3561-3572. 3. Walker, J.G.C., *Impact Erosion of Planetary Atmospheres.* Icarus, 1986. **68**: p. 87-98. 4. Melosh, H.J. and A.M. Vickery, *Atmospheric Erosion by High Speed Impact Ejecta.* EOS, 1988. **69**: p. 388. 5. Melosh, H.J. and A.M. Vickery, *Impact erosion of the primordial atmosphere of Mars.* Nature, 1989. **338**: p. 487-489. 6. Vickery, A.M. and H.J. Melosh, *Atmospheric erosion and impactor retention in large impacts, with application to mass extinctions,* in *Global catastrophes in Earth history; An interdisciplinary conference on impacts, volcanism, and mass mortality,* B. Sharpton and P. Ward, Editor. 1990, Geological Society of America: Boulder CO. p. 289-300.

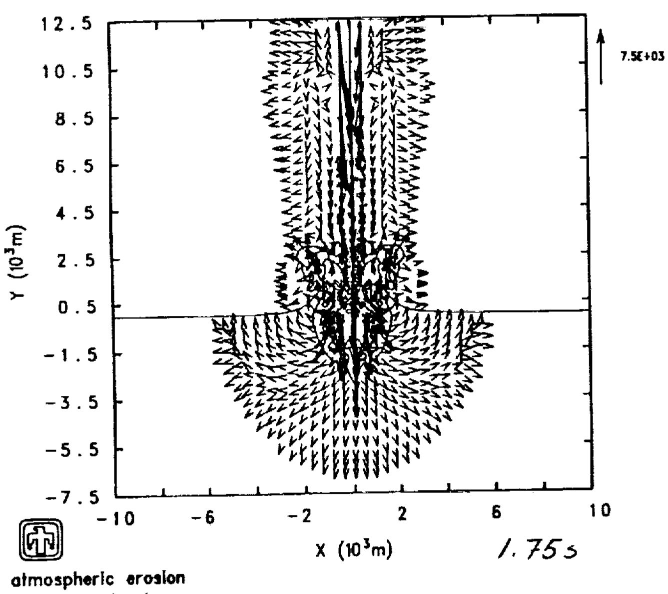


Figure 1. Full impact calculation of a 1-km diameter dunite projectile through a 1-bar CO2 atmosphere on Mars at 15 km/s. Time = 1.75 s.

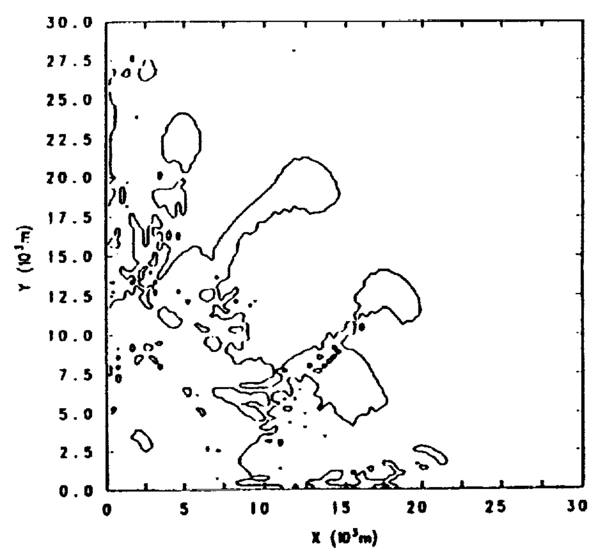


Figure 2. Material interface plot showing the originally hemispherical plume breaking up and mixing with the atmosphere. Time = 8.54 s.

5212-90
ABS. ONLY

P. 2

COMPARISON OF VISIBLE AND NEAR-INFRARED REFLECTANCE SPECTRA OF CM2 CARBONACEOUS CHONDRITES AND PRIMITIVE ASTEROIDS; F. Vilas, T. Hiroi, and M. E. Zolensky, NASA Johnson Space Center, Houston, Texas.

Spectra of primitive asteroids (here defined as C, P and D classes and associated subclasses) have been compared to the limited number of spectra of CM2 carbonaceous chondrites [1, 2]. An absorption feature located at 0.7 µm attributed to an Fe^{2+} - Fe^{3+} charge transfer absorption in iron oxides in phyllosilicates is apparent in some of the CM2 carbonaceous chondrite spectra and many of the asteroid spectra. Sawyer [2] has found a correlation between the area of the 0.7-µm feature and the mean semimajor axis of the asteroids. Spectra of a larger sample of carbonaceous chondrites, including 7 CM2 chondrites, covering a spectral interval of 0.30 - 2.5 µm have recently been obtained using the Relab instrument at Brown University. These spectra have been compared with spectrophotometric asteroid observations in a separate abstract in this volume [3]. We have taken those spectra of CM2 chondrites and isolated the UV, visible and near-infrared spectral regions in order to compare them with high-quality narrowband reflectance spectra (Fig. 1).

In order to study any existing features most effectively, each meteorite spectrum was treated as a continuum with discrete absorption features superimposed on it for the spectral interval which was roughly common with the asteroid spectra (0.49 - 1.0 µm). A simple linear continuum was defined by a linear least squares fit to the spectral data points of the meteorite. The continuum was then divided into each individual spectrum, thus removing a sloped background and allowing the intercomparison of residual spectral features. Figure 2 shows residual spectral features for the 7 CM2 chondrite spectra. Each spectrum shows the 0.7-µm feature seen in some earlier spectra, spectra of many asteroids, and spectra of some terrestrial phyllosilicates [4]. Some of these spectra show the shoulder located at 0.63 µm seen in some primitive asteroid spectra [5]. The width of the feature varies. In some spectra, an absorption feature near 0.9 µm is also present. This feature, presently unexplained, is in an area of an asteroid's spectrum that would be heavily affected by the incomplete removal of telluric water absorptions. Thus, comparisons of this feature with any similar feature in asteroid spectra must be conducted very carefully.

Sample C- and G-class asteroid spectra showing this feature are shown in Fig. 3. Sawyer [2] found that the 0.7-µm Fe^{2+}- Fe^{3+} feature was found predominantly in spectra of main-belt asteroids. Vilas and Gaffey [1] demonstrated that the spectral presence of this feature extends into the outer belt (heliocentric distances > 3.2 AU), but diminishes in intensity at the mean semimajor axes of the Hildas (4.0 AU) and is nonexistent at the distance of the Trojans (5.2 AU). Independent studies of the 3.0-µm water of hydration band also indicative of the presence of phyllosilicates also show a strong absorption in C- and G-class asteroids diminishing to nonexistent in the P- and D-class asteroids. It is reasonable to expect that the 0.7-µm absorption feature is indicative of aqueous alteration products. We examined whether change in this absorption feature correlated in any way with the sequence proposed by Browning et al. [6] for evidence of progressive aqueous alteration products in CM2 chondrites. The sample of common meteorites is limited to 3 (Murray, Mighei and Cold Bokkeveld), but loosely suggests that the absorption feature becomes slightly deeper and extends further into the near-IR.

Acknowledgements: This work is supported by the NASA Planetary Astronomy program, the NASA Origins of Solar Systems program, and the NAS/NRC RRA program.

References: [1]Vilas, F. and Gaffey, M. J., Science 1989;[2]Sawyer, S. R., Ph.D. Thesis, U. Texas, 1991; [3]Hiroi, T., Pieters, C. M., Zolensky, M. E. this volume; [4] King, T. V. V., Ph.D. Thesis, U. Hawaii, 1986; [5]Jarvis, K. S., Vilas, F., and Gaffey, M. J., this volume; [6]Browning, L. B., McSween, H. Y. and Zolensky, M. E., this volume.

SPECTRA OF CM2 CHONDRITES AND PRIMITIVE ASTEROIDS: Vilas, F. et al.

Fig. 1

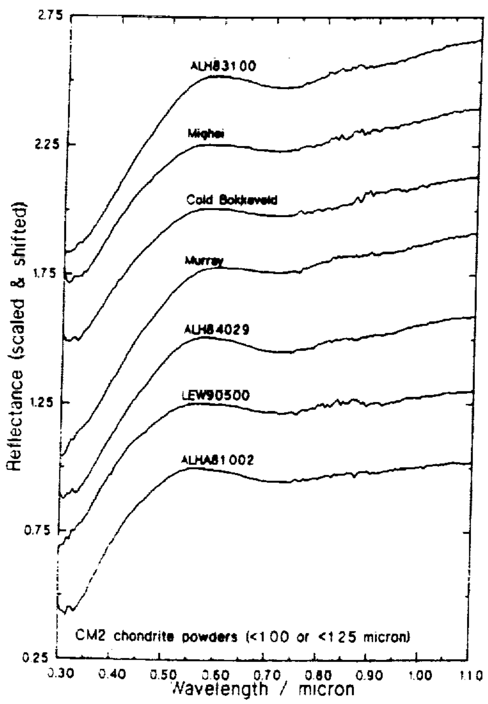


Fig. 2 CM2 CHONDRITE POWDERS WITH BACKGROUND CONTINUUM REMOVED

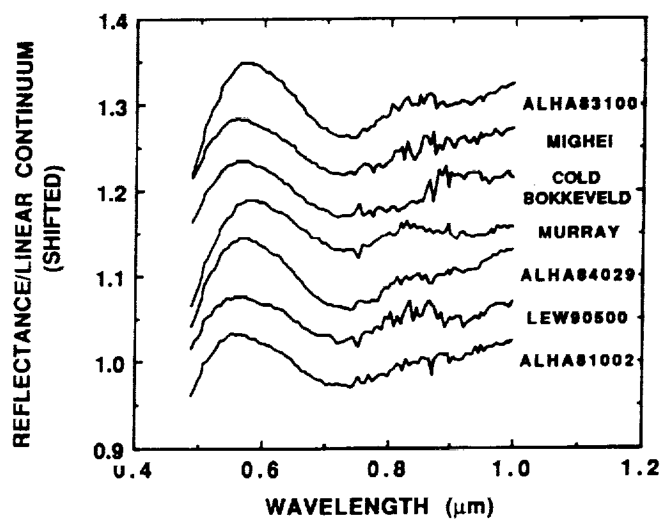
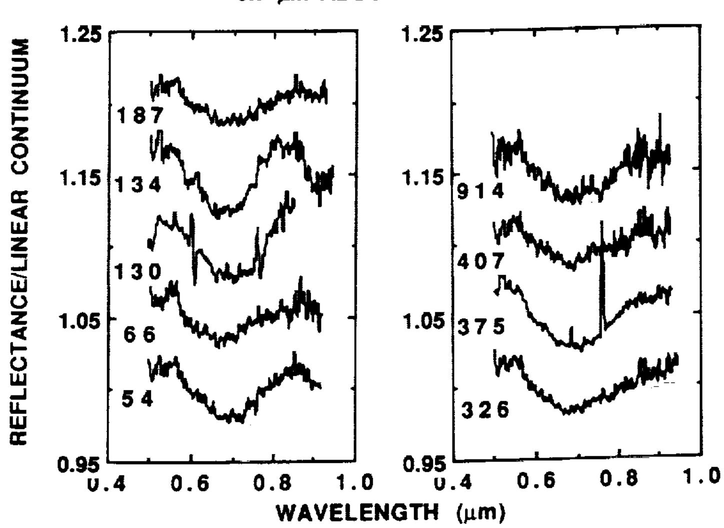


Fig. 3 MAIN-BELT C-CLASS ASTEROIDS 0.7 μm ABSORPTION FEATURE



S213-90 ABS. ONLY

N94-20849 168173 p-2

RECONDENSATION IN THE EARLY SOLAR SYSTEM: PHYSICAL CONDITIONS AND SOURCE MATERIAL; **A.V.Vityazev, V.A.Dorofeyeva, and A.B.Makalkin**, 1,3-Schmidt Institute of Physics of the Earth, Russian Acad.Sci., B.Gruzinskaya 10, 123810 Moscow, 2-Vernadsky Institute of Geochemistry, Russian Acad.Sci., Kosygin str.19, 117334 Moscow, Russia

Many physical processes in the solar nebula led to fractionation of the gaseous phase of the preplanetary material. We list some of these processes with corresponding type of fractionation in terms of Rock/Ice/Gas (Table 1). Recondensation from fractionated gas phase yields different compositions of condensates. In some details we consider one type of fractionation: impact heating with evaporation and subsequent recondensation of material during intercollisions of planetesimals. For thermodynamical simulation of recondensation in such a process one needs (a) $P-T$ parameters and (b) some initial source material to be heated, evaporated and recondensed. So these two problems are the main subject of the present abstract. In the other paper (1) we discuss results of the thermodynamical simulation.

According to the dynamical theory of planet formation, there should exist a long "planesimal" stage of evolution, when planetesimals grow by accumulation at intercollisions. The theory gives rather high collision velocities, at least at the late stages of planet formation (2,3): $v = (Gm_{max}/\theta r_{max})^{1/2} \approx 5(r_{max}/r_{\oplus})\text{km s}^{-1}$, where m_{max}, r_{max} are the mass and radius of the largest bodies in the mass spectrum $n(m)$ in the feeding zone of a planet, θ is Safronov number, G is gravitational constant, $r_{\oplus}$ is the radius of the Earth. At the zone of the terrestrial planets the relative velocities higher than 1 km/s existed at the time, when the large bodies were of lunar to martian size. From this moment at first very low, than more and more significant portions of material were involved in local evaporation at every collision. Estimates of $P-T$ parameters in the expanding explosion clouds at planetesimal collisions are presented in the book (3). The range of condensation pressures is rather high: from 10^{-6} to 10^{-2} bar. It depends on the relative velocity and sizes of colliding bodies and on the moment when condensation starts. Maximum temperatures of the evaporated material would not exceed 2000 K (3). Timescales when these $P-T$ conditions corresponded to recondensation events are from tens to 10^4 s (3). So for the first thermodynamical simulation of collisional impact recondensation 10^{-4} bar and 1500 K can be accepted as the reference data. These $P-T$ conditions can be applied equally to gas-abundant and gas-free stages of the early evolution of the solar system as far as pressure in the explosion cloud is higher than pressure in the nebula.

Other basic parameters necessary for this thermodynamic simulation are abundances of elements in colliding bodies, that is the source material to be evaporated and recondensed. We consider CI chondrite Orgueil as one extreme. It is an example of chondritic material least depleted in volatiles and most oxidized. Its elemental composition taken from the work (4) represents the most primitive material known from meteorites. Another extreme case for source material for impact recondensation is H5 chondrite Richardton. This is an example of material most depleted in volatiles and most reduced among ordinary chondrites. We used data (5) for its elemental composition. It is of interest to see what will be the effect of recondensation on their composition (1). But the simulation gives a mineral composition, so for better comparison of the processed material with the source one we have reconstructed the mineral composition of the source meteorites Orgueil and Richardton. Results are presented in Tables 2 and 3. For reconstruction of Orgueil mineral composition we used data (6,7) and other sources. Though similar to the model composition presented in (8),

our reconstruction yields much higher fraction of the oxidized sulfur, mostly in the form of epsomite. Reconstruction of the mineral composition of Richardton was made using the data (5). With the data available it's impossible to determine the composition of olivine and pyroxene. One can only say definitely, that 1 kg of the material contains 2.64 mole of olivine and 1.43 mole of pyroxene. The composition presented in Table 3 gives mole ratio forsterite/fayalite = 3.7, that approximately corresponds to olivine $Fe_{0.42}Mg_{1.58}SiO_4$ and pyroxene $Fe_{0.18}Mg_{0.82}SiO_3$ and their mass ratio ≈ 2.7.

References: (1) V.A. Dorofeyeva, A.B. Makalkin, M.V. Mironenko, A.V. Vityazev (1993) This volume. (2) V.S. Safronov (1969) *Evolution of the Protoplanetary Cloud and Formation of the Solar System* (Moscow, Nauka Press). (3) A.V. Vityazev, G.V. Pechernikova, V.S. Safronov (1990) *Terrestrial Planets: Origin and Early Evolution* (Moscow, Nauka Press). (4) E. Anders, M. Ebihara (1982) *Geochim. Cosmochin. Acta*, 46, 2363-2380. (5) J.A. Wood (1968) *Meteorites and the Origin of Planets* (New York, McGraw-Hill). (6) R.T. Dodd (1981) *Meteorites: A Petrologic-Chemical Synthesis* (Cambridge Univ. Press). (7) B. Nagy (1975) *Carbonaceous Meteorites* (New York, Elsevier Sci. Publ. Co.). (8) K.K. Turekian, S.P. Clark (1969), *Earth Planet. Sci. Lett.*, 6, 346-348.

Table 1. Fractionation in the gas phase
(R=Rock component, I=ices (H_2O, CH_4, NH_3, et al., G=H_2+He).

Fractionation type	Physical mechanism.
R enrichment relat. to I+G	Settling and subsequent evaporation of silicate dust (at electrical discharges). Impact evaporation at collisions of meteorite parent bodies.
R + I enrichment relative to G	Dissipation of H_2 from the solar nebula. Settling and subsequent evaporation of dust of cometary composition. Evaporation of cometary nuclei at collisions. Complete evaporation of interstellar dust at infall onto surface of the nebula.
I enr.to R+G, or I toG to R or I toR to G	Complete evaporation of ices with partial evaporation of silicates at the shock front on the nebula surface. Evaporation of ices (with partial evaporation of silicate dust) at collisions of cometary nuclei.

Table 2
Mineral Composition of Carbonaceous Chondrite CI Orgueil (Reconstruction)

Mineral	Formula	Mass %
Chlorite	$Mg_{3.6}Fe_{2.4}Si_4O_{14}\cdot 4H_2O$	5.2
Montmorillonite	$Mg_{0.161}Al_{2.33}Si_{3.67}O_{11}\cdot H_2O$	51.9
Epsomite	$MgSO_4\cdot 7H_2O$	23.1
Magnetite	Fe_3O_4	15.2
Sulfur	S	1.5
Anhydrite	$CaSO_4$	3.1

Table 3
Mineral Composition of Ordinary Chondrite H5 Richardton (Reconstruction)

	Mineral	Formula	Mass %
Olivine	Forsterite	Mg_2Si0_4	29.3
	Fayalite	Fe_2SiO_4	11.4
Pyroxene	Enstatite	$MgSiO_3$	11.8
	Ferrosilite	$FeSiO_3$	3.4
Feldspar	Albite	$NaAlSi_3O_8$	9.5
	Anorthite	$KAlSi_3O_8$	0.6
	Orthoclase	$CaAl_2Si_2O_8$	2.0
	Diopside	$CaMg(SiO_3)_2$	3.9
	Troilite	FeS	6.0
	Metal	Fe	18.3
	Other	(Ti, Cr *et al.*)	3.8

THE CLEMENTINE MISSION SCIENCE RETURN AT THE MOON AND GEOGRAPHOS; R. W. Vorder Bruegge[1], M.E. Davies[2], D.M. Horan[3], P.G. Lucey[4], C.M. Pieters[5], A.S. McEwen[6], S. Nozette[7], E.M. Shoemaker[6], S.W. Squyres[8], and P.C. Thomas[8]. [1]SAIC, 400 Virginia Ave., S.W., Ste. 810, Wash., D.C., 20024. [2]RAND Corp., 1700 Main St., Santa Monica, CA, 90407. [3]Naval Research Lab., Code 8111, 4555 Overlook Ave., S.W., Wash., D.C., 20375-5000, [4]U. Hawaii, Planetary Geoscience Div., 2525 Correa Road, Honolulu, HI, 96822. [5]Brown U., Dept. Geological Sciences, Providence, RI, 02912. [6]USGS, 2255 N. Gemini Dr., Flagstaff, AZ, 86001. [7]SDIO/TNI, The Pentagon, R 1E167, Wash., D.C., 20301-7100, [8]Cornell U., 312 Space Sciences Bldg., Ithaca, NY, 14853.

Introduction: The Clementine Mission is being built and flown by the Naval Research Laboratory under the sponsorship of the Strategic Defense Initiative Organization of the United States Department of Defense in joint-cooperation with NASA, and will explore the Moon and the near-Earth asteroid (NEA) 1620 Geographos with lightweight sensors developed by the Lawrence Livermore National Laboratory. A NASA Science Team for this mission will be selected by way of a NRA in April 1993. The instrument suite includes imaging cameras that cover a spectral range from the near-ultraviolet to the mid-infrared, a laser ranger, and, potentially, a charged particle telescope. To be launched in early 1994, Clementine will be in lunar orbit from February through May 1994, at which time it will depart the Moon for a flyby of 1620 Geographos in August 1994. This mission represents an outstanding opportunity for scientists interested in the Moon and asteroids. It is anticipated that the data returned from this mission will permit: an assessment of global lunar crustal heterogeneity at a resolution of less than 1 km; an assessment of the lithologic heterogeneity of Geographos at a scale of 100 m or better; and an assessment of surface processes on Geographos on the order of 10 m. This abstract describes the basic mission of Clementine and some of the key scientific questions that will be addressed. Additional material on the Clementine mission, its data handling and processing, and its instrument suite is presented elsewhere in this volume [1, 2, 3].

Clementine Mission: Clementine will be launched in late-January 1994 using a Titan-IIG rocket and will be inserted into a 5-hour, elliptical polar orbit at the Moon with a perilune of ~400 km at 30°S latitude. After one lunar-month, the perilune will be rotated to 30°N latitude, where it will remain for another lunar-month. During this period a global imaging data set will be obtained, as well as altimetry coverage between 60°N and 60°S. On May 3, 1994, the spacecraft will leave lunar orbit and enter an Earth-centered phasing orbit. Following two Earth swingbys, the spacecraft will make a close lunar swingby on May 27 and depart for an encounter with Geographos on August 31. The Geographos flyby distance is currently baselined at 100 km.

Four instruments to be tested by Clementine will provide the most valuable scientific return. These include ultraviolet/visible (UV/Vis) and near-infrared (NIR) imaging systems, a mid-infrared imaging system (usually referred to as the "long-wave" IR or LWIR), and a laser ranger (LIDAR) high resolution imaging and ranging system. The LIDAR ranger will provide a lunar altimetry data set between 60°N and 60°S with along-track spacing of ~1 km and across-track spacing of ~40 km at the equator. The vertical resolution will be limited by 40-m range bins, though the actual performance may vary with albedo and surface roughness. Some basic characteristics of the imaging systems are provided in Table 1. Three of these cameras will have multispectral capability via filter wheels. The bandpass centers for these filters were selected to maximize the return of lithologic data and are shown in Figure 1. The fourth camera (LWIR) has a single broadband filter. The multispectral capabilities of the Clementine cameras will permit it to address many of the same questions addressed by Galileo at the Moon and at Gaspra but with broader spectral coverage and at a somewhat higher resolution.

Clementine at the Moon: The global data set collected by Clementine at the Moon will permit investigation of a variety of key questions based on the compositional heterogeneity of the surface. Based on similar Galileo multispectral data, Belton and co-workers [4] determined that the ejecta from the Orientale impact basin was derived primarily from the crust with little, if any, mantle penetration and excavation. This finding is consistent with the formation of Orientale at a late stage

in the basin-forming epoch, after a thick lunar crust had been established, and is one example of how impact craters may be used as probes of the lunar interior. In another example Pieters [5] used telescopic reflectance spectra to determine that the impact event which created the 61 km-diameter crater Bullialdus excavated material from a compositionally-layered pluton within the uppermost 6 km of the lunar crust. The spatial resolution of the Clementine multispectral data should permit global lithological mapping on a scale as good or better than that which Galileo obtained and which can be obtained for the near-side of the Moon from Earth-based telescopes.

In another experiment, the Clementine LIDAR ranging experiment will provide a key data set for a variety of investigations. By combining the topography with gravity data, it becomes possible to map the density distribution of the lunar crust. It also provides a key information resource in almost all lunar geological studies [6]. The topography can be used in structural studies to estimate basin volumes and lava flow thicknesses, as well as to estimate lithospheric loads in flexure studies.

Clementine at Geographos: The August 1994 flyby of 1620 Geographos will permit investigation of the relationship of NEAs to Main Belt asteroids, comets, and meteorites. The specific measurements and scientific objectives for Galileo imaging at Gaspra [7] will hold for Clementine at Geographos: Global properties - size/shape, volume, period and pole position, cratering statistics and 'age' of surface; Surface morphology - crater morphology as a function of diameter, ejecta patterns, evidence of past internal activity, spallation features; Compositional features - surface composition and compositional heterogeneity; and Regolith properties - ejecta dispersal, stratigraphy, photometric properties. A primary goal in the exploration of asteroids is to examine the diversity of these objects. Key differences between Gaspra and Geographos are location and size. Gaspra is a mainbelt object approximately four times the size of the NEO Geographos. It will be interesting to examine the effects these differences have on some of the processes on small bodies such as cratering rate [8] and regolith processes [9-11].

References: (1) G. Shoemaker, LPSC XXIV (this volume), 1993. (2) A. McEwen, LPSC XXIV (this volume), 1993. (3) P. Lucey, LPSC XXIV (this volume), 1993. (4) M.J.S. Belton *et al.*, *Science*, **255**, p. 570, 1992. (5) C.M. Pieters, *Geophysical Res. Lett.*, **18**, p. 2129, 1991. (6) LGO Science Workshop Members, Contributions of a Lunar Geoscience Observer (LGO) Mission to Fundamental Questions in Lunar Science pp. 86, 1986. (7) M.J.S. Belton *et al.*, *Space Sci. Rev.*, **60**, p. 413, 1992. (8) C. Chapman *et al.*, 29th Plenary Meeting of COSPAR (Abstracts of the World Space Congress), p. 348, 1992. (9) Thomas *et al.*, *EOS, Trans. AGU*, **v. 73**, #43, p. 334, 1992. (10) McEwen *et al.*, 29th Plenary Meeting of COSPAR (Abstracts of the World Space Congress), p. 348, 1992. (11) C. Chapman *et al.*, LPSC XXIII, p. 219, 1992.

Table 1 - Some Characteristics of the Clementine Imaging Sensors

Instrument	Array Size	Bandpass (microns)	# Filters	Lunar Coverage	Pixel Resolution (m) Moon	Geographos
UV/Vis	288 x 384	0.25 - 1.0	5 or 6	Global	125 - 325	~ 25
NIR	256 x 256	1.0 - 3.0	6	Global	200 - 500	~ 40
LWIR	128 x 128	7.0 - 9.5	1	Partial (TBD)	50 - 125	~ 10
LIDAR	288 x 384	0.4 - 0.75	4	Partial (TBD)	40 - 100	< 5

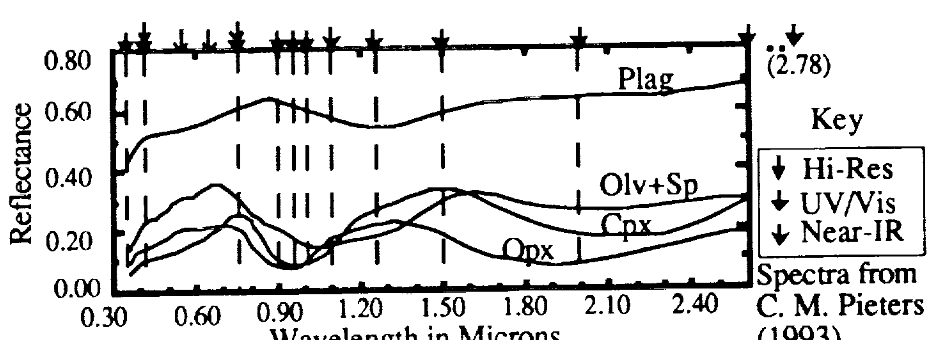


Figure 1. Clementine multispectral filter set superposed on reflectance data for four lunar mineral separates. 0.95 micron band may be replaced by a broadband filter for navigational purposes.

J215-25
ABS. ONLY

N94-20851

p. 2

ALUMINUM-26 ACTIVITIES IN METEORITES; J.F. Wacker, Battelle, Pacific Northwest Laboratories, P.O. Box 999, Richland, WA 99352

We report ^{26}Al activities for 686 Antarctic meteorites and 46 non-Antarctic meteorites. The data set includes new results for 253 Antarctic and 5 non-Antarctic meteorites. Most of the Antarctic specimens were collected from the Allan Hills region, but specimens from other regions have been measured as well. The non-Antarctic specimens include freshly fallen meteorites, in which short-lived radionuclides (*e.g.*, ^{22}Na, ^{54}Mn, ^{57}Co, etc.) were also measured. The data have been analyzed for terrestrial age distributions, identification of samples with unusual activities, pairing of specimens, and comparison of Antarctic and non-Antarctic activity distributions.

Terrestrial ages Terrestrial ages for individual specimens are generally determined using ^{36}Cl or ^{14}C. Ages of individual specimens based on ^{26}Al are generally unreliable due to variations in the ^{26}Al production rate caused by shielding effects, unusual exposures or undersaturation. Nevertheless, ^{26}Al can provide information on terrestrial ages of meteorite populations and provide useful guidance in identifying and selecting samples with long terrestrial ages. Comparisons of ^{26}Al activities and ^{36}Cl terrestrial ages [1] for Antarctic Ls and Hs show that older specimens, especially with ages >100 kyr (for Hs) or >250 kyr (Ls), have lower than normal ^{26}Al activities. Almost one half of the low activity samples have long terrestrial ages, indicating that ^{26}Al is useful in identifying old samples with about 50% success. Samples with low ^{26}Al but young ages are still of interest since they often have experienced unusual irradiation histories.

Unusual samples Several of the specimens show higher than saturation activities (59±9 for L and 55±8 for H chondrites [2]). Although many of these samples have recovered masses less than 100 g (*e.g.*, META 78008 [2] and Salem [3,4]), some high activity samples have large recovered masses. A notable example of the latter is ALHA 83101 (639.2 recovered mass). Two samples were measured, ALHA 83101.1 (515.1 g) and ALHA 83101.2 (23.1 g), with ^{26}Al activities of 90 and 113 dpm/kg, respectively. The high ^{26}Al activity in ALHA 83101 may indicate exposure to solar cosmic rays (SCRs), but atmospheric ablation should have removed most of the SCR-implanted material of the sample, given a typical range ~1 cm for SCRs [5]. Nevertheless, ALHA 83101 is a good candidate for either SCR exposure or an unusual irradiation history and it should be analyzed for noble gases and other radionuclides, such as ^{10}Be, ^{53}Mn.

One specimen had an unusually low ^{26}Al activity. EETA 83274 (L3) had an ^{26}Al activity of 18.9±0.9 dpm/kg. This activity is well below the L-chondrite saturation value of 59±9 dpm/kg and corresponds to a terrestrial age of 1.2±.2 Myr. The weathering and fracturing classes are B and A, suggesting a short terrestrial residence time and possibly a short cosmic ray exposure.

Pairings Aluminum-26 provides a useful means of identifying and confirming the existence of paired specimens. Recently analyzed meteorites include over 40 specimens from the Elephant Moraine region. Twelve L6s (EETA 83206, 83238, 83239, 83241, 83243, 83252, 83271, 83312, 83335, 83348, 83363, and 84304) have ^{26}Al activities from 70 to 84 dpm/kg, strongly suggesting that these samples belong to a single shower. The terrestrial age of EETA 83206, based on ^{36}Cl, is 45±45 kyr [1]. The high activity in the 12 samples also implies that they may have experienced an unusual cosmic ray exposure history, as may also be the case for a group of ALHA L6s. Two LL6 chondrites were analyzed (EETA 82608 and 83204, with ^{26}Al activities of 40±4 and 52±4, respectively), however, their ^{26}Al activities suggest independent falls. Other potential pairings were revealed by comparing the non-ALHA H and ALHA H distributions. The ALHA H distribution may have two components, one that has a broad ^{26}Al distribution and contains specimens with longer terrestrial ages, while the other is strongly peaked at 55 dpm/kg and represents younger specimens. The 55 dpm/kg peak in the ALHA H distribution has specimens from all compositional groups, suggesting that it was unlikely due to a shower. A group of ALHA

ALUMINUM-26 ACTIVITIES IN METEORITES; J.F. Wacker

H6s form a peak at 35 dpm/kg, suggesting a shower. The ALHA L distribution also appears to have several peaks, suggesting shower components.

Antarctic/non-Antarctic comparisons We have continued to examine and compare the distribution of ^{26}Al in Antarctic and non-Antarctic chondrites, in light of suggestions that these two groups of meteorites may be compositionally different [6,7]. A working hypothesis is that Antarctic/non-Antarctic differences ought to show up in the terrestrial age distributions of the Antarctic meteorites. If the compositional flux of meteorites is variable, then older meteorites should show greater differences. Previous reports have shown that Antarctic chondrites have average terrestrial ages of ~200 kyr , with ages up to ~1 Myr [1]. An average age of 200 kyr should shift the distribution of ^{26}Al activities for Antarctic chondrites to values that are typically ~20% lower than those of non-Antarctic ones. Average activities for ALHA L and H chondrites are 51 and 53 dpm/kg, by comparison, average (saturation) ^{26}Al activities for non-Antarctic L and H chondrites are 55 and 59 dpm/kg [2]. The ALHA Ls (111 specimens, corrected for known pairs) show the expected distribution, with an average ^{26}Al activity corresponding to a terrestrial age of 140 kyr. In contrast, the ALHA Hs (254 specimens, corrected for known pairings) show an unexpected behavior as their ^{26}Al distribution is similar to that of the non-Antarctic Hs. Thus, ALHA Hs are indistinguishable from modern specimens on the basis of ^{26}Al activities. This similarity suggests that the majority of ALHA Hs may be recent falls — within the last ~50,000 years. If Antarctic and non-Antarctic H chondrites sample different compositional groups, then a gradual shift in the composition of the incoming flux appears to be ruled-out by the ^{26}Al data [8,9]. This observation agrees with results obtained from cosmic ray exposure ages of Antarctic and non-Antarctic meteorites [10]. These results, however, may be consistent with suggestions of meteoroid streams [6,7,11,12] or may imply that Hs are more rapidly destroyed than Ls by terrestrial weathering.

REFERENCES [1] Nishiizumi K. *et al.*, (1989) *EPSL,* **93**, 299. [2] Evans J.C. and Reeves J.H. (1987) *EPSL* ,**82**, 223. [3] Evans J.C. *et al.*, (1987) *LPSC XVIII,* 271. [4] Nishiizumi K. *et al.*, (1990) *Meteoritics,* **25**, 392. [5] Michel R. *et al.*, (1982) *EPSL,* **59**, 33. [6] Dennison J.E. and Lipschutz M.E. (1987) *GCA,* **51**, 741. [7] Koeberl C. and Cassidy W.A. (1991) *GCA,* **55**, 3. [8] Wacker J.F. (1990) *BAAS,* **22**, 1124. [9] Wacker J.F. (1991) *Meteoritics,* **26**, 404. [10] Schultz L. *et al.*, (1991) *GCA,* **55**, 59. [11] Wood C.A. (1982) *LPSC XIII,* 873. [12] Dodd R.T. (1989) *Meteoritics,* **24**, 262.

S216-25 ABS ONLY

N94-20852

p. 2

RARE EARTH ELEMENTS IN INDIVIDUAL MINERALS IN SHERGOTTITES.

Meenakshi Wadhwa and Ghislaine Crozaz. McDonnell Center for the Space Sciences and Dept. of Earth and Planetary Sciences, Washington University, St. Louis, MO 63130.

Shergottites (i.e., Shergotty, Zagami, EETA79001, ALHA77005 and LEW88516) are an important set of achondrites because they comprise the majority of the SNC group of meteorites (nine, in total, known to us), which are likely to be samples of the planet Mars. Study of these meteorites may therefore provide valuable information about petrogenetic processes on a large planetary body other than Earth. Rare earth element distributions between various mineral phases have been found to be useful in geochemically modelling the petrogenesis of various rock types (terrestrial and meteoritic). However, with the exception of a few ion microprobe studies [1, 2, 3, 4, 5] and analyses of mineral separates [6, 7], there has previously not been any comprehensive effort to characterize and directly compare REE in individual minerals in each of the five known shergottites. We have, therefore, made ion microprobe analyses on thin sections of each of the shergottites. Minerals analysed were pyroxenes (pigeonite and augite), maskelynite and whitlockite. Table 1 gives REE concentrations in each mineral type in each shergottite.

As can be seen in Table 1, whitlockite is the mineral that contains the highest REE concentrations in every shergottite. In each case, bulk rock REE abundances are dominated by REE concentrations in whitlockite even though modal abundances of whitlockite in the shergottites range from ~<0.5% up to only ~1.5%. In fact, except for Eu (a substantial fraction of which is located in the maskelynite), the REE pattern of the whitlockite is almost parallel to the whole rock REE pattern for each shergottite. Mass balance calculations indicate that the fraction of REE located in the whitlockite is sensitive to the absolute modal abundance of whitlockite. On average, in the shergottites, ~70±25% of the La (representing LREE), ~25±10 of the Eu and ~ 35±15% of the Dy (representing HREE) are located in the whitockite; ~15±5% of the Eu is located in the maskelynite, while the remaining fraction of the REE are located in the pyroxene.

REE zoning in pyroxene, which is known to be among the first minerals to crystallize in the shergottites (based on petrography and phase relations), is an important indicator of crystallization history. Pigeonites and augites in all the shergottites are extensively zoned in their REE concentrations, as can be seen from the core and rim compositions given in Table 1. Moreover, there is a smooth variation of REE compositions in pyroxenes between these core and rim compositions, suggesting closed system crystal fractionation. These pyroxenes were obviously not in bulk equilibrium with their "parent" melt, but their cores (which do not seem to have undergone any post-crystallization re-equilibration and have retained their original compositions) were in equilibrium with this parent melt. As a result, estimates of the REE compositions of the shergottite parent melts can be made by inverting the core compositions of the clinopyroxenes using appropriate distribution coefficients (such as those determined in [8] for Shergotty pyroxenes). In all cases, we find that the REE abundances calculated in the melt in equilibrium with the low calcium pyroxene are lower than the abundances in the melt in equilibrium with the high calcium pyroxene, implying that the pigeonites began crystallization before the augites in the shergottites. In addition, REE patterns of the shergottite parent melts calculated in this manner are parallel to the whole rock REE patterns of each of the shergottites. This again supports a closed system fractional crystallization mechanism for the shergottites, despite their "cumulate" textures. As described in [5] for the new shergottite LEW88516 and for ALHA77005, closed system fractionation and the apparently cumulate textures in the shergottites need not necessarily be mutually exclusive (as is required by the strict definition of "cumulate" systems) if the accumulating crystals began crystallization in a relatively large volume system that nevertheless remained closed to the influx of fresh magma.

REE IN MINERALS IN SHERGOTTITES: Wadhwa M. and Crozaz G.

TABLE 1. REE in minerals in the shergottites: core and rim compositions are given for 'LCa Px' (low calcium pyroxene) and 'HCa Px' (high calcium pyroxene) as 'core/rim'; 'Poik' and 'Non-Poik', in the case of pyroxenes in ALHA77005 and LEW88516, denotes 'poikilitic' and 'non-poikilitic'. REE concentrations in maskelynite and whitlockite are averages of all measurements on these grains, with '±' reflecting the range of concentrations present in these minerals. REE concentrations in pyroxene and maskelynite are in ppb, while those in whitlockite are in ppm. The number in parentheses is the number of grains of each mineral type analysed.

SHERGOTTITE	MINERAL	REE									
		La	Ce	Nd	Sm	Eu	Gd	Tb	Dy	Ho	Tm
SHERGOTTY	LCa Px (13)	14/51	53/221	70/296	47/206	18/63	103/486	26/114	229/1128	52/264	28/143
	HCa Px (3)	33/97	147/410	290/696	162/534	58/89	317/837	72/205	526/1322	112/245	45/141
	Maskelynite (2)	89 ± 3	178 ± 8	81 ± 10	27 ± 1	337 ± 47	22 ± 3	4 ± 1	21 ± 3	6 ± 1	-
	Whitlockite (4)	147 ± 5	356 ± 13	239 ± 9	81 ± 6	22 ± 1	120 ± 9	24 ± 2	157 ± 3	32 ± 2	11 ± 1
ZAGAMI	LCa Px (23)	15/50	44/149	42/158	35/106	10/39	82/242	20/61	194/619	51/141	24/86
	HCa Px (7)	67/102	238/363	220/336	112/171	38/54	373/543	86/119	691/922	143/225	69/115
	Maskelynite (2)	70 ± 35	160 ± 36	83 ± 11	23 ± 11	247 ± 130	22 ± 9	4 ± 2	19 ± 2	6 ± 1	-
	Whitlockite (4)	113 ± 10	280 ± 11	177 ± 12	62 ± 6	19 ± 2	91 ± 8	18 ± 2	128 ± 18	25 ± 3	10 ± 1
EETA79001	LCa Px (20)	3.5/13	15/60	29/148	32/206	13/63	84/422	28/94	235/950	63/231	29/80
- Lithology A	HCa Px (*)	-	-	-	-	-	-	-	-	-	-
	Maskelynite (2)	33 ± 1	64 ± 3	55 ± 5	18 ± 2	445 ± 10	33 ± 3	4 ± 1	23 ± 4	-	-
	Whitlockite (3)	24 ± 6	64 ± 17	63 ± 22	42 ± 12	13 ± 7	72 ± 23	15 ± 2	107 ± 22	22 ± 6	8 ± 2
EETA79001	LCa Px (23)	32/53	77/161	96/155	99/167	31/70	245/406	68/106	617/713	154/173	61/99
- Lithology B	HCa Px (5)	78/97	97/644	257/360	191/384	64/82	547/970	154/212	1202/1748	267/365	136/141
	Maskelynite (3)	30 ± 11	42 ± 30	32 ± 6	18 ± 10	351 ± 130	21 ± 9	4 ± 2	18 ± 5	3 ± 2	-
	Whitlockite (4)	30 ± 4	74 ± 11	75 ± 14	45 ± 6	14 ± 2	81 ± 10	18 ± 2	118 ± 16	24 ± 3	8 ± 1
ALHA77005	LCa Px Poik (29)	1/4	4/21	8/47	7/53	2/12	16/122	4/30	30/273	9/84	6/42
	HCa Px Poik (4)	30/157	147/531	271/654	256/544	82/278	469/918	104/245	732/1826	187/412	72/110
	LCa Px Non-Poik (21)	11/50	48/154	52/252	57/243	19/69	84/612	22/152	233/1214	89/265	50/127
	HCa Px Non-Poik (3)	37/133	225/1769	439/559	463/464	145/159	816/1020	215/219	1565/1683	330/394	120/154
	Maskelynite (3)	62 ± 5	130 ± 57	68 ± 14	20 ± 8	443 ± 110	34 ± 15	4 ± 1	21 ± 4	-	-
	Whitlockite (4)	27 ± 2	65 ± 2	54 ± 1	31 ± 2	10 ± 1	55 ± 1	11 ± 1	75 ± 2	16 ± 1	6 ± 1
LEW88516	Low-Ca Px Poik (25)	1/2.5	4.9/32	9.1/62	9.5/63	4.4/22	23/218	5.7/57	66/571	16/143	9.2/71
	High-Ca Px Poik (3)	19/24	122/135	220/264	175/205	75/85	514/565	122/121	812/842	160/205	69/72
	LCa Px Non-Poik (15)	5/21	44/83	31/133	28/124	8/40	74/274	28/72	20/768	46/216	24/85
	HCa Px Non-Poik (2)	43/68	185/403	384/610	337/535	78/124	700/1112	166/263	1359/2157	311/425	146/206
	Maskelynite (6)	70 ± 20	140 ±13	73 ± 23	22 ± 12	468 ±150	33 ± 4	5 ± 1	26 ± 14	6 ± 1	-
	Whitlockite (6)	41 ± 4	106 ± 5	81 ± 8	45 ± 6	13 ± 2	75 ± 8	13 ± 2	98 ± 10	20 ± 2	7 ± 1

* Not analysed.

References: [1] Lundberg *et al.* (1988) GCA **52**, 2147-2163. [2] Lundberg *et al.* (1990) GCA **54**, 2535-2547. [3] Wadhwa *et al.* (1991) Meteoritics **26**, 404-405. [4] Wadhwa and Crozaz (1992) Meteoritics **27**, 302-303. [5] Harvey *et al.* (1992) GCA (submitted). [6] Smith *et al.* (1984) Proc. 14th LPSC, Part 2, JGR **89**, B612-B630. [7] Laul *et al.* (1986) **50**, 909-926. [8] McKay *et al.* (1986) GCA **50**, 927-937.

ORIGIN OF HIGH-Ti LUNAR ULTRAMAFIC GLASSES; T.P. Wagner and T. L. Grove, Department of Earth, Atmospheric and Planetary Sciences, Massachusetts Institute of Technology, Cambridge, MA 02139 P-2

We have performed a series of high pressure melting experiments on a synthetic analog of the Apollo 14 Black Glass. At 15 kb and 1400 °C, olivine is the liquidus phase. At 25 kb and 1450 °C, orthopyroxene and Cr-spinel crystallize. A multiple saturation point with olivine + orthopyroxene + spinel on the liquidus occurs at 20 kb and 1440 °C. We propose that the high-Ti ultramafic glass evolved from a low-Ti Green Glass generated deep in the lunar interior that assimilated shallow-level, late stage cumulates of magma ocean differentiation. Heat for assimilation is provided by superheat of the low-Ti magma and melts high-Ca pyroxene and ilmenite cumulates at a depth of 100 km. This model is a variant of that proposed by Hubbard and Minear [1] and rejected by Ringwood and Kesson [2].

Table 1. Olivine + orthopyroxene multiple saturation boundaries for lunar ultramafic glasses.

Glass composition	Temperature (°C)	Pressure (kb)	TiO_2 wt. %	Reference
Apollo 15 Green	1525	20	0.26	[3]
Apollo 14 VLT	1520	22	0.55	[4]
Apollo 17 VLT	1500	18	0.63	[5]
Apollo 17 Orange	1482	22	9.12	[6]
Apollo 15 Red	1463	25	13.8	[7]
Apollo 14 Black	1440	20	16.4	[3]

Table 1 summarizes the results of elevated pressure crystallization experiments on lunar ultramafic glass compositions. As previously noted [7,8,9] a remarkable characteristic of the phase relations is the similarity among their high pressure multiple saturation boundaries. These magmas would have formed between 500 km (Apollo 15 Red) and 360 km (Apollo 17 VLT), assuming a simple batch melting process. The results in Table 1 come from 5 different laboratories. Considering that inter laboratory differences in piston cylinder studies are commonly +/- 2 kb [10], the pressures of multiple saturation are remarkably close and indicate a pressure of origin of 22 kb. There is a significant temperature variation (85 °C) that is correlated with TiO_2 content; higher TiO_2 corresponding to lower temperature of multiple saturation. This temperature effect can not be due to inter laboratory differences, since the maximum and minimum values in Table 1 come from the same laboratory. We propose that the temperature drop results from assimilation of a component with a lower melting temperature.

Previous models for the origin of lunar ultramafic glasses A process must be identified that can lead to a great diversity in chemical composition in ultramafic glasses that all come from the same depth (or depth interval). This part of the lunar interior is significantly deeper (by 140 km) than the portion where the differentiates of a lunar magma ocean reside (0 to 300 km). The low-Ti Apollo 15 green glass has rare earth element abundances that are consistent with its derivation from a chondritic, undifferentiated lunar interior [11]. The remaining lunar ultramafic glasses show systematic variations in TiO_2 content [8] and display geochemical characteristics indicative of contributions from at least two other sources: a high-Ti cumulate source and a KREEP-like large ion lithophile and incompatible element enriched source [12]. Longhi [9] proposes that the low-Ti ultramafic glasses formed by polybaric near-fractional melting of the deep lunar interior during adiabatic decompression over a depth range from 1000

to 100 km. Following terrestrial models of fractional melting and melt aggregation, the multiple saturation point of low-Ti green glass corresponds to the mean pressure of melt segregation (400 km). This model satisfies the geochemical requirements of Apollo 15 green glass, and is consistent with models of the thermal structure of the deep lunar interior [13]. To generate the ultramafic glasses with variable TiO_2, Ringwood and Kesson [2] proposed that dense pods of TiO_2-rich magma ocean cumulates from shallow depth sank into the undifferentiated lunar mantle and melted there to form hybridized zones. Partial melting of these zones led to the range of observed ultramafic glasses. Ringwood and Kesson rejected cumulate assimilation at shallower depths based on heat budget constraints and mass balance considerations. If the hi-Ti glasses were produced by melting of deep hybridized zones, there is the potential that they would sink into the lunar interior, as the high-Ti magmas becomes denser than their surroundings at depths exceeding about 500 km [14]. Hess [15] has proposed a cumulate sinking model that overcomes this difficulty.

Proposed model for the origin of Apollo 14 Black Glass We suggest a variant of the model of [1] that involves assimilation of shallow mantle consisting of the late-stage Ti-rich cumulates of the magma ocean. In magma ocean models these cumulates would be present over a depth range of 100 to 150 km [16]. The base of the lithosphere lies near this depth at 3.2 b.y. [13]. Low-Ti ultramafic magmas are produced by near-fractional adiabatic melting as in [10] and rise into the cooler shallow lithosphere. When these magmas reach a depth of 100 km, they have a potential superheat of >160 ^oC (T of Green Glass multiple saturation - liquidus T of Black Glass at 100 km). This superheat provides thermal energy to melt the shallow level cumulates. Major element mass balance models produce the Black Glass from low-Ti Green Glass by assimilation of cumulates in the proportions:

Black Glass + 0.02 Olivine = 0.69 Green Glass + 0.03 high-Ca Clinopyroxene + 0.30 Ilmenite

This mass balance requires that about 50 cal/gm of heat be supplied to assimilate the high-Ti cumulates. A superheat of 160 ^oC will provide about 49 cal/gm. As the Black and Green glasses represent the extremes of the low-Ti to high-Ti ultramafic glass trends [8], the entire spectrum of compositions can be reproduced by this process. With continued ascent through shallower lithosphere, the high-Ti magmas pass through the KREEP-rich trapped residual liquid, and inherit the trace element characteristics of this component. Previous models call upon a large scale mixing process that disrupts the magma ocean cumulates and distributes them over a large region of the lunar mantle. In these models the difference in temperature of multiple saturation must be caused by differences in the mantle interior temperature which influence the adiabatic decompression melting process. A revived Hubbard and Minear model has the advantage of simplicity; it does not require reshuffling of magma ocean cumulates.

References [1] Hubbard and Minear, 1975, Lunar Sci VI, 405-406. [2] Ringwood and Kesson, 1976, Proc Lunar Sci Conf 7th, 1697-1722. [3] This study. Also see Green and Ringwood, 1973, Earth Planet. Sci. Lett., 19, 1-8 and Kesson, 1975, Proc. Lunar Sci Conf 6th, 921-944 for earlier experiments on the Apollo 15 Green and Apollo 15 Red glass, respectively. [4] Chen and Lindsley, 1983, Proc Lunar Planet Sci Conf 14th, B335-342. [5] Chen et al., 1982, Proc Lunar Planet Sci Conf 13th, A171-A181. [6] Green, 1975, Proc Lunar Sci Conf 6th, 871-893. [7] Delano, 1980, Proc Lunar Sci Conf 11th, 251-288. [8] Delano, 1986, Proc Lunar Planet Sci Conf 16th, D201-D213. [9] Longhi, 1992, Proc Lunar Planet Sci Conf 22nd, 343-353. [10] Johannes et al, 1971, Contrib Mineral Petrol 32, 24-38. [11] Taylor, 1975, Lunar Science: A post-Apollo view. Pergamon Press, 372 p. [12] Shearer et al, 1990, Geochim Cosmochim Acta 54, 851-867. [13] Solomon and Head, 1979, J Geophys Res 84, 1667-1682. [14] Delano, 1990, Proc Lunar Planet Sci Conf 20, 3-12. [15] Hess, 1991, Geophys Res Lett 18, 2069-2072. [16] Taylor and Jakes, 1974, Proc Lunar Sci Conf 5th, 1287-1305.

RHENIUM-OSMIUM ISOTOPE SYSTEMATICS OF ORDINARY CHONDRITES AND IRON METEORITES. R.J. Walker, Dept. of Geology, Univ. MD, College Park, MD 20742, J.W. Morgan, M.F. Horan and J.N. Grossman, U.S. Geological Survey, Reston, VA 22092

Using negative thermal ionization mass spectrometry, Re and Os abundances were determined by isotope dilution and $^{187}Os/^{186}Os$ measured in 11 ordinary chondrites, and also in 1 IIB and 3 IIIB irons. In addition, $^{186}Os/^{188}Os$ and $^{189}Os/^{188}Os$ ratios were precisely determined for 3 *unspiked* ordinary chondrites as a means of constraining the intensity of any neutron irradiation these meteorites may have experienced.

Ordinary Chondrites. The H-group ordinary chondrites examined by this study were chosen both to span the maximum range of metamorphic temperatures (H3 to H6), and because they are unshocked or lightly shocked. Where comparisons are possible, Re and Os elemental abundance data agree well with previous determinations [1,2]. Our other results fall within the H chondrite range previously determined, except Changde (H5), which falls squarely in the L chondrite range [1]. The $^{187}Os/^{186}Os$ and $^{187}Re/^{186}Os$ ratios for these whole-rock chondrite samples range from 1.055 to 1.089 and from 3.419 to 4.016, respectively. The range in Os isotopic compositions and Re/Os ratios contrasts with the generally higher and more variable $^{187}Os/^{186}Os$ and $^{187}Re/^{186}Os$ ratios reported for metal separated from ordinary chondrites (1.067-1.164 and 3.82-5.00, respectively) [3]. We note that several of the samples analyzed by Luck and Allegre [3] are moderately to heavily shocked [2]. Our data, except Xingyang, plot systematically below the IIA iron meteorite isochron of Horan *et al.* [4], however, they do not form an isochronous array (Table 1 and Figure 1). Δ_{Os} values (per mil deviation of $^{187}Os/^{186}Os$ from the IIA isochron which is defined as having a slope=0.07824 and an initial $^{187}Os/^{186}Os$=0.8007 [4]) range from +7.1 to -36.7. There is no correlation between metamorphic grade and Δ_{Os} value. Three of the meteorites were analyzed in duplicate. The Δ_{Os} values for duplicate analyses of two (Forest Vale and Forest City) agreed well, whereas duplicate analyses of Allegan did not agree well.

There are a number of possible explanations for the isotopic heterogeneities observed in these H-chondrites, and their offsets from the IIA isochron. For example, Forest Vale falls about 36 per mil below the IIA isochron, with duplicate analyses giving a model age of about 3 Ga. These results could be consistent with a later major reequilibration event occurring approximately 1.5 billion years following accretion, however, this meteorite shows no evidence of ^{40}Ar loss (age = 4.52±0.03 Ga [5]). Evidence of substantial neutron irradiation has been found in Forest Vale metal [6]. Since ^{187}Os has a high neutron capture cross section, we considered the possibility of neutron burn-up leading to depletion of this isotope. Measurable loss of ^{187}Os would necessarily lead to significant, but smaller, variations in other Os isotopes. Os isotope ratios were measured on unspiked samples of Allegan, Forest City and Forest Vale, meteorites with average Δ_{Os} values of -0.5, -16 and -35, respectively. Except for variations in ^{187}Os, no variations between meteorites were noted in the isotopic ratios of any other isotopes above the 0.5 per mil level of resolution. From the lack of detectible deviation in $^{186}Os/^{188}Os$ ratios, we estimate a maximum neutron fluence of 5 x $10^{18}/cm^2$, implying a change in $^{187}Os/^{188}Os$ of no more than 1.3 per mil.

The isotopic variations could also conceivably be the result of: 1) chemical differentiation in some portions of the solar system during its first 100 million years, 2) primordial heterogeneities, or 3) alteration, reequilibration, or contamination processes that occurred long after initial accretion. For example, a negative Δ_{Os} offset of as much as 5 could be the result of early accretion, followed by evolution of the parent body for the IIA irons with an average $^{187}Re/^{186}Os \geq 6$ for 50-100 Ma. Thus, the IIA irons may have a substantially younger Re-Os closure age than these H-chondrites. This scenario, however, would only be consistent with a single offset from the IIA isochron, and cannot account for variations among the meteorites that presumably come from the same parent body. It also requires that the IIA parent body evolved with a significantly higher time-integrated Re/Os ratio than any known chondrites. Those chondrites with the larger variations from the IIA isochron must reflect either primordial heterogeneities, or the result of processes that occurred much later in the history of the solar system, such as reequilibration, or late stage alteration/contamination. These possibilities will be evaluated via the careful examination of individual chondrite components.

Irons. Reexamination of the Re-Os systematics of IIAB and IIIAB irons that were previously examined by the less-precise resonance ionization technique has continued [7]. New data are provided in Table 1. The single IIB examined, Central Missouri, has a Δ_{Os} value of +7.7. This value is within uncertainty of the value reported for Mount Joy (+9.9)[4]. Together, the two samples hint that a IIB isochron may have nearly the same slope as the IIA isochron, but with a substantially higher initial ratio. Two of the IIIB irons have Δ_{Os} values within analytical uncertainty of the IIA isochron, suggesting very similar systematics to the IIA's. The value for Campbellsville, however, is +25.7 (not shown in figure), and plots well above the IIA isochron.

References. [1] J.W. Morgan and J.F. Lovering, *Geochim. Cosmochim. Acta* 31, 1893-1909, 1967. [2] J.W. Morgan, M.J. Janssens, H. Takahashi, J. Hertogen and E. Anders, *Geochim. Cosmochim. Acta* 49, 247-259, 1985. [3] J.M. Luck and C.J. Allegre, *Nature* 302, 130-132, 1983. [4] M.F. Horan, J.W. Morgan, R.J. Walker and J.N. Grossman, *Science* 255, 1118-1121, 1992. [5] G. Turner, M.C. Enright and P.H. Cadogan, Proc. *Lunar Planet. Sci. Conf. 9th*, 989-1025, 1978. [6] J.S. Kim and K. Marti, *Lunar and Planetary Science XXIII*, 689-670, 1991. [7] J.W. Morgan, R.J. Walker and J.N. Grossman, *Earth Planet. Sci. Lett.* 108, 191-202.

Table 1. Rhenium and Os isotopic and compositional data for chondrites and irons. Concentrations are given as parts per billion. Uncertainties are 1 and 2 per mil for $^{187}Os/^{186}Os$ and $^{187}Re/^{186}Os$, respectively, except for the irons with uncertainties of 2 and 4 per mil, respectively. Δ_{Os} is defined in the text.

Type	Meteorite	Re	Os	$^{187}Os/^{186}Os$	$^{187}Re/^{186}Os$	Δ_{Os}
H3	Dhajala	73.91	816.9	1.072	3.637	-12.2
	Sharps	74.52	876.1	1.061	3.419	-6.7
	Bremervörde	62.49	673.8	1.089	3.755	-5.0
H4	Avanhandava	78.75	842.7	1.088	3.757	-6.1
	Forest Vale	80.37	840.7	1.065	3.842	-33.0
	Forest Vale	83.31	833.9	1.074	4.016	-36.7
H5	Anlong	96.96	1048.	1.087	3.718	-4.2
	Changde	44.66	498.2	1.072	3.604	-9.9
	Allegan	79.33	888.5	1.081	3.589	-0.5
	Allegan	76.72	860.2	1.074	3.585	-6.6
	Forest City	78.64	862.8	1.071	3.664	-15.0
	Forest City	69.60	802.3	1.055	3.486	-17.2
H6	Guareña	84.17	982.5	1.069	3.444	-1.1
	Xingyang	86.21	976.7	1.086	3.549	+7.1
Group						
IIB	Central Missouri	1.428	12.98	1.156	4.428	+7.7
IIIB	Grant	2.673	24.48	1.147	4.394	+2.3
	Campbellsville	3.390	17.89	1.436	7.661	+25.7
	Tieraco Creek	2.879	27.32	1.130	4.240	-2.4

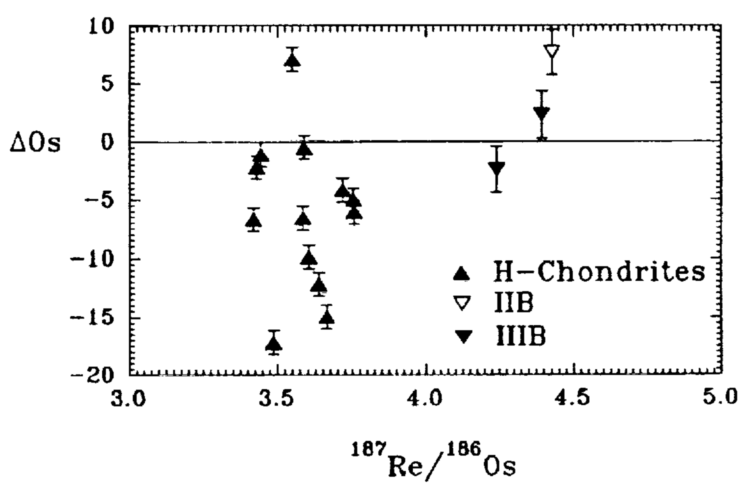


Figure 1. Δ_{Os} *vs.* $^{187}Re/^{186}Os$ plot for whole-rock ordinary chondrites and iron meteorites. Δ_{Os} is the per mil deviation in $^{187}Os/^{186}Os$ from the IIA isochron. The IIA isochron from Horan *et al.* [4] is show as a horizontal line. It has a slope of 0.7824 and an intercept of 0.8007.

DIFFUSION-CONTROLLED MAGNESIUM ISOTOPIC FRACTIONATION OF A SINGLE CRYSTAL FORSTERITE EVAPORATED FROM THE SOLID STATE; Jianhua Wang[1], Andrew M. Davis[4], Akihiko Hashimoto[3] and Robert N. Clayton[1,2,4]; [1]Department of the Geophysical Sciences, [2]Department of Chemistry, [4]Enrico Fermi Institute, University of Chicago, Chicago, IL 60637; [3]Harvard-Smithsonian Center for Astrophysics, Cambridge, MA 02138

Though the origin of calcium- and aluminum-rich inclusions (CAIs) in carbonaceous chondrites is still a disputed issue, evaporation is no doubt one of the most important processes for the formation of CAIs in the early solar nebula. The mechanism for production of large isotopic mass fractionation effects in magnesium, silicon, oxygen and chromium in CAIs can be better understood by examining isotopic fractionation during the evaporation of minerals. We have performed new evaporation experiments on single-crystal forsterite. We measured the magnesium isotopic distribution near the evaporating surfaces of the residues using a modified AEI IM-20 ion microprobe to obtain rastered beam depth profiles. A theoretical model was used to explain the profiles and allowed determination of the diffusion coefficient of Mg^{++} in forsterite at higher temperatures than previous measurements. The gas/solid isotopic fractionation factor for magnesium for evaporation from solid forsterite was also determined and found to be nearly the same as that for evaporation of liquid Mg_2SiO_4.

A previous study of the evaporation of synthetic liquid Mg_2SiO_4 revealed that isotopic fractionation of magnesium, silicon and oxygen follows a Rayleigh fractionation curve with close to inverse-square-root of mass fractionation factor, whereas little isotopic fractionation is detected in bulk residues from evaporation of solid forsterite [1]. Wang *et al.* [2] examined the isotope fractionation profiles of magnesium in residues of synthetic polycrystalline forsterite evaporated below the melting temperature and found that the distribution of magnesium isotopes near the evaporating surface was diffusion-controlled. In the Rayleigh fractionation model, instantaneous mixing (homogeneity) of the residues is assumed. This is rarely the case in the experiments and in nature because diffusion is slow enough to prevent instantaneous mixing of the residue during the evaporation process. Diffusion must be considered when modeling isotopic fractionation during the transformation process of a reservoir. Modeling of the evaporation of synthetic polycrystalline forsterite with loosely bonded single crystals is extremely complicated, as both volume and grain boundary diffusion must be considered, in addition to gas transport through a porous medium. In addition, the surface area of the synthetic polycrystalline aggregate is not well-known. For these reasons, we have performed new evaporation experiments on single-crystal forsterite.

A single crystal of synthetic forsterite (provided by Dr. Robert C. Morris of Allied Signal Corp.) was sliced perpendicular to its *a*-axis and polished on both surfaces. These slices were cut into small chips for evaporation experiments at 1800, 1750, 1600 and 1500°C for 1 to 96 hours. The evaporation runs were performed in a vacuum furnace [3] at a pressure of $\leq 10^{-6}$ torr. The weight and the surface area of each chip were measured before and after the evaporation run to determine the evaporation rate. Measured evaporation rates from short duration experiments tend to have higher values than those from longer experiments, probably due to the existence of defects on the crystal surface. All measured evaporation rates for single crystal forsterite are lower than those measured by Hashimoto [3], especially at lower temperatures (Figure 1). This discrepancy is apparently the result of the underestimate of the surface area in the polycrystalline forsterite used in the earlier experiments.

Magnesium isotopic fractionation effects in the single crystal forsterite residues occur over <10 µm, so that our previous method of spot analyses of sections through residues [2] could not be used. Instead, magnesium isotopic profiles perpendicular to the evaporating surfaces of the residues have been measured by depth profiling using a modified AEI IM-20 ion microprobe with rastered beam. The primary beam intensities were 30-35 nA with a rastered area of ~100 × 100 µm. In order to obtain a depth profile of only the central, flat-bottomed area of the raster pit, a digital aperture was used to collect signal from the central 52 or 25% of the total rastered area. In each measurement, signal collection was begun 2 minutes after turning on the primary beam to allow the Mg^+ signal to stabilize. Each measurement of 500–1000 cycles through ^{26}Mg, ^{25}Mg and ^{24}Mg took 5–7 hours and sampled the rastered area to a depth of up to 10 µm. Depth profiles of single-crystal forsterite starting material were measured before and after each isotope profile of a residue to standardize the results and correct for instrumental drift. A 500-scan analysis of forsterite starting material shows a constant magnesium isotopic composition with depth (or time) with a standard deviation for average of 25 scans of about ±1.5‰ (1σ) for $\delta^{26}Mg$. All evaporation experiments were long enough and the chips of the forsterite were thick enough that steady state isotope profiles were produced near the evaporating surface and the magnesium isotopic composition of the inner portion of the residue was not disturbed. The depth of each the raster pit was measured using a Sloan surface profiler with a precision of ±0.1 µm.

A theoretical model incorporating diffusion has been developed to study the isotope fractionation effects for

MG ISOTOPES IN FORSTERITE EVAPORATION RESIDUES; Wang J. *et al.*

transformation of a nonmixed reservoir. The present model uses a one-dimensional approach, assuming that the reservoir is shaped like a slab with phase transition at only one surface (or both surfaces) and the coordinate of length is always perpendicular to the surface. The first step in solving this problem is consideration of a semiinfinite slab. This involves solving a partial differential equation with a moving boundary and a solution was found using the Laplace transform [4]. There is also a steady state solution: $R(x)/R_o = 1 + (\alpha-1)e^{-x}$, where R is the ratio of a minor isotope to an abundant isotope, α is the fractionation factor between the solid and the gas phase and x is nondimensionalized distance from the evaporating surface relative to the diffusion coefficient and the evaporation rate. The next step is to consider a slab with finite thickness. A set of partial differential equations was solved numerically using the Crank-Nicolson implicit method. The results of this model were used to interpret magnesium isotopic fractionation in the single-crystal forsterite residues.

By plotting $\ln\delta^{26}Mg$ (relative to the starting material) vs. depth from the evaporating surface, we can obtain the diffusion coefficient for Mg^{++} from the slope (v/D) and the fractionation factor of magnesium between its gas phase species and solid forsterite from the intercept ($\ln 1000(\alpha-1)$). Figure 2 shows the variation of the diffusion coefficient of Mg^{++} in forsterite along the *a*-axis with temperature. The D_o and E_D deduced from this plot are 5.23×10^6 cm²/sec and 630 kJ/mole respectively for the temperature range of 1500 to 1800 °C. These results are different from Morioka's measurement of 1.54×10^3 cm²/sec and 444 kJ/mole for the temperature range of 1300-1400 °C for Mg^{++} diffusion in forsterite along *c*-axis [5]. Previous work (see references in [5]) on cation diffusion in olivine and forsterite revealed that cations diffuse faster along *c*-axis than *a*- and *b*-axis. This anisotropic diffusion effect is not enough to account for the difference between the present study and Morioka's data. The average fractionation factor for $^{26}Mg/^{24}Mg$ between its gas species and forsterite crystal is 0.9725. This is greater than the ideal kinetic fractionation factor of 0.9608 for magnesium evaporating as Mg atoms, but it is very close to the value measured for evaporation of liquid Mg_2SiO_4, 0.9696 [1]. One possibility for these differences is that other species such as MgO (α=0.975) were involved in evaporation. The outermost layer enriched in heavy magnesium could also have been burned away during the first two minutes before data collection. The reprecipitation of the evaporated species on the crystal surface may reduce the measured fractionation factor.

References: [1] A.M. Davis *et al.* (1990) *Nature* **347**, 655-658. [2] J. Wang *et al.* (1991) *LPSC* **22**, 1461-1462. [3] A. Hashimoto (1990) *Nature* **347**, 53-55. [4] V.G. Smith *et al.* (1955) *Can. J. Phys.* **33**, 723-745. [5] N. Morioka (1981) *GCA* **45**, 1573-1580.

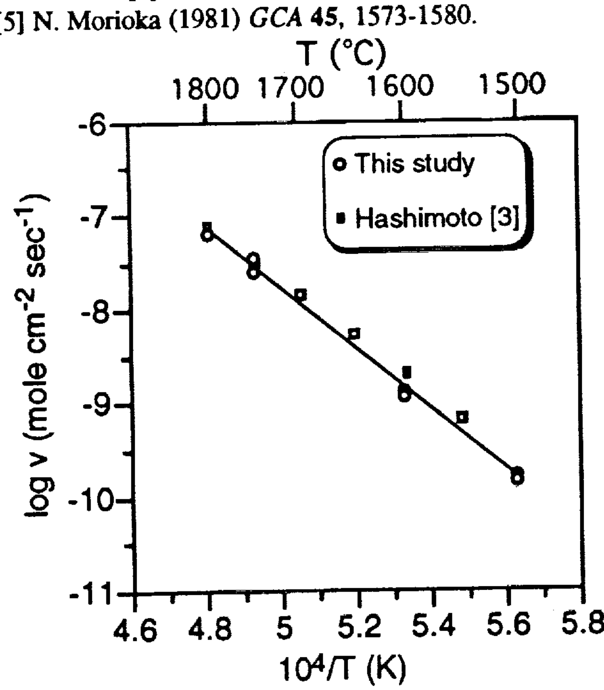


Fig. 1. Plot of evaporation rate of forsterite against evaporation temperature. The line is a linear fit to the single crystal forsterite evaporation experiments.

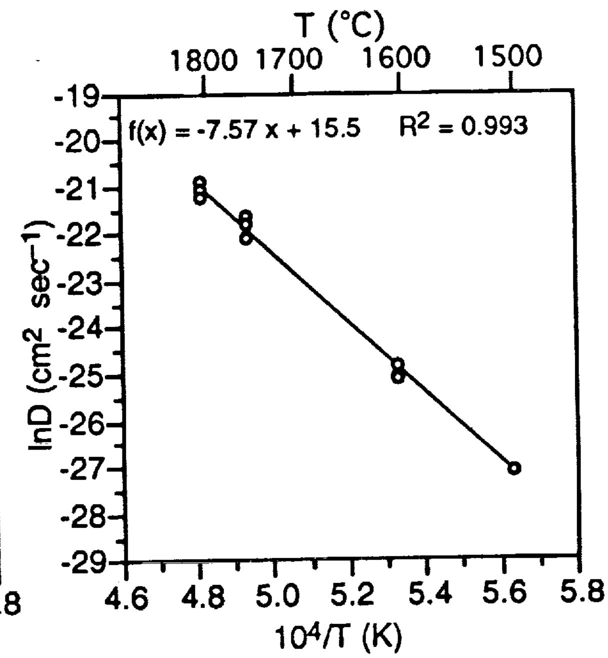


Fig. 2. Plot of Mg diffusion coefficient versus its evaporation temperature. The line is a linear fit to the data.

S220-91
ABS. ONLY

N94-20856

LIMITS ON DIFFERENTIATION OF MELT "SHEETS" FROM BASIN-SCALE LUNAR IMPACTS

PAUL H. WARREN, Institute of Geophysics and Planetary Physics, UCLA, Los Angeles, CA 90024-1567

In the literature on cratering, one frequently finds allusions to the "sheet" of impact melt that supposedly forms in the aftermath of any large impact. The presumption seems to be that either (1) most of the impact melt is formed virtually at the surface, or else (2) most of the melt inevitably collects into a near-surface, roughly sill-shaped "sheet," soon after the impact. However, in basin-scale impacts on the mature Moon, neither of these scenarios appears likely. Differentiation of impact melts on the Moon is hampered by similarity in density vs. the porous lunar crust, and by the adverse melt/"displaced" matter ratio that results from the lunar g.

Understanding the fate of melts generated by basin-scale impacts is a prerequisite for accurate interpretation of lunar crustal genesis. Recent studies of the Sudbury Complex [e.g., 1] indicate that its "irruptive" is almost entirely impact melt, formed in connection within a crater of apparent diameter $D_a \sim 200$ km. The Sudbury magma underwent extensive fractional crystallization. For example, the mg ratio in augites shows cryptic variation from 0.79 to 0.25; and the upper granophyre layer (roughly 1/2 of the total "irruptive") is enriched in K and incompatible elements by a factor of ~2.8, and depleted in CaO by a factor of ~3.6, compared to the other main layer (the norite) [2]. The impact melt of the similar-sized Chicxulub crater apparently differentiated to a similar degree [3]. The once canonical view that impact melts almost never differentiate has thus been disproved. A simple Sudbury-Moon analogy led Grieve et al. [1] to conjecture that "some misinterpretation of the origin of . . . so-called pristine lunar highland samples has been made and some are primordial impact melt rocks from large impact events." The many petrologists who have studied nonmare rocks all have different views of this problem. Certainly the term "plutonic" has been abused, in recent lunar literature. But does the new interpretation of Sudbury require a complete revision of the pristine rock concept?

Various factors affect the degree to which an impact melt undergoes differentiation. Obviously, only a large-scale mass of melt will cool slowly enough to differentiate. The volume of melt generated at Sudbury was probably smaller than that generated in the largest known lunar impacts by two orders of magnitude. For example, assuming for Serenitatis $D_a = 880$ km [4], the implied transient crater diameter D_{tr} is ~473 km; the similarly estimated D_{tr} for Sudbury is ~106 km. The volume of impact melt V_m, calculated from eqn. 7.10.2 of [5], or from eqn. 6 of [6], adjusted for g, is roughly 60× greater for Serenitatis (assuming equivalent impact velocity) than for Sudbury. If both impact melts efficiently collected into analogously shaped "sheets" within the craters, the sheet thickness would have been 3× greater at Serenitatis than at Sudbury. Besides cooling rate, the efficiency with which a melt body will differentiate is probably sensitive to the degree to which fluid motions supply fresh melt to crystal/melt interfaces. The tendency to convect is governed by the Rayleigh number Ra, $\propto$ thickness^3, g^1, and μ^{-1}, where μ is the melt viscosity. The effect of the ~1.24 wt% water in the Sudbury [2] would be offset by its high average SiO_2 (~63 wt%). At a likely differentiation T of 1000°C, μ calculated à la [7] would be 1.3×10^5 poise. The 1200°C μ for a melt of A-17 noritic breccia composition [8] is 86 poise. Thus, Ra should have been 2-4 orders of magnitude higher in a 3× thicker Serenitatis "sheet." However, the noritic Apollo-17 poikilitic impact breccias that appear to be Serenitatis impact melts [9] have fine-grained, clast-laden textures, and could hardly be mistaken for endogenous igneous rocks, as the Sudbury "irruptive" rocks once were [2]. Still less do the poikilitic Serenitatis products texturally resemble lightly brecciated "meteorite-free" lunar norites (e.g., 78235, with grains up to 10 mm across).

Differentiation of basin-scale impact melts on the Moon is hampered by two factors: (1) an adverse density relationship, and (2) an adverse melt/"displaced" matter ratio. In large impacts, most of the melt originally forms at great depth. Cintala and Grieve [10] have modeled the depth distribution of impact melts. They find (Fig. 1) that in large-scale events the maximum depth of melting is ~3× the max. depth of excavation d_{maxx} (assumed ~$D_{tr}/9$), and that the melt initially forms in a roughly spherical volume, directly beneath ground zero. A perfect sphere extending to 3.0× d_{maxx} would have only 7.3% of its volume above d_{maxx}. The true geometry is undoubtedly complex, but it seems clear that most of the melt in a basin-scale lunar impact forms too deep, by many tens of km, to land at the surface in the immediate aftermath of the impact (in addition, some of the fraction excavated from the transient crater travels beyond the final crater rim). In the modification stage, the roughly 93% of the impact melt below d_{maxx} will rapidly mingle with the "displaced" but not ejected material of the transient crater (in the largest events, some of the melt will be even deeper than the base of the transient cavity). The ratio of "displaced" to melted matter will be higher by a factor of four in an impact at lunar g than in a terrestrial one [5]. Thus, where a terrestrial impact melt might be cooled by mingling with 10% unmelted clasts, a lunar impact melt will be chilled by mingling with 40% unmelted clasts.

Fig. 2 shows density calculated à la [11] for averaged lunar impact melt compositions from Ap15 (Imbrium), Ap16 (group 2, Nectaris?), and Ap17 (Serenitatis), and also for the Sudbury composition

[12,13,8,2]. The 1000°C, 0.1-GPa density of the Sudbury melt is 2.44 g cm^{-3}. At 1.0 GPa (by conservative extrapolation), it is only 2.55 g cm^{-3}; i.e., 0.21 g cm^{-3} lower than the average density of the country rock [14], 0.13 g cm^{-3} lower than the density of the a liquidus phase (feldspar), and 0.31 g cm^{-3} lower than the aggregate density of the cumulates of the lower half of the complex. Thus, the Sudbury impact melt must have efficiently segregated up and away from the solids amidst which it mingled, and from the crystals it grew as it cooled. In contrast, the 1200°C, 0.1-GPa densities calculated for the average lunar impact melt compositions are all ≈ 2.76 g cm^{-3}. A typical estimate for the average zero-porosity density of the lunar crust would be 2.9 g cm^{-3}. However, the upper ~20 km of the crust has porosity from brecciation, and the "displaced" matter of a basin-scale impact would probably be porous as well. Assuming 5% porosity is representative of the region where most of the impact melt first forms, and that this region is compositionally "average," the implied country rock density is 2.76 g cm^{-3}—identical to that of the melt. Thus, the melt generated by a lunar basin-scale impact will not efficiently rise and aggregate into a single large "sheet." Instead, pockets of impact melt that originally form deep in the crust may typically remain almost stationary, or rise only to a level where the porosity of the surrounding country rock translates into neutral buoyancy. During 1200°C crystallization of whatever melt manages to aggregate into a large, nearly clast-free sheet, the density of the melt (~2.76 g cm^{-3}) would be ~ 0.20 g cm^{-3} less than the density of the aggregate liquidus assemblage (feldspar + pyroxene), but 0.05 g cm^{-3} *greater than* the density of a major liquidus phase (feldspar). Unless the magma was very thick, it would tend to become choked with feldspar, turning off convective motions, and thus also fractional crystallization.

Lunar impacts with D_a >> 900 km will generate more melt in the mantle than in the crust. Minor mantle-derived components might help to explain why the average *mg* ratio of the Ap15/Ap16/Ap17 impact melt breccias (0.70) is almost as high as some estimated bulk-Moon *mg* ratios. Major fractions of the melts formed by the largest impacts (South Pole-Aitken has D_a ~2200 km) surely rose into the lower crust, where they probably underwent extensive differentiation. However, the basins this large are all extremely ancient (or else too young for significant sampling of the lower crust beneath them through subsequent great impacts). Deep crustal igneous intrusions generated by basin-scale impacts even older than the oldest observable basins must have been enhanced by heat remaining from the lunar magmasphere (itself possibly an amalgamation of impact melts), and it seems pointless to distinguish a rock putatively formed in such a mode from a "purely" endogenous (pristine) rock. However, it should be acknowledged that if, as widely assumed, the Mg-suite rocks postdate the magma ocean, and if the "cataclysm" hypothesis of lunar cratering is not correct, then many of the Mg-suite rocks probably owe their existence, *in part*, to impact melting.

References: [1] Grieve R. et al. (1991) *JGR* **96**, 22753. [2] Naldrett A. & Hewins R. (1984) in *The Geology and Ore Deposits of the Sudbury Structure* (Pye et al., eds.), 235. [3] Sharpton V. L. et al. (1993) *Nature*, in press. [4] Head J. (1979) *Moon Planets* 21, 439. [5] Melosh H. J. (1989) *Impact Cratering: A Geologic Process*. [6] Grieve R. & Cintala M. (1992) *Meteoritics*, in press. [7] Shaw H. (1972) *A. J. Sci.* **272**, 870. [8] Rhodes J. et al. (1974) *PLSC* **5**, 1097. [9] Ryder G. & Spudis P. (1981) in *Multi-Ring Basins* (Merrill & Schultz, eds.), 133. [10] Cintala M. & Grieve R. (1991) *LPS* **XXII**, 215. [11] Bottinga Y. & Weill D. (1970) *A. J. Sci.* **269**, 169. [12] Lindstrom M. M. et al. (1990) *PLPSC* **20**, 77. McKinley J. P. et al. (1984) *PLPSC* **14**, B513. [14] Gupta V. et al. (1984) in *The Geology and Ore Deposits of the Sudbury Structure* (Pye et al., eds.), 381.

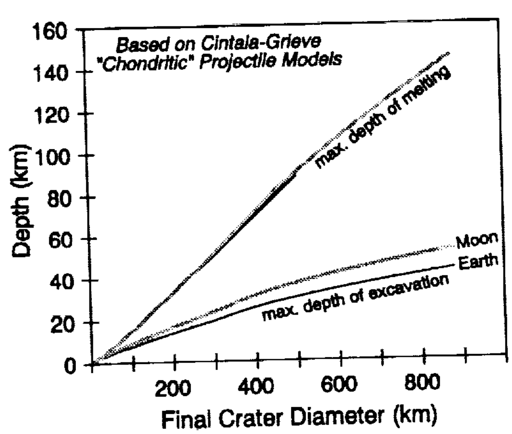
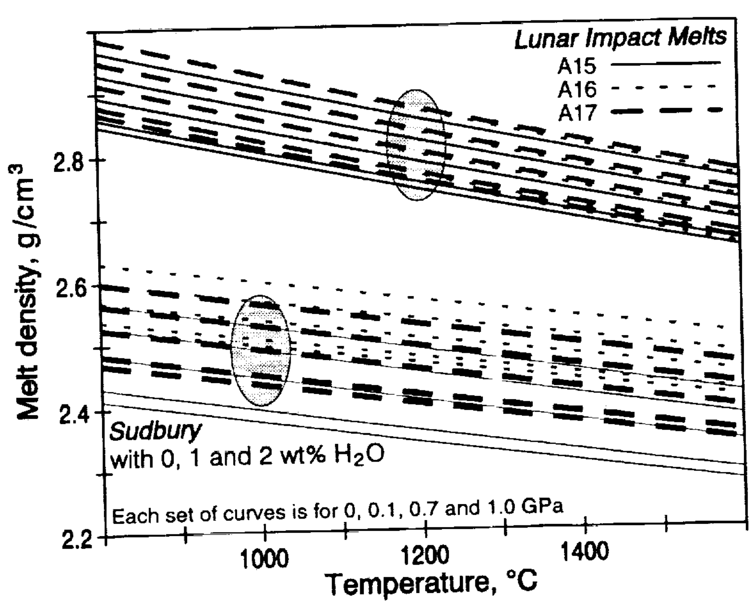


Fig. 1

Fig. 2 →



S221-90
ABS. ONLY

N94-20857

p. 2

CONSORTIUM STUDY OF LUNAR METEORITES YAMATO-793169 AND ASUKA-881757: GEOCHEMICAL EVIDENCE OF MUTUAL SIMILARITY, AND DISSIMILARITY VS. OTHER MARE BASALTS

Paul H. Warren
Institute of Geophysics and Planetary Physics, University of California, Los Angeles, CA 90024
Marilyn M. Lindstrom
SN2, NASA Johnson Space Center, Houston, TX 77058

Compositions of bulk powders and separated minerals from two meteorites derived from the mare lava plains of the Earth's Moon, Yamato-793169 and Asuka-881757, indicate a remarkable degree of similarity to one another, and clearly favor lunar origin. However, these meteorites are unlike any previously studied lunar rock. In both cases, the bulk-rock TiO_2 content is slightly greater than the level separating VLT from low-Ti mare basalt, yet the Sc content is much higher than previously observed except among high-Ti mare basalts. Conceivably, the Sc enrichment in A881757 reflects origin of this rock as a cumulate from a mare magma of "normal" Sc content, but this seems unlikely. Mineral-separate data suggest that most of the Sc is in pyroxene, and a variety of evidence weighs against the cumulus hypothesis as a major cause for the high Sc. The remarkable similarity between Y793169 and A881757 suggests the possibility that they were derived from a single source crater on the Moon.

As described in a companion abstract [1], the samples allocated for this study include homogenized powders generated from a large mass (indirectly 14 g) of the coarse-grained A881757, and from a smaller mass (0.51 g) of the relatively fine-grained Y793169; and also small chips, used to obtain mineral separates, from A881757. The bulk samples were studied by INAA and electron probe fused bead analysis at JSC and UCLA, and by RNAA at UCLA. Mineral separate analyses are exclusively from INAA at the JSC lab. In an earlier study [2], bulk analyses were also obtained (at JSC) for pieces of a 0.25-g chip of A881757, but in many respects the newer, powder samples are probably more representative of the composition of this extraordinarily coarse-grained mare gabbro.

In the TiO_2-based classification system for mare basalts, our averaged new data indicate that Y793169 (2.2 wt%) and A881757 (2.4 wt%) are both low-Ti. Earlier analyses (of distinct chips) reported by Yanai and Kojima [3] indicate 1.55 and 1.66 wt%, respectively. Considering all of the available evidence, it appears that these meteorites have higher TiO_2 than the customary upper bound for VLT (1.5 wt%), yet lower TiO_2 than nearly all previously known "low-Ti" mare basalts. Viewed in relation to the extraordinarily low *mg* ratios of these meteorites (by all accounts ~33 mol%), their TiO_2 contents are marginally consistent with kinship to previously-studied VLT (very-low-Ti) mare basalts. In another popular classification system, our averaged new data indicate that A881757 is low-Al (10.3 wt% Al_2O_3), and Y793169 (11.1 wt%) is marginally high-Al. The ambiguities posed by these two mare meteorites suggest that the traditional major element system for mare basalt classification cannot always be relied upon to effectively delineate affinities among the various mare materials.

Lindstrom et al. [2] noted that A881757 is uncommonly Sc-rich. On a plot of Sc vs. Ti (Fig. 1), Y793169 and A881757 plot near one another, and at roughly 2× the Sc content of most Apollo/Luna low-Ti mare basalts. At least in A881757, most of the Sc apparently resides in pyroxene. Two 32–35 mg pyroxene separates were found to contain 138–143 μg/g, which is much higher than the bulk-rock, and 3.6× higher than an opaque separate that appears to consist mainly of chromian ulvöspinel (Ti was not directly measured in these separates; the values used in Fig. 1 are based on analyses by Yanai [4]). The texture of A881757 is in some ways similar to those of cumulate eucrites [4]. Thus, conceivably the extraordinarily high Sc content arose through accumulation of pyroxene (and possibly other Sc-rich phases) from a relatively "normal" mare basaltic melt. However, by analogy with the compositions of Apollo 15 partial cumulates, especially the olivine-free 15388 [5], and cumulate eucrites, and moreover based on available crystal/melt distribution coefficients, it seems unlikely that a plausible (probably <<40 wt%, inferred from REE and *mg* evidence) cumulus component in A881757 could account for most of the separation between it and "normal" mare basalts on Fig. 1 [6]. Moreover, in the opinion of Takeda et al. [7], A881757 is "not a cumulate rock"; and Y793169, which is much finer grained than A881757, appears similar on Fig. 1. The high Sc contents of these meteorites probably reflect partial melting of a Sc-rich source (or sources) in the lunar mantle.

Rare earth element (REE) concentrations in A881757 and Y793169 are generally higher than those of

VLT mare basalts and in the range of low-Ti mare basalts. However, the unfractionated middle-REE/heavy-REE ratios of these two meteorites resemble the typical pattern of VLT mare basalt and contrast with the convex REE patterns of most low-Ti mare basalts. Mineral analyses show that the bulk of the middle-heavy REE are in pyroxene and not symplectite.

A881757 and Y793169 resemble VLT mare basalts in having high Sc/Sm ratios despite moderate Ti/Sm (Fig. 2). These meteorites resemble low-Ti basalts in terms of moderate overall REE contents and V/Sm and Cr/Sm ratios, and they even resemble high-Ti basalts in having high Sc coupled with low V. Neither meteorite shows the enrichments in K and Ge that remain peculiar to mare basalts from Apollo 14, apparently due to assimilation of the K-rich granitic and Ge-rich KREEPy materials that are uncommonly abundant in the Apollo 14 region.

A set of remarkable similarities between Y793169 and A881757 (from our data: their extraordinarily high Sc despite low Ti, and extraordinarily low *mg*; other workers [1,8–10] have demonstrated similar ages, $^{238}U/^{204}Pb$, and times of blast-off from the Moon) suggests that these two meteorites might be paired, in the sense of having left the Moon in a single cratering-ejection event. The geochemical contrasts between this duo and previously available mare basalts show that the full diversity of the lunar maria, and the factors that govern variability among mare basalts, are still poorly understood. The diversity and lack of systematics among lunar mare basalt compositions, reinforced by Y793169 and A881757, are consistent the magma ocean cumulate model for genesis of the mare source regions. The relationship between geochemistry and age among mare basalts seems more complex that previously supposed, perhaps because the compositional stratification that develops in the pile of magma ocean cumulates is too disorderly to conform with any model for depth-time-temperature evolution of the lunar interior.

Acknowledgments. We are grateful to our colleagues at the National Institute of Polar Research, especially K. Yanai and H. Kojima, for providing the samples, and to many other consortium members, especially C. Koeberl and H. Takeda, for helpful discussions. We also thank G. W. Kallemeyn and D. W. Mittlefehldt for technical assistance.

References: [1] Yanai K. et al. (1993) this volume. [2] Lindstrom M. M., Mittlefehldt D. W. and Martinez R. R. (1991) *Abstracts, 16th Symp. Antarct. Meteorites*, 102. [3] Yanai K. and Kojima H. (1991) *Proc. NIPR Symp. Antarct. Meteorites*, **4**, 70. [4] Yanai K. (1991) *Proc. Lunar Planet. Sci.*, **21**, 317. [5] Ryder G. and Steele A. (1988) *Proc. Lunar Planet. Sci. Conf.*, **18**, 273. [6] Warren P. H. and Kallemeyn G. W. (1993) *Proc. NIPR Symp. Antarct. Meteorites*, **6**, submitted. [7] Takeda H., Arai T. and Saiki K. (1992) *Abstracts, 17th Symp. Antarct. Meteorites*, 109. [8] Nishiizumi K. et al. (1992) *Abstracts, 17th Symp. Antarct. Meteorites*, 129. [9] Eugster O. (1992) *Abstracts, 17th Symp. Antarct. Meteorites*, 208. [10] Torigoe N. et al. (1993) this volume.

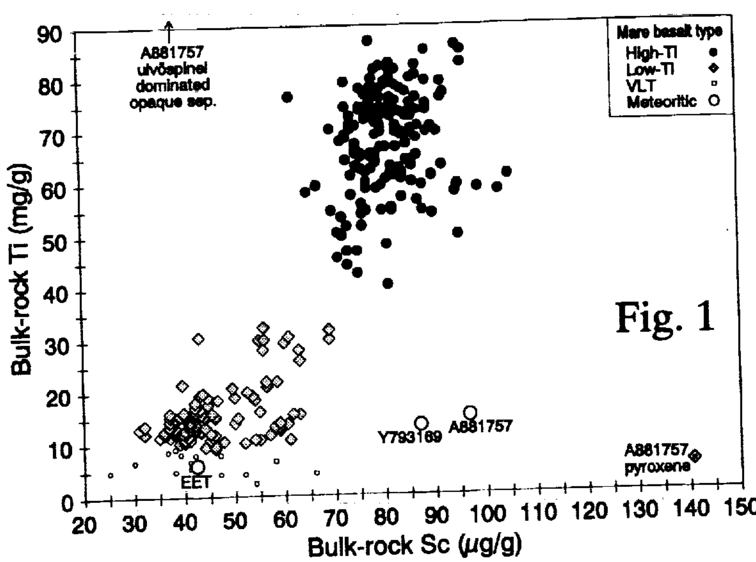


Fig. 1

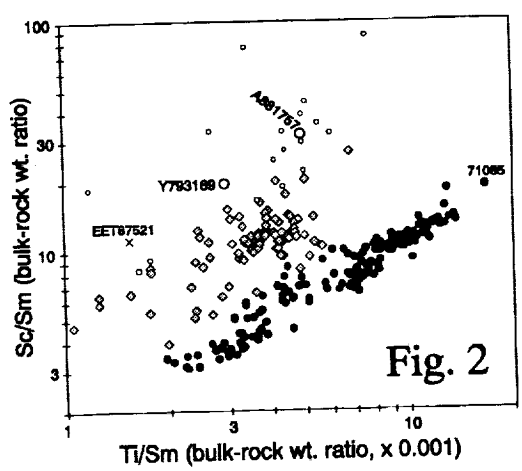


Fig. 2

MAGNETIC RECORD IN CHONDRITE METEORITES; P. J. Wasilewski, J. L. Faris, and M. V. O'Bryan, Astrochemistry Branch, NASA, Goddard Space Flight Center, Greenbelt, Maryland.

In this paper we summarize what we know about the magnetic record in chondrite meteorites based on new data and previously published results. Strips from thin slabs of chondrite meteorites were cut into near cubical subsamples (several mm on edge) numbering ~60 to ~120 per meteorite. A common orientation was assigned to each subsample from a given meteorite in order to ensure that we could discover the vector makeup of the bulk meteorite. The new data set includes: Shaw (L7), Roy, (L5/6), Claytonville (L5), Plainview (H5), Etter (H5), Leoville (C3V), and Allende (C3V). In addition to these new results, literature data of sufficient detail, e.g. Bjurbole (L4), ALH 769 (L6), Abee (E4), Allende (C3V) and Olivenza (L5) is considered.

Previously measured (and unpublished) alternating field and thermal demagnetization of 23 meteorites are utilized to assess bulk meteorite magnetic records. The validation of the natural remanence (NRM) in the meteorites is in part based on the ratio (called REM) of the NRM to the saturation remanence (SIRM).

The REM's cover a range of several orders of magnitude and no apparent correlation is noted when compared to Taylor-Heymann or Dodd-Jarosewich shock classifications (though the sample sets here are small).

- Most of the bulk magnetic vector records are ideal when either alternating field or thermal demagnetization results are considered.
- When the bulk is divided into subsamples, the large subsample data set exhibits scatter which can range from near random, to near hemispheric scatter to a noisy excursion.
- During demagnetization of the bulk, the randomness and scatter in the subsample record is muted and what appears to be an overprint record is noted - there are few exceptions.
- This overprint record is now being considered in terms of the fine grain (in matrix and silicate) and tetrataenite contributions separated from the noisy Kamacite record.
- The meaning of the paleofield estimates for a bulk meteorite brings into question the validity of technique. What is the REM (I don't recall any paleofield estimate rendering this judgement)? How is the vector record constructed? Each meteorite is in a sense a breccia processed to varying degree by thermophysical events. What is the role of mineralogical anomalies? Even in high metamorphic grades a great deal of fine metal can be observed and tetrataenite and Fe carbide - Fe intergrowths (such as in Abee) can result in anomalous remanence, including apparent self reversal in the Fe carbide intergrowths (in the analysis of the vector record the thermal demagnetization is more effective than the alternating field technique)

MAGNETIC RECORD IN CHONDRITE METEORITES: P. J. Wasilewski, et al.

In the very friable meteorites (ALH 769 (L6) and Bjurbole (L4) subsamples and individual components (metal grains, chondrules) exhibit a great degree of scatter. Only the matrix appears coherent and the bulk behaves well.

In Allende (C3V) exceptional bulk stability and subsample stability is noted. Chondrules may be ultra-stable or random when demagnetized.

Most class 5 and 6 chondrites (H or L) exhibit vector patterns which suggest the presence of magnetic fields during the cooling of the meteorites. The detailed vector maps of the 7 chondrite meteorites will be discussed in terms of the various scenarios that could possibly produce the observed records. There appears to be overwhelming evidence that different types of magnetic recording scenarios are responsible for the observed records in chondrite meteorites.

We will summarize the state of our knowledge about magnetic field records in chondrite meteorites.

S223-92 ABS. ONLY

N94-20859

p. 2

AGB STARS AS A SOURCE OF SHORT-LIVED RADIOACTIVE NUCLEI IN THE SOLAR NEBULA. G. J. Wasserburg[1], R. Gallino[2], M. Busso[3] and C. M. Raiteri[3], [1]Lunatic Asylum, Division of Geological & Planetary Sciences, Caltech, Pasadena CA 91125. [2]Istituto di Fisica Generale dell' Universita, Torino, [3]Osservatorio Astronomico di Torino, Torino.

The purpose of this study is to estimate the possible contribution of some short-lived nuclei to the early solar nebula from AGB sources. Low mass (1 to $3M_\odot$) AGB stars appear to provide a site for synthesis of the main *s* process component for solar system material with an exponential distribution of neutron irradiations $\propto \exp[-\tau/\tau_0]$ (where τ is the time integrated neutron flux with a mean neutron exposure τ_0) for solar ($\odot$) abundances with $\tau_0 = 0.28\ mb^{-1}$ [1]. Previous workers have estimated the synthesis of key short-lived nuclei which might be produced in AGB stars [2,3]. While these calculations [2] exhibit the basic characteristics of nuclei production by neutron exposure, there is need for a self-consistent calculation that follows AGB evolution and takes into account the net production from a star and dilution with the cloud medium. Many of the general approaches and the conclusions arrived at here have been presented earlier by Cameron *et al.*[2]. We have evaluated the production of nuclei for a star of 1.5 $M_\odot$ during the thermal pulsing of the AGB phase. Calculations were done for a series of thermal pulses with $\tau_0 = 0.12$ and $0.28\ mb^{-1}$. These pulses involve *s* nucleosynthesis in the burning shell at the base of the He zone followed by the ignition of the H burning shell at the top of the He zone. After about 10-15 cycles the abundances of the various nuclei in the He zone become constant. Computations of the abundances of all nuclei in the He zone were made following Gallino *et al.* [4]. We consider the mass of the solar nebula to consist of some initial material of approximately solar composition plus some contributions from AGB stars. We have calculated the ratios of the masses required from the AGB He burning zone to the ISM necessary to produce the observed value of $^{107}Pd/^{108}Pd$ in the early solar system and applied this dilution factor to all other relevant nuclei. The ratio of the number of each stable s nucleus per gram of matter in the He zone to the solar concentrations is $q^s_{He}/q^s_\odot$ determined in the calculations for the He shell. The resulting relative abundances of radioactive nucleus r to a stable nucleus s calculated for the early solar nebula are given in Table 1 for instant addition. We have also calculated the relative abundances in a cloud that has undergone continuous addition of AGB ejecta over a time t. Here the rate of AGB He shell ejection per unit mass of the cloud ($\dot{M}_{He}/M_C$) were determined from $(^{107}Pd/^{108}Pd)_\odot$, the production in the He zone, $q_{He}^{108Pd}/q_\odot^{108Pd}$ and $\bar{\tau}_{^{107}Pd}$. They provide a self-consistent set of relative isotopic abundances for the nuclei considered for each model and can thus be compared with the existing data on extinct nuclides in the early solar system. Free decay over an interval Δ will shift the values by $e^{-\Delta/\bar{\tau}}$. Table 1 shows the solar nebular abundances for the case of a single addition for a model with $\tau_0 = 0.12\ mb^{-1}$ (1A) and $\tau_0 = 0.28\ mb^{-1}$ (1B). Column $N^r_\odot/N^s_\odot$ corresponds to the ratio in the salted solar nebula for the isotopes r and s, and can be compared with the observations. N^r_{He}/N^s_{He} is the ratio of r/s in the helium zone and $q^s_{He}/q^s_\odot$ is the ratio of the concentrations (per gram) of s in the He zone to that of s in the ISM. Note that all nuclei that appear in the main *s* chain have roughly comparable abundances with the exception of $^{205}Pb/^{204}Pb$ that is enhanced. ^{129}I is only produced very weakly [2] due to the calculated short life time for ß decay of the 27.8 KEV excited state of ^{129}I, and the multiple neutron capture on Te. ^{60}Fe is also produced in very low, but non-negligible, amounts by multiple neutron capture on the Fe seed. The ratio $q^s_{He}/q^s_\odot$ shows that for many of these nuclei there is an enhancement of between 10 to 10^3 over solar. It is evident that the ratios N^r_{He}/N^s_{He} are roughly independent of τ_0 as shown earlier [2]. However, there is a substantial increase of $^{60}Fe/^{56}Fe$ (x10) with the increase in τ_0. In Table 1A (1B) we list the salted solar nebula values calculated using $M_{He}/M_\odot = 1.7\times10^{-6}$ (1.4×10^{-7}) as determined by matching the observed $^{107}Pd/^{108}Pd$ ratio. It is evident that a very small amount of matter from the He shell is sufficient to provide all of the ^{107}Pd in the solar nebula. Assuming that the ejecta from an AGB star has a ratio of envelope to He shell of 50, this corresponds to an ejected mass of $8.5\times10^{-5}M_\odot$ of AGB matter in order to salt $1M_\odot$ of ISM. A single $1.5M_\odot$ AGB star could provide enough ^{107}Pd to salt $10^4M_\odot$ of ISM (for $\tau_0 = 0.12mb^{-1}$). The calculated results for

$^{93}Zr/^{92}Zr$, $^{99}Tc/^{100}Tc$, $^{135}Cs/^{133}Cs$ and $^{205}Pb/^{204}Pb$ are all approximately comparable ($\sim 10^{-5}$) for τ_0 = 0.12mb^{-1}. They are only slightly changed for τ_0 = 0.28mb^{-1}. $^{182}Hf/^{180}Hf$ is substantially lower. It is of interest to note that $^{60}Fe/^{56}Fe$ has a substantial contribution from an AGB source, although it is about twenty times lower than reported by Shukolyukov and Lugmair [5] from differentiated planetary materials. One would obtain $^{60}Fe/^{56}Fe$ =4x10^{-9} for the case of $M_{He}/M_\odot$ = 1.1x10^{-5} (3.0x10^{-6}). If we consider ^{26}Al production in the H burning zone [3] we would require the ratio of ejected H burning zone to the He zone to be 25 in order to match both the ^{107}Pd and the ^{26}Al. Results for continuous production, ejection and mixing from multiple AGB sources over a cloud life time are given in Table 2. It can be seen that for τ_0 = 0.12 mb^{-1}, that the ratios $N_\odot^r/N_\odot^s$ are all $\sim 10^{-5}$ for the first five pairs. $^{60}Fe/^{56}Fe$ is present at a much reduced value and $^{129}I/^{127}I$ is grossly underproduced. The requirement of ^{26}Al production demands a high value for the rate of H shell ejection $\dot{M}_H/M_C$. We note that the ejection rate of $\dot{M}_{He}/M_C$ = 1.8x10^{-7} my^{-1} is almost two orders of magnitude less than the average over galactic history. In conclusion it appears that the presence of ^{107}Pd, ^{93}Zr, ^{99}Tc, ^{135}Cs and ^{205}Pb in a presolar cloud can be readily explained by AGB sources and would have well defined abundances. Some ^{60}Fe is expected from AGBs and much more could be obtained under higher neutron fluxes under *s* processing conditions. ^{26}Al could be provided by ejecta from H zone burning but it does not appear to be coupled with AGB pulsing unless the ejection of H zone material is far more efficient than that of matter from the He zone. A study of net increased ^{26}Al production in an extended H zone will be presented to see if ^{26}Al and ^{107}Pd can both be matched. ^{129}I cannot be due to AGB sources unless there is some major error in the parameters used and if the neutron flux is much increased. There is a major problem with an AGB source since only a small amount of AGB material can contaminate a large volume. The mixing and dilution mechanisms are not understood by us. Division Contribution 5229(793). References:[1]Iben I. and Renzini A. (1982) *Ap.J. 259*, L79; 263 L23 [2] Cameron A.G.W., Thielemann F.K. and Cowan J.J. (1992) *Physics Reports*, in press . [3] Forestini M., Paulus G., Arnould M. (1991) *Astron. & Astrophy. Dec.*, 123. [4] Gallino R., Busso M., Picchio G., Raiteri C. and Renzini A. (1988) *Ap.J. 334*, L45 [5]Shukolyukov and Lugmair (1992) *LPSC XXIII*, 1295. [6]Käppeler F., Gallino R., Busso M., Picchio G. and Raiteri C.M. (1990) *Ap.J. 354*, 630.

Table 1. AGB-ISM instant mix A) $M_{He}/M_\odot$ = 1.7x10^{-6} ; B) $M_{He}/M_\odot$ = 1.4 x 10^{-7}

A	$N_\odot^r/N_\odot^s$	N_{He}^r/N_{He}^s	$q_{He}^s/q_\odot^s$	B $N_\odot^r/N_\odot^s$	N_{He}^r/N_{He}^s	$q_{He}^s/q_\odot^s$
$^{107}Pd/^{108}Pd$	2 x10^{-5} *	0.163	72.4	2 x10^{-5} *	0.158	891
$^{93}Zr/^{92}Zr$	7.5 x10^{-5}	0.331	134	5.6 x10^{-5}	0.344	1158
$^{99}Tc/^{100}Ru$	3.9 x10^{-5}	0.181	128	3.6 x10^{-5}	0.176	1461
$^{135}Cs/^{133}Cs$	8.4 x10^{-6}	0.445	11.1	2.2 x10^{-5}	0.712	222
$^{182}Hf/^{180}Hf$	2.9 x10^{-7}	0.0115	14.8	3.5 x10^{-6}	0.0241	1030
$^{205}Pb/^{204}Pb$	3.9 x10^{-5}	1.66	13.9	2.8 x10^{-4}	1.83	1083
$^{129}I^{127}I$	2.2 x10^{-8}	2.9 x10^{-3}	4.5	5.7 x10^{-8}	2.6 x10^{-3}	79.3
$^{60}Fe/^{56}Fe$	7.3 x 10^{-10}	6.6 x10^{-4}	0.653	1.8 x 10^{-10}	2.6 x10^{-3}	0.52
[$^{26}Al/^{27}Al$	5 x10^{-5} **	$M_H/M_\odot$ = 4.4x10^{-5}]		[5 x10^{-5} **	$M_H/M_\odot$ = 4.4x10^{-5}]	

*Reference value chosen to determine $M_{He}/M_\odot$. All other values are calculated from model. **Reference value to determine $M_H/M_\odot$. [ ] Burning of ^{25}Mg to ^{26}Al in H burning shell of mass M_H.

Table 2. AGB-ISM continuous production and mixing

	$N_\odot^r/N_\odot^s$ (τ_0=0.12)	$N_\odot^r/N_\odot^s$ (τ_0=0.28)		$N_\odot^r/N_\odot^s$ (τ_0=0.12)	$N_\odot^r/N_\odot^s$ (τ_0=0.28)
$^{107}Pd/^{108}Pd$	2.0x10^{-5} *	2.0x10^{-5} *	$^{182}Hf/^{180}Hf$	4.0x10^{-7}	4.8x10^{-6}
$^{93}Zr/^{92}Zr$	1.8x10^{-5}	1.3x10^{-5}	$^{205}Pb/^{204}Pb$	8.3x10^{-5}	6.0x10^{-4}
$^{99}Tc/^{100}Ru$	8.2x10^{-6}	9.2x10^{-7}	$^{129}I/^{127}I$	5.4x10^{-8}	7.1x10^{-8}
$^{135}Cs/^{133}Cs$	3.4x10^{-5}	7.8x10^{-6}	$^{60}Fe/^{56}Fe$	1.2x10^{-10}	3.0x10^{-11}

[$^{26}Al/^{27}Al$ = 5x10^{-5}**, $\dot{M}_H/\dot{M}_C$ = 3.2x10^2, τ_0=0.12; $\dot{M}_H/\dot{M}_C$ = 3.8x10^3, τ_0=0.28]

*Reference value used to determine $\dot{M}_{He}/M_C$. Values for τ_0 = 0.12 mb^{-1} and 0.28 mb^{-1} are $\dot{M}_{He}/M_C$ = 1.8 x 10^{-7} and 1.5 x 10^{-8} per million years. **Reference value to determine $\dot{M}_H/M_\odot$.

S204-90
ABS. ONLY

168184

N94-20860

MULTIPLICITY OF CHONDRULE HEATING EVENTS AND THE COARSENING OF CHONDRULE TEXTURES. John T. Wasson, Institute of Geophysics and Planetary Physics, University of California, Los Angeles, CA 90024, USA.

Our studies of compound chondrules show that most chondrules experienced at least two thermal events that produced appreciable amounts of melt. I suggest that chondrules were subjected to a hierarchy of brief heating events, the number increasing exponentially with decreasing intensity, and that some of intermediate intensity deposited enough heat to partially melt mesostasis glass and promote the growth of mafic mineral grains. This scenario can account for textures that require improbably low monotonic cooling rates in laboratory simulations, and also for the rarity of glassy chondrule textures despite the ease with which these are produced in the laboratory [1].

Simulations of chondrule grain growth by Hewins, Lofgren and their coworkers indicate chondrule subsolidus cooling rates of 0.03-1 K s^{-1}. Such slow cooling rates seem to require that chondrules be immersed in a thermal blanket at the time of their formation. Sahagian and Hewins [2] showed that a 1000-km thick opaque nebular cloud would be an adequate blanket.

There is increasing evidence that most meteoritic chondrules were subjected to more than one flash-heating event. Studies at UCLA (e.g., [3]) of compound chondrules imply that most chondrules experienced two heating events of sufficient magnitude to melt appreciable fractions of the final assemblage. Chondrules are often surrounded by coarse-grained rims postdating chondrule formation [4]; these rims appear to have been coarsened by partly melting a fine-grained precursor rim, probably by the same process that melted chondrules.

All mechanisms proposed to produce flash heating yield a hierarchy of intensity levels, either because of the natural variability in the energy source or because of the variable efficiency of energy transfer to the precursor material. As an example of the latter, the reheating of chondrules by radiant energy from lightning strokes will decrease with increasing distance from the channel of the stroke. Because lightning channels were far longer than the dimensions of a chondrule, the amount of radiant energy intercepted by the chondrule decreased linearly with distance from the bolt axis.

Terrestrial lightning bolts reach temperatures of 30000 K and remain at temperatures above 5000 K for about 0.001 s. For modeling purposes I assume that the bolt radiates like a 5000-K black body for a period of 0.1 s, the longer duration allowing for the much more intense photon flux early in the bolt lifetime. I calculate that a chondrule located at the bolt margin, receiving the full flux and absorbing 5 % of it would absorb enough photons to increase the temperature of solid silicates by 1380 K (and, of course, to vaporize some of the assemblage). This is an upper limit since some of the energy would be reemitted during the 0.1-s period. A chondrule at a distance 5X greater from the center of the bolt would receive a fluence 5X smaller, sufficient to raise the temperature 280 K; in this case the fraction of energy lost during the irradiation was probably negligible. The number of chondrules within this larger

cylindrical shell was 24X greater than that within the bolt. In addition there were probably other heating events that failed to generate temperatures high enough to melt large fractions of mm-size chondrules but were still sufficient to raise temperatures of preexisting chondrules to the range where appreciable crystal growth could occur.

Petrographic observations at UCLA indicate that the mesostasis of highly unequilibrated chondrules is somewhat darker than that of phenocryst minerals; thus, the mesostasis would experience a greater degree of radiant heating.

It seems possible that the average chondrule experienced hundreds of heating events sufficient to raise the temperature of the mesostasis to incipient melting. Although this predicts formation of a series of overgrowth layers, it is not clear that these could be resolved by microscopic or microprobe observations, since the anticipated gradient would probably be similar to that produced by fractional crystallization of a melt.

Independent of the mechanism responsible for heating the chondrules, it is clear that the process was repeated in order to produce most non-sibling compound chondrules and to produce coarse-grained chondrule rims. It follows that there were other heating events whose record is more difficult to resolve, and that it is an oversimplification to model chondrule grain growth in terms of a single period of monotonic cooling following chondrule formation.

REFERENCES: [1] Hewins R.H. and Radomsky P.M. (1990), Meteoritics 25, 309-318; [2] Sahagian D.L. and Hewins R.H. (1992), Lunar Planet. Sci. 23, 1197-1198; [3] Wasson J.T. (1993), Meteoritics 28, in press; [4] Rubin A.E. (1984), Geochim. Cosmochim. Acta 48, 1779-1789.

EQUILIBRIUM AND FRACTIONAL CRYSTALLIZATION OF A PRIMITIVE SHERGOTTITE COMPOSITION. L.E. Wasylenki, Caltech 170-25, Pasadena, CA 91125; J.H. Jones, SN4, NASA-JSC, Houston, TX 77058; L. Le and A.J.G. Jurewicz, Lockheed ESC, C23, 2400 NASA Rd. 1, Houston, TX 77058.

INTRODUCTION. The shergottites are a subset of the SNC meteorites, which are believed to have come from Mars. Petrologic studies of these basaltic meteorites suggest that the most primitive shergottite composition is the groundmass of EETA79001 (A lithology). This inference is based on (i) its high Mg# relative to the other shergottites [1]; (ii) its normative olivine [1]; and (iii) its lack of the cumulate crystals found in most other SNC meteorites [2]. However, the relationship between this primitive composition and the compositions of the other, more evolved shergottites cannot be discovered through petrologic investigations alone. Therefore, liquidus phase relations were experimentally determined for a synthetic EETA79001A groundmass composition (from [1]) at 1 bar and QFM in order to find whether the bulk compositions of other shergottites could be derived by simple equilibrium or fractional crystallization of the EETA79001A groundmass composition.

EXPERIMENTAL. Three synthetic compositions were fused from reagent oxides and carbonates. Eg1, which was used for higher temperature runs, was based upon estimates of the EETA79001A groundmass composition from [1]. Eg3, which was used for equilibrium runs below 1150°C, was based upon Eg1 melt at 1150°C plus 5% equilibrium olivine. Eg4, used in fractional crystallization runs below 1250°C, was based upon Eg1 melt at 1250° plus 5% equilibrium pyroxene. (The 5% crystal component was added to ensure that the compositions would be saturated in the appropriate minerals.) Extra Fe_2O_3 (2.4 wt.%) was added to all three compositions to compensate for iron loss to platinum. Before the experiments, the starting material was made into a homogeneous glass: the fused starting material was ground into powder (<75 microns), pressed into 125 mg pellets, hung on Pt loops, and equilibrated at 1350°C for 24 hours to allow iron loss to Pt to occur. Samples were air quenched before being mounted for the actual experimental runs, which are described below. Run products were drop-quenched in water and analyzed with the NASA-JSC electron microprobe.

EQUILIBRIUM CRYSTALLIZATION EXPERIMENTS. For these experiments charges were held at constant temperatures ranging from 1300°C to 1075°C for 48 hours. Olivine (Fo_{78}) appears on the liquidus between 1300°C and 1290°C. Pyroxene (En76, Wo4) appears at ~1250°C, and at this point olivine goes into reaction relation with the liquid. Figure 1 shows the amount of olivine and pyroxene present in charges from the 1300° to 1150°C Eg1 experiments and demonstrates the peritectic nature of the olivine-pyroxene boundary. As temperature decreases, pyroxene gradually becomes more calcic and less magnesian: at 1175°C, pyroxene (En65, Wo8) is present. Plagioclase (An_{70}) begins to crystallize at 1100°C along with a trace of hercynitic spinel, and at 1075°C accessory titanomagnetite is present. K_D(Fe/Mg) values are 0.28-0.33 for olivine and 0.24-0.27 for pyroxene. Figure 2 illustrates the melt compositions of our run products, suggesting approximate phase boundaries.

FRACTIONAL CRYSTALLIZATION EXPERIMENTS. For these experiments charges were held at constant temperature for 24 hours and then subjected to a linear temperature decrease of either 2 or 5°C/hour. The ramp rate did not greatly affect melt compositions. Samples of Eg1 were run from 1290°C to 1250°C and samples of Eg4 from 1250° to 1200°C and from 1250° to 1150°C. Olivine crystals in these experiments were weakly zoned from Fo_{78} at 1290° to Fo_{76} at 1250°. Pyroxene ranged from En_{69},Wo_5 at 1250° to En_{66},Wo_6 at 1150°C. Analyzed pigeonite grains were zoned and unzoned and had varying compositions, suggesting multiple nucleation events. No augite was observed. Figure 2 shows the melt compositions from the 2°C/hr experiments for comparison with the equilibrium crystallization experiments and with experiments by [1] and [3].

CONCLUSIONS. Figure 2 shows our results along with the bulk compositions of the other shergottites (from [2], [4]). It appears that it is not possible to derive the bulk compositions of the other shergottites from this primitive composition through either equilibrium or fractional crystallization. None of our run products contained glasses close to the bulk compositions of other shergottites and, in contrast to melting experiments on Shergotty and Zagami by [3], we did not observe augite in any of our charges. Whereas it may be possible to derive the compositions of the interstitial liquids of Shergotty or Zagami [3], which are cumulate meteorites, by fractional crystallization of our starting composition, no equilibrium low-pressure process seems capable of producing the composition of EETA79001B (Figure 2).

REFERENCES. [1] Longhi J. and Pan V. (1989) *Proc. Lunar Planet. Sci. Conf. 19th.*, pp. 451-464. [2] McSween H. (1985) *Rev. of Geophys.*, Vol. 23, No. 4, pp. 391-416. [3] Stolper E. and McSween H. (1979)

CRYSTALLIZATION OF A PRIMITIVE SHERGOTTITE COMPOSITION: Wasylenki L.E. et al.

Geochim. Cosmochim. Acta, Vol. 43, pp. 1475-1498. [4] Bertka C. and Holloway J. (1988) *Proc. Lunar and Planet. Sci. Conf. 18th*, pp. 723-739.

Figure 1

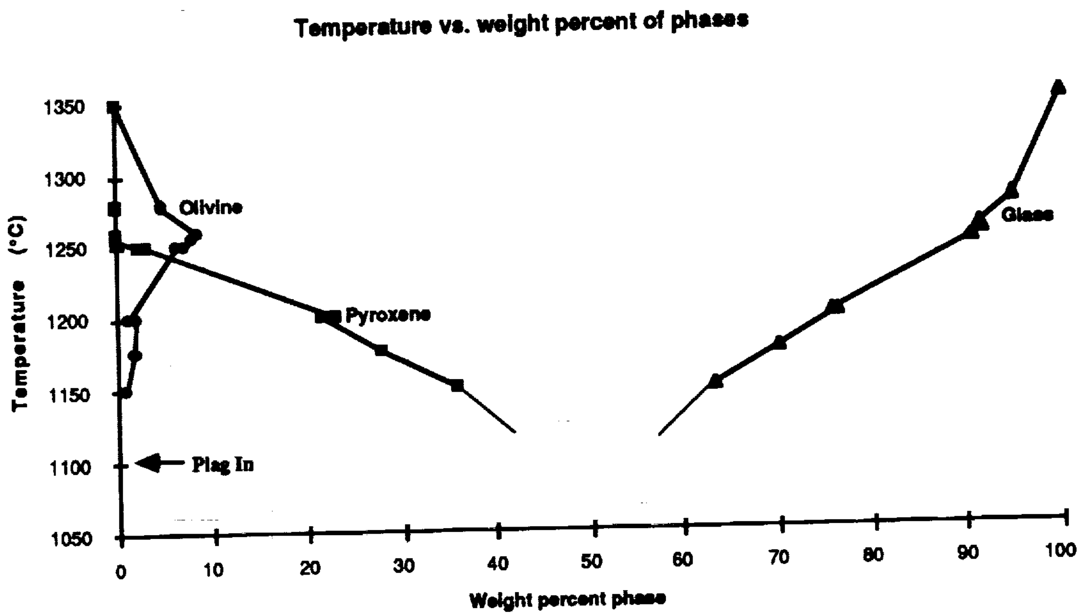
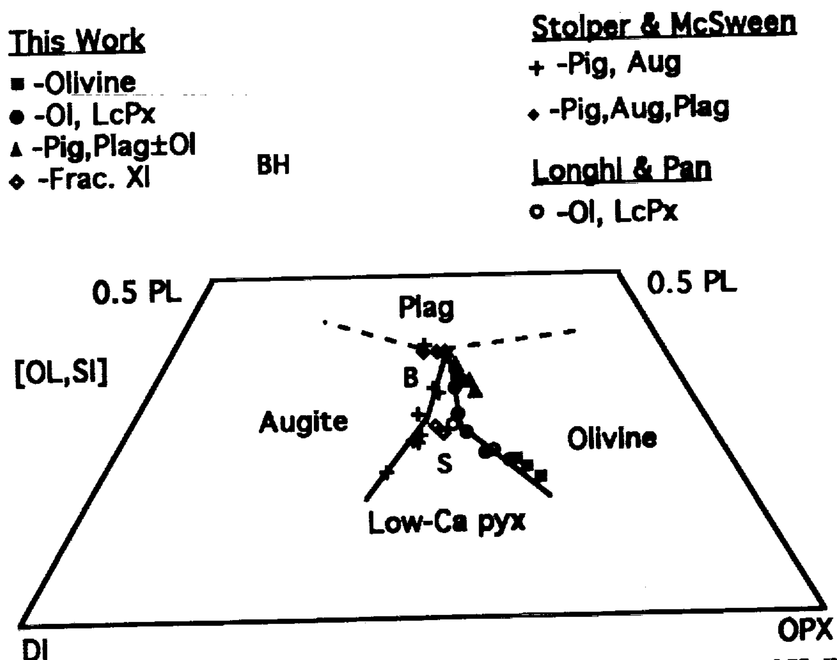


Figure 2



S = Shergotty; B = EETA79001B; BH = Minimum melt of Bertka and Holloway [4]

S226-91
ABS. ONLY

N94-20862

HIGH D/H RATIOS OF WATER IN MAGMATIC AMPHIBOLES IN CHASSIGNY: POSSIBLE CONSTRAINTS ON THE ISOTOPIC COMPOSITION OF MAGMATIC WATER ON MARS; L.L Watson, I.D. Hutcheon, S. Epstein, and E.M. Stolper, Division of Geological and Planetary Sciences, California Institute of Technology, Pasadena, CA 91125.

p. 2

Abstract. We have measured the D/H ratios of kaersutitic amphiboles contained in magmatic inclusions in the SNC meteorite Chassigny using the ion microprobe. A lower limit on the δD_{SMOW} of the amphiboles is +1420 ± 47 ‰. Assuming Chassigny comes from Mars and the amphiboles have not been subject to alteration after their crystallization, this result implies either that recycling of D-enriched martian atmosphere-derived waters into the planetary interior has taken place, or that the primordial hydrogen isotopic composition of the interior of Mars differs significantly from that of the Earth ($\delta D_{SMOW} \sim 0$ ‰). In addition, the measurements indicate that the amphiboles contain < 0.3 wt. % water. This is much lower than published estimates, and indicates a less-hydrous Chassigny parent magma than previously suggested.

Introduction. The D/H ratio of water in the martian atmosphere is enriched by a factor of 5.15 relative to the Earth [1] and weathering products in the nakhlite meteorites ("N" of the SNC group, thought to be possibly martian samples [2,3]) have also been shown to contain water significantly enriched in deuterium [4,5]. These D enrichments are thought to result from massive escape of hydrogen (relative to the heavier deuterium) from the martian upper atmosphere throughout its history [6,7]. A measurement of the D/H ratio of magmatic (interior) water would provide important constraints on the extent of such hydrogen loss because the D/H ratio of the martian interior likely reflects its original value (which has been assumed to be near the terrestrial value of 1.5×10^{-4} [8]) since unlike the Earth with its subduction zones, recycling of near-surface and atmosphere-derived waters to the martian deep interior is generally considered to be an unimportant process.

The SNC meteorite Chassigny ("C" of the acronym SNC) contains cumulus olivine crystals that trapped small (up to ~150 μm in diameter) pockets of melt during growth [9,10]. After entrapment, the inclusions partially crystallized, and the residual melt became progressively enriched in water. This led ultimately to the stabilization of kaersutite, a titanium-rich amphibole. Based on the crystal chemistry of the amphibole group and analyses of the Chassigny kaersutites with the electron microprobe and qualitative ion microprobe analyses, these kaersutite crystals have previously been suggested to contain hydroxyl as a major constituent [9,10]; Johnson et al. [10] estimated that they contain 1.5 wt.% water as hydroxyl groups. The amphiboles occur *only* in the interiors of the melt inclusions and are 10-30 μm in size. Thus, although the bulk meteorite is very poor in water, the amphiboles in the inclusions are thought to have concentrated magmatic water in structural sites. The goal of this work has been to measure the D/H ratio of the water in these amphiboles as a means of constraining the D/H ratio of magmatic water on another planet, possibly Mars.

Measurements. The D/H ratio of the kaersutites cannot be determined by conventional heating/extraction techniques since they are much too small and few in number to separate from the bulk meteorite. We have measured the D/H ratio of four single crystal kaersutites, ranging in size from 15 to 30 μm, in thin section USNM 624-1 on the PANURGE ion microprobe at Caltech. A large instrumental fractionation of the two hydrogen isotopes makes these measurements difficult [11]. This fractionation is strongly dependent upon the major element composition of the material being studied, requiring D/H standards with chemical compositions similar to that of the Chassigny kaersutite. Since no suitable terrestrial standard was available because the meteoritic kaersutites are outside of the range of common terrestrial amphibole compositions, we synthesized three glasses of the same bulk composition as the kaersutite (from [10]) containing dissolved water of various hydrogen isotopic compositions. The hydrous glasses were synthesized in a piston-cylinder apparatus at 10 kbar and 1550°C. Small chips of each glass were mounted and polished for ion microprobe analysis and the remaining sample was heated on a conventional extraction line to determine the δD of the dissolved water. Ion microprobe measurements of D/H ratios were made using a mass resolving power of ~1200, sufficient to resolve D^+ and H_2^+, and a $^{16}O^-$ primary beam of ~1.5 nA focused to a diameter of 3 to 5 μm.

Results. The H^+ intensity on the standard glasses ranged from 24100 to 65000 counts per second, increasing with the water content of 0.7 to 1.9 wt. %. The H^+ count rate varied from 5300 to 10000 counts per second on the Chassigny kaersutites. The background H^+ intensity measured on anhydrous silicates

was ~2000-3500 cps. No correction for H^+ or D^+ arising from adsorbed water was applied due to the large uncertainty in the D/H ratio and absolute abundance of this background component.

The instrumental fractionation factor, α, corresponds to the ratio of the measured D/H ratio to the absolute D/H ratio such that $\alpha = (D/H)_{measured}/(D/H)_{true}$. The three standards had δD_{true} values of +48, +592 and +1130 ‰ (where δD is expressed as a per mil difference relative to the D/H ratio of standard mean ocean water). $\delta D_{measured}$ values for these glasses correlate linearly with δD_{true} and yield $\alpha = 0.607 \pm 0.014$ (2σ) (Fig. 1). Using this fractionation factor, δD_{true} values of four Chassigny kaersutites in three different magmatic inclusions range from +853 ± 55 to +1420 ± 47 ‰ (Fig. 1). The δD values increase with the H^+ count rate suggesting that the H^+ and D^+ signals contain contributions from both adsorbed water and water structurally bound in the kaersutite. A measurement of the isotopic composition of the background gives a δD_{true} value of -127 ± 59 ‰ thus any correction will increase the actual δD values. Thus the δD values reported here should be taken as lower limits.

Discussion. The low count rates for the meteoritic amphiboles compared to the standards suggests that these crystals contain less hydrogen (water) than the 1.5 wt.% previously implied based on electron probe totals and measurement of ~0.5 wt. F [10]. Our data are consistent with a water content of <0.3 wt. %. Estimates of the water content of the parental magmas of Chassigny [10] and of its minimum depth of crystallization (~11 km [10]) will require downward revision since less water is needed in coexisting melt to stabilize an amphibole containing so little water.

The high D/H ratio of the water in the kaersutites is unexpected. Based on models of the origin of the solar system [8] it has been predicted that martian "juvenile" water would have approximately the same D/H ratio as the Earth corresponding to a δD_{SMOW} value of ~ 0 ± 100 ‰. Although we cannot rule out post-crystallization exchange of the hydrogen in the amphibole with heavier surface or atmosphere-derived (meteoric) waters, the facts that the hydrogen is thought to be structurally-bound in the amphibole and that the olivine "containers" show no evidence of alteration make this unlikely. Chassigny differs in this respect from the nakhlites, for example, which contain alteration in the form of reddish-brown "iddingsite" type veins [12,13]. If the measured D/H ratio of the kaersutites is in fact representative of the isotopic composition of the water dissolved in the Chassigny parental magma, either some sort of recycling of heavy atmosphere-derived waters into the magma source region must have taken place or the isotopic composition of the "primordial" water of the mantle of the Chassigny parent body (Mars?) differs significantly from the terrestrial mantle. Moreover, this implies that the deuterium enrichment of the martian atmosphere due to hydrogen escape is less extreme than previously thought.

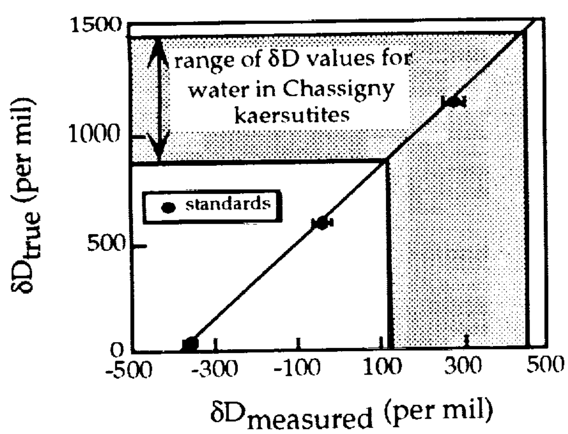


Fig. 1. Corrected hydrogen isotopic composition of water in Chassigny kaersutites (δD_{true}) versus to the values measured by ion microprobe ($\delta D_{measured}$). The symbols represent the standards used to calibrate the correction factor.

References. [1] Bjoraker, G.L. *et al.* (1989) In *Proc. 4th Int. Conf. Mars, Tucson*, 69-70. [2] Bogard, D.D. and Johnson, P. (1983) Science, *221*, 651-654. [3] McSween, H. (1985) Rev. Geophys., *23*, 391-416. [4] Kerridge, J.F. (1988) In *Lunar and Plan. Sci. XIX*, 599-600. [5] Watson, L.L. *et al.* (1991) In Workshop on the Martian Surface and Atmosphere Through Time, *LPI Tech. Rept. 92-02*, 156-166. [6] Owen *et al.* (1988) Science, *240*, 1767-1770. [7] Yung, Y.L. *et al.* (1988) Icarus, *76*, 146-159. [8] Yung, Y.L. and Dissly, R.W. (1992) In Isotope Effects in Gas Phase Chemistry, *ACS Symp. Series 502*, 369-389. [9] Floran *et al.* (1978) Geochim. Cosmochim. Acta, *42*, 1213-1229. [10] Johnson *et al.* (1990) Geochim. Cosmochim. Acta, *55*, 349-366. [11] Deloule, E. *et al.* (1991) In *Stable Isotope Geochemistry: A Tribute to Samuel Epstein*, 53-62. [12] Bunch, T.E. and Reid, A.M. (1975) Meteoritics, *10*, 303-315. [13] Gooding, J.L. et al. (1991) Meteoritics, *26*, 135-143.

5227-91
ABS. ONLY
N94-20863
p. 2

ARCUATE AND CIRCULAR STRUCTURES IN THE THARSIS REGION: EVIDENCE OF CORONAE ON MARS. T. R. Watters, J. R. Zimbelman, Center for Earth and Planetary Studies, National Air and Space Museum, Smithsonian Institution, Washington, D.C. 20560, D. H. Scott, Branch of Astrogeology, U.S. Geological Survey, 2255 North Gemini Drive, Flagstaff, AZ 86001

Arcuate and circular structures are evident in the Tharsis region of Mars. They involve concentric graben and fracture systems and are often associated with volcanic centers. The most prominent example is Alba Patera, a low relief volcanotectonic center. It is surrounded by a graben system comprised of the Alba and Tantalus Fossae and part of the Ceranius Fossae system that are thought to have formed during the Early Amazonian [1]. The graben concentric to Alba Patera form an annulus that is 600 km in diameter (figure 1A). Many of the north-trending graben of Ceranius Fossae were clearly influenced by Alba Patera. Graben are deflected around and in some cases merge with the Alba-concentric system. Other prominent circular structures have been described on the Tempe Terra plateau [2,3]. The annulus of graben and fractures forming these structures is approximately 250 km in diameter (figure 1B). Graben formed over a period extending from the Late Noachian through the Hesperian with the most pronounced arcuate graben forming during the Noachian [3]. These structures are also associated with volcanic centers. One of the graben sets encircles a volcanic dome and a caldera-like depression [2]. As in the case of Alba Patera, northeast-trending graben associated with Tempe and Mareotis Fossae are deflected and often merge with the concentric graben. Another set of arcuate graben occur near the prominent scarp that marks the western boundary of the Lunae Planum plateau [4]. These graben appear to have been part of a circular structure that had a diameter on the order of 600 km, although this can not be confirmed because of subsequent extensive faulting and erosion. The graben that comprise this system formed over a period extending from the Late Noachian through the Early Hesperian [4].

The similarity between Alba Patera and coronae on Venus was observed prior to the Magellan mission [5]. Magellan imagery of Venusian coronae has revealed a number of striking similarities between these structures, Alba Patera, and the other circular structures on Mars. Coronae on Venus are circular to ovoidal volcanotectonic features that range in diameter from 60 to over 1000 km [6,7]. Concentric graben form partial to complete tectonic annuli. More regionally extensive graben systems are deflected toward, and in many cases merge with, the concentric graben [see 6]. Volcanic flows and domes dominate the surface enclosed within the concentric graben. However, distinctive differences exist between coronae on Venus and the structures on Mars. Circular structures on Mars lack radial graben crosscut by concentric graben. There is also no evidence of the complex topography associated with coronae on Venus. The differences between coronae on Venus and the suspected coronae on Mars may be largely due to the difference in the thickness of the elastic lithosphere on the two planets. One model proposed for the origin of coronae on Venus [6-8] involves the ascent of a mantle diapir (figure 2A). Mantle flow above the rising diapir results in uplift of the lithosphere and the development of a gentle topographic dome and radial faulting. Once the diapir impinges on the base of the lithosphere it spreads out radially eventually resulting in the uplift of a circular plateau with concentric faulting. Magma may rise through fractures above the diapir to feed volcanism. As the flattened diapir cools, relaxation forms a central depression, a raised rim and a surrounding moat. On Mars, a similar mechanism with a similar diameter diapir would not be expected to have the same effect on the lithosphere. Assuming the lithosphere was on the order of 100 km thick (~3X that of Venus) when the circular structure formed, forces resulting from mantle flow may not have been sufficient to uplift the lithosphere into a dome and thus no radial faulting would occur (figure 2B). As the diapir reaches the base of the lithosphere and spreads out, buoyant material will gain sufficient leverage to uplift the lithosphere and generate concentric faulting. By analogy with the mechanics of laccolith development and hydraulic fracturing, leverage should be achieved when the buoyant material spreads over a distance equal to about 3 to 4 times the effective thickness of the overburden [9]. Cooling of the diapir will result in some relaxation of the topography and additional concentric faulting. The topographic expression of the interaction between the diapir and the lithosphere would be expected to be greatly subdued on Mars because of the large difference in lithospheric thickness. The lack of circular structures with diameters below 200 km suggests a lower limit to the size that coronae could form on Mars.

CIRCULAR STRUCTURES ON MARS: Watters T.R. et al.

References Cited: [1] Tanaka, K.L., *Proc. LPSC XX*, 515-523, 1990. [2] Scott, D.H., *JGR, 87*, 9839-9851, 1982. [3] Scott, D.H., and J.M. Dohm, *Proc. LPSC XX*, 503-513, 1990. [4] Watters, T.R., and M.J. Tuttle, *LPSC XXI*, 1308-1309, 1990. [5] Barlow, N.G., and J.R. Zimbelman, *LPSC XIX*, 35-36, 1988. [6] Squyres, S.W., et al., *JGR, 97*, 13611-13634, 1992. [7] Stofan, E.R., et al., *JGR, 97*, 13347-13378, 1992. [8] Janes, D.M., et al., *JGR, 97*, 13055-13067, 1992. [9] Pollard, D.D., and A.M. Johnson, *Tectonophysics, 18*, 311-354, 1973.

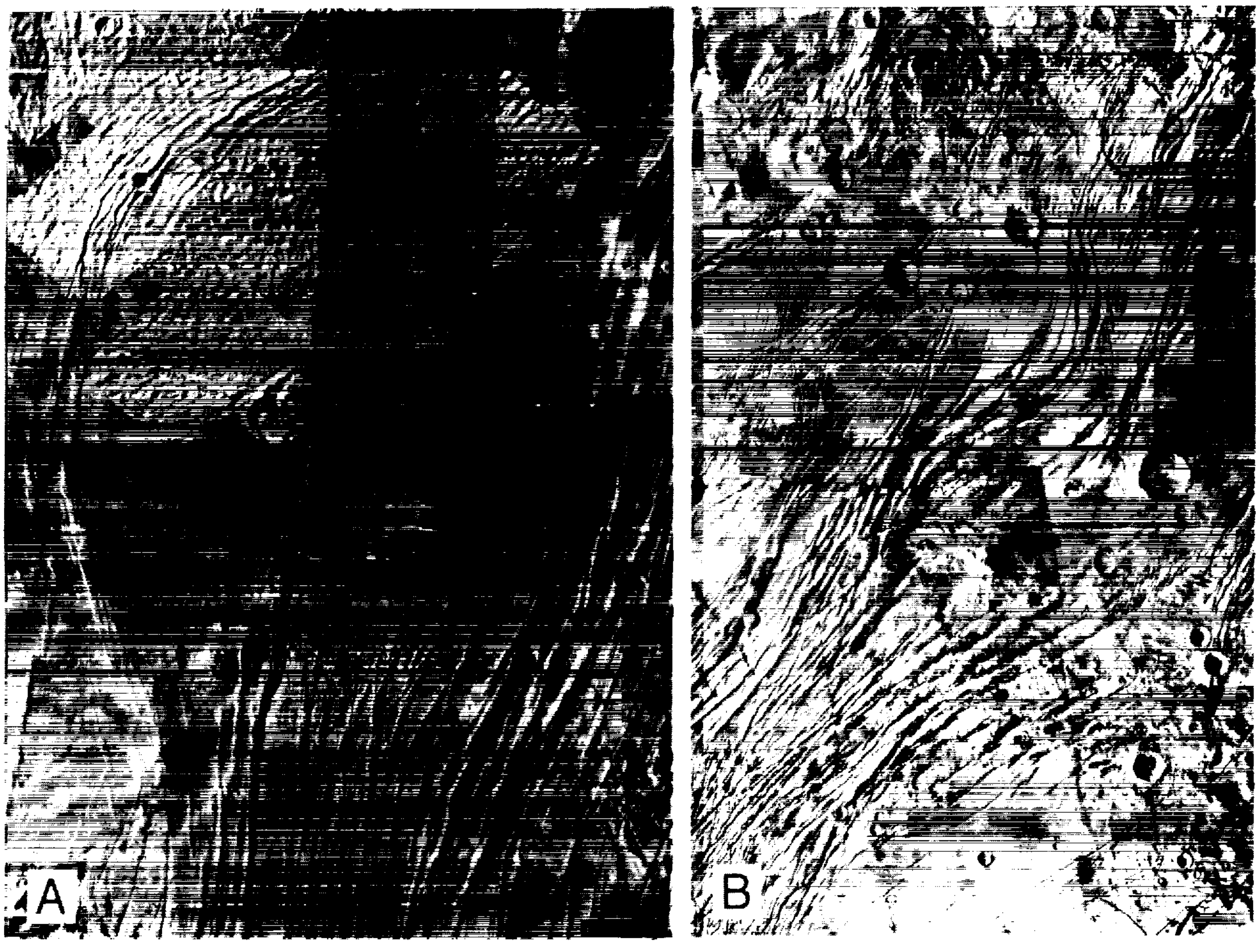


Figure 1. Circular structures on Mars that may be analogous to Coronae on Venus. (A) Alba Patera and (B) circular structures in Tempe Terra (arrow indicates a volcanic dome).

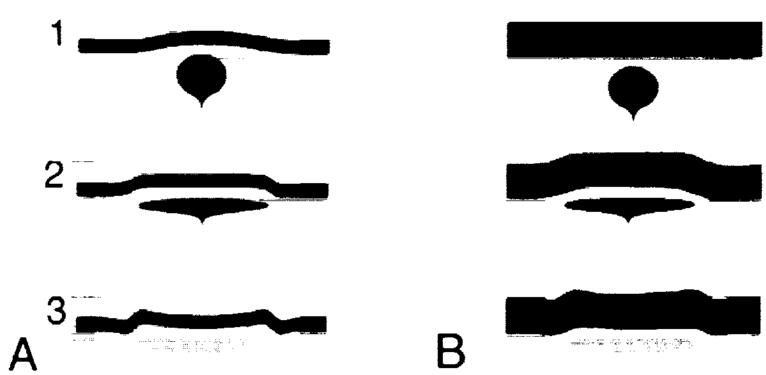


Figure 2. Conceptual model of the formation of (A) a Venusian corona (after Squyres et al. [6]) and (B) a circular structure on Mars.

N94-20864

A FRESH LOOK AT CRATER SCALING LAWS FOR NORMAL AND OBLIQUE HYPERVELOCITY IMPACTS;

A.J. Watts, D.R. Atkinson, S.R. Rieco, J.B. Brandvold, S.L.Lapin, C.R. Coombs; POD Associates, Inc., 2309 Renard Place SE, Suite 201, Albuquerque, NM 87106.

P. 2

INTRODUCTION

With the concomitant increase in the amount of man-made debris and an ever increasing use of space satellites, the issue of accidental collisions with particles becomes more severe. While the natural micrometeoroid population is unavoidable and assumed constant, continued launches increase the debris population at a steady rate.[1,2] Debris currently includes items ranging in size from microns to meters which originated from spent satellites and rocket cases. To understand and model these environments, impact damage in the form of craters and perforations must be analyzed. Returned spacecraft materials such as those from LDEF and Solar Max have provided such a testbed. From these space-aged samples various impact parameters (i.e., particle size, particle and target material, particle shape, relative impact speed, etc.) may be detetermined. These types of analyses require the use of generic analytic scaling laws which can adequately describe the impact effects. Currently, most existing analytic scaling laws are little more than curve-fits to limited data and are not based on physics, and thus are not generically applicable over a wide range of impact parameters. During this study, we have generated a series of physics-based scaling laws for normal and oblique crater and perforation formation into two types of materials: aluminum and Teflon.

BACKGROUND

Due to orbital mechanics and satellite geometries, very few impacts involve "normal" collisions. Christiansen[3] has shown that the angle of approach modifies the resulting penetration, thus, in order to correctly interpret the environment and the consequential impact effects, the effect of obliquity must be properly understood. Similarly, density of both the projectile and target must be known. Presently, it is assumed that most micrometeoroids have a density of ~0.5 g/cm^3 [4] while the debris value is ~4.7 g/cm^3 for particles <1 cm, and decreases with particle size[1] since most large pieces are not chunky pseudo-spheres, but rather odd-shaped items which, on average behave as if partly porous. In addition, target and projectile yield strengths, fracture strength, and melt energy properties must also be understood.

DAMAGE INTERPRETATION AND MODELLING

Impact damage ranges from simple pitting, erosion and cratering for impacts into plastically yielding materials, through conchoidal and star cracking for brittle targets, to complete perforation, large-scale spallation/fragmentation, and material melting and vaporization. LDEF data indicate additional effects, such as delaminations of multilayered material and the generation of rings of ejected material, and/or permanently deformed material. These impact effects may be enhanced by the introduction of thermal cycling, UV and AO embrittlement and erosion. These effects may be synergistic and may alter material properties so as to modify impact cratering, star cracking and perforation effects.

To correctly interpret the space environment, the resulting modes of impact damage and the potential methods which may be employable to mitigate the effects, one MUST properly understand the rules of impact damage. Unfortunately, existing experimental facilities cannot replicate the complet range of conditions. As a result, one must rely on either extrapolation of experimental data obtained at lower speeds or with non-typical materials, or from computer models. Although computer modelling eases the interpretation of material responses, it does not necessarily provide all the required data and is expensive and time consuming: thus the need for analytic scaling laws.

WATTS' SCALING LAWS

Many scaling laws are simple curve-fits to limited data derived by investigators fitting their own data. These laws rarely agree on the proper power index to be applied to impact velocities or densities, nor do they agree on whether to use such terms as hardness numbers or yield strengths. Also, these parameters are often only applied to the target and not the impactor, despite the fact that one must deal with both bodies. These are but a few of the problems evident in the current scaling laws.

Keeping these conditions in mind, using actual spacecraft data, CTH[5] hydrocode computer models and, laboratory data, POD has developed generically applicable scaling laws for predicting crater diameters, penetration depths, and the Ballistic Limit perforation conditions for both aluminum and Teflon for any impact angle of incidence; equations 1, 2, 3 respectively.

$$(d_c/d_p)=1.0857(\rho_p/\rho_t)^{0.2857}(\rho_t/Y_t)^{0.2857}(c_t/c_p)^{0.2857}(u_0\cos\theta)^{0.5714}/(1+(\rho_t/\rho_p)^{1/2})^{0.5714} \quad (1)$$

$$P/d_p=(1/4)(4/3)^{1/3}(\rho_p/\rho_t)^{1/3}(\rho_t/Y_t)^{1/3}\{(c_{0t}+s(u_0\cos\theta-u_{t,crit})/(1+(\rho_t/\rho_p)^{1/2}))(u_0\cos\theta-u_{t,crit})\}^{1/3} \quad (2)$$

$$T/d_p = (1/8)(4/3)^{1/3}(\rho_p/\rho_t)^{1/3}(\rho_t/Y_t)^{1/3}\{(c_{0t}+s(u_0\cos\theta-u_{t,crit})/(1+(\rho_t/\rho_p)^{1/2}))(u_0\cos\theta-u_{t,crit})\}^{1/3} + (1/4)\{\rho_p(u_0\cos\theta)^2/(2\sigma_t(1+(\rho_t/\rho_p)^{1/2})^2)\}^{1/N} \quad (3)$$

In addition, POD has also developed and validated criteria for predicting partial and complete projectile ricochets; equations 4 and 5, respectively.

$$\sin\theta \geq c_{0t}/u_0 + s\cos\theta/(1+(\rho_t/\rho_p)^{1/2}) \quad (4)$$

$$\tan\theta = r_c/d_p = 1/2\ (d_c/d_p) \quad (5)$$

Equation 3 actually has TWO parts, one relating to the crater depth, and one relating to the reflection of the shock pulse from the target rear surface. The former term depends on tensile strength and has roughly a 2/3 index for impact speed, while the latter term depends on tensile strength and has roughly a unit index for impact speed. Thus, both target yield strength and tensile strength are strong drivers for determining perforations.These equations satisfy dimensional analysis; however, these equations were derived from physics and thus suffer none of the irregularities which hamper the other existing scaling laws. In comparisons to CTH hydrodynamic code calculations, these equations closely matched the predictions for both aluminum and Teflon. In comparison with experimental data[6], these equations also closely matched the data for aluminum and Teflon.

REFERENCES: (1) Kessler D.J. *et. al.* (1987) *NASA TM-100471*. (2) Kessler D.J. (1990) Updates to *NASA TM-100471*. (3) Christiansen E.L. (1992) Design and performance equations for advanced meteor./debris shields, 1992 Hypervelocity Impact Symposium, Austin, TX. (4) Cour-Palais B.G. et al. (1969) *NASA SP-8013*. (5) Bell R.L. et al (1991) The CTH Code, Sandia Nat'l Lab (6) Horz F. et al. (1992) 1992 Hypervelocity Impact Symposium, Austin, TX.

COAGULATION OF GRAINS IN STATIC AND COLLAPSING PROTOSTELLAR CLOUDS

S.J. Weidenschilling (Planetary Science Institute) and T.V. Ruzmaikina (Lunar and Planetary Laboratory, Univ. of Arizona, Tucson, and Schmidt Inst. of Earth Physics, Moscow)

The wavelength dependence of extinction in the diffuse interstellar medium implies that it is produced by particles of dominant size $\sim 10^{-5}$ cm. There is some indication that in the cores of dense molecular clouds, sub-μm grains can coagulate to form larger particles; this process is probably driven by turbulence [1]. The most primitive meteorites (carbonaceous chondrites) are composed of particles with a bimodal size distribution with peaks near 1 μm (matrix) and 1 mm (chondrules). Cameron [2] suggested that grains could coagulate during collapse of the presolar cloud, with the short free-fall time ($\sim 10^5$y) offset by higher densities and turbulent velocities. Models for chondrule formation that involve processing of presolar material by chemical reactions [3] or through an accretion shock during infall [4-6] assume that aggregates of the requisite mass could form before or during collapse. Most evaluations of grain aggregation have been simple comparisons of collision timescales with cloud lifetimes and free-fall times; only Cameron computed actual size distributions of aggregates. The effectiveness of coagulation during collapse has been disputed [7,8]; it appears to depend on specific assumptions [9]. Here we report the first results of detailed numerical modeling of spatial and temporal variations of particle sizes in presolar clouds, both static and collapsing.

Static Clouds: Observations of present-day star-forming regions imply that solar-type stars are formed by collapse of small (radius R $\sim 10^{17}$ cm) dense cores in molecular clouds. A core of mass slightly exceeding $M_\odot$ is sufficient to make the Sun and a low-mass solar nebula. Stable Bonnor-Ebert spheres can be considered as models of the cloud cores; the degree of density concentration to the center depends on external pressure at the cloud surface. We consider spherically symmetric clouds with mass $M = 1.1M_\odot$, R = 1.4x10^4 AU and temperature T = 10°K (isothermal sound speed 1.9x10^4 cm/s). We consider clouds with three density distributions: uniform density, singular isothermal sphere ($\rho \propto r^{-2}$), and uniform central density with $\rho \propto r^{-2}$ in the outer part. We assume a Kolmogorov turbulence spectrum with maximum eddy size 0.1R. The turbulent velocity V is chosen to be either uniform or $\propto r^{-1/2}$ (constant turbulent pressure). Particle relative velocities are modeled from Völk *et al.* [10] as modified by Mizuno *et al.* [11] for the small scale eddies. We divide the cloud into 20 radial zones and compute the evolution of the size distribution in each. Particles can migrate between zones by turbulent diffusion and radial settling.

Particle Properties: The static cloud has an initially uniform grains/gas mass ratio of 0.014, with all grains initially 0.1 μm diameter. Aggregates are assumed to have uniform density or a fractal structure. The simplest assumption of perfect sticking yields an upper limit on aggregate size. We also use the sticking criterion of Chokshi *et al.* [12] with material properties of H_2O ice; impacts at less than a size-dependent critical velocity result in sticking. Erosion and disruption are allowed at higher velocities, assuming an impact strength of 10^6 erg/g.

Collapsing Clouds: The output size distribution of the static case is used as the initial state in the collapse, which follows Shu's [13] similarity solution for $\rho(r,t)$. We compute the collisional evolution of particles in a parcel of turbulent gas with sonic velocity of the largest eddies, $V=c$, as ρ increases during infall. Two assumptions are used to estimate the strength of turbulence: (a) constant largest eddy length scale $L = 0.1R$, and (b) $L = \min(0.1R, cr/\dot{r})$, which causes the inner size scale of smallest eddies to decrease during collapse. The collapse is followed to $r = 3$ AU; ρ increases by $\sim 10^5$.

Results: Particle growth occurs in the static case for either sticking criterion. For uniform aggregate density, sizes ~$100(V/c)$ μm are reached after 10^7y; for perfect sticking aggregate size increases roughly as t^2. Fractal aggregates yield sizes $\sim 10^2$ times larger, but with very low densities ($\sim 10^{-3}$g/cm^3). Still larger particles can form in the inner part of a centrally condensed cloud, but would be lost into the star during collapse. We model the size evolution during collapse only for the outer zone of the cloud; this material would land in the disk. For case (a), particle motions become more correlated and relative velocities decrease during collapse as ρ increases because the response time to drag forces varies as ρ^{-1}, while the turnover time of the smallest eddies decreases as $\rho^{-1/2}$. There are few collisions and very little change in the size distribution. In the more physically plausible case (b), the strength of turbulence and relative velocities increase during collapse, and collisions occur much more often. If perfect sticking is assumed, further growth occurs, as much as several orders of magnitude in mass. However, impact velocities also increase during collapse, and can cause net

destruction of aggregates due to high-speed collisions. For impact strength 10^6 erg/g, the aggregates striking the circumstellar disk at 3 AU are $\leq 10\ \mu m$ in final size.

Thus, we show the possibility of a significant growth of interstellar dust grains in turbulent molecular cloud cores before and during their collapse. Fluffy aggregates grow faster than compact grains. The sticking efficiency and impact strength are important parameters determining the evolution of size and mass of aggregates. Further investigation of these parameters is needed to restrict initial size distribution of aggregates in protostellar clouds and circumstellar disks.

This research is supported by NASA Origins of Solar Systems program, contract No. NASW-4616.

References:

[1] B.T. Draine (1985). In *Protostars and Planets II*, D. Black and M. Matthews, Eds. U. of Ariz., Tucson, 621-640.
[2] A.G.W. Cameron (1975) *Icarus* 24, 128.
[3] D. Clayton (1980) *Ap.J.* 239, L37.
[4] J. Wood (1984) *EPSL* 11, 70.
[5] T. Ruzmaikina (1990) *LPSCXXI*, 1053.
[6] T. Ruzmiakina and W. Ip (1993) *Icarus*, submitted.
[7] T. Kusaka, T. Nakano, and C. Hayashi (1970) *Prog. Theor. Phys.* 44, 1580.
[8] P. Cassen and A. Boss (1988), in *Meteorites and the Early Solar System*, J. Kerridge and M. Matthews, Eds., U. of Ariz., Tucson, 304-328.
[9] G.P. Horedt (1975) *Prog. Theor. Phys.* 54, 1224.
[10] H. Völk, F. Jones, G. Morfill, and S. Röser (1980) *Astron. Astrophys.* 85, 316.
[11] H. Mizuno, W. Markiewicz, and H. Völk (1988) *Astron. Astrophys.* 195, 183.
[12] A. Chokshi, A. Tielens, and D. Hollenbach (1993) *ApJ.*, in press.
[13] F. Shu (1977) *ApJ.* 214, 488.

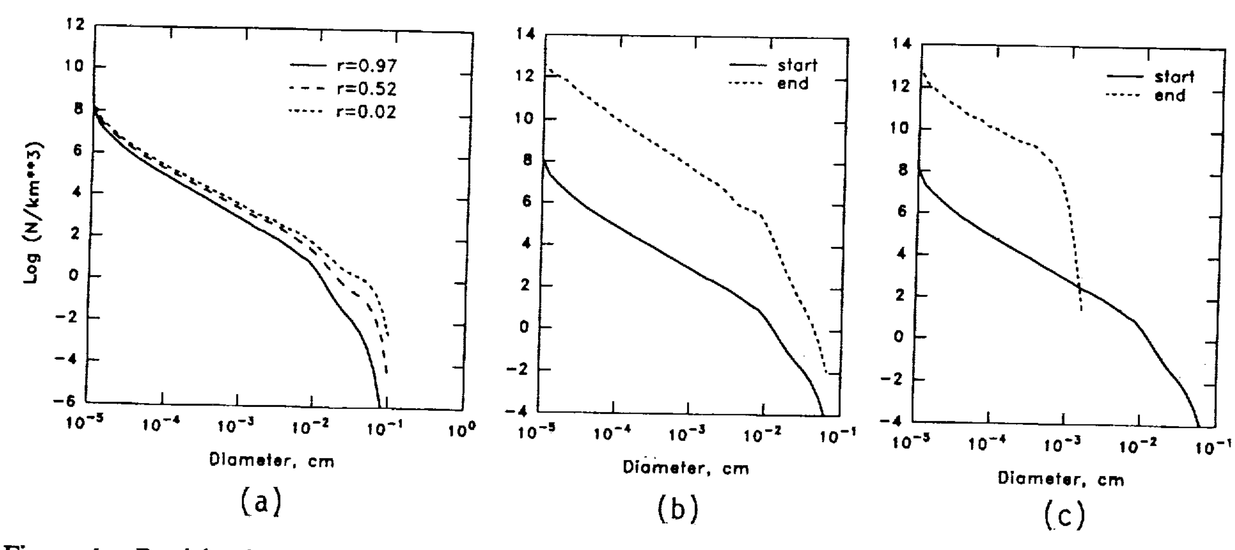


Figure 1. Particle size distribution for a static and collapsing cloud, presented as number density per logarithmic diameter interval $2^{1/3}$. Impact strength 10^6 erg/g. Fractal structure assumed at $d < 30\ \mu m$, where Chokshi *et al.* criterion predicts perfect sticking. Larger aggregates have constant density. (a) Static Bonner-Ebert sphere at $t = 10^7$y. $V = c$ at outer edge, $\propto \rho^{-1/2}$ in interior. Three radial locations shown. (b) Initial and final (r = 3 AU) size distributions for collapse of outer shell of (a), assuming uniform turbulence strength. There is little change in the size distribution, only increased concentration due to compression of gas. (c) Same as (b), but with increasing strength of turbulence during collapse. Collisions destroy most aggregates of size $> 10\ \mu m$.

S230-90
ABS. ONLY

N94-20866

THE FORMATION OF FEO-RICH PYROXENE AND ENSTATITE IN UNEQUILIBRATED ENSTATITE CHONDRITES: A PETROLOGIC-TRACE ELEMENT (SIMS) STUDY. M.K. Weisberg[1], M. Prinz[1], R.A. Fogel[1], and N. Shimizu[2]. (1) Dept. Mineral Sci., American Museum Natural History, New York, NY 10024. (2) WHOI, Dept. Geology and Geophys., Woods Hole, MA 02543. p. 2

FeO-rich pyroxenes (Fe-Pyx) are a major constituent of some of the chondrules and fragments in unequilibrated enstatite chondrites (UEC). They contain structurally oriented zones of Cr-, Mn-, V-rich, FeO-poor enstatite (En) that has a red cathodoluminescence and is associated with µm-sized blebs of low-Ni, Fe-metal, and in some cases silica. This represents clear evidence for the process of reduction. The Fe-pyx is nearly always rimmed by minor element-poor En having a blue CL. More commonly, red and blue En occur as larger grains in chondrules and fragments throughout the UEC's, unassociated with Fe-pyx, constituting the major silicate phases. REE abundance patterns of the Fe-pyx are LREE-depleted and red En has a similar pattern. Blue En rims, however, have a flat REE pattern at ~1xChondritic (Ch). The Fe-pyx in UEC's originated from an earlier generation of chondrules that formed in a nebular region that is more oxidizing than that required for enstatite chondrites. Following solidification these chondrules were introduced to a more reducing nebular environment. Some of the red En crystals that are common throughout UEC's may be the products of reduction of Fe-pyx. Blue En rims grew onto the surfaces of the Fe-pyx and red En via condensation from the nebula.

INTRODUCTION: Enstatite chondrites record the most reducing conditions known in the early solar system. Their oxidation state may be the result of condensation in a nebular region having an enhanced C/O ratio [1], reduction of more oxidized materials in a reducing nebula, reduction during metamorphic reheating in a parent body [2], or a combination of these events. The presence of more oxidized Fe-rich silicates [3,4,5,6], two types of En (distinguished by red and blue CL) [7,8], and the juxtaposition of Fe-pyx surrounded by blue En in the UEC's is intriguing and led us to examine the question of enstatite chondrite formation. Previously, we presented data on the petrologic-geochemical characteristics of the Fe-pyx and coexisting red and blue En [9]. Here we report on minor and trace element abundances (determined by ion probe-SIMS) on these three types of pyroxenes in the following meteorites: Kota Kota and LEW87223 (EH3), MAC88136 (EL3), St. Marks (EH4), and Hvittis (EL6). More data are currently being collected.

RESULTS: Fe-pyx (Fs_{4-37}) grains occur in some chondrules and fragments in UEC's and show evidence of the onset of reduction. They contain µm-sized blebs of low Ni (<1%), Fe-metal associated with (low-FeO) red En, and in some cases silica, along grain boundaries, twin lamellae, veins, and fractures. Fe-pyx chondrules and fragments are nearly always rimmed, or partially rimmed, by blue En. Electron probe analyses (WDS) show that Fe-pyx is enriched in minor elements which range (in wt.%) from 0.5-1.7 Cr_2O_3, 0.1-0.8 MnO, <0.1-2.6 Al_2O_3, 0.5-3.1 CaO. Minor elements determined by SIMS (Table 1) agree with the WDS data and, in addition, show that Fe-pyx has up to 148 ppm V and 787 ppm Ti. REE patterns were measured in 3 Fe-pyx grains and all have LREE-depleted patterns with La~0.1-0.2xCh and Yb~0.5-1xCh (Avg. La/Yb=0.2). **Red En** ($Fs_{<4}$) occurs along structurally controlled zones within the Fe-pyx as well as individual crystals in chondrules and fragments, unassociated with Fe-pyx. It is a major silicate component in UEC's. Minor and trace element abundances are generally similar to that of Fe-pyx (Table 1), and they have similar REE patterns (Fig. 1). **Blue En rims** are characterized by minor element concentrations below electron microprobe detection limits (<0.03wt.%) but, in some cases, have Na_2O (up to 0.07%) and Al_2O_3 (up to 2%) abundances that are higher than in Fe-pyx and red En. Ion probe analyses, however, reveal up to (in ppm) 91 Ti, 11 V, 434 Cr, 161 Mn, and 1 Sr (Table 1). The REE pattern for blue En differs significantly from that of Fe-pyx and red En and is flat at ~1xCh. **En in EH4 and EL6 chondrites** has blue CL, with Ti, V, and Cr abundances similar to the blue En rims; however, some blue En rims have much higher Al, Na, Mn and Sr concentrations. In addition, the REE patterns of these pyroxenes are LREE-depleted with La <0.07xCh for Hvittis (EL6) and below detection for St. Marks (EH4); HREE are flat at ~1xCh. and the Hvittis En has a large negative Eu anomaly.

DISCUSSION: 1) The occurrence of chondrules that consist mainly of Fe-pyx suggests that all Fe-pyx fragments in UEC's originated from broken chondrules [5,9]. The fractionated REE pattern of Fe-pyx, typical of that expected for crystal/melt partitioning of REE's in pyroxene, is consistent with this interpretation. 2) The high Fe content of the Fe-pyx testify to formation in a nebular region that is more oxidizing than that required for enstatite chondrites. 3) The similarity in REE patterns, trace element contents and the numerous reduction features found in red En and Fe-

pyx strongly imply formation of some red En, a major silicate component in UEC's, by reduction of Fe-pyx. Some red En may have crystallized from chondrule melts having Fe-pyx-like precursors. 4) The blue En rims did not form via crystallization from a melt. Crystallization of pyroxene from any known chondrule melt composition would not produce pyroxene which is so remarkably low in Cr and Mn; partition coefficients of these elements in pyroxene are too high [10]. Additionally, the flat REE pattern of blue En rims is not that expected from crystal/melt partitioning of REE's in pyroxene. Growth during parent body metamorphism is also an untenable hypothesis. UEC's are relatively unmetamorphosed and rims having sharp boundaries, like the blue En rims, are not observed in metamorphosed chondrites (e.g., ordinary chondrites). Secondly, metamorphism of enstatite chondrites appears to reduce all minor element abundances in En; therefore, the high Al, Na, Mn and Sr contents of some blue En rims are inconsistent with their growth during subsolidus heating on a parent body. Finally, the REE's in the Fe-pyx, red En, and equilibrated En in the EH4 and EL6 chondrites exhibit a similar LREE-depleted pattern, whereas the blue rims have a flat 1xCh pattern. The blue En with REE concentrations that are near C1, imply a nebular condensation origin. Their low FeO contents are consistent with a nebular environment classically thought of as having given rise to the E chondrites; a nebula with low fO_2.

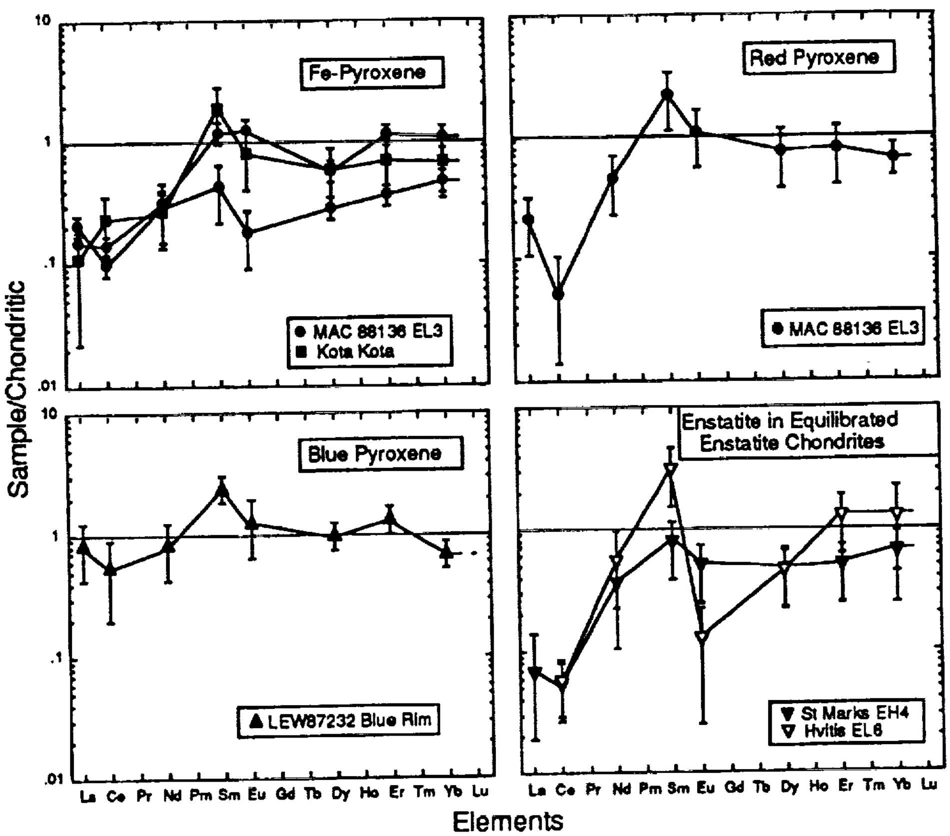


Figure 1. REE's in the three types of low-Ca pyroxene from enstatite chondrites. (Error bars = %MD.)

Table 1. Minor/trace element abundances (ppm) in pyroxene from enstatite chondrites.

	Fe-pyx	Red	Blue	Hvittis	St. Marks
Ti	33-787	153-230	7-91	17	37
V	42-148	66-102	9-11	4	17
Cr	2028-6638	2448-3132	314-434	177	399
Mn	805-3201	503-1530	154-161	57	63
Sr	1-3	bd-3	0.4-1	bd	0.4
# grains	5	2	3	1	1

bd-below detection.

REFERENCES: [1] Larimer J.W. and Bartholomay M. (1979) GCA 43, 1455-1466. [2] Ringwood A.E. (1966) GCA 30, 41-104. [3] Rambaldi E. et al. (1983) EPSL 66, 11-24. [4] Rambaldi E. et al. (1984) Nature 311, 138-140. [5] Lusby D. et al. (1987) JGR 92, E679-E965. [6] Kitamura M. et al. (1988) Proc. NIPR Symp. Antarc. Met. 1, 38-50. [7] Leitch C.A. and Smith J. V. (1982) GCA 46, 2083-2097. [8] McKinley S.G. et al. (1984) JGR 89, B567-572. [9] Weisberg M.K. et al. (1992) LPSC XXIII, 1509-1510. [10]Lofgren G.E. and DeHart J.M. (1992) LPSC XXIII, 801-802.

GEOLOGY AND RADIOPHYSICAL PROPERTIES OF THE VENERA AND VEGA LANDING SITES. C. M. Weitz, Jet Propulsion Laboratory, 4800 Oak Grove Drive, Pasadena, CA 91109; A. T. Basilevsky, Brown University, Dept. of Geology, Providence, RI, 02912, Permanent affiliation: Vernadsky Institute, Russian Academy of Science, 117975 Moscow.

Introduction: We have produced geologic maps for all seven Venera and Vega landing sites. Because the radius of error for each landing site is 150 km, we have mapped the entire landing circle centered about the estimated landing point. We found correlations between the Magellan imagery and the lander TV panoramas and geochemical measurements made at the landing site. Radiophysical properties, including backscatter cross-sections, altimetry, emissivity, and rms slopes, were determined for each landing circle. After mapping the geology of the landing circles, we mapped the regional geology of the seven sites and determined the geologic history of these large regions.

Geology of the Landing Sites: Geologic mapping of the seven Venera/Vega landing sites has shown that the dominant type of terrain at these sites is plains. The Venera 8 site contains ridged and fractured plains and a younger plains-forming volcanic complex [1]. A 23-km-diameter pancake dome and several smaller steep-sided domes were also identified within the landing circle. Geologic mapping of the Venera 9 site, which is located on the eastern slope of Beta Regio, has shown the geology of this area to be dominated by fractured plains with complex ridge terrain (CRT) units located both inside and outside the landing circle. A large trough oriented transverse to Devana Chasma cuts through the plains and a lava channel in the plains. The Venera 10 site contains an elder and a younger plains unit and the same CRT mapped at the Venera 9 site. The younger plain unit consists of lava flows from a gentle-sloped 60-km-diameter dome. Concentric fractures in the plains to the northeast indicate uplift of some of the CRT and adjacent plains to the west of the fractures. The Venera 13 site is dominated by plains that are radar-dark in the SAR imagery because of a mantling of fine debris. At least four steep-sided domes surround the landing circle. A 200-km coronalike feature and its associated flows are located in the southeast of the landing circle. A lineament belt trending NW-SE from a large CRT unit to the west cuts through the plains and domes in the site and lava flows from volcanism to the west both embay and are disrupted by the lineament belt. This lineament belt continues to the southeast where it disrupts the Venera 14 site. The Venera 14 geology shows a site dominated by radar-bright and -dark lava flows from a 75-km-diameter gentle-sloped volcano. Heavily fractured terrain, possibly representing CRT, has been embayed and infilled by the plains. Concentric fracture systems can be identified to the west and south of the volcano. Geologic mapping of the Vega 1 site has shown that the site consists of ridged radar-bright and -dark plains covered by debris and wind streaks. The Vega 2 site contains similar (and probably the same) radar-bright and -dark plains. The plains here, however, do not have the debris visible at the Vega 1 site but the Vega 2 site is disrupted by numerous lineations resulting from activity associated with Dali Chasma to the south.

Magellan and Lander Correlations: Based upon Magellan data and the lander geochemical [2] and TV panoramas [3], we have been able to suggest the most likely material in the Magellan imagery sampled by the landers. Lamprophyrelike lavas, silicic ash beds, or the pancake dome are the most likely material sampled at the Venera 8 site [1]. At the Venera 9 site, the sampled tholeiitic material most likely represents fractured plains. Plains from either the gentle-sloped dome or from earlier volcanic activity are the most probable tholeiitic material sampled at the Venera 10 site. Lavas from a steep-sided dome or a coronalike feature at the Venera 13 site might match the nontholeiitic composition measured by the lander. Basalts erupted from a gentle-sloped volcano represent the most likely tholeiitic material sampled by the lander at the Venera 14 site. At both the Vega 1 and 2 sites, the landers measured the tholeiitic composition of the radar-bright or -dark plains at these sites.

At the Venera 8 and 13 sites, where a non-tholeiitic composition was measured for the surface material, the Magellan imagery revealed that both these sites have unusual volcanic features associated with them, such as steep-sided domes and coronalike features with flows. Unusual volcanic activity was not observed inside the landing circle at the other five sites and at these sites the landers measured geochemical signatures of tholeiitic basalts. This correlation indicates that the geochemistry measured by the landers correlates well with the morphology seen in the Magellan imagery. A strong correlation also exists between the SAR imagery and the TV panoramas taken by the Venera 9, 10, 13, and 14 landers. The Venera 9 panorama showed cobbles on a sloped landing surface. The SAR imagery shows a fractured plain for the Venera 9 landing site. Both Venera 10 and 13 TV panoramas showed soil on the plains and the SAR imagery shows radar-dark debris on the plains. The Venera 14 TV panorama showed a plain with almost no debris and the SAR imagery of the site shows mottled lava flows with no debris covering the flows.

Radiophysical Properties: Backscatter cross-sections, altimetry, emissivity, and rms slopes were calculated for each Venera/Vega landing circle. The minimum, mean, and maximum values for each radiophysical parameter are shown in Table 1. Most of the variations in backscatter, emissivity, and rms slopes reflect variations in roughness at each site. The Venera 8 and Vega 1 and 2 sites consist predominantly of plains so the radiophysical

GEOLOGY OF THE VENERA AND VEGA LANDING SITES. C.M. Weitz and A. T. Basilevsky

properties within the landing circle are typical values for the venusian plains. The Venera 9 site has the highest backscatter cross-sections, altimetry, emissivity, and rms slopes of all the sites because it is located on the eastern slope of Beta Regio and the uplift associated with Beta Regio has caused the site to become elevated and heavily fractured. In addition, CRT within the landing circle is also a cause of the high radiophysical parameters within the landing circle. Altimetry data for the Venera 9 site shows that the lava channel does not follow the W-E slope associated with Beta Regio so this indicates that the uplift of Beta post-dates the emplacement of the plains. The Venera 10 site also has high backscatter, altimetry, emissivity, and rms slopes within the landing circle because it contains CRT. The plains within the landing circle appear quite smooth in the SAR so this is why the emissivity, backscatter, and rms slopes are lower than at the Venera 9 site. The Venera 13 site has some of the lowest radiophysical properties for all the sites because the landing circle contains plains that are covered by a layer of debris that has decreased the backscatter and emissivity at the site. The lava flows from the Venera 14 volcano have large variations in backscatter and emissivity. The Venera 14 and the Vega 1 and 2 sites have emissivity variations that do not correlate to variations in backscatter, unlike the other four sites. This indicates that there may be compositional and/or differences in vesicularity in the lava flows at these three sites.

Conclusions Geologic mapping of the Venera/Vega site and their regional geology has enabled us to determine a geologic history for these sites and the larger regions that contain them. Complex ridge terrain, complex terrain, and some heavily fractured plain represent the oldest geologic units at all the sites. Vast plains from regional-scale volcanism later embayed all three geologic units. Disruption of the plains by both extension and compression caused fractures and ridges to disrupt much of plains. Volcanism from local volcanic sources (i.e. steep-sided domes, coronae, rifting) post-date the vast plains. Lineament belts associated with both rifting and uplift from mantle upwelling have caused severe disruption of the older geologic units. The plains at the Venera 9 and Vega 1, 2 sites represent vast outpourings of lava associated with regional-scale plain-forming volcanic eruptions. Both the Venera 9 and Vega 2 sites have an elder plains that has been heavily fractured by major rifting and uplift adjacent to these two sites. The plains at the Venera 8, 10, 13, and 14 sites represent more restrictive flows that formed "spots". The volcanic activity associated with the Venera 8, 10, 13, and 14 sites is probably the result of hot-spot, plume-driven volcanic activity.

The geology of the Venera 9 site confirms earlier observations that Rhea Mons represents pre-existing CRT uplifted and then later disrupted by Devana Chasma [4]. Identification of a lava channel at the Venera 9 site that does not follow the topography associated with the uplift of Beta Regio to the west indicates that the plains formed before the uplift of Beta. Geologic mapping of the Venera 10 site has shown that there has been uplift and fracturing of CRT and older plains. Lineament belts in the Venera 13 and 14 sites extend between major sites of volcanic activity (i.e. volcanoes, rifting, coronalike features) on both the plains and CRT. This suggests that lineament belts in this region represent extensional zones associated with mantle upwelling. Geologic mapping of the Vega 1 and 2 sites and their regional geology indicates that the CRT has been embayed and infilled by vast eruptions of plains volcanism. The large volcanoes in Atla Regio and Sapas Mons post-date these vast plains. Dali Chasma and its associated activity to the south have caused severe disruption of the surrounding plains.

References: [1] Basilevsky et al., *JGR*, **97**, E10, 16,315-16,335, 1992; [2] Surkov, Cosmochemical exploration of planets and moons, Moscow, Navda Press, 1985; [3] Basilevsky et al., *Bull. Amer. Geol. Soc.*, **96**, 137-144, 1985; [4] Senske et al., *JGR*, **97**, E8, 13,395-13,420.

TABLE 1. Minimum, Maximum, and Mean Radiophysical Properties at Each Landing Site

Landing Site	Incidence Angle (deg)		Backscatter (DN)			Altimetry (km)			Emissivity			Rms Slope (deg)		
	Min	Max	Min	Mean	Max	Min	Mean	Max	Min	Mean	Max	Min	Mean	Max
Venera 8	41	42	92	111.2	129	6051.4	6051.85	6052.3	0.805	0.834	0.855	1.0	2.88	7.3
Venera 9	41	42	88	120.8	164	6051.4	6052.89	6053.7	0.82	0.857	0.89	1.3	4.03	10.6
Venera 10	45	45	81	112.5	157	6051.1	6052.02	6053.3	0.785	0.825	0.88	0.4	2.24	9.0
Venera 13	42	43	87	106.7	146	6051.9	6052.25	6053.5	0.775	0.811	0.84	1.0	2.61	5.3
Venera 14	40	42	85	116.6	155	6051.0	6052.29	6053.1	0.77	0.810	0.84	1.3	3.11	9.3
Vega 1	45	45	90	107.5	135	6051.0	6051.32	6052.0	0.825	0.852	0.875	1.0	2.25	5.8
Vega 2	42	43	94	115.9	148	6052.1	6052.60	6053.2	0.82	0.851	0.885	0.8	2.13	7.1

A STUDY OF CARBONATES, SULFATES, AND PHOSPHATES USING THERMAL EMISSION SPECTROSCOPY; M.L. Wenrich and P.R. Christensen, *Department of Geology, Arizona State University, Tempe, Arizona 85287-1404*

Thermal emission spectroscopy is useful for identifying mineralogies including carbonates, sulfates, and phosphates. Each of these groups of minerals has a distinct emissivity profile that allows for general identification (e.g., carbonate). Laboratory data are being collected that suggest the potential for determining specific composition of these minerals (e.g., calcite, magnesite). Previous studies of Mars suggest that the above groups of minerals should be present. On Mars fine-grained mineralogies are likely to be intimately mixed due to aeolian activity. Mixtures of calcite with palagonite will be studied to determine the volume percent requirement for salt identification and to understand the complexities of fine-grained mixtures observed by thermal emission. Further work with mixtures will include sulfate and phosphate mineralogies.

There are several lines of evidence that suggest carbonates should be present on Mars. Mars is thought to have had an early wet, "warm" (>273 K) climate maintained by a thick CO_2 atmosphere [1,2,3] with a pressure of ~3 to 5 bars. However, Mars' present atmospheric pressure ranges from ~6 to 10 mbar CO_2 [4]. This implies that the CO_2 inventory was significantly depleted since the early history of the planet by either 1) loss into space; 2) adsorption onto regolith materials; or 3) removal of the CO_2 by combining the molecule into carbonate rocks [3,5,6]. A previous study [5] estimates that loss into space and adsorption of CO_2 into the regolith are not sufficient to account for the CO_2 depletion; therefore, an additional reservoir, such as carbonate precipitation, is required [7]. On Earth a reduction of atmospheric CO_2 occurred by extensive carbonate precipitation fixing atmospheric CO_2 through reactions with H_2O and available cations such as Ca^{++} and Mg^{++}. This process may also have caused the CO_2 depletion on Mars. The reaction requires liquid water; current surface pressures and temperatures on Mars preclude the presence of liquid water, but large geomorphic features such as outflow channels and dendritic valley networks indicate that substantial water has been available during Mars' past. The abundance of liquid water may have enabled the reaction to proceed and fix the atmospheric CO_2 into carbonate deposits. An abundance of cations is also required for the carbonate precipitation, but several studies [3,8,9] have shown that weathering of basalts could have provided enough cations to maintain the reaction.

Mars is generally accepted to be the parent body from which the SNC (the Shergotty, the Nakhlite, and Chassigny) meteorites were derived [10,11]. All of these meteorites contain small amounts of carbonate as determined by C/O ratio, energy dispersive x-ray spectrometry (EDS), scanning electron microscopy (SEM), and x-ray diffraction analyses [12,13]. These carbonates are considered to have formed on the parent body, Mars, rather than as a result of terrestrial chemical alteration.

Carbonate formation is probably still occurring under present martian surface conditions. Although no large surficial bodies of liquid water presently exist on Mars' surface, Booth and Kieffer [8] established that carbonates will also form under non-aqueous conditions, such as with minimal frosts equivalent to a mere 20 pr µm of water. These vapor-derived carbonate deposits may not be as volumetrically significant as earlier deposits may have been, but they may be areally extensive. Additionally, carbonates may presently be forming as a result of weathering of primary materials [7,9]. Gooding [9] and Clark and VanHart [14] suggest that calcium- and magnesium-bearing pyroxenes, plagioclases, and olivines would decompose to produce calcite ($CaCO_3$) and magnesite ($MgCO_3$) among other products.

Previous workers [15,16] have sought to identify surface carbonate deposits on Mars using Earth-based visible and near infrared reflection spectroscopy (0.35-4.2 µm) during the 1986 and 1988 oppositions. Based on subtle spectral reflectance features and an assumption of mixing carbonate with palagonite (a basalt alteration product), upper limits for carbonate were determined to be 3 to 5 wt % for the 1986 and 1988 data, respectively. However, the possibilities for carbonate identification were limited by the large "footprint" of the spectrometer, which varied from ~2000 km to ~900 km (during the 1986 and 1988 oppositions, respectively).

Based on thermo-dynamic considerations and analyses of the SNC meteorites, several carbonate compositions such as calcite, magnesite, and siderite are primary martian candidates [9,13,17,18]. The thermal infrared (5.9-25 μm) spectra for these carbonates can be seen in Figure 1. Typical strong absorption features in calcite (Iceland spar) occur at ~6.6, 11.3, and 24.8 μm due to fundamental vibrations of the C-O bonds. A comparison of calcite to siderite shows that the siderite absorption features are displaced to shorter wavelengths of ~6.4, 11.2, and, 24.6 μm. These band shifts potentially will allow for specific carbonate composition to be determined. These and other analyses will provide insight into the data received from Mars by the Thermal Emission Spectrometer (TES) aboard the Mars Observer spacecraft. The TES was specifically designed to operate within the infrared window that contains fundamental carbonate vibrations. Unlike the large spatial "footprint" that results from Earth-based spectroscopy, the spatial resolution of the TES is 3 km. Because of the high spatial resolution and that the C-O bonds produce fundamental vibrations within the infrared range, the TES instrument will return spectra that should allow for identification of carbonates if they exist on the surface.

Due to extensive aeolian activity on Mars, dust is thought to be an important surface component. Palagonite is considered to be a terrestrial analog to Mars dust based on similar spectral reflectance properties in the visible and near infrared range [19]. To understand the limitation of using emissivity data to determine carbonate presence and composition, further work will be done using thermal emission spectroscopy to analyze fine-grained calcite in intimate mixtures with palagonite to determine volume percentage requirements for salt identification and to understand the complexities of mixtures observed by thermal emission.

Additionally, thermal emission studies will be conducted using various sulfates and phosphates that are predicted by the Viking landers and the SNC analyses to be on the martian surface.

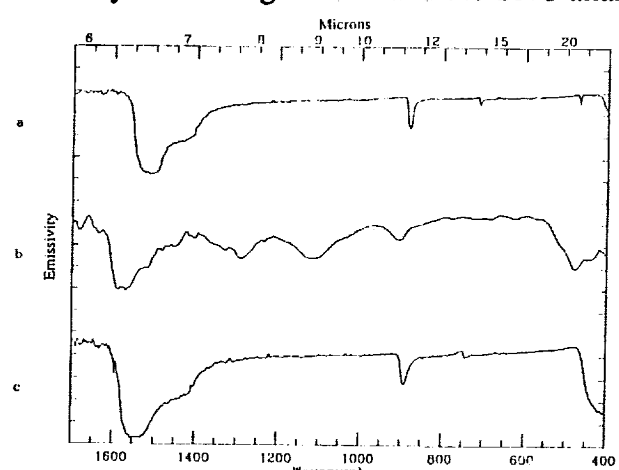


Figure 1. *Spectra of carbonate as emissivity varies with wavenumber: a) calcite, b) magnesite, c) siderite. Spectra are vertically displaced and separately scaled.*

References: [1] Masursky, H. (1973) *J. Geophys. Res., 78*, 4037-4047. [2] Pollack, J.B. (1979) *Icarus, 37*, 479-453. [3] Kahn, R. (1985) *Icarus, 62*, 175-190. [4] Carr, M.H. (1981) *The Surface of Mars*, Yale University Press. [5] Zent, A.P. et al. (1987) *Icarus, 71*, 241-249. [6] Carr, M.H. (1989) *Icarus, 79*, 311-327. [7] Fanale, F.P. (1976) *Icarus, 28*, 179-202. [8] Booth, M.C. and H.H. Kieffer (1978) *J. Geophys. Res., 83*, 1809-1815. [9] Gooding, J.L. (1978) *Icarus, 33*, 483-513. [10] Wood, C.A. and L.D. Ashwal (1981) *Proc. LPSC 12th*, 1359-1375. [11] McSween, H.Y., Jr. (1985) *Rev. Geophys. Space Phys., 23*, 391-416. [12] Gooding, J.L. et al. (1988) *Geochim. et Cosmochim. Acta, 52*, 909-915. [13] Gooding, J.L. (1992) *LPI Tech. Report, 92-04, Part 1*, 16-17. [14] Clark, B.C. and P.C. VanHart (1981) *Icarus, 45*, 370-378. [15] Blaney, D.L. and T.B. McCord (1989) *J. Geophys. Res., 94*, 10159-10166. [16] Blaney, D.L. (1990) University of Hawaii, PhD dissertation. [17] Chatzitheodoridis, E. and G. Turner (1990) *Meteoritics, 25*, 354. [18] Wentworth, S.J. and J.L. Gooding (1991) *LPSC 22nd*, 1489-1490. [19] Evans and Adams (1980) *Proc. LPSC 10th*, 1829.

WEATHERING FEATURES AND SECONDARY MINERALS IN ANTARCTIC SHERGOTTITES ALHA77005 AND LEW88516. Susan J. Wentworth[1] and James L. Gooding[2]. [1]C23/Lockheed ESC, 2400 NASA Rd. 1, Houston, TX 77058. [2]SN2/Office of the Curator, NASA Johnson Space Center, Houston, TX 77058 USA.

The shergottite meteorites Allan Hills, Antarctica, A77005 (ALHA77005) and Lewis Cliffs, Antarctica, 88516 (LEW88516) are known to be closely similar in their igneous petrological and geochemical characteristics. Comparative SEM/EDS studies suggest greater contrast in their contents of secondary minerals; aqueous alteration appears to be more diverse in ALHA77005 than in LEW88516. Fusion crusts of both meteorites bear sulfates of Antarctic origin. The interior of LEW88516 contains traces of Na- and Ca-sulfates and a S,Cl-bearing iron silicate "rust"; the interior of ALHA77005 is distinguished by K,Fe-sulfate, a discrete low-Al silicate clay, free silica, and an unusual Mg,Fe-phosphate.

Introduction. Our previous work has shown that all three sub-groups of the shergottite, nakhlite, and chassignite (SNC) clan of meteorites contain aqueous precipitates of probable pre-terrestrial origin [1-4]. Results achieved through 1992 have been summarized elsewhere [5]. In the context of secondary minerals, the most thoroughly studied shergottite has been Elephant Moraine, Antarctica, A79001 (EETA79001). The recognition of LEW88516 as the latest SNC specimen [6], and its close similarity with ALHA77005, invite a comparative study of the latter two meteorites, and with EETA79001, from the perspective of aqueous alteration. Previous studies of alteration products in ALHA77005 (based on thin sections only) were reported in [7] and our preliminary results for LEW88516 were given in [6].

Samples and Methods. Samples included untreated chips, up tp several millimeters in size, of interior and exterior (fusion crusted) portions of ALHA77005 and LEW88516. Procedures were the same as those used for our previous studies of the SNCs [1-4]: samples were examined by scanning electron microscopy (SEM) with a JEOL 35CF, and by qualitative energy-dispersive X-ray spectrometry (EDS) using a PGT system with a thin-window detector capable of detecting light elements such as oxygen and carbon.

Results and Discussion. The fusion crusts of the two meteorites (exterior chips ALHA77005,70 and LEW88516,17-1) are quite similar except that the former is more vesicular (possibly indicating a higher indigenous volatile content). Secondary aluminosilicates (and salts on LEW88516) of definite Antarctic origin partially fill vesicles and fractures on both fusion crusts, as previously documented for non-SNC Antarctic stony meteorites [8].

Interior samples of the two meteorites (ALHA77005,72 and LEW88516,17-2) are grossly similar in that traces of secondary minerals are present in both (Table 1 and Figs. 1-3). Fig. 1a shows vesicular maskelynite in LEW88516 which is very clean (except for a trace of Na-sulfate elsewhere; Fig. 3), whereas a similar area in ALHA77005 (Fig. 1b) contains abundant K,Fe-sulfate. We note that our ALHA77005 sample is larger than our LEW88516 sample so that relative volumetric abundances of secondary minerals are still unclear. The suite of secondary phases in ALHA77005 (Figs. 1, 2) is not common in other SNCs. The Mg, Fe-phosphate (Fig. 1b) and silica granules (Fig. 2a) may be equivalent to similar phases found in the EETA79001 shergottite, however, and low-Al clay is a component of Nakhla [2]. The Ca-sulfate in LEW88516 is similar to that seen in other SNCs but the Na-sulfate has not previously been identified in an interior sample of any other SNC; we note that Na-sulfate (e.g., thenardite) is known as a native mineral in Antarctic soils. Ca-sulfate and sialic rust (poorly crystalline iron oxyhydroxide rich in Si and Al) are also typical of Antarctic weathering products [8] so that caution must be exercised in their interpretation here. Additional application of microstratigraphic controls [1-4] will be used to distinguish terrestrial from extraterrestrial salts and clays.

References: [1] Gooding J. L. et al. (1988) *Geochim. Cosmochim. Acta, 52,* 909-915. [2] Gooding J. L. and Wentworth S. J. (1991) *Lunar Planet. Sci. XXII,* 461-462. [3] Gooding J. L. et al. (1991) *Meteoritics, 26,* 135-143. [4] Wentworth S. J. and Gooding J. L. (1993) in preparation. [5] Gooding J. L. (1992) *Icarus, 99,* 28-41. [6] Lindstrom M. M. et al. (1992) *Lunar Planet. Sci. XXIII,* 783-784. [7] Smith J. V. and Steele I. M. (1984) *Meteoritics, 19,* 121-133. [8] Gooding J. L. (1986) *Geochim. Cosmochim. Acta, 50,* 2215-2223.

WEATHERING OF SHERGOTTITES ALHA77005 AND LEW88516: Wentworth S. J. and Gooding J. L.

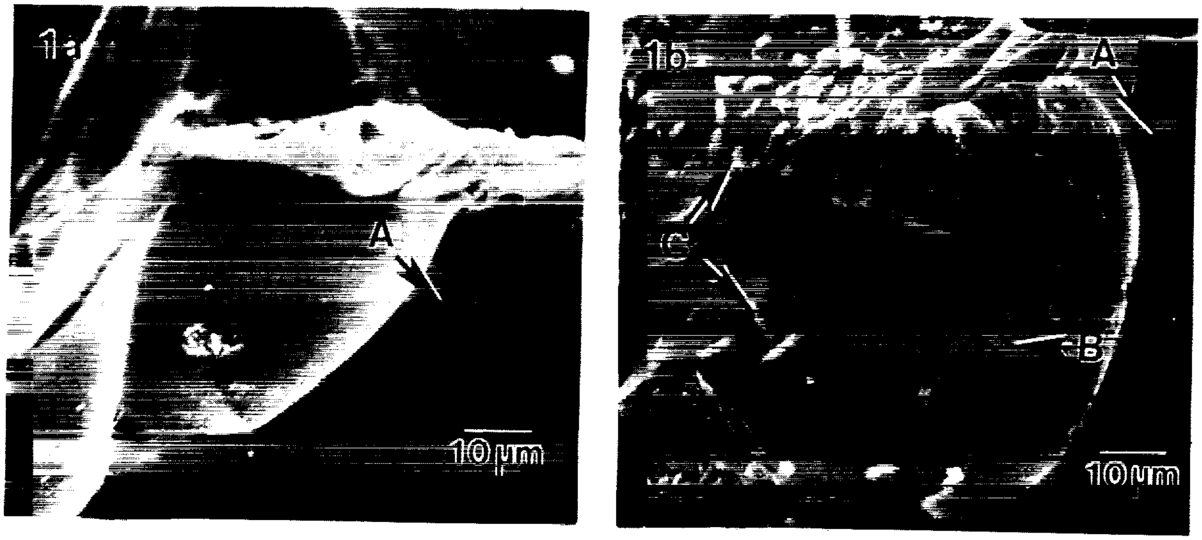


Figure 1. Vesicular maskelynite in interior of (a) LEW88516 and (b) ALHA77005. A = maskelynite; B = phosphate-maskelynite mixture; C = K, Fe-sulfate.

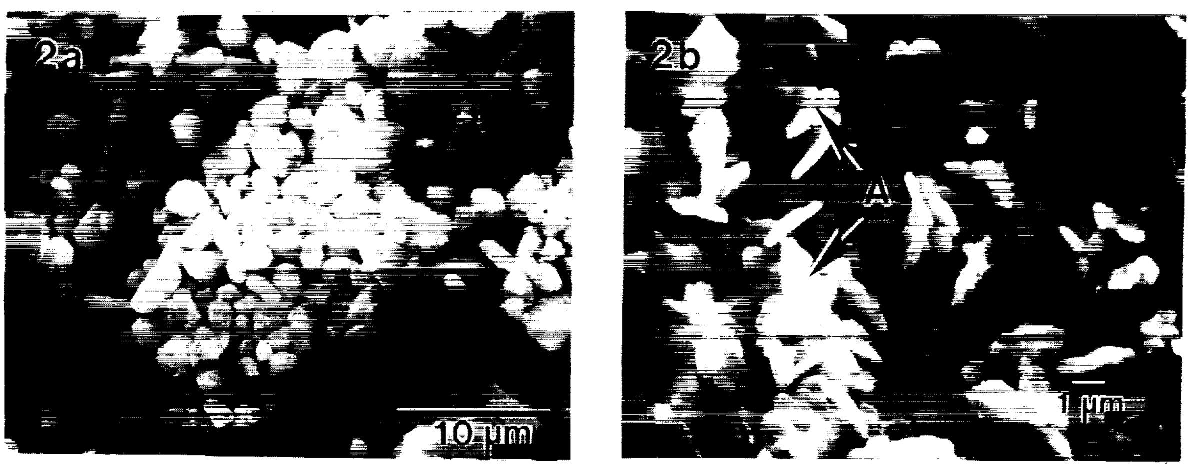


Figure 2. (a) Silica granules and (b) low-Al silicate clay (A) on pyroxene substrates in ALHA77005 interior.

Table 1. Secondary minerals in shergottite interior samples

Secondary Mineral	LEW88516	ALHA77005
Ca-sulfate	yes	
Na-sulfate	yes	
Sialic rust	yes	
K, Fe-sulfate		yes
Mg, Fe-phosphate		yes
Aluminosilicate clay		yes
Silica		yes

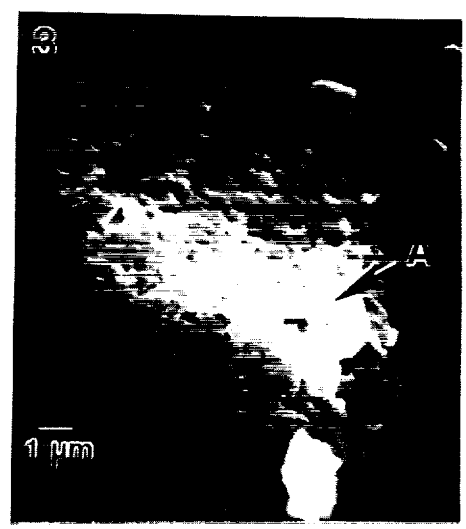


Figure 3. Na-sulfate (A) on maskelynite substrate in LEW88516 interior.

N94-20870
P-2

PETROLOGY AND GEOCHEMISTRY OF VLT GLASSES FROM DOUBLE DRIVE TUBE 79001/2; S. J. Wentworth[1], D. J. Lindstrom[2], R. R. Martinez[1], and D. S. McKay[2]. [1]LESC, 2400 NASA Rd. 1, Houston, TX 77058; [2]NASA Johnson Space Center, Houston, TX 77058.

Introduction. As a part of our more general studies of soils from Apollo 17 double drive tube 79001/2 (Station 9, Van Serg Crater) [1], we are analyzing glasses from the 79001/2 core by a multidisciplinary approach including SEM/EDS and INAA. We recently [2] reported preliminary results for a wide variety of 79001/2 glasses, including common and unusual compositional types of both mare and highland origin. Our efforts are currently focused on VLT (very low-Ti; $TiO_2 < 1$ wt%) mare glasses, which are common in 79001/2 and have also been found in other Apollo 17 soils [3]. One of our primary objectives is to determine whether any or all of the Apollo 17 VLT glasses represent pristine volcanic compositions. In addition, we wish to define the range of VLT glass compositions and possible relationships between the glasses and VLT lithic samples, for which some geochemical data have been obtained previously [4].

Samples and Techniques. The samples being used for this study are polished grain mounts from the 90-150 µm sieve fractions of samples from different depths of 79001/2. Thus far, glasses have been analyzed by SEM/EDS and electron microprobe in six samples representing the entire length of 79002 (0-12 cm depth below the lunar surface). Based on electron microprobe results, some of the glasses were chosen for high-sensitivity INAA [5]. Glass disks were drilled from the polished grain mounts with a microdrilling device, with individual disks ranging in diameter from about 50 to 100 µm (~0.1-0.5 µg).

Results and Discussion. Although data acquisition is not yet complete, it is clear that one of the unusual features of 79002 is its high abundance of VLT glasses. Excluding intermediate and high Ti mare glasses, which have not been tallied entirely, we have analyzed 133 glasses by electron microprobe from the six 79002 samples; VLT glasses comprise about 38% of this total. The VLT glasses seem to be unevenly distributed in 79002, ranging from 12-40% in samples from different depths.

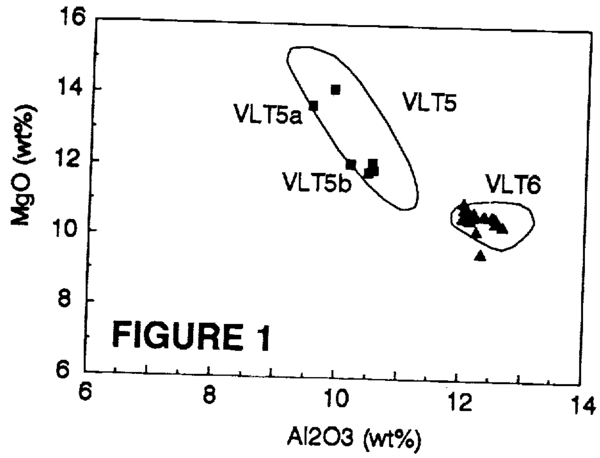
Major and trace element compositions of the VLT glasses (Table 1; Figs. 1-3) show the two distinct groupings of VLT compositions first identified by [3], which were based on major element microprobe data for other Apollo 17 VLT glasses. We have provisionally labelled the two groups as VLT5 and VLT6, after the nomenclature of [3] (their Mare 5 and Mare 6 glasses). Major element compositions of the VLT5 glasses are consistently higher in MgO and lower in Al_2O_3 than are the VLT6 glasses (Fig. 1. Minor and trace element abundances show similar distinctions; e.g., Co contents are nearly twice as high for the VLT5 glasses as those in the VLT6 glasses (Fig. 2). REE patterns for the two groups are also different (Fig. 3),with total REE abundances for VLT5 glasses being about 1.5X lower than those of the VLT6 group. Note that previous trace element analyses of VLT lithic fragments [4] revealed only the VLT5 REE pattern.

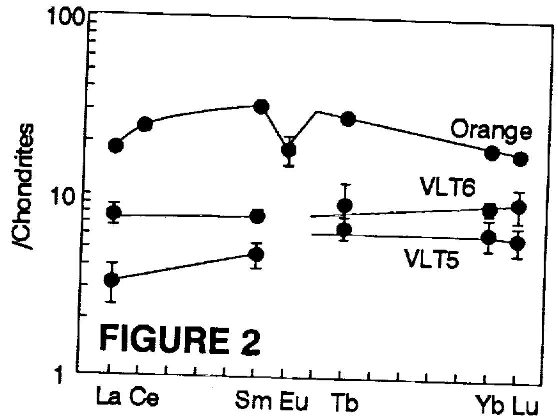
The VLT5 group was considered by [3] to represent a continuum, although our major element data suggest two groups, which we have labelled as VLT5a and VLT5b on fig. 3. Their diagram ([3], p. 1444) also suggests a split of the VLT5 into two groups. So far we have done INAA work on only one of the VLT5a group (79002,143-32), and it is clear that its trace element composition is very distinct, having higher Co and much lower Sc contents than the 5b group(Fig. 2).

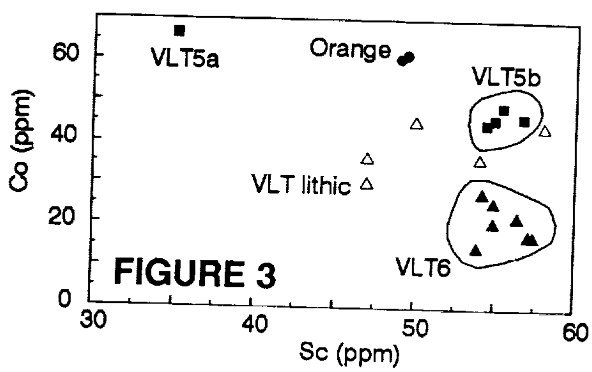
Standard criteria have been established by [6] to identify pristine volcanic lunar glasses, including: (1) an absence of schlieren and exotic inclusions; (2) intrasample homogeneity; (3) intersample homogeneity (clustering); (4) high Mg/Al ratios; (5) uniform, Mg-correlated Ni abundances; and (6) surface-correlated and trapped volatiles. The VLT glasses seem to fit most of the criteria. SEM/EDS of whole spheres of 79002 VLT glasses have not yet yielded any indication of surface-related volatiles; but surfaces of the glasses have been affected by micrometeorite processes. Figure 4 shows a pristine-looking VLT5 spherule with dendritic olivine crystals; the partial agglutinate coating is a common feature of all glasses in 79002. Note that the microdrilling techniques used for the INAA samples are accurate enough to eliminate problems such as contamination by agglutinitic material. Figure 5 is an example of a typical VLT6 glass. The VLT6 glasses commonly contain droplets of metallic Fe, although the VLT5 glasses do not. There is no indication that these are meteoritic metals rich in Co and Ni, so we assume they are indigenous to the volcanic glasses. The Apollo 17 orange and black volcanic glasses also contain occasional metallic Fe droplets [7].

PETROLOGY AND GEOCHEMISTRY OF VLT GLASSES: Wentworth S.J. et al.

References. [1] McKay D. S. et al. (in preparation). [2] Lindstrom D. J. et al. (1992) *Apollo 17 Workshop*, 29-31. [3] Warner R. D. et al. (1979) *Proc. LPSC 10th*, 1437-1456. [4] Wentworth S. J. et al. (1979) *Proc. LPSC 10th*, 207-233. [5] Lindstrom D. J. (1990) *Nucl. Instr. Meth. Phys. Res. A299*, 584-588. [6] Delano J. W. (1986) *Proc. LPSC 16th*, D201-D213. [7] Morris R. V., Gose W. A., and Lauer H.V. (1978) *Proc. Lunar Planet. Sci. Conf. 9th*, 2033-2048.







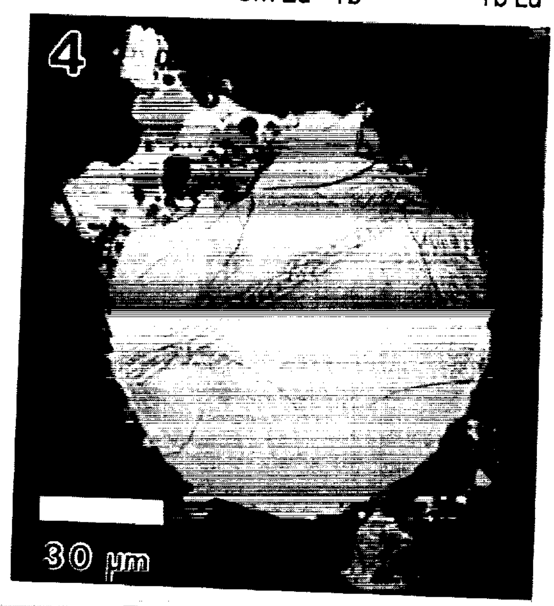
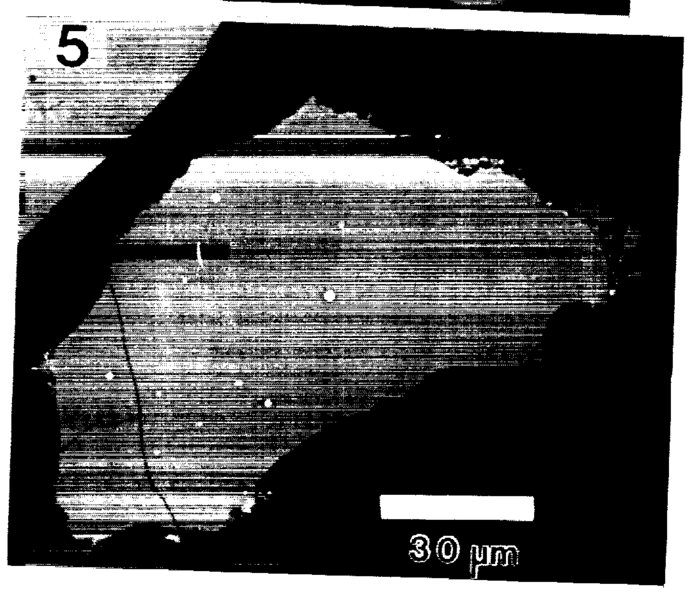


TABLE 1. Compositions of VLT glasses in 79001/2.

	VLT5a	VLT5b	VLT6
(wt%) n=	2	4	21
SiO2	45.51	46.70	46.39
TiO2	0.68	0.79	0.87
Al2O3	9.72	10.43	12.25
Cr2O3	0.49	0.77	0.52
FeO	18.54	17.73	17.65
MnO	0.23	0.28	0.27
MgO	13.93	11.98	10.54
CaO	9.85	9.76	10.67
Na2O	0.23	0.13	0.16
K2O	0.01	0.01	0.02
P2O5	0.02	0.02	0.03
Total	99.22	98.61	99.38
CaO/Al2O3	1.01	0.94	0.87
Mg/Mg+Fe	0.57	0.55	0.52
(ug/g) n=	1	4	7
Sc	35.1	55.4	55.5
Cr	3200	5250	3550
Co	66.5	46.6	
La	1.1	1.05	2.5
Ce	<9	4.2	8.5
Sm	0.97	0.97	1.6
Tb	<0.7	.35	.48
Yb	1.22	1.40	2.0
Lu	0.17	.20	0.33



S235-96
ABS ONLY
N94-20871
p. 2

VARIETY IN PLANETARY SYSTEMS; George W. Wetherill, DTM, Carnegie Institution of Washington, Washington, D.C. 20015.

Observation of circumstellar disks, regular satellite systems of outer planets, and planet-size objects orbiting pulsars support the supposition that formation of planetary systems is a robust, rather than a fragile, byproduct of the formation and evolution of stars. The extent to which these systems may be expected to resemble one another and our Solar System, either in overall structure or in detail remains uncertain. When the full range of possible stellar masses, disk masses, and initial specific angular momenta are considered, the possible variety of planetary configurations is very large.

Numerical modeling indicates a difference between the formation of small, inner, terrestrial planets and the outer planets. The accumulation of 10 km diameter planetesimals into 10^{26}-10^{29}g "planetary embryos" proceeds by rapid runaway growth (1). The final size and the escape velocity of runaway embryos increases with heliocentric distance (2), whereas the gravitational binding energy of the Sun decreases with heliocentric distance. As a consequence, in the inner Solar System embryo escape velocities and resulting relative velocities are ~ 4 km/sec, considerably less than the 13 km/sec Solar System escape velocity at 1 AU. Growing terrestrial planets will thus be trapped deeply within the Sun's gravitational potential well, and despite stochastic effects caused by close planetary encounters, will evolve in a relatively predictable way.

On the other hand, at 10 AU, the situation is reversed. A one $M_\oplus$ embryo will have an escape velocity of ~ 10 km/sec, well above the 4 km/sec Solar System escape velocity at that distance. Another difference is introduced by the thermally dependent condensation of volatile compounds and the ability of the large outer Solar System embryos to accrete nebular gas by gravitational capture. Growth of outer planets will thus be characterized by non-linear and quite possibly unstable competing tendencies of bodies to perturb one another into highly eccentric comet-like or hyperbolic orbits, or to experience damping of eccentricity by gas accretion and other gravitational interactions between massive embryos and nebular gas (3,4). These gas-embryo phenomena will be critically dependent upon the relative timing of embryo growth and dispersal of the gaseous component of the disk. There could be a natural self-regulating process that frequently leads to planetary systems resembling our own. More likely, relatively small natural variations in the distribution of angular momentum, mass, and temperature in the disk, and the timing of loss of residual nebular gas will lead to a variety of outer planet configurations, that include systems containing ~ 4 gas giants, as well those containing nothing but failed Jupiters,

VARIETY IN PLANETARY SYSTEMS; Wetherill, G.W.

either in nearly circular orbits like Uranus and Neptune, or systems with large numbers of massive bodies in highly eccentric orbits. Investigation of neighboring planetary systems may recapitulate the experience of planetary exploration that each newly investigated one will be different in some important way.

These differences in outer planet systems may also be expected to have significant effects on the associated terrestrial planets. Their morphological, atmospheric, chemical, and biological evolution is influenced by material transferred from the outer Solar System, as well as by asteroidal material accelerated into the terrestrial planet region by giant planet perturbations.

This is illustrated by calculations that have been carried out of the expected terrestrial cometary bombardment history for several outer planet configurations (Table 1). Systems in which ~ 15 $M_\oplus$ Jupiter and Saturn cores simply failed to capture significant quantities of nebular gas preserve a very large "Kuiper belt" reservoir of short period comets, resulting in a terrestrial cometary flux throughout geological time ~ 10^3 times greater than in our Solar System. In such systems "K-T boundary" impacts will occur on a ~ 10^5 year time scale. The volatile inventory of such planets could differ greatly from that of Earth. Smaller, but still significant increases in terrestrial impact rates are found for systems in which Jupiter and Saturn have their present mass, but the masses of Neptune and Uranus are only one $M_\oplus$. It may be speculated that the habitability of Earth for highly evolved organisms is dependent not only on terrestrial planet configurations, but on those of the outer Solar System as well. Perhaps it should be expected that we have a Jupiter: otherwise we wouldn't be here.

Perihelion passage rates of short period comets at 1 AU (arbitrary units)

	Time before present (m.y.): 0-3500	3500-4000	4000-4500
Present Solar System	3.6×10^3	3.8×10^4	1.9×10^7
"Failed" Jupiters in low eccentricity orbits	3.9×10^6	4.9×10^7	7.3×10^8
1 $M_\oplus$ Neptune and Uranus	6.1×10^4	1.3×10^5	8.4×10^5

REFERENCES

(1) Wetherill G.W., Stewart G.R. (1989) *Icarus 77*, 350-357.
(2) Lissauer J.J. (1987) *Icarus 69*, 249-265.
(3) Ward W.R. (1988) *Icarus 73*, 330-348.
(4) Takeda H. (1988) *Prog. Theor. Phys. Suppl. 96*, 196-210.

ELEVATION AND IGNEOUS CRATER MODIFICATION ON VENUS: IMPLICATIONS FOR MAGMATIC VOLATILE CONTENT. R.W. Wichman Dept. of Space Studies, Univ. of North Dakota, Grand Forks, ND 58202.

Introduction: Although most impact craters on Venus preserve nearly pristine crater rim and ejecta features [1], a small number of craters have been identified showing clear evidence of either igneous intrusion emplacement (floor-fracturing) beneath the crater floor [2] or of volcanically embayed exterior ejecta deposits [1,3]. Since the volcanically embayed craters consistently occur at higher elevations than the identified floor-fractured craters, I propose that igneous crater modification on Venus is elevation dependent. This abstract describes how regional variations in magmatic neutral buoyancy [4] could produce such elevation dependent crater modification and considers the implications for typical magmatic volatile contents on Venus.

Crater Modification and Elevation: Despite the abundance of surface volcanic features on Venus, only ~4-6% of the recognized venusian impact craters are clearly embayed by exterior volcanic flow units [1,3]. Igneous crater modification may be more common on Venus than this number indicates, however, since episodes of crater-controlled igneous activity should primarily affect the crater interior and not the exterior crater rim or ejecta units used to define the volcanically embayed craters above. Looking at crater interiors, the youngest craters on Venus (those with dark parabolic ejecta deposits) characteristically exhibit a radar bright floor unit [5]. In contrast, nearly two thirds of the recognized venusian craters contain dark floor deposits which might reflect crater-flooding volcanic events. While many of the dark-floored craters also appear to be distinctly shallower than the younger, bright-floored craters [6], however, these dark crater-filling units could as easily reflect fine-grained aeolian deposits emplaced by regional surface winds or impact-induced atmospheric turbulence as volcanic lava flows. Therefore, although the dark-floored venusian craters are consistent with widespread crater-filling volcanism, they do no require such igneous crater modification events.

A few craters, however, show strong resemblances to lunar floor-fractured craters (FFC) [2]. Specifically, three craters on Venus[1] show unequivocal examples of moat-delimited floor plate uplifts comparable to those in extensively modified lunar FFC. At least seven other venusian craters[2] exhibit less distinctive patterns of polygonal or concentric floor fractures which appear to be comparable to fracture patterns in less extensively modified lunar craters. Since the lunar FFC frequently contain ponded mare deposits [7,8,9], and since the best model for crater floor failure and uplift on the Moon requires emplacement of a crater-centered intrusion at depth [8,10,11], these ten venusian craters exhibit the most conclusive evidence on Venus for the interactions of impact structures with sub-surface magma bodies.

As shown by figures 1 and 2, the distribution of FFC on Venus as a function of elevation is distinctly different from the distribution of volcanically embayed craters. Specifically, while the FFC occur almost entirely below the mean planetary radius (MPR) of 6051.8 km and have a mean elevation of ~475 m below MPR, the volcanically embayed craters primarily occur at higher elevations, with a mean of ~340 m above MPR (figures). These two elevation distributions are statistically independent with a p-value of ~0.006, and chi-square tests suggest that the preferred elevation ranges of these distributions do not reflect random modification events within the global crater population.

Neutral Buoyancy Model: Igneous crater modification on Venus thus appears to vary systematically with elevation. Since magmatic neutral buoyancy levels on Venus should increase with elevation [4], these changes in regional magma depth provide a possible source for the observed dichotomy between floor-fractured crater modification at low elevations and the peripherally flooded craters at higher elevations. Specifically, if FFC reflect deformation over a shallow, crater-centered intrusion [8,10,11], this dichotomy in post-impact volcanism can result from variations in the depth of regional magmas relative to the breccia lens beneath a crater floor.

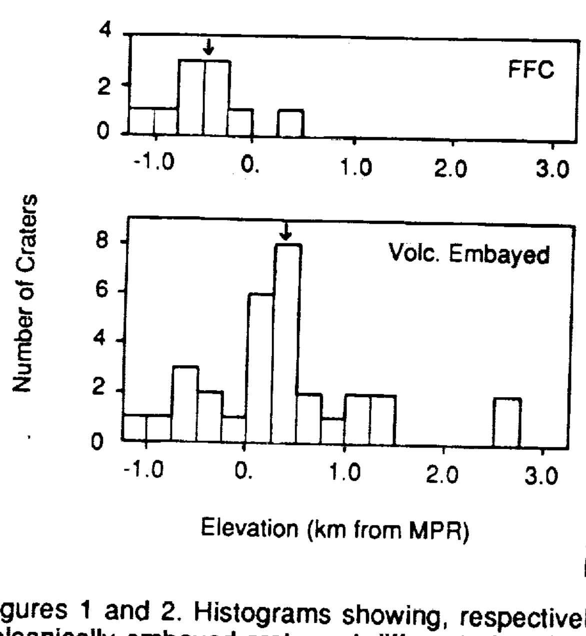
To illustrate the effects of such variations in magma depth on crater modification, consider a fresh crater 40 km in diameter with an apparent depth of ~1.0-1.25 km. By analogy to the terrestrial Ries crater [12], the intensity of brecciation beneath such a crater should decrease rapidly with depth and the depth-dependence of breccia densities should define a fairly shallow magmatic buoyancy trap (~0.5-1.5 km beneath the crater floor). Consequently, for magma levels shallower than ~1.5 km beneath a regional surface, magmas entering the crater should be vented directly onto the crater floor. For regional magma depths between ~1.5 and ~2.5 km, magmas entering the crater should be trapped within the impact breccia, thereby allowing floor-fracturing on the surface. Finally, for magma levels much deeper than ~2.5-3.0 km, magmas should not encounter significant brecciation effects, suggesting that volcanism in this case is likely to be independent of the impact structure.

FLOOR-FRACTURED CRATERS AND MAGMATIC VOLATILES ON VENUS: R.W. Wichman

In addition to these effects of NBZ depths on crater modification, however, the effect of atmospheric pressures on magmatic buoyancy also should inhibit FFC formation at higher elevations. Specifically, enhanced volatile exsolution at the higher elevations decreases magma buoyancies relative to the modeled breccia densities, thereby reducing the stability of a breccia-defined magma trap. Since significant crater modification requires magma pressures on the order of 100-200 bar [2,11], such destabilization allows magmas to escape to the surface at higher elevations (presumably within the crater) instead of driving surface failure and floor uplift within the crater.

Magmatic Volatiles: Since the modeled depth of magmatic neutral buoyancy on Venus depends on both elevation and magmatic volatile content [4], this model for the distribution of venusian FFC also can be used to constrain typical magma volatile concentrations on Venus. Based on the calculations of Head and Wilson [4], for example, NBZ should not develop at elevations below MPR on Venus for basaltic magmas with less than ~0.4 wt% combined CO_2 + SO_2. Since the corresponding NBZ depths in the highlands for these magmas range between ~1400 and ~2700 m, the consistently low elevation of FFC on Venus is incompatible with a record of predominantly volatile-poor volcanism. Alternatively, for ~0.4 wt% CO_2 + SO_2, predicted highland magma depths range from ~2500 to ~3200 m and continue to increase for higher volatile concentrations. In the lowland plains, however, such NBZ depths are not attained until ~0.55 wt% CO_2 + SO_2 [4]. Water contents show no significant effect on NBZ depth until concentrations exceed 0.5 wt%, then depths jump to over 2700 m even at the lowest elevations [4].

Summary: Development of lunar-like floor-fractured craters appears to be restricted to lowland plains elevations on Venus, while volcanic embayments outside the crater rim are significantly more common at higher elevations. This dichotomy in igneous crater modification is consistent with predicted changes in regional magma depths relative to a shallow breccia lens beneath the crater floor and suggests that typical magmas on Venus contain between ~0.4-0.5 wt % CO_2 + SO_2 and <0.5 wt% H_2O. Further, since the variation in magmatic neutral buoyancy with elevation should favor crater-filling volcanism at lower elevations, any change in the appearance of dark-floored craters with elevation may provide a basis for distinguishing volcanically flooded crater interiors from fine-grained sedimentary deposits collected within a crater.



REFERENCES: [1] Schaber, G.G. et al (1992) *J. Geophys. Res. 97*, 13257-13301. [2] Wichman, R.W. and Schultz, P.H. (1992) *Internatl. Coll. Venus, LPI Contrib. No. 789*, p. 131-132. [3]Phillips, R.J. et al (1992) *J. Geophys. Res. 97*, 15923-15948. [4] Head, J.W. and Wilson, L. (1992) *J. Geophys. Res. 97*, 3877-3903. [5] Campbell, D.B. et al (1992) *J. Geophys. Res. 97*, 16249-16278. [6] Sharpton, V.L. (1992) *Internatl. Conf. Large Meteorite Imp. Planet. Evoln., LPI Contrib. No.790*, 65-66. [7] Schultz, P.H. (1974) *Lunar Sci. Conf. 5*, 681-683. [8] Schultz, P.H. (1976) *Moon 15*, 241-273. [9] Bryan, W.B. et al (1975) *Proc. Lunar.Sci. Conf. 6*, 2563-2570. [10] Wichman, R.W. and Schultz, P.H. (1991) *Lunar Planet. Sci. Conf. 22*, 1501-1502. [11] Wichman, R.W. (1993) *Post-impact Modification of Craters and Multi-ring Basins on the Earth and Moon by Volcanism and Crustal Failure*. PhD Thesis, Brown University. [12] Pohl, J. et al (1978) *Impact and Explosion Cratering*, (D.J. Roddy, R.O. Pepin and R.B. Merrill, eds), 343-404.

Figures 1 and 2. Histograms showing, respectively, the number of floor-fractured craters (FFC) and volcanically embayed craters at different elevations on Venus. Crater elevation data is separated into 250 m bins and referenced to a mean planetary radius of 6051.8 km. Arrows indicate mean elevation of each crater population; for reference, mean elevation of all craters on Venus is ~50 m.

[1] Venusian craters with moat-defined floor plates are Mona Lisa, Barrymore, and an unnamed crater at (-18.5, 70.5).

[2] Venusian craters with well-developed polygonal or concentric fractures are Leyster, Barrera, Lebrun, Potanina, Yablochkina, Piaf and Wheatley.

S237-91
ABS. ONLY

N94-20873

p 2

LARGE FLOOR-FRACTURED CRATERS AND ISOSTATIC CRATER MODIFICATION: IMPLICATIONS FOR LITHOSPHERIC THICKNESS ON VENUS. R.W. Wichman, Dept. of Space Studies, Univ. of North Dakota, Grand Forks, ND 58202-7306 and P.H. Schultz, Dept. of Geological Sciences, Brown Univ., Providence RI 02912

Introduction: Several of the largest craters on Venus, including Mead, Meitner and Isabella, exhibit well-developed floor fracture patterns combining a central set of radial features with a peripheral set of concentric fractures. This pattern strongly resembles the fracture patterns observed in the largest floor-fractured craters on the Moon (eg. Humboldt, Gauss, Petavius). Although most lunar floor-fractured craters apparently reflect crater modification by igneous intrusions and volcanism [1,2,3], we propose that the fractures in these larger craters represent domical flexure events in response to post-impact isostatic uplift. Since the extent of uplift and surface failure in this model depends on both the size of the basin cavity and the local lithospheric thickness, this interpretation also provides a means for constraining lithospheric thicknesses on Venus. Based on the apparent onset diameter of isostatic crater modification, we derive lithospheric thickness estimates for the Moon of ~80-100 km, and for Venus of ~50-70 km.

Large Floor-fractured Craters: As noted in a companion abstract [4], ten craters on Venus show patterns of concentric or polygonal fractures resembling failure patterns observed in lunar floor-fractured craters. These craters are comparable in size (~20-90 km) to most of the lunar examples, and three craters in particular contain well-defined, moat-like structures around a scarp-bounded central floor plate identical to features observed in the most extensively modified craters on the Moon [5]. Since formation of such uplifted floor plates is best modeled by deformation over a shallow, crater-centered intrusion [3], we have identified these ten craters as likely sites for igneous crater modification on Venus [4,5].

In addition to these proposed floor-fractured craters, however, four of the largest craters on Venus (Table) exhibit a distinctive pattern of floor modification structures unlike those observed in the majority of lunar floor-fractured craters. As illustrated at Isabella (figure 1), this pattern comprises a central set of irregular radial lineaments inside an annulus of concentric fractures near the edge of the central basin floor. Further, the two largest proposed floor-fractured craters below 100 km in diameter (Potanina and Mona Lisa) also exhibit radiating structures inside a fracture annulus (Table), but in both instances, these central features contain prominent polygonal elements as well. Based on these observations, therefore, crater modification on Venus appears to vary with crater size. For craters smaller than ~80-100 km, failure produces predominantly concentric and polygonal fracture patterns, whereas radial fractures dominate failure within the central floor of larger craters.

A similar variation in crater modification with crater size also occurs on the Moon. Specifically, although most floor-fractured craters on the Moon exhibit polygonal or concentric fractures consistent with uplift and failure of the crater floor over a crater-centered intrusion [1,3], the largest floor-fractured craters on the Moon (eg. Humboldt, D=207 km; Gauss, D=177 km, Petavius, D=177 km; and Schrödinger, D=320 km) feature predominantly radial fracture patterns with peripheral concentric elements, minimal volcanism and negligible changes in apparent crater depth [1,3]. These failure patterns might reflect cone-sheet-like failure over very deep igneous intrusions [3], but there is little independent evidence for such intrusions beneath these craters. For the terrestrial Sudbury structure (D_{rim} ~180 km), which also shows evidence for an early episode of crater-centered radial fracturing [3,6], geophysical evidence precludes emplacement of any large contemporaneous intrusion at depth [7]. We therefore favor an alternative origin for these radial fracture patterns related to post-impact isostatic uplift in large craters.

Isostatic Flexure Mechanism: To first order, the excavation of an impact crater on any planet should create a negative load favoring isostatic uplift and flexure of the crater floor and surrounding lithosphere [3,8]. Since most craters are significantly smaller than the relative stiffness length of the respective planetary lithospheres, however, significant crater-centered uplift or deformation is likely only for the largest craters on any given planet [9]. Both cavity collapse and mantle uplift at these scales may limit the magnitude of such large cavity loads, but total isostatic equilibration of large craters by these processes seems unlikely. Even at larger multi-ring basin scales, clear signatures of post-impact, basin-centered uplift can be recognized [10,11].

Based on the work of Baldwin [8] and Brotchie and Silvester [9], therefore, crater-centered uplifts during post-impact isostatic equilibration should produce failure by domical flexure of the crater floor. Since such flexure results in a central sequence of radial failure inside a narrow region of concentric fracturing [12], this mechanism can produce the distinctive failure patterns observed on Venus. Further, since small craters should not induce sufficient isostatic adjustments to initiate failure, this model also explains the restriction of such failure to the largest craters on both the Moon and Venus.

Implications for Lithospheric Thickness: In addition to explaining the apparent transition from igneous crater modification at small crater diameters to domical flexure at large crater diameters, the isostatic crater modification model also provides a basis for estimating the thickness of the flexural elastic lithosphere on Venus. Specifically, if the smallest craters containing a combined radial and concentric failure pattern are identified with the transition diameter at which isostatic uplift first initiates failure, this crater size provides a model for the load required to achieve a specific lithospheric yield strength. Since the transition diameter on Venus appears to be between 80 and 100 km (Table), figure 2 shows modeled hoop stresses for these diameters over a range of lithospheric thicknesses. In each case, a cylindrical load equivalent in diameter to the crater floor was assumed in order to partially account for the effects of cavity collapse and subsurface mantle uplifts on crater equilibration. If we then assume that the failure strength of the crater floor materials is ~300 bar, roughly equivalent to terrestrial rock strengths [13], the indicated lithospheric thickness for Venus is on the order of 48-72 km. A similar calculation for the Moon, where apparent crater depths are greater and the transition diameter is between 175 and 200 km, indicates a lunar lithospheric thickness of ~80-100 km. These latter values are consistent with the maximum lithospheric thicknesses (>75 km and 100-150 km) derived by [14] for flexure on the Moon in response to basin-filling mare loads.

Craters showing rad./conc. fracture combination

crater	lat	long	dia (km)
Isabella	-29.7	204.1	170
Klenova	78.1	104.2	140
Meitner	-55.6	321.6	150
Mead	12.5	57.2	280
Mona Lisa*	25.5	25.0	85
Potanina*	31.7	53.0	90

* strong polygonal components in central radial features

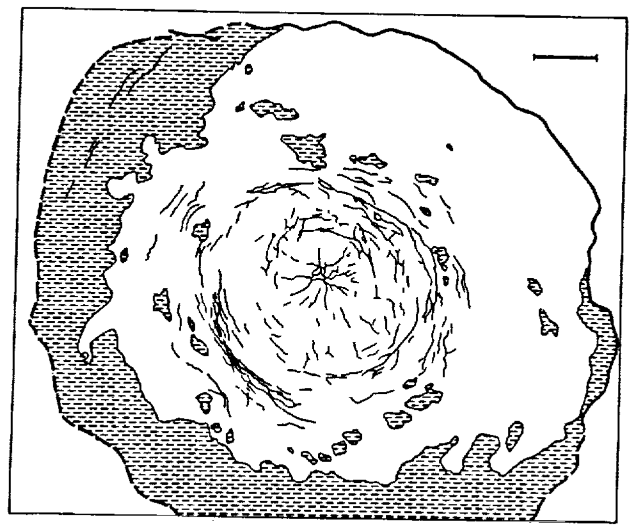


Figure 1. Sketch map of floor features in the crater Isabella. Heavy line marks location of crater scarp, hashured regions denote crater massif and wall regions. Scale bar is 20 km.

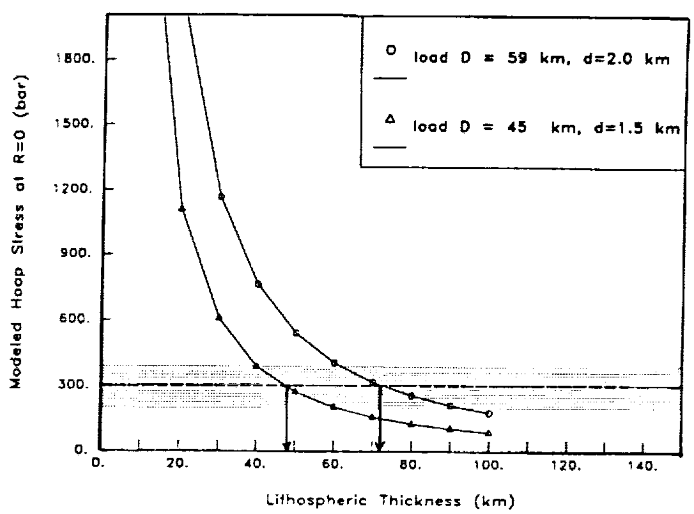


Figure 2. Modeled hoop stresses due to isostatic floor uplift on Venus for crater diameters of 80 and 100 km.

REFERENCES: [1] Schultz, P.H. (1976) *Moon 15,* 241-273. [2] Wichman, R.W. and Schultz, P.H. (1991) *Lunar Planet. Sci.Conf. 22,* 1501-1502. [3] Wichman, R.W. (1993) *Post-impact Modification of Craters and Multi-ring Basins on the Earth and Moon by Volcanism and Crustal Failure.* PhD Thesis, Brown University. [4] Wichman, R.W. (1993) this volume. [5] Wichman, R.W. and Schultz, P.H. (1992) *Internatl. Coll. Venus, LPI Contrib. No. 789,* p. 131-132. [6] Wichman, R.W. and Schultz, P.H. (1992) *Internatl. Conf. Large Meteorite Imp. Planet. Evoln., LPI Contrib. No. 790,* p.79-80. [7] Milkereit, B. et al (1992) *Geology 20,* 807-811. [8] Baldwin, R.B. (1968) *J. Geophys. Res. 73,* 3227-3229. [9] Brotchie, J.F. and Silvester, R. (1969) *J. Geophys. Res. 74,* 5240-5252. [10] Wichman, R.W. and Schultz, P.H. (1992) *Lunar Planet. Sci. Conf. 23,* 1521-1522. [11] Wichman, R.W. and Schultz, P.H. (1992) *Internatl. Conf. Large Meteorite Imp. Planet. Evoln., LPI Contrib. No. 790,* p.80-81. [12] Withjack, M.O. and Scheiner, C. (1982) *AAPG Bull. 66,* 302-316. [13] Comer, R.P. et al (1979) *Proc. Lunar Planet. Sci. Conf. 10,* 2441-2463. [14] Solomon, S.C. and Head, J.W. (1980) *Rev. Geophys. Space Phys. 18,* 107-141.

DEGRADATION SEQUENCE OF YOUNG LUNAR CRATERS FROM ORBITAL INFRARED SURVEY; M A. Wieczorek; SUNY at Buffalo, Dept. of Physics and Astronomy, Buffalo, NY 14260; W. W. Mendell, SN4/Planetary Science Branch, NASA Johnson Space Center, Houston, TX 77058. p. 2

Using new software, nighttime thermal maps of the lunar surface have been generated from data obtained by the Apollo 17 Infrared Scanning Radiometer (ISR) in lunar orbit [1]. Most of the thermal anomalies observed in the maps correspond to fresh lunar craters because blocks on the lunar surface maintain a thermal contrast relative to surrounding soil during the lunar night. Craters of Erastosthenian age and older - relatively young by lunar standards - have developed soil covers that make them almost indistinguishable from their surroundings in the thermal data. Thermal images of Copernican age craters show various stages of a degradation process, allowing the craters to be ranked by age. The ISR data should yield insights into lunar surface evolution as well as a more detailed understanding of the bombardment history after formation of the great mare basins.

Data available for analysis was collected along the Apollo 17 ground track, primarily to the west of the Apennines across Oceanus Procellarum into the highlands north and west of Mare Orientale. Seventeen craters located in the maria and highlands were grouped into seven distinct classes based on their infrared morphology [2]. Temperatures of the central peak, rim/wall, floor and ejecta as well as the distance covered by the ejecta and crater halos are listed in Table I—Class 1 being the least degraded and Class 7 the most degraded. In constructing a series of degradational states the following assumptions were used: 1) all impacts form in a similar manner and have similar morphologies; 2) the youngest craters will have the largest thermal enhancements because of the lack of weathering on exposed impact melt and boulders; and 3) as ejecta deposits evolve to soils, a cool, featureless halo is left as a remnant. It should be noted that relative ages cannot be extracted from the different crater classes unless the two craters being compared have similar sizes. Smaller craters are expected to degrade faster than larger ones due to different erosional rates from mass wasting processes. From Table I it appears that smaller craters occupy a larger percentage of the more highly degraded classes. We believe that this reflects a nonlinear scaling of erosional rates with crater size.

Of all the craters examined, a small unnamed crater located at 259E, 2.56N, approx. 5 km to the southeast of Lenz Crater has the largest thermal anomalies within the crater rim and ejecta deposit and is interpreted as the youngest, least degraded crater examined. Zond imagery show this crater to posses a high albedo ejecta deposit spanning over ten crater radii. It is also readily identifiable in Galileo imagery. The infrared data show a thermally enhanced ejecta blanket extending about 10 crater radii from the edge of the rim crest.

Class 2 craters have an enhanced ejecta deposit spanning one crater radius from the edge of the rim crest and a cool halo extending another crater radius beyond the ejecta. Temperatures within the rim are lower than in the crater near Lenz but are still considerably enhanced.

Class 3, 4, and 5 craters show a general decline in central peak, floor, rim/wall, and ejecta temperatures. The peak and rim/wall temperatures are consistently higher than the floor temperatures for Classes 3, 4, 5, and 6. This suggests that much of the early degradation within the rim is a consequence of mass wasting, avalanching, and the migration of surface materials from the crater rim and peak to the floor [3]. As slumping and avalanching occur, impact melt and boulders within the floor will be covered by loose material and at the same time new outcrops are exposed on the walls and peaks. Because the crater rim spans more surface area than the central peak, it would be expected that the floor would first lose its thermal enhancement, followed by the central peak, and finally by the rim.

Class 3 craters show a slight decrease in the ejecta radius and halo radius with respect to Class 2, whereas Class 4 craters are characterized primarily by their lack of an enhanced ejecta. In its place, however, is a cool featureless halo that spans from the crater rim to a distance of about two crater radii. Temperatures within the crater rim are again appreciably decreased with respect to Class 3. Class 5 craters show the final result of crater ejecta weathering. Halos and ejecta deposits are entirely absent or have been considerably degraded by the addition of small

IR MAPS OF LUNAR CRATER EROSION: Wieczorek, M. A. and Mendell, W. W.

thermal enhancements surrounding the crater. This sequence is interpreted as being due to the effects of small sub-resolution impacts excavating blocky material from beneath the thin, fine-grained surface cover.

Although Marius is the only crater in this data set which occupies Class 6, an extrapolation of degradation behaviors suggests that the last thermally enhanced portion of a crater should be its rim. Marius is characterized by not having a noticeable crater halo or enhanced ejecta, and by the absence of a central peak and floor enhancement. Beyond this class of degradation there should be no noticeable thermal enhancements within the crater. Class 7 craters are not believed to be the end of a crater degradation sequence within the maria even though they are extremely degraded in the infrared. In contrast to Marius, the last stage of crater degradation in the highlands seems to be its floor. This characteristic thermal signature may be caused by the lack of, or decrease in the number of, buried boulders in the regolith, or by accelerated rates of erosion by means of mass wasting.

Table I. Crater Classifications Based on Thermal Data

Crater	Diameter (km)	Solar Phase Angle (°) *	Central Peak Temp.†	Floor Temp.†	Rim/Wall Temp.†	Ejecta Temp.†	Ejecta Radius ‡	Halo Radius ◊
Class 1								
Lenz A	12.5	207	68	58	51	5 - 50	1 - 11	
Class 2								
Olbers A	43	208	30	25 - 38	14 - 30	5 - 15	1	1-2.5 (?)
Aristarchus	40	260.5	30	25-40	17 - 29	5 - 12	1	1 - 2.5
Class 3								
Kepler	32	223	21	8 - 12	8 - 18	0 - 3	0.8	0.8 - 2.5
Reiner	31	206.5	20	4 - 12	12 - 31	2	0.8	0.8 - 2
Copernicus	93	241	28	0 - 6	11 - 13	3	0.7	0.7 - 1.7
Class 4								
Galilaei	18	222.5		5 - 8	8 - 25			2
Bessarion A	13	246		7 - 10	7 - 33			1.5
Milichius	13	231		15 - 20	12 - 28			1.8 (?)
Class 5								
Pytheas	20	265	17	2.5 - 7	7 - 12			(?)
T. Mayer C	15.5	235		5 - 15	5 - 15			
Herman	20	204	14	8 - 13	8 - 20			(?)
Class 6								
Marius	42	234		0	15 - 18			
Class 7 (Highlands)								
Schlüter	90	178	6	5 - 8	5			
T. Mayer A	17	233		5	5			
Conon	20	262	3	4 - 6	0 - 4			
Eratosthenes	61	249	8	0 - 5	0 - 5			

* 0° = noon, 90° = sunset, 180° = midnight, 270° = sunrise
† All temperatures are with respect to either the surrounding mare or highlands.
‡ Ejecta distances measure the amount of thermal enhancement beyond the crater rim crest.
◊ Crater halo distances are measured in crater radii with respect to the edge of the ejecta deposit.

References:

[1] Mendell W. W. (1975) *Proc. Lunar. Sci. Conf. 6th*, p. 2711-2719. [2] Mendell W. W. & Wieczorek, M.A. (1993) LPSC XXIV. [3] Mendell W. W. (1976) *Proc. Lunar Sci. Conf. 7th*, p. 2705-2716.

ABS ONLY N94-20875

A LONG-TERM CHANGE OF THE AR/KR/XE FRACTIONATION IN THE SOLAR CORPUSCULAR RADIATION; R. Wieler, H. Baur, and P. Signer, ETH-Zürich, NO C61, CH-8092 Zürich, Switzerland p. 2

Abstract: Solar noble gases in an ilmenite separate from breccia 79035 (antiquity > 1 Ga) were analyzed by closed system stepped etching (CSSE). All five gases show the familiar two-component structure: first solar-wind (SW) gases are released, followed by gases from solar energetic particles (SEP). Element patterns in 79035 are similar to those of 71501 ilmenite (ref. 1; antiquity <100 Ma). SW-He-Ne were partly lost, but SEP-He-Ne-Ar are retained (nearly) unfractionated. Constant Ar/Kr/Xe ratios indicate that ilmenites contain an unfractionated sample of the heavy SW-SEP noble gases. Ar/Kr/Xe ratios in the solar corpuscular radiation are, however, different from "solar system" values, whereby the Kr/Xe difference in 79035 is about twice as large as in 71501. We propose that Xe is less fractionated than Kr and Ar, though its first ionisation potential (FIP) is higher than the "cutoff" at ~11.5eV, above which all elements in SEP are usually assumed to be depleted by a roughly constant factor. SW-Ne may be isotopically slightly heavier in the ancient SW trapped by 79035, as proposed earlier (2,3).

In this work we extend our previous CSSE studies (1) of solar noble gases *including Kr and Xe* to a lunar sample irradiated at least 1 Ga ago (breccia 79035, ilmenite separate, 42-64μm). This sample was particularly gently etched in the first steps. Surprisingly, the first three steps, each releasing ≤0.5‰ of the total 36-Ar, showed an SEP-like trapped component plus relatively large concentrations of cosmogenic gases. Steps 4ff contain much less cosmogenic and more solar gas with a SW-like isotope pattern. Thus, a very minor easily etchable phase that has completely lost its SW-gases must be responsible for steps 1-3. We will not discuss these steps here and refer to the actual step 4 as the "initial" etching step.

Element ratios: 4-He/36-Ar and 20-Ne/36-Ar patterns (Fig. 1) are very similar to earlier ones: ratios are below SW values (4) in the first steps but approach or reach SW ratios in the second half of the gas release. This indicates fractionating loss of solar wind He-Ne but (nearly) unfractionated retention of SEP-He-Ne-Ar in ilmenites (1). Unlike He/Ar and Ne/Ar, the Ar/Kr and Kr/Xe ratios are almost constant in 79035, as in 71501 (1). However, the average 84-Kr/132-Xe in 79035 is about 50% lower than in 71501 (4.75 vs. 8.97). Similar differences were previously reported (5) and interpreted to reflect possibly a variable Xe abundance in the SW (6,3). The present data offer strong additional support to this view: We argued (1) that the constant Ar/Kr/Xe ratios in CSSE runs, together with the conclusion that even the light gases He and Ne are not fractionated in the later steps, clearly suggest that the heavy gases in ilmenites are unfractionated samples both of the incoming SW and SEP. Ar/Kr/Xe ratios, however, do not agree with tabulated solar system values (ref.7, "SS" in Fig. 1). If ilmenite indeed retains unfractionated SW- and SEP-Ar-Kr-Xe, these gases seem thus to fractionate in the corona. The Kr/Xe fractionation factor thereby decreased about twofold since breccia 79035 was irradiated. Note that we postulate that Kr/Xe below SS in ilmenite is *not* due to a noble gas loss on the Moon. We find no evidence for SS-like Kr/Xe in the early release fractions as has been postulated for stepped combustion/pyrolysis runs (8). Our highest 4-He/36-Ar ratios in 79035 do not exceed the highest values in 71501, but the maximum is reached much earlier in the breccia than in the soil. We thus believe that the higher bulk 4-He/36-Ar of 79035 reflects a relatively smaller loss of SW-He from this sample rather than a higher 4-He/36-Ar ratio in the ancient SW (3).

Fig. 2 shows Ar-Kr-Xe fractionation factors relative to SS values versus their first ionisation potentials (FIP). All noble gases have FIP above 11.5 eV, the usually assumed "cutoff" value for FIP-related fractionation in SEP. Thus FIP may not be the only relevant parameter, or the cutoff seems to be larger for noble gases. To explain the different Kr/Xe ratios in ancient and recently exposed samples, Wiens et al. (9) proposed that the FIP cutoff might have been higher in the ancient sun.

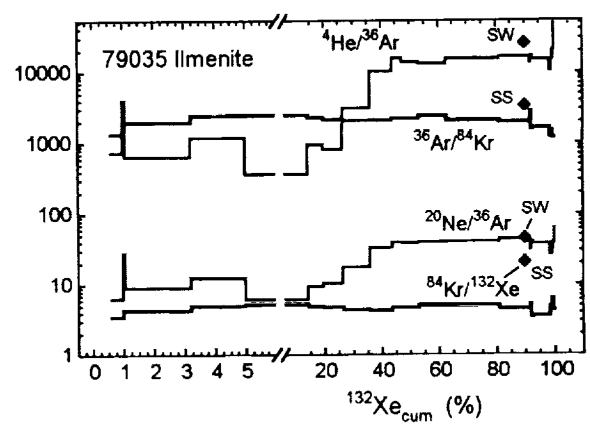


Fig. 1: 4-He/36-Ar and 20-Ne/36-Ar approach solar wind (SW, ref. 4) values in the last etching steps. This indicates that SEP-He-Ne-Ar - *and by inference also solar Kr and Xe* - is unfractionated in lunar ilmenites. 36-Ar/84-Kr and 84-Kr/132-Xe ratios are constant throughout the run but below "solar system" (SS, ref. 7) ratios, suggesting noble gas fractionation in the solar corpuscular radiation.

He-Ne-Ar isotopes: We concluded (10, 1) that ilmenites release in the first CSSE steps isotopically unfractionated SW noble gases, because recently irradiated 71501 ilmenite shows in the first steps isotopic compositions identical to modern SW. The more ancient 79035 ilmenite thus should allow us to rule on the long term constancy/variability of the isotopic composition of SW noble gases (3). Both samples show essentially the same 20-Ne/22-Ne value of 13.8 in their first step. However, in 79035 this first step comprises a mere 3.8‰ of the total 132-Xe, compared to 13% in the case of 71501. Steps 2-4 of 79035 (accounting for 4% of the total Xe) form a "plateau" at 20-Ne/22-Ne = 13.5. This value may thus represent SW-Ne in 79035 ilmenite, possibly showing a secular decrease of this ratio in the past >1Ga, as has often been postulated (e. g. 2, 3). The high ratio of 13.8 in step 1 may either be due to a minor contamination with recently irradiated soil (R. H. Becker, pers. comm.) or reflect a lower penetration depth of the lighter Ne isotope. We prefer the first explanation, since ratios light/heavy element are not enhanced in step 1.

Measured 3-He/4-He in the first 79035 steps is within ±8% of the SW value derived from 71501 ilmenite (1,10). 3-He/4-He in the SW to be inferred from these data is, however, rather uncertain due to cosmogenic 3-He. A possible secular increase of this ratio (2,3) is confined by these and earlier 79035 CSSE data (1,10) to less than about 7%. 36-Ar/38-Ar in the SW in 71501 and 79035 are indistinguishable.

20-Ne/22-Ne of SEP-Ne in 79035 is ~11.1, slightly lower than the value of 11.2 in 71501. Both, 3-He/4-He and 36-Ar/38-Ar in SEP in 79035 are similar to the 71501 values (1,10) but less well determined due to rather large corrections for cosmogenic gases.

Kr-Xe Isotopes: The CSSE steps with pure SW-Ne should also allow us to determine the isotopic composition of SW-Kr-Xe. SW-Kr in 71501 ilmenite is very slightly heavier than atmospheric Kr (86-Kr/84-Kr = 0.3041, ref. 1), i. e. heavier than most current estimates for SW-Kr (e. g. 11). In 79035 we now determine 86-Kr/84-Kr = 0.3018, lighter by ~0.4‰ per amu than the 71501 value and close to the range preferred in (11). Hence, the isotopic composition of SW-Kr possibly also changed since the time 79035 was irradiated. Surprisingly, however, SW-Kr would have become isotopically heavier, unlike SW-He and -Ne. Both, Kr and Xe in 79035 get isotopically heavier with increasing step number, analogous to He-Ne-Ar and similar to 71501. This corroborates the existence of (heavy) SEP-Kr-Xe inferred in (1).

Acknowledgments: Work supported by the Swiss National Science Foundation.

References: **(1)** Wieler R. et al. (1992) *Lun. Planet. Sci. XXIII*, 1525. **(2)** Pepin R. O. (1980) *In: The Ancient Sun*, 411. **(3)** Becker R. H. and Pepin R. O. (1989) *Geochim. Cosmochim. Acta* **53**, 1135. **(4)** Geiss J. et al. (1972) *NASA SP-315*, 14.1. **(5)** Hintenberger H. et al. (1974) *Proc. Lun. Sci. Conf. 5th*, 2005. **(6)** Kerridge J. F. (1980) *In: The Ancient Sun*, 475. **(7)** Anders, E. and Grevesse N. (1989) *Geochim. Cosmochim. Acta*, **53**, 197. **(8)** Frick U. et al. (1988) *Proc. Lun. Planet. Sci. Conf. 18th*, 87. **(9)** Wiens R. C. et al. (1992) *Proc. Lun. Planet. Sci. Conf. 22*, 153. **(10)** Benkert J.-P. et al. (1993) *J. Geophys. Res. (Planets)*, submitted. **(11)** Pepin R. O. (1991) *Icarus* **92**, 2.

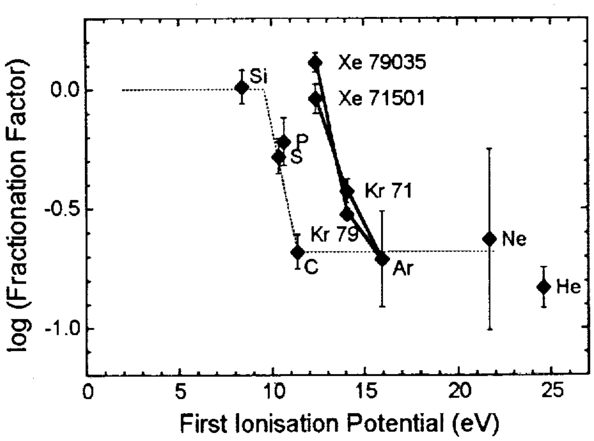


Fig. 2: Fractionation factors of solar Ar, Kr, and Xe in two lunar ilmenites, relative to solar system values (7). Kr and Xe points anchored to Ar as given in (7), data of other elements also from (7). Kr and Xe errors reflect 2σ of mean of 36-Ar/84-Kr and 36-Ar/132-Xe in main CSSE steps, but not uncertainty of Ar/Si fractionation. Xe/Kr in the ancient solar corpuscular radiation sampled by 79035 is twice as high as in recently irradiated soil 71501. The indicated FIP "cutoff" seems too low to explain the noble gas data.

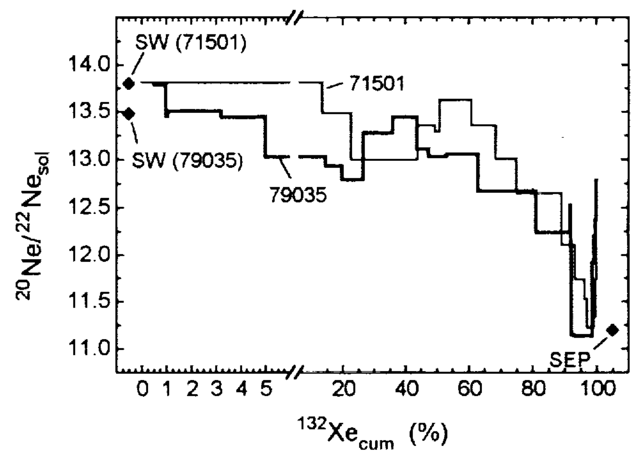


Fig. 3: 20-Ne/22-Ne of solar component versus cumulative fraction of 132-Xe released. Breccia 79035 indicates a ~2% lower 20-Ne/22-Ne in the ancient solar wind, compared to recently irradiated soil 71501 (the first step of 79035 may show contamination with recently irradiated fine dust). Both samples show the presence of SEP-Ne with 20-Ne/22-Ne = 11.1-11.2.

S240-91
ABS. ONLY
N94-20876
p. 2

MULTISPECTRAL STUDIES OF SELECTED CRATER- AND BASIN-FILLING LUNAR MARIA FROM GALILEO EARTH-MOON ENCOUNTER 1;

D.A. Williams and R. Greeley, *Department of Geology, Arizona State University, Tempe, Arizona 85287*; G. Neukum and R. Wagner, *German Aerospace Research Establishment (DLR), Inst. for Planetary Exploration, Berlin/Oberpfaffenhofen, Germany.*

New visible and near-infrared multispectral data of the Moon were obtained by the Galileo spacecraft in December, 1990 [1]. These data were calibrated with Earth-based spectral observations of the nearside to compare compositional information to previously uncharacterized mare basalts filling craters and basins on the western near side and eastern far side [1]. A Galileo-based spectral classification scheme, modified from the Earth-based scheme developed by Pieters [2], designates the different spectral classifications of mare basalt observed using the 0.41/0.56 μm reflectance ratio (titanium content), 0.56 μm reflectance values (albedo), and 0.76/0.99 μm reflectance ratio (absorption due to Fe^{2+} in mafic minerals and glass) [3]. In addition, age determinations from crater counts and results of a linear spectral mixing model were used to assess the volcanic histories of specific regions of interest [3]. These interpreted histories were related to models of mare basalt petrogenesis in an attempt to better understand the evolution of lunar volcanism.

The following general results were obtained: 1) mare basalts on the western near side and eastern far side have much less variability in titanium content than near side maria [4]; and 2) weaker absorptions at 1 μm suggest these basalts may have an inherently different mafic mineralogy than those on the near side [4,5]. Spectral differences suggest evidence for compositional variations for maria in the Grimaldi, Orientale, Mendel-Rydberg, and Apollo basins, implying evolution in basalt composition or multiple source regions for these mare basalts [3]. Specifically, mare units in the Grimaldi basin (cratering model ages: 2.49-3.25 Ga) contain medium- (<4 wt.% TiO_2) and medium-high-titanium (3-7 wt.% TiO_2) basalts, whereas the mare units in the neighboring Crüger region have evolved from older medium-high-titanium (3-7 wt.% TiO_2) basalts to younger, medium-titanium (<4 wt.% TiO_2) basalts, spanning ~0.4 Ga (cratering model ages: 3.18-3.46 Ga) during the upper-Imbrian. The intermediate-titanium (<4-7 wt.% TiO_2) mare units in the Mendel-Rydberg basin (cratering model age: 3.44 Ga) show evidence of multiple lava flows with different compositions. Likewise, spectral variations in the Apollo maria (cratering model ages: 3.63-3.71 Ga) suggest the presence of multiple lava flows with different compositions. The youngest basalts in Apollo have high titanium contents (>6 wt.% TiO_2), and have been interpreted as part of an upper-Imbrian period of regional volcanism in the South Pole-Aitken basin [4]. Mixing model analyses suggest ancient maria covered by crater ejecta (cryptomaria) may be present in several old basins, including Schiller-Zucchius [6,7], Mendel-Rydberg (prior to the Orientale impact), and S.P.-Aitken after the basin impact in the pre-Nectarian [8].

These results show several general trends: 1) maria filling basins have higher titanium contents than maria filling small craters (most basin maria have ~3-7 wt.% TiO_2 vs crater maria having <4 wt.% TiO_2); 2) the only occurrence of high-titanium basalt (>6 wt.% TiO_2) on the lunar far side occurs within the 505 km diameter Apollo basin, which is superposed on the 2300 km diameter S.P.-Aitken basin; and 3) there is no global correlation of titanium content with cratering model age or crustal thickness; correlations seem to be related to specific geographic regions [3].

From these general trends several implications regarding basalt petrogenesis can be made: 1) higher-titanium magmas are restricted to regions where the crust is inferred to be thinner due to excavation by basin impacts (Procellarum or S.P.-Aitken); 2) denser high-titanium magmas apparently ascend to a buoyancy trap as diapirs and extrude on the far side surface only in regionally compensated areas of a superposed impact (Apollo) within S.P.-Aitken. This observation agrees with modeling of Head and Wilson (1992) [9]; 3) the compositional variations of western near side/eastern far side basalts implies there are local heterogeneities of basalt sources in specific geographic regions (assuming that differences in titanium content observed by Galileo are due to differences in primary magma composition); and 4) if convective overturn [10] is

responsible for heterogeneity of mare basalts, it may have occurred on a regional, rather than global, scale to cause the apparent heterogeneities inferred for western near side/eastern far side regions. The next stage of this research is to analyze the spectral data of the western far side (eastern limb) and the north polar region of the Moon obtained by Galileo during Earth-Moon Encounter 2 (December, 1992), apply our classification scheme, and determine if the maria in this region of the Moon are more similar to the widely varying compositions of nearside maria or to the relatively homogeneous maria of the western near side and eastern far side.

REFERENCES: [1] Belton, M.J.S. et al. (1992), *Science 255*, 570-576; [2] Pieters, C. (1978), *Proc. 9th Lunar Planet. Sci. Conf.*, 2825-2849; [3] Williams, D.A. (1992), Masters Thesis, Arizona State University, 145 pp.; [4] Greeley, R. et al. (in review), *J. Geophys. Res.*; [5] Pieters, C.M. et al. (in review), *J. Geophys. Res.*; [6] Mustard, J.F. et al. (1992), *Lunar Planet Science XXIII*, 957-58; [7] Head, J.W. et al. (in review), *J. Geophys. Res.*; [8] Wilhelms, D.E. (1987), *USGS Prof. Paper #1348*; [9] Head, J.W. and L. Wilson (1992), *Geochima Cosmochima Acta 56*, 2155-2175; [10] Neal, C.R. and L.A. Taylor (1992), *Geochima Cosmochima Acta 56*, 2177-2211.

Equilibrium Models of Mass Distribution and Collisional Lifetimes of Asteroids. David R. Williams and George Wetherill, DTM, Carnegie Institution of Washington, 5241 Broad Branch Road N.W., Washington DC 20015.

An understanding of the steady state distribution expected in the present day asteroid belt is important to our understanding of the collisional evolution of the asteroids and their physical properties. We have extended earlier work to show that, in the absence of gravity, a simple power law distribution as a function of mass with constant exponent will give an equilibrium distribution of asteroids for all bodies much smaller than the largest asteroids. This result holds for realistic fragmentation mechanisms and is independent of the physical properties of the asteroids. Inclusion of the effects of gravity on disruption and fragmentation of asteroids precludes an analytic solution to this problem, and rules out a simple power law distribution. We are currently calculating numerical solutions in order to determine the expected steady state mass distribution in the asteroid belt.

In order to understand the relationship of the asteroids and meteorites to the early solar system, we must understand their collisional and thermal histories. For example, we need to know whether a given asteroid is likely to be a pristine relic of the initial formation of the asteroids or a collisional fragment of a larger body, i.e. we need to know the collisional lifetime of a given asteroid. The collisional lifetime of an asteroid is a function of the number of asteroids with which it can collide. Because smaller asteroids greatly outnumber larger ones, the majority of collisions an asteroid experiences will be with bodies smaller than itself. At collisional velocities of approximately 5 km/sec, small asteroids will be able to catastrophically disrupt bodies many times their size [1]. Unfortunately, even for the present asteroid belt the number of asteroids is not well known for those with diameters less than 30 to 40 km. Therefore, while the collisional lifetimes are very sensitive to the number of smaller asteroids, the number of smaller asteroids is not well constrained. In addition, the physical properties of even the present asteroids are not well known, and there is much more uncertainty regarding the properties of primordial asteroidal bodies. It is therefore important to understand the extent to which the collisional evolution is actually dependent on physical properties.

One approach to this problem is to assume that smaller asteroids have reached a steady state distribution over the age of the solar system, so that the number of bodies of a given mass lost due to collisions is equal to the number of fragments supplied by collisions involving larger asteroids. (Obviously, this assumption breaks down at the largest asteroids, because there are no larger bodies to resupply them.) This approach was taken by Dohnanyi [2,3], who derived an integro-differential equation for the change in number of particles as a function of particle mass. The mass distribution is represented as a power law function of the form $N(m)dm = Am^{-\alpha})dm$, where N equals the number of particles of mass m to m + dm, A and α are constants. Collisions can be one of two types. For small projectiles, cratering occurs, with the cratering fragments being lost to space. For collisions involving projectiles above a certain cutoff mass, catastrophic disruption is assumed to occur, in which the target body is fragmented and dispersed. The projectile, defined as the smaller of any two bodies involved in a collision, is completely fragmented in both types of collisions. Dohnanyi [2,3] assumes the cutoff mass is directly proportional to the mass of the target body. He further assumed that the largest fragment resulting from any collision was directly proportional to the size of the impactor [2] or to the size of the target [3]. If physical properties are assumed to be independent of mass, an analytic solution can be found for bodies much smaller than the largest body. Dohnanyi [2,3] obtained the important result that a steady state is found for $\alpha = 11/6$, independent of the material properties assumed, when cratering collisions are ignored and only catastrophic collisions are taken into account.

EQUILIBRIUM MODELS OF ASTEROID MASS DISTRIBUTION : Williams, D. R., and G. Wetherill

We have extended Dohnanyi's formulation to show that $\alpha = 11/6$ is an exact solution when cratering collisions are included, and also for the case in which catastrophic collisions are neglected and cratering collisions are assumed to represent the sole mechanism of mass distribution. Therefore, the equilibium values are not affected by the relative importance of cratering collisions versus catastrophic collisions in the asteroid belt. We have reformulated the equation using a more realistic model for fragmentation due to catastrophic collisions, in which largest fragment size (M_b) is a function of both target mass (M_t) and projectile mass (M_p) with the form $M_b = \lambda M_t^{1+\beta} M_p^{-\beta}$, where λ and β are constant. Note that fragment size is inversely proportional to projectile mass, because larger projectiles impart more energy into the target and tend to break it into smaller pieces. The steady state value, $\alpha = 11/6$, holds for this case as well, showing this solution is quite insensitive to details of the fragmentation mechanism.

One important factor which is not taken into account in these solutions and which invalidates the self-similarity assumption of the asteroid physical properties is gravity. Larger asteroids, by nature of their higher gravity, are more resistant to catastrophic distuption and to loss of fragments. We have formulated a particle flux equation which takes into account the effect of self-gravity on the cutoff collision size for catastrophic disruption, the fragment size distribution, and the loss of fragments during cratering collisions. The projectile mass required to cause a catastrophic collision is given by $M_p = (c_1 + c_2 M_t^{0.5}) M_t$, where c_1 and c_2 are constants. The value of c_1 is taken from [2] and the value of c_2 is determined using pi-scaling theory [4]. The largest fragment size is also a function of the target mass. We assume that the smallest possible projectile mass which can result in a catastrophic collision will leave a largest fragment one-half the mass of the original target. For cratering collisions, the largest possible projectile has a mass just below the cutoff mass, and will eject a mass of material just under one-half the mass of the target, by definition. The largest fragment is assumed to be a constant proportion of the mass ejected from the crater. These equations do not permit an analytic solution, but it is obvious that a power law with a constant exponent will not result in a steady state distribution, due to the mass dependent effects of gravity. Gravity would be expected to prolong the collisional lifetimes of the largest asteroids, which in turn would result in less lower mass fragments being produced. Gravity becomes less important than internal strength at diameters of about 1 to 10 km, so we would expect to see some deficit of particles near this mass range. At smaller sizes, the distribution should approach a Dohnanyi-type power law as the effects of gravity become less important. We are currently solving these equations numerically to find steady state solutions for the asteroid belt. We will compare these solutions to the actual observations of the asteroids, and discuss their implications and the stability of the solutions to the assumptions involving physical parameters and fragmentation mechanisms.

REFERENCES.

[1] Moore, H.J. and D.E. Gault (1965). *Astrogeologic Studies, U.S.G.S. Ann. Prog. Rept.*, 127-150

[2] Dohnanyi, J.S. (1969). *J. Geophys. Res., 74*, 2531-2554

[3] Dohnanyi, J.S. (1972). *Icarus, 17*, 1-48

[4] Melosh, H.J. (1989). *Impact Cratering: A Geological Process*, Oxford Univ. Press, N.Y.

FORMATION OF PERCHED LAVA PONDS ON BASALTIC VOLCANOES: INTERACTION BETWEEN COOLING RATE AND FLOW GEOMETRY ALLOWS ESTIMATION OF LAVA EFFUSION RATES. L. Wilson[1,2] and E. A. Parfitt[1] [1]Geological Sciences Department, Brown University, Providence, RI 02912. [2]Environmental Science Division, Lancaster University, Lancaster LA1 4YQ, U.K.

p. 2

Perched lava ponds are infrequent but distinctive topographic features formed during some basaltic eruptions. Two such ponds, each ~ 150 m in diameter, formed during the 1968 eruption at Napau Crater [1] and the 1974 eruption of Mauna Ulu [2], both on Kilauea Volcano, Hawai'i. Each one formed where a channelised, high volume flux lava flow encountered a sharp reduction of slope: the flow spread out radially and stalled, forming a well-defined terminal levée enclosing a nearly circular lava pond. We describe a model of how cooling limits the motion of lava spreading radially into a pond and compare this with the case of a channelised flow. The difference in geometry has a major effect, such that the size of a pond is a good indicator of the volume flux of the lava forming it. Lateral spreading on distal shallow slopes is a major factor limiting the lengths of lava flows.

Theoretical Considerations If a Newtonian lava with viscosity μ and bulk density ρ moves with mean speed U and thickness D down a plane inclined at α to the horizontal, the equation of motion in the x coordinate direction is (1),

$$U (\partial U/\partial x) = g \sin \alpha - [(K \mu U) / (D^2 \rho)]$$

where g is the acceleration due to gravity and K is a constant which depends on the cross-sectional geometry of the flow. For flows which are much wider than they are deep, K = 3, whereas for flows in a semicircular channel, K = 8 [3]. Eq. (1) assumes that a steady state prevails, i.e. there are no changes of velocity with time.

The lava motion is found by combining (1) with a continuity equation expressing conservation of volume of the flowing material. For a flow in a channel of uniform width the volume flux V_c is: (2)

$$V_c = U_c D_c W_c$$

where W_c is the channel width, and U_c and D_c are the velocity and flow depth in the channel geometry case. The channel width does not change with x, so U_c and D_c are constant, and eq. (1) simplifies to (3).

$$U_c = (D_c^2 \rho g \sin \alpha) / (K \mu)$$

Each of U_c and D_c can be eliminated in turn between eqs. (2) and (3) to give (4a), (4b).

$$D_c = [(V_c K \mu) / (W_c \rho g \sin \alpha)]^{1/3}$$

$$U_c = [(V_c^2 \rho g \sin \alpha) / (W_c^2 K \mu)]^{1/3}$$

The time, t_c, needed for a given batch of lava in the flow to travel a distance x_c is given by (5),

$$t_c = x_c / U_c$$

since the velocity U_c is constant. Eliminating U_c with eq. (2) we have (6).

$$t_c = (D_c W_c x_c) / V_c$$

For a flow in a semicircular pond the continuity relation is (7),

$$V_p = \pi x_p U_p D_p$$

where the velocity and depth are U_p & D_p, respectively, at a distance x_p from the centre of curvature. Since V_p now involves a dependence on x_p, it follows that both U_p and D_p will be functions of x_p, and so in general it is no longer possible to neglect the term $[U (\partial U/\partial x)]$ in eq. (1). However, we have integrated eqs. (1) and (7) simultaneously using numerical methods and find that, over a wide range of values of V_p and x_p, analytical solutions obtained neglecting the term $[U (\partial U/\partial x)]$ differ by less than 1% from numerical solutions. Expressions for the variations of U_p and D_p with x_p are found by eliminating each of U_p and D_p in turn between eqs. (3) and (7), giving (8a)

$$D_p (x) = [(V_p K \mu) / (\pi x_p \rho g \sin \alpha)]^{1/3} \quad (8b).$$

and

$$U_p (x) = [(V_p^2 \rho g \sin \alpha) / (\pi^2 K \mu x_p^2)]^{1/3}$$

Both U_p and D_p decrease with increasing x_p, with U_p showing the most rapid change. Since U_p is a function of x_p, the time t_p needed for a batch of lava to travel outward from its source is found from (9).

$$dx = U \, dt$$

Substituting eq. (8b) for U and integrating from an initial small radius x_{p0}: (10).

$$t_p = (3/5) [(\pi^2 K \mu) / (V_p^2 \rho g \sin \alpha)]^{1/3} (x_p^{5/3} - x_{p0}^{5/3})$$

Since x_{p0}, having a value of at most a few metres, will generally be very much smaller than the distance at which

the flow stops, we can approximate (10) by

$$t_p = (3/5)\,[(\pi^2 K \mu) / (V_p^2 \rho g \sin\alpha)]^{1/3}\, x_p^{5/3} \qquad (11).$$

By analogy [4] with engineering data on the cooling of a fluid in a pipe, motion of a lava flow stops when a thermal cooling wave has penetrated from the flow surface to a distance which is some critical fraction q of the flow thickness D. In time τ a cooling wave penetrates a distance $\lambda \approx (\kappa \tau)^{1/2}$ as long as heat transfer is entirely limited by the thermal diffusivity, κ, of the flow material, rather than by the ability of the environment to remove heat. This is a good approximation at times more than a few minutes after a given batch of material has been erupted [5], so the time to cessation of flow, T, is

$$T = (q^2 D^2) / \kappa \qquad (12),$$

where κ is ~10^{-6} m^2/s for all silicates. Field data show that q^2 has a value close to (1/300) [6]. This model ignores lava rheology changes as a function of distance from the vent and hence time since eruption. Instead, it establishes a correlation, with the theoretically expected functional form, between maximum flow length and effusion rate. The changes in rheology, and consequent deceleration and eventual cessation of motion, are all included through the value used for q^2. We can now find cooling-limited travel distances for the above flow geometries. For flow in a channel, we equate T given by eq. (12) to t_c given by eq. (6). Identifying D in equation (12) with D_c given by eq. (4a) and writing $x_c = X_c$ for the distance travelled:

$$X_c = [1/(300\,\kappa)]\,[V_c / W_c]^{4/3}\,[(K \mu) / (\rho g \sin\alpha)]^{1/3} \qquad (13).$$

For flow in a semicircular pond, we equate T from eq. (12) to t_p in eq. (11), explicitly identify D in eq. (12) with D_p from eq. (8a) and solve for x_p. Putting $x_p = X_p$ when the motion stops,

$$X_p = [(V_p^4 K \mu) / (2^6\, 3^6\, 5^3\, \pi^4\, \kappa^3\, \rho g \sin\alpha)]^{1/7} \qquad (14).$$

Discussion Eqs. (13) and (14) show the relatively weak dependence of flow length on the lava properties μ and ρ, the environmental factors g and α, and the geometric parameter K, especially in the case of motion in a pond; the most important control on flow length is the volume flux V. We have calibrated eq. (14) above by comparing the predicted and observed eruption rates of the events producing the Mauna Ulu and Napau ponds on Kilauea [7]. The Mauna Ulu pond has a radius of 70-80 m which implies an eruption rate of 12.6-16.0 m^3/s on a slope of sin α ~0.025, to be compared with a rate inferred from the deflation of the summit magma chamber of 13.3-18.2 m^3/s; the Napau pond, formed on a shallower slope ($\sin\alpha = 0.008$), has a radius of ~75 m implying V = 10.7 m^3/s, to be compared with an estimated rate of ~ 11.9 m^3/s. The agreement is encouragingly close in both cases.

Consider now a case where V = 200 m^3/s (at the upper end of the range of common eruption rates of basaltic lavas on Earth [8]; $\sin\alpha = 0.025$ (roughly the average along strike slope of the East Rift Zone of Kilauea); ρ = 2000 kg/m^3 (a moderately vesicular basalt); μ = 30 Pa s [9] and K = 3, implying a relatively high ratio of flow width to depth in the channel case. Then for a flow in a channel 10 m wide, the maximum potential travel distance is X_c =103 km whereas X_p, the maximum distance travelled by an unchannelised (ponded) flow, is only 339 m. Thus if a previously channelised flow encounters topography which causes or allows lateral spreading, flow thinning caused by the change in geometry can produce a dramatic difference in the subsequent possible travel distance. We argue that this is the main cause of the development of perched lava ponds (and of the cessation of advance of many lava flows). The influences of α, g and μ are so weak (seventh root in the case of radial motion, cube root for channelised flows) that X_c/X_p will always be ~300 for mafic lavas with V ~200 m^3/s. The dependance of X_c/X_p on V in the table below shows that topographic spreading will be particularly important for very high effusion rates such as those postulated [10] to explain the long lava flows found on Venus.

$V/(m^3/s)$	2	5	10	25	50	100	200	500	1000	10^4
X_c/X_p	9	18	31	62	105	179	303	610	1034	5979

References

[1] Jackson, D.B. et al. [1975] U.S.G.S. Prof. Paper 890. [2] Tilling, R.I. et al. (1987) Chapter 16 in U.S.G.S. Prof. Paper 1350. [3] Knudsen, J.G. & Katz, D.L. [1958] Fluid dynamics and heat transfer. McGraw-Hill. 576 pp. [4] Hulme, G. & Fielder, G. [1977] Phil. Trans. Roy. Soc. Lond. A. 285, 227-234. [5] Head, J.W. & Wilson, L. [1986] J. geophys. Res. 91, 9407-9446. [6] Pinkerton, H. & Wilson, L. [1988] Lunar plan. Sci. XIX, 937-938. [7] Wilson, L. & Parfitt, E.A. [1992] (sub judice, J. Volcanol. geotherm. Res.) [8] Wilson, L. & Head, J.W. [1981] J. geophys. Res., 86, 2971-3001. [9] Heslop, S.E.et al. [1989] Bull. Volcanol. 51, 415-432. [10] Wilson, L. et al.[1990] Lunar plan. Sci. XXI, 1347-1348.

5243-46
ABS. ONLY

N94-20879

A CLASSIFICATION SCHEME FOR THE MORPHOLOGY OF LAVA FLOW FIELDS. L. Wilson[1,2], H. Pinkerton[1], J.W. Head[2] and K. Magee Roberts[2]. [1]Environmental Sci. Div., Lancaster Univ., Lancaster LA1 4YQ, U.K. [2]Dept. Geological Sci., Brown Univ., Providence RI 02912 USA

Introduction: Analysis of the processes controlling the advance of lava flows[1-3] shows that, if no other factors intervene, thermal constraints will act to limit the maximum length of a flow being fed at a given volume or mass effusion rate from a vent. These constraints can be characterised through the Grätz number[4], which takes on a large value at the vent and decreases down flow. Early application of this principle[5] showed that, despite the many subtleties of modes of heat loss from flows[6], motion apparently ceases when the Grätz number has decreased to a value close to 300. Recent analyses of flow units from the 1983-86 Pu'u 'O'o eruption of Kilauea and of other, more silicic lava flow units confirm this finding[2].

Discussion: There are several factors which may intervene to prevent a flow reaching its maximum potential cooling-limited length. These factors are particularly important when they cause the formation of a compound flow field, the large-scale features of which may be more amenable to measurement than the geometries of individual flow units[7]. The presence of well-preserved and areally very extensive examples of such compound flow fields on Venus[8-10] has prompted us to attempt to classify as many as possible of the factors which are relevant to mapping such flow fields and to deriving eruption rate estimates from their morphologies. For this purpose we categorise flows as follows:

Classification Scheme:

Cooling-limited flows: Effusion from the vent is steady; the flow front thickens and slows as the lava rheology responds to progressive cooling; the flow front eventually stops due to this cooling and the central channel of the flow does not drain. If the vent remains active, a break-out flow must form from some point on the margin of the initial flow unit.

Volume-limited flows: The steady advance of the front of the flow stops when effusion from the vent stops; the central channel of the flow unit may drain, in which case part of the original flow front continues to advance, but at a decreasing rate (and forming a thinner and narrower flow unit) as the channel drains. No normal break-out flows are associated with a volume-limited flow. A volume-limited flow is by definition shorter than a cooling-limited flow formed at the same effusion rate.

Accidentally-breached flows: If the central channel of a flow becomes blocked due to the breaking off of parts of the levee or channel wall, a break-out flow will form from a point somewhere upstream of the blockage. The accidentally-breached parent flow will be shorter than if it had not been breached.

Break-out flows: These form either from the sides or fronts of cooling limited flows if effusion at the vent continues after the front of the first flow unit has stopped due to cooling, or from the sides of accidentally breached flows. A break-out flow may itself become cooling-limited, volume-limited, etc.

Captured flows: If pre-existing topography down slope of a vent confines a flow unit to a channel which is narrower than the width which the flow would have adopted (by forming its own cooled levees) if it had been erupted on a flat inclined plane, the flow will be deeper than it would otherwise have been, and will also reach a greater cooling- limited length than if it had not been captured. If topographic data and morphological measurements are available at sufficiently high resolution, captured flows may be distinguished from other flow types by having differing patterns of correlation of flow width and thickness with substrate slope: for non-captured flows, the total flow width, central channel width and flow thickness will all increase systematically with decreasing substrate slope[11].

Tube-fed flows: These are flows fed by a roofed-over tube system. This may be just the interior of a single, parent, cooling-limited flow unit, the central channel of which has become

C-9

completely solid, or may be a more complex system of earlier flow units. Once magma has emerged from the roofed-over tube system, the flow units formed obey the same rules as those given above for flows fed from a primary vent. The only significant difference may be that, although magma cools only slowly within a tube system, the lava forming tube-fed flows may be systematically slightly cooler than lava emerging from a primary vent on the same volcano; the consequent higher initial viscosity of tube-fed lava will lead to cooling-limited flow units that are somewhat shorter than those fed from a primary vent at the same effusion rate.

Applications: Where a compound flow field consists of many flow units which have been produced by a long-lived eruption, much of which may have taken place at a relatively constant effusion rate, it is to be expected that many of the flow units will be cooling limited, each such flow being connected to one or more break-out flows which is itself cooling-limited. The last flow unit in such a sequence will, of course, be volume limited. The first step in the analysis of a compound flow field must be the application of traditional mapping methods, identifying discrete units, determining superposition relationships between units or groups of units, and looking for continuity relationships between adjacent units. Once a connected group of units has been mapped, a histogram of the lengths of the units may be plotted, and the following relationships are expected. In the simplest circumstances, there will be a high peak in the distribution corresponding to the length, L, of a single cooling-limited flow unit. There may also be significant peaks at lengths which are integer multiples of this basic length (2L, 3L, etc.), corresponding to groups of two or more flow units where each is a break-out flow from the front of an earlier unit but has not been recognised as such because of inadequate resolution in the images used. The sharpness of the peak(s) will depend on the constancy of the effusion rate: a declining effusion rate will lead to the formation of shorter cooling-limited flows, resulting in a skewing of the histogram peak towards lengths somewhat shorter than L. Superimposed on the simple pattern due to cooling limited flows will be a distribution of lengths arising from volume limited and accidentally breached flows (all of which must have lengths shorter than L by various amounts) and of captured flows (all of which have lengths greater than L). As long as the "noise" represented by these other flows does not swamp the main peak due to cooling-limited flows, it will be possible to use the flow length, L, at which the peak occurs to estimate the mean effusion rate feeding the flow field. Examples of several of these flow types and fields on Venus are described elsewhere[10].

References: 1) Pinkerton, H. and Wilson, L. (1988) *LPSC XIX*, 937; 2) Pinkerton, H. and Wilson, L. (1992) Factors controlling the lengths of channel-fed lava flows, submitted to *Bull. Volcanol.*; 3) Pinkerton, H. and Wilson, L. (1992) *LPSC XXIII*, 1083; 4) Knudsen, J.G. and Katz, D.L. (1958) *Fluid dynamics and heat transfer*. McGraw Hill; 5) Hulme, G. and Fielder, G. (1977) *Phil. Trans. Roy. Soc.* A285, 227; 6) Crisp, J. A. and Baloga, S. M. (1990) *JGR*, 95, 1255; 7) Kilburn, C.R.J. and Lopes, R.M.C. (1991) *JGR*, 96, 19721; 8) Magee Roberts, K. *et al.* (1992) JGR, 97, 15991; 9) Lancaster, M. *et al.* (1992) *LPSC XXIII*, 753 ; 10) Head, J., Magee Roberts, K., Wilson, L., and Pinkerton, H. (1993) Lava flow field morphological classification and interpretation: Examples from Venus, this volume; 11) Wilson, L. *et al.* (1987) *Ann. Rev. Earth Plan. Sci.*, 15, 73.

S244-89
ABS ONLY

N94-20880

p. 2

CERN-Derived Analysis of Lunar Radiation Backgrounds;

Thomas L. Wilson[1] and Robert Svoboda[2]; [1]NASA Johnson Space Center/SN3, Houston, Texas 77058. [2]Louisiana State University, Baton Rouge, Louisiana 70803.

The Moon produces radiation which background-limits scientific experiments there. Early analyses of these backgrounds have either failed [1-3] to take into consideration the effect of charm [4] in particle physics (because they pre-dated its discovery), or have used branching ratios which are no longer strictly valid [5-9] (due to new accelerator data). We are presently investigating [10] an analytical program for deriving muon and neutrino spectra generated by the Moon, converting an existing CERN computer program known as GEANT which does the same for the Earth. In so doing, this will (1) determine an accurate prompt neutrino spectrum produced by the lunar surface; (2) determine the lunar subsurface particle flux; (3) determine the consequence of charm production physics upon the lunar background radiation environment; and (4) provide an analytical tool for the NASA astrophysics community with which to begin an assessment of the Moon as a scientific laboratory versus its particle radiation environment. This will be done on a recurring basis with the latest experimental results of the particle data groups at Earth-based high-energy accelerators [11,12], in particular with the latest branching ratios for charmed meson decay. This will be accomplished for the first time as a full 3-Dimensional simulation.

Such a study is important because the Space Science Board of the National Academy of Sciences has set forth broad guidelines [13] for NASA research which include neutrino astrophysics and neutrino astronomy as potential new fields of emphasis for the future exploration of space. The strategic study of NASA's Space Physics Division [14,15] includes a lunar neutrino telescope as a candidate experiment for a mature lunar base, in part because the Moon has no appreciable atmosphere (only an exosphere) and the noisy atmospheric neutrinos of Earth are 60 Earth-radii away [16,17]. This attribute of the barren Moon ignores, however, the fact that any planetary object (Earth or Moon) produces prompt neutrinos as a consequence of cosmic ray bombardment on its surface, altering the hadronic chemistry of its planetary regolith and producing mesons which in turn decay into neutrinos when they survive long enough to do so.

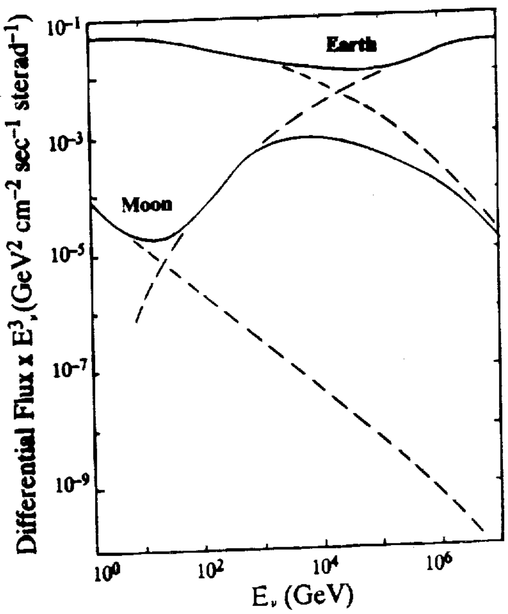


Figure 1. Charm on the Moon [Adapted from Volkova (1989)]

As a consequence, science (and physics in particular) on the Moon is confronted with several problems: (a) Our understanding of cosmic ray interaction with planetary surfaces has changed radically since the Apollo program due to the discovery of charm in quantum particle physics; and (b) Earlier work addressing this subject is out of date, due to new results on charm from the particle data groups.

The history of this problem of neutrino physics on the Moon [2] is almost as long as that for neutrino astronomy on Earth [18]. From the outset, prompt generation of neutrinos was recognized and treated early on as a problem of primary cosmic ray interaction with a rarefied medium [3,8]. Following the discovery of charm in particle physics, however, these results were recalculated for the Moon

CERN-Derived Analysis; Wilson, T.L. and Svoboda, R.

[7,5,6] by taking into account charmed meson decay. These results are illustrated in Figure 1, showing the effect, and in Figure 2, giving an Earth-versus-Moon flux comparison in the presence of charm. At 10 GeV in Figure 1, the ambient neutrino background is clearly lower than that on Earth. Similarly at 10^4 GeV, one could argue that a lunar neutrino experiment is hardly justified - illustrating why an Earth-versus-Moon radiation background analysis is important.

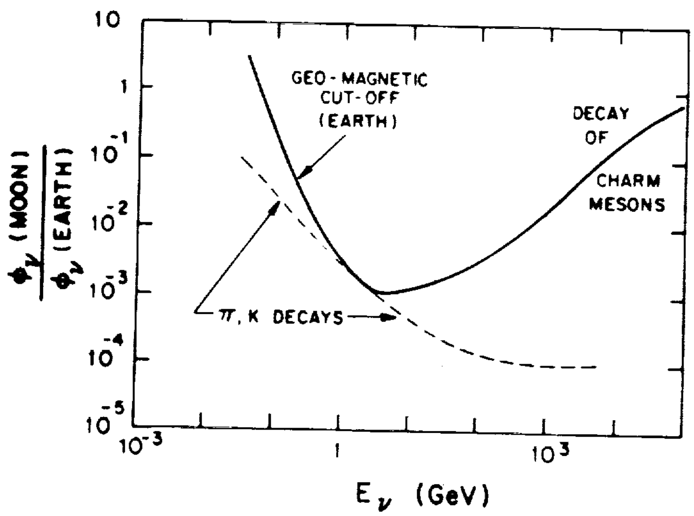


Figure 2. Moon-Versus-Earth Flux Comparison for neutrinos. [Cherry and Lande (1985)]

The current problem with this earlier work (e.g., Figures 1 and 2) is that it was calculated at a time when the energy dependence of charm production was not well understood. The particle data groups [11,12] have since published significant new data on charm production. The original naming convention of charmed mesons discussed by Cherry & Lande [7] is not even used anymore, and the branching ratios assumed by everyone [7,5,9] have changed, in some cases significantly.

The study discussed here represents a relatively simple work-around to the above muon-neutrino albedo problem for the Moon which brings the analysis in line with contemporary high-energy physics.

References:

[1] Trombka, J.I., *et al.*, Ap. J. **212**, 925 (1977); Adler, I., and Trombka, J.I., Phys. Chem. Earth, Vol. X, 17 (1977). [2] Volkova, L.V., and Zatsepin, G.T., *9th ICRC* (London), Vol. 2, 1039 (1965). [3] Volkova, L.V., in *Cosmic Rays No. 10 - International Geophysics Project*, 128-131 (Science Publications, Moscow, 1969). [4] E.g., Gaillard, M.K., Lee, B.W., and Rosner, J.L., Rev. Mod. Phys. **47**, 277 (1975), Note added in proof. [5] Volkova, L.V., in *Cosmic Gamma Rays, Neutrinos, and Related Astrophysics*, Shapiro, M.M., and Wefel, J.P., eds. (Kluwer, 1989). [6] Cherry, M.L., in *Neutrino Astrophysics*, Jones, W.V., Kerr, F.J., and Ormes J.F., eds., AIP Conf. Proc. **203**, 299 (American Institute of Physics, New York, 1990). [7] Cherry, M.L., and Lande, K., in *Lunar Bases and Space Activities of the 21st Century*, Mendell, W., ed. (Lunar and Planetary Institute, Houston, Texas, 1985), 335. [8] Volkova, L.V., and Zatsepin, G.T., *Akad. Nauk SSR, Phys. Series, Bulletin*, **49**, 143 (1985). [9] Volkova, L.V., *Nuovo Cim.* **10C**, 465 (1987). [10] Wilson, T.L. and Svoboda, R., unpublished (1992). [11] Hikasa, K., *et al.* Phys. Rev. **D45**, No. 11, Part II (1992). [12] Hernandez, J.J., *et al.*, Phys. Lett. **B239**, 1 (1990). [13] NRC (National Research Council) *Space Science in the 21st Century: Imperatives for the Decades 1995 to 2015* (National Academy Press, Washington DC, 1988), 7 volumes. [14] Shawhan, S., *et al.*, *Space Physics Strategy - Implementation Study* (Space Physics Division, NASA Headquarters, 1991), Vol. 1 and Vol. 2. [15] *Space Physics Missions Handbook*, with Supplement (Space Physics Division, NASA Headquarters, 1991), Section **6.2**. [16] Wilson, T.L.. in *Physics and Astrophysics from a Lunar Base*, Potter, A.E., and Wilson, T.L., eds., AIP Conf. Proc. **202**, 53 (American Institute of Physics, New York, 1990). [17] Wilson, T.L., in *Astrophysics from the Moon*, Mumma, M.J., and Smith, H.J., eds., AIP Conf. Proc **207**, 608 (American Institude of Physics, New York, 1990). [18] Bahcall, J., *Neutrino Astrophysics* (Cambridge University Press, 1989).

S245-65
ABS. ONLY

N94-20881

MULTIVARIATE STATISTICAL ANALYSIS: PRINCIPLES AND APPLICATIONS TO COORBITAL STREAMS OF METEORITE FALLS; Wolf S. F. and Lipschutz M. E., Dept. of Chemistry, Purdue University, W. Lafayette, IN 47907

Multivariate statistical analysis techniques (linear discriminant analysis and logistic regression) can provide powerful discrimination tools which are generally unfamiliar to the planetary science community. Their use can be illustrated by the following example. Dodd et al. (1992) used fall parameters to identify a group of 17 H chondrites ("Cluster 1") that were part of a coorbital stream which intersected Earth's orbit in May, from 1855-1895, and can be distinguished from all other H chondrite falls. Using multivariate statistical techniques, Dodd et al. (1992) demonstrated that a totally different criterion, labile trace element contents – hence thermal histories – of 13 Cluster 1 meteorites are distinguishable from those of 45 non-Cluster 1 H chondrites. Here, we focus upon the principles of multivariate statistical techniques and illustrate their application using non-meteoritic and meteoritic examples.

Fig. 1 depicts data for the two cases: a) 4 easily-measured parameters for 50-sample sets of 2 different iris populations; b) data for 10 labile trace elements in 13- and 45-sample sets of H chondrites. For the non-meteorite case, we describe classification methods and the results of univariate (1-dimensional) and multivariate analysis (2-, 3- and 4-dimensional). Table 1 lists the multivariate results, showing a decrease in the number of misclassifications and an increase in D(Y) – a dimensionless standard distance describing population separation – as more parameters are considered.

For the 10 parameters of the H chondrite case (Fig. 1b) excellent separation is achieved using either multivariate technique (Fig. 2). In our talk, we apply the methods of randomization-simulation (Lipschutz and Samuels, 1991), test-validation, and compensation for over-determination to these data. All results demonstrate that Cluster 1 H chondrites are distinguishable from all other falls beyond any reasonable doubt.

Work supported by NASA grant NAG 9-48.

REFERENCES

Dodd, R. T., Wolf, S. F., and Lipschutz, M. E. (1992) Science submitted.

Lipschutz, M. E. and Samuels, S. M. (1991) Geochim. Cosmochim. Acta 55, 19-47.

Table 1. Multivariate discrimination of two iris populations.

Dimensions	Parameters	Misclassifications	$D_p(Y)$
2	Petal length Petal width	6	3.193
3	Petal length Petal width Sepal length	3	3.534
4	Petal length Petal width Sepal length Sepal width	3	3.710

MULTIVARIATE STATISTICAL ANALYSIS: Wolf S. F. and Lipschutz M. E.

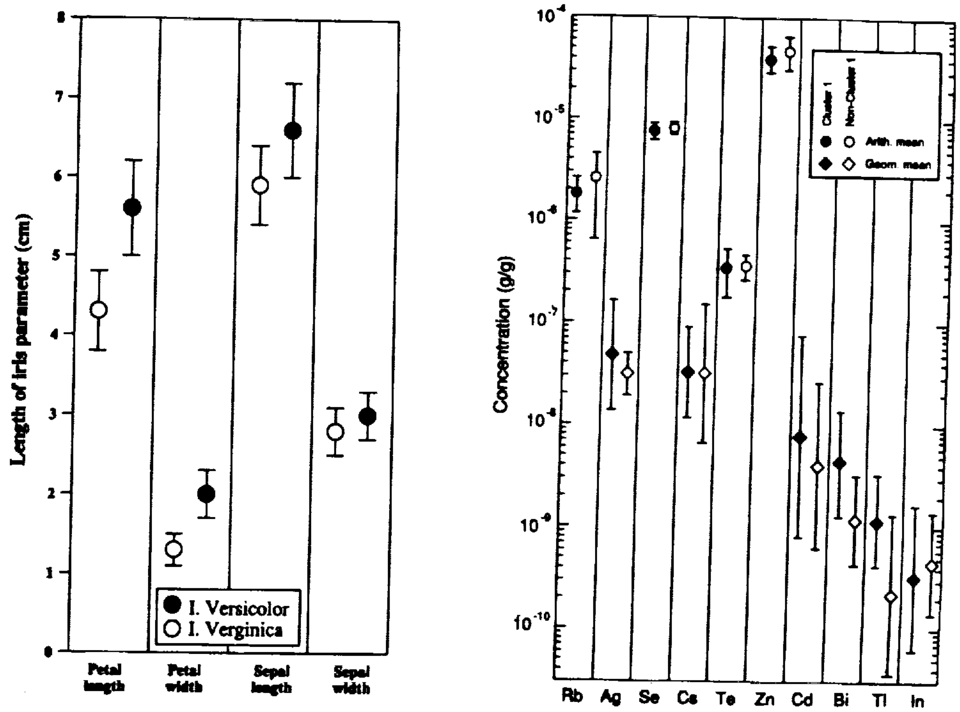


Fig. 1. Mean and one standard deviation for data for: a) 4 parameters in 2 iris populations; b) 10 labile trace elements in 2 H chondrite fall populations.

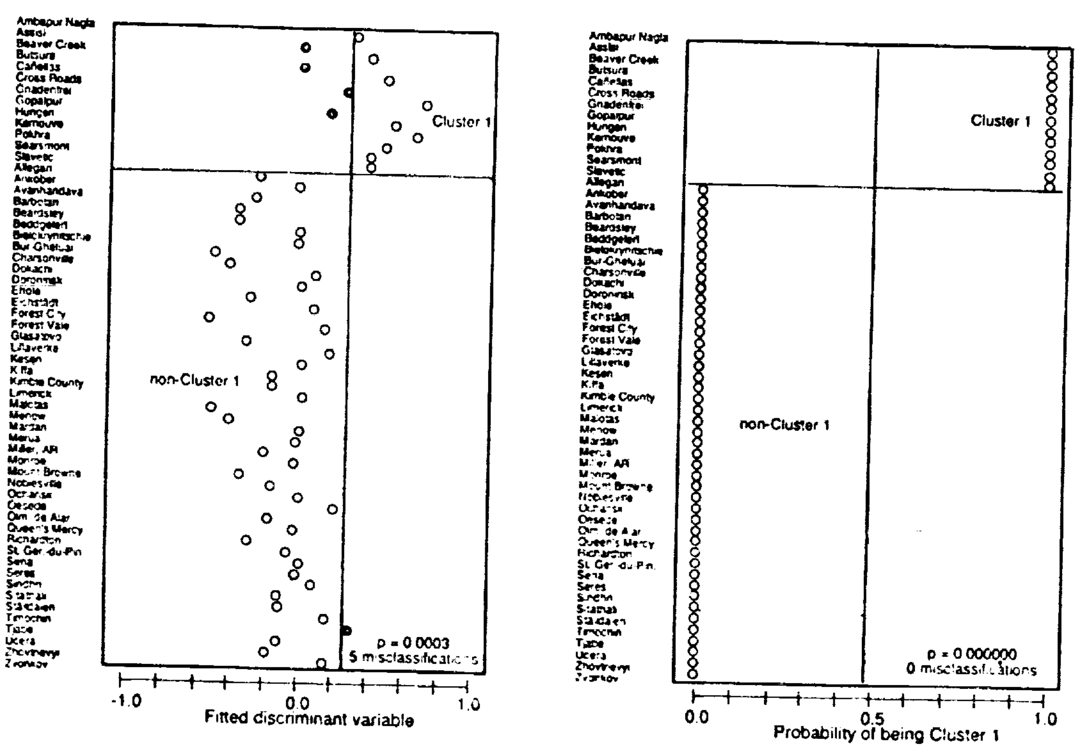


Fig. 2. Very strong evidence for a compositional difference between H chondrite fall populations by: a) linear discriminant analysis; b) logistic regression.

CHARACTERIZATION OF THE MARQUEZ DOME BURIED IMPACT CRATER USING GRAVITY AND MAGNETIC DATA; A.M. Wong, A.M. Reid, and S.A. Hall, *Dept. of Geosciences, The University of Houston, Houston, TX 77204*, V.L. Sharpton, *Lunar and Planetary Institute, Houston, TX 77058*

Introduction. The buried impact crater, Marquez Dome, located in Leon County in east central Texas, is an approximately 15 kilometer diameter structure whose central uplift is now partially exposed due to headward erosion of the post-impact cover. The central uplift is approximately 3 kilometers in diameter and the rocks within it have been uplifted more than 1200 meters above their regional level[1]. The crater rim remains buried and previous attempts[1,2] to determine its location have had to rely on seismic reflection data and geologic well logs. These attempts have been somewhat successful in mapping the extent of the disturbed zone around Marquez Dome, but more limited in their ability to image the shallow buried rim. In an attempt to define accurately the whole Marquez Dome structure and assist in the selection of drilling sites, a geophysical investigation involving gravity and magnetic data over the central uplift and the surrounding area has been undertaken.

Geological setting. The Marquez Dome structure is located in the East Texas Basin which was created by a late Triassic rifting event. The basin existed in a near-shore environment and was the site of almost constant sedimentary deposition. Depositional units include a mixture of terrigenous sands, fluvio-deltaic silts, shales, shelf carbonates, and evaporites. The units vary in thickness but in the area surrounding Marquez Dome are basically tabular and exhibit a gentle 2 to 3 degree dip to the southeast[2].

Geophysical signature. The disturbance to this well layered stratigraphy in the early Tertiary, caused by impact, crater formation, and subsequent in-filling, should produce an identifiable gravity anomaly that will give an indication of the crater's true extent. A previous regional gravity study has already identified a 2.5 mGal positive Bouguer gravity anomaly associated with the central peak[1]. The same disturbed stratigraphy also yields a magnetic anomaly. Preliminary magnetic data show a total intensity magnetic anomaly associated with the central uplift (see Fig. 1). The anomaly may be distorted by the iron-rich Carrizo sandstone that subcrops less than 2 kilometers to the east of the center of the uplift.

Field data collection. A program to collect gravity and magnetic data over and around Marquez Dome is currently underway. Based on the magnitude of the gravity anomaly over the central uplift and the magnitude of gravity and magnetic anomalies over other impact craters of similar size in sedimentary targets, precisions of +/- 0.1 mGals and +/- 1 nT are used in the acquisition of the data. Contour maps will be examined for evidence of any concentric trends that correspond to the central uplift, annular basin, or the crater rim. Data will also be plotted as profiles that traverse the structure. These profiles will serve to emphasize any changes in the gradient of the fields

CHARACTERIZATION OF THE MARQUEZ DOME: Wong, A.M. et al.

that may correspond to the location of the crater rim or the flanks of the central uplift. Preliminary magnetic and gravity maps, based primarily on surveys of the area of the central uplift, are shown in Figures 1 and 2. Additional measurements of the region surrounding the central uplift are in progress.

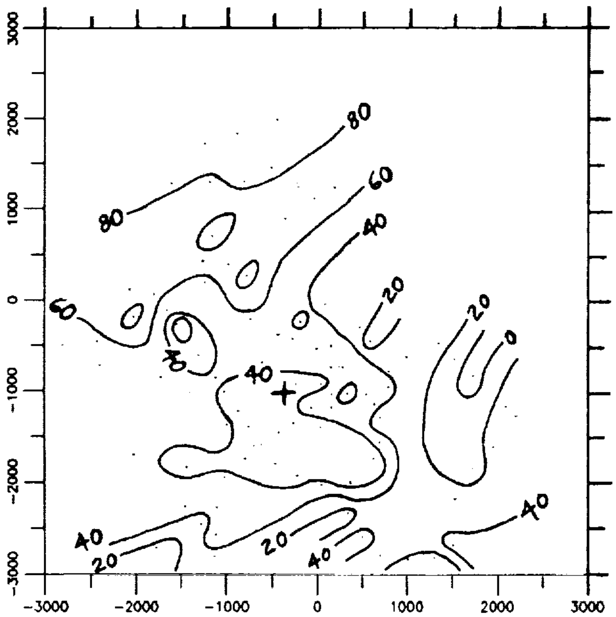


Figure 1.
TOTAL INTENSITY MAGNETIC ANOMALY MAP OF THE MARQUEZ DOME CENTRAL UPLIFT. MAP COORDINATES ARE IN METERS. THE CENTER OF THE CENTRAL UPLIFT IS MARKED BY (+). OBSERVATION STATIONS ARE MARKED BY (.). CONTOUR INTERVAL IS 20 nT.

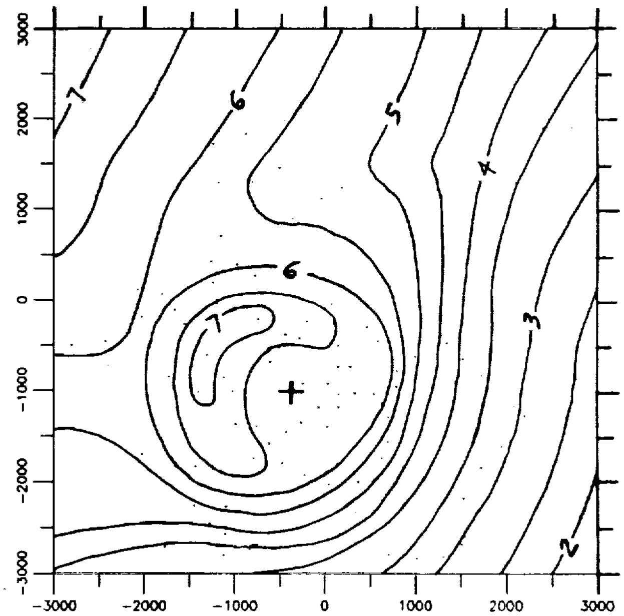


Figure 2.
BOUGUER GRAVITY ANOMALY MAP OF THE MARQUEZ DOME CENTRAL UPLIFT. MAP SYMBOLS ARE THE SAME AS FIGURE 1. CONTOUR INTERVAL IS 0.5 mGal.

References. [1]Sharpton, V.L., and Gibson, J.W.Jr. (1990) The Marquez Dome Impact Structure, Leon County, Texas. In *Lunar and Planetary Science XXI*, pp. 1136-1137. Lunar and Planetary Institute, Houston. [2]Gibson, J.W.Jr. (1990) MS Thesis, The University of Houston.

S247-91
ABS. ONLY

N94-20883

P-2

MORPHOLOGIC CLASSES OF IMPACT BASINS ON VENUS

Wood, Charles A. and Wesley Tam, Space Studies, University of North Dakota, Grand Forks, ND 58202

An independent survey of 60% of Venus has resulted in the detection of 35 impact basins and associated transitional rings. Contrary to previous studies we identify central peak basins, as well as peak ring basins. But no unambiguous multi-ring basins have been detected. A new class of crateriform - expanded peak structure - has been noticed, which is transitional in diameter, but apparently not in structure, between central peak and peak ring basins.

Impact basins are the largest features on most solid planets and moons in the solar system. Their existence, diameters, and morphologies provide clues to a planet's crustal structure, surface age, thermal history, and erosional processes. Since their discovery thirty years ago by Hartmann and Kuiper (1), impact basins, with their tantalizing near-regularities, have provided considerable fun for ring counters, modelers, and other hand wavers. Each planet and moon has been found to have its own variations, but all appear to be variants on the basic diameter-dependent morphologic sequence recognized on the Moon (2): *central peak basins* [crater-like structures containing both a central peak and an inner ring; the protobasin of Pike and Spudis (3)], *peak ring basins* [two ring basin of (3)], and *multi-ring basins* (with three or more rings).

The completion of Magellan's mapping has led to the first systematic cataloging of basins on Venus. Schaber and others (4) have identified 33 basins and an additional 10 possible basins. Their more definite basins include 27 peak ring basins and 6 multi-ring basins. They found no central peak basins on Venus. Alexopoulos and McKinnon (5) also reported their identification of 52 peak-ring and 3 multi-ring basins.

Independently of the work of (4) and (5) we have searched for basins on the collection of Magellan photographic prints provided by the NASA Planetary Geology Office. These prints cover only ~60% of the surface of Venus; the main gap occurs between longitudes 210° and 330°. We have recognized 35 basins (Table). Our results differ from previous analyses. We found 10 central peak basins, and 17 peak ring basins, but failed to identify any multi-ring basins. Many of the inner rings are irregular or incomplete; we accept Schultz's convincing evidence (6) that such ring deformation is due to oblique impact. CP basins on Venus have larger peak and ring masses than do lunar examples.

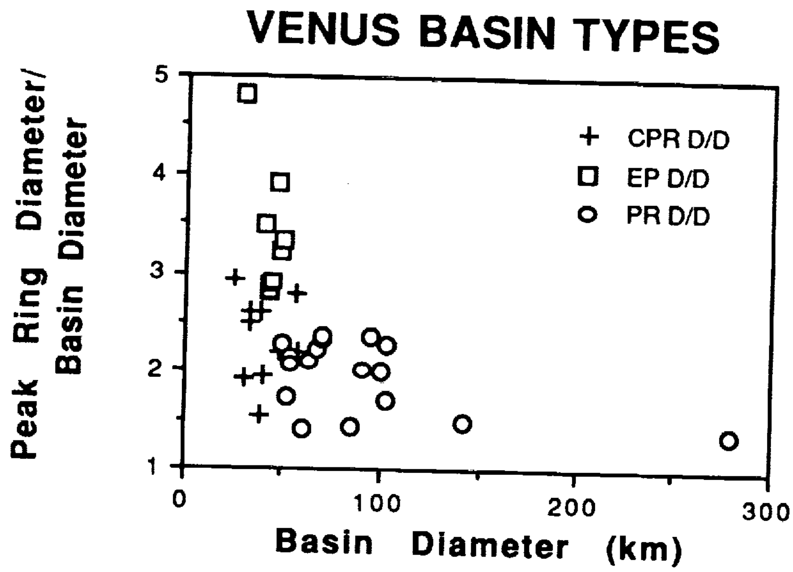
PARTIAL LIST OF VENUS IMPACT BASINS

Name	Lat	Long	D	Dr	Type
Fredegunde	-50.50	93.15	25	8	CPR?
Simonenko	-26.70	97.60	29	6	EP
Erxleben	-50.79	39.65	30	16	CPR
Ferrier	15.75	111.32	32	12	CPR?
Sitwell	16.63	190.40	32	13	CPR?
Flagstad	-54.31	18.85	38	25	CPR?
Zenobia	-29.32	28.55	39	15	CPR
Agnesi	-39.40	37.50	40	20	CPR?
no name	2.34	198.26	40	12	EP
Manzolini	25.68	91.25	42	15	EP
Tiyoni	-47.60	95.65	43	15	EP
Corpman	0.30	151.80	44	15	EP
Khatun	40.33	87.00	47	12	EP
Danilova	-26.30	337.05	48	22	CPR
Cunitz	14.47	350.90	48	15	EP
Wharton	55.65	61.99	50	22	PR
Zhilova	66.38	125.55	50	15	EP
de Beauvoir	1.95	96.05	52	30	PR
Cori	25.45	73.00	54	25	PR
Vigier Lebrun	17.25	141.15	54	26	PR
Carreno	-3.87	16.10	56	20	CPR?
Yablochkina	48.26	195.32	58	26	CPR?
Hepworth	5.10	94.60	60	42	PR
Aglaonice	-26.60	339.55	63	30	PR?
Stuart	-30.75	20.20	67	30	PR
Boulanger	-26.60	99.20	70	30	PR
Andreianova	-3.00	68.77	70	30	PR
Mona Lisa	25.65	25.20	85	58	PR
Bonnevie	-36.10	126.90	91	45	PR?
Greenaway	22.95	145.20	95	40	PR
Joliet-Curie	-1.60	62.50	100	50	PR
Cochran	51.85	143.35	103	45	PR
Cleopatra	65.85	7.15	103	60	PR?
Klenova	78.15	104.20	142	95	PR?
Mead	12.50	57.20	280	200	PR?

D = basin diameter; Dr = ring diameter.

We have also found a new class of transitional structure (from central peak craters to basin morphology) which we call *expanded peak* craters (EP). These have apparently also been noticed by Alexopoulos and McKinnon (5). EP appear to be normal craters with relatively small diameter rings in place of their central peaks. The average ratio of basin diameter to peak ring diameter for EP is 3.4, compared to 2.3 for central peak, and 1.95 for peak ring basins.

VENUS BASINS: Wood, C.A. and Tam, W.



Our available photography shows only two of the proposed multi-ring basins (Mead and Klenova), but we have examined photos of the other one (Meitner) in reference (4). Mead shows no evidence of a third ring; indeed Mead is admittedly classified as a multi-ring basin by (4) largely because of its large size. Klenova has two, nearly contacting inner rings, somewhat like Orientale's Inner and Outer Rook rings, but they are contained within an outer ring that looks like a normal crater rim. Meitner appears to be a peak ring basin with a very low and perhaps incomplete outer circular trace. Images available to us make it difficult to discern if the trace is of ejected material or is structural. What is missing from all proposed multi-ring basins on Venus is a scarp-like, Cordillera style ring. Considering the exquisite preservation of impact features on Venus, the lack of true multi-ring scarp morphologies may mean that they never formed. Additionally, the smallest unequivocal multi-ring basins on other planets have onset diameters of > 300 to 400 km (3);Venus' putative multi-ring basins are as small as 86 km wide (Mona Lisa; ref. 4). At this moment we have seen no evidence that Venus has any true multi-ring basins, rather some of its peak ring basins may have modifications unfamiliar from other planets.

Conclusions: Impact basins exist on Venus. Identified morphological classes include central peak basins and peak ring basins as on the Moon, Mercury, and Mars, but, unlike those planets, no multi-ring basins have been unambiguously recognized, presumably because such basins would have formed before the planet-wide resurfacing event, 0.5 by ago. Alternatively, according to the ring tectonic model of Melosh (7) the poor development of multi-ring basins may imply that Venus had a thick lithosphere during basin-formation time. A new morphologic type, expanded peak structures, has been discovered that is transitional in diameter between central peak basins and peak ring basins, but ring diameter ratios suggest they are not part of the basin continuum. Central peak basins are more abundant (percentage wise) on Venus than on any other planet, and thus transitional structures (expanded peak and peak ring basins) are much more prevalent that elsewhere. Melosh's (7) model would explain this observation as indicating that the upper layers of Venus act more like a Bingham fluid than does the crust of other planets.

REFERENCES: 1: Hartmann, WK and GP Kuiper (1962) *Comm. Lunar Planet. Lab. 1*, 51-66. **2:** Hartmann, WK and CA Wood (1971) *The Moon 3*, 3-78. **3:** Pike, RJ and PD Spudis (1987) *Earth, Moon Planets 39*, 129-194. **4:** Schaber, GG and others (1992) *J. Geophys. Res. 97*, 13,257-13,301. **5:** Alexopoulos, JS and WB McKinnon (1992) *Internat. Coll. Venus* (LPI Pub. # 789), 2-4. **6:** Schultz, PH (1992) *J. Geophys. Res. 97*, 16,183-16,248. **7:** Melosh, HJ (1989) *Impact Cratering*. Oxford University Press, NY, p. 180.

5248-90
ABS. ONLY

N94-20884

p. 2

LREE VARIABILITY IN CM MATRICES: ANOTHER LOOK AT METEORITE "COMPACTION AGES"; D. S. Woolum and Karen Poelstra, Calif. State Univ., CA 92634; C. Alexander, Washington Univ., St. Louis, MO 63130; T. Ireland, ANU, Canberra

Recent Neon-21 analyses [1] indicate that individual grains in some CM meteorites show the effects of enhanced exposures to energetic particles beyond that which can be attributed to conventional cosmic ray exposure. The exposures clearly occurred prior to the final compaction of the CM meteorites. These exposures were of such a magnitude that they require that we either have to revise our understanding of regolith dynamics and the time scales involved in the regolith activity of meteorite parent bodies, or must invoke an exposure of the irradiated grains to an enhanced energetic particle environment, an environment which would most likely be produced by an early active sun. Constraints on the compaction ages of the meteorites which exhibit the large precompaction exposures could play a critical role in resolving this issue [5].

So-called "compaction ages" have been reported previously for CM meteorites [2], but these CM "compaction ages" are model-dependent and rest on assumptions that may not be true. The chronometer used in the reported CM compaction age studies is extinct Pu-244. Briefly, the basic idea is to determine the track densities on the very surfaces of large isolated actinide-element-free mineral grains (primarily olivine grains) imbedded in the fine-grained CM matrix. The normal sources of the nuclear particle tracks at the grain surfaces are galactic and solar cosmic rays and the energetic charged products of the fissioning of U (essentially all coming from the matrix, since olivine incorporates only negligible amounts of U). Grains showing surface track densities greater than can be explained by the known U content of the matrix and the known galactic cosmic ray exposure age are of primary interest. Some of these (a few percent of the total; Hohenberg, et al., 1990) can be explained by exposure to solar flares, presumably in the regolith at the surface of its parent body; these grains can be identified by their extremely high surface densities and their steep track density depth profile. Non-solar- flare-irradiated grains with excess track densities are most plausibly explained by the grains' exposure to the CM matrix very early, prior to the decay in the adjacent matrix of the now-extinct Pu-244 radionuclide, which decays by fission and has a short, 72 Gyr half-life. The excess track density attributable to Pu, is a function of the "contact time", the time period during which the grain was exposed to the Pu-bearing matrix, and a "contact age" (a term we prefer to the more commonly used, but the possibly misleading, term: "compaction age") can be determined as long as an initial Pu abundance can be inferred.

In the original work [2], the Pu-fission track densities on the surfaces of isolated grains in selected CM meteorites were observed to vary by about two orders of magnitude. This variability was interpreted as being due to a variability of Pu in the matrix of these meteorites, and the authors argued on this basis that the average track density for each meteorite and the average chondritic initial Pu/U could be used to determine a compaction age for the individual meteorites. Ages progressing from 4.22 up to 4.42 Gyr were determined for Nogoya (youngest), Mighei, Murchison, Cold Bokkeveld, and Murray (oldest), based on the initial Pu/U ratio given by [3]. In the

interim, a re-evaluation of the initial Pu/U ratio has resulted in a value for that ratio that is lower by about a factor of two [4], which would translate into revised compaction ages ranging between 4.32 and 4.52 Gyr. These new ages compound the problem in explaining the precompaction exposures with unusually long regolith exposures even further. There does not appear to be time enough between 4.56 Gyr and the inferred compactions. For example, for Murchison, the excess Neon-21 observed requires at the very least 100 Myr regolith exposure with present day fluxes and with the total exposure spent at a depth corresponding to the peak in the production profile; a more realistic exposure history would indicate more like several hundred Myr regolith exposures. Because of the inherent importance of the question of meteorite compaction ages and their relevance to the interpretation of the Neon-21 data, we have undertaken to re-evaluate the CM "compaction ages".

One of the key assumptions in the reported ages is that the fission track variability is due to Pu variability in the matrix. While Pu is now extinct, there are ways to assess the likelihood of this assumption. Cosmochemically, Pu is expected to behave either like an actinide (e.g., like U) or like the LREE (especially Ce, Sm Nd), depending on redox conditions. If Pu variability of up to two orders of magnitude is the explanation for the fission track variability, then one would expect to find comparable variability in either the actinides or the LREE. Based on neutron-induced fission track maps of CM sections, Macdougall and Kothari [2] determined that, in general, U appeared homogeneously distributed on the 100 micron scale spatially in the CM matrix.

We report here the results of our assessment of the LREE variability in CM matrices. We have determined the Ce, Nd, Sm abundances in the matrices of CM meteorites Murchison, Murray, Mighei, Nogoya, and Cochabamba by ionmicroprobe analyses performed at Washington University, St. Louis. We have focussed our analyses specifically on the matrix abutting isolated olivine grains. This is the only "brand" of matrix that counts in the calculation of the Macdougall/Kothari compaction ages, since fission fragment ranges are only about 15 microns.

We find that the LREE abundances in the matrices abutting isolated mineral grains vary significantly, by about a factor of six for all CM meteorites analyzed, although the elemental ratios are all roughly chondritic. To the extent that it is fair to compare the LREE data from CM polished sections from one set of meteorite samples (kindly provided to us by Mike Zolensky and Chuck Meyer) with the track densities obtained from separate samples, both reported by [2] and obtained by us (preliminary work in progress), we conclude that the absolute variation of the LREE abundances, while significant, does not explain the two orders of magnitude variation of the surface track densities observed, if Pu cosmochemically followed the LREE and all the grains' actual matrix contact ages were truly synchronous.

REFS: [1] Hohenberg C. M., et al. (1989) GCA 54, 2133. [2] Macdougall D. J. and Kothari B. K. (1976) EPSL 33, 36. [3] Podosek F. A. (1970) EPSL 8, 183. [4] Hudson G. B., et al. (1988) Proc. Lunar Planet. Sci. Conf. 19th,547. [5] Woolum D. S. and Hohenberg C. M. (1993) In, Protostars and Planets III, Univ. Arizona Press, Tucson (in press).

5249-90
ABS ONLY

N94-20885

THE CARBON COMPONENTS IN SNC METEORITES OF FELDSPATHIC HARZBURGITE COMPOSITION; I.P.Wright, C.Douglas and C.T.Pillinger, Dept. of Earth Sciences, Open University, Walton Hall, Milton Keynes MK7 6AA, England.

p-2

Two meteorites collected in Antarctica, ALH A77005 and LEW 88516, have characteristics which link them to the shergottite group of SNC meteorites (*e.g.* 1). Essentially, ALH A77005 and LEW 88516 are feldspathic harzburgites (*e.g.* 2), being comprised of roughly equal quantities of olivine and pyroxene, with an additional few percent of feldspar which has subsequently been converted to maskelynite by shock (2,3). The meteorites represent samples of a cumulate rock which is itself composed of two different lithologies: in one, large pyroxenes poikilitically enclose olivine crystals, while the other consists of interstitial areas made up of pyroxene, olivine, maskelynite, whitlockite, troilite, ilmenite and chlorapatite (1). It has been proposed that meteorites such as ALH A77005 (and LEW 88516) are relict samples of the source peridotite from which the other shergottites formed (3). As such it should be informative to study in detail the carbon components present within these samples, in order to make comparisons with data from other shergottites (e.g. 4). Although not plutonic in origin (2), and therefore not sampling a truly deep source, analyses of ALH A77005 and LEW 88516 should assist with attempts to define the bulk carbon isotopic composition of Mars. This has been assessed previously through analyses of carbon of presumed magmatic origin in other SNC meteorites (4,5), but the carbon isotopic compositions obtained seem to be at variance with what might be expected. It is important to constrain the carbon isotopic composition of Mars as well as possible so that models of atmospheric evolution, based on carbon isotopic data (6,7), can yield the most reliable results.

As detailed in Wright *et al.* (5), the isotopic composition of magmatic carbon on Mars appears to fall in the region of $\delta^{13}C$ = -20 to -30‰. This is substantially different to carbon of a juvenile composition in the Earth's mantle, which has $\delta^{13}C$ of -5 to -7‰. The apparent difference in carbon isotopic composition between the two planets is difficult to explain. Even if heterogeneous accretion is advocated, with differing sorts of late-stage veneers on the two planets, while it is possible to comprehend the Earth's $\delta^{13}C$ value in terms of known meteorite groups (*i.e.* C1 and C2 carbonaceous chondrites have $\delta^{13}C$ in the range -5 to -10‰), the data for Mars are at odds with meteoritic evidence. In order to provide some new information on this subject, ALH A77005 and LEW 88516 have been re-analysed by high-resolution (*i.e.* 25°C temperature increments), stepped combustion. This technique gives a measure of the variation of carbon concentration and stable isotopic composition with temperature (from ambient to *ca.* 1300°C, where melting begins).

A previous analysis of ALH A77005 (4) showed it to contain 141 ppm carbon with a $\Sigma\delta^{13}C$ of -28.7‰. Notwithstanding what appear to be three separate releases of carbon (200-400°C, 500-600°C and 900-1200°C), $\delta^{13}C$ values hardly deviate from the mean value. The results for the new analysis of ALH A77005 show 153 ppm carbon and a $\Sigma\delta^{13}C$ value of -26.4‰, in good agreement with the previous experiment. In detail, an obvious high temperature release of carbon is missing in the new analysis; it is likely that the release of carbon at 900-1200°C in the original extraction was the result of metal contamination, arising from the use of a stellite (stainless steel) pestle and mortar, during sample preparation. The analysis reported herein is from a sample which was manipulated in an agate pestle and mortar (as, indeed, are all analyses of SNC meteorites now performed in our laboratory). In the original analysis, 27 ppm carbon with $\Sigma\delta^{13}C$ of -27.6‰ were released from 900-1200°C; in the new analysis only 4.4 ppm carbon are liberated over the equivalent temperature range. Curiously the $\Sigma\delta^{13}C$ value recorded from 900-1200°C in the new analysis is -24.2‰, which is indistinguishable from that acquired previously. Since 900-1200°C is the temperature range over which magmatic carbon could be released, it would seem that this new

analysis of ALH A77005 provides an upper limit to the possible concentration of this component. It is considered to be an upper limit since, as demonstrated by the previous analysis of ALH A77005, contaminants can burn at high temperatures (there is also a contribution from system blank which is not accounted for here). The $\Sigma\delta^{13}C$ of -24.2‰ is no different to that proposed earlier for magmatic carbon in SNC meteorites (5).

In the analysis of LEW 88516 (sub-sample 8) a discrete release of carbon is discernible at 1000-1150°C. This amounts to 2.63 ppm carbon with $\Sigma\delta^{13}C$ of -22.2‰. However, on the basis of the $\delta^{13}C$ values recorded at different steps it appears that this carbon does not arise from a single component. From 1000-1050°C, 1.2 ppm carbon are released with $\delta^{13}C$ of -32.8‰, while from 1050-1100°C, 0.78 ppm carbon with $\delta^{13}C$ of -7.4‰ are evolved. The isotopically light material would be compatible with what has been found previously in SNC meteorites, and ascribed to martian magmatic carbon. On the other hand, the $\delta^{13}C$ value of -7.4‰ is perhaps more like what would be anticipated for magmatic carbon, based on the experience of terrestrial samples. However, SNC meteorites suffer from the complication of a component believed to be trapped martian atmospheric CO_2, present in shock-produced glass, which has $\delta^{13}C$ as high as +27‰ (8). Depending upon the location of magmatic carbon in SNC meteorites it may not be possible, using stepped combustion, to successfully resolve trapped CO_2 from the evolution of magmatic species. For instance, if magmatic carbon is dissolved in minerals, this may be released at a similar temperature to that where glass melts and liberates trapped CO_2. For the analysis of ALH A77005, trapped CO_2 was observed at temperatures greater than 1200°C, whereupon 0.5 ppm carbon with $\delta^{13}C$ of +15.9‰ was released. This tends to suggest that in this sample, at least, trapped CO_2 was resolved. The component with $\delta^{13}C$ of -7.4‰ in LEW 88516 may simply represent a mixing of trapped CO_2 and magmatic carbon with a $\delta^{13}C$ of -32.8‰. In any case an isotopically light component was observed at high temperatures in LEW 88516, which is consistent with previous analyses of SNC meteorites. Thus, it would seem apparent that magmatic carbon in SNC meteorites is distinctly different to that on Earth.

It is known that xenoliths from terrestrial basalts contain carbonaceous matter in the form of particles in cracks, and semi-continuous films in microcracks (9). The particles are considered to be graphite intercalation products, while the films are complex mixtures of organic and possibly graphitic compounds. These materials are thought to have formed abiotically by the reaction of volcanic gases with chemically active crack surfaces. Interestingly attempts to measure the carbon isotopic compositions of the carbonaceous materials using stepped heating extractions (10) have shown that they may combust at temperatures up to 1200°C and have $\delta^{13}C$ values of *ca.* -25‰, even though co-existing CO_2 fluid inclusions have $\delta^{13}C$ of about -5‰. It seems entirely possible that the SNC meteorite samples studied herein may show evidence for the presence of carbonaceous matter (with $\delta^{13}C$ of *ca.* -25‰), while any CO_2 originally present (with $\delta^{13}C$ of -5‰?) has been degassed from the samples without forming fluid inclusions.

References: (1) M.M.Lindstrom *et al.* (1992), *Lunar Planet. Sci.*, **XXIII**, 783-784; (2) H.Y.McSween (1985), *Rev. Geophys.*, **23**, 391-416; (3) H.Y.McSween *et al.*, (1979), *Science*, **204**, 1201-1203; (4) I.P.Wright *et al.* (1986), *Geochim. Cosmochim. Acta*, **50**, 983-991; (5) I.P.Wright *et al.*, (1991), *Workshop on the Martian Surface and Atmosphere Through Time, Boulder, Colorado*, 156-157; (6) I.P.Wright *et al.*, (1990), *J. Geophys. Res.*, **95**, 14789-14794; (7) B.M.Jakosky (1991), *Icarus*, **94**, 14-31; (8) C.P.Hartmetz *et al.*, (1991),*Workshop on the Martian Surface and Atmosphere Through Time, Boulder, Colorado*, 54-55; (9) E.A.Mathez (1987), *Geochim. Cosmochim. Acta*, **51**, 2339-2347; (10) F.Pineau and E.Mathez (1990), *Geochim. Cosmochim. Acta*, **54**, 217-227.

5250-90
ABS. ONLY

N94-20886

FURTHER CARBON ISOTOPE MEASUREMENTS OF LEW 88516; I.P.Wright, C.Douglas and C.T.Pillinger, Dept. of Earth Sciences, Open University, Walton Hall, Milton Keynes MK7 6AA, England.

p. 2

Douglas *et al.* (1) have previously analysed the carbon content and isotopic composition of a crushed sample (sub-sample 13) of the shergottite, LEW 88516. The powder, which was prepared from a relatively large portion of the meteorite in order to obtain a representative sample, was distributed amongst the scientific community. However, it is probable that the preparation procedure was not optimised for the purposes of carbon measurements. Indeed, it was found that LEW 88516,13 contained over 1200 ppm carbon (1), a concentration which is greater than that present in any other SNC meteorite (2,3). That a close relative, ALH A77005, contains only 141 ppm carbon (3) seems to implicate the preparation procedure as being responsible for the apparently high carbon content of LEW 88516. However, it may also be the nature of the fine powder which has resulted in contamination. The observation of a high carbon content in LEW 88516,13 highlights the extreme difficulty of trying to obtain representative samples of whole-meteorites for this kind of investigation. Presented herein are some further measurements of LEW 88516 which should serve to clarify some of the issues raised by the previous investigation.

A repeat analysis of LEW 88516,13 using high-resolution stepped combustion gave the following results: 1614.5 ppm carbon and $\Sigma\delta^{13}C$ = -23.7‰ (compared with 1215.2 ppm carbon and $\Sigma\delta^{13}C$ = -21.2‰, for the previous analysis). In contrast, a non-powdered sample from the interior of the meteorite (LEW 88516,8), prepared for analysis in our own laboratory, was found to contain only 75.9 ppm carbon with $\Sigma\delta^{13}C$ of -25.6‰. This carbon content is now the lowest recorded from any SNC meteorite and is clearly more like what would have been anticipated from a sample of this nature. It is considered that the enhanced levels of carbon in LEW 88516,13 are the result of an input to the sample of extraneous materials. Terrestrial contamination in Antarctica prior to collection is discounted since an analysis of an exterior sample of the meteorite (LEW 88516,9) yielded a carbon concentration of 91.2 ppm, which is only marginally greater than the interior fragment. Because of analytical difficulties experienced at low temperatures of this extraction it is not possible to derive a satisfactory $\Sigma\delta^{13}C$ value for LEW 88516,9 although it is unlikely that there would be any substantial difference to the other samples.

The addition of carbon in LEW 88516,13 cannot necessarily be ascribed simply to contamination during the crushing of the sample; carbon-bearing components could have been added at any time after crushing by exposure of the sample to the atmosphere. In this regard it is important to consider the apparent discrepancy in yields between the two analyses of LEW 88516,13. Since this sample is a fine powder it would have been anticipated that the carbon yields from the two experiments would be comparable. The difference is not the result of an analytical problem since the absolute yields released from each extraction (2094 and 1660 ng carbon) are way in excess of the detection limit of the capacitance manometer, used to determine the quantity of CO_2 gas produced during the combustion procedure. Perhaps the difference in carbon yield between the two analyses demonstrates that, even though the sample is finely powdered, some characteristic of the carbon-bearing material results in variable quantities of it being extracted from the reservoir. For instance, the carbon may occur as a thin film on the surfaces of individual particles. In which case selection effects, such as removal of samples with differing mean grain size, may cause a variation in carbon yield between analyses (coarser grains are likely to have risen to the top of the powder and have been extracted for the first analysis). The situation may have been further complicated by coagulation of grains, the effects of static charge *etc.*, which may have acted to preferentially leave some of the materials within the reservoir. It should be noted that the two

analyses of LEW 88516,13 utilised 1.7232 and 1.0114 mg of powder respectively; in total this represents about 70% of the entire allocation of the sample. Since each analysis was performed on a significant fraction of the total sample, problems associated with removal of material from the reservoir are more than likely to have caused the disparity in carbon yields between the two experiments. A further consideration is that the second analysis, which produced a higher carbon concentration, was performed two months after the first; it has to be considered that the addition of contamination was time-dependent. The remaining sample will be used to assess this.

Looking in detail at the carbon released from the new analysis of LEW 88516,13 it can be seen that there are several carbon-bearing components present (this cannot be done effectively with the previous analysis since that sample was analysed using 100°C temperature increments). If it is assumed that the vast majority of the carbon in LEW 88516 is the result of laboratory contamination then proper characterisation may allow the identification of contaminants in other samples where proportionately lower quantities are present. Between room temperature and 250°C, 147 ppm carbon are liberated with a $\Sigma\delta^{13}C$ value of *ca.* -25‰. The $\delta^{13}C$ values then show a plateau at -22‰ over five consecutive temperature steps (between 250 and 400°C), with a corresponding yield amounting to 1200 ppm. Between 375 and 475°C, 230 ppm carbon are released with $\Sigma\delta^{13}C$ of -29‰. The carbon released over these three temperatures ranges will be non-committally referred to as LC1 (0-250°C), LC2 (250-400°C) and LC3 (375-475°C). Evidence for similar components is also found in a further Antarctic shergottite, EET A79001, although in different experiments the exact temperature intervals may vary by ±25°C. In LEW 88516,8, LC1 amounts to 22.5 ppm carbon with $\Sigma\delta^{13}C$ of -28‰, while LC2 and LC3 account for 21 and 22 ppm carbon respectively, with corresponding $\Sigma\delta^{13}C$ values of -20.7‰ and -29.9‰. Since the temperature ranges of combustion for LC1, LC2 and LC3 overlap it is inevitable that there may be some slight disparity between the calculated $\Sigma\delta^{13}C$ values. Nonetheless, it is considered that there is good agreement between the carbon isotopic compositions recorded for LC1, LC2 and LC3 in sub-samples 13 and 8 of the meteorite. Of interest here are the relative quantities of the three different sorts of carbon present in the various fractions of LEW 88516. In LEW 88516,8, LC1,LC2 and LC3 occur in roughly equal quantities, whereas in LEW 88516,13, the ratio of LC2/LC1 is about 8, and LC3/LC1 is 1.6. In other words, LC2 is 60 times more abundant in LEW 88516,13 compared to sub-sample 8, whereas the equivalent factors for LC1 and LC3 are only 6.5 and 10.5 respectively.

As yet it is not possible to derive the nature of LC1, LC2 and LC3, although they are apparently resolvable on a volatility basis. In this respect, LC1 would be considered to represent volatile atmospheric contaminants (such as hydrocarbons *etc.*), which are only very loosely bound to the sample. LC2 is less volatile in nature; its carbon isotopic composition ($\delta^{13}C$ = -21 to -22‰) should eventually help in its identification. LC3 is more refractory still, having a combustion temperature which is consistent with identification as a fairly complicated organic material (terrestrial spores or pollen might be a suitable example). The overall enhancement of LC1, LC2 and LC3 in LEW 88516,13 can be explained on the basis of the higher surface area of the sample. However, an alternative explanation is that LEW 88516,13 samples parts of the meteorite not included in LEW 88516,8. In which case some of the low-temperature carbon could be of pre-terrestrial origin. Thus, whilst the results obtained from LEW 88516,13 might not appear to be of direct relevance to the study of SNC meteorites, further investigations of the sample could, in the long term, lead to a better understanding of the indigenous components in these meteorites.

References: (1) C.Douglas *et al.* (1992), *Meteoritics*, **27**, 215-216; (2) R.H.Carr *et al.* (1985), *Nature*, **314**, 248-250; (3) I.P.Wright *et al.* (1986), *Geochim. Cosmochim. Acta*, **50**, 983-991.

S25/-46
ABS. ONLY

N94-26887

p. 2

SHOCK ATTENUATION AT THE SLATE ISLANDS REVISITED; Wu S., Institute of Mineral Deposits, Chinese Academy of Geological Science, Beijing, China, P.B. Robertson and R.A.F. Grieve, Geological Survey of Canada, Ottawa, Canada

The Slate Islands, off the north shore of L. Superior, represent the emergent portion of the central uplift of a complex crater with an estimated diameter of 30 km (1). Previous systematic studies of the shock metamorphism at the Slate Islands have concentrated on the orientation of shatter cones, complemented by paleomagnetic data (5), and observations of the distribution of planar deformation features in quartz (6) to locate the "shock center" and to estimate the rate of shock pressure decay from the center. The impact origin of the Slate Islands, however, has not been accepted by Sage (2,3), who attributes the shock metamorphic effects to the intrusion of diatreme breccias. This argument, in turn, has been used by others (e.g., 4) to dispute the established relationship between shock metamorphism and impact and to argue that the existence of planar deformation features in quartz from K/T boundary deposits does not require the occurrence of a hypervelocity impact event. Because of Sage's continuing assertion that the planar deformation features at Slate Islands are associated with breccia dikes and have, therefore, an endogenic origin, we have extended the earlier analysis to a more spatially extensive suite of samples than observed previously (Fig. 1).

The methodology used to determine the shock pressures recorded by the planar deformation features in quartz is that used previously (6), with orientations determined by the U-stage for 25 quartz grains in each sample. An additional 24 samples were examined, bringing the total number of samples examined to 42 and making the Slate Islands the most intensively studied impact structure in Canada from the perspective of planar deformation features in quartz. Samples with quartz but no planar deformation features have been assigned a recorded shock pressure of 5.5 GPa, provided they occur within the outer limit of shatter cone development. As with other complex impact craters, shatter cones are developed at Slate Islands out to a greater radial distance than are planar deformation features (7). The combined data sets (6 and this work) clearly indicate the relatively systematic radial decay of recorded shock pressure from a central location on Patterson Island. The "shock center" based on the development of planar deformation features is located < 1 km south of the "shock center" based on shatter cone orientations (5). Using the planar deformation feature data, Fig. 2 shows attenuation of the rate of recorded shock pressure with distance from the shock center. As previously, this is normalized to the distance to the edge of the peripheral trough, which is taken to approximate the edge of the transient cavity (6). The rate of decay is similar to previous estimates for the Slate Islands and Charlevoix but slower than that derived from comparable observations at Manicouagan. We interpret this difference as due to the effects of erosion, with Manicouagan being less deeply eroded than the Slate Islands or Charlevoix structures. The relatively high variation in recorded shock pressure in some samples at an equivalent radial distance (Fig. 2) has been noted previously and attributed to grain size effects (8).

Planar deformation features also have been observed in clasts in one of the breccia dikes located on the east coast of Patterson Island, where the surrounding country rocks do not display planar deformation features in quartz. This evidence of the deformation chronology agrees with observations by Sage (3) for a breccia dike on the west coast, and is complemented by the occurrence of shatter cones in some breccia clasts (1). We interpret these observations to indicate that brecciation occurred after passage of the shock wave, making these dikes so-called type-B breccia dikes (9). The higher recorded shock levels in clasts compared with levels in the adjacent country rocks, and the presence of clasts of now missing, stratigraphically higher lithologies (1) indicate that the dikes formed during cavity growth with material being driven down into the target. As well, the occurrence of clasts with recorded shock pressures of ~ 13 GPa within cm of country rocks displaying no planar deformation features conflicts with the argument of Sage (2,3) that the source of energy for the development of shock metamorphic effects is diatreme intrusion.

CONCLUSIONS:

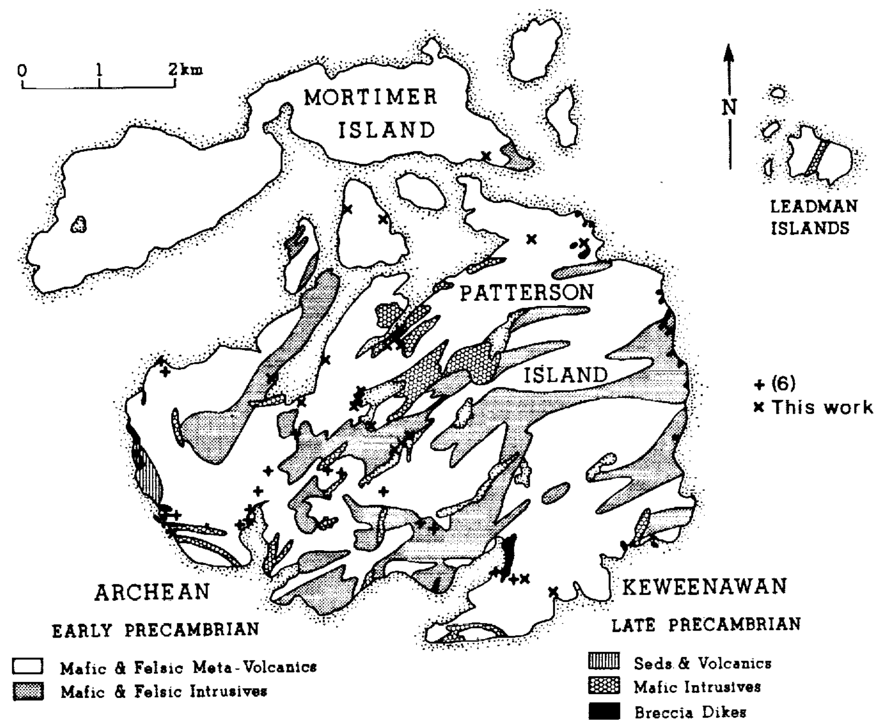
This study of a more extensive suite of Slate Islands samples confirms previous interpretations. It indicates clearly that recorded shock pressures, as determined by planar deformation feature orientations, increased towards the center. The "shock center" is very close, (considering the structural movements during cavity modification) to that from an independent determination from shatter cone orientations. Shock metamorphism at a higher level in breccia clasts than in the adjacent country rocks is evidence that the shock event preceded the formation of the breccia dikes. These observations, which are consistent with those at other impact

SLATE ISLANDS REVISITED: **Wu S. et al.**

structures, are all contrary to the interpretation by Sage (2,3) that breccia dike formation by diatreme action was the source of the shock event. There is no plausible reason to consider the Slate Islands as anything but the emergent portion of the central uplift of a complex impact crater. It cannot be cited as an example of endogenic shock in arguments regarding evidence of impact in the terrestrial stratigraphic record.

REFERENCES: (1) Halls, H.C. and Grieve, R.A.F. (1976) Can. Jour. Earth Sci., 13, 1301-1309. (2) Sage, R.P. (1978) Bull. Geol. Soc. Amer., 89, 1529-1540. (3) Sage, R.P. (1991) Ont. Geol. Surv. Rpt. 264, 111 p. (4) Officer, C.B. (1992) Terra Nova, 4, 394-404. (5) Stesky, R.M. and Halls, H.C. (1983) Can. Jour. Earth Sci., 20, 1-18. (6) Robertson, P.B. and Grieve, R.A.F. (1977) Impact and Explosion Cratering, 687-702. (7) Lakomy, R. (1990) LPSC XXI, 676-677. (8) Grieve and Robertson (1976) Contrib. Min. Pet., 38, 37-49. (9) Lambert, P. (1981) Multi-ring Basins, 59-78.

Fig. 1. Sample locations and general geology of the Slate Islands.



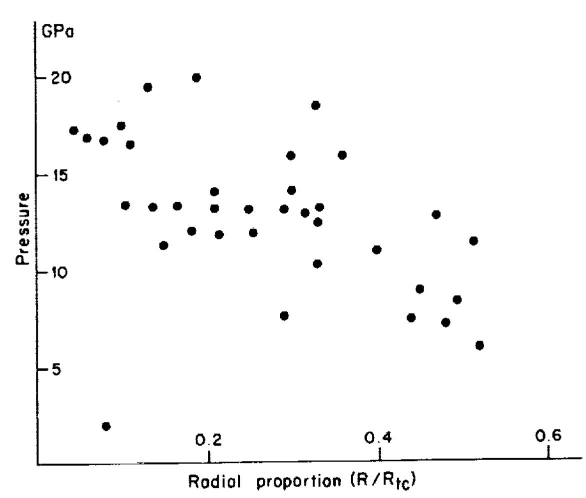


Fig. 2. Attenuation of shock pressure (GPa) with distance from shock center.

S252-43 ABS. ONLY

N94-20888

CONVEX SET AND LINEAR MIXING MODEL;

P. Xu and R. Greeley, *Department of Geology, Arizona State University, Tempe, Arizona 85287-1404*

p. 2

Summary. A major goal of optical remote sensing is to determine surface compositions of the Earth and other planetary objects. For assessment of composition, single pixels in multi-spectral images usually record a mixture of the signals from various materials within the corresponding surface area. In this report, we introduce a closed and bounded convex set as a mathematical model for linear mixing. This model has a clear geometric implication because the closed and bounded convex set is a natural generalization of a triangle in n-space. The endmembers are extreme points of the convex set. Every point in the convex closure of the endmembers is a linear mixture of those endmembers, which is exactly how linear mixing is defined. With this model, some general criteria for selecting endmembers could be described. This model can lead to a better understanding of linear mixing models.

Introduction. A major goal of optical remote sensing is to determine surface compositions of the Earth and other planetary objects. In order to quantify the areal abundances of surface materials, the effects of atmospheric attenuation, illumination geometry, and particle size must be removed from the data, as discussed elsewhere [3]. For assessment of composition, single pixels in multi-spectral images usually record a mixture of the signals from various materials within the corresponding surface area. Two types of models are generally used to quantify the abundances of surface materials in single pixel: *linear mixing models* (macroscopic scale or "checkerboard") [1,7,9] and *non-linear mixing models* (microscopic scale or intimate) [2,4,6]. Mathematically, linear mixing models are expressed as sets of linear equations in which the spectral mixture is a linear combination of component (endmember) spectra:

$$\sum_{i=1}^{k} f_i \mathbf{Re}_i = \mathbf{Rm} \text{ such that } 0 \le f_i \le 1 \text{ for all } i \text{ and } \sum_{i=1}^{k} f_i = 1 \qquad (1)$$

in which **Rm** is the column vector of the spectral mixture, $\mathbf{Re}_i$ is the column vector of *ith* endmember spectral, f_i is the fraction of *ith* endmember in the spectral mixture, and k is the number of endmembers. As a first-order approximation, non-linear mixing models can also be expressed as a set of linear equations except that the reflectance (**R**) is replaced by single-scattering albedo (**W**) in equation (1) [4,8]. In this report, we show how models can be related to a convex set for application to both linear and non-linear mixing models (the effects of instrumental noise are not discussed).

Convex Set. The following definitions and theorems regarding convex set are from [5]. Let v_1, v_2, v_3 be different vectors or points in n-space; the *line segment* is the set of all points: $t_1v_1 + t_2v_2$, with $t_1, t_2 \ge 0$ and $t_1 + t_2 = 1$. A *triangle* is the set of points: $t_1v_1 + t_2v_2 + t_3v_3$, $t_i \ge 0$ for i =1,2,3 and $t_1 + t_2 + t_3 = 1$. Let S be a subset of $\mathbf{R}^n$, S is *convex* if given points P, Q in S, the line segment joining P to Q is also contained in S. Let S be a convex set and let P be a point of S, P is an *extreme point* of S if there do not exist points Q_1, Q_2 of S with $Q_1 \neq Q_2$ such that P can be written in the form: $P = tQ_1 + (1-t)Q_2$ with $0 < t < 1$. Some theorems about convex set are:

(1) Let $P_1, ..., P_n$ be points of $\mathbf{R}^m$. Any convex set which contains $P_1, ..., P_n$ also contains all linear combinations $x_1P_1 + ... + x_nP_n$, such that $0 \le x_i \le 1$ for all i, and $x_1 + ... + x_n = 1$.

(2) Let $P_1, ..., P_n$ be points of $\mathbf{R}^m$. The set of all linear combinations $x_1P_1 + ... + x_nP_n$ with $0 \le x_i \le 1$ for all i, and $x_1 + ... + x_n = 1$, is a convex set which is also called the convex closure of points $P_1, ..., P_n$.

(3) Let S be a closed, bounded, convex set. Then S is the convex closure of its extreme points.

Convex Set and Linear Mixing Model. From the definitions and theorems about the convex set, we see a correspondence between the closed, bounded convex set and linear mixing models.

CONVEX SET AND LINEAR MIXING MODEL: Xu, P. and Greeley, R.

We view the spectra of endmembers and their mixture as vectors or points in n-space. Then the endmembers correspond to extreme points of a convex set and the set of all possible mixtures of the endmembers correspond to the convex set which is the convex closure of its extreme points. We propose that closed and bounded convex set be a mathematical model for linear mixing. The advantages of this model are that: (1) the endmember of linear mixing is clearly stated as an extreme point; (2) the closed and bounded convex set is a natural generalization of a triangle in n-space which has geometric implication; and (3) every point in the convex closure of the endmembers satisfies the condition that the fraction of each endmember in the mixture is non-negative and all fractions equal unity. However, in the linear equation representation of linear mixing, the geometric significance is not apparent and the endmembers are not checked for their extremity. In the light of the convex set, the linear mixing model involves the following steps:

(1) define all the possible endmembers which could be selected from either a spectral library or the multi-spectral images;
(2) find at least two endmembers which constitute the smallest convex set which "contain" the mixture point (this "containment" may be in a least-square sense);
(3) solve the linear equations to obtain the fractions of each endmembers in the mixture.

If step (2) fails, it means that the mixture point is not in any of the convex closures of the endmembers defined in step (1) or that the endmembers defined in step (1) cannot model the mixture. Step (2) ensures that the fraction solutions of step (3) are not negative, nor greater than one. With the convex set model, some general criteria for endmember selection can be formulated. When the endmember is selected from multi-spectral images, the extreme point or vertex of the data cluster would generally be a better candidate. The third endmember should not be in the line segment joining the other two endmembers. Generally speaking, an endmember in the convex closure of the other endmembers is not a good choice of endmember. However, there may be the case in which an endmember is in the convex closure of the other endmembers; if so, the endmembers should be broken into several groups and the mixture will have the fractions in terms of only one group of endmembers.

Conclusions. There is correspondence between a closed, bounded convex set and linear mixing models. We propose that the closed and bounded convex set be a mathematical model for linear mixing. This model has a clear geometric implication because the closed and bounded convex set is a natural generalization of a triangle in n-space. The endmembers are extreme points of the convex set. Every point in the convex closure of the endmembers is a linear mixture of those endmembers, which is exactly how linear mixing is defined. With this model, some general criteria for selecting endmembers could be described. This model can lead to a better understanding of linear mixing models.

References.

[1] Adams, J.B., et al. (1971), *Proc. Apollo 12 Lunar Sci Conf.*, 2183-2195.
[2] Hapke, B. (1981), *J. Geophys. Res.*, *86*, 3039-3054.
[3] Johnson, P. E., et al. (1992), *J. Geophys. Res.*, *97*, 2649-2657.
[4] Johnson, P.E., et al. (1983), *J. Geophys. Res.*, *88*, 3557-3561.
[5] Lang, S. (1971), *Linear Algebra*, Addison-Wesley.
[6] Mustard, J.F., et al. (1987), *J. Geophys. Res.*, *92*, E617-E626.
[7] Nash, D.B., et al. (1974), *J. Geophys. Res.*, *79*, 1615-1621.
[8] Sabol, D.E., et al. (1992), *J. Geophys. Res.*, *97*, 2659-2672.
[9] Singer, R.B., et al. (1979), *Proc. 10th Lunar Planet. Sci. Conf.*, 1835-1848.

S253-46 ABS. ONLY

N94-20889

p. 2

STABLE NI ISOTOPES AND ^{10}Be AND ^{26}Al IN METALLIC SPHEROIDS FROM METEOR CRATER, ARIZONA; S. Xue, G.F. Herzog, G.S. Hall[1], J. Klein, R. Middleton and D. Juenemann[2]. 1) Dept. Chemistry, Rutgers Univ., New Brunswick, NJ 08903; 2) Dept. Physics, Univ. Pennsylvania, Philadelphia, PA 19104.

Introduction. The Canyon Diablo spheroids, which are found around Meteor Crater, Arizona [1], are nickel-enriched objects with diameters from <0.1 to several mm. Previous studies have suggested that the enrichment of nickel resulted either from shock-melting of S-rich areas followed by solidification of the liquids under strongly non-equilibrium conditions at rapid cooling rates during flight outward from the crater [2]; or from the selective oxidation of iron [3]. Isotopic studies are an effective tool for constraining the degree of open-system evaporation experienced by a system. The purpose of this study was to see whether Ni isotopes had been fractionated by volatilization during spheroid formation. In addition, the cosmogenic nuclides ^{10}Be and ^{26}Al were measured to try to estimate the depths in the parent meteorite from which the spheroids came.

Experimental methods. Spheroids with diameters between 0.5 and 1.0 mm were kindly supplied by C. Moore. Two sets of spheroids (I [n=14] and II [n=7]) were weighed and dissolved in 1 cm^3 of 9 M HCl (Ultrex). We took separate aliquots of these solutions and diluted them for compositional and isotopic analyses. We used a two-column anion exchange procedure (with 9 M HCl and 2.2 M HCl) to minimize contamination due to iron and zinc, which interfere at masses 58 and 64. The recovery of nickel was incomplete from Set I spheroids. For this reason the anion exchange procdure was modified slightly to insure complete Ni recovery for Set II spheroids. After anion exchange the eluate was evaporated and taken up in 50 cm^3 of 2% HNO_3. Composition and isotopic abundances of Ni were measured with PlasmaQuad PQ2+ ICP-MS instrument (VG Elemental) operated in peak-scanning mode [4]. The measured Ni isotopic data were corrected for procedural blanks and for interferences due to variable, residual concentrations of Fe and Zn. Below, the average Ni isotopic ratios of the spheroids are reported as δ-values, where $\delta^{y}Ni \equiv \{[^{y}Ni/^{58}Ni]_{sample}/[^{y}Ni/^{58}Ni]_{terrestrial}-1\}x1000$. The procedures used for the ^{10}Be and ^{26}Al analyses were similar to those described by Vogt and Herpers [5], except that we used minicolumns (2-3 cm^3) for both anion and cation exchange. The ^{10}Be and ^{26}Al activities of the spheroids were determined by accelerator mass spectrometry (AMS) at the University of Pennsylvania, following our standard analytical procedures [6,7].

Results. Nickel concentrations of the Canyon Diablo spheroids range from 7% to 37%, but fall mostly between 11% and 16%, as do those reported elsewhere (i.e., 13 to 22% Ni [3]). We estimate the precision of the measured nickel ratios to be as follows: (60/58, 0.3%; 61/58, 1%; 62/58, 0.6%; 64/58, 1.3%). The relative standard deviations of the averages calculated for all the Canyon Diablo spheroids (assuming no fractionation in any of them) are slightly higher than those of standards, e.g., for 60/58, Δ= ±0.28% for the spheroids vs. ±0.26% for the standards. We attribute this small difference to presence of low concentrations of impurities in the spheroid solutions.

The average δ-values of the two sets of Canyon Diablo spheroids, normalized to the average of nine Ni standards taken to represent the terrestrial values, are given in Table 1. There were no obvious differences in the results for sample sets I and II. For most of the spheroids, the δ-values and isotopic fractionation (Φ) are zero within the range of analytical error. However, there are a few exceptions. Two spheroids of Set II had positive values for δ^{60} and δ^{62} and Φ

Table 1. Average Ni isotopic abundances in Canyon Diablo spheroids.

Sample	Mass (mg)	Ni(%)	$\delta^{60}Ni$	$\delta^{61}Ni$	$\delta^{62}Ni$	$\delta^{64}Ni$	Φ (%/AMU)
Set I (avg)	0.73	16.2	0±1	-6±4	-3±2	2±5	-0.1±0.1
Set II (avg)	1.10	14.2	5±2	4±5	7±2	30±13	0.3±0.1
All	0.86	15.3	2±1	-3±3	0±2	11±6	0.0±0.1

(the average mass fractionation). The δ^{64}Ni values, which are all positive, vary by about a factor of ten, probably because of unidentified interferences (MgAr?).

Table 2 shows the results of the AMS analyses for three Canyon Diablo spheroids. The ^{10}Be activities range from 0.5 ± 0.5 to 1.5 ± 0.8 dpm/kg. The errors are large because the samples were small and because we used a commercial atomic absorption solution ($^{10}Be/^{9}Be \sim (3 \pm 2) \times 10^{-14}$) as a carrier. The ^{26}Al activities in spheroids are at background levels ($^{26}Al/^{27}Al \leq 4 \times 10^{-15}$) and are presented as upper limits.

Discussion. The small observed degree of fractionation of nickel isotopes limits the extent of Ni loss during spheroid formation: If we assume Rayleigh distillation and take $\delta^{62} \leq 2$, we find that less than 3% of the Ni evaporated. The well-known enhancement of Ni/Fe ratios in the spheroids compared to bulk Canyon Diablo thus confirms the Fe losses of ~50-70% that Kelly et al. [3] inferred and attributed to the selective oxidation of Fe: One thinks of a film of iron oxide stripped off during the high-speed flight of the spheroid or of subaerial weathering. Now it has been suggested that metallic deep-sea spherules also underwent substantial loss of Fe (through oxidation [8]) and of Ni [4]. In the spherules, however, Ni (and Fe and O) isotopes are strongly fractionated, perhaps because the spherules remained at higher temperatures for longer times. Measurement of Fe and O isotopic abundances in the spheroids would be useful.

Most hand samples of Canyon Diablo contain >0.8 dpm/kg of ^{10}Be and ^{26}Al [9]. The ^{26}Al activities in the two spheroids analyzed are considerably lower. As it happens, an ^{26}Al activity of 0.8 dpm/kg was measured for a hand sample with a ^{21}Ne concentration just twice the lowest value observed in any Canyon Diablo sample. One possible interpretation of our ^{26}Al data is that the spheroids represent material from greater shielding depths than have been analyzed before. Table 2 shows the pre-atmospheric depths of the spheroids inferred from the ^{26}Al production rate profiles of Ref. [10]. Two cautions are in order, however. First, the spheroids are known to include light elements [1,3]. To the extent that these elements come from the incorporation of terrestrial silicaceous material, then the masses we have used are too high, the activities too low and the depths too high by ~10-15 cm. We note in this context that soils near Meteor Crater are expected to contain 0.1-0.5 dpm/kg of ^{10}Be, which may help explain the high ^{10}Be activity in spheroid G. On the other hand, to the extent that the light elements are native to the meteorite (e.g., S, C, and/or P) then the production rates of ^{10}Be and ^{26}Al in space would have been higher and our calculated depths (which assume production on iron and nickel only) too low. Our second caution is that Be and Al could have been lost from the molten state either as a result of oxidation or direct vaporization. Such losses have been inferred for Fe, Ni, and Mn from metallic deep-sea spherules but not for Be or Al (see [4]). An analysis of ^{59}Ni would be a decisive way to determine the preatmospheric depth of the precursor material.

Table 2. ^{10}Be and ^{26}Al activities in Canyon Diablo spheroids.

Sample	^{10}Be (dpm/kg)	^{26}Al (dpm/kg)	Depth (cm)[10] ^{10}Be	Depth (cm)[10] ^{26}Al
Spher-A	<0.5	<0.11	>32	>57
Spher-D	0.7±0.7	<0.02	25	>100
Spher-G	1.5±0.8		14	

References [1] Mead C. et al. (1965) *Amer. Mineral. 50*, 667-681. [2] Blau P.J. et al. (1973) *J. Geophys. Res. 78*, 363-374. [3] Kelly W.R. et al. (1974) *Geochim. Cosmochim. Acta 38*, 533-543. [4] Herzog G.F. et al. (1992) *Lunar Planet. Sci. XXIII*, 527-528. [5] Vogt S. and Herpers U. (1988) *Fresenius Z. Anal. Chemie 331*, 186-188. [6] Middleton R. and Klein J. (1986) *Proc. Workshop Tech. Accel. Mass Spectrom.*, Oxford, England, pp. 76-81. [7] Middleton R. and Klein J. (1987) *Phil. Trans. Roy. Soc. London A323*, 121-143. [8] Davis A. et al. (1991) *Lunar Planet. Sci XXII*, 281-282. [9] Nishiizumi K. (1987) *Nucl. Tracks Radiat. Meas. 13*, 209-273. [10] Kohman T.P. and Bender M.L. (1967) In *High-Energy Nuclear Reactions in Astrophysics* (ed. B.S.P. Shen), W.A. Benjamin, Inc., 169-245.

S254-18
ABS ONLY

N94-20890

P-2

GEOMETRICAL ANALYSIS OF THE MICROCRATERS FOUND ON LDEF SAMPLES.

Kazuo Yamakoshi[1],Hideo Ohashi[1],Motosaku Noma[2], Hirohisa Sakurai[2], Kazuo Nakashima[2],Ken'ichi Nogami[3] and Rie Omori[3]

[1] Institute for Cosmic Ray Research, Univ. Tokyo ,Tanashi, Tokyo 188, Japan.

[2] Faculty Sci., Yamagata Univ., Koshirakawa, Yamagata 990, Yamagata,Japan.

[3] Lab.Phys.,Dokkyo Univ. School Medicine, Mibu, Shimotsuga-gun,Tochigi,Japan.

In this work, diameters(D) and depthes(T) of microcraters found on LDEF samples were measured and their origins were deduced by the (D/T) ratios, which distinguish projectile materials. From the results, one iron and several stony projectiles could be recognized.

The satellite LDEF was retrieved in Jan.1991 by the space-shuttle "Columbia". Two aluminum clamp samples; "A07,C03" and "A08,C03" are curated from NASA in August 1992 to us. 16 microcraters were found on the LDEF samples.

It is well known, the ratio of diameter(D) to depth(T), (D/T), is independent of the projectile's velocity and weight and dependentonly on the combination of the target and projectile materials [1],[2].

From simulation results of aluminum targets, iron and stone (or plastic) projectiles make (D/T) ≒ 1 and ≒ 2 ,respectively [1],[2]. In Fig.1, (D/T)≒ 1 for iron projectiles to aluminum targets and (D/T)≒ 3.5 for iron projectiles to iron targets obtained in simulation experiments for wide ranges of projectile's velocity[2]. Nagel and Fechtig (1980) [1] gave (D/T) ≒ 2, when plastic grains collided aluminum targets. There are no data about aluminum-stone combination in simulation experiments, thus (D/T) ≒ 2 is used instead of stony projectiles.

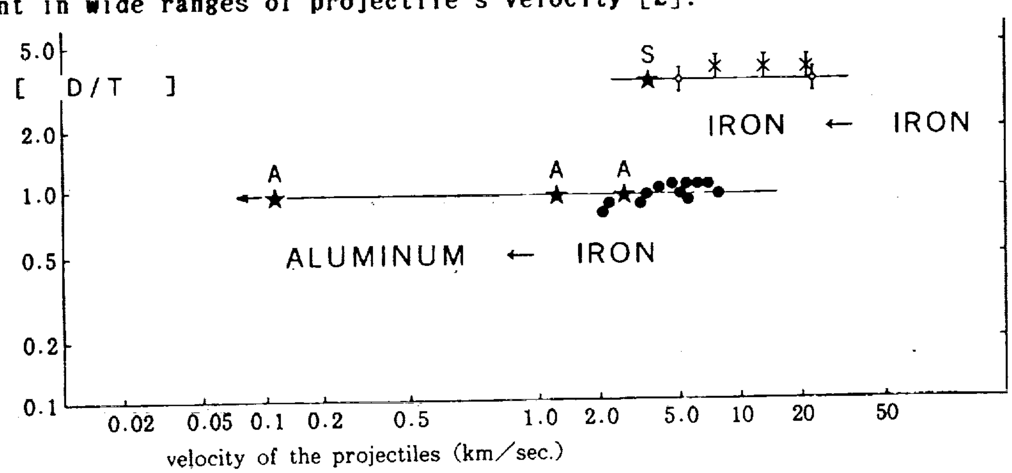
In this work, the dimensions of the microcraters found on LDEF aluminum plates are measured using a laser-microscope[3]. The data are shown in Table 1,in which one iron and seven or more stony projectiles can be found. In the cases of (D/T) > 2, it is expected to be shallowed due to residues of the projectiles at the bottoms. The residues can be seen as irregular structures from the cross-section of some shallower craters,so X-ray microanalysis is expected to give us fruitful results. This (D/T) method used in this work is a good clue to estimate the projectilematerials, however, it has a weak point. It can not discriminate the impact craters which are induced by cosmic meteoroids or artificial debris. In order to cover the weak points, the analyses of the chemical compositions of

the residues remained in the craters will be very effective.

Table 1. The Dimensions of the Microcraters of LDEF Samples.

[Sample Code]		[Diameter] D;(μm)	[Depth] T;(μm)	[D/T] RATIOS	[REMARKS]
[A07,C03]	A	457.16	203.27	2.14	stony,
	B	51.035	25.80	1.98	stony, projection?
	C	74.383	12.84	5.79	residue? or small angle
	D	112.020	51.31	2.18	stony,
	E	123.45	111.37	1.11	iron,
	F	34.028	12.90	2.64	
	G	313.13	92.99	3.37	residue?
	H	282.27	71.12	3.97	residue?
[A08,C03]	J	118.76	56.76	2.09	stony, projection?
	K	138.661	33.27	4.17	residue? or small angle
	L	185.53	96.60	1.91	stony,
	M	152.463	71.56	2.13	stony,
	N	339.81	118.53	1.80	stony?
	O	139.624	57.53	2.43	
	P	369.71	114.54	3.23	

Fig.1. (D/T) Ratios obtained in simulation experiments, in which projectiles were iron and stainless steel and targets were aluminum and iron, are nearly constant in wide ranges of projectile's velocity [2].



REFERENCES:[1] Nagel K.& Fechtig H.; Planet.Space Sci.,28(1980) 567~573.

[2] Yamakoshi K.;Proc.of Workshop on Space Debris,ISAS SP-11 (1990),39~50.

[3] by the courtesy of Laser Technics Co.,Ltd. using MODEL #1LM21H.

5255-39
ABS. ONLY
N94-20891
p-2

ANTIPODAL FRAGMENT VELOCITIES FOR POROUS AND WEAK TARGETS AT CATASTROPHIC IMPACTS; M. Yanagisawa and T. Itoi, Univ. Electro-Communications, Chofu-shi, Tokyo 182, JAPAN.

Mortar, porous alumina and sand targets, which were spherical in shape, 11 to 15 cm in diameter, were impacted normally by plastic (polycarbonate) projectiles of nearly 1 g in mass at velocities about 6 km/s. Fragment velocity at the antipole of impact site (antipodal velocity, V_a), for each experiment, was obtained from two Flash X-ray images recorded prior to and at predetermined delayed time after impact event. It has been revealed that the velocities for the same E/M_t (impact energy divided by target mass) depend strongly on target material, and differ about an order of magnitude between the sand and basalt.

Target is hanged in the impact chamber of Electromagnetic Railgun Facility at Inst. Space Astronaut. Sci. [1] between Flash X-ray tube and 43 x 35 cm film cassette. Just before hitting the target projectile cuts thin wire placed in the path of its trajectory at $l = 52$ cm before impact point. At the predetermined delay (T = 1, 2 or 4 msec) after electric circuit detecting the wire broken, the X-ray tube irradiate a 35 nsec pulse. Thus, radiograph at $t_1 = T - l / v_0$ after the impact is obtained (Fig. 1), where v_0 is projectile velocity. Small sensors are glued on the targets for some experiments to monitor the initiation of antipodal movement and obtain the time between the initiation and the image acquisition, t_2. Target diameters, D, divided by $(t_1 - t_2)$ correspond to mean shock wave velocities in the targets, U_s. We calculate V_as by dividing the displacement of antipole between the two radiographs by t_2 or $(t_1 - D / U_s)$.

Results are summarized in Table 1. and V_as are plotted against E/M_t in Fig. 2 with the values reported by Fujiwara and Tsukamoto (1980) [2] for basalt targets. V_as are apparently smaller for porous or weak targets than dense and hard ones at the same E/M_t. V_as are also lower for the Porous alumina targets than solid ones in oblique impact experiments by Nakamura and Fujiwara (1991) [3].

V_a would represent relative velocities of large fragments at catastrophic impact. Then, it is inferred that porous or weak asteroids would easily re-accumulate gravitationally, so they could be shattered but hard to be dispersed. Such objects would lessen their size through cratering erosion rather than catastrophic disruption.

ACKNOWLEDGMENTS: This work was supported by ISAS. We greatly owe A. Yamori for firing electromagnetic railgun for our experiments.

REFERENCES: [1] Kawashima, N., Yamori, A., Yanagisawa, M., Kubo, H., Kono, M. and Teii, S. (January 1993) *IEEE Tran. Mag.* [2] Fujiwara, A. and Tsukamoto, A. (1980) *ICARUS, 44,* 142. [3] Nakanura, A. and Fujiwara, A. (1991) *ICARUS, 92,* 132.

ANTIPODAL FRAGMENT VELOCITY AT IMPACT: Yanagisawa, M. and Itoi, T.

Table 1. Experimental Results

Shot #	Material*	Target mass (kg)	Projectile mass (g)	Impact velocity (km/s)	E/M_t x 10^4 (J/kg)	V_a (m/s)
O-118	Mortar	1.5	1.1	6.7	1.6	16.9
O-119	Mortar	3.4	1.1	5.9	0.55	6.64
O-121	Sand	2.4	1.1	6.9	1.1	1.4
O-122	Sand	2.2	1.1	7.1	1.2	3.2
O-145'	Porous alumina	1.1	1.2	3.7	0.72	4.2
I-1	Porous alumina	0.94	1.1	5.0	1.5	8.1
I-2 **	Porous alumina	1.0	1.2	3.7	0.83	3.3

* Mortar targets are made of commercial mortar including some glue. They would have 20 or 30 % porosity judging from their low bulk density, 1.9 g/cm^3. Each porous alumina target consists of two hemispheres glued together. The glued boundary affected the fragmentation seriously and antipodal hemisphere was not shattered when projectile hit the center of the other hemisphere. Nominal density and porosity are 1.4 g/cm^3 and 60 %, and U_s was 2.8 km/s. Sand targets are thin spherical paper bags filled with non-cohesive sand (not quartz sand). We assume the effect of paper sheet on V_a being negligible. Their density is 1.4 g/cm^3, and the porosity would be about 50 %. U_s was 0.3 km/s.

** Oblique impact due to unexpected projectile trajectory. The projectile could lessen its mass and velocity before impact due to some problem of the gun.



Fig. 1. Radiograph at 0.9 msec after impact in Shot # O-118.

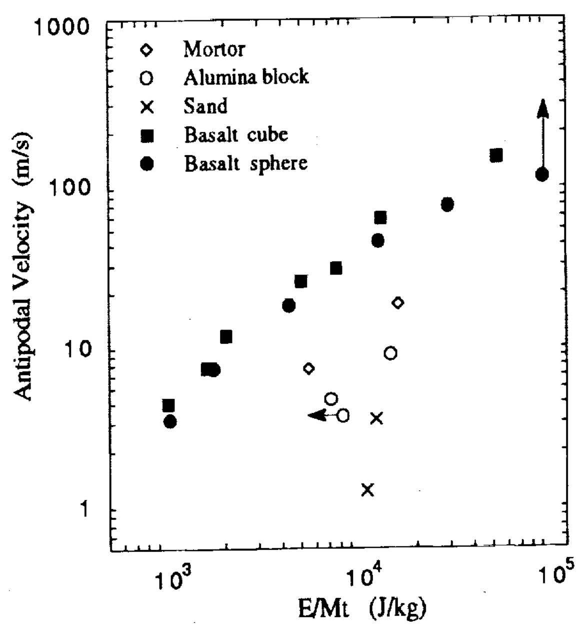


Fig. 2. V_as for porous and basalt[2] targets.

S256-90
ABS. ONLY

N94-20892

P-2

REGOLITH BRECCIA CONSISTING OF H AND LL CHONDRITE MIXTURE

Keizo Yanai and Hideyasu Kojima, Department of Antarctic Meteorites, National Institute of Polar Research, 9-10, Kaga 1-chome, Itabashi-ku, Tokyo 173 Japan

Antarctic meteorite Yamato-8424(Y-8424) is a regolith breccia that is homogenized mixture of H and LL chondrite components. The breccia consists mainly of a fine-grained material with mineral fragments of olivine, pyroxene and Fe-Ni metal with traces of plagioclase.

Y-8424 is a small irregular shaped stone(mostly complete) weighing 9 grams[1] and it is covered with a dull-black fusion crust. The surface of the stone shows a dark brown to brown to do weathering effect, however the interior(sawing surface) is very fresh with relatively large and very fresh Fe-Ni metal grains in dark grey fine material.

In the thin section (Fig. 1), Y-8424 shows typical negolith breccia consisting mainly of fine-grained matrix and less amount of mineral fragments. The mineral fragments are olivines, pyroxenes and Fe-Ni metal ranging 0.2-0.4 mm, excepting 1 mm Fe-Ni metal grain (center of bottom in Fig. 1). The matrix is fine grains under 50μm, consisting of olivines, pyroxenes, troilite, Fe-Ni metal and traces of plagioclase within very fine recrystallized. Most troilites distributed as under 30μm grains along the grain boundaries in the whole section. Some relatively large fragments may be traced as parts of chondrules. Therefore it indicates that the specimen is originallv chondrite.



Figure 1. Photomicrograh of the thin section of Yamato-8424, regolith breccia of H and LL chondrite mixture. Field view 6.5 mm wide.

The result of the EPMA analyses of constituent minerals show an unusual features such as Fig. 2. Olivines and low-Ca pyroxenes in both mineral fragments and fine grains in matrix, appear as the bimodal trequency patterns in their compositions. Olivines are recognized three groups for their compositions such as an average composition Fa17.5, Fa23.0 and

Fa28.7. Especially two remarkable peaks of them are conspicuous and they are corresponded to those of H and LL chondrite groups. Low-Ca pyroxenes are comprised largely two compositional groups such as an average composition Fs15.8 and Fs22.8, and they are also corresponded to H chondrite group and L-LL groups. Both olivines and pyroxenes drove from at least two chondrite groups, and they distribute uniformly in the whole section as mixture.

The texture and unusual compositional patterns indicate that Y-8424 is the regolith breccia and it is the mixture of the different chondritic materials. The mixing of the materials should be carried out on the parent bodies before the breaking of them. It seems that the Yamato-8424 regolith breccia had been formed by the mixing on the surface of the chondrite parent body(bodies) by the intense collisions of the H or L or LL chondrite bodies, during the early stage of the solar system.

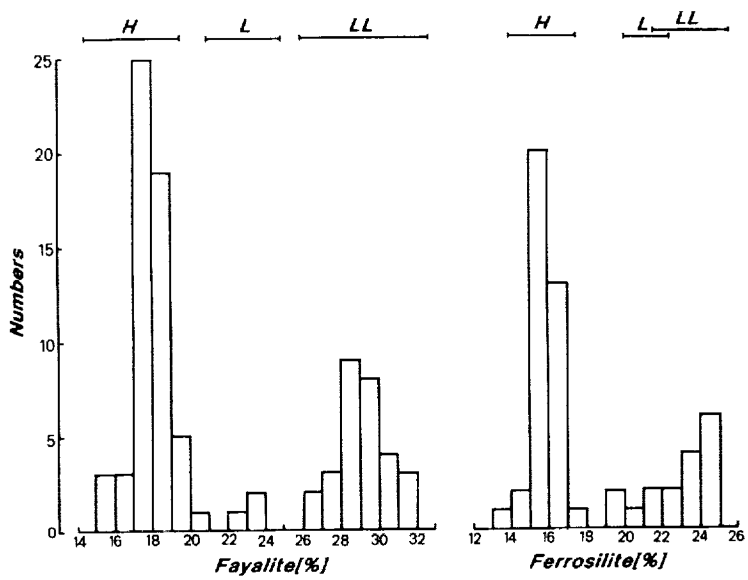


Figure 2. Frequencies of Fa and Fs compositions, correspond to H, L and LL chondrites.

Reference: [1] Yanai, K. and Kojima, H. (1987): Photographic Catalog of the Antarctic Meteorites. p298, NIPR Tokyo.

S257-90 ABS. ONLY

N94-20893

p. 2

CONSORTIUM REPORTS ON LUNAR METEORITES YAMATO 793169 AND ASUKA 881757, A NEW TYPE OF MARE BASALT; Keizo Yanai[1], Hiroshi Takeda[2], M. M. Lindstrom[3], M. Tatsumoto[4], N. Torigoe[4], K. Misawa[1], P. H. Warren[5], G. W. Kallemeyn[5], C. Koeberl[6], H. Kojima[1], K. Takahashi[7], A. Masuda[7], K. Nishiizumi[8]. [1]Natnl. Inst. Polar Res., 1-9-10 Kaga, Itabashi-Ku, Tokyo 173, Japan, [2]Mineral. Inst., Faculty of Sci., Univ. of Tokyo, Hongo, Tokyo 113, Japan, [3]SN2 NASA Johnson Space Center, Houston, TX 77058, [4]USGS, MS 963, Denver, CO, [5]Inst. Geophys. Planet. Phys., UCLA, Los Angeles, CA 90024, [6]Inst. Geochemistry, University of Vienna, Vienna, Austria, [7]Earth Sciences Lab, Riken, Wako, Saitama 351-01, Japan, [8]Dept of Chemistry, UCSD, La Jolla, CA 92093.

Consortium studies on lunar meteorites Yamato 793169 and Asuka 881757 (formerly Asuka-31) were performed to characterize these new samples from unknown locations in the lunar mare. Both meteorites are coarse-grained mare rocks having low Mg/Fe ratios (bulk mg'=30-35) and low TiO_2 (1.5-2.5% in homogenized bulk samples). They are intermediate between VLT and low-Ti mare basalts. Although these meteorites are not identical to each other, their mineral and bulk compositions, isotopic systematics and crystallization ages are remarkably similar and distinct from those of all other mare basalts. They appear to represent a new type of low-Ti mare basalt that crystallized at about 3.9Ga. These meteorites are inconsistent with the canonical correlation between the TiO_2 contents and ages of mare basalts and suggest that our knowledge of lunar volcanism is far from complete.

Samples: Because of the coarse-grained textures of these mare rocks, homogenized powders were prepared from large chips for bulk analyses. Samples of Y793169 allocated to this study include sample ,20 (512 mg), from which homogenized powdered samples ,41 (119 mg) and ,42 (125 mg) were prepared. Sample ,41 was sent to UCLA for further subdivisions to 5 groups for INAA. The bulk wet chemical analysis was done at NIPR using 0.639 g (,53) [1,2]. The homogenized sample of A881757 ,56 (5,908 g) was prepared from a 14.414 g chip (,20) by removing fusion crust. Sample ,56 was subdivided and sent to 5 INAA groups and one for age determination (,85). The bulk analyses at NIPR used 3.547 g (,51).

Mineralogy and petrography: Mineralogical studies showed that both meteorites are coarse-grained rocks consisting mainly of pigeonite, plagioclase and opaque minerals [1,2,3,4]. Pyroxenes are highly variable in composition, ranging from pigeonites and augites with mg' 50-60 to Fe-rich hedenbergites. Exsolution lamellae are rare in pyroxenes and have only been observed in a few grains. Plagioclases are often highly shocked (maskelynitized); they are highly anorthitic. On average, the FeO content in A881757 plagioclase is considerably lower than those in plagioclases of VLT and low-Ti mare basalts. Opaques and other residual phases are concentrated in areas of symplectite (A881757) or glassy mesostasis (Y793169). The most abundant opaque minerals are ilmenite, ulvöspinel and chromite. These opaque phases coexist with Fe-rich pyroxenes and Na-rich plagioclases, and minor amounts of fayalite, silica, troilite, metal and phosphate. The modal abundance of opaque phases varies between thin sections, but is consistently several percent, which is higher than that typically observed in VLT mare basalts. The bulk TiO_2 content calculated from mineral compositions and modal proportions in one thin section is 1.8 wt %, which is within the range of TiO_2 contents measured in bulk samples (below).

Major and trace element composition: Major element analyses of homogenized powders of Y793169 and A881757 determined by INAA and FB-EMP[4,5,6,7] are very similar to one another and only slightly different from the earlier NIPR wet chemical analyses [1]. Thus the homogenized samples appear to be fairly representative samples, in contrast to the small chip of A881757 analyzed by [8]. Both mare meteorites have very low Mg/Fe (bulk mg' 31-35) and low TiO_2 (1.5-2.5%). Variations in Mg/Fe and TiO_2 are related to heterogeneity in modal proportions of opaque phases. These analyses bridge the gap from VLT to low-Ti mare basalts. Both meteorites have LREE-depleted patterns that are flat in the middle-heavy REE with a small negative Eu anomaly. REE concentrations are higher than those in most VLT and low-Ti mare

LUNAR METEORITES YAMATO 793169 AND ASUKA 881757; Yanai K. et al.

basalts. The very high Sc concentrations are the most significant difference between A881757 and Y793169 meteorites and other mare basalts. Sc contents in the meteorites are a factor of two higher than in VLT and low-Ti mare basalts. A companion abstract [9] discusses these high Sc concentrations and shows that they are strong evidence for a new magma type.

Ages and isotopic systematics: The U-Pb ages (USGS) of A881757 (3.93 Ga) and Y793169 (3.94 Ga) are slightly older than the Rb-Sr [3.84±0.03 (USGS); 3.75±0.07 (Riken)] and Sm-Nd [3.87±0.05 (USGS); 3.82±0.09 (Riken)] ages of A881757. The younger Sm-Nd age of Y791369 (3.47±0.18) is probably due to a later disturbance of the Sm-Nd system [10]. Despite these variations, we note that the reliable ages of these mare meteorites (3.75-3.94 Ga) are distinctly higher than those of returned samples of low-Ti (3.2-3.5 Ga) and for VLT (3.4 Ga) mare basalts. The Pb isotopic composition of these mare meteorites are non-radiogenic and the estimated $^{238}U/^{204}Pb$ (μ) values for the source are 7 and 9 ± 6, respectively. These μ values are extremely low compared with those of typical lunar mare basalts (100-300), and are even lower than those (25-55) estimated for green and orange glasses, and that (12-15) for Luna 24170 VLT basalt [11]. The εNd values for the A881757 and Y793169 sources (7.3;5.8) are higher than that (3.2) for Luna VLT basalt 24170 [12], suggesting that the source of mare meteorites is different from that for Luna 24 VLT basalt. The high εNd is consistent with the REE pattern which suggests a higher Sm/Nd ratio for the meteorite source region than for those of other mare basalts. The initial $^{87}Sr/^{86}Sr$ value for A881757 of 0.69910 at 3840 Ma indicates that the $^{87}Rb/^{86}Sr$ value for A881757 is 0.18. This value is similar to those of Luna 16 LT and Luna 24 VLT basalts. These low U/Pb and large positive εNd values for these meteorites are different from those for low-Ti and VLT basalts and imply isotopically distinct source reservoirs for these mare meteorites.

Exposure histories: Both Y793169 and A881757 were exposed to cosmic rays in a small body in space (4π exposure) for approximately one million years. They fell to Earth as independent falls, however, based on comparison of ^{10}Be, ^{26}Al and ^{36}Cl results with ^{21}Ne of Eugster [13]. If both meteorites were ejected from the Moon in the same event, they were both buried at least several meters below the lunar surface before ejection. Possibly A881757 was buried a few meters deeper than Y793169.

Conclusion: Meteorites Y93169 and A881757 are coarse-grained igneous rocks from the lunar mare. They are very similar to each other in mineral and bulk composition, crystallization ages, isotopic systematics and time of blast-off from the moon. Their bulk compositions are distinct from those of Apollo and Luna mare basalts, but are generally intermediate between VLT and low-Ti mare basalts [14]. Their crystallization ages are similar to those of high-Ti basalts, but much older than those of VLT or low-Ti basalts, and their isotopic characteristics are unique. These lunar meteorites represent a new type of mare magma which does not fit standard classification schemes nor correspond to previous ideas of relationships between TiO2 contents and ages. Each new sample of the moon's surface provides important clues to lunar evolution and sometimes challenges current theories.

ACKNOWLEDGMENTS: We are indebted to NIPR for the consortium samples, and to Drs. H. Eugster and J. S. Delaney for their data and for discussion. We thank the PIs of the studies and their co-investigators who are not listed in this abstract for their technical assistance.

REFERENCES: [1] Yanai K. and Kojima H. (1991) Proc. NIPR Symp. Antarct. Meteorites, 4, 70-90. [2] Yanai K. (1991) Proc. Lunar Planet. Sci. 21, 317-324. [3] Takeda H. et al. (1992) Abstr. 17th Symp. Ant. Met., NIPR, 109-112 [4] Koeberl C. et al. (1992) Ibid. 219-222. [5] Warren P. H. and Kallemeyn G. W. (1992) Ibid. 113. [6] Fukuoka T. (1992) Ibid. 251-253. [7] Lindstrom M. M., unpublished. [8] Lindstrom M. M. et al. (1991) Abstr. 16th Symp. Antarctic Meteorites, 102-105. [9] Warren P.H. and Lindstrom M.M. (1993) this volume. [10] Torigoe N. et al, this volume. [11] Wasserburg G. J. et al (1978) Mare Crisium, 657-678. [12] Unruh D. M. and Tatsumoto M. (1978) Ibid. 679-694. [13] Eugster O. (1992) Abstr. 17th Symp. Ant. Met., NIPR, 208-210. [14] Papike J. J. et al (1976) Rev. Geophys. Space Phys. 14, 475-540.

5258-90
ABS. ONLY

N94-20894

PRELIMINARY AEM STUDY OF THE MICROSTRUCTURE AND COMPOSITION OF METAL PARTICLES IN ORDINARY CHONDRITES ; C. W. Yang, D. B. Williams, and J. I. Goldstein, Department of Materials Science and Engineering, Lehigh University, Bethlehem, PA 18015

p. 2

The purpose of this study is to examine the microstructure and composition of the metal particles in ordinary chondrites using analytical electron microscopy (AEM) techniques. Since the phases produced within the metal particles are very fine, the application of various AEM techniques for structural and chemical characterization is critical. However, thin specimen preparation for AEM study has proven very difficult because of the matrix silicate which is present. This is the first AEM study of the metal particles in chondrites. A type 6 chondrite, Saint Severin (LL6), was selected for examination because the metal phases have been reheated into the single phase taenite region (>700°C), and cooled slowly to lower temperatures. A combination of electron optical instruments was employed including a field emission gun (FEG) JEOL 840F high resolution scanning electron microscope (HRSEM), a JEOL 6300F FEG-HRSEM, a Philips 400T AEM, and a JEOL 733 electron probe microanalyzer (EPMA).

Figs. 1a and 1b are HRSEM images of a taenite particle in the Saint Severin ordinary chondrite. The taenite particle is surrounded by silicate (S). From the high Ni border moving into the particle, the microstructure includes the outer taenite rim (TR) which corresponds to clear taenite 1 (CT1) in iron meteorites (52 - 46 wt% Ni), and the cloudy zone (CZ, 45 - 30 wt% Ni). The outer taenite rim contains three sub-zones (1, 2, 3). The size of the constituents of the cloudy zone changes along the Ni concentration gradient. Fig. 1c shows further high magnification image of the center of the cloudy zone. The microstructure shown in Fig. 1 is consistent with the observation of Duffield[1]. The microstructure and the chemistry are closely related to each other.

Fig. 2a is a transmission electron microscope (TEM) bright field image of the cloudy zone in Saint Severin. The average Ni content of this region is 37 wt% Ni. Comparing the size of the phases with the HRSEM image (Fig.1c) and Ni content determined by EPMA, this region is also in the middle of the cloudy zone. The CZ region in the taenite particles contains two phases.The structure of the cloudy zone of Saint Severin is very similar to that of Carlton iron meteorite and Estherville stony-iron meteorite as investigated by Zhang[2] and Reuter[3], respectively. The cloudy zone forms by spinodal decomposition[3]. According to a recent Fe-Ni phase diagram[4], the taenite in the composition range from 41 wt% Ni to 28 wt% Ni transforms spontaneously into Ni-rich regions (light regions in Fig. 2a, island phase) and Ni-poor regions (dark regions in Fig. 2a, honeycomb phase) defined by the miscibility gap. The Ni-rich region undergoes the ordering transformation and forms tetrataenite. As the temperature decreases, the Ni-poor region decreases in Ni content and transforms to martensite. The selected area diffraction (SAD) pattern (Fig. 2c), as indexed in Fig. 2d, is composed of the fcc <110> zone axis pattern, two bcc <111> zone axis patterns which are in a twinning orientation relationship, and weak superlattice diffraction spots which can be observed on the negative although they are not clear on the print. The superlattice spot is due to the ordering of the parent fcc phase to tetrataenite. The twinning plane is $(002)_{fcc}$. The centered dark field (CDF) image (Fig. 2b) taken from a $(0\bar{1}1)$ bcc spot in Fig. 2c shows that the honeycomb phase has a bcc structure. The microstructure of other taenite particles in Saint severin will also be described.

References [1] Duffield C.E., Williams D.B., and Goldstein J.I. (1991) *Meteoritics* , *26* , 97 [2] Zhang J. (1991) *Ph.D Dissertation, Lehigh Univ.* [3] Reuter K.B., Williams D.B., and Goldstein J.I. (1988) *Geochim. Cosmochim. Acta* , *52* , 617 [4] Reuter K.B., Williams D.B., and Goldstein J.I. (1989) *Met. Trans., 20A* , 719

PRELIMINARY AEM STUDY OF THE METAL PARTICLES IN CHONDRITES: Yang C. W. et al.

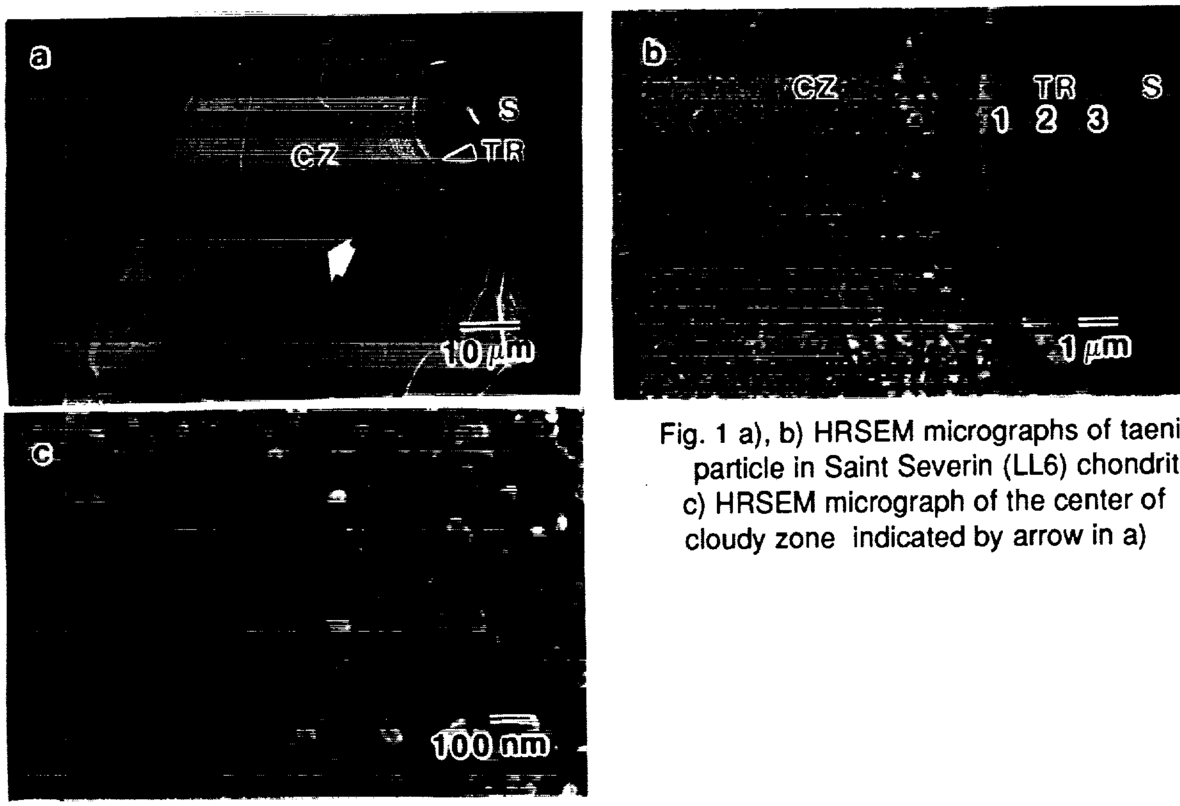


Fig. 1 a), b) HRSEM micrographs of taenite particle in Saint Severin (LL6) chondrite, c) HRSEM micrograph of the center of cloudy zone indicated by arrow in a)

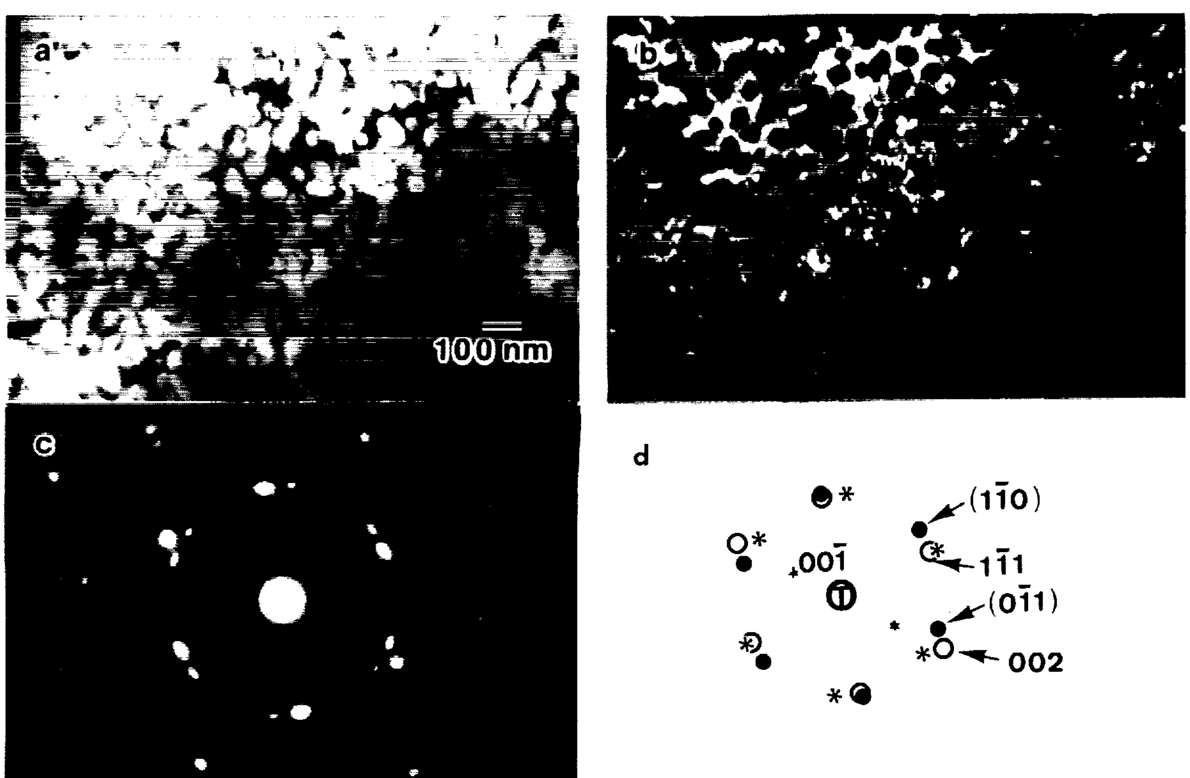


Fig. 2 a) TEM bright field image of CZ region of Saint Severin chondrite, b) centered dark field image from a (01̄1) bcc spot, c) SAD pattern, d) indexing of SAD pattern; ● hkl: bcc[111] zone axis pattern; ∗hkl: another bcc[111] zone axis pattern; O hkl: fcc[110] zone axis pattern; • superlattice diffraction spots (observed on the negative)

Micrometeorite Pre-Solar Diamonds from Greenland Cryoconite?

P.D.Yates.

Space Science Department, European Space Research and Technology Center, 2200 AG Noordwijk, The Netherlands.

Introduction.

An acid-resistant residue prepared from Greenland cryoconite has been investigated to determine whether the micrometeorite component within the cryoconite contains pre-solar material analogous to that found in primitive chondritic meteorites. The residue has been analysed for carbon content and stable isotopic composition [1], by electron probe micro-analysis (EPMA) for major element chemistry and then by a combination of X-ray diffraction (XRD) and transmission electron microscopy (TEM) to elucidate the structure of any constituent mineral phases. The cryoconite sample, which was collected *ca*. 25km inland of the ice margin at the latitude of Søndre Strømfjord on the west coast of Greenland, was processed by Dr.J.W.Arden at the University of Oxford following procedures used on bulk meteorite samples for the isolation of pre-solar dust components (see [2] for details of the experimental methods).

Results.

1) Stable carbon isotopes.

The results of the stable carbon isotope analysis have been previously reported [1], but suggested that the residue contained meteoritic pre-solar diamond and silicon carbide (SiC). Furthermore, the abundance of these components within the micrometeorite fraction of the cryoconite was estimated to be in excess of the maximum values obtained for the most primitive meteorites [3].

2) Electron probe micro-analysis.

The major element chemistry of the residue revealed it to be largely constituted of a mixture of micron-sized metallic alloy grains. These grains were composed of aluminium, titanium or a chromium-titanium-iron composite, and were often found embedded in larger (up to *ca*.400μm diameter) grains that were rich in silicon (Si) and zirconium (Zr).

3) X-ray diffraction.

The residue yielded a complex pattern of diffraction lines, but from which only the mineral zircon ($ZrSiO_4$) could be positively identified. The presence of zircon explained the Si and Zr from the EPMA results, but it was somewhat surprising, considering their abundance within the residue, that no lines characteristic of the metallic alloys were identified.

4) Transmission electron microscopy.

The TEM results confirmed the presence of zircon, but also revealed rutile (TiO_2) and, more importantly, diamond. The diamonds were present within the residue as an aggregate of crystals with a mean grain size of *ca*.5nm; this is comparable to that of pre-solar diamonds isolated from primitive meteorites [4]. This being said, individual diamonds were observed within the aggregate approaching 30nm in diameter which is greater than any reported from the primitive meteorites. The aggregation of the diamonds allowed a good electron diffraction pattern to be obtained; three rings at 2.06Å, 1.26Å and 1.08Å were seen, which corresponds to diamond (111), (220) and (311) respectively. These results show an excellent correlation with the values obtained for diamonds from an acid-resistant residue of Allende, where spacings of of 2.06Å, 1.26Å and 1.07Å were observed [4].

Unfortunately no SiC grains were identified. However, pre-solar SiC is present within the primitive meteorites at a reduced concentration with respect to pre-solar diamond (*i.e.* a maximum of 941ppm for diamond and 14ppm for SiC [3]). Correspondingly, if the micrometeorites mirror their larger counterparts in the relative concentrations of pre-solar

material, then intuitively SiC would be more difficult to isolate. It is also apparent that this problem would be exacerbated if, unlike the diamonds, the SiC did not aggregate together during the preparation protocols.

Conclusions.

The bulk of the cryoconite residue was found to be composed of metallic alloys. It is well established that aerospace activities have produced a debris belt about the Earth composed largely of metals, refractory oxides and silicate grains [5]. Orbital decay of such debris particles allows them to enter the Earth's atmosphere, where they are subject to the same collection mechanisms as extraterrestrial dust. It is therefore perhaps not surprising that similar material has become concentrated along with the micrometeorites in the cryoconite samples. Given this possible source it is perhaps feasible to explain why the alloys in the residues could not be identified by XRD, as intuitively the ablation processes that formed them are not replicated in the formation of terrestrial alloys from which the XRD standards are derived.

The stable carbon isotopic analysis of the residue had suggested the presence of pre-solar diamond and SiC components analogous to those isolated from the primitive meteorites. Examination of the residue by TEM has confirmed these tentative conclusions for the diamond, although no SiC was isolated. The carbon isotope analysis also implied that the concentration of the pre-solar material within the micrometeorite fraction of the cryoconite was greater than even the most primitive meteorites. Although the TEM results can not verify these conclusions, it is still considered possible that they could be valid, *i.e.* some micrometeorites may be composed of almost pure fine grained matrix. Notwithstanding that the mean grainsize of the cryoconite diamonds was similar to that from the primitive meteorites, a few larger grains were observed. It is therefore possible to speculate that the respective sources of the diamonds for the micrometeorites and their larger counterparts may be different.

Further work.

Two new residues have been prepared using larger aliquots of cryoconite in an attempt to verify the results reported here. These residues are currently undergoing TEM and stable carbon isotope analysis. Pre-solar SiC and diamonds are known to be the hosts of isotopically light nitrogen, possessing mean $\delta^{15}N$ values of -625‰ [6] and -343‰ [7] respectively, and consequently the residues are also scheduled for stable nitrogen istopic analysis

Acknowledgements.

Dr. Martin Lee performed the TEM analyses at the University of Essex, and Dr. Gordon Cressey of the Natural History Museum is thanked for interpretation of the XRD results.

References.

[1] Yates P.D., Arden J.W., Wright I.P., Pillinger C.T. and Hutchison R. (1992) *Meteoritics*, **27**, 309. [2] Alexander C.M.O'D., Arden J.W., Ash R.D. and Pillinger C.T. (1990) *Earth and Planet.Sci.Letts.*, **99**, 220. [3] Huss G.R. (1990) *Nature*, **347**, 159. [4] Lewis R.S., Tang Ming, Wacker J.F., Anders E. and Steel E. (1987) *Nature*, **326**, 160. [5] Kessler D.J. and Cour-Palais B.G. (1978) *J.Geophys.Res.*, **83**, 2637. [6] Russell S.S., Ash R.D., Pillinger C.T. and Arden J.W. (1991) *Meteoritics*, **26**, 390. [7] Russell S.S., Arden J.W. and Pillinger C.T. (1991) *Science*, **254**, 1180.

5260-91 ABS. ONLY

N94-20896

THE CONNECTION BETWEEN VENUS' FREE OBLIQUITY AND ITS CMB OBLATENESS;

C. F. Yoder, Jet Propulsion Laboratory,Cal Tech,Pasadena,CA 91109.

p. 2

The most striking feature of Venus rotational state is its slow retrograde rotation which is apparently maintained by a balance between solid tidal friction and thermal tidal torques[1]. Solid tides tend to drive the spin toward sychronous rotation while thermal tides drive it away. A balance is achieved at a specific rate because of the inverse frequency dependence of the thermal tide[2] to the semi-diurnal heating. Atmospheric models have been constructed to estimate the thermal tidal torque[3,4] based on ground heating. The solid friction dissipation factor $Q \approx 50$ can be deduced assuming rotation has achieved steady state. The most perplexing feature of Venus orientation is its non-zero free obliquity $\varepsilon \approx 1.5°$ relative to its orbit[4]. Although solid tides and perhaps atmospheric tides tend to increase the free obliquity on a time $1/K_t = 4QCa^3\omega/(3k_2n^2M_{sun}R^3) \approx 1\times10^8$yr, viscous friction(CMF) at a core-mantle boundary(CMB) resulting from the differential angular orientation $\Delta\varepsilon$ of the core and mantle spin axes should have damped the free obliquity on a time scale as short as 10^6 yr[5,6].One means of achieving a balance similar to that controlling rotation is to introduce a comparatively large CMB ellipticity $e_c = (C_c-A_c)/C_c = (a_c-c_c)/a_c$ to reduce $\Delta\varepsilon$ such that there is a balance between solid-thermal tides and CMF. The balance depends not so much on the potential frequency dependence of the tides as on the quadratic dependence of CMF on $\Delta\varepsilon$ if the layer is turbulent.

The CMF torque acting on the fluid core is $K_c(\omega-\omega_c)$. For turbulent CMB friction[7], I find K_c is logarithmically dependent on core viscosity ν, and

$$K_c = \frac{45\pi}{32}\left(\frac{\delta u}{u_o}\right)^3 \sin\Delta\epsilon|\omega|; \quad \frac{\delta u}{u_o} = \frac{0.4}{\ln\left|\frac{\delta u}{u_o}\frac{\sin\Delta\epsilon\omega R_c^2}{\nu}\right|}$$

Generally, these equations must be solved by iteration. The value for K_c is near $7\times10^{-3}\Delta\varepsilon|\omega|$ for the expected core parameters.

The dynamical model describing the response of the core spin m_c in the space-fixed frame is

$$(D+i\sigma_c+K_c)\,m_c = -i\omega Dp$$

where $D=d/dt$ and $\sigma_c = -e_c\,\omega$ is the unperturbed, free core nutation(FCN) frequency. The mantle pole variable $p = \sin\varepsilon\ \exp{-i\phi}$ depends on both the obliquity and the orientation angle ϕ of the equator on the invariable plane.

The whole body dynamical equation appropriate for slow precessional motion is[8]

$$((1-e_o)D^2+\omega(iD-\sigma_o-iK_{ta}))\,p = -\omega\sigma_o P-\alpha Dm_c$$

where $P=\sin I\ \exp{-i\Omega}$ describes the slowly changing orbit orientation, $\sigma_o = -1.5e_o\,n^2/\omega$ is the

unperturbed precession rate of the free obliquity, $e_o=J_2(MR^2/C)$ is the dynamic ellipticity, $\alpha=C_c/C$ is the ratio of moments of inertia and $K_{ta}=\lambda K_t$ is the combined solid-thermal tide contribution($\lambda \approx 2.5$).

The precession frequency associated with the free obliquity is real if $K_{ta}=(\sigma_o/\sigma_c)^2 K_c$. Now K_c is proportional to $\Delta\varepsilon$ and from the core equation we find $\Delta\varepsilon=(\sigma_o/\sigma_c)\varepsilon$. The resulting value for e_c is (adopting Q=50, α=0.1, kinematic viscosity ν=0.1 cm^2 /sec),

$$e_c=30e_o=4x10^{-4}$$

This is to be compared with Earth's non-hydrostatic CMB ellipticity=1.2×10^{-4} [9]. One possible explanation for this large core e_c is that Venus lower mantle boundary layer (i.e. equivalent D" layer) is either much thinner or stiffer or even absent. In any case, this large e_c must be matched with a large and negative density anomaly within the lower mantle to contrabalance the contribution of e_c to the external J_2 gravity coefficient.

References:[1]Gold, T. and S. Soter(1969) *Icarus*, **11**, 356-366.[2]Ingersoll, A.P. and A. R. Dobrovolskis(1978) *Nature*,275, 37-38.[3]Dobrovolskis, A.R. and A.P. Ingersoll(1980) *Icarus*, **41**,1-17.[4]Dobrovolskis, A.R.(1980) *Icarus*, **41**, 18-35.[5]Ward,W. R. and DeCampli(1979)*Ap. J. (Letters)*,**230**,*l*117.[6]Yoder, C.F. and W.R. Ward(1979) *Astrophys. J.*, **233**, L33-L37. [7]Yoder, C. F.(1981) *Phil. Trans. Roy. Soc. London*, **A303**,327-246[8]Sasao, T., S. Okubo and M. Saito(1969) in Nutation and the Earth's Rotation, (M.L. Smith and P.L. Bender eds.),165-183. [9]Herring, T.A., C. R. Gwinn and I. I. Shapiro(1986)*J. Geophys. Res.*, **91**, 4755-4765.

TRACE ELEMENT COMPOSITIONS OF SPINEL-RICH REFRACTORY INCLUSIONS FROM THE MURCHISON METEORITE;

S. Yoneda[1], P.J. Sylvester[1,*], S.B. Simon[1], L. Grossman[1,2] and A. Hsu[3]. [1]Department of the Geophysical Sciences, [2]Enrico Fermi Institute, The University of Chicago, Chicago, IL 60637, USA. [3]Illinois Math and Science Academy, Aurora, IL 60506, USA. *Present address: Research School of Earth Sciences, The Australian National University, GPO Box 4, Canberra, ACT 2611, Australia.

Abstract: Three spinel-rich, perovskite-bearing, pyroxene-rimmed, hibonite-free inclusions from the Murchison C2 chondrite have volatility-controlled, modified group II REE patterns. Two have high Eu/Yb ratios, two have small positive Ce anomalies and one has high refractory siderophiles for a group II inclusion. Two additional spinel-rich inclusions have subchondritic Ce/La ratios and negative Eu and Yb anomalies, the Eu anomalies being larger than the Yb ones. One of these inclusions is enriched in La relative to all HREE and the other is enriched in HREE relative to all LREE except La, possibly suggesting the presence of an ultrarefractory component in the latter. One hibonite-rich inclusion has a group III REE pattern with a negative Ce anomaly. A calcium dialuminate-bearing inclusion known to have crystallized from a melt at 2100-1800K has a modified group II REE pattern, rather than a pattern which would be predicted from the evaporation expected from such a droplet, *e.g.*, a group III or ultrarefractory pattern. Volatile element contents of these inclusions are among the lowest found in any refractory inclusions.

Introduction: Recent ion microprobe studies of refractory lithophiles in hibonite-bearing inclusions in C2 chondrites reveal a huge variety of volatility-controlled fractionations among these elements [1-4]. It is probable, however, that, among refractory inclusions in these meteorites, pyroxene-rimmed, spinel-rich, hibonite-free objects are at least as abundant as hibonite-bearing ones. The only trace element data reported for spinel-rich, hibonite-free inclusions come from ion microprobe studies of lithophile elements in Mighei inclusions [5,6]. Here we report preliminary INAA data on refractory lithophile and siderophile elements in splits of five hibonite-free, spinel-pyroxene inclusions in addition to two hibonite-bearing ones, all weighing between 3 and 11 μg and all newly collected from the Murchison C2 chondrite by freeze-thaw disaggregation followed by heavy liquid separation and hand-picking, as in [7]. The remaining fraction of each inclusion was made into a polished thin section and studied by SEM and EPMA.

M92B1, B3 and B7: These three inclusions are very similar to one another in mineralogy and petrography, all having a massive core of Mg-, Al-spinel with numerous, accessory perovskite grains (<5-10 μm) and a fluffy rim composed mostly of aluminous diopside. All three also have volatility-controlled, modified group II REE patterns (Fig. 1). These formed by condensation of the REE remaining in the gas after removal of the most refractory REE in an ultrarefractory condensate at a lower temperature than was the case for normal group II REE patterns [8-10]. This causes fractions of the most refractory of the LREE to be removed along with the refractory HREE, resulting in smaller LREE/HREE ratios and smaller fractionations among the HREE than is the case for normal group II patterns. Thus, La/Lu is 1.98±0.06, 3.98±0.26 and 1.16±0.04 and Tb/Lu is 0.51±0.10, 0.83±0.20 and 0.75±0.06 relative to C1 chondrites in B1, B3 and B7, respectively, compared to values around 50 and 20 in normal group II patterns [11]. Unusual features of the REE patterns include high Yb/Eu ratios in B1 and B3, 3.1±0.5 and 4.5±1.2, respectively, and small positive Ce anomalies in B1 and B7, with Ce/La of 1.56±0.03 and 1.21±0.03, respectively, all relative to C1 chondrites. The positive Ce anomalies are probably due to the fact that Ce is more volatile than La in a gas of solar composition, causing more of the Ce than the La to be left in the gas after removal of the refractory REE fraction in the earlier condensate [8]. The shape of the REE pattern of B1, including its positive Ce anomaly and its Eu/Yb ratio, is almost identical to that of spinel-perovskite nodule 2 of Mighei 3483-3-8 [5]. Enrichment factors for refractory siderophiles are uniformly low in B1 and B3, those for Ir being 0.115±0.003 and 1.75±0.03, respectively, relative to C1 chondrites, but are extraordinarily high for group II inclusions [12] in B7, with Ir=11.1±0.2 × C1.

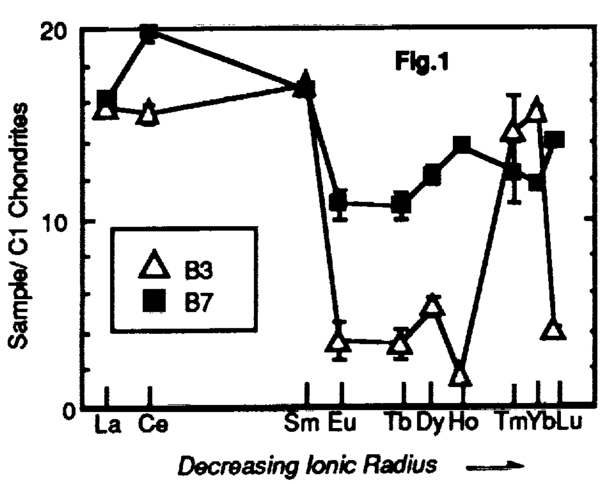
M92B2, B5 and B9: These three inclusions differ in mineralogy and petrography from one another but are grouped together because of similarities in their REE patterns. B5 has the mineralogical and textural characteristics of the three spinel-rich inclusions discussed above. B9 consists of massive spinel but differs from the other spinel-rich inclusions in containing irregular grains (<5 μm) of accessory melilite in addition to perovskite and in lacking a pyroxene rim. B2 is composed of numerous plates of hibonite (~40 μm across) with minor perovskite. All three have REE patterns with affinities to group IIIs, *i.e.*, they have large negative Eu and Yb anomalies, with B2, B5 and B9 having Eu/Sm ratios of 0.15±0.04, <0.071 and 0.19±0.07, respectively, and Yb/Lu ratios of 0.094±0.006, 0.360±0.005 and 0.52±0.02, respectively, all relative to C1 chondrites (Fig. 2). Such patterns are thought to have formed by condensation of REE at a high enough temperature that the condensed fraction of Eu and Yb, the two most volatile REE, was considerably less than that of all the other REE [13]. Eu anomalies are larger than Yb anomalies in B5 and B9, a characteristic found in a minority of hibonite-rich samples [3, 14] but also found in the group III, spinel-rich inclusion Mighei 3483-3-4 [5]. In addition, all three of these inclusions have negative Ce anomalies, the Ce/La ratios of B2, B5 and B9 being 0.79±0.02, 0.49±0.01 and 0.37±0.02, respectively, relative to C1 chondrites. This may be due to a slightly higher equilibration temperature for these

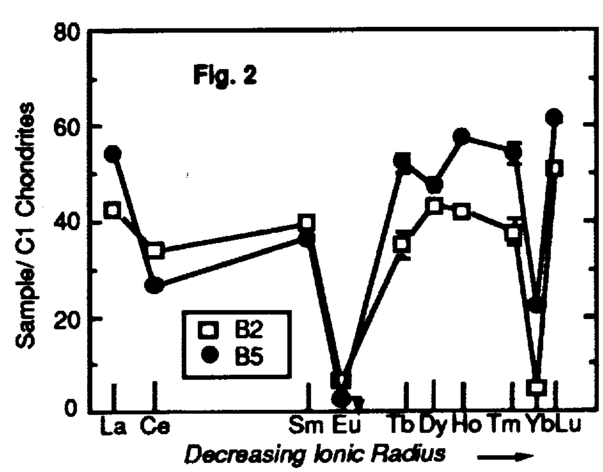
inclusions than is the case for normal group III inclusions, causing Ce, the next most volatile REE after Eu and Yb, to be incompletely condensed as well. Otherwise, B2 is the closest of the three to having a normal group III REE pattern, in that the other REE are approximately uniformly enriched at about 41 × C1 chondrites. In B9, however, La has a much higher enrichment factor, ~27, than all other REE which, except for Ce, Eu and Yb, have approximately uniform enrichment factors of ~15, relative to C1 chondrites. In B5, the enrichment factor for La, 54, is not only much higher than that for Ce but also than that for Sm, 36, suggesting that it may be incorrect to have inferred a negative Ce anomaly for this object based on the previously mentioned, low Ce/La ratio. Except for La, LREE are depleted relative to all HREE except for Yb, with enrichment factors varying from ~47 for Dy to ~61 for Lu, possibly due to the presence of an ultrarefractory component, as in [2]. In each of these inclusions, refractory siderophiles have uniform enrichment factors which are lower than those of most refractory lithophiles, that for Ir being 0.16±0.01, 1.24±0.02 and 2.93±0.04 in B2, B5 and B9, respectively.

M92B6: This is a spinel-, hibonite- and calcium dialuminate-bearing inclusion that appears to have crystallized from the outside of a molten droplet inward at extremely high temperatures [15]. Despite the fact that the temperature interval for crystallization of this object is so high, from at least 2100 to 1800 K, that the droplet would be extremely unstable with respect to evaporation in a low-pressure gas of solar composition, the REE pattern is neither group III nor ultrarefractory, patterns which could result from high-temperature evaporation, but instead is a modified group II, with C1 chondrite-normalized enrichment factors for LREE, Tb, Tm and Lu being ~35, 14, 23 and 2.4, respectively. Group II patterns were also found in all four calcium dialuminate-bearing inclusions from the Saharan meteorites investigated by BISCHOFF et al. [16]. As is usual in group II inclusions [12], refractory siderophiles are enriched in B6 much less than in most group I inclusions, Ir having an enrichment factor of only 1.1 relative to C1 chondrites.

Volatile Elements: As was also found by EKAMBARAM et al. [14] in their trace element study of refractory inclusions in Murchison, these objects have much lower concentrations of volatile elements than coarse-grained inclusions in Allende. Except for 1950 ppm Na in B3 and 28 ppb Au in B2, the Na concentrations of all inclusions studied here lie in the range of 265-640 ppm and the Au concentrations are all <4.3 ppb, placing them well within the field of coarse-grained inclusions from the reduced subgroup of C3V chondrites, the refractory inclusions with the lowest concentrations of these elements [17]. Despite the pervasive, low-temperature, parent-body alteration history alleged for C2 chondrites such as Murchison, such processes have had only a trivial impact on the volatile element contents of refractory inclusions in this meteorite.

References: [1] FAHEY, A. J. et al. (1987) *GCA* **51**, 329. [2] HINTON, R.W. et al. (1988) *GCA* **52**, 2573. [3] IRELAND, T.R. et al. (1988) *GCA* **52**, 2841.[4] IRELAND, T.R. (1990) *GCA* **54**, 3219. [5] MACPHERSON, G.J. and DAVIS, A.M. (1991) In *LPS XXII*, p. 841. [6] DAVIS, A.M. and MACPHERSON, G.J. (1992) *Meteoritics* **27**, 212. [7] MACPHERSON, G.J. et al. (1980) In *LPS XI*, p. 660. [8] MACPHERSON, G.J. et al. (1989) *Meteoritics* **24**, 297. [9] MAO, X.-Y. et al. (1990) *GCA* **54**, 2121. [10] SYLVESTER, P.J. et al. (1992) *GCA* **56**, 1343. [11] CONARD, R. (1976) M.S. Thesis, Oregon State University. [12] GROSSMAN, L. and GANAPATHY, R. (1976) *GCA* **40**, 967. [13] BOYNTON, W.V. (1978) In *Protostars and Planets*, p. 427. [14] EKAMBARAM, V. et al. (1984) *GCA* **48**, 2089. [15] SIMON, S. et al. (1993) This volume. [16] BISCHOFF, A. et al. (1992) *Meteoritics* **27**, 204. [17] BISCHOFF, A. et al. (1987) In *LPS XVIII*, p. 81.





S262-90
ABS. ONLY

p. 2

INTER- AND INTRA- CRYSTALLINE OXYGEN ISOTOPE DISTRIBUTION OF FASSAITES IN ALLENDE CAI; Hisayoshi Yurimoto [1], Hiroshi Nagasawa [2] and Yoshiharu Mori [3], [1] Institute of Geoscience, The University of Tsukuba, Tsukuba, Ibaraki 305, Japan, [2] Department of Chemistry, Gakushuin University, Mejiro, Tokyo 171, Japan, [3] National Laboratory for High Energy Physics (KEK), Tsukuba, Ibaraki 305, Japan.

Calcium, aluminium-rich inclusions (CAIs) from carbonaceous chondrite are believed to be among the first solids to have formed in the early solar system and thus to preserve a record of conditions and processes that prevailed early in the solar nebula. We have measured inter- and intra- crystalline oxygen isotope distribution of fassaite in Type B1 CAI of Allende meteorite. Secondary ion mass spectrometry (SIMS) using negative Au^- primary ion was applied to *in situ* oxygen isotope ratio analysis on an polished thin section of the CAI.

Samples and Experimental Methods: The sample used in this study was a polished thin section (HN3-1c) from Allende HN3-1 Type B1 CAI. Petrological characteristics of the inclusion is described by NAGAHARA et al.[1]. Oxygen isotope data for individual minerals in the inclusion were reported by Mayeda et al. [2]. The polished thin section was coated with ~30 nm of gold film for SIMS analysis. Oxygen isotope ratios were measured by the Tsukuba University CAMECA IMS-3F ion microprobe equipped with BLAKE-V ion source [3]. All O isotopic measurements were made with a focused negative primary ion beam of gold. Primary beam currents were adjusted for each run to obtain a $^{16}O^-$ count rate of ~3×10^5 counts s^{-1}. The beam size was 10~20 μm in diameter. A mass resolution power was set to ~2,000 (1% valley), which was sufficient to resolve all significant interferences. Measurements were made by cycling through the mass sequences 16 and 18 in a magnetic peak jumping mode. After the magnetic peak jumping, a precise peak centering of each mass was made by electrostatic peak switching scan. Principle of the electrostatic peak switching equipment was described by SLODZIAN et al. [4]. Secondary ion signals were detected with electron multiplier operated in a pulse counting mode. Signals measured in the electron multiplier were corrected for the counting system dead time. The isotopic composition measured by the SIMS differs from true isotopic composition of the sample by the matrix dependent instrumental mass fractionation. In order to correct the instrumental mass fractionation, a terrestrial augite megacryst from alkali-olivine basalt, Taka-shima, Japan was prepared as an internal standard. A measurement run consisted of 100 cycles was divided into "blocks" of 10 cycles each for purpose of time interpolation and peak centering.

Results and Discussion: Intra and inter-crystalline distribution of $\delta^{18}O$ values for fassaite crystals in HN3-1 CAI are shown in Table 1. The delta values were represented the deviation from the terrestrial volcanic augite standard from Taka-shima, Japan. Two distinguished types of fassaite in the CAI were analyzed in this study. One is the large, blocky fassaite crystals, the other is the fassaite crystals enclosed in melilite in the interiors (core melilite) of the CAI. No discrepancy of oxygen isotope compositions were observed for both types of fassaite grains

OXYGEN ISOTOPE DISTRIBUTION IN ALLENDE CAI: Yurimoto et al.

analyzed, which value are about -30 ‰ relative to the terrestrial volcanic augite. Slightly large value of #07 was due to primary beam overlap for surrounding melilite crystal. Present results is consistent with the previous data determined by conventional method [2]. In order to detect intra-crystalline distribution, we analyzed $\delta^{18}O$ at four different spots in a large fassaite single crystal. Locations of the SIMS analysis are shown in Fig. 1, and the values are represented in Table 1. The results indicate that there are no clear evidence for heterogeneous $\delta^{18}O$ distribution in the fassaite single crystal.

In conclusion, present data indicate that O isotope composition is homogeneous inside of fassaite grains as well as among grains in the HN3-1 CAI, and that the $\delta^{18}O$ value (-24.14 ‰ relative to SMOW) determined by [2] could be applied to most fassaite grains. The results suggest that most fassaite grains are preexisting solids like spinel grains.

Table 1. Intra- and inter-crystalline oxygen isotope distribution of fassaite grains in HN3-1.

analysis point	$\delta^{18}O_{taka}$† (‰)	2σ
large, blocky crystal		
#01	-29	5
#02	-28	5
#03	-34	5
#04	-32	6
average of #01-04	-31	2
#09	-31	7
#12	-37	6
#13	-35	6
crystals in core melilite		
#06	-25	5
#07	-18*	5

Locations of #01, 02, 03, and 04 are in a single crystal of fassaite grain (see Fig. 1).

†delta value relative to the Taka-shima augite standard. *A part of primary beam overlapped with the surrounding melilite crystal.

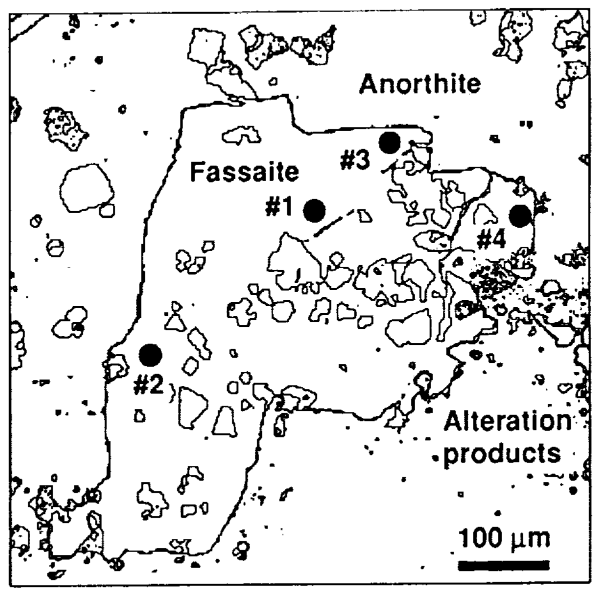


Fig. 1. A large, blocky fassaite single crystal in HN3-1 CAI. The crystal coexsists with anorthite and alteration products. Many small grains in the figure correspond to spinel crystals. Locations of the SIMS analysis are shown in solid circles.

References: [1] Nagahara, H., Nagasawa, H., Nakamura, N., and Matsui, T. (1987) *Lunar Planet. Sci.* **XVIII**, 694-695. [2] Mayeda, T. K., Clayton, R. N., and Nagasawa, H. (1986) *Lunar Planet. Sci.* **XVII**, 562-563. [3] Yurimoto, H., Mori, Y. and Yamamoto, H. (1993) *Rev. Sci. Instrum.* (in press). [4] Slodzian, G., Lorin, J. C., Dennebouy, R., and Havette, A. (1984) *Secondary Ion Mass Spectrometry SIMS IV*, ed. by Benninghoven, A., Okano, J., Shimizu, R., and Werner, H. W. Springer-Verlag Berlin, 153-157.

5263-46
ABS. ONLY N94-20899
p-2

AGE AND THERMOCHRONOLOGY OF K-FELDSPARS FROM THE MANSON IMPACT STRUCTURE;

P. K. Zeitler, Dept. of Earth and Environmental Sciences, 31 Williams Drive, Lehigh University, Bethlehem, PA 18015-3188; M. J. Kunk, U.S. Geological Survey, Reston, VA 22092.

As a contribution to the effort to obtain a precise age for the Manson Impact Structure, we are approaching the problem from a thermochronological perspective, with the goal of extracting an age from $^{40}Ar/^{39}Ar$ age-spectrum analysis of partially overprinted K-feldspars taken from granitoid clasts. We find that shocked feldspars from Manson generally show a strong overprint in their age spectra, with more than 50% of each spectrum being reset. The reset portions of the age spectra correspond to gas lost from very small diffusion domains, and a characteristic of the Manson samples is the very large range in apparent diffusion dimensions that they display, with the smallest domains being some 400 times smaller than the largest domains. It is also noteworthy that the small domains comprise a substantial portion of the volume of the feldspars (50% or more). These observations are consistent with the extreme shock experienced by these samples. In detail, the spectra we have measured to date are saddle-shaped and show minimum ages of between 67 and 72 Ma, which we interpret to be maximum estimates for the age of the impact. In the case of one sample (M1-678.3; K-feldspar from a large syenite block located well below the apparent melt-matrix breccia in the M1 borehole), isotope-correlation analysis suggests the presence of a non-atmospheric trapped Ar component ($^{40}Ar/^{36}Ar$ of 660 ± 40), and an age of about 65.3 ± 0.5 Ma (2σ). Our interpretation of our results is that the shock of impact greatly reduced the diffusion-domain sizes of our samples, making them susceptible to significant Ar loss during heating associated with impact. It appears that while our feldspars were partially open to Ar loss, they equilibrated with a non-atmospheric Ar component, probably related to impact-related degassing of old basement around the impact site.

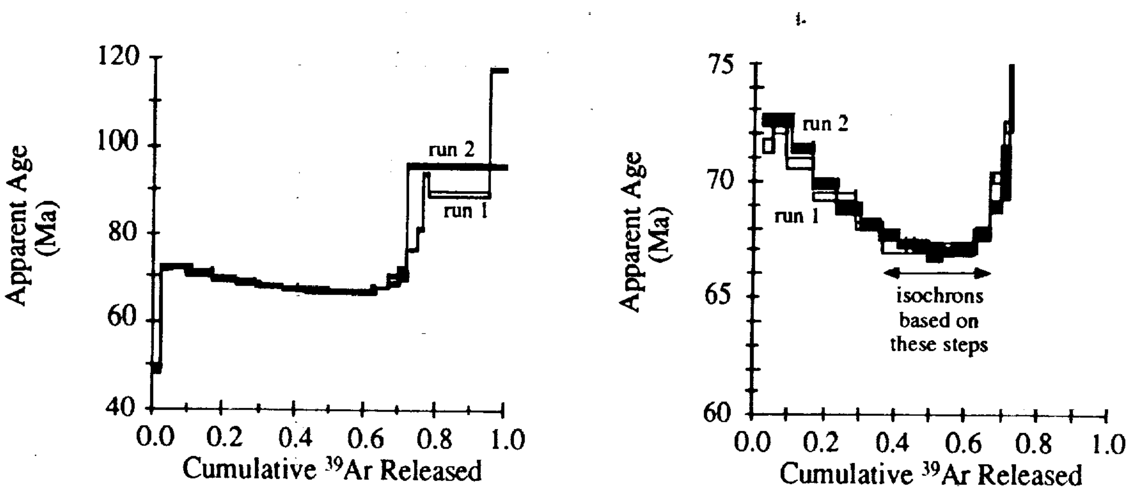
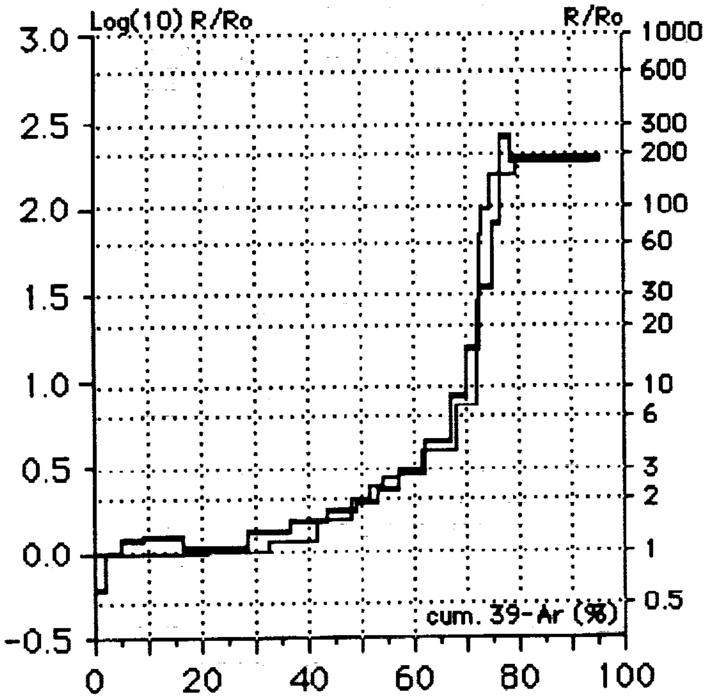


Figure 1. Age spectra from two preliminary analyses of sample M1-678.3 K-feldspar. The minimum age reached in the saddle is about 67 ± 0.7 Ma (2σ). Fish Canyon sanidine (27.79 Ma) and MMhb-1 hornblende (520.4 Ma) were used as irradiation monitors; Haitian tektites included in the irradiation package gave an age of 65.0 ± 0.2 Ma.

MANSON STRUCTURE THERMOCHRONOLOGY: Zeitler P.K. and Kunk M.J.



GRAIN-SIZE DISTRIBUTION:

	size*	volume (%)	Tc bulk (10°C/m.y.)
1	0.45	38.00	122.7
2	1.70	34.00	142.8
3	200.00	28.00	234.9

*Sizes relative to the smallest APPARENT size= 1.0

Figure 2. R/Ro plot for M1-678.3 K-feldspar. Thin line is model calculated from parameters given above. Note range in domain sizes of over 400, and large volume of small domains. Note also the low closure temperature of the smaller domains.

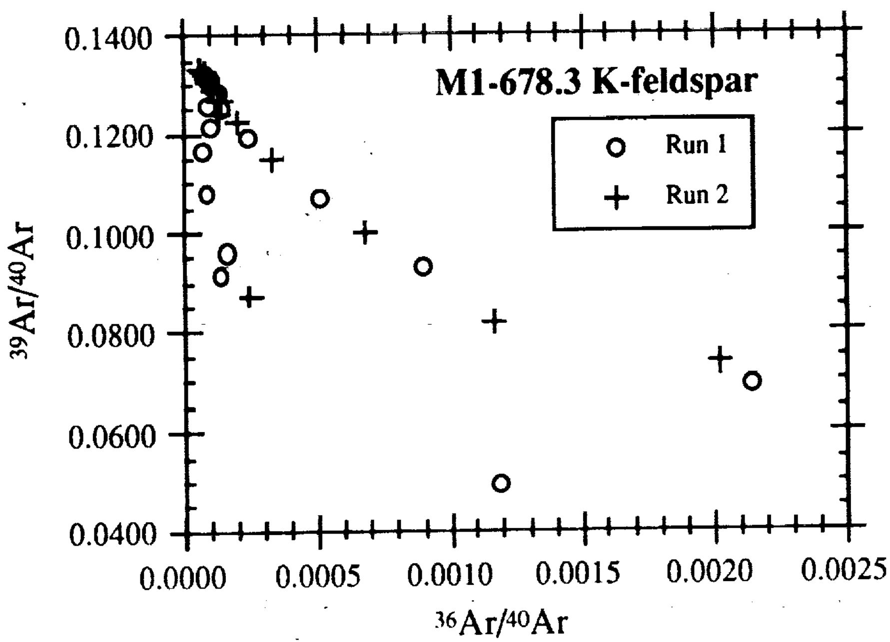


Figure 3. Isotope correlation plot for two analyses of sample M1-678.3 K-feldspar. The most radiogenic analyses define reasonable mixing lines between a trapped component (40/36 of about 660) and a radiogenic component corresponding to an age of about 65.3 ± 0.5 Ma (2σ).

5264-91 ABS. ONLY

N94-20900

p. 2

SPECTRAL ANALYSIS OF CHEMISORBED CO_2 ON MARS ANALOG MATERIALS, A. P. Zent, SETI Institute and NASA Ames Research Center, Moffett Field, Ca 94035, T. L. Roush, San Francisco State University, San Francisco, Ca 94132 and NASA Ames Research Center, Moffett Field, 94035.

Introduction: The goal of this work is to estimate the mass of CO_2 that may have been removed to a quasi-stable reservoir on the martian surface by chemisorption, and to estimate the spectral effects of chemisorbed CO_2 in remotely-sensed martian spectra. Our approach is to characterize the conditions most favorable for the formation of carbonate on common terrestrial oxide minerals, and to search for infrared spectral bands that result from chemisorption of CO_2 molecules onto oxide and other Mars analog materials.

The role of CO_2 in establishing paleo-temperatures ≥ 273 K is unknown [1]. It appears that a CO_2 greenhouse may not have been adequate under any circumstances [2]; however, if a CO_2 was responsible for elevated surface temperatures, then most of that CO_2 must still be in the near-surface environment since no identifiable escape mechanism will remove it after the decline of channeling. The most reasonable reservoir is carbonate, and there are remote sensing techniques which can be used to search for that carbonate [3]. We are investigating CO_2 chemisorption as a permanent CO_2 sink, and to aid in interpretation of remotely-sensed IR spectra of Mars.

A common effect reported in CO_2 adsorption studies of some oxide adsorbents is the formation of a layer of carbonate or bicarbonate anions [4]. The process that forms carbonate is chemisorption, an activated process that is promoted by an increase in temperature - quite the opposite of physical adsorption. Chemisorption is not reversible in the sense that physical adsorption is.

Experiment: We exposed fresh surfaces of common oxide minerals that have carbonate counterparts to atmospheric CO_2 and/or H_2O for various periods of time and then examined the spectra of the powders to see if bands characteristic of the carbonate anion had developed.

Natural oxide and hydroxide samples were prepared by powdering the bulk minerals, seiving to ≤ 38 μm, and sealing the powders in serum vials, all under N_2. Experimental samples were purged with CO_2 and evacuated repeatedly for up to 1 hour. Controls remained under N_2. The effects of H_2O were tested by identical aliquots of powder, some of which were exposed to DDH_2O in amounts corresponding to less than a 1:1 water:powder ratio. Samples and controls are tested after 1, 8, 22 and 60 days; 0.2 mg of powder were mixed with 200 mg of KBr and pressed into pellets. The pellets were placed in a spectrometer environment chamber, which was purged with dry nitrogen gas.

Transmission spectra were acquired from 2.5 to 25 μm with a resolution of 1 cm^{-1}. Individual spectra were corrected for thickness (*t*) and concetration (*C*) by converting the transmission (I/I_o), to extinction, ε, according to

$$\varepsilon = \frac{-\log_{10}(I/I_o)}{Ct} \qquad 1$$

In this representation, absorptions appear as peaks. The extinction coefficients for each sample were ratioed against, and separately subtracted from ,their respective controls.

$Ca(OH)_2$: This hydroxide was included in order to test the sensitivity of our spectral technique to detection of the carbonate anion. $Ca(OH)_2$ is known to form carbonate and bicarbonate ions on exposure to CO_2 [e.g.5]. There were pronounced effects on the $Ca(OH)_2$ spectrum that correspond to the formation of the carbonate anion in the spectral regions of 1300-1400, 1063, 879 and 680 cm^{-1} [6,7] (Fig. 1). The oxide and hydroxides of Ca do not occur in nature, because the partial pressure of CO_2 is too high, and carbonate

is the stable form. This is in contrast to the other oxides and hydroxides used in this study, all of which are naturally occuring oxides and hydroxides.

Natural Oxides and Hydroxides: We chose goethite (FeO.OH) and pyrolusite (MnO_2) for initial short-term experiments, and are currently conducting long-term experiments with goethite, hematite (Fe_2O_3), pyrolustite and brucite $Mg(OH)_2$. To date, the experiments have been carried for up to 72 hours, with no change in the spectral features that can be definitively related to the appearence of surficial carbonate anions. if we assume that we can detect a monolayer of chemisorbed carbonate ions, a reasonable limit, then we can estimate that the formation rate of the carbonate to be less than $5x10^{13}$ molecules g^{-1} s^{-1}. If the detection limit is 0.1 monolayers, then the production limit is less than the value of 10^{13} molecules g^{-1} s^{-1} that was claimed by Booth and Kieffer [8]. We wil present data from long duration exposures that will permit us to characterize the formation rate of carbonate anion at sensitivities well below 10^{13} molecules g^{-1} s^{-1}

Palagonite and Montmorillonite: Powdered samples of both materials were exposed to 100 kPa of CO_2 for 24 hours , and spectra were examined for band formation. No spectral changes were identified that might be related to dry carbonate formation. In these cases, the samples previously existed as powders, and contamination of the mineral surfaces by terrestrial H_2O and atmospheric gases may have affected their reactivity to CO_2.

Summary: Exposure to 100 kPa of CO_2 for 24 hours at 25° C produced easily detectable amounts of chemisorbed carbonate and possible bicarbonate ion on the surface of $Ca(OH)_2$. There was no spectral evidence for the formation of either carbonate or bicarbonate upon exposure of montmorillonite, palagonite, goethite, or pyrolusite to the same conditions. There is not yet evidence to suggest that significant rates of dry carbonate formation might have occured on Mars, nor is there any reason to suspect that infrared studies of the martian regolith must account for chemisorbed CO_2.

[1] Pollack *et al.*, *Icarus*, **71**, 203-224, 1987; [2] Kasting, J., *Icarus*, **94**, 1-13, 1991; [3] Pollack *et al.*, *J. Geophys. Res.*, **95**, 14595 - 14627, 1990; [4] Sposito, G., *Surface Chemistry of Soils* Oxford, 1984; [5] Rosynek, M., D. Magnuson, *J. Catal.*, **48**, 417-421, 1977; [6] Gadsden, J. A. *Infrared spectra of minerals and related inorganic compounds*, Butterworths, 1975; [7]. White, W. B., in *The Infrared Spectra of Minerals*, Mineral. Soc. Amer. Monograph 4, 1974; [8] Booth, M. C., H. H. , Kieffer, *J. Geophys. Res*, **83**,1809-1815,1978.

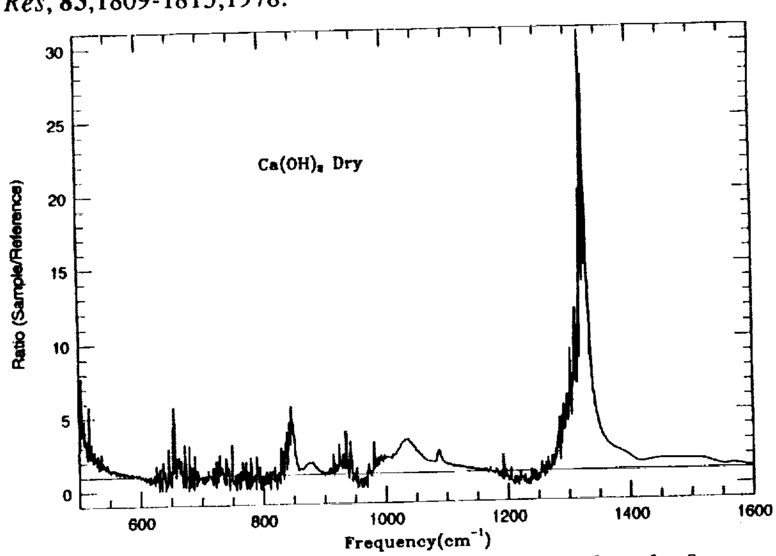


Fig. 1 Ratio of the absorption coefficients of the sample and reference powders of $Ca(OH)_2$. The absorption increase near 1300 cm is due to formation of carbonate anion.

LEWIS CLIFF 87057: A NEW METAL-RICH E3 CHONDRITE WITH SIMILARITIES TO MT. EGERTON, SHALLOWATER AND HAPPY CANYON. Y. Zhang, P.H. Benoit and D.W.G. Sears. Cosmochemistry Group, Department of Chemistry and Biochemistry, University of Arkansas, Fayetteville, Arkansas 72701, USA.

The Antarctic meteorites LEW87057, LEW87220, LEW87223, LEW87234, LEW87237, and LEW87285 were described as paired E3 chondrites by Brian Mason (*Antarctic Meteorite Newsletters*, 12(1) and 15(1,2)). LEW87223 is texturally unusual, containing abundant chondrules and jagged troilite grains which are enclosed in metal. Our INAA data show that the siderophile element abundance in two splits of LEW87223 are higher than the EH range, while chalcophile elements (Cr excepted) are highly depleted. Mineral compositions are unlike those normally found in EH or EL chondrites or aubites, and in some respects resemble those of several anomalous enstatite meteorites such as Shallowater, Mt. Egerton and Happy Canyon. The bulk and mineral compositions are consistent with the addition of EL chondrite metal to an EL3 chondrite with the removal of sulfides other than troilite which is now Cr-rich. We suggest that this meteorite is an EL3 chondrite into which metal was introduced and sulfides redistributed during an event involving impact melting and brecciation.

INTRODUCTION

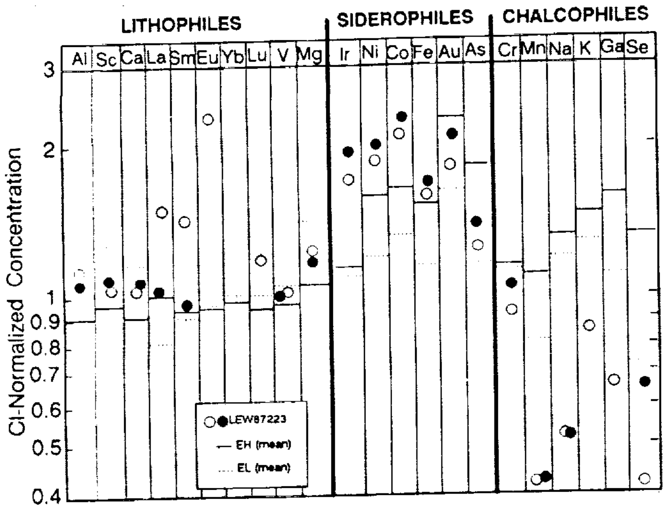
Enstatite meteorites consist of the EH and EL classes (which are chondritic in composition but with complex and poorly understood thermal histories)[1,2], the igneous aubrites[3,4] the Mt. Egerton stony-iron[5], the Horse Creek iron[6], the metal-rich aubrite Shallowater and a number of impact melts such as Happy Canyon (EL6)[7] and Ilafegh 009 (EL6)[8,9]. They probably originated on a number of distinct parent-bodies[7]. Shallowater, unlike other aubrites, is unbrecciated, metal-bearing (9 wt%), diopside-free, and shows a positive Eu anomaly[10]. It probably experienced a complex cooling history associated with impact mixing and repeated break-up[10]. Mt. Egerton consists of Fe-free, low-Ca pyroxene and Si-bearing metal similar to enstatite chondrites, but in very different proportions probably also due to mixing during impact[5]. Here, we present the results of our study of LEW87223 (part of the LEW87057 pairing group[11]), another unusual enstatite meteorite which is a metal-rich E3 chondrite in some respects similar to the unusual enstatite meteorites.

RESULTS

Mineralogy and petrography. The LEW87223 hand-specimen is highly weathered although our thin section looked fresh. It contains a closely-packed aggregate of fractured and otherwise altered chondrules surrounded by abundant metal, which encloses large masses of irregular-shaped troilite. A modal analysis of a small thin section (~0.7 x 0.5 cm, 509 points) shows clinoenstatite (61wt%), metal (23%), sulfides (12%) and other phases (4%). By comparison, EH and EL chondrites are typically 22 and 19 wt% metal, and 11 and 8.0 wt% sulfide, respectively[12]. A small xenolith of plagioclase was also observed in our section (LEW87223, 18).

Bulk chemistry. Using our previous INAA methods[13], we analyzed two splits (150 mg and 100 mg) of LEW87223 in two separate irradiations (Fig.1). While the Fe/Mg ratio (1.2) corresponds to the normal EH value[13]; Ir, Ni and Co are much higher than the EH range; chalcophiles are much lower than the EH and EL ranges (although Cr is less depleted than the others); Al, Sc, Ca, V and Mg are intermediate between EH and EL values. The Ni/Ir weight ratio (23.9), which is an important parameter for distinguishing EH and EL chondrites, is lower than EH chondrite (31.0) and comparable to EL (24.8) and Shallowater (24.5)[10,14]. Like Shallowater and Mt. Egerton, the REE display a strong Eu enrichment, although our REE data are preliminary[10,15]. While 10 other E chondrites analyzed in the same two irradiations had compositions similar to EH or EL group averages, the composition of LEW87223 corresponds to no known enstatite meteorite class.

Mineral chemistry. The mineral compositions of LEW87223 also defy simple assignment to the EH or EL class. Like EL chondrites, LEW87223 contains alabandite but it is unusually Fe-rich (42 %FeS), Si in the kamacite and Ni in the metal are in the EL3 range, phosphide compositions are in the EH5,6 range, and Cr and Ti in the troilite have much higher values than typical of the EH and EL classes and resemble Shallowater, Mt. Egerton and Happy Canyon (Fig.2)[3,4]. The CaO in enstatite is intermediate to EH and EL chondrites.



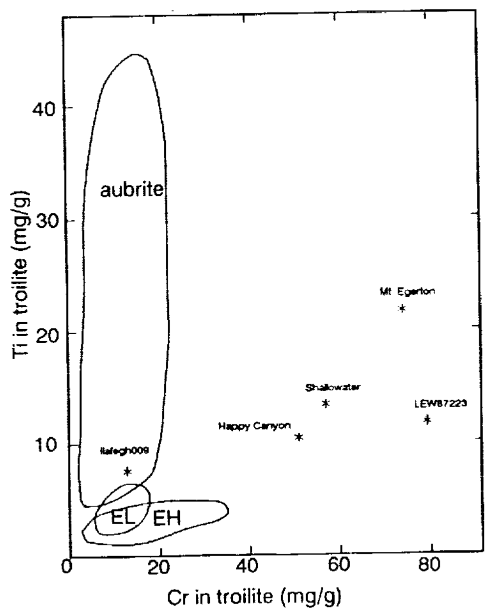


Fig. 1. (Left) CI-normalized concentration ratios for two splits of LEW87223 analyzed by INAA. The data suggest that the meteorite is an EL chondrite to which metal has been added and sulfides, other than Cr-bearing troilite, were removed.

Fig. 2. (Right) Titanium and Cr concentrations in the troilite of enstatite meteorites. Like Shallowater, Happy Canyon and Mt. Egerton, troilite in LEW87223 has high concentrations of these minor elements.

DISCUSSION

In terms of bulk composition LEW87223 is highly anomalous. These compositional properties are not due to weathering (which might leach Na and K but could not increase siderophiles while lowering lithophiles) or sample heterogeneity, which produces much smaller effects. The bulk composition can be explained by the addition of about 12% metal with EL proportions of siderophiles to starting material of EL composition, with the removal of the sulfides, other than troilite, to explain the depletion in chalcophiles. At the same time, the Cr content of the FeS was increased and the FeS content of the residual alabandite was increased. A positive Eu anomaly was produced, although experimental details of how REE behave in sulfide systems is not available; REE are known to be located in the sulfides in E chondrites[16]. The unusual sulfide-metal structures were presumably produced, and the xenolith introduced, by this process. The meteorite may be described as a metal-rich EL3 chondrite showing several signs of an igneous event, such as the Eu anomaly, the low abundance of sulfides other than troilite and the metal-sulfide structures. Mineral compositions are also highly unusual and unlike the EH or EL group. They most closely resemble those of Shallowater, Mt. Egerton and Happy Canyon. We suggest that LEW87223 is an EL3 chondrite to which considerable metal and the xenolith were added by impact and brecciation which was accompanied by a small amount of partial melting.

1, Sears *et al.* (1982) *GCA* **46**, 597. 2, Zhang *et al.* (1992) *Meteoritics* **27**, 310. 3, Watters and Prinz (1980) *LPS XI*, 1225. 4, Watters and Prinz (1979) *Proc. LPS X*, 1073. 5, McCall (1965) *Miner. Mag.* **35**, 241. 6, Buchwald (1985) *Handbook of Iron Meteorites*. 7, Keil (1989) *Meteoritics* **24**, 195. 8, Bischoff *et al.* (1992) *LPS XXIII*, 105. 9, McCoy *et al* (1992) *LPS XXIII*, 869. 10, Keil *et al* (1989) *GCA* **53**, 3291. 11. Mason in *Antarctic Meteorite Newsletter* (1989 and 1992), **12(1)** and **15(1,2)**. 12, Keil (1968) *JGR* **73**, 6945. 13, Weeks and Sears (1985) *GCA* **49**, 1525. 14, Wasson and Kallemeyn (1988) *Phil. Trans. R. Soc. Lond. A* **325**, 535. 15, Wolf *et al* (1983) *GCA* **47**, 2257. 16, Sears *et al.* (1983) *EPSL* **62**, 180-192. NASA grant NAG 9-81.

S266-90
ABS. ONLY

N94-20902

p. 2

CHEMICAL ZONING AND DIFFUSION OF CA, AL, MN, AND CR IN OLIVINE OF SPRINGWATER PALLASITE. Y. Zhou and Ian M. Steele, Dept. of Geophysical Sciences, University of Chicago, 5734 S. Ellis Ave., Chicago, IL 60637.

The pallasites, consisting mainly of Fe-Ni metal and olivine (1,2), are thought to represent the interior of a planetary body which slowly cooled from high temperature. Although the olivines are nearly homogeneous (3), ion microprobe studies revealed variations of Ca, Ti, Co, Cr, and Ni near grain edges (4,5). These variations were thought to represent diffusion in response to falling temperature of the parent body. Pallasite cooling rates have been estimated based on kamacite-taenite textures (6) but results differ by x100. In principle elemental profiles in olivine can allow estimates of cooling rate if diffusion coefficients are known; in addition, given a cooling rate, diffusion coefficients could be derived. Data are presented which show that apparent diffusion profiles can be measured for Al, Ca, Cr and Mn which qualitatively agree with expected diffusion rates and have the potential of providing independent estimates of pallasite cooling rates.

Experimental: Below we present electron microprobe profiles for Mn, Cr, Al, and Ca from Springwater pallasite as determined by electron microprobe. Operating conditions were selected to obtain maximum sensitivity: 20kV, 200nA, focused beam, PHA on, 1200sec count time. Concentrations (ppmw) for the 4 minor elements are approximately: Mn - 2750; Cr - 140; Al - 10; Ca - 64. Spectral scans confirmed a linear background with no interfering peaks. A total of 18 concentration profiles from edge to interior were obtained from 6 different olivine grains. Profile locations were chosen to avoid cracks and large grains were chosen so sections near the grain center were likely. The grain orientation was not known and attempts to determine orientation using backscattered electron diffraction were unsuccessful. While profiles discussed below are the most common, anomalous profiles were obtained which did not show a simple increase or decrease in concentration relative to grain edge, but there is no apparent reason for these complex profiles. Particular attention was paid to the phases adjacent to the olivine grain which may affect the profile by acting as a sink or source of a particular element.

Results: A typical profile is shown in Fig.1 where the adjacent phase is Fe-Ni metal. Two types of trends are seen which are common to nearly all profiles. The profiles for Al, Ca and Cr, all show a concentration decrease at the olivine grain edge relative to the olivine center; in contrast, the profile for Mn is highest at the grain edge and decreases toward the grain center. The profile for Mn is always much smoother than for the other three elements due to the 10 to 100x higher concentration; the apparent scatter in profiles for Al, Ca, and Cr can be attributed to counting statistics. The Mn decrease toward the grain interior can be interpreted as partitioning of Mn between olivine and metal where Mn favors olivine as temperature decreases (assuming ideal solid solution). Therefore, the Mn will migrate from the neighboring metal into olivine in response to the overall cooling. At high temperature, the diffusion is rapid and the time to reach equilibrium throughout the grain is short relative to the rate of temperature decrease. At low temperatures, on the other hand, diffusion within the olivine becomes slow and the Mn does not diffuse from the grain edge resulting in high concentrations at the metal-olivine boundary. The increasing concentrations for Al, Ca, and Cr toward the grain center indicate that these elements are diffusing out of olivine during cooling. A similar character for Ni has been observed (4). In contrast to Mn, the equilibrium Al, Ca, and Cr content in olivine decreases during cooling. This conclusion which is true for Ni (3) is speculative for the 3 elements described here because the adjacent metal phase does not contain these 3 elements in detectable quantities. It is possible that Cr is incorporated into the olivine structure as Cr^{+2} (7) at the reducing conditions indicated by the low Ni in Springwater olivine. Other phases, however, including chromite, troilite, and various phosphates (stanfieldite, whitlockite) may better act as sinks especially for Cr and Ca but require long distance grain boundary migration. A sink for Al is more difficult to identify but both phosphates and chromite may incorporate minor amounts; the bulk Al is very low in pallasites so no Al phase is required. There are indications the the slope of the profiles are dependent on the adjacent phases (metal, troilite, schreibersite) but sufficient data have not been obtained to verify relationships. If true however, limits can be placed on the distance over which equilibrium was achieved.

While crystallographic orientation of our analyzed grains is not known, there is a dependence of direction and diffusion rate (8) which has been observed for C3 (9) and terrestrial olivine (10). Fig. 2 illustrates the measured profiles for one Springwater olivine grain at 0, 45, and

90 degrees in the plane of the polished section. The profiles for Cr, Al, and Ca are essentially identical in the 3 directions, but if there are differences due to direction, they would probably be masked by the statistical fluctuation. On the other hand, Si diffusion in olivine is isotropic (11) and Al may be similar. The profiles for Mn, however are distinctly different and the 45° profile reflects rapid diffusion relative to the 0° and especially the 90° profile.

A comparison of the profiles for Al, Ca, and Cr on Fig. 2 shows that Al has the sharpest profile with a near-constant composition reached about 110μm from the grain edge. Both Ca and Cr profiles appear to extend beyond 250μm although Cr may become flat near 250μm. Qualitatively, the diffusion coefficients can be ordered as Ca>Cr>Al. The slow diffusion of Al is consistent with substitution in part in tetrahedral sites as concluded for C3 olivine grains (12). Quantitative interpretation suffers many uncertainties including: 1) the valance state of Cr; 2) the occurrence of Al in two sites, tetrahedral and octahedral, for charge balance; 3) unknown or poorly known diffusion coefficients for Al and Cr.

References: (1) Buseck, P.R. (1977) GCA 41, 711-740; (2) Scott, E.R.D. (1977) GCA 41, 693-710; (3) Buseck, P.R. and Goldstein, J.I. (1969) BGSA 80, 2141-2158; (4) Leitch, C.A. et al. (1979) LPS X, 716-718; (5) Reed, S.J.B. et al. (1979) EPSL 43, 5-12; (6) Narayan, C. and Goldstein, J.I. (1985) GCA 49, 397-410; (7) Smith, J.V. et al. (1983) JGR 88, B229-236; (8) Morioka, M. and Nagasawa, H. (1991) in "Diffusion, Atomic Ordering, and Mass Transport", editor, J.Ganguly, 177-197; (9) Steele, I.M. (1992) LPS XXIII, 1353-1354; (10) Jurewicz, A.J.G. and Watson, E.B. (1988) CMP 99, 186-201; (11) Jaoul, O. et al. (1981) Geodyn. Ser. 4, 95-100, AGU, Washington; (12) Steele, I.M. (1986) GCA 50, 1379-1395. Acknowledgement: NASA NAG 9-47 for support.

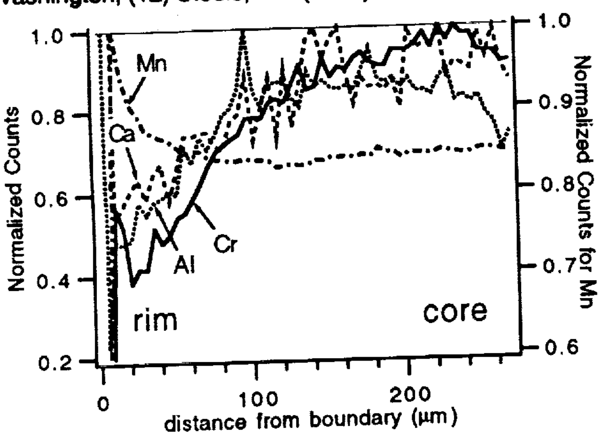


Fig. 1. Typical concentration profile for Al, Ca, Cr, and Mn in Springwater olivine. The olivine rim (left) is adjacent to Fe-Ni metal. Al, Ca, and Cr show a depletion at the olivine-metal boundary relative to the olivine center. Mn shows an enrichment at the olivine rim and rapidly levels off. The scatter for Al, Ca, and Cr is mostly due to counting statistics.

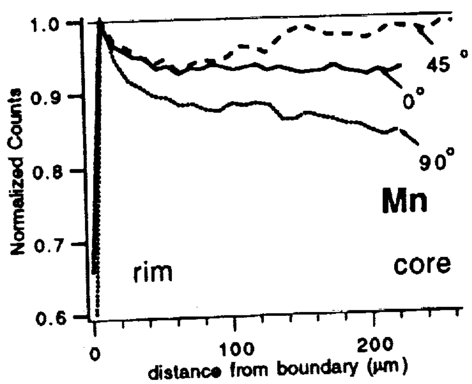
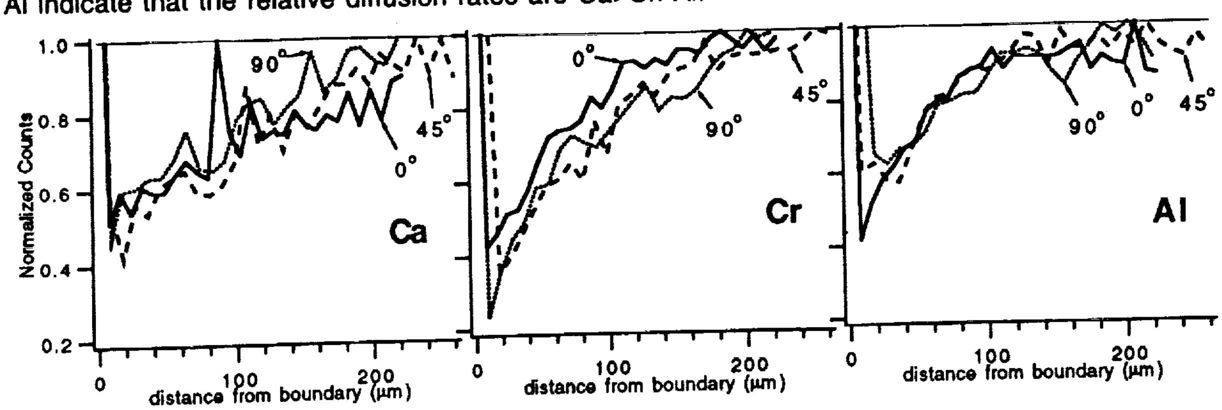


Fig. 2. Rim to core profiles for Al, Ca, Cr, and Mn in 3 directions in a single olivine grain. Fe-Ni metal occurs at the olivine rim. For Ca, Cr and Al the three profiles in the 0, 45 and 90° direction are identical within statistics suggesting no large diffusion anisotropy. For Mn, however, the profiles are distinctly different with the 0° profile indicating a fast diffusing direction. The slopes of the profiles for Ca, Cr, and Al indicate that the relative diffusion rates are Ca>Cr>Al.



5267-91
ABS-ONLY

N94-20903

COMPARISON OF FLANK MODIFICATION ON ASCRAEUS AND ARSIA MONTES VOLCANOES, MARS. James R. Zimbelman (CEPS/NASM, Smithsonian Institution, Washington, DC 20560)

p-1

Geologic mapping of the Tharsis Montes on Mars is in progress as part of the Mars Geologic Mapping Program of NASA (1). Mapping of the southern flanks of Ascraeus Mons at 1:500,000 scale was undertaken first (2), followed by detailed mapping of Arsia Mons (3), and mapping of Pavonis Mons will begin later this year. Results indicate that each of the Tharsis volcanoes displays unique variations on the general 'theme' of a martian shield volcano (1,4). Here we concentrate on the flank characteristics on Ascraeus Mons and Arsia Mons, the northernmost and southernmost of the Tharsis Montes, as illustrative of the most prominent trends.

Both Ascraeus and Arsia Montes have relatively uniform flank slopes of 4° to 5° (6), consistent with the broad profile typical of shield volcanoes. Both volcanoes have calderas at their summit, although at Ascraeus Mons there is a nested complex of six (7) or more (8) collapse events, while Arsia Mons has only a single 100-km-diameter caldera (7). Both volcanoes have erosional scarps with about 300 m of relief on their western flanks, at an elevation of 10 km on Ascraeus Mons (2) and an elevation of 15 km on Arsia Mons (3). Elevation differences for the scarps may be correlated to the overall age of the constructs obtained from some (9) but not all (10) crater counts. Both volcanoes have low thermal inertias indicative of a covering of fine dust (11), even after corrections for elevation-dependent thermal conductivity (12). Arcuate ridges within isolated hollows along the scarp on Arsia Mons (422A27, 38 m/pixel) are interpreted here to be sand dunes, consistent with a recent reevaluation of thermal conductivities on the martian volcanoes (13). The southern flanks of Ascraeus Mons have subtle terraces at about 50 km spacing and generally lack graben within 100 km of the caldera rim (1). In contrast, the southern flanks of Arsia Mons have few graben within 100 km from the summit while the northern and western flanks have graben up to the caldera rim (1). Nonuniform tensional forces have been exerted on the Arsia Mons shield to produce this pattern. Such extensional asymmetries may be indicative of nonuniform stresses within the shields (14), perhaps related to their location on the side of the Tharsis crustal uplift (15). The details mapped on both volcanoes should provide new constraints on various geological and geophysical processes inferred to be active on the martian volcanoes.

REFERENCES: 1) Zimbelman J.R. and Edgett K.S. (1992) Proc. Lunar Planet. Sci. 22, 31-44. 2) Zimbelman J.R. (1991) Trans. AGU 72(44), 279. 3) Zimbelman J.R. (1991) Trans. AGU 72(17), 182. 4) Zimbelman J.R. and Edgett K.S. (1991) GSA Abs. Prog. 23(5), A401. 5) Zimbelman J.R. (1992) Trans. AGU 73(43), 325. 6) USGS (1991) Map I-2160. 7) Mouginis-Mark P.J. (1981) Proc. Lunar Planet. Sci. 12B, 1431-1447. 8) Zimbelman J.R. (1984) Ph.D. Diss., Arizona St. Univ., in NASA TM-88784, 271-572. 9) Plescia J.B. and Saunders R.S. (1979) Proc. Lunar Planet. Sci. 10th, 2841-2859. 10) Neukum G. and Hiller K. (1981) JGR 86, 3097-3121. 11) Kieffer H.H. et al. (1977) JGR 82, 4249-4291. 12) Zimbelman J.R. (1986) Trans. AGU 67, 1074. 13) Bridges N.T. (1992) Trans. AGU 73(43), 323. 14) Thomas P.J. et al. (1990) JGR 95, 14345-14355. 15) McGovern P.J. and Solomon S.C. (1992) Lunar Planet. Sci. XXIII, 885-886.

S268-46 ABS ONLY

N94-20904

p-2

NUMERICAL SIMULATION OF LAVA FLOWS; APPLICATIONS TO THE TERRESTRIAL PLANETS.

James R. Zimbelman and Bruce A. Campbell (CEPS/NASM, Smithsonian Inst., Wash., DC 20560), Juliana Kousoum (Thom. Jefferson H.S. for Sci. and Tech., Alexandria, VA 22312), and Derrick J. Lampkin (Ohio St. Univ., Columbus, OH 43210).

Lava flows are the visible expression of the extrusion of volcanic materials on a variety of planetary surfaces. A computer program described by Ishihara et al. (1) appears to be well suited for application to different environments, and we have undertaken tests to evaluate their approach. Our results are somewhat mixed; the program does reproduce reasonable lava flow behavior in many situations, but we have encountered some conditions common to planetary environments for which the current program is inadequate. Here we present our initial efforts to identify the 'parameter space' for reasonable numerical simulations of lava flows.

The program uses the steady state solution of the Navier-Stokes' equation for a Bingham fluid with constant thickness that flows down an inclined plane. Lava motion stops when the thickness is less than the critical depth, which depends on yield strength, gravity, density, and underlying slope. Heat loss occurs solely through radiation from the flow. Limited field data for basaltic flows were used to derive expressions for yield strength and viscosity as a function of temperature. This simplified program was able to reproduce the general shape and thickness of several historic flows in Japan, all of which were emplaced on relatively large slopes (generally > 3^{o}).

The program provided in the Ishihara paper was modified to accommodate current computer capabilities, and it ran successfully when error traps were added to exclude calculations near zero slope. Reasonable flows were produced for slopes >1^{o}. The Ishihara radiation algorithm produces very little cooling of the flows, so that they tend to be volume-limited by the lava supply rate. Several simulations were run on inclined planes to investigate the effect of varying slope, gravity, eruption temperature, and effusion rate while keeping all other parameters constant. Resulting flows varied considerably in shape and thickness, and the aspect ratio (length/width) should prove to be a useful quantity for comparison to real flows.

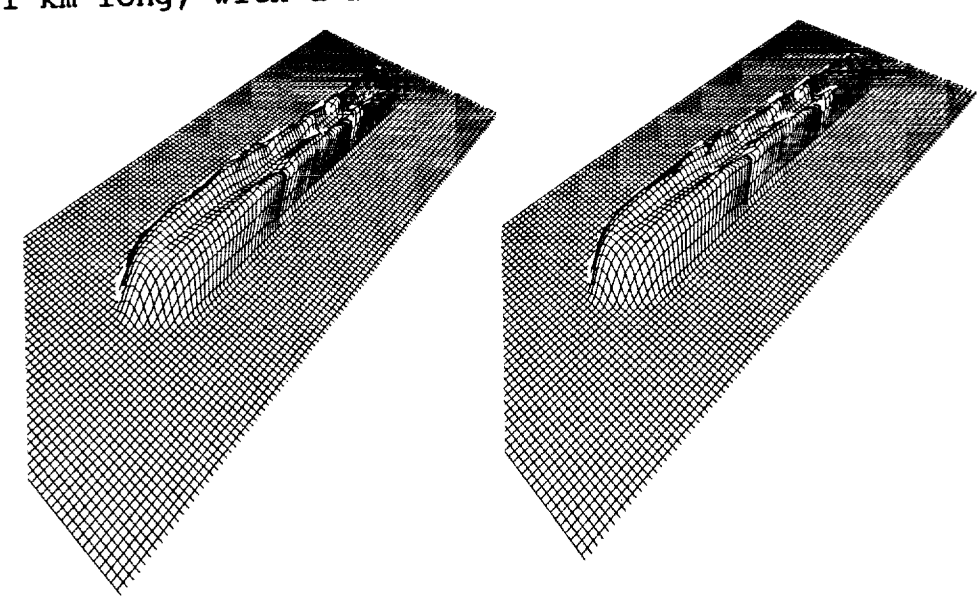
The program did not run satisfactorily on DEMs derived from contour maps if these topographic models contained significant areas of zero slope. Modifications were made to allow for pressure-driven flow on very shallow slopes, with the constraint that the flow front was not allowed to exceed the angle of repose, and for floating-point topographic arrays (Fig. 1). More modifications will certainly be needed to address other limitations that affect the modeling of flowing lava (see 2).

With proper awareness of the model limitations, simulations should be applicable to planetary environments. **Earth:** The current program is best suited for flow emplacement on surfaces sloping >1^{o}, such as flows on the flanks of shield volcanoes like Kilauea. Modeling the well-documented Puu Oo flows (3) will provide calibration for the cooling algorithm and the rheologic

conditions for basalt used in the program. **Moon:** Distinct lava flows are visible in Mare Imbrium (4), found on slopes of 0.1° to 0.2° (5). The youngest Imbrium flows (4) have isolated leveed channels and large length/width ratios. Cooling and rheology algorithms likely will need to be changed to simulate such flows. **Mars:** Many distinct lava flows are present in the Tharsis area (6), typically on slopes of 1° to 5° (7). The program should be quite applicable to the best examples of these flows. **Venus:** Several of the lava flow fields identified on Venus (8) include individual flows traceable for hundreds of kilometers. Magellan altimetry indicates that flows in East Kawelu Planitia were emplaced on extremely shallow slopes of 0.02° to 0.07° (9). The program will be used to evlauate the need to accommodate cooling processes in the dense venusian atmosphere, and possibly eruption temperature and/or rheologic changes, to reproduce the observed aspect ratios of venusian flows on shallow slopes. Continued modelling should provide constraints on likely lava thickness, eruption temperature, and effusion rates for discreet lava flows observed on Venus.

REFERENCES: 1) Ishihara et al., 1990, in IAVCEI Proc. Volc., 2, Lava Flows and Domes, (J. Fink, ed), Springer-Verlag, 174-207. 2) Campbell and Zimbelman, 1993, LPS XXIV, this volume. 3) Wolfe et al., 1989, USGS Prof. Pap. 1463, 1-98. 4) Schaber, 1973, Proc. LPSC 4th, 73-92. 5) LTO (250) maps 39C2, 40A1, 40A4. 6) Carr, 1981, Surface of Mars, Yale Univ. Pr., 87-105. 7) USGS Map I-2112, 1991. 8) Head et al., 1992, J. Geophys. Res. 97, 13153-13197. 9) Helgerud and Zimbelman, 1993, LPS XXIV, this volume.

Figure 1. Stereoscopic view of lava flow simulation on an inclined plane [Parameters used: flow rate = 30 $m^3\ s^{-1}$, effusion duration = 3 hr, calc interval = 1 s, grid cell size = 10 m, slope = 3°, gravity = 9.8 $m\ s^{-2}$, eruption temp = 1400 K, lava density = 2500 $kg\ m^{-3}$]. View is for one hour after cessation of effusion, so that lava has drained from the central channel. Flow is 1 km long, with a maximum thickness at front of 6 m.



CHEMICAL COMPOSITION OF NEW ACAPULCOITES AND LODRANITES.

J. Zipfel and H. Palme, MPI für Chemie, Saarstrasse 23, 6500 Mainz, Germany.

The bulk compositions of two Antarctic Lodranites, MAC 88177 and FRO 90011 and two Acapulcoites, ALH 81261 and Monument Draw were determined with instrumental neutron activation analysis. Acapulcoites have essentially chondritic major and trace element abundances but achondritic texture. They consist, of entirely recrystallized, fine grained mineral assemblages. Chondrules are extremely rare, one relict radiating pyroxene chondrule was described in Monument Draw (MD) (1). The coarse grained Lodranites also have achondritic textures, but they are different compositionally with depletions in Al, Na and incompatible elements probably a result of separation of a partial, feldspar-rich melt (2). MAC 88177 is significantly more depleted in incompatible elements than FRO 90011 suggesting a higher degree of partial melting for the MAC-Lodranite. The chemical data support a genetic relationship between Lodranites and Acapulcoites inferred earlier from oxygen isotopes, petrology and mineral composition (1).

Analytical results of the four meteorites are presented in the Table. FRO 90011, found in 1990/1991 EUROMET in Antarctica, has a total mass of only 1.8 g and was initially classified as an Acapulcoite (3). Oxygen isotopes (4) are in the range of those for Acapulco- and Lodran-like meteorites (5). Two pieces A and B of 84 and 95 mg, respectively were analyzed. Results for both samples reflect different modal compositions. Higher contents of siderophiles in B indicate a higher metal content while higher concentrations of Al, Na and K possibly reflect the presence of plagioclase. The bulk chemical data clearly demonstrate the chemical similarity of FRO 90011 and the achondritic group of Lodranites. In addition, samples of MAC 88177 (lodranite), ALH 81261 and Monument Draw (two Acapulcoites) were analyzed. A detailed description of MD is in progress (6).

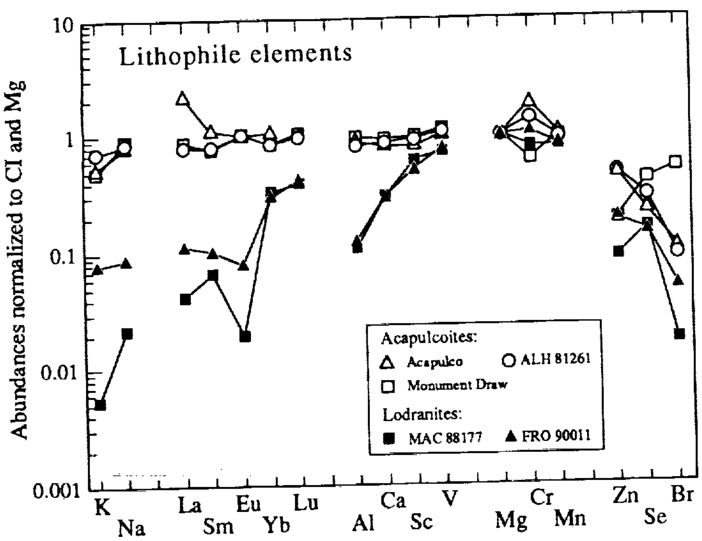
Relative abundances (CI and Mg - normalized) of the lithophile elements of the investigated meteorites are plotted in the Figure. Acapulcoites and Lodranites form two clearly separated groups. All Acapulcoites define a narrow compositional range in incompatible and compatible elements. They have approximately chondritic abundances for most elements with the exception of some minor depletion in K. Volatile elements such as Zn, Se and Br are slightly depleted relative to CI, Zn and Br are, however, enriched when compared to ordinary chondrites while Se has similar abundances (7). Of the Acapulcoites MD has the lowest abundances of Cr and Zn, a possible indication of chromite fractionation as chromite is the major host phase for Cr and Zn. The high Se of MD reflects a higher troilite content which is supported by the observation of large troilite and metal veins in MD (1). Data for Acapulco (7) are shown for comparison. Except for enrichment in LREE and Cr, Acapulco is similar to Monument Draw and ALH 81261. Mobilisation of chromite, indicated by high Cr in Acapulco and low Cr in MD, requires a high degree of partial melting to allow mechanical separation of chromite crystals. From the different composition of matrix metal and tiny metal inclusions inside olivine and orthopyroxene grains of Acapulco (8) it was inferred that Acapulco was at least heated to 1400 °C, which caused partial melting of metal and silicates in Acapulco.

In Lodranites incompatible lithophile elements (K, LREE) and Na, Al and Ca are strongly depleted. The extent of depletion is more pronounced in MAC 88177 whereas compatible elements have similar and chondritic abundances in both Lodranites. An essentially uniform chondritic abundance level is found for siderophile and chalcophile elements in Lodranite FRO 90011 and the Acapulcoites. This implies that in FRO 90011 only a silicate partial melt was extracted but not the coexisting sulfide rich melts. All examined Lodranites have a negative Eu anomaly indicating removal of Eu. This is surprising since there is no obvious reason why the partial melt should preferentially accomodate Eu. Apparently, after melting of plagioclase (positive Eu anomalies) no re-equilibration between melt and residuum was achieved. Thus the separation of the plagioclase rich melt must have occurred relatively fast. This is supported by the strong depletion in Na, which is generally not considered a very incompatible element, but resides predominantly in plagioclase in chondritic meteorites.

The Acapulcoites representing an unfractionated and almost undepleted counterpart of the Lodranites could be the parent material for Lodranites. Acapulco is to various degrees enriched in incompatible elements (LREE, U). However, it is unlikely that partial melts from the Lodranites are responsible for this enrichment. Since these melts are enriched in K and Na but Acapulco is not. Probably phosphate entrainment is responsible for the unusual LREE enrichment of Acapulco, since phosphates are high in U and REE but low in K.

In summary, Lodranites may represent residues from partial melting of an Acapulcoite parent body. Details of formation and fractionation of partial melts are unclear (e.g. why are silicate melts lost but sulfides are retained?). A better understanding of these processes will ultimately lead to a better insight in the initial stages of planetary differentiation.

CHEMICAL COMPOSITION OF NEW ACAPULCOITES AND LODRANITES: Zipfel J. and Palme H.



Lit.: (1) McCoy T.J. et al. (1992), LPSC **XXIII**, 871-872; (2) Bild R.W. and Wasson J.T. (1976), Min. Mag. **40**, 721-735; (3) Wlotzka F. (1992), Meteoritics **27**, 479-480; (4) Franchi I.A. et al. (1992), Meteoritics **27**, 222; (5) Clayton R.N. et al. (1992), LPSC **XXIII**, 231-232; (6) McCoy T.J. et al. (1993), in prep.; (7) Palme H. et al. (1981) Geochim. Cosmochim. Acta **45**, 727-752; (8) Zipfel J. et al. (1992), LPSC **XXIII**, 1585-1586.

Table: Bulk composition of Lodranites and Acapulcoites

	Lodranites					*Acapulcoites*		
	MAC 88177		***FRO90011 A #***	***FRO90011 B #***		***ALHA 81261***	***Monument Draw I****	
wt. mg	180.8		83.87	94.49		126.5	119.75	
[%]		s.d.			s.d.			s.d.
Mg	20.52	3	19.06	15.87	3	15.48	14.7	5
Al	0.18	10	0.13	0.23	5	1.12	1.2	5
Ca	0.56	10	0.49	0.48	15	1.25	1.3	10
Fe##	13.73	3	20.11	28.43	3	21.81	22.4	3
[ppm]								
Na	242	3	282	1260	3	6880	7075	3
K	6	25	31	110	10	603	393	10
Sc	7.72	3	6.25	5.16	5	8.65	9.05	3
V	80.3	3	101.0	62.0	5	91.7	96.5	5
Cr	4140	4	6990	3420	3	5970	2460	3
Mn	3190	3	3210	2580	3	2700	2600	3
Co	196	3	480	931	3	673	700	3
Ni	4230	4	8920	16300	4	13600	17900	4
Cu	35	15	37	63	25	<180	190	20
Zn	65	6	144	113	5	243	99	7
Ga	3.1	4	6.1	11.4	5	9.3	6.9	10
As	0.926	3	1.450	3.130	5	1.960	2.660	7
Se	6.14	7	5.85	4.23	7	8.66	11.50	5
Br	0.09	20	0.24	0.20	20	0.36	1.90	25
Mo				1.50	30	1.10	1.00	15
Ru			1.02	1.73	20	1.2	1.4	20
La	0.022	25	0.062	0.043	10	0.330	0.338	8
Sm	0.022	5	0.034	0.025	10	0.190	0.175	5
Eu	0.0024	35	0.0033	0.0130	30	0.0940	0.0860	15
Yb	0.118	7	0.100	0.092	15	0.240	0.220	15
Lu	0.020	10	0.026	0.015	15	0.039	0.041	15
Re			<0.034	0.133	15	0.067	0.081	8
Os			0.837	1.570	15	0.930	0.990	10
Ir	0.025	5	0.722	1.550	3	0.756	0.822	3
Au	0.056	3	0.137	0.290	3	0.186	0.248	3
U	<0.01		0.042	<0.0300	25	0.019	<0.025	30

preliminary data; * McCoy et al. (in prep.); ## total Fe; s.d. standard deviation in %.

S270-90
ABS. ONLY

N94-20906

p. 2

DIFFUSE REFLECTANCE SPECTRA OF ORTHOPYROXENE, OLIVINE, AND PLAGIOCLASE AS A FUNCTION OF COMPOSITION AND STRUCTURE

M.E. Zolensky[1], L. Le[2], C. Galindo[2], R. Morris[1], V. Lauer[2] and F. Vilas[1]; [1]Solar System Exploration Division, NASA Johnson Space Center, Houston, TX 77058; [2]Lockheed ESCO, 2400 NASA Rd. 1, Houston, TX 77058.

Although many similarities exist between meteorite spectra and "primitive" asteroids , there are unexplained discrepancies [1]. These discrepancies do not appear to arise from grain size effects [2&3]. Assuming that primitive meteorites did in fact originate from the "primitive" asteroids, we believe that there are two testable explanations for the observed spectral discrepancies: compositional or structural differences. We have begun to synthesize and collect reflectance and Mossbauer spectra of pertinent materials, beginning with olivine, pyroxene and plagioclase (all found in primitive meteorites), and to assess the possible effects composition may have on spectral features. Our study focuses on the combination of composition *and* structural effects.

We have synthesized olivines, pyroxenes, plagioclases and related glasses in gas-mixing furnaces (with controlled oxygen fugacities) at variable melting and quench-rate conditions. Typically, non-crystalline or structurally disordered materials are promoted by elevated melt temperatures, increased time held at the peak temperature, and high quench rates. Diffuse reflectivity spectra (350-2100 nm) were obtained at room temperature using a Cary-14 spectrophotometer configured with a 9-inch diameter integrating sphere, and are shown for olivines and orthopyroxenes in Figure 1. The identity of all synthesis products was established by powder X-ray diffraction, and some by Mossbauer spectroscopy.

Olivines have been synthesized at only two compositions, because of the high temperature required for melting of Fo_{100}, and difficulty in quenching same under these conditions. Our attempts to quench non-crystalline olivine were unsuccessful, as expected. Note that water-quenched runs (vs. slower air quenched) yielded olivines characterized by reflectivity spectra with less spectral contrast for their ~1.0 μm Fe^{2+} bands. However, the interpretation of these spectra is complicated by the presence of optically-opaque magnetite particles (detected in Mossbauer spectra). We are now attempting to synthesize olivines without accompanying magnetite or metal.

Pyroxenes were synthesized at En_{50}, En_{75} and En_{100}. The crystalline Fe-bearing pyroxenes all displayed spectra typical of orthopyroxenes, i.e., ~1.0 and 2.0 μm Fe^{2+} bands. Glasses with pyroxene compositions were successfully fabricated in the water-quenched runs. In addition to the two bands discussed above, these spectra appear to have a third, broad band centered near 1.2 μm. In the few pyroxenes so analyzed to date, Mossbauer spectra provided no evidence for the presence of magnetite or metal. Synthesized enstatites (En_{100}), of course, had flat reflectance spectra; some with a slightly negative slope.

Plagioclase was synthesized at meteoritically appropriate compositions An_{100}, An_{15} and $An_{10}Ab_{85}Or_5$. In all cases the reflectance spectra were flat (because they contain no iron), with slightly negative slopes.

REFERENCES: [1] Vilas and Gaffey (1989) *Science 246*, 790-792; [2] Miyamoto et al. (1981) *Memoirs of the National Institute of Polar Research Special Issue 20*, 345-361; [3] Miyamoto et al. (1982) *Memoirs of the National Institute of Polar Research Special Issue 25*, 291-307

DIFFUSE REFLECTANCE SPECTRA: Zolensky M.E. et al.

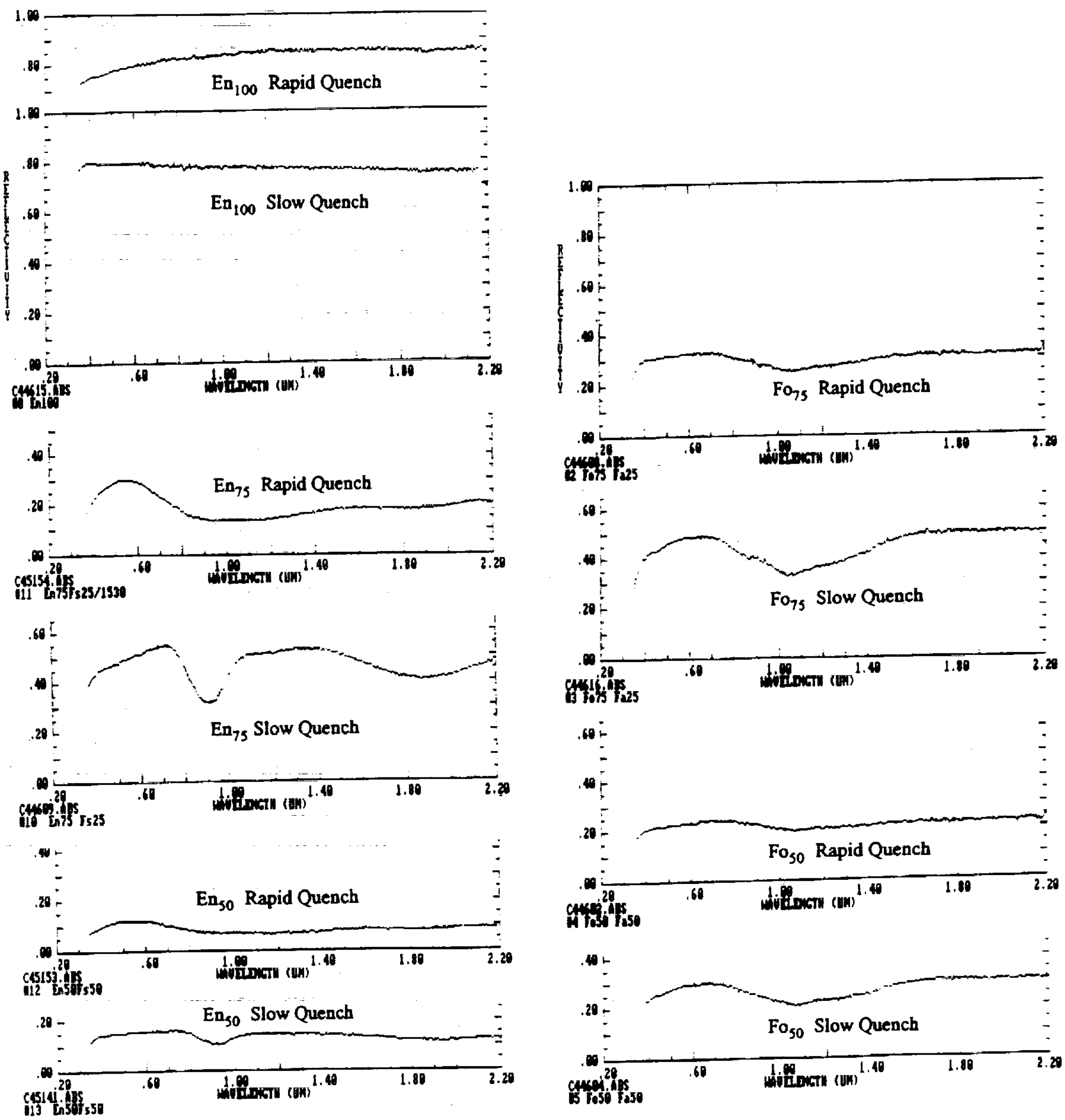


Figure 1 Spectral Reflectance Spectra of Synthesized Orthopyroxenes, Glasses of Orthopyroxene Compositions and Olivines

MINERALOGY OF DARK CLASTS IN PRIMITIVE VS DIFFERENTIATED METEORITES

M.E. Zolensky[1], M.K. Weisberg[2], R.A. Barrett[3] and M. Prinz[2]; [1]SN2, NASA Johnson Space Center, Houston, TX 77058; [2]American Museum of Natural History, New York, NY 10024; [3]Lockheed ESCO, 2400 NASA Rd. 1, Houston, TX 77058.

The presence of dark lithic clasts within meteorites can provide information concerning asteroidal regolith processes, the extent of interactions between asteroids, and the relationship between meteorite types, micrometeorites and interplanetary dust particles. Accordingly, we have been seeking and characterizing dark clasts found within carbonaceous chondrites, unequilibrated ordinary chondrites, howardites and eucrites. We find that unequilibrated chondrites in this study contain fine-grained, anhydrous unequilibrated inclusions, while the howardites often contain inclusions from geochemically processed, hydrous asteroids (type 1 and 2 carbonaceous chondrites). Eucrites and howardites contain unusual clasts, not easily classified.

The most abundant dark clasts that we studied are uniformly fine-grained assemblages dominated by olivine and pyroxenes, and, based on mineralogy as well as oxygen isotopic compositions, appear to be genetically related to their host chondrites. Using HRTEM, we examined the dark clasts in Dhajala (H3.8) and Manych (LL3.1), previously described by Nehru et al. [1], and clasts in Allende and Vigarano (CV3), as described by Johnson et al [2]. Dhajala and Manych clasts are mineralogically simple, containing mainly olivine, OPX $\pm$ CPX, generally sub-micrometer to a few micrometers in grain size. Accessory minerals (as fragments 50-100 µm in size) include Fe-Ni metal, pyrrhotite $\pm$ pentlandite, and Ca-phosphates. One relatively fine-grained clast in Manych consists mainly of olivine (Fo_{63-65}) and pyroxene (En_{53-63} Wo_{19-28}, with significant Cr, Mn, Al and Na), and with accessory Fe-Ni metal and glass. This clast also contains elliptical augen with complexly intergrown laths of pyroxene ($En_{63}Wo_{19}$) and an unidentified Al-rich phase. Normally zoned, coarse-grained olivine aggregates are also present within the augen as well as the clast matrix. More complexity is shown by the fine-grained clasts in Allende and Vigarano, which contain predominantly normally-zoned olivine (Fo_{93-46}), enstatite and diopside, often in overgrowth relationships. In one Allende clast, olivine compositions are Fo_{56-65}, and accessory phases include awaruite and glass. This clast shows arcuate banding [2].

Many dark clasts in howardites resemble CM chondrites, but have been variously heated; a clast in G'Day is one example. It consists mainly of aluminous serpentine (Al is anti-correlated with Mg/Fe). Serpentine lattice fringes are slightly corrugated, a probable indication of heating. Other important phases are pyrrhotite, pentlandite, enstatite, augite, forsterite, and metal. This clast also contains a sinuous aggregate of spinel rimmed by serpentine. This is a common type of altered CAI in CM chondrites [3]. Numerous clasts in Kapoeta (howardite) also resemble CM chondrites. They contain subsidiary clasts of olivine (Fo_{57-100}, sometimes zoned), OPX (En_{94-100}), pyrrhotite $\pm$ pentlandite, calcite, and layered serpentine (Mg/Fe=0.37-2.7), all set within a matrix consisting mainly of serpentine. One of these clasts contains abundant sinuous inclusions of spinel, with an inner rim of serpentine (Mg/Fe=0.15-0.38) and outer rim of diopside (fig. 1a). In most respects, these clasts are identical to one previously reported from the EET 87513 howardite [4].

One highly unusual Kapoeta (howardite) clast contains OPX, olivine (Fo_{69-99}), and pyrrhotite. Grains and framboids of magnetite are present, generally enclosed within calcite. This, and other calcite masses in this clast are rimmed by stoichiometric hedenbergite (fig. 1b). This inclusion is clearly related to C1 and C2 chondrites.

LEW 87295 (eucrite) contains an intriguing polymict inclusion which consists of 100-micrometer sized aggregates and mineral fragments. The components are 1) uniformly fine-grained (sub-micrometer) aggregates of olivine ($\sim Fo_{33-49}$), pyrrhotite $\pm$ pentlandite, and Ca-phosphates, one with a more iron-rich rim, similar to several larger inclusions described above; 2) clasts containing anhydrous, aluminous ferromagnesian grains with the approximate composition of Fo_{25} with patchy rims of Fo_{28}; these may be heated serpentine; 3) aggregates of unheated serpentine; 4) aggregates of magnesian olivine (Fo_{94-100}) and pyroxene (En_{89-94}); 5) rounded aggregates of enstatite rimmed by diopside; and 6) individual anhedral grains of OPX (En_{45-54}), pyrrhotite, and pentlandite. The matrix consists of fragmental grains of olivine and OPX, surrounded by spongy ferromagnesian

silicate material which is probably poorly crystalline (heated?) serpentine. Clearly, this polymict clast records several stages of formation, reaction, alteration, and accretion, all predating incorporation into LEW 87295.

Zolensky et al. [4&5] reported that 1) clasts in the LEW 85300 eucrite are mineralogically most similar to CV3 chondrites, but are compositionally unique; 2) most clasts within the EET 87513 and Bholghati howardites are mineralogically compatible with CM chondrites heated to varying degrees, and 3) the remaining clasts from Bholghati are conceivably heated CI chondrite material. The results of this study suggest the following relationships between dark clasts found in primitive and differentiated meteorites. Eucrites contain unusual clasts which are not easily classified. Howardites contain these unusual types as well as CM- and CI-like chondrite material, heated to varying degrees. Type 3 CV and ordinary chondrites host fine-grained, generally anhydrous inclusions (although evidence of hydrated clasts has been reported in Plainview and Abbott ordinary chondrites [6&7]). In other words, unequilibrated chondrites tend to contain anhydrous, fine-grained, unequilibrated inclusions, while the howardites often contain inclusions (sometimes heated) from geochemically processed, hydrous asteroids (type 1 and 2 carbonaceous chondrites). Increased sampling of dark clasts in various chondrites and differentiated meteorites, as well as oxygen isotopic data on more clast types, will help decipher relationships among dark clasts, meteorite types, micrometeorites and interplanetary dust particles.

Acknowledgments: We thank Aurora Pun, Paul Buchanan, and Elbert King for samples and discussions.

References: [1] Nehru et al. (1991) *Meteoritics 26*, 377; [2] Johnson et al. (1990) *GCA 54*, 819-830; [3] MacPherson et al. (1988) in *Meteorites and the Early Solar System*, pp. 746-807; [4] Zolensky et al. (1992) *LPSC XXIII*, ; [5] Zolensky et al. (1992) *Meteoritics 27*, in press; [6] Fodor and Keil (1976) GCA 40, 177-189; [7] Fodor et al. (1976) *New Mexico Geol. Soc. 6*, 206-218.

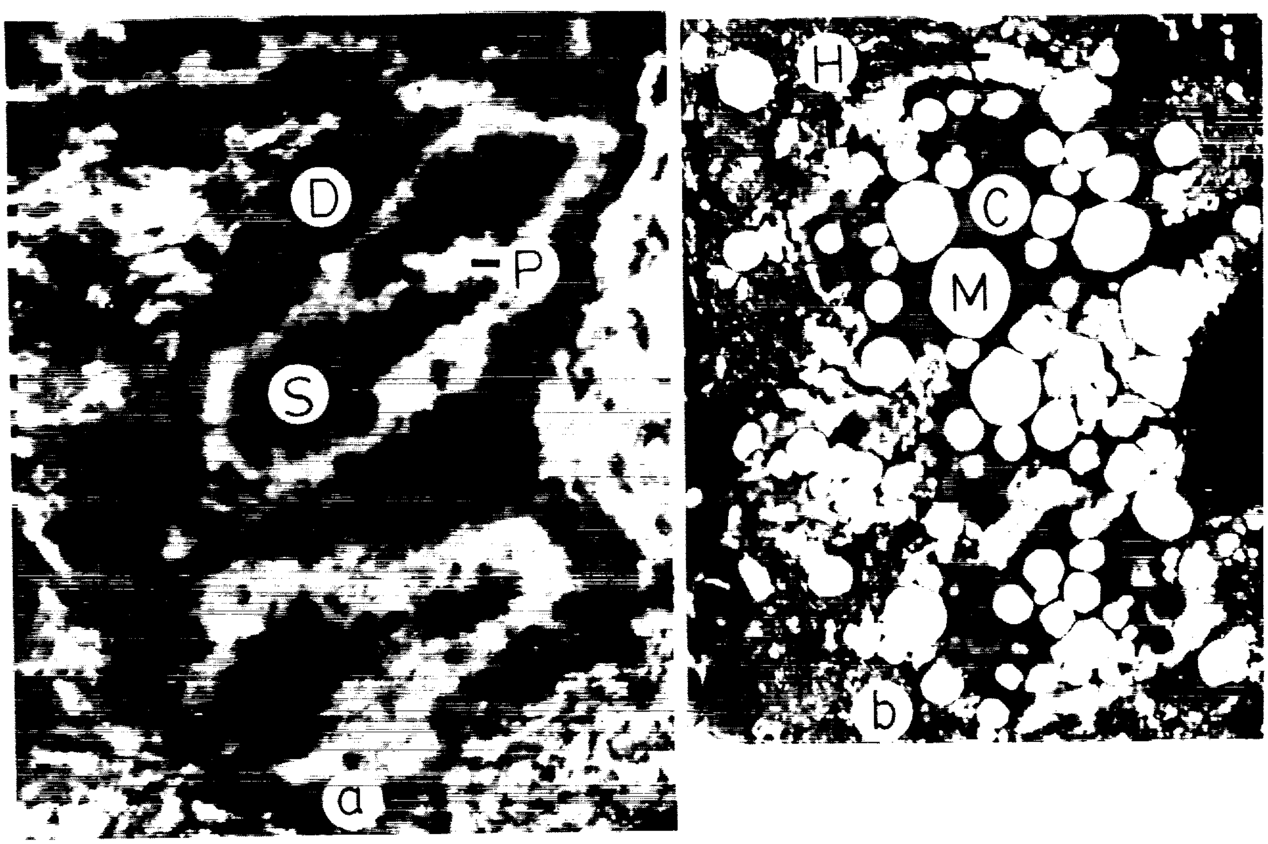


Figure 1 From Kapoeta (a) a sinuous inclusion of spinel (S) with rims of serpentine (P) and diopside (D); (b) a clast with magnetite framboids (M) enclosed within calcite (C), in turn rimmed by hedenbergite (H).

K, U, and Th behavior in Martian environmental conditions

Zolotov, M.Yu., T.V. Krot, and L.V. Moroz, Vernadsky Institute of Geochemistry and Analytical Chemistry, Russian Academy of Sciences, Moscow, Russia

The speculations on the K, U, and Th behavior in the Martian environments show that aeolian and aqueous processes leads to the preferential accumulation of K, U, and Th in fine dust material. The separation of K, U, and Th on Mars is smaller in scale to that on Earth.

The possibility of K, U, and Th content determination from orbit and *in situ* allows consideration of those elements as geochemical indicators in the planetary studies. In the case of Mars the unambiguous interpretations of such data in terms of igneous rocks are remarkably constrained by the widespread rock alteration and the existence of exogenic deposits. Besides, the terrestrial experience indicates that K, U, and Th contents could be used as indicators of environmental geochemical processes. Thus the determination of K, U, and Th contents in the Martian surface materials could provide the indirect data on the conditions of some exogenic geological processes.

K, U, and Th in Martian igneous rocks. The morphological features [1], near-infrared spectral data [2], chemical composition of soil [3] as well as of SNC-meteorites [4] are supporting a concept of predominating mafic igneous rocks on the Martian surface. The remote sensing in concern with K, U, and Th measurements in the surface materials carried out on Mars 5 and Phobos 2 also could be considered as an evidence of mainly mafic composition [5, 6]. These data in association with SNC-meteorite studies [4,7] do not indicate any detectable differences of Martian and terrestrial mafic rocks in terms of U, Th, and K contents. The chemical forms of these elements in igneous rocks on both planets are probably similar. K, U, and Th are considered to exist partly in disseminated form and partly accumulated in host minerals. The latter are presented by biotite, phlogopite (especially K, U, and Th), apatite; sometimes magnetite, titanomagnetite, and ilmenite (particularly U and Th) in mafic and ultramafic rocks. The host minerals in acidic and alkaline rocks are as following: K-feldspar, biotite, leucite, nepheline (for K), monazite, zircon, sphene, allanite, pyrochlore, biotite and apatite (for U and Th). In volcanic facies these elements are mainly incorporated in the interstitial glass and groundmass [8].

Mechanical weathering and migration. The geochemical behavior of K, U, and Th on Mars in the absence of liquid water is controlled by the fate of their host minerals, which depends on their hardness, size and density being the main agents of particle migration. Low stability of glass and groundmass in respect of weathering especially in basic volcanic rocks is assumed to be favorable for the preferential aeolian removal of K, U, and Th in fine weathered products. Such phenomena upon the weathering of more uniform rocks as ash deposits or aphyric basalts could be suppressed or completely absent. Some small enrichment in U and Th could be observed in lag deposits on basic rocks characterized as accumulation sites of magnetite, titanomagnetite or ilmenite. Lag deposits of granites should be highly enriched in resistant to weathering U and Th host minerals of high specific gravity.

Aeolian particle size separation [9] could result in relatively dust enrichment in K, U, and Th due to predominant concentration of fine particles of Fe-oxyhydroxides, smectites, and palagonites (see below). The separation in aqueous environment seems to be feasible only in lakes or hypothetical "ocean" with predominant enrichment in K, U, and Th of clay minerals in central parts of those basins.

Chemical weathering. Terrestrial weathering could lead to the relative depletion or enrichment in K, U, and Th depending on the primary rock type, conditions and duration of weathering process. Thus the unambiguous prediction of the geochemical behavior of K, U, and Th on Mars is very difficult.

During the period of existence of liquid water on the Martian surface the associated environments such as acidic [10] oxidized conditions and high CO_2 pressure [11] were favorable for K, U, and Th leaching. These conditions could be proposed only for initial stages of Martian geologic history [11], whereas the subsequent period was characterized of water depletion and low temperature providing the low weathering rates and preferential accumulation of these elements in autigenic minerals *in situ* instead of aqueous removal.

The weathered Martian basalts could be depleted in K and possibly in U due to high weathering rate of glass. Th mobility could be rather substantial only in extremely acidic environment [12]. The weathered gabbro rocks are proposed to be depleted in K and U because of fast biotite destruction [13]. The weathered Martian acidic and alkaline rocks are supposedly enriched in Th and, in some cases, in U in accord with high refractory properties of corresponding host minerals. Some relative enrichment in K could be confined to intermediate weathering stages due to autigenic clay formation as well as low solubility of K-feldspar [14]. The formation of laterite weathering crust usually enriched in U and Th and extremely depleted in K is found to be not plausible due to low temperature,

K, U, and Th behavior: Zolotov M.Yu. et al.

dryness of corresponding environment, and limited time of weathering. On the base of terrestrial experience [15] it is possible to assume that Martian palagonites could be depleted in K and possibly enriched in U and Th due to sorption by amorphous oxyhydroxides. At the same time the potassium removed from palagonite especially in "dry" environment could be mostly incorporated in autigenic clays.

Aqueous transport and deposition. Most intensive processes of the aqueous transport supposedly were widespread only at the period of small valley network formation being very restricted in time and space at the subsequent geological periods. Potassium evidently was transported in the ionic form while its accumulation in the outflow, river or ground waters looks like rather unlikely due to the potassium depletion of igneous rocks as well as high rate of its removal from aqueous solutions followed by the formation of autigenic minerals and ion exchange in clays. The formation of illites in Martian environment is considered as unlikely improbable process because of the potassium depletion and acidic environment. The accumulation of K in jarosite and alunite is also constrained by low K content. During the evaporation or freezing of lakes the potassium could be removed from solutions predominantly by clay mud. In the freezing of outflow waters K should accumulate in unfrozen waters and could be deposited in a form of K-Mg chlorides.

The ancient Martian climatic conditions possibly involving the CO2 rich atmosphere and oxidizing environment were favorable for the U migration in a form of uranyl (UO2++) complexes. The acidic environment assumed for Martian aqueous solutions [10] is favorable for the hexavalent uranium transport in uranyl complexes and tetravalent thorium transport in a form of sulfate and chloride complexes. High sulfate content in the aqueous solutions are proposed as an U and Th migration factor in the acidic environment [12,16]. However the U and Th content in Martian waters were hardly much above 0.1 and 0.01 ppb due to a number of negative factors as following: low content of those elements in primary rocks; abundant inorganic sorbents; lack of organic matter, disequilibrium in water-rock system at low temperature and low solubility of UO2 and ThO2.

The substantial accumulation of U on the geochemical reducing barriers at the surface or nearsurface is practically implausible due to absence of organic matter deposits and exogenic sulfide occurrences. The preferred sorption of U and Th from waters by amorphous Fe-oxyhydroxides [12,16] should be a main factor of U and Th accumulation. The coprecipitation of U,Th-complex compounds with the oxyhydroxides also could be proposed at the sites of ground water leakage. At the same time the U accumulation is excluded at the outflows or outbursts of the deep seated reduced waters. Clay minerals are also considered as slightly less important exogenic host minerals of U and Th relative to the oxyhydroxides. The subordinate role could be assigned to the autigenic phosphates due to presumable depletion in phosphorus in the aqueous solutions the latter being provided by relative stability of apatite upon weathering process as well as the absence of conditions for the accumulation of phosphorites. The accumulation of U upon evaporation of the aqueous solutions or its deposition in channel calcretes or phoscretes could be abundant only in the areas of acidic rock predominance.

Conclusions. Aeolian removal and separation of K, U, and Th host minerals is considered to be the principal factor in the migration and concentration of those elements. Mechanical and chemical weathering associated with aeolian and aqueous processes leads to the preferential accumulation of K, U, and Th in amorphous Fe-oxyhydroxides, smectites, and palagonite-like materials considered as primary components of Martian dust. In addition, local enrichment of K, U, and Th may be present in exogenic materials such as aeolian lag deposits, weathering crusts, channel floor deposits, paleolake and outflow deposits. The separation of K, U, and Th in the Martian environment is smaller in scale to that on Earth because of the absence of large quantities of acidic rocks, the low water/rock ratio, weak aqueous separation, and the absence of organic matter on Mars.

Acknowledgments: This work was supported by Max-Plank-Institut fur Chemie (Mainz, Germany). We are grateful to Prof. H. Wanke for that support.

References: 1. Greeley R. and P. Spudis, Rev. Geoph. Sp. Phys. 19, 13, 1981; 2. Singer R. Adv. Space Res. 5, 59, 1985; 3. Clark B. et al. JGR 87, 10059, 1982; 4. McSween T. Rev. Geoph. Sp. Phys. 23, 391, 1985; 5. Basilevsky A. et al. Geochimiya, N1, 10, 1981; 6. Surkov Yu. et al. Nature 341, 595, 1989; 7. Dreibus G. and H. Wanke Proc. 27-th Int. Geol Cong., V.11, 1, 1984; 8. Handbook of Geochemistry (ed. K. Wedepohl), 1967; 9. Christensen P. JGR 91, 3533, 1986; 10. Burns R. Proc 18 LPSC, 713, 1988; JGR 95, 14169, 1990; 11. Pollack J. et al. Icarus 71, 203, 1987; 12. Langmuir D and J. Herman Geoch. Cosm. Acta 44, 1753, 1980; 13. Fritz S. Chem. Geol. 68, 275, 1988; 14. Middelburg J. et al. ibid, 253; 15. Jercinovic M. et al. Geochim. Cosm. Acta 54, 2679, 1990; 16. Langmuir D. ibid, 42, 547, 1978.

ON DUST EMISSIONS FROM THE JOVIAN SYSTEM; H. A. Zook[1], E. Grün[2], M. Baguhl[2], A. Balogh[3], S. J. Bame[4], H. Fechtig[2], R. Forsyth[3], M. S. Hanner[5], M. Horanyi[6], J. Kissel[2], B.-A. Lindblad[7], D. Linkert[2], G. Linkert[2], I. Mann[8], J. A. M. McDonnell[9], G. E. Morfill[10], J. L. Phillips[4], C. Polanskey[5], G. Schwehm[11], N. Siddique[2], P. Staubach[2], J. Svestka[12], and A. Taylor[9]; [1]NASA Johnson Space Center, Houston, TX 77058, USA, [2]Max-Planck-Institut für Kernphysik, Postfach 103980, 69 Heidelberg 1, Germany, [3]Imperial College, London, UK, [4]LANL, Univ. of California, Los Alamos, NM 87545, USA, [5]Jet Propulsion Laboratory, Pasadena, CA 91109, USA, [6]LASP, Univ. of Colorado, Boulder, CO, USA, [7]Lund Observatory, 221 Lund, Sweden, [8]MPI für Aeronomie, 3411 Katlenburg-Lindau, Germany, [9]University of Kent, Canterbury, CT2 7NR, UK, [10]MPI für Extraterrestrische Physik, 8046 Garching, Germany, [11]ESA ESTEC, 2200 AG Noordwijk, The Netherlands, [12] Prague Observatory, 11846 Prague 1, CSFR.

As described by Grün et al.[1,2], the dust impact detector on the Ulysses spacecraft detected a totally unexpected series of dust streams in the outer solar system near the orbit of Jupiter. Five considerations lead us to believe that the dust streams emanate from the jovian system itself: 1. The dust streams only occur within about 1 AU of the jovian system, with the strongest stream being the one closest to Jupiter (about 550 R_J away); 2. The direction from which they arrive is never far from the line-of-sight direction to Jupiter; 3. The time period between streams is about 28 (+/-3) days; 4. The impact velocities are very high--mostly around 40 km/s; and 5. We can think of no cometary, asteroidal, or interstellar source that could give rise to the above four phenomena; such streams have never before been detected.

In Figure 1 is plotted the logarithm of the dust grain impact rate, in events per day, versus time, in days, for a 400 day period centered on Jupiter closest approach (CA) on Feb. 8, 1992. Depicted is a continuous four-impact running average of all impacts with dust masses above the detector threshold ($4*10^{-15}$g at 20 km/s to $6*10^{-16}$g at 40 km/s impact velocity). 16 hours before CA, sensitivity was reduced, partly to protect the instrument, so that grains smaller than about 10^{-13}g could not be detected. Full sensitivity was restored about 16 hours after CA. The Ulysses spacecraft velocity well away from Jupiter, but with respect to Jupiter, is about 14 km/s.

The eye is immediately struck by the rough periodicity of the six dust streams before and after Jupiter CA (2 streams before and 4 after). The average period between streams is 28 to 29 days. A second feature is that the streams only occur within about 1 AU (approx. 2100 R_J) distance from Jupiter and average about 505 R_J apart; the most intense stream is the one closest to Jupiter. A third feature, again striking, is observed in Fig. 2 where each dust grain impact is represented as a symbol on a plot showing spacecraft rotation angle versus days from CA. Large grains ($m>5*10^{-14}$g) are shown as diamonds and small grains as "plus signs". The dust detector points nearly perpendicular (85 degrees) to the spacecraft rotation axis which, in turn, points continuously to Earth; zero degrees rotation means the dust detector then points, during spacecraft rotation, closest to ecliptic north. It is seen that each stream (shown as "plusses" inside an enclosed field) is made up of small grains that arrive from a single direction (allowing for the 140 degree sensor field-of-view). It is further seen that the radiant of approach of each stream changes by about 150 degrees in rotation angle from before CA to after CA. The direction from which the streams appear to arrive is, in all cases, close to the line of sight direction to Jupiter.

3274-91
ABS. ONLY

N94-20910

p. 2

WRINKLE RIDGES, REVERSE FAULTING, AND THE DEPTH PENETRATION OF LITHOSPHERIC STRESS IN LUNAE PLANUM, MARS; *M.T. Zuber*, Department of Earth and Planetary Sciences, Johns Hopkins University, Baltimore, MD 21218-2681.

Tectonic features on a planetary surface are commonly used as constraints on models to determine the state of stress at the time the features formed. Quantitative global stress models applied to understand the formation of the Tharsis province on Mars constrained by observed tectonics [1-3] have calculated stresses at the surface of a thin elastic shell and have neglected the role of vertical structure in influencing the predicted pattern of surface deformation. Wrinkle ridges in the Lunae Planum region of Mars form a conentric pattern of regularly spaced features in the eastern and southeastern part of Tharsis and formed due to compressional stresses related to the response of the Martian lithosphere to the Tharsis bulge [1,4,5]. Structurally, the ridges are on the order of 1 km wide, several hundreds of meters high, and are interpreted to be the surface manifestation of reverse faulting in combination with a smaller component of folding [6,7]. The ridges are located in Early Hesperian-aged plains materials that are interpreted to be flood basalts [8] with thicknesses <1 km [9-11]. As observed in the exposures of valley walls in areas such as the Kasei Valles, the surface plains unit is underlain by an unconsolidated impact-generated megaregolith that grades with depth into structurally competent lithospheric basement. The ridges have alternatively been hypothesized to reflect deformation restricted to the surface plains unit ("thin skinned deformation" [12]) and deformation that includes the surface unit, megaregolith and basement lithosphere ("thick skinned deformation" [13,14]). The nature of ridge formation has important implications for the interpretation of geophysical models of the Tharsis region. If the ridges formed normal to the maximum compressive stress direction at the surface, then these features can be used to constrain the state of stress determined in elastic spherical shell models [1-3]. If, however, the ridges nucleated at depth and propagated to te surface, then the orientations of the ridges may have been controlled by a different stress state. Even if ridge-related faults nucleated within the surface plains unit, it is necessary to understand the extent to which vertical mechanical structure affects the near-surface state of stress.

We have adopted a finite element approach to quantify the nature of deformation associated with the development of wrinkle ridges in a vertically-stratified elastic lithosphere. We used the program TECTON [15], which contains a slippery node capability that allowed us to explicitly take into account the presence of reverse faults believed to be associated with the ridges. In this study we focused on the strain field in the vicinity of a single ridge when slip occurs along the fault. We considered two initial model geometries. In the first, the reverse fault was assumed to be in the surface plains unit, and in the second the initial fault was located in lithospheric basement, immediately beneath the weak megaregolith. We are interested in the conditions underwhich strain in the surface layer and basement either penetrates or fails to penetrate through the megaregolth. We thus address the conditions required for an initial basement fault to propagate through the megaregolith to the surface, as well as the effect of the megareolith on the strain tensor in the vicinity of a fault that nucleates in the surface plains unit.

Figure 1a shows the central part of a two-dimensional cartesian finite element grid that treats the surface unit, megaregolith and basement as layers with different Young's moduli. The Young's modulus of the megaregolith layer is assumed to be an order of magnitude less than that of the surface and basement layers. The grid contains a 20° dipping reverse fault that extends through the surface plains layer. The entire grid has 2319 nodes and 2856 elements; 250 m displacement is imposed along the fault. The broad upwarping of the surface is a consequence of elastic flexure of the surface plains layer. Figure 1b is a contour plot showing the second invariant of the strain tensor for a larger portion of grid than shown in Figure 1a. This quantity is a measure of the tendency for strain to concentrate in a particular location. Despite the presence of the weak megaregolith, significant strain is transmitted to lithospheric basement in the area beneath the faulted surface layer.

Figure 2a shows a similar calculation with the reverse fault instead initially located at the top of the lithospheric basement layer, just beneath the megaregolith. In this model the ridge forms due to fault propagation folding in which ridge topography is a consequence of elastic continuum deformation above the fault. Figure 2b contours the second invariant of strain and demonstrates that, despite the presence of the weak megaregolith layer, strain is transmitted to the surface layer.

In both examples, the surface plains unit, megaregolith and lithospheric basement are involved in the deformation, which is a consequence of fault slip presumed to be associated with the development of wrinkle ridges. For the lithospheric structure assumed in these preliminary calculations, the surface layer and basement are coupled sufficiently to allow the transmission of strain so that deformation is not confined to the near-surface as required in thin-skinned deformation models. We are currently investigating parameter sensitivities to further clarify the nature of this coupling, in order to better understand the relationship between wrinkle ridge-related faulting, lithosphere structure, and the style of Tharsis deformation.

References: [1]Banerdt, W.B. et al. (1982) *JGR, 87,* 9723, 1982. [2]Willemann, R.J. and D.L. Turcotte, *JGR 87,* 9793. [3]Banerdt, W.B., et al. (1992) in *Mars,* ed. H.H. Kieffer, B.M. Jakosky and M.S. Matthews, 249, Univ. Ariz. Press, Tucson. [4]Maxwell, T.A. (1982) *JGR, 87,* A97. [5]Watters, T.R. and T.A. Maxwell (1986) *JGR, 91,* 8113. [6]Plescia, J.B. and M.P. Golombek (1986) *GSAB, 97,* 1289. [7]Watters, T.R. (1988) *JGR, 93,* 10236. [8]Greeley, R. and P. Spuidis (1981) *Rev. Geophys., 19,* 13. [9]DeHon, R.A. (1982) *JGR, 87,* 9821. [10]DeHon, R.A. (1988) LPI Tech. Rept. 88-05, p. 54, Houston. [11]Frey, H. and T. Grant (1988) *JGR, 95,* 14249-14263. [12]Watters, T.R. (1991) *JGR, 96,* 15599. [13]Zuber, M.T. and L.L. Aist (1990) *JGR, 95,* 14215. [14]Golombek, M. et al. (1989) *LPI tech. Rept. 89-06,* p. 36, Houston. [15]Melosh, H.J. and A.R. Raefsky (1980) *GJRAS, 60,* 333.

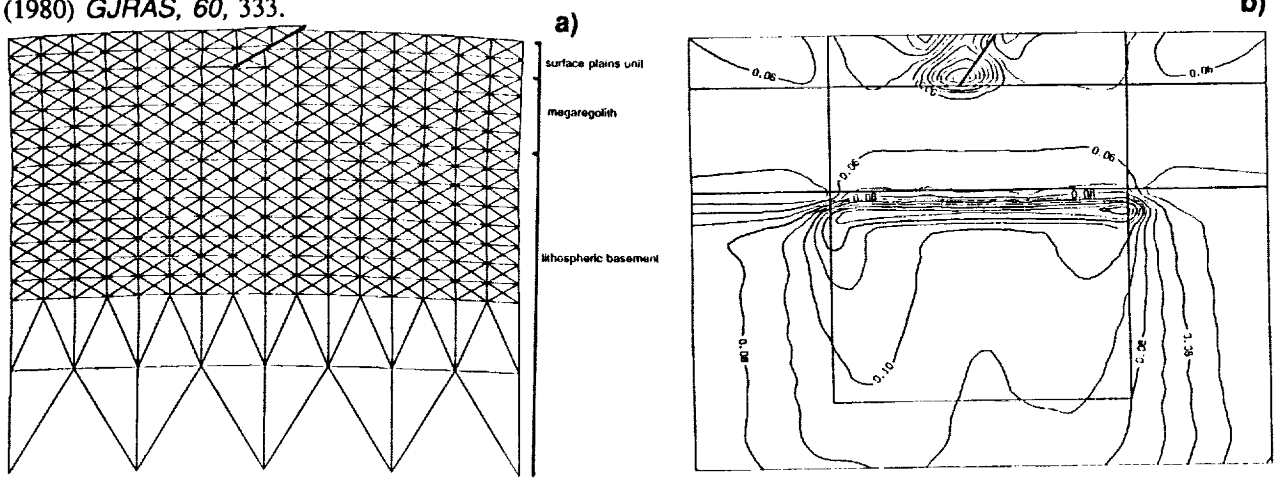


Figure 1. (a) Deformation grid and *(b)* contours of second invariant of strain tensor for a horizontally shortening model Martian lithosphere with a 20°-dipping reverse fault with 250-m displacement. The fault is located in the surface plains unit. The megaregolith is characterized by a Young's modulus an order of magnitude less than the surface plains unit and basement. Note the transmission of strain through the megaregolith to basement.

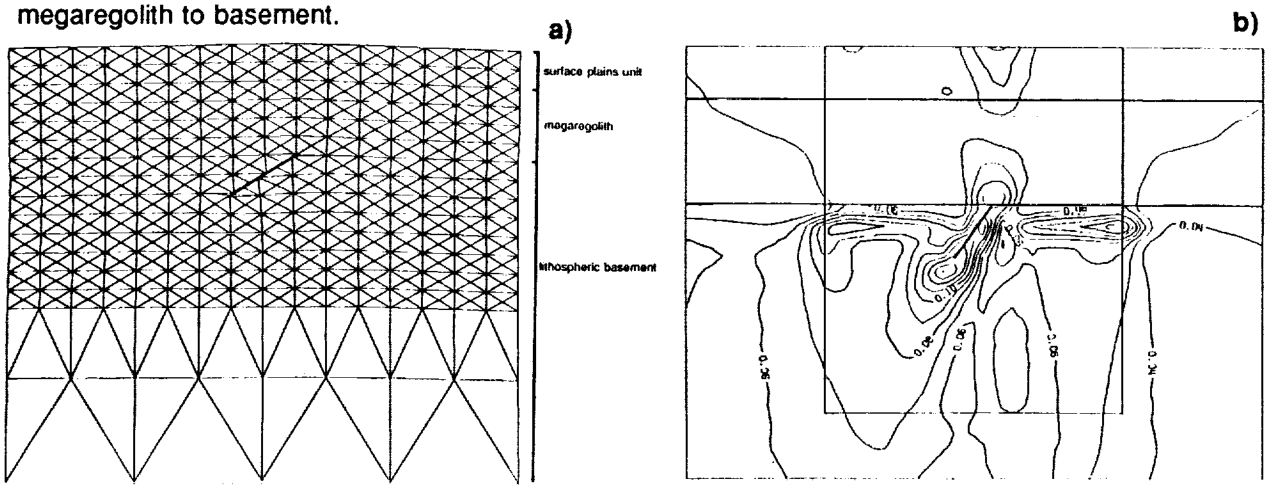


Figure 2. Same as above, except the fault is located at the top of the lithospheric basement layer. Note the transmission of strain through the megaregolith to the surface layer.

N94-20911
168235
p. 2

POSSIBLE FLEXURAL SIGNATURES AROUND OLYMPUS AND ASCRAEUS MONTES, MARS;
M.T. Zuber[1,2], *B.G. Bills*[2], *H.V. Frey*[2], *W.S. Kiefer*[2,3], *R.S. Nerem*[2], and *J.H. Roark*[2,4], [1]Department of Earth and Planetary Sciences, Johns Hopkins University, Baltimore, MD 21218, [2]Laboratory for Terrestrial Physics, NASA/Goddard Space Flight Center, Greenbelt, MD 20771, [3]Now at: Lunar and Planetary Institute, Houston, TX 77058, [4]Astronomy Department, University of Maryland, College Park, MD 20742.

The effective elastic thickness (h) of the lithosphere provides a measure of the thermal and mechanical state of a planet's shallow interior. An estimate of h in the vicinity of a feature that constitutes a load on a planetary surface can be determined from the flexural response of the lithosphere to the load. This approach has been applied to Mars by calculating radial stresses associated with lithospheric flexure associated with surface loads, and comparing the results to the positions of circumferential graben surrounding the major Martian shield volcanoes and mascon basins [1,2]. However, many prominent surface loads on Mars, most notably the Olympus Mons volcano, do not exhibit flexural graben. In these instances application of the above method can provide only a lower limit of effective elastic thickness [*cf.* 3]. An alternative method of determining h is to calculate the vertical displacements associated with the flexural loading and to compare the amplitude and shape of the flexural profile to observed topography. This method has not been applied to flexural problems on Mars because of the poor resolution of Martian topographic data. However, previous analyses have shown that the lithosphere around major volcanic shields should exhibit vertical deflections of order 1 km over horizontal baselines of order 100 km [1,2]. We were thus motivated to search for the presence of flexural troughs in the existing Mars topography data.

The primary data set that we utilized was a 50th degree and order spherical harmonic expansion that we performed on the Mars Digital Topographic Model (DTM)[4]. Figure 1 shows topographic profiles across three prominent volcanic shields: Pavonis, Ascraeus and Olympus Montes. We also investigated Arsia and Elysium Montes and Alba Patera. Of these features, we have identified possible flexural troughs around Olympus and Ascraeus Montes, denoted by the arrows in the figure. These are the two youngest, and highest, of the major Tharsis shields. These signatures are also present in the Mars DTM. A previous analysis of an earlier verison of the DTM [5] failed to identify the candidate flexural trough around Olympus Mons.

If these features are a consequence of lithospheric flexure in response to the volcanic loads, then h can be constrained from the deflection profiles. We have performed a preliminary calculation of effective elastic thickness for Olympus Mons by treating the volcanic load (q) as a series of superposed cylinders with density 2900 kg m^{-3}. We solved the flexural equation for a thin spherical shell [6]

$$\nabla^2 w + w/l^4 = q/D \tag{1}$$

where w is the vertical displacement, $l\{=D/[(Eh^3/R^2)+\rho g]\}$ is the flexural length, $D[=Eh^3/12(1-\nu^2)]$ is the flexural rigidity of the lithosphere, E is Young's modulus, ν is Poisson's ratio, R is the radius of Mars, $\rho=\rho_m-\rho_p$, and g is the acceleration due to gravity. The solution of (1) for a uniform cylindrical load in which $r_p<<R$ is [7]

$$w = [q/(Eh/R^2+\rho g)]\ [d\ ker'(d)\ ber(x) - d\ kei'(d)\ bei(x) + 1] \tag{2}$$

for $x \le d = r_p/l$ and

$$w = [qd/(Eh/R^2+\rho g)]\ [ber'(d)\ ker(x) - bei'(d)\ kei(x)] \tag{3}$$

for $x \ge d$. The zero-order Bessel-Kelvin functions *ber*, *bei*, *ker*, and *kei* and their derivatives were evaluated following [1]. We found a best-fit elastic thickness of 50 km. This is in contrast to the lower limit of 150 km found using the absence of flexural graben as a constraint. The value we determine is in the range though somewhat greater than values (20–30 km) for the other Tharsis montes that exhibit circumferential graben [1].

The Mars Observer Laser Altimeter (MOLA), with its 330-m along-track spatial resolution, 1.5-m vertical resolution, and 30-m global vertical accuracy [8], is expected to provide a high quality, geodetically referenced topographic model of Mars which should permit the detection of flexural displacements

associated with many major topographic loads. If the features we identified are real, they will be detectable with MOLA. Flexural troughs should also be observed in association with most of the other features we examined. MOLA topography should permit independent estimates of effective elastic thickness in the vicinity of these features and new estimates in areas with loads that lack associated concentric graben, such as the polar layered terrains [9].

References: [1]Comer, R.P. et al. (1985) *Rev. Geophys., 23,* 61. [2]Hall, J.L. et al. (1986) *JGR, 91,* 11377. [3]Thurber, C.H. and M.N. Toksoz (1978) *GRL, 5,* 977. [4]Wu, S.S.C. et al. (1986) *NASA TN-88383,* 614. [5]Comer, R.P. et al. (1981) *LPSC XII,* 166, LPI, Houston. [6]Brotchie, J.F. and R. Silvester (1969) *JGR, 74,* 5240. [7]Brotchie, J.F. (1971) *Modern Geol., 3,* 15. [8]Zuber, M.T., et al. (1992) *JGR, 97,* 7781. [9]Zuber, M.T. (1992) *LPSC XXIII,* 1593, LPI, Houston. [10]Smith, D.E. (1992) this issue.

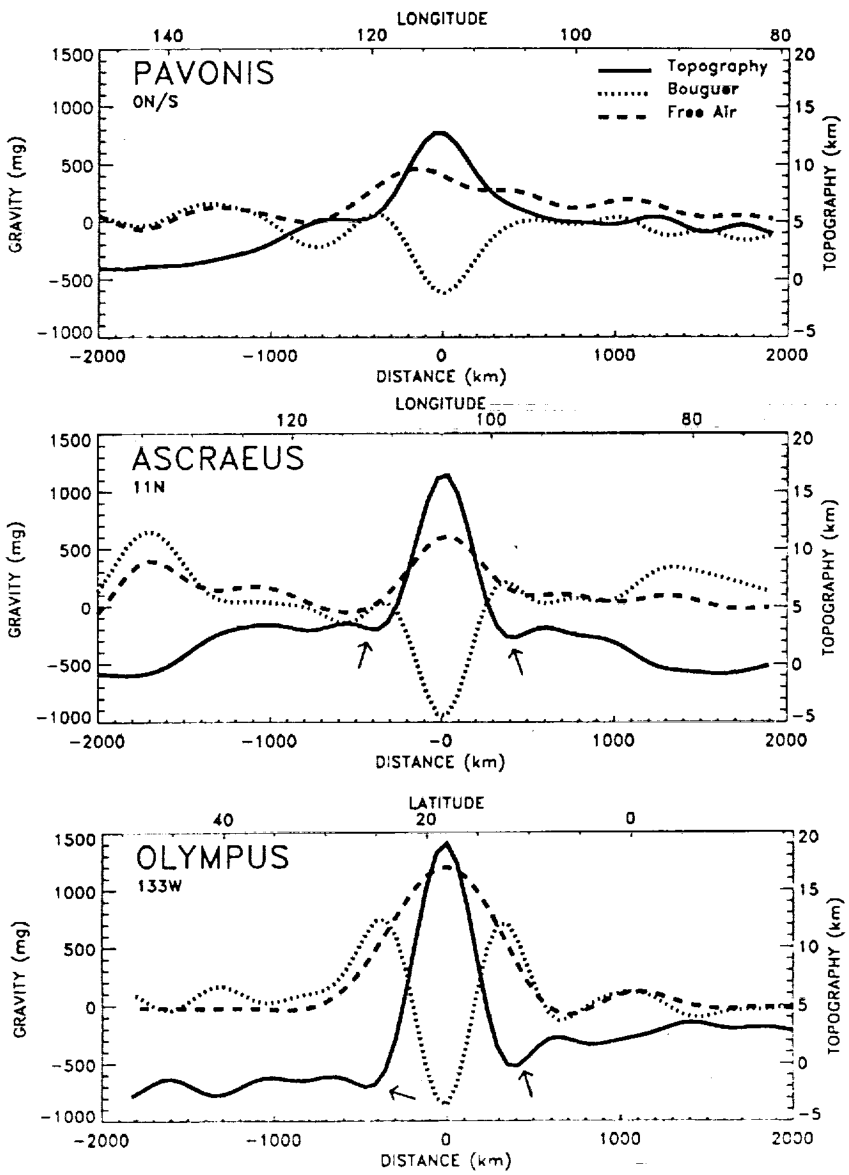


Figure 1. Profiles of topography, and Bouguer and free air gravity anomalies across three Martian volcanoes. Olympus and Ascraeus Montes display possible flexural troughs (arrows). Pavonis Mons does not. Topography is from a 50^{th} degree and order spherical harmonic expansion of the MarsDTM [4]. Gravity is taken from Goddard Mars Model-1 (GMM-1) [10].

OMIT TO END

AUTHOR INDEX*

*Page numbers refer to the first page of an abstract on which an author appears.

SAMPLE INDEX*

*Page numbers refer to the first page of an abstract in which a sample is mentioned.

METEORITE INDEX*

*Page numbers refer to the first page of an abstract in which a meteorite is mentioned.

KEYWORD INDEX*

*Page numbers refer to the first page of an abstract in which a term is mentioned.